Exploring the Influence of Azo Ligands in Catalysis: Ruthenium-Catalyzed C–C and C–N Bond Formation and Ligand-Catalyzed CO_2 Capture

THESIS SUBMITTED FOR THE DEGREE OF

DOCTOR OF PHILOSOPHY (SCIENCE)

JADAVPUR UNIVERSITY

By

Supriyo Halder

DEPARTMENT OF CHEMISTRY

JADAVPUR UNIVERSITY

KOLKATA-700032

July, 2025

Prof. (Dr.) K. Pramanik
Professor
Department of Chemistry
Inorganic Chemistry Section

JADAVPUR UNIVERSITY
KOLKATA700032, INDIA
Tel: 91+033+ 2457 2781
Mob: +91-8910935661
email: kausikis.pramanik@jadavpuruniversity.in

CERTIFICATE FROM THE SUPERVISOR

This is to certify that the thesis titled "***Exploring the Influence of Azo Ligands in Catalysis: Ruthenium-Catalyzed C-C and C-N Bond Formation and Ligand-Catalyzed CO_2 Capture***" submitted by **Mr. Supriyo Halder**, who enrolled on September 2, 2019 (Registration No.- **SCHEM1106319**) for the Ph.D. (Science) degree at the Jadavpur University, is an account of original research conducted by him under my supervision. I further declare that no portion of this thesis has been submitted earlier for the award of any degree, diploma, or academic award at any other university or institution. It is further confirmed that he has satisfied all the regulatory criteria concerning both the conduct and duration of the research.

3/7/2025
Dr. Kausikisankar Pramanik
Professor of Chemistry
Jadavpur University
Kolkata-700032

(Dr. Kausikisankar Pramanik)
Professor
Department of Chemistry
Jadavpur University
Kolkata – 700 032

Declaration

I hereby declare that this written submission reflects my original work and creative approach, expressed in my own words. Wherever the ideas or contributions of others have been incorporated, they have been appropriately acknowledged and cited using credible and authentic sources. I further affirm that I have upheld the principles of academic integrity and honesty throughout this work. I have not misrepresented, fabricated, or falsified any data, methodology, or source. I fully understand that any breach of these principles may result in disciplinary action by the University and may also lead to legal or academic consequences from the original sources that were either not properly cited or used without appropriate permission.

Date: 03/07/2025

Supriyo Halder

Supriyo Halder
Jadavpur University
Registration no**. SCHEM1106319**
Index no. **63/19/Chem./26**


Dedicated
to my parents
&
my teachers

Acknowledgements

"It is sometimes easier to make a molecule than to figure out how it works." — Roald Hoffmann, Nobel Laureate in Chemistry

First and foremost, I express my heartfelt gratitude to the **Almighty** for **His** boundless grace and blessings. It is through **His** divine will and guidance that I have been granted the strength, patience, and perseverance to complete this work.

It is with immense pride and deep satisfaction that I present this dissertation, a culmination of years of effort and learning. This endeavour would not have been possible without the intellectual legacy of countless scientists whose pioneering work in the vast and intricate field of Chemistry laid the foundation for my own research.

It is my pleasure to express deepest and most sincere appreciation to my respected supervisor, ***Prof.*** (***Dr.) Kausikisankar Pramanik***, Professor, Department of Chemistry, Jadavpur University, Kolkata. His insightful guidance, constant support and unwavering encouragement have been instrumental throughout my research journey. I am profoundly grateful for his expertise, meticulous supervision, and the inspiring mentorship he has offered at every stage of this work. His foresight and pragmatic approach have served as a constant beacon, shaping the direction and quality of this thesis.

I would also extend my profound gratitude and earnest respect to ***Dr. Sanjib Ganguly*** of St. Xavier's College, Kolkata, for his invaluable mentorship and continuous encouragement. His insightful suggestions and generous access to laboratory resources played a critical role in the successful execution of my research.

I am also deeply indebted to the members of my Research Advisory Committee (RAC) **Prof. Surajit Chattopadhyay** (University of Kalyani), **Prof. Kajal Krishna Rajak** (Head,

Department of Chemistry, JU, Kolkata) for their valuable suggestions, insightful advice, and continuous support during the annual RAC meetings.

I am extremely grateful to **Prof. Samaresh Bhattacharyya**, **Prof. Subrata Mukherjee**, **Prof. S. K. Baitalik**, **Prof. J. P. Naskar**, and **Dr. Bibhuti Bhushan Shaw** of the Department of Chemistry, Jadavpur University, for their continuous academic support and encouragement.

I owe special thanks to **Dr. Koushik Sarkar**, Assistant Professor, Department of Chemistry, St. Xavier's College, Kolkata whose expert suggestions and heartfelt concern provided both intellectual direction and moral support during critical stages of my research. I am equally grateful to **Dr. Rahul Sharma,** Associate Professor, Department of Chemistry, St. Xavier's College, Kolkata, for their constant encouragement and meaningful contributions to the progress of this work.

I would like to extend my sincere gratitude to my esteemed research collaborators **Prof. Soumyajit Roy** (IISER Kolkata), **Dr. Subhadip Roy** (The ICFAI University, Tripura), **Dr. Shyama Charan Mandal** (Stanford University, USA), **Ms. Nischal Bharadwaj** (IIT, Indore). Their steadfast support, intellectual collaboration, and shared enthusiasm greatly contributed to the advancement and successful completion of this research work.

Working alongside my juniors, **Aritra Paul** and **Aritra Das**, has been a genuinely rewarding experience. Their dedication, enthusiasm, and positive spirit added great value to this journey and made the research environment both productive and enjoyable.

I would also like to acknowledge my esteemed colleagues: **Dr. Sarat Chandra Patra**, **Dr. Shuvam Pramanik**, **Dr. Tapas Ghorui**, **Mr. Debasish Jana**, **Mr. Sampad Malik, Mr. Gopal Kanrar** for their unwavering cooperation and encouragement throughout this academic journey.

A special word of thanks is due to **Dr. Soumitra Dinda**, whose constant support and motivational presence were invaluable. His belief in my potential and his guidance during the most challenging phases of this work made a profound difference. This thesis would not have been possible without him.

It would be truly remiss of me not to acknowledge my contemporaries **Dr. Debopam Sinha, Dr. Mitali Majumdar, Dr. Tapashi Das, Dr. Roumi Patra**, **Mr. Uday Shee, Mr. Rakesh Debnath, Mr. Supriya Debnath, Ms. Sneha Ray**, **Mr. Biswajit Khutia, Dr. Ashoke Patra** (RKMRC, Narendrapur)**, Mr. Anik Roy** (RKMRC, Narendrapur), **Mr. Dibakar Halder** (RKMRC, Narendrapur), **Dr. Abhijit Nayek** (IACS, Kolkata), **Dr. Ujjwal Maji** (IACS, Kolkata) whose support and assistance in various capacities have been invaluable throughout the course of my study. Their camaraderie, encouragement, and help at different stages of this journey are deeply appreciated and warmly remembered.

I remain deeply indebted to the entire staff of my department for their unwavering cooperation, continuous support, and behind-the-scenes efforts that ensured a smooth and conducive environment for my research. Their dedication and willingness to assist, often without recognition, played a crucial role in facilitating both my academic and administrative needs throughout this journey.

I am profoundly grateful to my parents, **Mr. Sujit Kumar Halder** and **Mrs. Pratima Halder**, whose unwavering belief in me, along with their boundless love and sacrifices, have been the cornerstone of my journey. Their quiet strength, enduring support, and constant encouragement provided me with the courage to face every obstacle along the way. I am equally thankful to my parents-in-law, **Dr. Nityananda Naskar** and **Mrs. Malabika Naskar** and brother-in-law **Dr. Kaushik Naskar** (Jadavpur University) for their heartfelt blessings, encouragement, and kindness, which have brought immense comfort and strength throughout this endeavour.

Lastly, and most importantly, I extend my heartfelt thanks to my wife, **Srijita Naskar**, who has been not only a constant source of emotional strength but also a supportive colleague throughout the course of my research. Her patience, encouragement, and unwavering presence have been invaluable.

I also like to express my sincere appreciation to all my teachers, friends, relatives, and well-wishers whose support and goodwill, even if not mentioned individually, have meant a great deal to me and contributed in various ways to this journey.

I extend my sincere thanks to the **University Grants Commission (UGC)** for awarding me the fellowship and contingency grants that financially supported my research work. I am also deeply grateful to **Jadavpur University**, **St. Xavier's College (Autonomous), Kolkata**, **IISER Kolkata**, and **IACS Kolkata** for providing the essential infrastructural support and research facilities that greatly aided the progress of my work. To those whose names do not appear here, please know that your contributions have not gone unnoticed. Your support and encouragement have meant more to me than words can express.

Supriyo Halder

July, 2025

Preface

This thesis, entitled ***"Exploring the Influence of Azo Ligands in Catalysis: Ruthenium-Catalyzed C–C and C–N Bond Formation and Ligand-Catalyzed CO_2 Capture"***, presents a comprehensive study on recent developments in coordination chemistry involving π-acidic azo-oxime and bis-azo-diamine ligands. Commenced in July 2018, the research centers on the strategic design and synthesis of coordination complexes featuring custom-designed diaryl azo-oxime and bis-azo-diamine ligands. Particular attention is given to investigating the redox behaviour, optoelectronic characteristics, and catalytic performance of these complexes in facilitating C–C and C–N bond formation, as well as in CO_2 capture applications.

The outcomes of this work are organized into six structured chapters, following a general introduction that lays the theoretical foundation for the study.

Chapter 1: This chapter represents a general introduction to the thesis, with a brief overview of redox-noninnocent azo-oxime ligands and a new bis-azo-diamine ligand. The central section summarizes the research objectives, methodologies, and key outcomes of the study. The final part contains the details of physical methods, computational approaches, and instrumentation employed for the characterization of the synthesized compounds.

Chapter 2: This chapter summarises the synthesis of four new ruthenium(II) complexes having general formula *trans*-[Ru(L)(CO)Cl(PPh_3)$_2$] using azo-oxime ligands, in which the aryl (Ar) substituent is systematically varied. Structural analysis reveals subtle variations in the Ru–N_{azo} and Ru–N_{oxime} bond lengths, primarily influenced by the electronic properties of the aryl group within the ligand framework. We also extensively studied the electrochemical behaviour of all complexes and found that reductive responses are associated with electron uptake within the coordinated azo-oxime ligand framework, leading to the formation of meta-stable one-electron reduced anion radical species.

Chapter 3: This chapter demonstrates that *trans*-[Ru(L)(CO)Cl(PPh_3)$_2$] complexes act as efficient, tunable electron transfer catalysts, with activity governed by the electron accepting ability of the azo-oxime ligand. They catalyse (i) α-alkylation of ketones with primary alcohols and (ii) synthesis of 2-substituted quinolines. Mechanistic studies indicate a ligand-centered, redox-driven process initiated by an azo-oxime-based anion radical Ru(II) complex *via* HAT mechanism. The metal center serves mainly as a structural template, with electron withdrawing ligand groups enhancing the catalytic activity.

Chapter 4: This chapter details the synthesis and characterization of an air- and moisture-stable Ru(II) complex, *trans*-[Ru(NpL)(CO)Cl(PPh_3)$_2$], featuring phenyl-azo-naphthaldoxime ligand and its application as a pre-catalyst for the aerobic dehydrogenative coupling of benzyl alcohols with *o*-aminobenzamides to form quinazolin-4(3H)-ones. Mechanistic and theoretical studies reveal a ligand-centered HAT pathway, with the azo group driving aldehyde formation, followed by base-assisted condensation. The method offers low catalyst loading, mild conditions, and high efficiency.

Chapter 5: This chapter reports the synthesis and characterization of a bis-azo-diamine ligand and its effective use in catalytically converting CO_2 into C_3 products. The transformation proceeds *via* a triplet diradical pathway, forming acetic acid and ethanol through glyoxal intermediates. Electron transfer sustains the catalytic cycle, leading to the formation of ethanol, acetone and acetic acid, with acetic acid reacting with formyl species to yield C_3 products. The study highlights the potential of fluxional redox-active catalysts for sustainable CO_2 utilization and outlines future directions for catalyst optimization and scalability.

Chapter 6: This chapter discusses the synthesis and characterization of a hexacoordinated ruthenium(III) complex featuring a bis-azo-diamido ligand. The complex has been successfully employed as a catalyst for the direct dehydrogenative N-alkylation of aromatic amines using primary alcohols. Mechanistic studies suggest that one of the azo moieties within the ligand

framework plays a crucial role in the dehydrogenation step, while the ruthenium center remains redox-insensitive. The preferred pathway involves hydrogen atom transfer (HAT) from the alcohol to the azo group, leading to aldehyde formation. The resulting aldehyde then condensed with an aromatic primary amine to form a Schiff base (Ar–N=CH–R), which undergoes hydrogenation *via* the metal-assisted "Borrowing Hydrogenation" (BH) pathway, yielding the desired N-alkylated aromatic amine.

INDEX

Content **Page No.**

1. Introduction, Experimental Methodology, and Research Overview

1.1 General introduction 1

1.2 Azo-oximes: A potential redox non-innocent ligand 3

1.3 Bis-azo aromatic ligand 6

1.4 Summary of the research work 7

1.5 Experimental details 10

1.6 References 14

2. Design, Synthesis, and Structural Elucidation of Ruthenium(II) Complexes with Redox-Active Diaryl-Azo-Oxime Ligands

2.1 Introduction 20

2.2 Results and Discussion 22

2.3 Experimental Section 47

2.4 Conclusion 51

2.5 References 51

2.6 Appendix 55

3. Catalytic Applications of Ruthenium(II) Complexes bearing Redox-Active Aryl-Azo-Oximes: α-Alkylation of Ketones and Formation of 2-Substituted Quinolines

3.1 Introduction 66

3.2 Results and Discussion 70

3.3 Conclusion 83

3.4 Experimental Section 84

3.5 References 86

3.6 Appendix 90

4. Dehydrogenative Coupling for Synthesis of Quinazolin-4(3H)-ones *via* Tandem Reaction using Ruthenium(II)-Phenyl-Azo-Naphthaldoxime: An Experimental and Theoretical Investigation

4.1 Introduction 148

4.2 Results and Discussion 150

4.3 Conclusion 175

4.4 Experimental Section 175

4.5 References 179

4.6 Appendix 183

5. Coordination Dynamics and Electrocatalytic Activity of a Redox-Active Bis-Azo-Diamine Scaffold in Selective CO_2 Reduction to C2/C3 Products

5.1 Introduction 268

5.2 Results and Discussion 270

5.3 Conclusion 285

5.4 Experimental Section 285

5.5 References 288

5.6 Appendix 290

6. Sustainable Route Towards N-Alkylated Amines *via* Alcohol Dehydrogenation Catalysed by Bis-Azo-Diamido Coordinated Ruthenium(III) Complex

6.1 Introduction 298

6.2 Results and Discussion 303

6.3 Conclusion 325

6.4 Experimental Section 326

6.5 References 329

6.6 Appendix 333

Summary and Outlook 408

List of Publications 411

Chapter 1

Introduction, Experimental Methodology, and Research Overview

1.1 General introduction

Harnessing the redox activity and chemical noninnocence of ligands has recently emerged as a powerful strategy in the development of advanced catalytic systems.[1] A growing class of ligand frameworks now demonstrates the ability to reversibly store and release electrons, accessing multiple oxidation states with ease. These ligands are not only electronically versatile but also structurally resilient, maintaining their integrity across various redox states without undergoing undesirable bond cleavage that could disrupt catalytic performance. Redox-active ligands often feature either high-energy filled π-bonding orbitals or low-energy empty π* antibonding orbitals, enabling them to participate in redox events at potentials that are comparable to or even milder than those required for metal-centered redox transformations. This unique property allows ligands to act as electron reservoirs, facilitating redox processes without forcing the metal center into energetically unfavourable oxidation states. As a result, ligand-centered redox activity can provide alternative pathways for catalysis, reducing energy demands and expanding the range of accessible chemical transformations.

The concept of redox noninnocent ligands has its origins in the pioneering work of Prof. Christian Klixbüll Jørgensen in 1966,[2] who introduced the classification of ligands as either *innocent* or *noninnocent* to address the ambiguity surrounding the assignment of oxidation states to metal centers. According to this formalism, innocent ligands allow for an unambiguous determination of the metal oxidation state, whereas noninnocent ligands complicate this assignment due to their ability to participate in redox processes themselves. Redox noninnocent ligands are typically considered a subset of redox-active ligands; however, the key distinction lies in the interpretive challenge they pose when determining the distribution of electrons between the metal and ligand in a given complex. In complexes containing redox-active ligands, oxidation states can generally be determined with clarity through experimental and computational methods. In contrast, the electronic structure of complexes with redox

noninnocent ligands is often ambiguous due to extensive metal–ligand electronic delocalization.[3] This ambiguity, rather than being a limitation, has proven to be a valuable feature in catalysis. Inspired by nature, recent advancements in the field have exploited redox noninnocence to design biomimetic catalysts. Several metalloenzymes such as hydrogenases,[4] galactose oxidase,[5] and cytochrome P-450[6] are known to utilize ligand-based radical intermediates as part of their catalytic mechanisms, highlighting the critical role of ligand noninnocence in biological redox chemistry. One of the key advantages offered by redox noninnocent ligands, particularly in bioinorganic systems, is the reduction in reorganization energy during electron transfer events. This is attributed to the ability of these ligands to delocalize electron density, thus stabilizing multiple oxidation states and facilitating rapid and efficient electron flow. Moreover, in some metalloenzymatic systems, multiple noninnocent ligands can operate in tandem, enabling communication between spatially distant redox centers through long-range electron transfer pathways. This cooperative behaviour offers a valuable design principle for constructing advanced synthetic catalysts capable of emulating complex biological functions.

Redox noninnocence in transition metal complexes typically arises from strong electronic coupling between the metal center and the coordinated ligand, leading to an inherently ambiguous electronic structure. In such systems, the conventional assignment of oxidation states becomes challenging, making the concept of redox noninnocence particularly relevant. A diverse array of ligand scaffolds has been identified as redox-active, with many displaying noninnocent behaviour under specific coordination environments. Representative examples include donor-substituted diarylamines,[7] dithiolenes,[8] and salen-type ligands along with their derivatives.[9] Other notable classes encompass dipyrrins and their extended counterparts such as porphyrins,[10] 1,4-diimines and structurally related 2-iminopyridines,[11] bis(imino)pyridines,[12] 1,2-catechols and *o*-phenylenediamines,[13] formazanates,[14]

aminotropiminates,[15] β-diketiminates,[16] diaryl-azo-oximes,[17] azo based ligand such as 2,2-azobispyridine,[18] 2-(arylazo)pyridines and its arylamino derivatives,[19] and bis-azo aromatics.[20] These ligand frameworks are widely recognized for their ability to engage in reversible redox processes and significantly influence the electronic landscape of the metal complexes they form.

1.2 Azo-oximes: A potential redox non-innocent ligand

Oximes represent a distinct subclass of imines, characterized by the presence of a nitrogen–oxygen double bond functionality. They are typically synthesized through the nucleophilic addition of hydroxylamine or its derivatives to carbonyl compounds such as aldehydes and ketones. Based on their structural variations, oximes are broadly categorized into three types: hydroxy oximes (R_2C=NOH), oxime ethers (R_2C=NOR'), and oxime esters (R_2C=NOCOR'), each offering unique chemical properties and reactivity profiles. Due to their versatility and potential in various domains—including organic synthesis, medicinal chemistry, and coordination chemistry, oximes have garnered considerable attention in both fundamental and applied research.

Of particular interest are organic frameworks that simultaneously incorporate azo (–N=N–) and oxime (–C=N–OH) functionalities. Such molecules, upon coordination to transition metal centres, have been observed to exhibit redox non-innocent behaviour.[17] This unique feature stems from their ability to participate actively in redox processes, rather than serving merely as passive ligands. In these systems, the azo group can accept electrons through stepwise one-electron reductions into its low-lying π* orbital, a process that is often facilitated or modulated by the presence of the oxime moiety. The oxime group may also act as a photosensitizer, further enhancing the redox activity and photophysical properties of the resulting metal complexes. The synthesis of azo-oxime ligands is straightforward and historically well established. These

ligands are typically prepared by reacting aryl hydrazone precursors with isoamyl nitrite under mild conditions a synthetic route first introduced by Bamberger and Pemsel in 1903.[21] Mechanistically, the reaction is thought to proceed *via* the formation of a transient C-nitroso intermediate, which undergoes rapid isomerization to yield an aryl azo-oximate species. Upon subsequent treatment with dilute aqueous acid, the oximate is converted to the corresponding aryl-azo-oxime (Scheme 1.1). This transformation not only exemplifies elegant synthetic simplicity but also provides access to ligands with rich coordination and redox chemistry.

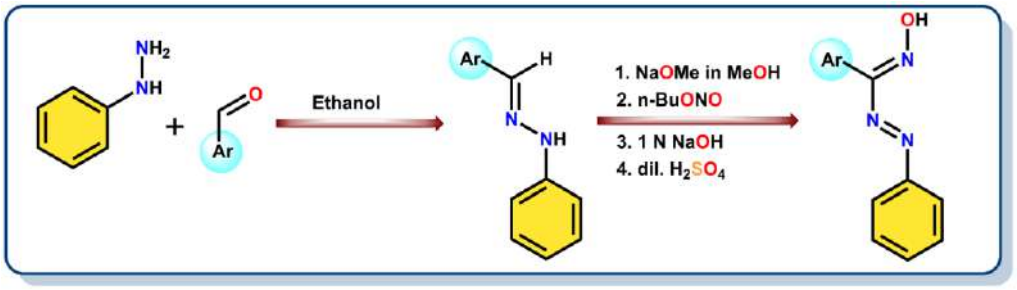

Scheme 1.1: Synthetic strategy of diaryl azo-oxime starting from aryl aldehyde and phenyl hydrazine

Aryl-azo-oximes are versatile ligands known for their ability to form stable coordination complexes with a wide range of transition metal ions. Their structural diversity and electronic richness make them particularly attractive for exploring new coordination architectures and functional materials. The coordination chemistry of these ligand dates back to 1941, when Louis Hunter and Carl B. Roberts first reported the synthesis of cobalt complexes using a series of azo-oxime ligands in ethanol. This pioneering work laid the groundwork for further investigations into the metal-binding capabilities of such systems. Subsequent studies, most notably by Prof. Animesh Chakravorty and his collaborators, significantly expanded the scope of this chemistry. They successfully synthesized and characterized numerous metal complexes of aryl-azo-oximes involving a diverse array of transition metals, including vanadium, manganese, nickel, cobalt, rhenium, ruthenium rhodium, iridium, palladium and platinum.[22] These investigations revealed that the multifunctional and flexi-dentate nature of aryl-azo-

oxime ligands featuring both azo (–N=N–) and oxime (–C=N–OH) donor groups—facilitates the formation of a broad spectrum of coordination motifs. Depending on the metal ion and reaction conditions, these ligands can adopt various binding modes, often leading to structurally robust and electronically tunable complexes.

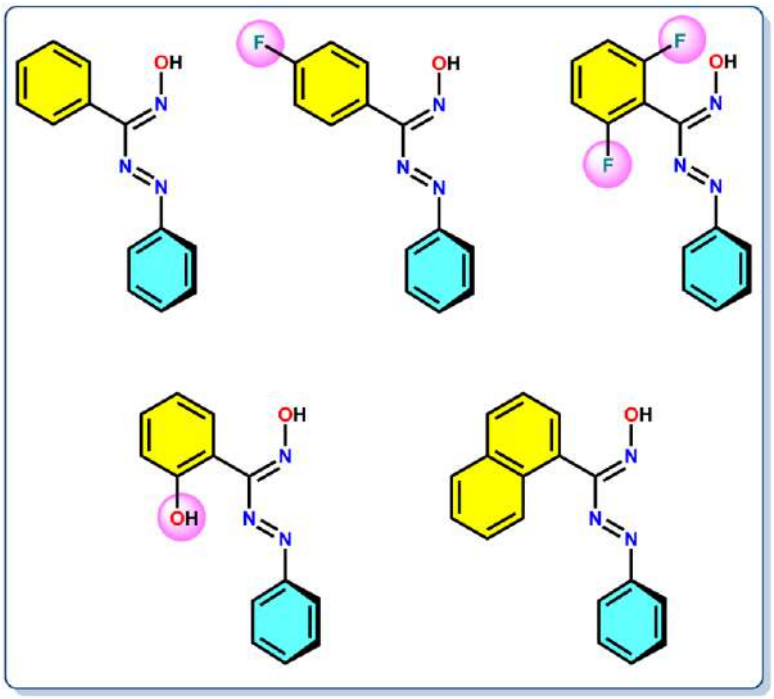

Scheme 1.2: The diaryl-azo-oxime ligands used in this research work

The aromatic azo functionality present in these ligands contributes significantly to their electronic properties, rendering them electron-rich and capable of engaging in π-conjugation. As a result, aryl-azo-oxime ligands exhibit moderate photoluminescence, functioning as chromophores with notable emissive characteristics. Interestingly, this luminescent behaviour is not limited to the free ligands alone; it often persists and, in some cases, is enhanced upon metal coordination. The resulting metal complexes frequently display emissive properties, making them promising candidates for applications in light-emitting materials, sensors, and photophysical studies.

In summary, the coordination chemistry of aryl-azo-oximes offers a rich platform for the development of functional metal complexes, with potential applications spanning catalysis, electronic materials, and photochemistry.

1.3 Bis-azo aromatic ligand

Azoaromatic compounds have attracted considerable attention in materials chemistry due to their distinctive combination of geometric flexibility and electronic properties.[23-24] One of their key features is the presence of a low-lying π* molecular orbital, which is responsible for strong absorption in the visible region an essential characteristic for their function as dyes. This electronic structure also imparts notable non-linear optical (NLO) properties, making them suitable candidates for applications in optical data storage and molecular electronics. Furthermore, the azo chromophore is capable of undergoing reversible photoinduced *E/Z* isomerization,[25] enabling its use in light-responsive systems. Structural modifications of azo compounds have also enabled their integration into mesogenic materials and liquid-crystalline polymers, broadening their scope in advanced materials design. Electrochemically, the accessible π* orbital can be populated through one- or two-electron reduction processes, either chemically or *via* electrochemical methods. This results in a well-defined two-step redox system involving the formation of a stable radical anion intermediate, followed by full reduction to a 1,2-disubstituted hydrazido ($2e^-$) species (Scheme 1.3). This redox behaviour underpins their utility in molecular electronics and redox-active coordination complexes.[26]

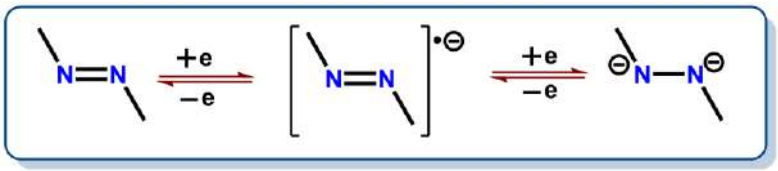

Scheme 1.3: Schematic depiction of $1e^-$ and $2e^-$ reduced azo anion radical

The interaction between azo-based ligands and one or more metal centers was first recognized in 1969 by Baldwin, Lever, and Parish. These systems exhibit a range of distinctive properties, including multiple accessible oxidation states, pronounced charge-transfer bands extending into the long-wavelength region, short metal–metal separations, diverse isomeric forms, and the remarkable stability of radical intermediates and mixed-valent species.[27] Similarly, the coordination chemistry of the unreduced 2-(arylazo)pyridine ligand was independently pioneered in the early 1980s by Prof. Animesh Chakravorty, Prof. Ronald A. Krause, and others.[28] In recent years, research group led by Prof. Sreebrata Goswami has made significant progress in the systematic exploration of transition metal complexes bearing azoaromatic ligands, aiming to better understand their structural and electronic properties.[29] In this study, we employed a bis-azo-diamino ligand that adopts a unique tetradentate planar coordination mode upon binding to transition metals. While this ligand has previously been explored as an intermediate in the synthesis of both cyclic and acyclic polyazo aromatic compounds most notably by the research group of Prof. Hermann Wegner.[30] But its coordination chemistry and potential for stabilizing metal complexes remain unexplored.

1.4 Summary of the research work

Chapter 2

In this chapter, we report the successful synthesis and comprehensive characterization of a series of four ruthenium(II) complexes with the general formula *trans*-[Ru(L)(CO)Cl(PPh_3)$_2$], where L represents a bidentate diaryl-azo-oxime ligand and the aryl (Ar) substituent is systematically varied to modulate electronic effects. The synthetic approach demonstrates the versatility of the azo-oxime framework in coordinating to the ruthenium centre through both azo and oxime donor sites. Structural analysis, based on single crystal X-ray diffraction (SCXRD) and supported by spectroscopic data, reveals subtle but discernible variations in the

Ru–N_{azo} and Ru–N_{oxime} bond lengths. These variations correlate with the electronic nature of the aryl substituents, indicating that electron donating and electron withdrawing groups exert a measurable influence on the coordination environment. Electrochemical studies were conducted to gain deeper insights into the redox properties of these complexes. Cyclic voltammetry data indicate that the observed reductive responses originate predominantly from electron uptake within the coordinated azo-oxime ligand framework. These reductions result in the formation of meta-stable, one electron reduced radical anion species, which are characteristics of ligand-centered redox activity.

Chapter 3

Here in this chapter, we demonstrate the precursor complexes *trans*-[Ru(L)(CO)Cl(PPh_3)$_2$] have potential as electron transfer catalysis, with their catalytic efficiency being tunable through controlled manipulation of the electron density within the azo-oxime framework. We have successfully utilized their catalytic performance in two distinct transformations: (i) α-alkylation of ketones using primary alcohols and (ii) the synthesis of 2-substituted quinoline derivatives from 2-aminobenzyl alcohols and substituted acetophenones or alkyl methyl ketones. A comprehensive study of the reaction scope has been conducted, and mechanistic insights have been derived from experimental observations. Our results indicate that the catalytic process is primarily ligand-centered and redox-driven during the dehydrogenation step. The reaction initiates with the formation of an azo-oxime-based anion radical complex of ruthenium(II), which serves as the active catalytic species. This complex facilitates the conversion of the starting alcohol into the corresponding carbonyl compound *via* a hydrogen atom transfer (HAT) mechanism. Notably, the metal center acts as a structural template rather than participating directly in redox processes. Furthermore, the catalytic efficiency is significantly influenced by the electronic nature of the pendant aryl groups in the ligand framework, with increased electron withdrawing character enhancing the catalytic performance.

Chapter 4

In this chapter, we report the synthesis and comprehensive characterization of an air- and moisture-stable ruthenium(II) complex, *trans*-[Ru(NpL)(CO)Cl(PPh_3)$_2$], using spectroscopic, electrochemical, and X-ray crystallographic methods, supported by theoretical analysis. The complex serves as an effective pre-catalyst for the aerobic dehydrogenative coupling of benzyl alcohols with *o*-aminobenzamides or N-substituted benzamides, affording quinazolin-4(3H)-ones. Mechanistic studies highlight the crucial role of the azo moiety in facilitating the dehydrogenation step, while the metal center remains redox-inactive. Theoretical analysis confirms that hydrogen atom transfer (HAT) from the alcohol to the azo group is the favoured pathway, leading to aldehyde generation. This is followed by base-promoted condensation under aerobic conditions, forming 2,3-dihydro-2-arylquinazolin-4(1H)-ones, which undergo further dehydrogenation to yield the final quinazolin-4(3H)-one products. The protocol features low catalyst loading, mild reaction conditions, and short reaction times, offering a practical and efficient alternative to conventional catalytic methods.

Chapter 5

This chapter presents the synthesis and characterization of a bis-azo-diamine ligand and its effective application in the catalytic valorization of CO_2 into C_3 products. The transformation proceeds *via* a distinctive triplet diradical pathway, initiating a cascade that converts CO_2 into acetic acid and acetone through glyoxal intermediates. The catalytic cycle is driven by electron transfer, enabling continuous catalyst regeneration while promoting the formation of acetone and acetic acid. Significantly, acetic acid further reacts with formyl species to yield C_3 products, emphasizing the catalyst's role in sustainable carbon recycling. This study highlights the potential of fluxional, redox-active catalysts in CO_2 utilization and offers a promising route for carbon capture. Ongoing research will aim to refine catalyst design and improve scalability for future practical implementation.

Chapter 6

This chapter describes the synthesis and detailed characterization of a novel hexacoordinated ruthenium(III) complex featuring a bis-azo-diamido ligand scaffold. The complex demonstrates excellent catalytic activity in the direct dehydrogenative N-alkylation of aromatic amines using primary alcohols as alkylating agents. Mechanistic investigations reveal that the dehydrogenation step is primarily mediated by one of the azo groups within the ligand, while the ruthenium center remains redox-inert throughout the process. The reaction proceeds *via* a hydrogen atom transfer (HAT) from the alcohol to the azo functionality, generating an aldehyde intermediate. This aldehyde subsequently condenses with an aromatic amine to form a Schiff base (Ar–N=CH–R), which is then reduced through a metal-assisted "Borrowing Hydrogenation" (BH) pathway to afford the final N-alkylated amine product. This catalytic system highlights the unique synergy between the redox-active ligand and the metal center in enabling efficient and sustainable N-alkylation under mild conditions.

1.5 Experimental details

1.5.1 Physical Measurements

Different physical methods have been used for the characterization and elucidation of the properties of the synthesized compounds and these are described in the subsequent chapters. These are briefly described below.

Elemental Analysis

Elemental analyses (C, H, N) of the ligands and their corresponding ruthenium complexes were carried out using a Perkin-Elmer 2400 Series II elemental analyser. This instrument operates based on thermal conductivity detection of combustion products such as CO_2, H_2O, and N_2. Samples weighing between 1.4 and 2.5 mg were introduced into a high-temperature combustion chamber, typically maintained between 900 and 980 °C. Combustion was

performed in the presence of pure oxygen, while pure helium served as the carrier gas to transport the resulting gases through the detection system.

Infrared Spectra

FT-IR spectra of all ligands and complexes were measured in Perkin-Elmer L-0100 spectrometer using diamond ATR.

NMR Spectra

^{1}H, ^{13}C, ^{19}F, and ^{31}P NMR spectra were recorded on Bruker AVANCE III spectrometers operating at 400 and 300 MHz, using deuterated solvents. Proton chemical shifts (δ) are reported in parts per million (ppm) relative to tetramethylsilane (TMS), with residual solvent signals used as internal standards ($CDCl_3$: δ 7.26 ppm). ^{1}H NMR data are presented as follows: chemical shift, multiplicity (s = singlet, d = doublet, dd = doublet of doublets, t = triplet, q = quartet, m = multiplet, br = broad), coupling constants (in Hz), and integration. ^{13}C NMR chemical shifts are also reported in ppm relative to TMS, using the solvent peak as the internal standard ($CDCl_3$: δ 77.16 ppm).

Electronic Spectra

Electronic spectra were recorded on Perkin-Elmer LAMBDA EZ-301 and a Shimadzu 1800 UV-Vis spectrometer (190-1100 nm). A matched pair of quartz cells of path length 1 cm was used.

Mass spectrometric data

Mass spectra were recorded using a Micromass Quadrupole Time-of-Flight (Q-TOF) micro-MS system equipped with an electrospray ionization (ESI) source. High-resolution mass spectra (HRMS) were obtained on the same instrument at a resolution of 5K or 7K, using polyethylene glycol as the internal reference standard.

Electrochemical Measurements

Cyclic voltammetry (CV) experiments were performed using a BASi Epsilon-EC electrochemical workstation at temperature of 298 K. The measurements of all ligand and complexes were conducted in dry, degassed dichloromethane/acetonitrile solutions (1:9 v/v), using 0.2 M tetrabutylammonium hexafluorophosphate (TBAP) as the supporting electrolyte. A conventional three-electrode setup was employed, consisting of a platinum disc as the working electrode, a platinum wire as the auxiliary electrode, and a saturated Ag/AgCl electrode as the reference electrode. Prior to each experiment, the electrolyte solution was thoroughly degassed by purging with high-purity argon to eliminate dissolved oxygen and moisture. All potentials reported are referenced against the Ag/AgCl electrode unless otherwise specified.

X-Ray Crystallographic studies

Single-crystal X-ray diffraction data were collected on a Bruker D8 QUEST diffractometer equipped with a Mo Kα radiation source (λ = 0.71073 Å), operated at 50 kV and 1 mA. A suitable crystal was mounted on a loop, and data acquisition was performed at a temperature of 273(2) K. Data collection, reduction, scaling, and absorption corrections were carried out using standard Bruker software packages. The crystal structure was solved using the ShelXT[31] program via intrinsic phasing methods and refined with full-matrix least-squares minimization on F^2 using ShelXL,[32] all within the Olex2[33] graphical user interface. All non-hydrogen atoms were located from difference Fourier maps and refined anisotropically.[34] Hydrogen atoms were positioned geometrically and refined using a riding model with isotropic displacement parameters. Complete crystallographic refinement details are provided in the associated CIF file. The crystallographic data have been deposited with the Cambridge Crystallographic Data Centre (CCDC) and can be obtained free of charge *via* www.ccdc.cam.ac.uk/data_request/cif.

Computational Studies

All computational studies were performed using the Gaussian 09 software package.[35] Geometry optimizations of ligands and complexes were carried out using their crystallographic coordinates as starting points, employing the (R/U)B3LYP[36] level of theory in the solution phase, without any simplification of the ligand framework. The optimized geometries showed overall good agreement with the experimental crystallographic data, with minor deviations attributed to crystal lattice distortions present in the solid state. To confirm the nature of the optimized structures, vibrational frequency analyses were conducted. All stationary points were verified as true minima on the potential energy surface, as evidenced by the absence of any imaginary frequencies ($N_{Imag} = 0$). Based on the optimized geometries, the absorption and emission spectra in dichloromethane (CH_2Cl_2) were computed using time-dependent density functional theory (TD-DFT)[37] combined with the conductor-like polarizable continuum model (CPCM)[38] to account for solvent effects. TD-DFT is widely recognized as a reliable method for predicting electronic excitation energies within the DFT framework, particularly for transition metal complexes.[39] To gain insight into the nature of the electronic transitions, natural transition orbital (NTO) analysis was performed using the transition density matrices[40] obtained from TD-DFT calculations. This approach provides a compact and intuitive representation of electronic excitations in terms of single-particle transitions, identifying the "hole" (occupied) and "electron" (unoccupied) NTOs that characterize each excitation. For the calculations, the ruthenium centers were described using the LANL2DZ[41] effective core potential with a double-ζ basis set, while a 6-311+G(d,p) basis set[42] was employed for all other atoms, except hydrogen, for which a 6-31G basis was used. Frontier molecular orbital (FMO) diagrams and electronic density plots were generated using GaussView 6.0. Additionally, the GaussSum 3.0 program[43] was employed to analyse the contribution of individual atoms or molecular fragments to the molecular orbitals.

1.6 References

[1] (a) V. Lyaskovskyy, B. de Bruin, *ACS Catal.*, **2012**, *2*, 270−279. (b) P. J. Chirik, K. Wieghardt, *Science*, **2010**, *327*, 794−795.

[2] C. K. Jorgensen, *Coord. Chem. Rev.*, **1966**, *1*, 164−178.

[3] (a) O. R. Luca, R. H. Crabtree, *Chem. Soc. Rev.*, **2013**, *42*, 1440−1459. (b) D. L. J. Broere, R. Plessius, J. I. van der Vlugt, *Chem. Soc. Rev.*, **2015**, *44*, 6886−6915.

[4] A. Volbeda, M.-H. Charon, C. Piras, E. C. Hatchikian, M. Frey, C. J. Fontecilla-Camps, *Nature*, **1995**, *373*, 580−587.

[5] C. D. Borman, C. G. Saysell, A. Sokolowski, M. B. Twitchett, C. Wright, A. G. Sykes, *Coord. Chem. Rev.*, **1999**, *190*, 771−779.

[6] J. Rittle, M. T. Green, *Science*, **2010**, *330*, 933−937.

[7] (a) S. B. Harkins, N. P. Mankad, A. J. M. Miller, R. K. Szilagyi, J. C. Peters, *J. Am. Chem. Soc.*, **2008**, *130*, 3478−3485. (b) D. Adhikari, S. Mossin, F. Basuli, J. C. Huffman, R. K. Szilagyi, K. Meyer, D. J. Mindiola, *J. Am. Chem. Soc.*, **2008**, *130*, 3676−3682. (c) D. Wang, S. V. Lindeman, A. T. Fiedler, *Inorg. Chem.*, **2015**, *54*, 8744−8754.

[8] (a) R. Eisenberg, H. B. Gray, *Inorg. Chem.*, **2011**, *50*, 9741− 9751. (b) A. Vlcek, *Coord. Chem. Rev.*, **2010**, *254*, 1357.

[9] (a) R. M. Clarke, K. Hazin, J. R. Thompson, D. Savard, K. E. Prosser, T. Storr, *Inorg. Chem.*, **2016**, *55*, 762−774. (b) D. de Bellefeuille, M. Orio, A.- L. Barra, A. Aukauloo, Y. Journaux, C. Philouze, X. Ottenwaelder, F. Thomas, *Inorg. Chem.*, **2015**, *54*, 9013−9026.

[10] (a) J. R. Pankhurst, N. L. Bell, M. Zegke, L. N. Platts, C. A. Lamfsus, L. Maron, L. S. Natrajan, S. Sproules, P. L. Arnold, J. B. Love, *Chem. Sci.*, **2017**, *8*, 108−116. (b) R. Gautam, T. M. Chang, A. V. Astashkin, K. M. Lincoln, E. Tomat, *Chem. Commun.*, **2016**, *52*, 6585−6588.

[11] (a) P. J. Chirik, *Acc. Chem. Res.*, **2015**, *48*, 1687−1695. (b) V. A. Williams, E. B. Hulley, P. T. Wolczanski, K. M. Lancaster, E. B. Lobkovsky, *Chem. Sci.*, **2013**, *4*, 3636−3648. (c) T. W. Myers, L. A. Berben, *Inorg. Chem.*, **2012**, *51*, 1480−1488.

[12] (a) D. Sieh, M. Schlimm, L. Andernach, F. Angersbach, S. Nückel, J. Schoffel, N. Susnjar, P. Burger, *Eur. J. Inorg. Chem.*, **2012**, *2012*, 444−462. (b) C. Romelt, T. Weyhermuller, K. Wieghardt, *Coord. Chem. Rev.*, **2019**, *380*, 287−317.

[13] (a) C. G. Pierpont, *Inorg. Chem.*, **2011***, 50,* 9766−9772. (b) S. Bera, S. Mondal, S. Maity, T. Weyhermüller, P. Ghosh, *Inorg. Chem.*, **2016**, *55*, 4746−4756.

[14] (a) J. B. Gilroy, E. Otten, *Chem. Soc. Rev.*, **2020**, *49*, 85−113. (b) A. Mandal, B. Schwederski, J. Fiedler, W. Kaim, G. K. Lahiri, *Inorg. Chem.*, **2015**, *54*, 8126−8135.

[15] C. Lichtenberg, I. Krummenacher, *Chem. Commun.*, **2016**, *52*, 10044−10047.

[16] (a) M. M. Khusniyarov, E. Bill, T. Weyhermüller, E. Bothe, K. Wieghardt, *Angew. Chem., Int. Ed.*, **2011**, *50*, 1652−1655. (b) K. Singh, V. Sridharan, D. Adhikari, *Inorg. Chem. Front.*, **2021**, *8*, 2078−2087.

[17] (a) K. C. Kalia, A. Chakravorty, *Inorg. Chem.*, **1969**, *8*, 2586−2590. (b) K. C. Kalia, A. Chakravorty, *Inorg. Chem.*, **1968**, *7*, 2016−2020. (c) A. Chakravorty, K. C. Kalia, *Inorg. Nucl. Chem. Lett.*, **1967**, *3*, 319−321 (d) I. Chakraborty, B. K. Panda, J. Gangopadhyay, A. Chakravorty, *Inorg. Chem.*, **2005**, *44*, 1054–1060. (e) S. Ganguly, S. Mukherjee, *J. Ind. Chem. Soc.*, **2005**, *82*, 898–902. (f) S. Ganguly, *J. Ind. Chem. Soc.*, **2004**, *81*, 327–329. (g) S. Ganguly, S. Karmakar, C. K. Pal, A. Chakravorty, *Inorg. Chem.*, **1999**, *38*, 5984–5987. (h) V. Manivannan, B. K. Dirghangi, C. K. Pal, A. Chakravorty, *Inorg. Chem.*, **1997**, *36*, 1526–1528; (i) S. Karmakar, A. Chakravorty, *Inorg. Chem.*, **1996**, *35*, 1935–1939.

[18] (a) A. Kirpal, L. Reiter, *Ber. Dtsch. Chem. Ges.* **1927**, *60*, 664. (b) W. Kaim, *Coord. Chem. Rev.*, **2001**, *219*, 463–488.

[19] (a) S. Banerjee, S. Bhattacharyya, B. K. Dirghangi, M. Menon, A. Chakravorty, *Inorg. Chem.*, **2000**, *39*, 6–13. (b) S. Samanta, P. Ghosh, S. Goswami, *Dalton Trans.*, **2012**, *41*, 2213–2226.

[20] (a) S. Roy, S. Pramanik, S. C. Patra, B. Adhikari, A. Mondal, S. Ganguly, K. Pramanik, *Inorg. Chem.*, **2017**, *56*, 12764−12774. (b) S. Roy, T. Ghorui, D. Jana, S. C. Patra, S. Pramanik, S. Moorthy, S. K. Singh, S. Mehta, A. Mondal, K. Pramanik, *Chem. Eur. J.*, **2025**, *31*, e202404027.

[21] E. Bamberger, W. Pemsel, *Ber.*, **1903**, *36*, 85−89.

[22] (a) C. Natarajan, A. N. Hussain, *Transition Met Chem.*, **1984**, *9*, 18–22. (b) S. Pal, D. Bandyopadhyay, D. Datta, A. Chakravorty, *J. Chem. Soc., Dalton Trans.*, **1985**, 159–162. (c) B. K. Ghosh, R. Mukherjee, A. Chakravorty, *Inorg. Chem.*, **1987**, *26*, 1946–1950. (d) S. Karmakar, S. B. Choudhury, A. Chakravorty, *Inorg. Chem.*, **1994**, *33*, 6148–6153. (e) S. Chattopadhyay, A. Chakravorty, *J. Chem. Sci.*, **1994**, *106*, 793. (f) S. Karmakar, A. Chakravorty, *Inorg. Chem.*, **1996**, *35*, 1935–1939. (g) K. Pramanik, S. Karmakar, S. B. Choudhury, A. Chakravorty, *Inorg. Chem.*, **1997**, *36*, 3562–3564. (h) V. Manivannan, B. K. Dirghangi, C. K. Pal, A. Chakravorty, *Inorg. Chem.*, **1997**, *36*, 1526–1528. (i) S. Ganguly, S. Karmakar, C. K. Pal, A. Chakravorty, *Inorg. Chem.*, **1999**, *38*, 5984–5987. (j) S. Ganguly, *J. Ind. Chem. Soc.*, **2004**, *81*, 327–329. (k) I. Chakraborty, B. K. Panda, J. Gangopadhyay, A. Chakravorty, *Inorg. Chem.*, **2005**, *44*, 1054–1060. (l) S. Ganguly, S. Mukherjee, *J. Ind. Chem. Soc.*, **2005**, *82*, 898–902. (m) S. Pramanik, S. Roy, T. Ghorui, S. Ganguly, K. Pramanik, *Dalton Trans.*, **2014**, *43*, 5317–5334.

[23] (a) Eich, M.; Wendorff, J. H. Reck, B. Ringsdorf, H. Makromol, *Chem. Rapid Commun.*, **1987**, *8*, 59–63. (b) U. Wiesner, M. Antonietti, C. Boeffel, H. W. Spiess, *Makromol. Chem.*, **1990**, *191*, 2133–2149. (c) A. Natansohn, P. Rochon, J. Gosselin, S. Xie, *Macromolecules*, **1992**, *25*, 2268–2273. (d) S. Hvilsted, F. Andruzzi, P. S. Ramanujam, *Optics Lett.*, **1992**, *17*, 1234–1236. (e) S. Hvilsted, F. Andruzzi, C. Kulinna, H. W. Siesler, P. S. Ramanujam, *Macromolecules*, **1995**, *28*, 2172–2183. (f) R. H. Berg, S. Hvilsted, P. S. Ramanujam, *Nature*, **1996**, *383*, 505–508. (g) A. Natansohn (Ed.), *Azobenzene-Containing Materials*, Wiley-VCH, Weinheim, **1999**. (h) P.-O. Astrand, P.S. Ramanujam, S. Hvilsted, K.L. Bak, S.P.A. Sauer, *J. Am. Chem. Soc.*, **2000**, *122*, 3482–3487.

[24] (a) R. Hildebrandt, M. Hegelich, H. -M. Keller, G. Marowsky, S. Hvilsted, N. C. R. Holme, P. S. Ramanujam, *Phys. Rev. Lett.*, **1998**, *81*, 5548–5551. (b) C. Kulinna, S. Hvilsted, C. Hendann, H.W. Siesler, P. S. Ramanujam, *Macromolecules*, **1998**, *31*, 2141–2151. (c) L. Andruzzi, A. Altomare, F. Ciardelli, R. Solaro, S. Hvilsted, P. S. Ramanujam, *Macromolecules*, **1999**, *32*, 448–454. (d) N. C. R. Holme, L. Nikolova, T. B. Norris, S. Hvilsted, M. Pedersen, R. H. Berg, P. H. Rasmussen, P. S. Ramanujam, *Macromol. Symp.*, **1999**, *137*, 83–103. (e) P. H. Rasmussen; P. S. Ramanujam, S. Hvilsted, R. H. Berg, *J. Am. Chem. Soc.*, **1999**, *121*, 4738–4743.

[25] (a) H. Knoll in *CRC Handbook of Organic Photochemistry and Photobiology* (Eds.: W. M. Horspool, F. Lenci), 2nd ed., CRC, Boca Raton, FL, **1996**. (b) V. Balzani, M. Venturi and

A. Credi, *Molecular Devices and Machines—A Journey into the Nanoworld*, Wiley-VCH GmbH, Weinheim, Germany, 1st ed., **2003**. (c) *Molecular Switches* (Eds.: B. L. Feringa, W. R. Browne), 2nd ed., Wiley-VCH, Weinheim, **2011**. (d) R. Reuter, H. A. Wegner, *Chem. Commun.*, **2011**, *47*, 12267–12276. (e) H. A. Wegner, *Angew. Chem. Int. Ed*., **2012**, *51*, 4787 – 4788.

[26] W. Kaim, *Coord. Chem. Rev.*, **2001**, *219*, 463–488.

[27] (a) D.A. Baldwin, A.B.P. Lever, R.V. Parish, *Inorg. Chem.*, **1969**, *8*, 107–115. (b) S. Panda, S. Dhara, A. Singh, S. Dey, G. K. Lahiri, *Coord. Chem. Rev.*, **2023**, *475*, 214895.

[28] (a) R. A. Krause, K. Krause, *Inorg. Chem.*, **1980**, *19*, 2600–2603. (b) R. A. Krause, K. Krause, *Inorg. Chem.*, **1982**, *21*, 1714–1720. (c) R. A. Krause, K. Krause, *Inorg. Chem.*, **1984**, *23*, 2195–2198. (d) V. Ferreira, R. A. Krause, S. Larsen, *Inorg. Chim. Acta*, **1988**, *145*, 29–38. (e) B. K. Ghosh, A. Chakravorty, *Coord. Chem. Rev.*, **1989**, *95*, 239–294.

[29] (a) S. Goswami, A. R. Chakravarty, A. Chakravorty, *Inorg. Chem.*, **1981**, *20*, 2246–2250. (b) S. Goswami, A. R. Chakravarty, A. Chakravorty, *Inorg. Chem.*, **1982**, *21*, 2737–2742. (c) S. Goswami, A. R. Chakravarty, A. Chakravorty, *Inorg. Chem.*, **1983**, *22*, 602–609. (d) S. Goswami, R. N. Mukherjee, A. Chakravorty, *Inorg. Chem.*, **1983**, *22*, 2825–2832. (e) B. K. Ghosh, S. Goswami, A. Chakravorty, *Inorg. Chem.*, **1983**, *22*, 3358–3360. (f) B. K. Ghosh, A. Mukhopadhyay, S. Goswami, S. Ray, A. Chakravorty, *Inorg. Chem.*, **1984**, *23*, 4633–4639. (g) G. K. Lahiri, S. Goswami, L. R. Falvello, A. Chakravorty, *Inorg. Chem.*, **1987**, *26*, 3365–3370. (h) A. K. Deb, P. C. Paul, Sreebrata Goswami, *J. Chem. Soc., Dalton Trans.*, **1988**, 2051–2054. (i) A. K. Deb, S. Goswami, *J. Chem. Soc., Dalton Trans.*, **1989**, 1635–1637. (j) G. K. Lahiri, S. Bhattacharya, S. Goswami, A. Chakravorty, *J. Chem. Soc.*, *Dalton Trans.*, **1990**, 561–565. (k) A. K. Deb, S. Choudhury, S. Goswami, *Polyhedron*, **1990**, *9*, 2251–2255. (l) A. K. Deb, M. Kakoti, Sreebrata Goswami, *J. Chem. Soc., Dalton Trans.*, **1991**, 3249–3251. (m) M. Kakoti, A. K. Deb, Sreebrata Goswami, *Inorg. Chem.*, **1992**, *31*, 1302–1304. (n) M. Kakoti, S. Chaudhury, A. K. Deb, S. Goswami, *Polyhedron*, **1993**, *12*, 783–789. (o) W. Kharmawphlang, S. Choudhury, A. K. Deb, S. Goswami, *Inorg. Chem.*, **1995**, *34*, 3826–3828. (p) P. Majumdar, A. K. Ghosh, L. R. Falvello, S. -M. Peng, S. Goswami, *Inorg. Chem.*, **1998**, *37*, 1651–1654. (q) P. Majumdar, S. -M. Peng, S. Goswami, *J. Chem. Soc., Dalton Trans.*, **1998**, 1569–1574. (r) S. Mandal, N. D. Paul, P. Banerjee, T. K. Mondal, S. Goswami, *Dalton Trans.*, **2010**, *39*, 2717–2726.

[30] (a) R. Reuter, H. A. Wegner, *Chem. Commun.*, **2011**, *47*, 12267–12276. (b) S. Bellotto, R. Reuter, C. Heinis, H. A. Wegner, *J. Org. Chem.*, **2011**, *76*, 9826−9834. (c) R. Reuter, H. A. Wegner, *Chem. Eur. J.*, **2011**, *17*, 2987 – 2995.

[31] (a) SAINT, Data Reduction and Frame Integration Program for the CCD Area-Detector System, Bruker Analytical X-ray Systems, Madison, Wisconsin, USA, 1997–2006. (b) G. M. Sheldrick, SADABS, Program for Area Detector Adsorption Correction, Institute for Inorganic Chemistry, University of Gőttingen, Germany, **1996**.

[32] G. M. Sheldrick, *Acta Crystallogr., Sect. C: Struct. Chem.*, **2015**, *71*, 3–8.

[33] G. M. Sheldrick, SHELXTL, v. 6.14; Bruker AXS Inc.: Madison, WI, **2003**.

[34] O. V. Dolomanov, L. J. Bourhis, R. J. Gildea, J. A. K. Howard, H. Puschmann, *J. Appl. Crystallogr.*, **2009**, *42*, 339–341.

[35] M. J. Frisch, G. W. Trucks, H. B. Schlegel, G. E. Scuseria, M. A. Robb, J. R. Cheeseman, G. Scalmani, V. Barone, B. Mennucci, G. A. Petersson, H. Nakatsuji, M. Caricato, X. Li, H. P. Hratchian, A. F. Izmaylov, J. Bloino, G. Zheng, J. L. Sonnenberg, M. Hada, M. Ehara, K. Toyota, R. Fukuda, J. Hasegawa, M. Ishida, T. Nakajima, Y. Honda, O. Kitao, H. Nakai, T. Vreven, J. A. Montgomery, Jr., J. E. Peralta, F. Ogliaro, M. Bearpark, J. J. Heyd, E. Brothers, K. N. Kudin, V. N. Staroverov, R. Kobayashi, J. Normand, K. Raghavachari, A. Rendell, J. C. Burant, S. S. Iyengar, J. Tomasi, M. Cossi, N. Rega, J. M. Millam, M. Klene, J. E. Knox, J. B. Cross, V. Bakken, C. Adamo, J. Jaramillo, R. Gomperts, R. E. Stratmann, O. Yazyev, A. J. Austin, R. Cammi, C. Pomelli, J. W. Ochterski, R. L. Martin, K. Morokuma, V. G. Zakrzewski, G. A. Voth, P. Salvador, J. J. Dannenberg, S. Dapprich, A. D. Daniels, O. Farkas, J. B. Foresman, J. V. Ortiz, J. Cioslowski and D. J. Fox, Gaussian 09 (Revision A.01), Gaussian, Inc., Wallingford CT, 2009.

[36] C. Lee, W. Yang, R.G. Parr, *Phys. Rev. B*, **1998**, *37*, 785−789.

[37] (a) J. Autschbach, T. Ziegler, S. J. A. Gisbergen, E. J. Baerends, *J. Chem. Phys.*, **2002**, *116*, 6930−6940. (b) K. L. Bak, P. Jørgensen, T. Helgaker, K. Rund, H. J. A. Jenson, *J. Chem. Phys.*, **1993**, *98*, 8873−8887. (c) T. Helgaker, P. Jørgensen, *J. Chem. Phys.*, **1991**, *95*, 2595−2601. (d) E. K. U. Gross, W. Kohn, *Adv. Quantum Chem.*, **1990**, *21*, 255−291.

[38] (a) M. Cossi, N. Rega, G. Scalmani, V. Barone, *J. Comput. Chem.*, **2003**, *24*, 669−681. (b) M. Cossi, V. Barone, *J. Chem. Phys.*, **2001**, *115*, 4708−4717. (c) V. Barone, M. Cossi, *J. Phys. Chem. A*, **1998**, *102*, 1995−2001.

[39] (a) T. Liu, H. X. Zhang, B. H. Xia, *J. Phys. Chem. A*, **2007**, *111*, 8724−8730. (b) A. Albertino, C. Garino, S. Ghiani, R. Gobetto, C. Nervi, L. Salassa, E. Rosenverg, A. Sharmin, G. Viscardi, R. Buscaino, G. Cross, M. Milanesio, J. Organomet. Chem., **2007**, *692*, 1377–1391. (c) X. Zhou, H. X. Zhang, Q. J. Pan, B. H. Xia, A. C. Tang, *J. Phys. Chem. A*, 2005, 109, 8809−8818. (d) X. Zhou, A. M. Ren, J. K. Feng, *J. Organomet. Chem.*, **2005**, *690*, 338−347.

[40] R. L. Martin, *J. Chem. Phys.*, **2003**, *118*, 4775–4777.

[41] (a) P. J. Hay, W. R. Wadt, *J. Chem. Phys.*, **1985**, *82*, 299−310. (b) P. J. Hay, W. R. Wadt, *J. Chem. Phys.*, **1985**, *82*, 270 283.

[42] (a) M. S. Gordon, J. S. Binkley, J. A. Pople, W. J. Pietro, W. J. Hehre, *J. Am. Chem. Soc.*, **1982**, *104*, 2797–2803; (b) J. S. Binkley, J. A. Pople, W. J. Hehre, *J. Am. Chem. Soc.*, **1980**, *102*, 939–947.

[43] N. M. O'Boyle, A. L. Tenderholt, K. M. Langner, *J. Comp. Chem.*, **2008**, *29*, 839–845.

Chapter 2

Design, Synthesis, and Structural Elucidation of Ruthenium(II) Complexes with Redox-Active Diaryl-Azo-Oxime Ligands

2.1 Introduction

The redox non-innocence[1] of coordinated ligands is gaining profound importance in the field of electron transfer catalysis since the metal redox and the ligand skeleton have the aptitude to stimulate the process in a collaborative manner with the catalyst swapping from one spin isomeric state to another.[2-4] Such reactions may proceed *via* formation of meta-stable ligand-centric coordinated radical and it is usually accompanied by conjoint proton coupled electron transfer (PCET)[5-6] or hydrogen atom transfer (HAT).[7-8] The chemistry of redox non-innocent ligands containing azo functions has developed over the past two and half decades[9-12] and at present the catalytic role of their complexes are under intense investigation.[13-16] In majority of the cases, ligands are tridentate azo pincers type where the ligated azo moieties have the competence to behave as electron pockets to store electron/s in the form of azo anion-radical. In addition, the reserved electron/s may be transferred to suitable centres to bring about catalytic reduction and this conception has been proficiently employed to synthesize several value-added chemicals of pharmaceutical and industrial importance, in a cost effective and atom efficient manner.

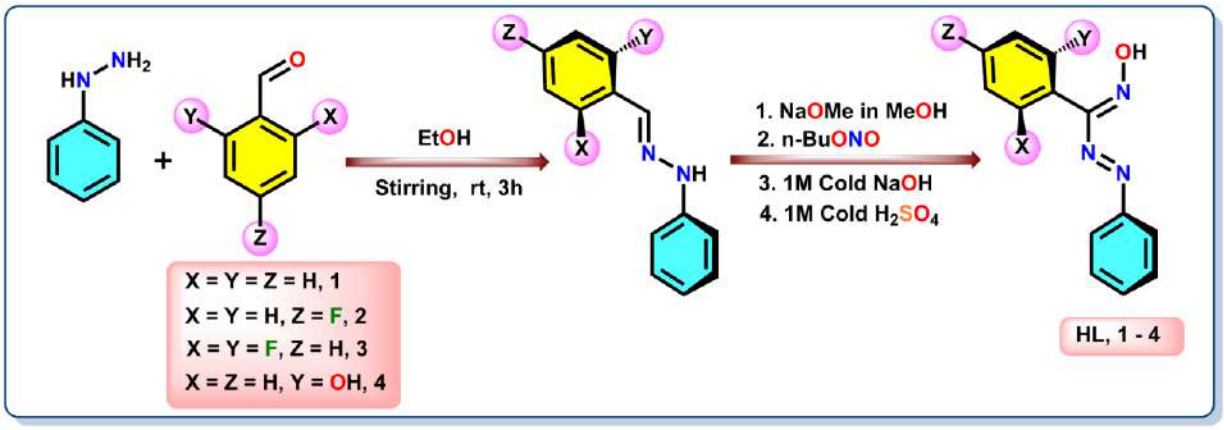

Scheme 2.1: Schematic representation of synthesis of diaryl-azo-oxime ligands (**1-4**)

We have been striving to explore and figure out the electron extracting ability of coordinated diaryl-azo-oximes in order to effectuate certain unusual redox transformations.[17-18] We are

further motivated to synthesize suitable complexes of azo-oximes where the ligand skeleton may become redox active in presence of ruthenium(II) and this perception may be skilfully employed to bring about electron-transfer catalysis for synthesis of value-added organic compounds in an atom efficient pathway. It is important to note that, to the best of our knowledge, electron-transfer catalysis involving azo-oximates has not been documented. In the present work, we have synthesized certain new ruthenium(II) complexes with four different diaryl-azo-oximes of type PhN=NC(Ar)NOH, HL (**1**-**4**) (Scheme 2.1), by varying the Ar groups (Scheme 2.2) in order to demonstrate how the pendant aryl group can play a crucial role in the ligand-centric redox catalysis (See Chapter 3). In fact, we have chosen the aryl groups in such a way that some are electron withdrawing and some have electron donor ability. The structural features, electrochemical properties and theoretical studies have been performed for the complexes *trans*-[RuL(CO)Cl(PPh_3)$_2$], **Ru1**-**Ru4** in order to have a perception of their prospects to bring about ligand-mediated redox transformation.

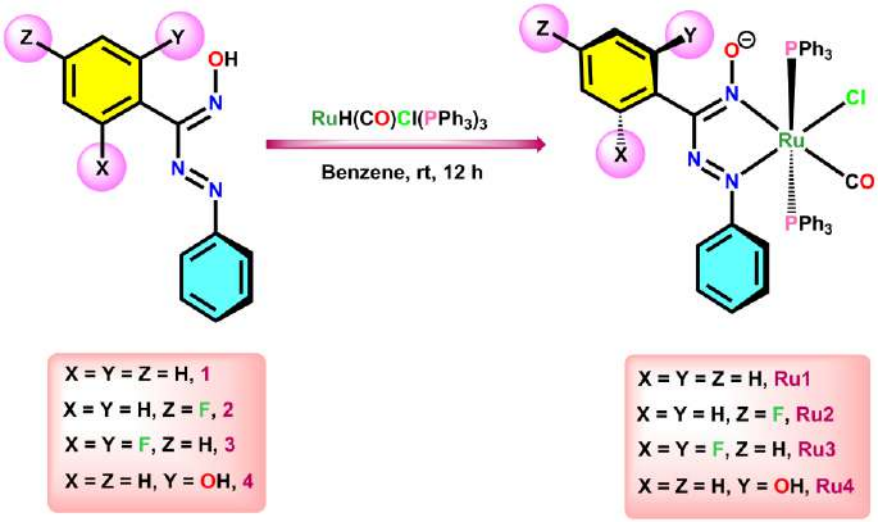

Scheme 2.2: Synthetic strategy of the ruthenium complexes of type *trans*-[Ru(L)(CO)Cl(PPh_3)$_2$], **Ru1**-**Ru4**

2.2 Results and Discussion

2.2.1 Synthesis and Characterization of the catalysts

The ligand **1** was synthesized following a reported procedure,[19-20] and similar methodologies were employed for the preparation of the other ligands **2**-**4** (Scheme 2.1), using phenylhydrazine and various aldehydes as starting materials. These ligands feature two distinct donor sites: $N_{oximato}$ and N_{azo} group, with the overall azo-oxime framework exhibiting electron-deficient character upon coordination. The ruthenium(II) complexes $[RuL(CO)Cl(PPh_3)_2]$ were obtained by stirring the ligands **1**-**4** with $[RuH(CO)Cl(PPh_3)_3]$ in a 1:1 molar ratio at room temperature in dry and degassed benzene for 12 h. The reaction afforded a dark pinkish-red solution, which, upon solvent removal and chromatographic purification, yielded the desired complexes in good yields. The diamagnetic nature of the resulting Ru(II) complexes was confirmed by their ^1H NMR spectra, with signals appearing in the range of 6.6–9.0 ppm (Figure 2.6.A9, 2.6.A12, 2.6.A16 and 2.6.A20). Furthermore, the presence of magnetically equivalent and trans-disposed PPh_3 ligands in all complexes was verified by $^{31}P\{^1H\}$ NMR spectroscopy (Figure 2.6.A11, 2.6.A15, 2.6.A19 and 2.6.A22). The solid-state crystal structure of ligand **3**, determined by single-crystal X-ray diffraction (SCXRD), provides key insights into its molecular conformation and bonding features (Figure 2.1). The structure reveals that the oxime, azo, and phenyl moieties are arranged in a nearly coplanar fashion, indicating extensive electron delocalization across these units. In contrast, the pendant difluorophenyl moiety is oriented almost orthogonally to the plane of the azo-oxime core, likely due to steric interactions or crystal packing effects that influence its spatial arrangement. The geometric parameters of key functional groups further support the observed structural features. The azo (–N=N–) linkage exhibits a bond length of 1.250(2) Å, which is consistent with a typical free azo bond and indicative of a well-delocalized π-system. Within the oxime unit, the C–N bond measures 1.285(2) Å, while the N–O bond length is 1.3707(19) Å. These bond lengths fall within

expected ranges for oxime functionalities and suggest partial delocalization of electron density between the nitrogen and oxygen atoms. Such structural characteristics are crucial for understanding the electronic properties and potential reactivity of **3**, especially in the context of coordination chemistry and redox behaviour. Comprehensive crystallographic details and selected metrical parameters are presented in Table 2.1 and Table 2.2, providing a thorough account of the molecular geometry. Similarly, molecular structures of ruthenium(II) complexes reveal that azo-oxime ligands act as bidentate monoanionic $N_{oximato}$ and N_{azo}, donors, forming a five-member ring but the oximato–O, owing to its inherent hardness, is not involved in coordination with the softer Ru(II). The two phosphine groups are in trans disposition. All the complexes of type *trans*-[RuL(CO)Cl$(PPh_3)_2$] crystallize in monoclinic space groups and details of crystallographic data are provided in Table 2.3. The ORTEP diagrams of complexes **Ru1**-**Ru4** are represented in Figures 2.2-2.5. It has been observed that there is a marked difference in the Ru–N_{azo} and Ru–N_{oxime} lengths in the complexes. They may be attributed primarily to electronic effects of pendant aryl group of the coordinated ligand. Also, it can be due to π–π stacking interactions between a phenyl ring of PPh_3 and the five-membered chelate ring. In the case of **Ru1** and **Ru2**, this interaction is stronger (Figure 2.6 and Table 2.5-2.8) as compared to

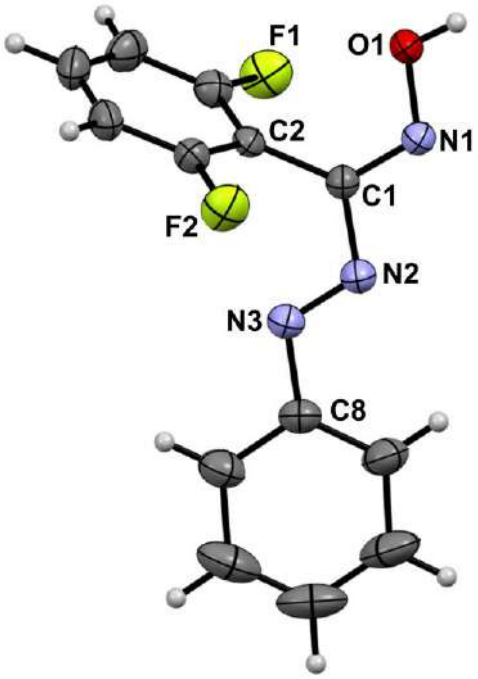

Figure 2.1: ORTEP diagram of ligand **1** (Thermal ellipsoids are set at 50% probability)

that in **Ru3** and hence the Ru–N lengths in the former two are somewhat longer than that of the latter. It is for the same reason that N–N lengths in **Ru1** and **Ru2** are slightly longer than that in **Ru3**. For **Ru4**, the Ru–N lengths are the longest and this may be explained based on oximato-O…O (hydroxyphenyl) interaction (2.598(4) Å) (Figure 2.7, Table 2.10), that leads to weakening of electron cloud delocalization within the azo-oxime skeleton. This is also reflected in N–O length which is much longer than that in other three. In the case of **Ru3**, there are two F-atoms in the pendant aryl group and weak intramolecular F…π interactions are observed. (Figure 2.6, Table 2.9).

Table 2.1: Crystallographic details of **3**

	3
Empirical formula	$C_{13}H_9N_3OF_2$
T/K	273.15
fw	261.23
Crystal system	Triclinic
Space Group	$P\bar{1}$
a/Å	12.5353(5)
b/*Å*	13.1282(5)
c/ *Å*	14.2648(6)
α/deg	112.829(2)
β/deg	111.535(2)
γ/deg	98.357(2)
V/ *Å*^{3}	1895.82(14)
Z	6
D_c/Mgm^{-3}	1.373
μ/mm^{-1}	0.111
F(000)	804
cryst size/mm^3	0.5×0.3×0.2
θ/deg	2.43– 26.07
Measured reflns	39820
Unique reflns	9983
[a]GOF on F^2	1.039
R1[b], wR2[c][$I>2\sigma(I)$]	0.0510, 0.1200
R1, wR2	0.0874, 0.1335
[a]GOF = $\{\Sigma[w(F_o{}^2-F_c{}^2)2]/(n-p)\}^{1/2}$. [b]R1 = Σ [$\lvert F_o\rvert-\lvert F_c\rvert$]/ Σ $\lvert F_o\rvert$. [c]wR2 = $[\Sigma\ [w(F_o{}^2-F_c{}^2)^2]/\ \Sigma\ [w(F_o{}^2)^2]]^{1/2}$ where w = 1/[$\sigma^2(F_o{}^2)+(aP)^2+bP]$, P = $(F_o{}^2+2F_c{}^2)/3$.	

Table 2.2: Crystallographic and theoretical metrical theoretical metrical parameters for **3**

Metrical Parameters	Bond length (Å)		Metrical Parameters	Bond angle (°)	
	Expt.	Theo.		Expt.	Theo.
N2–N3	1.250(2)	1.256	N1–C1–N2	111.40(15)	112.25
N1–O1	1.3707(19)	1.377	N1–C1–C2	125.76(16)	125.07
C1–N1	1.285(2)	1.287	N2–C1–C2	122.84(15)	122.66
C1–N2	1.411(2)	1.407	C1–N2–N3	113.28(15)	113.70
C8–N3	1.422(2)	1.415	N2–N3–C8	114.33(16)	114.91
C1–C2	1.488(2)	1.487	C1–N1–O1	113.40(14)	112.38

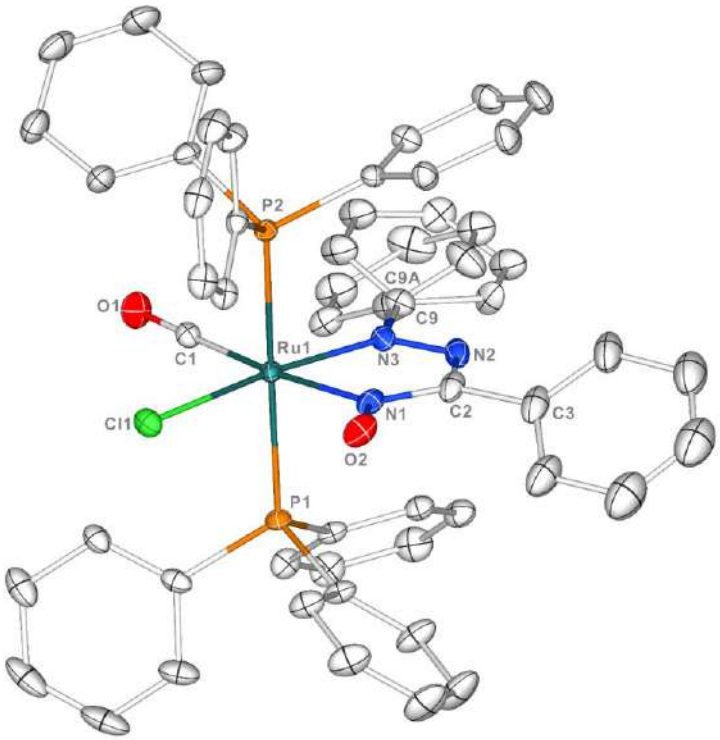

Figure 2.2: ORTEP diagram of **Ru1** with partial atom numbering scheme (Hydrogen atoms are omitted for clarity, and thermal ellipsoids are set at 50% probability)

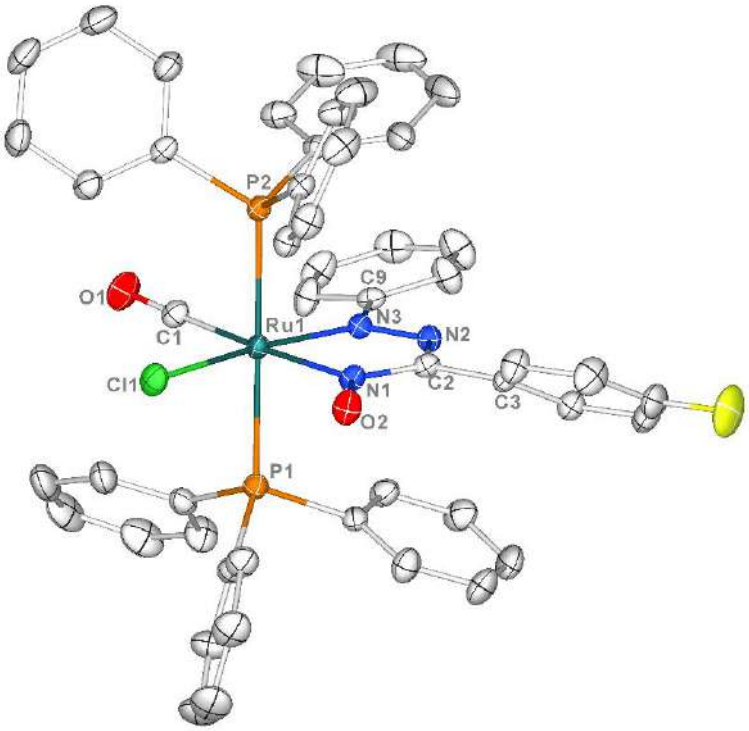

Figure 2.3: ORTEP diagram of **Ru2** with partial atom numbering scheme (Hydrogen atoms are omitted for clarity, and thermal ellipsoids are set at 50% probability)

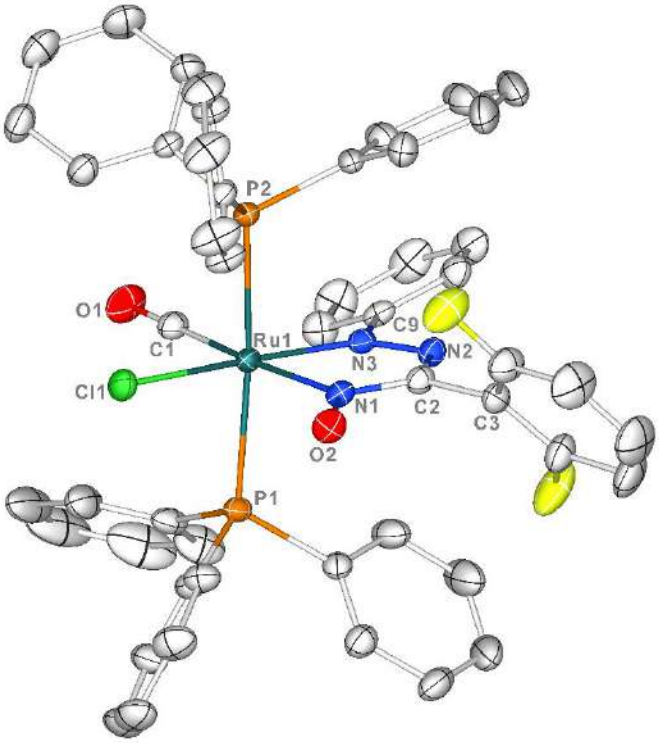

Figure 2.4: ORTEP diagram of **Ru3** with partial atom numbering scheme (Hydrogen atoms are omitted for clarity, and thermal ellipsoids are set at 50% probability)

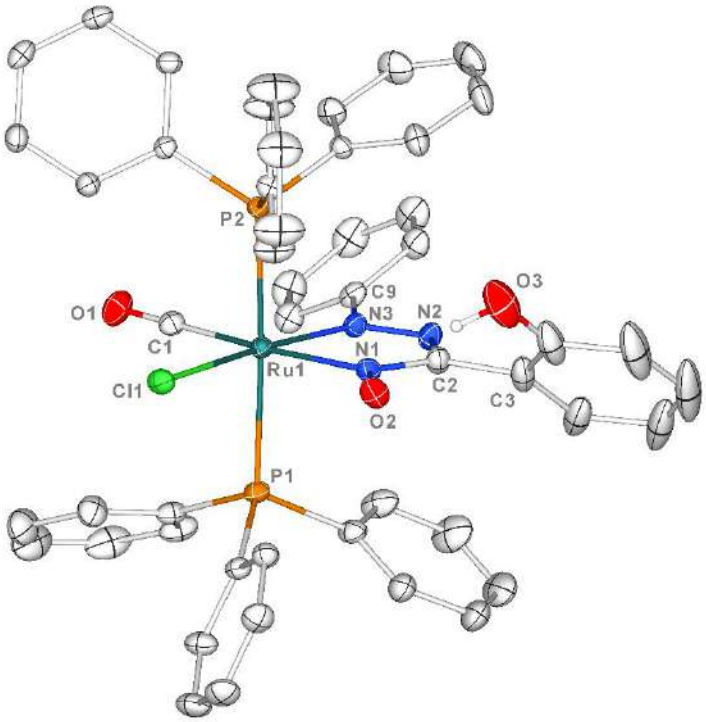

Figure 2.5: ORTEP diagram of **Ru4** with partial atom numbering scheme (Hydrogen atoms are omitted for clarity and thermal ellipsoids are set at 50% probability)

Table 2.3: Crystallographic details of **Ru1**, **Ru2**, **Ru3** and **Ru4**

	Ru1	**Ru2**	**Ru3**	**Ru4**
Empirical formula	$C_{50}H_{40}N_3ClO_2P_2Ru$	$C_{50}H_{39}N_3ClFO_2P_2Ru$	$C_{50}H_{38}N_3ClF_2O_2\ P_2Ru$	$C_{50}H_{40}N_3ClO_3P_2Ru$
T/K	273.15	273.15	273.15	273.15
fw	913.31	931.30	949.29	929.31
Crystal system	Monoclinic	Monoclinic	Monoclinic	Monoclinic
Space Group	P 1 21 1	P 1 21/n 1	P 1 21/c 1	P 1 21/c 1
a/Å	11.0288(4)	10.5558(3)	12.2380(5)	20.1633(17)
b/*Å*	16.7801(6)	21.1187(7)	18.6710(7)	12.2066(10)
c/ *Å*	12.7714(4)	19.2437(6)	20.9395(8)	18.6526(16)
α/deg	90	90	90	90
β/deg	113.1940(10)	94.6440(10)	99.9840(10)	109.084(3)
γ/deg	90	90	90	90
V/ *Å*^{3}	2172.50(13)	4275.8(2)	4712.1(3)	4338.6(6)
Z	2	4	4	4
D_c/Mgm^{-3}	1.396	1.447	1.338	1.423
μ/mm^{-1}	0.540	0.553	0.506	0.543
F(000)	936	1904	1936	1904

cryst size/mm^3	0.6×0.4×0.3	0.4×0.2×0.1	0.5×0.3×0.2	0.35×0.26×0.18
θ/deg	2.98–29.99	2.163–25.715	1.690–28.422	2.585–29.177
Measured reflns	41188	115966	160291	98620
Unique reflns	12639	8138	11794	11679
[a]GOF on F^2	1.055	1.249	1.142	1.086
R1[b], wR2[c][$I>2\sigma(I)$]	0.0315, 0.0824	0.0552, 0.0948	0.0496, 0.1068	0.0342, 0.0781
R1, wR2	0.0349, 0.0841	0.0655, 0.0989	0.0606, 0.1126	0.0460, 0.0887
[a]GOF = $\{\Sigma[w(F_o{}^2-F_c{}^2)2]/(n-p)\}^{1/2}$. [b]R1 = $\Sigma\,[\|F_o\|-\|F_c\|]/\Sigma\,\|F_o\|$. [c]wR2 = $[\Sigma\,[w(F_o^2-F_c^2)^2]/\Sigma\,[w(F_o^2)^2]]^{1/2}$ where $w = 1/[\,\sigma^2(F_o^2)+(aP)^2+bP]$, $P = (F_o^2+2F_c^2)/3$.				

Table 2.4: Selected crystallographic and theoretical bond length (Å) and bond angles (º) of **Ru1**, **Ru2**, **Ru3** and **Ru4**

Metrical Parameters	Ru1		Ru2		Ru3		Ru4
	Expt.	Theo.	Expt.	Theo.	Expt.	Theo.	Expt.
Ru1–N1	2.087(3)	2.132	2.083(3)	2.135	2.076(2)	2.140	2.0959(17)
Ru1–N3	2.040(3)	2.089	2.052(3)	2.080	2.042(2)	2.103	2.0300(16)
Ru1–C1	1.882(3)	1.900	1.878(4)	1.903	1.881(3)	1.899	1.886(2)
Ru1–Cl1	2.4384(9)	2.519	2.4213(11)	2.528	2.4239(8)	2.515	2.4239(5)
Ru1–P1	2.4233(8)	2.502	2.4283(11)	2.515	2.4257(7)	2.507	2.4225(6)
Ru1–P2	2.4124(7)	2.520	2.4075(11)	2.512	2.4223(7)	2.538	2.4103(16)
N2–N3	1.316(5)	1.285	1.303(4)	1.282	1.301(3)	1.286	1.296(2)
N1–O2	1.273(4)	1.254	1.265(4)	1.257	1.267(3)	1.253	1.302(2)
C1–O1	1.147(4)	1.148	1.147(5)	1.147	1.139(4)	1.147	1.137(3)
C2 –N1	1.359(5)	1.359	1.349(5)	1.357	1.343(4)	1.354	1.337(3)
C2– N2	1.332(6)	1.350	1.352(5)	1.352	1.349(4)	1.342	1.364(3)
C9–N3	1.456(4)	1.436	1.445(5)	1.435	1.444(4)	1.435	1.448(2)
C2–C3	1.486(6)	1.479	1.475(5)	1.477	1.477(4)	1.482	1.482(3)
N1–Ru1–N3	76.26(13)	75.26	76.40(12)	75.33	76.20(9)	75.42	75.69(7)
N1–Ru1–P1	89.47(8)	88.72	88.55(9)	88.49	89.24(7)	89.32	89.75(5)
N1–Ru1–P2	85.94(8)	89.42	91.98(9)	88.59	90.63(6)	92.02	90.12(5)
N3–Ru1–P1	91.10(8)	92.88	89.41(9)	91.85	93.88(6)	93.34	91.77(5)
N3–Ru1–P2	91.27(8)	93.82	90.41(9)	91.55	92.42(6)	94.41	93.57(5)
C1–Ru1–Cl1	87.64(10)	89.10	88.59(13)	87.28	86.97(11)	90.34	87.58(6)
C1–Ru1–P1	93.60(10)	93.36	93.50(13)	94.57	91.99(9)	91.83	91.32(6)
C1–Ru1–P2	91.26(10)	89.21	85.96(13)	88.71	88.67(9)	87.58	89.34(6)
Cl1–Ru1–P1	86.30(3)	86.89	89.89(4)	86.13	86.70(3)	87.58	86.787(18)
Cl1–Ru1–P2	90.72(3)	85.93	90.39(4)	90.02	86.85(3)	84.65	87.741(17)
N1–Ru1–Cl1	97.06(10)	96.64	93.36(9)	97.98	97.72(7)	95.33	93.36(9)

N3–Ru1–C1	99.16(14)	98.97	101.66(15)	99.46	99.09(12)	98.87	97.93(5)
P1–Ru1–P2	174.19(3)	172.33	179.39(4)	174.81	173.48(3)	172.21	174.454(17)

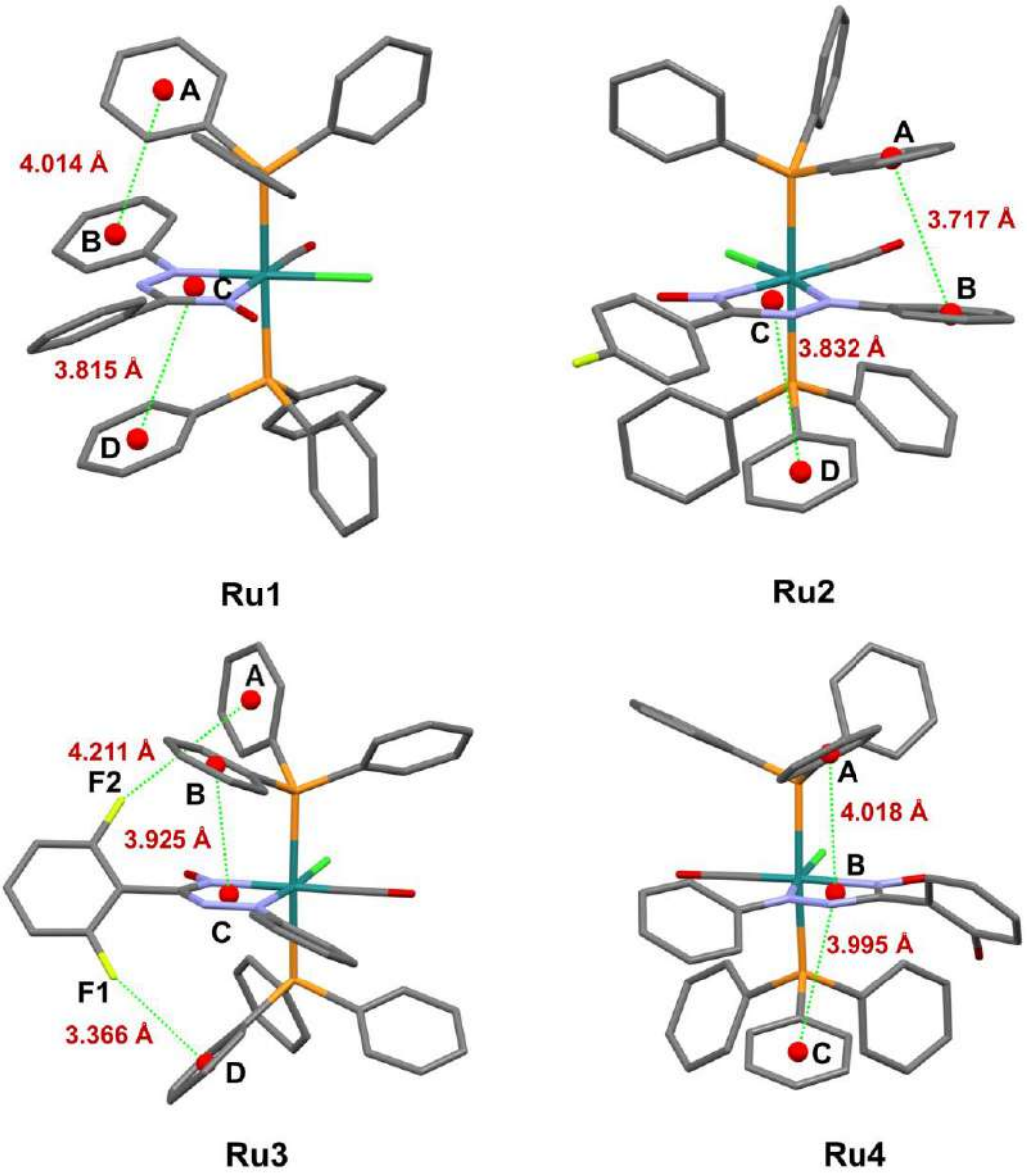

Figure 2.6: Intramolecular π–π stacking and F–π interactions in **Ru1, Ru2, Ru3** and **Ru4**

Table 2.5: Intra-molecular π-π stacking parameter* of **Ru1**

Stacking Parameters	Ring A–B	Ring C–D
d[$C_g(I) - C_g(J)$] Å/α°	4.041(3)/28.7(2)	3.815(2)/22.4(2)
d[Cg(*I*) – R(*J*)] Å/β°	3.575(2)/33.8	3.574(2)/40.6
d[Cg(*J*) – R(*I*)] Å/γ°	3.3597(17)/27.8	2.8973(14)/20.5

Table 2.6: Intra-molecular π-π stacking parameter* of **Ru2**

Stacking Parameters	Ring A–B	Ring C–D
d[$C_g(I) - C_g(J)$] Å/α°	3.717(3)/15.0(2)	3.832(2)/22.5
d[Cg(*I*) – R(*J*)] Å/β°	3.6640(19)/24.5	2.9612(13)/21.5
d[Cg(*J*) – R(*I*)] Å/γ°	3.383(2)/9.7	3.566(2)/39.4

Table 2.7: Intramolecular π-π stacking parameter*of **Ru3**

Stacking Parameters	Ring B–C
d[$C_g(I) - C_g(J)$] Å/α°	3.9251(19)/24.65(16)
d[Cg(*I*) – R(*J*)] Å/β°	3.0073(10)/22.1
d[Cg(*J*) – R(*I*)] Å/γ°	3.6371/40.0

Table 2.8: Intra-molecular π-π stacking parameter*of **Ru4**

Stacking Parameters	Ring A–B	Ring C–D
d[$C_g(I) - C_g(J)$] Å/α°	4.0174(15)/23.29(12)	3.9945(15)/30.76(12)
d[Cg(*I*) – R(*J*)] Å/β°	2.9498(8)/23.3	3.7882(12)/43.1
d[Cg(*J*) – R(*I*)] Å/γ°	3.6899(12)/42.8	2.9184(8)/18.5

*$C_g(I)$ = Centroid of ring *I*, $C_g(J)$ = Centroid of ring *J*, d[$C_g(I) - C_g(J)$] = Separation between two ring centroids, d[Cg(*I*) – R(*J*)] = Perpendicular distance of Cg(*I*) on ring *J*, d[Cg(*J*) – R(*I*)] = Perpendicular distance of Cg(*J*) on ring *I*, α = Dihedral angle between Planes *I* of ring *I* and plane *J* of ring *J*, β and γ = Angle between the vector $C_g(I) - C_g(J)$ and the normal to plane P(*I*) or P(*J*) from $C_g(I)$ and $C_g(J)$ respectively.

Table 2.9: Intramolecular F – π interaction parameter*of **Ru3**

Bond (X–Y)	d[($C_g(I)$ – Y]/Å	X–Y…$C_g(I)$/deg	d[X–$C_g(I)$]/ Å
C4–F1	3.336(3)	136.5(2)	4.405

*d[(Cg(*I*) – Y] = Distance between centroid of ring *I* (C_g) and Y, X–Y…$C_g(I)$ = Angle between C_g-Y vector and ring *I* normal in degree, d[Y–$C_g(I)$] = Distance between centroid of ring *I* (C_g) and X

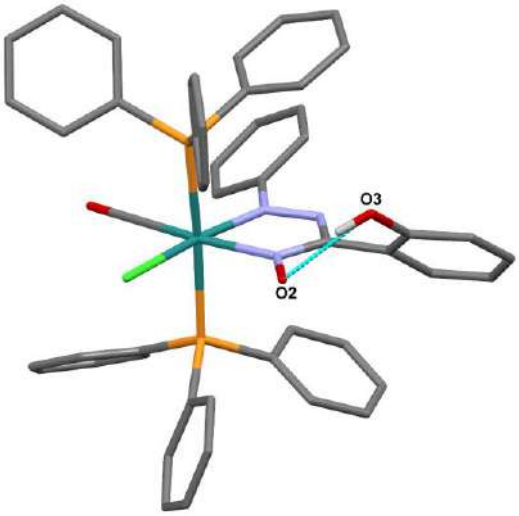

Figure 2.7: Intramolecular H-Bonding in **Ru4**

Table 2.10: Hydrogen bonding parameter of **Ru4**

Type of H-Bonding	Donor (D)	Acceptor (A)	D – A(Å)	D–H…..A(deg)
Intra-molecular	O3	O2	2.598(4)	155

2.2.2 Electronic Spectra

The UV-VIS absorption spectra of **Ru1, Ru2**, **Ru3** & **Ru4** were taken in dichloromethane solution at room temperature. All the spectra were plotted together with their respective theoretically calculated spectra except for **Ru4** (Figure 2.8). All complexes exhibit multiple transition and can be assigned as charge transfer (CT) transition within azo-oxime moiety with significant contribution from metal d-orbitals. Time-dependent density functional theory (TD-DFT) in dichloromethane was performed using the CPCM model to realize the absorption spectra. The major transitions along with their corresponding energies, characteristics and oscillator strengths (*f*) of all the complexes have been given in Table 2.11-2.13. Natural Transition Orbital (NTO) analysis was utilised to make out the basis of transitions and are represented in Table 2.14-2.16. A compact diagram of transition density amongst the ground and excited states in terms of expansion into single-particle transitions (hole and electron states

for each given excitation) is given by this method. The occupied and unoccupied NTO's are epitomized as 'electron' and 'hole'.

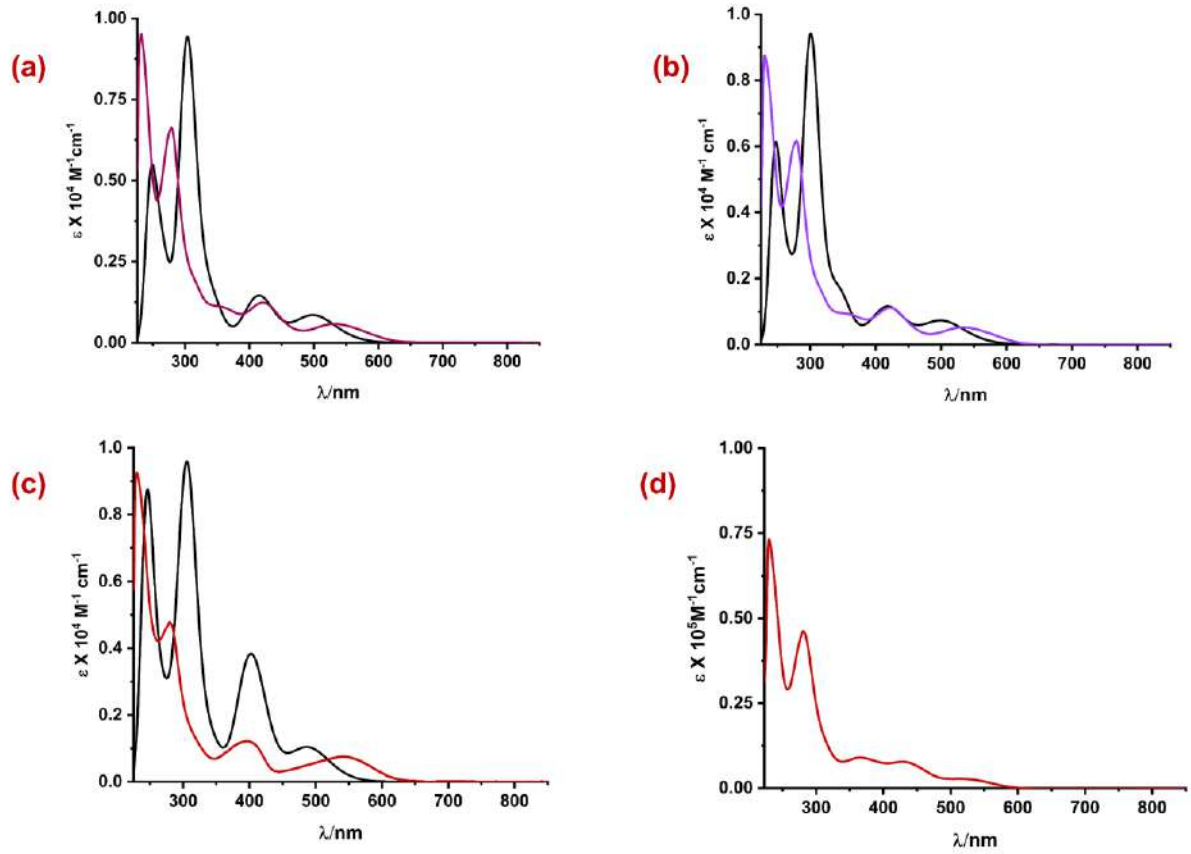

Figure 2.8: Experimental (a) Magenta for **Ru1**, (b) purple for **Ru2**, (c) marron for **Ru3** & (d) red for **Ru4** and Calculated (black) absorption spectra of **Ru1**, **Ru2** & **Ru3** respectively

In **Ru1**, the transition at 534 nm is computed to be near λ_{theo} = 498 nm (2.4871 eV, f = 0.0766) and ascribed as mainly [π(azo + oxime) → π*(azo + oxime) + d_{xz} → d_{yz}] ILCT with little d-d transition. The next band at 419 nm is quantified at near about λ_{theo} = 416 nm (2.9774 eV, f = 0.1186) and assigned as [π(Cl) → π*(azo + oxime)] LLCT transition along with some amount d-d transition. The band near UV region is observed at 277 nm which is calculated at λ_{theo} = 303 nm (4.0853 eV, f = 0.3764), having [π(PPh_3) → π*(Cl + PPh_3) + d_{yz} → d_{z^2}] ILCT combined with LLCT and d-d transition. The band at very near to UV region is detected at 232 nm which is evaluated at λ_{theo} = 247 nm (5.0059 eV, f = 0.0743), having [π(Cl + Oxime) → π*(PPh_3) + $d_{x^2-y^2}$ → d_{xz}] LLCT with slight contribution from d-d transition.

In **Ru2**, the lowest energy band at 528 nm is computed to be near λ_{theo} = 499 nm (2.4822 eV, *f* = 0.0634) and assigned as primarily [π(Azo + Oxime + Ph) → π*(Azo + oxime) + d_{xz} → d_{yz}] ILCT with small amount of d-d transition. The next following band at 420 nm is determined at close to λ_{theo} = 428 nm (2.8956 eV, *f* = 0.0221) and assigned as [π(Cl + Oxime) → π*(Azo + Oxime + Ph) + $d_{x^2-y^2}$ → d_{yz}] ILCT transition with some contribution from d-d transition. The band near UV region is observed at 358 nm which is calculated at λ_{theo} = 393 nm (3.1515 eV, *f* = 0.0294), having [π(PPh_3) → π*(Azo + Oxime + Ph) + d_{xz} → d_{yz}] LLCT combined with LLCT and d-d transition. The band at near to UV region is detected at 279 nm which is evaluated at λ_{theo} = 300 nm (4.1194 eV, *f* = 0.2933), having [π(PPh_3) → π*(PPh_3) + d_{yz} → d_{z^2}] ILCT with little contribution from d-d transition. Another band at near about UV region is computed at 232 nm and quantified at λ_{theo} = 246 nm (5.0202 eV, *f* = 0.0454), having [π(PPh_3) → π*(Ph + PPh_3) + d_{yz} → $d_{x^2-y^2}$] LLCT together with d-d transition.

For **Ru3**, the band with lowest energy is observed at 543 nm which is enumerated at λ_{theo} = 487 nm (2.5432 eV, *f* = 0.0612) and can be ascribed as mostly [π (Cl +Azo + Oxime + Ph) → π*(Azo + Oxime + Ph) + d_{xz} → d_{yz}] ILCT, LLCT as well as small amount of d-d transition. The next band appeared at 399 nm which is calculated at λ_{theo} = 406 nm (3.0510 eV, *f* = 0.1255) and can be ascribed as typically [π (Cl + Oxime) → π*(Azo + Oxime + Ph) + d_{xz} → d_{yz}] ILCT, LLCT along with minute amount of d-d transition. The band at 279 nm which composed with two transitions computed at λ_{theo} = 307 nm (4.0279 eV, *f* = 0.3605). The first transition can be assessed as mostly [π (Cl + Oxime + Ph + PPh_3) → π*(Cl + Azo + Oxime + PPh_3) + d_{xz} → d_{yz}] ILCT and d-d transition while another one may be designated as [π (Cl + Oxime) → π*(Cl + PPh_3) + d_{xz} → d_{z^2}] ILCT and d-d transition. The last band at 230 nm is determined at λ_{theo} = 248 nm (4.9841 eV, *f* = 0.0193) and can be attributed as [π (Cl + Oxime) → π*(PPh_3)] ILCT, LLCT and MLCT.

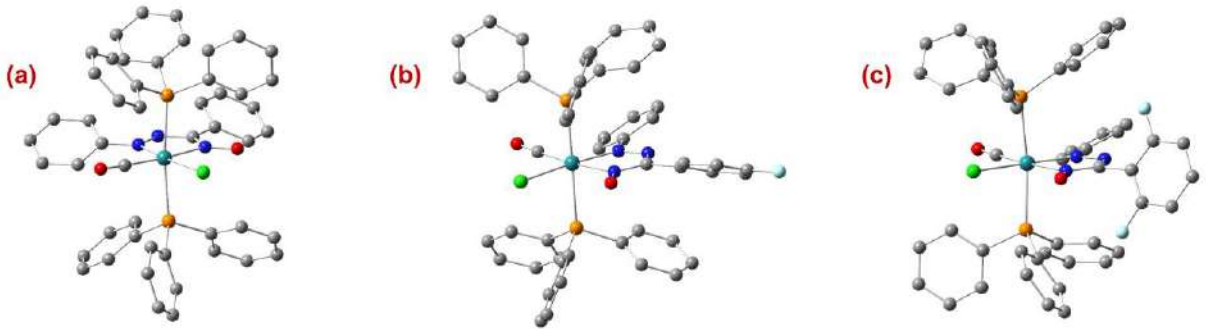

Figure 2.9: Optimized geometry of (a) **Ru1**, (b) **Ru2** and (c) **Ru3** at (R)B3LYP level of theory using 6-311+G(d,p) basis set for non-H atoms and LANL2DZ basis for Ru

Table 2.11: Main Optical Transition at the TD-DFT/(R)B3LYP level of theory using 6-311+G(d,p) basis set for non-H atoms and LANL2DZ basis for Ru for the complex **Ru1** with composition in terms of Molecular Orbital Contribution of the Transition, Computed Vertical Excitation Energies, and Oscillator Strength in Dichloromethane.

Transition	CI	Composition	E (eV)	Oscillator strength (*f*)	λ_{theo} (nm)
$S_0 \rightarrow S_2$	0.63328	HOMO → LUMO (80%)	2.4871	0.0766	498.50
$S_0 \rightarrow S_5$	0.63410	H−2 → LUMO (80%)	2.9774	0.1186	416.41
$S_0 \rightarrow S_{27}$	0.49547	H−3 → L+1 (49%)	4.0853	0.3764	303.48
$S_0 \rightarrow S_{83}$	0.32198	H−4 → L+4 (21%)	5.0059	0.0743	247.67

Table 2.12. Main Optical Transition at the TD-DFT/(R)B3LYP level of theory using 6-311+G(d,p) basis set for non-H atoms and LANL2DZ basis for Ru for the complex **Ru2** with composition in terms of Molecular Orbital Contribution of the Transition, Computed Vertical Excitation Energies, and Oscillator Strength in Dichloromethane

Transition	CI	Composition	E (eV)	Oscillator strength (*f*)	λ_{theo} (nm)
$S_0 \rightarrow S_2$	0.62095	HOMO → LUMO (77%)	2.4822	0.0634	499
$S_0 \rightarrow S_4$	0.53343	H−4 → LUMO (57%)	2.8956	0.0221	428
$S_0 \rightarrow S_6$	0.67492	H−3 → LUMO (91%)	3.1515	0.0294	393
$S_0 \rightarrow S_{27}$	0.39175	H−3 → L+1 (31%)	4.1194	0.2933	300
$S_0 \rightarrow S_{82}$	0.41354	H−3 → L+4 (34%)	5.0202	0.0454	246

Table 2.13: Main Optical Transition at the TD-DFT/(R)B3LYP level of theory using 6-311+G(d,p) basis set for non-H atoms and LANL2DZ basis for Ru for the complex **Ru3** with composition in terms of Molecular Orbital Contribution of the Transition, Computed Vertical Excitation Energies, and Oscillator Strength in Dichloromethane

Transition	CI	Composition	E (eV)	Oscillator strength (*f*)	λ_{theo} (nm)
$S_0 \rightarrow S_2$	0.62256	HOMO → LUMO (78%)	2.5432	0.0612	487.51
$S_0 \rightarrow S_5$	0.62859	H−2 → LUMO (79%)	3.0510	0.1255	406.37
$S_0 \rightarrow S_{24}$	0.34323 0.40551	H−2 → L+1 (24%) H−3 → L+1 (33%)	4.0279	0.3605	307.81
$S_0 \rightarrow S_{73}$	0.32840	H−4 → L+2 (22%)	4.9841	0.0193	248.75

Table 2.14: Natural transition orbitals (NTOs) for complex **Ru1** illustrating the nature of singlet excited states in the absorption bands in the range 200–800 nm. For each state, the respective number of the state, transition energy (eV), and the oscillator strength (in parentheses) are listed. Shown are only occupied (holes) and unoccupied (electrons) NTO pairs that contribute more than 15% to each excited state.

		Hole	Electron
534 nm	S_2 w = 0.8020 2.4871 (0.0766) 498.50 nm ILCT & d-d π (Azo + Oxime) → π* (Azo + Oxime) & d_{xz} → d_{yz}	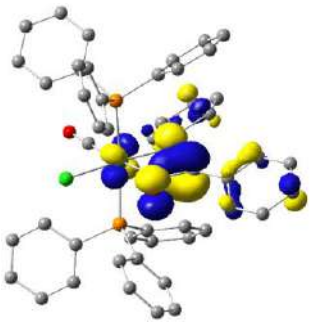	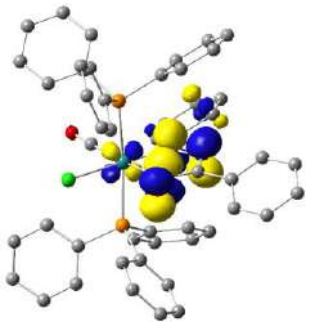
419 nm	S_5 w = 0.8041 2.9774 (0.1186) 416.41 nm LLCT & d-d π (Cl) → π* (Azo + Oxime) & d_{xz} → d_{yz}	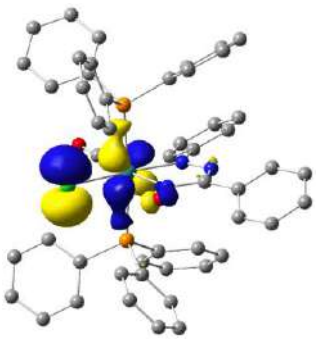	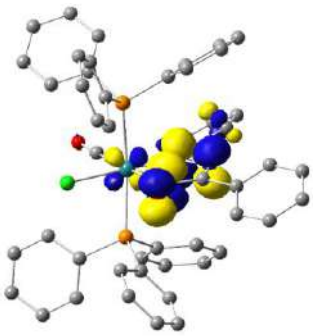

277 nm	S_{27} w = 0.4909 4.0853 (0.3764) 303.48 nm ILCT, LLCT & d-d π (PPh_3) → π* (Cl+ PPh_3) & $d_{yz} \rightarrow d_{z^2}$	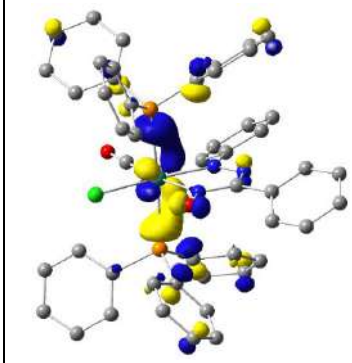	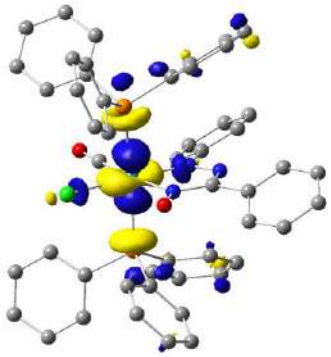
232 nm	S_{83} w = 0.2073 5.0059 (0.0743) 247.67 nm LLCT & d-d π (Cl + Oxime) → π* (PPh_3) & $d_{x^2-z^2} \rightarrow d_{xz}$	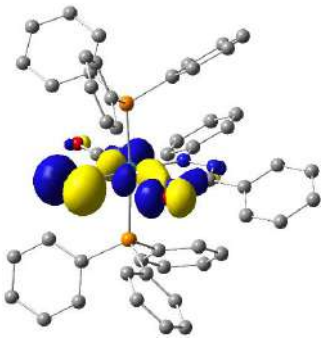	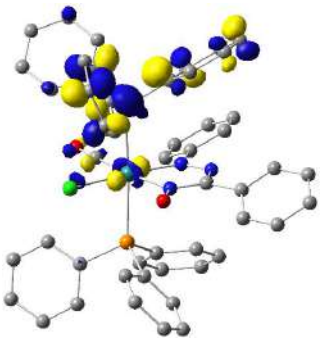

Table 2.15: Natural transition orbitals (NTOs) for complex **Ru2** illustrating the nature of singlet excited states in the absorption bands in the range 200–800 nm. For each state, the respective number of the state, transition energy (eV), and the oscillator strength (in parentheses) are listed. Shown are only occupied (holes) and unoccupied (electrons) NTO pairs that contribute more than 15% to each excited state

		Hole	**Electron**
528 nm	S_2 w = 0.7711 2.4822 (0.0634) 499.49 nm ILCT & d-d π (Azo + Oxime + Ph) → π* (Azo + Oxime) & $d_{xz} \rightarrow d_{yz}$	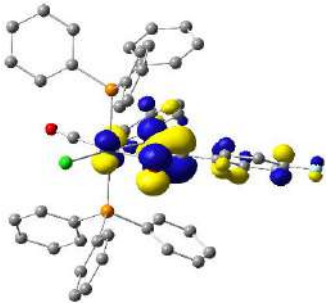	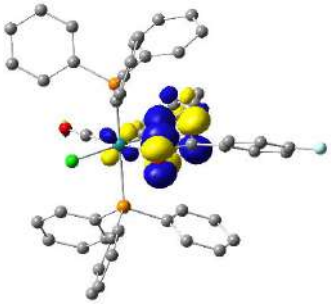

420 nm	*S4* w = 0.5689 2.8956 (0.0221) 428.18 nm ILCT & d-d π (Cl + Oxime) → π* (Azo + Oxime + Ph) & $d_{x^2-y^2} \rightarrow d_{yz}$	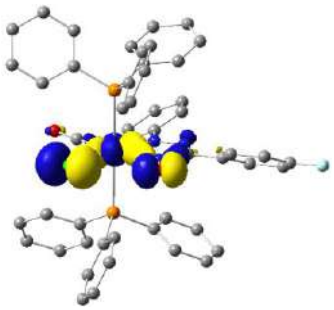	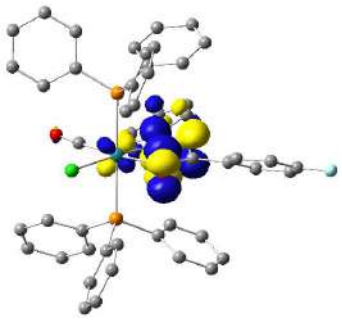
358 nm	*S6* w = 0.9110 3.1515 (0.0294) 393.41 nm LLCT & d-d π (PPh_3) → π* (Azo + Oxime + Ph) & $d_{xz} \rightarrow d_{yz}$	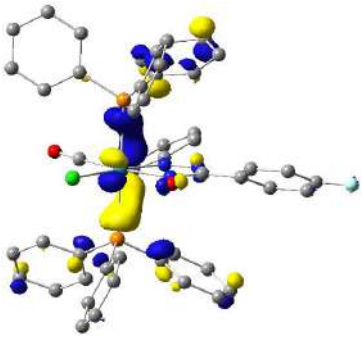	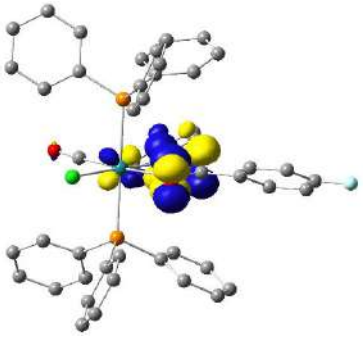
279 nm	*S27* w = 0.3069 4.1194 (0.2933) 300.97 nm ILCT & d-d π (PPh_3) → π* (PPh_3) & $d_{yz} \rightarrow d_{z^2}$	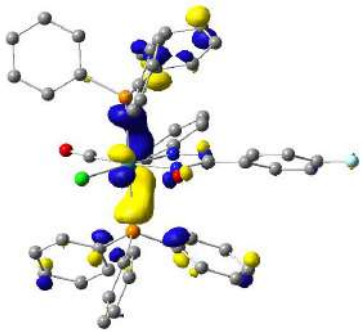	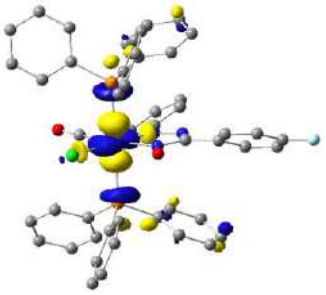
232 nm	*S82* w = 0.3420 5.0202 (0.0454) 246.97 nm LLCT & d-d π (PPh_3) → π* (Ph + PPh_3) & $d_{yz} \rightarrow d_{x^2-y^2}$	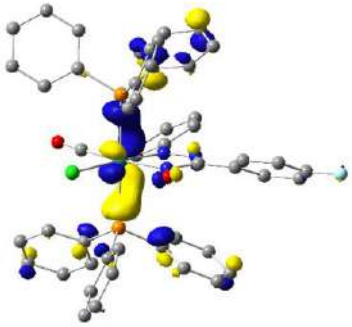	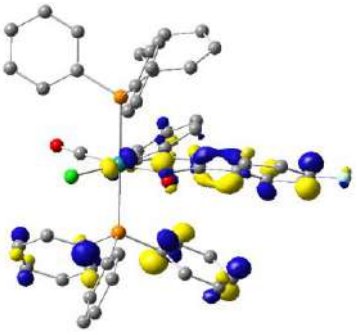

Table 2.16: Natural transition orbitals (NTOs) for complex **Ru3** illustrating the nature of singlet excited states in the absorption bands in the range 200–800 nm. For each state, the respective number of the state, transition energy (eV), and the oscillator strength (in parentheses) are listed. Shown are only occupied (holes) and unoccupied (electrons) NTO pairs that contribute more than 15% to each excited state.

		Hole	**Electron**
543 nm	*S_2* w = 0.7751 2.5432 (0.0612) 487.51 nm ILCT, LLCT & d-d π (Cl + Azo + Oxime + Ph) → π* (Azo + Oxime + Ph) & $d_{xz} \rightarrow d_{yz}$	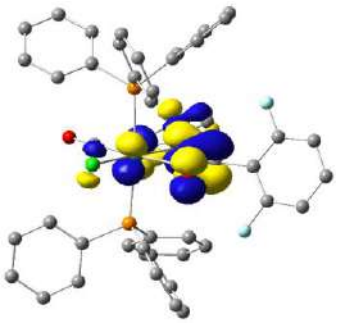	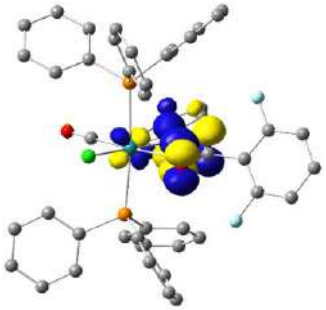
399 nm	*S_5* w = 0.7902 3.0510 (0.1255) 406.37 nm ILCT, LLCT & d-d π (Cl + Oxime) → π* (Azo + Oxime + Ph) & $d_{xz} \rightarrow d_{yz}$	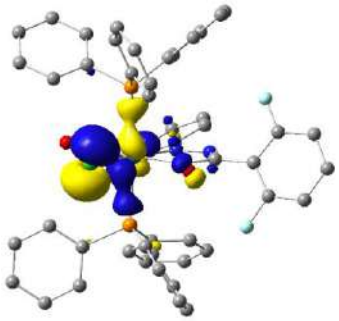	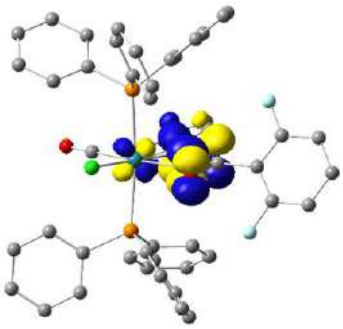
	S_{24} w = 0.2343 4.0279 (0.3605) 307.81 nm ILCT & d-d π (Cl + Oxime) → π* (Cl + PPh_3) & $d_{xz} \rightarrow d_z^2$	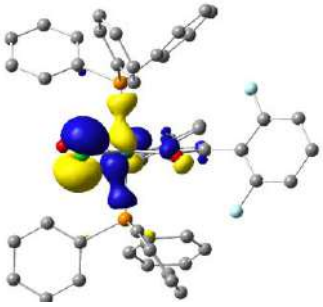	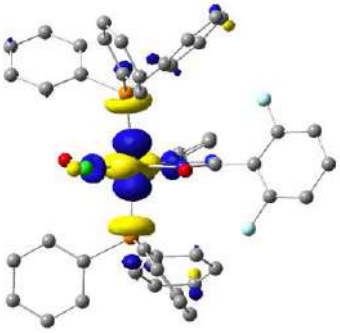

230 nm	S_{73} w = 0.2156 4.9841 (0.0193) 248.75 nm LLCT & MLCT π (Cl + Oxime) → π* (PPh_3)	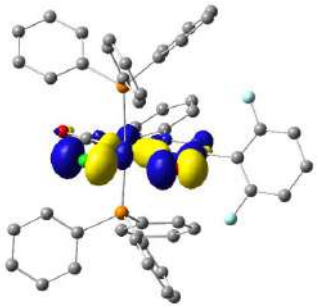	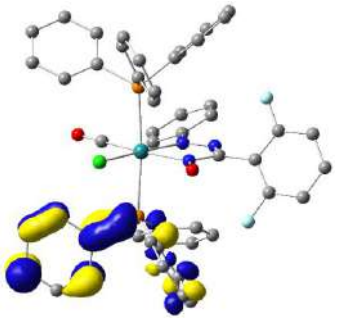

2.2.3 Electrochemistry

The complexes **Ru1**-**Ru4** undergo multiple single-electron quasi-reversible/reversible reductive responses within –0.59 and –1.32V, in acetonitrile/0.1M tetrabutyl ammonium hexafluorophosphate using glassy carbon as working electrode, and saturated Ag/AgCl as the reference electrode (Figure 2.10, Table 2.17). Theoretical considerations reveal that LUMO in all complexes is of π* character having very high contribution from the azo as well as oxime moieties of the coordinated ligand (Table 2.18-2.20). Hence the reductive couples are attributed to azo-oxime reduction of the ligand skeleton. It is evident from Table 2.17 that the one electron azo reductive couples become more negative as we move from **Ru3** → **Ru2** → **Ru1** → **Ru4**, suggesting that the electron acceptor ability is of the order **Ru3** > **Ru2** > **Ru1** > **Ru4**. The complexes *trans*-[RuL(CO)Cl(PPh_3)$_2$] (**Ru1**-**Ru4**) can also be transformed to the corresponding azo-oxime anion radical species [Ru($L^{\bullet-}$)(CO)Cl(PPh_3)$_2$] [**1a**]$^{\bullet-}$ - [**4a**]$^{\bullet-}$ *via* one-electron reduction upon refluxing with t-BuOK for 30 minutes. We have been able to isolate the metastable anion radical complex but couldn't grow X-ray quality single crystals even after persistent attempts. EPR spectra of these complexes in solution at 298 K display a single line isotropic spectra with g_{iso} = 1.999, thereby suggesting the formation of the ligand-centric anion radical complex (Figure 2.14). Optimization of the structure of one of the representative complex, **[Ru3]**$^{\bullet-}$ reveals that spin density is majorly concentrated over azo-oxime portion (Figure 2.14b). The UV-VIS absorption spectra of **[Ru3]**$^{\bullet-}$ in dichloromethane solution at room

temperature are provided in Figure 2.14c, along with their respective theoretically calculated spectra.

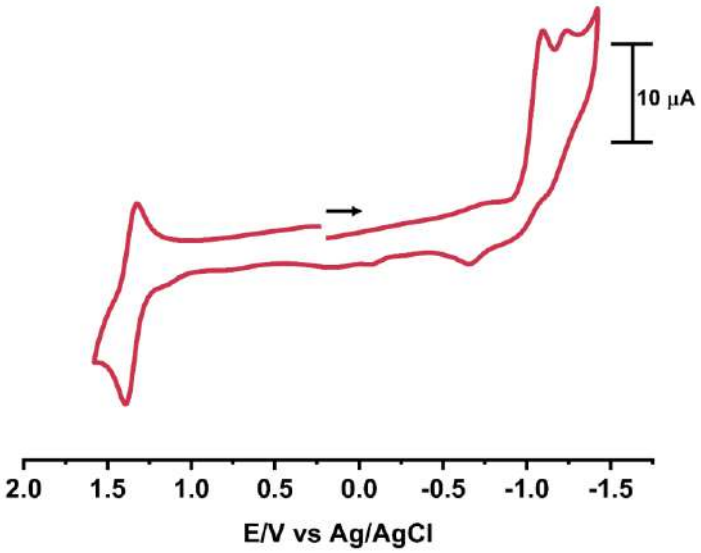

Figure 2.10: Cyclic voltammogram of **Ru3**

Table 2.17: Electrochemical data of Ru(II)-complexes with respect to Ag/AgCl

Complex	$E_{1/2}$/V (ΔE/mV)	
	Oxidation	Reduction
Ru1	+1.23(75[a])	–0.63 (E_p^2/V), –1.08 (E_p^2/V)
Ru2	+1.24(87[a])	–0.61(E_p^2/V), –1.09(E_p^2/V)
Ru3	+1.35(70)	–0.59 (110mV) V, –1.09(E_p^2/V)
Ru4	+1.16, 0.68(E_p^1/V)	–0.65(E_p^2/V), –0.97(E_p^2/V)
$E_{1/2}$ = ½(E_{pa} + E_{pa}), E_{pa} = anodic peak potential; E_{pc} = cathodic peak potential, ΔE = peak-to-peak separation		

Table 2.18: Frontier Molecular Orbital Composition (%) in the ground state for **Ru1**

Orbital	MO	Energy (eV)	Contribution (%)							Contribution
			Ru	Cl	CO	Azo	Oxime	Ph	PPh_3	
226	L+5	-0.92	4	1	2	0	2	9	83	π*(Oxime + PPh_3)
225	L+4	-0.98	1	0	1	1	1	4	91	π*(Ph + PPh_3)
224	L+3	-1.07	2	0	1	0	0	2	94	π*(PPh_3)
223	L+2	-1.09	3	0	3	0	4	11	79	π*(Ph + PPh_3)
222	L+1	-1.65	32	3	1	2	3	0	60	d_z^2 + π*(PPh_3)
221	LUMO	-2.61	6	0	2	35	39	13	4	π*(Azo + Oxime + Ph)

220	HOMO	-5.51	14	5	0	11	38	30	3	d_{xy} + π (Azo + Oxime + Ph)
219	H–1	-6.00	24	39	4	2	24	4	4	$d_{x^2-z^2}$ + π (Azo + Oxime + Ph)
218	H–2	-6.11	20	47	1	3	10	9	10	d_{xz} + π (Cl + Azo + Oxime + Ph)
217	H–3	-6.34	9	31	5	3	48	3	2	d_{xz} + π (Cl + Ph)
216	H–4	-6.51	13	1	0	3	1	7	76	d_{xz} + π (Ph + PPh_3)
215	H–5	-6.80	0	2	0	2	1	89	6	π (Ph + PPh_3)
HOMO–LUMO gap = 2.90 eV										

Table 2.19: Frontier Molecular Orbital Composition (%) in the ground state for **Ru2**

Orbital	MO	Energy (eV)	Contribution (%)							Contribution
			Ru	Cl	CO	Azo	Oxime	Ph	PPh_3	
230	L+5	-0.99	9	2	3	2	8	31	46	$d_{x^2-z^2}$ + π*(Oxime +Ph + PPh_3)
229	L+4	-1.01	2	0	2	0	1	2	93	π*(PPh_3)
228	L+3	-1.13	2	0	2	2	0	4	95	π*(PPh_3)
227	L+2	-1.25	0	0	2	1	1	0	96	π*(PPh_3)
226	L+1	-1.71	32	3	2	3	1	0	60	d_{z^2} + π* (PPh_3)
225	LUMO	-2.69	6	0	2	35	38	15	4	π*(Azo + Oxime + Ph)
224	HOMO	-5.58	14	5	0	10	38	30	3	d_{xz} + π (Azo + Oxime + Ph)
223	H–1	-6.08	25	42	4	2	19	4	6	d_{xy} + π (Azo + Oxime + Ph)
222	H–2	-6.14	20	44	2	3	15	7	10	d_{yz} + π (Cl + Oxime + Ph + PPh_3)
221	H–3	-6.46	8	29	6	3	51	2	2	d_{yz} + π (Cl + CO + Oxime + Ph)
220	H–4	-6.62	13	0	0	3	1	8	74	d_{xy} + π (Ph + PPh_3)
219	H–5	-6.89	0	0	0	0	0	3	96	π (PPh_3)
HOMO–LUMO gap = 2.89 eV										

Table 2.20: Frontier Molecular Orbital Composition (%) in the ground state for **Ru3**

Orbital	MO	Energy (eV)	Contribution (%)							Contribution
			Ru	Cl	CO	Azo	Oxime	Ph	PPh_3	
230	L+5	-0.90	1	1	2	0	4	8	84	π*(PPh_3)
229	L+4	-0.95	3	0	1	1	6	31	60	π*(Ph + PPh_3)
228	L+3	-1.04	4	0	3	1	2	25	64	$d_{x^2-z^2}$ + π*(Ph + PPh_3)
227	L+2	-1.09	0	0	2	1	1	4	92	π*(PPh_3)
226	L+1	-1.63	35	4	1	3	2	0	57	d_{z^2} + π*(PPh_3)
225	LUMO	-2.62	6	0	2	34	39	14	4	d_{xz} + π*(Azo + Oxime + Ph)
224	HOMO	-5.68	23	12	0	11	34	16	3	d_{xz} + π (Cl + Azo + Oxime + Ph)
223	H–1	-6.10	27	43	5	1	20	0	3	d_{xz} + π (Cl + CO + Oxime)
222	H–2	-6.17	10	43	0	4	11	13	19	d_{yz} + π (Cl + Azo + Oxime + Ph)
221	H–3	-6.43	6	21	5	4	59	1	4	d_{xz} + π (Cl + Oxime)
220	H–4	-6.50	14	2	0	3	2	6	73	d_{xz} + π (PPh_3)
219	H–5	-6.78	1	0	0	0	1	2	96	π (PPh_3)
HOMO–LUMO gap = 3.06 eV										

Table 2.21: Frontier Molecular Orbital Composition (**α-MO**) (%) in the ground state for [**3a**]$^{\bullet-}$

Orbital	MO	Energy (eV)	Contribution (%)							Contribution
			Ru	Cl	CO	Azo	Oxime	Ph	PPh_3	
235	L+5	1.55	2	0	0	2	1	26	69	π*(Ph + PPh_3)
234	L+4	1.46	4	0	0	0	1	0	97	π*(PPh_3)
233	L+3	1.44	1	0	0	0	3	0	98	π*(PPh_3)
232	L+2	1.34	2	0	1	0	1	1	95	π*(PPh_3)
231	L+1	1.20	0	0	0	0	0	1	99	π*(PPh_3)
230	LUMO	1.04	24	2	1	1	1	0	72	d_z^2 + π*(PPh_3)
229	HOMO	-1.01	6	0	1	35	34	21	3	d_{xz} + π (Azo + Oxime + Ph)
228	H–1	-2.63	13	3	1	13	41	26	3	d_{yz} + π (Azo + Oxime + Ph)
227	H–2	-2.94	7	3	5	2	80	1	1	d_{yz} + π (CO + Oxime)
226	H–3	-3.30	33	45	2	2	3	11	4	d_{xz} + π (Cl + Oxime + Ph)
225	H–4	-3.36	38	47	6	2	4	1	1	d_{xz} + π (Cl + CO)
224	H–5	-3.99	15	5	0	2	1	13	66	d_{xy} + π (Cl + Ph + PPh_3)
HOMO–LUMO gap = 2.05 eV										

Table 2.22: Frontier Molecular Orbital Composition (**β-MO**) (%) in the ground state for [**3a**]$^{\bullet-}$

Orbital	MO	Energy (eV)	Contribution (%)							Contribution
			Ru	Cl	CO	Azo	Oxime	Ph	PPh_3	
234	L+5	1.47	5	1	0	0	2	1	92	π*(PPh_3)
233	L+4	1.44	1	0	0	0	3	0	98	π*(PPh_3)
232	L+3	1.36	2	0	1	1	4	2	91	π*(PPh_3)
231	L+2	1.22	2	0	1	8	9	7	73	π*(Oxime + PPh_3)
230	L+1	1.16	6	1	3	11	16	7	56	π*(Azo + Oxime + PPh_3)
229	LUMO	1.00	18	1	1	8	9	5	58	d_z^2 + π*(Azo + Oxime + PPh_3)
228	HOMO	-2.03	8	1	0	22	34	33	2	d_{xz} + π (Azo + Oxime + Ph)
227	H–1	-2.71	6	2	6	2	82	0	1	d_{yz} + π (Oxime)
226	H–2	-3.35	41	43	1	2	3	5	5	d_{yz} + π (Cl)
225	H–3	-3.93	40	49	7	2	2	0	1	d_{xz} + π (Cl + CO)
224	H–4	-3.95	0	10	2	47	16	16	15	d_{yz} + π (Cl + Azo + Oxime + Ph)
223	H–5	-3.93	8	6	1	14	1	25	44	d_{xy} + π (Cl + Azo + Ph + PPh_3)
HOMO–LUMO gap = 3.03 eV										

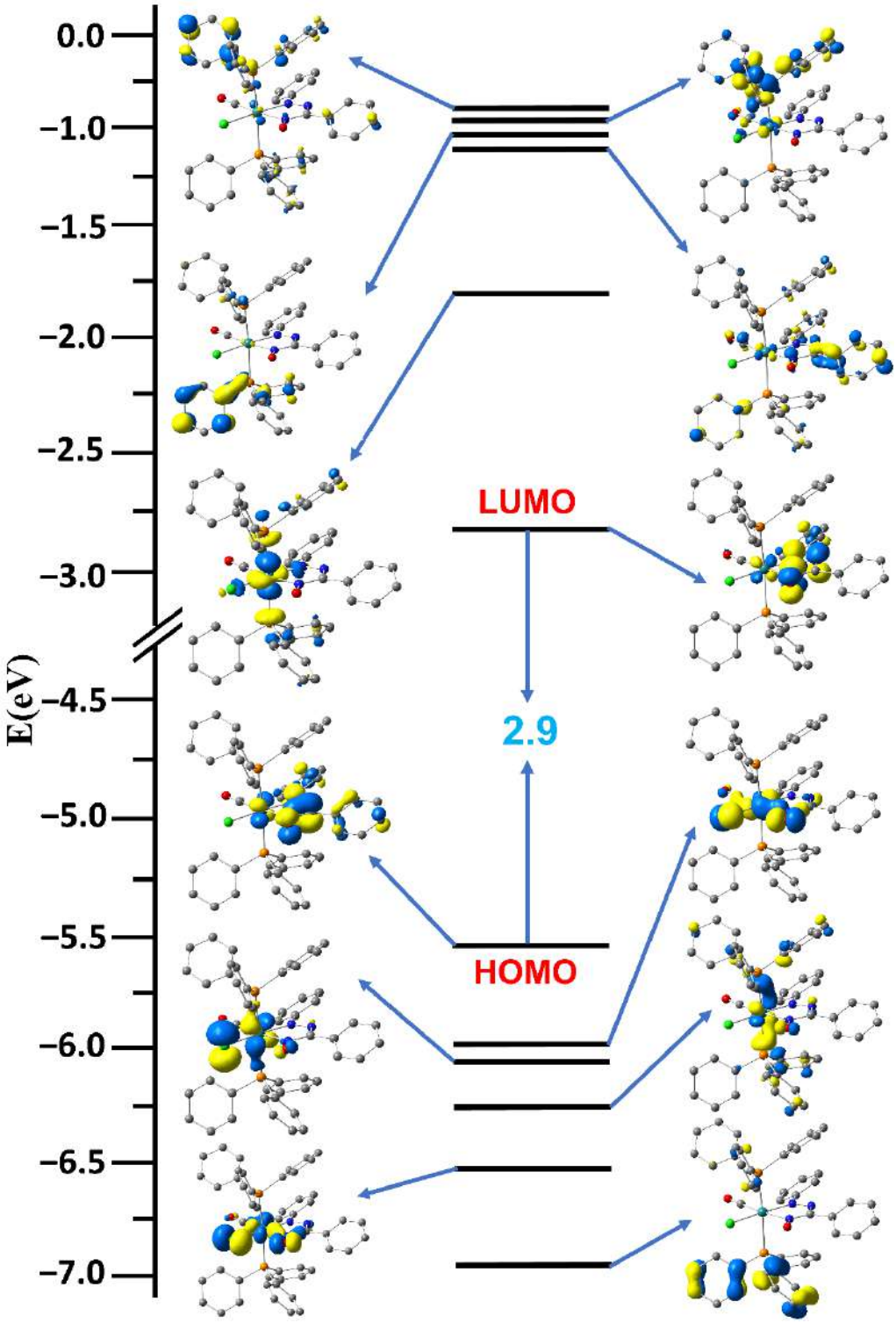

Figure 2.11: Partial FMO (Frontier molecular orbital) diagram and isodensity surface plots (isovalue = 0.06) for selected FMOs of **Ru1**. The arrows are used to highlight the HOMO–LUMO energy gap. All the DFT energy values are given in eV

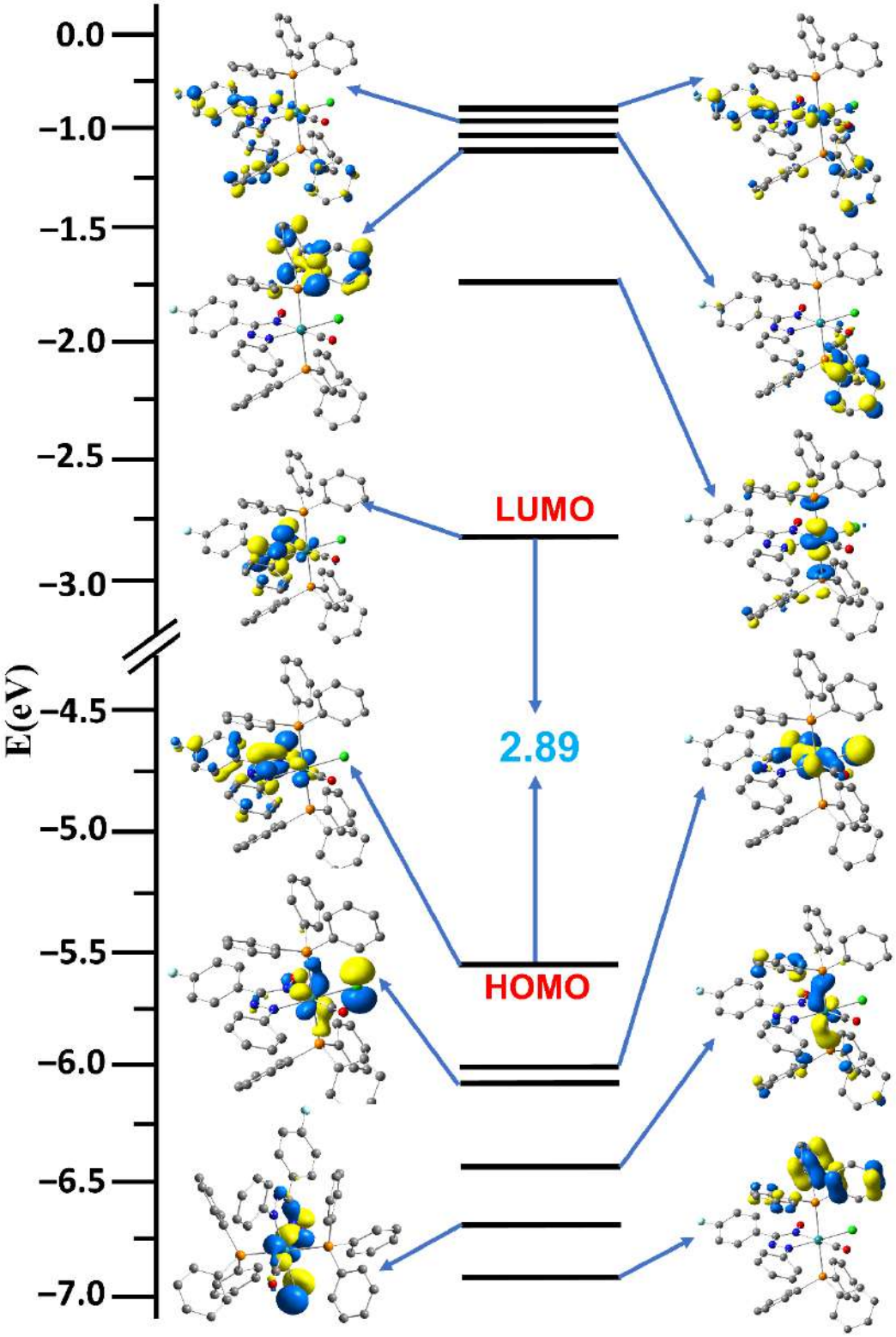

Figure 2.12: Partial FMO (Frontier molecular orbital) diagram and isodensity surface plots (isovalue = 0.06) for selected FMOs of **Ru2**. The arrows are used to highlight the HOMO–LUMO energy gap. All the DFT energy values are given in eV

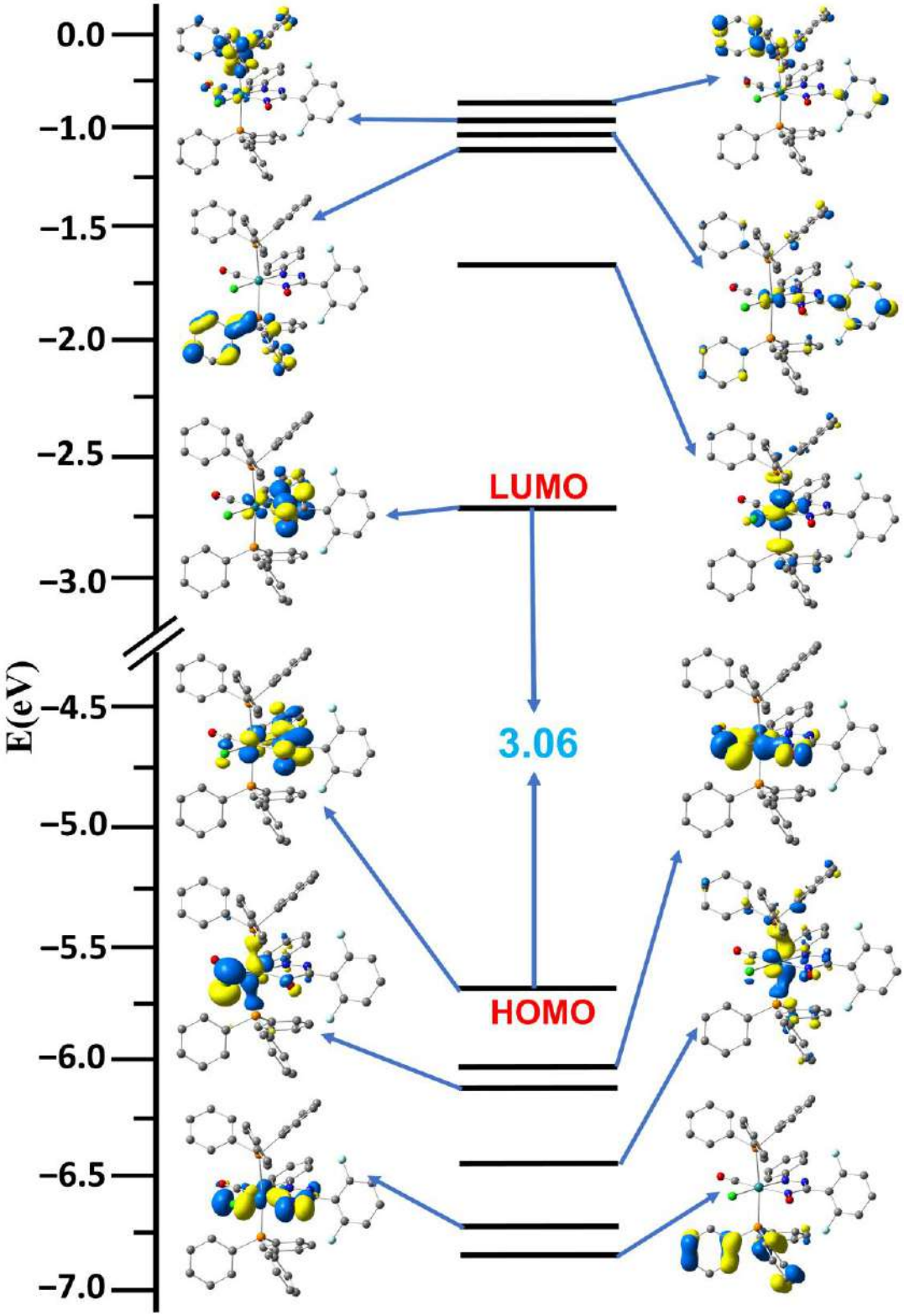

Figure 2.13: Partial FMO (Frontier molecular orbital) diagram and isodensity surface plots (isovalue = 0.06) for selected FMOs of **Ru3**. The arrows are used to highlight the HOMO–LUMO energy gap. All the DFT energy values are given in eV

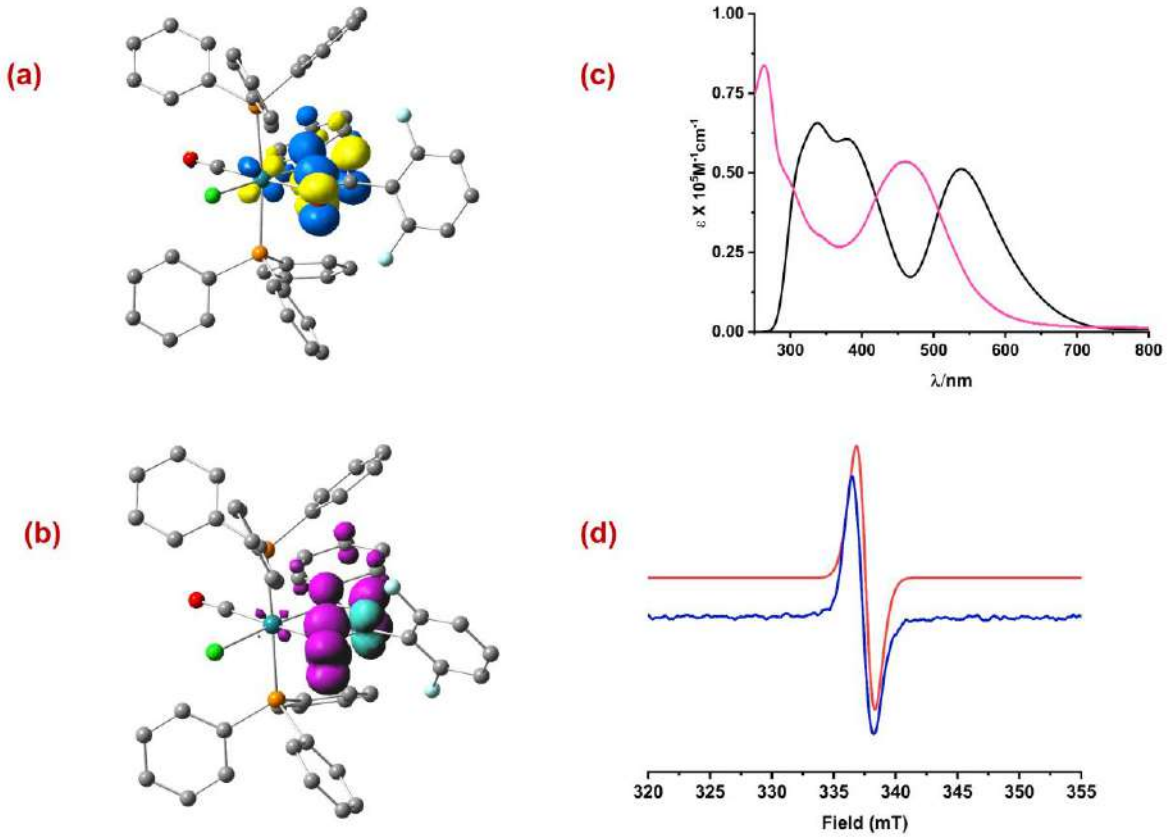

Figure 2.14: (a) LUMO of **Ru3**. (b) Mulliken spin Density plot of [**Ru3**]$^{\bullet-}$ (c) Experimental (pink) and calculated absorption (black) spectrum of [**Ru3**]$^{\bullet-}$ (d) Experimental (blue) and simulated (red) EPR spectrum of [**Ru3**]$^{\bullet-}$; Instrument settings: Microwave frequency 9.458 GHz; Microwave power 0.998 mW; Modulation frequency, 100 kHz.

2.3 Experimental Section

2.3.1 General Information

All the reactions mentioned in this work were performed under aerobic condition. Required reagents and solvent was used as soon as they received without any further synthetic manipulation. The following sources were used for purchase of required chemicals: phenyl hydrazine, benzaldehyde, 2-hydroxybenzaldehyde, 2,6-difluorobenzaldehyde and 4-fluorobenzaldehyde were purchased from TCI Chemical (India) Pvt. Ltd. Triphenylphosphine

(PPh_3) was obtained from Sigma-Aldrich. Ruthenium trichloride ($RuCl_3$. xH_2O) was taken from Arora-Matthey (India) Ltd. n-Butyl nitrite was prepared by using literature procedure[1].

Synthesis of ligands: All the reported diaryl-azo-oxime (**1**,**2**,**3** and **4**) ligands were prepared according to previously described method.[19]

(E)-(4-fluorophenyl)((E)-phenyldiazenyl)methanone oxime **(2):** Yield: 75%; ESI MS $[M + H]^+$; *m/z*: 244.0878 (calcd 244.0886); ^1H NMR (300 MHz, d^6-DMSO): δ 14.30 (s, 1H), 9.32 (dd, J = 22.5, 2.4 Hz, 2H), 9.23 – 9.15 (m, 3H), 9.05 – 8.87 (m, 4H). $^{13}C\{^1H\}$ NMR (101 MHz, $CDCl_3$): δ 164.94, 152.41, 132.39, 132.07 (d, J = 8.4 Hz), 129.64, 129.25, 123.53 (d, J = 2.9 Hz), 115.73 (d, J = 21.8 Hz), 115.30 (d, J = 21.7 Hz). ^{19}F NMR (377 MHz, $CDCl_3$): δ -110.16.

(E)-(2,6-difluorophenyl)((E)-phenyldiazenyl)methanone oxime **(3):** Yield: 65%, ESI MS $[M + H]^+$; *m/z*: 262.0796 (calcd 262.0792); ^1H NMR (400 MHz, d^6-DMSO): δ 13.32 (s, 1H), 7.74 (dd, J = 7.6, 2.2 Hz, 2H), 7.65 – 7.52 (m, 4H), 7.22 (t, J = 8.1 Hz, 2H); $^{13}C\{^1H\}$ NMR (101 MHz, d^6-DMSO): δ 160.43 (d, J = 8.6 Hz), 159.77 (t, J = 2.8 Hz), 157.96 (d, J = 8.7 Hz), 152.10, 134.05 – 132.10 (m), 130.06, 123.17, 112.00 (d, J = 20.5 Hz), 107.23 (t, J = 23.4 Hz); ^{19}F NMR (377 MHz, d^6-DMSO): δ -110.32.

(E)-(2-hydroxyphenyl)((E)-phenyldiazenyl)methanone oxime **(4):** Yield: 74%, ESI MS $[M + H]^+$; *m/z*: 242.0924 (calcd 242.0930); ^1H NMR (300 MHz, $CDCl_3$): δ 11.89 (s, 1H), 10.41 (s, 1H), 8.04 (dd, J = 6.6, 1.8 Hz, 2H), 7.71 – 7.57 (m, 4H), 7.41 – 7.31 (m, 1H), 7.09 (d, J = 8.3 Hz, 1H), 6.96 – 6.89 (m, 1H). $^{13}C\{^1H\}$ NMR (101 MHz, $CDCl_3$): 157.89, 157.63, 151.28, 134.19, 131.93, 129.79, 128.04, 123.58, 119.32, 117.75, 115.27.

2.3.2 General procedure for the synthesis of complexes *trans*-[Ru(L^-)(CO)Cl(PPh_3)$_2$] (Ru1-Ru4)

The diarylazooxime ligand (**HL**, 1-4) (0.1 mmol, 1equiv.**)** was dissolve in 20 ml of reagent grade benzene in 50 ml round bottom flask equipped with a magnetic stir bar. The precursor ruthenium complex, [RuH(CO)Cl(PPh_3)$_3$] (95 mg, 0.1 mmol, 1equiv.) was added as solid to the above solution and stirred for 12 h at room temperature. The resulting dark pinkish red coloured solution was evaporated to dryness under vacuum. The desired ruthenium-diarylazooxime complex was purified by column chromatography using silica gel and toluene/acetonitrile mixture was used as eluent. The suitable single crystal for SCXRD study was produced by solvent diffusion method where a solution of freshly purified ruthenium-diarylazooxime complex in CH_2Cl_2 was taken in a test tube with glass stopper and by using a syringe, n-hexane was added very carefully without any disturbance of the layer of CH_2Cl_2 solution.

***Analytical data of Ru1*:** The ligand was **1**. The complex was prepared according to general procedure. Reddish brown solid. Yield: 63 mg (69%). Anal. Calcd (%) for **[Ru1]** $C_{50}H_{40}N_3O_2ClP_2Ru$: C, 65.75; H, 4.41; N, 4.60. Found: C, 63.68; H, 4.39; N, 4.62. HRMS; [M + H] *m/z* = 914.1010 (calcd 914.1412); FT-IR/cm^{-1} υ =, 1966 ($\upsilon_{C=O}$), 1483 ($\upsilon_{N=N}$), 1089 (υ_{N-O}); ^{1}H NMR (400 MHz, $CDCl_3$): δ 7.47 – 7.43 (m, 12H), 7.38 (dd, *J* = 6.7, 3.1 Hz, 2H), 7.29 – 7.21 (m, 9H), 7.20 – 7.16 (m, 12), 7.10 (t, *J* = 7.2 Hz, 1H), 6.92 (t, *J* = 7.8 Hz, 2H), 6.83 (d, *J* = 8.1 Hz, 2H); ^{13}C{^{1}H} NMR (100 MHz, $CDCl_3$): 204.79, 204.66, 167.37, 155.33, 134.34, 134.29, 134.24, 130.86, 130.63, 130.41, 130.09, 128.04, 127.99, 127.94,127.79, 127.60, 127.57, 127.87; ^{31}P{^{1}H} NMR (161.99 MHz, $CDCl_3$): (δ, ppm) 21.64

***Analytical data of Ru2*:** The ligand was **2**. Dark brown solid. Yield: 69 mg (74%). Anal. Calcd (%) for **[Ru2]** $C_{50}H_{39}N_3O_2FClP_2Ru$: C, 64.48; H, 4.22; N, 4.51. Found: C, 63.41; H, 4.19; N, 4.49. HRMS; [M + H] *m/z* = 932.1204 (calcd 932.1317); FT-IR/cm^{-1} υ = 1960 ($\upsilon_{C=O}$), 1485

($\upsilon_{N=N}$), 1090 (υ_{N-O}); ^{1}H NMR (400 MHz, $CDCl_3$): δ 7.54 – 7.37 (m, 13H0, 7.27 – 7.30 (m, 8H), 7.25 – 7.12 (m, 11H), 7.13 (t, *J* = 8.0 Hz, 1H), 6.99 – 6.88 (m, 4H), 6.87 – 6.82 (m, 2H); $^{13}C\{^{1}H\}$ NMR (100 MHz, $CDCl_3$): 204.59, 204.47, 166.50, 163.38, 160.92, 155.45, 134.37, 134.32, 134.26, 134.03, 130.85, 130.62, 130.13, 130.39, 129.49, 128.06, 128.01, 127.96,127.89, 127.73, 126.90, 126.87, 122.94, 114.50, 114.29; $^{31}P\{^{1}H\}$ NMR (161.99 MHz, $CDCl_3$): (δ, ppm) 21.76; ^{19}F NMR (376.5 MHz, $CDCl_3$): (δ, ppm) -112.77.

***Analytical data of Ru3*:** The ligand was **3**. Purple red solid. Yield: 70 mg (74%); Anal. Calcd (%) for **[Ru3]** $C_{50}H_{38}N_3O_2F_2ClP_2Ru$: C, 63.26; H, 4.03; N, 4.43. Found: C, 63.20; H, 4.05; N, 4.40. HRMS; [M + H] *m/z* = 950.0700 (calcd 950.1223); FT-IR/cm^{-1} υ = 1987 ($\upsilon_{C=O}$), 1435 ($\upsilon_{N=N}$), 1090 (υ_{N-O}); ^{1}H NMR (400 MHz, $CDCl_3$): δ 7.60 – 7.50 (m, 12H), 7.31 – 7.22 (m, 9H), 7.21 – 7.17 (m, 12H), 6.99 (ddd, *J* = 8.4, 5.4, 3.2 Hz, 1H), 6.87 – 6.73 (m, 4H); $^{13}C\{^{1}H\}$ NMR (100 MHz, $CDCl_3$): 162.38, 162.30, 159.86, 159.79, 159.00, 154.61, 134.42, 134.37, 134.31, 131.21, 130.98, 130.75, 130.14, 128.10, 127.95, 127.90, 127.58, 127.25, 122.58, 11.52, 111.28; $^{31}P\{^{1}H\}$ NMR (161.99 MHz, $CDCl_3$): (δ, ppm) 20.18; ^{19}F NMR (376.5 MHz, $CDCl_3$): (δ, ppm) -107.60.

***Analytical data of Ru4*:** The ligand was **4**. Purple red solid. Yield: 68 mg (73%); Anal. Calcd (%) for **[Ru4]** $C_{50}H_{40}N_3O_3ClP_2Ru$: C, 64. 62; H, 4.34; N, 4.52. Found: C, 64.67; H, 4.37; N, 4.48. HRMS; [M + H] *m/z* = 930.0438 (calcd 930.1361); FT-IR/cm^{-1} υ = 1992 ($\upsilon_{C=O}$), 1433 ($\upsilon_{N=N}$), 1092 (υ_{N-O}), ^{1}H NMR (400 MHz, $CDCl_3$): δ 8.99 (s, 1H), 7.59 – 7.48 (m, 4H), 7.30 – 7.18 (m, 10H), 7.03 (t, *J* = 7.8 Hz, 1H), 6.89 (dd, *J* = 8.0, 15.0 Hz, 2H), 6.71 (t, *J* = 7.5 Hz, 1H); $^{13}C\{^{1}H\}$ NMR (100 MHz, $CDCl_3$): 203.38, 203.26, 203.13, 169.26, 157.42, 155.61, 134.33, 134.27, 134.22, 130.48, 130.43, 130.25, 130.02, 129.37, 128.20, 128.15, 128.04, 123.56, 119.62, 119.41, 118.40; $^{31}P\{^{1}H\}$ NMR (161.99 MHz, $CDCl_3$): (δ, ppm) 19.62.

2.4 Conclusion

In summary, we have successfully synthesized and characterized a series of four ruthenium(II) complexes of the general formula [RuL(CO)Cl(PPh_3)$_2$] (**Ru1**–**Ru4**), where **HL**$^{1\text{-}4}$ represent diaryl azo-oxime ligands of the type PhN=N–C(Ar)=NOH bearing electronically diverse aryl (Ar) substituents. Detailed structural investigations reveal that the coordination environment around the ruthenium center is influenced by subtle electronic effects imparted by the pendant aryl groups. Notably, variations in the Ru–N_{azo} and Ru–N_{oxime} bond lengths across the series correlate with the electronic nature of the aryl substituents. In complex **Ru4**, a noticeable elongation of the Ru–N bonds are observed, likely resulting from intramolecular hydrogen bonding between the oximato oxygen and the adjacent ortho-hydroxyphenyl moiety. All the ruthenium complexes also feature significant intramolecular π–π stacking interactions, contributing to their overall structural stability. In a related fashion, complex **Ru3** demonstrates distinct intramolecular fluorine–arene (F···π) interactions, which introduce subtle modifications to the coordination geometry and reinforce the molecular architecture. Electrochemical studies indicate that all four complexes display well-defined reductive responses, primarily associated with the azo-oxime ligand framework. These responses correspond to ligand-centered one-electron reduction processes, leading to the formation of metastable radical anion species. Overall, this work provides insights into the coordination behaviour and electronic properties of azo-oxime-based ruthenium(II) complexes, and underscores their potential as tunable platforms for electron-transfer catalysis.

2.5 References

[1] R. N. Mukherjee, *Inorg. Chem.*, **2020**, *59*, 12961–12977 and references therein.

[2] (a) V. Lyaskovskyy, B. de Bruin, *ACS Catal.*, **2012**, *2*, 270−279. (b) O. R. Luca, R. H. Crabtree, *Chem. Soc. Rev.*, **2013**, *42*, 1440−1459. (c) D. L. J. Broere, R. Plessiusa, J. I. V.

Vlugt, *Chem. Soc. Rev*., **2015**, *44*, 6886−6915. (d) M. Sutradhar, A. J. L. Pombeiro, J. A. L. da Silva, *Coord. Chem. Rev*., **2021**, *439*, 213911−213929.

[3] (a) J. L. Boyer, J. Rochford, M.-K. Tsai, J. T. Muckerman, E. Fujita, *Coord. Chem. Rev*., **2010**, *254*, 309−330. (b) S. Blanchard, E. Derat, M. Desage-El Murr, L. Fensterbank, M. Malacria, V. Mouriès-Mansuy, *Eur. J. Inorg. Chem*., **2012**, 376–389. (c) M. D. Kärkäs, B. Åkermark, *Dalton Trans*., **2016**, *45*, 14421−14461. (d) L. Zhang, S. Mathew, J. Hessels, J. N. H. Reek, F. Yu, *ChemSusChem*, **2021**, *14*, 234−250.

[4] (a) J. I. van der Vlugt, J. N. H. Reek, *Angew. Chem., Int. Ed.,* **2009**, *48*, 8832−8846. (b) R. H. Crabtree, *Chem. Rev*., **2017**, *117*, 9228–9246. (c) S. Liu, Y.-J. Lei, Z.-J. Xin, Y.-B. Lu, H.-Y. Wang, *J. Photochem. and Photobiol. A*: Chemistry, **2018**, *355*, 141−151. (d) G.B. Shul'pin, Y. N. Kozlov, L.S. Shul'pina, *Catalysts,* **2019**, *9*, 1046−1067. (e) N. P. van Leest, F. J. de Zwart, M. Zhou, B. de Bruin, *ACS Au,* **2021**, *1*, 1101–1115. (f) R. Mondal, A. K. Guin, G. Chakrabortya, N. D. Paul, *Org. Biomol. Chem*., **2022**, *20*, 296−328. (g) A. Nakada, T. Matsumoto, H.-C. Chang, *Coord. Chem. Rev.*, **2022**, *473*, 214804−214838.

[5] (a) M. H. V. Huynh, T. J. Meyer, *Chem. Rev*., **2007**, *107*, 5004–5064. (b) D. R. Weinberg, C. J. Gagliardi, J. F. Hull, C. F. Murphy, C. A. Kent, B. C. Westlake, A. Paul, D. H. Ess, D. G. McCafferty, T. J. Meyer, *Chem. Rev.*, **2012**, *112*, 4016–4093. (c) D. G. Nocera, *J. Am. Chem. Soc*., **2022**, *144*, 1069–1081.

[6] (a) C. J. Gagliardi, B. C. Westlake, C. A. Kent, J. J. Paul, J. M. Papanikolas, T. J. Meyer, *Coord. Chem. Rev*., **2010**, *254*, 2459−2471. (b) I. Siewert, *Chem. Eur. J.*, **2015**, *21*, 15078−15091. (c) R. E. Warburton, A. V. Soudackov, S. H. -Schiffe, *Chem. Rev.*, **2022**, *122*, 10599–10650.

[7] (a) H. Yang, X. Cui, X. Dai, Y. Deng, F. Shi, *Nat Commun.*, **2015**, *6*, 6478−6488. (b) L. Wang, J. Xiao, (**2016**) G. Guillena, D. Ramón, (eds) Topics in Current Chemistry Collections. Springer, Cham. (c) S. Rohe, A. O. Morris, T. McCallum, L. Barriault, *Angew. Chem., Int. Ed.,* **2018**, *57*, 15664−15669.

[8] (a) J. P. Roth, J. C. Yoder, T. -J. Won, J. M. Mayer, *Science*, **2001**, *294*, 2524−2526. (b) M. Nechab, S. Mondal, M. P. Bertrand, *Chem. Eur. J.*, **2014**, *20*, 16034−16059. (c) M. Kumar, A. Sinha, J. S. Francisco, *Acc. Chem. Res.*, **2016**, *49*, 877–883. (d) L. Capaldo, D. Ravelli, M. Fagnoni, *Chem. Rev*., **2022**, *122*, 1875–1924.

[9] (a) B. K. Ghosh, A. Chakravorty, *Coord. Chem. Rev.*, **1989**, *95*, 239−294. (b) M. Shivakumar, K. Pramanik, P. Ghosh, A. Chakravorty, *Inorg. Chem*., **1998**, *37*, 5968–5969. (c) N. Doslik, T. Sixt, W. Kaim, *Angew. Chem. Int. Ed.*, **1998**, *37*, 2403−2404. (d) A. Singh, S. Panda, S. Dey, G. K. Lahiri, *Angew. Chem. Int. Ed.*, **2021**, *60*, 11206−11210.

[10] (a) W. Kaim, *Dalton Trans*., **2003**, 761−768. (b) A Sanyal, S. Chatterjee, A. Castiñeiras, B. Sarkar, P. Singh, J. Fiedler, S. Záliš, W. Kaim, S. Goswami, *Inorg. Chem*., **2007**, *46*, 8584–8593. (c) N. D. Paul, T. Krämer, J. E. McGrady, S. Goswami, *Chem. Commun.*, **2010**, *46*, 7124−7126. (d) N. D. Paul, S. Samanta, S. Goswami, *Inorg. Chem*., **2010**, *49*, 2649–2655.

[11] (a) C. Remenyi, R. Reviakine, M. Kaupp, *J. Phys. Chem. A*, **2006**, *110*, 4021–4033. (b) B. Sarkar, S. Frantz, S. Roy, M. Sieger, C. Duboc, G. Denninger, H.-J. Kümmerer, W. Kaim, *J. Mol. Str.,* **2008**, *890*, 133−138. (c) W. Kaim, G. K. Lahiri, *Coord. Chem. Rev.*, **2019**, *393*, 1−8.

[12] (a) S. Pramanik, S. Roy, T. Ghorui, S. Ganguly, K. Pramanik, *Dalton Trans.*, **2014**, *43*, 5317–5334. (b) D. Sengupta, N. S. Chowdhury, S. Samanta, P. Ghosh, S. K. Seth, S. Demeshko, F. Meyer, S. Goswami, *Inorg. Chem*., **2015**, *54*, 11465–11476. (c) F. F. Khan, J. Klein, J. L. Priego, B. Sarkar, R. J.-Aparicio, G. K. Lahiri, *Inorg. Chem.*, **2018**, *57*, 12800–12810. (d) S. Panda, S. Dhara, A. Singh, S. Dey, G. K. Lahiri*, Coord. Chem. Rev*., **2023**, *475*, 214895−214920. (e) S. Roy, T. Ghorui, D. Jana, S. C. Patra, S. Pramanik, S. Moorthy, S. K. Singh, S. Mehta, A. Mondal, K. Pramanik, *Chem. Eur. J.*, **2025**, *31*, e202404027.

[13] (a) S. Sinha, R. Sikari, V. Sinha, U. Jash, S. Das, P. Brandao, S. Demeshko, F. Meyer, B. de Bruin, N. D. Paul, *Inorg. Chem.*, **2019**, *58*, 1935–1948. (b) S. Sinha, S. Das, R. Mondal, S. Mandal, N. D. Paul, *Dalton Trans.*, **2020**, *49*, 8448−8478. (c) R. Mondal, G. Chakraborty, A. K. Guin, S. Sarkar, N. D. Paul, *J. Org. Chem.*, **2021**, *86*, 13186−13197. (d) R. Mondal, A. K. Guin, S. Chakraborty, N. D. Paul, *J. Org. Chem.*, **2022**, *87*, 2921–2934. (e) A. A. Swatiputra, D. Mukherjee, S. Dinda, S Roy, K. Pramanik, S. Ganguly, *Dalton Trans.,* **2023**, *52*, 15627–15646.

[14] (a) C. C. H. Atienza, C. Milsmann, E. Lobkovsky, P. J. Chirik, *Angew. Chem., Int. Ed.*, **2011**, *50*, 8143–8147 and references therein. (b) K. Ohno, A. Nagasawa, T. Fujihara, *Dalton Trans*., **2015**, *44*, 368–376. (c) D. Sengupta, R. Bhattacharjee, R. Pramanick, S. P. Rath, N. S. Chowdhury, A. Datta, S. Goswami, *Inorg. Chem.*, **2016**, *55*, 9602–9610. (d) B. Goswami, M. Khatua, S. Samanta, *Dalton Trans.*, **2022**, *51*, 1454−1463. (e) Kamal, M. Khatua, S. Rani, B. Goswami, S. Samanta, *J. Org. Chem.*, **2023**, *88*, 5827−5843.

[15] (a) S. K. Hanson, R. Wu, L. A. Silks, *Org. Lett.*, **2011**, *13*, 1908−1911. (b) A. K. -Nezhad, F. Panahi, *ACS Catal.*, **2014**, *4*, 1686−1692. (c) C. Gunanathan, D. Milstein, *Chem. Rev.*, **2014**, *114*, 12024−12087. (d) E. M. Lane, K. B. Uttley, N. Hazari, W. Bernskoetter, *Organometallics*, **2017**, *36*, 2020− 2025. (e) P. Daw, Y. B.-David, D. Milstein, *ACS Catal.*, **2017**, *7*, 7456−7460. (f) S. Genç, B. Arslan, S. Gülcemal, S. Günnaz, B. Çetinkaya, and D. Gülcemal, *J. Org. Chem.*, **2019**, *84*, 6286−6297.

[16] (a) M. Chakraborty, D. Sengupta, T. Saha, and S. Goswami, *J. Org. Chem.*, **2018**, *83*, 7771−7778. (b) A. K. Bains, A. Kundu, S. Yadav, D. Adhikari, *ACS Catal.*, **2019**, *9*, 9051−9059. (c) A. K. Bains, D. Dey, S. Yadav, A. Kund, D. Adhikari, *Catal. Sci. Technol.*, **2020**, *10*, 6495−6500. (d) A. K. Bains, V. Singh, D. Adhikari, *J. Org. Chem*., **2020**, *85*, 14971–14979. (e) A. K Bains, A. Biswas, D. Adhikari, *Chem. Commun*., **2020**, *56*, 15442−15445.

[17] (a) A. Chakravorty, *Coord. Chem. Rev*. **1974**, *13*, 1–46. (b) R. Pramanick, R. Bhattacharjee, D. Sengupta, A. Datta, S. Goswami, *Inorg. Chem.*, **2018**, *57*, 6816–6824. (c) S. Das, R. Mondal, G. Chakraborty, A. K. Guin, A. Das, N. D. Paul, *ACS Catal.*, **2021**, *11*, 7498−7512.

[18] (a) S. Das, R. Mondal, A. K. Guin, N. D. Paul, *Org. Biomol. Chem.*, **2022**, *20*, 3105–3117. (b) S. Pal, S. Das, S. Chakraborty, S. Khanra, N. D. Paul, *J. Org. Chem.*, **2023**, *88*, 3650−3665. (c) S. Chakraborty, R. Mondal, S. Pal, A. K. Guin, L. Roy, N. D. Paul, *J. Org. Chem*., **2023**, *88*, 771−787.

[19] (a) K. C. Kalia, A. Chakravorty, *Inorg. Chem.*, **1968**, *7*, 2016–2020. (b) K. C. Kalia, A. Chakravorty, *J. Org. Chem.*, **1970**, *35*, 2231–2234

[20] (a) S. Pramanik, S. Roy, T. Ghorui, S. Ganguly and K. Pramanik, *Inorg. Chem.*, **2016**, *55*, 1461–1468. (b) S. Dinda, S. Pramanik, J. Basu, S. C. Patra, K. Pramanik and S. Ganguly, *Dalton Trans.*, **2022**, *51*, 10121–10135.

2.6 Appendix

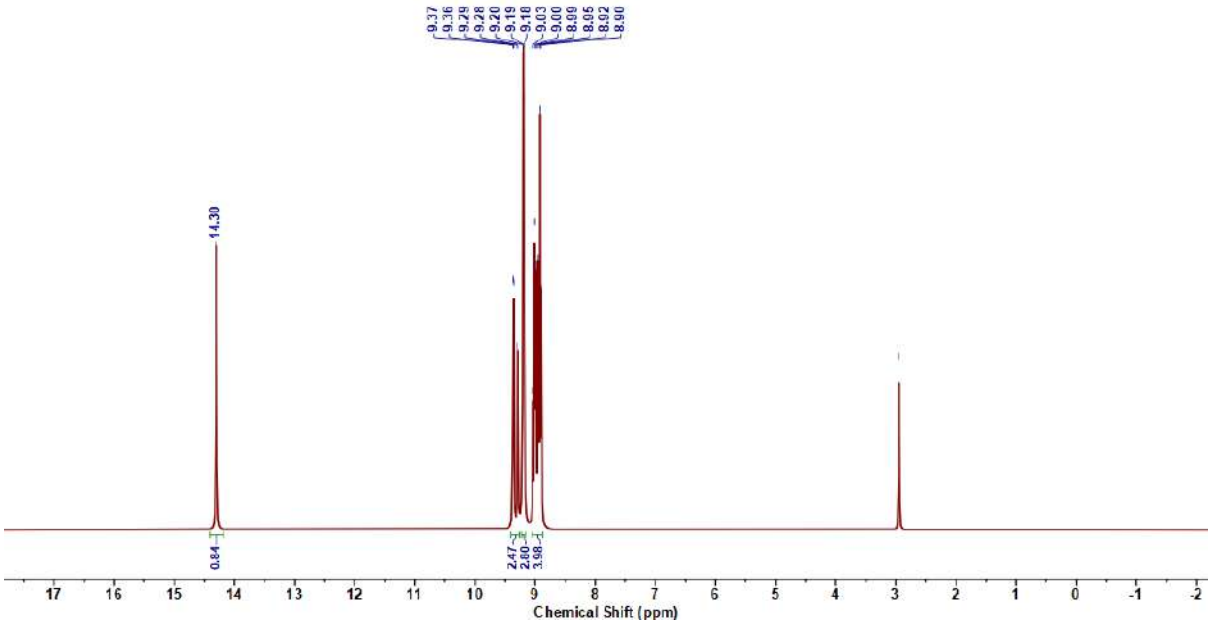

Figure 2.6.A1: ^{1}H NMR spectrum of **2**

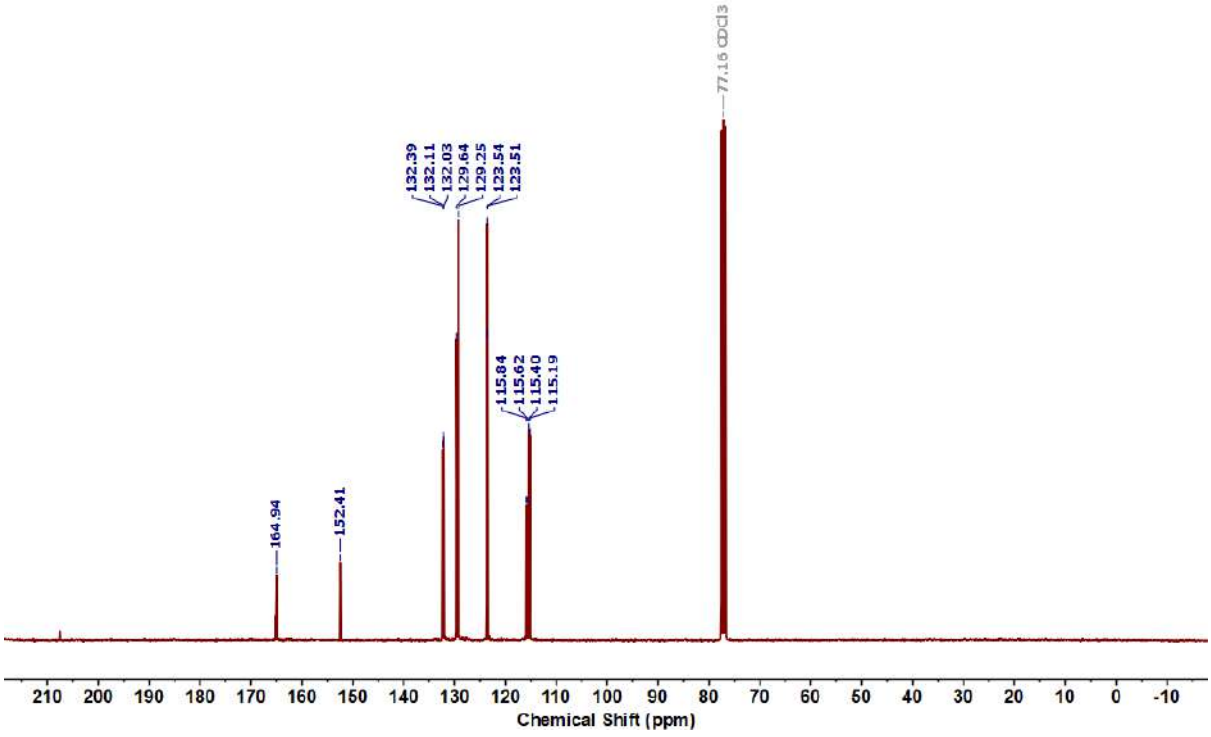

Figure 2.6.A2: $^{13}C\{^{1}H\}$ NMR spectrum of **2**

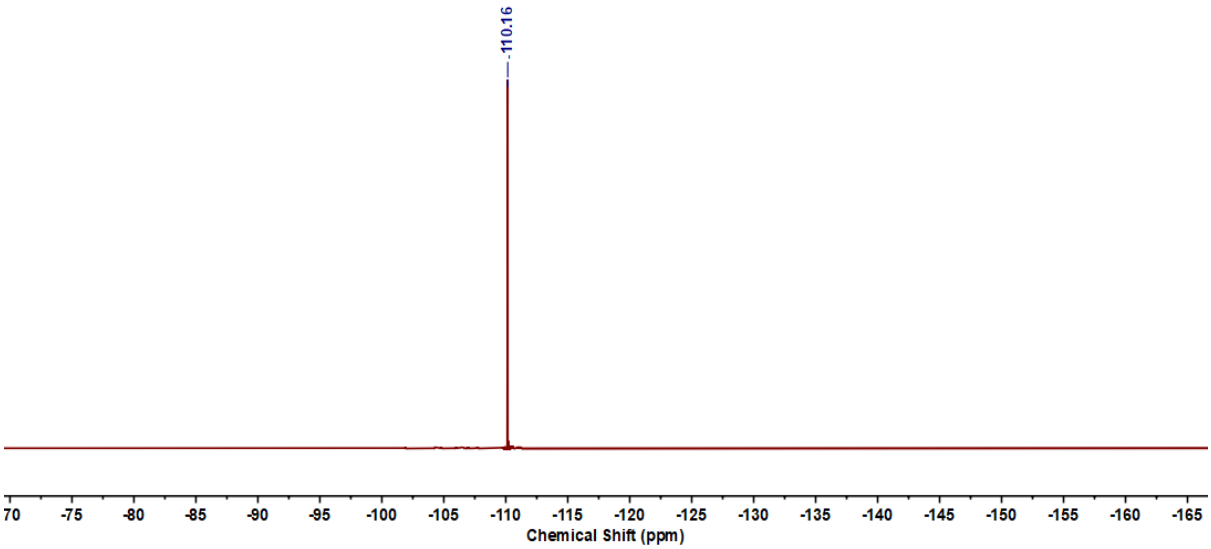

Figure 2.6.A3: ^{19}F NMR spectrum of **2**

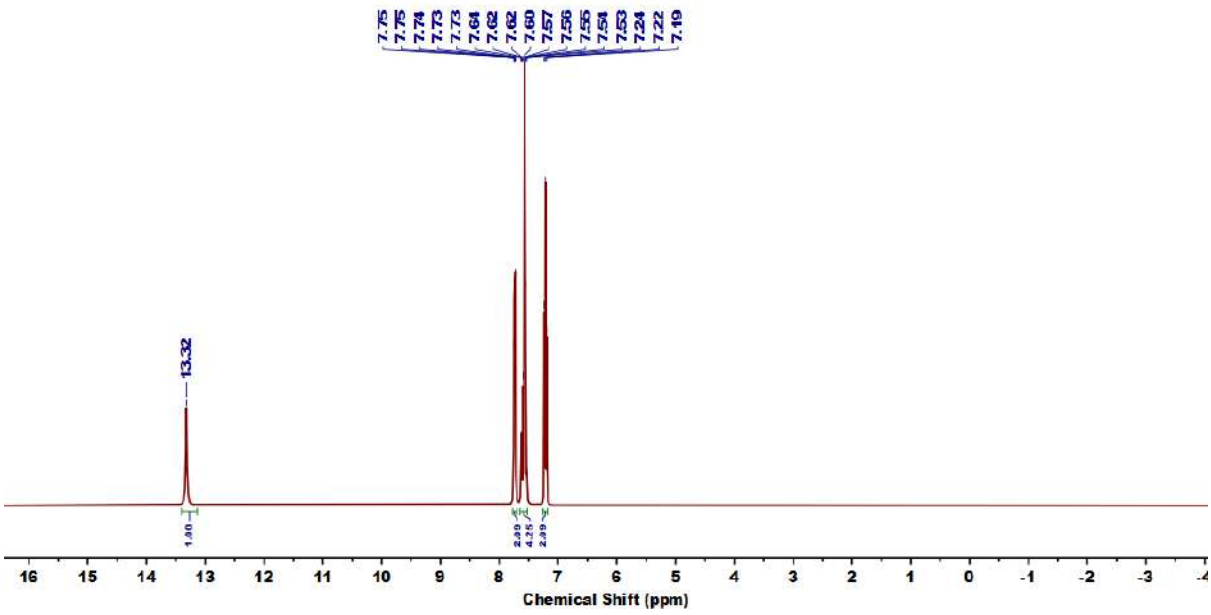

Figure 2.6.A4: ^{1}H NMR spectrum of **3**

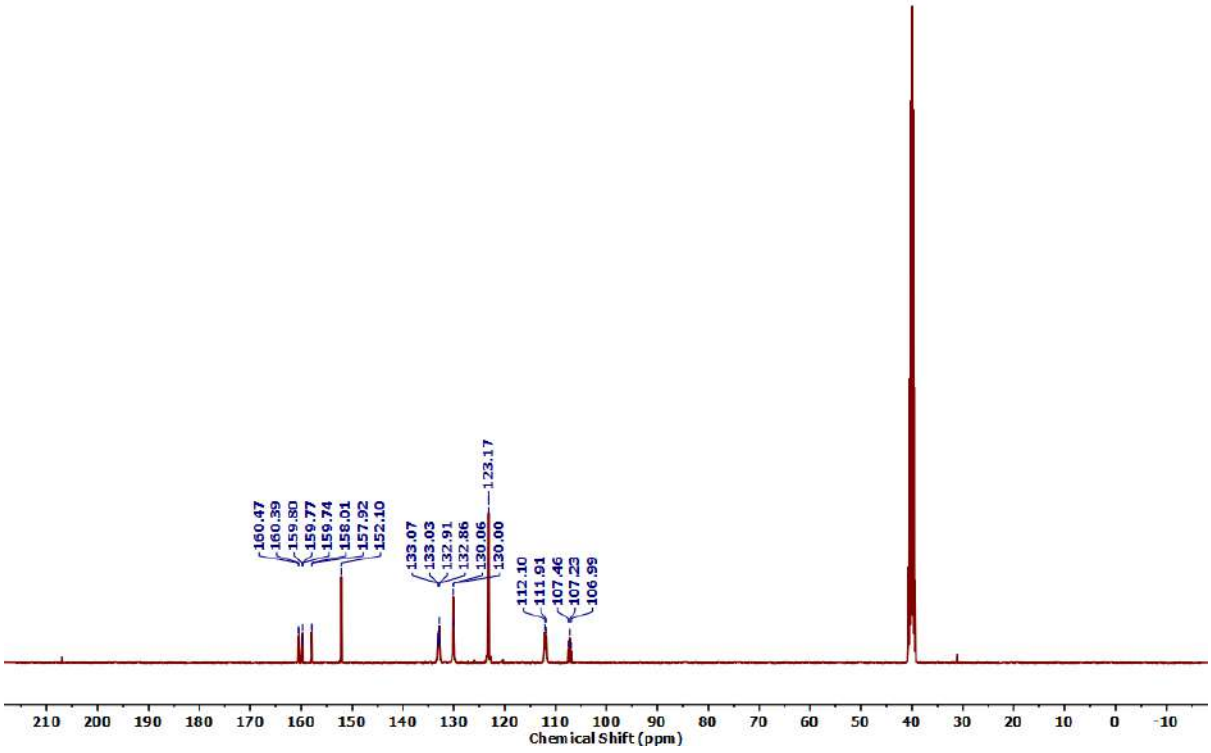

Figure 2.6.A5: $^{13}C\{^{1}H\}$ NMR spectrum of **3**

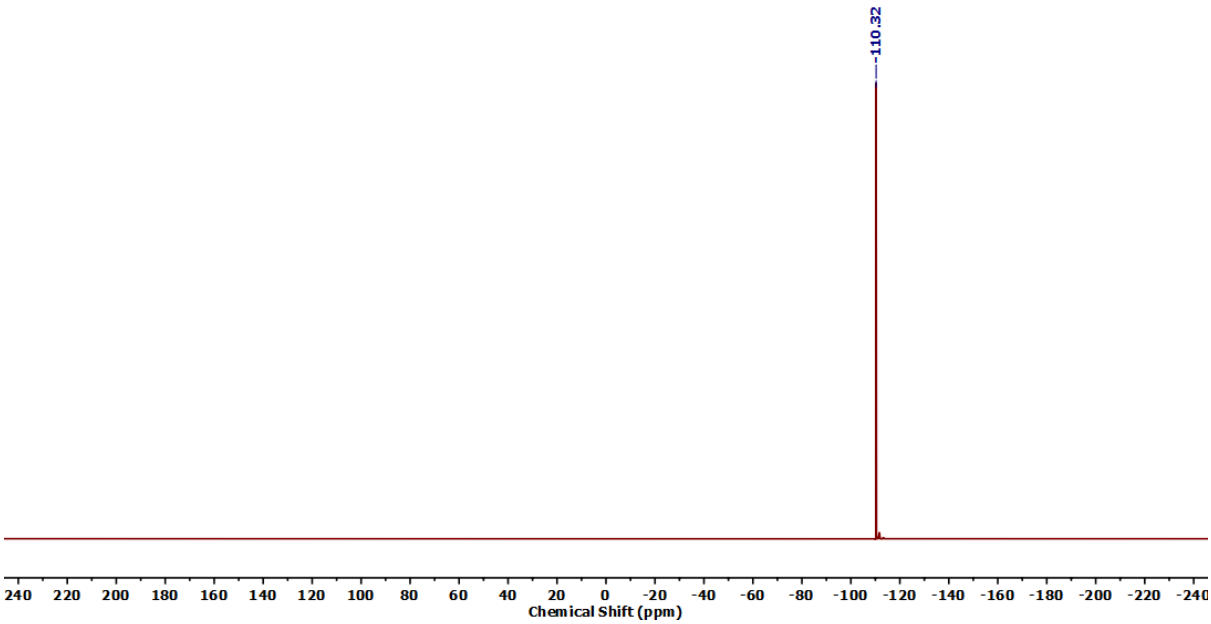

Figure 2.6.A6: ^{19}F NMR spectrum of **3**

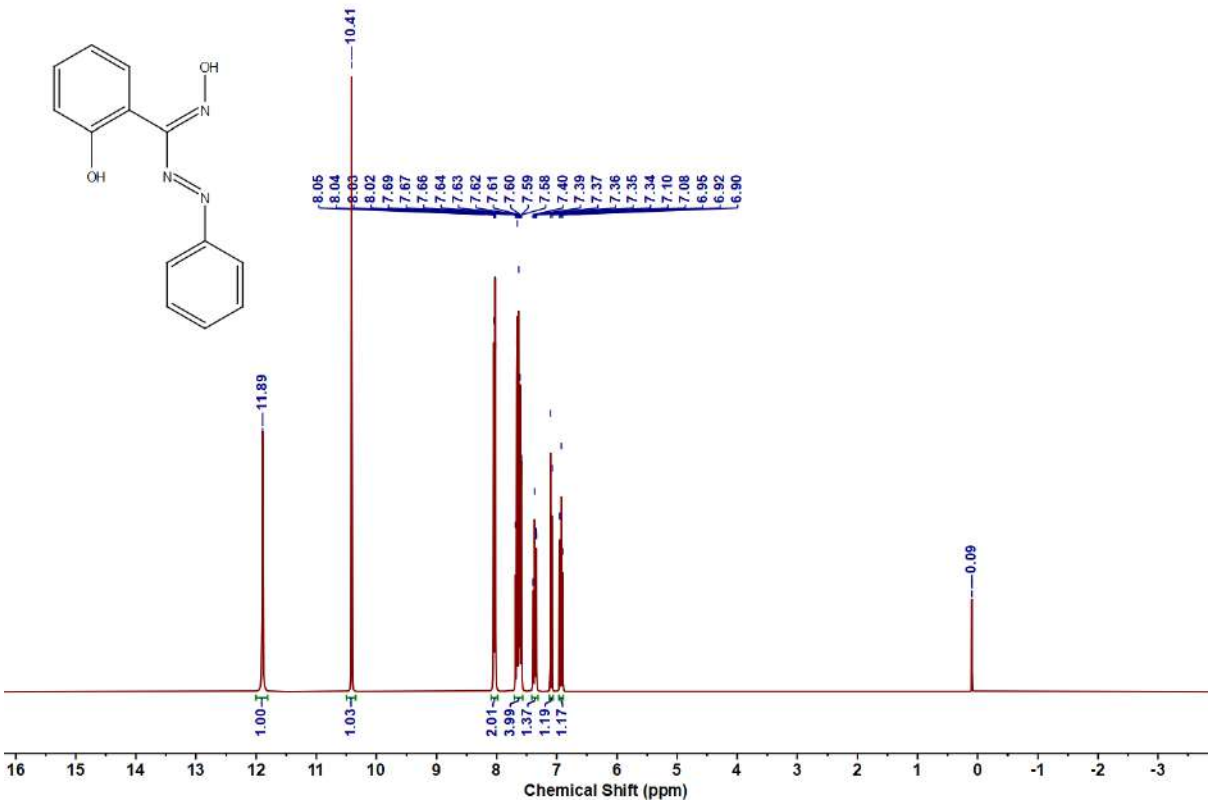

Figure 2.6.A7: ^{1}H NMR spectrum of **4**

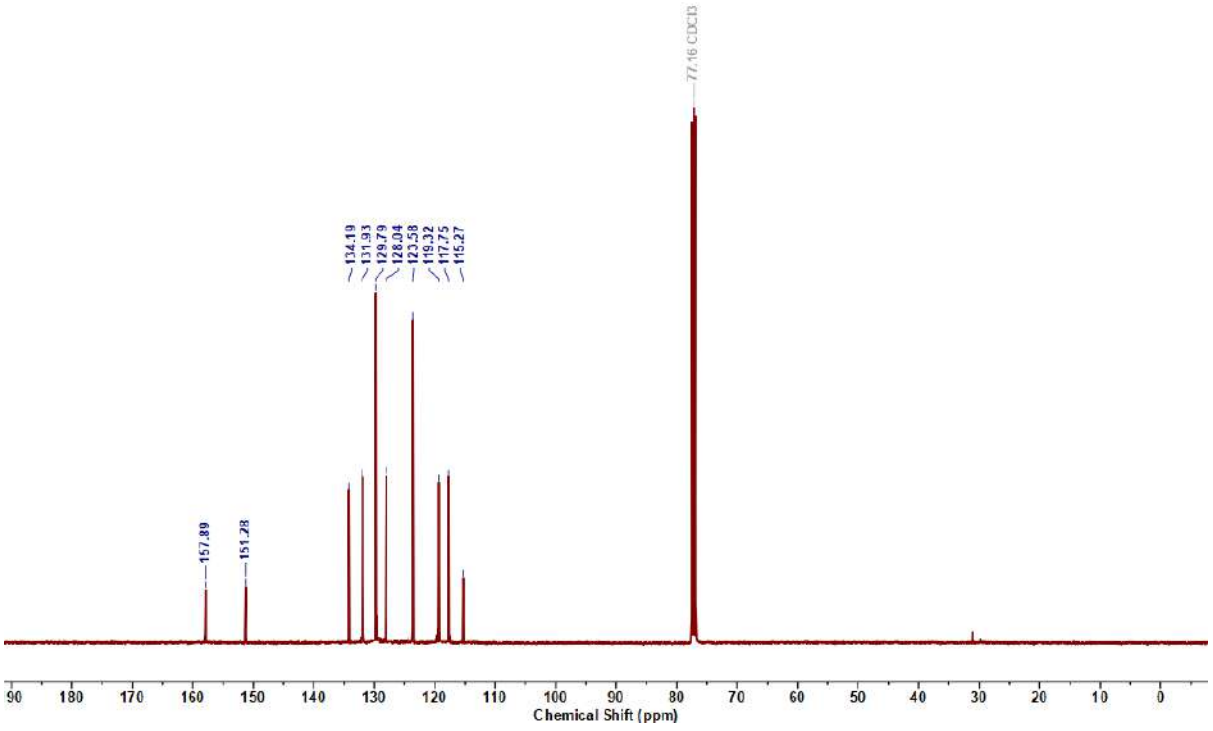

Figure 2.6.A8: ^{13}C{^{1}H} NMR spectrum of **4**

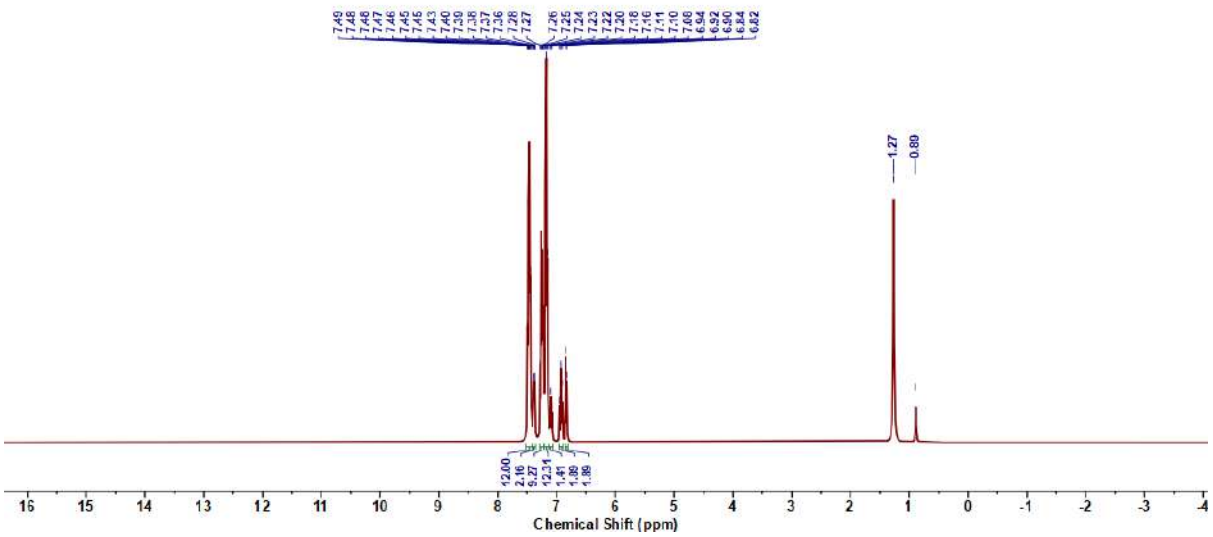

Figure 2.6.A9: ^{1}H NMR spectrum of **Ru1**

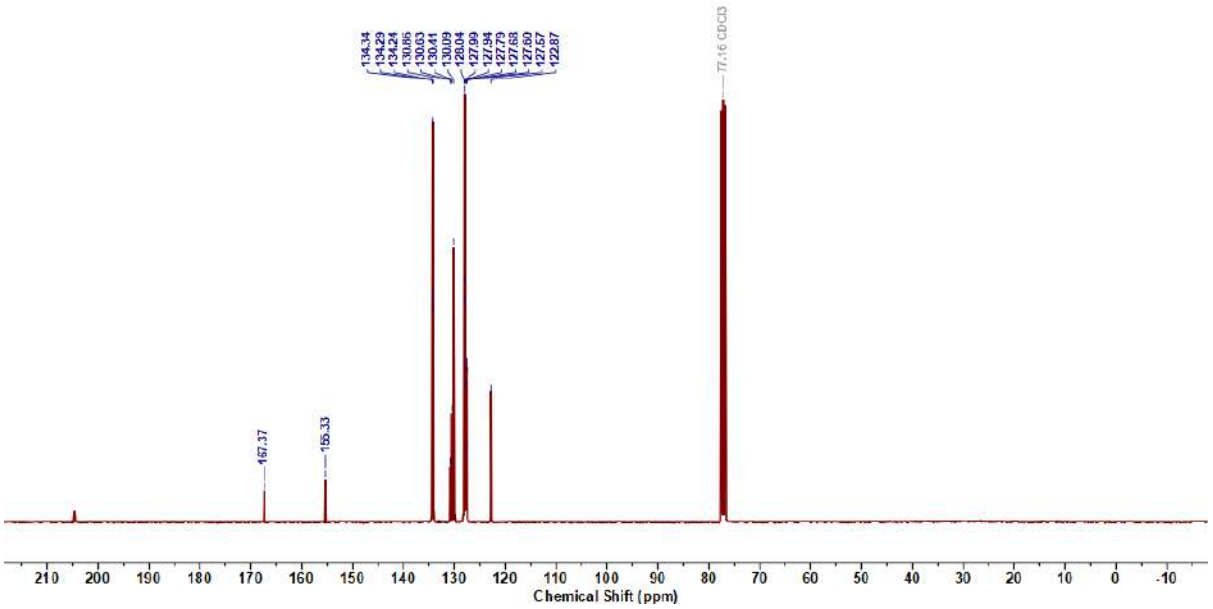

Figure 2.6.A10: ^{13}C{^{1}H} NMR spectrum of **Ru1**

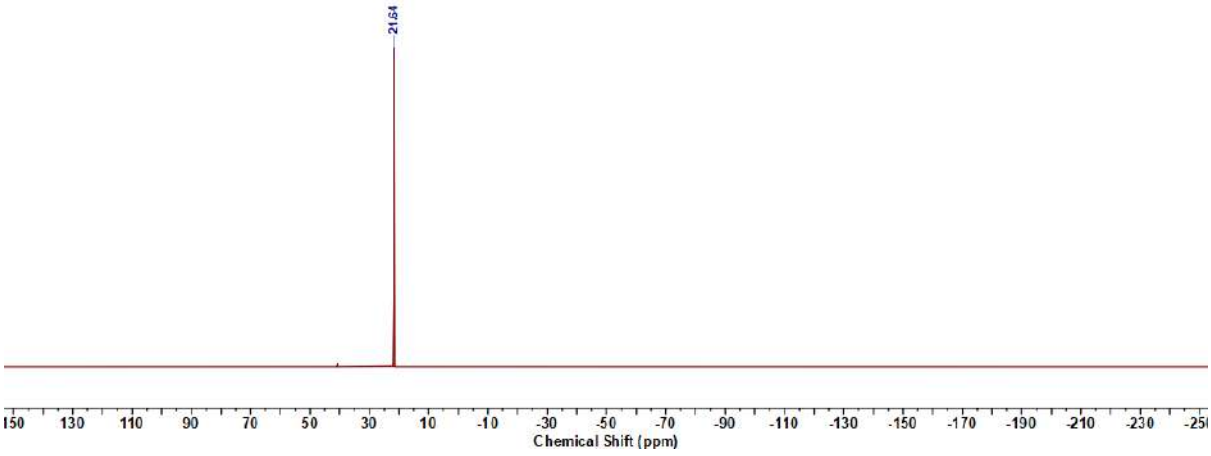

Figure 2.6.A11: $^{31}P\{^{1}H\}$ NMR spectrum of **Ru1**

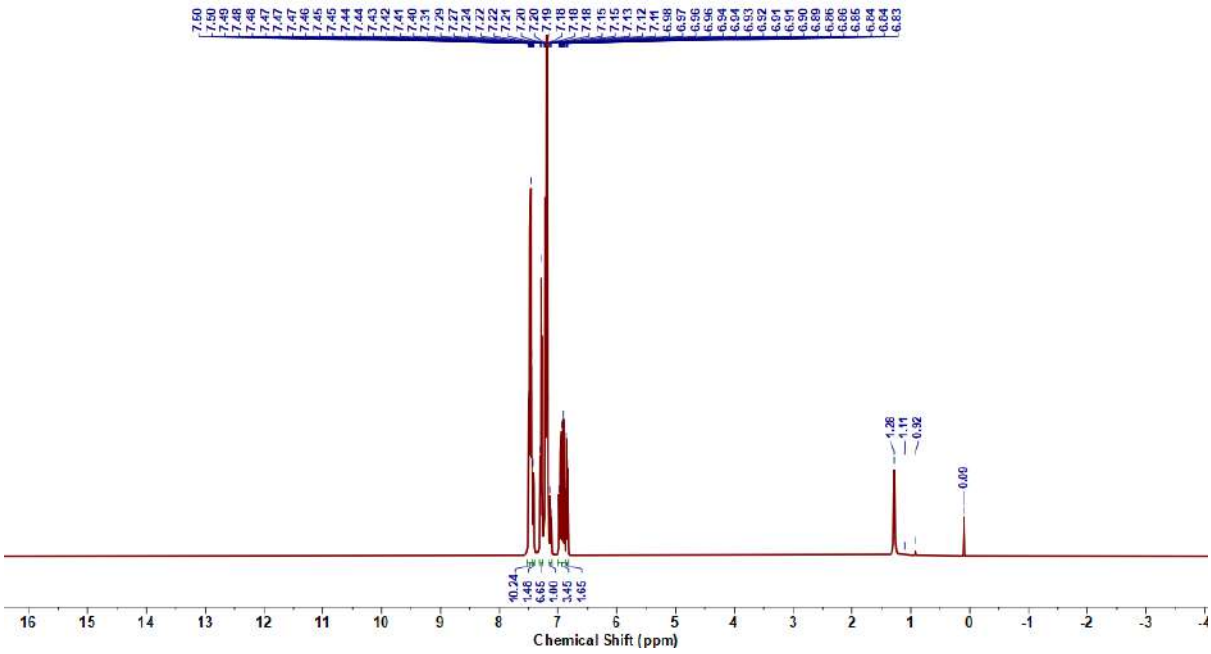

Figure 2.6.A12: ^{1}H NMR spectrum of **Ru2**

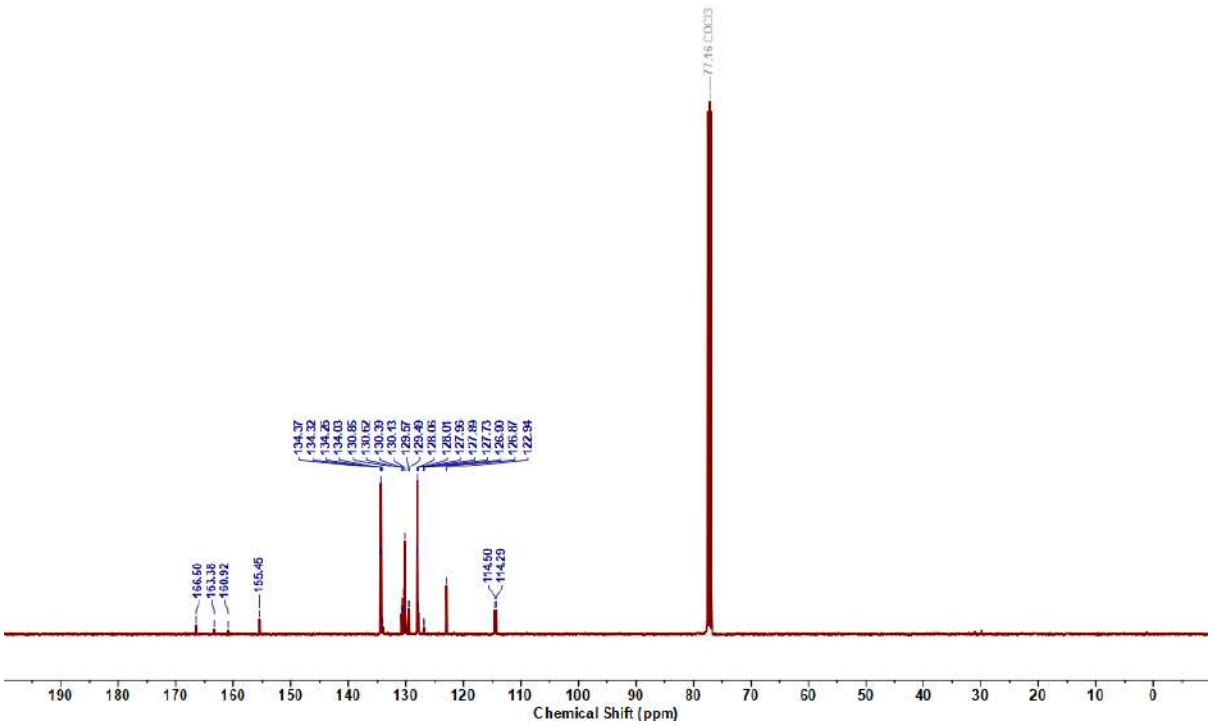

Figure 2.6.A13: $^{13}C\{^{1}H\}$ NMR spectrum of **Ru2**

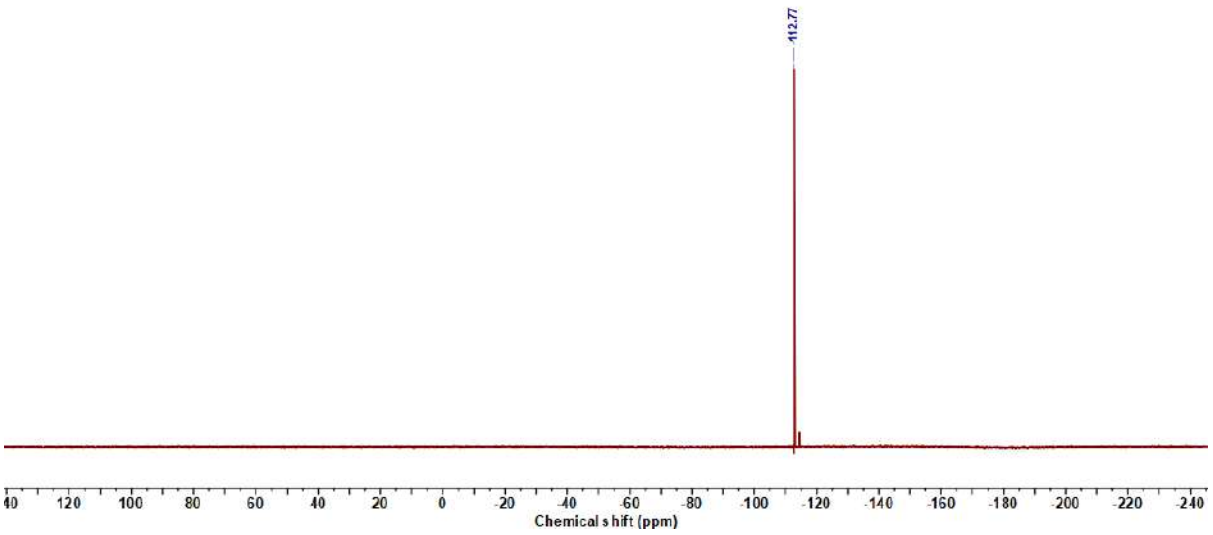

Figure 2.6.A14: ^{19}F NMR spectrum of **Ru2**

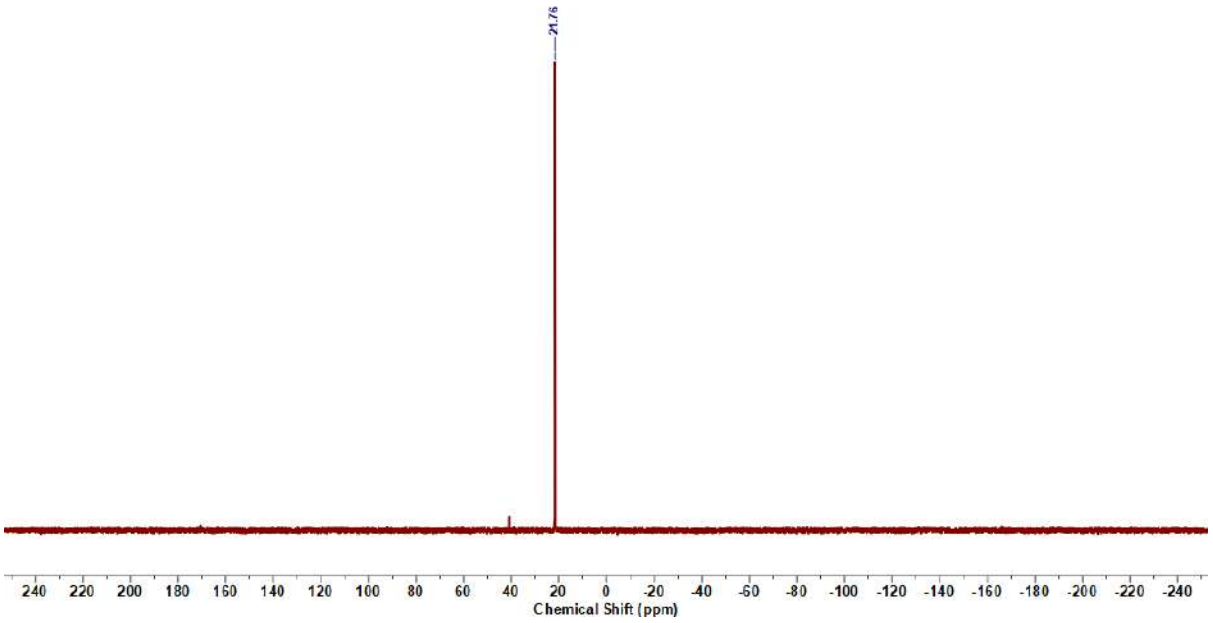

Figure 2.6.A15: $^{31}P\{^{1}H\}$ NMR spectrum of **Ru2**

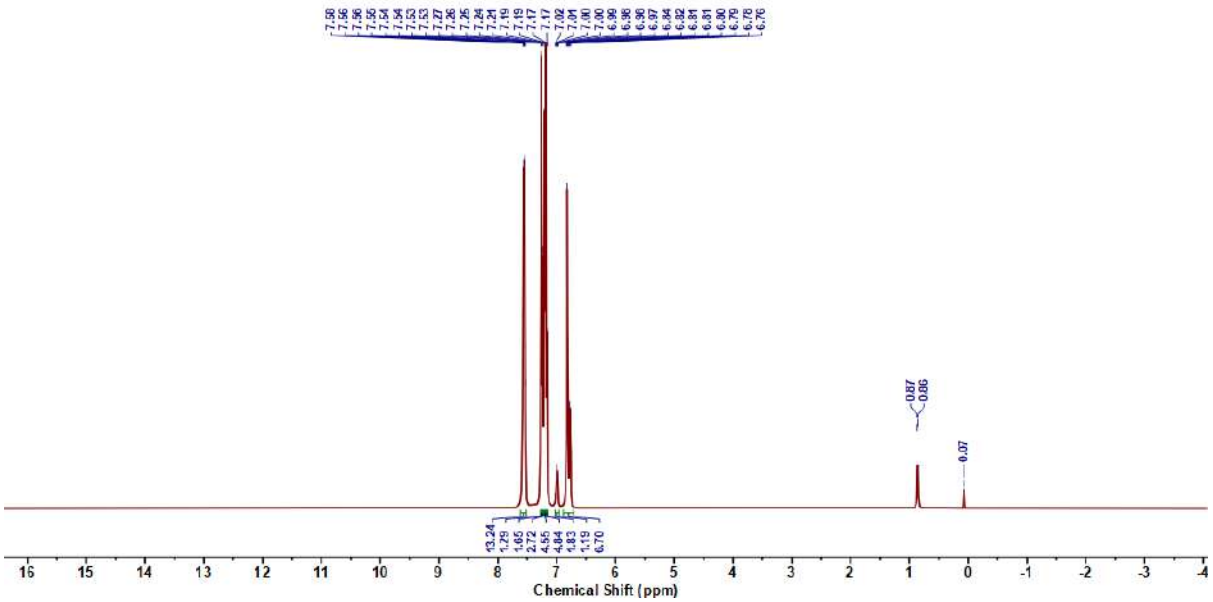

Figure 2.6.A16: ^{1}H NMR spectrum of **Ru3**

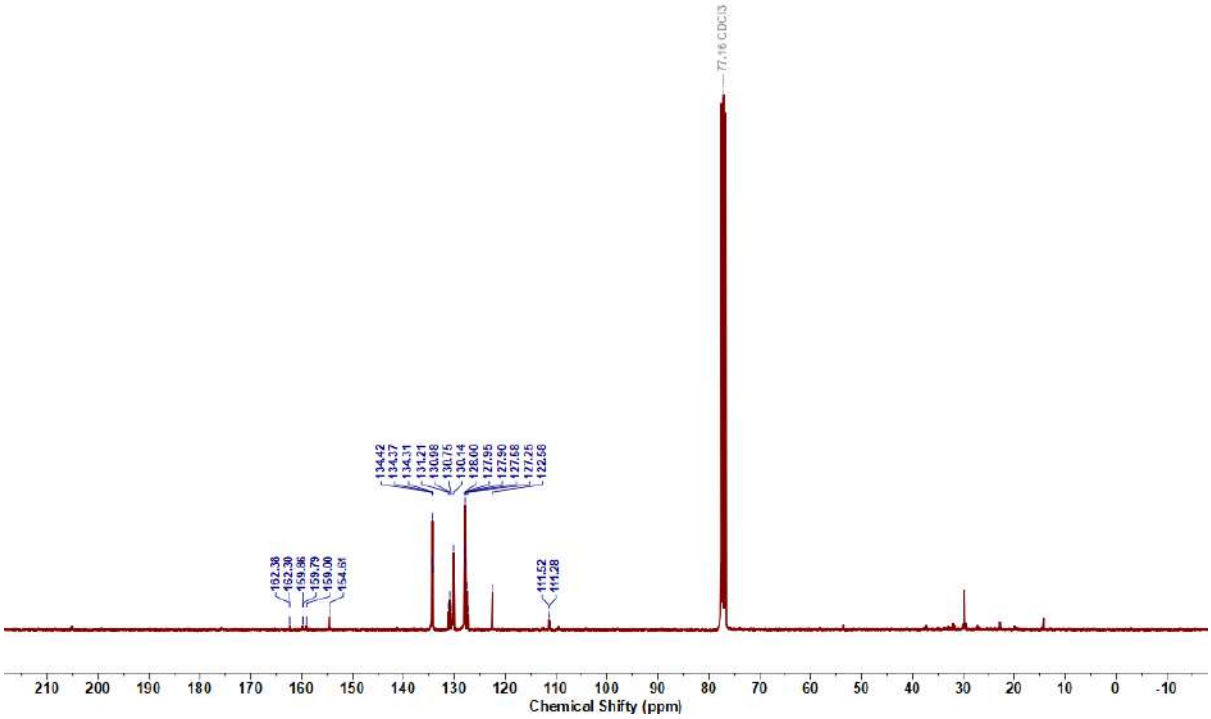

Figure 2.6.A17: $^{13}C\{^{1}H\}$ NMR spectrum of **Ru3**

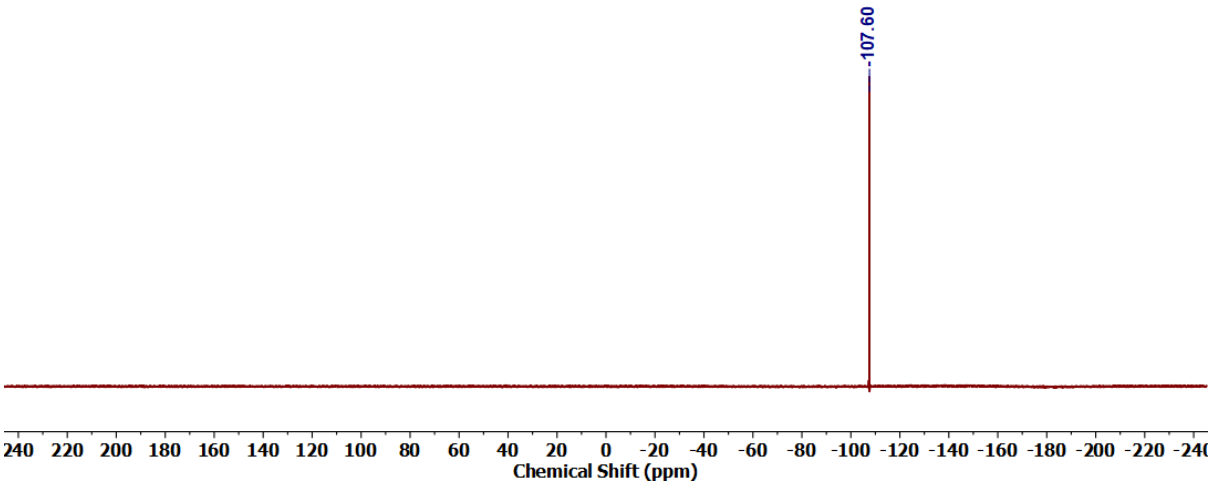

Figure 2.6.A18: ^{19}F NMR spectrum of **Ru3**

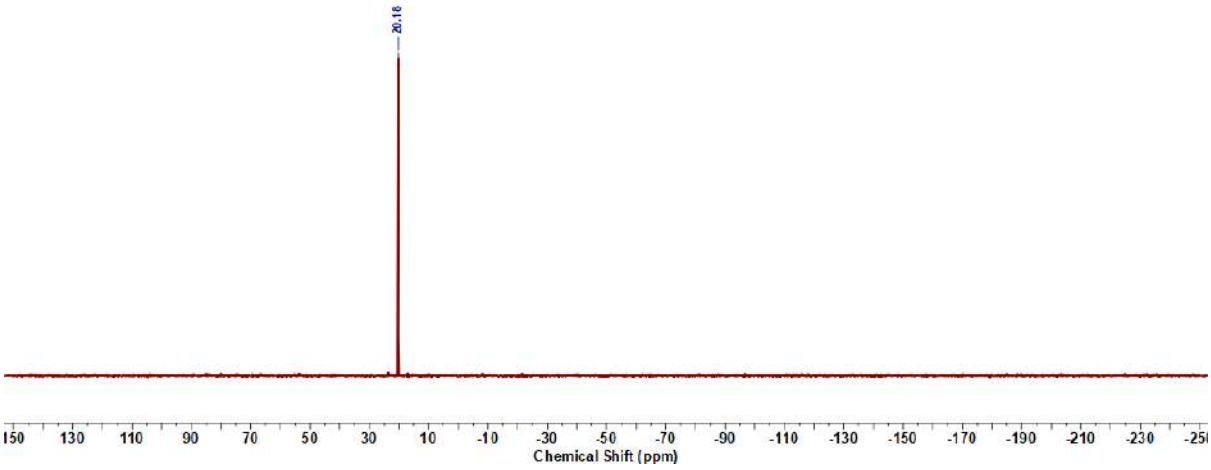

Figure 2.6.A19: $^{31}P\{^{1}H\}$ NMR spectrum of **Ru3**

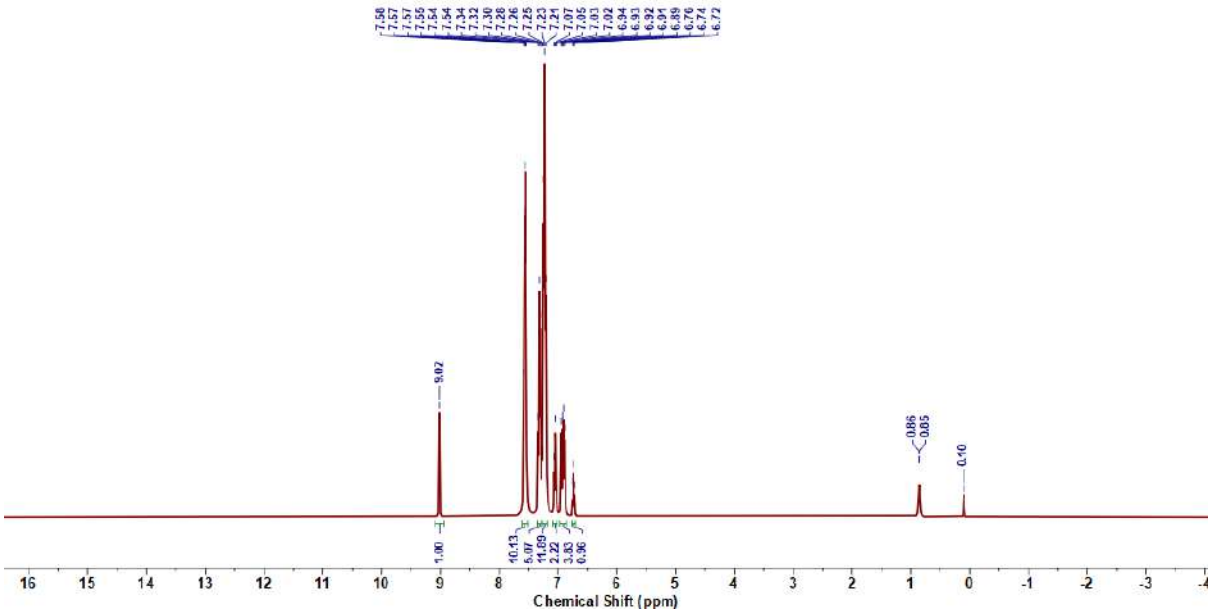

Figure 2.6.A20: ^{1}H NMR spectrum of **Ru4**

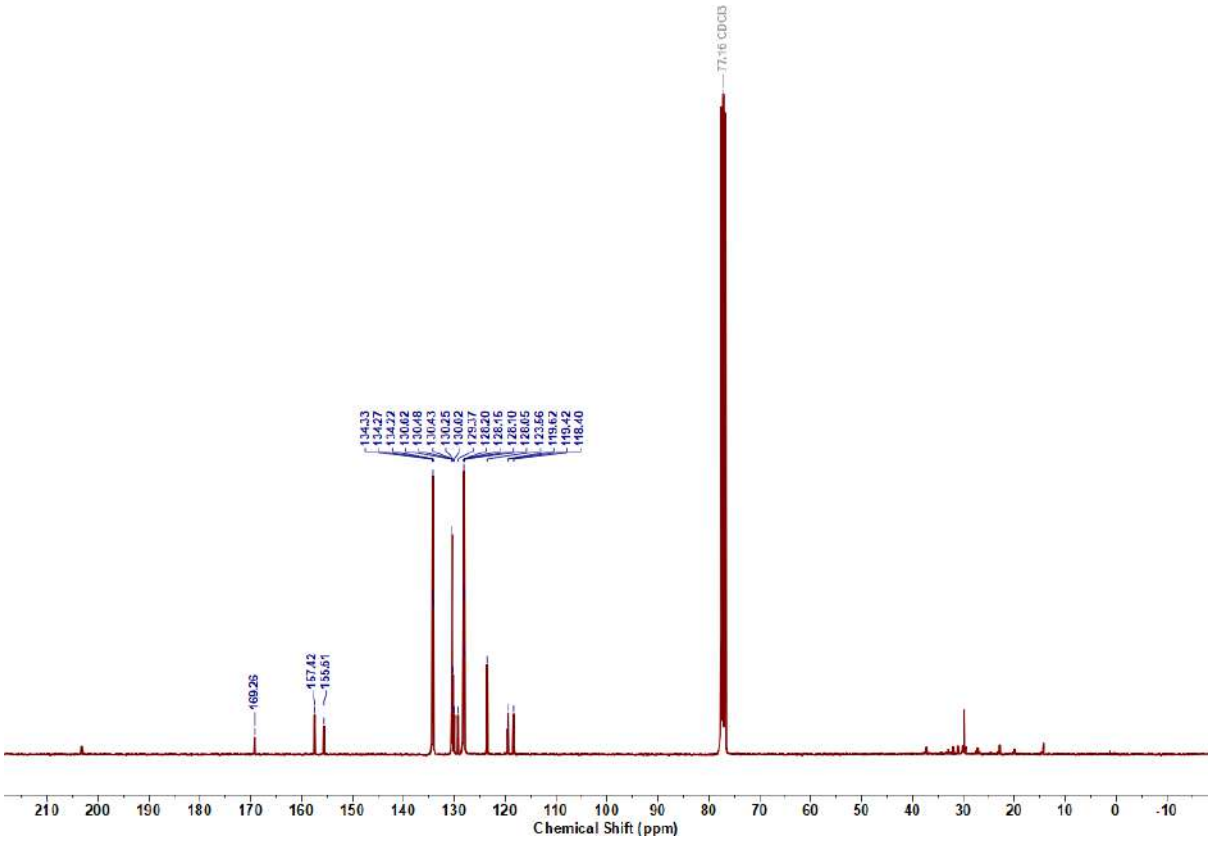

Figure 2.6.A21: $^{13}C\{^{1}H\}$ NMR spectrum of **Ru4**

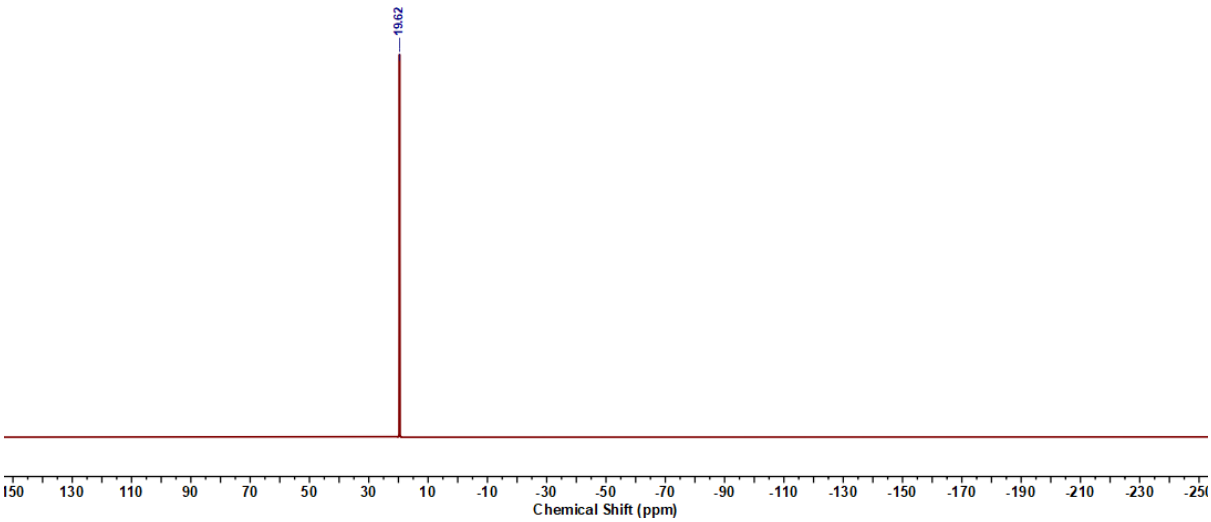

Figure 2.6.A22: $^{31}P\{^{1}H\}$ NMR spectrum of **Ru4**

Chapter 3

Catalytic Applications of Ruthenium(II) Complexes bearing Redox-Active Aryl-Azo-Oximes: α-Alkylation of Ketones and Formation of 2-Substituted Quinolines

3.1 Introduction

Nitrogen-based heterocycles are a fundamental class of compounds that are abundantly found in nature and play a crucial role in the structure of numerous natural products, pharmaceutical agents, and advanced organic materials.[1] Among them, quinolines, 2-aminoquinolines, and quinazolines stand out as essential frameworks present in a wide array of biologically and medicinally relevant molecules.[2] These heterocycles are known for their diverse therapeutic profiles, exhibiting activities such as antibacterial,[3] anti-inflammatory,[4] anticonvulsant,[5] antimalarial,[6] antiasthmatic,[7] anti-Alzheimer's,[8] and anticancer[9] effects. Similarly, α-alkylated carbonyl compounds have emerged as valuable pharmacophores due to their broad spectrumof biological activities, including antispasmodic, anti-inflammatory, analgesic, antidiabetic, antitumor, and antibacterial properties.[10]

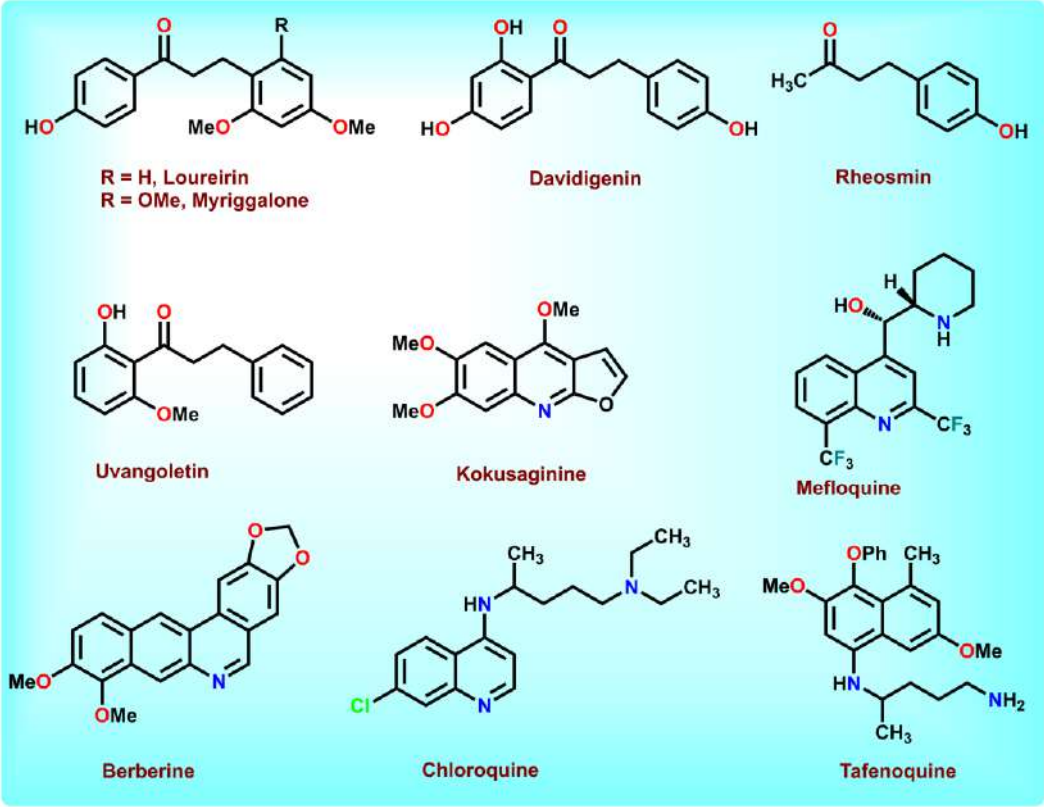

Scheme 3.1 Schematic illustration of pharmaceutically active compounds featuring 1,4-diaryl ketone cores, as well as amide and quinoline derivatives.

Over the years, considerable efforts have been devoted to the synthesis of nitrogen-containing heterocycles, employing both classical metal-free strategies and a range of metal-catalyzed multicomponent coupling reactions.[11,12] Despite the significant advancements achieved, many of the reported methodologies continue to face challenges such as prolonged multistep reaction sequences, reliance on pre-functionalized substrates, and the generation of substantial chemical waste. These limitations underscore the ongoing need for the development of alternative synthetic approaches that are not only efficient and atom-economical but also environmentally benign. In this context, designing methodologies that employ readily available and cost-effective starting materials while minimizing waste generation is highly desirable for the sustainable construction of nitrogen-rich heterocyclic frameworks.

Dehydrogenative functionalization of alcohols has recently gained prominence as an efficient and sustainable synthetic strategy for the construction of complex organic molecules, including nitrogen-containing heterocycles.[12] This methodology offers notable advantages in terms of atom economy and environmental compatibility, as it employs readily available, renewable alcohols and generates minimal waste. The resurgence of interest in this field has been fuelled by the development of innovative catalysts and catalytic systems that enable selective and efficient dehydrogenative transformations.[13-14] Significant progress has been made in applying this strategy to the synthesis of a wide range of N-heterocycles such as pyrroles,[15] pyridines,[16] pyrimidines,[17] quinolines,[18] quinazolinones,[19] and quinazolines,[20] demonstrating its utility in heterocyclic chemistry. Moreover, the scope of dehydrogenative functionalization has been extended to the synthesis of other high-value compounds, including amines, imines, amides, and esters, further emphasizing its broad applicability and growing importance in modern synthetic organic chemistry. This type of dehydrogenative C–N bond forming strategy can also be extended to C–C bond formation, offering a versatile approach to molecular construction. In this context, α-alkylated carbonyl scaffolds have emerged as important structural units due

to their broad spectrum of biological activities, including antibacterial, antispasmodic, anti-inflammatory, analgesic, antidiabetic, and antitumor properties (Scheme 3.1).[19]

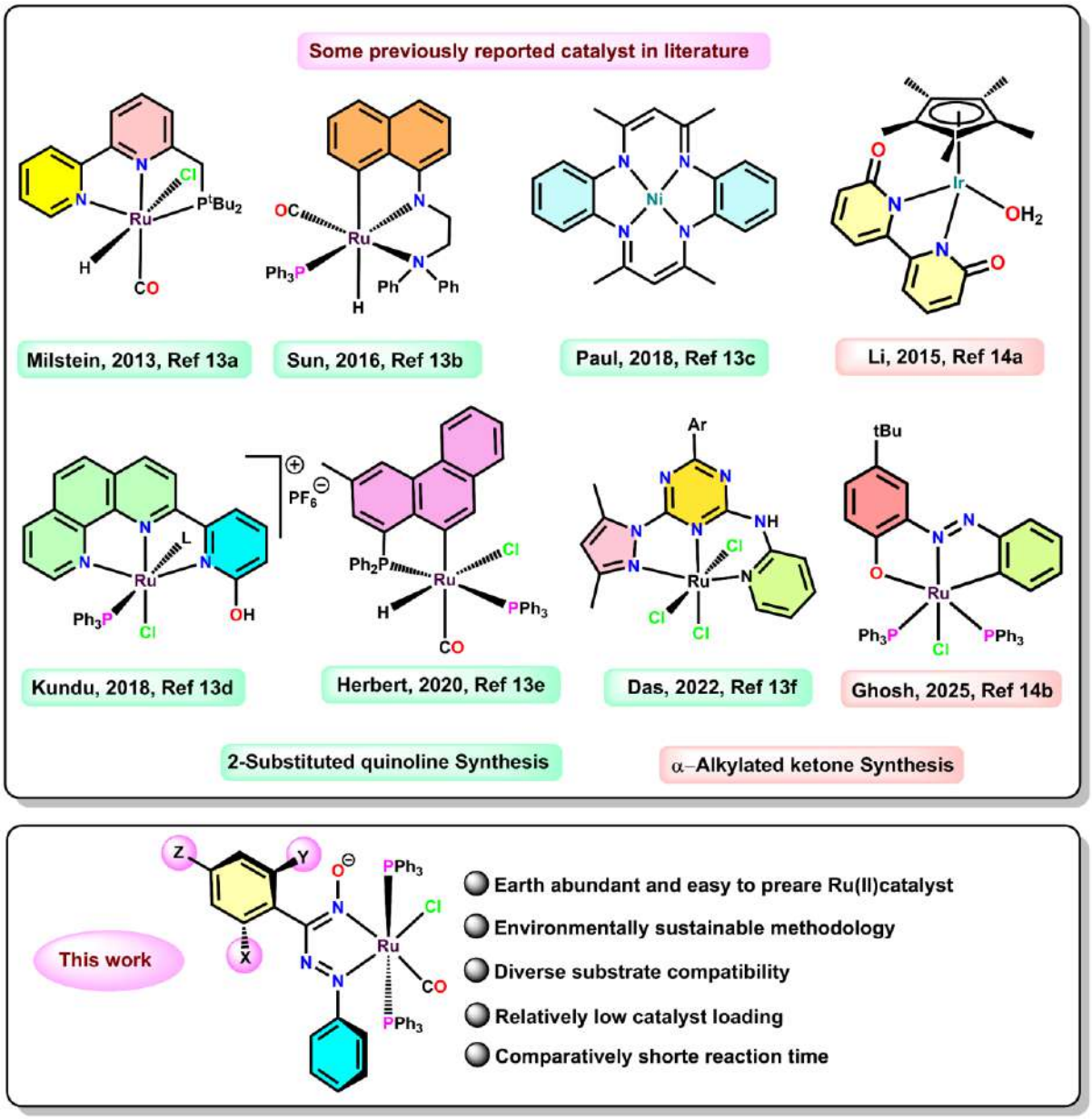

Scheme 3.2 Representative structures highly active ruthenium catalyst for alcohol dehydrogenation (AD)

Herein, we report a catalytic strategy for the α-alkylation of ketones with primary alcohols, followed by a dehydrogenative cyclization to afford 2-substituted quinolines, using a newly synthesized Ru(II) complex bearing an azo-oxime coordinated ligand. It is owing to the ability of coordinated ligand framework to accept an electron/s within the azo-oxime pocket that led

us to envisage that they may suitably employed as catalyst in certain electron transfer organic synthesis *via* conversion of alcohols to the corresponding carbonyls, followed by removal of hydrogen atom from diverse organic substrates, thereby facilitating coupling reactions.[13b,20] Detailed mechanistic investigations based on certain experimental data suggest that the catalytic cycle initiates with the formation of a coordinated azo anion-radical intermediate, which likely serves as the active species. This is followed by a hydrogen atom transfer (HAT) pathway that facilitates product formation. Furthermore, the presence of a dangling aryl group within the ligand framework was found to significantly influence both the catalytic efficiency and the yield of the desired quinoline products, highlighting its critical role in the overall transformation.

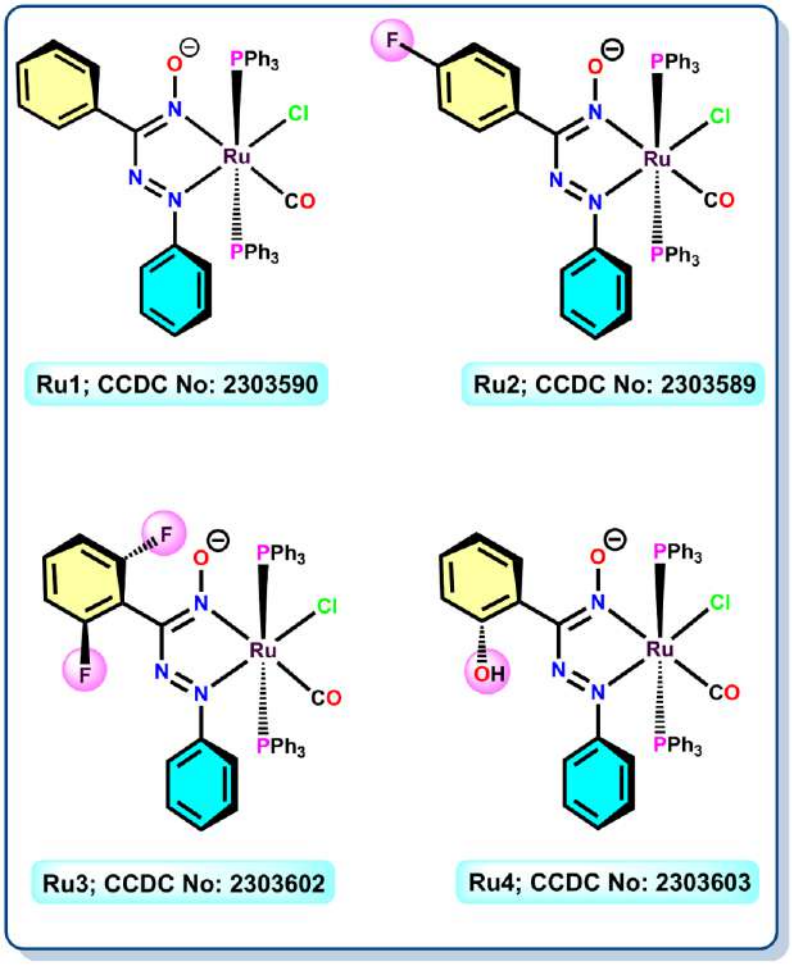

Scheme 3.3: The ruthenium(II) catalysts used in this study

3.2 Results and Discussion

3.2.1 Catalytic synthesis of α-alkylated ketones

The study commenced with the standardisation of reaction conditions for both type of reaction using aromatic primary alcohols. Our investigation began with catalyst screening for both types of reaction. Here we have used four redox active azo-oxime coordinated ruthenium(II) complexes which shown in Scheme 3.3. It has been observed that isolated yield for this reaction is highest with **Ru3** but in all cases, the yield is quite high (Table 3.1). Next, we investigated the optimized reaction conditions for the α-alkylation of ketones catalyzed by the synthesized ruthenium(II) complex. Initial screening with alkali metal hydroxide bases such as NaOH and KOH resulted in moderate product yields ranging from 50-75% (Table 3.2, Entry 1-4). However, when t-BuOK was employed in place of NaOH or KOH, a significant improvement in yield was observed (Table 3.2, Entry 5 & 6). To identify a potentially more effective base, a series of other bases such as Cs_2CO_3, K_2CO_3, and K_3PO_4 were tested under identical reaction conditions (Table 3.2, Entry 7-11). None of these alternatives outperformed t-BuOK, which remained the most effective base. Subsequently, we evaluated the influence of different solvents to determine whether a better alternative to toluene could be found. Solvents such as tetrahydrofuran (THF), acetonitrile, *N,N*-dimethylformamide (DMF), ethanol were tested (Table 3.2, Entry 12-15). In all cases, the yields were notably lower compared to toluene. This diminished efficiency is likely due to the coordinating ability of these solvents with the transition metal center, which may interfere the catalytic cycle. Additionally, lowering the catalyst loading to 0.001 mol% led to a significant reduction in product yield (Table 3.2, Entry 17). Therefore, the optimized reaction condition for this dehydrogenative synthesis of α-alkylated ketones is as follows: Ru3 catalyst (0.01 mol%), t-BuOK as base (1.0 equiv.) and toluene as a solvent. After establishing the optimized reaction conditions, we explored the substrate scope of the α-alkylation reaction. Acetophenone (**1a**) and benzyl alcohol (**2a**)

underwent smooth coupling to afford the corresponding α-alkylated ketone (**3a**) in 93% isolated yield (Table 3.3). Aryl ketones bearing electron-donating substituents at the *ortho*, *meta*, and *para* positions also reacted efficiently with benzyl alcohol (**2a**), delivering the desired products in good yields (**3b**: 85%, **3c**: 80%, **3d**: 86%, **3g**: 84%, **3h**: 90%). Furthermore, aromatic primary alcohols featuring either electron-donating or electron-withdrawing groups coupled successfully with acetophenone (**1a**), affording the corresponding alkylated products in yields of up to 92% (**3i**: 92%, **3j**: 83%, **3k**: 90%, **3l**: 83%, **3m**: 80%).

Table 3.1: Catalyst screening for α-alkylation of ketone

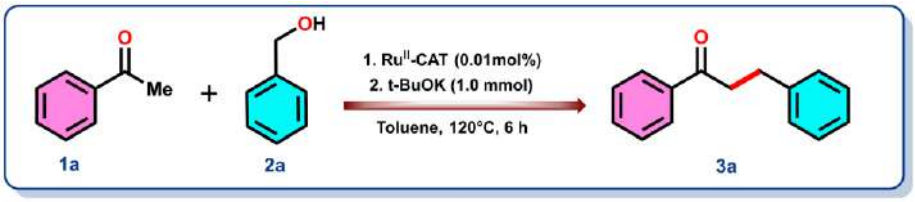

Entry	Ru^{II}-Catalyst	Yield of 3a (%)[b]
1	Ru1	78
2	Ru2	83
3	**Ru3**	**90**
4	Ru4	65

Table 3.2: Optimization of the Reaction Conditions for α -alkylation of ketones with primary alcohols *via* Catalytic Dehydrogenation by using Ru^{II}-Catalyst

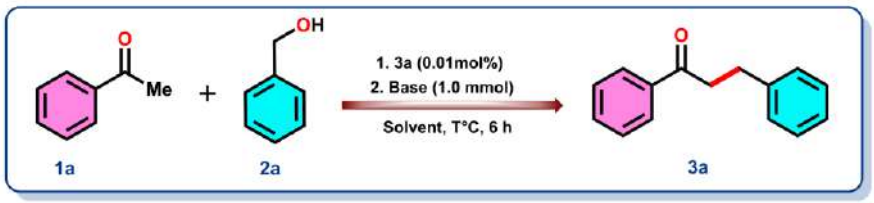

Entry	Catalyst (0.01 mol%)	Base	X	Solvent	T°C	Yield[b] (%)
1	Ru3	NaOH	0.5	Toluene	120	50
2	Ru3	NaOH	1.0	Toluene	120	75
3	Ru3	KOH	0.5	Toluene	120	50

4	Ru3	KOH	1.0	Toluene	120	65
5	Ru3	t-BuOK	0.5	Toluene	120	85
6	**Ru3**	**t-BuOK**	**1.0**	**Toluene**	**120**	**90**
7	Ru3	Cs_2CO_3	0.5	Toluene	120	40
8	Ru3	Cs_2CO_3	1.0	Toluene	120	45
9	Ru3	K_2CO_3	1.0	Toluene	120	50
10	Ru3	K_2CO_3	0.5	Toluene	120	46
11	Ru3	K_3PO_4	1.0	Toluene	120	38
12	Ru3	t-BuOK	1.0	THF	80	20
13	Ru3	t-BuOK	1.0	MeCN	80	10
14	Ru3	t-BuOK	1.0	DMF	120	trace
15	Ru3	t-BuOK	1.0	Ethanol	80	NR
16	Ru3	t-BuOK	1.0	Xylene	120	70
17	Ru3 (0.001 mol%)	t-BuOK	1.0	Toluene	120	42

*[a]Reaction conditions: **1a** (1 mmol), **2a** (1.1 mmol), **Ru3** (0.01 mol %), base (x equiv.), solvent (6 mL), 120 ºC (oil bath), 6 h. [b] Isolated yield*

Table 3.3: Substrate scope of α-alkylation of arylacetophenone

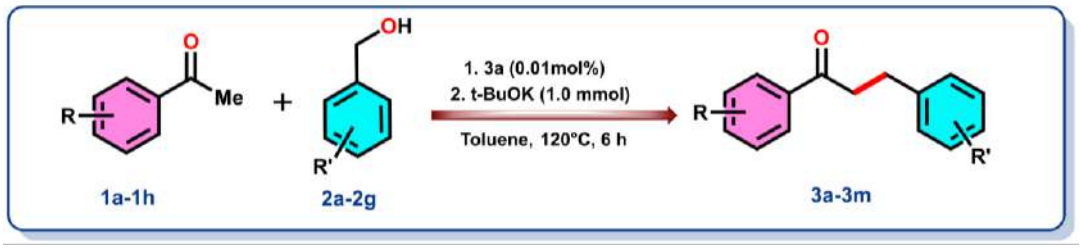

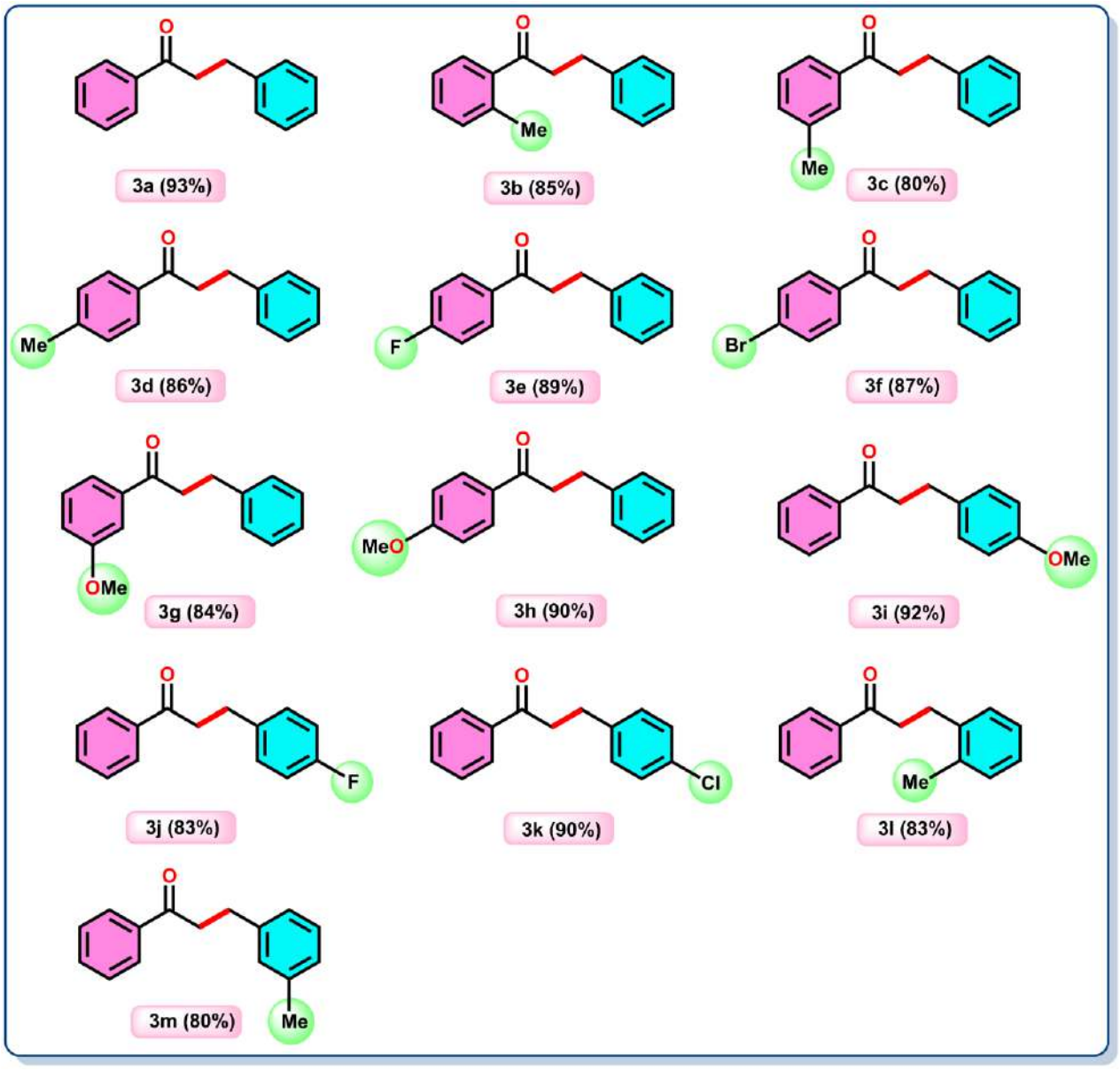

3.2.2 Catalytic synthesis of 2-substituted quinolines

To initiate our study, we carried out the reaction of *o*-aminobenzyl alcohol with acetophenone under a range of defined conditions, including variations in temperature, solvent, and catalyst loading, to identify the most effective catalyst for the dehydrogenative synthesis of 2-substituted quinolines. The catalytic performance of four ruthenium complexes (**Ru1**–**Ru4**) was systematically evaluated under identical reaction conditions (Table 3.4). Among these, **Ru3** emerged as the most efficient catalyst, affording the highest yield of the desired quinoline product. The remaining complexes (**Ru1**, **Ru2**, and **Ru4**) also facilitated the transformation with moderately high yields, demonstrating their catalytic competence, albeit to a lesser extent than **Ru3**. Following the identification of the most effective catalyst for this transformation, we turned our attention to optimizing the reaction conditions. The dehydrogenative cyclization proceeded most efficiently when the reaction was conducted in toluene at 85 °C for 5 h in the presence of *tert*-butoxide (t-BuOK) as the base. Under these conditions, high yields of the desired quinoline derivatives were obtained (Table 3.5). A marked decrease in yield was observed when the reaction temperature was lowered to 70 °C or when the reaction time was reduced to 3 h, indicating the critical role of thermal activation and sufficient reaction duration. Furthermore, increasing the temperature to 120 °C, extending the reaction time beyond 5 h, or increasing the catalyst loading did not lead to any significant improvement in yield, suggesting that the reaction conditions were already near optimal under the standard protocol. The scope of these cyclization reactions of o-amino benzyl alcohols with methyl ketones were examined and detailed in Table 3.6. 2-aminobenzyl alcohol (**4a**) reacts with series of aryl methyl ketones containing both electron donating and withdrawing group. Aryl methyl ketone containing electron donating at *ortho*, *meta* and *para* position successfully coupled with **4a** to give the corresponding 2-substituted quinolines isolated yield up to 94% (**5a**: 93%, **5b**: 90%, **5c**: 91%, **5d**: 94%, **5e**: 87%, **5f**: 85 %). Aryl methyl ketone containing strong electron withdrawing group

such as –F, –Br and –NO_2 at *ortho*, *meta* and *para* position also annulated with **4a** to produce desired products with good to excellent yield (**5g**: 85%, **5h**: 89%, **5i**: 92%, **5j**: 88%, **5k**: 65%, **5l**: 60%). Polyaromatic ketone such as 1-(naphthalen-2-yl)ethan-1-one (**1m**) is also react with **4a** to produce corresponding quinoline derivative (**5m**) with the isolated yield of 87%. Similarly, dialkyl ketone like 2-octanone is successfully coupled to form the corresponding 2-substuted quinoline (**5n**) with 75% yield.

Table 3.4: Catalyst screening for α-alkylation of ketone

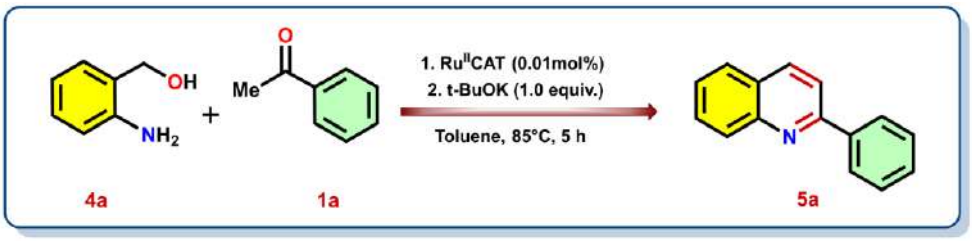

Entry	Ru^{II}-Catalyst	Yield of 6a (%)[b]
1	Ru1	80
2	Ru2	85
3	**Ru3**	**93**
4	Ru4	70

*[a] Reaction conditions: **4a** (1 mmol), **1a** (1.1 mmol), Ru^{II}-Catalyst (0.01 mol %), base (1.0 equiv.), toluene (6 mL), 85 °C (oil bath), 5 h reaction time, [b] Isolated yield.*

Table 3.5. Optimization of the Reaction Conditions for synthesis of 2-substituted quinoline derivatives from 2-amino benzyl alcohol/ 2-amino 5-chloro benzyl alcohol with substituted acetophenones/ alkyl methyl ketones using Ru-catalyst

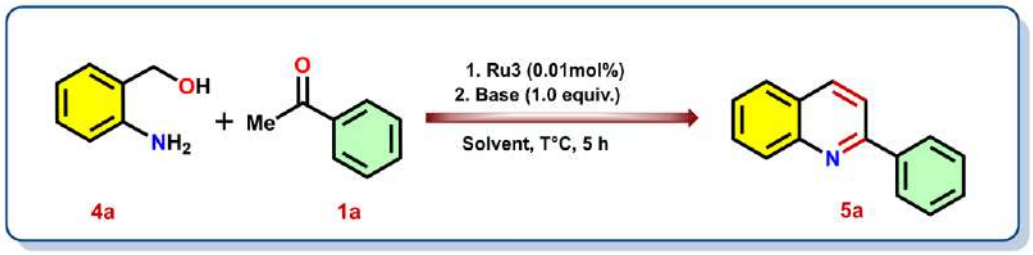

Entry	Catalyst (0.01 mol%)	Base	x (equiv.)	Solvent	T°C	Yield[b] (%)
1	Ru3	NaOH	0.5	Toluene	85	55
2	Ru3	NaOH	1.0	Toluene	85	62
3	Ru3	KOH	0.5	Toluene	85	70
4	Ru3	KOH	1.0	Toluene	85	75
5	**Ru3**	**t-BuOK**	**1.0**	**Toluene**	**85**	**93**
6	Ru3	t-BuOK	0.5	Toluene	85	80
7	Ru3	t-BuOK	0.5	Xylene	85	71
8	Ru3	t-BuOK	0.5	MeCN	85	trace
9	Ru3	Cs_2CO_3	1.0	Toluene	85	50
10	Ru3	K_2CO_3	0.5	Toluene	85	52
11	Ru3	K_2CO_3	1.0	Toluene	85	63
11	Ru3	Cs_2CO_3	0.5	Toluene	85	40
12	Ru3	K_3PO_4	0.5	Toluene	85	45
13	Ru3	K_3PO_4	1.0	Toluene	85	51
14	Ru3	t-BuOK	1.0	Toluene	100	94
15	Ru3	t-BuOK	1.0	Toluene	120	94

*[a]Reaction conditions: **4a** (1 mmol), **5a** (1.1 mmol), **Ru3** (0.01 mol %), base (x equiv.), solvent (6 mL), 85°C (oil bath), 5 h reaction time. [b] Isolated yield.*

Table 3.6: Substrate scope of 2-substituted quinolines

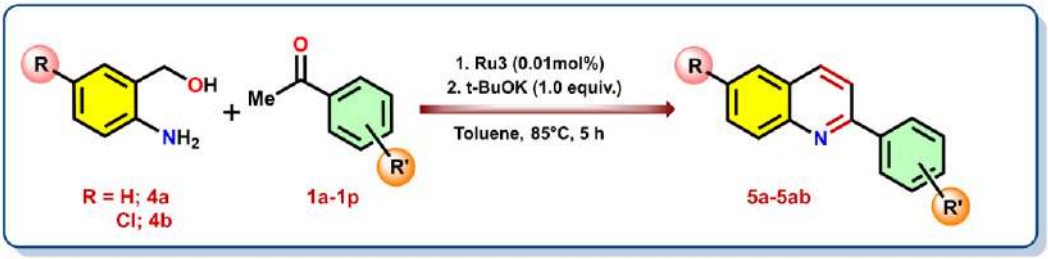

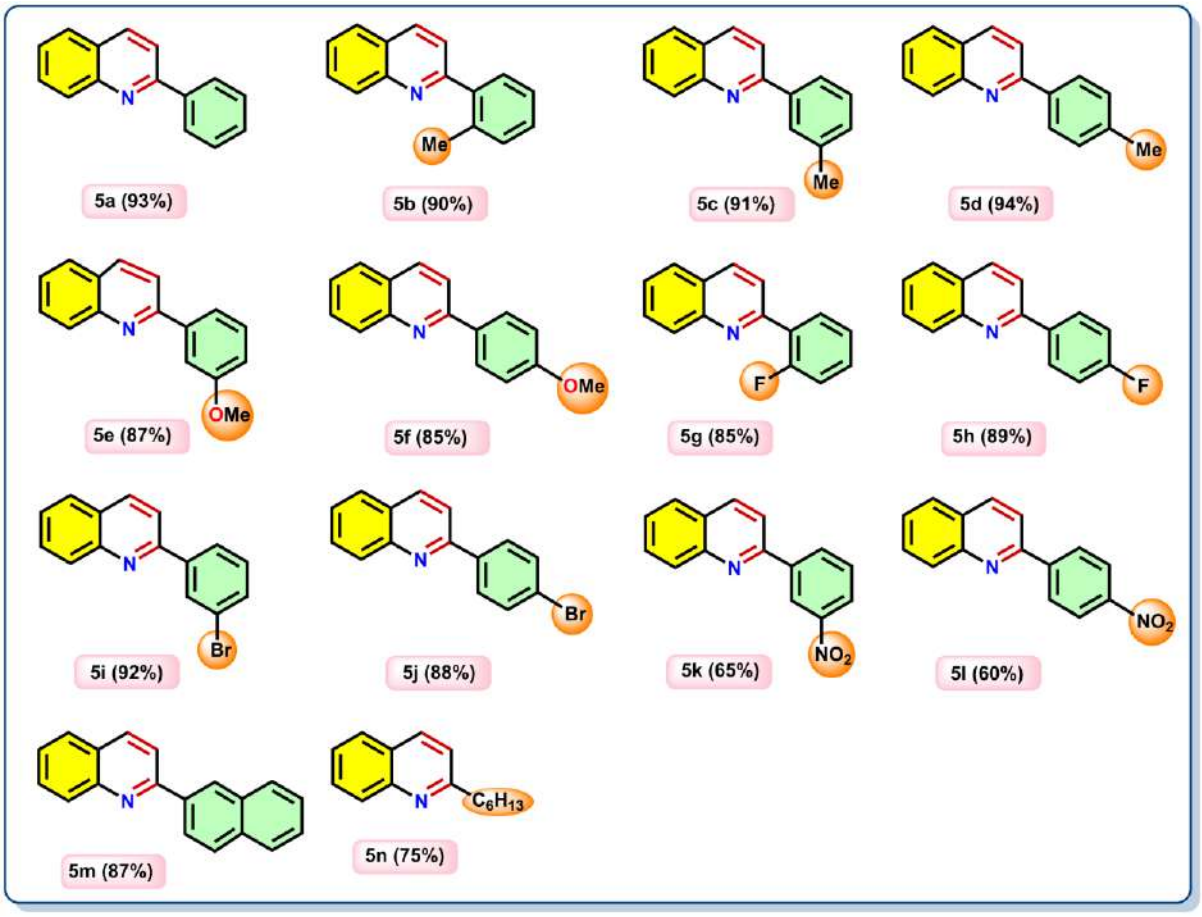

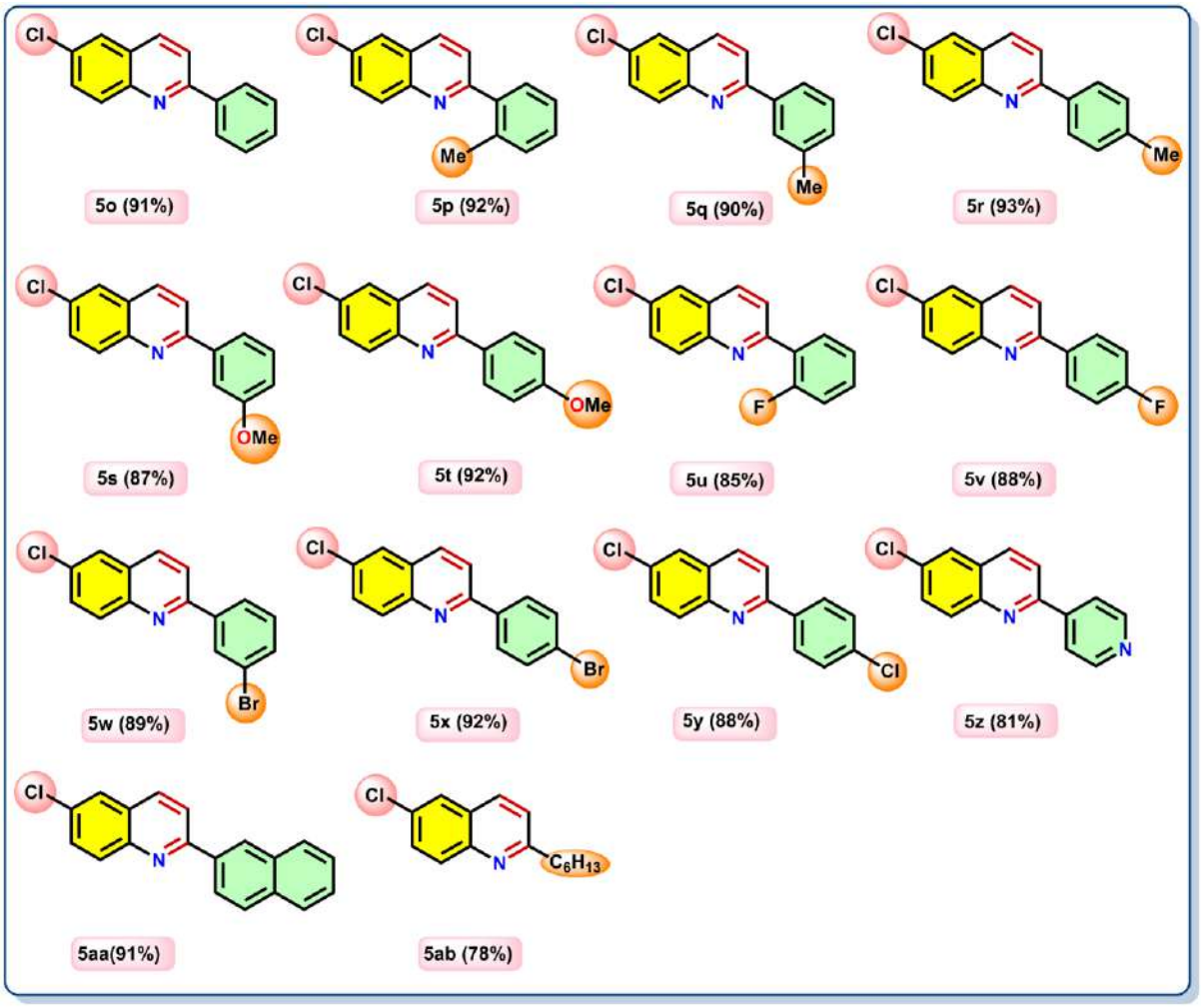

Additionally, 5-chloro-2-aminobenzyl alcohol (**4b**) effectively reacts with a variety of aryl and alkyl ketones to furnish the corresponding 2-substituted quinoline derivatives in good to excellent yields (Table 3.6). Aryl methyl ketones bearing electron-donating groups at the ortho, meta, or para positions underwent smooth annulation with **4b**, affording the desired quinoline products in yields of up to 94% (**5o**: 91%, **5p**: 92%, **5q**: 90%, **5r**: 93%, **5s**: 87%, **5t**: 92%). Similarly, aryl methyl ketones containing strong electron-withdrawing substituents such as –F, –Cl, and –Br at various positions also reacted efficiently with **4a**, yielding the corresponding quinolines in high yields (**5u**: 85%, **5v**: 88%, **5w**: 89%, **5x**: 92%, **5y**: 88%). Notably, a heteroaryl methyl ketone (**1p**) successfully coupled with **4b** to deliver quinoline derivative **6z** in 81% yield. Furthermore, a polyaromatic ketone such as 1-(naphthalen-2-yl)ethan-1-one (**1m**) underwent smooth cyclization with **4a**, furnishing product **5aa** in 91% yield. In addition,

an aliphatic dialkyl ketone like 2-octanone also participated in the reaction, producing 2-substituted quinoline **5ab** with a yield of 78%.

3.2.3 Mechanistic study

To elucidate the mechanism of these catalytic transformation and to and to have an insight into the coordinated azo-anion ligand radical intermediates formed during Ru(II)-catalyzed synthesis of α-alkylated ketones and 2-substituted quinolines, the following control experiments were performed under optimized reaction condition. Since the alkylation reactions were carried out at 120°C, the stability of catalyst was checked under aerobic condition and all of them *viz.*, **Ru1**, **Ru2**, **Ru3** and **Ru4** were found to be stable at 120°C in toluene and other organic solvent. In order to comprehend the homogeneity of catalytic transformations as well as the involvement of catalysts, mercury poisoning test was performed. The dehydrogenation of alcohol and subsequent coupling reactions were unaffected by the presence of mercury. The basic mechanism of catalytic transformation in both the above type of reactions appear to be similar.

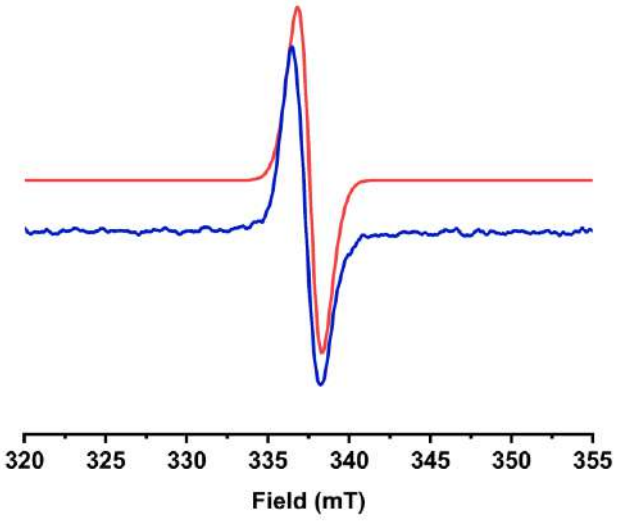

Figure 3.1: Experimental (blue) and simulated (red) EPR spectra of $[Ru_3]^{\bullet-}$ generated upon reaction of Ru3 with t-BuOK in toluene. Instrument settings: Microwave frequency 9.458 GHz; Microwave power 0.998 mW; Modulation frequency, 100 kHz.

The catalysis has been found to be initiated with the formation anion radical species *trans*-$[Ru(L^{\bullet-})(CO)Cl(PPh_3)_2]^-$ **[Ru1]$^{\bullet-}$**-**[Ru4]$^{\bullet-}$** *via* one-electron reduction of the catalyst *trans*-$[RuL(CO)Cl(PPh_3)_2]$ (**Ru1**-**Ru4**) in presence of t-BuOK. This conception has been ascertained by refluxing the catalyst with t-BuOK only for 30 minutes and performing EPR (g_{iso} = 1.999) with the reaction mixture (Figure 3.5). In order to confirm the participation of ligand-centric coordinated azo-anion radical intermediates/ other organic radical species during catalytic transformation, dehydrogenation of **2a** was carried out in presence of equivalent amount of radical scavenger, TEMPO (2,2,6,6-Tetramethylpiperidin-1-yl)oxyl), under optimised reaction condition (Scheme 3.5, Entry 1). Notably, the formation of corresponding aldehyde **2a′** is drastically reduced. Moreover, when we performed the coupling reaction between **1a** and **2a** as well as between **4a** and **1a**, the yield

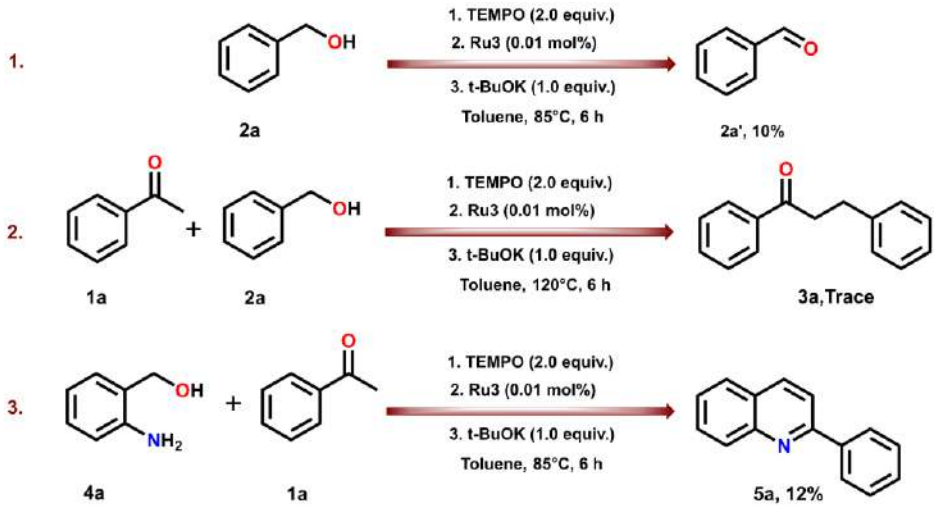

Scheme 3.4 Radical scavenging experiment for alcohol dehydrogenation and subsequent coupling reaction

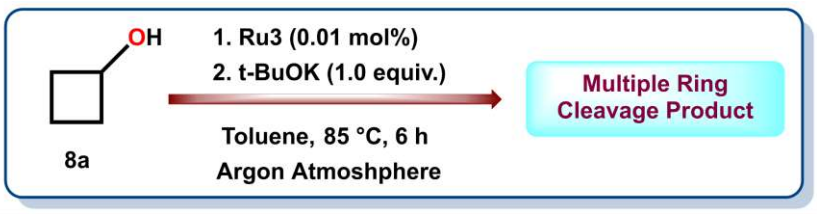

Scheme 3.5: Oxidation of radical clock substrate cyclobutanol under optimal condition

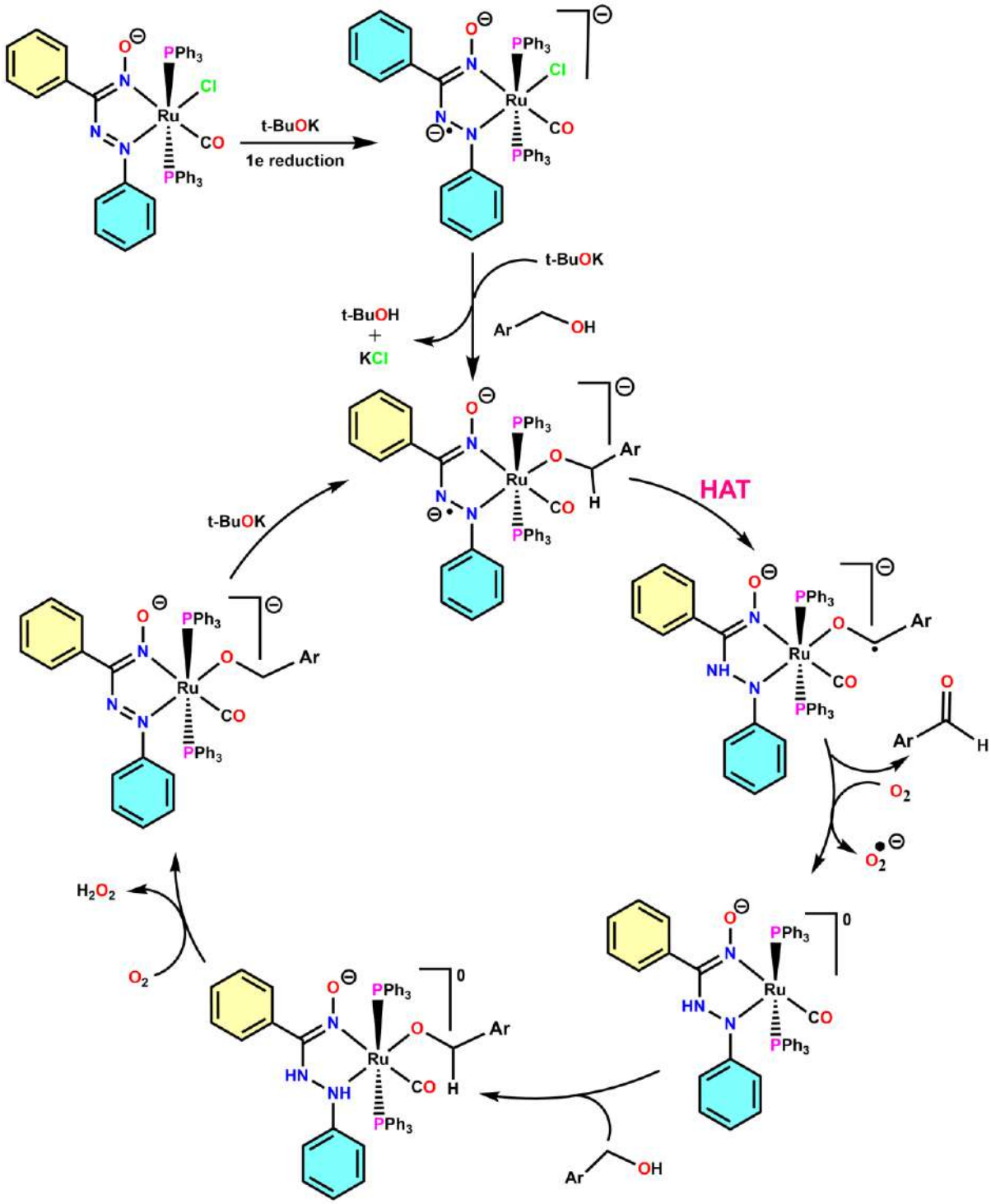

Scheme 3.6: plausible rection pathway of ruthenium(II) catalysed alcohol dehydrogenation

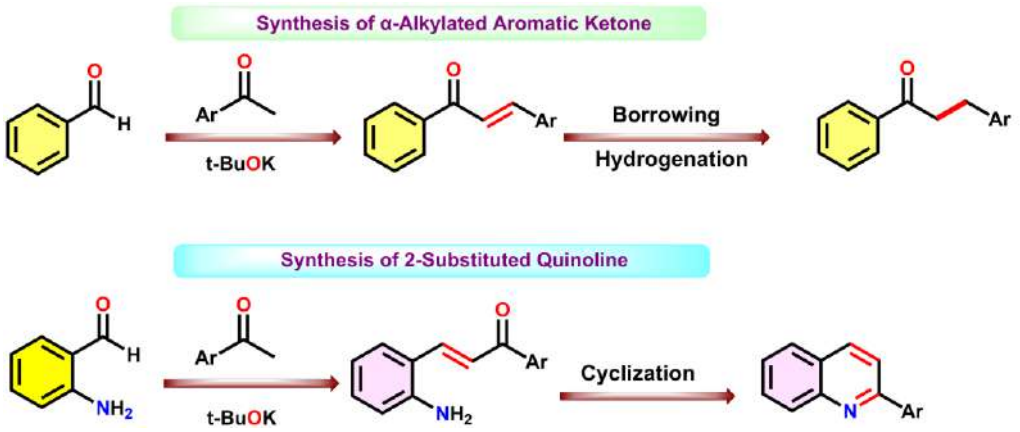

Scheme 3.7: Schematic depiction final product formation

of corresponding **3a** and **5a** reduced significantly, thereby demonstrating the active participation of radical intermediate (Scheme 3.4, Entry 2 & 3). To have further perception about the radical intermediate we carried out a reaction of 1-phenylethanol (**7a**) and **Ru3** (1 mol%) and 3 equivalents of t-BuOK in toluene under argon atmosphere. IR spectrum of the reaction mixture reveals that there are N–H stretches at 3032 and 3065 cm^{-1}, consistent with previous reports (See Figure 3.6.A1).[21] In order to support azo to hydrazo transformation the aforesaid reaction was carried out with deuterated 1-phenylethanol (**7a-D_2**) under an argon atmosphere (See Figure 3.6.A2). Analysis of IR spectrum of the reaction mixture revealed N–D attributions at 2117 and 2130 cm^{-1}. Therefore, *trans*-$[Ru(L^{\bullet-})(CO)Cl(PPh_3)_2]^-$ behaves as the active catalyst during the process.

In order to identify whether the oxidation of primary alcohol proceeds through a H^- ($2e^-$) or H-atom ($1e^-$) transfer process, we have oxidised a radical clock substrate cyclobutanol (**8a**) under optimal reaction condition (Scheme 3.5).[22] The ^1H NMR analysis revealed different ring cleavage products instead of $2e^-$ reduced product cyclobutanone (see Figure 3.6.A3). These experimental findings suggest that the coordinated azo-oximato ligand is actively participated in catalysis. The coordinated alkoxide radical is being transformed to corresponding aldehyde conceivably *via* removal of electron by molecular oxygen, the latter being converted to

superoxide. This conception is intuitive owing to lack of experimental evidences.[22b,23] The aldehyde so formed possibly reacts with methyl ketone in a single-pot reaction to form α,β-unsaturated carbonyl compound (aldol type condensation) which are further hydrogenated *via* "borrowing hydrogen (BH) catalysis" to form the reported organic products.[23c] For 2-substituted quinoline synthesis, similar aldol type condensation products are formed which further cyclized to quinoline moiety owing to greater stabilisation of aromatic ring than acyclic α,β-unsaturated carbonyl product (see Scheme 3.7). The catalytic cycle is completed by coordination of the second molecule of the 1º alcohol to the Ru(II) centre with concomitant removal of hydrogen peroxide in presence of aerial oxygen.[24] We have studied the catalytic organic synthesis by using four catalysts **Ru1**-**Ru4** and in both type of reactions, it has been found that yield is substantially higher upon using **Ru3** and in fact, the order of catalytic yield is with **Ru3** > **Ru2** > **Ru1** > **Ru4**. Thus, the pendant aryl group in the coordinated ligand framework must have some role during the process since the other portion of the catalysts remain unaltered. From Scheme 2.1 (Chapter 2), the pendant aryl groups in **1**, **2**, **3** and **4** are respectively phenyl, 4-fluorophenyl, 2,6-difluorophenyl and 2-hydroxyphenyl. Therefore, with decrease in electron withdrawal ability of pendant aryl group from **Ru3** → **Ru2** → **Ru1a**→ **Ru4**, the extent of catalysis decreases, thereby disclosing the role of these groups during the catalytic process.

3.3 Conclusion

In this work we have explored ruthenium(II) catalyzed synthesis of two types of reactions (1) α -alkylation of ketones with primary alcohols and (ii) synthesis of 2-substituted quinoline derivatives from 2-aminobenzyl alcohols and substituted acetophenones/ alkyl methyl ketone using alcohol dehydrogenation (AD) and borrowing hydrogenation (BH) strategy. The scope of catalytic reactions has been investigated at length and probable mechanism of catalysis have been provided from several experimental findings. The catalytic pathway has been found to be

practically ligand-centric redox-driven for the dehydrogenation process and the initial step involves formation of $[Ru(L^{\bullet -})(CO)Cl(PPh_3)_2]^-$, the latter behaving as the active catalyst. This led to the transformation of starting 1º alcohol to corresponding carbonyl *via* HAT pathway with the metal centre behaving as a template and is not involved in redox events. The catalysis has been found to be affected by the nature of pendant aryl groups within the coordinated ligand. With increase in electron withdrawal aptitude of the aryls, from **Ru4 → Ru1 → Ru2 → Ru3,** yield of products has increased appreciably, conceivably owing to their enhanced ability to form the corresponding anion radical to initiate the catalytic reaction.

3.4 Experimental Section

3.4.1 General Information

All the reaction mention in this paper were performed under aerobic condition. Required reagents and solvent was used as soon as they received without any further synthetic manipulation. The following sources were used for purchase of required chemicals: phenyl hydrazine, benzaldehyde, 2-hydroxybenzaldehyde, 2,6-difluorobenzaldehyde and 4-fluorobenzaldehyde were purchased from TCI Chemical (India) Pvt. Ltd. Triphenylphosphine (PPh_3) was obtained from Sigma-Aldrich. Ruthenium trichloride ($RuCl_3.\ xH_2O$) was taken from Arora-Matthey (India) Ltd. n-Butyl nitrite was prepared by using literature procedure[1].

3.4.2 Synthesis of a representative anion radical complex $[Ru3]^{\bullet -}$

To a solution of **Ru3** (0.05 mmol, 47.5 mg) in dry toluene (15 ml), t-BuOK (1.0 equiv., 112 mg) was added and refluxed for 30 min. The Purple red coloured solution was gradually turned into brownish yellow coloured solution. After 30 min the reaction mixture was cooled to room temperature and filtered through a silica pad to remove excess t-BuOK and other solid impurities. The solvent was rapidly evaporated to dryness under reduced pressure and extracted with n-heptane. The n-heptane solution was then evaporated as quickly as possible to obtain

brownish yellow solid compound **[Ru3]$^{\bullet-}$**. Yield: 30 mg (63%). Anal. Calcd (%) for **[Ru3]$^{\bullet-}$** $C_{50}H_{38}N_3O_2F_2ClP_2Ru$: C, 63.26; H, 4.03; N, 4.43. Found: C, 63.17; H, 4.06; N, 4.45. FT-IR/cm^{-1} υ = 1947 ($\upsilon_{C=O}$), 1367 ($\upsilon_{N=N}$), 1079 (υ_{N-O}).; λ_{max}/nm in CH_2Cl_2: 459, 303, 264.

3.4.3 Mercury poisoning test

To a mixture of *o*-aminobenzyl alcohol (**4a)** (246 mg, 2.0 mmol, 1 equiv.), acetophenone (**5a**) (0.26 ml, 2.2 mmol), t-BuOK (224 mg, 2.0 mmol, 1 equiv.), catalyst **Ru3** (0.2 mg, 0.01 mol%) taken in a 20 ml round bottomed flask containing 5 ml toluene along with a magnetic stir bar, 50 equiv. of mercury (738 mg) was added under open air atmosphere. The resulting mixture was heated at 85°C for 6h under stirring condition. After the completion of reaction organic part was extracted with EtOAc and purified by column chromatography using hexane/EtOAc (3:1 v/v). The isolated yield of the desired product (**6a**) was 89%. The similar procedure was applied for the reaction of **1a** and **2a**.

3.4.4 General Method for Synthesis of α-Alkylated Aromatic Ketones:

A mixture of catalyst **Ru3** (0.1 mg, 0.01 mol %), t-BuOK (1.0 equiv.), ketone (1.0 mmol), and 2-aromatic primary alcohol (1.1 mmol) was added to a 20 ml flat-bottom flask. To this, 6 mL of dry toluene was added. The reaction mixture was then placed in an oil bath preheated at 120°C equipped with a reflux condenser. The reaction was continued for 6 h under open air atmosphere. After completion, distilled water was added to the reaction mixture and organic part was extracted with EtOAc followed by washing with brine solution. The resulting organic part was evaporated to dryness under vacuum. The crude organic product was isolated through column chromatography using silica gel (60-120 mesh) as solid phase and hexane/EtOAc mixture as eluent.

3.4.5 General Method for one-pot Cascade Synthesis of Quinolines

A mixture of catalyst **Ru3** (0.1 mg, 0.01 mol %), t-BuOK (1.0 equiv.), ketone (1.0 mmol), and 2-aminobenzylalcohol/2-amino 5-chloro benzyl alcohol (1.0 mmol) was added to a 20 ml flat-bottom flask. To this, 6 mL of dry toluene was added. The whole reaction mixture was then placed in an oil bath preheated at 85 °C equipped with a reflux condenser. The reaction was continued for 5 h under aerobic condition. After completion, distilled water was added to the reaction mixture and organic part was extracted with EtOAc followed by washing with brine solution. The resulting organic part was evaporated to dryness under vacuum. The crude organic product was isolated through column chromatography using silica gel (60-120) as stationary phase and hexane/EtOAc mixture as eluent.

3.5 References

[1] (a) A. R. Katritzky, C. W. Rees, Comprehensive Heterocyclic Chemistry II; Elsevier: Oxford, **1996**. (b) K. Nepali, H.-Y. Lee, J.-P. Liou, *J. Med. Chem.*, **2019**, *62*, 2851–2893.

[2] (a) J. P. Michael, *Nat. Prod. Rep.*, **2008**, *25*, 166−187. (b) J. P. Michael, *Nat. Prod. Rep.*, **2002**, *19*, 742−760. (c) S. Vandekerckhove, M. D'hooghe, *Bioorg. Med. Chem.*, **2015**, *23*, 5098−5119. (d) S. Shagufta, I. Ahmad, *MedChemComm*, **2017**, *8*, 871−885.

[3] (a) P. Narender, U. Srinivas, M. Ravinder, B. A. Rao, C. Ramesh, K. Harakishore, B. Gangadasu, U. S. N Murthy, V. J. Rao, *Bioorg. Med. Chem.*, **2006**, *14*, 4600−4609. (b) P.-P. Kung, M. D. Casper, K. L. Cook, L. Wilson-Lingardo, L. M. Risen, T. A. Vickers, R. Ranken, L. B. Blyn, J. R. Wyatt, P. D. Cook, D. J. Ecker, *J. Med. Chem.*, **1999**, *42*, 4705−4713.

[4] (a) N. A. Santagati, E. Bousquet, A. Spadaro, G. Ronsisvalle, **1999**, *54*, 780−784. (b) G. Roma, M. Di Braccio, G. Grossi, F. Mattioli, M. Ghia, *Eur. J. Med. Chem.*, **2000**, *35*, 1021−1035.

[5] (a) L.-P. Guan, Q.-H. Jin, G.-R. Tian, K.-Y. Chai, Z.-S. Quan, *J. Pharm. Pharm. Sci.*, **2007**, *10*, 254−262. (b) V. G. Ugale, S. B. Bari, *Eur. J. Med. Chem.*, **2014**, *80*, 447−501.

[6] (a) R. G. Ridley, *Nature*, **2002**, *415*, 686−693. (b) P. Verhaeghe, N. Azas, M. Gasquet, S. Hutter, C. Ducros, M. Laget, S. Rault, P. Rathelot, P. Vanelle, *Bioorg. Med. Chem. Lett.*, **2008**, *18*, 396−401.

[7] (a) P. Benedetti, R. Mannhold, G. Cruciani, Ottaviani, *Bioorg. Med. Chem.*, **2004**, *12*, 3607−3617. (b) A. M. Alafeefy, A. A. Kadi, O. A. Al-Deeb, K. E. H. El-Tahir, N. A. Al-Jaber, *Eur. J. Med. Chem.*, **2010**, *45*, 4947−4952.

[8] (a) T. H. Thatcher, I. Luzina, R. Fishelevich, M. A. Tomai, R. L. Miller, A. A. Gaspari, *J. Invest. Dermatol.*, **2006**, *126*, 821−831. (b) J. F. M. da Silva, M. Walters, S. Al-Damluji, C. R. Ganellin, *Bioorg. Med. Chem.*, **2008**, *16*, 7254−7263.

[9] (a) Y. Zhang, M. D. Tortorella, J. Liao, X. Qin, T. Chen, J. Luo, J. Guan, J. J. Talley, Z. Tu, *ACS Med. Chem. Lett.*, **2015**, *6*, 1086−1090. (b) K. Juvale, J. Gallus, M. Wiese, *Bioorg. Med. Chem.*, **2013**, *21*, 7858−7873.

[10] J. Y. Fan, T. Yi, C. M. Sze-To, L. Zhu, W. L. Peng, Y. Z. Zhang, Z. Z. Zhao, H. B. Chen, *Molecules*, **2014**, *19*, 10650–10669.

[11] (a) P. A. Claret, *Comprehensive Organic Chemistry*; D. Barton, W. D. Ollis, Eds.; Pergamon Press: Oxford, **1979**; *Vol. 4*, pp 1479−1489. (b) G. Jones, *Comprehensive Heterocyclic Chemistry II*; A. R., Katritzky, C. W. Rees, E. F. V. Scriven, A. McKillop, Eds.; Pergamon: Oxford, **1996**; *Vol. 5*, pp 167−300. (c) R. D. Larsen, *Science of Synthesis*; D. S. Black, Ed.; Thieme: Stuttgart, **2005**; *Vol. 15*, pp 389−549. (d) V. V. Kouznetsov, L. Y. V. Méndez, C. M. M. Gómez, *Curr. Org. Chem.*, **2005**, *9*, 141−161. (e) R. D. Larsen, *Science of Synthesis* (D. S.Black Ed.; Thieme: Stuttgart), **2005**, *Vol. 15*, pp 551−660. (f) S. A. Yamashkin, E. A. Oreshkina, *Chem. Heterocycl. Compd.*, **2006**, *42*, 701− 718. (g) R. Martínez, D. J. Ramón, M. Yus, *J. Org. Chem.*, **2008**, *73*, 9778−9780. (h) S. Madapa, Z. Tusi, S. Batra, *Curr. Org. Chem.*, **2008**, *12*, 1116−1183. (i) R. I. Khusnutdinov, A. R. Bayguzina, U. M. Dzhemilev, *J. Organomet. Chem.*, **2014**, *768*, 75−114. (j) G. A. Ramann, B. J. Cowen, *Molecules* **2016**, *21*, 986−1008.

[12] (a) D. J. Connolly, D. Cusack, T. P. O'Sullivan, P. J. Guiry, *Tetrahedron*, **2005**, *61*, 10153−10202. (b) Y. Yan, Y. Zhang, C. Feng, Z. Zha, Z. Wang, *Angew. Chem., Int. Ed.*, **2012**, *51*, 8077−8081. (c) H. Yuan, W. -J. Yoo, H. Miyamura, S. Kobayashi, *Adv. Synth. Catal.*, **2012**, *354*, 2899−2904. (d) J. -P. Lin, F. -H. Zhang, Y. -Q. Long, *Org. Lett.*, **2014**, *16*, 2822−2825. (e) C. Li, S. An, Y. Zhu, J. Zhang, Y. Kang, P. Liu, Y. Wang, J. Li, *RSC Adv.*, **2014**, *4*,

49888−49891. (f) S. S. Alneyadi, I. A. Shehadi, I. M. Abdou, *Heterocycl. Commun.*, **2015**, *21*, 115. (g) M. Ramanathan, S. -T. Liu, *J. Org. Chem.*, **2017**, *82*, 8290−8295 and references cited therein.

[13] (a) D. Srimani, Y. Ben-David, D. Milstein, *Chem. Commun.*, **2013**, *49*, 6632–6634 (b) B. Pan, B. Liu, E. Yue, Q. Liu, X. Yang, Z. Wang, W. -H. Sun, *ACS Catal.*, **2016**, *6*, 1247–1253. (c) S. Parua, R. Sikari, S. Sinha, G. Chakraborty, R. Mondal, N. D. Paul, *J. Org. Chem.*, **2018**, *83*, 11154−11166. (d) M. Maji, K. Chakrabarti, B. Paul, B. C. Roy and S. Kundu, *Adv. Synth. Catal.*, **2018**, *360*, 722–729. (e) R. Mondal and D. E. Herbert, *Organometallics*, **2020**, *39*, 1310–1317. (f) D. Bhattacharyya, P. Adhikari, K. Deoria, A. Das, *Catal. Sci. Technol.*, **2022**, *12*, 5695–5702.

[14] (a) R. Wang, H. Fan, W. Zhao, F. Li, *Org. Lett.*, **2016**, *18*, 3558−3561. (b) S. Singh, R. Saini, V. K. Chaudhary, K. Ghosh, *Chem Asian J.*, **2025**, *20*, e202400811.

[15] (a) N. D. Schley, G. E. Dobereiner, R. H. Crabtree, *Organometallics*, **2011**, *30*, 4174−4179. (b) M. Zhang, H. Neumann, M. Beller, *Angew. Chem., Int. Ed.*, **2013**, *52*, 597−601. (c) M. Zhang, X. Fang, H. Neumann, M. Beller, *J. Am. Chem. Soc.* **2013**, *135*, 11384−11388. (d) S. Michlik, R. Kempe, *Nat. Chem.*, **2013**, *5*, 140−144. (e) D. Srimani, Y. Ben-David, D. Milstein, *Angew. Chem. Int. Ed.*, **2013**, *52*, 4012−4015.

[16] S. Michlik, R. Kempe, *Angew. Chem., Int. Ed.*, **2013**, *52*, 6326−6329.

[17] N. Deibl, K. Ament, R. Kempe, *J. Am. Chem. Soc.*, **2015**, *137*, 12804−12807.

[18] (a) M. Mastalir, M. Glatz, E. Pittenauer, G. Allmaier, K. Kirchner, *J. Am. Chem. Soc.*, **2016**, *138*, 15543−15546. (b) S. Shee, K. Ganguli, K. Jana, S. Kundu, *Chem. Commun.*, **2018**, *54*, 6883−6886. (c) S. Das, D. Maiti, S. De Sarkar, *J. Org. Chem.*, **2018**, *83*, 2309−2316.
(18) (a) M. Chen, M. Zhang, B. Xiong, Z. Tan, W. Lv, H. Jiang, *Org. Lett.*, **2014**, *16*, 6028−6031. (b) J. Fang, J. Zhou, Z. Fang, *RSC Adv.*, **2013**, *3*, 334−336.

[19] (a) K. Joule, J. A. Mills, *Heterocyclic Chemistry*, 5th ed., Wiley: Chichester, U. K., **2010**; b) S. Bongarzone, M. L. Bolognesi, *Expert Opin. Drug Discovery*, **2011**, *6*, 251.

[20] (a) K. Taguchi, H. Nakagawa, T. Hirabayashi, S. Sakaguchi, Y. Ishii, *J. Am. Chem. Soc.*, **2004**, *126*, 72−73 (b) T. Kuwahara, T. Fukuyama, I. Ryu, *Org. Lett.*, **2012**, *14*, 4703–4705.

[21] S. Sinha, S. Das, R. Sikari, S. Parua, P. Brandaŏ, S. Demeshko, F. Meyer, N. D. Paul, *Inorg. Chem.*, **2017**, *56*, 14084−14100.

[22] (a) R. Ray, S. Chandra, D. Maiti, G. K. Lahiri, *Chem. Eur. J.*, **2016**, *22*, 8814−8822. (b) Y. Ma, Z. Du, J. Liu, F. Xia, J. Xu, *Green Chem.*, **2015**, *17*, 4968−4973. (c) D. Sengupta, R. Bhattacharjee, R. Pramanick, S. P. Rath, N. S. Chowdhury, A. Datta, S. Goswami, *Inorg. Chem.*, **2016**, *55*, 9602−9610.

[23] S. Das, S. Sinha, U. Jash, R. Sikari, A. Saha, S. K. Barman, P. Brandao, N. D. Paul, *Inorg. Chem.*, **2018**, *57*, 5830−5841. (b) S. Das, R. Mondal, G. Chakraborty, A. K. Guin, A. Das, N. D. Paul, *ACS Catal.*, **2021**, *11*, 7498−7512. (c) 56. E. M. Lane, K. B. Uttley, N. Hazari, W. Bernskoetter, *Organometallics*, **2017**, *36*, 2020− 2025.

[24] R. Pramanick, R. Bhattacharjee, D. Sengupta, A. Datta, S. Goswami, *Inorg. Chem.*, **2018**, *57*, 6816−6824.

3.6 Appendix

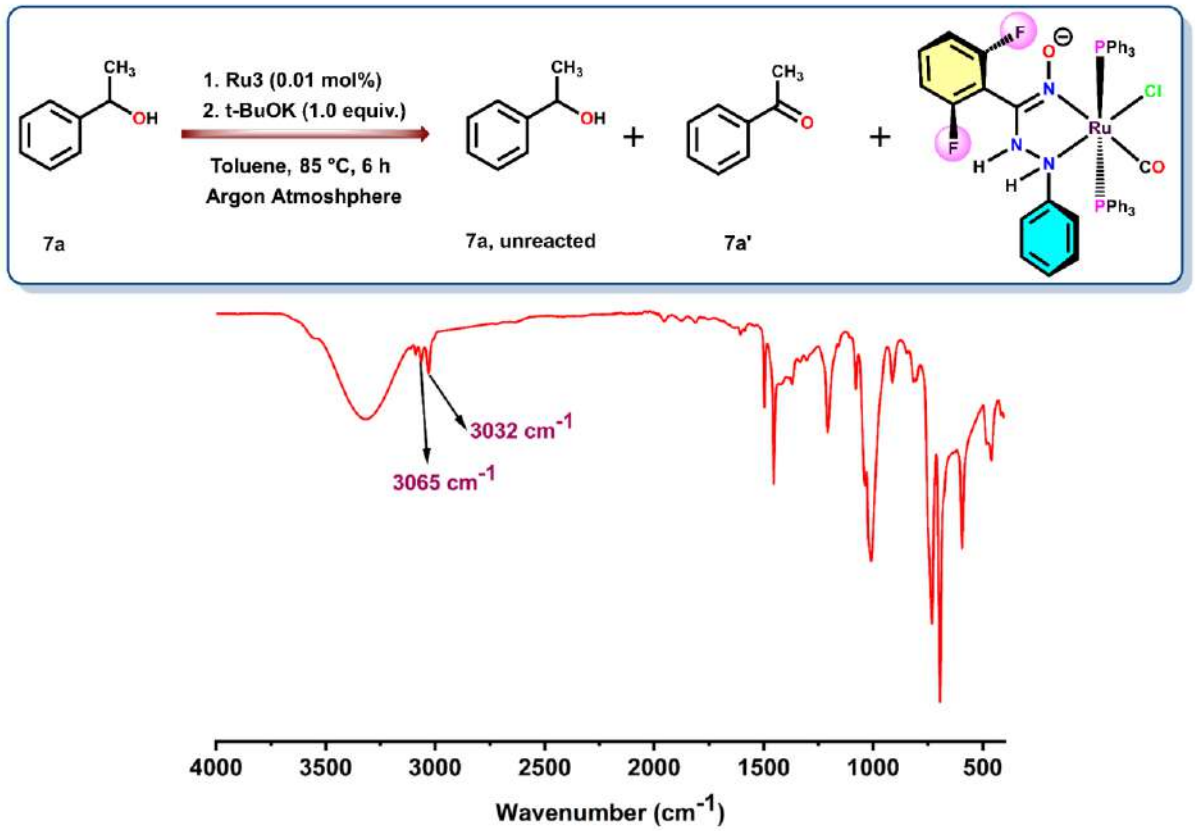

Figure 3.6.A1: IR spectrum of the reaction mixture involving stoichiometric alcohol dehydrogenation of deuterated 1-phenylethanol (**7a-d2**) under argon: involvement of azo/hydrazo redox couple with catalyst **Ru3**.

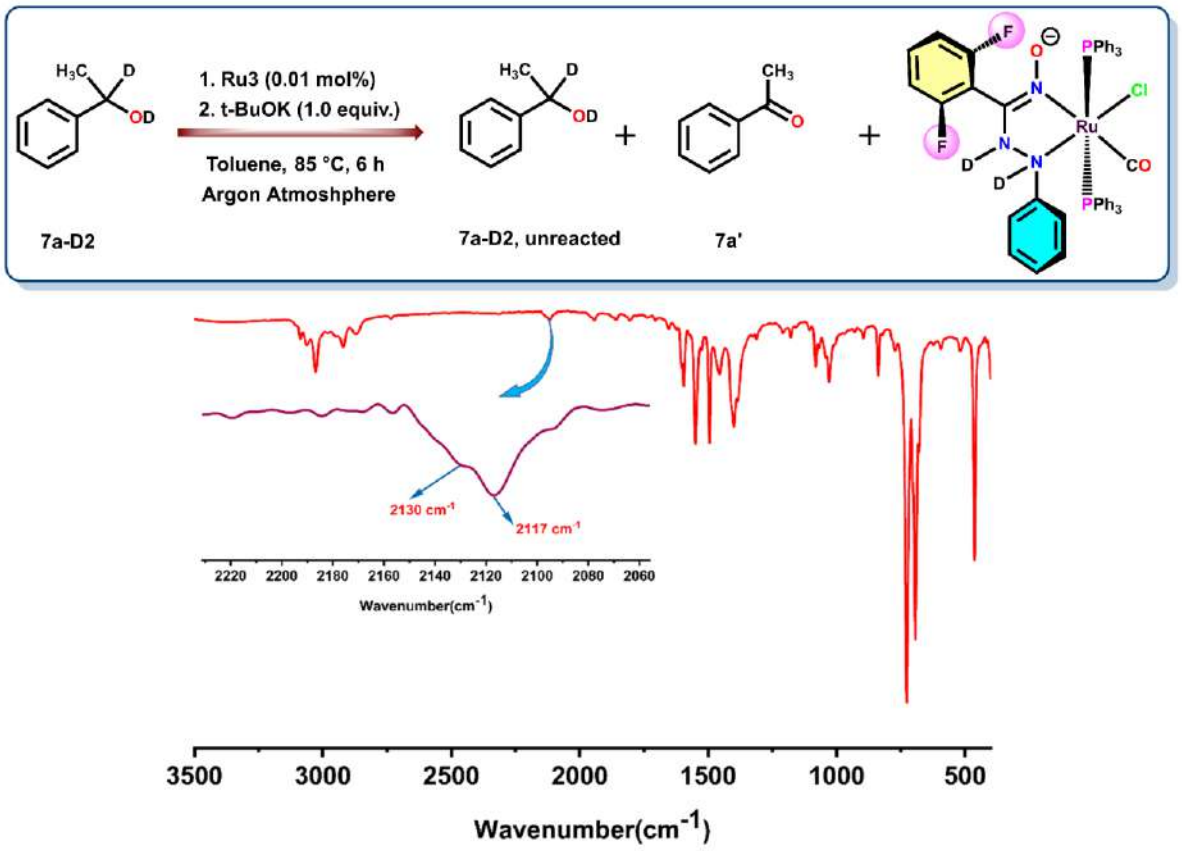

Figure 3.6.A2: IR spectrum of the reaction mixture involving stoichiometric alcohol dehydrogenation of deuterated 1-phenylethanol (**7a-D2**) under argon: involvement of azo/hydrazo redox couple with catalyst **Ru3**.

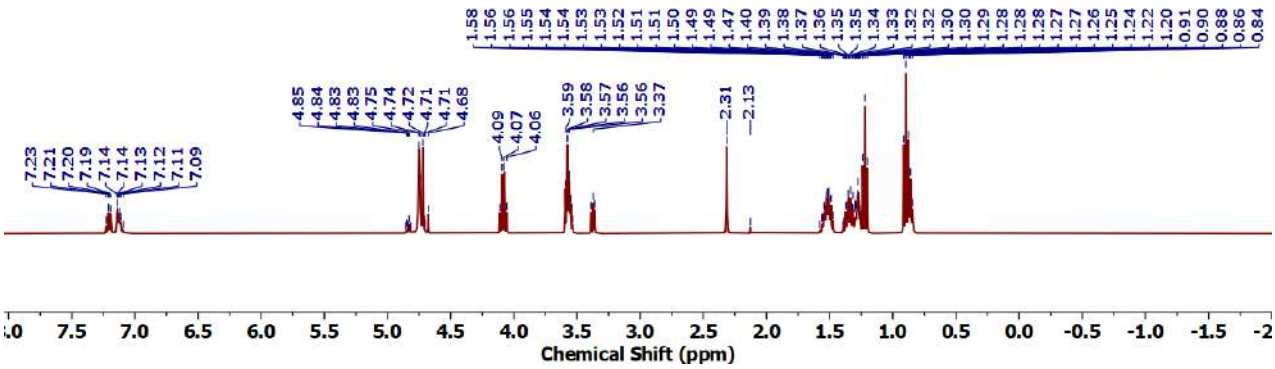

Figure 3.6.A3: ^{1}H NMR spectrum of reaction mixture of oxidation of cyclobutanol

3.6.1: NMR data of all synthesized α-alkylated ketones:

***1,3-diphenylpropan-1-one(3a)*:** Yield 93%, White solid. ^{1}H NMR (400 MHz, $CDCl_3$): δ 7.99 (dt, *J* = 7.1, 1.4 Hz, 2H), 7.63 – 7.54 (m, 1H), 7.48 (dd, *J* = 8.2, 6.7 Hz, 3H), 7.33 (d, *J* = 1.1 Hz, 1H), 7.32 – 7.28 (m, 3H), 7.28 – 7.25 (m, 1H), 7.23 (d, *J* = 4.7 Hz, 1H), 3.34 (t, *J* = 7.9 Hz, 2H), 3.15 – 3.06 (m, 2H). ^{13}C{^{1}H} NMR (75 MHz, $CDCl_3$): δ 199.37, 141.42, 136.99, 133.20, 128.74, 128.66, 128.56, 128.17, 126.27, 40.59, 30.26.

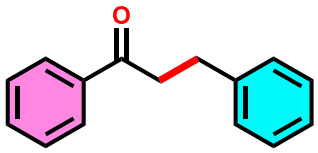

***3-phenyl-1-(o-tolyl)propan-1-one(3b)*:** Yield 85%, Colorless oil. ^{1}H NMR (400 MHz, $CDCl_3$): δ 7.66 – 7.61 (m, 1H), 7.41 – 7.36 (m, 3H), 7.32 (d, *J* = 7.3 Hz, 3H), 7.24 (d, *J* = 4.2 Hz, 2H), 3.30 – 3.22 (m, 2H), 3.09 (t, *J* = 7.6 Hz, 2H), 2.51 (s, 3H). ^{13}C{^{1}H} NMR (100 MHz, $CDCl_3$): δ 203.48, 141.30, 138.19, 138.02, 132.07, 131.35, 128.61, 128.53, 128.48, 126.23, 125.77, 43.32, 30.44, 21.35.

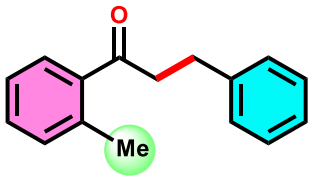

***3-phenyl-1-(m-tolyl)propan-1-one(3c)*:** Yield 80%, Yellow oil. ^{1}H NMR (400 MHz, $CDCl_3$): δ 7.83 – 7.74 (m, 2H), 7.43 – 7.27 (m, 7H), 3.40 – 3.25 (m, 2H), 3.16 – 2.92 (m, 2H), 2.43 (s, 3H). ^{13}C{^{1}H} NMR (100 MHz, $CDCl_3$) δ 199.58, 141.52, 138.53, 137.11, 133.93, 128.74, 128.66, 128.61, 128.57, 126.25, 125.40, 40.66, 30.34, 21.48.

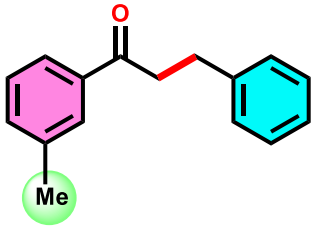

3-phenyl-1-(p-tolyl)propan-1-one(3d): Yield 86%, Colorless oil. ^{1}H NMR (400 MHz, $CDCl_3$): δ 7.96 – 7.84 (m, 2H), 7.40 – 7.19 (m, 7H), 3.31 (t, *J* = 8.1 Hz, 2H), 3.15 – 3.03 (m, 2H), 2.44 (s, 3H). ^{13}C{^{1}H} NMR (100 MHz, $CDCl_3$): δ 199.05, 143.97, 141.52, 134.48, 129.40, 128.63, 128.55, 128.29, 126.22, 40.47, 30.33, 21.76.

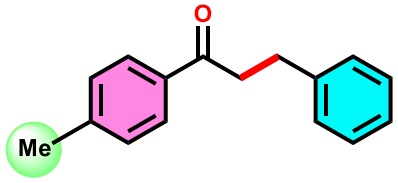

***1-(4-fluorophenyl)-3-phenylpropan-1-one(3e)*:** Yield 89%, White solid. ^{1}H NMR (400 MHz, $CDCl_3$): δ 8.11 – 7.91 (m, 2H), 7.39 – 7.21 (m, 5H), 7.20 – 7.10 (m, 2H), 3.43 – 3.22 (m, 2H), 3.11 (dd, *J* = 8.5, 6.8 Hz, 2H). ^{13}C{^{1}H} NMR (100 MHz, $CDCl_3$): δ 197.68, 167.47, 164.10, 141.22, 133.35 (d, *J* = 3.0 Hz), 130.74 (d, *J* = 9.2 Hz), 128.57 (d, *J* = 10.4 Hz), 126.28, 115.76 (d, *J* = 21.8 Hz), 40.44, 30.16. ^{19}F NMR (282 MHz, $CDCl_3$): δ -105.24.

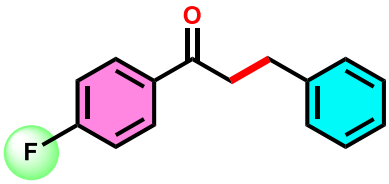

***1-(4-bromophenyl)-3-phenylpropan-1-one(3f)*:** Yield 87%, Light yellow solid, ^{1}H NMR (300 MHz, $CDCl_3$): δ 7.84 (d, *J* = 8.7 Hz, 1H), 7.61 (d, *J* = 8.7 Hz, 2H), 7.35 – 7.20 (m, 6H), 3.29 (t, *J* = 7.7 Hz, 2H), 3.08 (t, *J* = 7.6 Hz, 2H). ^{13}C{^{1}H} NMR (75 MHz, $CDCl_3$): δ 198.30, 141.11, 132.00, 129.66, 129.05, 128.66, 128.57, 128.50, 126.32, 40.50, 30.10.

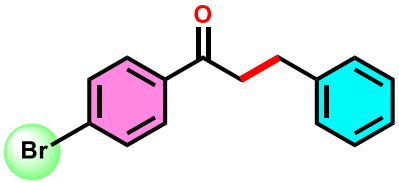

***1-(3-methoxyphenyl)-3-phenylpropan-1-one(3g)*:** Yield 84%, Yellow oil. ^{1}H NMR (300 MHz, $CDCl_3$): δ 7.61 – 7.52 (m, 2H), 7.39 (t, *J* = 7.9 Hz, 1H), 7.31 (t, *J* = 5.4 Hz, 3H), 7.25 (d, *J* = 3.0 Hz, 1H), 7.23 – 7.12 (m, 2H), 3.88 (s, 3H), 3.33 (t, *J* = 7.9 Hz, 2H), 3.11 (t, *J* = 7.9 Hz, 2H). ^{13}C{^{1}H} NMR (75 MHz, $CDCl_3$): δ 199.07, 159.88, 141.32, 129.64, 129.07, 128.58, 128.49, 126.19, 120.72, 119.61, 112.30, 55.45, 40.59, 30.21.

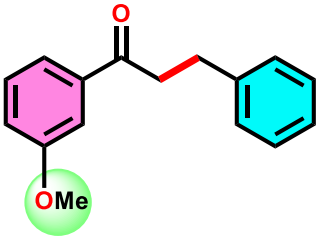

***1-(4-methoxyphenyl)-3-phenylpropan-1-one(3h)*:** Yield 90%, Yellow oil. ^{1}H NMR (400 MHz, $CDCl_3$): δ 8.07 – 7.87 (m, 2H), 7.45 – 7.07 (m, 5H), 7.01 – 6.87 (m, 2H), 3.89 (s, 3H), 3.28 (t, *J* = 8.2 Hz, 2H), 3.08 (t, *J* = 7.9 Hz, 2H). ^{13}C{^{1}H} NMR (100 MHz, $CDCl_3$): δ 197.97, 163.62, 141.62, 130.46, 130.18, 128.65, 128.57, 126.23, 113.89, 55.60, 40.25, 30.51.

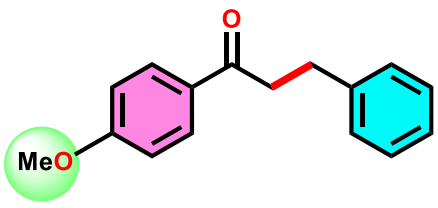

***3-(4-methoxyphenyl)-1-phenylpropan-1-one(3i)*:** Yield 92%, Brown solid. ^{1}H NMR (300 MHz, $CDCl_3$): δ 8.05 – 7.91 (m, 2H), 7.58 (ddt, *J* = 8.3, 6.6, 1.4 Hz, 1H), 7.52 – 7.44 (m, 2H), 7.20 (d, *J* = 8.5 Hz, 2H), 6.87 (d, *J* = 8.6 Hz, 2H), 3.82 (s, 3H), 3.30 (t, *J* = 7.3 Hz, 2H), 3.10 – 2.98 (m, 2H). ^{13}C{^{1}H} NMR (101 MHz, $CDCl_3$): δ 199.48, 158.12, 137.05, 133.41, 133.10, 129.43, 128.68, 128.12, 114.06, 55.36, 40.77, 29.40.

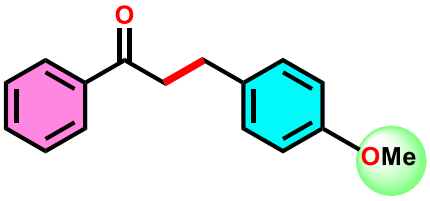

***3-(4-fluorophenyl)-1-phenylpropan-1-one(3j)*:** Yield 83%, White solid. ^{1}H NMR (400 MHz, $CDCl_3$) δ 7.98 (dd, *J* = 7.6, 1.9 Hz, 1H), 7.63 – 7.54 (m, 1H), 7.48 (td, *J* = 7.8, 1.8 Hz, 1H), 7.23 (ddt, *J* = 8.7, 5.3, 2.6 Hz, 1H), 7.00 (td, *J* = 8.8, 1.9 Hz, 1H), 3.31 (t, *J* = 8.4 Hz, 1H), 3.16 – 3.03 (m, 1H). ^{13}C{^{1}H} NMR (101 MHz, $CDCl_3$): δ 199.16, 162.78, 160.36, 137.06 – 136.99 (m), 133.25, 130.56 (d, *J* = 7.8 Hz), 129.97 (d, *J* = 7.9 Hz), 128.77, 128.16, 115.39 (d, *J* = 21.1 Hz). ^{19}F NMR (377 MHz, $CDCl_3$): δ -117.27.

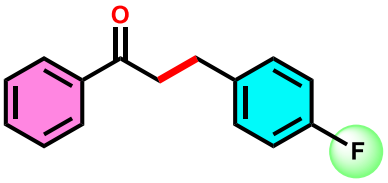

***3-(4-chlorophenyl)-1-phenylpropan-1-one(3k)*:** Yield 90%, Pale yellow solid. ^{1}H NMR (300 MHz, $CDCl_3$) δ 8.04 – 7.93 (m, 2H), 7.62 – 7.54 (m, 1H), 7.53 – 7.43 (m, 2H), 7.30 – 7.17 (m, 4H), 3.31 (t, *J* = 7.9 Hz, 2H), 3.07 (t, *J* = 7.5 Hz, 2H). ^{13}C{^{1}H} NMR (101 MHz, $CDCl_3$) δ 198.99, 139.90, 136.97, 133.29, 132.06, 129.96, 128.79, 128.75, 128.16, 40.27, 29.56.

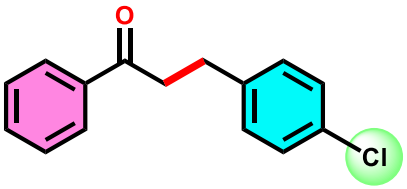

***1-phenyl-3-(o-tolyl)propan-1-one (3l)*:** Yield 83%, Yellow oil. ^{1}H NMR (300 MHz, $CDCl_3$): δ 8.04 – 7.96 (m, 1H), 7.62 – 7.54 (m, 1H), 7.48 (ddt, *J* = 8.3, 6.7, 1.3 Hz, 2H), 7.29 – 7.15 (m, 2H), 7.12 – 7.02 (m, 3H), 3.33 (t, *J* = 8.0 Hz, 2H), 3.11 – 3.00 (m, 2H), 2.36 (s, 3H). ^{13}C{^{1}H} NMR (75

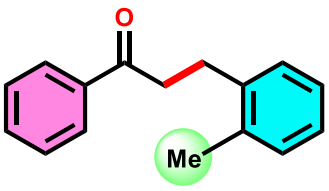

MHz, $CDCl_3$): δ 199.21, 139.36, 136.81, 135.92, 133.04, 130.33, 129.23, 128.71, 128.59, 128.01, 126.31, 126.17, 39.04, 27.47, 19.34.

***1-phenyl-3-(m-tolyl)propan-1-one(3m)*:** Yield 80%, Yellow oil. ^1H NMR (300 MHz, $CDCl_3$):

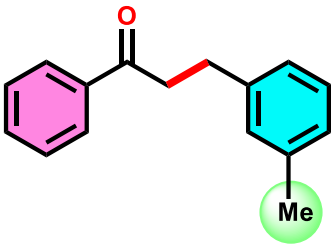

δ 8.05 – 7.97 (m, 1H), 7.60 – 7.55 (m, 1H), 7.48 (ddd, J = 8.3, 6.8, 1.0 Hz, 2H), 7.28 – 7.18 (m, 2H), 7.13 – 7.02 (m, 3H), 3.33 (t, J = 8.0 Hz, 2H), 3.11 – 3.00 (m, 2H), 2.36 (s, 3H). $^{13}C\{^1H\}$ NMR (75 MHz, $CDCl_3$) δ 199.48, 141.37, 138.26, 137.01, 133.19, 129.38, 128.74, 128.58, 128.19, 127.02, 125.53, 40.68, 30.21, 21.54.

3.7.2: NMR data of all synthesized 2-substituted quinoline derivatives:

***2-phenylquinoline(5a)*:** Yield 93%, White crystalline solid. ^1H NMR (400 MHz, $CDCl_3$): δ

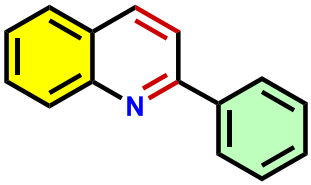

8.26 – 8.13 (m, 4H), 7.92 – 7.80 (m, 2H), 7.74 (ddd, J = 8.5, 6.9, 1.5 Hz, 1H), 7.59–7.43 (m, 4H). $^{13}C\{^1H\}$ NMR (100 MHz, $CDCl_3$): 157.50, 148.43, 139.82, 136.90, 129.88, 129.79,129.46, 128.97, 127.72, 127.58, 127.34, 126.41, 119.13.

***2-(o-tolyl)quinoline(5b)*:** Yield 90%, White crystalline solid. ^1H NMR (400 MHz, $CDCl_3$): δ

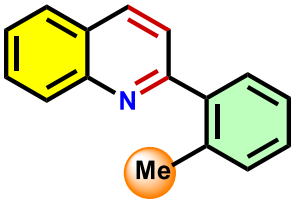

8.23 (t, J = 9.7 Hz, 2H), 7.89 (d, J = 8.1 Hz, 1H), 7.77 (t, J = 7.7 Hz, 1H), 7.57 (dq, J = 12.8, 7.0, 6.3 Hz, 3H), 7.36 (d, J = 5.5 Hz, 3H), 2.45 (s, 3H). $^{13}C\{^1H\}$ NMR (100 MHz, $CDCl_3$): δ 160.38, 147.96, 140.80, 136.21, 136.08, 129.79, 129.74, 129.67, 128.62, 127.62, 126.83, 126.52, 126.12, 122.49, 20.46.

***2-(m-tolyl)quinoline(5c)*:** Yield 91%, Pale yellow solid. ^{1}H NMR (400 MHz, $CDCl_3$): δ 8.26–

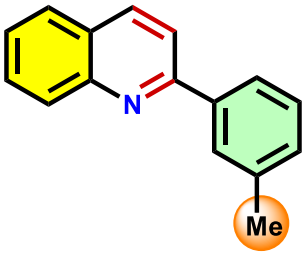

8.20 (m, 2H), 7.89 (d, *J* = 8.6 Hz, 1H), 7.85 (dd, *J* = 8.2, 1.5 Hz, 1H), 7.77 (dddd, *J* = 10.1, 8.5, 5.9, 2.1 Hz, 2H), 7.55 (ddd, *J* = 8.1, 6.9, 1.2 Hz, 1H), 7.45 (t, *J* = 7.6 Hz, 1H), 7.41–7.34 (m, 1H), 7.31 (ddt, *J* = 7.6, 1.9, 0.9 Hz, 1H), 2.51 (s, 3H). ^{13}C{^{1}H} NMR (100 MHz, $CDCl_3$): δ 157.71, 148.35, 139.73, 138.65, 136.89, 133.99, 130.27, 129.79, 128.86, 128.42, 127.58, 126.37, 125.72, 124.86, 119.30, 21.71.

***2-(p-tolyl)quinoline(5d)*:** Yield 94%, Pale yellow solid. ^{1}H NMR (400 MHz, $CDCl_3$): δ 8.19

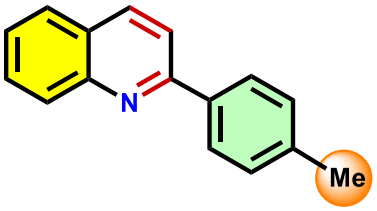

(d, *J* = 8.5 Hz, 2H), 8.08 (d, *J* = 8.2 Hz, 2H), 7.89 – 7.78 (m, 2H), 7.73 (ddd, *J* = 8.5, 6.9, 1.5 Hz, 1H), 7.52 (ddd, *J* = 8.1, 6.9, 1.2 Hz, 1H), 7.34 (d, *J* = 7.9 Hz, 2H), 2.45 (s, 3H). ^{13}C{^{1}H} NMR (100 MHz, $CDCl_3$): 157.44, 148.36, 139.52, 136.94, 136.79, 129.72, 129.69, 127.55, 127.20, 126.20, 118.99, 21.46.

***2-(3-methoxyphenyl)quinoline(5e)*:** Yield 87%, Pale yellow crystalline solid. ^{1}H NMR (300

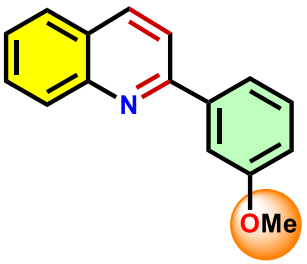

MHz, $CDCl_3$): δ 8.25 – 8.17 (m, 2H), 7.90 – 7.79 (m, 3H), 7.77 – 7.69 (m, 2H), 7.55 (d, *J* = 6.8 Hz, 1H), 7.46 (t, *J* = 7.9 Hz, 1H), 7.05 (dd, *J* = 8.2, 2.6 Hz, 1H), 3.95 (s, 3H). ^{13}C{^{1}H} NMR (75 MHz, $CDCl_3$): δ 160.15, 157.13, 148.21, 141.15, 136.82, 129.85, 129.73, 129.71, 129.60, 127.51, 126.37, 120.05, 119.13, 115.40, 112.74, 55.43.

***2-(4-methoxyphenyl)quinoline(5f)*:** Yield 85%, Light yellow solid. ^{1}H NMR (400 MHz,

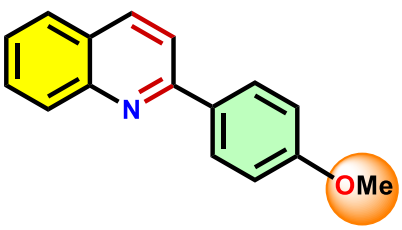

$CDCl_3$): δ 8.22 – 8.14 (m, 4H), 7.88 – 7.80 (m, 2H), 7.74 (ddd, *J* = 8.5, 6.9, 1.5 Hz, 1H), 7.52 (ddd, *J* = 8.1, 6.9, 1.2 Hz, 1H), 7.12 – 7.04 (m, 2H), 3.91 (s, 3H). ^{13}C{^{1}H} NMR

(100 MHz, $CDCl_3$): δ 160.97, 157.02, 148.35, 136.80, 132.32, 129.72, 129.59, 129.03, 127.55, 127.03, 126.05, 118.68, 114.36, 55.51.

***2-(2-fluorophenyl)quinoline(5g)*:** Yield 85%, White crystalline solid. ^1H NMR (400 MHz, $CDCl_3$): δ 8.31 (d, J = 8.9 Hz, 1H), 8.08 (dd, J = 8.7, 5.0 Hz, 2H), 7.99 (d, J = 8.0 Hz, 1H), 7.86 (d, J = 8.1 Hz, 1H), 7.78 (t, J = 7.7 Hz, 1H), 7.58 (t, J = 7.5 Hz, 1H), 7.40 (t, J = 7.7 Hz, 1H), 7.12 (d, J = 8.2 Hz, 1H), 6.99 (t, J = 7.6 Hz, 1H). $^{13}C\{^1H\}$ NMR (101 MHz, $CDCl_3$): δ 158.17, 144.93, 137.76, 136.36, 132.17, 130.99 (d, J = 8.6 Hz), 130.62, 129.82, 127.71 (d, J = 7.1 Hz), 127.63, 124.83 (d, J = 3.6 Hz), 122.61 (d, J = 8.1 Hz), 118.87 (d, J = 6.0 Hz), 116.39 (d, J = 22.8 Hz). ^{19}F NMR (282 MHz, $CDCl_3$): δ -117.26.

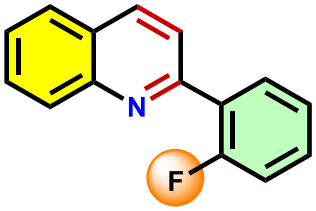

***2-(4-fluorophenyl)quinoline(5h)*:** Yield 89%, White crystalline solid. ^1H NMR (400 MHz, $CDCl_3$): δ 8.34 – 8.11 (m, 4H), 7.83 (dd, J = 8.5, 2.7 Hz, 2H), 7.75 (t, J = 7.7 Hz, 1H), 7.55 (t, J = 7.5 Hz, 1H), 7.23 (t, J = 8.7 Hz, 2H). $^{13}C\{^1H\}$ NMR (101 MHz, $CDCl_3$): δ 165.17, 162.69, 156.29, 148.32, 136.99, 135.89 (d, J = 3.2 Hz), 131.82 (d, J = 8.3 Hz), 129.81 (d, J = 15.6 Hz), 129.52 (d, J = 8.4 Hz), 127.57, 126.45, 118.68, 115.85 (d, J = 21.6 Hz). ^{19}F NMR (377 MHz, $CDCl_3$): δ -112.50.

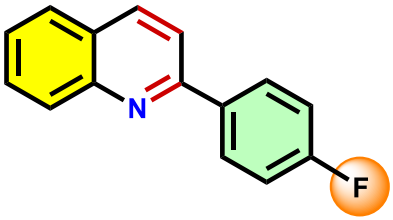

***2-(3-bromophenyl)quinoline(5i)*:** Yield 92%, Yellow crystalline solid. ^1H NMR (400 MHz, $CDCl_3$): δ 8.39 (s, 1H), 8.23 – 8.15 (m, 2H), 8.07 (d, J = 7.4 Hz, 1H), 7.84 – 7.71 (m, 3H), 7.64–7.50 (m, 2H), 7.38 (t, J = 7.9 Hz, 1H). $^{13}C\{^1H\}$ NMR (100 MHz, $CDCl_3$): δ 155.52, 148.21, 141.64, 137.01, 132.24, 130.64, 130.33, 129.91, 129.79, 127.53, 127.36, 126.67, 126.07, 123.19, 118.62.

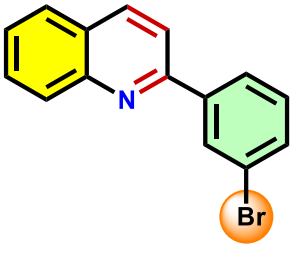

***2-(4-bromophenyl)quinoline(5j)*:** Yield 88%, Yellow crystalline solid. ^{1}H NMR (400 MHz, $CDCl_3$): δ 8.25 (dd, *J* = 8.6, 0.9 Hz, 1H), 8.12 – 8.05 (m, 2H), 7.90–7.80 (m, 4H), 7.71 – 7.60 (m, 4H). $^{13}C\{^{1}H\}$ NMR (100 MHz, $CDCl_3$): δ 197.10, 156.17, 148.36, 138.60, 137.14, 132.03, 129.96, 129.83, 129.24, 127.62, 127.39, 126.67, 124.09, 118.63.

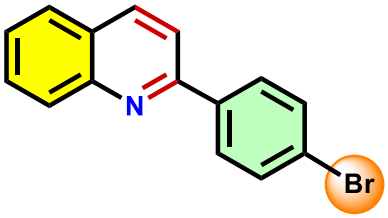

***2-(3-nitrophenyl)quinoline(5k)*:** Yield 65%, Yellow crystalline solid. ^{1}H NMR (300 MHz, $CDCl_3$): δ 8.40 (s, 3H), 8.37 – 8.32 (m, 1H), 8.25 (d, *J* = 8.5 Hz, 1H), 7.99 – 7.88 (m, 2H), 7.82 (ddd, *J* = 8.5, 6.9, 1.5 Hz, 1H), 7.63 (ddd, *J* = 8.1, 6.9, 1.2 Hz, 1H). $^{13}C\{^{1}H\}$ NMR (75 MHz, $CDCl_3$): δ 154.55, 141.28, 137.71, 135.87, 135.34, 133.53, 130.43, 129.97, 129.88, 127.71, 127.67, 127.29, 124.10, 122.62, 118.54.

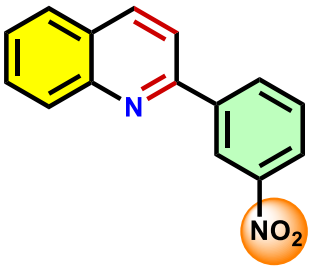

***2-(4-nitrophenyl)quinoline(5l)*:** Yield 60%, Yellow crystalline solid. ^{1}H NMR (300 MHz, $CDCl_3$): δ 8.40 (s, 3H), 8.37 – 8.32 (m, 1H), 8.25 (d, *J* = 8.5 Hz, 1H), 7.99 – 7.88 (m, 2H), 7.82 (ddd, *J* = 8.5, 6.9, 1.5 Hz, 1H), 7.63 (ddd, *J* = 8.1, 6.9, 1.2 Hz, 1H). $^{13}C\{^{1}H\}$ NMR (100 MHz, $CDCl_3$): δ 154.69, 148.60, 148.21, 145.35, 137.75, 130.55, 129.93, 128.59, 127.73, 127.54, 124.22, 118.98.

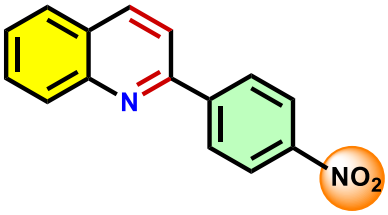

***2-(naphthalen-2-yl)quinoline(5m)*:** Yield 87%, Yellow crystalline solid. ^{1}H NMR (400 MHz, $CDCl_3$): δ 8.65 (d, *J* = 1.8 Hz, 1H), 8.41 (dd, *J* = 8.6, 1.8 Hz, 1H), 8.27 (dd, *J* = 8.6, 4.3 Hz, 2H), 8.04 (dd, *J* = 10.8, 8.6 Hz, 3H), 7.93 (dt, *J* = 7.1, 3.6 Hz, 1H), 7.90 – 7.75 (m, 4H), 7.57 (td, *J* = 6.4, 2.2 Hz, 3H). $^{13}C\{^{1}H\}$ NMR (101 MHz, $CDCl_3$): δ 157.32, 148.53, 137.12, 136.94, 134.02, 133.66, 129.89, 129.86, 128.97, 128.71, 127.86, 127.63, 127.38, 127.30, 126.85, 126.48, 126.47, 125.22, 119.30.

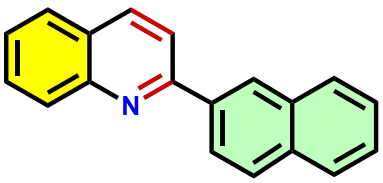

2-hexylquinoline(5n): Yield 75%, Yellow oil. ^{1}H NMR (400 MHz, $CDCl_3$): δ 8.06 (dd, *J* = 10.1, 8.4 Hz, 2H), 7.76 (dd, *J* = 8.0, 1.5 Hz, 1H), 7.68 (ddd, *J* = 8.4, 6.9, 1.5 Hz, 1H), 7.47 (ddd, *J* = 8.1, 6.9, 1.2 Hz, 1H), 7.29 (d, *J* = 8.4 Hz, 1H), 3.13 – 2.84 (m, 2H), 1.82 (q, *J* = 7.6 Hz, 2H), 1.38 – 1.29 (m, 5H), 0.94 – 0.85 (m, 4H). ^{13}C{^{1}H} NMR (100 MHz, $CDCl_3$): δ 163.17, 147.92, 136.25, 129.37, 128.83, 127.53, 126.76, 125.68, 121.42, 39.42, 31.80, 30.13, 29.31, 22.64, 14.15.

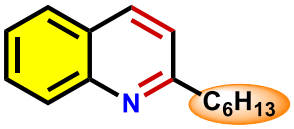

***6-chloro-2-phenylquinoline(5o)*:** Yield 91%, White crystalline solid. ^{1}H NMR (300 MHz, $CDCl_3$): δ 8.27 – 8.18 (m, 4H), 7.92 – 7.85 (m, 2H), 7.76 (ddd, *J* = 8.5, 6.9, 1.5 Hz, 1H), 7.59 – 7.49 (m, 3H). ^{13}C{^{1}H} NMR (75 MHz, $CDCl_3$): δ 157.52, 148.38, 139.79, 136.96, 129.84, 129.82, 129.47, 128.99, 127.73, 127.60, 127.32, 126.44, 119.18.

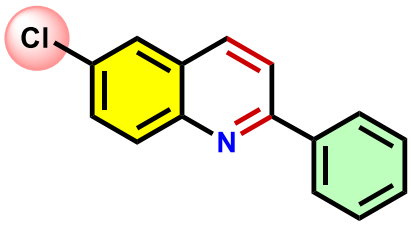

***6-chloro-2-(o-tolyl)quinoline(5p)*:** Yield 92%, White crystalline solid. ^{1}H NMR (300 MHz, $CDCl_3$): δ 8.13 (dd, *J* = 8.8, 6.5 Hz, 2H), 7.86 (d, *J* = 2.3 Hz, 1H), 7.69 (dd, *J* = 9.0, 2.3 Hz, 1H), 7.59 (d, *J* = 8.6 Hz, 1H), 7.52 (dd, *J* = 7.3, 2.5 Hz, 1H), 7.38-7.34 (m, 3H), 2.44 (s, 3H). ^{13}C{^{1}H} NMR (75 MHz, $CDCl_3$): δ 160.63, 146.36, 140.37, 136.10, 135.25, 132.18, 131.31, 131.07, 130.63, 129.76, 128.81, 127.39 126.26, 126.19, 123.33, 20.46.

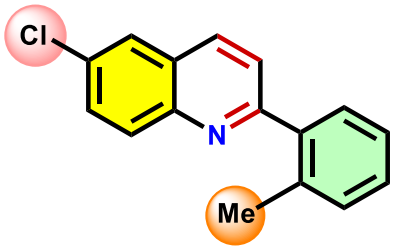

***6-chloro-2-(m-tolyl)quinoline(5q)*:** Yield 90%, White crystalline solid. ^{1}H NMR (400 MHz, $CDCl_3$): δ 8.13 (dd, *J* = 8.8, 2.8 Hz, 2H), 8.02 (d, *J* = 1.9 Hz, 1H), 7.92 (dd, *J* = 11.4, 8.3 Hz, 2H), 7.82 (d, *J* = 2.4 Hz, 1H), 7.68 (dd, *J* = 9.0, 2.4 Hz, 1H), 7.44 (t, *J* = 7.6 Hz, 1H), 7.32 (ddt, *J* = 7.5, 1.8, 0.9 Hz, 1H), 2.51 (s, 3H). ^{13}C{^{1}H} NMR

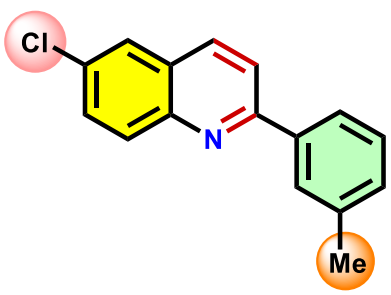

(101 MHz, $CDCl_3$): δ 157.71, 148.35, 136.89, 130.27, 129.78, 128.92, 128.86, 128.57, 128.42, 127.58, 127.32, 126.37, 125.72, 124.86, 119.30, 26.78.

***6-chloro-2-(p-tolyl)quinoline(5r)*:** Yield 93%, Yellow crystalline solid. ^1H NMR (300 MHz, $CDCl_3$): δ 8.13 (d, J = 2.6 Hz, 1H), 8.09 (q, J = 2.4 Hz, 2H), 8.07 (d, J = 1.9 Hz, 1H), 7.89 (d, J = 8.7 Hz, 1H), 7.81 (d, J = 2.4 Hz, 1H), 7.67 (dd, J = 9.0, 2.4 Hz, 1H), 7.36 (d, J = 7.9 Hz, 2H), 2.46 (s, 3H). $^{13}C\{^1H\}$ NMR (75 MHz, $CDCl_3$): δ 157.65, 146.78, 139.85, 136.51, 135.85, 131.79, 131.35, 130.59, 129.76, 127.75, 127.51, 126.24, 119.77, 21.49.

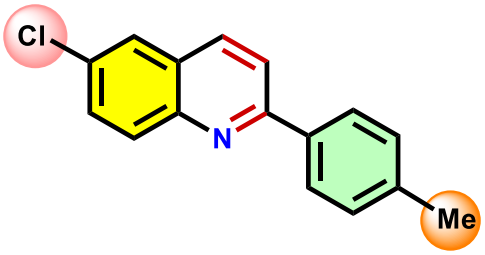

***6-chloro-2-(3-methoxyphenyl)quinoline(5s)*:** Yield 87%, Yellow crystalline solid. ^1H NMR (300 MHz, $CDCl_3$): δ 8.17 – 8.07 (m, 2H), 7.88 (dd, J = 8.6, 0.9 Hz, 1H), 7.84 – 7.76 (m, 2H), 7.74 – 7.64 (m, 2H), 7.45 (t, J = 7.9 Hz, 1H), 7.05 (ddd, J = 8.3, 2.6, 1.0 Hz, 1H), 3.95 (s, 3H). $^{13}C\{^1H\}$ NMR (75 MHz, $CDCl_3$): δ 160.27, 157.39, 146.66, 140.74, 135.91, 131.42, 130.66, 132.04, 129.98, 127.90, 126.23, 120.04, 119.98, 115.68, 112.79, 55.53.

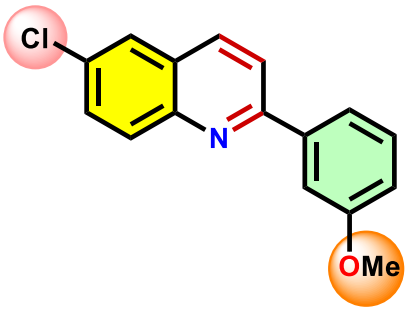

***6-chloro-2-(4-methoxyphenyl)quinoline(5t)*:** Yield 92%, Yellow crystalline solid. ^1H NMR (300 MHz, $CDCl_3$): δ 8.19 – 8.04 (m, 4H), 7.87 (d, J = 8.7 Hz, 1H), 7.80 (d, J = 2.4 Hz, 1H), 7.66 (dd, J = 9.0, 2.4 Hz, 1H), 7.12 – 7.01 (m, 2H), 3.91 (s, 3H). $^{13}C\{^1H\}$ NMR (75 MHz, $CDCl_3$): δ 161.14, 157.25, 146.81, 135.83, 131.90, 131.60, 131.23, 130.59, 129.00, 127.58, 126.25, 119.48, 114.43, 55.55.

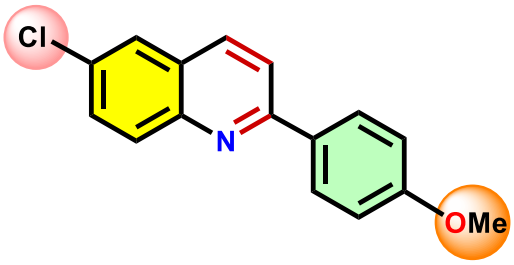

***6-chloro-2-(2-fluorophenyl)quinoline(5u)*:** Yield 85%, White crystalline solid. ^{1}H NMR (300

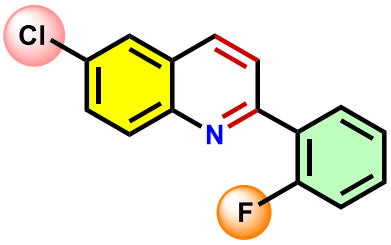

MHz, $CDCl_3$): δ 8.13 (td, *J* = 8.3, 6.4 Hz, 3H), 7.94 (dd, *J* = 8.7, 2.7 Hz, 1H), 7.86 (d, *J* = 2.4 Hz, 1H), 7.69 (dd, *J* = 9.0, 2.4 Hz, 1H), 7.47 (dddd, *J* = 8.2, 7.1, 5.0, 1.9 Hz, 1H), 7.35 (td, *J* = 7.5, 1.2 Hz, 1H), 7.23 (ddd, *J* = 11.3, 8.2, 1.3 Hz, 1H). ^{13}C{^{1}H} NMR (75 MHz, $CDCl_3$): δ 162.58, 159.27, 154.43 (d, *J* = 2.0 Hz), 146.82, 135.41, 132.48, 131.61 – 131.41 (m), 131.24 (d, *J* = 8.6 Hz), 130.73, 127.90, 127.64 (d, *J* = 11.8 Hz), 126.29, 124.89 (d, *J* = 3.5 Hz), 123.45 (d, *J* = 8.5 Hz), 116.46 (d, *J* = 22.9 Hz). ^{19}F NMR (377 MHz, $CDCl_3$): δ -117.02.

***6-chloro-2-(4-fluorophenyl)quinoline(5v)*:** Yield 88%, White crystalline solid. ^{1}H NMR (300

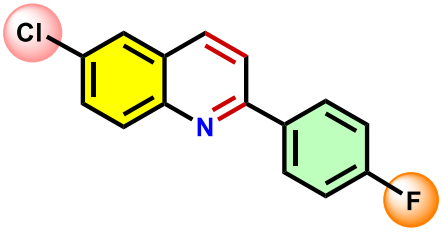

MHz, $CDCl_3$): δ 8.23 – 8.06 (m, 4H), 7.92 – 7.81 (m, 2H), 7.68 (dd, *J* = 9.0, 2.4 Hz, 1H), 7.29 – 7.18 (m, 2H). ^{13}C{^{1}H} NMR (75 MHz, $CDCl_3$): δ 165.73, 162.42, 156.59, 146.74, 136.13, 135.49 (d, *J* = 3.2 Hz), 132.14, 131.11 (d, *J* = 38.1 Hz), 129.53 (d, *J* = 8.5 Hz), 127.76, 126.30, 119.58, 116.01 (d, *J* = 21.6 Hz). ^{19}F NMR (282 MHz, $CDCl_3$): δ -111.98.

***2-(3-bromophenyl)-6-chloroquinoline(5w)*:** Yield 89%, Yellow crystalline solid. ^{1}H NMR

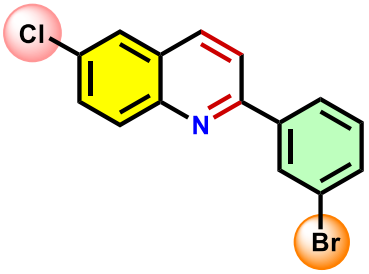

(400 MHz, $CDCl_3$): δ 8.35 (q, *J* = 1.9 Hz, 1H), 8.19 – 8.04 (m, 3H), 7.90 – 7.80 (m, 2H), 7.68 (dt, *J* = 9.0, 2.0 Hz, 1H), 7.60 (d, *J* = 8.2 Hz, 1H), 7.40 (td, *J* = 7.9, 1.6 Hz, 1H). ^{13}C{^{1}H} NMR (101 MHz, $CDCl_3$): δ 156.01, 146.79, 141.38, 136.23, 132.63, 132.54, 131.56, 131.00, 130.77, 130.52, 128.07, 126.32, 126.14, 123.38, 119.64.

***2-(4-bromophenyl)-6-chloroquinoline(5x)*:** Yield 92%, Yellow crystalline solid. ^{1}H NMR

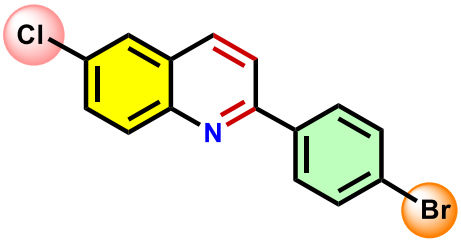

(300 MHz, $CDCl_3$): δ 8.20 – 8.03 (m, 4H), 7.88 (d, *J* = 8.7 Hz, 1H), 7.84 (d, *J* = 2.4 Hz, 1H), 7.74 – 7.63 (m, 3H). ^{13}C{^{1}H} NMR (75 MHz, $CDCl_3$): δ 156.41, 146.75, 138.17, 136.21, 132.33, 132.20, 131.43, 130.94, 129.17, 127.92, 126.32, 124.36, 119.48.

2-(4-chlorophenyl)-6-chloroquinoline(5y): Yield 88%, Yellow crystalline solid. ^{1}H NMR

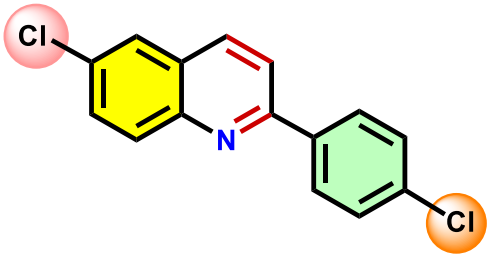

(300 MHz, $CDCl_3$): δ 8.19 – 8.07 (m, 4H), 7.88 (d, *J* = 8.6 Hz, 1H), 7.83 (d, *J* = 2.3 Hz, 1H), 7.69 (dd, *J* = 9.0, 2.3 Hz, 1H), 7.56 – 7.48 (m, 2H). ^{13}C{^{1}H} NMR (75 MHz, $CDCl_3$): δ 156.35, 146.73, 137.70, 136.18, 135.96, 132.29, 131.40, 130.91, 129.23, 128.89, 127.88, 126.30, 119.51.

***6-chloro-2-(pyridin-4-yl)quinoline(5z)*:** Yield 81%, Brownish yellow crystalline solid. ^{1}H

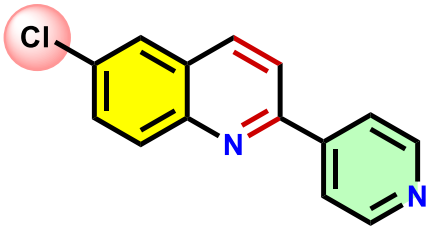

NMR (300 MHz, $CDCl_3$): δ 8.84 – 8.76 (m, 2H), 8.22 (dt, *J* = 8.5, 1.3 Hz, 1H), 8.14 (d, *J* = 9.0 Hz, 1H), 8.10 – 8.02 (m, 2H), 7.94 (d, *J* = 8.7 Hz, 1H), 7.86 (d, *J* = 2.4 Hz, 1H), 7.72 (dd, *J* = 9.0, 2.4 Hz, 1H). ^{13}C{^{1}H} NMR (75 MHz, $CDCl_3$): δ 154.82, 150.66, 146.82, 146.34, 136.47, 133.18, 131.73, 131.23, 128.51, 126.35, 121.66, 119.38.

***6-chloro-2-(naphthalen-2-yl)quinoline(5aa)*:** Yield 91%, Yellow crystalline solid. ^{1}H NMR

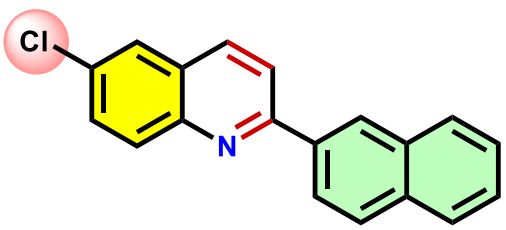

(300 MHz, $CDCl_3$): δ 8.61 (d, *J* = 1.8 Hz, 1H), 8.37 (dd, *J* = 8.6, 1.8 Hz, 1H), 8.16 (dd, *J* = 8.8, 4.1 Hz, 2H), 8.09 – 7.96 (m, 3H), 7.96 – 7.88 (m, 1H), 7.83 (d, *J* = 2.4 Hz, 1H), 7.70 (dd, *J* = 9.0, 2.4 Hz, 1H),

7.57 (dt, J = 6.3, 3.5 Hz, 2H). $^{13}C\{^{1}H\}$ NMR (75 MHz, $CDCl_3$): δ 157.46, 146.85, 136.58, 135.97, 134.07, 133.57, 132.07, 131.43, 130.74, 128.96, 128.78, 127.86, 127.32, 127.00, 126.55, 126.29, 124.98, 120.04.

***6-chloro-2-hexylquinoline(5ab)*:** Yield 78%, Yellow oil. ^{1}H NMR (300 MHz, $CDCl_3$): δ 8.04 – 7.90 (m, 1H), 7.79 – 7.69 (m, 1H), 7.65 – 7.53 (m, 1H), 7.33 (dd, J = 8.4, 1.6 Hz, 0H), 2.97 (dd, J = 8.6, 7.2 Hz, 1H), 1.89 – 1.75 (m, 1H), 1.49 – 1.33 (m, 2H), 0.99 – 0.84 (m, 1H). $^{13}C\{^{1}H\}$ NMR (75 MHz, $CDCl_3$): δ 163.47, 146.29, 135.20, 131.26, 130.46, 130.14, 127.30, 126.12, 122.23, 39.25, 31.69, 29.82, 29.18, 22.54, 14.02.

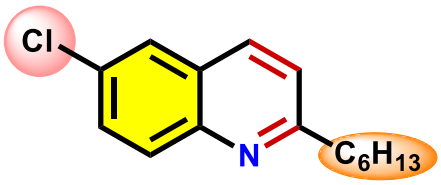

3.6.2 Copies of NMR spectra of all synthesized compounds

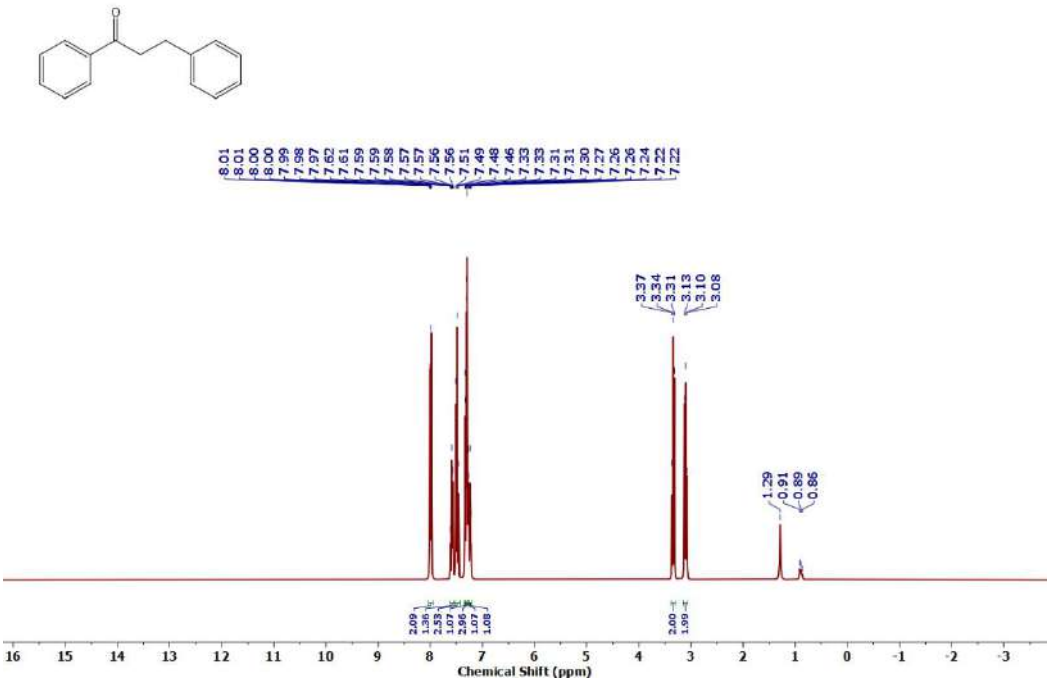

Figure 3.6.A4: ^{1}H NMR spectrum of **3a**

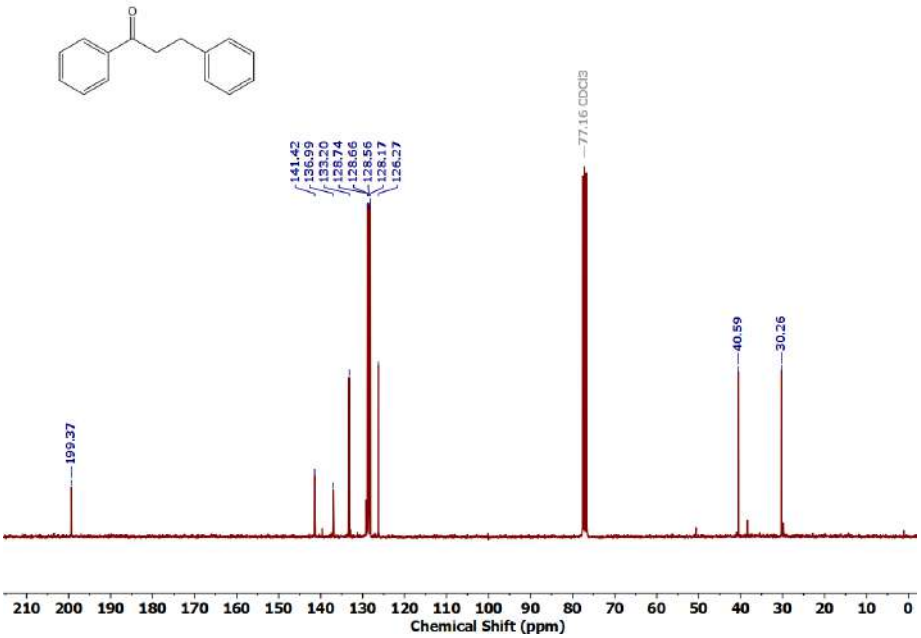

Figure 3.6.A5: $^{13}C\{^{1}H\}$ NMR spectrum of **3a**

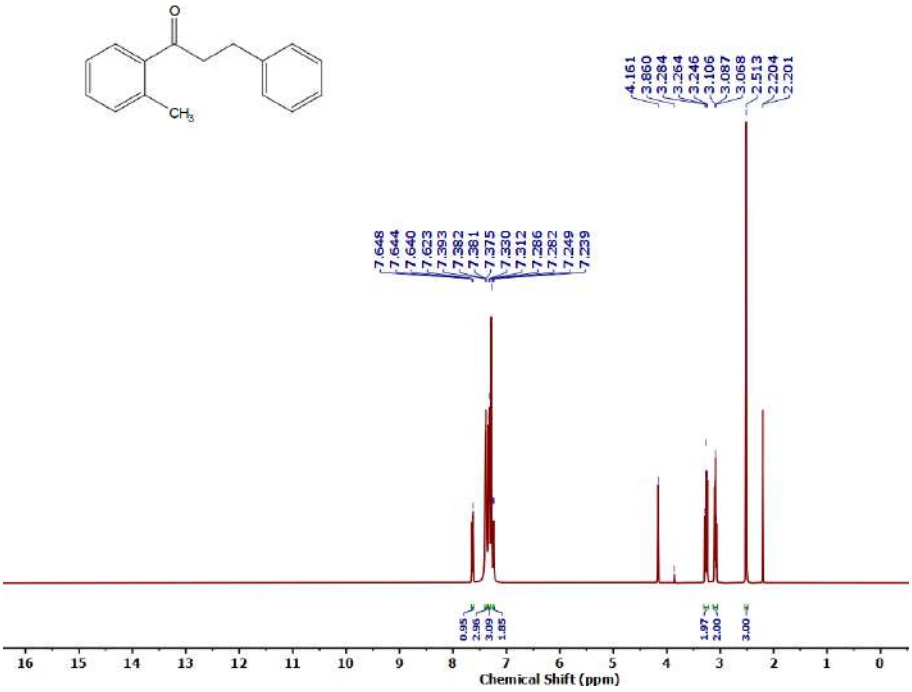

Figure 3.6.A6: ^{1}H NMR spectrum of **3b**

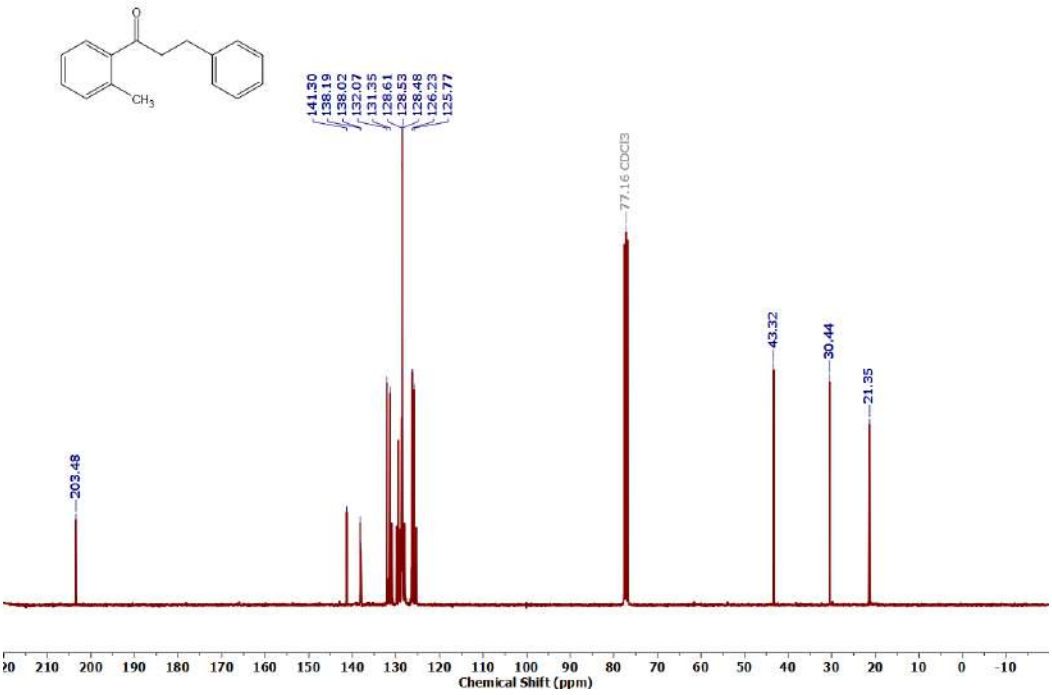

Figure 3.6.A7: $^{13}C\{^{1}H\}$ NMR spectrum of **3b**

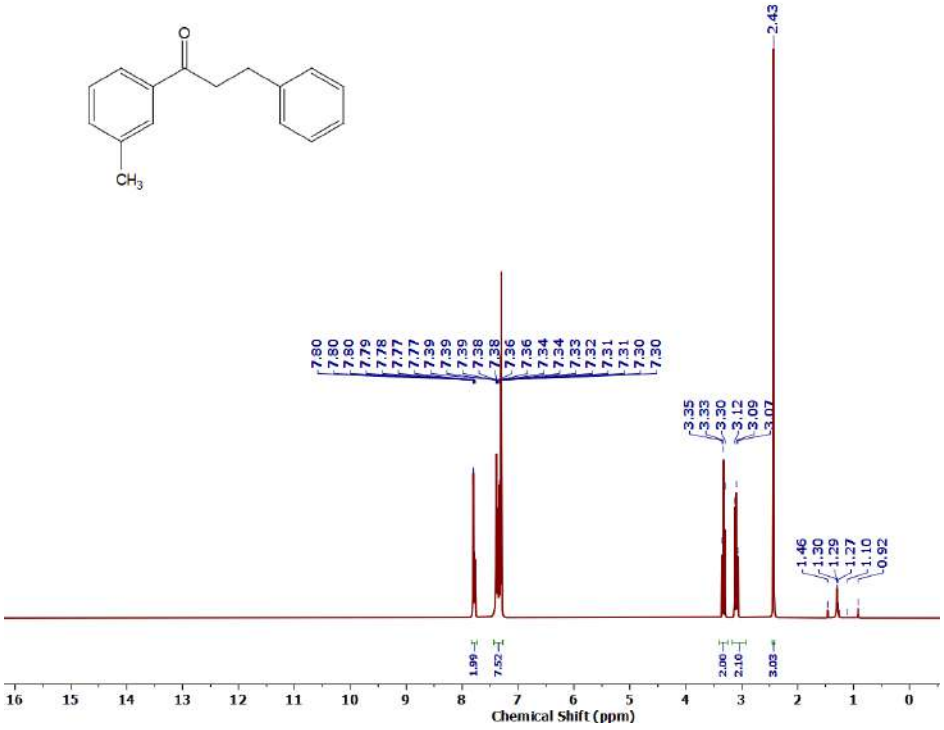

Figure 3.6.A8: ^{1}H NMR spectrum of **3c**

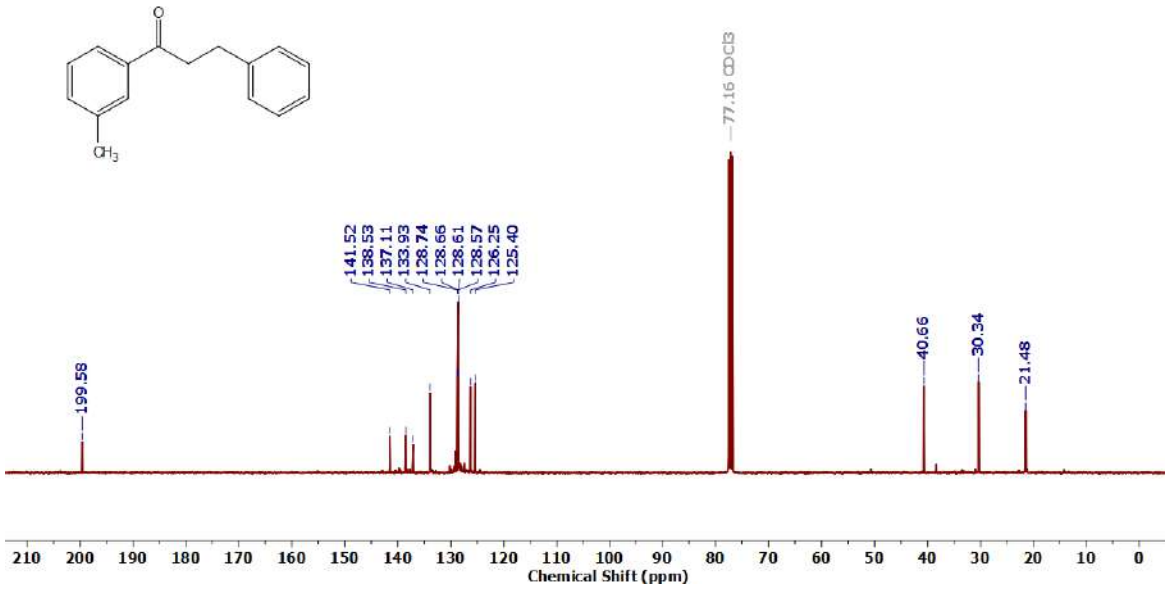

Figure 3.6.A9: $^{13}C\{^{1}H\}$ NMR spectrum of **3c**

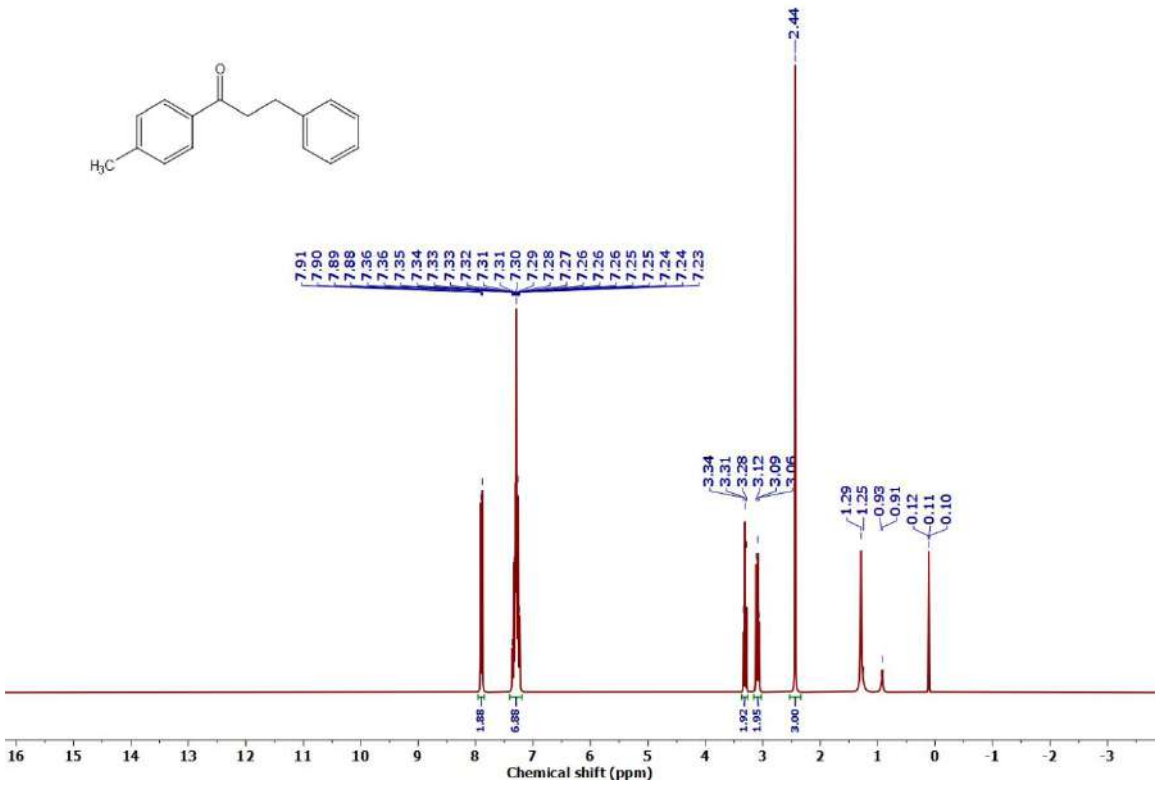

Figure 3.6.A10: ^{1}H NMR spectrum of **3d**

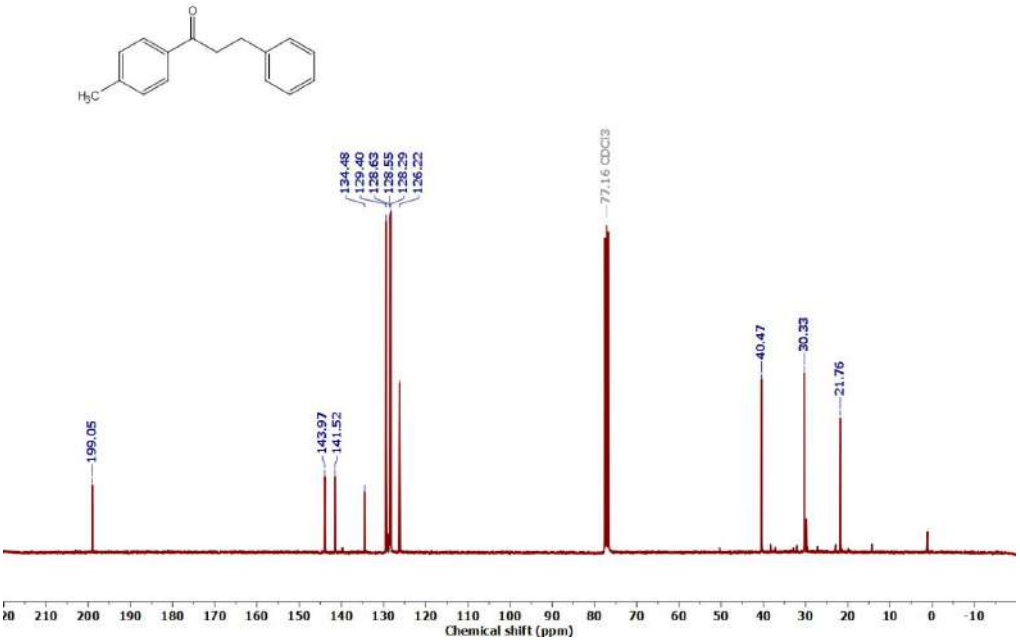

Figure 3.6.A11: $^{13}C\{^{1}H\}$ NMR spectrum of **3d**

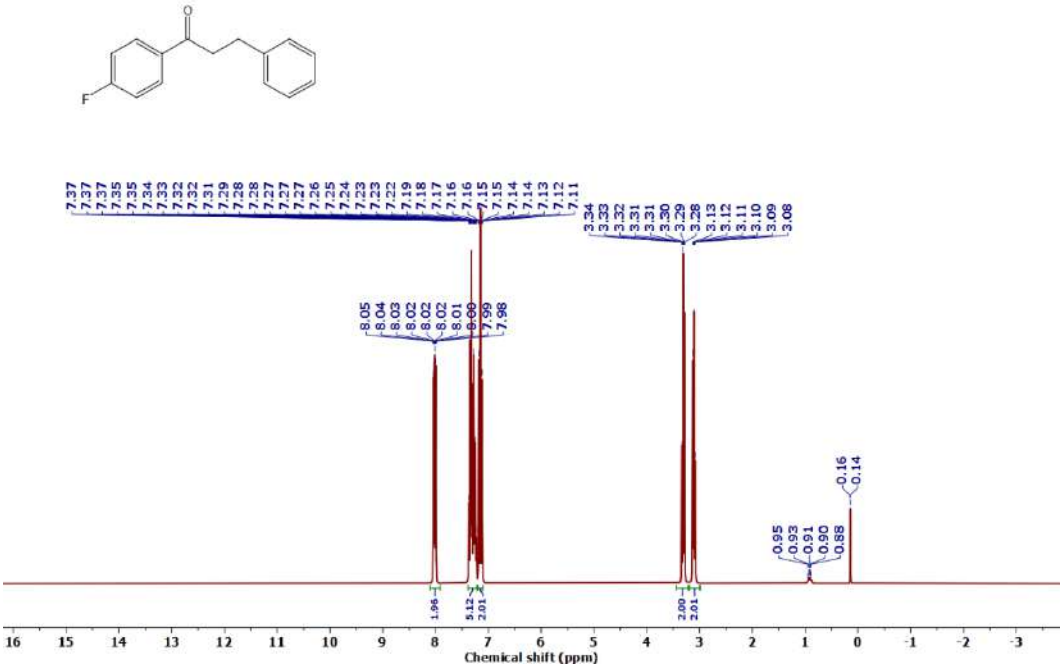

Figure 3.6.A12: ^{1}H NMR spectrum of **3e**

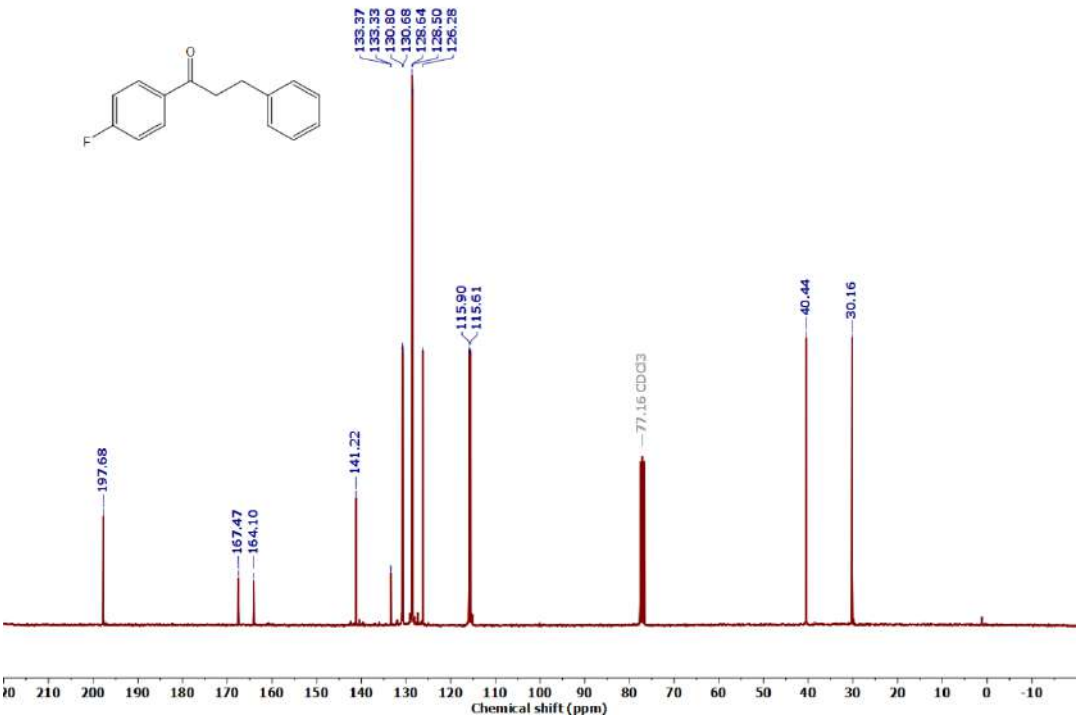

Figure 3.6.A13: $^{13}C\{^{1}H\}$ NMR spectrum of **3e**

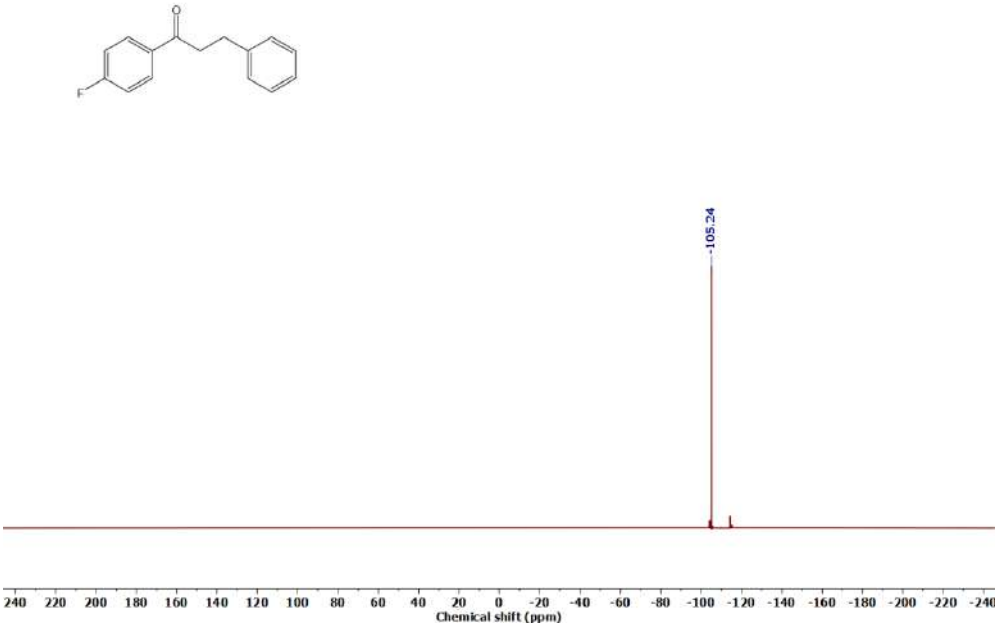

Figure 3.6.A14: ^{19}F NMR spectrum of **3e**

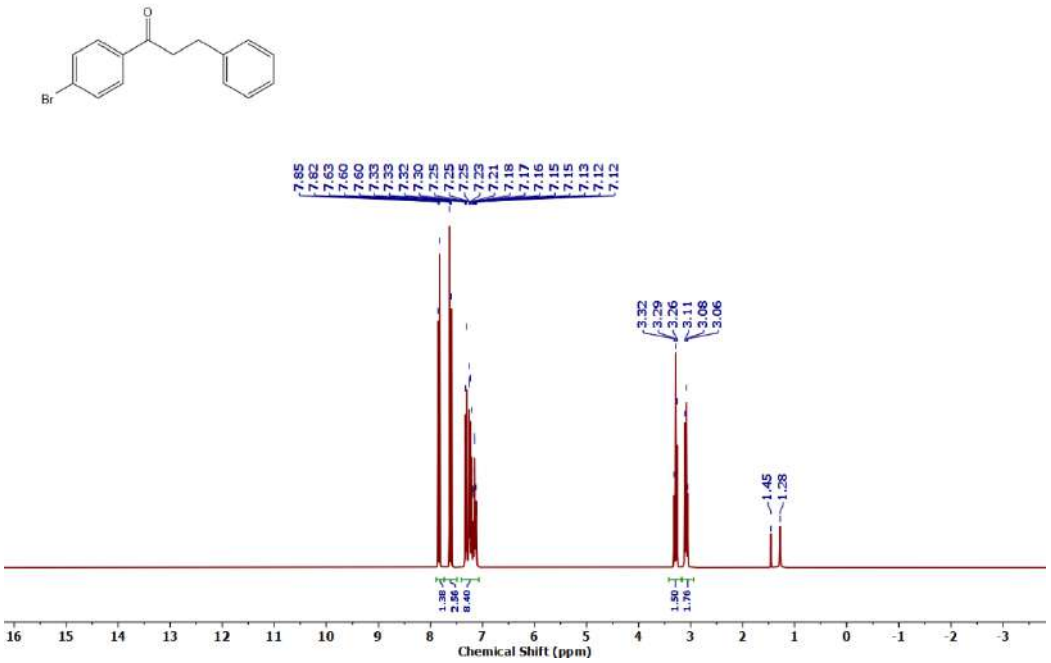

Figure 3.6.A15: ^{1}H NMR spectrum of **3f**

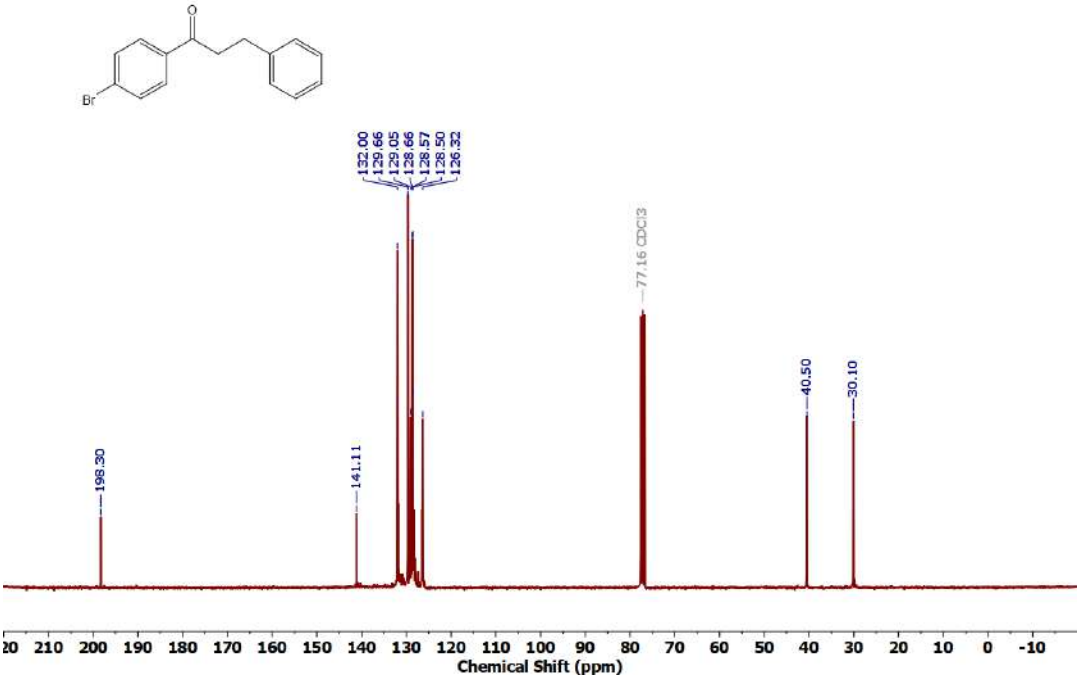

Figure 3.6.A16: ^{13}C{^{1}H} NMR spectrum of **3f**

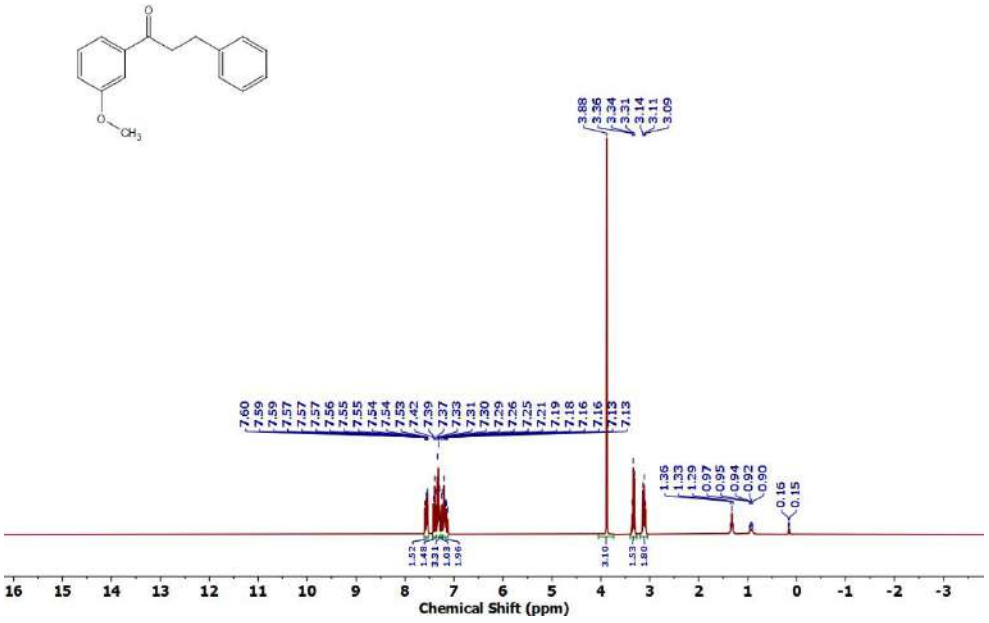

Figure 3.6.A17: ^{1}H NMR spectrum of **3g**

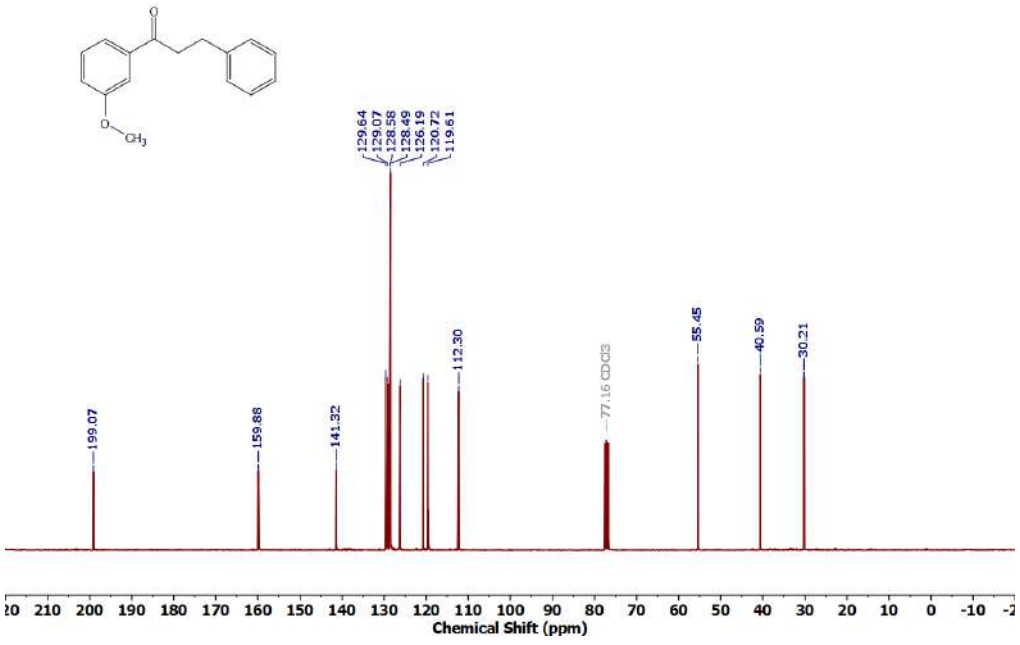

Figure 3.6.A18: ^{13}C{^{1}H} NMR spectrum of **3g**

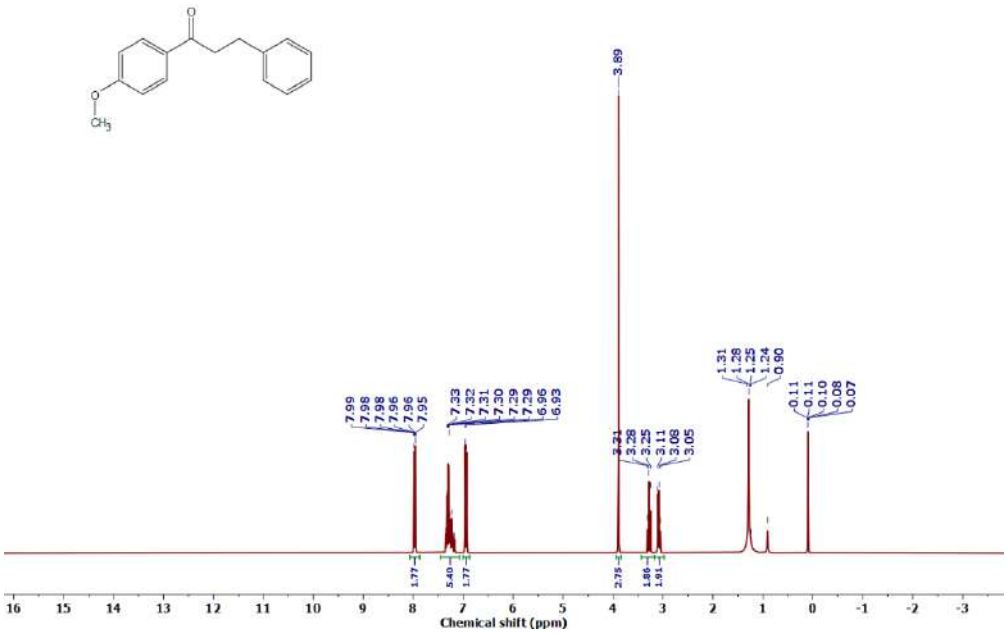

Figure 3.6.A19: ^{1}H NMR spectrum of **3h**

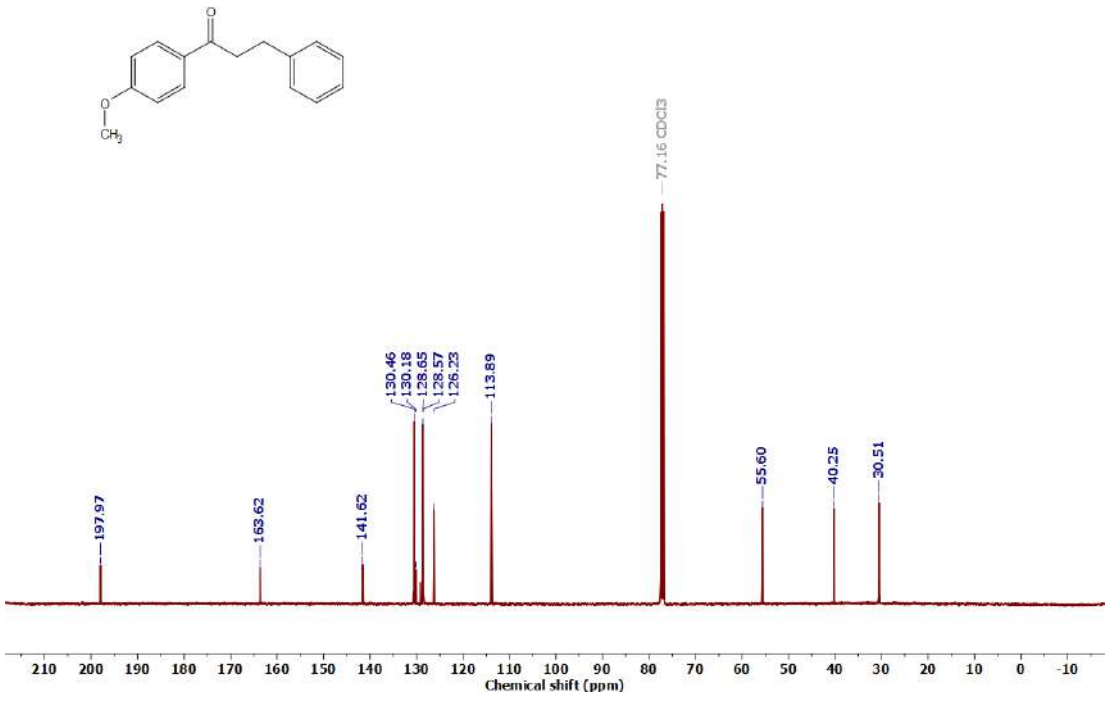

Figure 3.6.A20: ^{13}C{^{1}H} NMR spectrum of **3h**

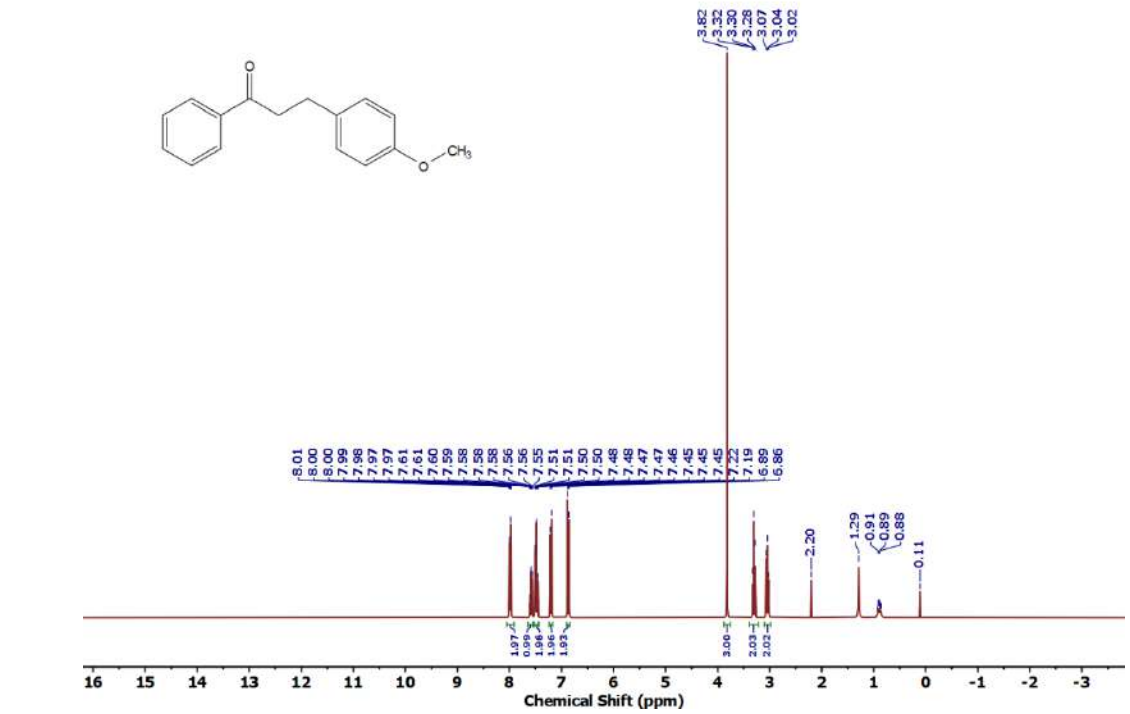

Figure 3.6.A21: ^{1}H NMR spectrum of **3i**

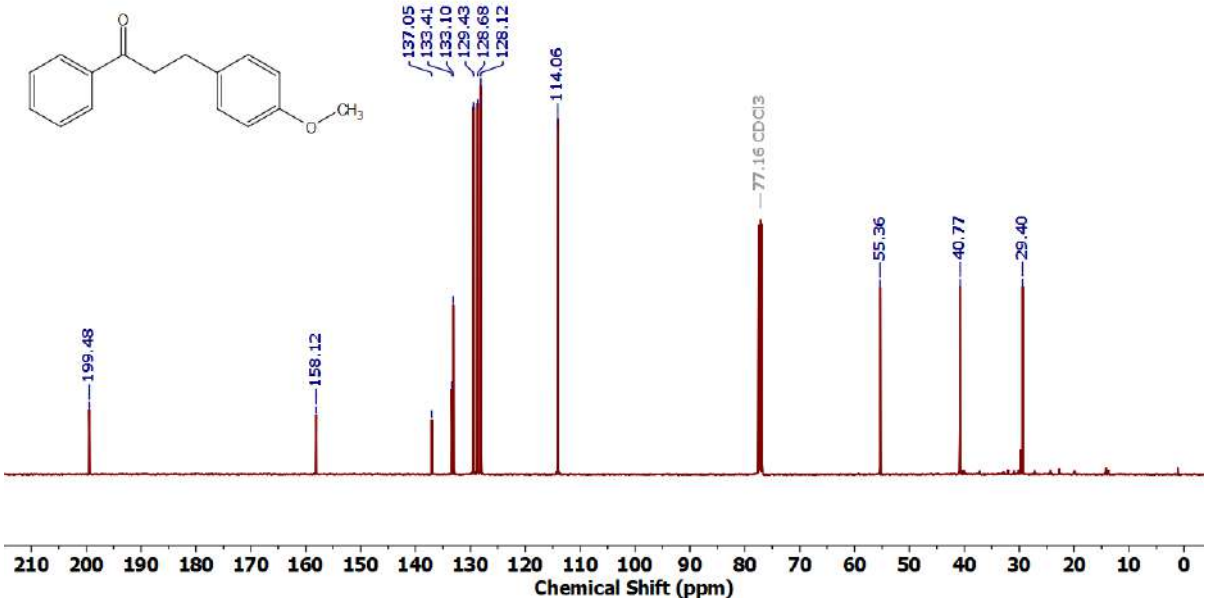

Figure 3.6.A22: $^{13}C\{^{1}H\}$ NMR spectrum of **3i**

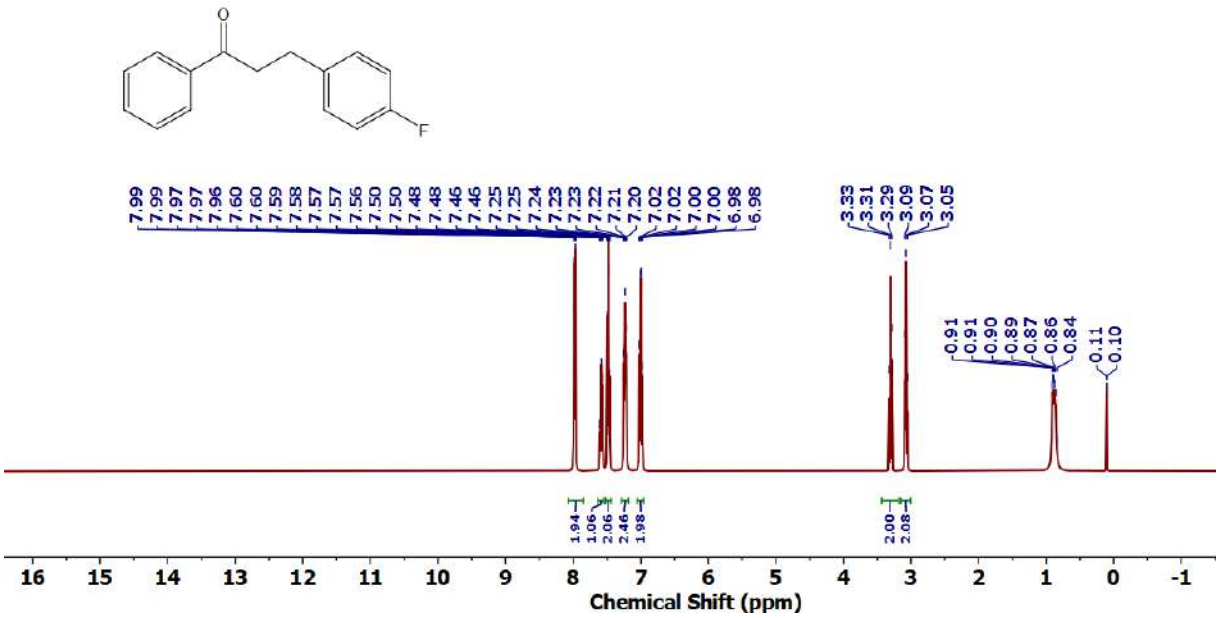

Figure 3.6.A23: ^{1}H NMR spectrum of **3j**

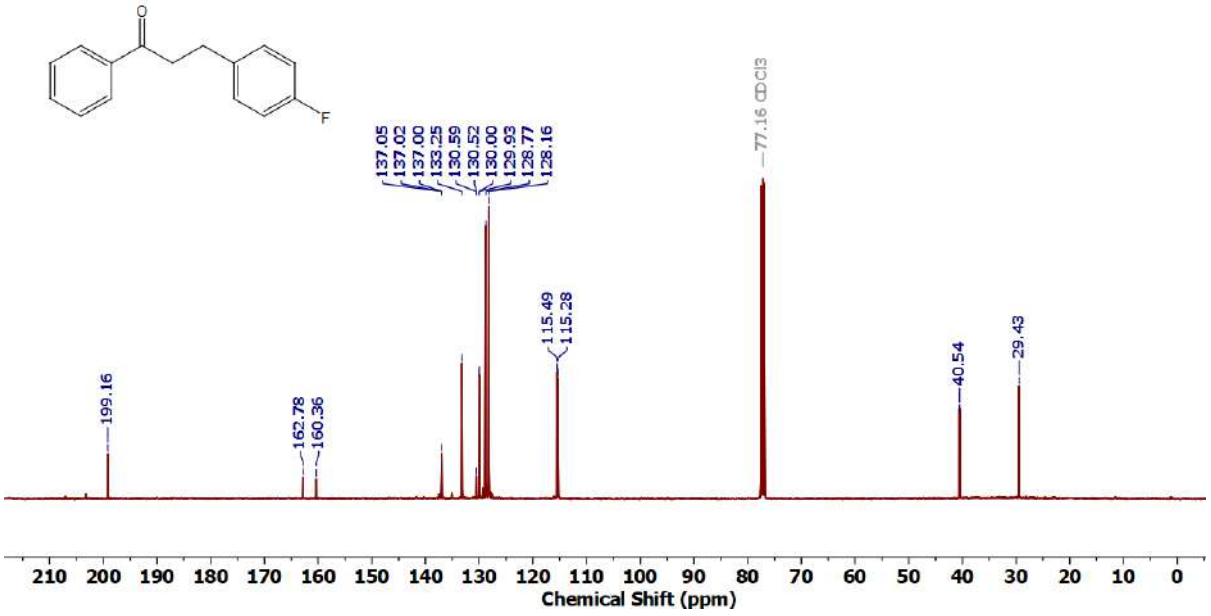

Figure 3.6.A24: $^{13}C\{^{1}H\}$ NMR spectrum of **3j**

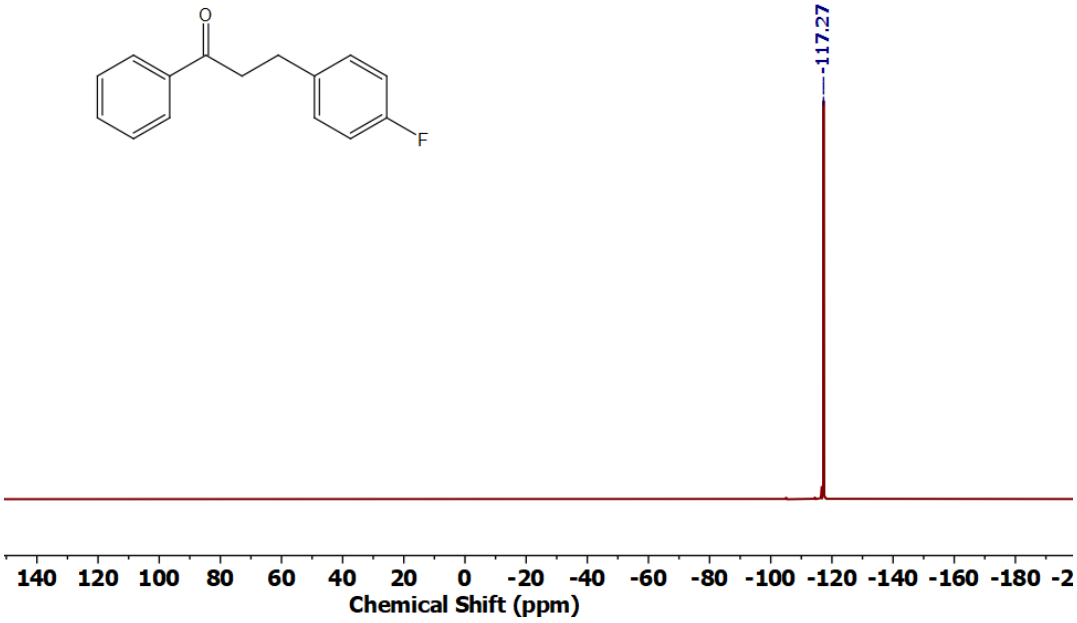

Figure 3.6.A25: ^{19}F NMR spectrum of **3j**

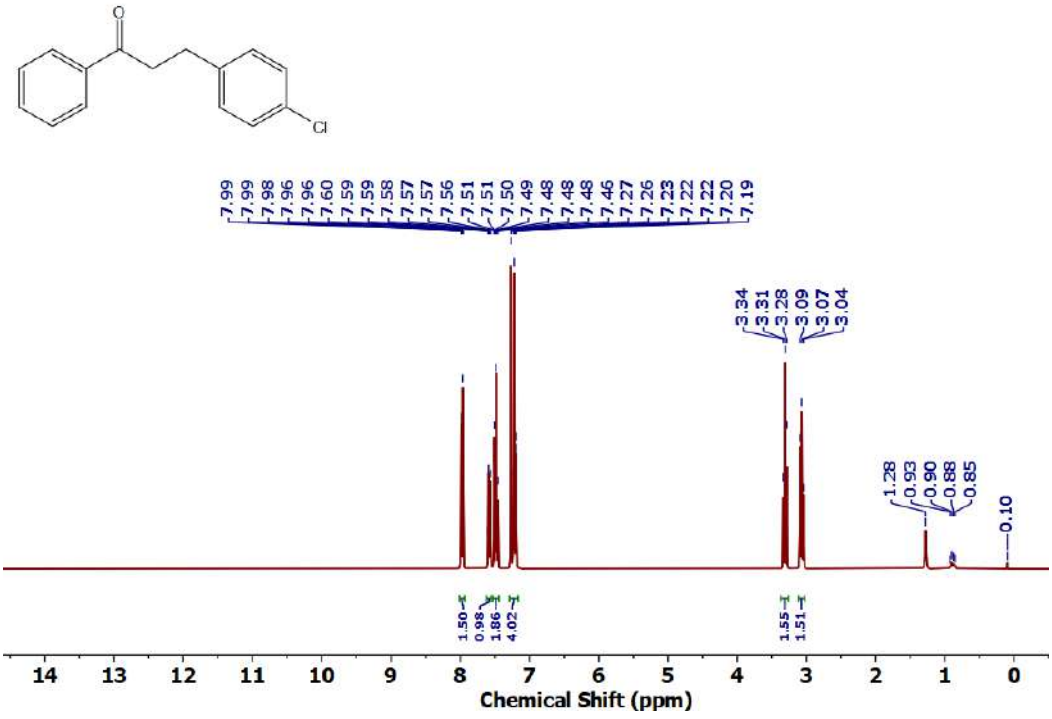

Figure 3.6.A26: ^{1}H NMR spectrum of **3k**

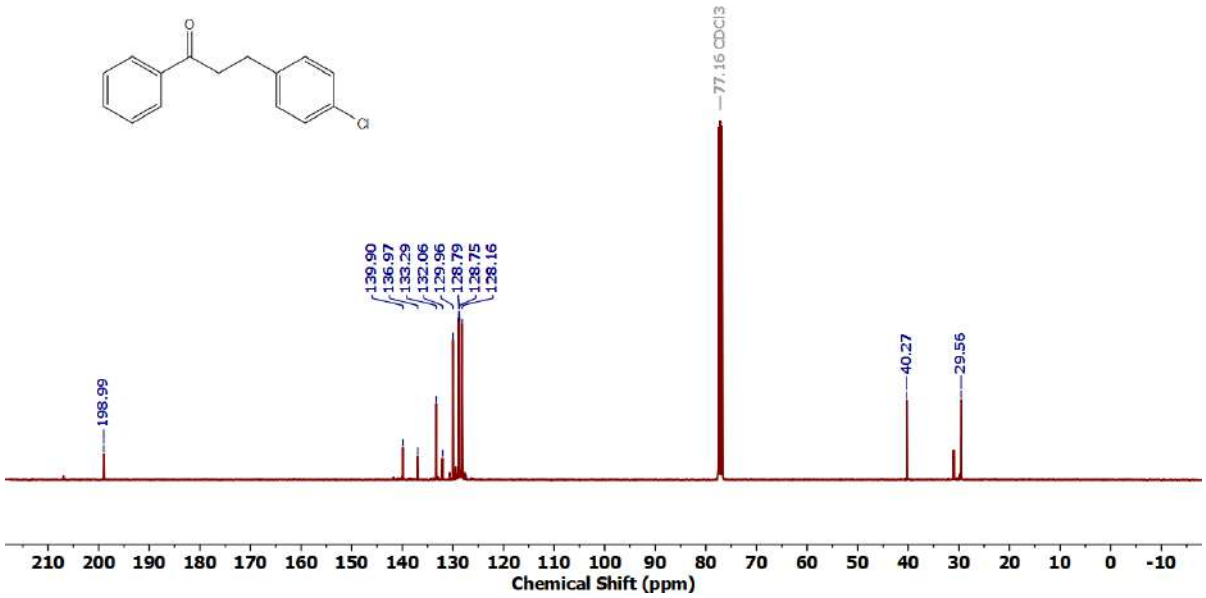

Figure 3.6.A27: $^{13}C\{^{1}H\}$ NMR spectrum of **3k**

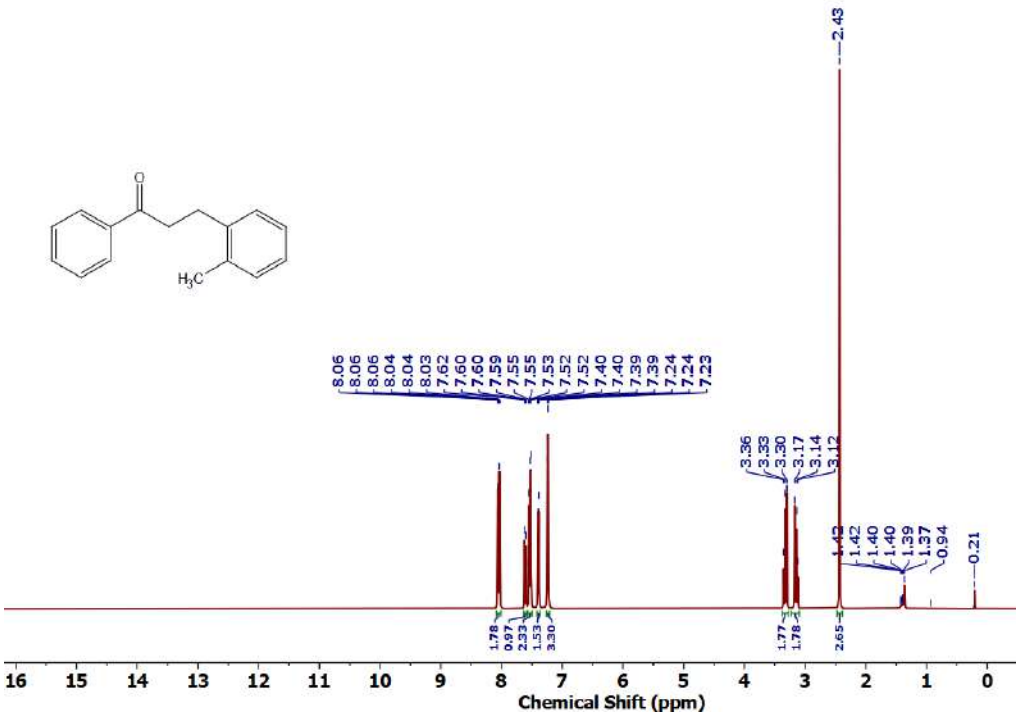

Figure 3.6.A28: ^{1}H NMR spectrum of **3l**

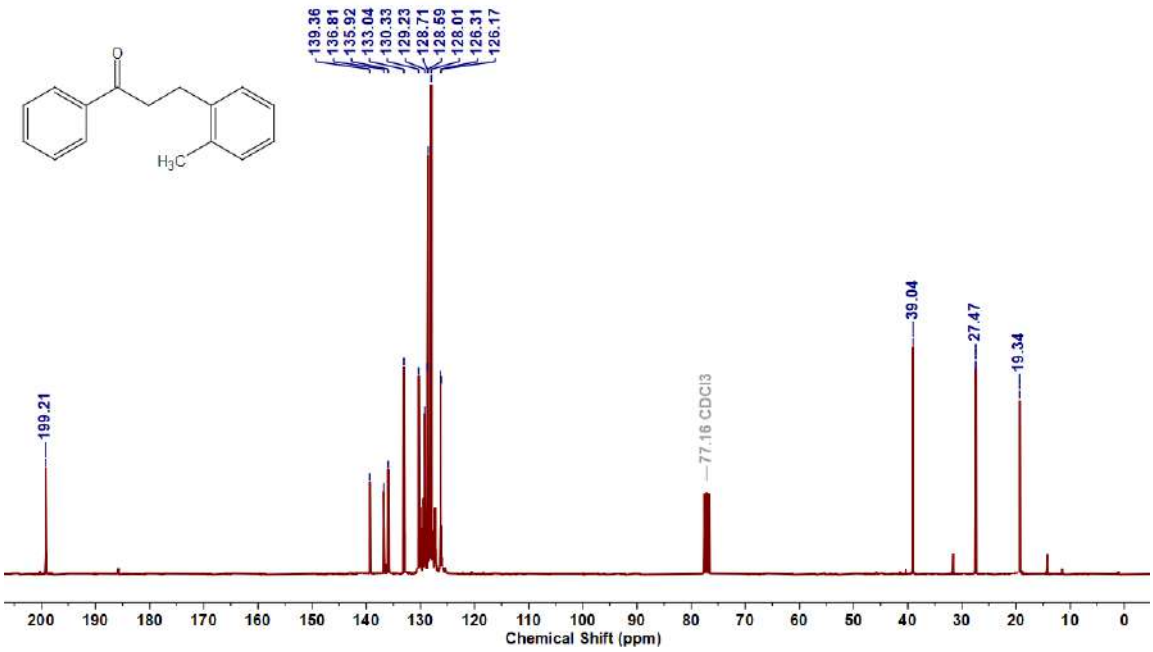

Figure 3.6.A29: $^{13}C\{^{1}H\}$ NMR spectrum of **3l**

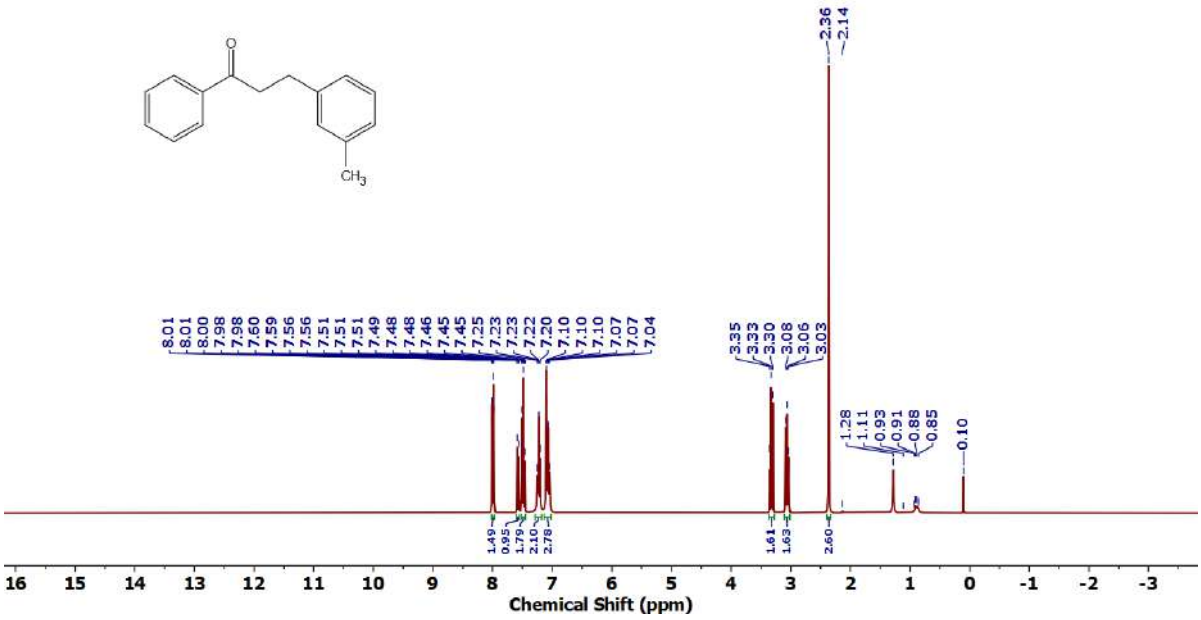

Figure 3.6.A30: ^{1}H NMR spectrum of **3m**

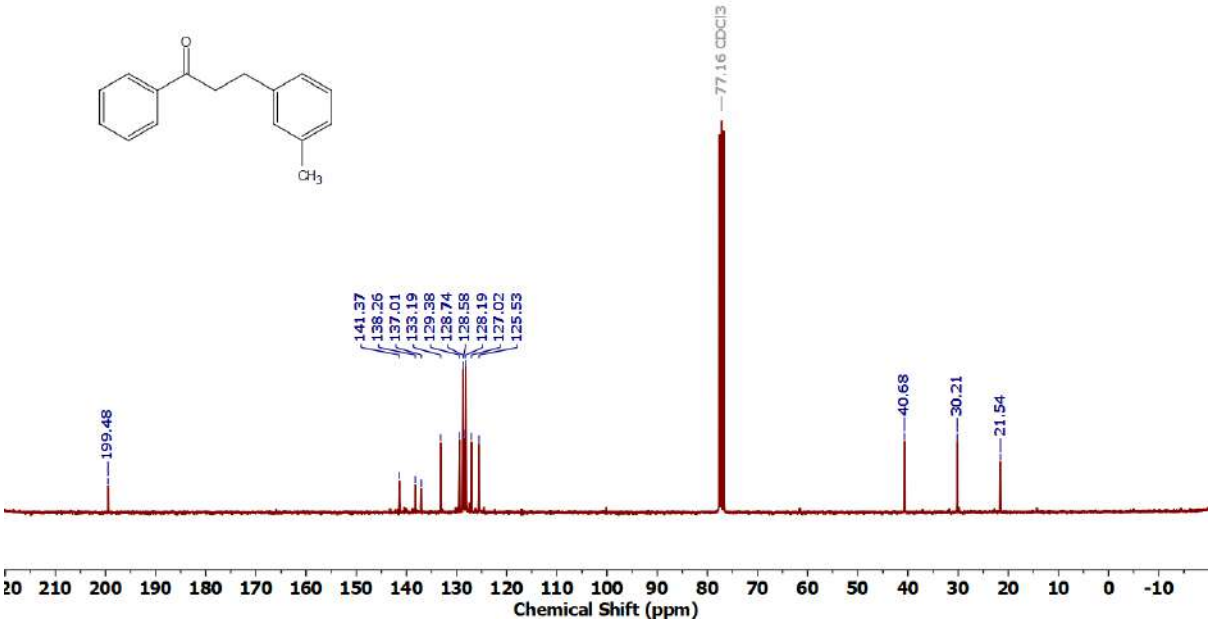

Figure 3.6.A31: $^{13}C\{^{1}H\}$ NMR spectrum of **7m**

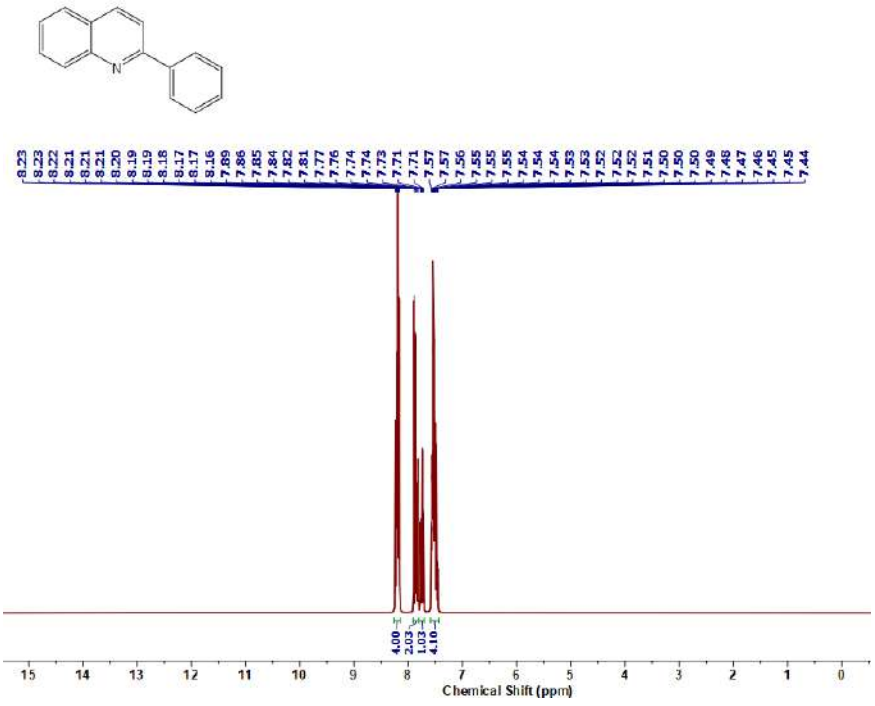

Figure 3.6.A32: ^{1}H NMR spectrum of **5a**

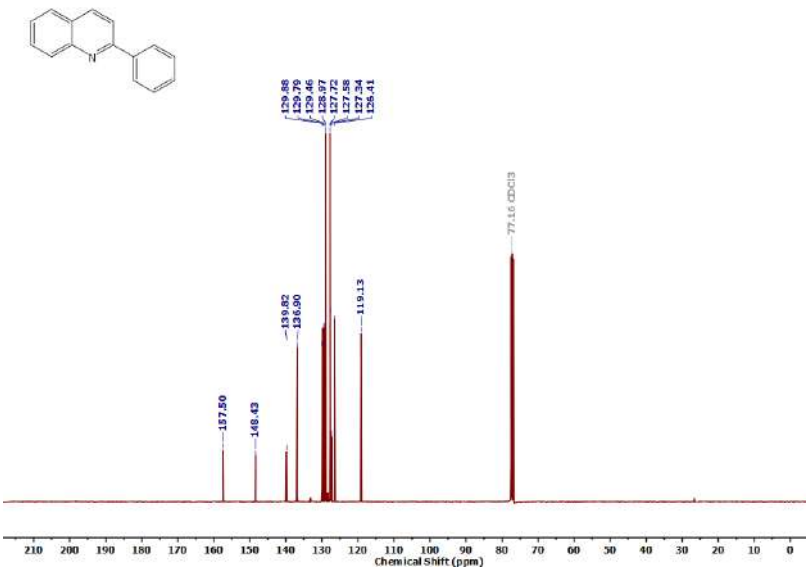

Figure 3.6.A33: $^{13}C\{^{1}H\}$ NMR spectrum of **5a**

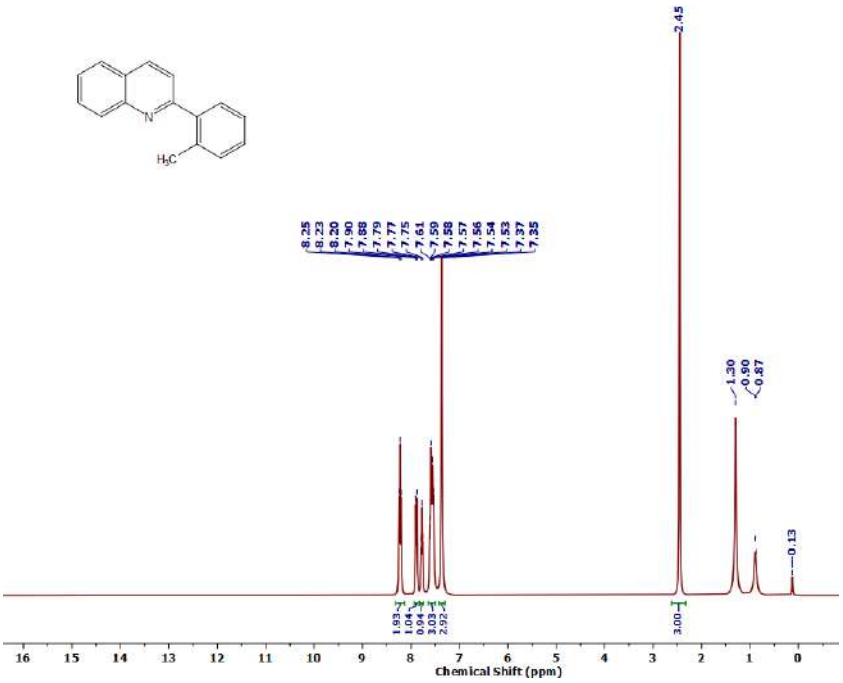

Figure 3.6.A34: ^{1}H NMR spectrum of **5b**

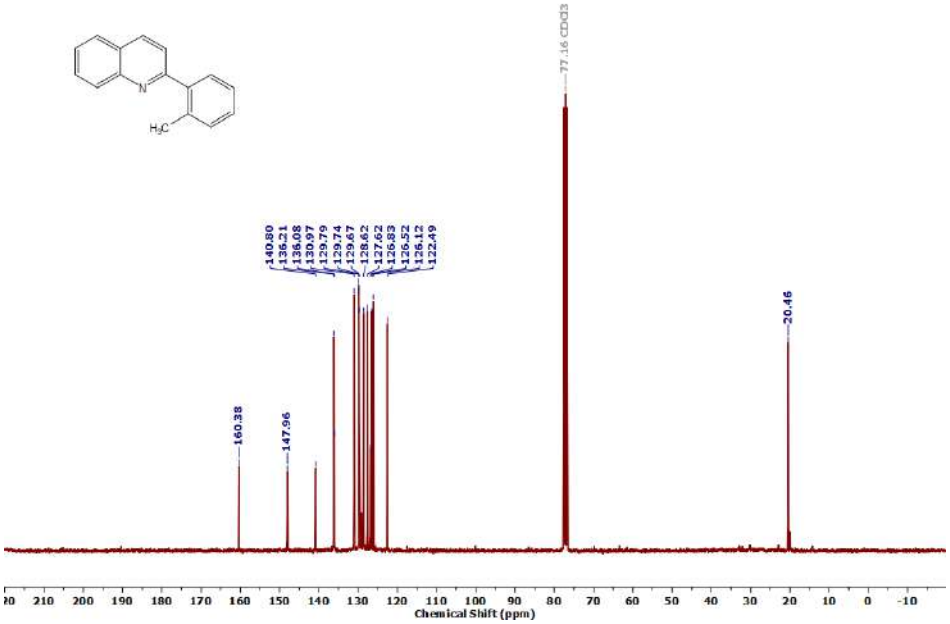

Figure 3.6.A35: $^{13}C\{^{1}H\}$ NMR spectrum of **5b**

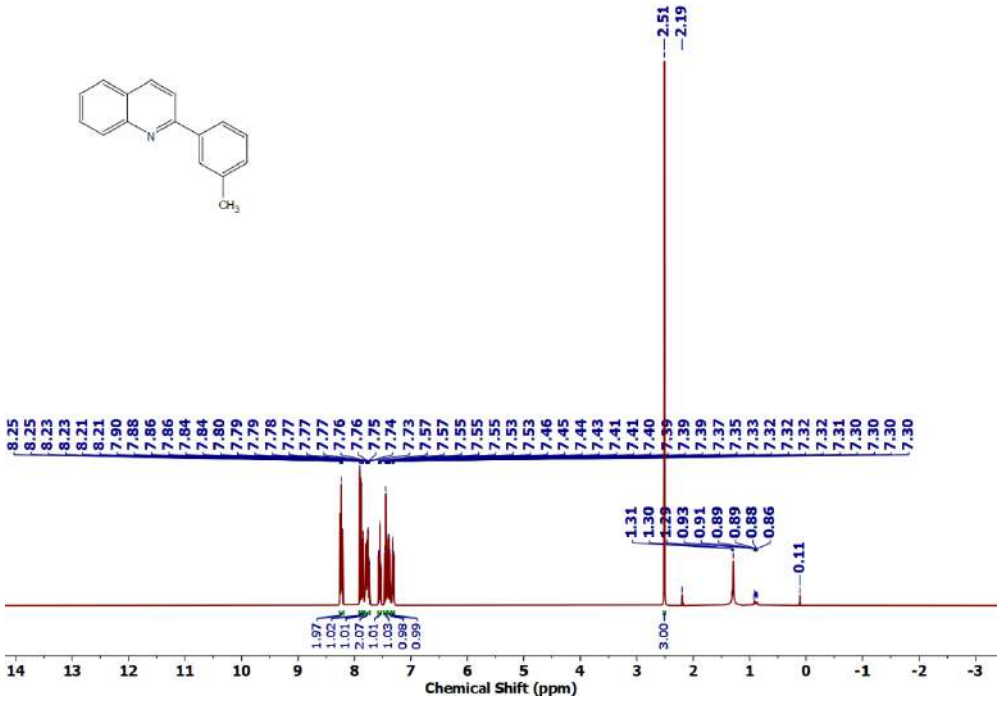

Figure 3.6.A36: ^{1}H NMR spectrum of **5c**

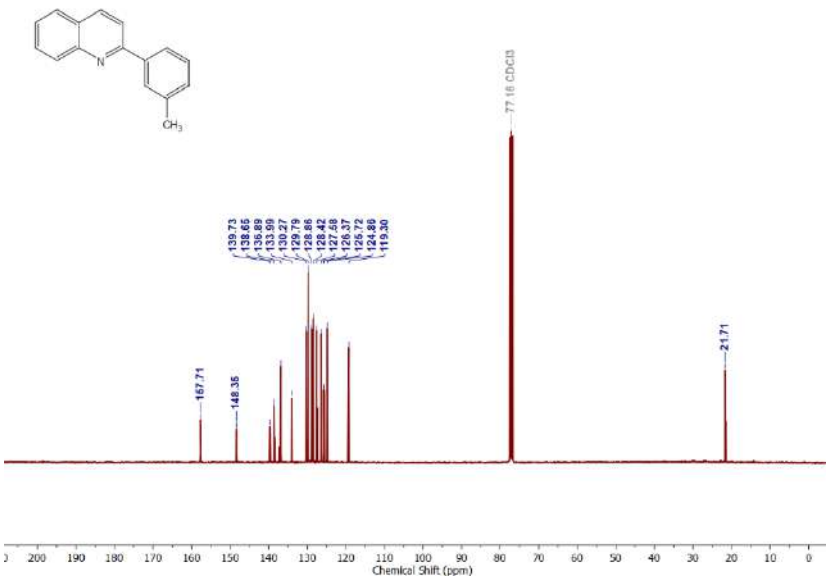

Figure 3.6.A37: $^{13}C\{^{1}H\}$ NMR spectrum of **5c**

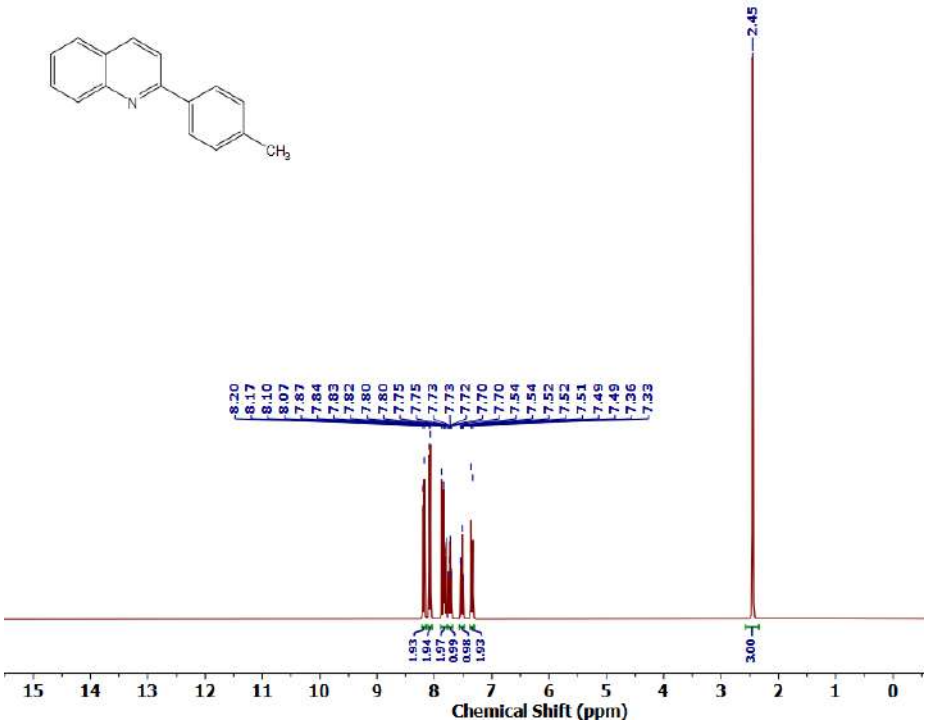

Figure 3.6.A38: ^{1}H NMR spectrum of **5d**

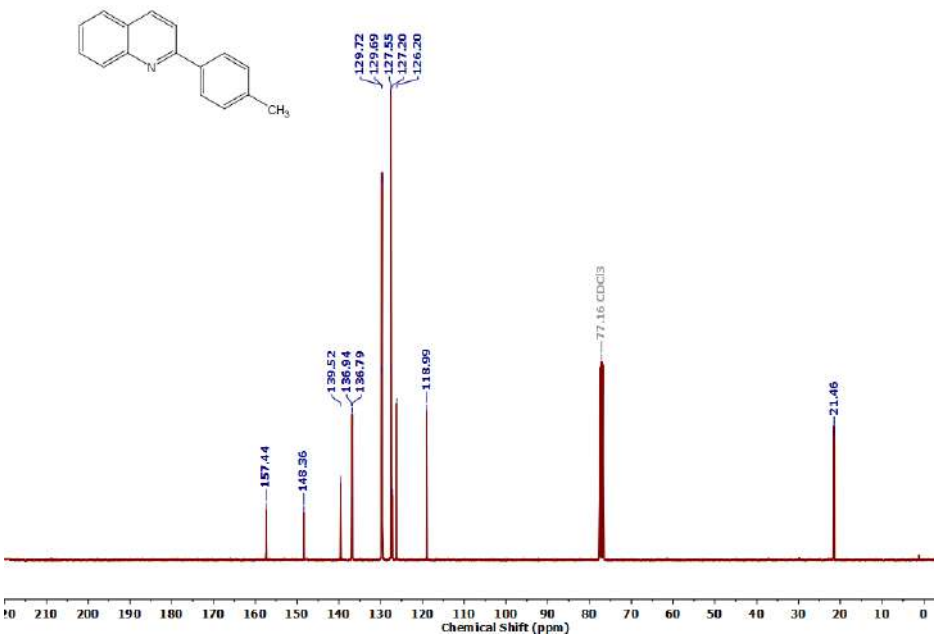

Figure 3.6.A39: $^{13}C\{^{1}H\}$ NMR spectrum of **5d**

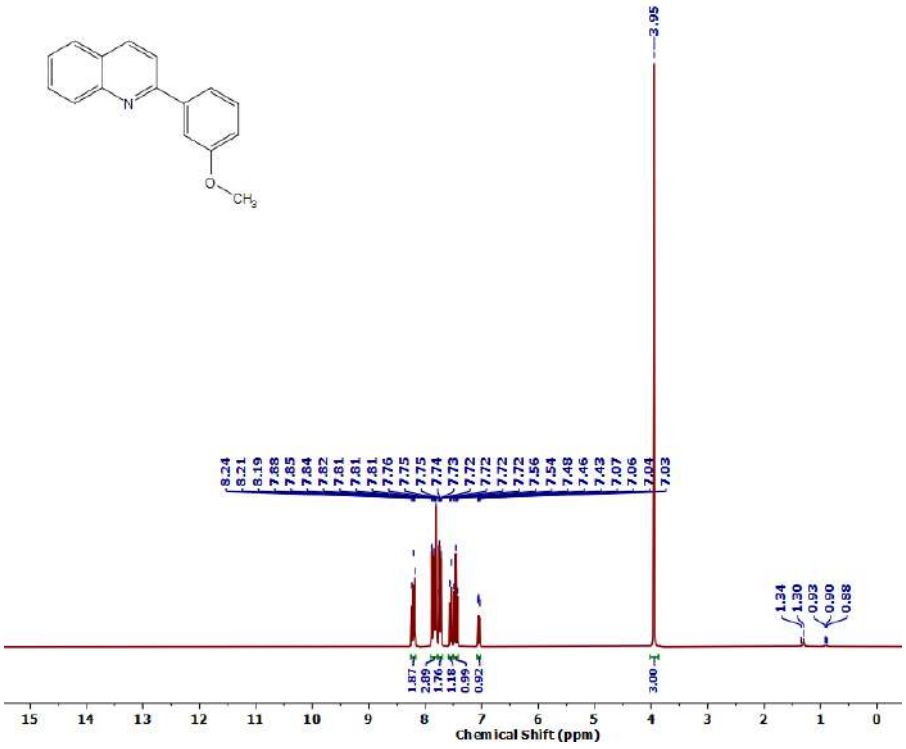

Figure 3.6.A40: ^{1}H NMR spectrum of **5e**

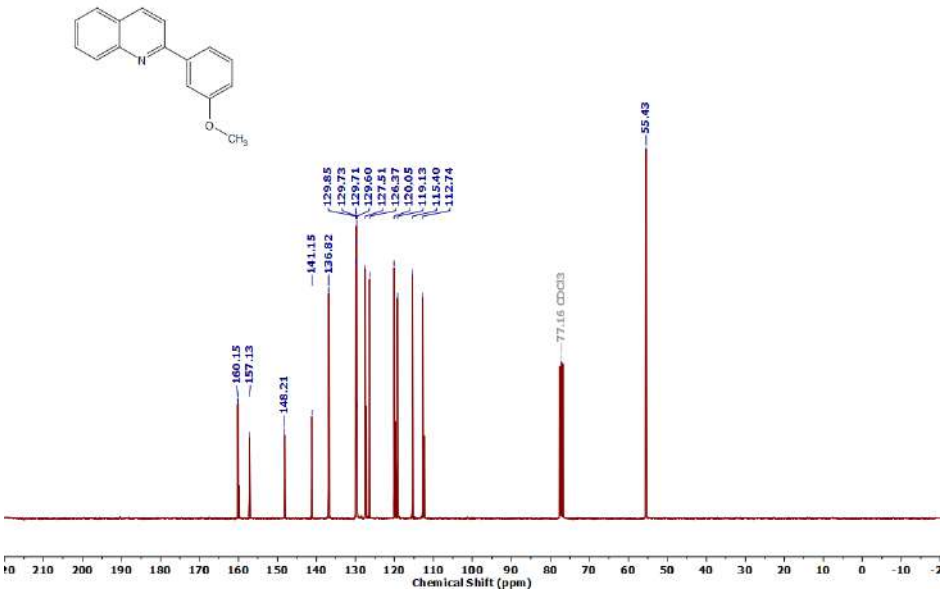

Figure 3.6.A41: $^{13}C\{^{1}H\}$ NMR spectrum of **5e**

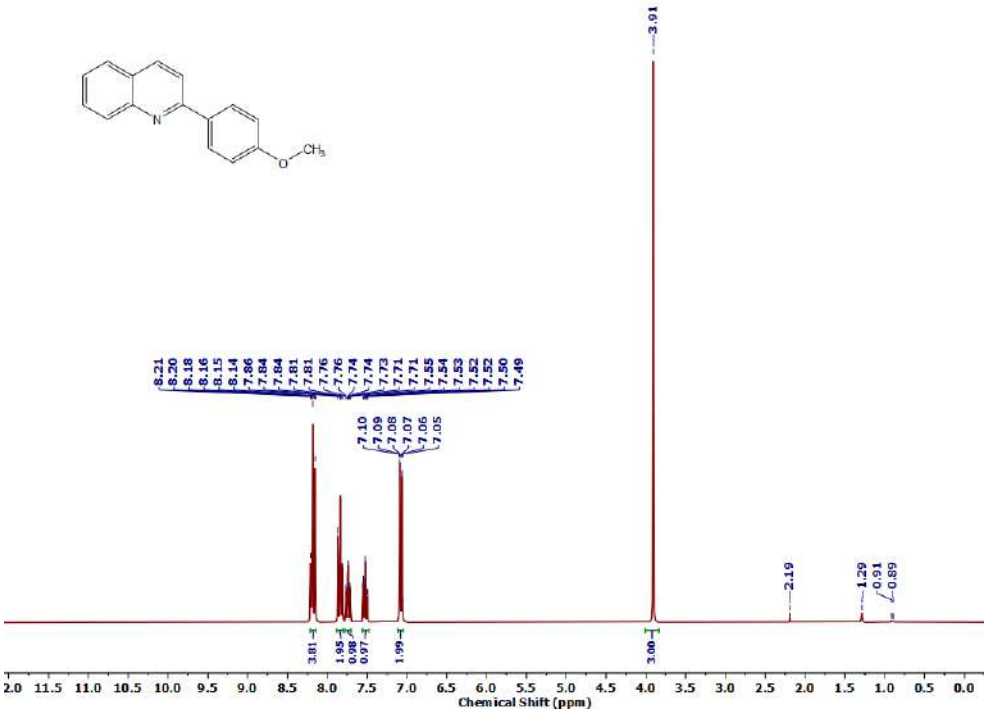

Figure 3.6.A42: ^{1}H NMR spectrum of **5f**

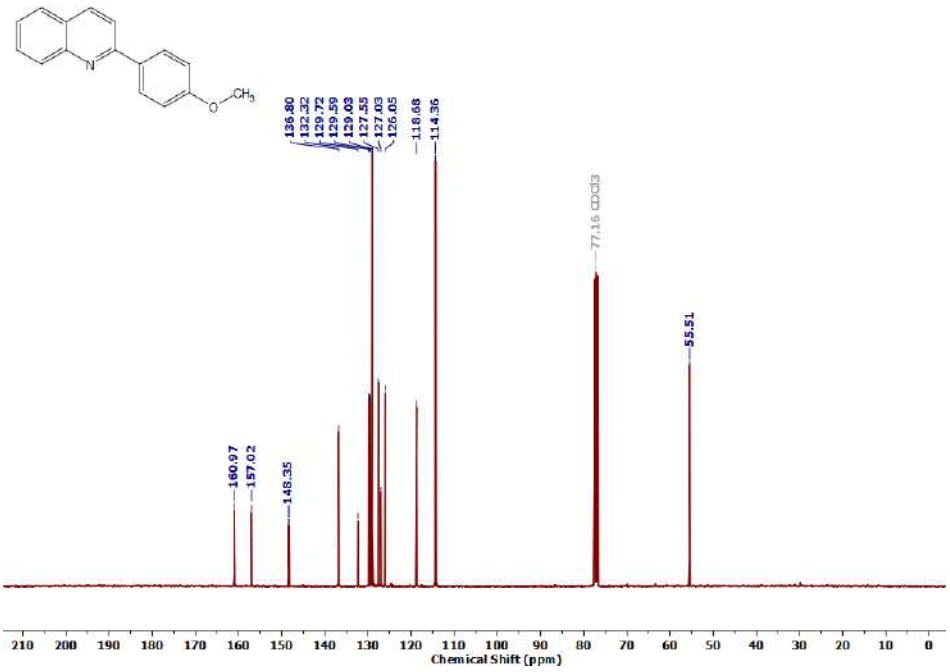

Figure 3.6.A43: $^{13}C\{^{1}H\}$ NMR spectrum of **5f**

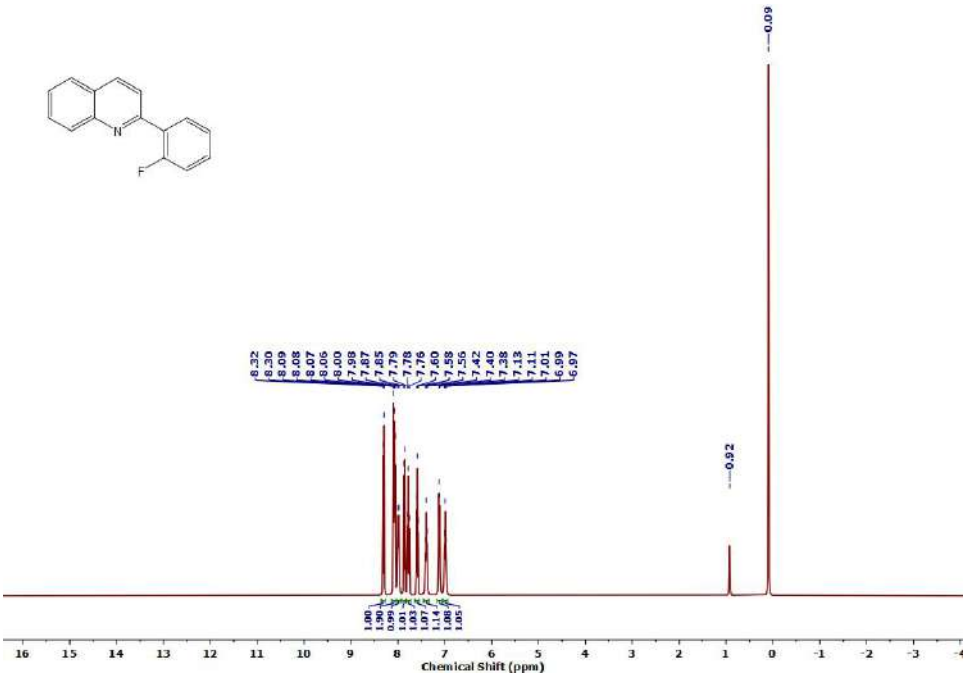

Figure 3.6.A44: ^{1}H NMR spectrum of **5g**

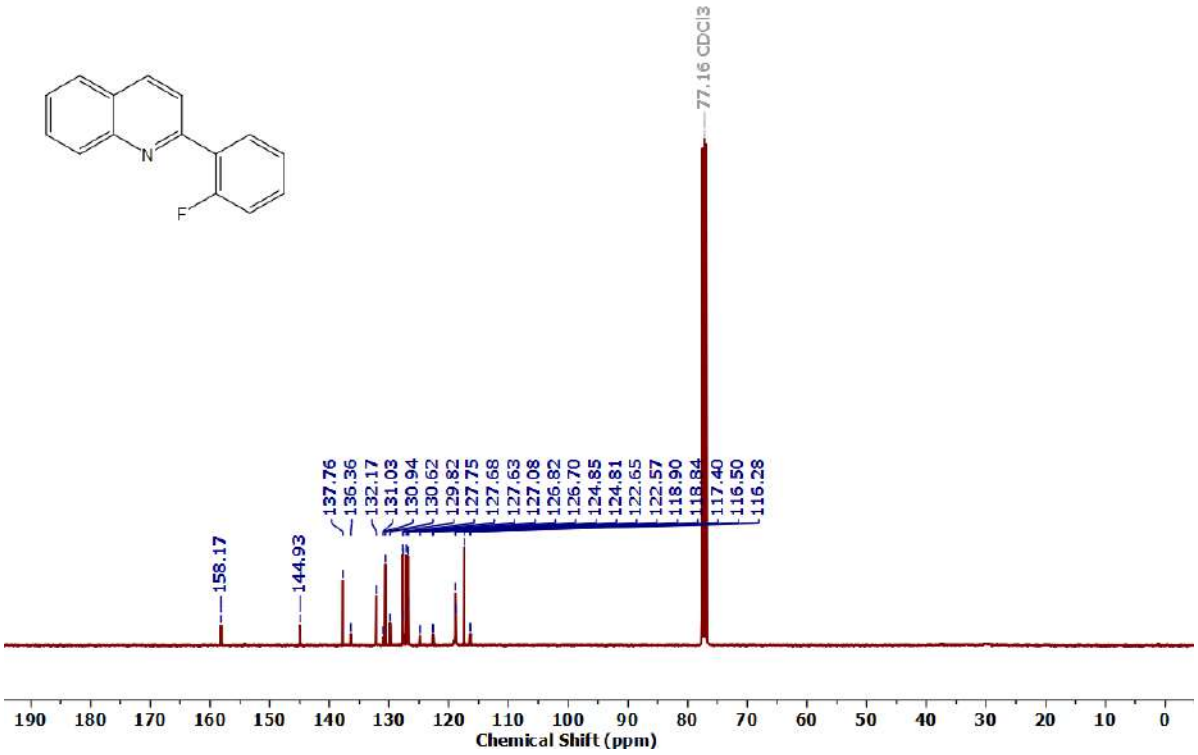

Figure 3.6.A45: $^{13}C\{^{1}H\}$ NMR spectrum of **5g**

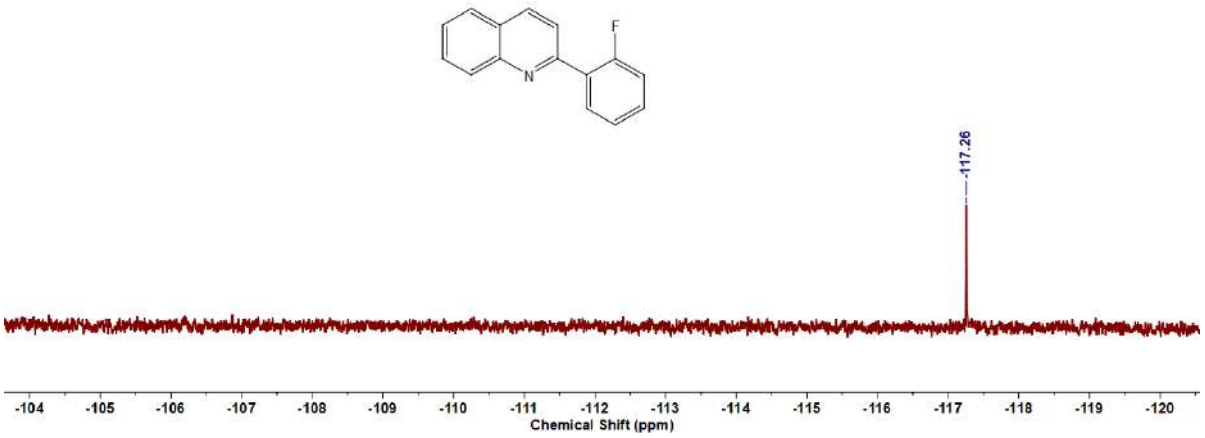

Figure 3.6.A46: ^{19}F NMR spectrum of **5g**

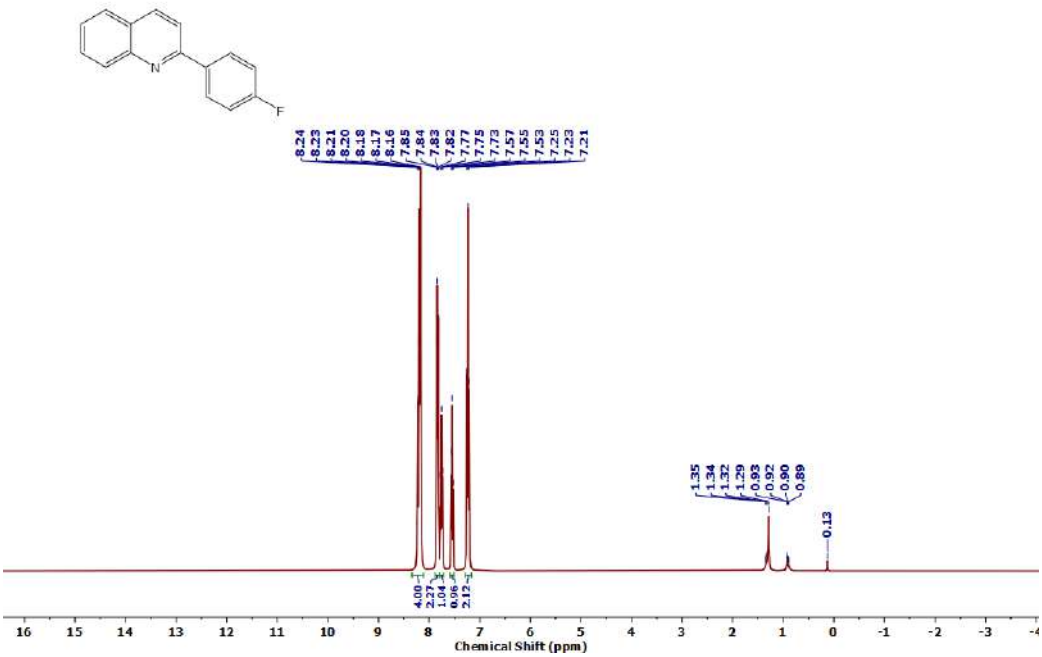

Figure 3.6.A47: ^{1}H NMR spectrum of **5h**

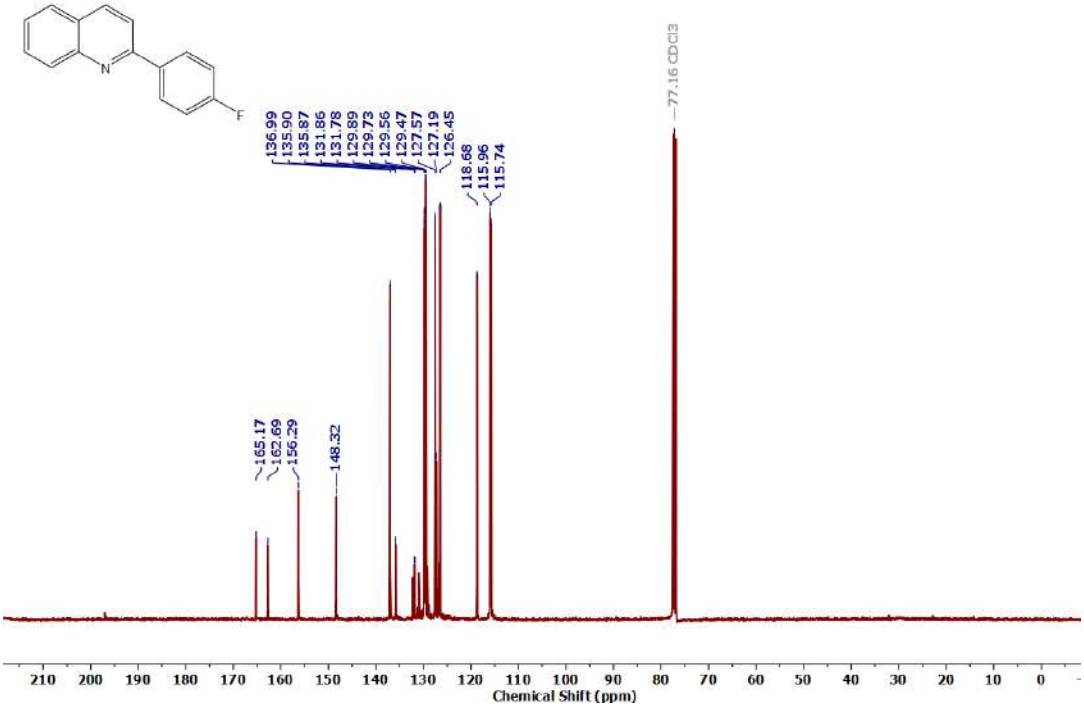

Figure 3.6.A48: ^{13}C{^{1}H} NMR spectrum of **5h**

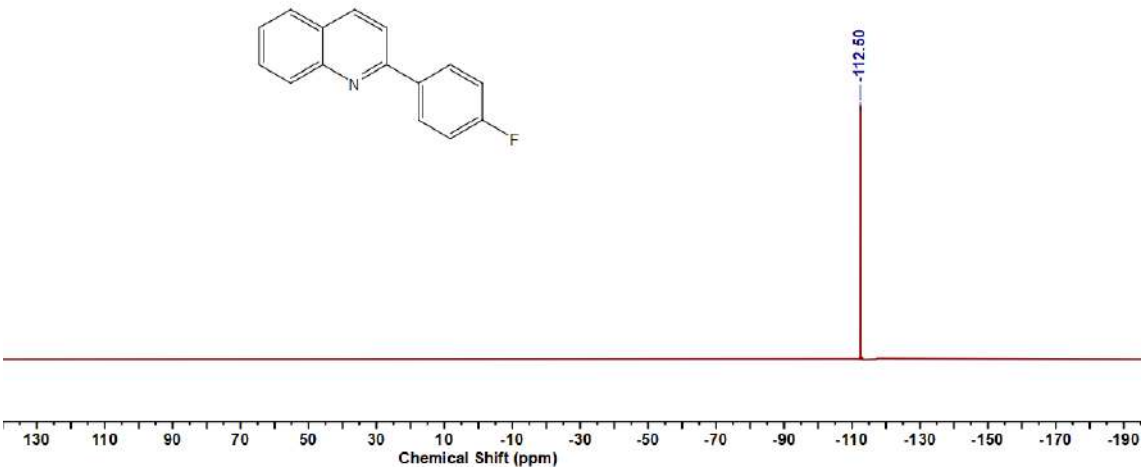

Figure 3.6.A49: ^{19}F NMR spectrum of **5h**

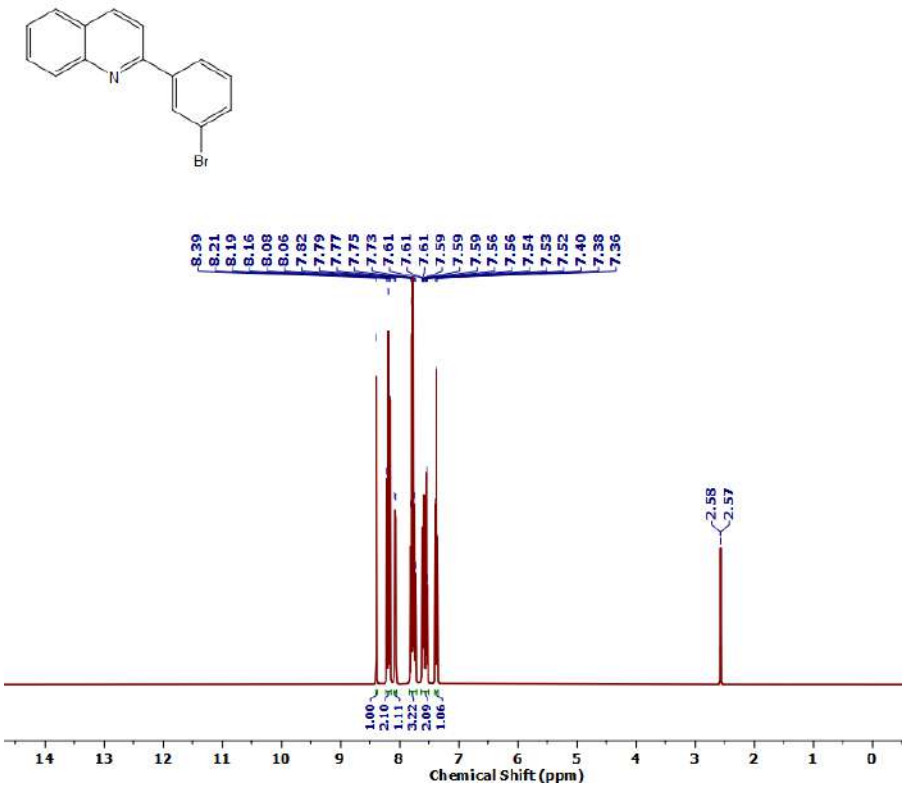

Figure 3.6.A50: ^{1}H NMR spectrum of **5i**

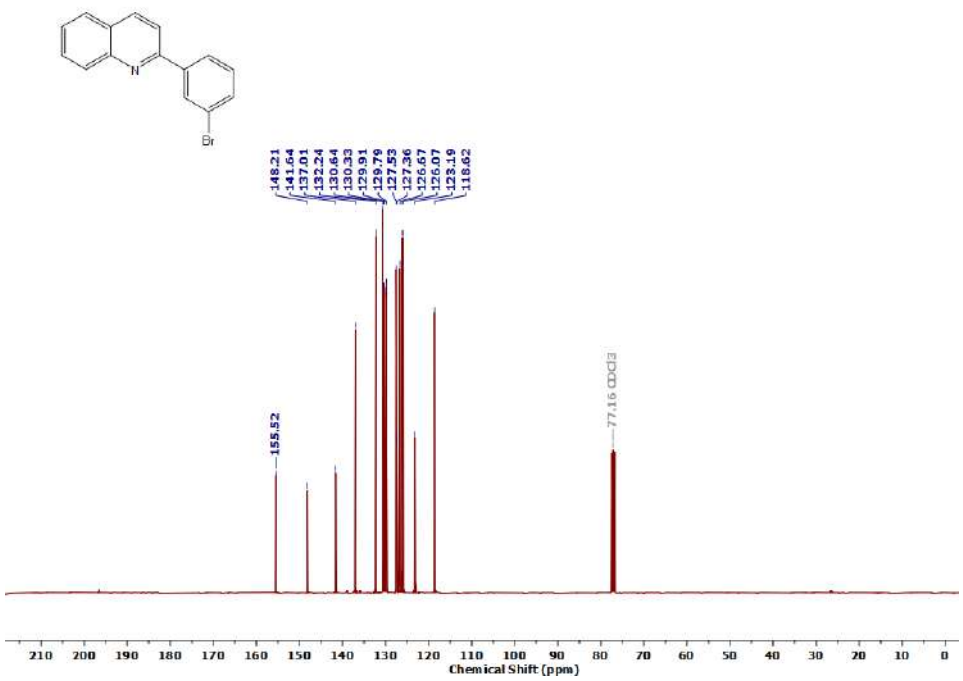

Figure 3.6.A51: $^{13}C\{^{1}H\}$ NMR spectrum of **5i**

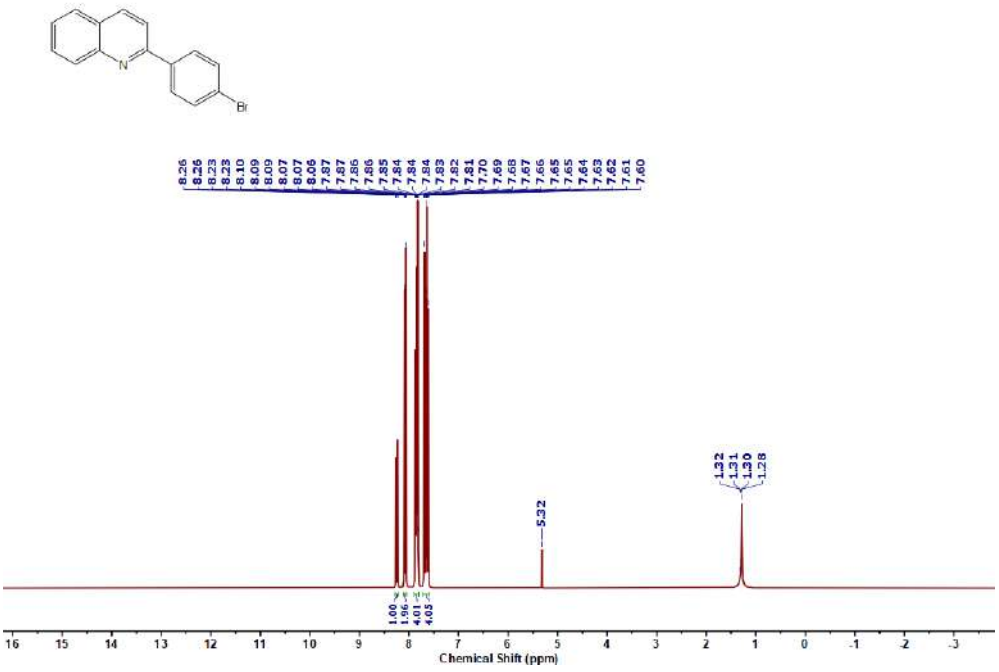

Figure 3.6.A52: ^{1}H NMR spectrum of **5j**

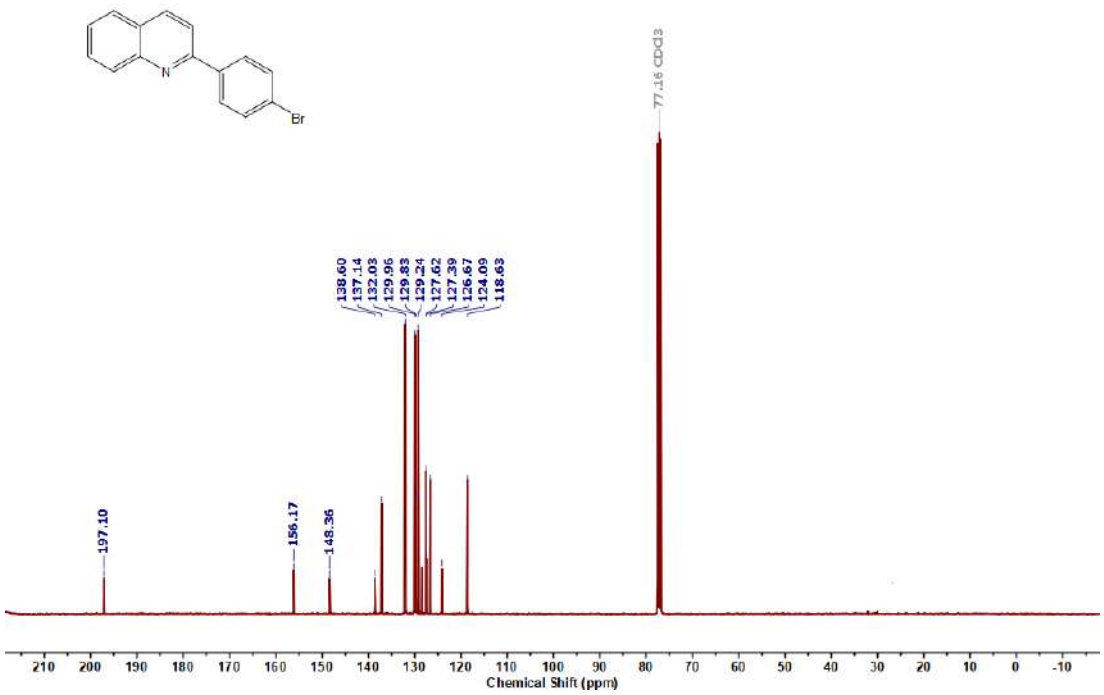

Figure 3.6.A53: $^{13}C\{^{1}H\}$ NMR spectrum of **5j**

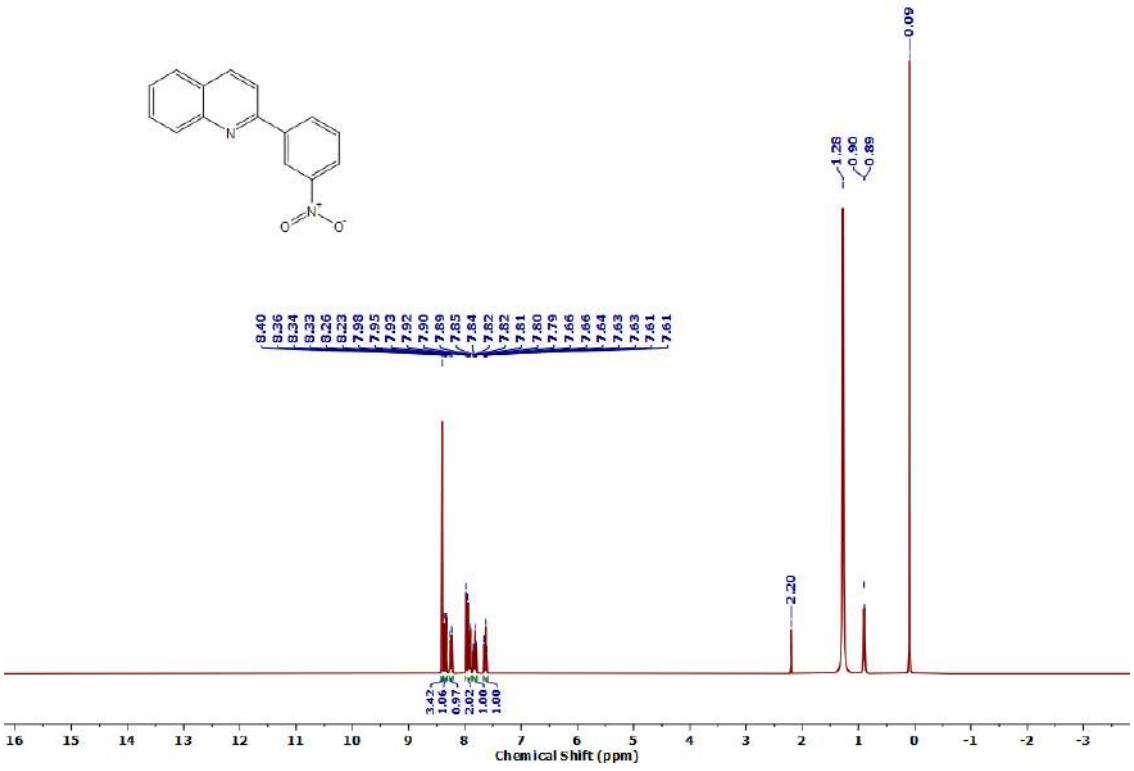

Figure 3.6.A54: ^{1}H NMR spectrum of **5k**

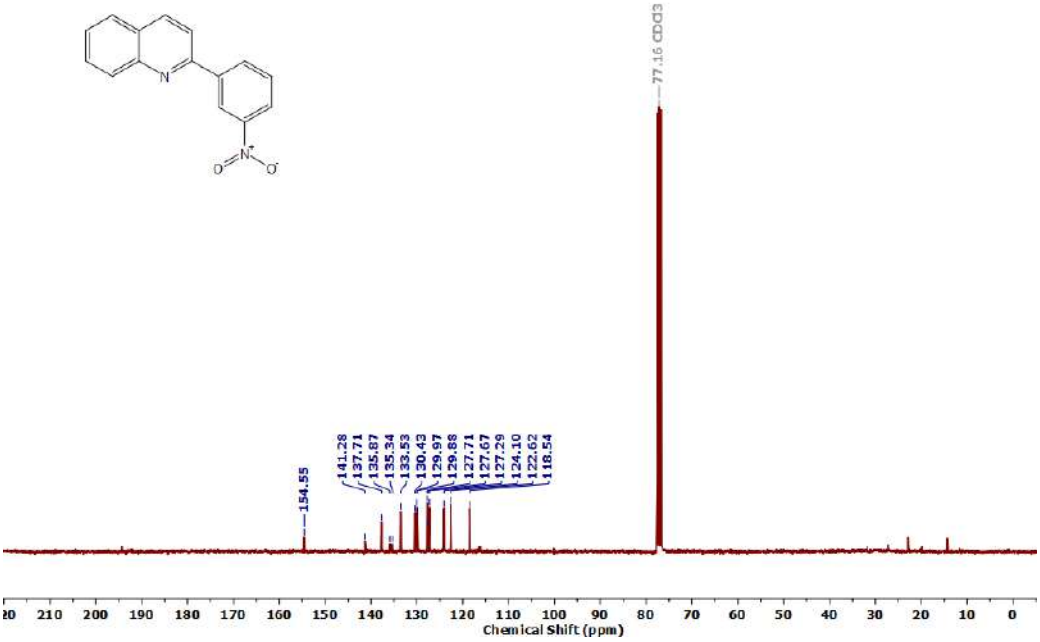

Figure 3.6.A55: $^{13}C\{^{1}H\}$ NMR spectrum of **5k**

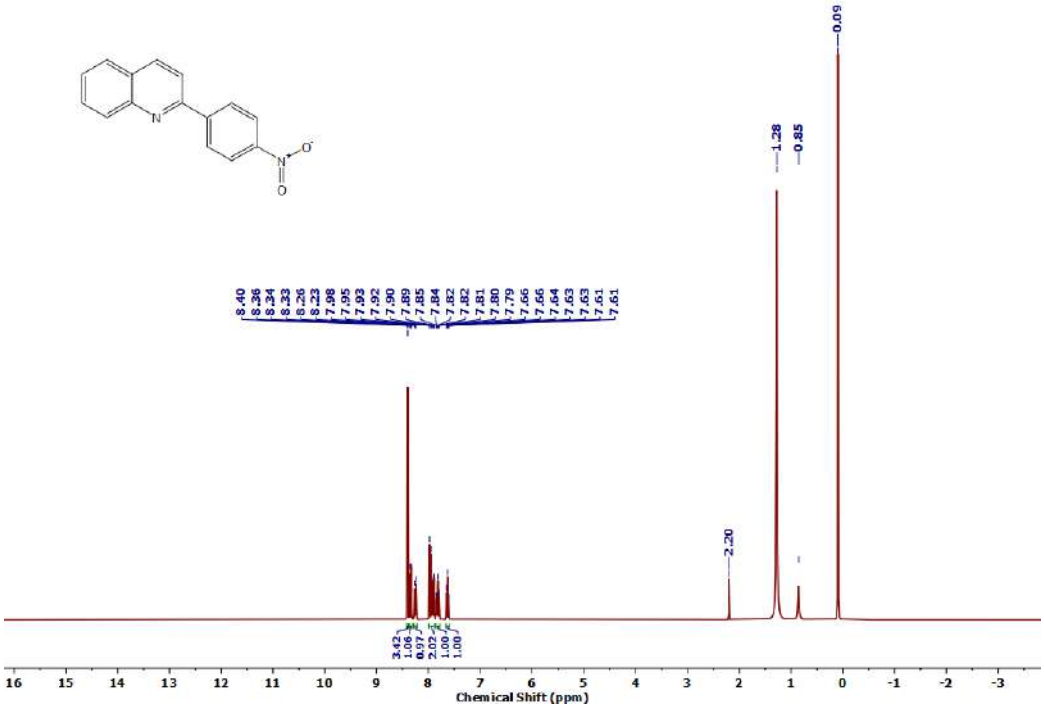

Figure 3.6.A56: ^{1}H NMR spectrum of **5l**

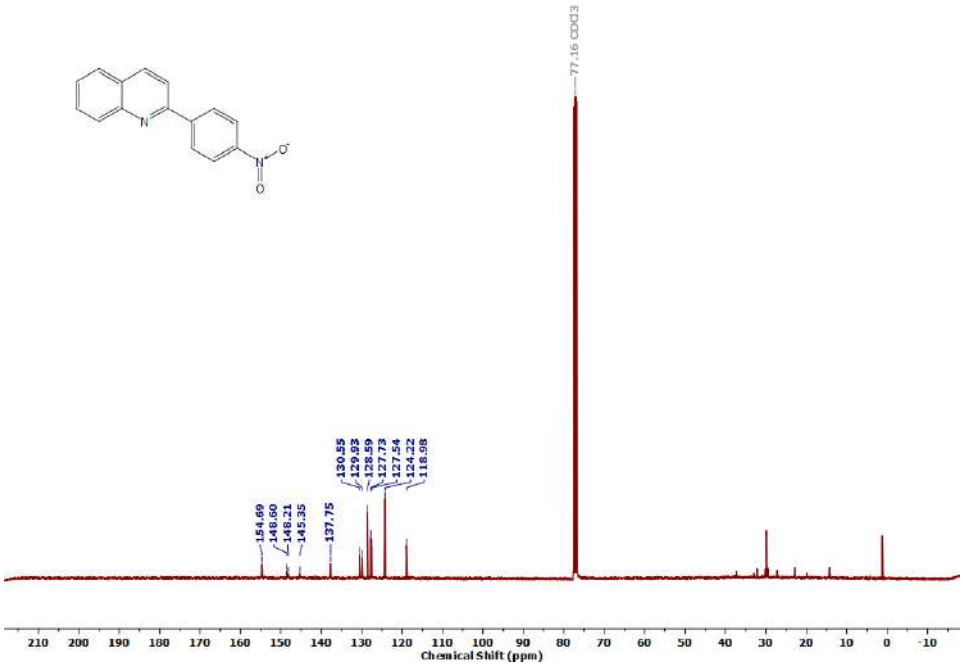

Figure 3.6.A57: $^{13}C\{^{1}H\}$ NMR spectrum of **5l**

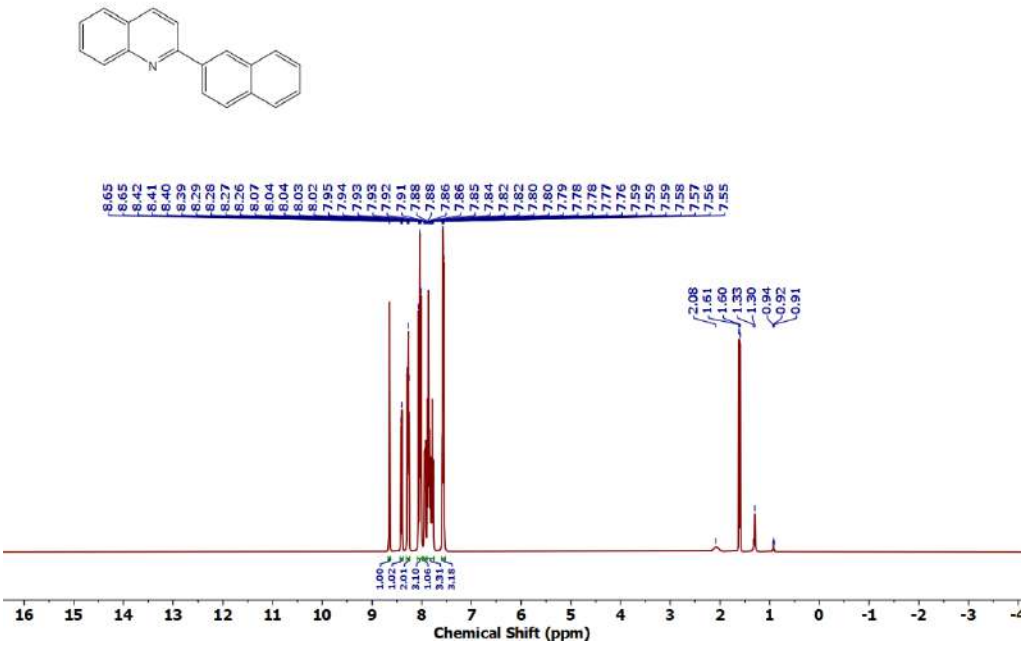

Figure 3.6.A58: ^{1}H NMR spectrum of **5m**

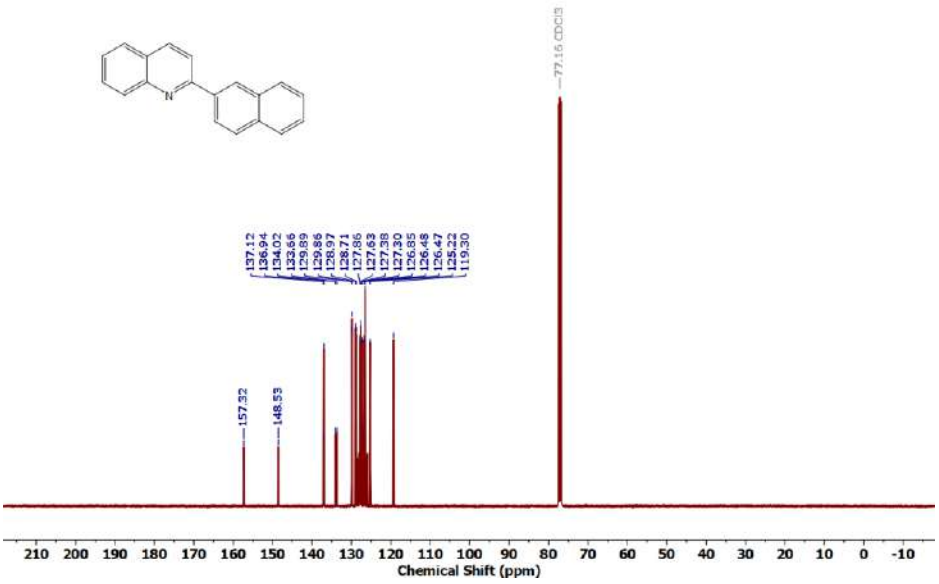

Figure 3.6.A59: $^{13}C\{^{1}H\}$ NMR spectrum of **5m**

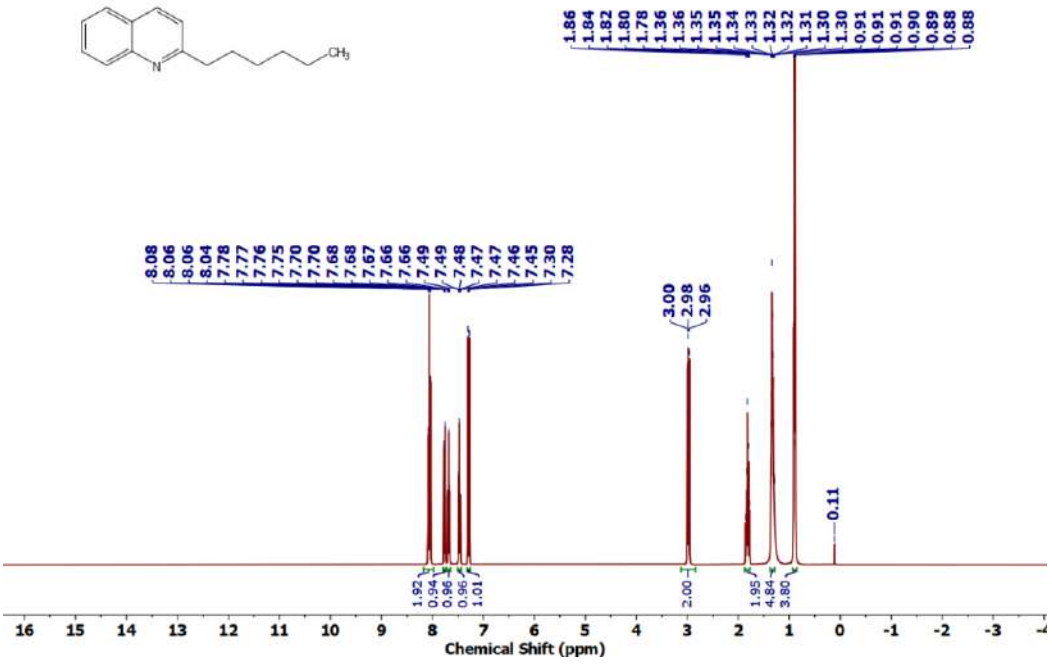

Figure 3.6.A60: ^{1}H NMR spectrum of **5n**

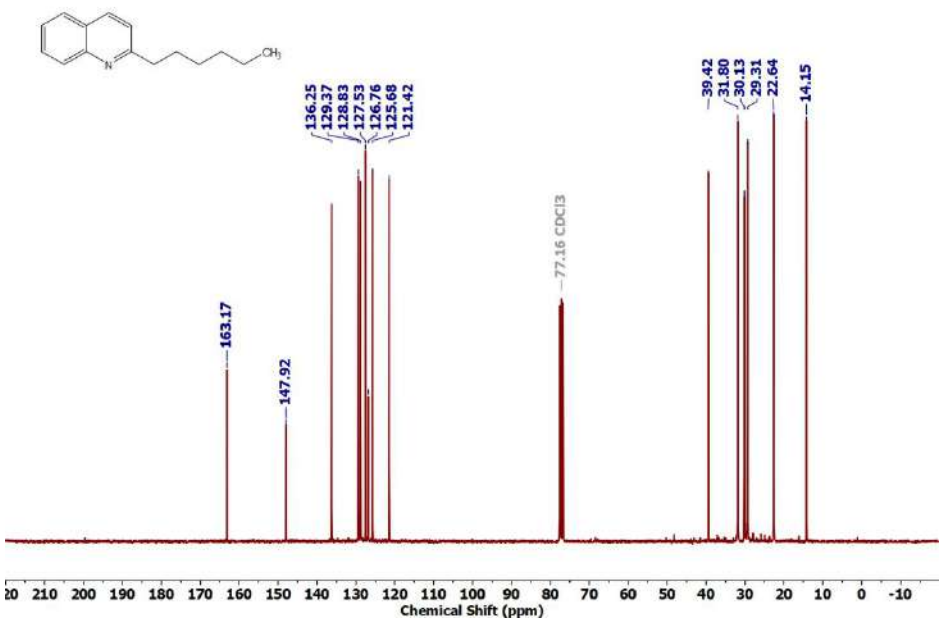

Figure 3.6.A61: $^{13}C\{^{1}H\}$ NMR spectrum of **5n**

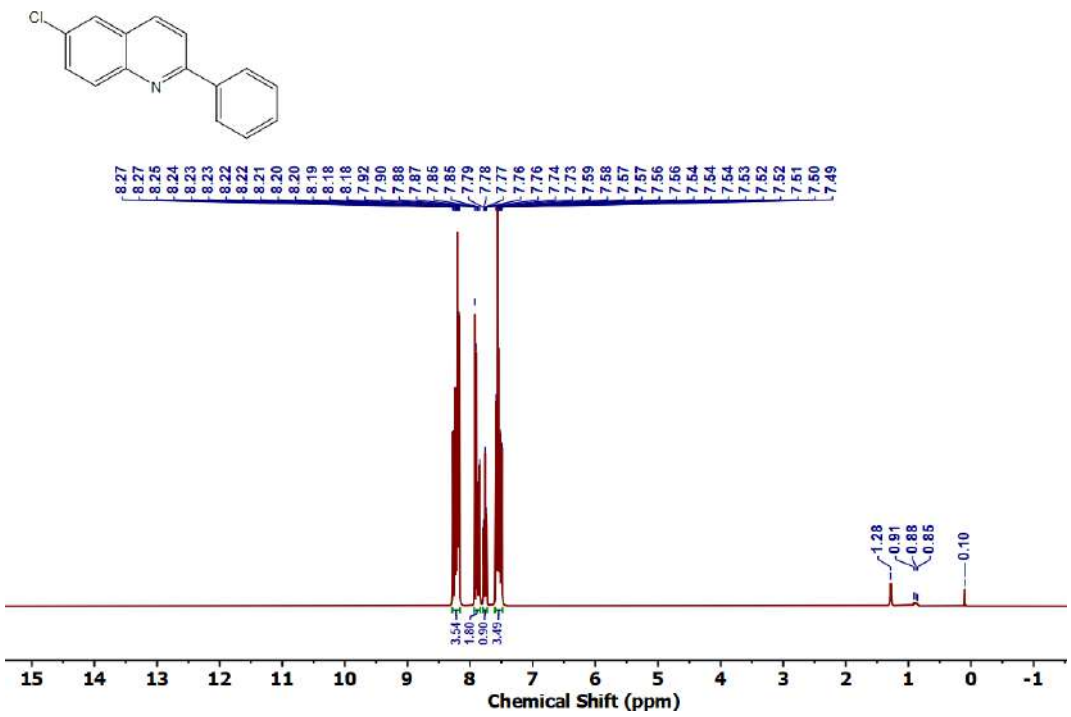

Figure 3.6.A62: ^{1}H NMR spectrum of **5o**

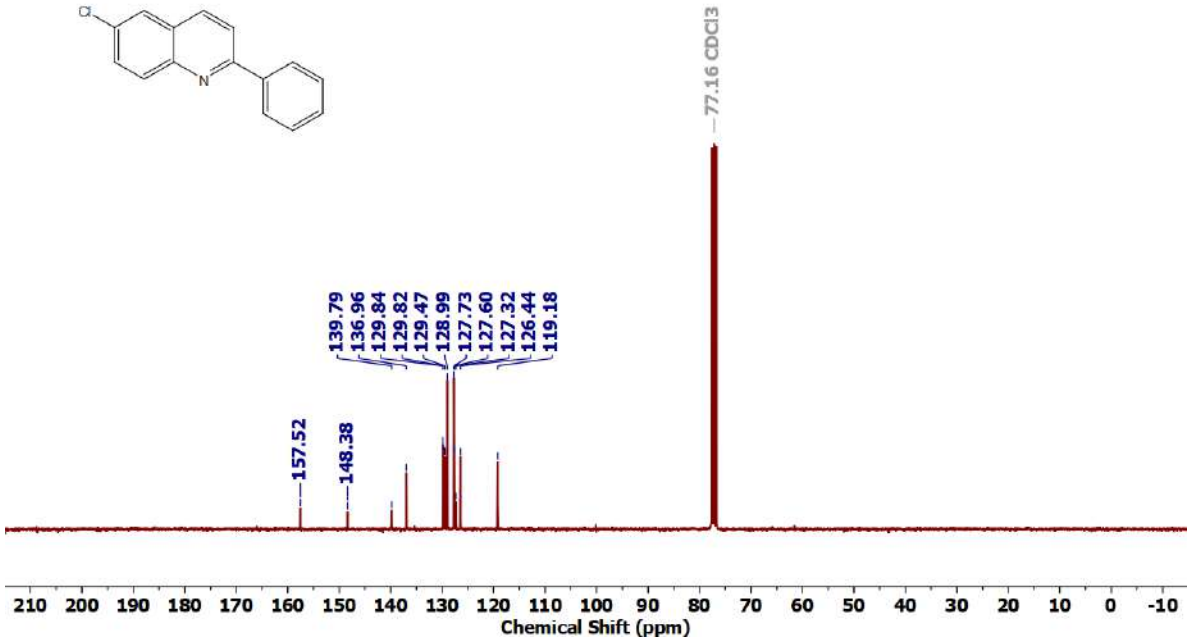

Figure 3.6.A63: $^{13}C\{^{1}H\}$ NMR spectrum of **5o**

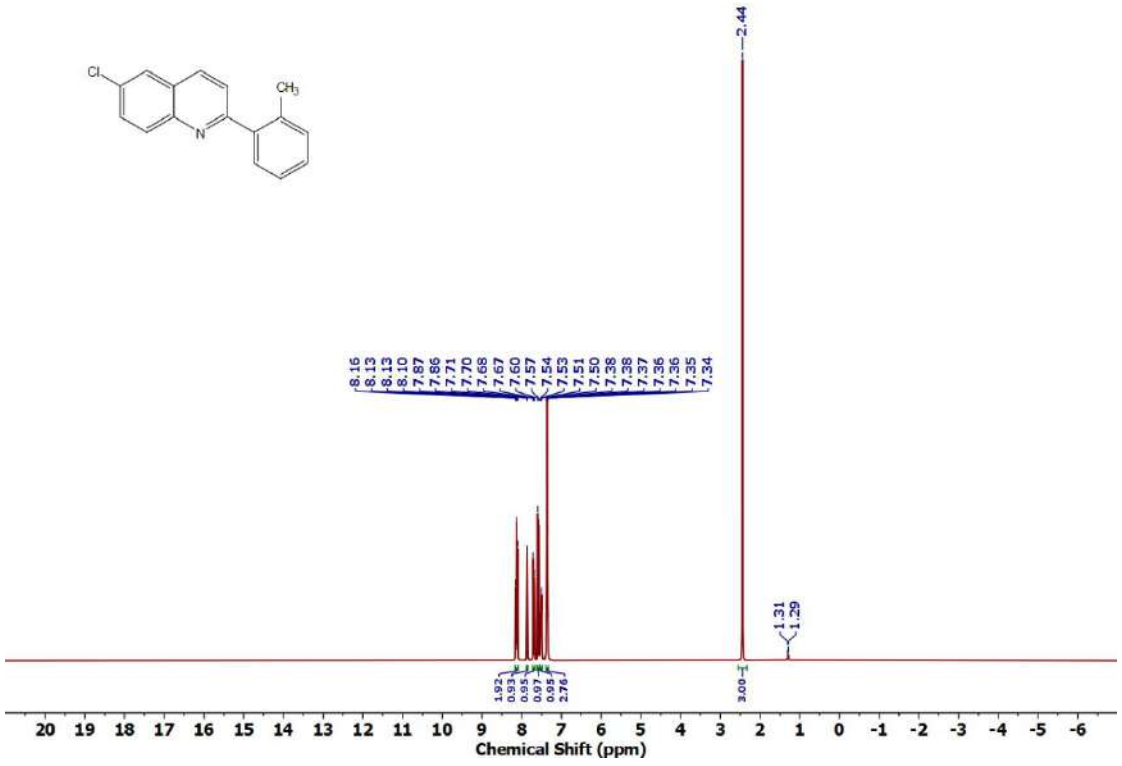

Figure 3.6.A64: ^{1}H NMR spectrum of **5p**

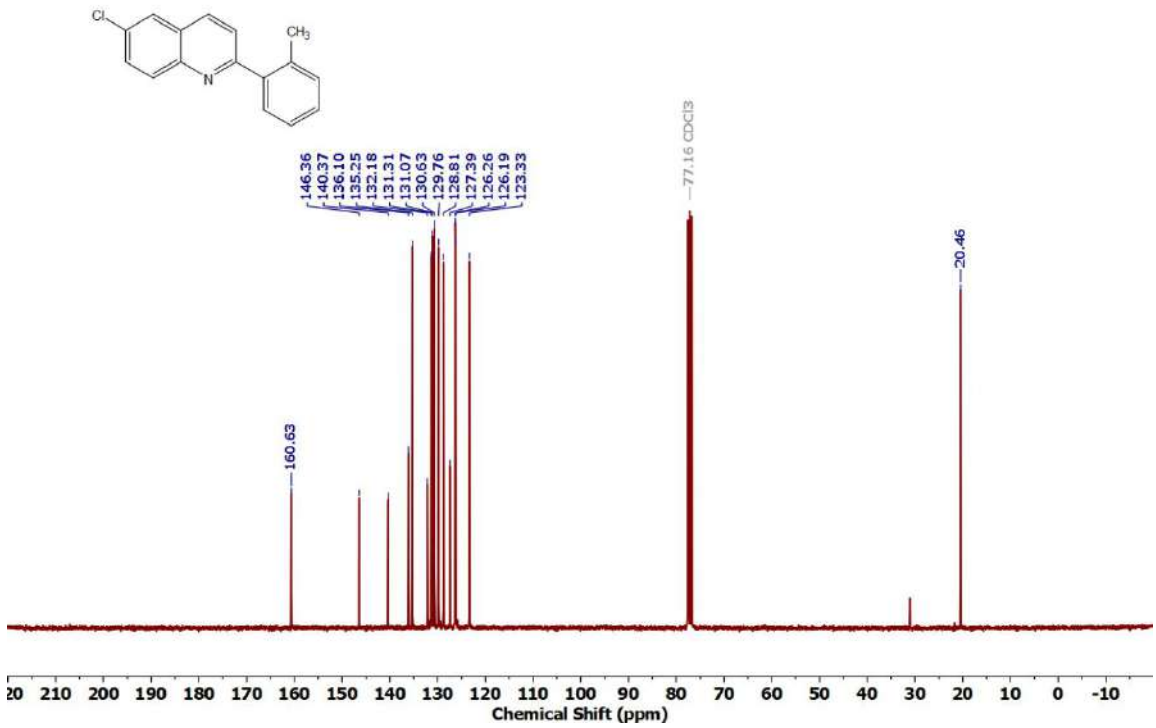

Figure 3.6.A65: $^{13}C\{^{1}H\}$ NMR spectrum of **5p**

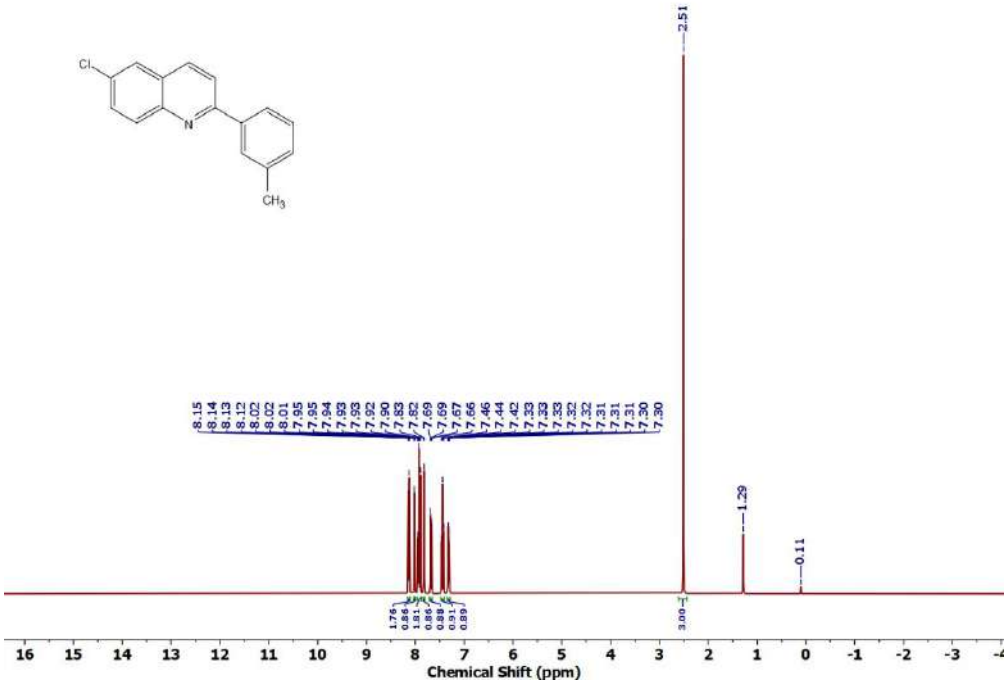

Figure 3.6.A66: ^{1}H NMR spectrum of **5q**

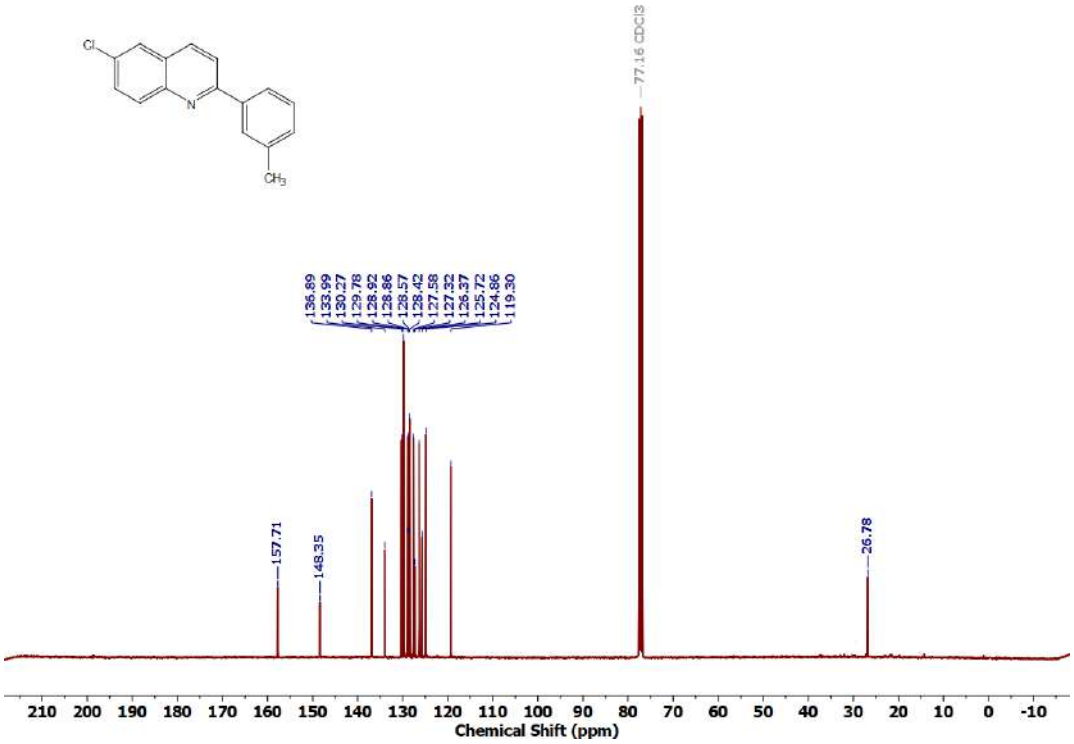

Figure 3.6.A67: $^{13}C\{^{1}H\}$ NMR spectrum of **5q**

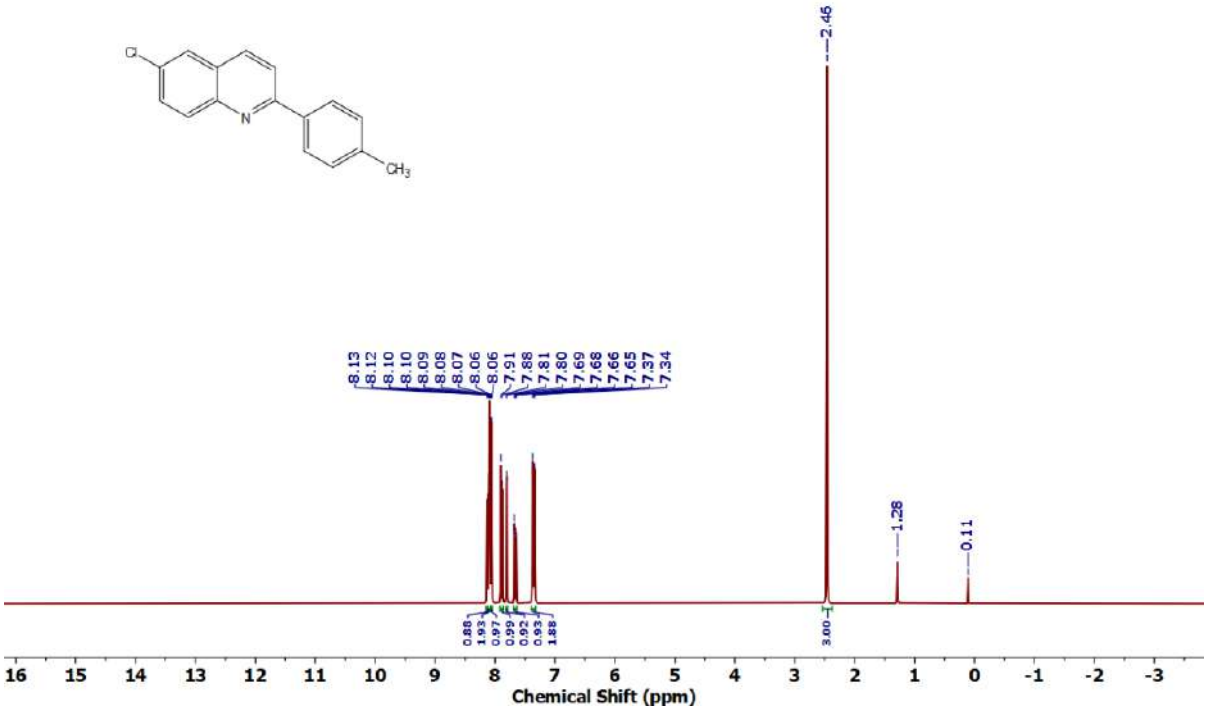

Figure 3.6.A68: ^{1}H NMR spectrum of **5r**

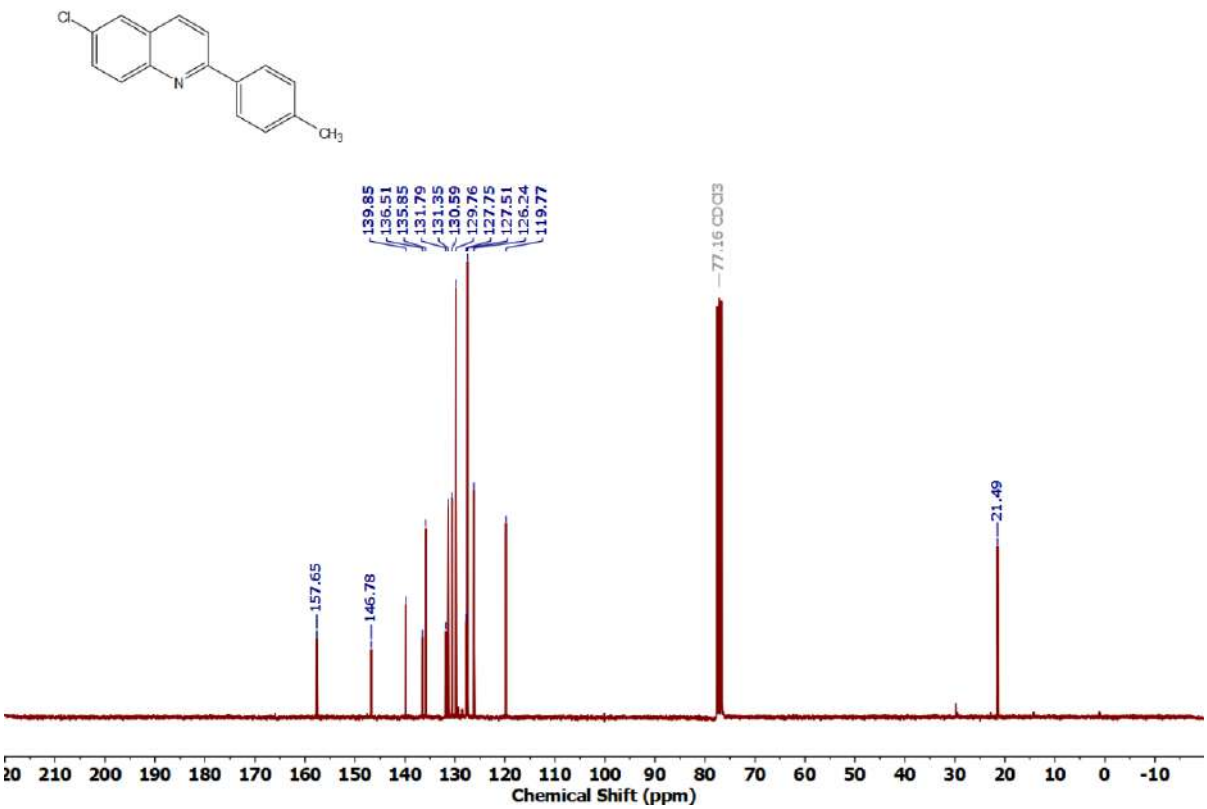

Figure 3.6.A69: $^{13}C\{^{1}H\}$ NMR spectrum of **5r**

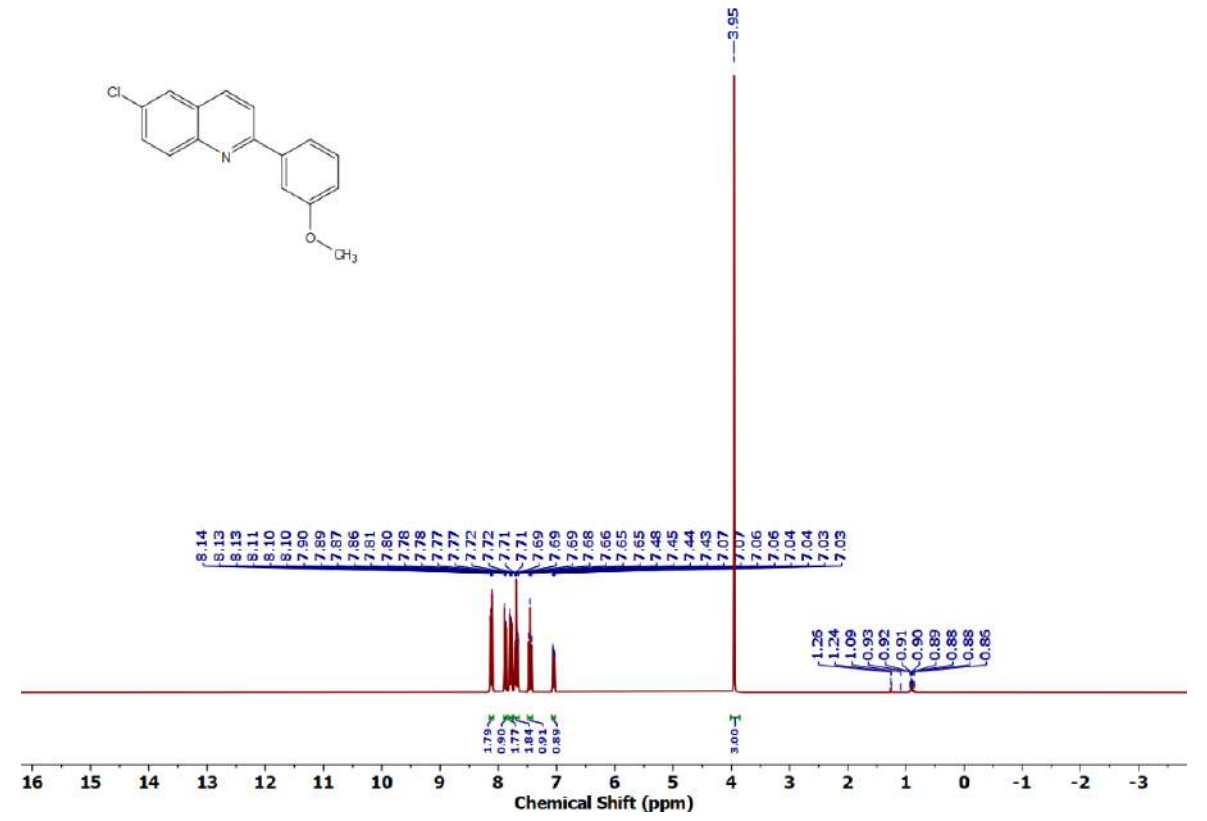

Figure 3.6.A70: ^{1}H NMR spectrum of **5s**

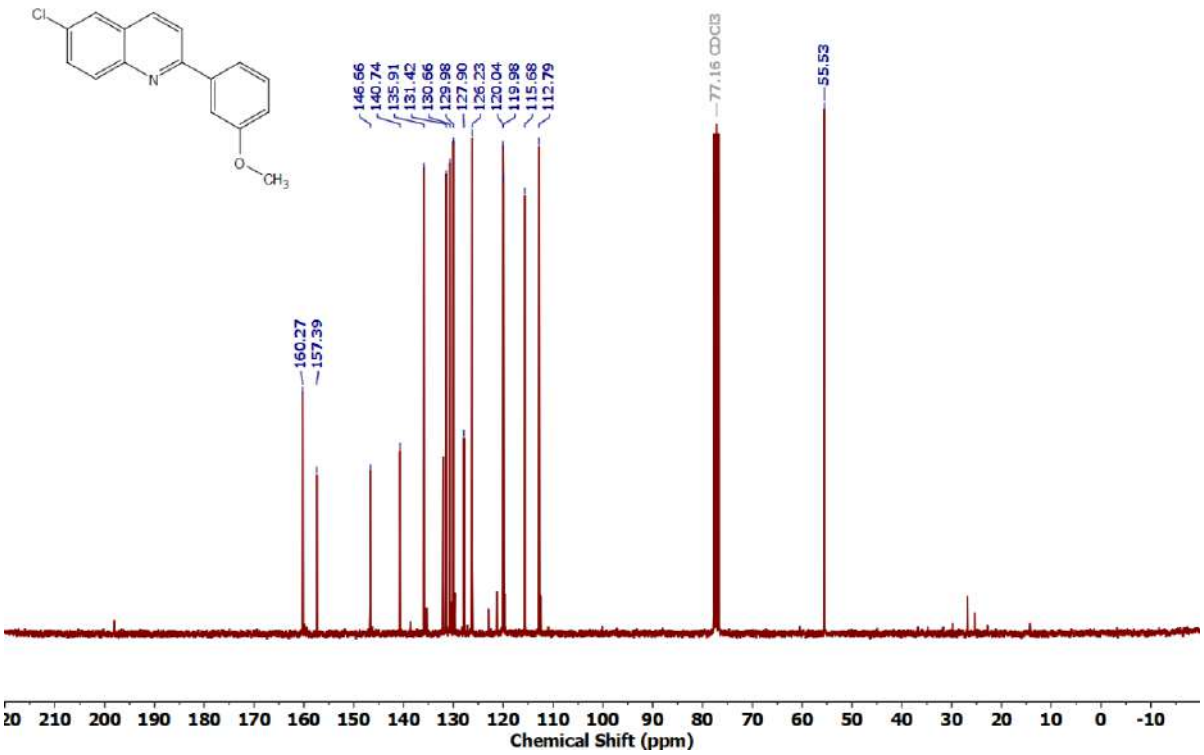

Figure 3.6.A71: $^{13}C\{^{1}H\}$ NMR spectrum of **5s**

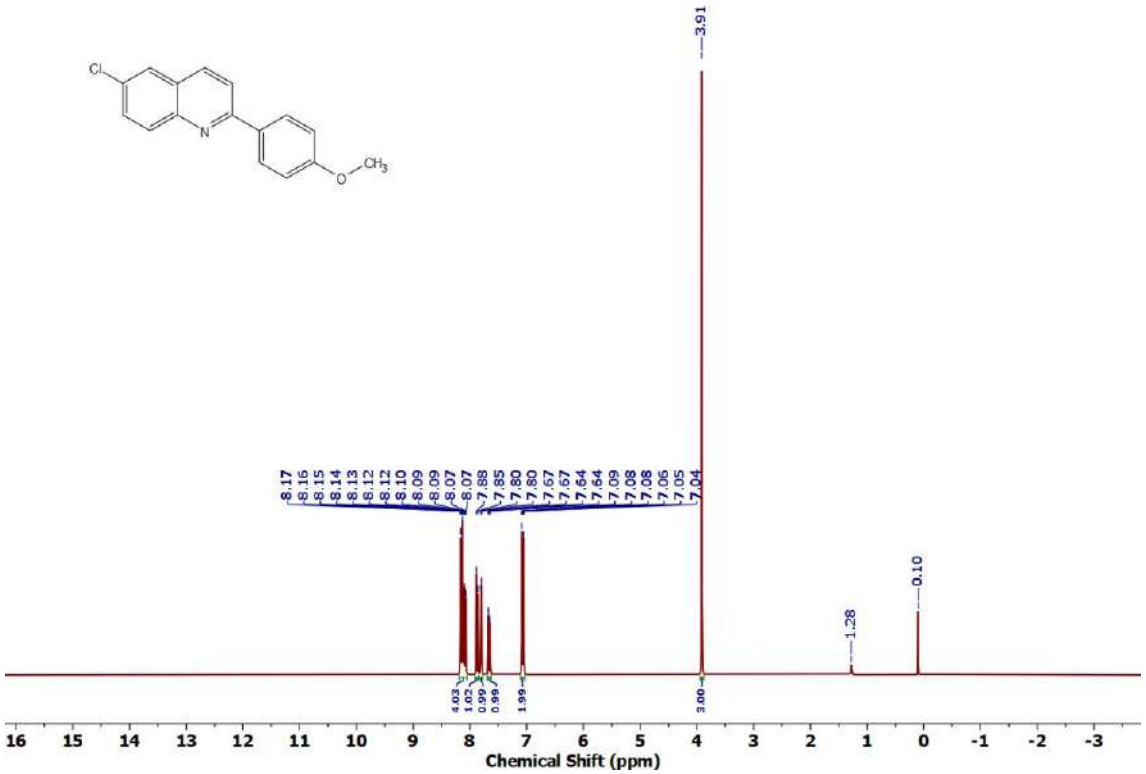

Figure 3.6.A72: ^{1}H NMR spectrum of **5t**

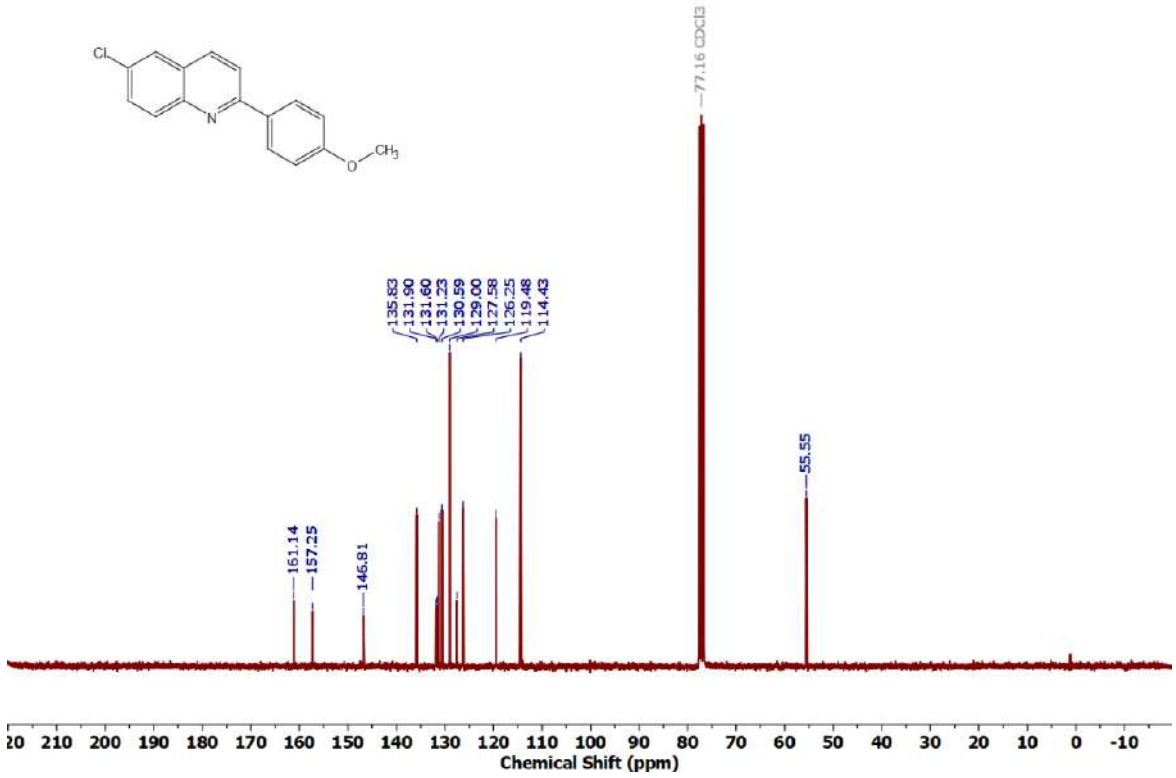

Figure 3.6.A73: $^{13}C\{^{1}H\}$ NMR spectrum of **5t**

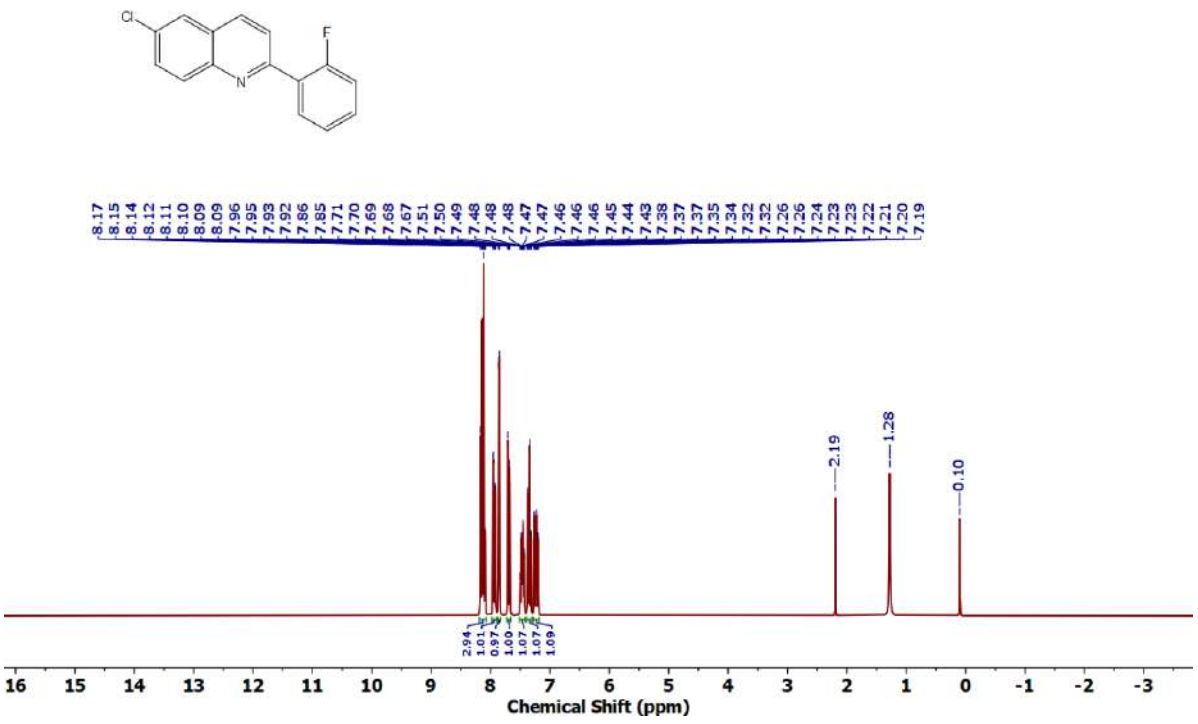

Figure 3.6.A74: ^{1}H NMR spectrum of **5u**

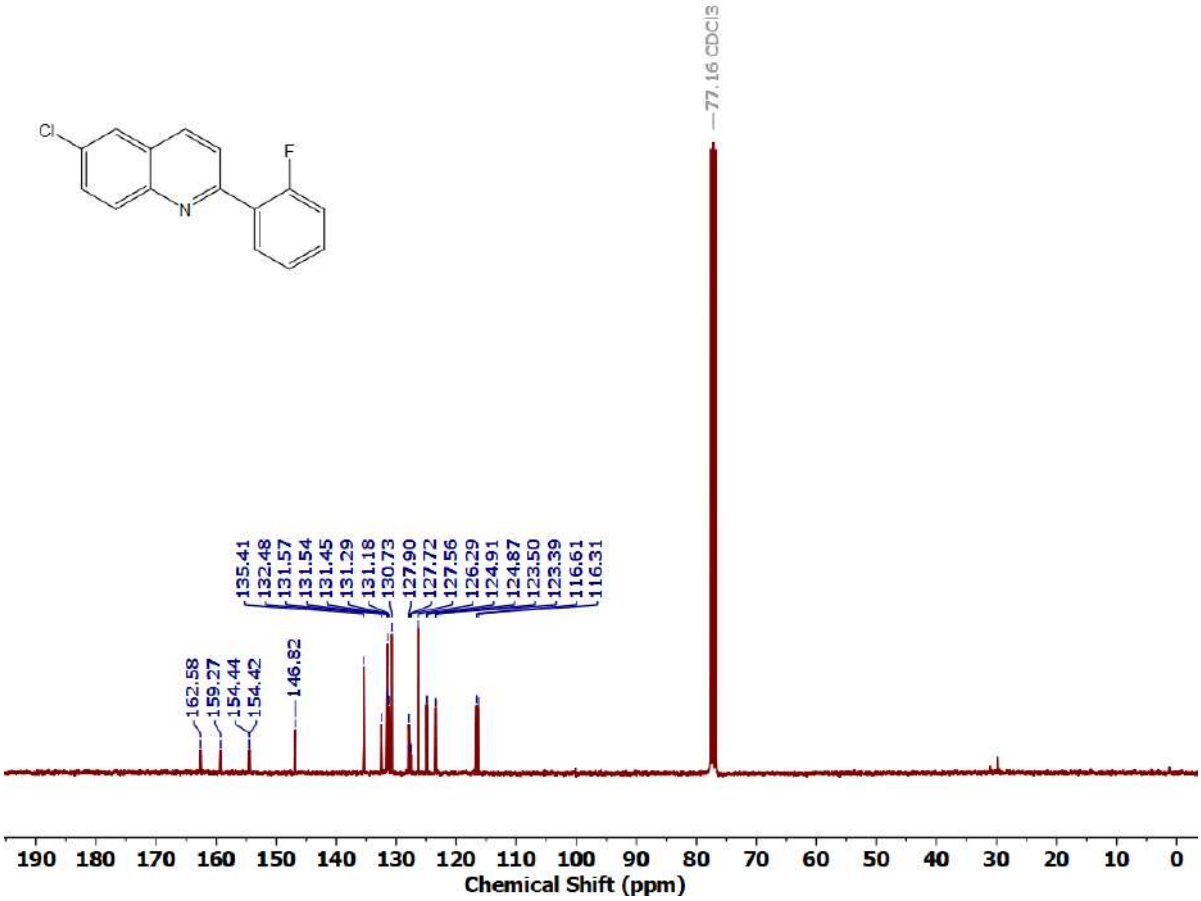

Figure 3.6.A75: $^{13}C\{^{1}H\}$ NMR spectrum of **5u**

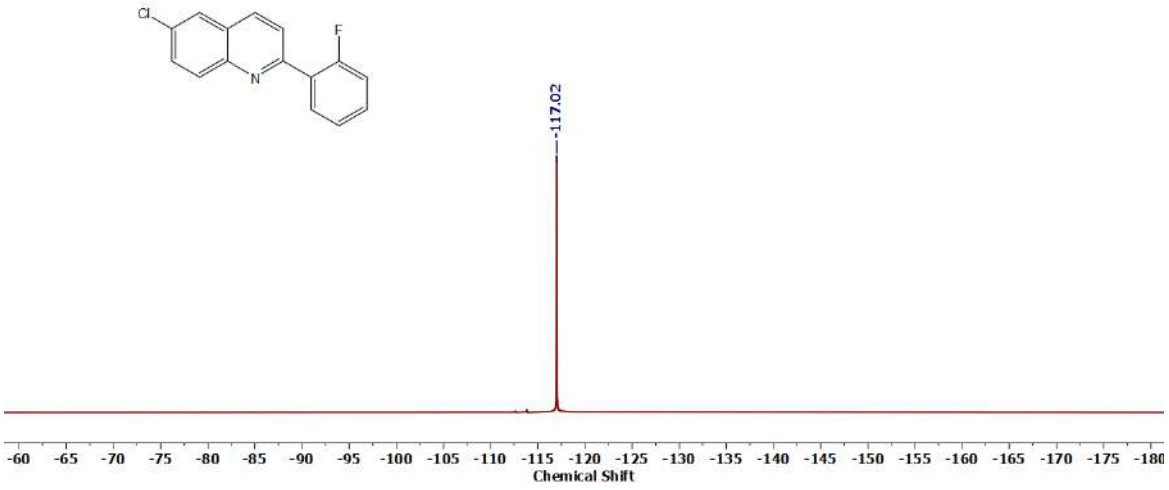

Figure 3.6.A76: ^{19}F NMR spectrum of **6u**

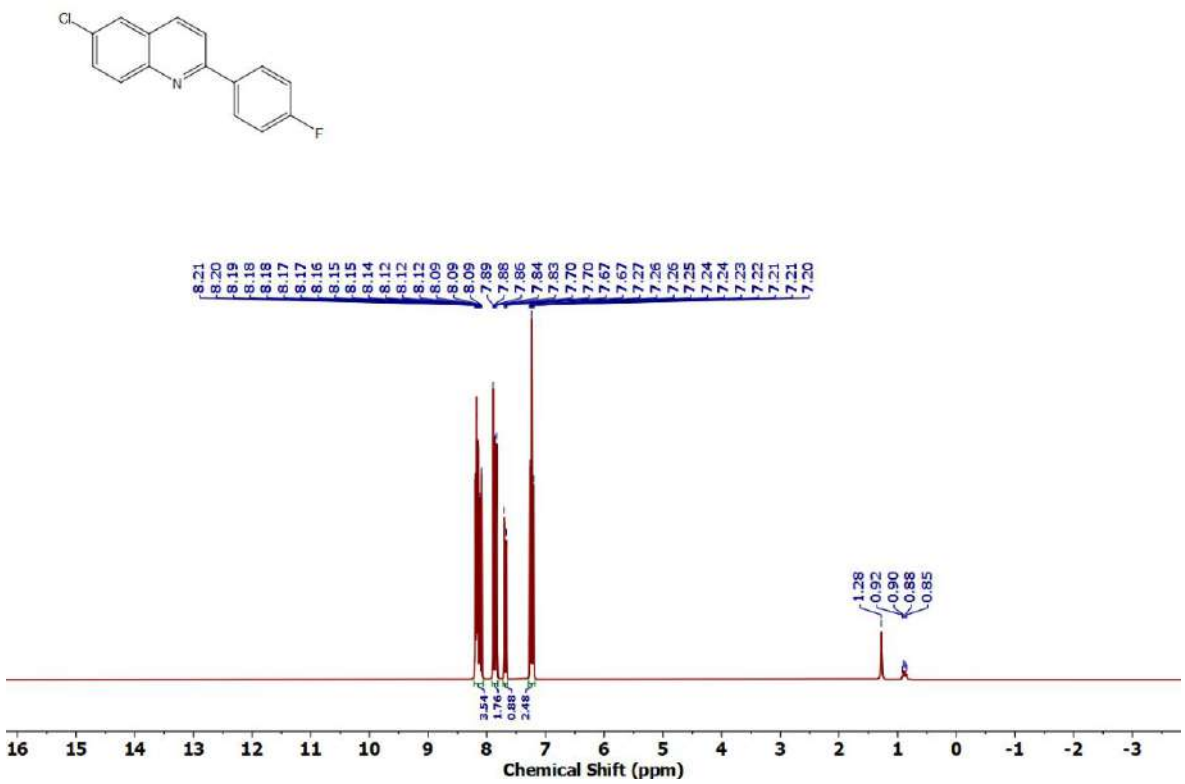

Figure 3.6.A77: ^{1}H NMR spectrum of **5v**

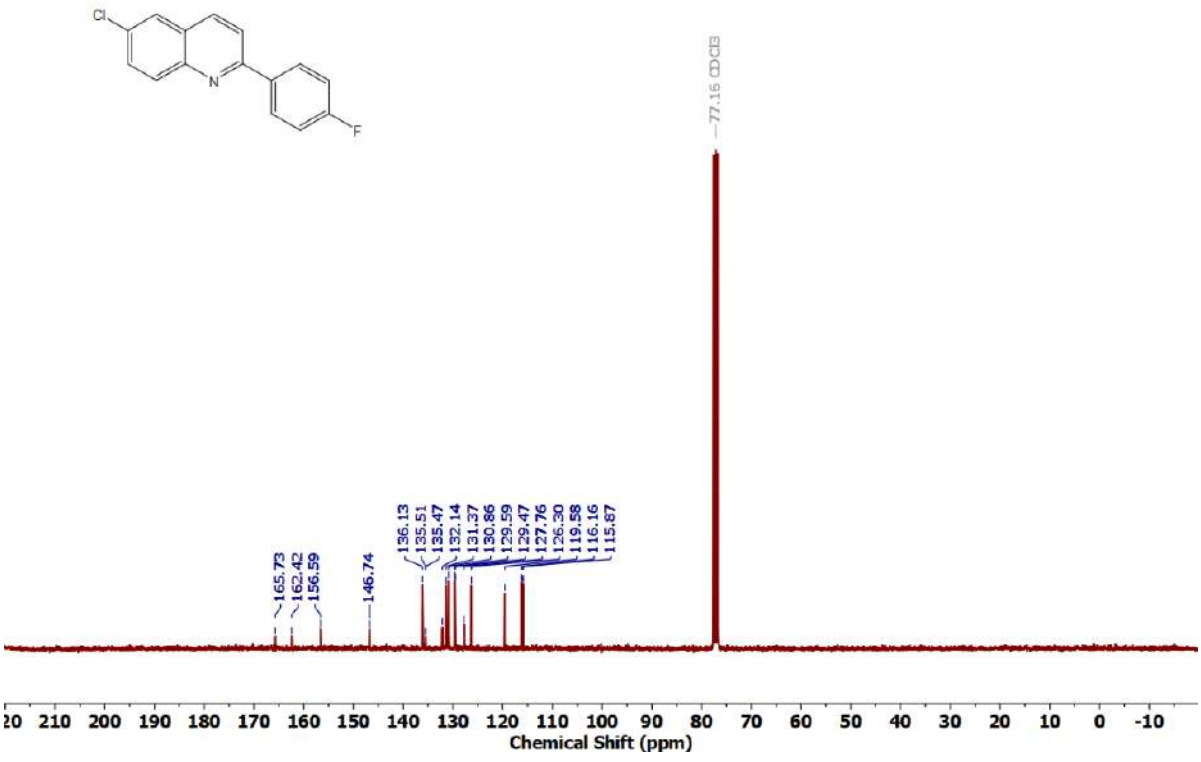

Figure 3.6.A78: ^{13}C{^{1}H} NMR spectrum of **5v**

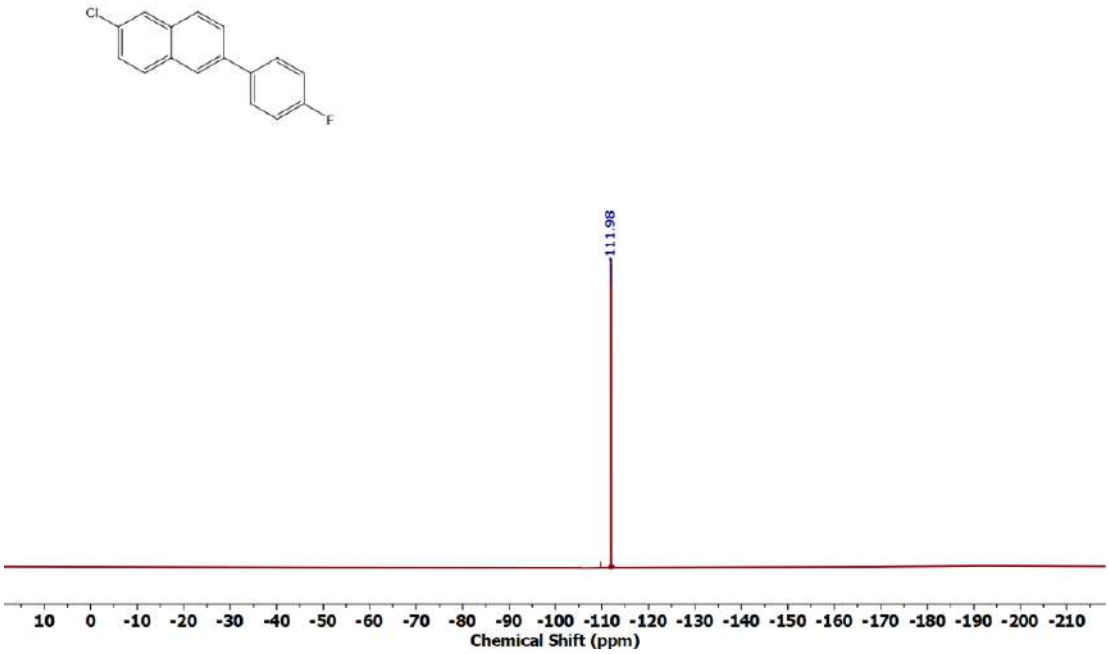

Figure 3.6.A79: ^{19}F NMR spectrum of **5v**

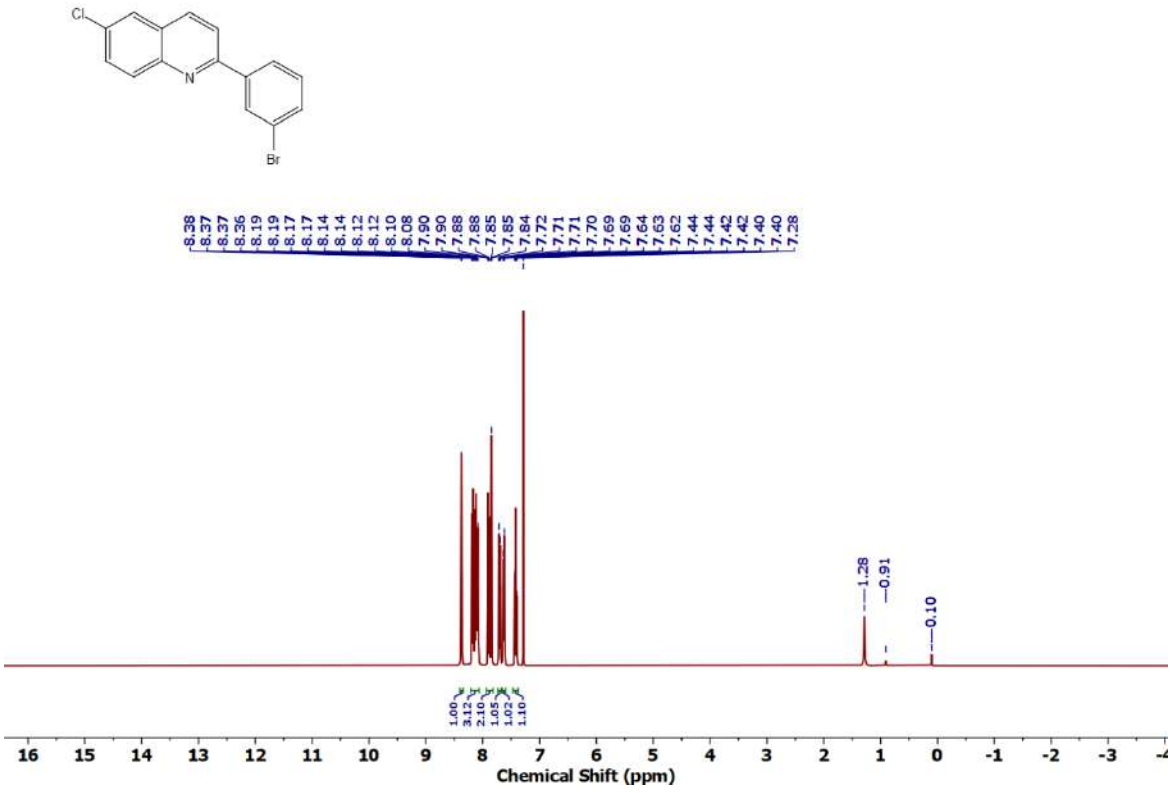

Figure 3.6.A80: ^{1}H NMR spectrum of **6w**

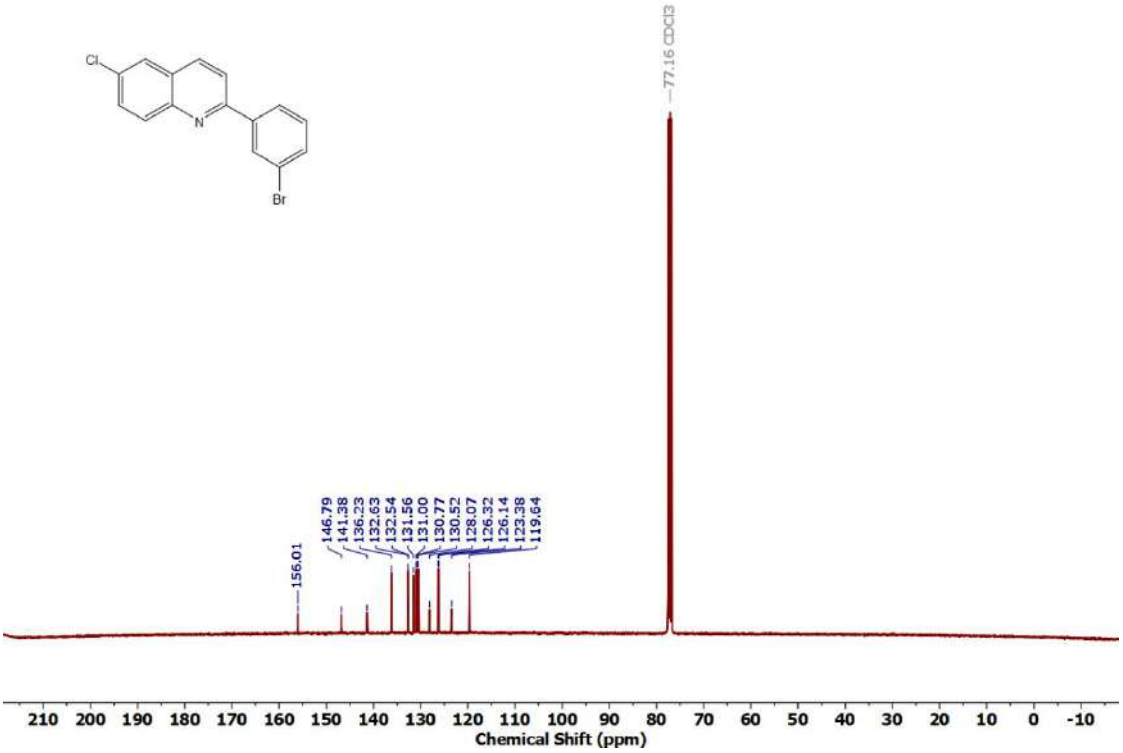

Figure 3.6.A81: $^{13}C\{^{1}H\}$ NMR spectrum of **5w**

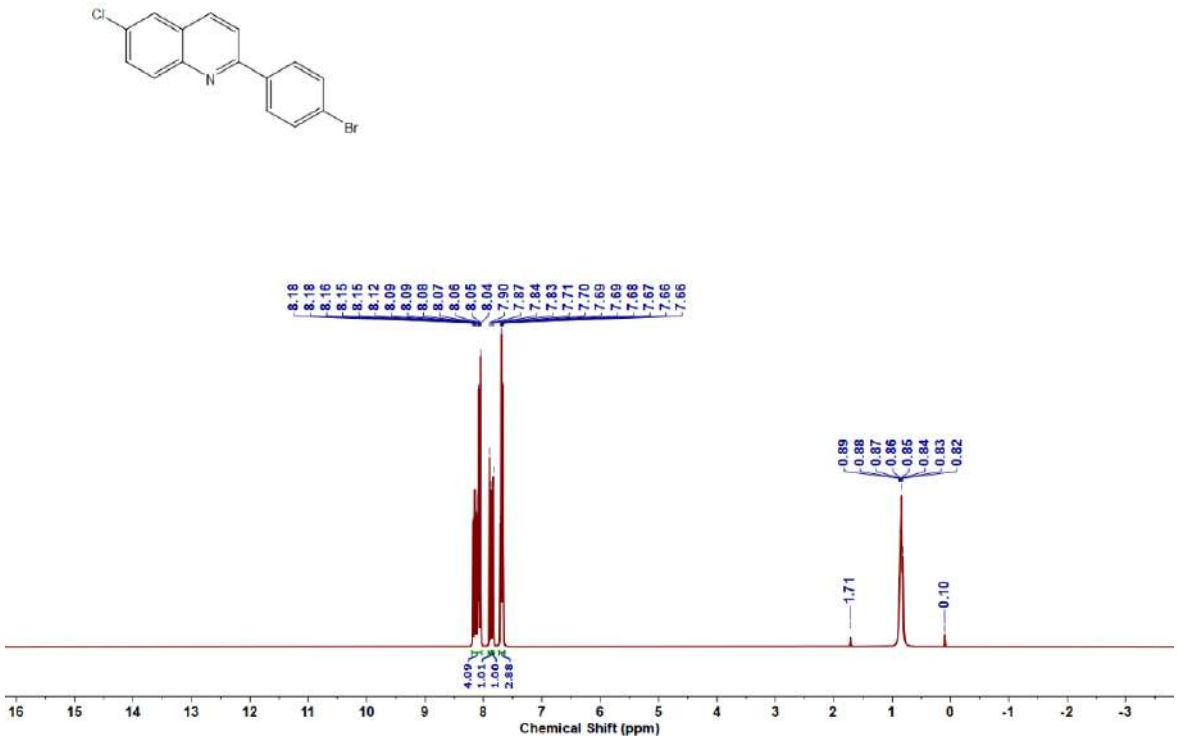

Figure 3.6.A82: ^{1}H NMR spectrum of **5x**

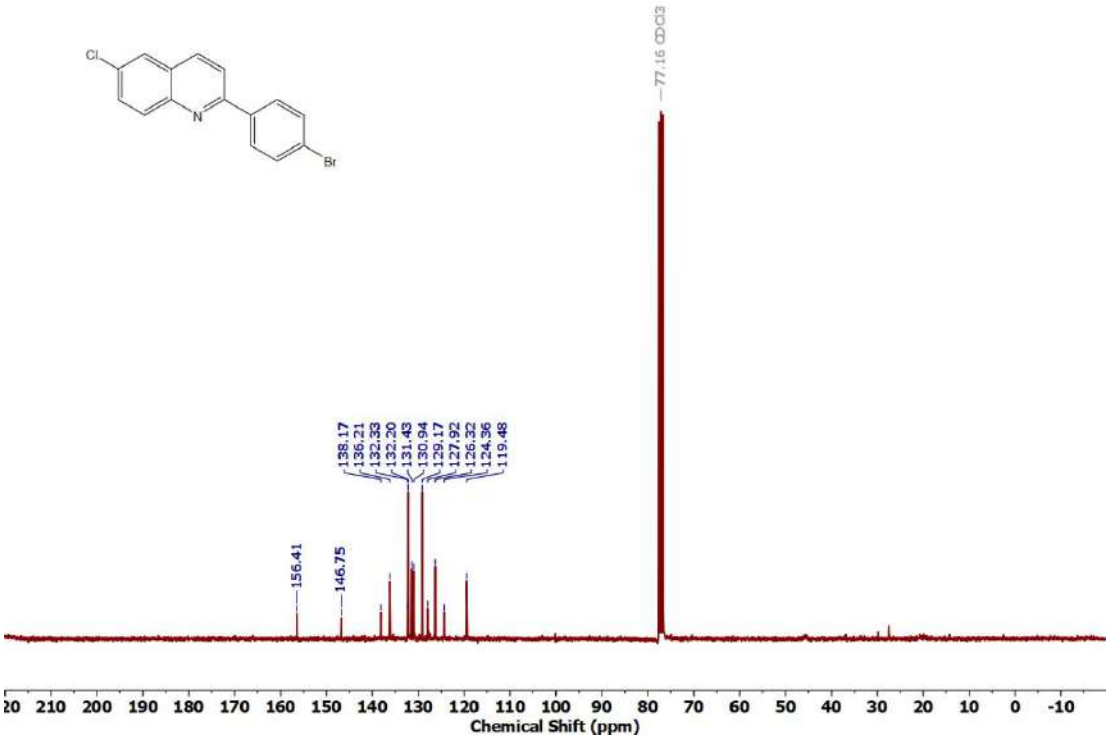

Figure 3.6.A83: $^{13}C\{^{1}H\}$ NMR spectrum of **5x**

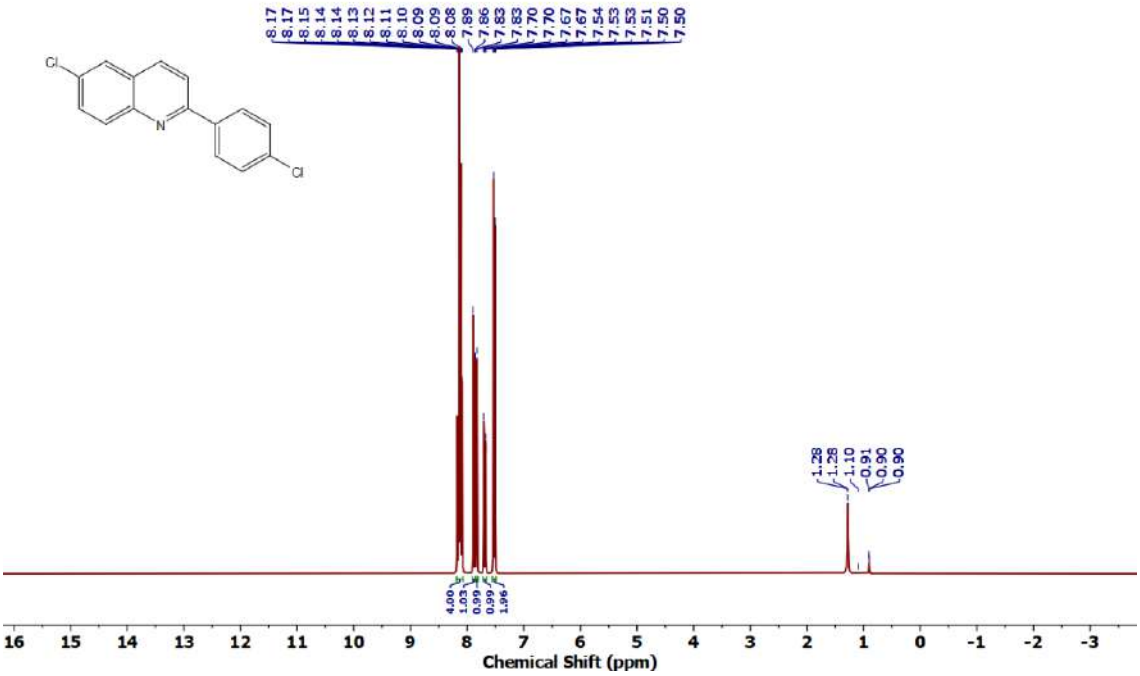

Figure 3.6.A84: ^{1}H NMR spectrum of **5y**

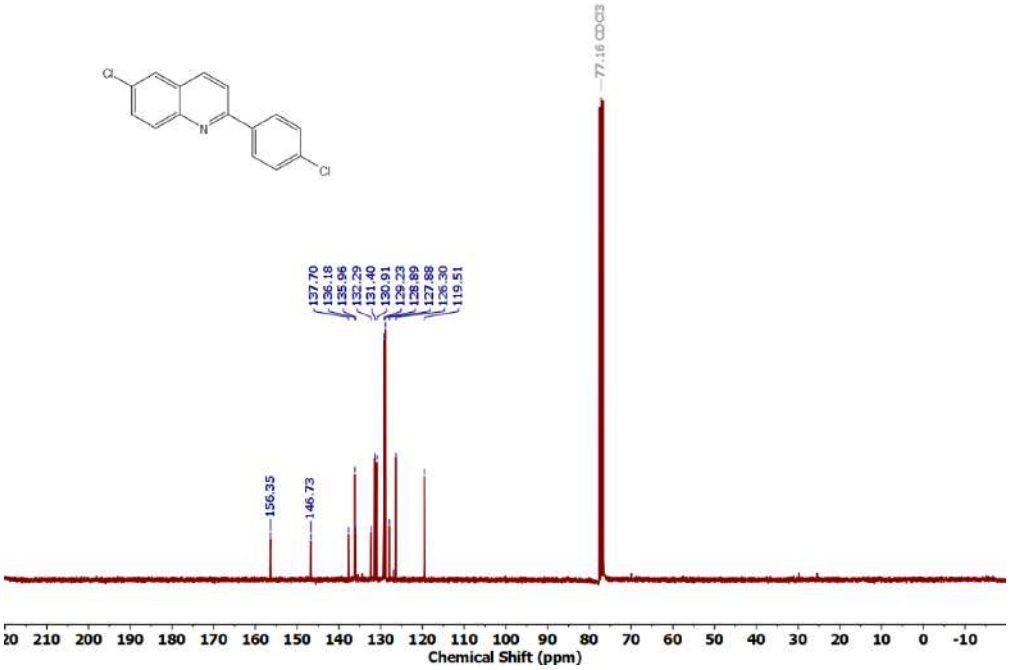

Figure 3.6.A86: $^{13}C\{^{1}H\}$ NMR spectrum of **5y**

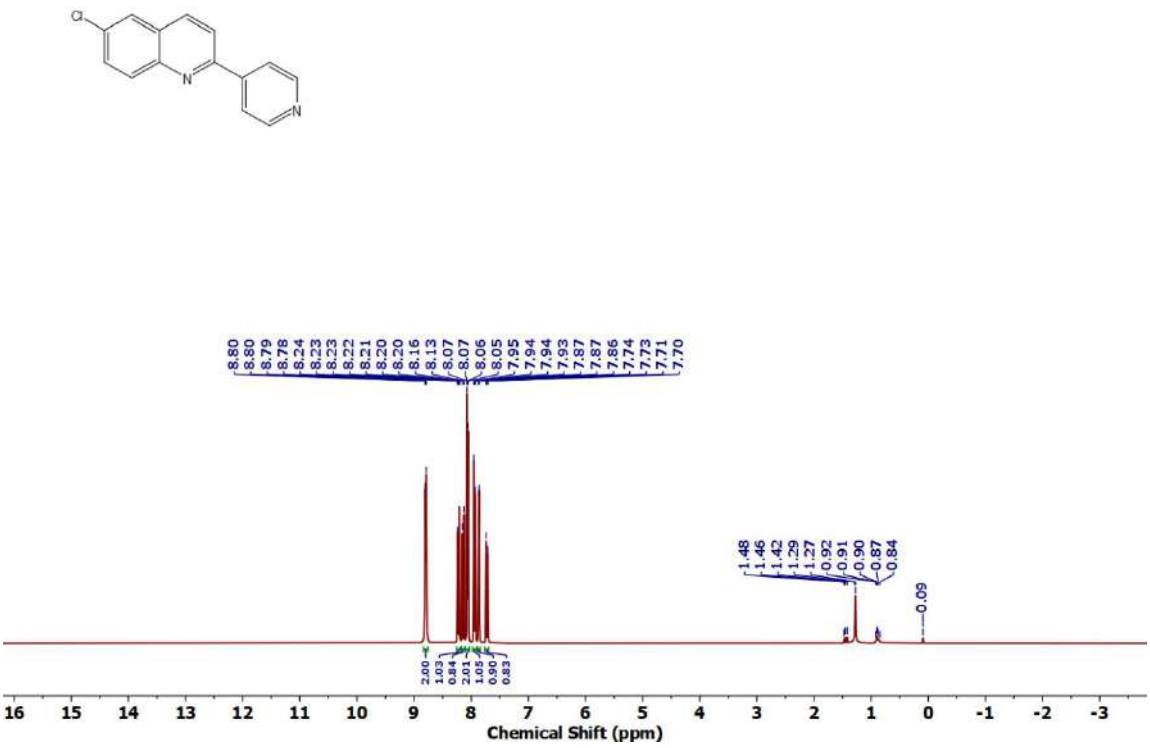

Figure 3.6.A87: ^{1}H NMR spectrum of **5z**

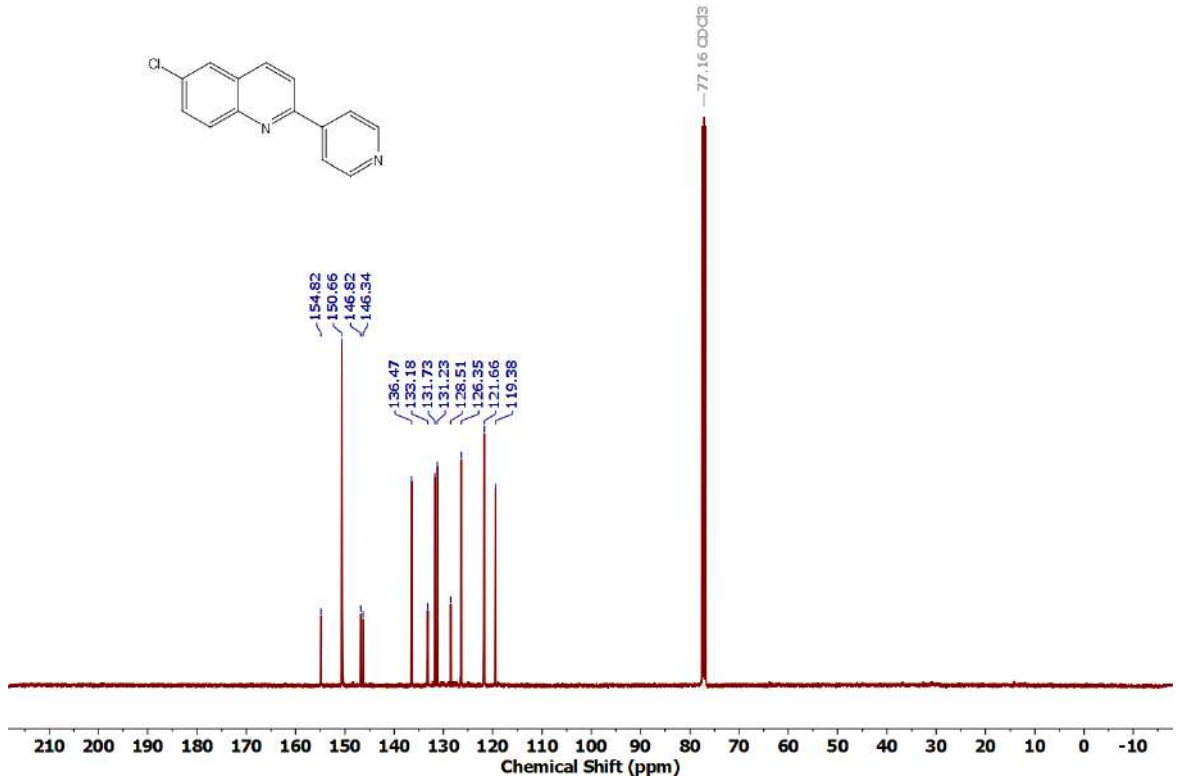

Figure 3.6.A88: $^{13}C\{^{1}H\}$ NMR spectrum of **5z**

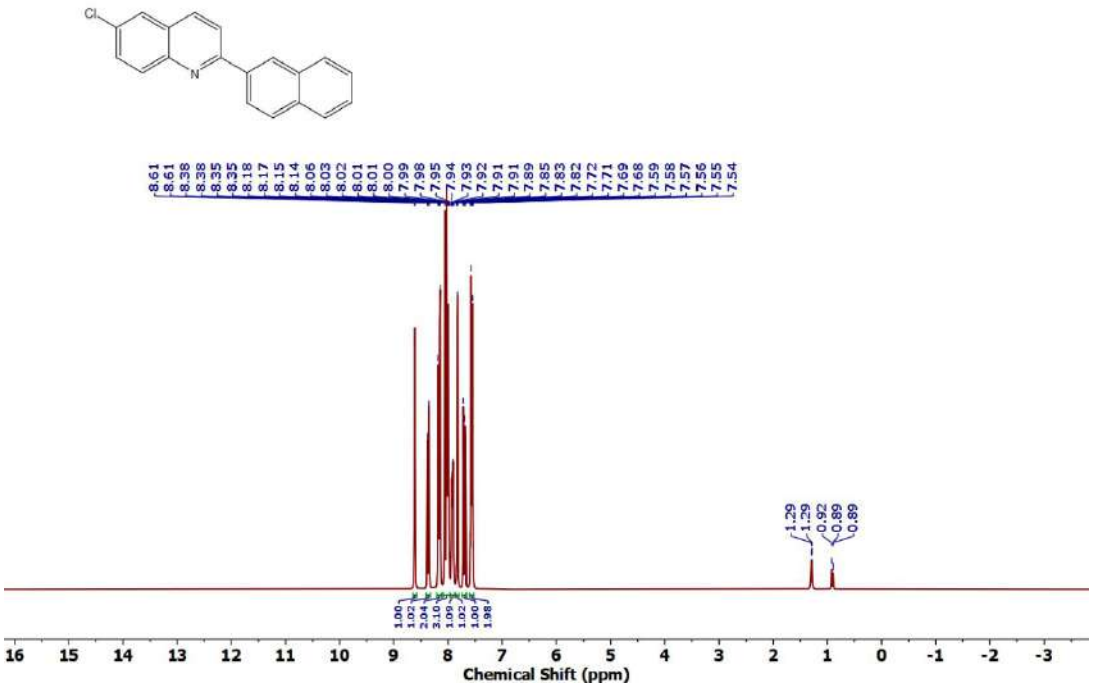

Figure 3.6.A89: ^{1}H NMR spectrum of **5aa**

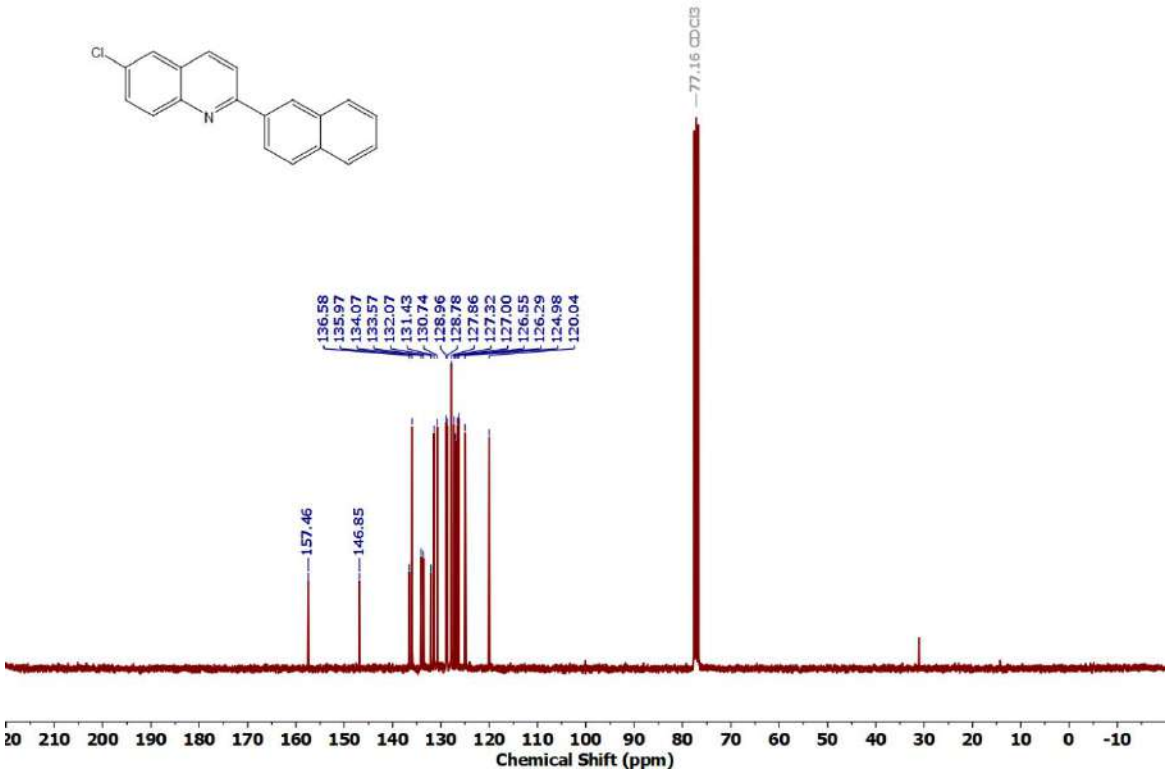

Figure 3.6.A90: $^{13}C\{^{1}H\}$ NMR spectrum of **5aa**

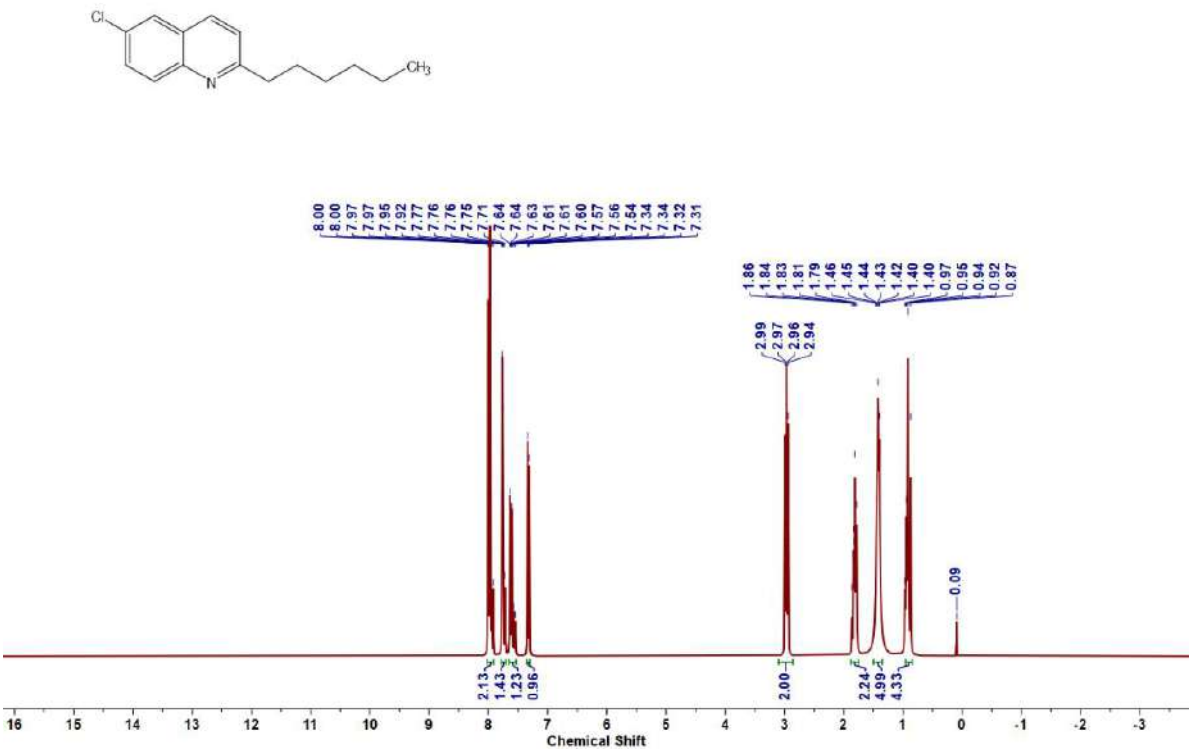

Figure 3.6.A91: ^{1}H NMR spectrum of **5ab**

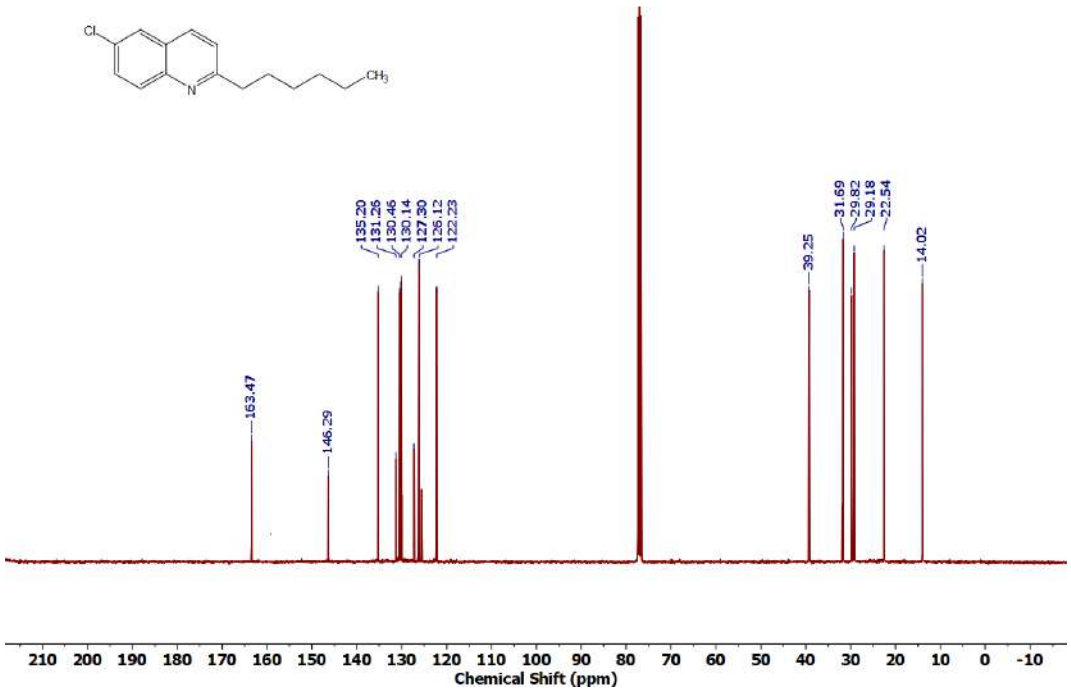

Figure 3.6.A92: $^{13}C\{^{1}H\}$ NMR spectrum of **5ab**

Chapter 4

Dehydrogenative Coupling for Synthesis of Quinazolin-4(3H)-ones *via* Tandem Reaction using Ruthenium(II)-Phenyl-Azo-Naphthaldoxime: An Experimental and Theoretical Investigation

4.1 Introduction:

N-heterocycles have been found to be in plenitude in natural products due to their intimate biological relevance. This leads to extensive research towards the development of innovative, sustainable and greener methods for synthesis of aza-heterocycles.[1] The quinazolinone moiety is present as a building block in a wide range of naturally occurring alkaloids that have been sequestered from natural resources like microorganisms, plants, and animals.[2,3] Quinazolin-4(3H)-ones and their substituted analogues have gained significant attention owing to various pharmacological activities, such as anti-inflammatory,[4] antimicrobial,[5] anticancer,[6,7] antihypertensive,[8] dihydrofolate reductase inhibition,[9] and Tyrosine Kinase inhibition[10]. Despite significant progress in this area, it has been found that in most cases multi-step synthesis is required. This creates unwanted byproducts and often needed hazardous chemicals for catalytic transformation. Furthermore, the precursor molecules are often expensive and less available.[11,12] Accordingly, it is always challenging to develop cost-effective and atom efficient production of substituted quinazolin-4(3H)-ones. There have been some reports of transition metal catalysed synthesis of substituted quinazolin-4(3H)-ones *via* dehydrogenative functionalization of aliphatic and aromatic alcohols and this strategy is quite promising since it is a single-step, economical, environment friendly synthesis starting from readily available precursors and generates hydrogen or water as the only byproducts (Scheme 4.1).[13-15] We were inquisitive regarding the electron trapping aptitude of coordinated azooximes[16] for the past few years and this led us to explore their ability to bring about dehydrogenative functionalization of aliphatic and aromatic primary alcohols to form value added products.[17-19] As a continuation of our previous work, in this study we have utilized phenyl-azo-naphthaldoxime NpLH, **1** to synthesize a ruthenium(II) complex *trans*-[Ru(NpL)(CO)Cl(PPh_3)$_2$], **2** (Scheme 4.2). The structural, electrochemical, and theoretical studies of **2** have been performed in order to have a comprehension of their competence to bring about electron transfer catalysis.

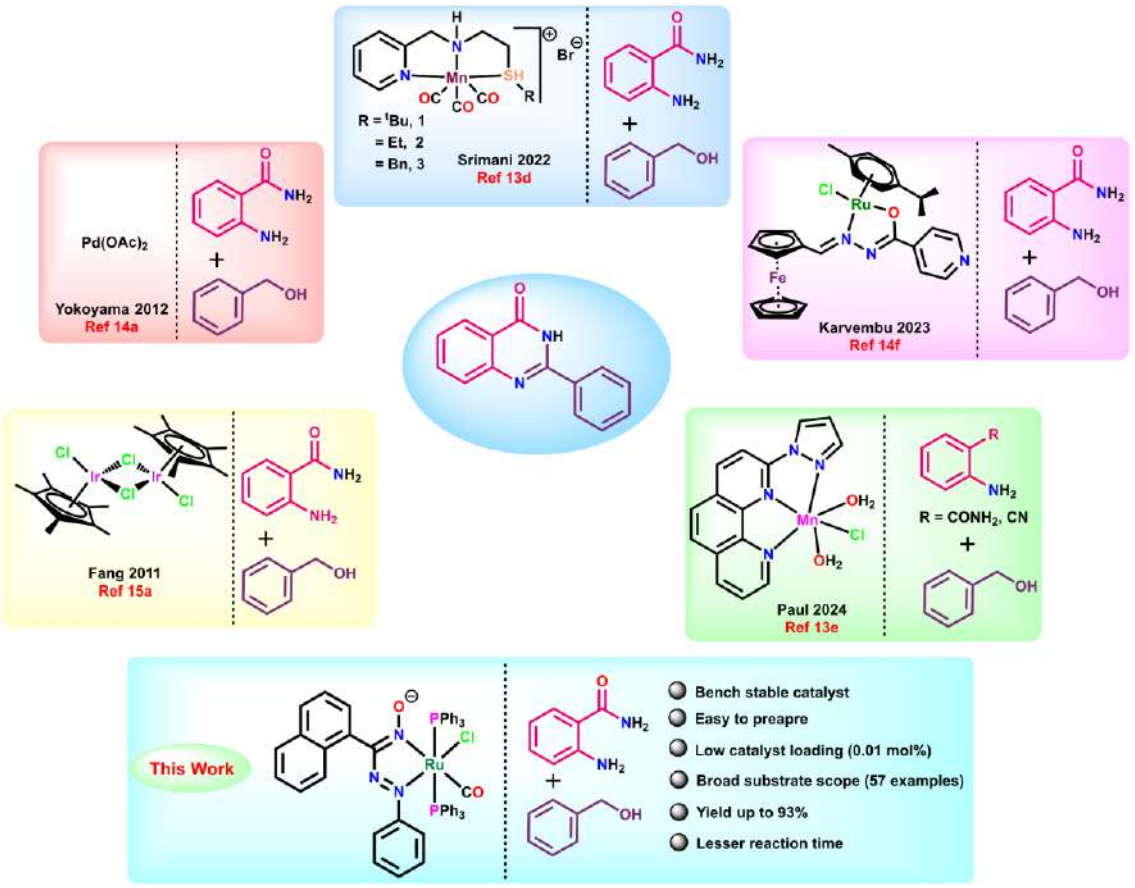

Scheme 4.1: Different transition metal catalysed dehydrogenative synthesis of Quinazolin-4(3H)-ones using o-aminobenzamides and benzyl alcohols

The ruthenium(II) complex have been successfully employed to catalyse the single-pot synthesis of 2-substituted quinazolinones in excellent yields (up to 93%) starting from *o*-aminobenzamides and substituted benzyl alcohols. Furthermore, it acts as an efficient catalyst for one-step transformation of N-substituted benzamides and primary alcohols to 2,3-disubstituted quinazolinones in very good yields (Scheme 4.2). The major advantage of this catalyst lies in its air- and moisture-insensitivity, thereby tolerating the catalytic transformation under aerobic conditions. In addition, it requires low catalyst loading (0.01%) and time-economic synthesis of a wide range of quinazolin-4(3H)-ones. To gain deeper insights of catalytic transformation by dehydrogenation pathway, we have investigated the plausible mechanism by using density functional theory (DFT) calculations. Both experimental data and theoretical analysis have provided a detailed interpretation of the reaction pathway along with a reaction free energy profile diagram.

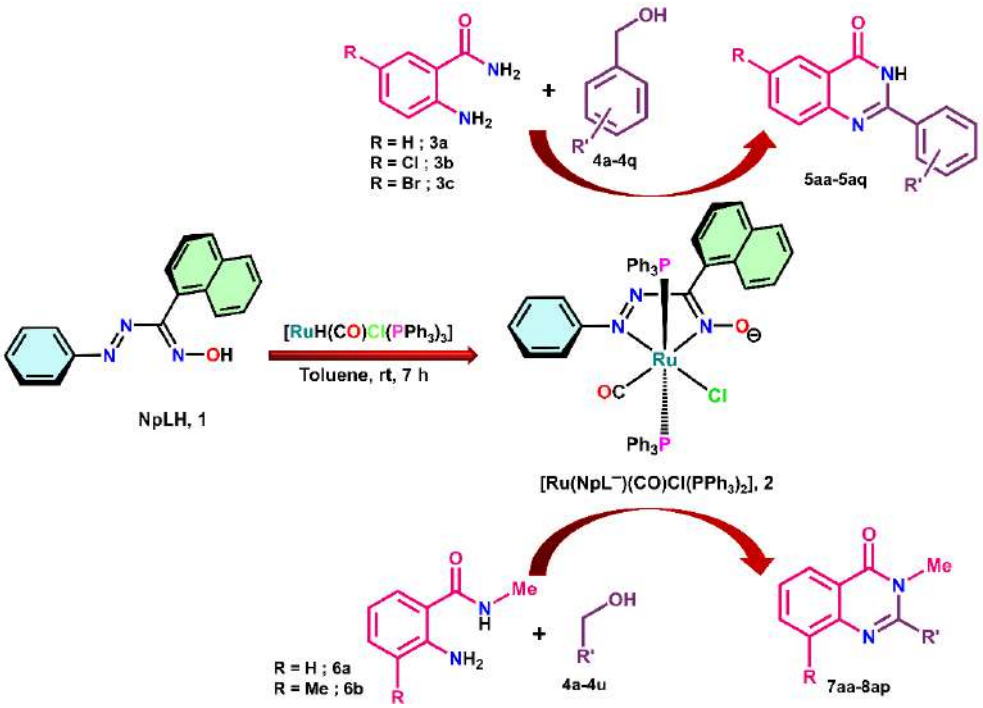

Scheme 4.2: Schematic representation of catalyst (complex **2**) synthesis and the catalytic synthesis of substituted quinazolin-4(3H)-ones *via* dehydrogenative functionalization of primary alcohols

4.2 Results and discussion

4.2.1 Synthesis and characterization of the catalyst

The ligand NpLH, **1** has been prepared starting from phenyl hydrazine and 1-naphthaldehyde and characterised by spectroscopically (See Experimental Section, Figure 4.6.A1–4.6.A4).[20] It possesses two donor centres *viz*., $N_{oximato}$ and N_{azo} which typically act as electron deficient moiety during coordination. When metal precursor [RuH(CO)Cl(PPh_3)$_3$] is added to the ligand solution in toluene in 1:1 molar ratio at room temperature and stirred for about 7 h, a dark brownish-red solution was formed. Upon subsequent chromatographic separation it gave *trans*-[Ru(NpL)(CO)Cl(PPh_3)$_2$], **2** in very high yield (66%). The ^{1}H-NMR spectrum of ruthenium(II) complex gave signals within the region of 6.23–7.80 (Figure 4.6.A5). Two magnetically equivalent triphenylphosphine moieties are oriented in trans position in the complex which can be substantiated by ^{31}P{1H} NMR (Figure 4.6.A7).

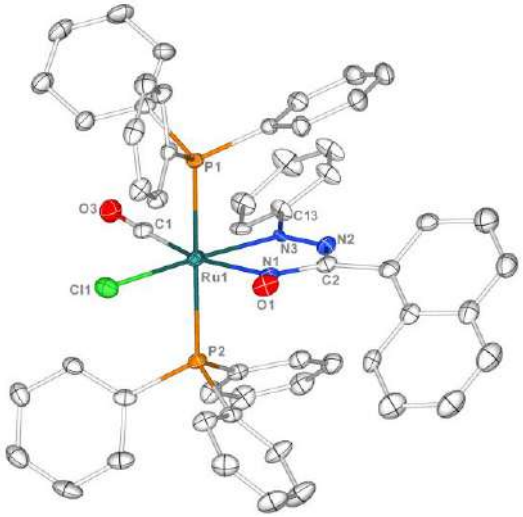

Figure 4.1 ORTEP diagram of **2** (CCDC No. **2370526**) with partial atom numbering scheme (Thermal Ellipsoids are set at 40%). Only one orientation of the disordered ligand **L** is shown and hydrogen atoms are omitted for clarity

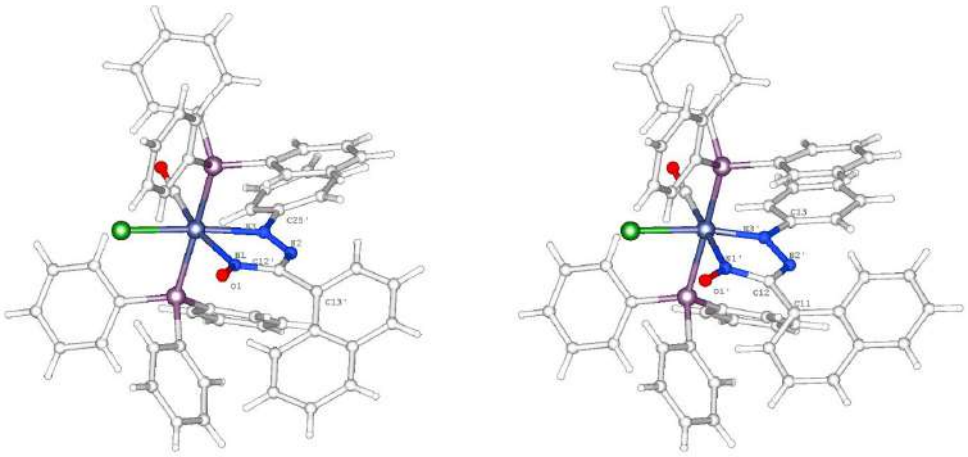

Figure 4.2: Two different of positional orientation of disordered ligand

The complex *trans*-[Ru(NpL)(CO)Cl(PPh_3)$_2$] **2** crystallizes in monoclinic P2_1 space group and its ORTEP diagram is depicted in Figure 4.1. Details of crystallographic parameters are presented in Table 4.1 and Table 4.2. The **NpL** ligand moiety is disordered over two positions [(C12'–C22'/C25'–C30'/N2/N3/N1/O1) and (C2–C12/C13–C18/N2'/N3'/N1'/O1') with equal occupancies (Figure 4.2). In the complex, chelation occurs through N_{azo} and $N_{oximato}$ donor atoms from the ligand **1** and two PPh_3 groups are positioned trans to each other. The

ligand **1** acts as a bi-dentate uninegative ligand, forming a distorted octahedral complex with ruthenium(II). Analysis of the six coordinated geometry around the ruthenium center by the continuous-shape measures (CShMs) method of SHAPE software supports the same (Table 4.3). Due to the disorder involving the ligand atoms, the N–N length spans a range of

Table 4.1 Crystallographic details of **2**

	2
Empirical formula	$C_{54}H_{42}ClN_3O_2P_2Ru$
T/K	273.15K
fw	963.419
Crystal system	Monoclinic
Space Group	$P2_1$
a/Å	11.039(4)
b/*Å*	16.981(6)
c/ *Å*	12.791(4)
α/deg	90
β/deg	112.626(4)
γ/deg	90
V/ *Å*^{3}	2213.1(13)
Z	2
D_c/Mgm^{-3}	1.446
μ/mm^{-1}	0.534
F(000)	986.7
cryst size/mm^3	0.31 × 0.25 × 0.13
θ/deg	3.44 – 50.66
Index ranges	-13 ≤ h ≤ 13, -20 ≤ k ≤ 20, -15 ≤ l ≤ 15
Measured reflns	19418
Unique reflns	7687
[a]GOF on F^2	1.055
R1[b], wR2[c][*I*>2*σ*(*I*)]	0.0457, 0.0961
R1, wR2	0.0585, 0.1023
Largest diff. peak/hole / e Å^{-3}	0.76/-0.74
Flack parameter	0.13(2)
[a]GOF = $\{\Sigma[w(F_o^2-F_c^2)2]/(n-p)\}^{1/2}$. [b]R1 = Σ [$\|F_o\|-\|F_c\|$]/ Σ $\|F_o\|$. [c]wR2 = $[\Sigma [w(F_o^2-F_c^2)^2]/ \Sigma [w(F_o^2)^2]]^{1/2}$ where w = 1/[$\sigma^2(F_o^2)+(aP)^2+bP]$, P = $(F_o^2+2F_c^2)/3$.	

Table 4.2 Selected Bond Lengths (Å) and Bond Angles (degree) for complex **2**

Metrical Parameters	Expt.	Metrical Parameters	Expt.
Ru1–N1	2.138(10)	Cl1–Ru1–P2	90.45(5)
Ru1–N3	2.217(9)	P1–Ru1–P2	174.53(4)
Ru1–N1'	2.067(10)	P1–Ru1–Cl1	86.52(5)
Ru1–N3'	1.855(10)	C1–Ru1–P2	90.34(14)
Ru1–P1	2.4272(14)	C1–Ru1–Cl1	87.55(17)
Ru1–P2	2.4147(13)	C1–Ru1–P1	94.08(14)
Ru1–Cl1	2.4349(16)	N1–Ru1–P2	84.6(3)
Ru1–C1	1.877(5)	N1–Ru1–Cl1	105.2(2)
N2–N3	1.226(13)	N1–Ru1–P1	91.8(3)
N2'–N3'	1.392(16)	N1–Ru1–C1	166.3(3)
N1–O1	1.246(11)	N3–Ru1–P2	91.6(3)
N1'–O1'	1.230(13)	N3–Ru1–Cl1	176.7(3)
C12'–N1	1.399(14)	N3–Ru1–P1	91.3(3)
C12'–N2	1.326(14)	N3–Ru1–N1	72.4(4)
C12–N1'	1.405(15)	N1'–Ru1–P2	87.0(3)
C12–N2'	1.324(16)	N1'–Ru1–Cl1	89.7(3)
C13–N3'	1.480(12)	N1'–Ru1–P1	88.5(3)

Table 4.3 Summary of Shape analysis of complex **2**

Complex	Metal centre	Hexagon HP-6 (D_{6h})	Pentagonal pyramid PPY-6 (C_{5v})	Octahedron OC-6 (Oh)	Trigonal prism TPR-6 (D_{3h})	Johnson pentagonal pyramid J2 JPPY-6 (C_{5v})
2	Ru	30.146	23.380	1.745	13.685	25.493

1.226(13) - 1.392(16) Å. Weak C–H···X (X= O, N and Cl) interactions are found to be operative in the crystal lattice. Selected bond lengths and bond angles are summarized in Table 4.2. Electrochemical experiments of **2** were performed in dichloromethane/acetonitrile (1:9 v/v) at room temperature using saturated Ag/AgCl was used as reference electrode. Multiple irreversible reductive couples within the potential range of -0.73 to -1.07V (Figure 4.3, Table 4.4) were observed and these are primarily attributed to reduction of the coordinated ligand,

with very high contribution from both oxime as well as azo functions (Table 4.5). This driven us to believe that the azo-oxime group of coordinated ligand may be exploited in electron transfer catalysis. The optimised geometry of complex **2** and some calculated bond length as well as bond angle are given in Figure 4.4a. We also obtain calculated absorption spectrum of complex **2** from DFT studies which is plotted along with the experimental absorption spectrum (Figure 4.4b).

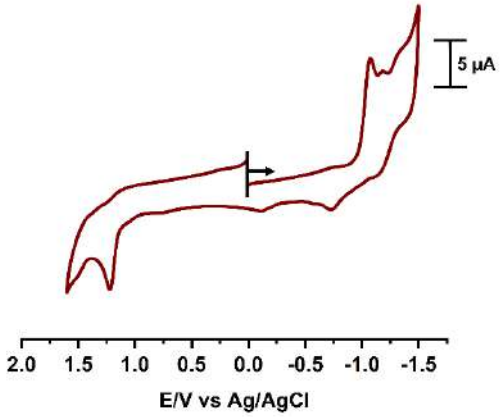

Figure 4.3: Cyclic Voltammogram of complex **2**

Table 4.4: Electrochemical data of Ru(II)-complex **2** with respect to Ag/AgCl

Complex	$E_{1/2}$**/V (Δ*E*/mV)**	
	Oxidation	**Reduction**
2	+1.22 (E_p^1/V)	-0.72 (E_p^2/V), -1.07 (E_p^2/V)
$E_{1/2} = ½(E_{pa} + E_{pa})$, E_{pa} = anodic peak potential; E_{pc} = cathodic peak potential, Δ*E* = peak-to-peak separation		

Table 4.5: Frontier Molecular Orbital Composition (%) in the ground state for complex **2**

MO No.	MO	E(eV)	Contribution (%)								Contribution
			Ru	Cl	CO	Azo	Oxime	Nap	Ph	PPh_3	
239	L+5	-1.02	3	1	2	0	2	0	1	92	$d_{x^2-z^2}$ + π*(Oxime +Ph + PPh_3)
238	L+4	-1.09	1	0	0	0	0	0	1	98	π*(PPh_3)
237	L+3	-1.09	2	0	1	0	1	3	2	91	π*(PPh_3)
236	L+2	-1.32	2	0	0	3	2	87	4	2	π*(PPh_3)
235	L+1	-1.68	32	4	1	2	2	0	0	60	d_{z^2} + π* (PPh_3)
234	LUMO	-2.61	6	0	2	33	40	2	13	4	π*(Azo + Oxime + Ph)
233	HOMO	-5.50	11	4	0	9	34	30	11	2	d_{xz} + π (Azo + Oxime + Naph)
232	H–1	-5.95	21	26	1	3	6	37	1	4	d_{xy} + π (Cl + Oxime + Naph)
231	H–2	-6.09	25	35	4	1	24	9	0	2	d_{yz} + π (Cl + Oxime + Naph)
230	H–3	-6.24	2	29	0	5	11	21	14	18	π (Cl + Oxime + Naph + Ph + PPh_3)
229	H–4	-6.34	8	28	5	3	50	4	1	2	d_{xy} + π (Cl + Oxime)
228	H–5	-6.58	12	0	0	2	2	3	5	76	d_{yz} + π (PPh_3)

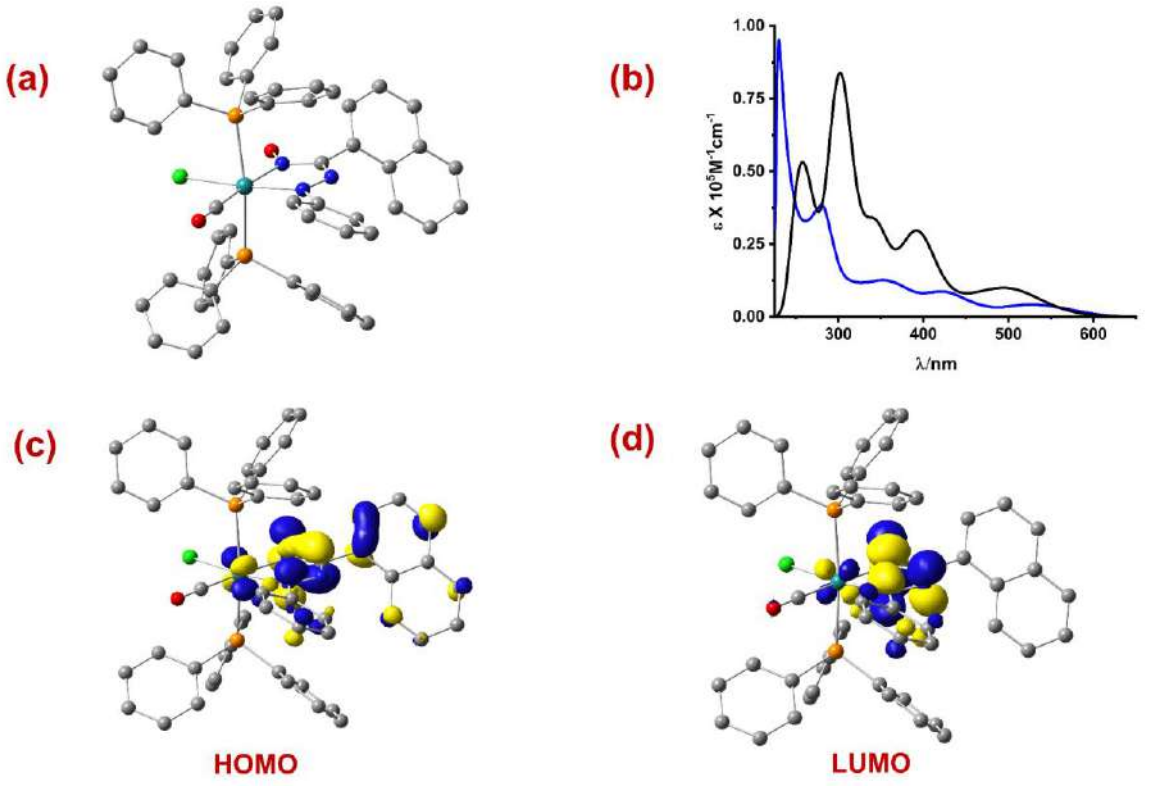

Figure 4.4: (a) The optimized geometry of complex **2** at B3LYP/6311+G(d,p) level of theory and Selected bond lengths (Å) and bond angles (degrees): Ru1–N1 2.136, Ru1–N3 2.097, Ru1–Cl1 2.515, Ru1–P1 2.527, Ru1–P2 2.505, N2–N3 1.287, N1–O2 1.253, N1–Ru1–N3 75.26,

N3–Ru1–C1 99.18, N1–Ru1–P1 91.93 **(b)** Experimental (blue) and calculated (black) absorption spectra of **2**, **(c)** HOMO & **(d)** LUMO of **2**

Table 4.6: Main Optical Transition at the TD-DFT/B3LYP/6-311+G(d,p) Level for the **2** with composition in terms of Molecular Orbital Contribution of the Transition, Computed Vertical Excitation Energies, and Oscillator Strength in Dichloromethane

Transition	CI	Composition	E (eV)	Oscillator strength (*f*)	λ_{theo} (nm)
$S_0 \rightarrow S_2$	0.59780	HOMO → LUMO (71%)	2.4652	0.0535	502.93
$S_0 \rightarrow S_6$	0.64955	H─3 → LUMO (84%)	3.0984	0.0884	400.15
$S_0 \rightarrow S_7$	0.62377	H─4 → LUMO (78%)	3.1989	0.1194	387.58
$S_0 \rightarrow S_{11}$	0.66728	HOMO → L+2 (89%)	3.5954	0.1446	344.84
$S_0 \rightarrow S_{31}$	0.38812	HOMO → L+4 (30%)	4.1305	0.0220	300.16
$S_0 \rightarrow S_{70}$	0.34435	H─3 → L+4 (24%)	4.7953	0.0167	258.55

Table 4.7: Natural transition orbitals (NTOs) for complex **2** illustrating the nature of singlet excited states in the absorption bands in the range 200–800 nm. For each state, the respective number of the state, transition energy (eV), and the oscillator strength (in parentheses) are listed. Shown are only occupied (holes) and unoccupied (electrons) NTO pairs that contribute more than 20% to each excited state

		Hole	Electron
528 nm	S_2 w = 0.7147 2.4652 (0.0535) 502.93 nm ILCT & d-d π (Azo + Oxime + Naph + Ph) → π* (Azo + Oxime + Ph) & d_{xz} → d_{yz}	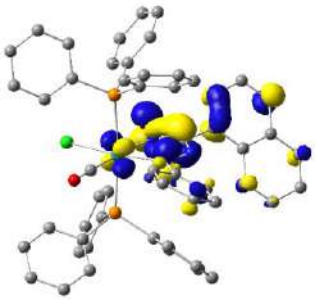	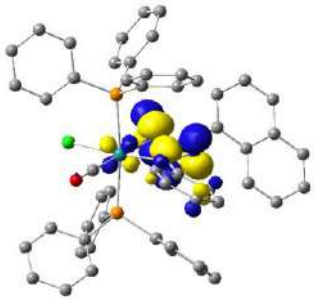
425 nm	S_6 w = 0.8438 3.0984 (0.0884) 400.15 nm ILCT, LLCT & d-d π (Cl + Ph) → π* (Azo + Oxime + Ph) & $d_{x^2-y^2}$ → d_{yz}	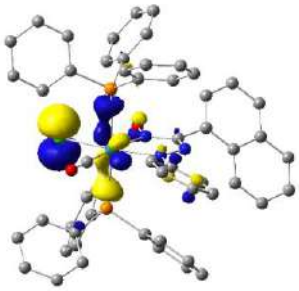	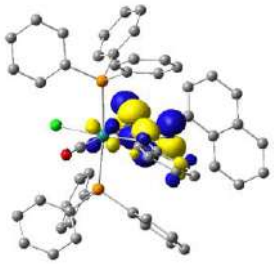
	S_7 w = 0.7781 3.1989 (0.1194) 387.58 nm LLCT & d-d π (Cl + Ph + PPh_3) → π* (Azo + Oxime + Ph) & d_{xz} → d_{yz}	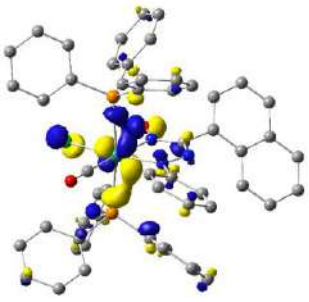	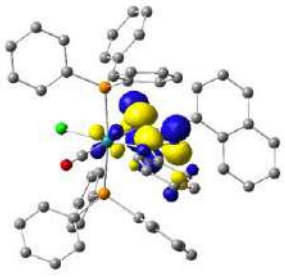

352 nm	S_{11} w = 0.8905 3.5954 (0.1446) 344.84 nm MLCT & ILCT π (Azo + Oxime + Naph + Ph) & d_{yz} → π* (Naph)	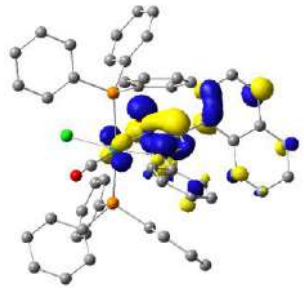	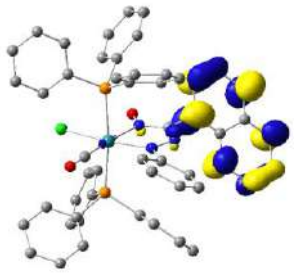
278 nm	S_{31} w = 0.3012 4.1305 (0.0220) 300.16 nm LLCT & d-d π (Azo + Oxime + Naph + Ph) → π* (PPh_3) & d_{yz} → $d_{x^2-y^2}$	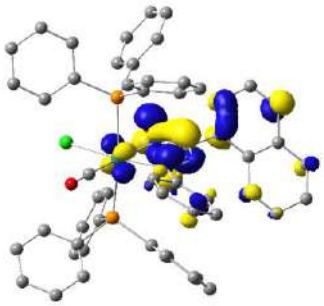	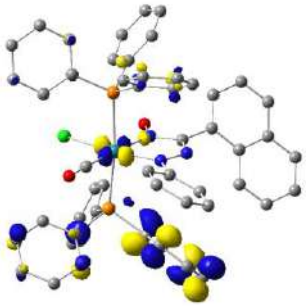
230 nm	S_{70} w = 0.2371 4.7953 (0.0167) 258.55 nm LLCT & d-d π (Cl + Ph) → π* (PPh_3) & d_{yz} → $d_{x^2-y^2}$	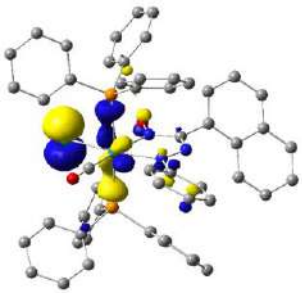	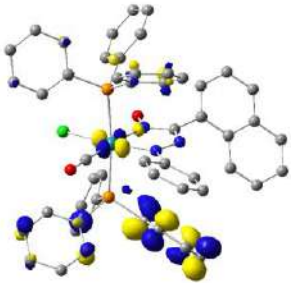

4.2.2 Catalytic activity

The classical approaches for synthesis of quinazolin-4(3H)-ones require strong oxidants and are usually multi-step, time-consuming processes. They generally require expensive catalysts and generate unwanted by products.[11-12] Consequently, synthesis of substituted quinazolin-4(3H)-ones via the functionalization of sustainable alcohols and *o*-aminobenzamides using less expensive and abundantly obtainable catalysts under aerobic conditions is of paramount significance.[13-15] The ruthenium(II) complex of phenyl-azo-naththaldoxime, trans-

[Ru(NpL)(CO)Cl(PPh$_3$)$_2$], **2** has been used as an efficient catalyst to synthesize a wide variety of substituted quinazolin-4(3H)-ones as depicted in Scheme 4.3.

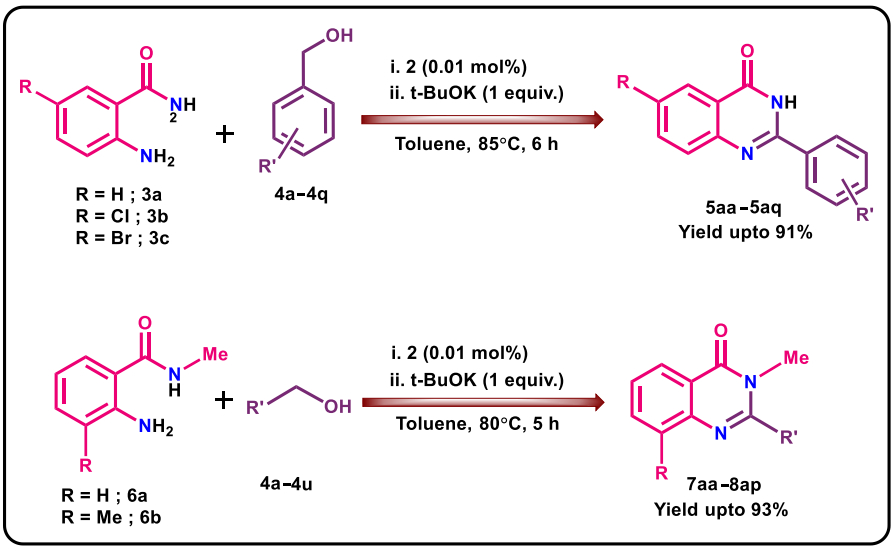

Scheme 4.3: The schematic representation catalytic synthesis of substituted quinazolin-4(3H)-ones

4.2.3 Optimization of reaction conditions

We initiated our investigation to find out the optimum reaction condition for synthesis of quinazolin-4(*3H*)-one by reacting *o*-aminobenzamide (**3a**) with benzyl alcohol (**4a**) in the presence of catalyst **2**. Various control experiments were conducted by adjusting different reaction parameters such as solvents, bases, temperature, *etc*. to determine the optimal reaction condition. The details of optimized conditions are summarized in Table 3.8.

The reaction between **3a** and **4a** proceeded quite efficiently in the presence of 0.01 mol% of **2** and inorganic bases like NaOH and KOH in toluene. When the amount of base is increased from 0.5 equiv. to 1.0 equiv., no significant improvement in yield of **5aa** was observed (Table 4.8, Entry 1–4). A similar outcome was found in the case of coupling between **6a** and **4a** resulting in **7aa**. The yields of both **5aa** and **7aa** increase significantly when t-BuOK (Table 4.8, Entry 5) was used as the base, instead of NaOH or KOH, in toluene at 85°C and 80°C,

respectively. However, reducing the amount of t-BuOK led to a lower yield of the desired product (Table 4.8, Entry 6).

We have performed the coupling reactions in various solvents including xylene, acetonitrile (MeCN), N,N-dimethylformamide (DMF) and tetrahydrofuran (THF) (Table 4.8, Entry 7−12). However, none of them outperformed toluene. In addition, bases other than t-BuOK, like Et_3N, i-Pr_2NEt along with alkali metal carbonates and phosphate such as K_2CO_3, Cs_2CO_3, & K_3PO_4 were used. Unfortunately, these alternative bases led to a substantial reduction in the yields of both **5aa** and **7aa** (Table 4.8, Entry 13−20).

Upon carrying out the reaction at elevated temperature (100−110ºC), the yields of both **5aa** and **7aa** slightly decreased (Table 3.8, Entry 21−22). At the same time, a significant reduction in yield was observed at lower temperatures (60°C) and reaction is practically insignificant at room temperature (Table 4.8, Entry 23−24). In absence of catalyst **2**, **5aa** and **7aa** are produced in a trace amount while no reaction took place in absence of bases (Table 4.8, Entry 25−26).

Table 4.8: Optimization of the reaction conditions for the synthesis of 2-substituted and 2,3-disubstituted quinazolinones *via* catalytic dehydrogenation using catalyst **2**[a,b,c,d]

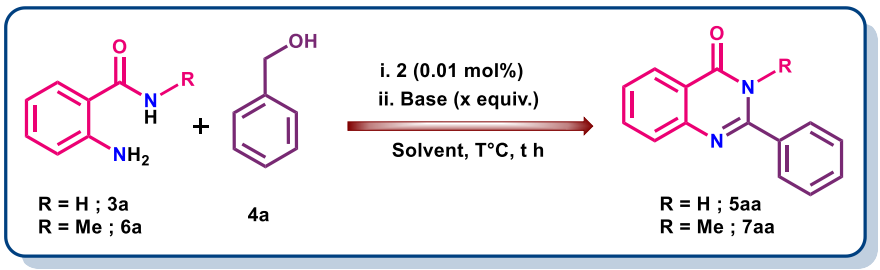

					For 5aa			For 7aa		
Entry	**Catalyst (0.01 mol%)**	**Base**	**X (equiv.)**	**Solvent**	**TºC**	**Time (h)**	**Yield[c] (%)**	**TºC**	**Time (h)**	**Yield[c] (%)**
1	2	NaOH	0.5	Toluene	85	6	73	80	5	78
2	2	NaOH	1.0	Toluene	85	6	79	80	5	82
3	2	KOH	0.5	Toluene	85	6	58	80	5	60
4	2	KOH	1.0	Toluene	85	6	62	80	5	62
5	**2**	**t-BuOK**	**1.0**	**Toluene**	**85**	**6**	**91**	**80**	**5**	**93**

6	2	t-BuOK	1.0	Toluene	85	6	87	80	5	80
7	2	t-BuOK	0.5	Xylene	85	6	75	80	5	79
8	2	t-BuOK	0.5	MeCN	82	6	Trace	80	5	Trace
9	2	t-BuOK	0.5	DMF	85	6	Trace	80	5	Trace
10	2	t-BuOK	1.0	DMF	85	6	Trace	80	5	Trace
11	2	t-BuOK	0.5	THF	85	6	35	80	5	30
12	2	t-BuOK	1.0	THF	85	6	45	80	5	40
13	2	Et_3N	1.0	Toluene	85	6	NR	80	5	NR
14	2	i-Pr_2NEt	1.0	Toluene	85	6	NR	80	5	NR
15	2	Cs_2CO_3	0.5	Toluene	85	6	38	80	5	48
16	2	Cs_2CO_3	1.0	Toluene	85	6	46	80	5	55
17	2	K_2CO_3	0.5	Toluene	85	6	55	80	5	62
18	2	K_2CO_3	1.0	Toluene	85	6	60	80	5	67
19	2	K_3PO_4	0.5	Toluene	85	6	25	80	5	30
20	2	K_3PO_4	1.0	Toluene	85	6	30	80	5	35
21	2	t-BuOK	1.0	Toluene	100	6	90	100	5	91
22	2	t-BuOK	1.0	Toluene	110	6	88	110	5	90
23	2	t-BuOK	1.0	Toluene	60	6	20	60	5	28
24	2	t-BuOK	1.0	Toluene	rt	6	NR	rt	5	NR
25	–	t-BuOK	1.0	Toluene	80	6	Trace	80	5	Trace
26	2	–	–	Toluene	80	6	NR	80	5	NR

*[a]Reaction conditions: **3a** (1 mmol), **4a** (1.1 mmol), Catalyst **2** (0.01 mol %), base (x equiv.), solvent (5 mL), 85 ºC (oil bath), 6 h. [c]Isolated yield after column chromatography, [d]Under air.*

*[b]Reaction conditions: **6a** (1 mmol), **4a** (1.1 mmol), Catalyst **2** (0.01 mol %), base (x equiv.), solvent (5 mL), 80 ºC (oil bath), 5 h. [c]Isolated yield after column chromatography, [d]Under air.*

4.2.4 Substrate Scope

In order to evaluate the breadth of this synthetic approach, we investigated its applicability across various alcohols and *o*-aminobenzamides (Table 4.9). We have used a wide array of benzyl alcohols with substituents at *ortho*, *meta,* and *para* positions. Benzyl alcohols with electron-donating groups reacted efficiently under the current catalytic protocol, yielding the corresponding 2-substituted quinazolinones in high yields (Table 4.9, **5ab:** 89%, **5ad**: 88%, **5ag**: 90%, **5ah**: 85%, **5ai**: 87%). Also, benzyl alcohols with moderate (−Cl, −Br) to strong

electron-withdrawing groups (−F, $-CF_3$) reacted quite effectively with *o*-aminobenzamides to afford the desired quinazolinones in good to excellent yields (Table 4.9, **5ae**: 79%, **5af**: 76%, **5aj**: 81%, **5ak**: 77%, **5al**: 74%, **5am**: 80%). Furthermore, an aromatic polycyclic alcohol such as naphthalen-1-ylmethanol was found to undergo smooth conversion under same catalytic conditions, producing the corresponding quinazolinone in excellent yield (Table 4.9, **5ap**: 86%). Heteroaryl alcohols including pyridin-2-ylmethanol, thiophen-2-ylmethanol, and furan-3-ylmethanol also reacted successfully to give the desired 2-substituted quinazolinones (Table 4.9, **5ar**: 68%, **5as**: 70%, **5at**: 73%). The substrate compatibility was further expanded to different substituted *o*-aminobenzamides as coupling partners. We have successfully able to couple substituted benzamides such as 2-amino-5-chlorobenzamide (**3b**) and 2-amino-5-bromobenzamide (**3c**) with benzyl alcohol and 4-methylbenzyl alcohol, yielding the corresponding quinazolinones (Table 4.9, **5ac**: 74%, **5an**: 72%, **5ao**: 70%).

The compatibility of substrate is also evaluated with N-substituted-2-aminobenzamide. Benzyl alcohols with both electron-donating and withdrawing groups successfully reacted with N-methyl-2-aminobenzamide (**6a**) to produce corresponding N-substituted quinazolinones (Table 4.10). Notably, the benzyl alcohols with electron-withdrawing substituents acted as a superior coupling partners compared to those with electron-donating groups to form the corresponding 2,3-disubstituted quinazolinones in excellent yields (Table 4.10, **7ad**: 92%, **7ae**: 89%, **7aj**: 94%, **7ak**: 86%, **7al**: 81%, **7am**: 90%). Analogous outcomes were also observed for 2-amino-N,3-dimethylbenzamide (**6b**) (Table 4.10). This protocol is effective for heteroaryl alcohols, yielding the corresponding products **7ao** and **7ap** with isolated yields of 75% and 76% respectively (Table 4.10). In addition, polyaromatic alcohol like naphthalen-1-ylmethanol coupled proficiently with both N-methyl-2-aminobenzamide (**6a**) and 2-amino-N,3-dimethylbenzamide (**6b**), resulting in the corresponding products with good yields, specifically 87% for **7an** and 82% for **8an**, as presented in Table 4.10. It is worth mentioning that benzyl

alcohols containing $-NO_2$ group at *ortho*, *meta,* and *para* positions failed to couple with any of the *o*-aminobenzamides under this optimized reaction conditions.

We have also extended our investigation with aliphatic primary alcohols to assess their suitability for this reaction. It is possibly owing to their enhanced stability and robustness that these are a bit more demanding to activate than their aryl and heteroaryl counterparts under the present standardized protocol. To obtain higher product yields, we have modified the reaction conditions by increasing the temperature to 100°C and extending the reaction time to 16 h to achieve the corresponding 2-alkylated quinazolinones in appreciable yields. By using this approach, we were fruitfully able to couple between N-methyl-2-aminobenzamide (**6a**)/ 2-amino-N,3-dimethylbenzamide (**6b**) with suitable aliphatic alcohols like *n*-propanol, *n*-butanol, *n*-hexanol and *n*-octanol under the above modified reaction conditions (Table 4.10, **7ar**: 45%, **7as**: 48%, **7at**: 57%, **7au**: 60%, **8ao**: 46%, **8ap**: 55%).

Table 4.9: Substrate scope with different alcohols

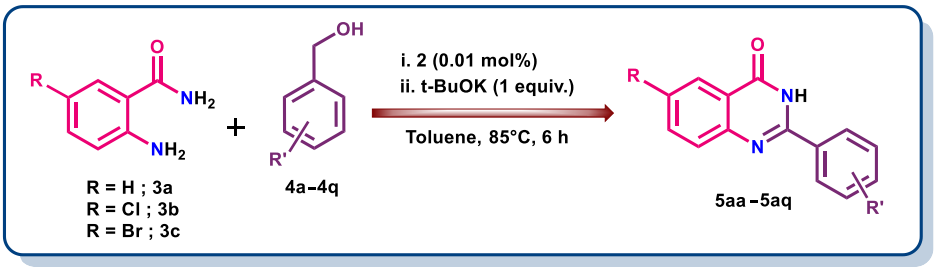

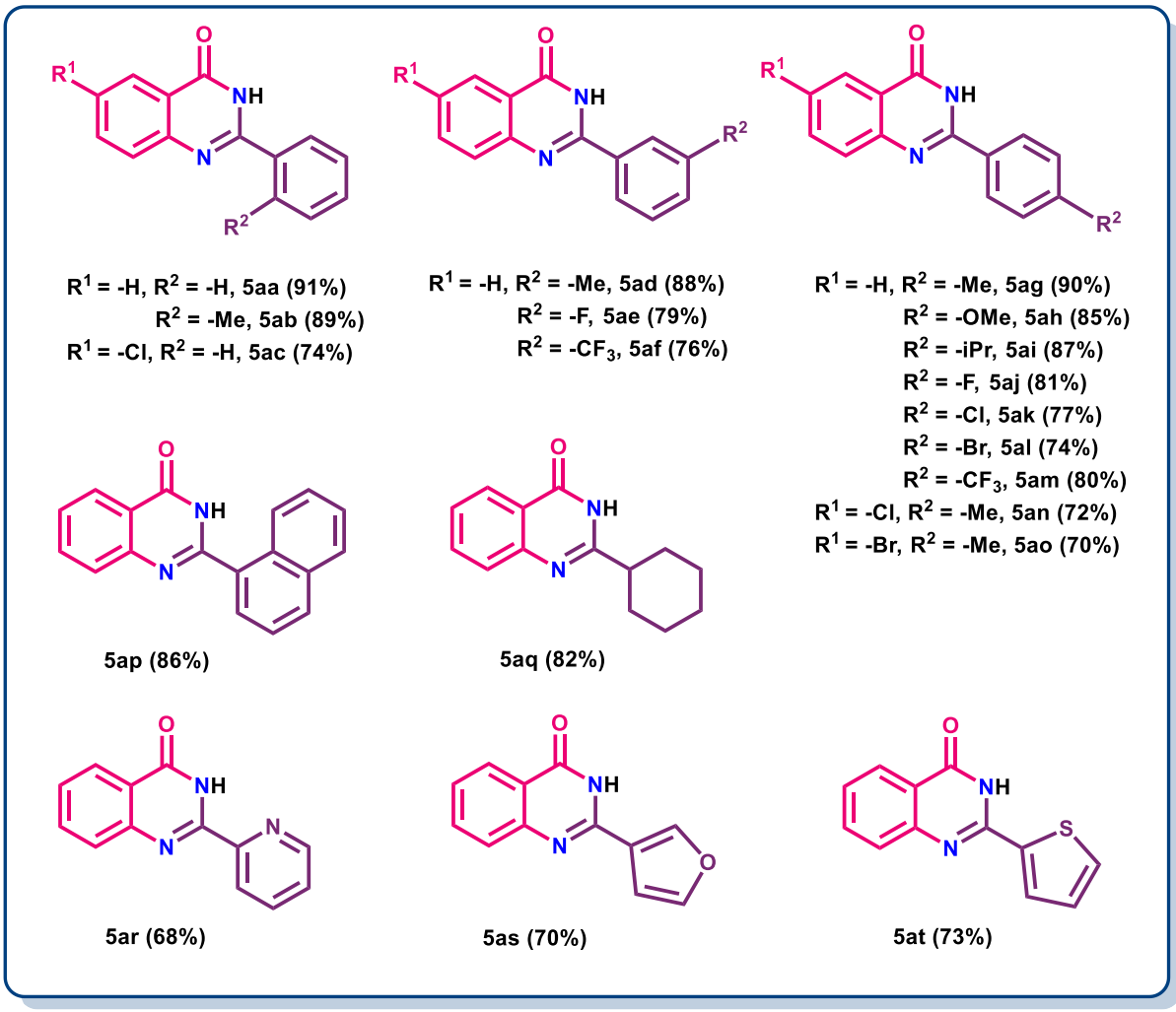

Table 4.10: Substrate scope with various benzamides and benzyl alcohols

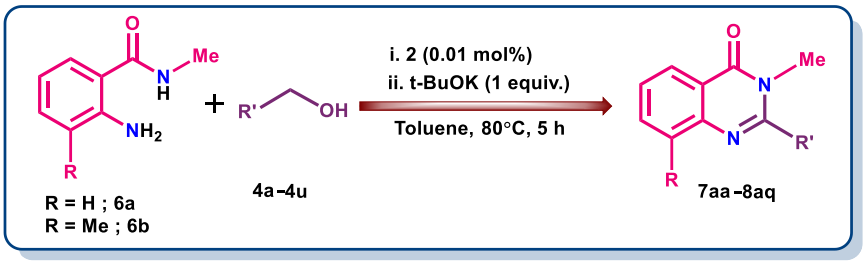

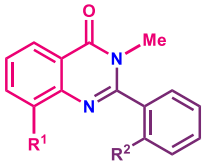

R^1 = -H, R^2 = -H, 7aa (93%)
R^2 = -Me, 7ab (85%)
R^1 = -Me, R^2 = -H, 8aa (85%)
R^2 = -Me, 8ab (83%)

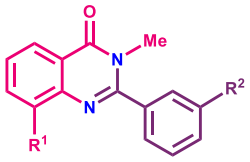

R^1 = -H, R^2 = -Me, 7ac (88%)
R^2 = -F, 7ad (92%)
R^2 = -CF_3, 7ae (89%)
R^1 = -Me, R^2 = -Me, 8ac (85%)
R^2 = -F, 8ad (92%)
R^2 = -CF_3, 8ae (90%)

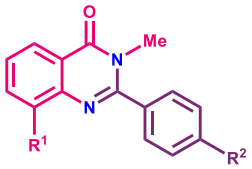

R^1 = -H, R^2 = -Me, 7af (91%)
R^2 = -OMe, 7ag (84%)
R^2 = -iPr, 7ah (86%)
R^2 = -Ph, 7ai (87%)
R^2 = -F, 7aj (94%)
R^2 = -Cl, 7ak (86%)
R^2 = -Br, 7al (81%)
R^2 = -CF_3, 7am (90%)

R^1 = -Me, R^2 = -Me, 8af (90%)
R^2 = -OMe, 8ag (87%)
R^2 = -iPr, 8ah (86%)
R^2 = -Ph, 8ai (84%)
R^2 = -F, 8aj (95%)
R^2 = -Cl, 8ak (88%)
R^2 = -Br, 8al (85%)
R^2 = -CF_3, 8am (92%)

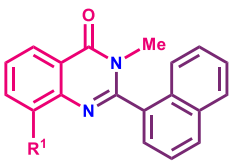

R^1 = -H, 7an (87%)
R^1 = -Me, 8an (82%)

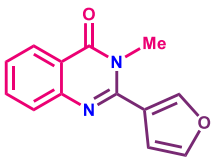

7ao (75%)

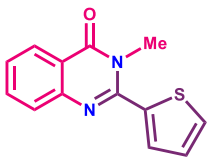

7ap (76%)

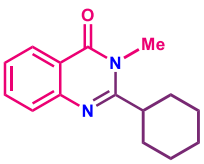

7aq (79%)

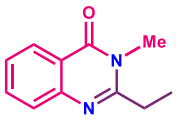

7ar (45%)*

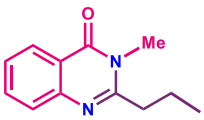

7as (48%)*

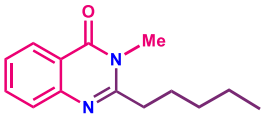

7at (57%)*

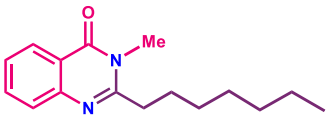

7au (60%)*

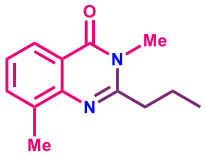

8ao (46%)*

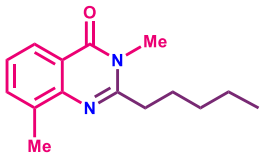

8ap (55%)*

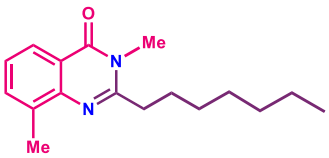

8aq (61%)*

*Temperature: 100°C, Reaction Time: 16 h

4.2.5 Mechanistic investigation

In order to have a perception of the catalytic reaction pathway for synthesis of quinazolinone-4(3*H*)-ones and its *N*-methyl derivatives, few control experiments were undertaken under standard and optimised reaction condition. The ruthenium catalyst is indeed robust since the transformations were accomplished at relatively high temperatures. Furthermore, it is stable even at 110 ºC in toluene and in other common organic solvents under both aerobic and inert conditions. We have scrutinized the homogeneity of the catalytic reaction and active involvement of **2** through mercury poisoning test. Oxidation of primary alcohols as well as dehydrogenative coupling reaction between primary alcohols and benzamides were found to progress efficiently under the above-mentioned conditions.

The dehydrogenative coupling between **3a** and **4a** as well as **6a** and **4a** result in **5aa** and **7aa** with 89% and 91% yield respectively (See Experimental section for details). The above experimental findings clearly indicate the non-involvement of ruthenium nano particle and active participation of molecular ruthenium catalyst **2** during the course of reaction. In order to check the possible involvement of any organic radical species during the reaction, the dehydrogenation of **4a** was conducted in presence of radical scavenger **TEMPO** (2,2,6,6-tetramethylpiperidin-1-yl)oxyl), under optimised condition. It was observed that ruthenium catalysed dehydrogenation of alcohols remains unchanged in presence of **TEMPO** (Scheme 4.5). The corresponding aldehyde **4a'** was obtained in 90% as dehydrogenation product. Furthermore, the coupling reaction between **3a** and **4a** progresses efficiently even in presence of **TEMPO** with > 90% yield. For further validation, we have carried out the dehydrogenation of a radical clock substrate, cyclobutanol(**12a**) under optimised condition. The formation of cyclobutanone(**12a'**) as solitary product (Scheme 4.6) clearly supports the non-involvement of ketyl radical species during the dehydrogenation of primary alcohol catalysed by ruthenium(II). Therefore, this dehydrogenation reaction possibly proceeds *via* two-electron hydride transfer pathway.

Subsequently, we carried out the sub-stoichiometric dehydrogenation of 1-phenylethanol (**10a**) under nitrogen atmosphere in presence 1 equiv. t-BuOK and 0.1 equiv. of **2**. The reaction was analysed by IR spectroscopy (Figure 4.6.A10). Surprisingly, instead of N=N stretches (expected at around 1433 cm^{-1}) for catalyst **2**, the reaction mixture showed N–H stretch at 3029 and 3063 cm^{-1}, suggesting the probable conversion of azo-chromophore to its two-electron reduced hydrazido analog.[21] Also, when the same sub-stoichiometric reaction was performed by using deuterated 1-phenylethanol (**10a-D_2**), the corresponding N–D stretching frequencies were observed at 2160 and 2169 cm^{-1} (Figure 4.6.A11).[21] These observations are in keeping with the probable participation of azo/hydrazo redox couple during dehydrogenation of alcohols. It is worth mentioning that upon performing the same reaction under aerobic condition, N–H stretch was not observed. Instead, it was found that hydrogen peroxide was formed and this is clear evidence in favour of formation of hydrazido intermediate during dehydrogenation process. The latter further reacts with dioxygen to form hydrogen peroxide[21], thereby regenerating the active catalyst. Possibly Additionally, the dynamic involvement of azo functionality is further substantiated by the fact that the above alcohol dehydrogenation reactions did not proceed effectively in presence of $[RuH(CO)Cl(PPh_3)_3]$ under optimal reaction condition.

Finally, to inspect the prospect of transfer hydrogenation, the dehydrogenation of **10a** was performed in presence of easily reducible substrate like 4-methoxybenzaldehyde. Under inert atmosphere, dehydrogenation of **10a** did not occur and only traces of acetophenone were obtained (confirmed by TLC, Scheme 4.7) whereas in aerobic condition, corresponding dehydrogenated product acetophenone was obtained in good yield (91%) (Scheme 4.7). Nonetheless, in both cases we did not find transfer hydrogenated product i.e., 4-methoxybenzylalcohol.

In order to have an insight into the probable mechanistic path for formation of 2-phenylquinazolin-4(1*H*)-one (**5aa**) from pre-formed 2,3-dihydro-2-phenylquinazolin-4(1H)-one (**5aa'**), dehydrogenation of **5aa'** was performed under analogous reaction condition as in the case of dehydrogenation of alcohols. **5aa'** is efficiently transformed to **5aa** with about 89% yield (Scheme 4.4) along with the formation of hydrogen peroxide *via* hydrogenation of dioxygen (Scheme 4.8). Upon performing the dehydrogenation reaction under inert condition, the reaction practically does not occur and only trace amount of **5aa'** was observed in TLC plate. It is worthy to mention here that dehydrogenation of **5aa'** in presence of TEMPO, proceeds smoothly[21].

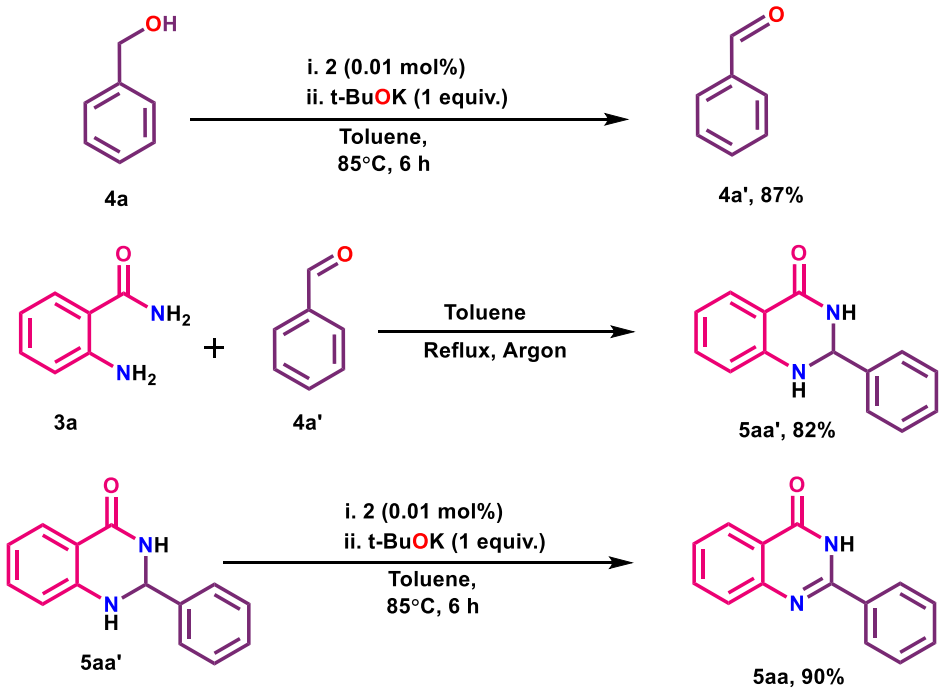

Scheme 4.4: Control experiment for oxidation of alcohol and dehydrogenation amine

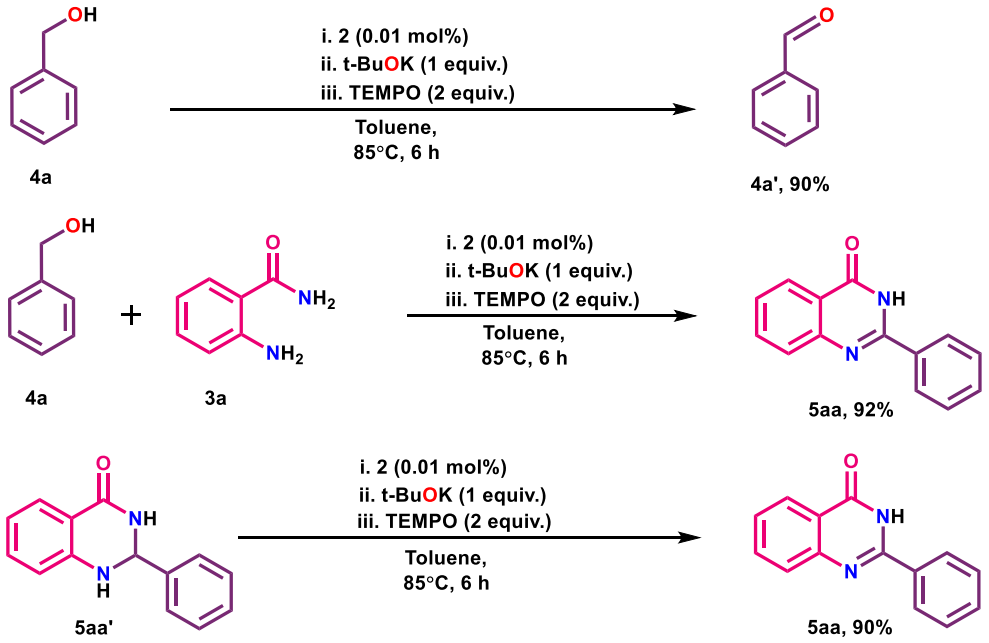

Scheme 4.5: Progress of the reaction in presence of radical scavenger

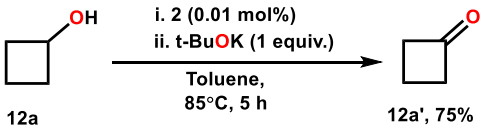

Scheme 4.6: Dehydrogenation of radical clock substrate cyclobutanone

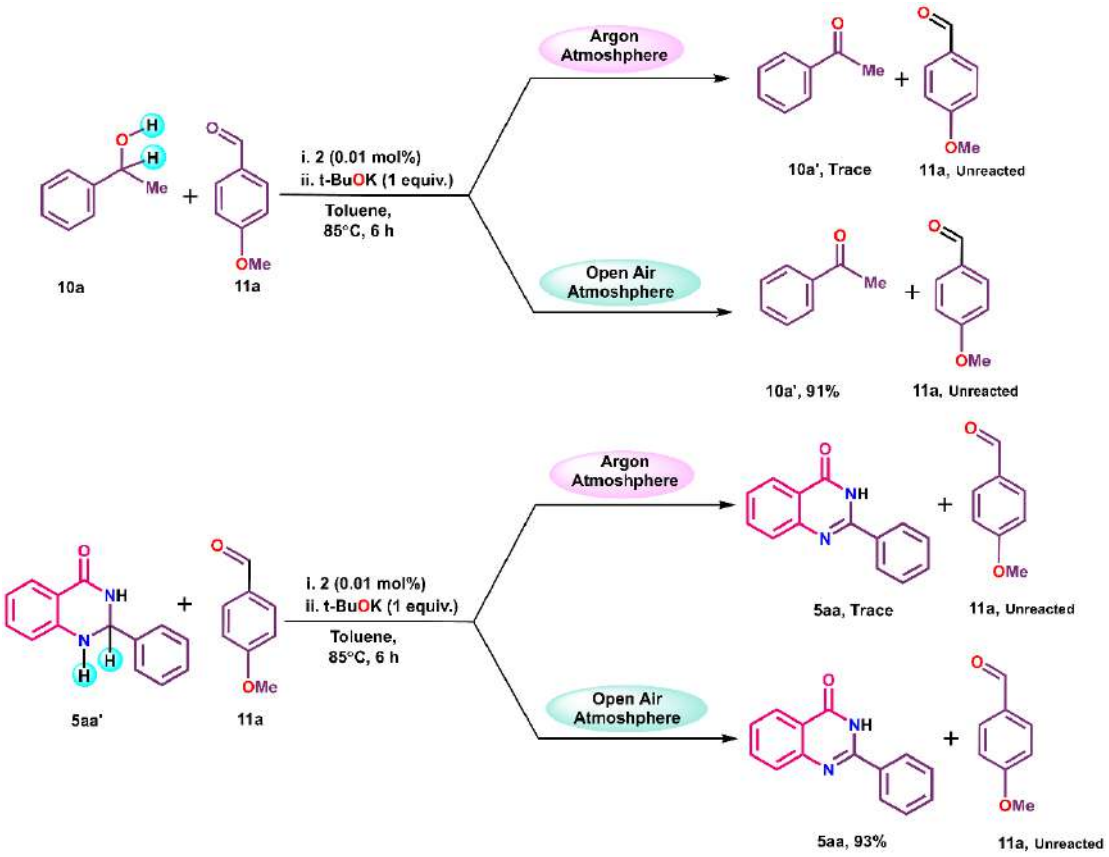

Scheme 4.7: Transfer hydrogenation reaction to prove evolution of H_2 production

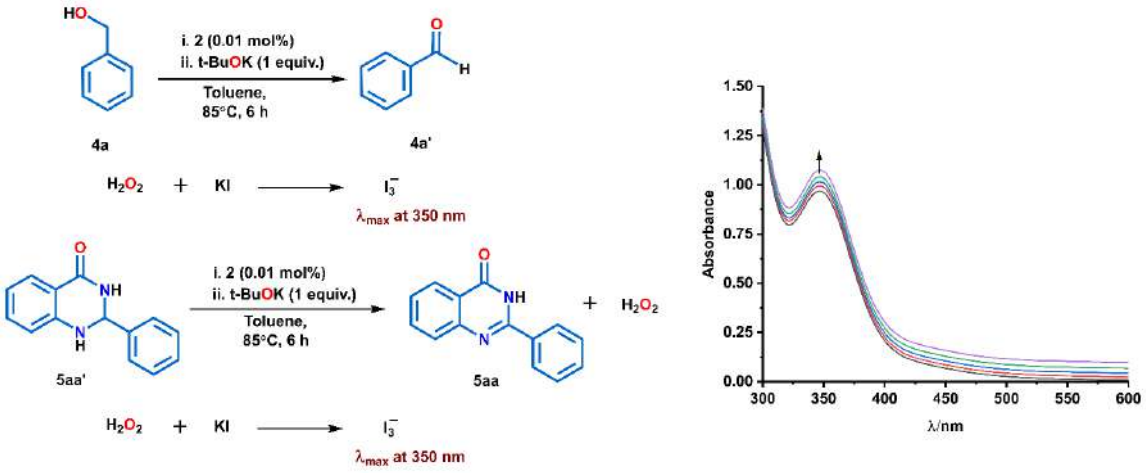

Scheme 4.8: Detection of H_2O_2 and identification of λ_{max} of triiodide (I_3^-) anion at 350 nm

4.2.6 Theoretical investigation of dehydrogenative functionalization

To substantiate the experimental findings as well as to gain deeper perceptions of the mechanistic pathway of dehydrogenation reaction, we have performed density functional theory (DFT) calculations. By applying experimental outcomes and DFT calculations, we intend to comprehend the detailed reaction along with the corresponding reaction free energy changes of the elementary steps that occur during dehydrogenation.

To gain mechanistic insights of the dehydrogenation using *trans*-[Ru(NpL)(CO)Cl(PPh_3)$_2$] **2**, all plausible mechanistic pathways of the dehydrogenation reaction. Specifically, we studied the dehydrogenation of benzyl alcohol ($PhCH_2OH$) to benzaldehyde (PhCHO). The catalytic cycle and reaction free energy of all elementary steps are provided in Scheme 4.9 and Figure 3.5. Initially, the active catalyst (intermediate 2, formed via rupture of Ru–Cl bond) interacts with the reactant $PhCH_2OH$, forming intermediate **2** with a reaction energy of -2.35 eV. This step is exergonic due to stronger interactions between Ru and the oxygen atom of $PhCH_2OH$. Thereafter, the hydrogen atom from the hydroxyl group (OH) of $PhCH_2OH$ can be transferred to a nitrogen atom in the ligand sphere. There are two types of nitrogen atoms present: in intermediate **3**, the hydrogen is transferred to the NH group directly attached to Ru, while in intermediate **4**, the hydrogen is transferred to another nitrogen atom in the ligand sphere. The calculated reaction free energies indicate that both steps are endergonic, but the formation of intermediate **4** from intermediate **2** is 0.85 eV more favourable than the formation of intermediate **3** from intermediate **2**. Therefore, the reaction will proceed via intermediate 4 rather than intermediate 3. Once intermediate 4 is formed, the other nitrogen becomes reactive and abstracts the hydrogen from the CH_2 group of $PhCH_2OH$. This step is highly exergonic, driving the reaction forward. In the next step, the removal of the product PhCHO from intermediate **5** leads to the formation of intermediate **6**. This step is highly endergonic, necessitating specific experimental conditions for the reaction. The highly endergonic nature

of this step is due to the strong Ru–O interaction that must be broken to release PhCHO from intermediate **5** and form intermediate **6**. The breaking of energy demanding M–O bond has been observed earlier also.[22] Besides, there can be other possibility of formation of intermediate 1 and H_2O_2 from intermediate **5**. The presence of O_2 leads to the formation of H_2O_2 from intermediate **6**, regenerating intermediate 1 and allowing the reaction to proceed in the next cycle of the catalytic process.

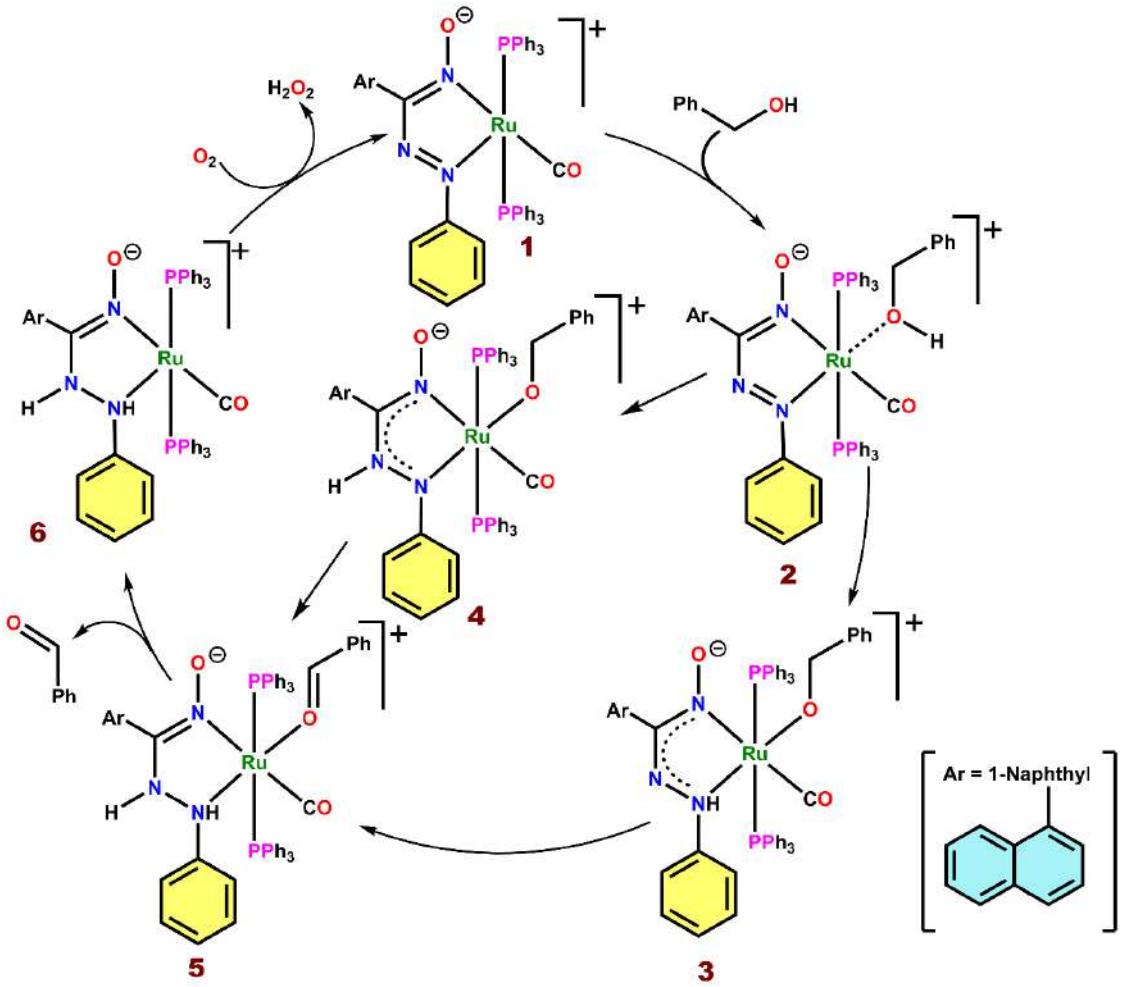

Scheme 4.9: Plausible mechanistic pathways for dehydrogenation of benzyl alcohol ($PhCH_2OH$) to benzaldehyde (PhCHO) using Ru(II)-based catalyst

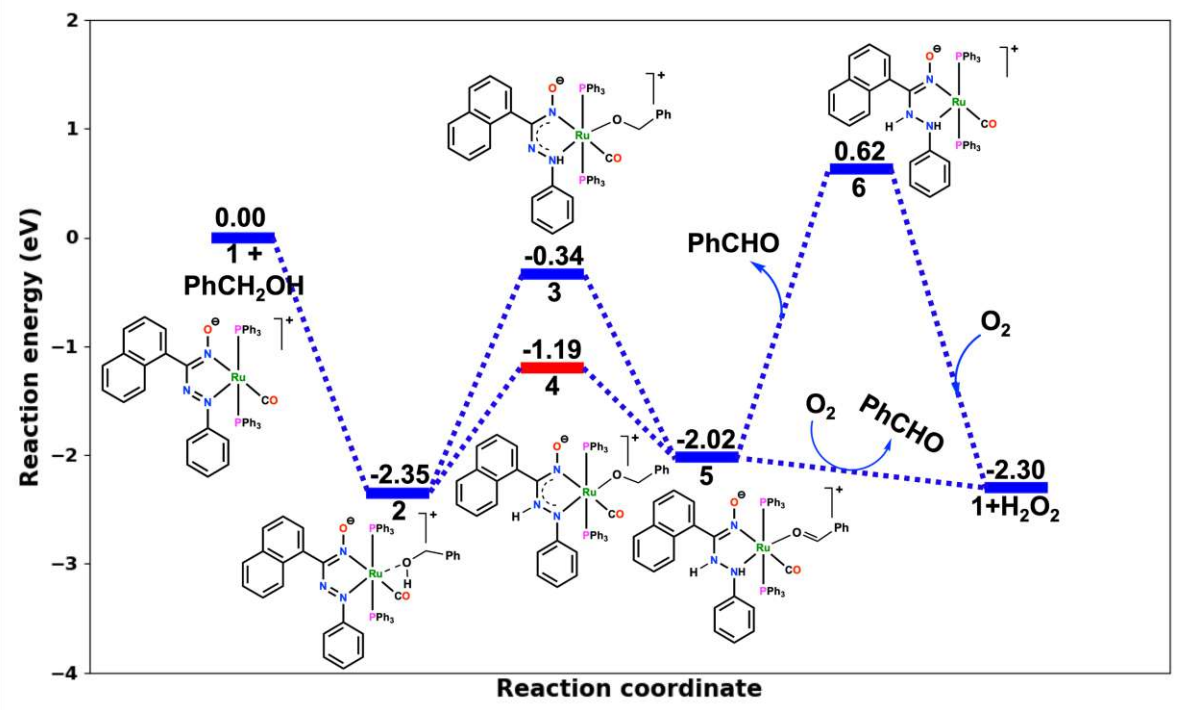

Figure 4.5: The reaction free energy profile diagram of every elementary step for dehydrogenation of benzyl alcohol ($PhCH_2OH$) to benzaldehyde (PhCHO) using Ru-based catalyst. All the reaction free energies are in eV

The benzaldehydes formed *via* the above process possibly undergoes condensation with *o*-amino benzamides/ N-substituted benzamides under aerobic conditions in presence of t-BuOK to form 2,3-dihydro-2-arylquinazolin-4(1H)-one, that binds to the Ru(II) centre of the catalyst through N1. Thereafter, the H atom of N1 is transferred to the coordinated azo-N, followed by walking of second H from adjacent C2 to the other N of the azo moiety of the ligand skeleton. The substituted quinazolin-4(3H)-ones formed *via* catalytic dehydrogenation is then released and the coordinated hydrazido moiety is converted back to azo to regenerate the active catalyst and the catalytic cycle continues (Scheme 4.10).

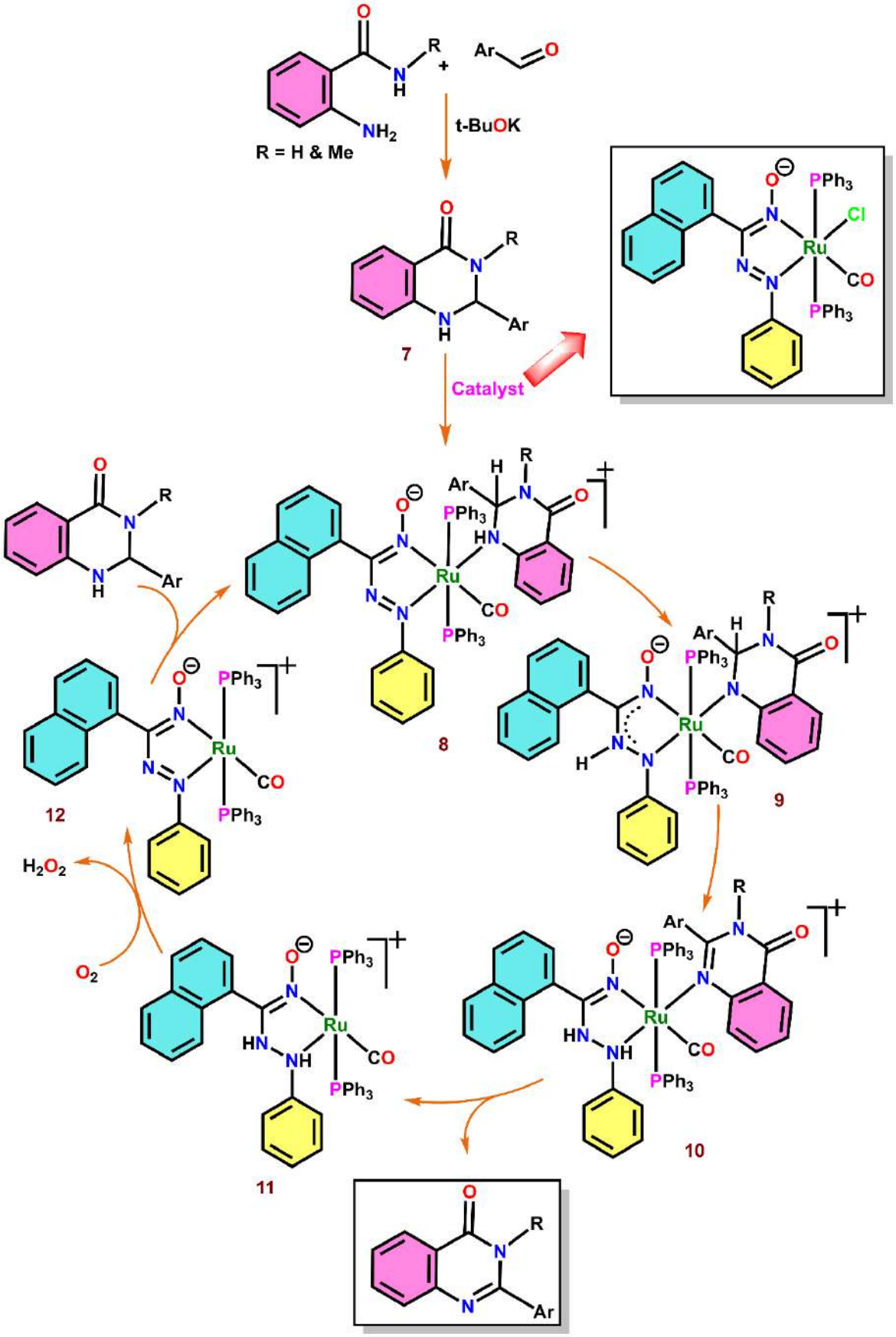

Scheme 4.10: Plausible mechanism of final product formation

4.3 Conclusion

In this work, an air- and moisture-stable ruthenium(II) complex *trans*-[Ru(NpL)(CO)Cl(PPh_3)$_2$], **2** has been synthesized and characterized by spectral, electrochemical, X-ray diffraction studies and the results have further been supplemented by theoretical scrutiny. It serves as a good pre-catalyst for dehydrogenative functionalization of a wide range of benzyl alcohols to quinazolin-4(3H)-ones via condensation with diverse o-amino benzamides as well as N-substituted benzamides under aerobic conditions. We have explored the underlying catalytic pathway where the azo moiety in the coordinated ligand skeleton plays a crucial role in dehydrogenative coupling although the metal centre remains redox inert during the entire course. The mechanism has been further substantiated by theoretical study, where dehydrogenation of benzyl alcohols to benzaldehydes have been ascertained by considering all the possible pathways. The calculated reaction free energies point towards the HAT from alcoholic-OH to the coordinated azo-N linked to phenyl group, followed by transfer of benzylic-H to the other N centre of azo moiety. Therefore, the more favourable dehydrogenation reaction pathway is via 1 → 2 → 4 → 5 → 6 rather than 1 → 2 → 3 → 5 → 6. Subsequently, the aldehydes undergo condensation with o-amino benzamides/ N-substituted benzamides under aerobic conditions to form 2,3-dihydro-2-arylquinazolin-4(1H)-one in the presence of t-BuOK which further catalytically transformed into wide varieties of quinazolin-4(3H)-ones. Notably, this methodology is promising since it has the following advantages over earlier catalytic protocols: low catalyst loading, short duration and low reaction temperature.

4.4 Experimental Section

4.4.1 General Information

All the reactions reported in this work were performed in aerobic condition. All the necessary reagents and solvents were used immediately without any further manipulation. Phenyl

hydrazine, 1-naphthaldehyde were purchased from TCI Chemical (India) Pvt. Ltd. Triphenylphosphine (PPh_3) was taken from Sigma-Aldrich. Silica gel (60−120 mesh) taken from Merck was used for column chromatographic separation of the products. Ruthenium trichloride ($RuCl_3$. xH_2O) was received from Arora-Matthey (India) Ltd. n-Butyl nitrite was synthesised according to literature procedure.[20]

4.4.2 Synthesis of ligands

The ligand **1** was synthesized according to previously described method.[20]

(E)-naphthalen-1-yl((E)-phenyldiazenyl)methanone oxime: Orange solid, Yield: 850 mg (77%). HRMS; [M + H] m/z = 276.1158 (calcd 276.1137); FT-IR/cm^{-1} υ =, 3165 (υ_{O-H}), 1450 ($\upsilon_{N=N}$), 1048 (υ_{N-O}); ^1H NMR (400 MHz, DMSO): δ 12.70 (s, 1H), 8.00 (t, *J* = 8.4 Hz, 2H), 7.67 – 7.56 (m, 3H), 7.56 – 7.43 (m, 5H), 7.37 – 7.29 (m, 2H). $^{13}C\{^1H\}$ NMR (101 MHz, DMSO): δ 166.89, 151.98, 132.80, 131.80, 129.93, 129.35, 128.88, 128.33, 128.24, 126.97, 126.50, 125.96, 125.22, 125.11, 122.39.

4.4.3 Synthesis of complex *trans*-[Ru(NpL)(CO)Cl(PPh_3)$_2$] (2)

The diarylazooxime ligand (**1**) (28 mg, 0.1 mmol, 1equiv.**)** was dissolved in 25 ml of reagent grade toluene in 100 ml round bottom flask which is equipped with a magnetic stir bar. The ruthenium complex, [RuH(CO)Cl(PPh_3)$_3$] (95 mg, 0.1 mmol, 1equiv.) was added to the above solution and kept in stirring condition for 7 h at room temperature. The dark purple red coloured solution was then evaporated to dryness under reduced pressure. The obtained residue was purified by column chromatography using silica gel (60-120 mesh) and toluene/acetonitrile mixture was used as eluent. The desired single crystals of complex **2** for X-Ray diffraction study were obtained through solvent diffusion method.

***trans*-[Ru(NpL)(CO)Cl(PPh_3)$_2$] (2):** Dark purple red coloured crystalline solid. Yield: 62 mg (66%). HRMS: $[M]^+$ m/z = 964.1989 (calcd 964.1563); FT-IR/cm^{-1} υ = 1964 ($\upsilon_{C=O}$), 1433

($\upsilon_{N=N}$), 1090 (υ_{N-O}), 511 (υ_{Ru-P}) ; ^{1}H NMR (300 MHz, $CDCl_3$): δ 7.78 (dd, J = 8.2, 5.3 Hz, 2H), 7.63 – 7.45 (m, 12H), 7.41 – 7.18 (m, 21H), 7.11 – 6.95 (m, 3H), 6.94 – 6.77 (m, 3H), 6.24 (d, J = 7.1 Hz, 1H). $^{13}C\{^{1}H\}$ NMR (101 MHz, $CDCl_3$): δ 168.06, 154.94, 134.63, 134.57, 134.52, 134.16, 133.70, 131.56, 131.04, 130.82, 130.59, 130.31, 130.02, 129.02, 128.84, 128.72, 128.64, 128.31, 128.22, 128.18, 128.13, 127.80, 127.32, 126.12, 126.03, 125.37, 124.96, 122.86. $^{31}P\{^{1}H\}$ NMR (121 MHz, $CDCl_3$): δ 21.34.

4.4.4 Mercury Poisoning Test

To a mixture of *o*-aminobenzamide (**3a)** (272 mg, 2.0 mmol, 1 equiv.), benzyl alcohol (**4a**) (238 mg, 2.2 mmol), t-BuOK (224 mg, 2.0 mmol, 1 equiv.), catalyst **2** (0.2 mg, 0.01 mol%) taken in a 20 ml round bottomed flask containing 5 ml toluene along with a magnetic stir bar, 50 equiv. of mercury (738 mg) was added under open air atmosphere. The resulting mixture was heated at 85°C for 6h under stirring condition. After the completion of reaction organic part was extracted with EtOAc and purified by column chromatography using hexane/EtOAc (3:1 v/v). The isolated yield of the desired product (**5aa**) was 89%. The similar procedure was applied for the reaction of **6a** and **4a**.

4.4.5 Detection of hydrogen peroxide (H_2O_2) during Ru catalysed dehydrogenation of benzyl alcohol

During the dehydrogenation of benzyl alcohol, the formation of H_2O_2 was detected by means of spectrophotometrically following the steady growth of the characteristic absorption band for I_3^- at 350 nm. The reaction between benzyl alcohol (**4a**) and catalyst 2 was carried out under open air condition in 25 mL oven-dried round bottom flask containing 2 mmol of **4a** and 0.01 mol% (0.2 mg) Catalyst **2**, 2 mmol (112 mg) of t-BuOK in 5 mL of dry toluene. Then reaction mixture was heated under stirring condition at 85°C for 6 h. After the completion of reaction 15 mL of water was added to the reaction mixture, and the whole solution was extracted two times with CH_2Cl_2. The aqueous part was then acidified with dilute H_2SO_4 up to pH 2 to prevent

further oxidation. Thereafter, 1 mL of a 10% KI solution and few drops of 3% solution of $(NH4)_2MoO_4$ were added. As a result, H_2O_2 oxidizes I^- to I_2, which reacts with excess I^- to produce I_3^- in accordance with the following chemical steps:

A. $H_2O_2 + 2I^- + 2H^+ \rightarrow 2H_2O + I_2$;

B. $I_2(aq) + I- \rightarrow I_3^-$.

4.4.6 General Method for Synthesis of 2-substituted and 2,3-disubstituted quinazolinone derivatives

A mixture of catalyst **2** (0.01 mol %), t-BuOK (1 equiv.), substituted 2-aminobenzamide/ disubstituted 2-aminobenzamide (1.0 mmol, 1 equiv.), and primary alcohol (1.1 mmol) and 5 mL of dry toluene was added to the oven dried 25 ml round bottom flask. Then the reaction mixture was placed in a preheated oil bath at required temperature along with a reflux condenser. The reaction was continued for designated time under open air atmosphere. After completion, the reaction mixture was evaporated to dryness under vacuum in order to remove solvent and volatile impurities. The residue was subjected to column chromatography using silica gel (60-120 mesh) and Hexane/EtOAc (3:1 v/v) mixture as eluent.

4.4.7 General Method for Synthesis of 2-substituted and 2,3-disubstituted quinazolinone derivatives:

A mixture of catalyst **2** (0.01 mol %), t-BuOK (1 equiv.), N-substituted 2-aminobenzamide (1.0 mmol, 1 equiv.), and primary alcohol (1.1 mmol) and 5 mL of dry toluene was added to the oven dried 25 ml round bottom flask. Then the reaction mixture was placed in a preheated oil bath at 80°C along with a reflux condenser. The reaction was continued for 5 h under open air atmosphere. After completion, the reaction mixture was evaporated to dryness under vacuum in order to remove solvent and volatile impurities. The residue was subjected to column chromatography using silica gel (60-120 mesh) and Hexane/EtOAc (3:1 v/v) mixture as eluent.

4.5 References

[1] (a) A. R. Katritzky, C. W. Rees, E. F. V. Scriven, *Comprehensive Heterocyclic Chemistry II. Eds*, Elsevier: Oxford, **1996**. (b) T. Nomura, Z. Z. Ma, Y. Hano, Y. J. Chen, *Heterocycles*, **1997**, *46*, 541−546. (c) J. A. Joule, K. Mills, *Heterocyclic Chemistry*, Blackwell: Oxford UK, 5th Edn. **2010**. (d) A. A. Al-Mulla, *Pharma Chem.*, **2017**, *9*, 141−147.

[2] Reviews on quinazolinone alkaloid: (a) J. P. Michael, *Nat. Prod. Rep.*, **2003**, *20*, 476−493. (b) J. P. Michael, *Nat. Prod. Rep.*, **2004**, *21*, 650−668. (c) D. J. Connolly, D. Cusack, T. P. O'Sullivan, P. J. Guiry, *Tetrahedron*, **2005**, *61*, 10153−10202. (d) J. P. Michael, *Nat. Prod. Rep.*, **2005**, *22*, 627−646. (e) S. B. Mhaske, N. P. Argade, *Tetrahedron*, **2006**, *62*, 9787−9826. (f) L. He, H. Li, J. Chen, X. F. Wu, *RSC Adv.*, **2014**, *4*, 12065−12077.

[3] (a) I. Khan, A. Ibrar, N. Abbas, A. Saeed, *Eur. J. Med. Chem.*, **2014**, *76*, 193−244. (b) I. M. Abdou, S. S. Al-Neyadi, *Heterocycl. Commun.*, **2015**, *21*, 115−132. (c) U. A. Kshirsagar, *Org. Biomol. Chem.*, **2015**, *13*, 9336−9352. (d) I. Khan, A. Ibrar, W. Ahmed, A. Saeed, *Eur. J. Med. Chem.*, **2015**, *90*, 124−169. (e) X. F. Shang, S. L. Morris-Natschke, Y. Q. Liu, X. Guo, X. S. Xu, M. Goto, J. Li, G. Z. Yang, K. H. Lee, *Medicinal Research Rev.*, **2018**, *38*, 775−828. (f) M. Bhat, S. L. Belagali, S.V. Mamatha, B.K. Sagar, E. Vijaya Sekhar, *Studies in Natural Products Chemistry*, **2021**, *71*, 185−219.

[4] (a) V. Alagarsamy, S. Meena, K.V. Ramaseshu, V.R. Solomon, T.D. Kumar, K. Thirumurugan, *Chem Biol Drug Des*, **2007**, *70*, 254−260. (b) A. A.-M. Abdel-Aziz, L. A. Abou-Zeid, K. E. H. ElTahir, M. A. Mohamed, M. A. A. El-Enin, A. S. El-Azab, *Bioorganic & Medicinal Chemistry*, **2016**, *16*, 3818−3828. (c) S. K. Verma, R. Verma, K.P. Rakesh, D. C. Gowda, *European Journal of Medicinal Chemistry Reports*, **2022**, *6*, 100087−100101. (d) S. K. Wahan, B. Sharma, P. A. Chawla, *J. Heterocyclic Chemistry*, **2022**, *59*, 239−257.

[5] (a) S. Farooq, A. Mazhar, I. U. Haq, N. Ullah, *Arabian J. Chem.*, **2020**, *12*, 9145−9165. (b) O. P. Osarodion, *GSC Biological and Pharmaceutical Sciences*, **2020**, *11*, 212−220. (c) P. R. Patel, H. Joshi, U. Shah, M. Bapna, B. Patel, *Asian Pacific Journal of Health Sciences*, **2021**, *8*, 61−66.

[6] (a) S. Poudapally, S. Battu, L. R. Velatooru, M. S. Bethu, J. V. Rao, S. Sharma, S. Sen, N. Pottabathini, V. B. R. Iska, V. Katangoor, *Bioorganic & Medicinal Chemistry Letters*, **2017**, *27*, 1923−1928. (b) K.P. Rakesh, H.K. Kumara, H.M. Manukumar, D. C. Gowda, *Bioorganic Chemistry*, **2019**, *87*, 252−264. (c) S. Gatadi, G. Pulivendala, J. Gour, S. Malasala, S. Bujji, R.

Parupalli, M. Shaikh, C. Godugu, S. Nanduri, *J. Mol. Struct.*, **2020**, *1200*, 127097−127109. (d) A. A. Noser, M. E. Naggar, T. Donia, A. H. Abdelmonsef, *Molecules*, **2020**, *25*, 4780−4799. [7] (a) M. A. Mohamed, R. R. Ayyad, T. Z. Shawer, A. A. M. Abdel-Aziz, A. S. El-Azab, *European Journal of Medicinal Chemistry*, **2016**, *112*, 106−113. (b) W. Dohle, F. L. Jourdan, G. Menchon, A. E. Prota, P. A. Foster, P. Mannion, E. Hamel, M. P. Thomas, P. G. Kasprzyk, E. Ferrandis, M. O. Steinmetz, M. P. Leese, B. V. L. Potter, *J. Med. Chem.*, **2018**, *61*, 1031–1044. (c) A. I. Khodair, M. A. Alsafi, M. S. Nafie, *Carbohydrate Research*, **2019**, *486*, 107832−107844. (d) H. S. A. ElZahabi, M. S. Nafie, D. Osman, N. H. Elghazawy, D. H. Soliman, A. A. H. EL-Helby, R. K. Arafa, *European Journal of Medicinal Chemistry*, **2021**, *222*, 113609−113624.

[8] (a) V. Alagarsamy, U. S. Pathak, *Bioorganic & Medicinal Chemistry*, **2007**, *15*, 3457−3462. (b) K. Magyar, L. Deres, K. Eros, K. Bruszt, L. Seress, J. Hamar, K. Hideg, A. Balogh, F. Gallyas Jr., B. Sumegi, K. Toth, R. Halmosi, *Biochimica et Biophysica Acta (BBA) - Molecular Basis of Disease*, **2014**, *1842*, 935−944. (c) R. Venkatesh, S. Kasaboina, H. K. Gaikwad, S. Janardhan, R. Bantu, L. Nagarapu, G. N. Sastry, S. K. Banerjee, *European Journal of Medicinal Chemistry*, **2015**, *96*, 22−29. (d) U. Chatturong, H. Martin, P. Totoson, K. Ingkaninan, P. Temkitthawon, S. Sermsenaphorn, T. Somarin, A. Konsue, M. P. Gleeson, C. Demougeot, K. Chootip, *Vascular Pharmacology*, **2022**, *147*, 107111−107119. (e) U. Chatturong, K. Chootip, H. Martin, M. Tournier-Nappey, K. Ingkaninan, P. Temkitthawon, S. Sermsenaphorn, T. Somarin, A. Konsue, M. P. Gleeson, P. Totoson, C. Demougeot, *European Journal of Pharmacology*, **2023**, *953*, 175829−175835.

[9] (a) P. Singla, V. Luxami, K. Paul, *Journal of Photochemistry and Photobiology B: Biology*, **2017**, *168*, 156−164. (b) T. S. Patel, S. F. Vanparia, U. H. Patel, R. B. Dixit, C. J. Chudasama, B. D. Patel, B. C. Dixit, *European Journal of Medicinal Chemistry*, **2017**, *129*, 251−265. (c) A. H. Romero, N. Rodríguez, H. Oviedo, *Bioorganic Chemistry*, **2019**, *83*, 145−153. (d) Y. Li, Y. Ouyang, H. Wu, P. Wang, Y. Huang, X. Li, H. Chen, Y. Sun, X. Hu, X. Wang, G. Li, Y. Lu, C. Li, X. Lu, J. Pang, T. Nie, X. Sang, L. Dong, W. Dong, J. Jiang, X. You, *European Journal of Medicinal Chemistry*, **2022**, *228*, 113979–113995. (e) Z. Zhu, C. Chen, J. Zhang, F. Lai, J. Feng, G. Wu, J. Xia, W. Zhang, Z. Han, C. Zhang, Q. Yang, Y. Wang, B. Liu, T. Li, S. Wu, *J. Med. Chem.*, **2023**, *66*, 13946–13967.

[10] (a) X. Qin, Y. Lv, P. Liu, Z. Li, L. Hu, C. Zeng, L. Yang, *Bioorganic & Medicinal Chemistry Letters*, **2016**, *26*, 1571–1575. (b) T. O. Mirgany, A. N. Abdalla, M. Arifuzzaman,

A. F. M. Motiur Rahman, H. S. Al-Salem, *Journal of Enzyme Inhibition and Medicinal Chemistry*, **2021**, *36*, 2055–2067. (c) M. Mortazavi, M. Divar, T. Damghani, F. Moosavi, L. Saso, S. Pirhadi, M. Khoshneviszadeh, N. Edraki, O. Firuzi, *Frontiers in Chemistry*, **2022**, *10*, 1–21. (d) M. F. Zayed, *Sci. Pharm.*, **2023**, *91*, 18–51.

[11] (a) O. V. Larionov, D. Stephens, A. Mfuh, G. Chavez, *Org. Lett.*, **2014**, *16*, 864−867. (b) K. D. Kim, J. H. Lee, *Org. Lett.*, **2018**, *20*, 7712−7716. (c) W. Jo, S. Y. Baek, C. Hwang, J. Heo, M. H. Baik, S. H. Cho, *J. Am. Chem. Soc.*, **2020**, *142*, 13235−13245. (d) L. Biesen, T. J. J. Muller, *Adv. Synth. Catal.*, **2021**, *363*, 980−1006.

[12] (a) R. Cheng, T. Guo, D. Z. Negrerie, Y. Du, K. Zhao, *Synthesis*, **2013**, *45*, 2998−3006. (b) S. Laclef, M. Harari, J. Godeau, I. S. Afonso, L. Bischoff, C. Hoarau, V. Levacher, C. Fruit, T. Besson, *Org. Lett.*, **2015**, *17*, 1700−1703. (c) L. Åkerbladh, L. R. Odell, *J. Org. Chem.*, **2016**, *81*, 2966−2973. (d) A. Clemenceau, Q. Wang, J. Zhu, *Org. Lett.*, **2017**, *19*, 4872−4875. (e) S. Y. Lee, C. H. Cheon, *J. Org. Chem.*, **2018**, *83*, 13036−13044. (f) L. C. Wang, S. Du, Z. Chen, X. F. Wu, *Org. Lett.*, **2020**, *22*, 5567−5571.

[13] (a) S. Das, S. Sinha, D. Samanta, R. Mondal, G. Chakraborty, P. Brandaõ, N. D. Paul, *J. Org. Chem.*, **2019**, *84*, 10160–10171. (b) S. Sinha, S. Das, R. Mondal, S. Mandal, N. D. Paul, *Dalton Trans.*, **2020**, *49*, 8448–8459. (c) R. Mondal, G. Chakraborty, A. K. Guin, S. Pal, N. D. Paul, *Tetrahedron*, **2021**, *100*, 132479−132488. (d) D. Pal, A. Mondal, D. Srimani, *Catal. Sci. Technol.*, **2022**, *12*, 3202–3208. (e) S. Mondal, S. Chakraborty, S. Khanra, S. Chakraborty, S. Pal, P. Brandão, N. D. Paul, *J. Org. Chem.*, **2024**, *89*, 5250–5265.

[14] (a) H. Hikawa, Y. Ino, H. Suzuki, Y. Yokoyama, *J. Org. Chem.*, **2012**, *77*, 7046−7051. (b) A. J. A. Watson, A. C. Maxwell, J. M. J. Williams, *Org. Biomol. Chem.*, **2012**, *10*, 240–243. (c) J. B. Peng, H. Q. Geng, W. Wang, X. Qi, J. Ying, X. F. Wu, *Journal of Catalysis*, **2018**, *365*, 10–13. (d) Z. L. Ren, H. H. Kong, W. T. Lu, M. Sun, M. W. Ding, *Tetrahedron*, **2018**, *74*, 184–193. (e) W. Zhang, C, Meng, Y. Liu, Y. Tang, F. Li, *Adv. Synth. Catal.*, **2018**, *360*, 3751–3759. (f) A. Ravindran N E, M. Yadav, M. M. Tamizh, N. Bhuvanesh, S. Sarkar, R. Karvembu, *Asian J. Org. Chem.*, **2023**, *12*, e202200675.

[15] (a) J. Zhou, J. Fang, J. Org. Chem., **2011**, *76*, 7730–7736. (b) F, Li, L. Lua, J. Ma, *Org. Chem. Front.*, **2015**, *2*, 1589–1597.

[16] (a) S. Pramanik, S. Roy, T. Ghorui, S. Ganguly, K. Pramanik, *Inorg. Chem.*, **2016**, *55*, 1461–1468. (b) S. Roy, S. Pramanik, S. C. Patra, B. Adhikari, A. Mondal, S. Ganguly, K.

Pramanik, *Inorg. Chem.*, **2017**, *56*, 12764–12774. (c) S. Dinda, S. Roy, S. C. Patra, S. Bhandary, K. Pramanik, S. Ganguly, *New J. Chem.*, **2020**, *44*, 3737–3747. (d) R. Mukherjee, *Inorg. Chem.*, **2020**, *59*, 12961−12977. (e) S. Dinda, S. Pramanik, J. Basu, S. C. Patra, K. Pramanik, S. Ganguly, *Dalton Trans.*, **2022**, *51*, 10121–10135. (f) S. Halder, S. Naskar, D. Jana, G. Kanrar, K. Pramanik, S. Ganguly, *New J. Chem.*, **2024**, *48*, 8181–8194.

[17] (a) H. Fuse, H. Mitsunuma, M. Kanai, *J. Am. Chem. Soc.*, **2020**, *142*, 4493–4499. (b) P. Chandra, T. Ghosh, N. Choudhary, A. Mohammad, S. M. Mobin, *Coord. Chem. Rev.*, **2020**, *411*, 213241–213299. (c) A. K. Guin, R. Mondal, G. Chakraborty, S. Pal, N. D. Paul, *J. Org. Chem.*, **2022**, *87*, 7106–7123. (d) A. A. Swatiputra, D. Mukherjee, S. Dinda, S. Roy, K. Pramanik, S. Ganguly, *Dalton Trans.*, **2023**, *52*, 15627–15646 and references therein. (e) M. Khatua, B. Goswami, A. Devi, Kamal, S. Hans, S. Samanta, *Inorg. Chem.*, **2024**, *63*, 9786–9800. (f) Kamal, S. Samanta, *J. Org. Chem.*, **2024**, *89*, 1910−1926.

[18] (a) Z. Shao, Y. Wang, Y. Liu, Q. Wang, X. Fub, Q. Li, *Org. Chem. Front.*, **2018**, *5*, 1248–1256. (b) T. Mori, C. Ishii, M. Kimura, *Org. Process Res. Dev.*, **2019**, *23*, 1709–1717. (c) M. Trincado, J. Bösken, H. Grützmacher, *Coord. Chem. Rev.*, **2021**, *443*, 213967–214000. (d) A. M. Pandey, N. K. Digrawal, N. Mohanta, A. B. Jamdade, M. B. Chaudhari, G. S. Bisht, B. Gnanaprakasam, *J. Org. Chem.*, **2021**, *86*, 8805–8828. (e) M. Maji, D. Panja, I. Borthakur, S. Kundu, *Org. Chem. Front.*, **2021**, *8*, 2673–2709. (f) S. Nandi, I. Borthakur, K. Ganguli, S. Kundu, *Organometallics*, **2023**, *42*, 1793−1802. (g) S. Bansal, B. Punji, *ChemCatChem*, **2024**, *16*, 1–11.

[19] (a) J. Rana, R. Babu, M. Subaramaniana, E. Balaraman, *Org. Chem. Front.*, **2018**, *5*, 3250–3255. (b) B. C. Roy, K. Ganguli, S. A. Samim, S. Kundu, *Asian J. Org. Chem.*, **2021**, *10*, 1218–1232. (c) S. Yin, Q. Zheng, J. Chen, T. Tu, *Journal of Catalysis*, **2022**, *408*, 165–172. (d) I. Borthakur, S. Kumari, S. Kundu, Dalton Trans., **2022**, *51*, 11987–12020. (e) I. Borthakur, A. Sau, S. Kundu, *Coord. Chem. Rev.*, **2022**, *451*, 214257–214292.

[20] (a) K. C. Kalia, A. Chakravorty, *Inorg. Chem.*, **1968**, *7*, 2016–2020. (b) K. C. Kalia, A. Chakravorty, *J. Org. Chem.*, **1970**, *35*, 2231–2234.

[21] (a) D. Sengupta, R. Bhattacharjee, R. Pramanick, S. P. Rath, N. Saha Chowdhury, A. Datta and S. Goswami, *Inorg. Chem.*, **2016**, *55*, 9602–9610. (b) S. Sinha, S. Das, R. Sikari, S. Parua, P. Brandaõ, S. Demeshko, F. Meyer, N. D. Paul, *Inorg. Chem.*, **2017**, *56*, 14084–14100. (c) S. P. Rath, D. Sengupta, P. Ghosh, R. Bhattacharjee, M. Chakraborty, S. Samanta, A. Datta, S.

Goswami, *Inorg. Chem.*, **2018**, *57*, 11995–12009. (d) S. Das, S. Sinha, D. Samanta, R. Mondal, G. Chakraborty, P. Brandaõ, N. D. Paul, *J. Org. Chem.*, **2019**, *84*, 10160–10171.

[22] (a) S. C. Mandal, K. S. Rawat, B. Pathak, Phys. *Chem. Chem. Phys*., **2019**, *21*, 3932–3941. (b) K. A. Moltved, K. P. Kepp, *ChemPhysChem*, **2019**, *20*, 3210–3220.

4.6 Appendix

4.6.1 NMR data of all synthesized compounds

***2-phenylquinazolin-4(3H)-one (5aa)[9]*:** Yield: 202 mg (91%), White solid. ^{1}H NMR (300

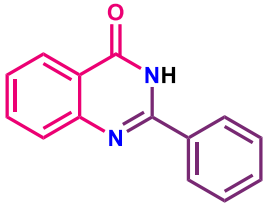

MHz, DMSO): δ 12.55 (s, 1H), 8.25 – 8.12 (m, 3H), 7.90 – 7.81 (m, 1H), 7.75 (dd, *J* = 8.3, 1.3 Hz, 1H), 7.61 – 7.50 (m, 4H). ^{13}C{^{1}H} NMR (75 MHz, DMSO): δ 162.24, 152.32, 148.73, 134.59, 132.72, 131.39, 128.60, 127.76, 127.50, 126.58, 125.86, 120.98.

***2-(o-tolyl)quinazolin-4(3H)-one (5ab)[9]*:** Yield: 210 mg (89%), White solid. ^{1}H NMR (300

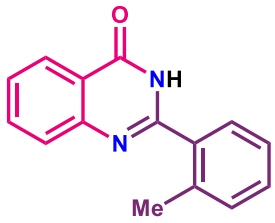

MHz, DMSO): δ 12.48 (brs, 1H), 8.18 (dd, *J* = 7.9, 1.5 Hz, 1H), 7.85 (ddd, *J* = 8.5, 7.1, 1.6 Hz, 1H), 7.70 (dd, *J* = 8.2, 1.2 Hz, 1H), 7.54 (ddd, *J* = 15.1, 7.1, 1.4 Hz, 2H), 7.48 – 7.41 (m, 1H), 7.39 – 7.30 (m, 2H), 2.39 (s, 3H). ^{13}C{^{1}H} NMR (75 MHz, DMSO): δ 161.78, 154.51, 136.12, 134.51, 134.06, 130.54, 129.96, 129.14, 127.10, 126.69, 125.81, 125.70, 120.93, 19.54.

***6-chloro-2-phenylquinazolin-4(3H)-one (5ac)[9]*:** Yield: 190 mg (74%), White crystalline solid.

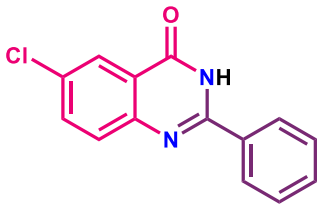

^{1}H NMR (300 MHz, DMSO): δ 12.69 (s, 1H), 8.23 – 8.13 (m, 2H), 8.09 (d, *J* = 2.5 Hz, 1H), 7.87 (dd, *J* = 8.7, 2.5 Hz, 1H), 7.77 (d, *J* = 8.7 Hz, 1H), 7.67 – 7.50 (m, 3H). ^{13}C{^{1}H} NMR (75 MHz, DMSO): δ 161.44, 152.97, 147.46, 134.73, 132.52, 131.63, 130.78, 129.71, 128.67, 127.88, 124.91, 122.25.

***2-(m-tolyl)quinazolin-4(3H)-one (5ad)[9]*:** Yield: 208 mg (88%), White solid. ^{1}H NMR (300 MHz, DMSO): δ 12.47 (s, 1H), 8.16 (dd, *J* = 8.0, 1.5 Hz, 1H), 8.07 – 7.93 (m, 2H), 7.84 (ddd, *J* = 8.5, 7.0, 1.6 Hz, 1H), 7.75 (dd, *J* = 8.2, 1.3 Hz, 1H), 7.52 (ddd, *J* = 8.2, 7.0, 1.3 Hz, 1H), 7.47 – 7.38 (m, 2H), 2.41 (s, 3H). ^{13}C{^{1}H} NMR (75 MHz, DMSO): δ 162.21, 152.38, 148.79, 137.92, 134.59, 132.65, 132.01, 128.51, 128.30, 127.50, 126.53, 125.85, 124.90, 121.00, 20.98.

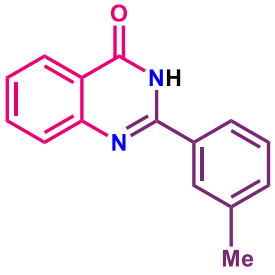

***2-(3-fluorophenyl)quinazolin-4(3H)-one (5ae)[9]*:** Yield: 190 mg (79%), White crystalline solid. ^{1}H NMR (300 MHz, DMSO): δ 12.61 (s, 1H), 8.17 (dd, *J* = 7.9, 1.4 Hz, 1H), 8.09 – 7.98 (m, 2H), 7.86 (ddd, *J* = 8.5, 7.0, 1.6 Hz, 1H), 7.79 – 7.74 (m, 1H), 7.66 – 7.51 (m, 2H), 7.45 (tdd, *J* = 8.5, 2.6, 1.0 Hz, 1H). ^{13}C{^{1}H} NMR (75 MHz, DMSO): δ 163.75, 162.19, 151.10, 148.51, 135.05 (d, *J* = 8.0 Hz), 134.78, 130.82 (d, *J* = 8.2 Hz), 127.67, 127.00, 125.94, 123.99 (d, *J* = 2.8 Hz), 121.16, 118.33 (d, *J* = 21.1 Hz), 114.59 (d, *J* = 23.8 Hz). ^{19}F NMR (282 MHz, DMSO): δ -112.44.

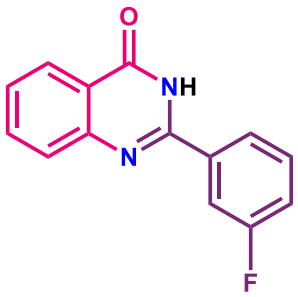

***2-(3-(trifluoromethyl)phenyl)quinazolin-4(3H)-one (5af)[9]*:** Yield: 220 mg (76%), White crystalline solid. ^{1}H NMR (300 MHz, DMSO): δ 12.78 (s, 1H), 8.58 – 8.45 (m, 2H), 8.18 (dd, *J* = 7.9, 1.5 Hz, 1H), 7.97 (d, *J* = 7.9 Hz, 1H), 7.91 – 7.76 (m, 3H), 7.56 (ddd, *J* = 8.1, 6.9, 1.4 Hz, 1H). ^{13}C{^{1}H} NMR (101 MHz, DMSO): δ 162.66, 151.51, 148.87, 135.17, 134.20, 132.23, 130.32, 129.92 (d, *J* = 32.2 Hz), 128.30 (d, *J* = 3.9 Hz), 127.47, 126.36, 124.95 (d, *J* = 4.0 Hz), 123.10, 121.64. ^{19}F NMR (377 MHz, DMSO): δ -61.18.

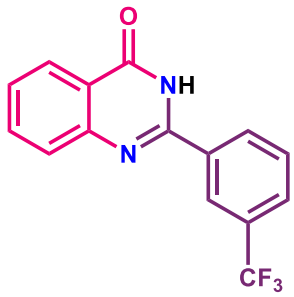

***2-(p-tolyl)quinazolin-4(3H)-one (5ag)[9]*:** Yield: 212 mg (90%), White solid. ^{1}H NMR (300

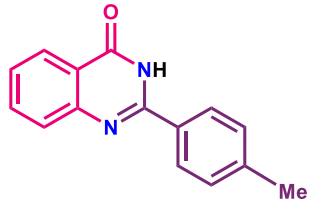

MHz, DMSO): δ 12.48 (s, 1H), 8.20 – 8.06 (m, 3H), 7.83 (ddd, *J* = 8.5, 7.0, 1.6 Hz, 1H), 7.73 (dd, *J* = 8.3, 1.2 Hz, 1H), 7.51 (ddd, *J* = 8.1, 7.0, 1.3 Hz, 1H), 7.36 (d, *J* = 8.0 Hz, 2H), 2.40 (s, 3H). ^{13}C{^{1}H} NMR (101 MHz, DMSO): δ 162.24, 152.21, 148.82, 141.43, 134.56, 129.88, 129.18, 128.59, 127.41, 126.38, 125.82, 120.90, 20.98.

***2-(4-methoxyphenyl)quinazolin-4(3H)-one (5ah)* :** Yield: 214 mg (85%), White crystalline

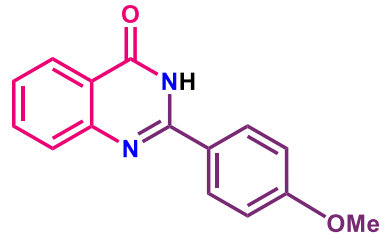

solid. ^{1}H NMR (300 MHz, DMSO): δ 12.42 (s, 1H), 8.25 – 8.09 (m, 3H), 7.82 (ddd, *J* = 8.4, 7.0, 1.6 Hz, 1H), 7.70 (ddd, *J* = 8.2, 6.9, 1.5 Hz, 1H), 7.49 (ddd, *J* = 8.1, 7.0, 1.3 Hz, 1H), 7.15 – 7.04 (m, 2H), 3.85 (s, 3H). ^{13}C{^{1}H} NMR (75 MHz, DMSO): δ 161.92, 151.92, 148.98, 134.63, 131.20, 129.51, 127.97, 127.34, 126.21, 125.88, 124.84, 120.73, 114.06, 55.52.

***2-(4-isopropylphenyl)quinazolin-4(3H)-one (5ai)[9]*:** Yield: 230 mg (87%), White solid. ^{1}H

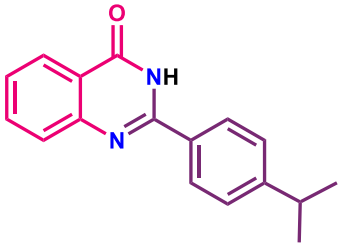

NMR (300 MHz, DMSO): δ 12.49 (s, 1H), 8.15 (td, *J* = 7.4, 1.6 Hz, 3H), 7.83 (t, *J* = 8.4 Hz, 0H), 7.73 (d, *J* = 8.1 Hz, 1H), 7.55 – 7.47 (m, 1H), 7.41 (d, *J* = 8.2 Hz, 2H), 2.97 (hept, *J* = 6.9 Hz, 1H), 1.24 (d, *J* = 6.9 Hz, 6H). ^{13}C{^{1}H} NMR (75 MHz, DMSO): δ 162.29, 152.24, 152.13, 148.87, 134.59, 130.33, 127.85, 127.46, 126.59, 126.42, 125.86, 120.93, 33.40, 23.62.

***2-(4-fluorophenyl)quinazolin-4(3H)-one (5aj)[9]*:** Yield: 194 mg (81%), White solid. ^{1}H NMR

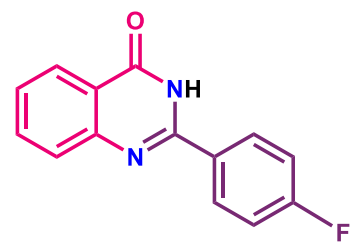

(400 MHz, DMSO): δ 12.58 (s, 1H), 8.31 – 8.21 (m, 2H), 8.16 (dd, *J* = 8.0, 1.6 Hz, 1H), 7.85 (ddd, *J* = 8.5, 7.1, 1.6 Hz, 1H), 7.74 (dd, *J* = 8.3, 1.2 Hz, 1H), 7.53 (ddd, *J* = 8.1, 7.1, 1.2 Hz,

1H), 7.44 – 7.35 (m, 2H). $^{13}C\{^{1}H\}$ NMR (75 MHz, DMSO): δ 162.27, 151.45, 148.61, 134.64, 130.38 (d, *J* = 9.1 Hz), 129.25 (d, *J* = 3.1 Hz), 128.28, 127.40, 126.61, 125.86, 120.87, 115.64 (d, *J* = 21.9 Hz). ^{19}F NMR (282 MHz, DMSO): δ -109.07.

***2-(4-chlorophenyl)quinazolin-4(3H)-one (5ak)[9]*:** Yield: 198 mg (77%), White crystalline solid. ^{1}H NMR (300 MHz, DMSO): δ 12.63 (s, 1H), 8.27 – 8.13 (m, 3H), 7.90 – 7.81 (m, 1H), 7.75 (d, *J* = 8.1 Hz, 1H), 7.68 – 7.60 (m, 2H), 7.58 – 7.50 (m, 1H). $^{13}C\{^{1}H\}$ NMR (75 MHz, DMSO): δ 162.19, 151.36, 148.60, 136.32, 134.70, 131.57, 129.64, 128.71, 127.55, 126.80, 125.89, 121.03.

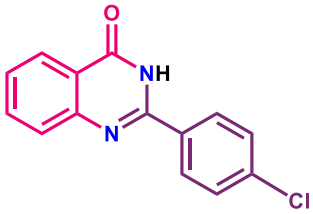

***2-(4-bromophenyl)quinazolin-4(3H)-one (5al)[9]*:** Yield: 223 mg (74%), White solid. ^{1}H NMR (300 MHz, DMSO): δ 12.60 (s, 1H), 8.21 – 8.08 (m, 3H), 7.85 (ddd, *J* = 8.5, 7.0, 1.6 Hz, 1H), 7.79 – 7.71 (m, 3H), 7.57 – 7.45 (m, 1H). $^{13}C\{^{1}H\}$ NMR (75 MHz, DMSO): δ 162.24, 151.55, 148.63, 134.78, 131.70, 129.87, 128.63, 127.59, 126.89, 125.94, 125.30, 121.06.

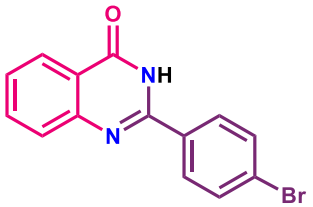

***2-(4-(trifluoromethyl)phenyl)quinazolin-4(3H)-one (5am)[9]*:** Yield: 232 mg (80%), White solid. ^{1}H NMR (300 MHz, DMSO): δ 12.76 (s, 1H), 8.38 (d, *J* = 8.0 Hz, 2H), 8.18 (d, *J* = 7.9 Hz, 1H), 7.93 (d, *J* = 8.0 Hz, 2H), 7.86 (d, *J* = 7.5 Hz, 1H), 7.78 (d, *J* = 8.2 Hz, 1H), 7.57 (t, *J* = 7.4 Hz, 1H). $^{13}C\{^{1}H\}$ NMR (75 MHz, DMSO): δ 162.16, 151.20, 148.42, 136.62, 134.75, 131.33, 130.90, 128.74, 127.67, 127.13, 125.91, 125.61 – 125.40 (m), 121.21. ^{19}F NMR (282 MHz, DMSO): δ -61.34.

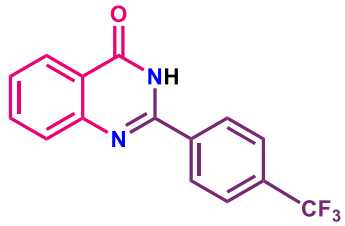

***6-chloro-2-(p-tolyl)quinazolin-4(3H)-one (5an)[9]*:** Yield: 195 mg (72%), White crystalline solid. ^{1}H NMR (300 MHz, DMSO): δ 12.64 (s, 1H), 8.10 (d, *J* = 8.8 Hz, 3H), 7.86 (dd, *J* = 8.7, 2.5 Hz, 1H), 7.75 (d, *J* = 8.7 Hz, 1H), 7.37 (d, *J* = 8.0 Hz, 2H), 2.40 (s, 3H). ^{13}C{^{1}H} NMR (75 MHz, DMSO): δ 161.37, 152.79, 141.75, 134.68, 130.56, 129.63, 129.24, 128.58, 127.78, 126.48, 124.86, 122.13, 21.01.

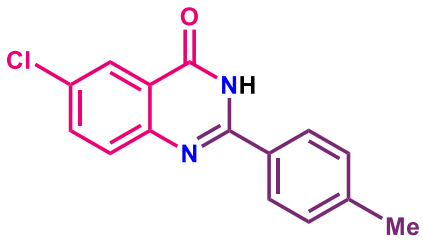

***6-bromo-2-(p-tolyl)quinazolin-4(3H)-one (5ao)[9]*:** Yield: 221 mg (70%), White crystalline solid. ^{1}H NMR (300 MHz, DMSO): δ 12.64 (s, 1H), 8.22 (d, *J* = 2.4 Hz, 1H), 8.09 (d, *J* = 8.2 Hz, 2H), 7.97 (dd, *J* = 8.7, 2.4 Hz, 1H), 7.68 (d, *J* = 8.7 Hz, 1H), 7.36 (d, *J* = 8.1 Hz, 2H), 2.40 (s, 3H). ^{13}C{^{1}H} NMR (75 MHz, DMSO): δ 161.35, 153.01, 141.88, 137.49, 134.70, 129.81, 129.33, 128.05, 127.86, 126.52, 125.93, 118.80, 21.08.

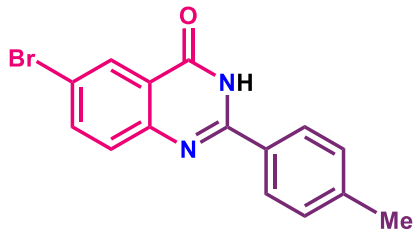

***2-(naphthalen-1-yl)quinazolin-4(3H)-one (5ap)[9]*:** Yield: 234 mg (86%), White crystalline solid. ^{1}H NMR (300 MHz, DMSO): δ 12.69 (s, 1H), 8.23 (dd, *J* = 7.9, 1.5 Hz, 1H), 8.20 – 8.10 (m, 2H), 8.09 – 8.03 (m, 1H), 7.88 (ddd, *J* = 8.5, 7.1, 1.6 Hz, 1H), 7.80 (dd, *J* = 7.1, 1.3 Hz, 1H), 7.74 (dd, *J* = 8.3, 1.2 Hz, 1H), 7.67 (d, *J* = 8.2 Hz, 1H), 7.64 – 7.55 (m, 3H). ^{13}C{^{1}H} NMR (75 MHz, DMSO): δ 161.95, 153.72, 148.76, 134.59, 133.16, 131.75, 130.43, 130.28, 128.38, 127.72, 127.50, 127.12, 126.85, 126.42, 125.90, 125.24, 125.12, 121.26.

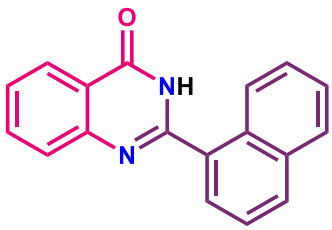

***2-cyclohexylquinazolin-4(3H)-one (5aq)*[9]:** Yield: 187 mg (82%), White solid. ^{1}H NMR (300 MHz, DMSO): δ 12.10 (s, 1H), 8.11 – 8.03 (m, 1H), 7.77 (ddd, *J* = 8.6, 7.1, 1.6 Hz, 1H), 7.63 – 7.55 (m, 1H), 7.46 (ddd, *J* = 8.1, 7.1, 1.2 Hz, 1H), 2.58 (ddd, *J* = 11.7, 8.3, 3.4 Hz, 1H), 1.85 (dd, *J* = 32.4, 12.3 Hz, 4H), 1.73 – 1.50 (m, 3H), 1.40 – 1.24 (m, 3H). ^{13}C{^{1}H} NMR (101 MHz, DMSO): δ 162.37, 161.23, 149.41, 134.71, 129.08, 127.44, 126.38, 126.13, 121.42, 43.30, 30.67, 25.97.

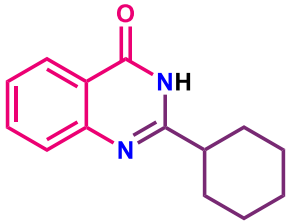

***2-(pyridin-2-yl)quinazolin-4(3H)-one (5ar)*[9]:** Yield: 152 mg (68%), White crystalline solid. ^{1}H NMR (300 MHz, DMSO): δ 11.85 (s, 1H), 8.77 (ddd, *J* = 4.9, 1.7, 0.9 Hz, 1H), 8.47 (dt, *J* = 8.0, 1.1 Hz, 1H), 8.19 (dd, *J* = 7.9, 1.5 Hz, 1H), 8.09 (td, *J* = 7.8, 1.7 Hz, 1H), 7.92 – 7.79 (m, 2H), 7.67 (ddd, *J* = 7.6, 4.8, 1.2 Hz, 1H), 7.58 (ddd, *J* = 8.1, 6.9, 1.5 Hz, 1H). ^{13}C{^{1}H} NMR (101 MHz, DMSO): δ 160.82, 150.00, 148.99, 148.71, 148.39, 138.01, 134.69, 127.67, 127.25, 126.60, 126.11, 122.19, 121.97.

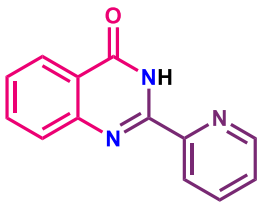

***2-(furan-3-yl)quinazolin-4(3H)-one (5as)*[9]:** Yield: 148 mg (70%), White crystalline solid. ^{1}H NMR (300 MHz, DMSO): δ 12.43 (s, 1H), 8.63 (s, 1H), 8.13 (dd, *J* = 7.8, 1.6 Hz, 1H), 7.90 – 7.76 (m, 2H), 7.67 (dd, *J* = 8.2, 1.2 Hz, 1H), 7.50 (ddd, *J* = 8.2, 7.1, 1.2 Hz, 1H), 7.17 (dd, *J* = 1.9, 0.8 Hz, 1H). ^{13}C{^{1}H} NMR (75 MHz, DMSO): δ 161.95, 148.89, 147.25, 145.10, 144.82, 134.65, 127.12, 126.35, 125.92, 121.49, 121.01, 109.10.

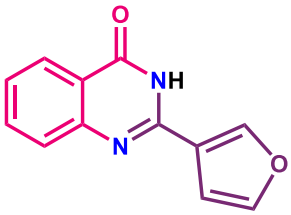

***2-(thiophen-2-yl)quinazolin-4(3H)-one (5at)*[9]:** Yield: 167 mg (73%), White crystalline solid. ^{1}H NMR (400 MHz, DMSO): δ 12.64 (s, 1H), 8.24 (dd, *J* = 3.8, 1.1 Hz, 1H), 8.13 (dd, *J* = 7.9, 1.6 Hz, 1H), 7.87 (dd, *J* = 5.0, 1.1 Hz, 1H), 7.81 (ddd, *J* = 8.5, 7.2, 1.6 Hz, 1H), 7.66 (dd, *J* = 8.3, 1.2 Hz, 1H),

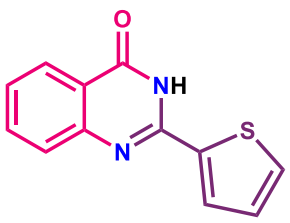

7.49 (ddd, *J* = 8.1, 7.1, 1.2 Hz, 1H), 7.24 (dd, *J* = 5.0, 3.8 Hz, 1H). $^{13}C\{^{1}H\}$ NMR (75 MHz, DMSO): δ 161.84, 148.66, 147.86, 137.39, 134.73, 132.21, 129.43, 128.55, 126.97, 126.37, 126.02, 120.89.

***3-methyl-2-phenylquinazolin-4(3H)-one (7aa)[10]*:** Yield: 220 mg (93%), White crystalline solid. ^{1}H NMR (300 MHz, $CDCl_3$): δ 8.40 – 8.31 (m, 1H), 7.77 (dt, *J* = 3.9, 1.3 Hz, 2H), 7.65 – 7.45 (m, 6H), 3.52 (s, 3H). $^{13}C\{^{1}H\}$ NMR (75 MHz, $CDCl_3$): δ 162.86, 156.27, 147.43, 135.51, 134.45, 130.21, 129.02, 128.12, 127.62, 127.14, 126.82, 120.66, 34.39.

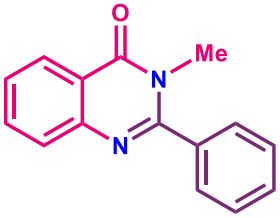

***3-methyl-2-(o-tolyl)quinazolin-4(3H)-one (7ab)*:** Yield: 213 mg (85%), Colourless crystalline solid. ^{1}H NMR (400 MHz, $CDCl_3$): δ 8.36 (d, *J* = 8.5 Hz, 1H), 7.82 – 7.71 (m, 2H), 7.52 (ddd, *J* = 8.3, 6.3, 2.1 Hz, 1H), 7.44 – 7.38 (m, 1H), 7.33 (d, *J* = 3.1 Hz, 3H), 3.35 (s, 3H), 2.26 (s, 3H). $^{13}C\{^{1}H\}$ NMR (75 MHz, $CDCl_3$): δ 162.53, 156.05, 147.41, 135.31, 135.12, 134.41, 130.83, 129.95, 127.54, 127.12, 126.75, 126.59, 120.73, 32.79, 19.17.

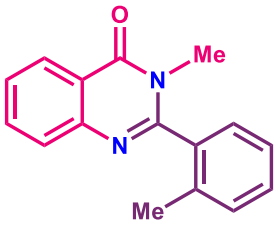

***3-methyl-2-(m-tolyl)quinazolin-4(3H)-one (7ac)*:** Yield: 220 mg (88%), White crystalline solid.^{1}H NMR (300 MHz, $CDCl_3$): δ 8.38 – 8.29 (m, 1H), 7.82 – 7.72 (m, 2H), 7.50 (dq, *J* = 10.1, 3.6 Hz, 1H), 7.45 – 7.25 (m, 4H), 3.50 (d, *J* = 1.4 Hz, 3H), 2.45 (s, 3H). $^{13}C\{^{1}H\}$ NMR (75 MHz, $CDCl_3$): δ 162.80, 156.44, 147.41, 138.96, 135.39, 134.36, 130.87, 128.79, 128.60, 127.55, 127.01, 126.75, 125.04, 120.60, 34.32, 21.53.

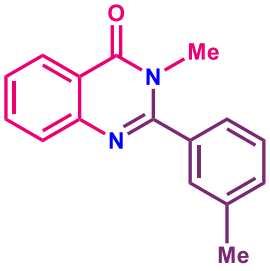

***2-(3-fluorophenyl)-3-methylquinazolin-4(3H)-one (7ad)*:** Yield: 234 mg (92%), White crystalline solid. ^{1}H NMR (300 MHz, $CDCl_3$): δ 8.35 (ddd, *J* = 8.0, 1.5, 0.7 Hz, 1H), 7.85 – 7.70 (m, 2H), 7.60 – 7.47 (m, 2H), 7.42 – 7.19 (m, 3H), 3.52 (s, 3H). ^{13}C{^{1}H} NMR (75 MHz, $CDCl_3$): δ 164.45, 162.65, 161.15, 154.83 (d, *J* = 2.6 Hz), 147.21, 137.29 (d, *J* = 7.7 Hz), 134.58, 130.86 (d, *J* = 8.3 Hz), 127.54 (d, *J* = 15.9 Hz), 126.87, 123.96 (d, *J* = 3.3 Hz), 120.72, 117.36 (d, *J* = 21.0 Hz), 115.65 (d, *J* = 23.2 Hz), 34.30. ^{19}F NMR (282 MHz, $CDCl_3$): δ -110.97.

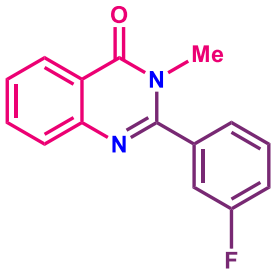

***3-methyl-2-(3-(trifluoromethyl)phenyl)quinazolin-4(3H)-one (7ae)*:** Yield: 271 mg (89%), White crystalline solid. ^{1}H NMR (400 MHz, $CDCl_3$): δ 8.39 – 8.32 (m, 1H), 7.91 (td, *J* = 1.7, 0.8 Hz, 1H), 7.86 – 7.72 (m, 4H), 7.72 – 7.66 (m, 1H), 7.55 (ddd, *J* = 8.1, 6.8, 1.5 Hz, 1H), 3.51 (s, 3H). ^{13}C{^{1}H} NMR (101 MHz, $CDCl_3$): δ 162.57, 154.68, 147.17, 136.21, 134.64, 131.84, 131.53 (d, *J* = 1.6 Hz), 129.62, 127.64, 127.57, 127.02 (q, *J* = 3.7 Hz), 126.90, 125.34 (q, *J* = 3.9 Hz), 122.36, 120.72. 34.29. ^{19}F NMR (377 MHz, $CDCl_3$): δ -62.77.

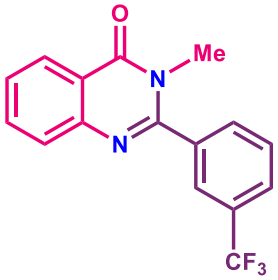

***3-methyl-2-(p-tolyl)quinazolin-4(3H)-one (7af)*:** Yield: 228 mg (91%), White crystalline solid. ^{1}H NMR (300 MHz, $CDCl_3$): δ 8.34 (dt, *J* = 8.0, 1.1 Hz, 1H), 7.83 – 7.71 (m, 2H), 7.59 – 7.44 (m, 3H), 7.35 (d, *J* = 8.0 Hz, 2H), 3.53 (s, 3H), 2.46 (s, 3H). ^{13}C{^{1}H} NMR (75 MHz, $CDCl_3$): δ 162.93, 156.44, 147.42, 140.44, 134.40, 132.58, 129.60, 128.10, 127.54, 127.00, 126.78, 120.56, 34.44, 21.57.

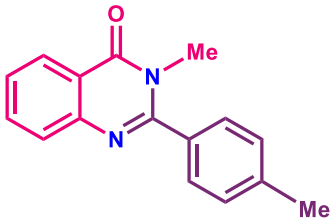

***2-(4-methoxyphenyl)-3-methylquinazolin-4(3H)-one (7ag)*:** Yield: 224 mg (84%), White solid. ^{1}H NMR (300 MHz, $CDCl_3$): δ 8.33 (dt, *J* = 8.0, 1.2 Hz, 1H), 7.78 – 7.74 (m, 2H), 7.59 – 7.46 (m, 3H), 7.08 – 7.01 (m, 2H), 3.89 (s, 3H), 3.55 (s, 3H). ^{13}C{^{1}H} NMR (75 MHz,

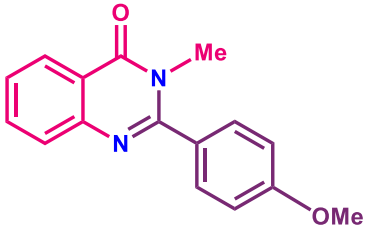

$CDCl_3$): δ 163.02, 161.07, 156.16, 147.41, 134.37, 129.88, 127.77, 127.46, 126.90, 126.76, 120.45, 114.31, 55.58, 34.57.

***2-(4-isopropylphenyl)-3-methylquinazolin-4(3H)-one (7ah)*:** Yield: 239 mg (86%), White

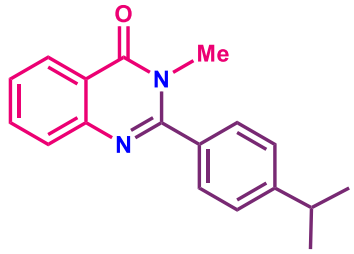

crystalline solid. ^{1}H NMR (300 MHz, $CDCl_3$): δ 8.39 – 8.30 (m, 1H), 7.80 – 7.72 (m, 2H), 7.58 – 7.43 (m, 3H), 7.43 – 7.35 (m, 2H), 3.54 (s, 3H), 3.01 (hept, *J* = 6.8 Hz, 1H), 1.31 (d, *J* = 6.9 Hz, 6H). ^{13}C{^{1}H} NMR (75 MHz, $CDCl_3$): δ 162.94, 156.46, 151.27, 147.46, 134.38, 132.92, 128.16, 127.56, 127.08, 126.97, 126.76, 120.55, 34.47, 34.25, 23.96.

***2-([1,1'-biphenyl]-4-yl)-3-methylquinazolin-4(3H)-one (7ai)*:** Yield: 272 mg (87%), White

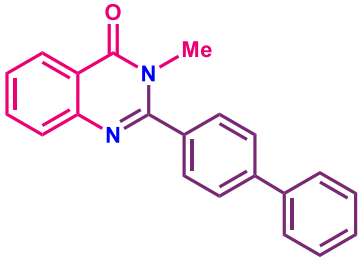

crystalline solid. ^{1}H NMR (300 MHz, $CDCl_3$): δ 8.37 (d, *J* = 7.9 Hz, 1H), 7.81 – 7.75 (m, 3H), 7.66 (dd, *J* = 6.0, 2.0 Hz, 3H), 7.60 (ddt, *J* = 5.5, 3.7, 1.6 Hz, 1H), 7.55 – 7.41 (m, 5H), 3.59 (s, 3H). ^{13}C{^{1}H} NMR (101 MHz, $CDCl_3$): δ 162.91, 156.09, 147.47, 143.17, 140.17, 134.46, 134.23, 129.08, 128.68, 127.68, 127.62, 127.32, 127.17, 127.14, 126.81, 120.62, 34.48.

***2-(4-fluorophenyl)-3-methylquinazolin-4(3H)-one (7aj)*:** Yield: 239 mg (94%), White

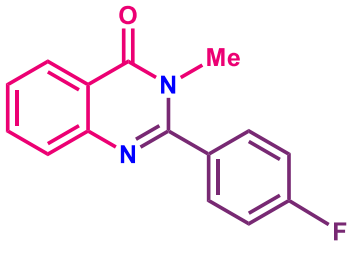

crystalline solid. ^{1}H NMR (300 MHz, $CDCl_3$): δ 8.34 (ddd, *J* = 8.0, 1.5, 0.7 Hz, 1H), 7.82 – 7.72 (m, 2H), 7.65 – 7.57 (m, 2H), 7.53 (ddd, *J* = 8.2, 6.6, 1.7 Hz, 1H), 7.29 – 7.20 (m, 2H), 3.52 (s, 3H). ^{13}C{^{1}H} NMR (101 MHz, $CDCl_3$): δ 164.99, 162.64 (d, *J* = 30.3 Hz), 155.29, 147.29, 134.52, 131.65 (d, *J* = 3.5 Hz), 130.42 (d, *J* = 8.5 Hz), 127.57, 127.27, 126.85, 120.63, 116.19 (d, *J* = 22.2 Hz), 34.40. ^{19}F NMR (282 MHz, $CDCl_3$): δ -109.62.

***2-(4-chlorophenyl)-3-methylquinazolin-4(3H)-one (7ak)*:** Yield: 232 mg 86%, White solid.

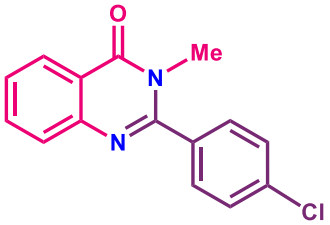

^{1}H NMR (300 MHz, $CDCl_3$): δ 8.34 (dd, *J* = 7.9, 1.5 Hz, 1H), 7.84 – 7.69 (m, 2H), 7.60 – 7.47 (m, 5H), 3.51 (s, 3H). ^{13}C NMR (75 MHz, $CDCl_3$): δ 162.70, 155.16, 147.21, 136.50, 134.56, 133.79, 129.68, 129.30, 127.56, 127.35, 126.84, 120.61, 34.39.

***2-(4-bromophenyl)-3-methylquinazolin-4(3H)-one (7al)*:** Yield: 255 mg (81%), Colourless solid.

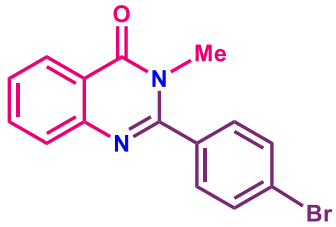

^{1}H NMR (300 MHz, $CDCl_3$): δ 8.34 (dt, *J* = 8.1, 1.2 Hz, 1H), 7.76 (dt, *J* = 4.8, 1.5 Hz, 2H), 7.71 – 7.63 (m, 1H), 7.57 – 7.49 (m, 4H), 3.50 (s, 3H). ^{13}C NMR (75 MHz, $CDCl_3$): δ 162.78, 156.21, 147.34, 134.39, 131.75, 130.15, 129.76, 128.94, 128.07, 127.08, 126.73, 120.56, 34.32.

***3-methyl-2-(4-(trifluoromethyl)phenyl)quinazolin-4(3H)-one (7am)*:** Yield: 274 mg (90%), White crystalline solid.

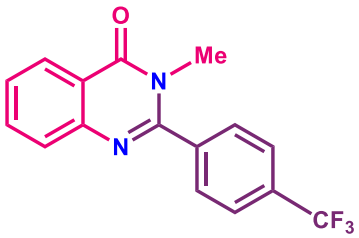

^{1}H NMR (300 MHz, $CDCl_3$): δ 8.37 (ddd, *J* = 8.0, 1.5, 0.7 Hz, 1H), 7.83 (td, *J* = 6.6, 1.1 Hz, 3H), 7.79 – 7.72 (m, 3H), 7.56 (ddd, *J* = 8.2, 6.8, 1.6 Hz, 1H), 3.52 (s, 3H). ^{13}C NMR (75 MHz, $CDCl_3$): δ 162.56, 154.81, 147.17, 138.81, 134.68, 132.31 (d, *J* = 32.9 Hz), 128.77, 127.64 (d, *J* = 4.4 Hz), 126.92, 126.13 (q, *J* = 3.7 Hz), 121.97, 120.75, 34.30. ^{19}F NMR (282 MHz, $CDCl_3$): δ -62.93.

***3-methyl-2-(naphthalen-1-yl)quinazolin-4(3H)-one (7an)*:** Yield: 249 mg (87%), White crystalline solid.

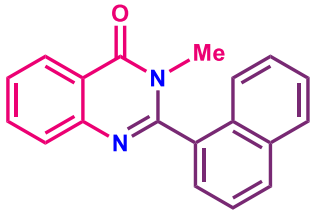

^{1}H NMR (300 MHz, $CDCl_3$): δ 8.48 – 8.39 (m, 1H), 8.08 – 8.00 (m, 1H), 8.00 – 7.95 (m, 1H), 7.84 – 7.78 (m, 2H), 7.66 – 7.49 (m, 6H), 3.34 (s, 3H). ^{13}C NMR (101 MHz, $CDCl_3$): δ 162.58, 155.58, 147.53, 134.56, 133.71, 132.83, 130.42, 130.40, 128.87, 127.76, 127.74, 127.38, 126.92, 126.87, 126.27, 125.56, 124.38, 120.96, 33.23.

***2-(furan-3-yl)-3-methylquinazolin-4(3H)-one (7ao)*:** Yield: 169 mg (75%) , White crystalline solid. ^{1}H NMR (400 MHz, $CDCl_3$): δ 8.31 (ddd, *J* = 8.0, 1.5, 0.7 Hz, 1H), 7.97 (dd, *J* = 1.6, 0.9 Hz, 1H), 7.80 – 7.68 (m, 2H), 7.58 (t, *J* = 1.7 Hz, 1H), 7.49 (ddd, *J* = 8.1, 6.7, 1.6 Hz, 1H), 6.83 (s, 1H), 3.71 (s, 3H). ^{13}C{^{1}H} NMR (75 MHz, $CDCl_3$): δ 162.71, 149.75, 147.43, 143.90, 143.60, 134.44, 127.38, 127.05, 126.84, 121.73, 120.36, 110.84, 33.53.

***3-methyl-2-(thiophen-2-yl)quinazolin-4(3H)-one (7ap)*:** Yield: 184 mg (76%), White solid. ^{1}H NMR (300 MHz, $CDCl_3$): δ 8.36 – 8.27 (m, 1H), 7.80 – 7.69 (m, 2H), 7.62 – 7.42 (m, 3H), 7.18 (dd, *J* = 5.1, 3.7 Hz, 1H), 3.79 (s, 3H). ^{13}C{^{1}H} NMR (75 MHz, $CDCl_3$): δ 162.86, 150.20, 147.30, 137.14, 134.49, 129.93, 129.57, 127.58, 127.54, 127.16, 126.87, 120.24, 34.25.

***2-cyclohexyl-3-methylquinazolin-4(3H)-one (7aq)*:** Yield: 191 mg (79%), White solid. ^{1}H NMR (300 MHz, $CDCl_3$): δ 8.26 (dd, *J* = 8.0, 1.6 Hz, 1H), 7.75 – 7.61 (m, 2H), 7.42 (ddd, *J* = 8.2, 6.8, 1.5 Hz, 1H), 3.68 (s, 3H), 2.83 (tt, *J* = 11.4, 3.1 Hz, 1H), 2.04 – 1.69 (m, 8H), 1.41 (ddd, *J* = 11.5, 8.2, 3.5 Hz, 2H). ^{13}C{^{1}H} NMR (75 MHz, $CDCl_3$): δ 162.96, 160.34, 147.53, 134.02, 127.19, 126.76, 126.26, 120.32, 42.48, 31.16, 30.15, 26.29, 25.91.

***2-ethyl-3-methylquinazolin-4(3H)-one (7ar)*:** Yield: 85 mg (45%), White solid. ^{1}H NMR (300 MHz, $CDCl_3$): δ 8.32 – 8.23 (m, 1H), 7.80 – 7.63 (m, 2H), 7.45 (ddd, *J* = 8.2, 6.8, 1.5 Hz, 1H), 3.66 (s, 3H), 2.90 (q, *J* = 7.4 Hz, 2H), 1.43 (t, *J* = 7.4 Hz, 3H). ^{13}C{^{1}H} NMR (101 MHz, $CDCl_3$): δ 162.68, 158.08, 147.31, 134.24, 126.95, 126.87, 126.50, 120.31, 30.45, 29.03, 11.22.

***3-methyl-2-propylquinazolin-4(3H)-one (7as)*:** Yield: 97 mg (48%), White solid. ^{1}H NMR

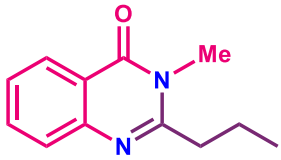

(300 MHz, $CDCl_3$): δ 8.30 – 8.21 (m, 1H), 7.72 (t, *J* = 7.6 Hz, 1H), 7.63 (d, *J* = 6.9 Hz, 1H), 7.43 (t, *J* = 8.2 Hz, 1H), 3.64 (s, 3H), 2.87 – 2.76 (m, 2H), 1.88 (h, *J* = 7.4 Hz, 2H), 1.10 (t, *J* = 7.4 Hz, 3H). ^{13}C{^{1}H} NMR (101 MHz, $CDCl_3$): δ 162.67, 157.14, 147.30, 134.17, 126.91, 126.80, 126.41, 120.28, 37.69, 30.63, 20.41, 14.00.

***3-methyl-2-pentylquinazolin-4(3H)-one (7at)*:** Yield: 131 mg (57%), White solid. ^{1}H NMR

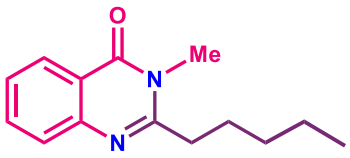

(300 MHz, $CDCl_3$): δ 8.31 – 8.21 (m, 1H), 7.79 – 7.60 (m, 2H), 7.44 (ddd, *J* = 8.1, 6.9, 1.4 Hz, 1H), 3.64 (s, 3H), 2.89 – 2.78 (m, 2H), 1.91 – 1.79 (m, 2H), 1.56 – 1.32 (m, 4H), 0.95 (t, *J* = 7.0 Hz, 3H). ^{13}C{^{1}H} NMR (101 MHz, $CDCl_3$): δ 162.71, 157.40, 147.37, 134.17, 126.93, 126.82, 126.40, 120.29, 35.88, 31.69, 30.67, 26.73, 22.56, 14.10.

***2-heptyl-3-methylquinazolin-4(3H)-one (7au)*:** Yield: 155 mg (60%), White solid. ^{1}H NMR

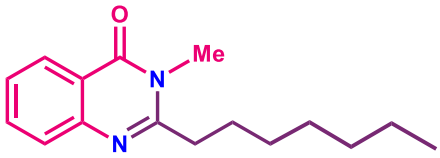

(300 MHz, $CDCl_3$): δ 8.26 (dd, *J* = 8.0, 1.5 Hz, 1H), 7.72 (ddd, *J* = 8.4, 6.9, 1.6 Hz, 1H), 7.64 (dd, *J* = 8.3, 1.4 Hz, 1H), 7.43 (ddd, *J* = 8.1, 6.9, 1.4 Hz, 1H), 3.64 (s, 3H), 2.91 – 2.74 (m, 2H), 1.84 (p, *J* = 7.5 Hz, 2H), 1.51 – 1.42 (m, 2H), 1.32 (tt, *J* = 9.0, 5.3 Hz, 6H), 0.97 – 0.84 (m, 3H). ^{13}C{^{1}H} NMR (75 MHz, $CDCl_3$): δ 162.71, 157.41, 147.35, 134.17, 126.91, 126.80, 126.39, 120.27, 35.91, 31.81, 30.66, 29.48, 29.14, 27.03, 22.71, 14.17.

***3,8-dimethyl-2-phenylquinazolin-4(3H)-one (8aa)*:** Yield: 213 mg (85%), White crystalline

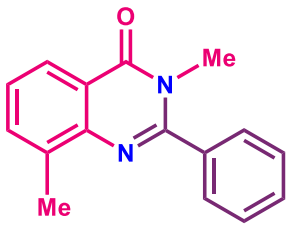

solid. ^{1}H NMR (300 MHz, $CDCl_3$): δ 8.23 – 8.16 (m, 1H), 7.65 – 7.59 (m, 3H), 7.54 (dp, *J* = 5.3, 2.0 Hz, 3H), 7.40 (t, *J* = 7.6 Hz, 1H), 3.53 (s, 3H), 2.62 (s, 3H). ^{13}C{^{1}H} NMR (75 MHz, $CDCl_3$): δ 163.39,

154.69, 146.13, 136.20, 135.90, 134.89, 130.05, 128.75, 128.54, 126.61, 124.39, 120.56, 34.51, 17.43.

3,8-dimethyl-2-(o-tolyl)quinazolin-4(3H)-one (8ab) **:** Yield: 219 mg (83%), White solid. ^{1}H

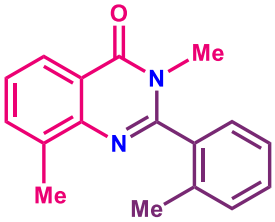

NMR (300 MHz, $CDCl_3$): δ 8.27 – 8.18 (m, 1H), 7.68 – 7.58 (m, 1H), 7.49 – 7.30 (m, 5H), 3.36 (s, 3H), 2.61 (s, 3H), 2.29 (s, 3H). $^{13}C\{^{1}H\}$ NMR (75 MHz, $CDCl_3$): δ 163.09, 154.42, 146.23, 136.26, 135.67, 134.92, 130.84, 129.76, 127.92, 126.64, 126.41, 124.43, 120.77, 32.92, 19.39, 17.62.

3,8-dimethyl-2-(m-tolyl)quinazolin-4(3H)-one (8ac)**:** Yield: 225 mg (85%), White crystalline

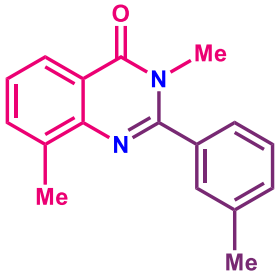

solid. ^{1}H NMR (300 MHz, $CDCl_3$): δ 8.20 (dt, J = 8.0, 1.0 Hz, 1H), 7.66 – 7.57 (m, 1H), 7.49 – 7.30 (m, 5H), 3.52 (s, 3H), 2.63 (s, 3H), 2.48 (s, 3H). $^{13}C\{^{1}H\}$ NMR (75 MHz, $CDCl_3$): δ 163.41, 154.93, 146.20, 138.69, 136.20, 135.88, 134.89, 130.81, 129.06, 128.66, 126.57, 125.55, 124.42, 120.60, 34.50, 21.62, 17.50.

2-(3-fluorophenyl)-3,8-dimethylquinazolin-4(3H)-one (8ad): Yield: 247 mg (92%), White

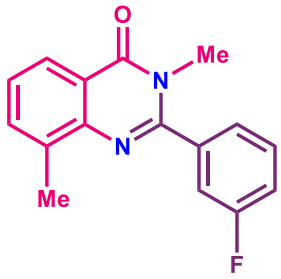

crystalline solid. ^{1}H NMR (300 MHz, $CDCl_3$): δ 8.22 – 8.17 (m, 1H), 7.63 (ddd, J = 7.4, 1.7, 0.9 Hz, 1H), 7.53 (td, J = 8.0, 5.6 Hz, 1H), 7.46 – 7.33 (m, 3H), 7.30 – 7.21 (m, 1H), 3.53 (s, 3H), 2.62 (s, 3H). $^{13}C\{^{1}H\}$ NMR (101 MHz, $CDCl_3$): δ 163.99, 163.22, 161.53, 153.33 (d, J = 2.6 Hz), 145.97, 137.79 (d, J = 7.8 Hz), 136.33, 135.06, 130.54 (d, J = 8.3 Hz), 126.95, 124.49, 124.32 (d, J = 3.2 Hz), 120.69, 117.19 (d, J = 21.0 Hz), 116.03 (d, J = 23.0 Hz), 34.44, 17.42. ^{19}F NMR (282 MHz, $CDCl_3$): δ -111.42.

***3,8-dimethyl-2-(3-(trifluoromethyl)phenyl)quinazolin-4(3H)-one (8ae)*:** Yield: 286 mg (90%), White crystalline solid. ^{1}H NMR (300 MHz, $CDCl_3$): δ 8.24 – 8.15 (m, 1H), 7.93 (t, *J* = 1.7 Hz, 1H), 7.88 – 7.77 (m, 2H), 7.75 – 7.58 (m, 2H), 7.42 (t, *J* = 7.6 Hz, 1H), 3.53 (s, 3H), 2.62 (s, 3H). ^{13}C{^{1}H} NMR (101 MHz, $CDCl_3$): δ 163.11, 153.17, 145.88, 136.49 (d, *J* = 26.5 Hz), 135.12, 131.89 (d, *J* = 1.5 Hz), 131.43 (d, *J* = 32.9 Hz), 129.39, 127.07, 126.82 (d, *J* = 3.8 Hz), 125.64 (d, *J* = 3.9 Hz), 125.16, 124.48, 122.45, 120.67, 34.40, 17.36. ^{19}F NMR (282 MHz, $CDCl_3$): δ -62.72.

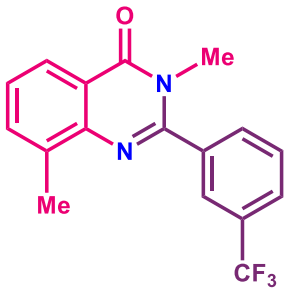

***3,8-dimethyl-2-(p-tolyl)quinazolin-4(3H)-one (8af)*:** Yield: 238 mg (90%), White crystalline solid. ^{1}H NMR (400 MHz, $CDCl_3$): δ 8.19 (dd, *J* = 8.0, 1.6 Hz, 1H), 7.61 (dt, *J* = 7.3, 1.3 Hz, 1H), 7.56 – 7.50 (m, 2H), 7.43 – 7.31 (m, 3H), 3.54 (s, 3H), 2.62 (s, 3H), 2.47 (s, 3H). ^{13}C NMR (101 MHz, $CDCl_3$): δ 163.52, 154.86, 146.24, 140.30, 136.19, 134.85, 133.15, 129.41, 128.55, 126.49, 124.41, 120.54, 34.56, 21.56, 17.45.

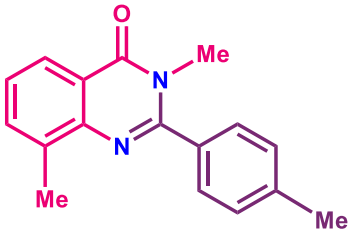

***2-(4-methoxyphenyl)-3,8-dimethylquinazolin-4(3H)-one (8ag)*:** Yield: 244 mg (87%), Colourless solid. ^{1}H NMR (300 MHz, $CDCl_3$): δ 8.18 (dd, *J* = 8.0, 1.6 Hz, 1H), 7.65 – 7.57 (m, 3H), 7.38 (t, *J* = 7.6 Hz, 1H), 7.09 – 7.01 (m, 2H), 3.91 (s, 3H), 3.57 (s, 3H), 2.63 (s, 3H). ^{13}C{^{1}H} NMR (75 MHz, $CDCl_3$): δ 163.63, 161.06, 154.60, 146.23, 136.07, 134.84, 130.31, 128.31, 126.40, 124.40, 120.41, 114.11, 55.58, 34.73, 17.44.

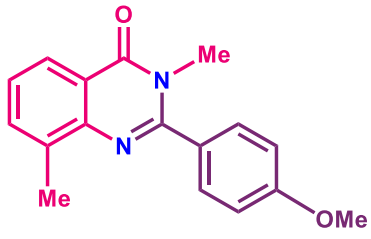

***2-(4-isopropylphenyl)-3,8-dimethylquinazolin-4(3H)-one (8ah)*:** Yield: 251 mg (86%), White solid. ^{1}H NMR (300 MHz, $CDCl_3$): δ 8.24 – 8.15 (m, 1H), 7.66 – 7.52 (m, 3H), 7.45 – 7.34 (m, 3H), 3.55 (s, 3H), 3.02 (hept, *J* = 6.9 Hz, 1H), 2.63 (s, 3H), 1.33 (d, *J* = 6.9 Hz, 6H). ^{13}C{^{1}H}

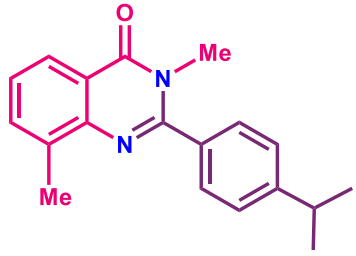

NMR (75 MHz, $CDCl_3$): δ 163.53, 154.91, 151.12, 146.23, 136.15, 134.85, 133.37, 128.65, 126.85, 126.48, 124.40, 120.52, 34.65, 34.23, 23.98, 17.48.

***2-([1,1'-biphenyl]-4-yl)-3,8-dimethylquinazolin-4(3H)-one (8ai)*:** Yield: 274 mg (84%),

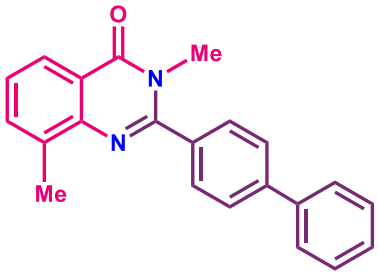

White crystalline solid. ^1H NMR (300 MHz, $CDCl_3$): δ 8.22 (ddd, J = 8.0, 1.6, 0.7 Hz, 1H), 7.80 – 7.72 (m, 3H), 7.72 – 7.61 (m, 4H), 7.55 – 7.49 (m, 2H), 7.46 – 7.38 (m, 2H), 3.61 (s, 3H), 2.66 (s, 3H). $^{13}C\{^1H\}$ NMR (75 MHz, $CDCl_3$): δ 163.44, 154.53, 146.18, 143.03, 140.24, 136.22, 134.92, 134.66, 129.11, 129.08, 128.06, 127.47, 127.32, 126.64, 124.43, 120.57, 34.63, 17.48.

***2-(4-fluorophenyl)-3,8-dimethylquinazolin-4(3H)-one (8aj)*:** Yield: 255 mg (95%), White

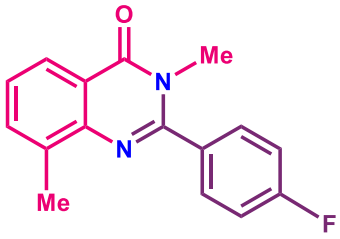

crystalline solid. ^1H NMR (300 MHz, $CDCl_3$): δ 8.22 – 8.17 (m, 1H), 7.68 – 7.60 (m, 3H), 7.41 (t, J = 7.6 Hz, 1H), 7.28 – 7.20 (m, 2H). 3.54 (s, 3H), 2.63 (s, 3H). $^{13}C\{^1H\}$ NMR (101 MHz, $CDCl_3$): δ 165.01, 163.40, 162.52, 153.79, 146.05, 136.23, 135.04, 132.09, 132.06, 130.84, 130.75, 126.80, 124.49, 120.59, 116.09, 115.87, 34.59, 17.43. ^{19}F NMR (282 MHz, $CDCl_3$): δ -109.99.

***2-(4-chlorophenyl)-3,8-dimethylquinazolin-4(3H)-one (8ak)*:** Yield: 250 mg (88%), White

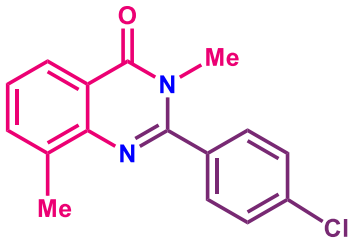

solid. ^1H NMR (400 MHz, $CDCl_3$): δ 8.19 (dd, J = 8.3, 1.6 Hz, 1H), 7.66 – 7.49 (m, 5H), 7.41 (t, J = 7.6 Hz, 1H), 3.53 (s, 3H), 2.62 (s, 3H). $^{13}C\{^1H\}$ NMR (75 MHz, $CDCl_3$): δ 163.30, 153.65, 146.01, 136.38, 136.27, 135.04, 134.29, 130.06, 129.11, 126.87, 124.48, 120.60, 34.52, 17.41.

***2-(4-bromophenyl)-3,8-dimethylquinazolin-4(3H)-one (8al)*:** Yield: 280 mg (85%), White solid. ^{1}H NMR (300 MHz, $CDCl_3$): δ 8.24 – 8.15 (m, 1H), 7.73 – 7.66 (m, 2H), 7.65 – 7.59 (m, 1H), 7.56 – 7.49 (m, 2H), 7.41 (t, *J* = 7.6 Hz, 1H), 3.53 (s, 3H), 2.61 (s, 3H). ^{13}C{^{1}H} NMR (75 MHz, $CDCl_3$): δ 163.31, 153.71, 146.02, 136.29, 135.07, 134.76, 132.08, 130.26, 126.90, 124.65, 124.49, 120.61, 34.51, 17.42.

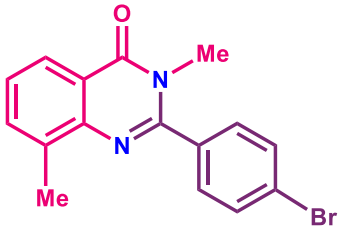

***3,8-dimethyl-2-(4-(trifluoromethyl)phenyl)quinazolin-4(3H)-one (8am)*:** Yield: 293 mg (92%), White crystalline solid. ^{1}H NMR (300 MHz, $CDCl_3$): δ 8.25 – 8.16 (m, 1H), 7.80 (q, *J* = 8.3 Hz, 4H), 7.64 (ddd, *J* = 7.4, 1.8, 1.0 Hz, 1H), 7.43 (t, *J* = 7.6 Hz, 1H), 3.53 (s, 3H), 2.62 (s, 3H). ^{13}C{^{1}H} NMR (75 MHz, $CDCl_3$): δ 163.13 153.30, 145.93, 139.24 (d, *J* = 1.5 Hz), 136.39, 135.15, 132.11 (d, *J* = 32.8 Hz), 129.09, 127.13, 125.91 (d, *J* = 3.8 Hz), 124.52, 122.06, 120.72, 34.41, 17.41. ^{19}F NMR (282 MHz, $CDCl_3$): δ -62.89.

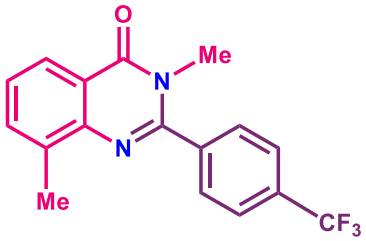

***3,8-dimethyl-2-(naphthalen-1-yl)quinazolin-4(3H)-one (8an)*:** Yield: 246 mg (82%), White crystalline solid. ^{1}H NMR (300 MHz, $CDCl_3$): δ 8.34 – 8.24 (m, 1H), 8.09 – 7.93 (m, 2H), 7.71 – 7.60 (m, 4H), 7.60 – 7.41 (m, 3H), 3.31 (s, 3H), 2.61 (s, 3H). ^{13}C{^{1}H} NMR (75 MHz, $CDCl_3$): δ 163.06, 153.94, 146.34, 136.40, 135.02, 133.66, 133.41, 130.64, 130.15, 128.80, 127.56, 126.84, 126.74, 126.49, 125.53, 124.65, 124.51, 120.93, 33.26, 17.63.

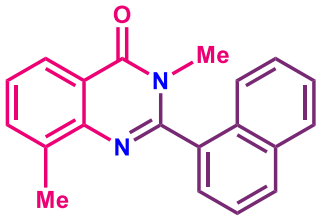

***3,8-dimethyl-2-propylquinazolin-4(3H)-one (8ao)*:** Yield: 99 mg (46%), White crystalline solid. ^{1}H NMR (300 MHz, $CDCl_3$): δ 8.12 (dd, *J* = 7.9, 1.3 Hz, 1H), 7.58 (dt, *J* = 7.2, 1.2 Hz, 1H), 7.33 (t, *J* = 7.6 Hz, 1H), 3.64 (s, 3H), 2.86 – 2.78 (m, 2H), 2.62 (s, 3H), 1.96 (h, *J* = 7.4 Hz, 2H), 1.13 (t, *J*

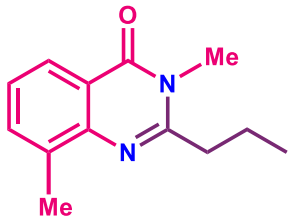

= 7.4 Hz, 3H). ^{13}C NMR (75 MHz, $CDCl_3$): δ 163.05, 155.17, 145.81, 135.52, 134.47, 125.79, 124.32, 120.11, 37.29, 30.23, 19.71, 17.15, 13.83.

***3,8-dimethyl-2-pentylquinazolin-4(3H)-one (8ap)*:** Yield: 134 mg (55%), White crystalline solid. ^{1}H NMR (300 MHz, $CDCl_3$) δ 8.12 (dd, *J* = 8.0, 1.6 Hz, 1H), 7.57 (d, *J* = 7.2 Hz, 1H), 7.33 (t, *J* = 7.6 Hz, 2H), 3.64 (s, 3H), 2.84 (t, *J* = 7.5 Hz, 2H), 2.62 (s, 3H), 1.91 (p, *J* = 7.1 Hz, 2H), 1.48 (ddt, *J* = 12.5, 9.3, 4.7 Hz, 4H), 0.97 (t, *J* = 6.9 Hz, 3H). ^{13}C{^{1}H} NMR (75 MHz, $CDCl_3$): δ 163.14, 155.61, 145.86, 135.58, 134.63, 125.93, 124.46, 120.21, 35.44, 31.54, 30.43, 26.13, 22.69, 17.35, 14.16.

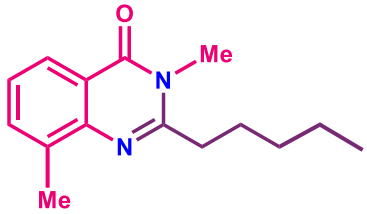

4.7.2 Copies of NMR spectra of all synthesized compounds

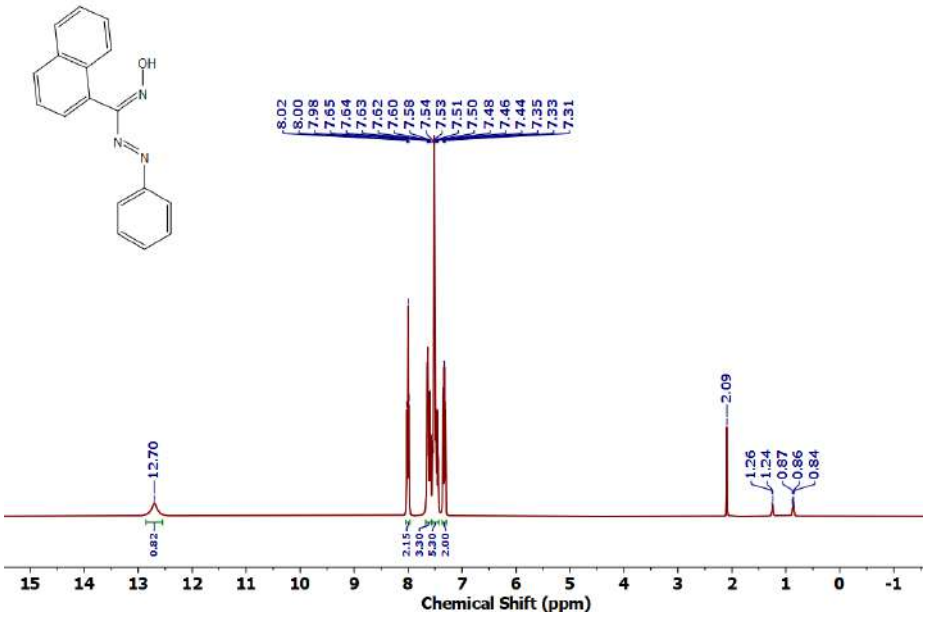

Figure 4.6.A1: ^{1}H NMR spectrum of ligand **1**

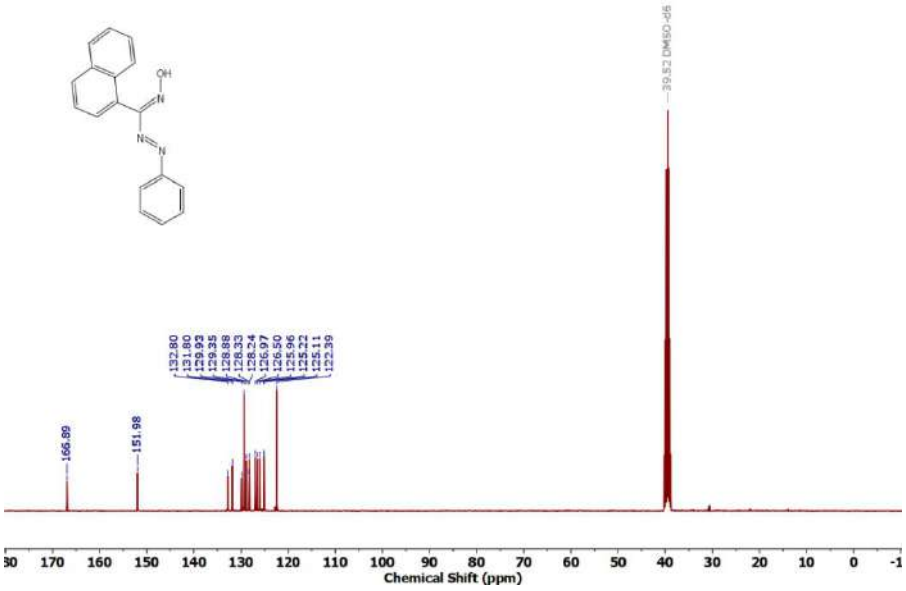

Figure 4.6.A2: $^{13}C\{^{1}H\}$ NMR spectrum of ligand **1**

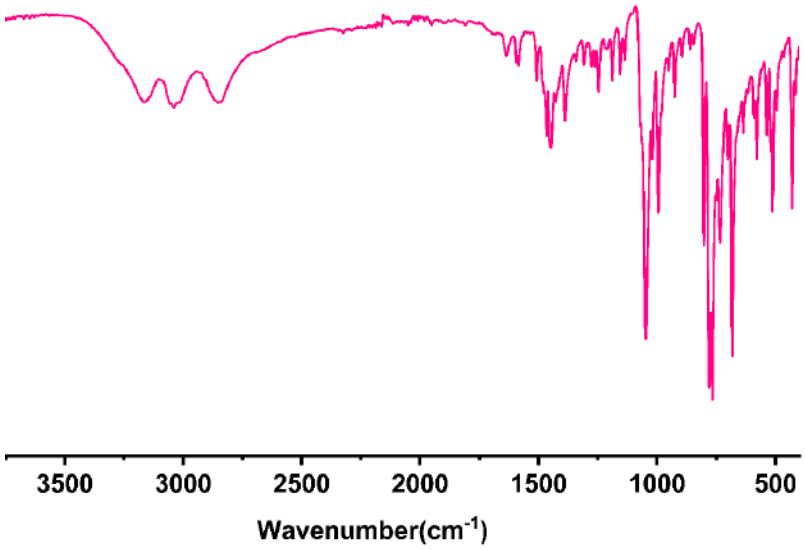

Figure 4.6.A3: IR spectrum of ligand **1**

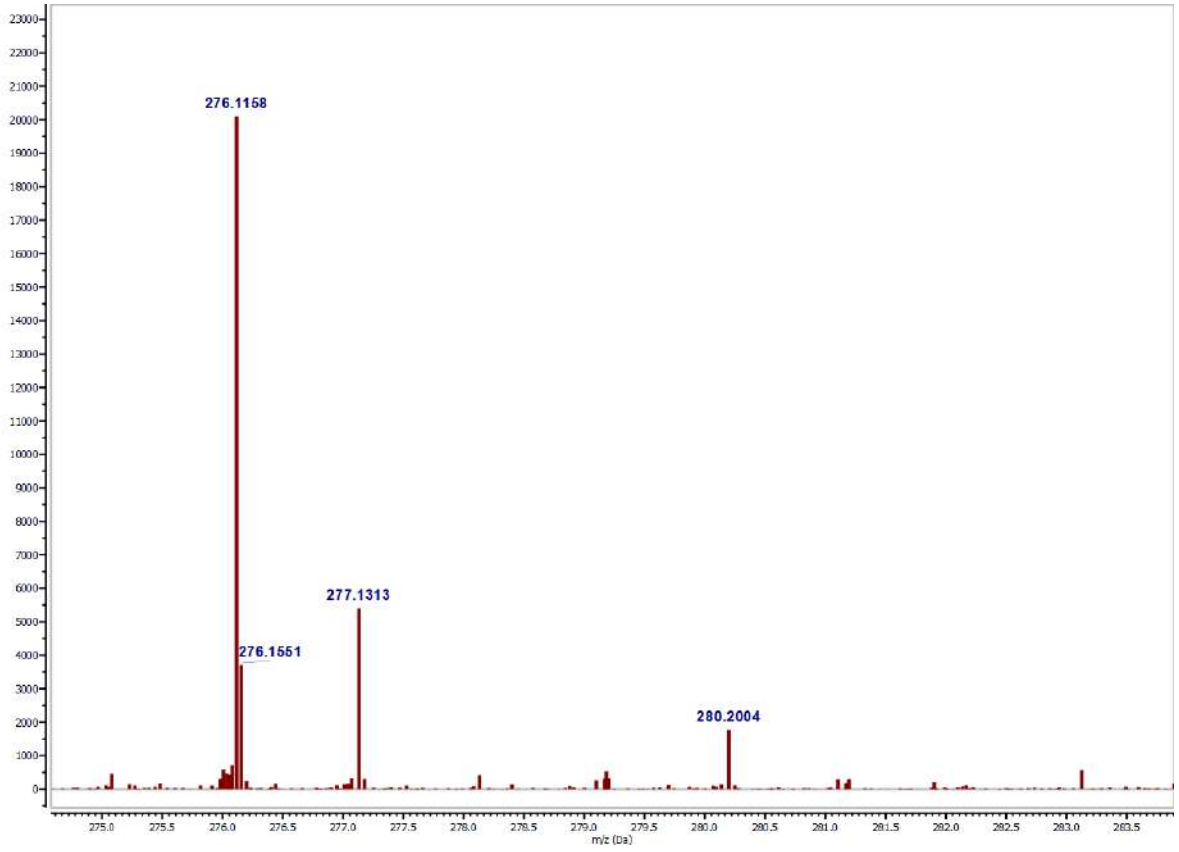

Figure 4.6.A4: HRMS spectrum of **1**

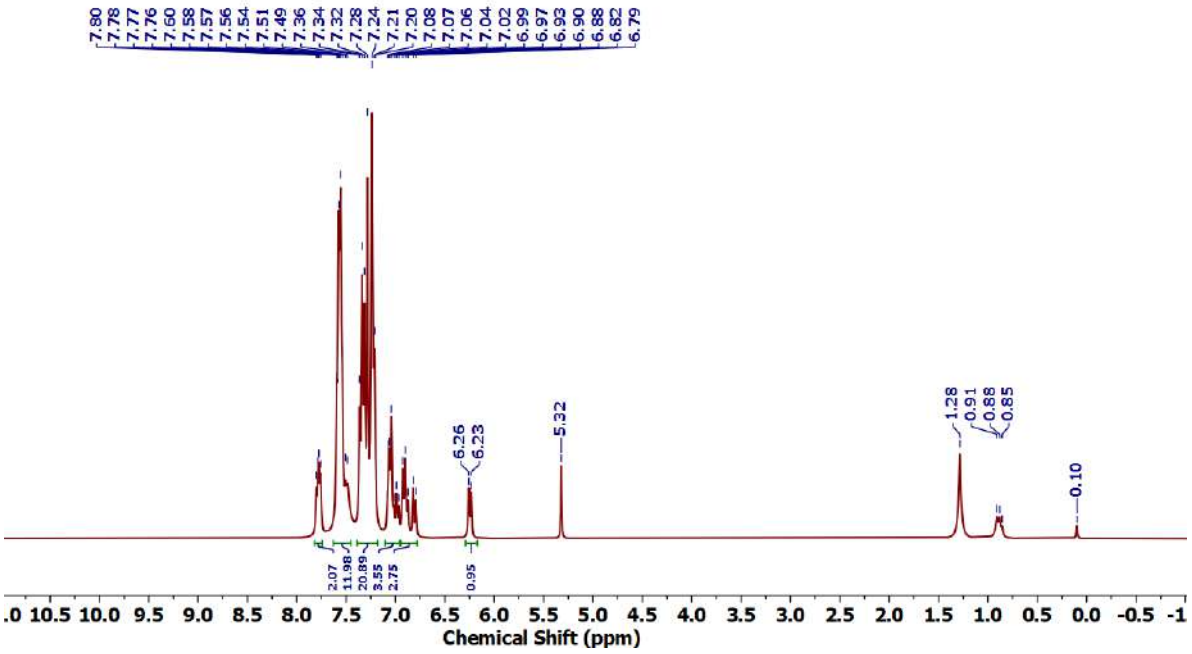

Figure 4.6.A5: ^{1}H NMR spectrum of **2**

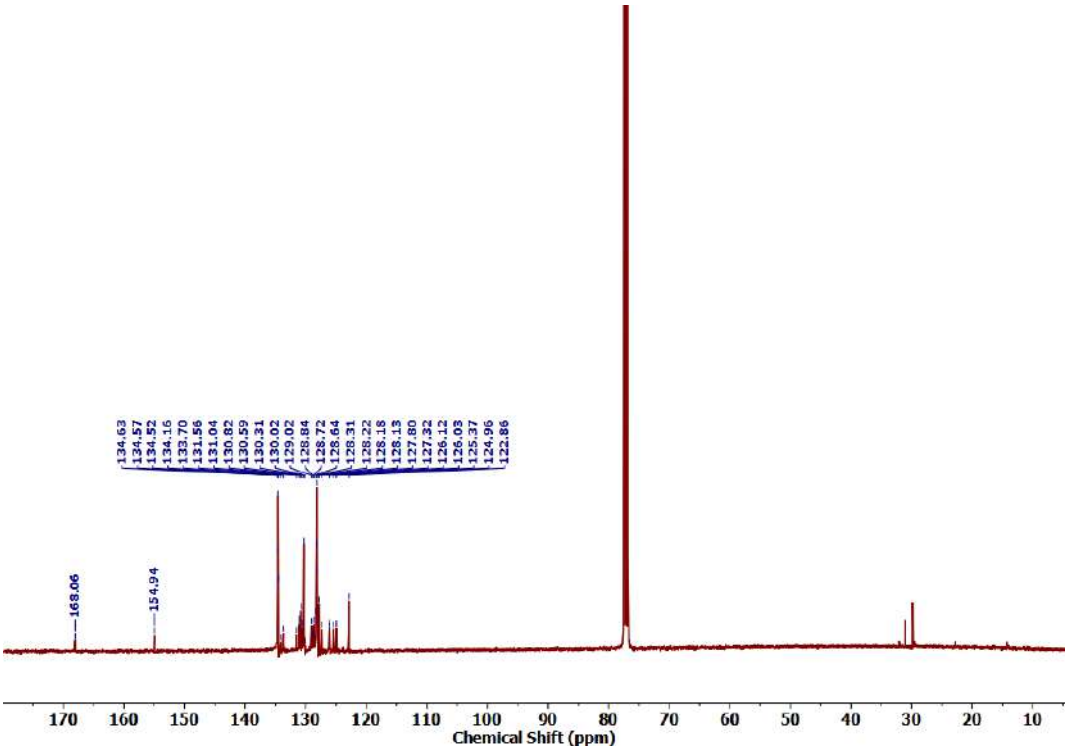

Figure 4.6.A6: $^{13}C\{^{1}H\}$ NMR spectrum of **2**

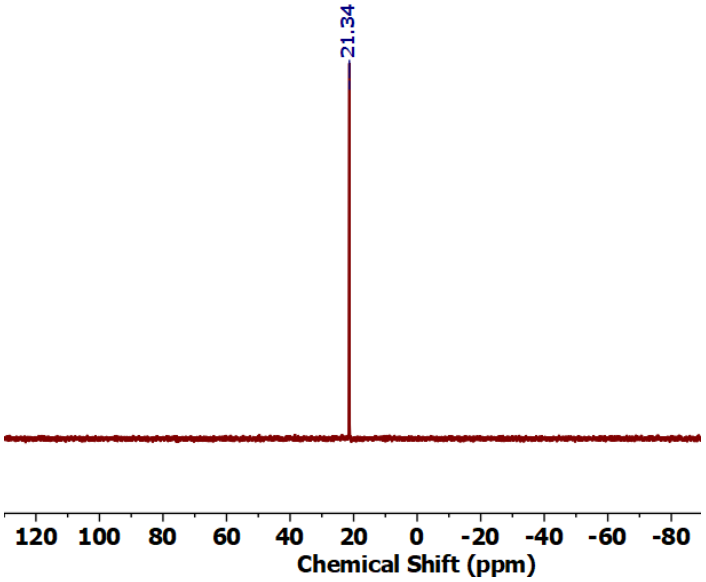

Figure 4.6.A7: $^{31}P\{^{1}H\}$ NMR spectrum of **2**

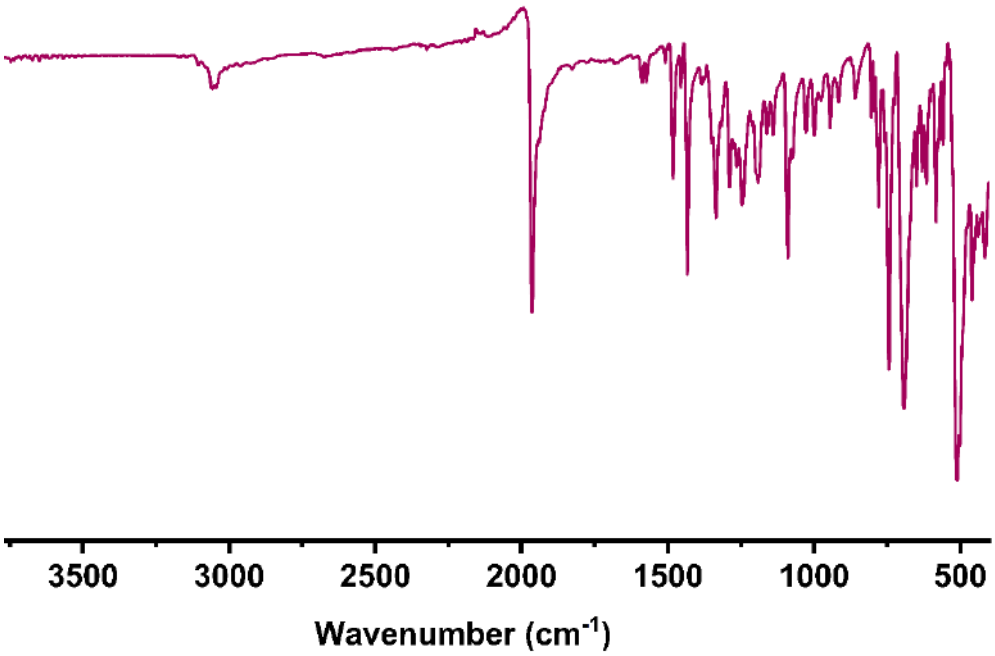

Figure 4.6.A8: IR spectrum of **2**

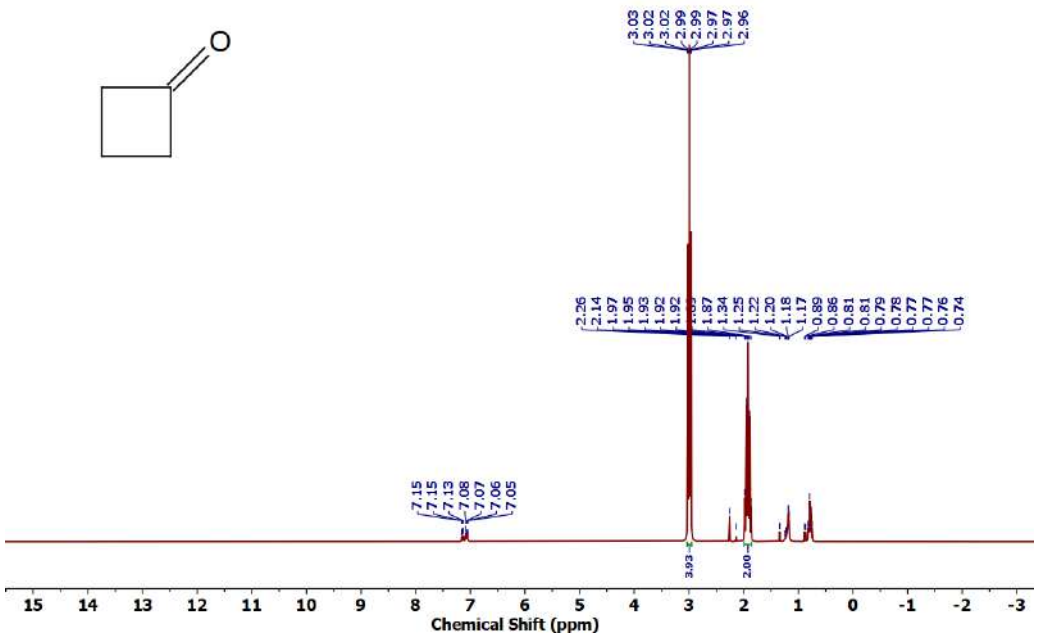

Figure 4.6.A9: ^{1}H NMR spectrum of cyclobutanone

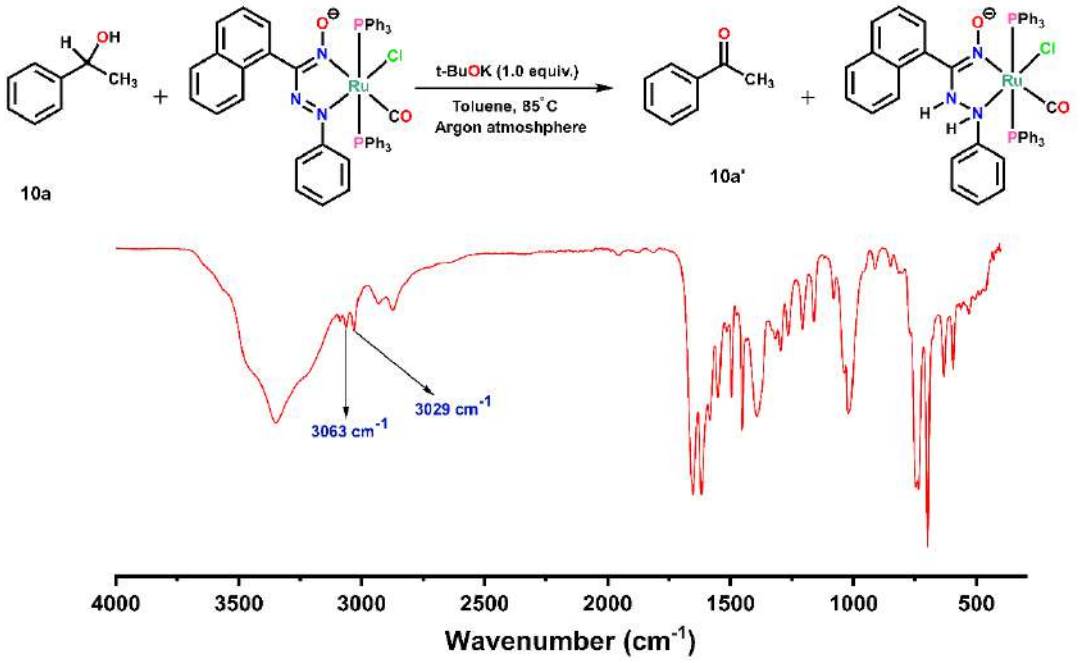

Figure 4.6.A10: IR spectrum of the reaction mixture obtained from stoichiometric alcohol dehydrogenation of 1-phenylethanol (**10a**) under argon: involvement of azo/hydrazo redox conversion with catalyst **2**.

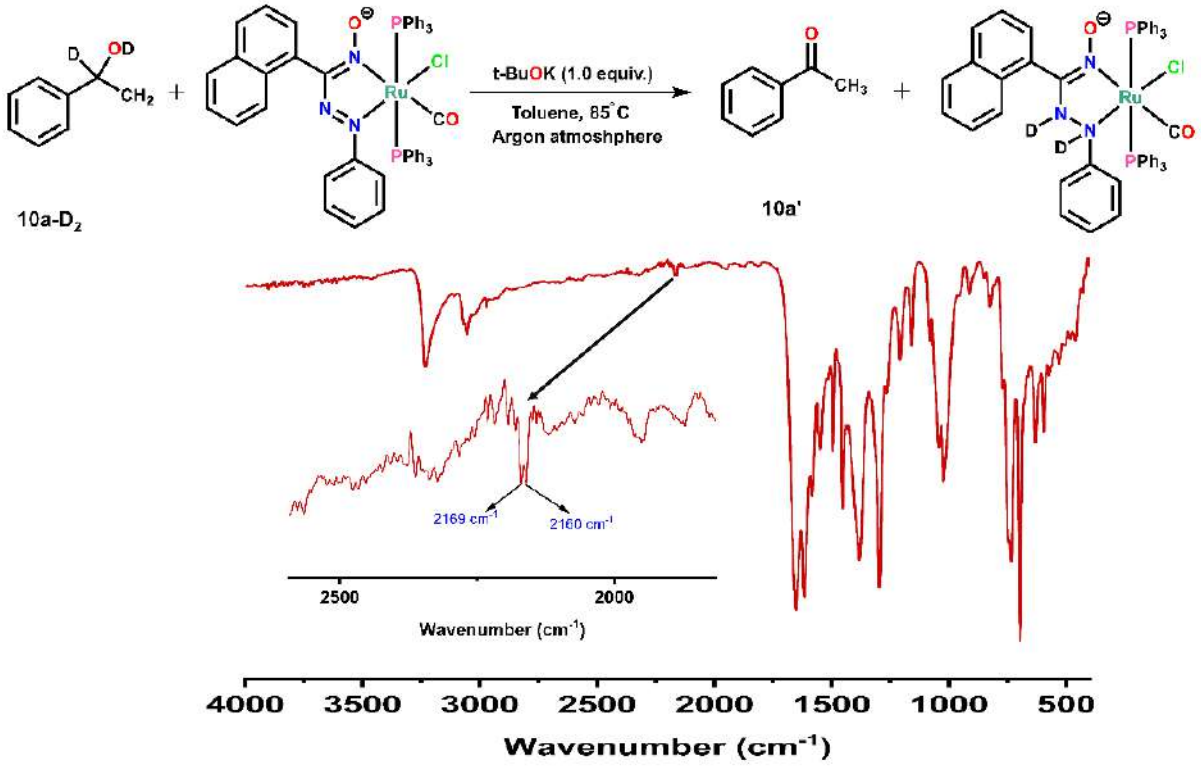

Figure 4.6.A11: IR spectrum of the reaction mixture obtained from stoichiometric alcohol dehydrogenation of 1-phenylethanol (**10a-D$_2$**) under argon: involvement of azo/hydrazo redox conversion with catalyst **2**.

4.6.2 Copies of ^{1}H, ^{13}C and ^{19}F NMR spectra all synthesized Quinazolin-4(3H)-ones

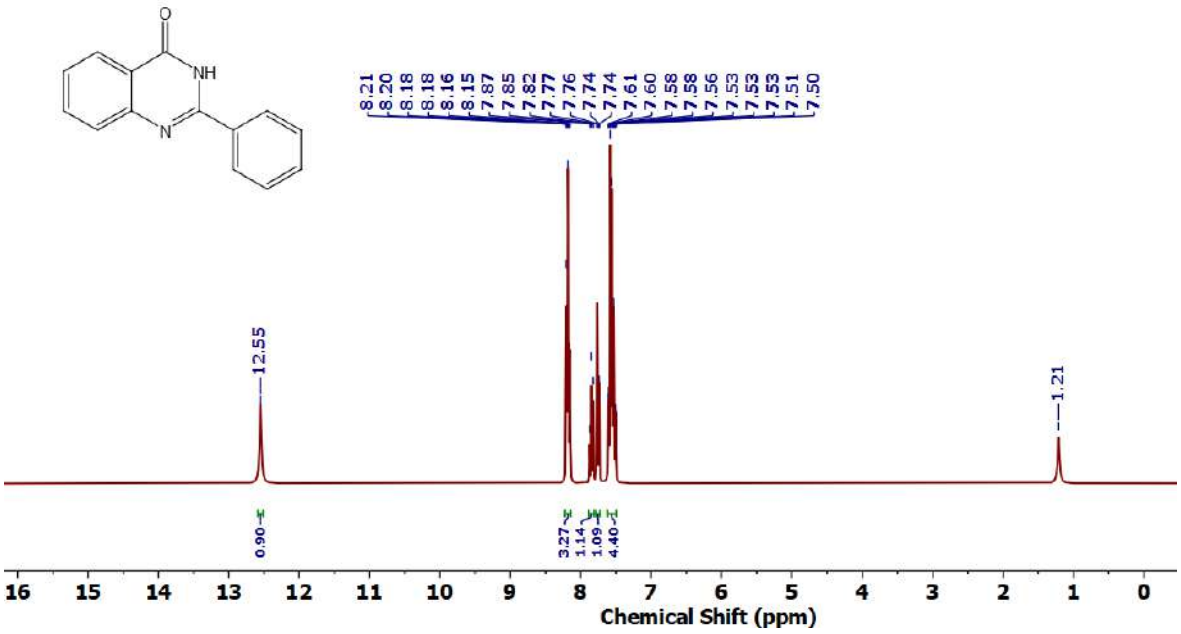

Figure 4.6.A12: ^{1}H NMR spectrum of **5aa**

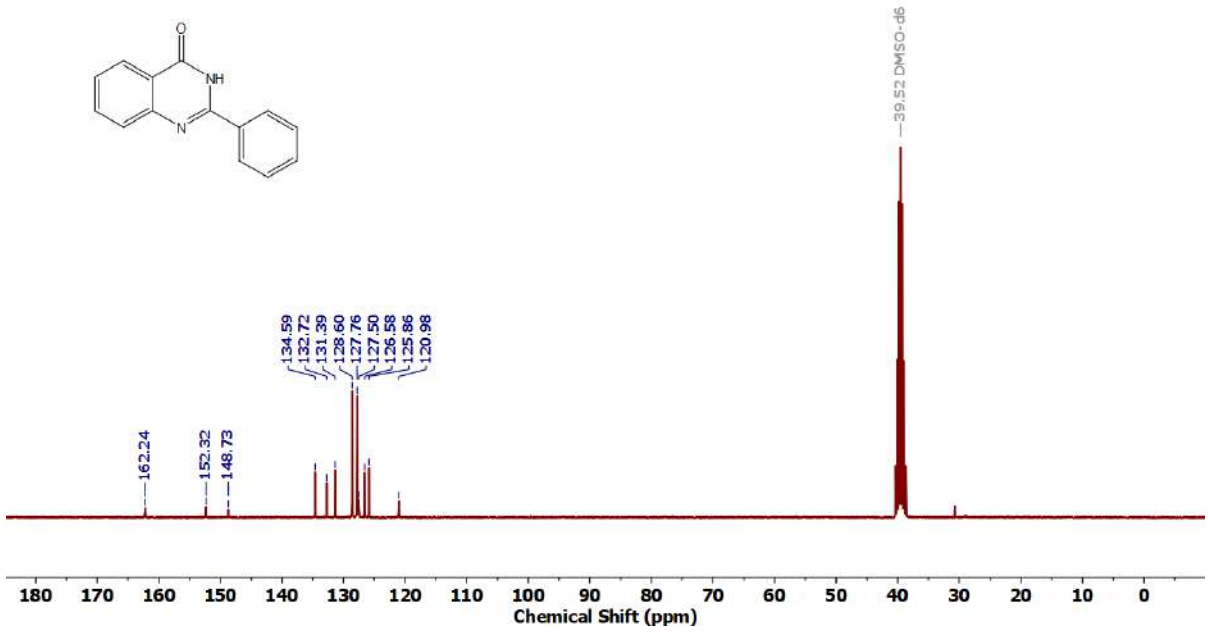

Figure 4.6.A13: $^{13}C\{^{1}H\}$ NMR spectrum of **5aa**

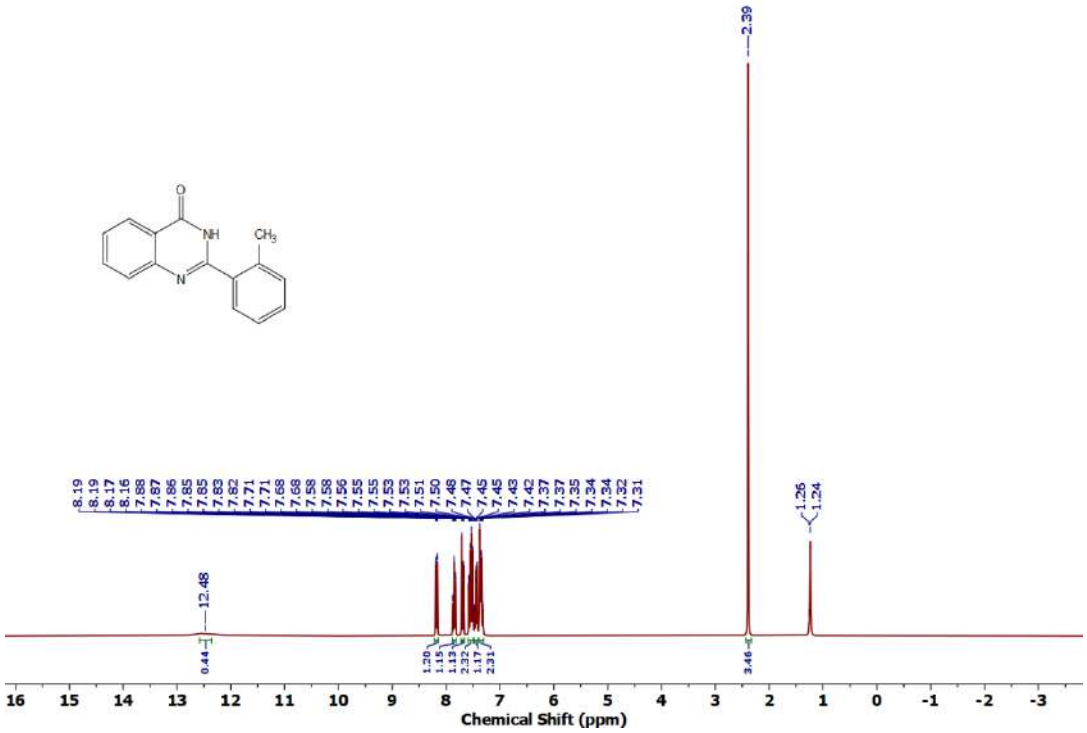

Figure 4.6.A14: ^{1}H NMR spectrum of **5ab**

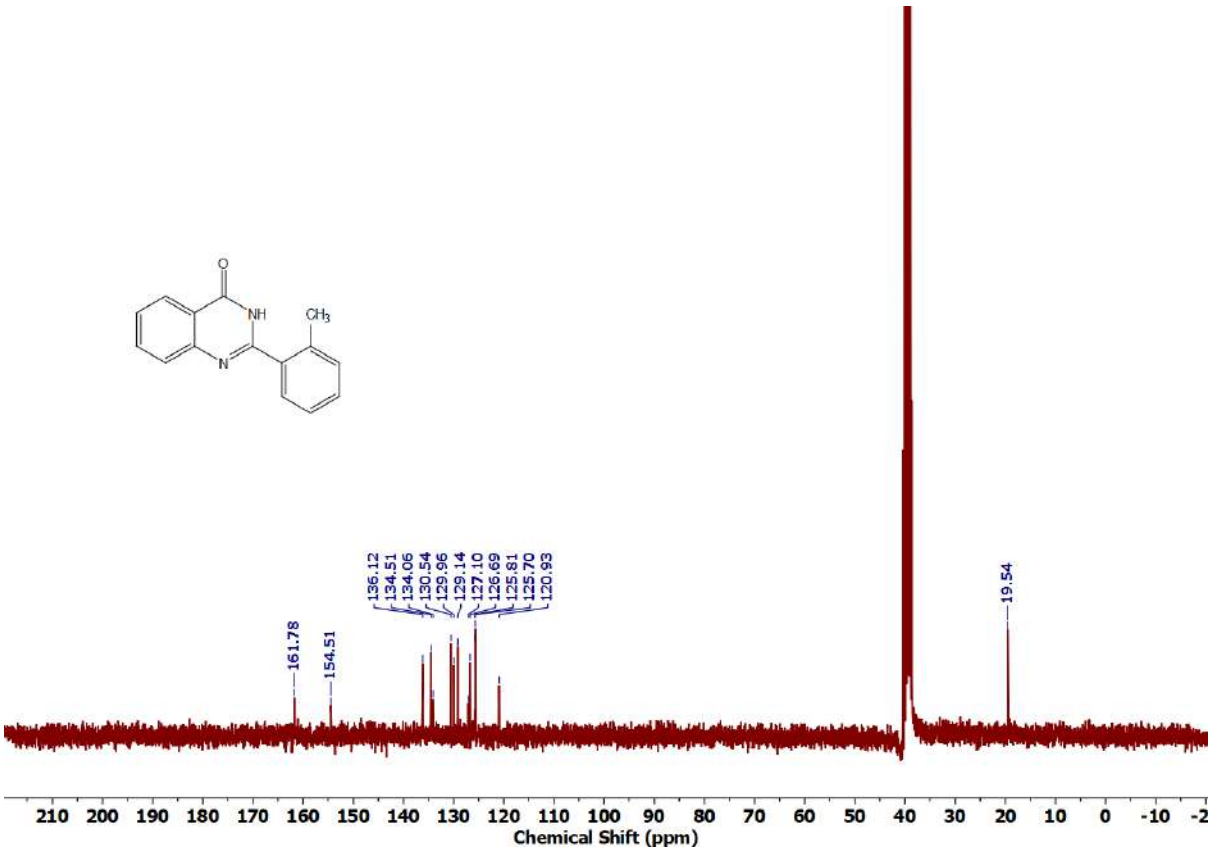

Figure 4.6.A15: ^{13}C{^{1}H} NMR spectrum of **5ab**

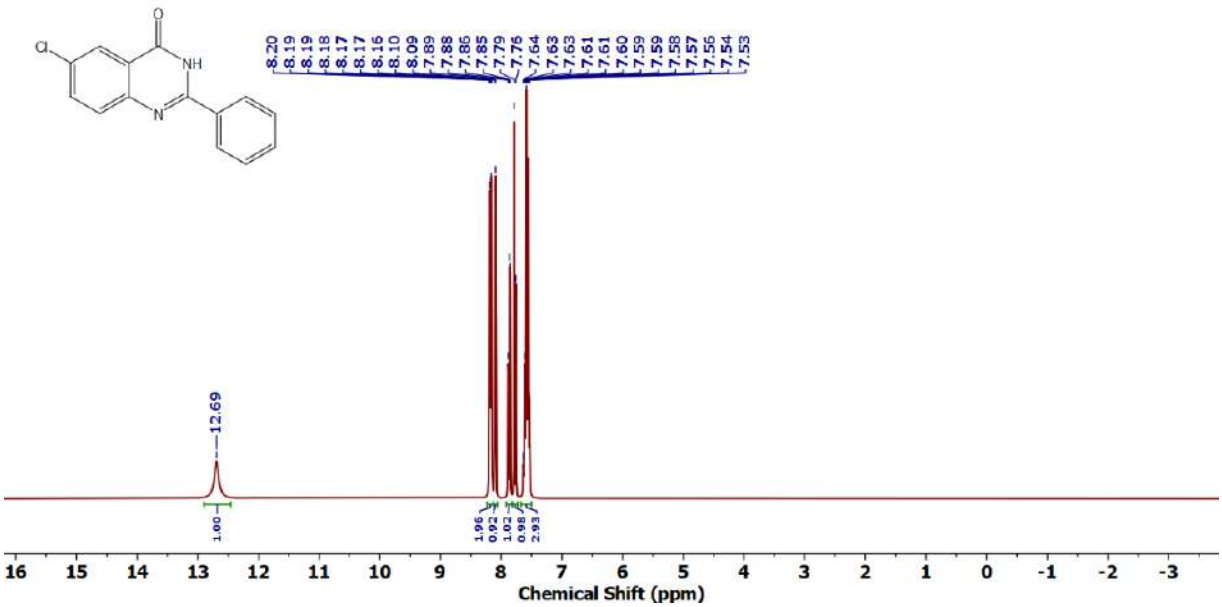

Figure 4.6.A16: ^{1}H NMR spectrum of **5ac**

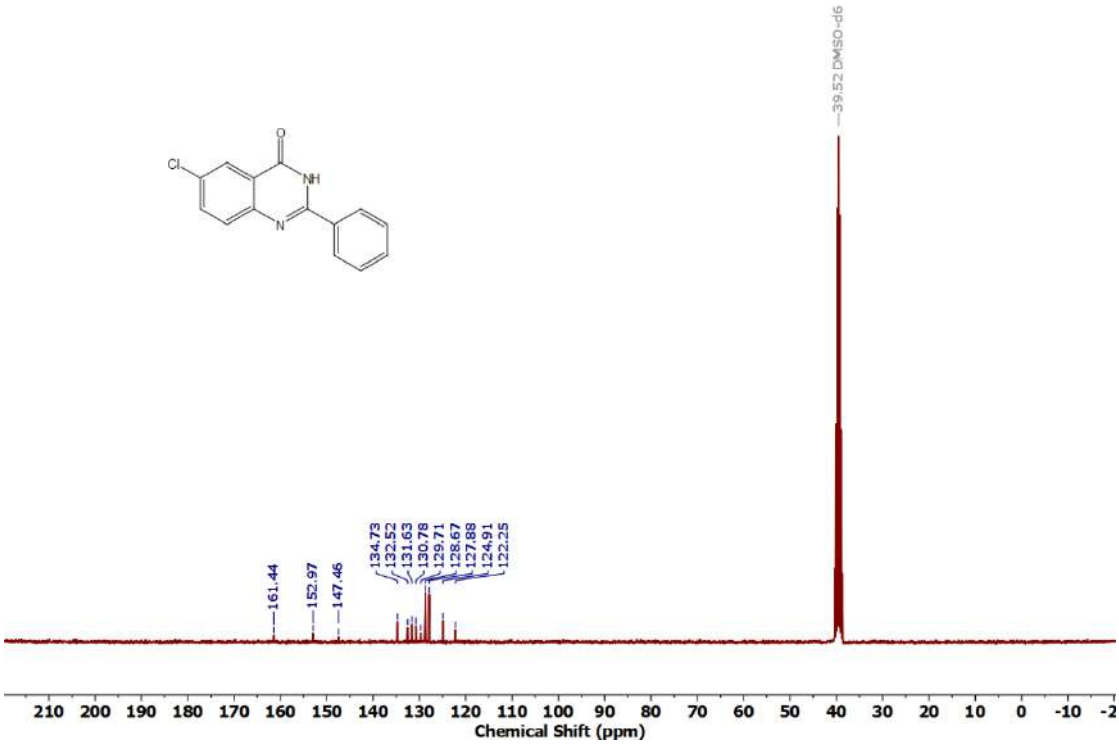

Figure 4.6.A17: ^{13}C{^{1}H} NMR spectrum of **5ac**

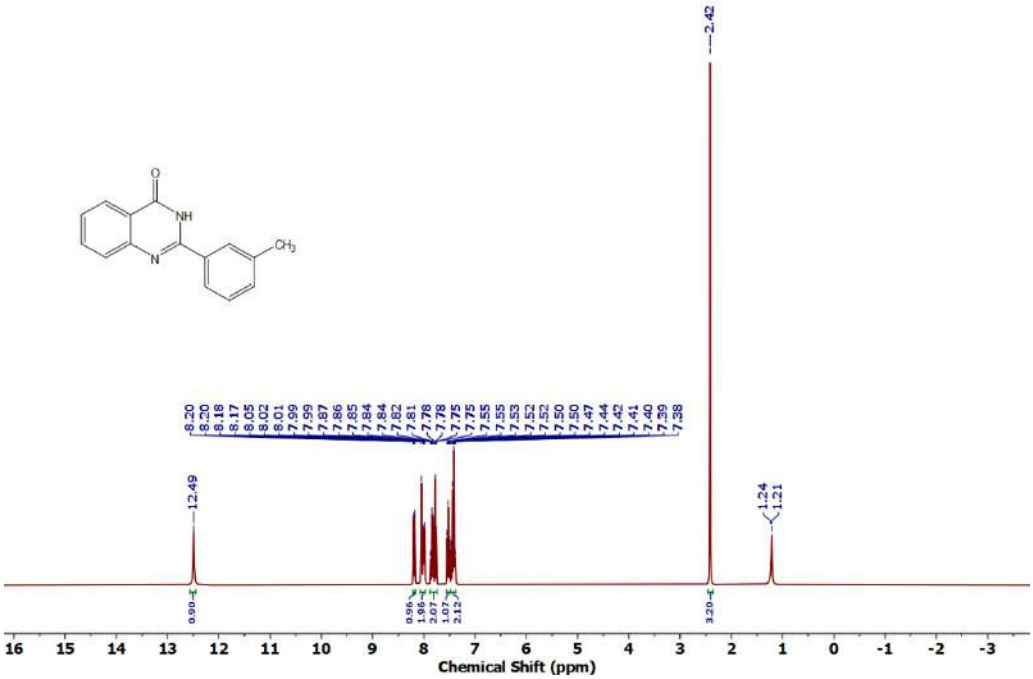

Figure 4.6.A18: ^{1}H NMR spectrum of **5ad**

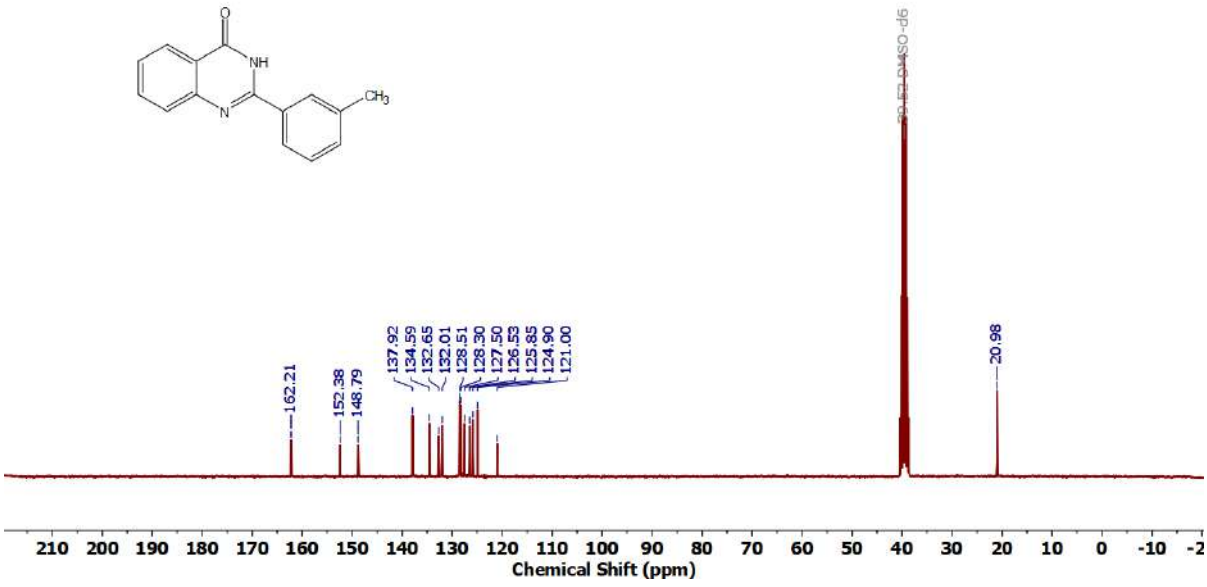

Figure 4.6.A19: ^{13}C{^{1}H} NMR spectrum of **5ad**

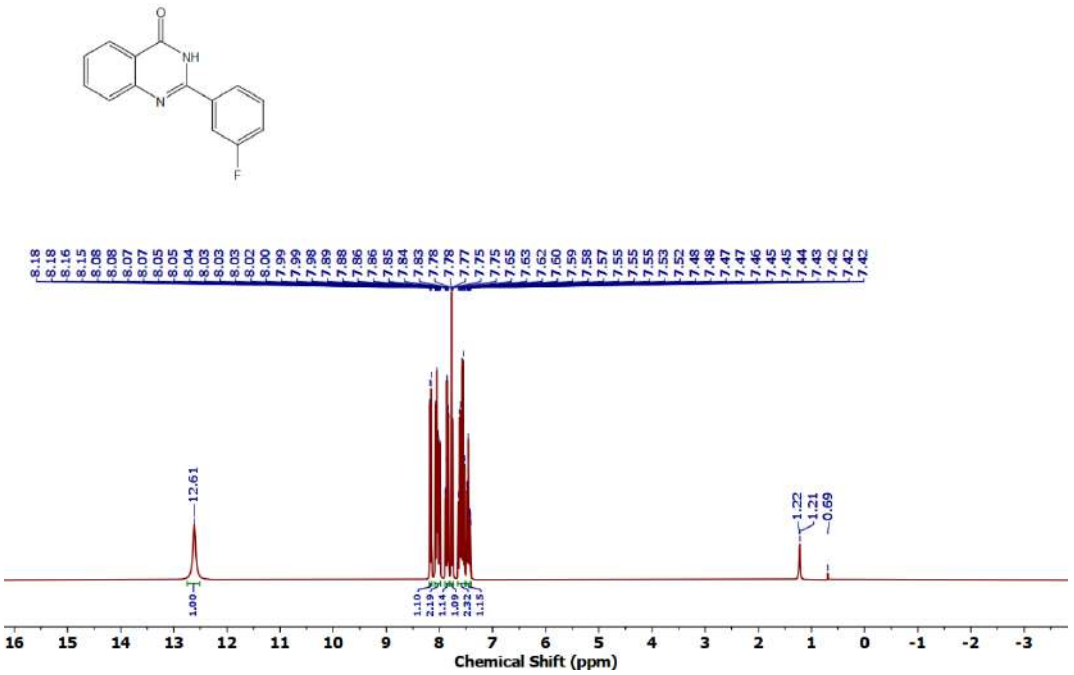

Figure 4.6.A20: ^{1}H NMR spectrum of **5ae**

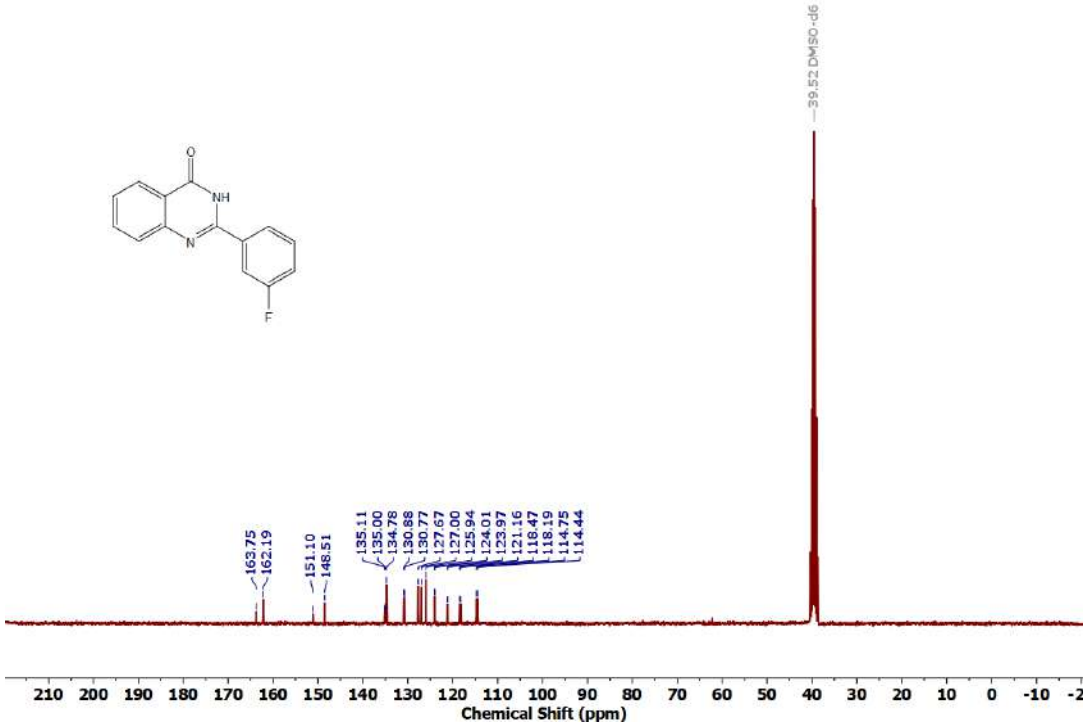

Figure 4.6.A21: ^{13}C{^{1}H} NMR spectrum of **5ae**

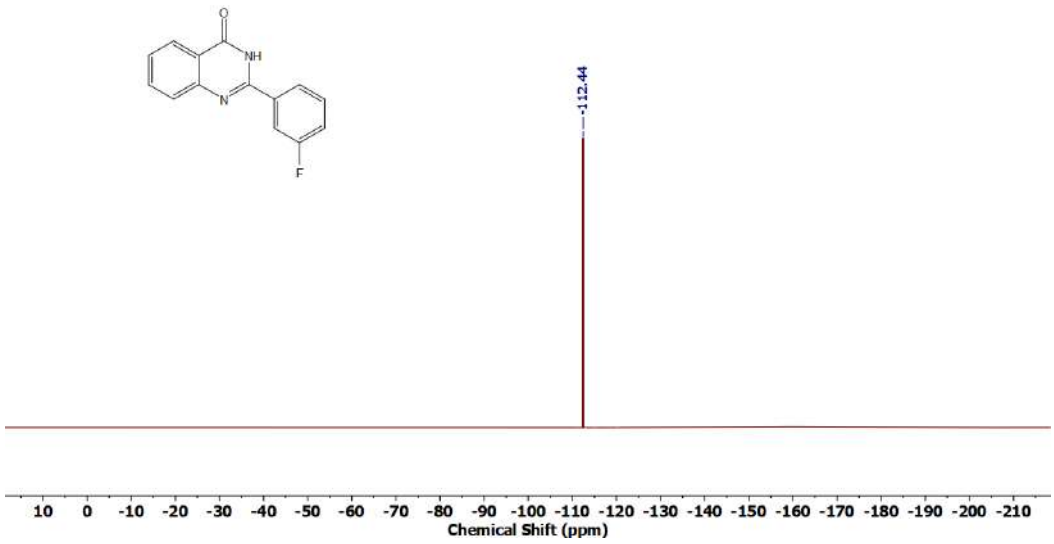

Figure 4.6.A22: ^{19}F NMR spectrum of **5ae**

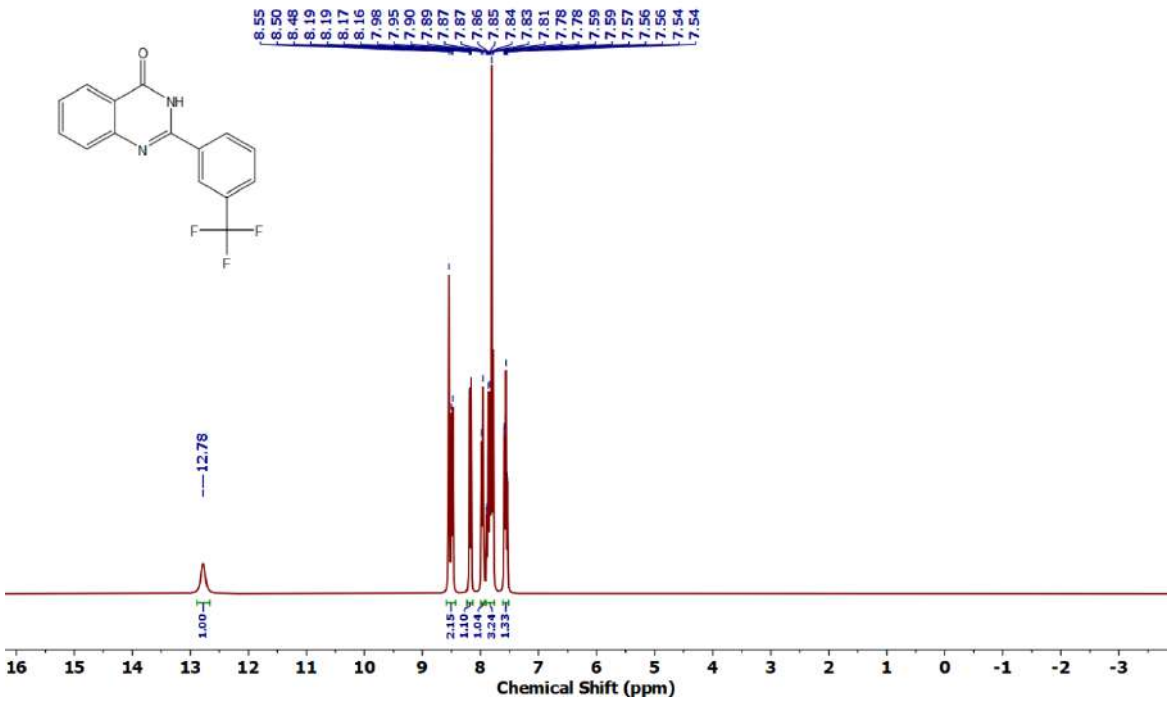

Figure 4.6.A23: ^{1}H NMR spectrum of **5af**

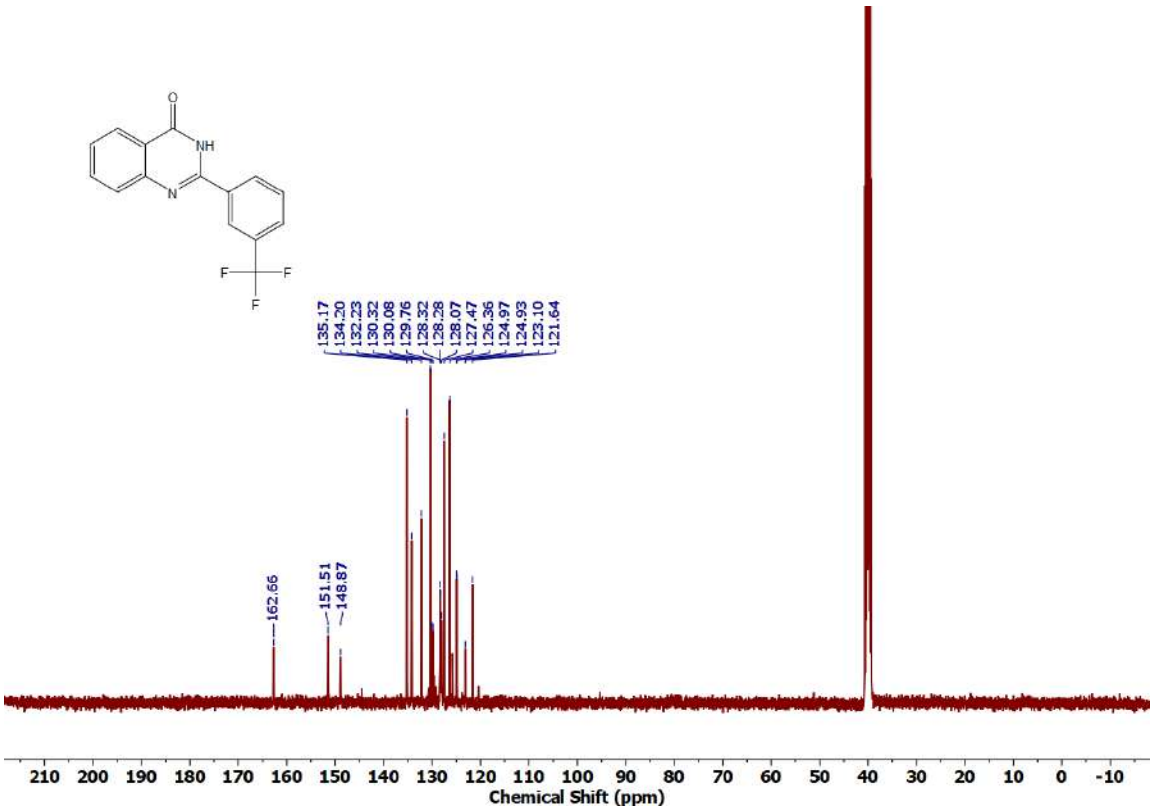

Figure 4.6.A24: $^{13}C\{^{1}H\}$ NMR spectrum of **5af**

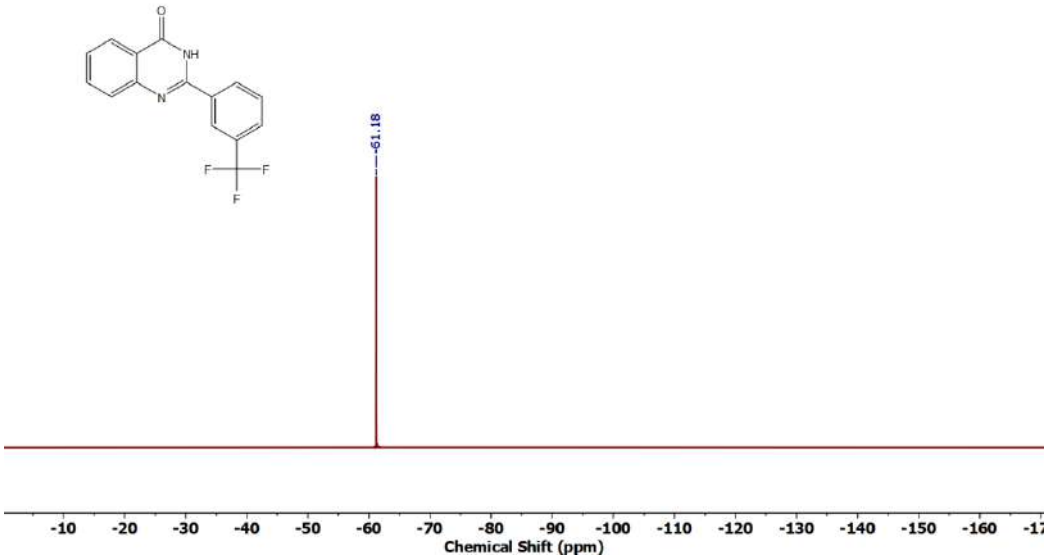

Figure 4.6.A25: ^{19}F NMR spectrum of **5af**

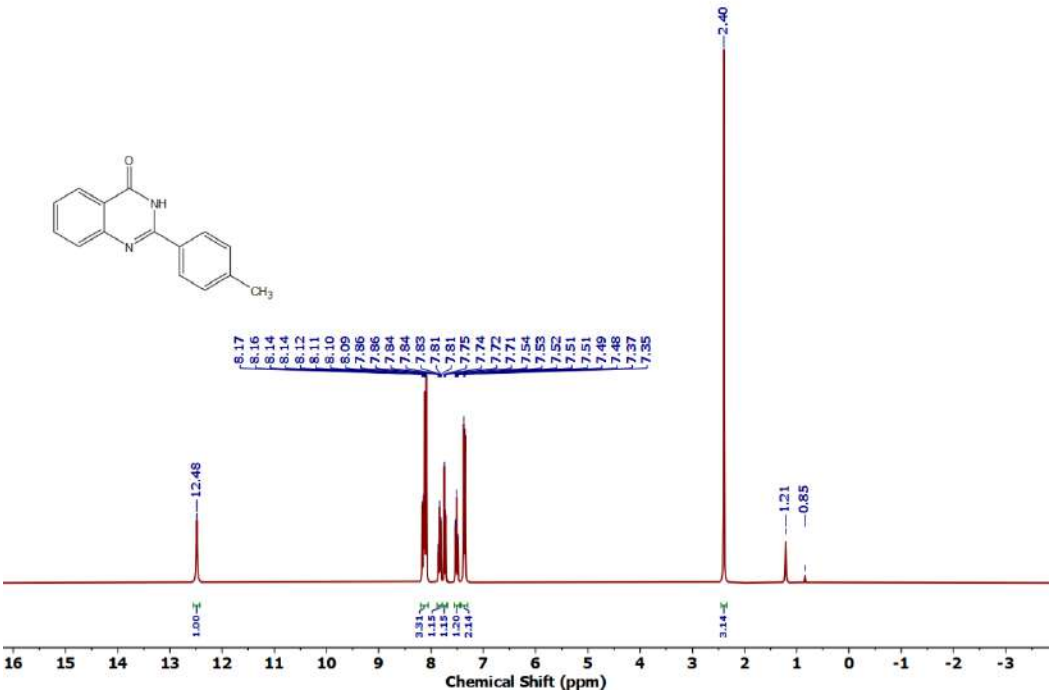

Figure 4.6.A26: ^{1}H NMR spectrum of **5ag**

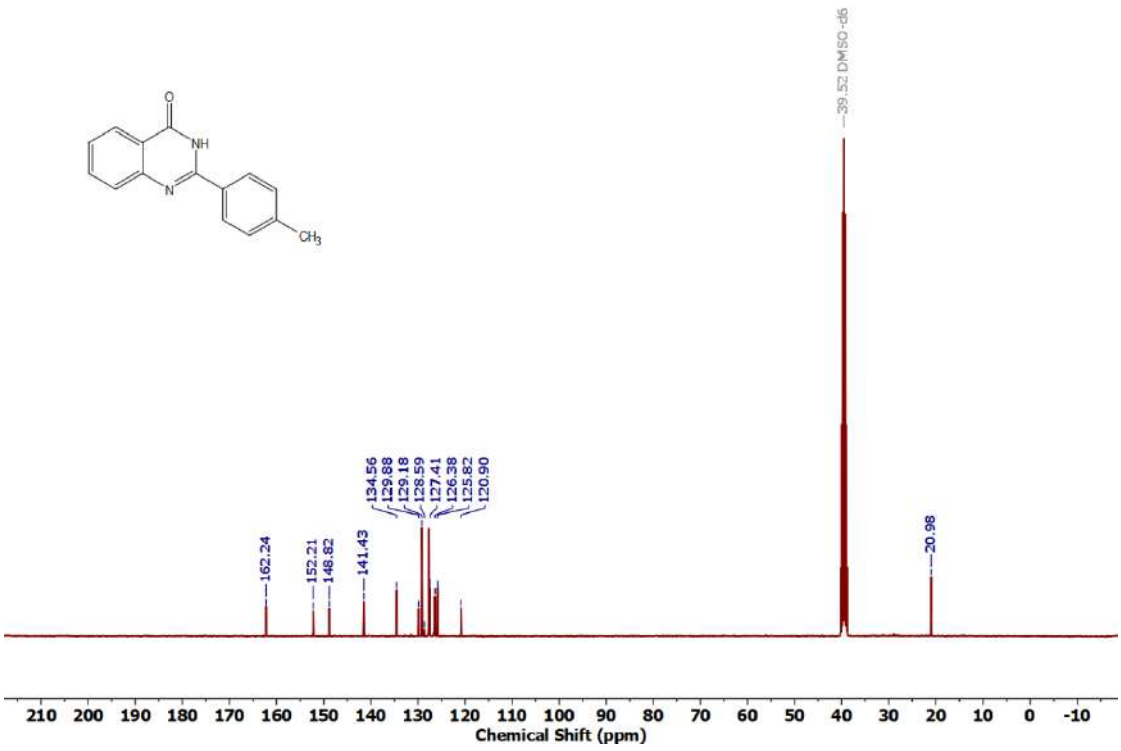

Figure 4.6.A27: $^{13}C\{^{1}H\}$ NMR spectrum of **5ag**

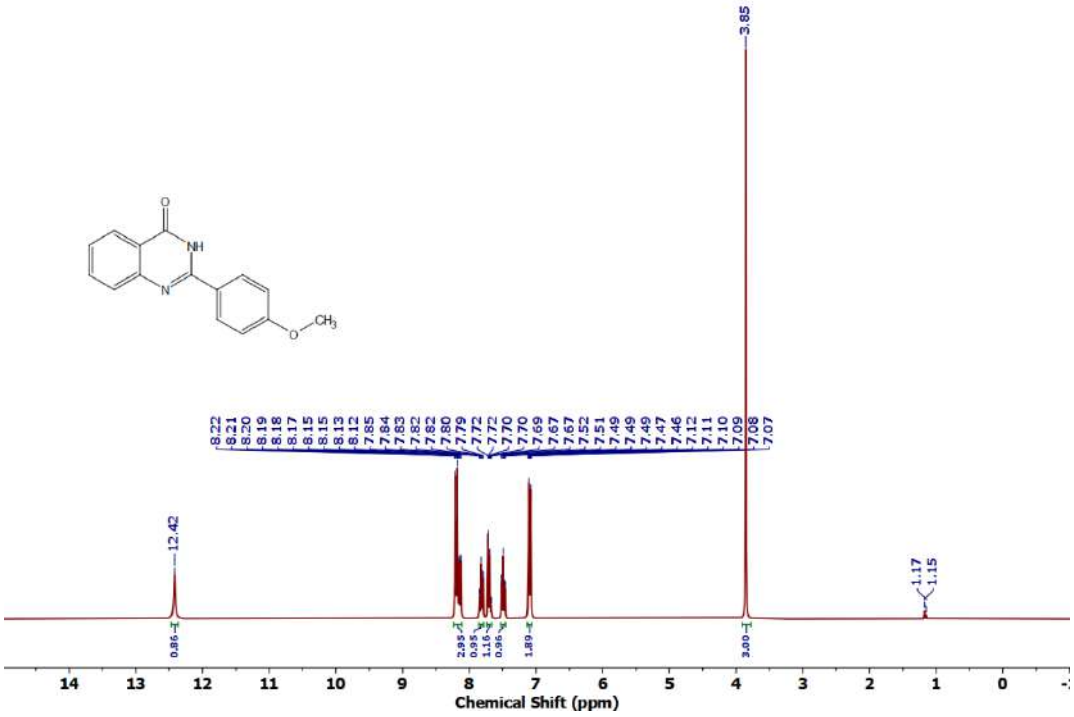

Figure 4.6.A28: ^{1}H NMR spectrum of **5ah**

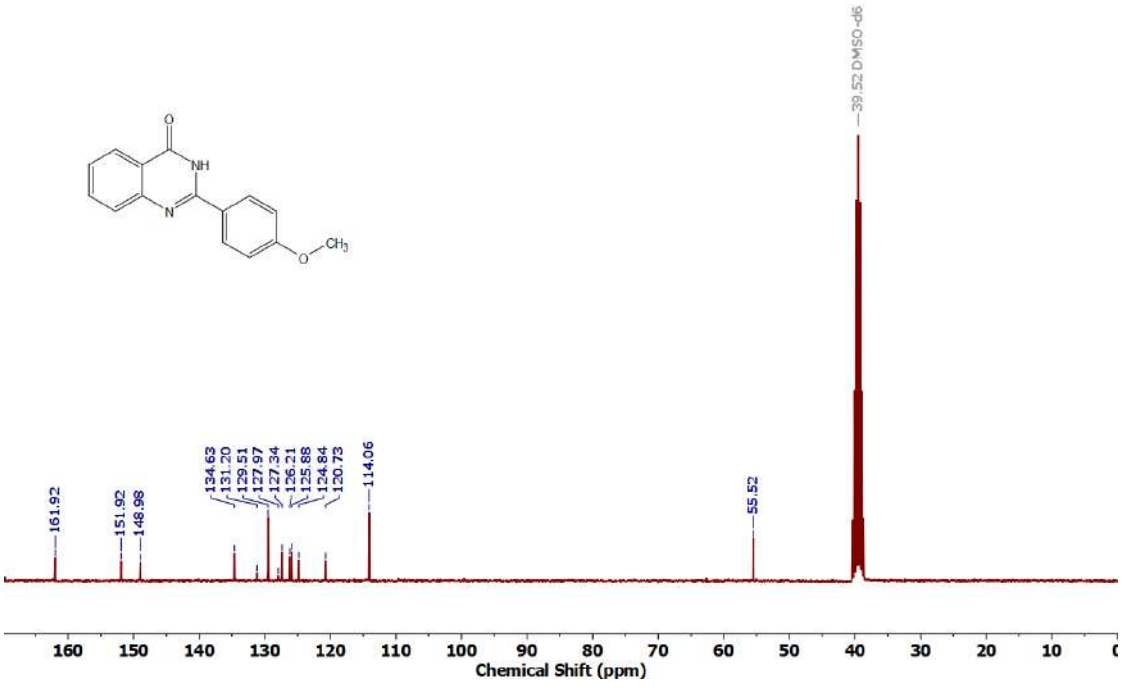

Figure 4.6.A29: ^{13}C{^{1}H} NMR spectrum of **5ah**

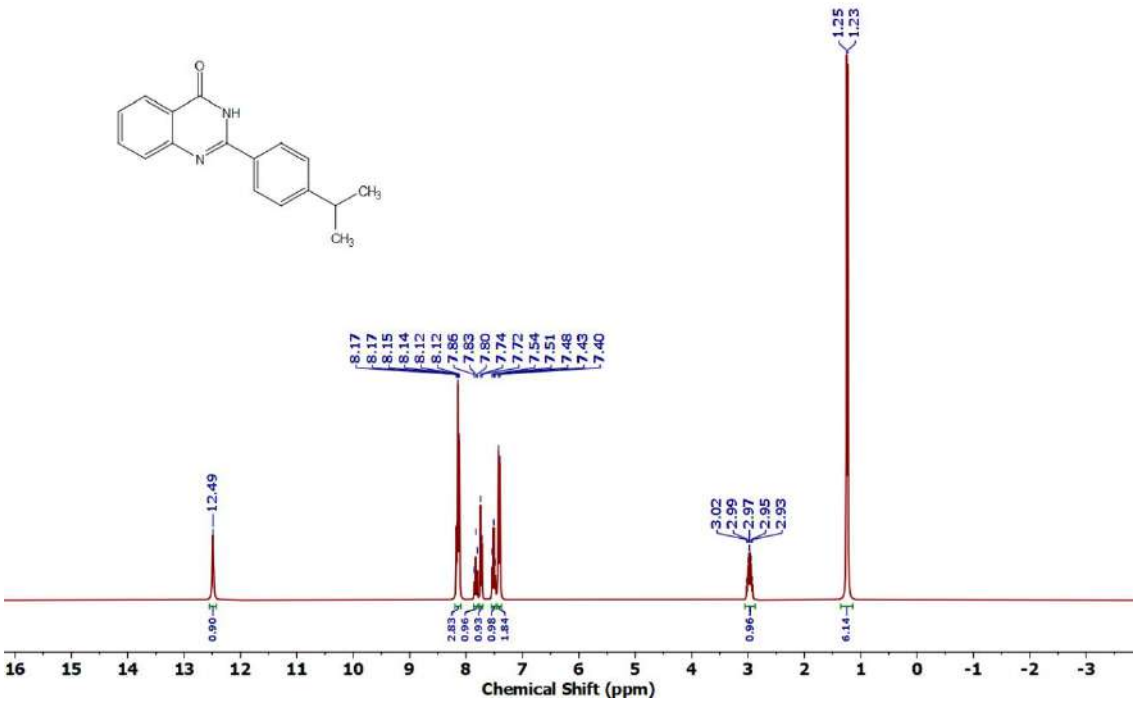

Figure 4.6.A30: ^{1}H NMR spectrum of **5ai**

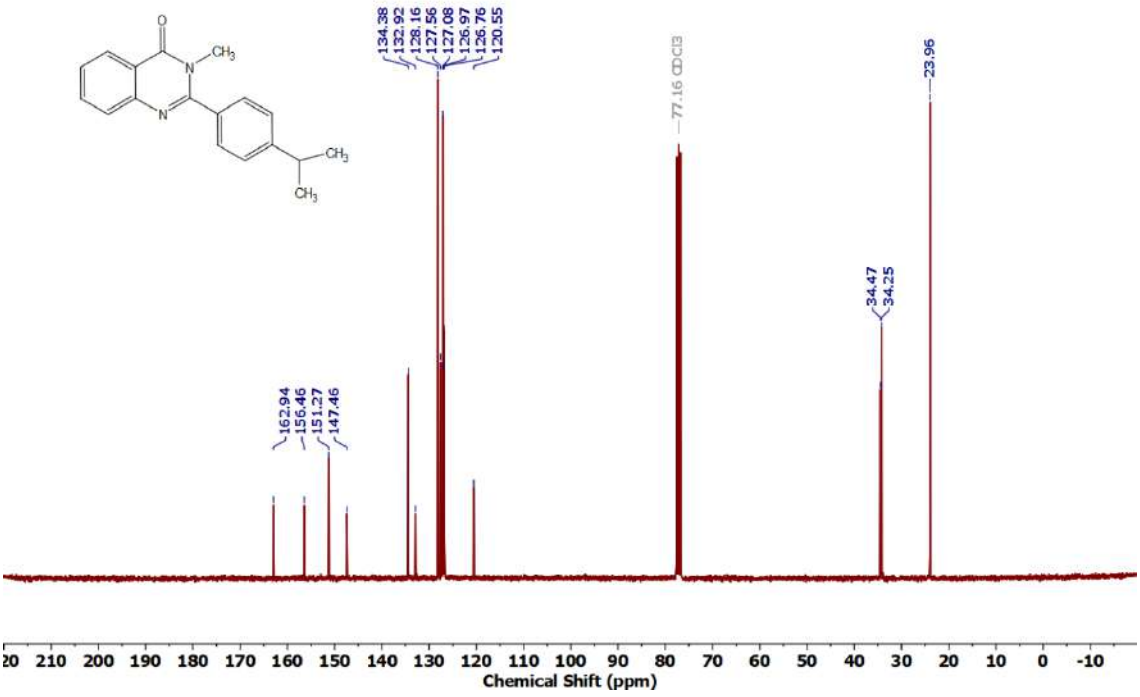

Figure 4.6.A31: ^{13}C{^{1}H} NMR spectrum of **5ai**

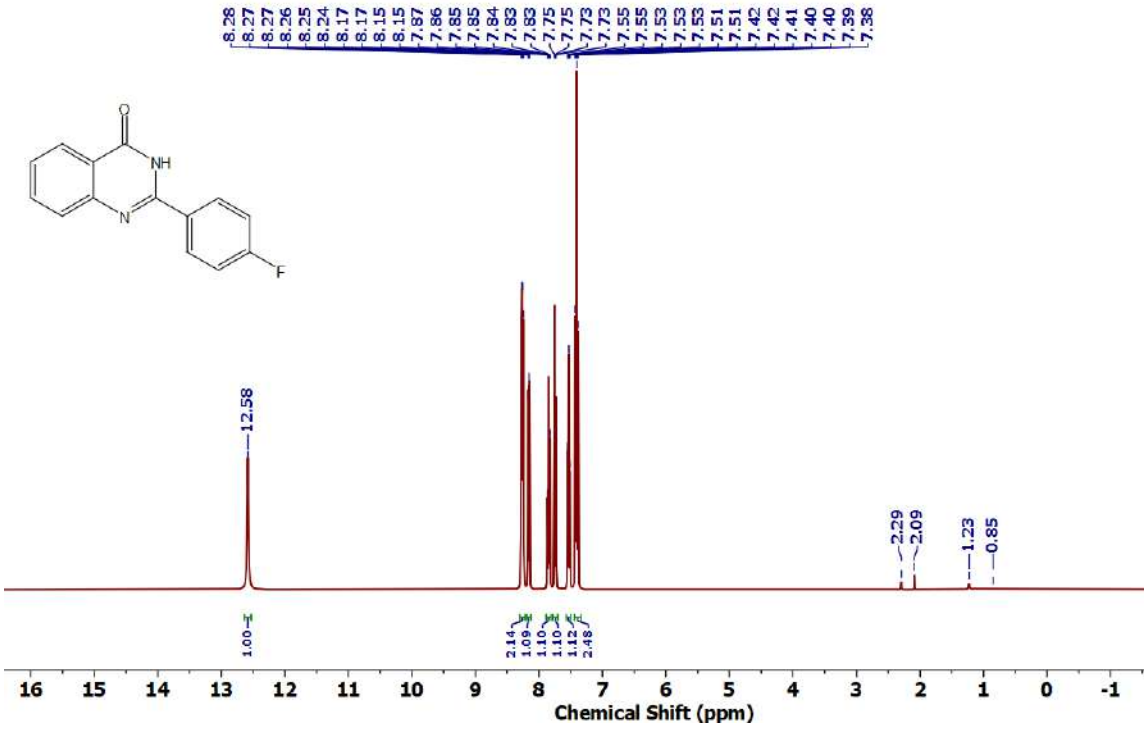

Figure 4.6.A32: ^{1}H NMR spectrum of **5aj**

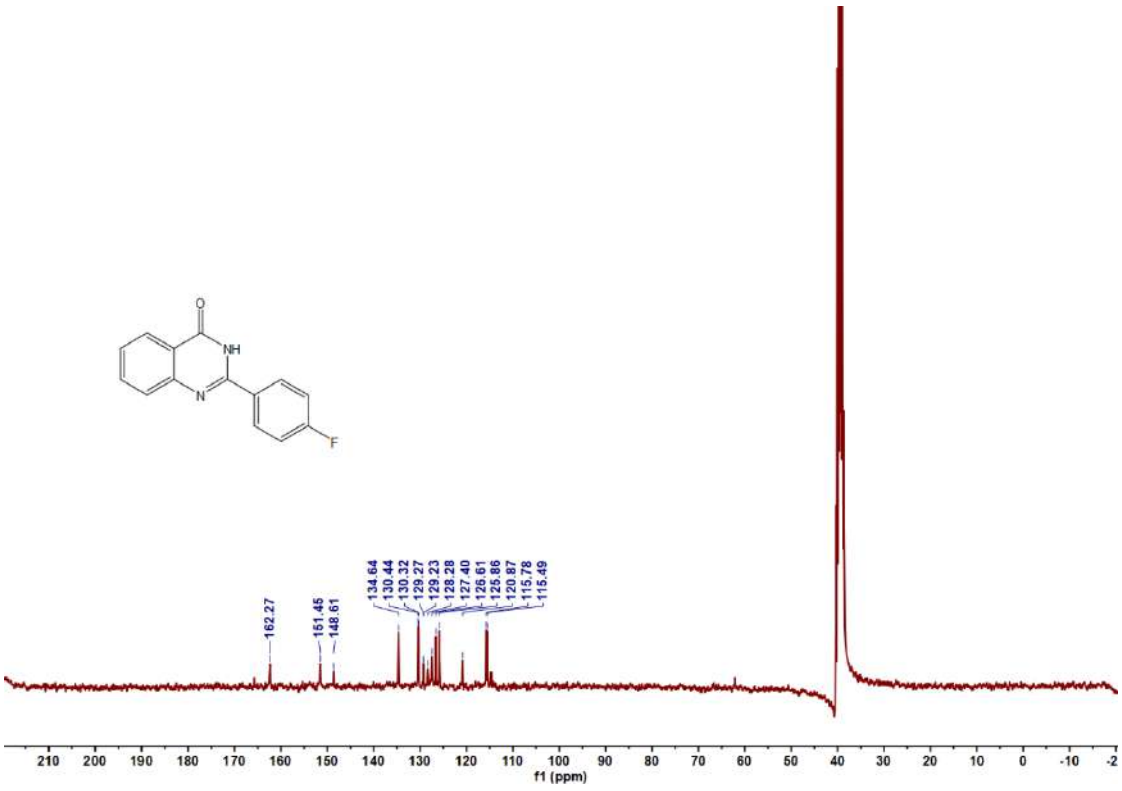

Figure 4.6.A33: ^{13}C{^{1}H} NMR spectrum of **5aj**

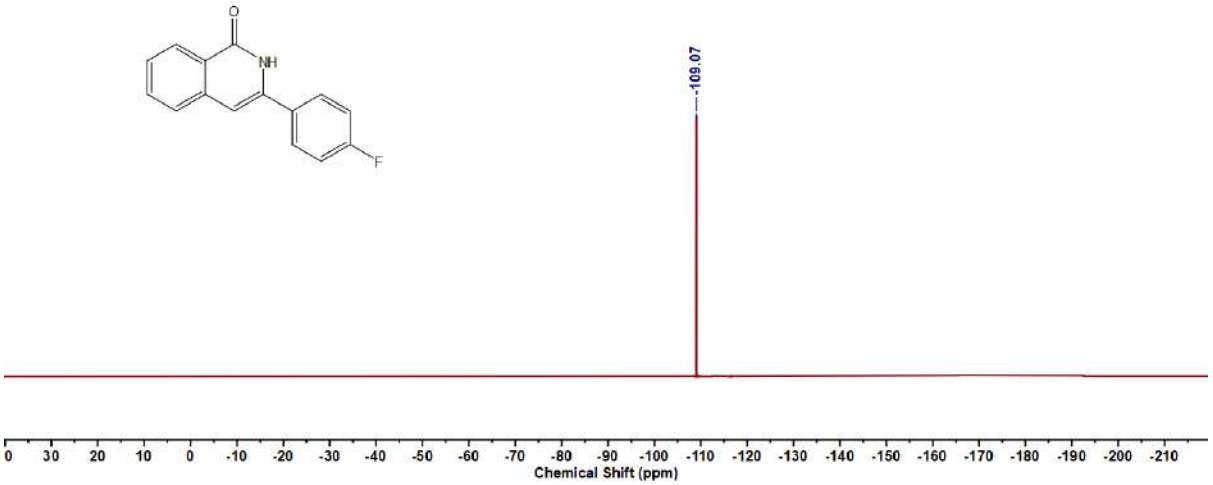

Figure 4.6.A34: ^{19}F NMR spectrum of **5aj**

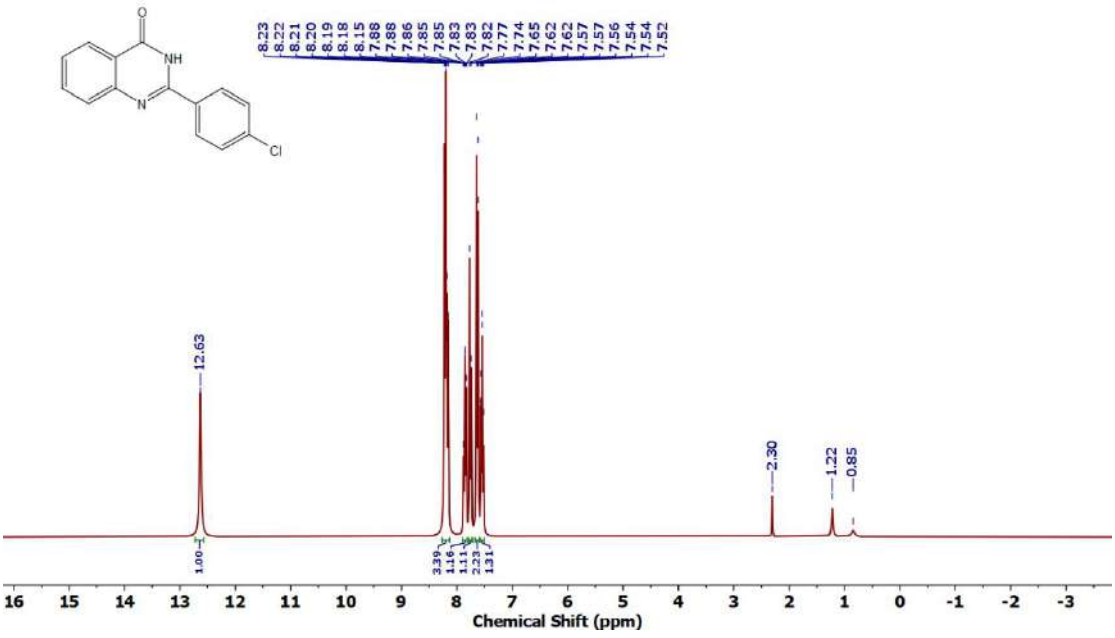

Figure 4.6.A35: ^{1}H NMR spectrum of **5ak**

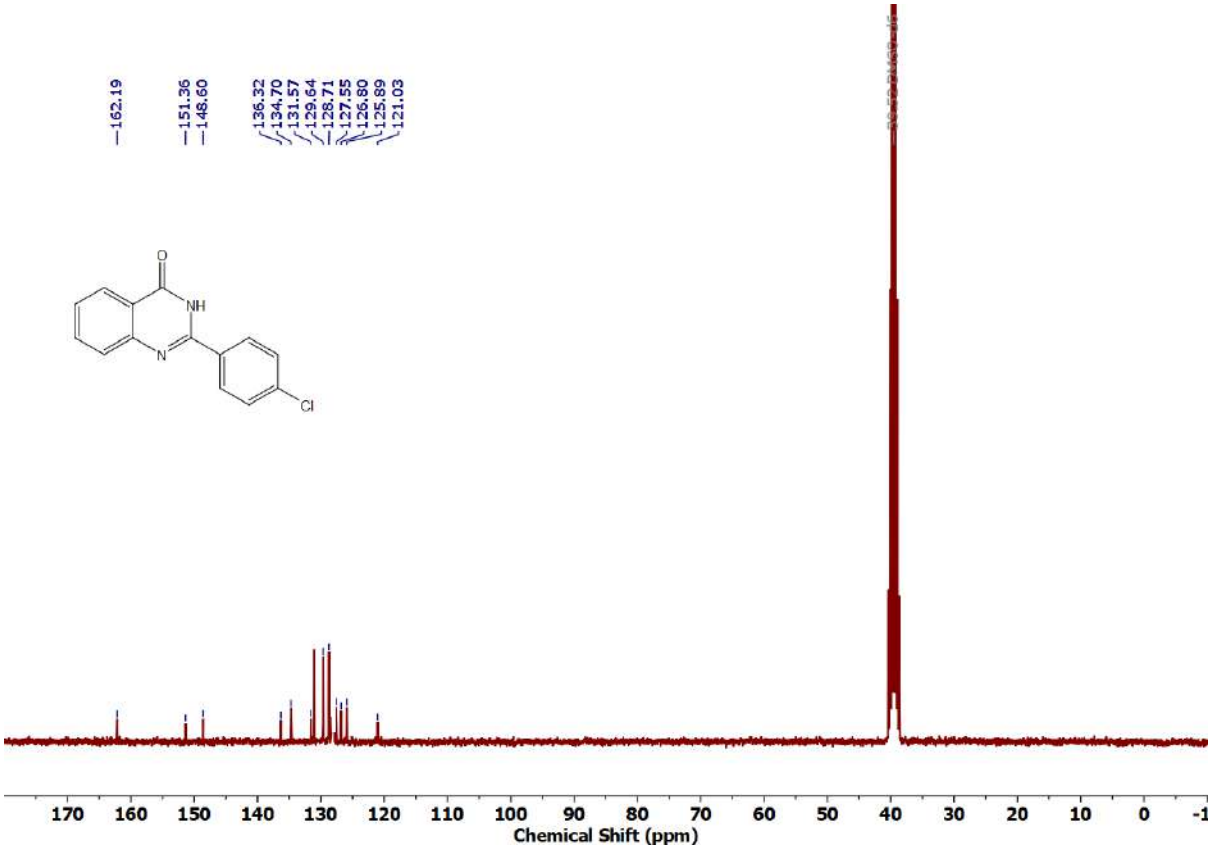

Figure 4.6.A36: $^{13}C\{^{1}H\}$ NMR spectrum of **5ak**

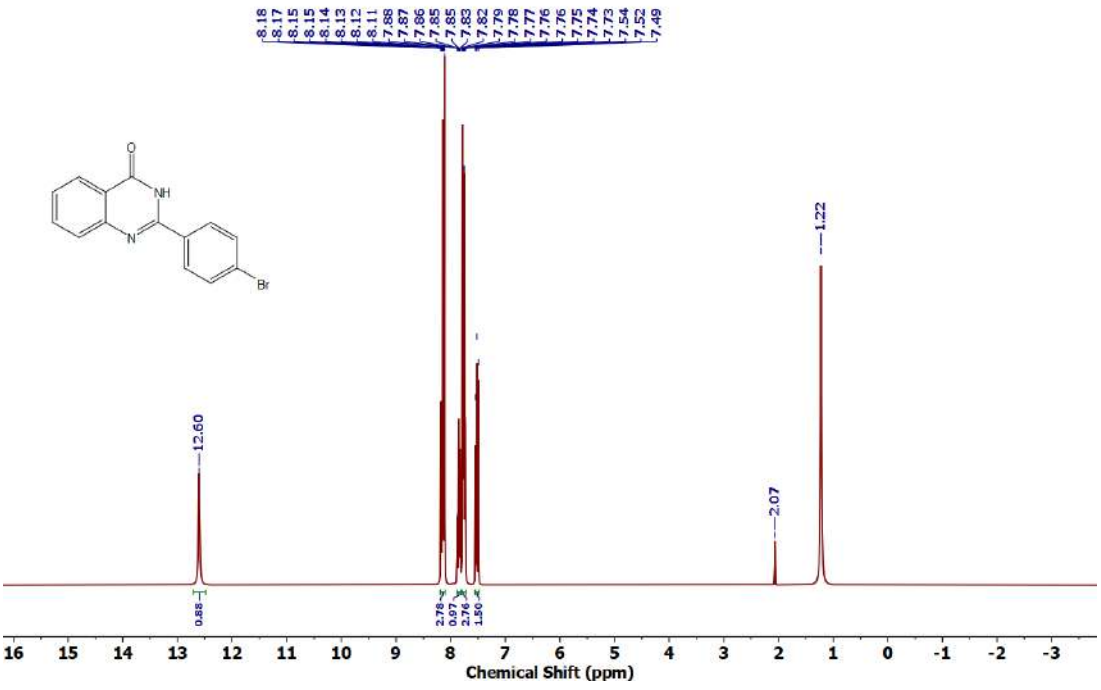

Figure 4.6.A37: ^{1}H NMR spectrum of **5al**

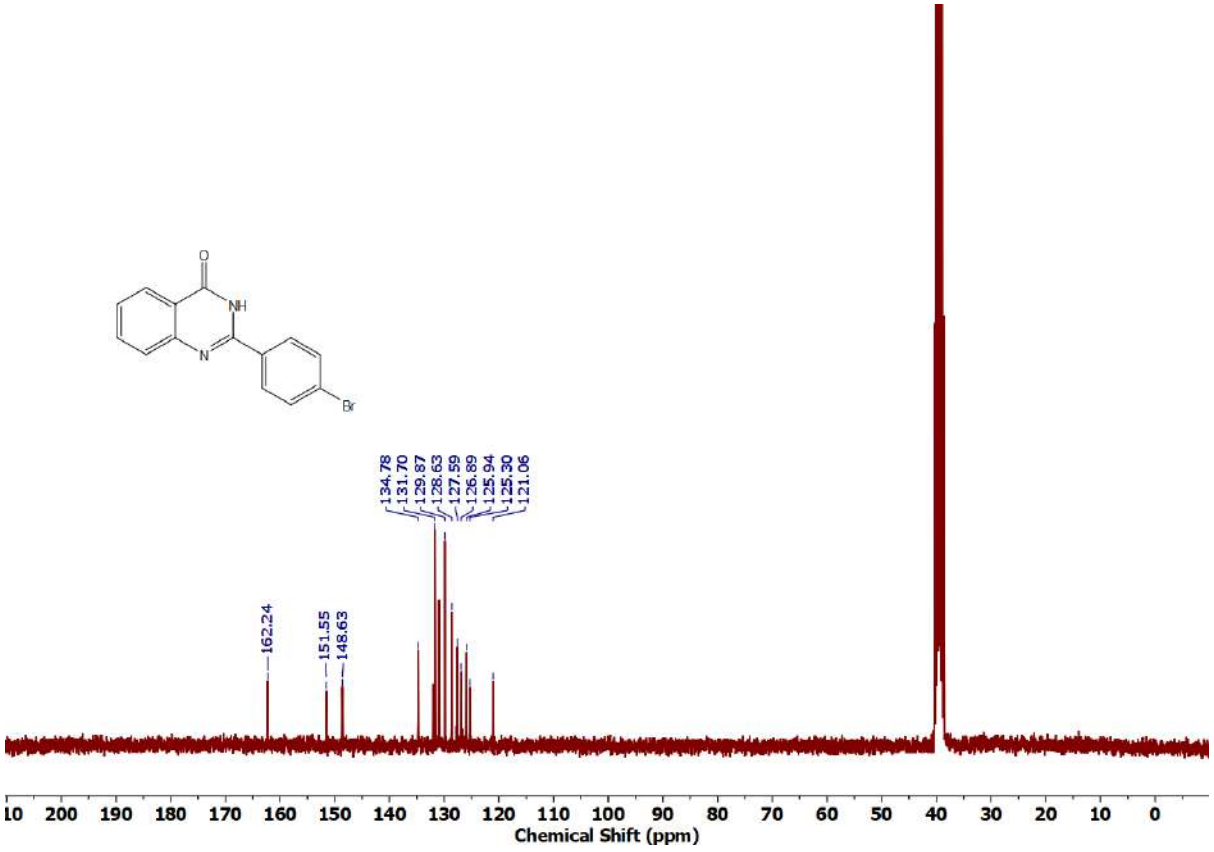

Figure 4.6.A38: $^{13}C\{^{1}H\}$ NMR spectrum of **5al**

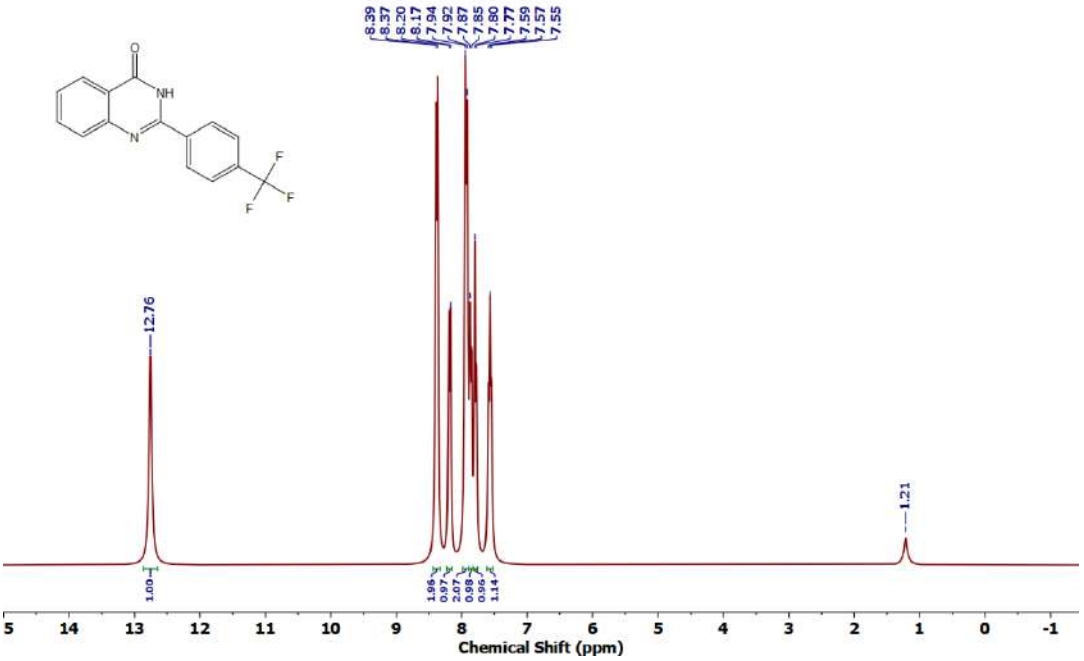

Figure 4.6.A39: ^{1}H NMR spectrum of **5am**

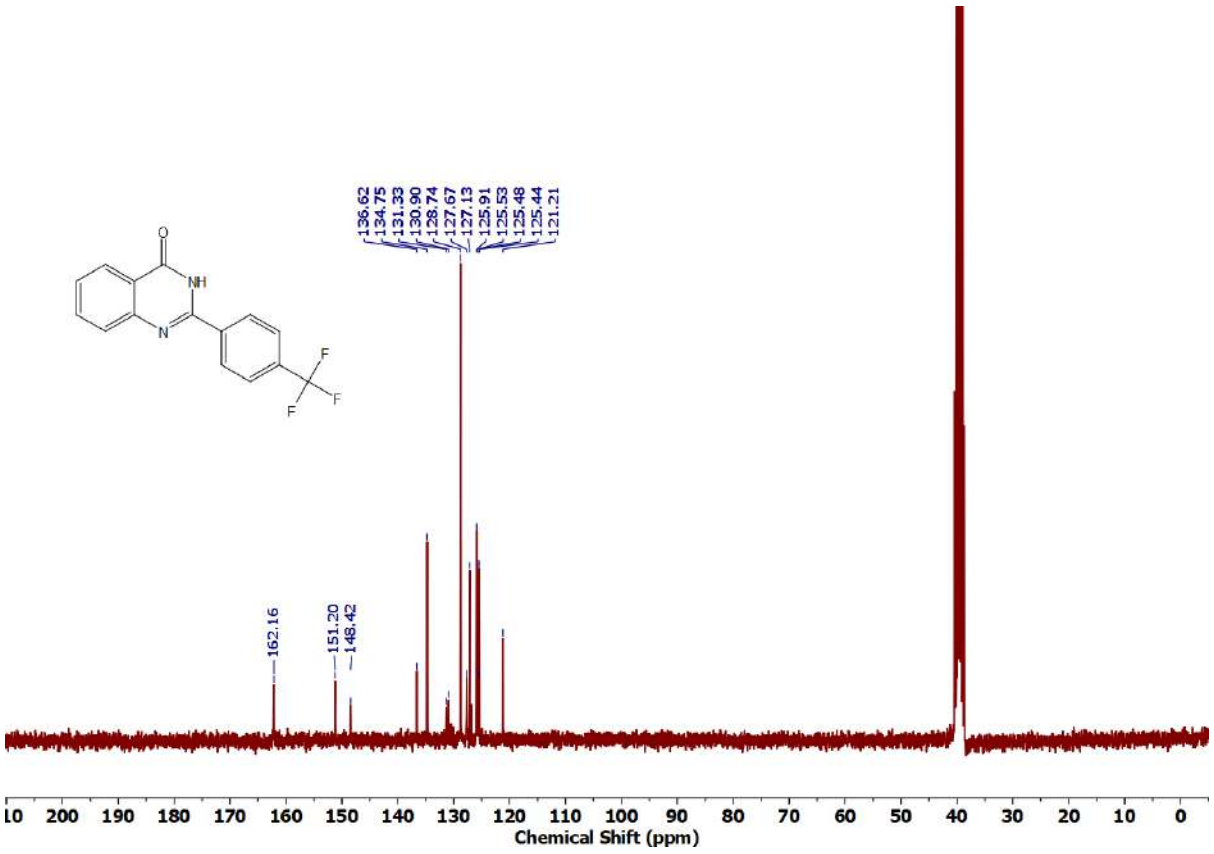

Figure 4.6.A40: $^{13}C\{^{1}H\}$ NMR spectrum of **5am**

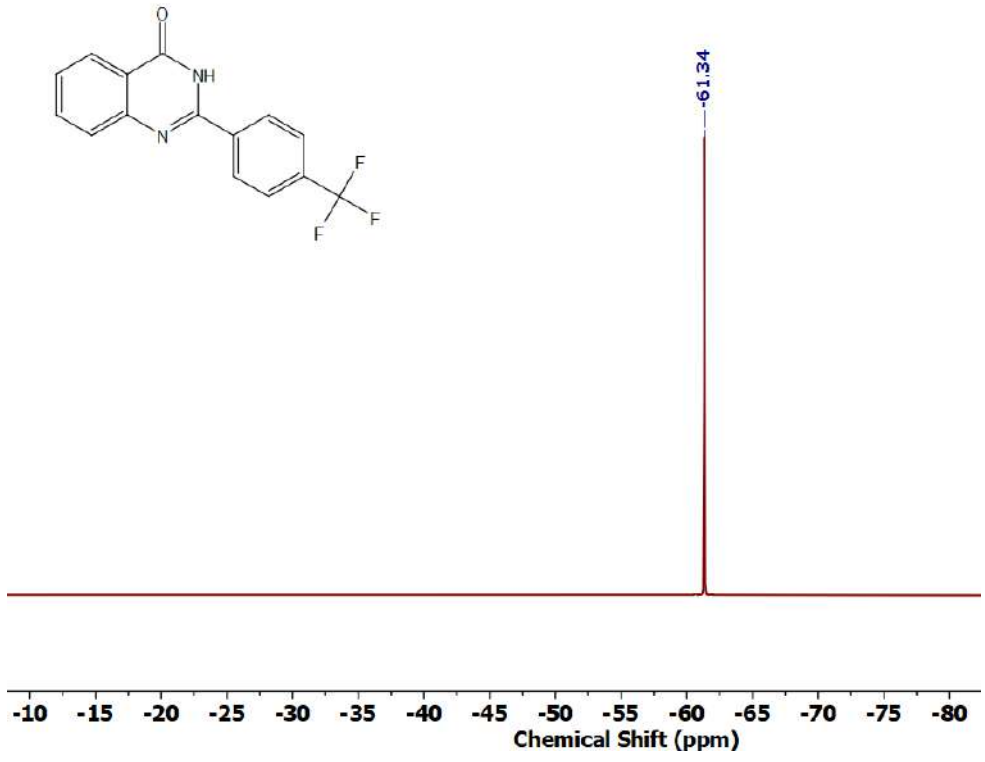

Figure 4.6.A41: ^{19}F NMR spectrum of **5am**

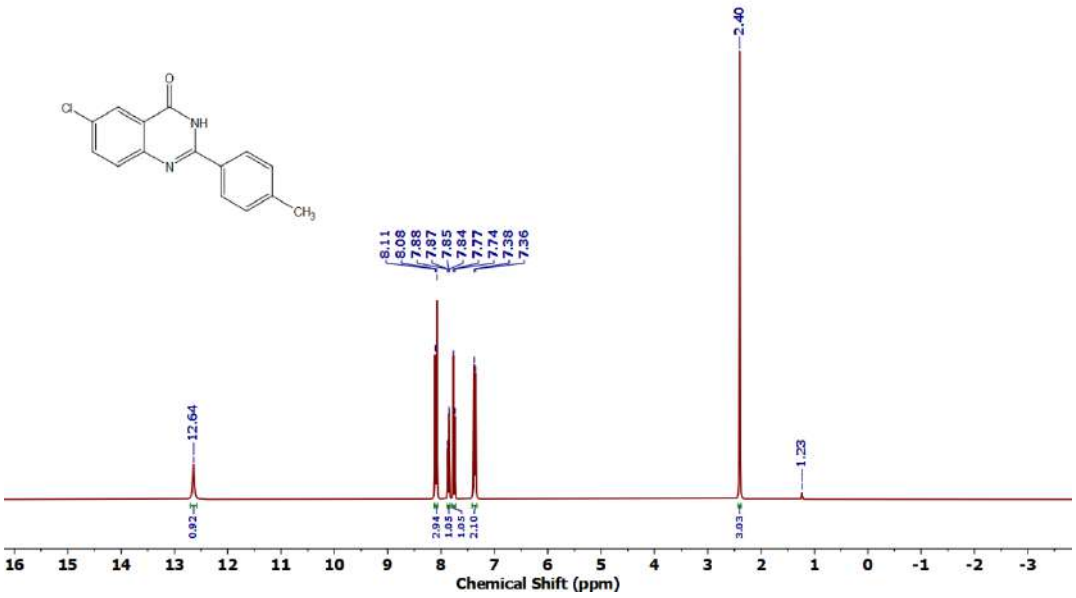

Figure 4.6.A42: ^{1}H NMR spectrum of **5an**

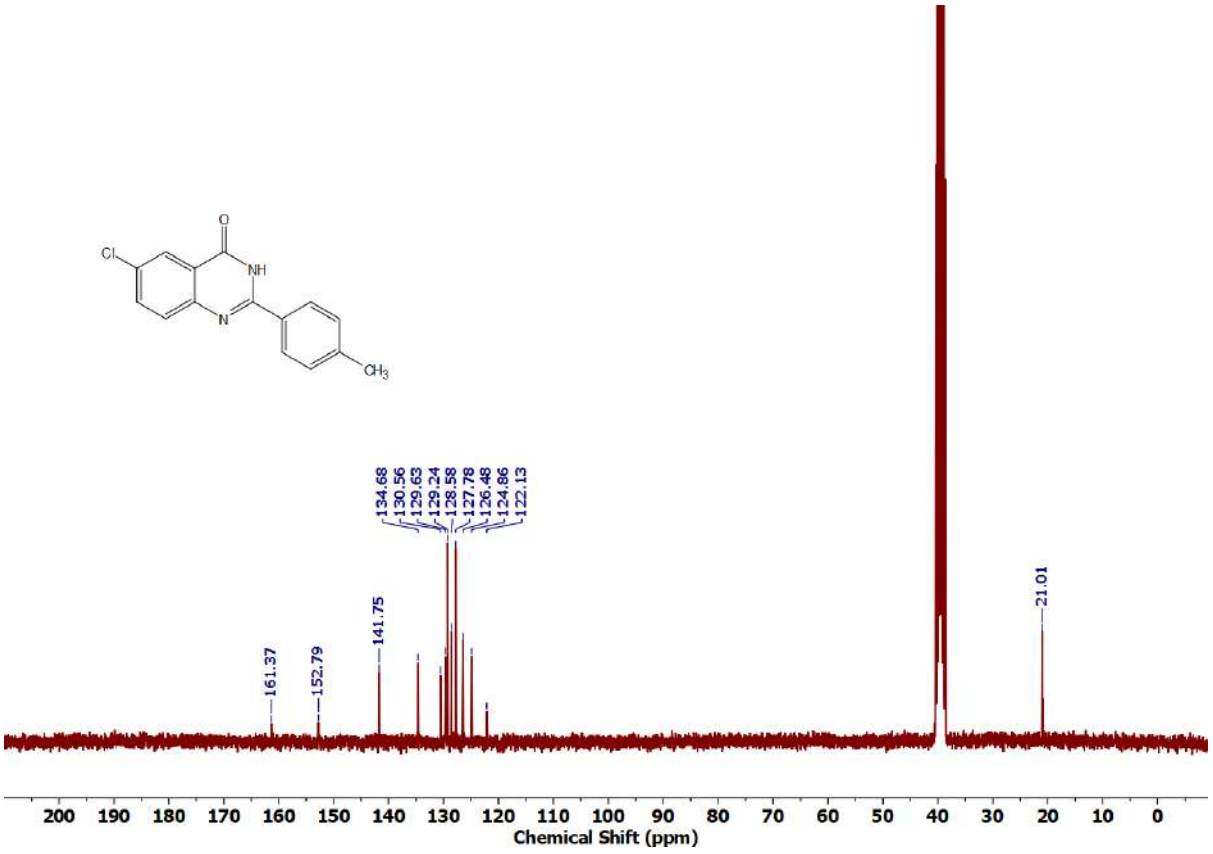

Figure 4.6.A43: ^{13}C{^{1}H} NMR spectrum of **5an**

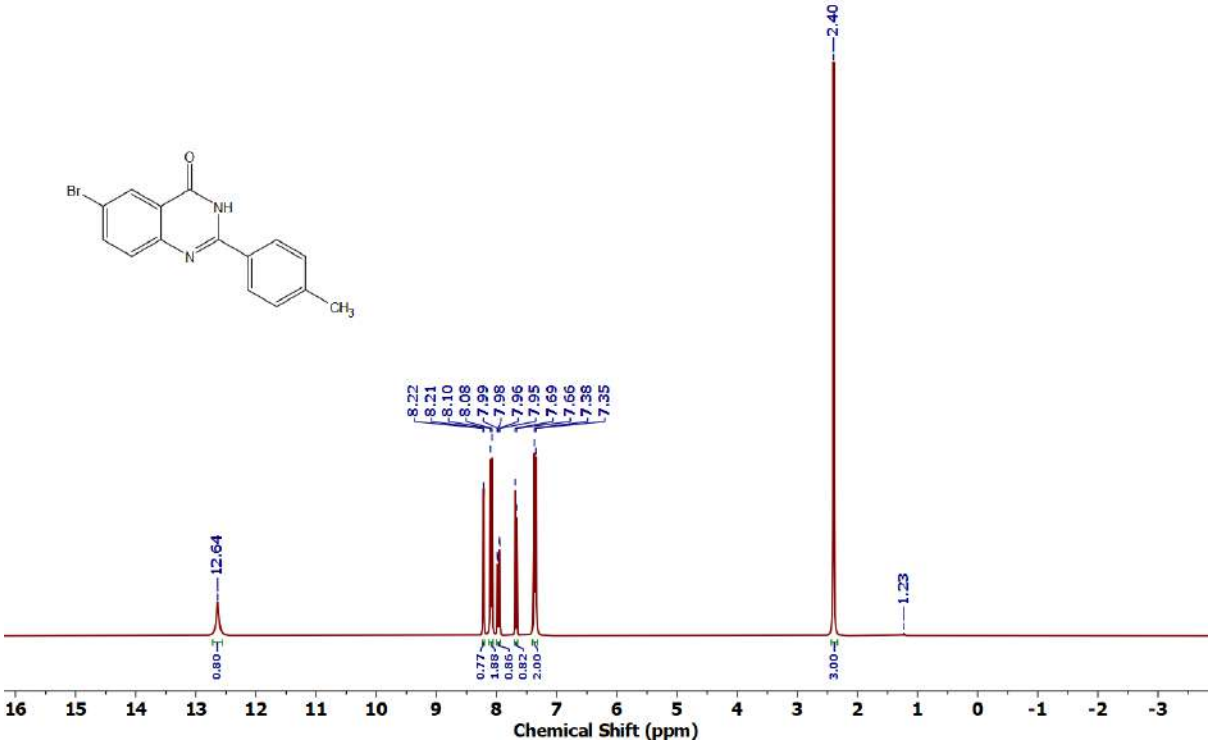

Figure 4.6.A44: ^{1}H NMR spectrum of **5ao**

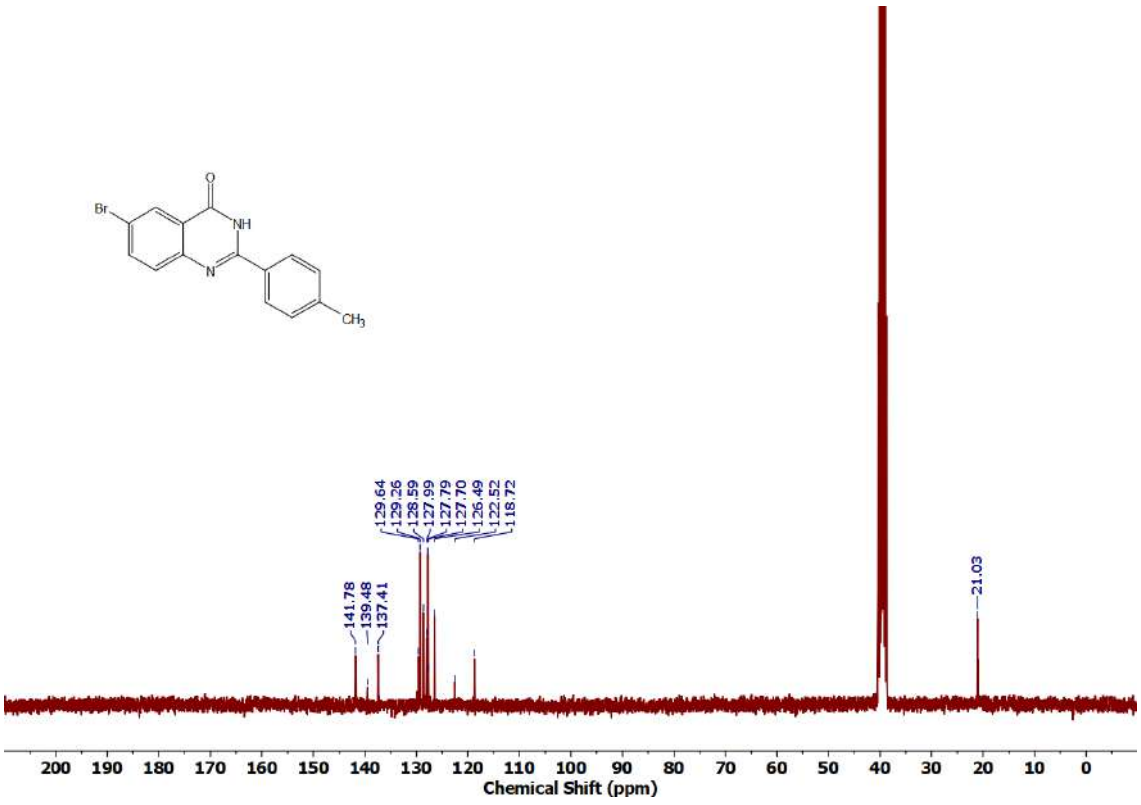

Figure 4.6.A45: ^{13}C{^{1}H} NMR spectrum of **5ao**

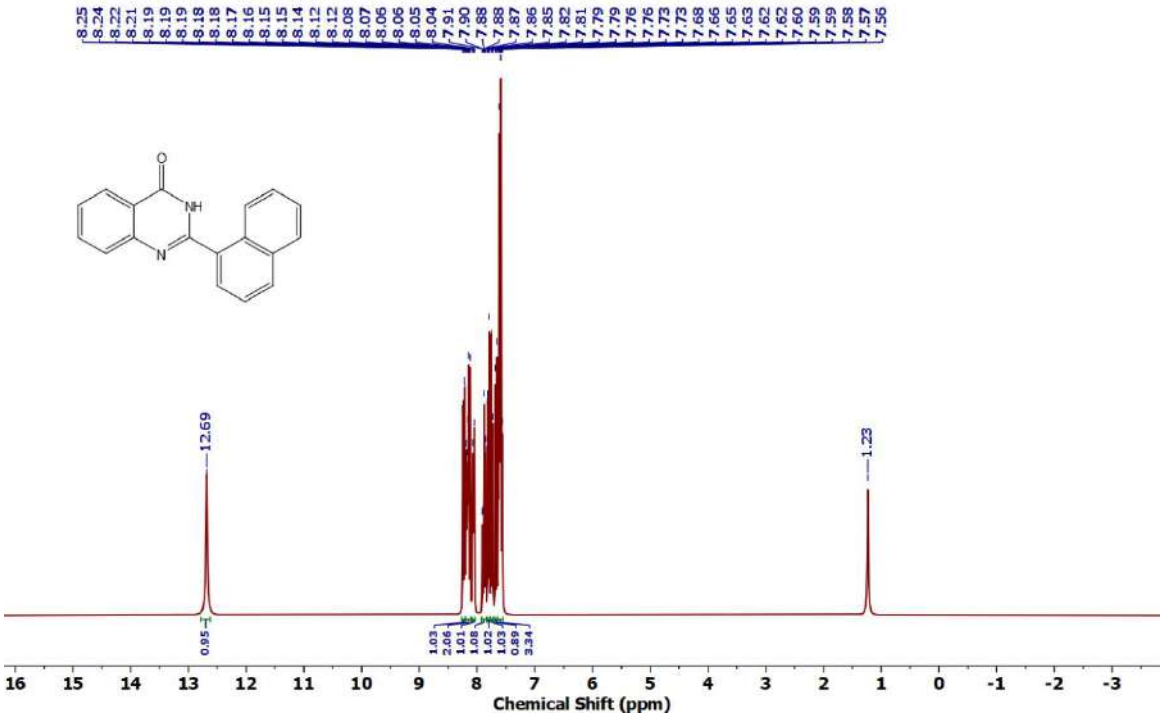

Figure 4.6.A46: ^{1}H NMR spectrum of **5ap**

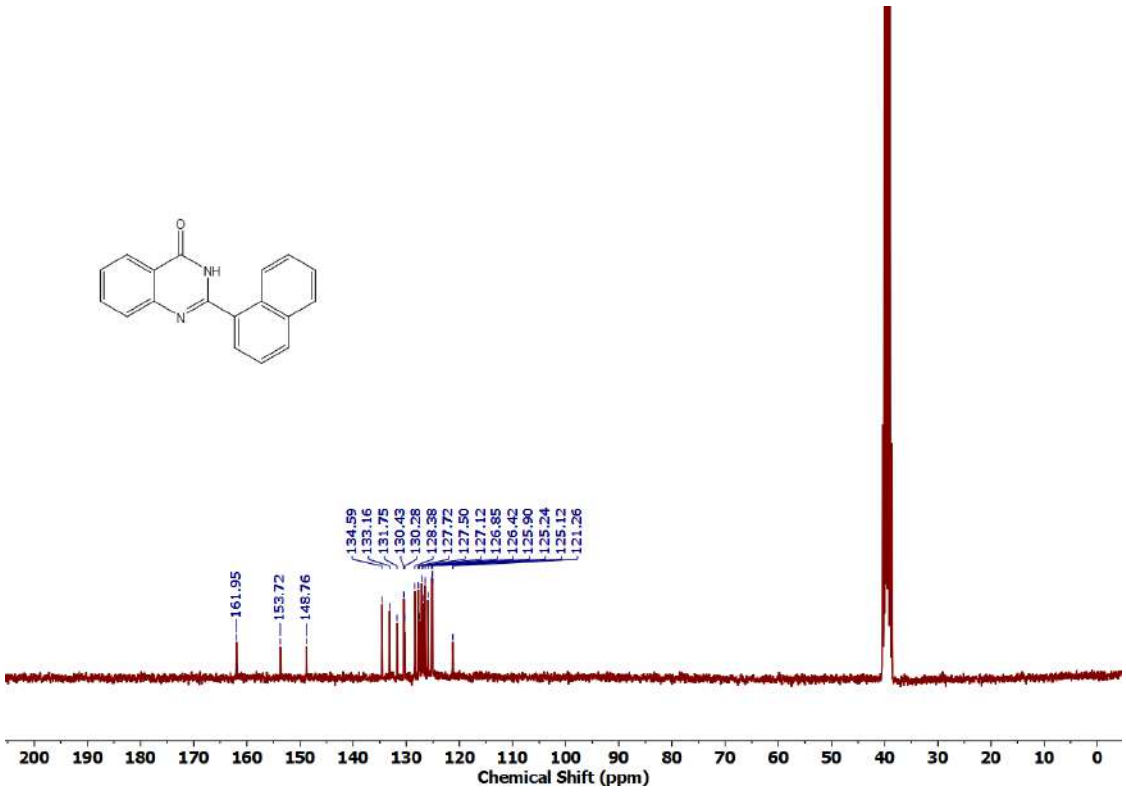

Figure 4.6.A47: ^{13}C{^{1}H} NMR spectrum of **5ap**

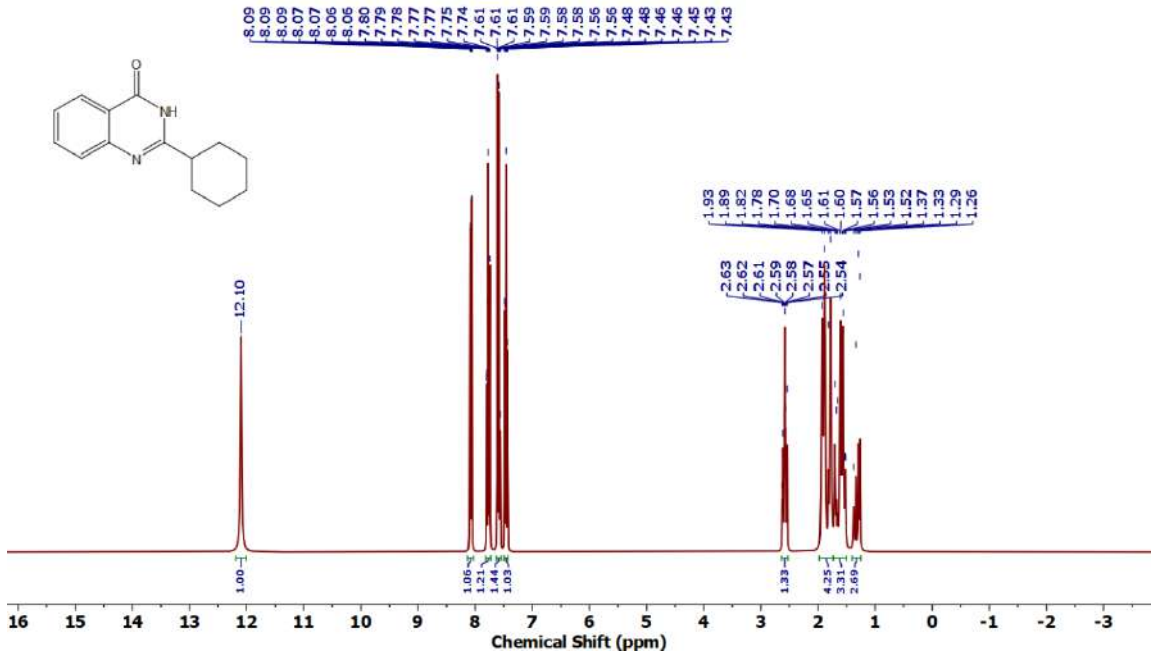

Figure 4.6.A48: ^{1}H NMR spectrum of **5aq**

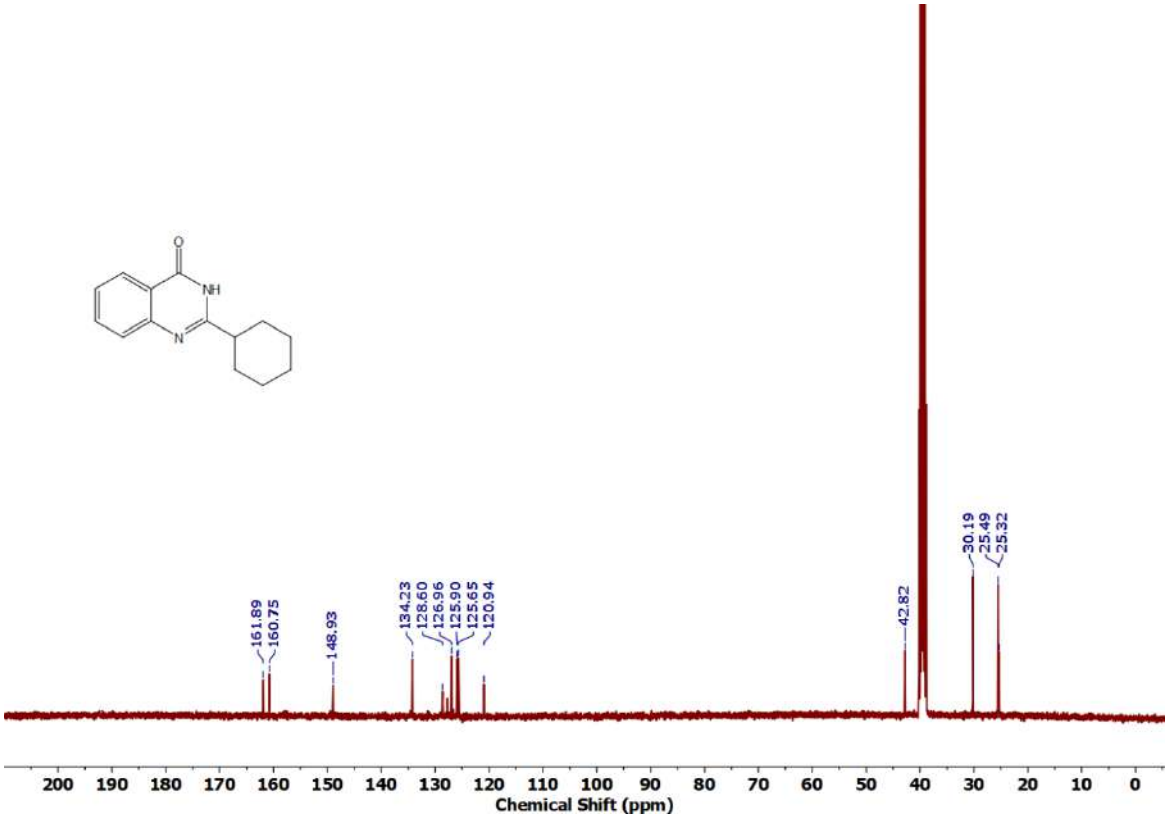

Figure 4.6.A49: ^{13}C{^{1}H} NMR spectrum of **5aq**

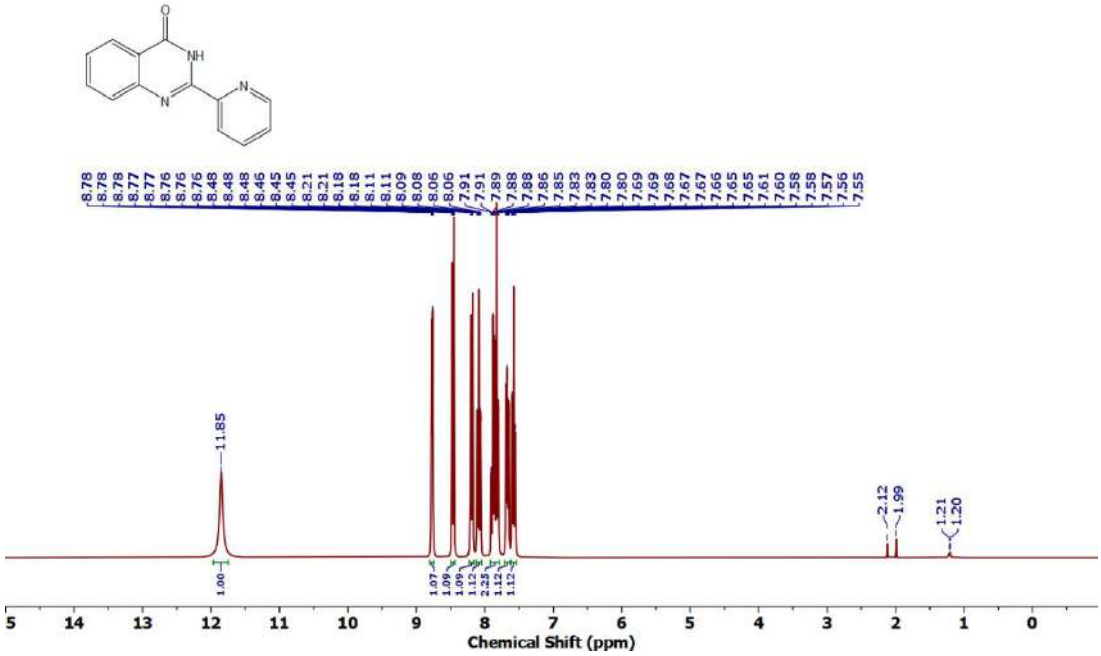

Figure 4.6.A50: ^{1}H NMR spectrum of **5ar**

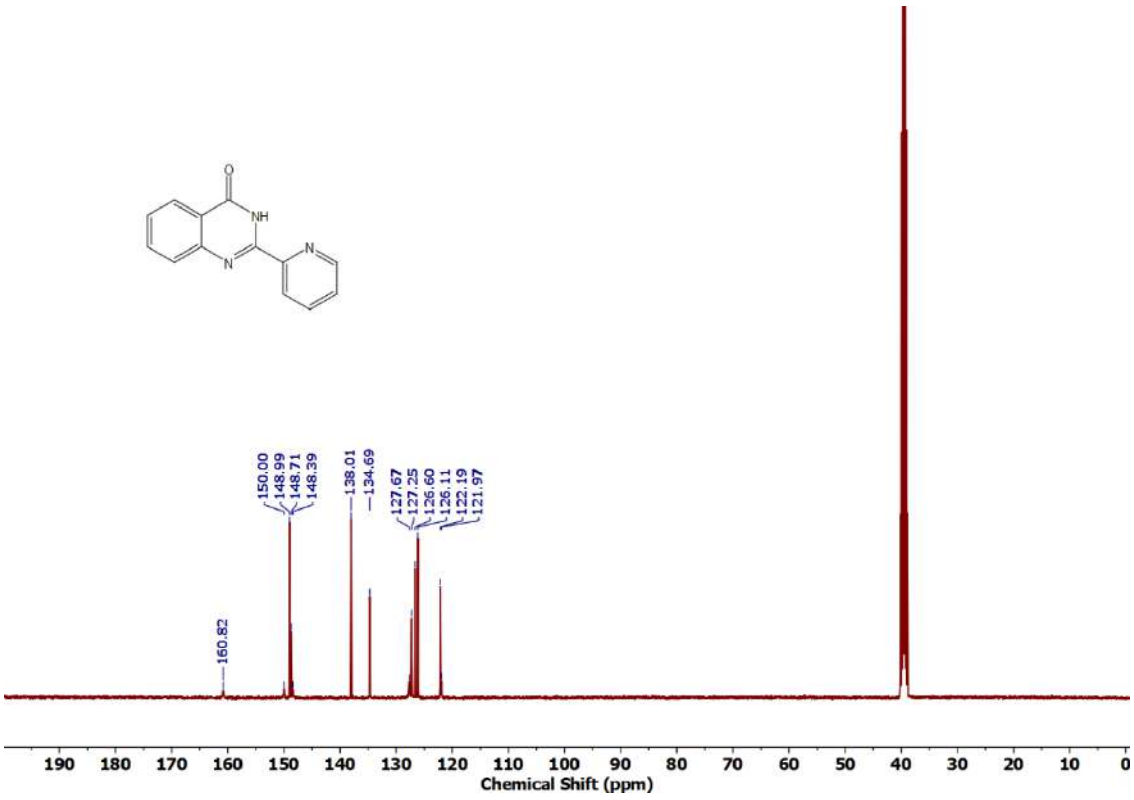

Figure 4.6.A51: ^{13}C{^{1}H} NMR spectrum of **5ar**

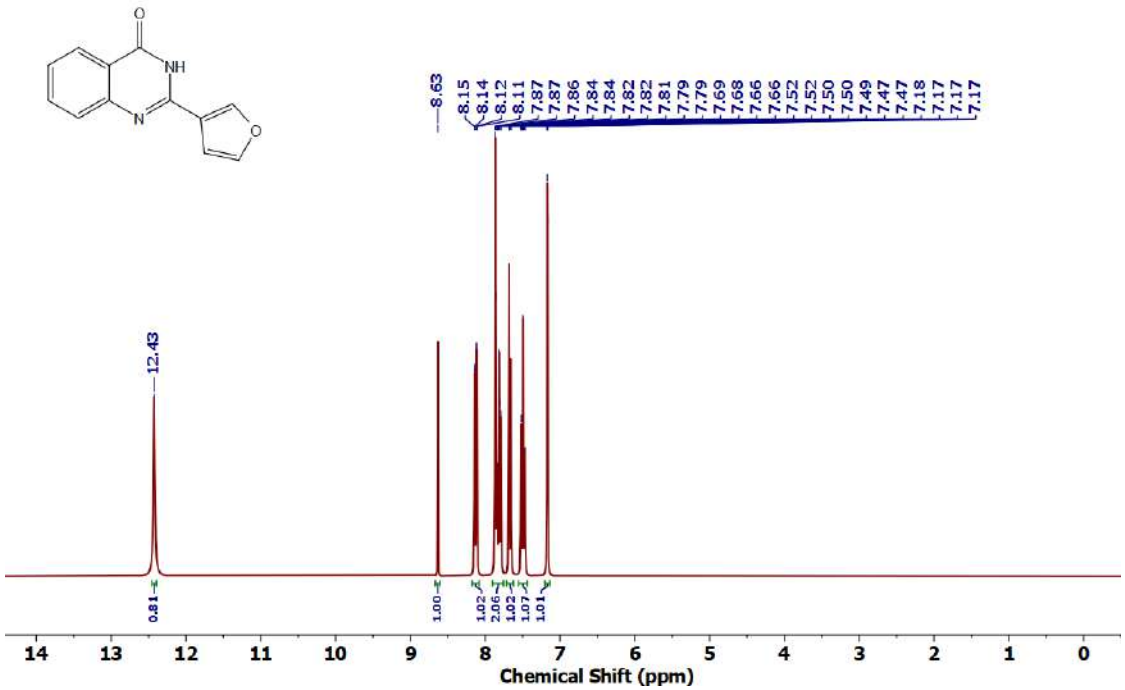

Figure 4.6.A52: ^{1}H NMR spectrum of **5as**

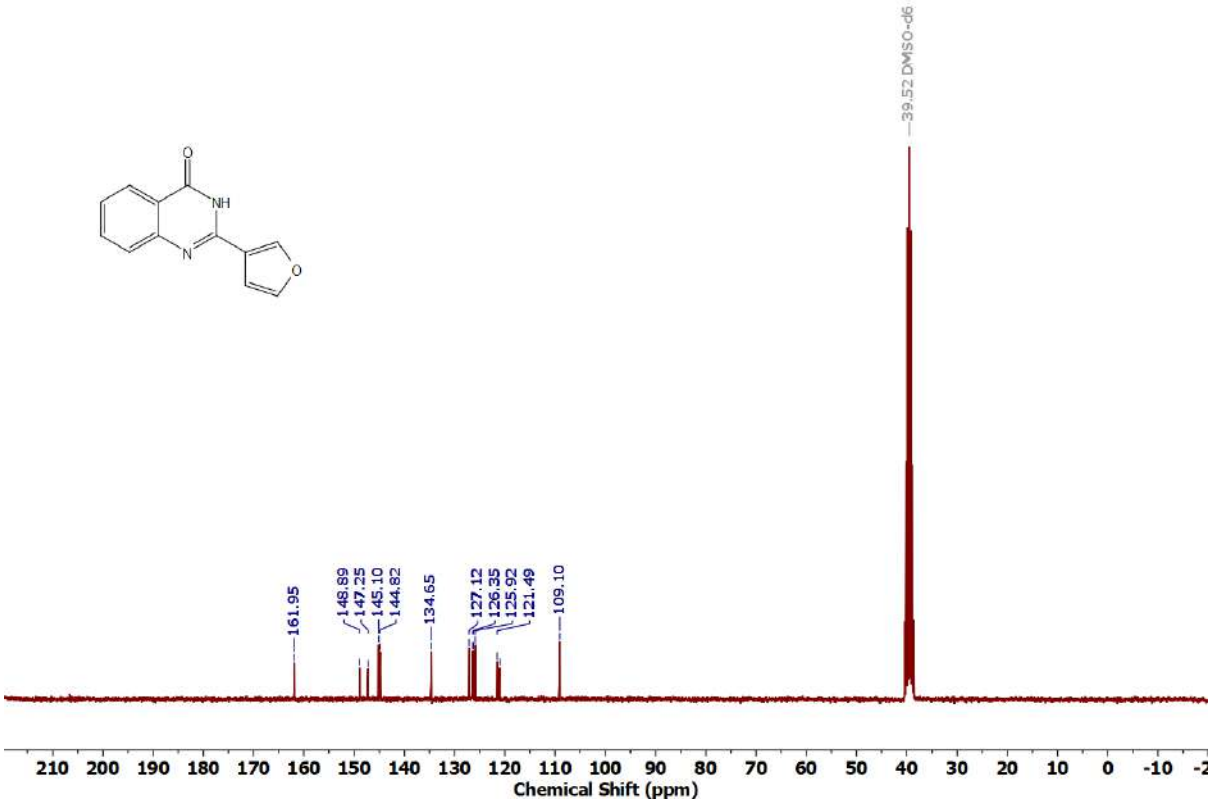

Figure 4.6.A53: ^{13}C{^{1}H} NMR spectrum of **5as**

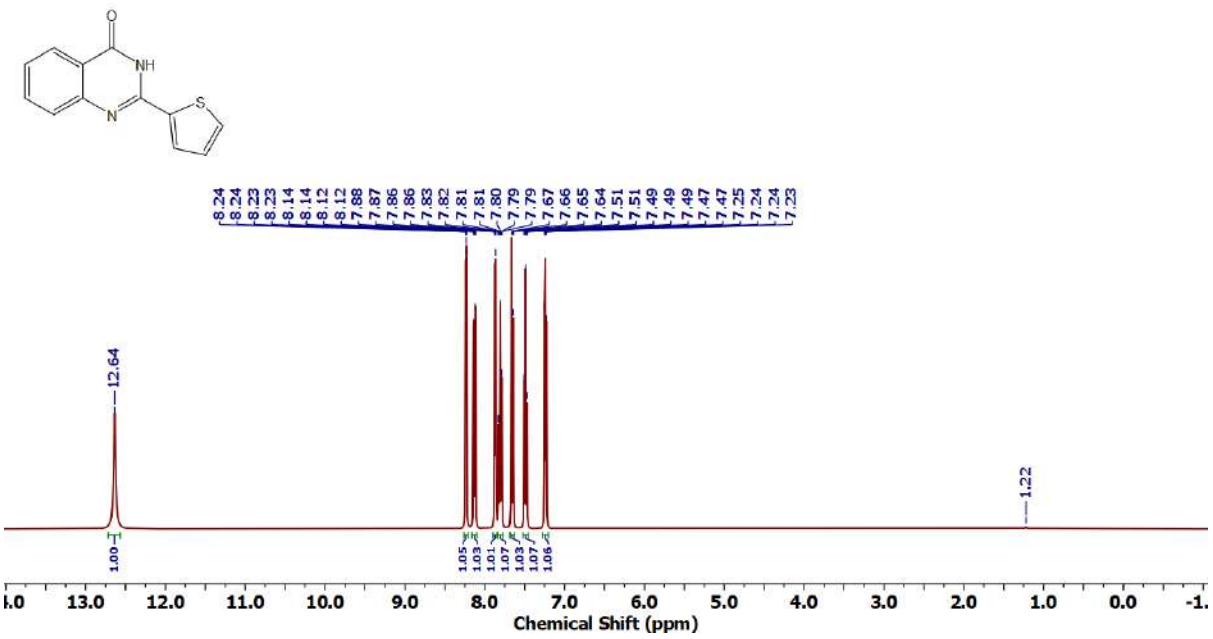

Figure 4.6.A54: ^{1}H NMR spectrum of **5at**

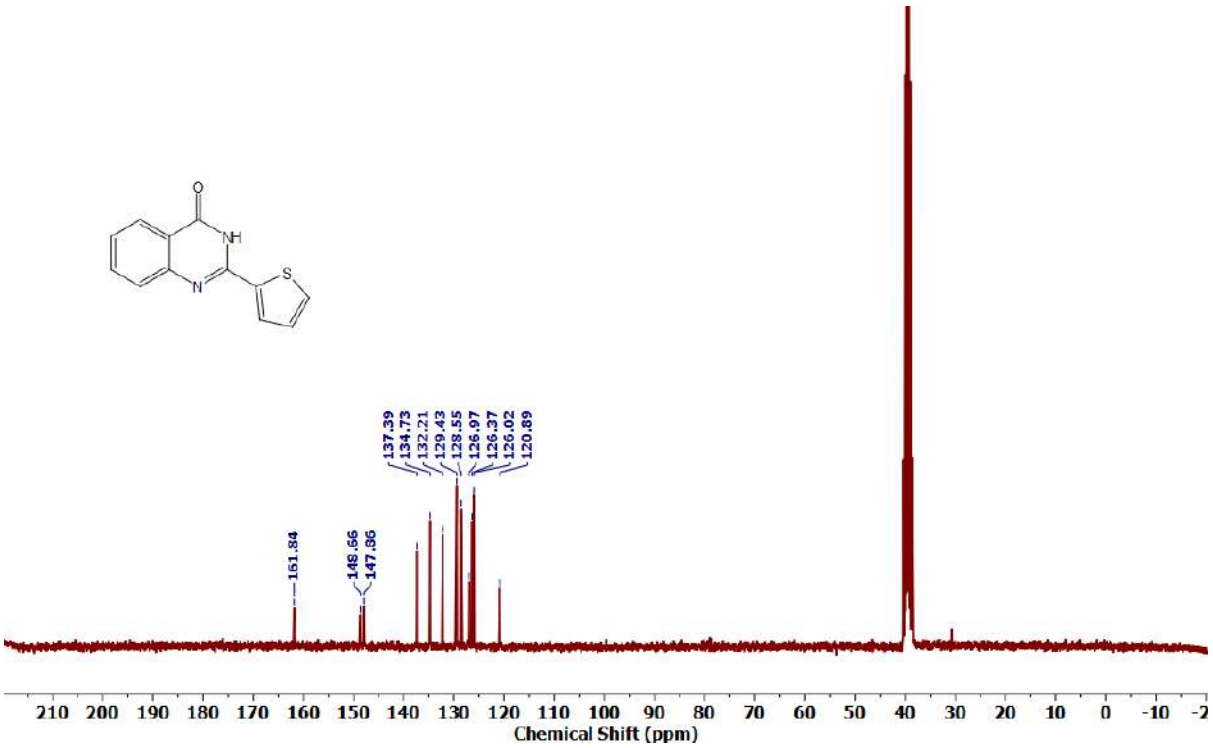

Figure 4.6.A55: ^{13}C{^{1}H} NMR spectrum of **5at**

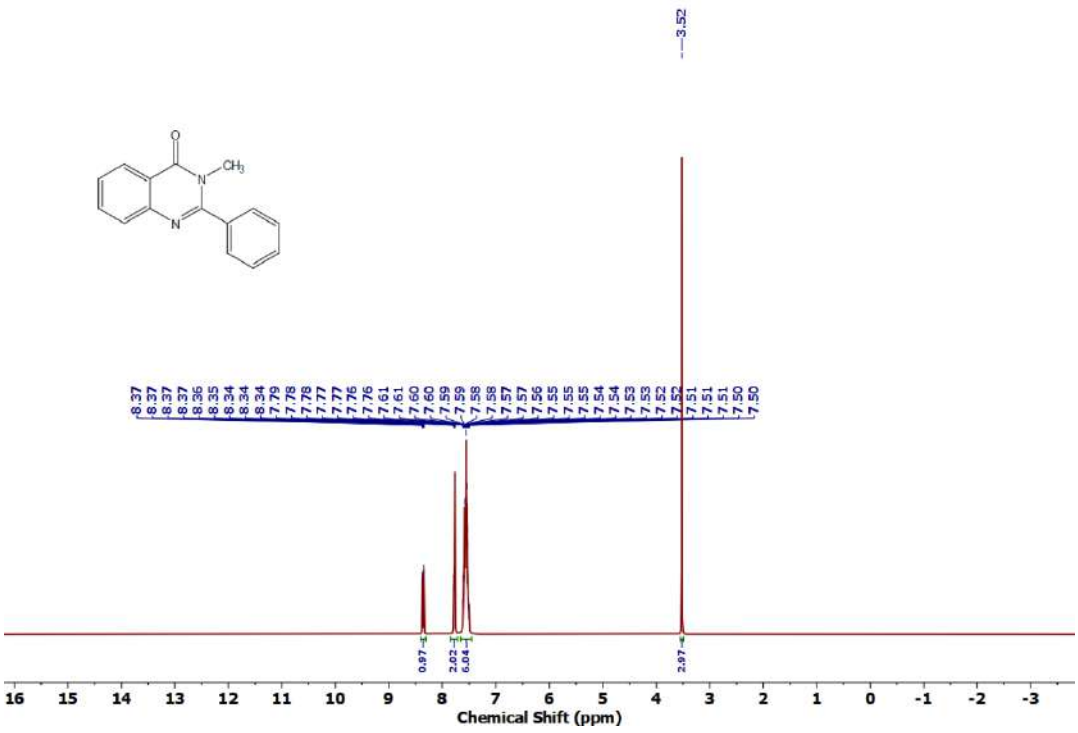

Figure 4.6.A56: ^{1}H NMR spectrum of **7aa**

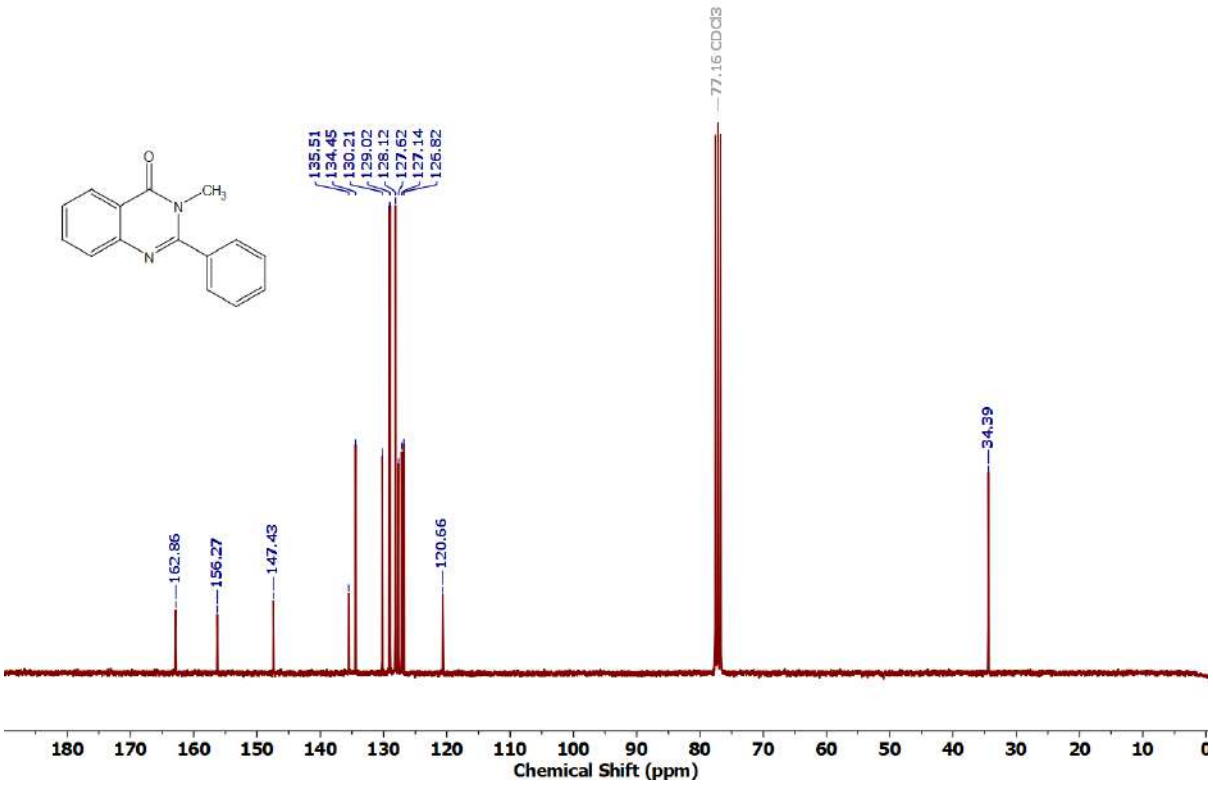

Figure 4.6.A57: ^{13}C{^{1}H} NMR spectrum of **7aa**

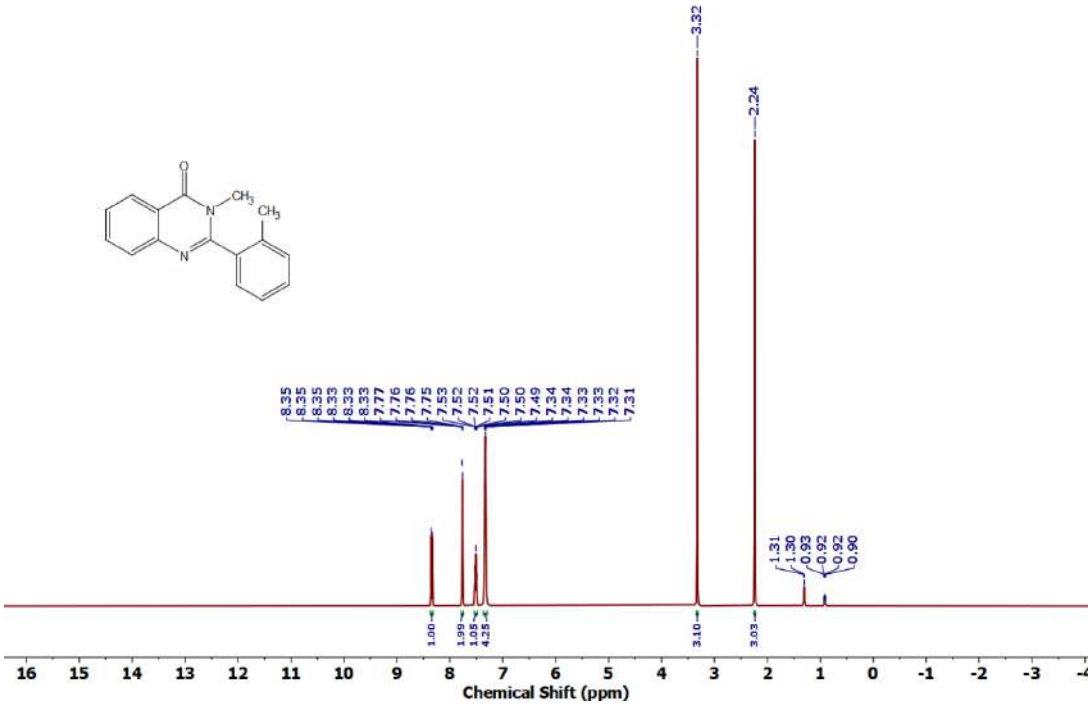

Figure 4.6.A58: ^{1}H NMR spectrum of **7ab**

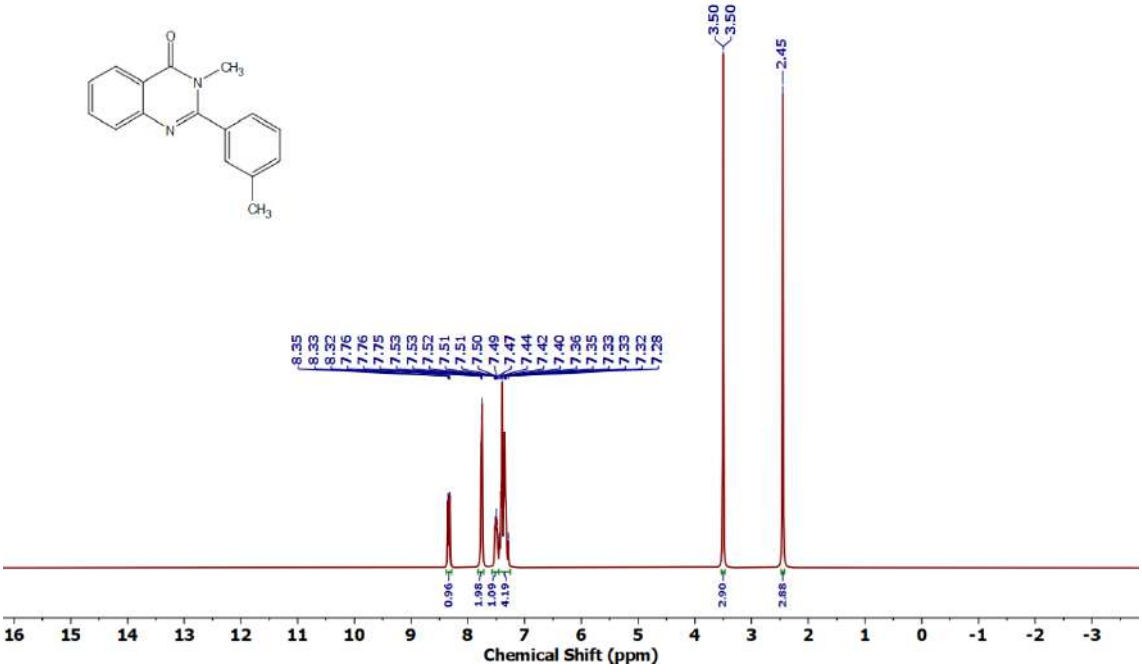

Figure 4.6.A59: ^{1}H NMR spectrum of **7ac**

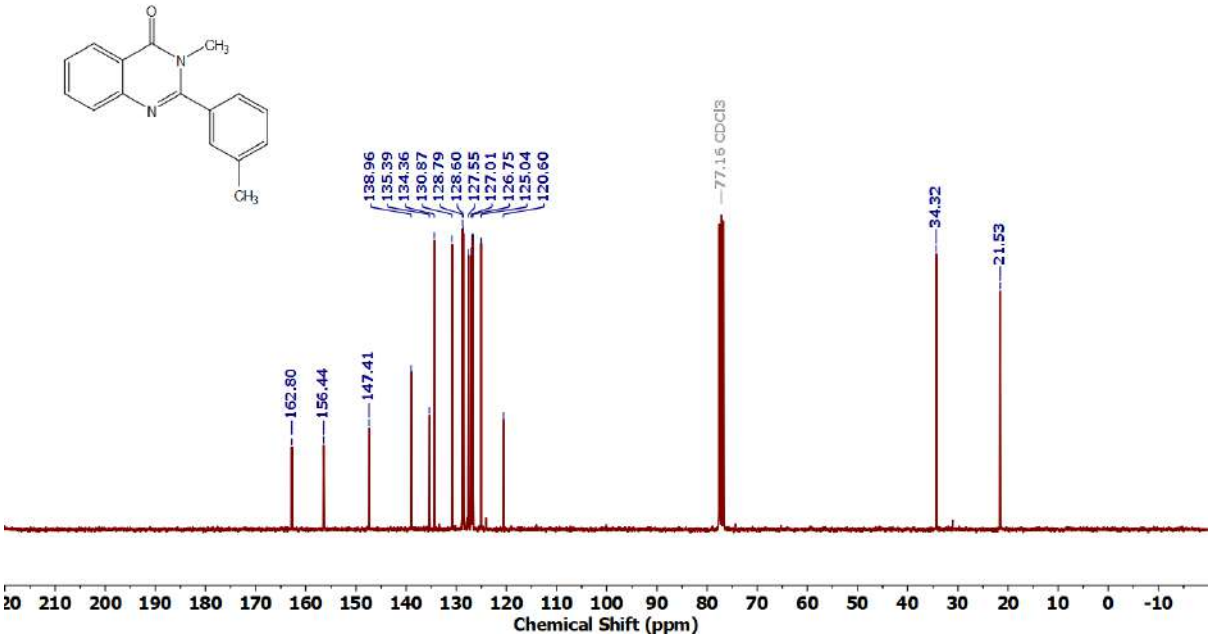

Figure 4.6.A60: $^{13}C\{^{1}H\}$ NMR spectrum of **7ac**

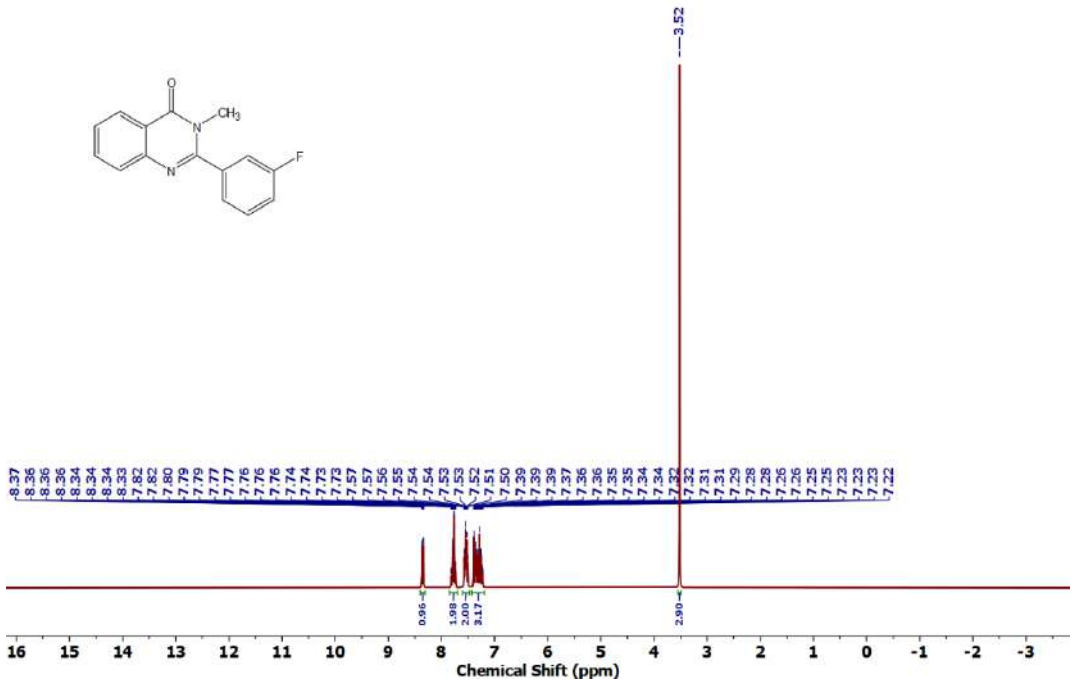

Figure 4.6.A61: ^{1}H NMR spectrum of **7ad**

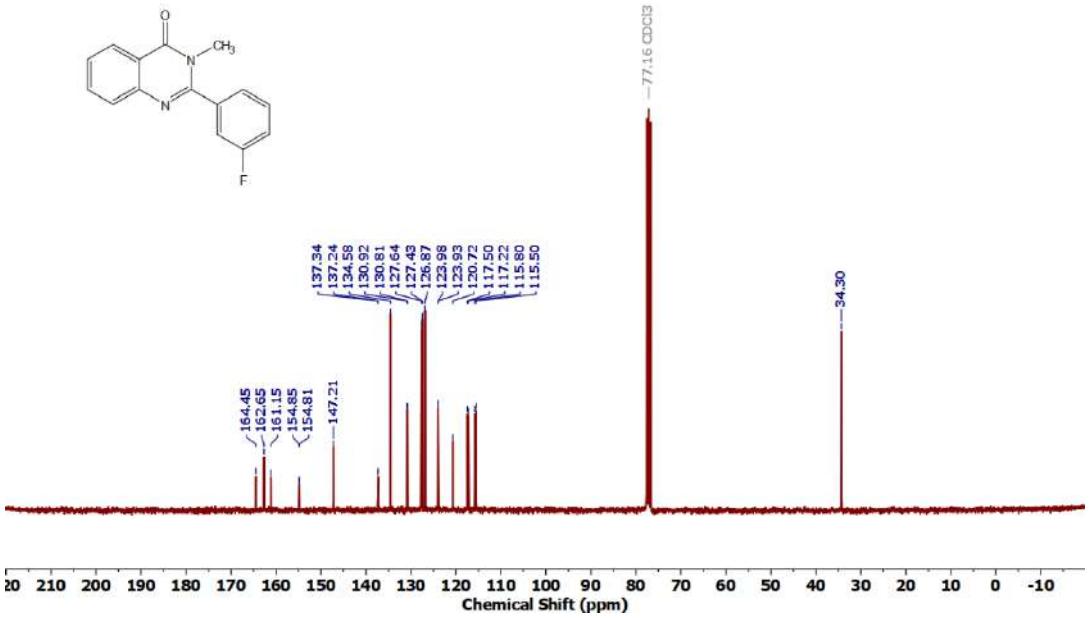

Figure 4.6.A62: $^{13}C\{^{1}H\}$ NMR spectrum of **7ad**

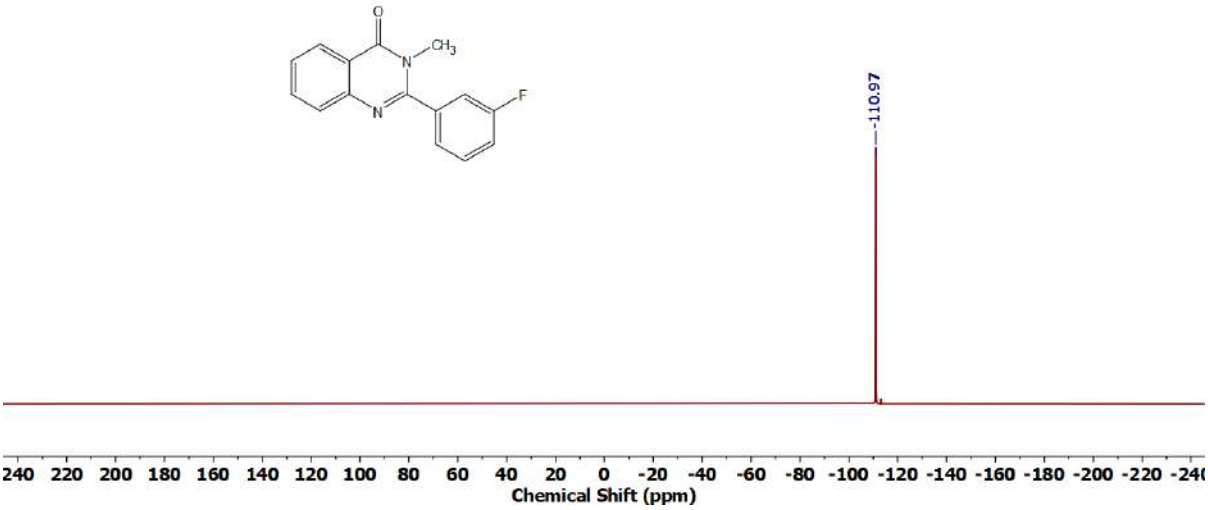

Figure 4.6.A63: ^{19}F NMR spectrum of **7ad**

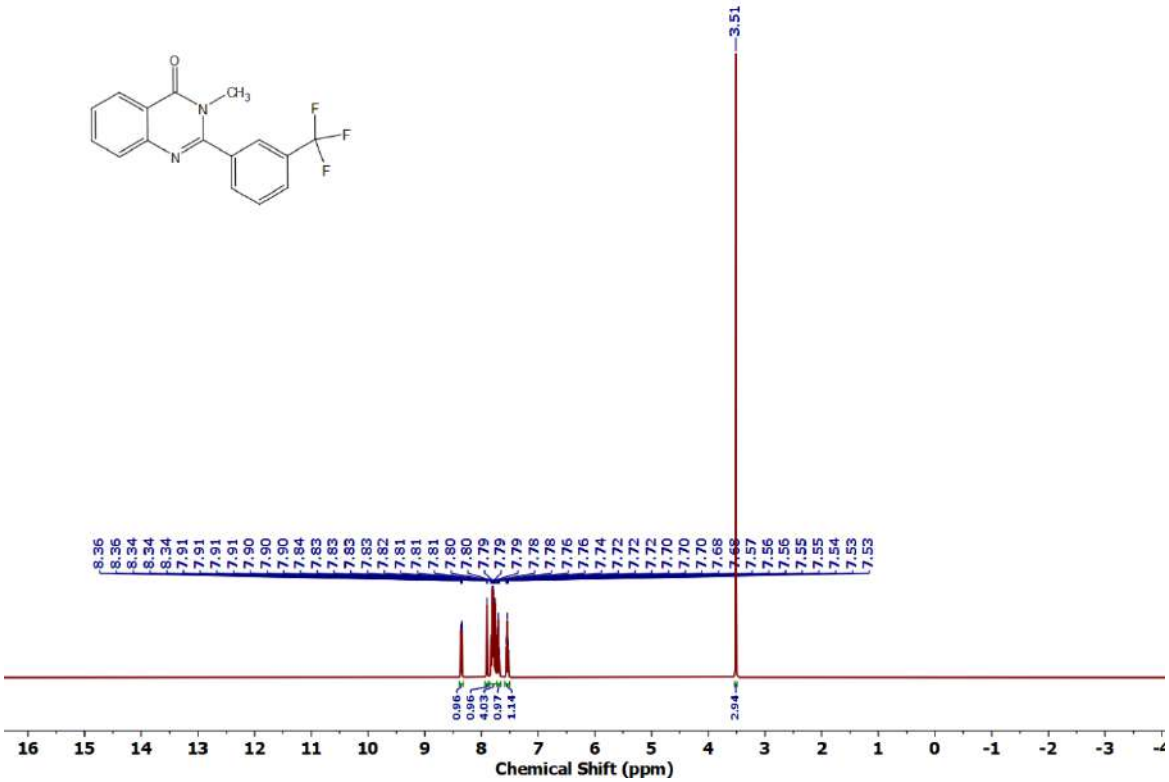

Figure 4.6.A64: ^{1}H NMR spectrum of **7ae**

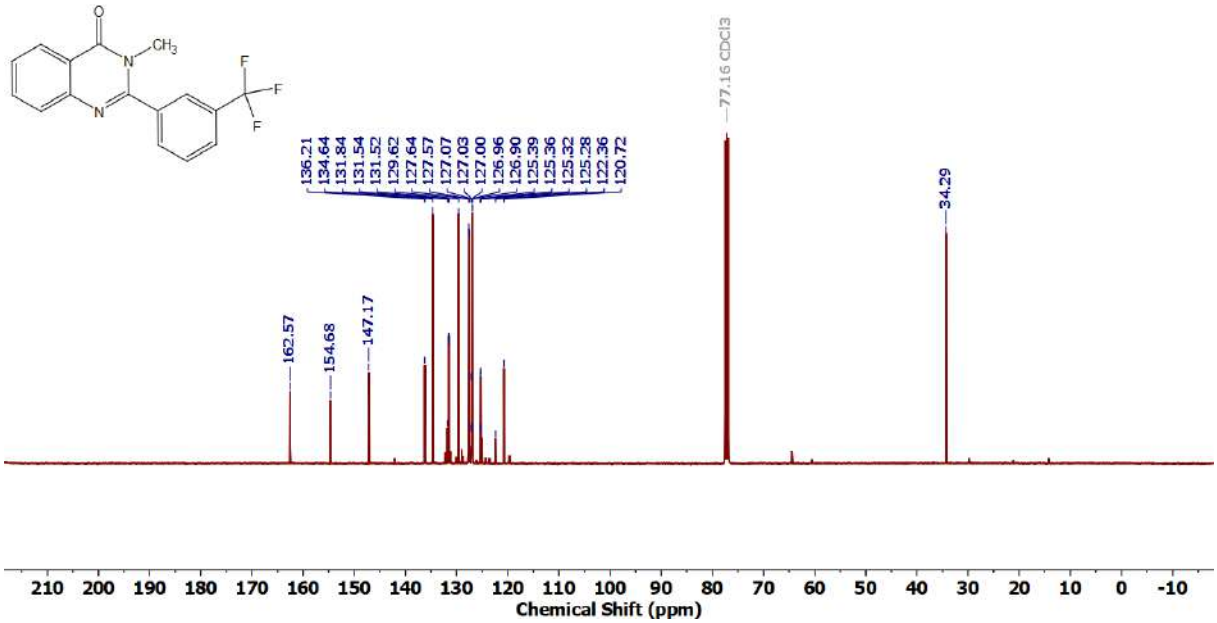

Figure 4.6.A65: ^{13}C{^{1}H} NMR spectrum of **7ae**

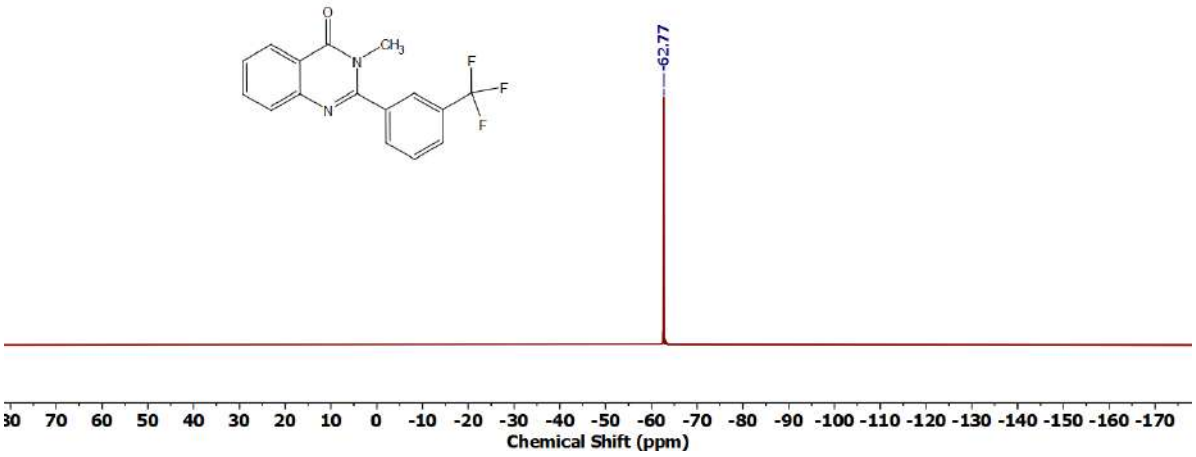

Figure 4.6.A66: ^{19}F NMR spectrum of **7ae**

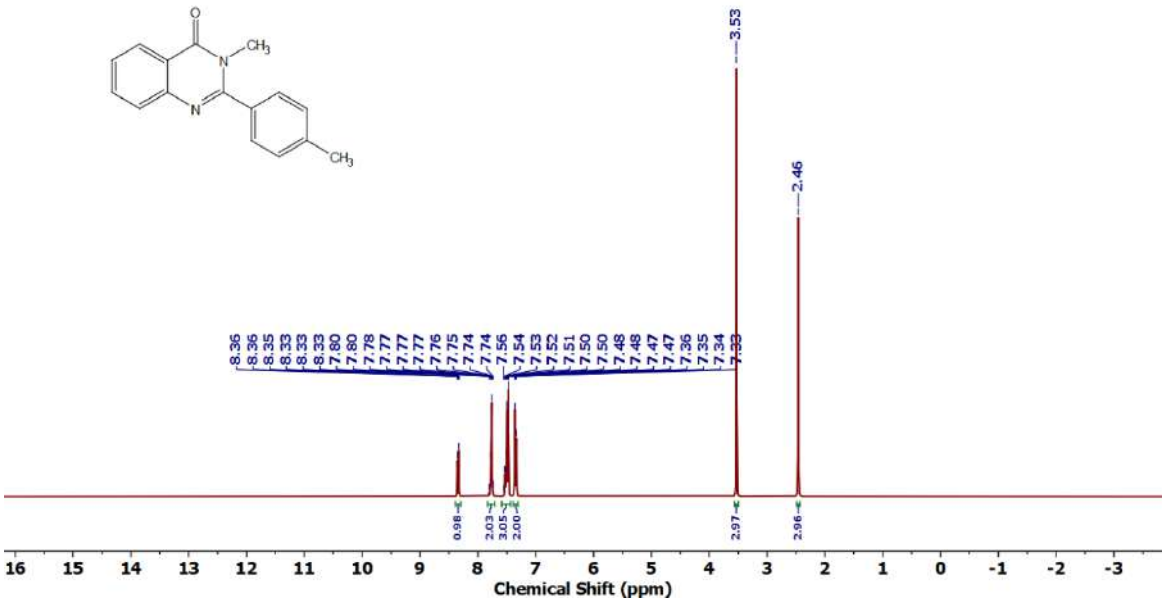

Figure 4.6.A67: ^{1}H NMR spectrum of **7af**

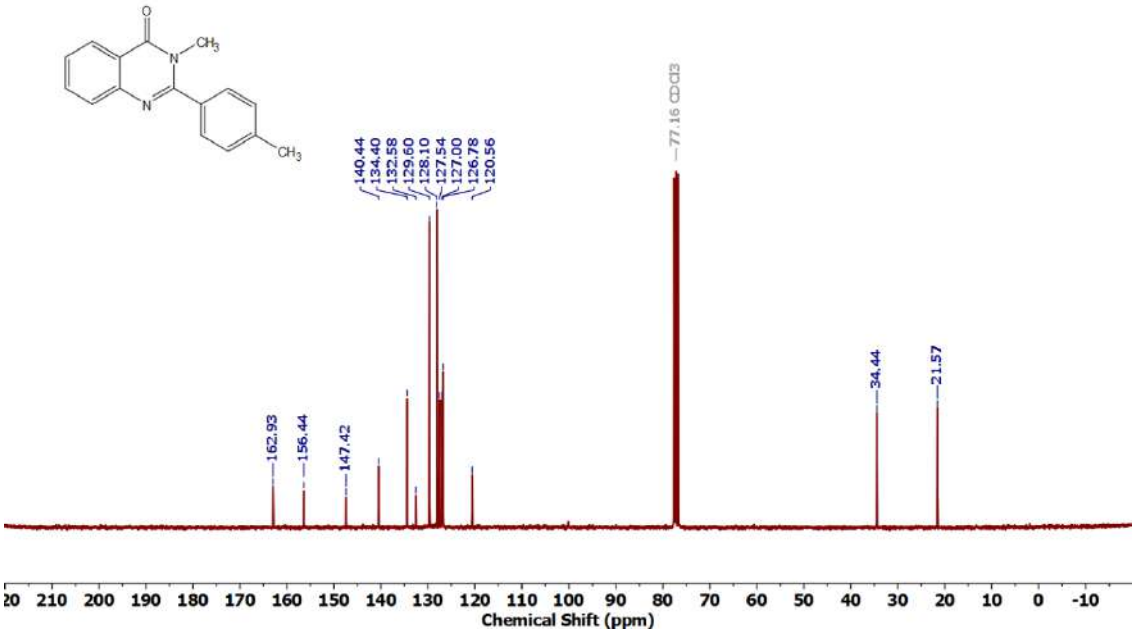

Figure 4.6.A68: $^{13}C\{^{1}H\}$ NMR spectrum of **7af**

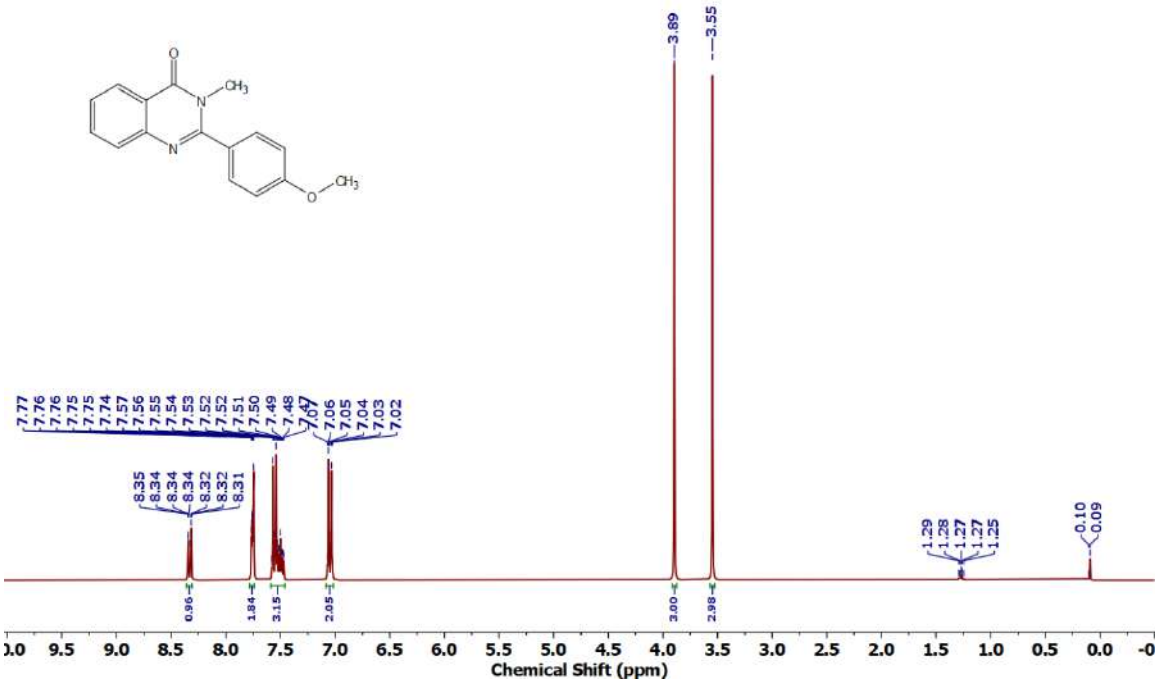

Figure 4.6.A69: ^{1}H NMR spectrum of **7ag**

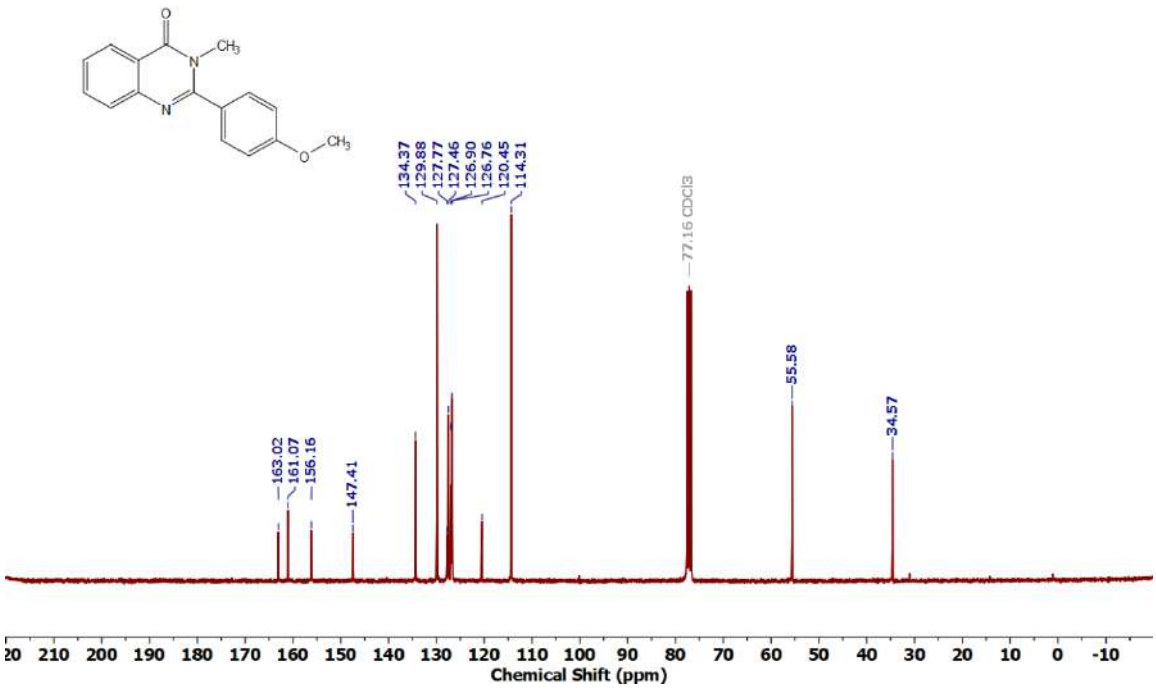

Figure 4.6.A70: $^{13}C\{^{1}H\}$ NMR spectrum of **7ag**

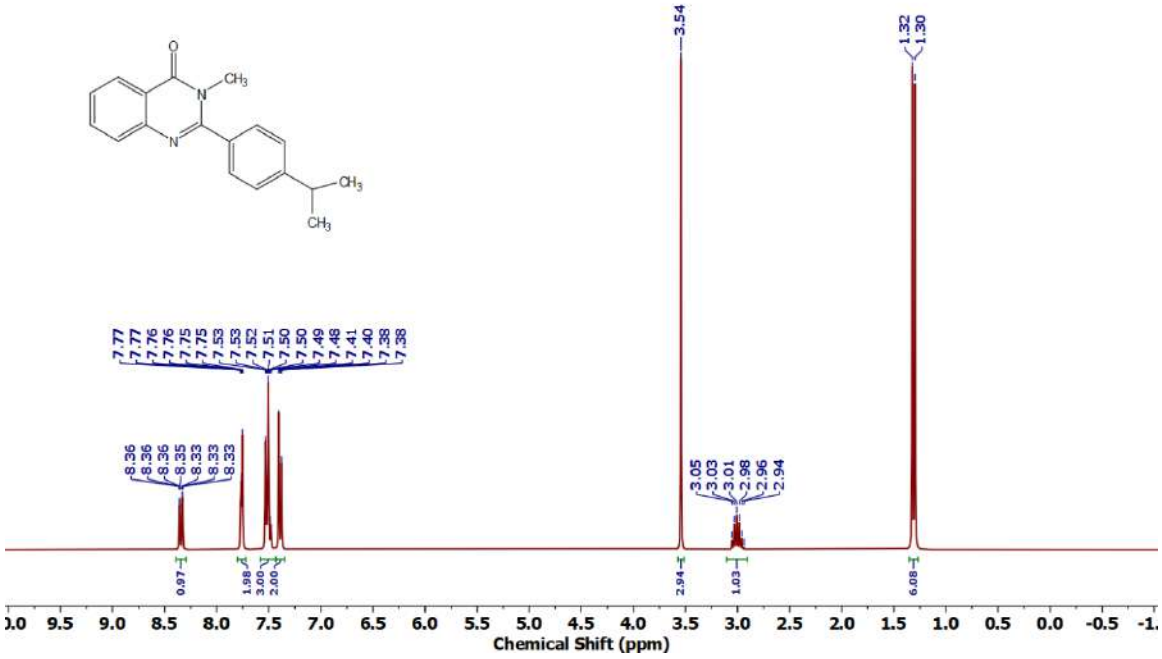

Figure 4.6.A71: ^{1}H NMR spectrum of **7ah**

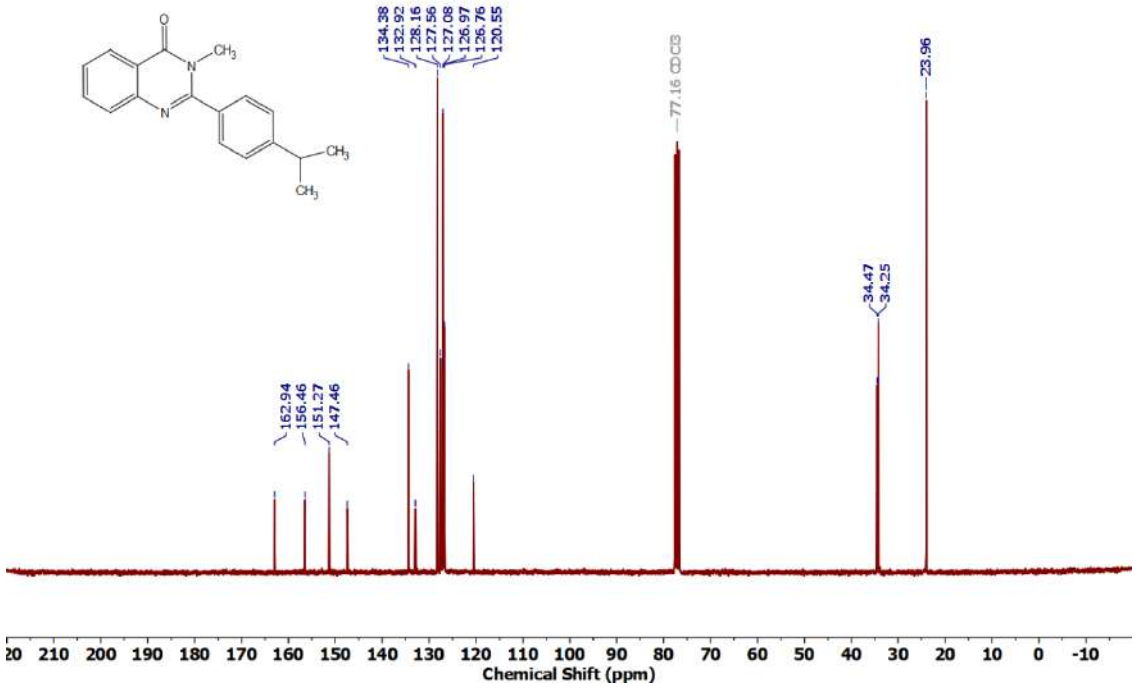

Figure 4.6.A72: $^{13}C\{^{1}H\}$ NMR spectrum of **7ah**

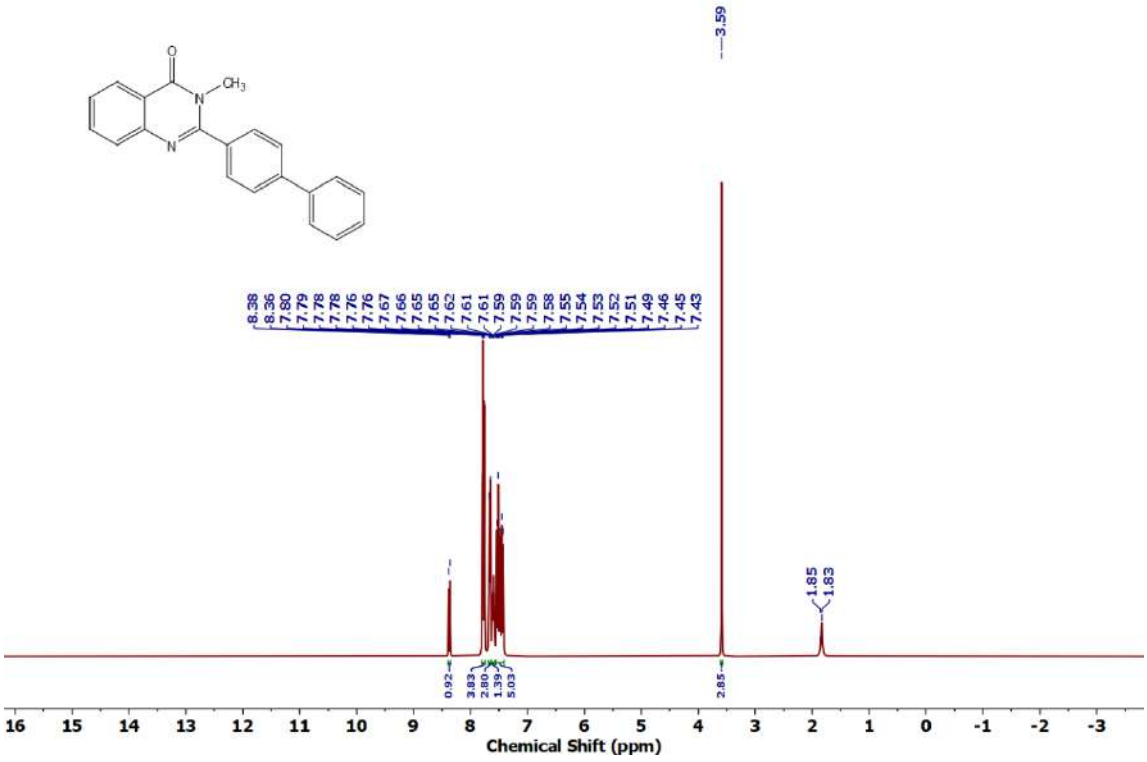

Figure 4.6.A73: ^{1}H NMR spectrum of **7ai**

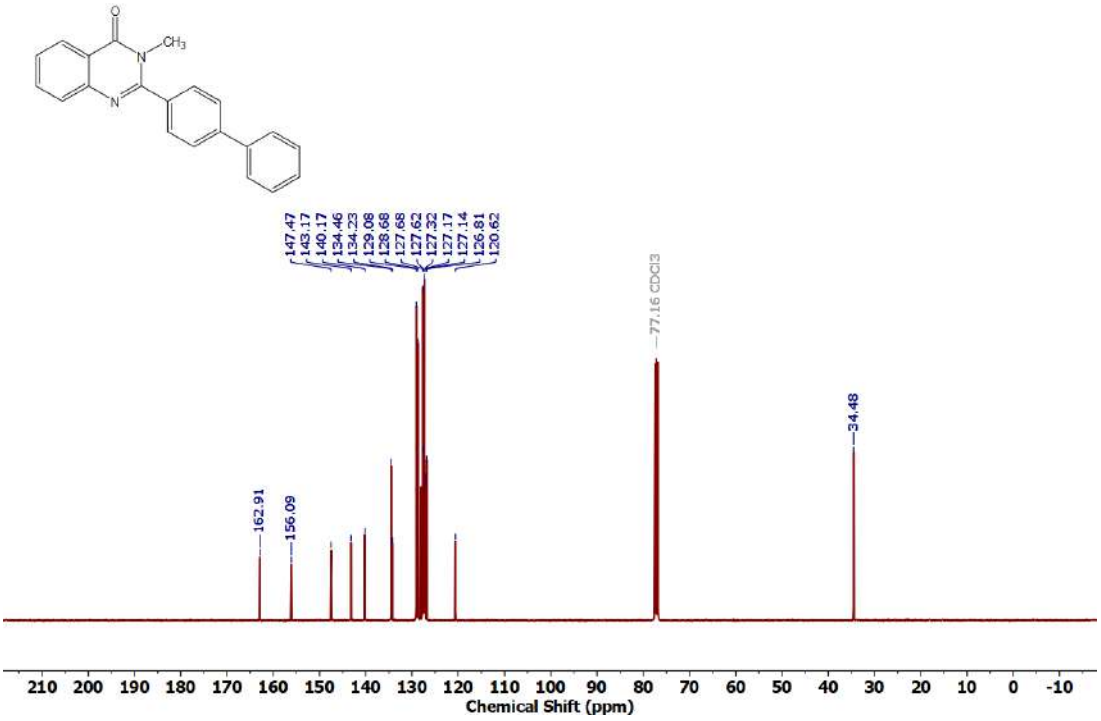

Figure 4.6.A74: $^{13}C\{^{1}H\}$ NMR spectrum of **7ai**

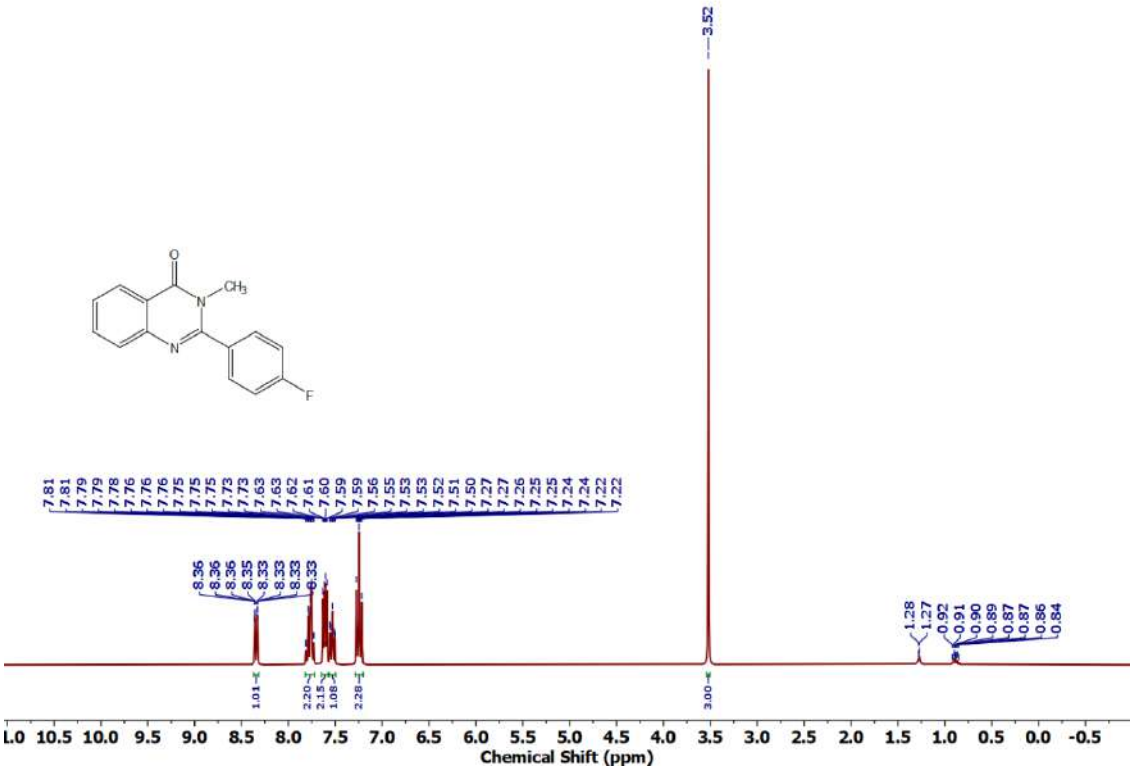

Figure 4.6.A75: ^{1}H NMR spectrum of **7aj**

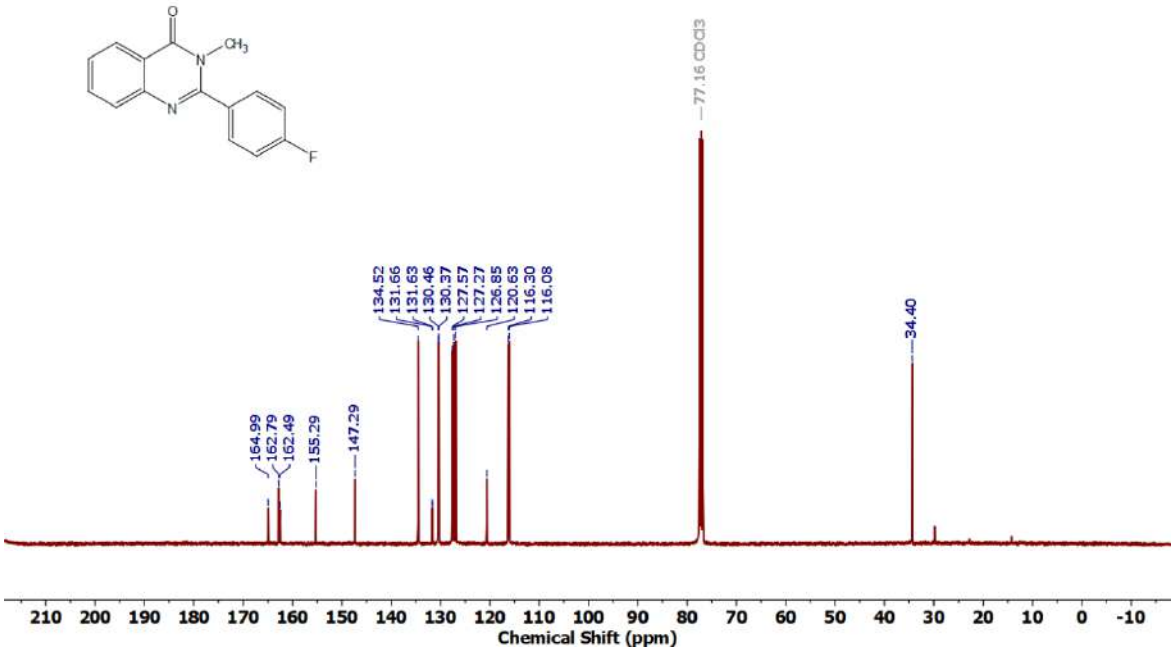

Figure 4.6.A76: $^{13}C\{^{1}H\}$ NMR spectrum of **7aj**

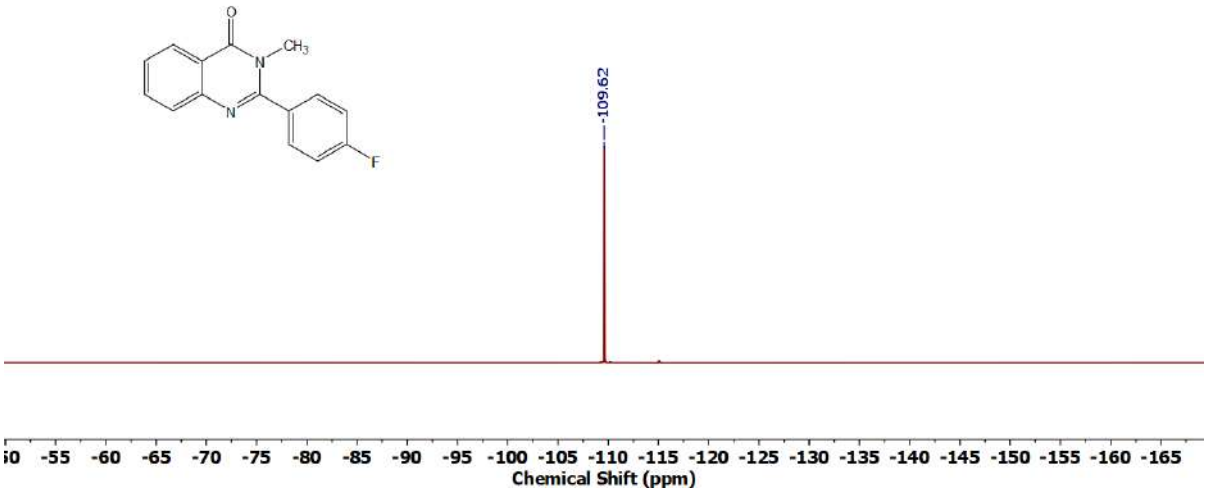

Figure 4.6.A77: ^{19}F NMR spectrum of **7aj**

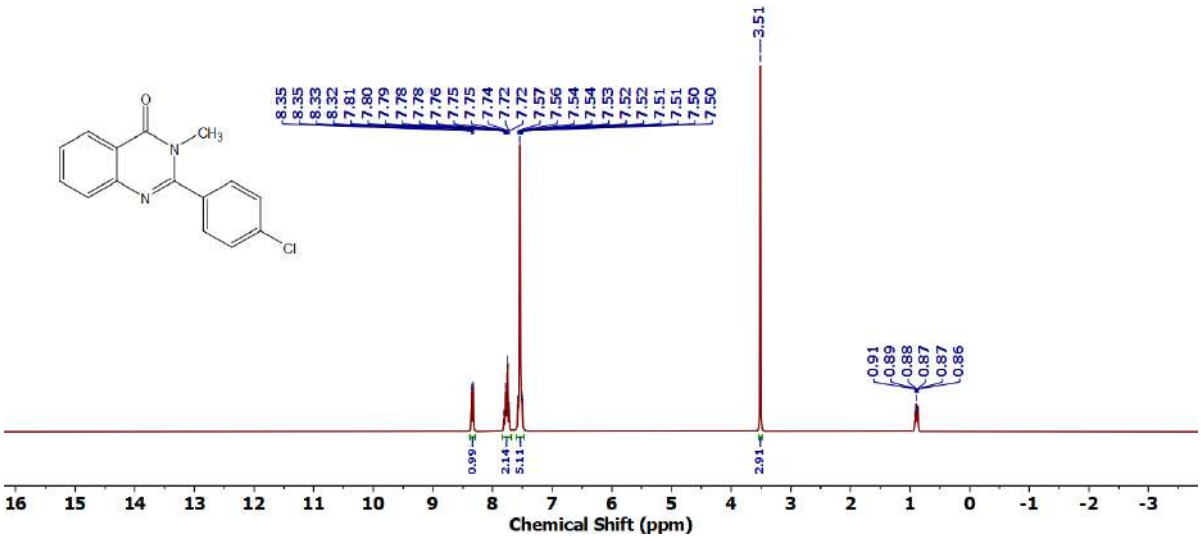

Figure 4.6.A78: ^{1}H NMR spectrum of **7ak**

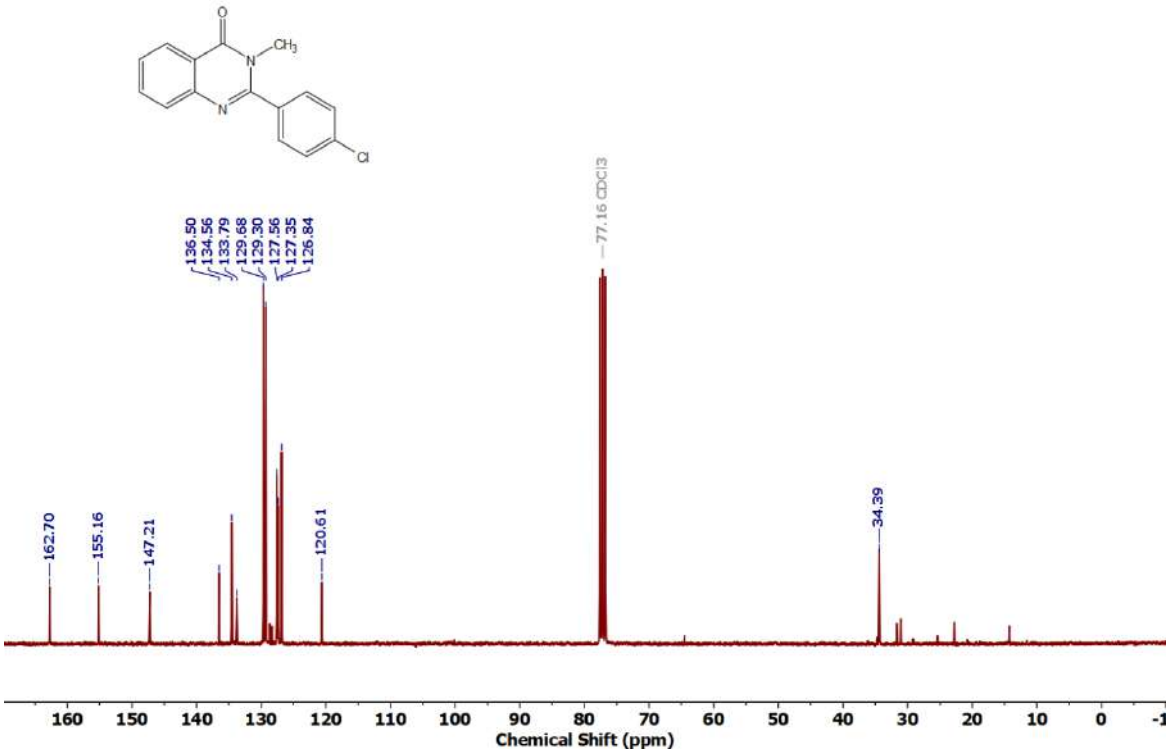

Figure 4.6.A79: ^{13}C{^{1}H} NMR spectrum of **7ak**

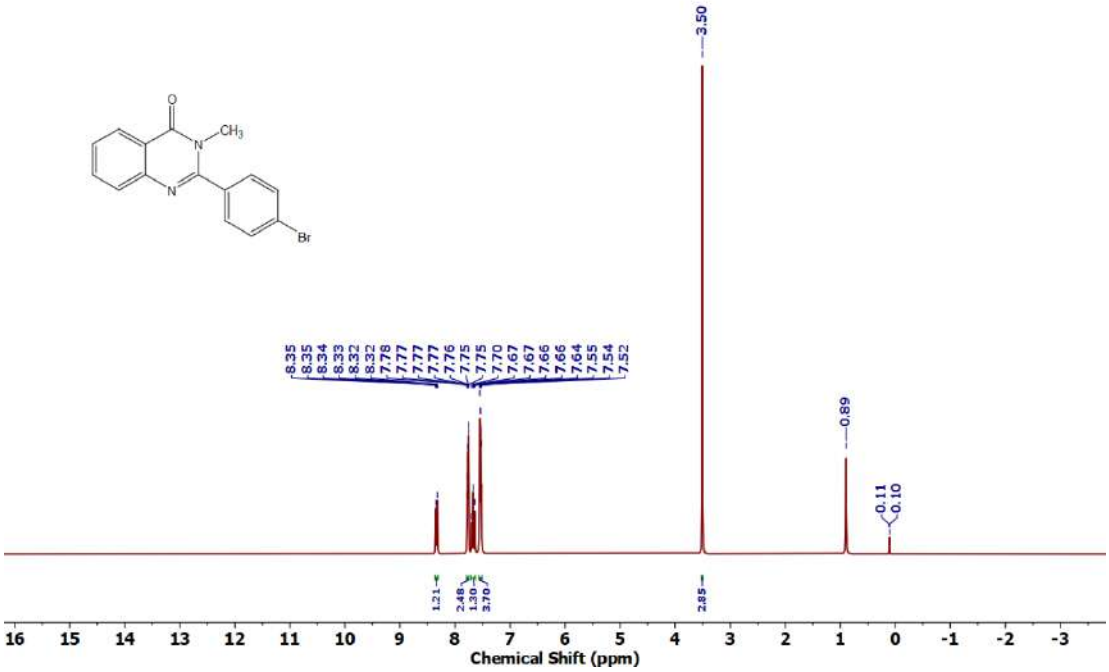

Figure 4.6.A80: ^{1}H NMR spectrum of **7al**

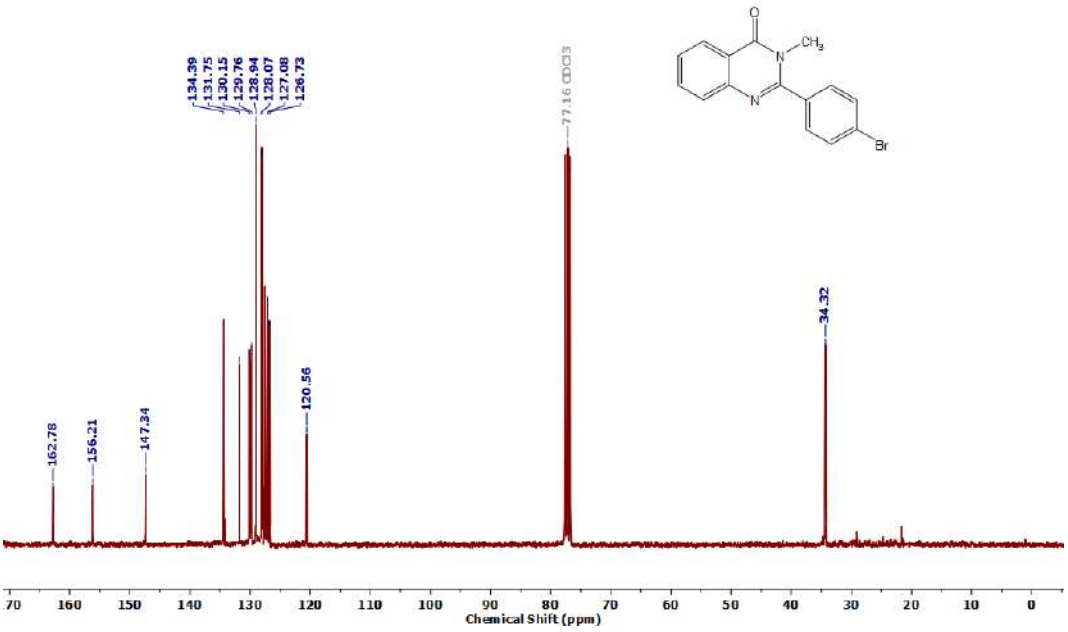

Figure 4.6.A81: ^{13}C{^{1}H} NMR spectrum of **7al**

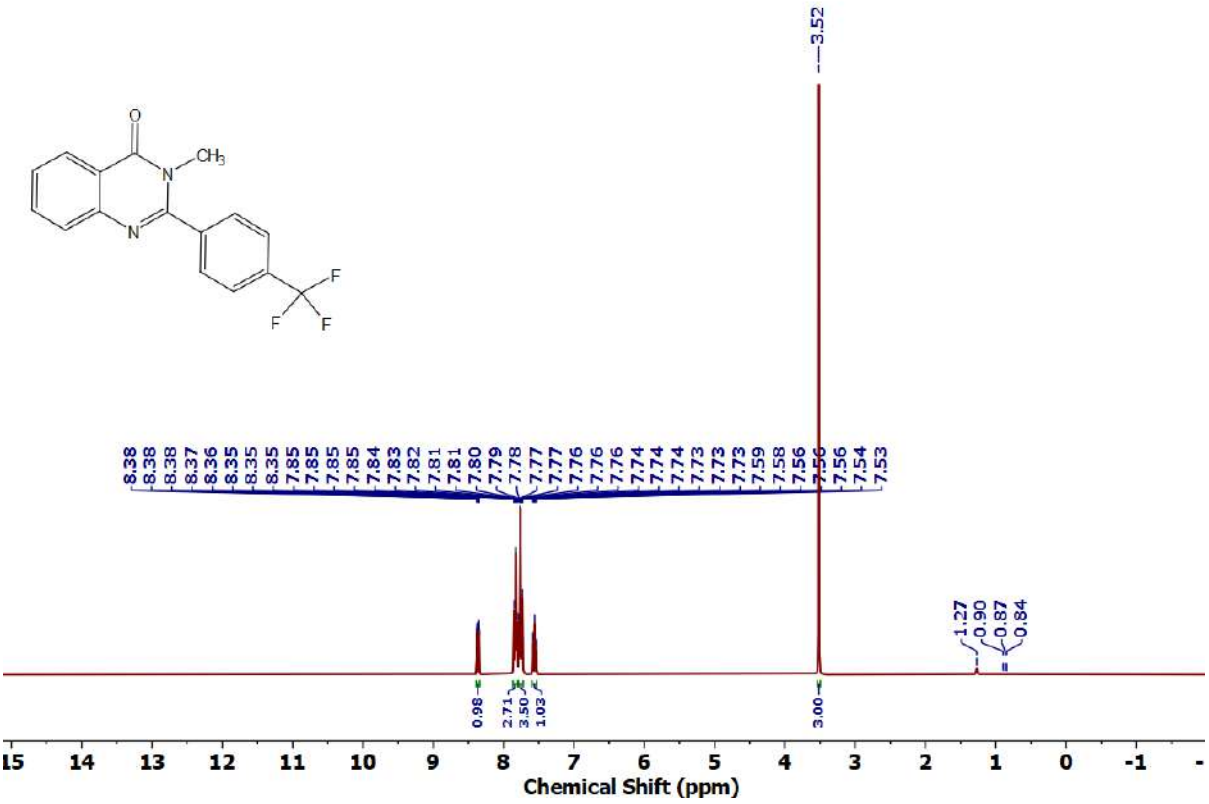

Figure 4.6.A82: ^{1}H NMR spectrum of **7am**

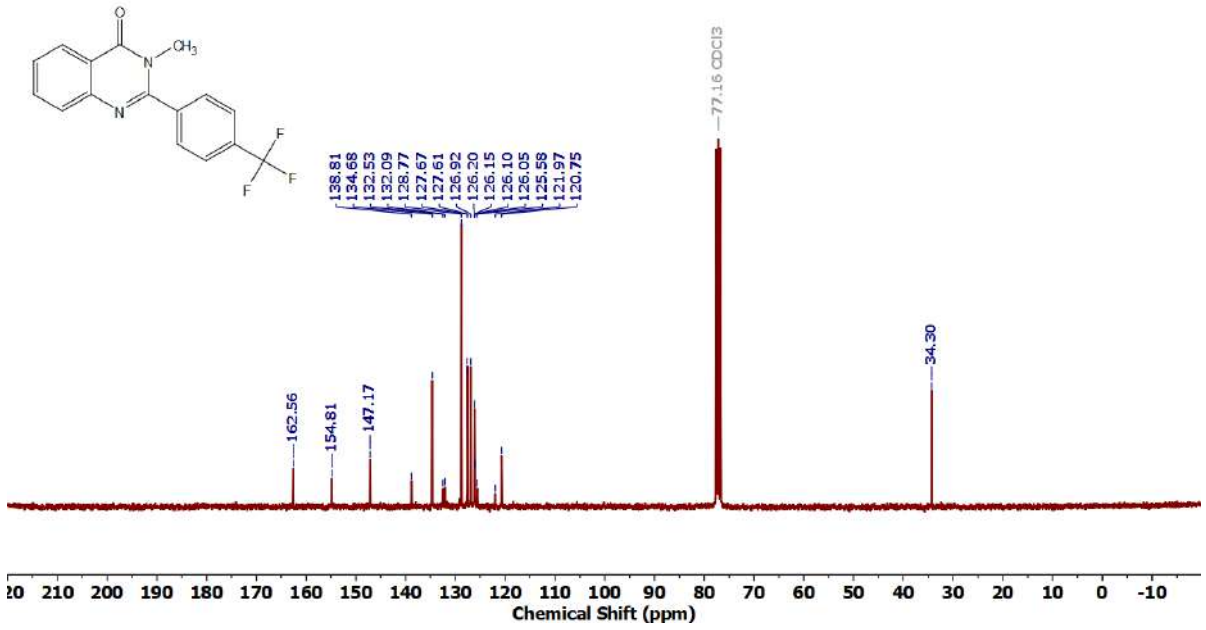

Figure 4.6.A83: ^{13}C{^{1}H} NMR spectrum of **7am**

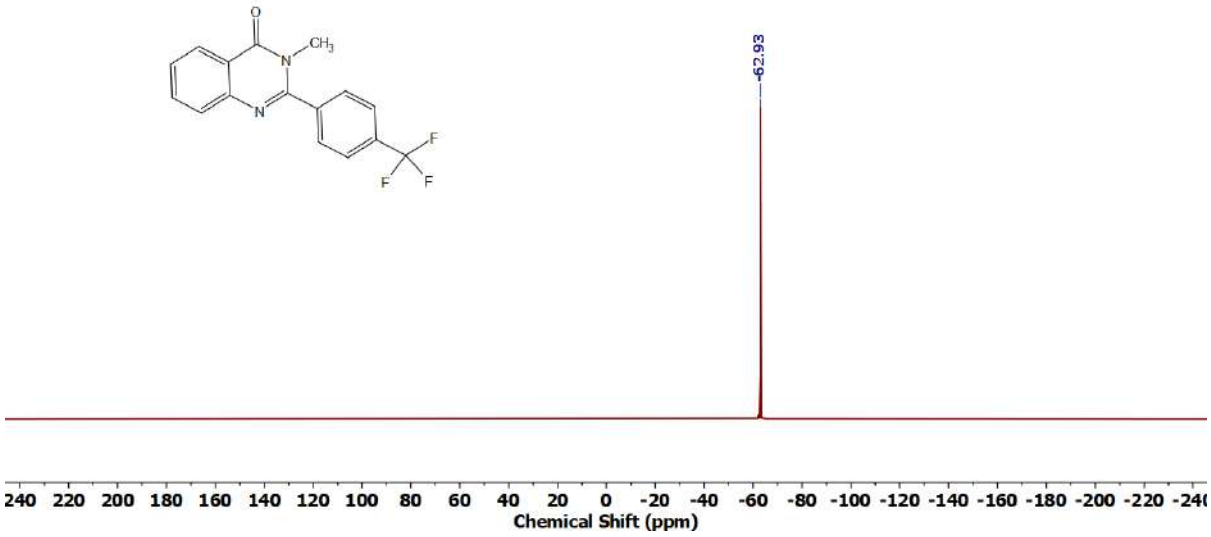

Figure 4.6.A84: ^{19}F NMR spectrum of **7am**

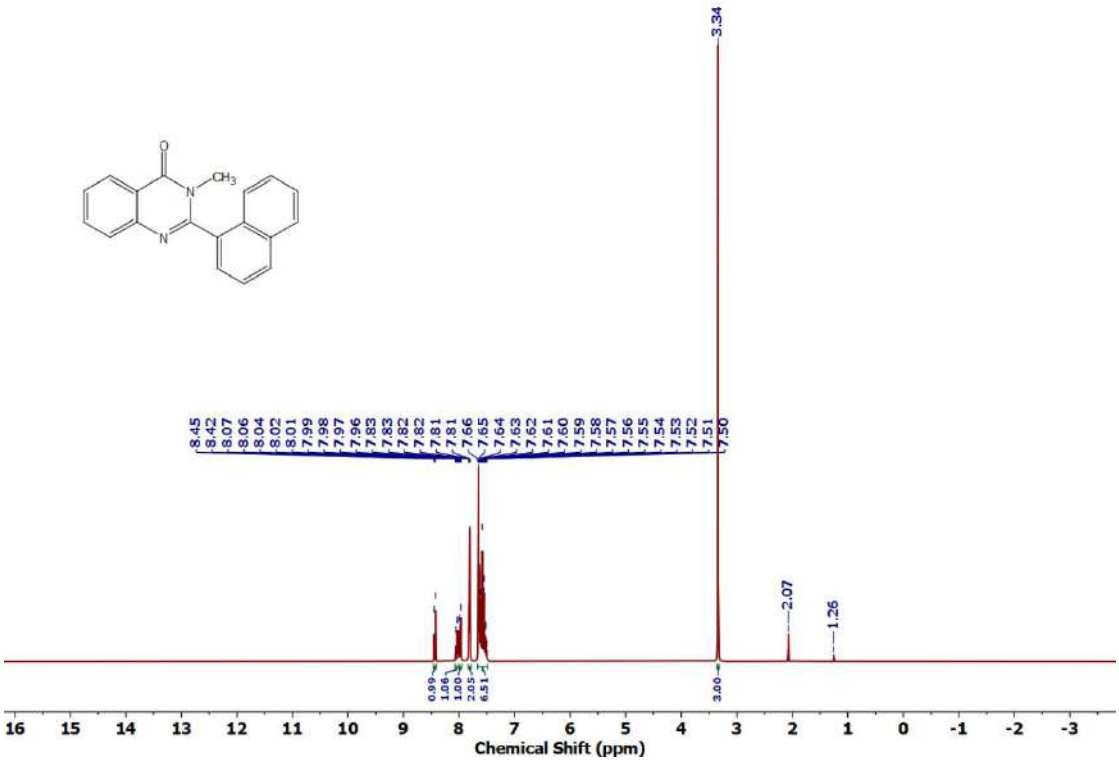

Figure 4.6.A85: ^{1}H NMR spectrum of **7an**

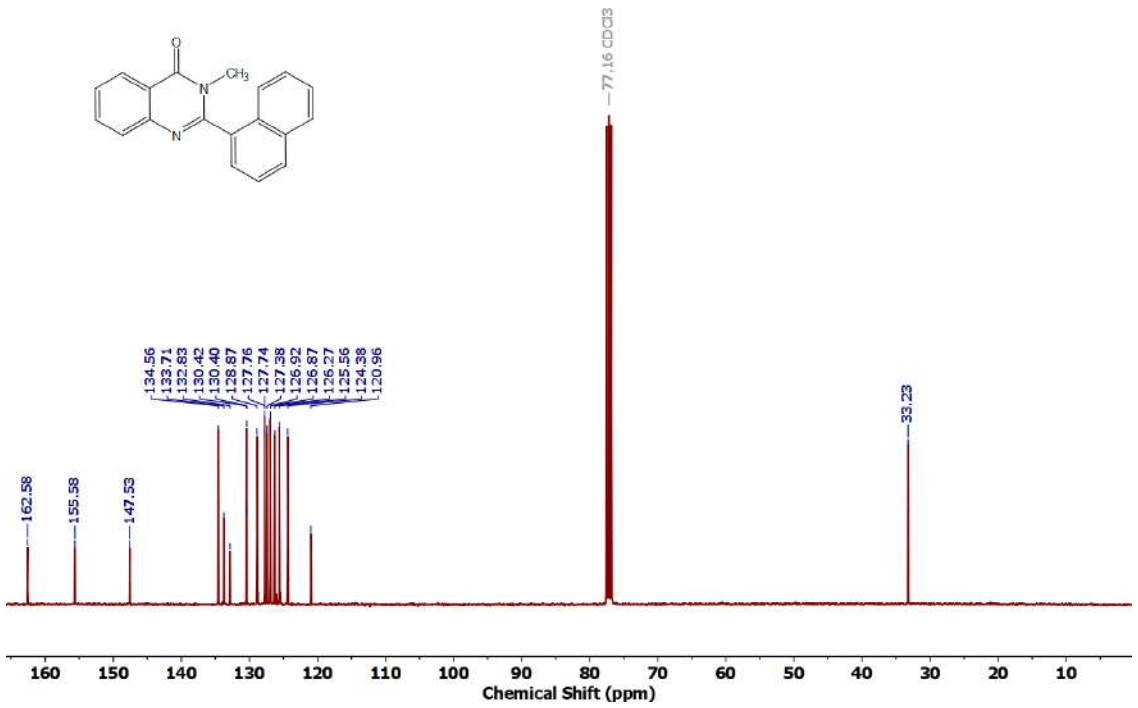

Figure 4.6.A86: $^{13}C\{^{1}H\}$ NMR spectrum of **7an**

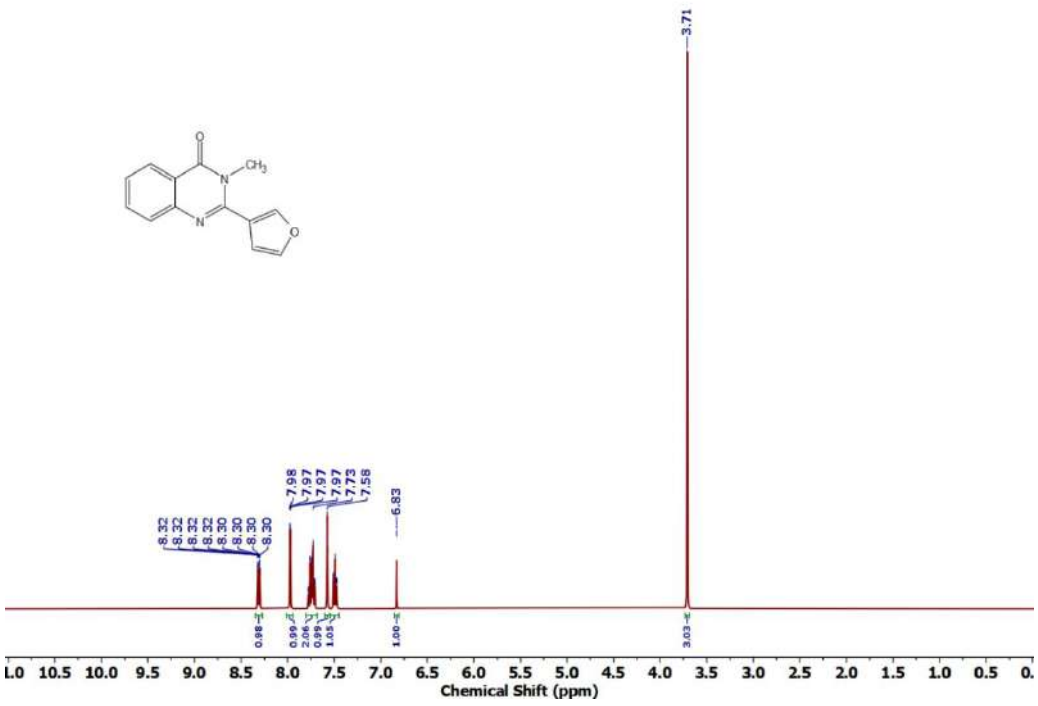

Figure 4.6.A87: ^{1}H NMR spectrum of **7ao**

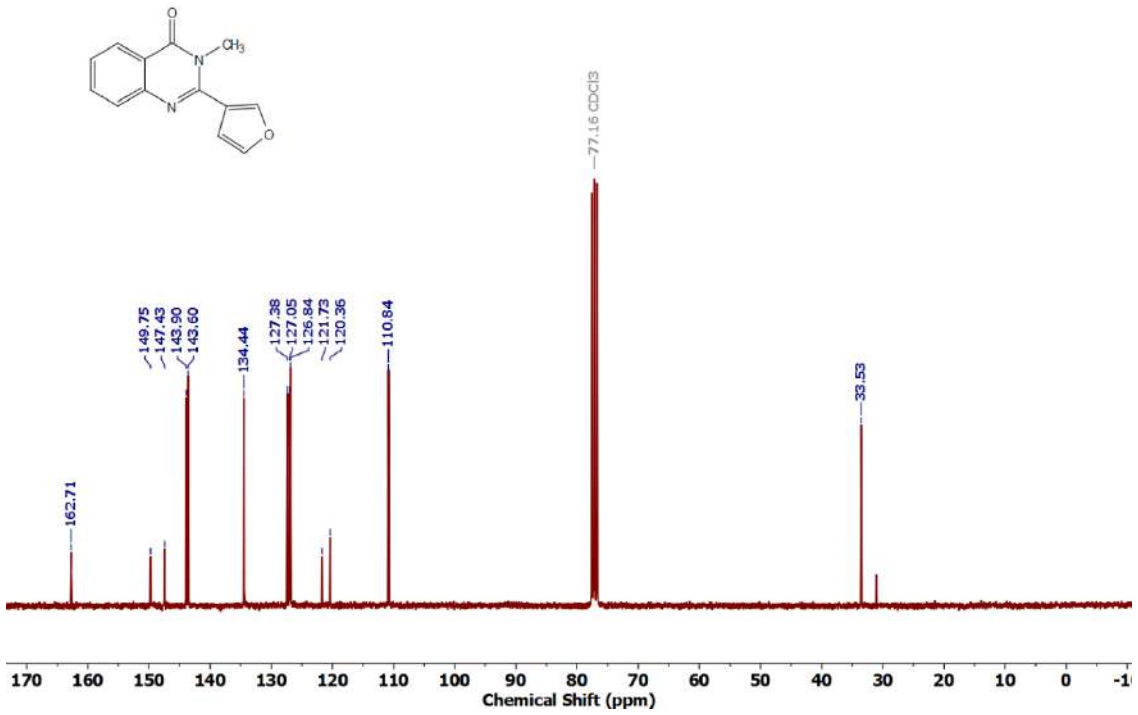

Figure 4.6.A88: $^{13}C\{^{1}H\}$ NMR spectrum of **7ao**

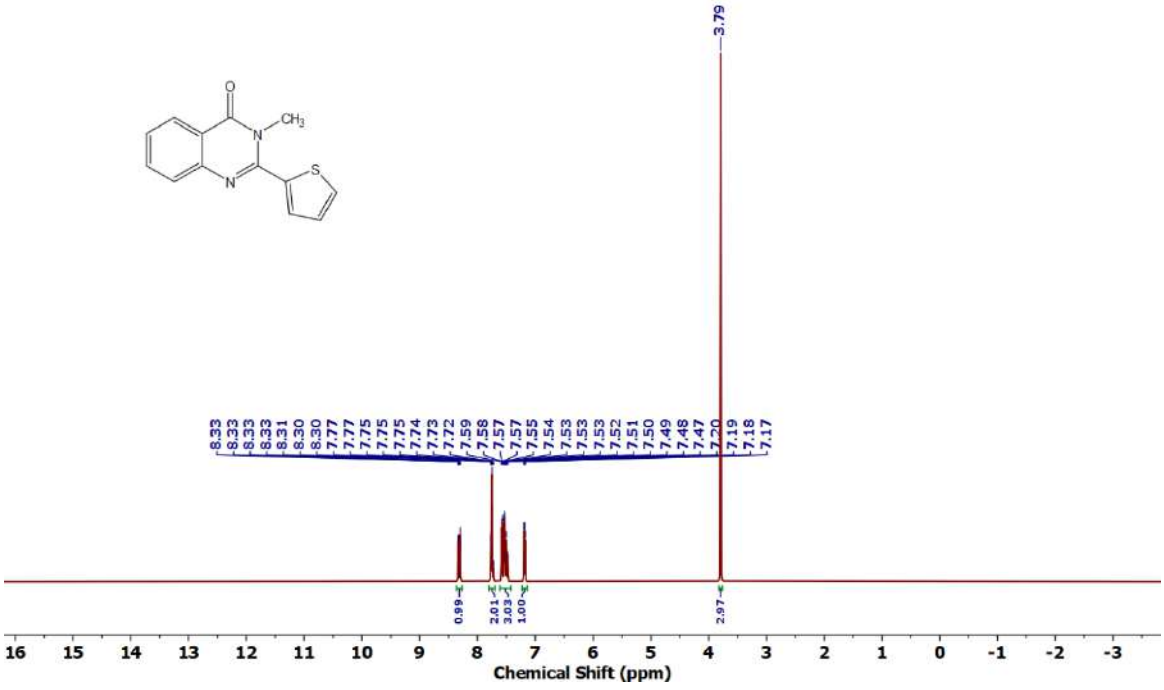

Figure 4.6.A89: ^{1}H NMR spectrum of **7ap**

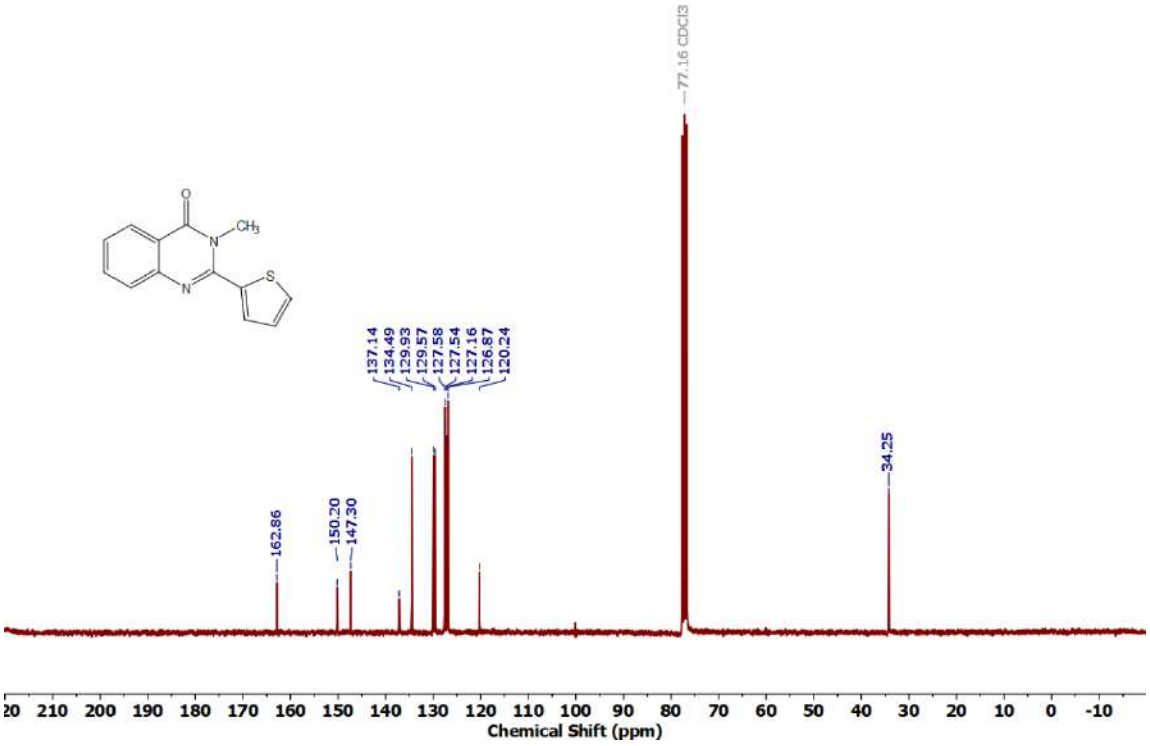

Figure 4.6.A90: $^{13}C\{^{1}H\}$ NMR spectrum of **7ap**

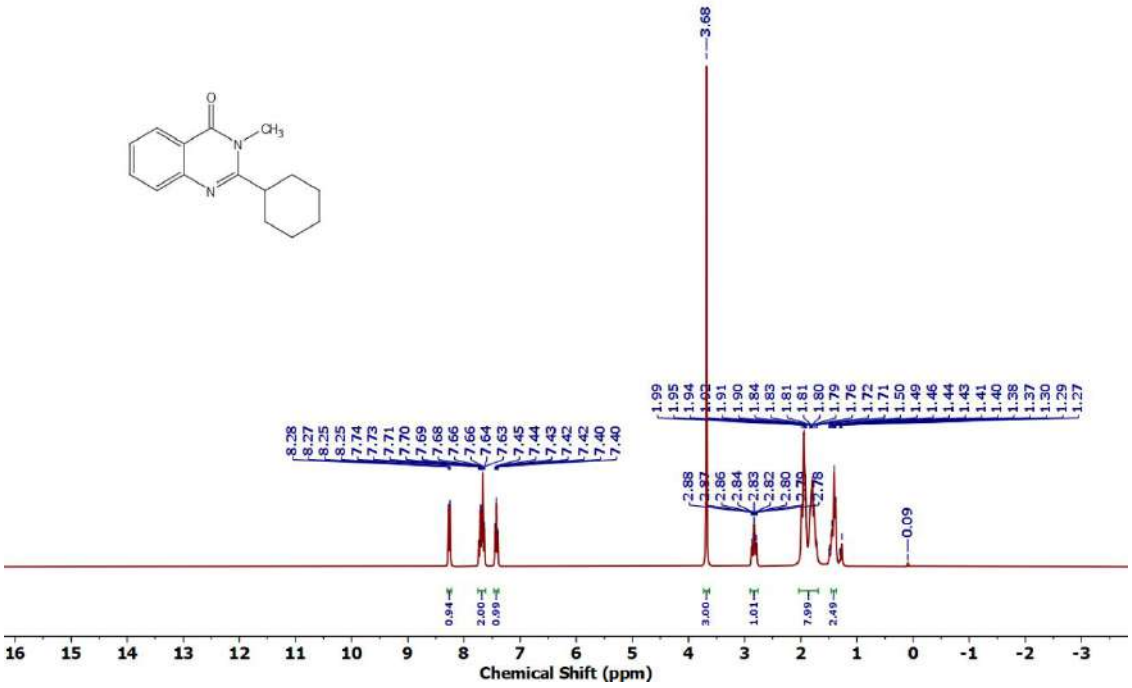

Figure 4.6.A91: ^{1}H NMR spectrum of **7aq**

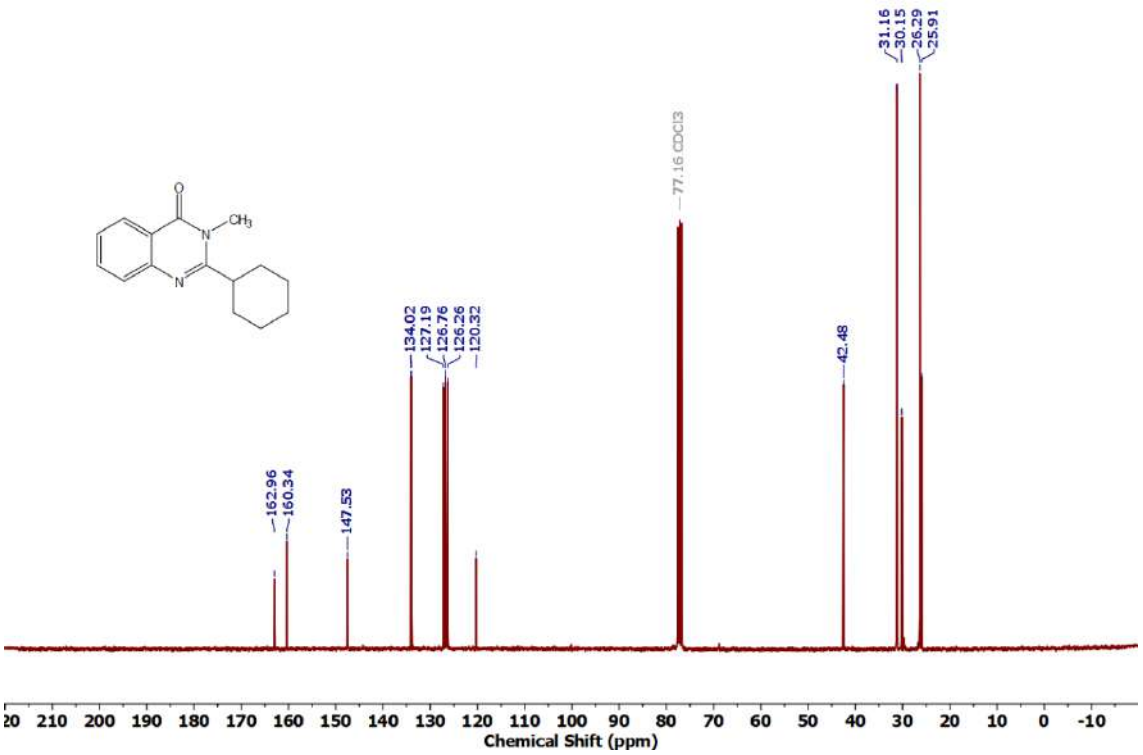

Figure 4.6.A92: $^{13}C\{^{1}H\}$ NMR spectrum of **7aq**

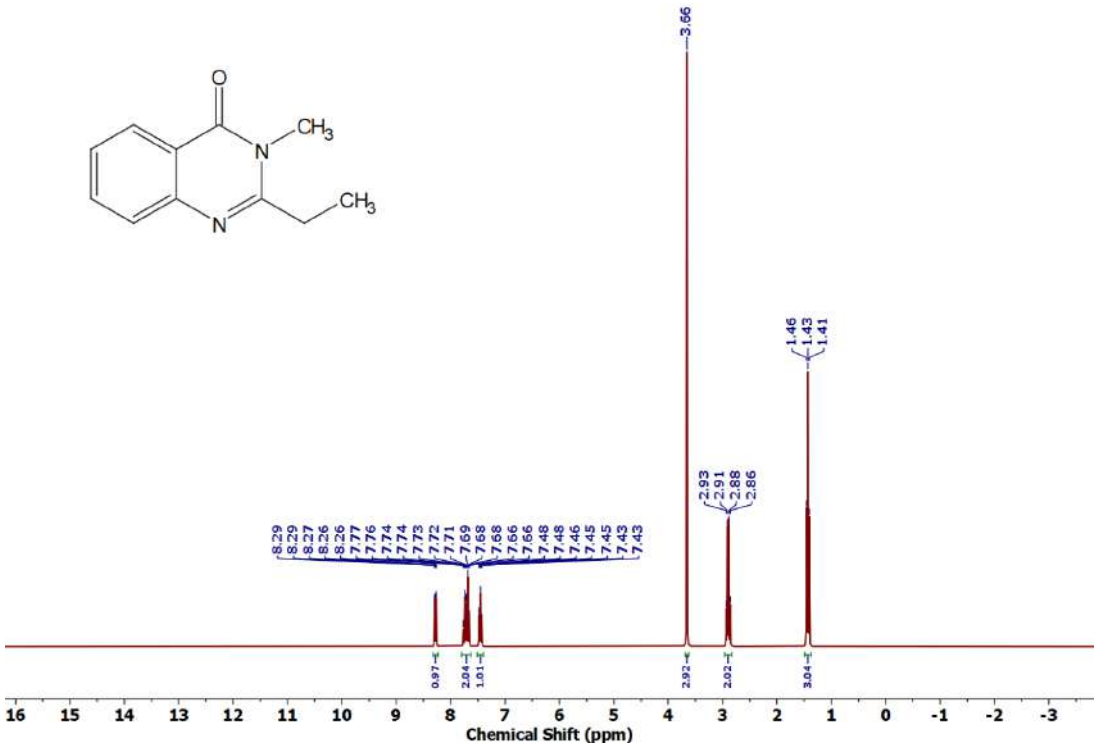

Figure 4.6.A93: ^{1}H NMR spectrum of **7ar**

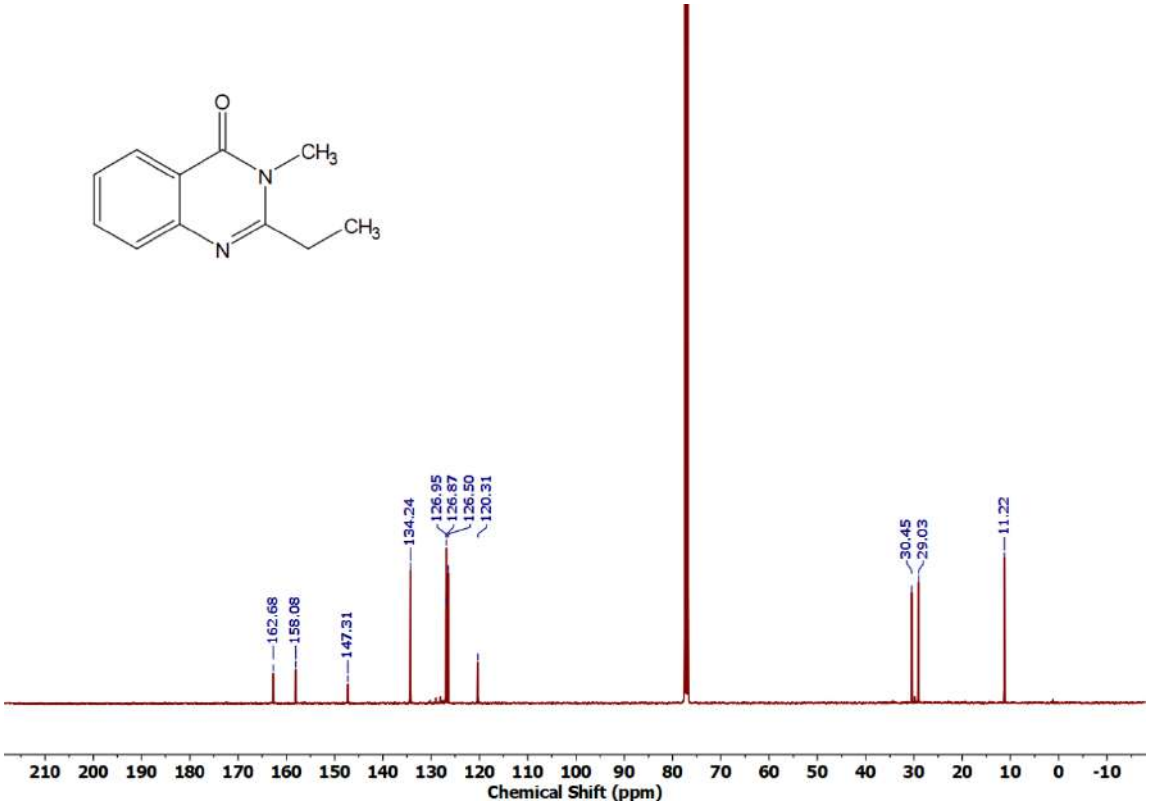

Figure 4.6.A94: $^{13}C\{^{1}H\}$ NMR spectrum of **7ar**

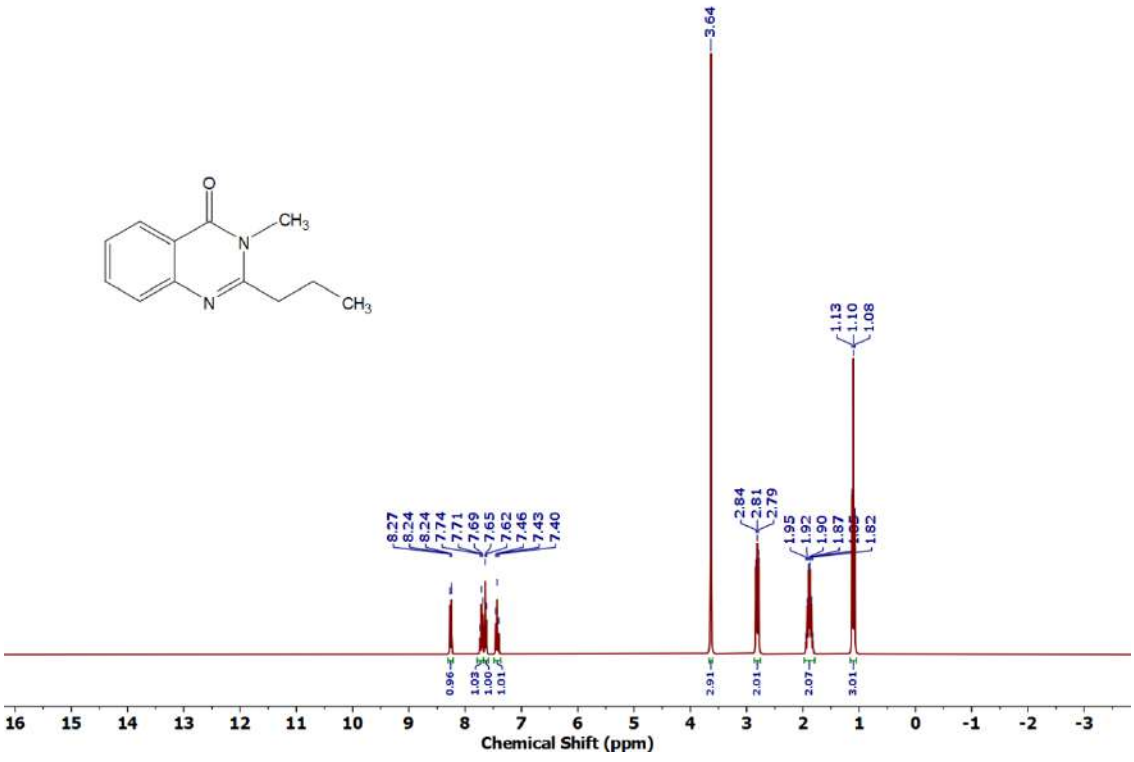

Figure 4.6.A95: ^{1}H NMR spectrum of **7as**

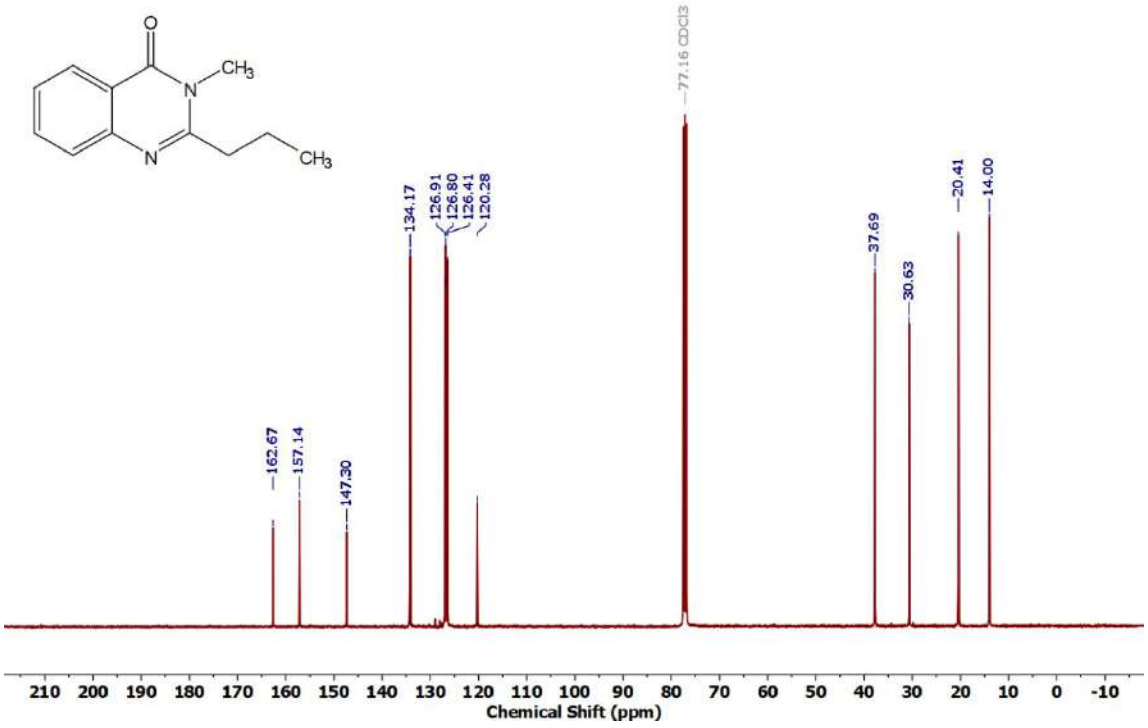

Figure 4.6.A96: $^{13}C\{^{1}H\}$ NMR spectrum of **7as**

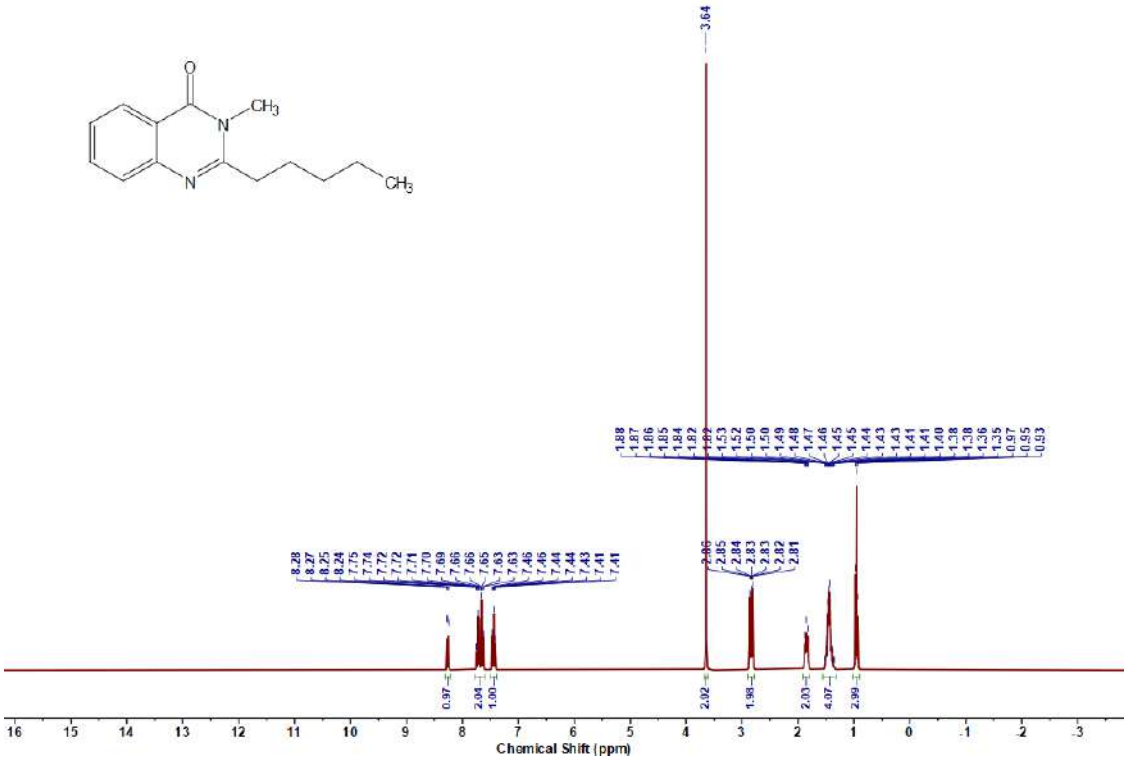

Figure 4.6.A97: ^{1}H NMR spectrum of **7at**

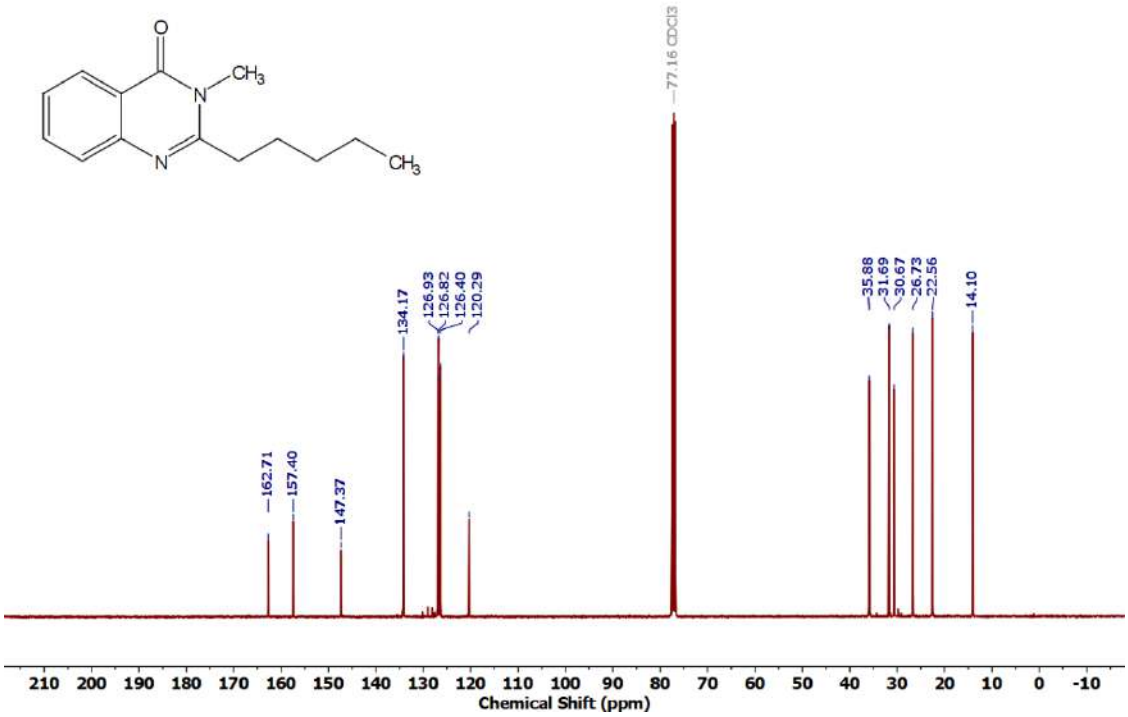

Figure 4.6.A98: $^{13}C\{^{1}H\}$ NMR spectrum of **7at**

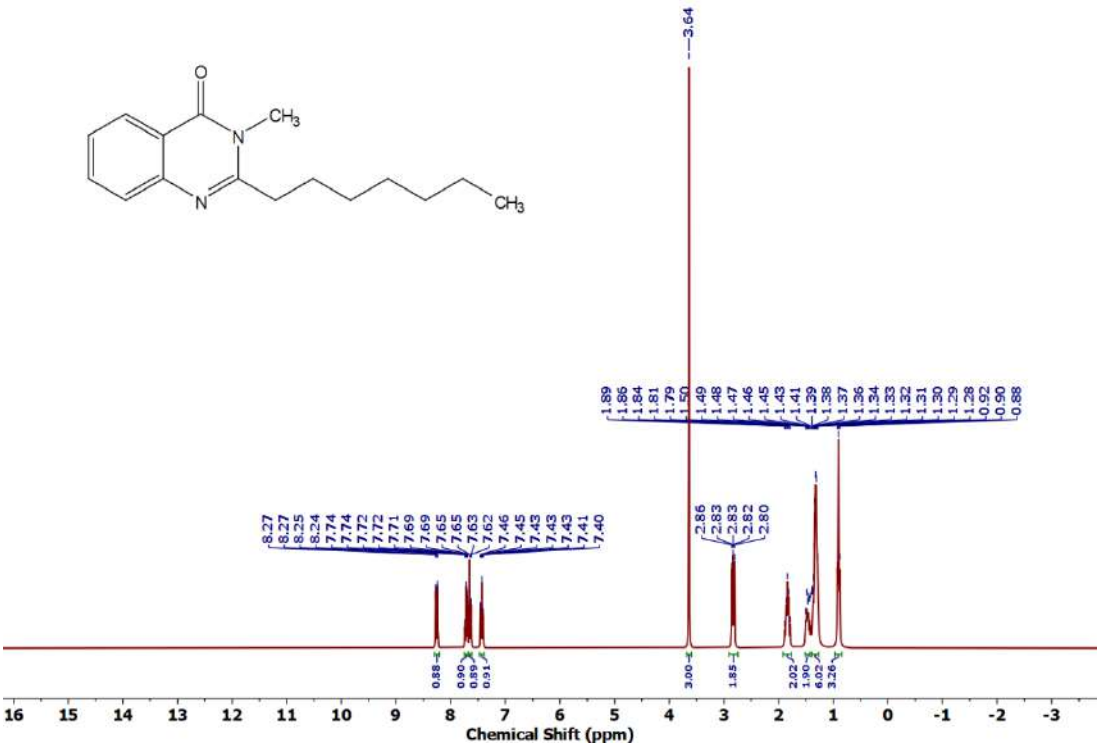

Figure 4.6.A99: ^{1}H NMR spectrum of **7au**

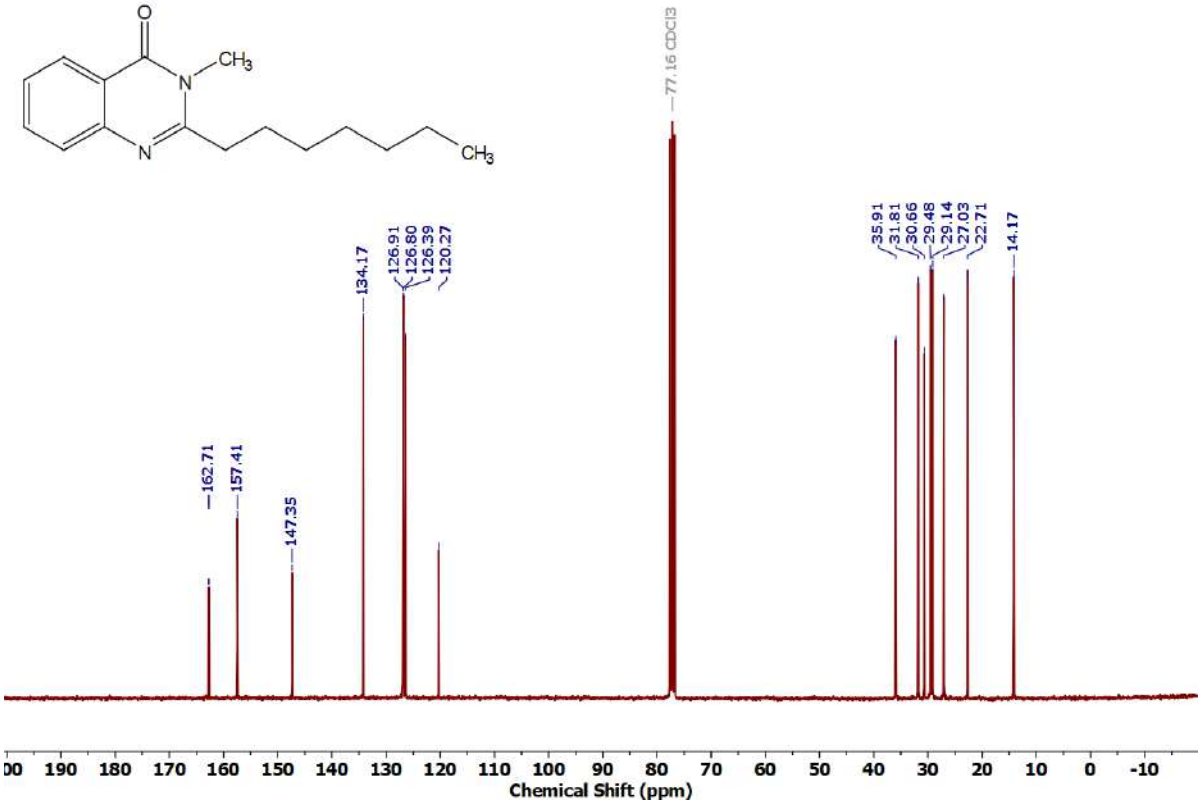

Figure 4.6.A100: $^{13}C\{^{1}H\}$ NMR spectrum of **7au**

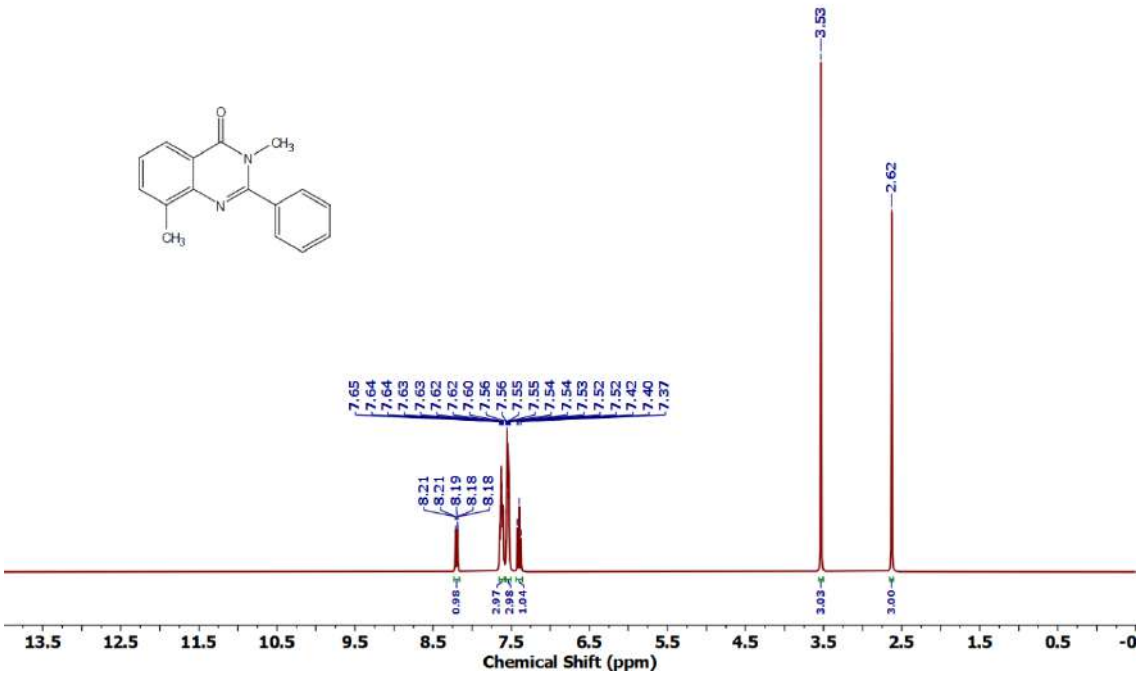

Figure 4.6.A101: ^{1}H NMR spectrum of **8aa**

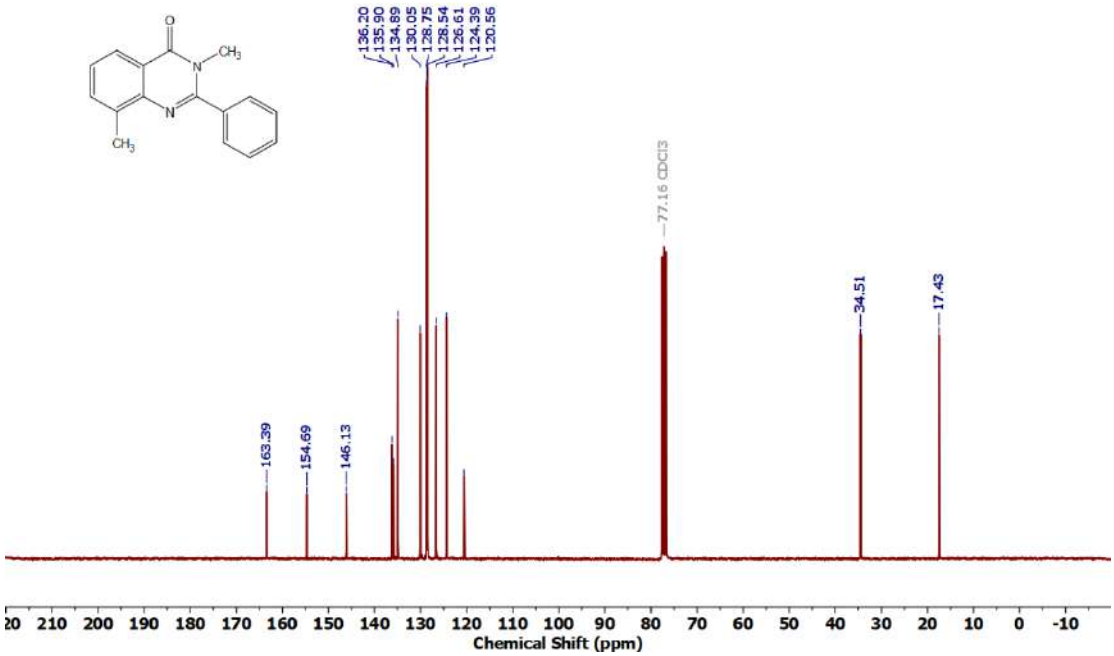

Figure 4.6.A102: $^{13}C\{^{1}H\}$ NMR spectrum of **8aa**

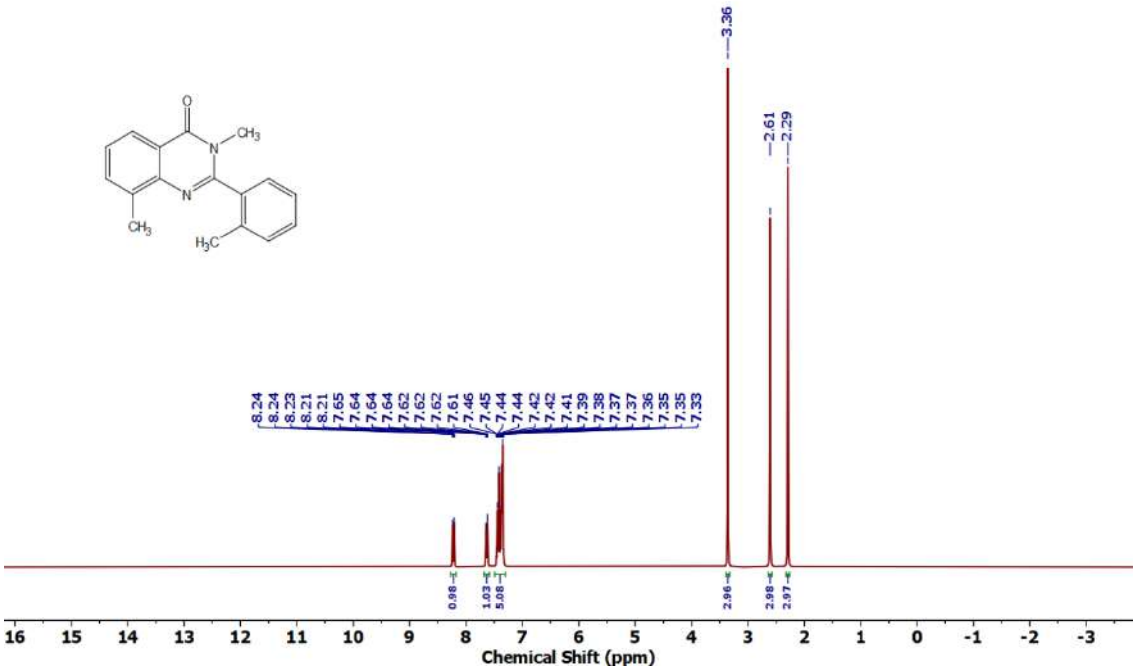

Figure 4.6.A103: ^{1}H NMR spectrum of **8ab**

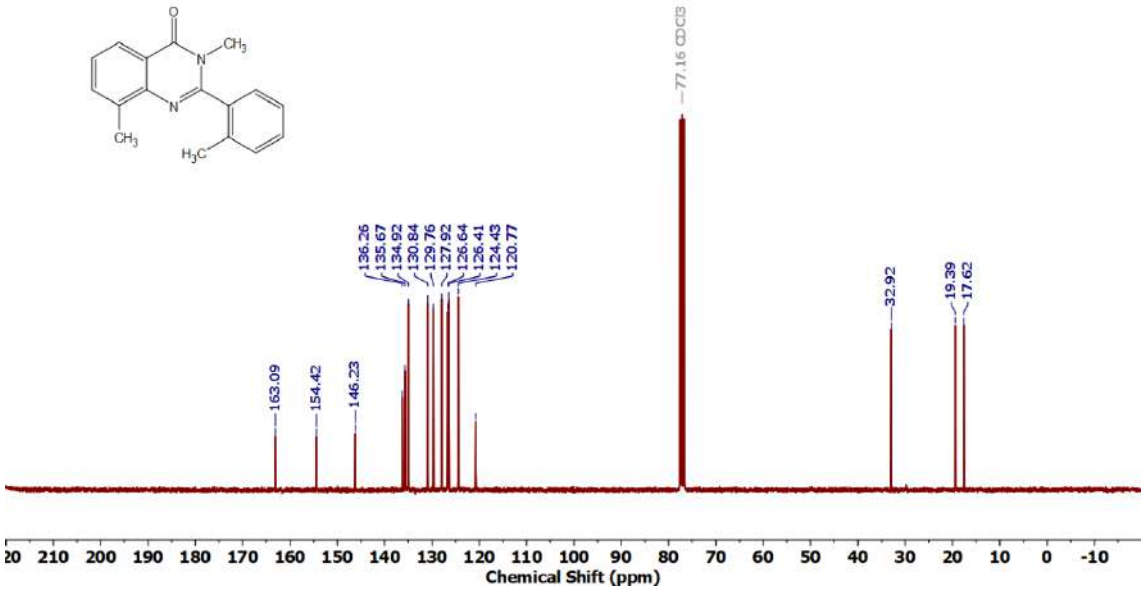

Figure 4.6.A104: $^{13}C\{^{1}H\}$ NMR spectrum of **8ab**

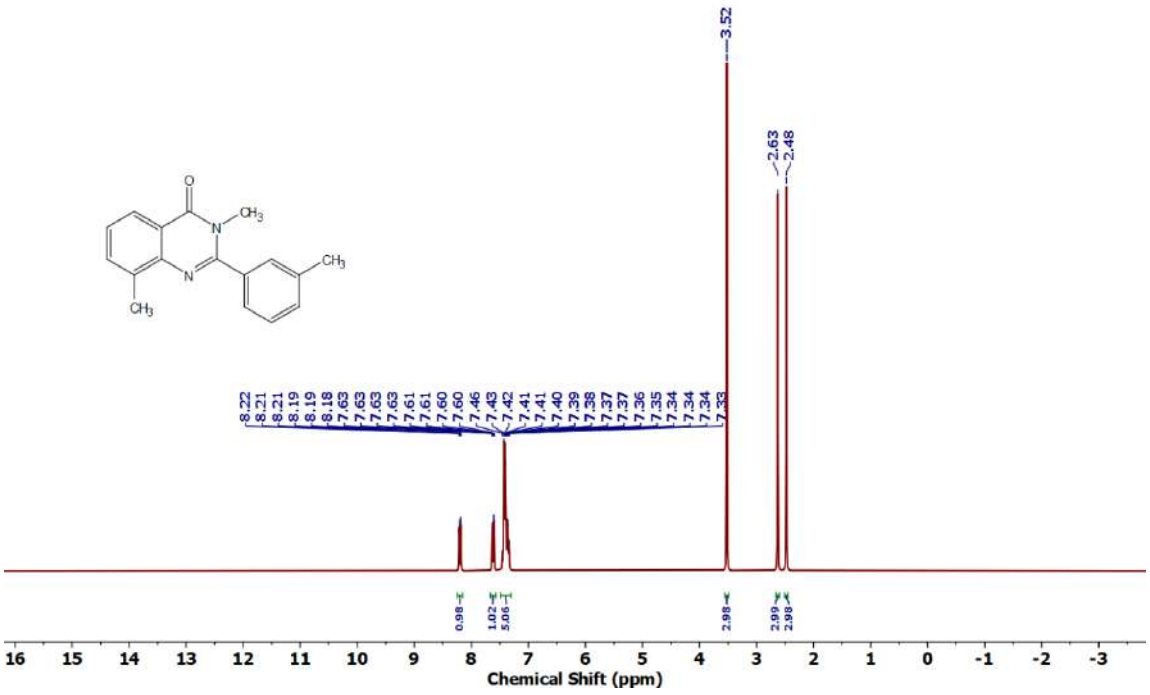

Figure 4.6.A105: ^{1}H NMR spectrum of **8ac**

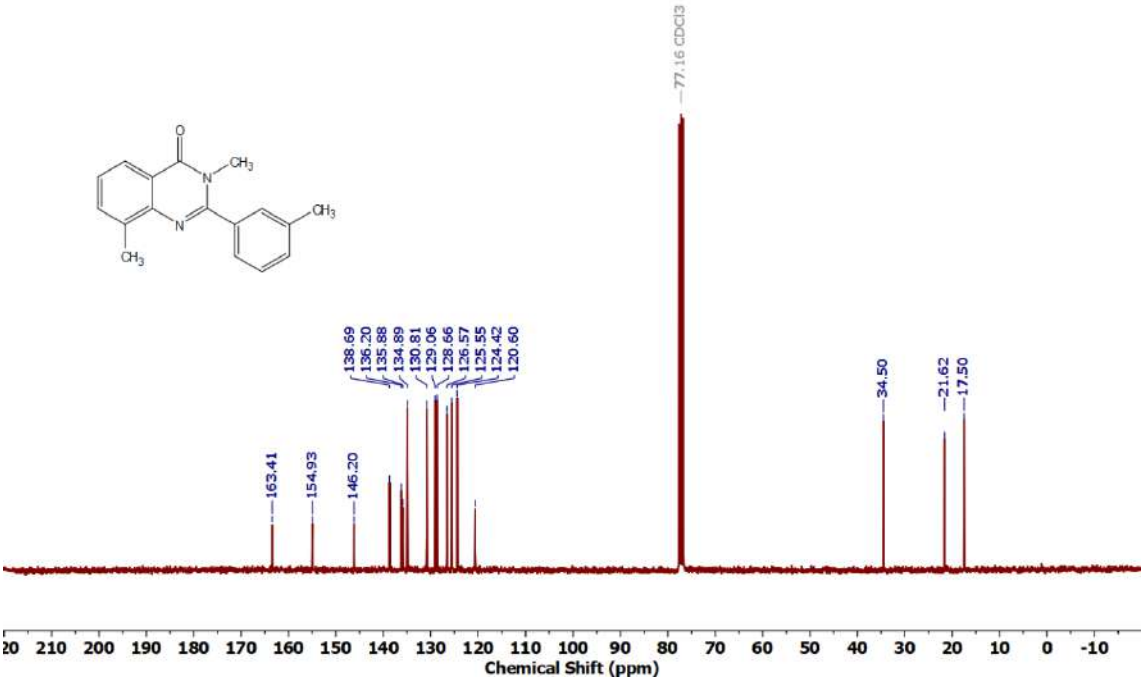

Figure 4.6.A106: $^{13}C\{^{1}H\}$ NMR spectrum of **8ac**

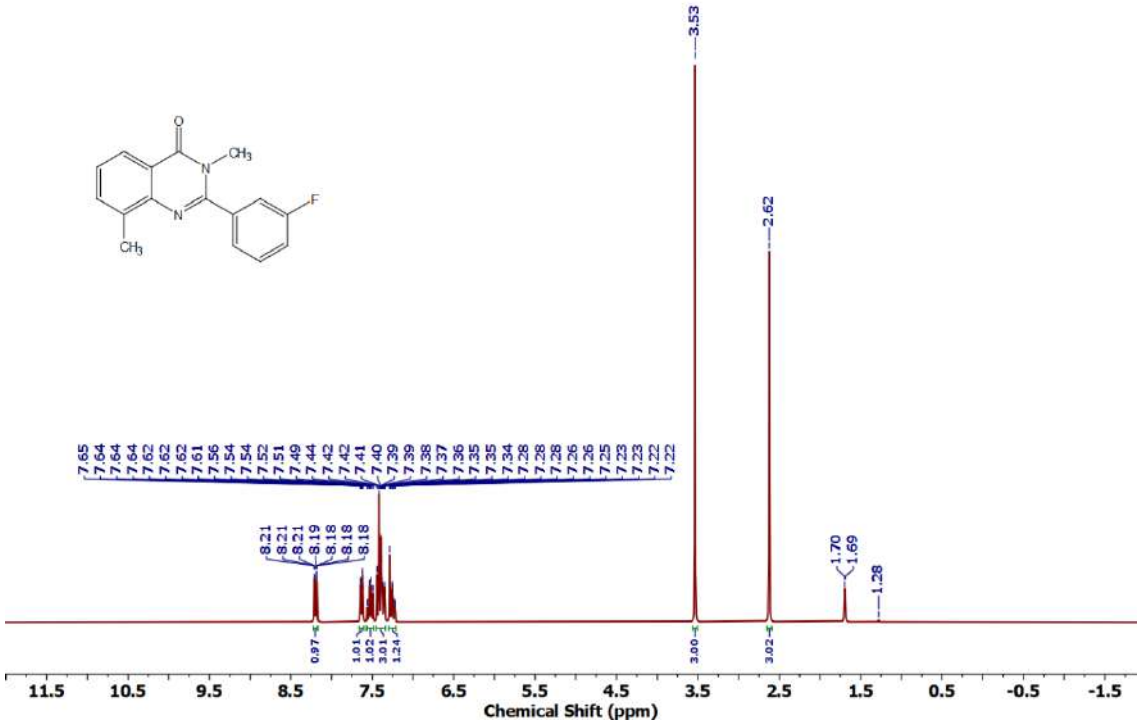

Figure 4.6.A107: ^{1}H NMR spectrum of **8ad**

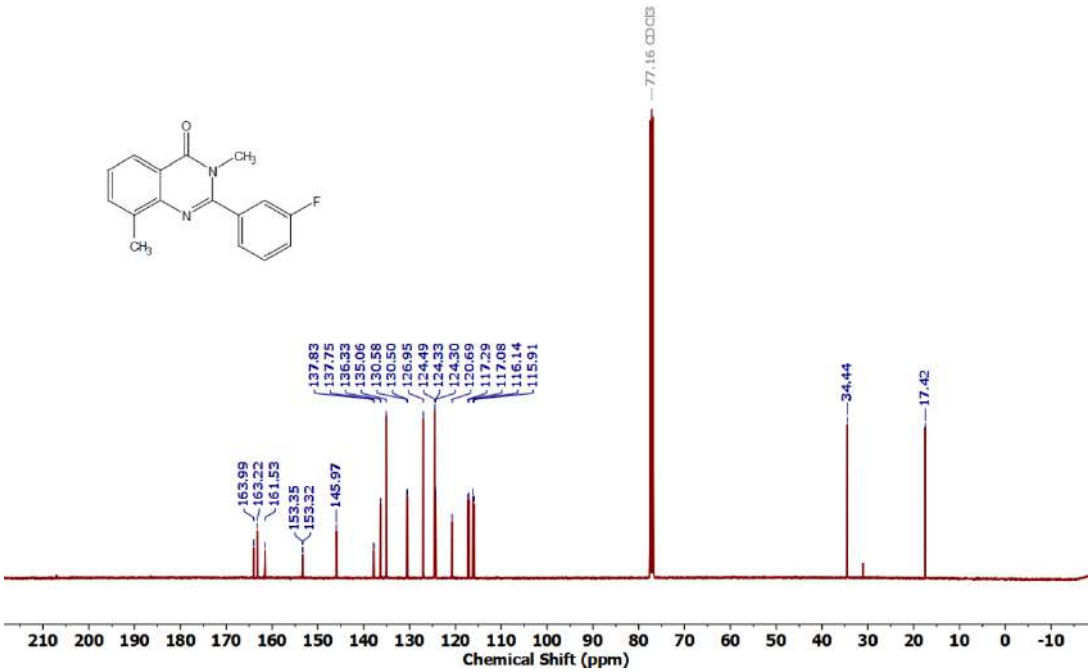

Figure 4.6.A108: $^{13}C\{^{1}H\}$ NMR spectrum of **8ad**

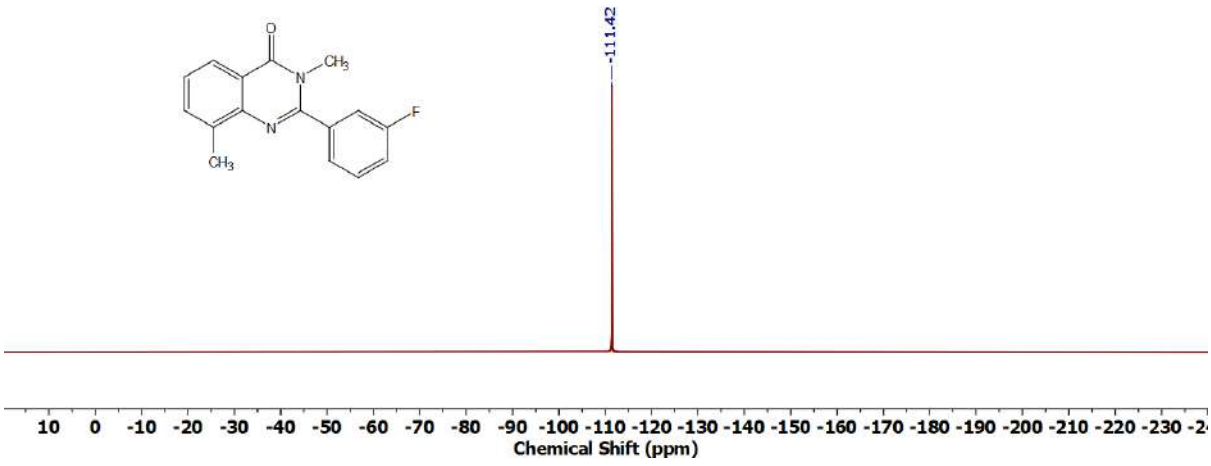

Figure 4.6.A109: ^{19}F NMR spectrum of **8ad**

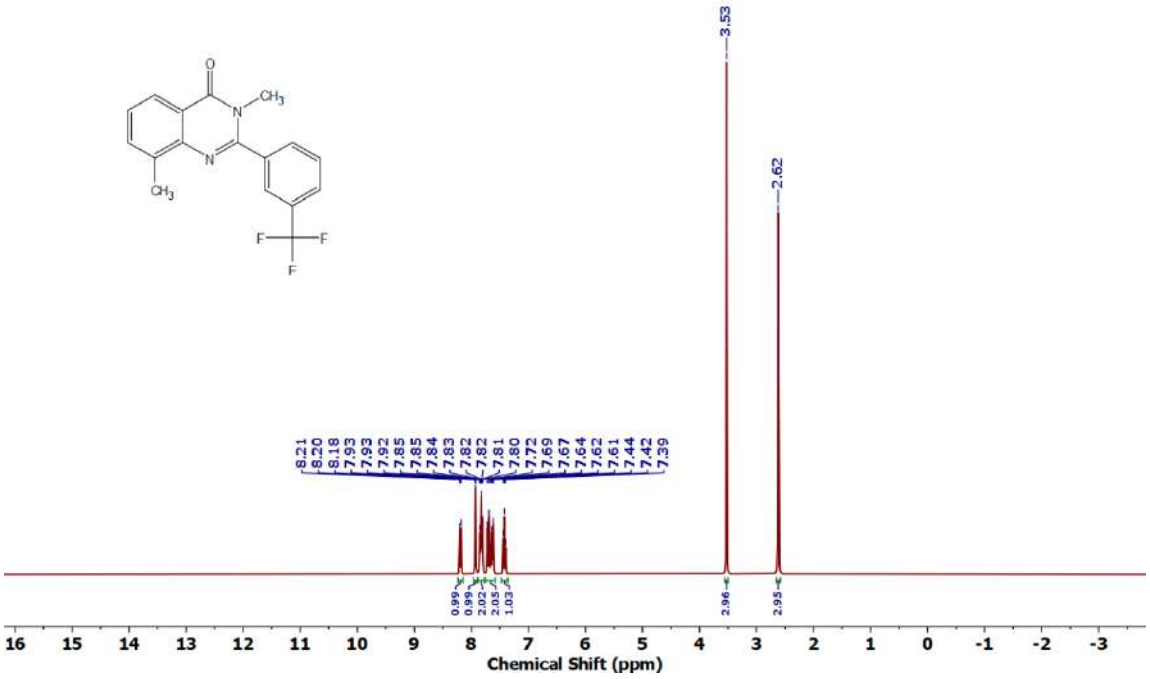

Figure 4.6.A110: ^{1}H NMR spectrum of **8ae**

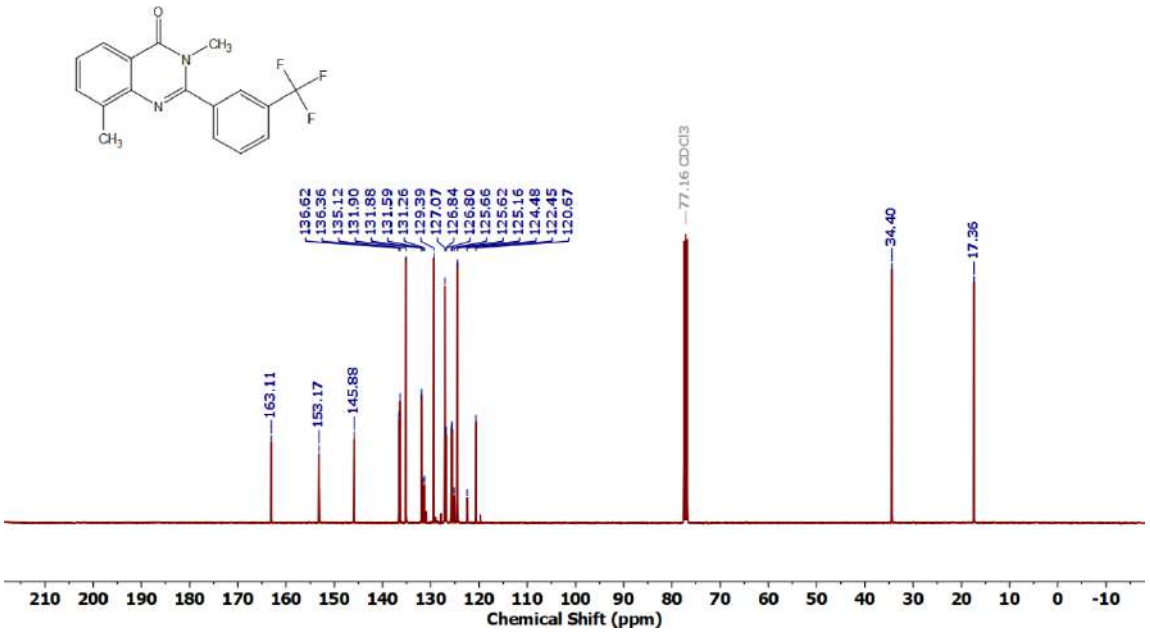

Figure 4.6.A111: ^{13}C{^{1}H} NMR spectrum of **8ae**

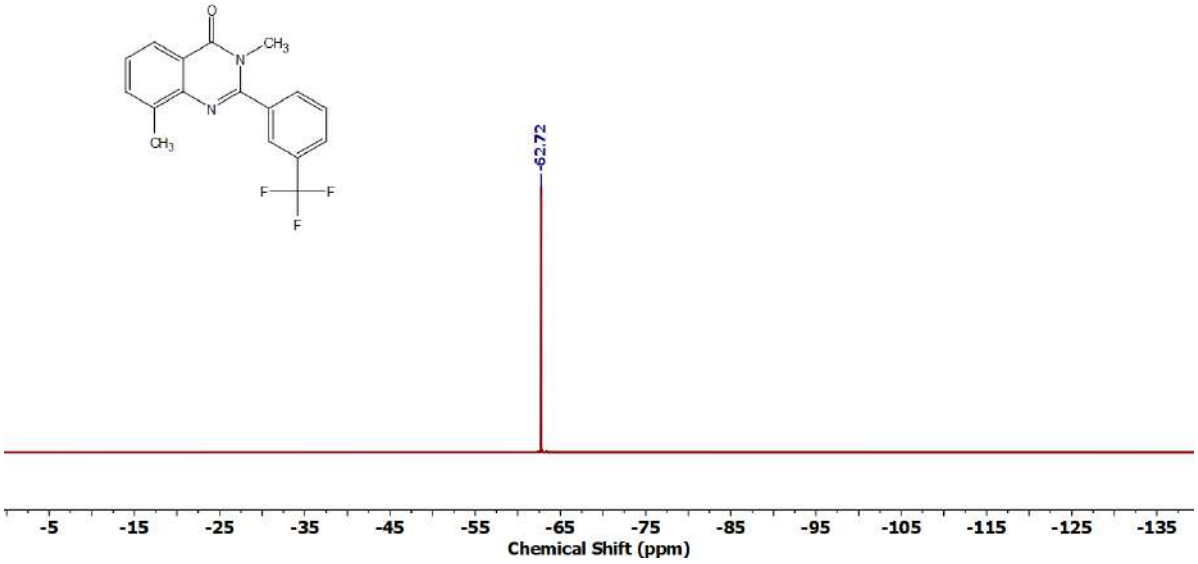

Figure 4.6.A112: ^{19}F NMR spectrum of **8ae**

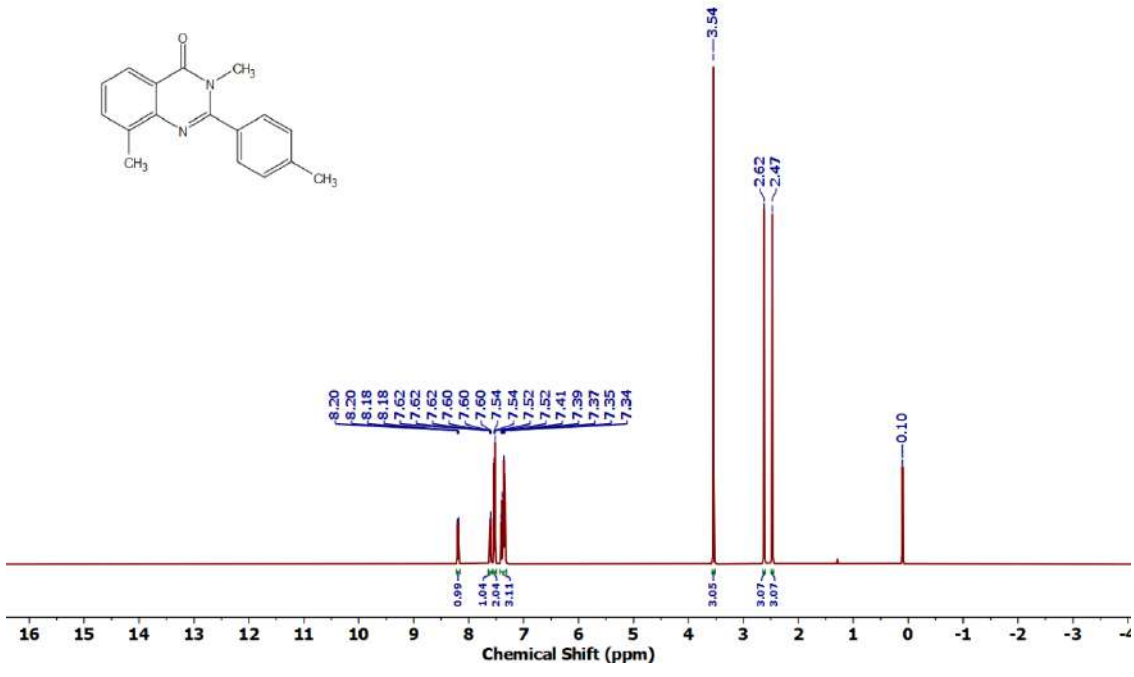

Figure 4.6.A113: ^{1}H NMR spectrum of **8af**

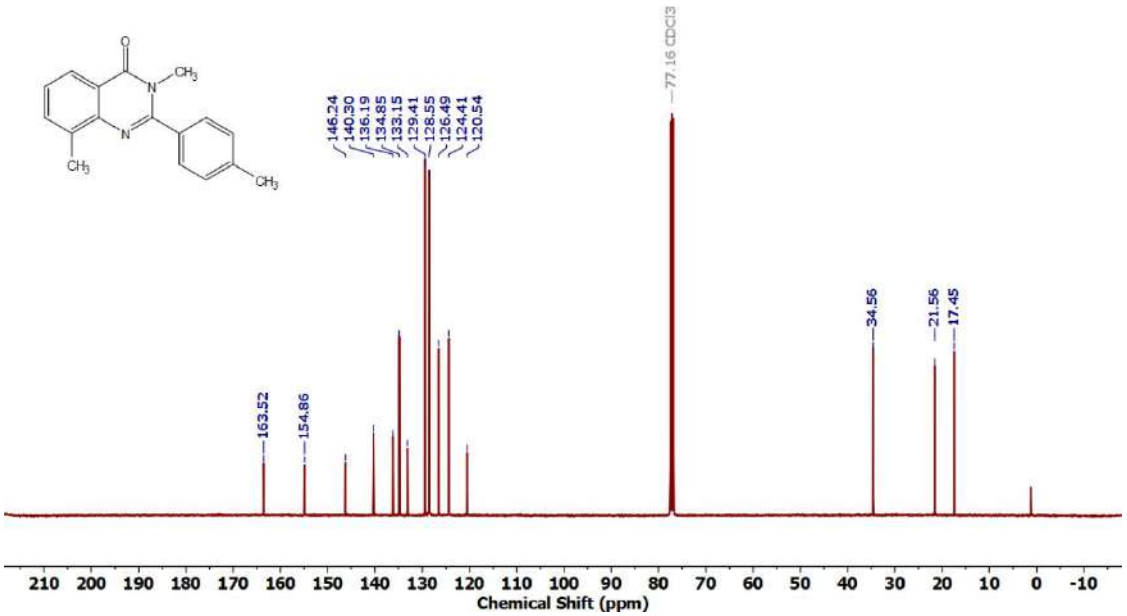

Figure 4.6.A114: $^{13}C\{^{1}H\}$ NMR spectrum of **8af**

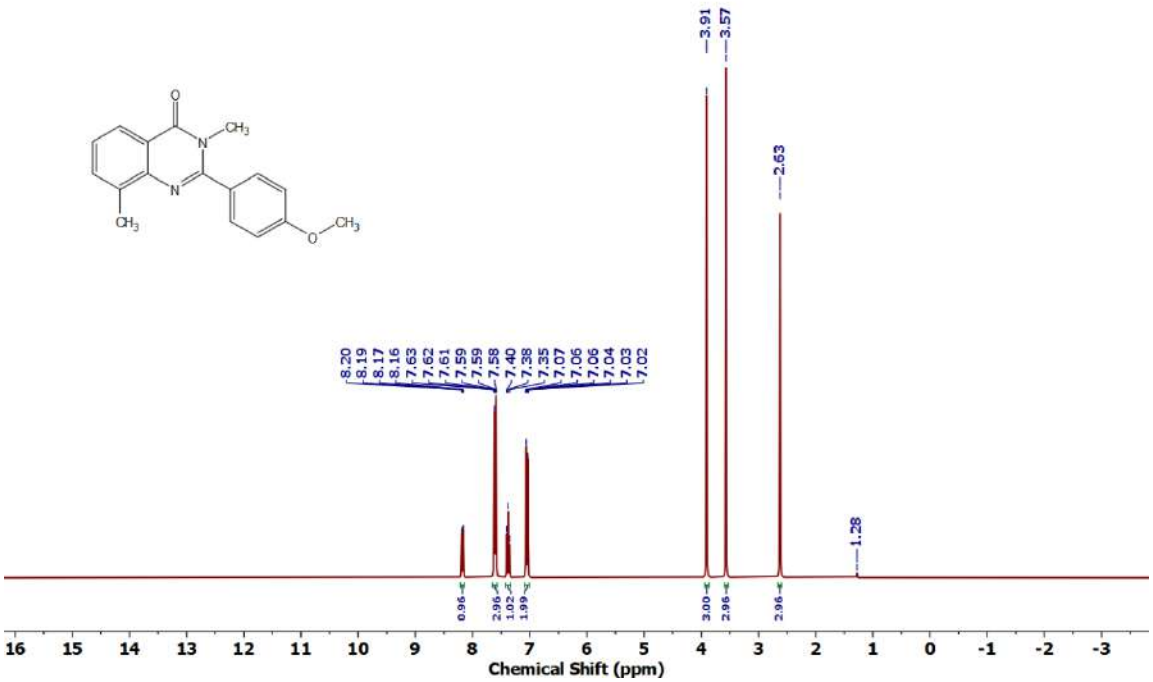

Figure 4.6.A115: ^{1}HNMR spectrum of **8ag**

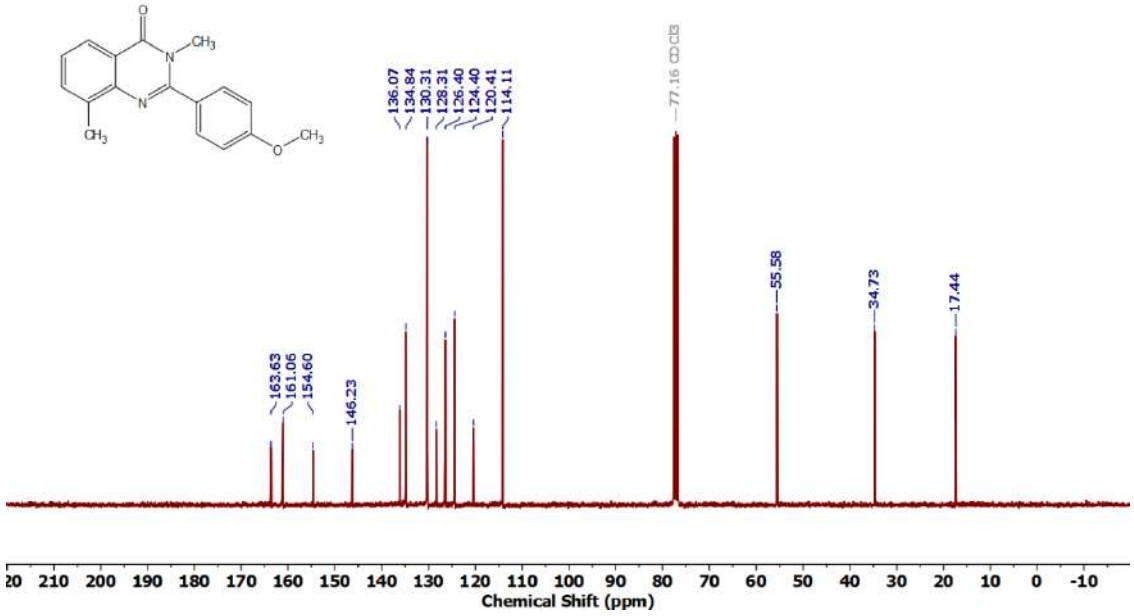

Figure 4.6.A116: $^{13}C\{^{1}H\}$ NMR spectrum of **8ag**

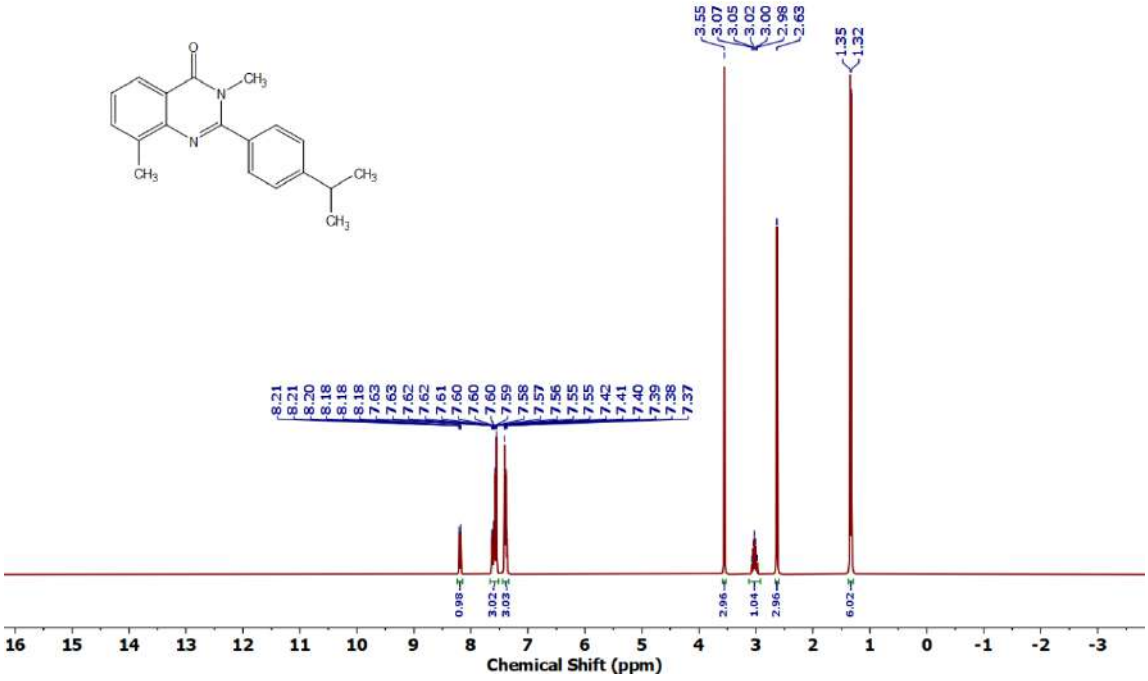

Figure 4.6.A117: ^{1}H NMR spectrum of **8ah**

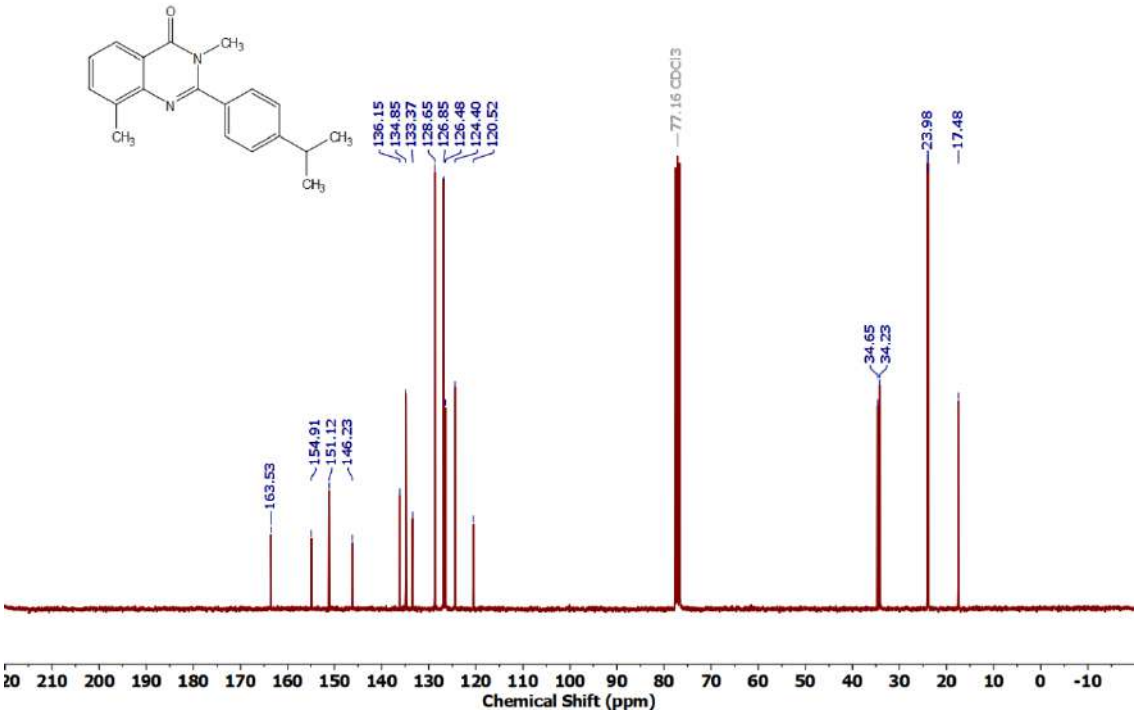

Figure 4.6.A118: $^{13}C\{^{1}H\}$ NMR spectrum of **8ah**

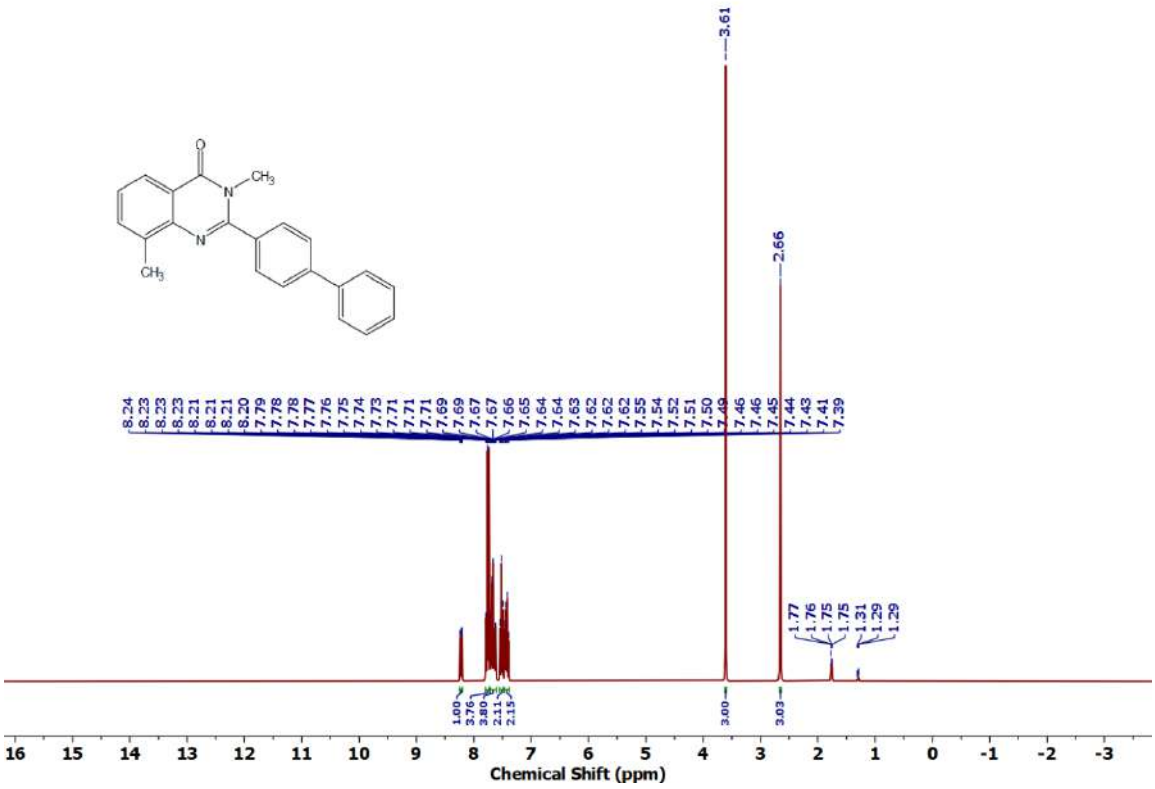

Figure 4.6.A119: ^{1}H NMR spectrum of **8ai**

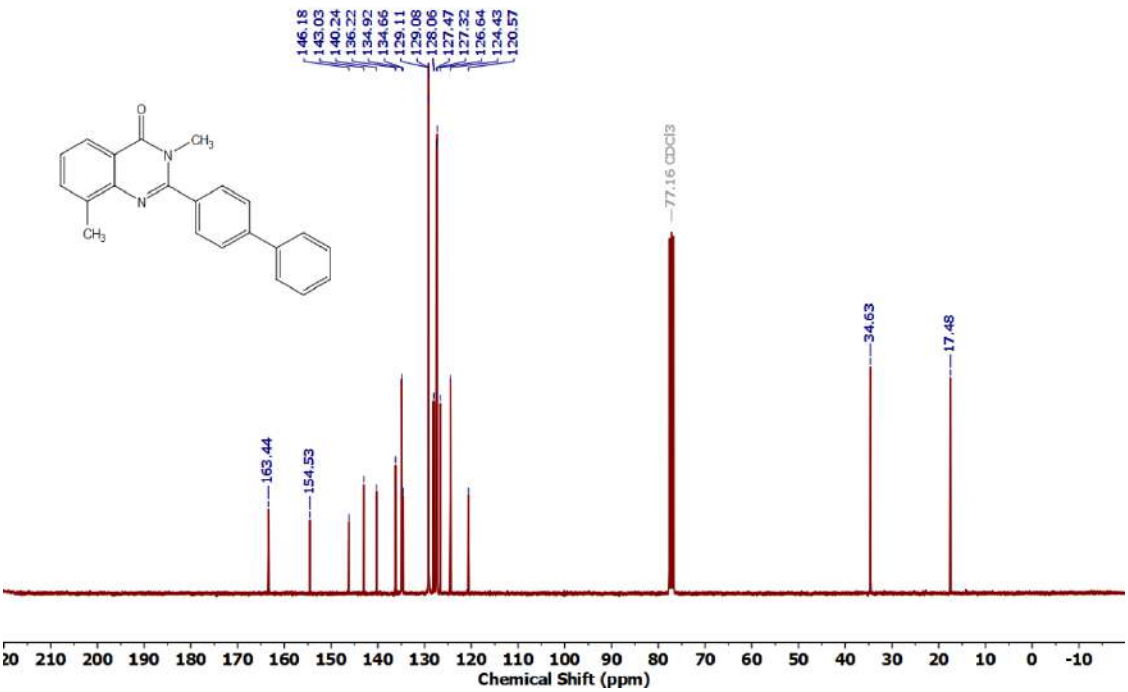

Figure 4.6.A120: $^{13}C\{^{1}H\}$ NMR spectrum of **8ai**

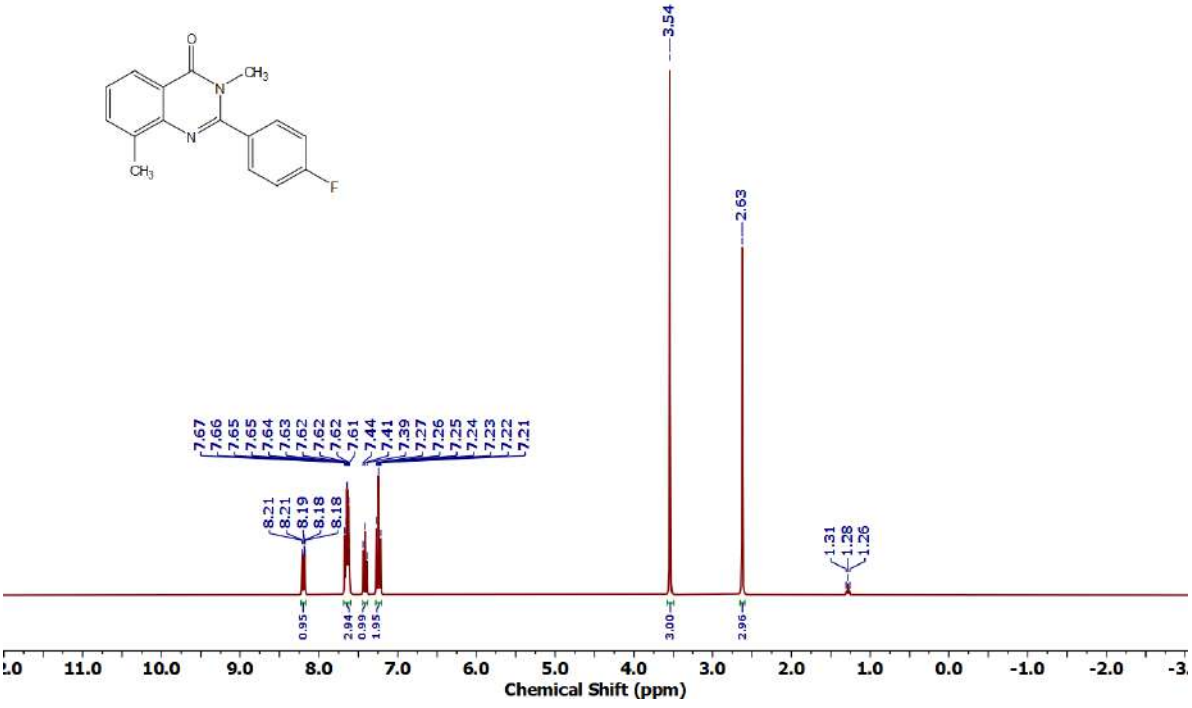

Figure 4.6.A121: ^{1}H NMR spectrum of **8aj**

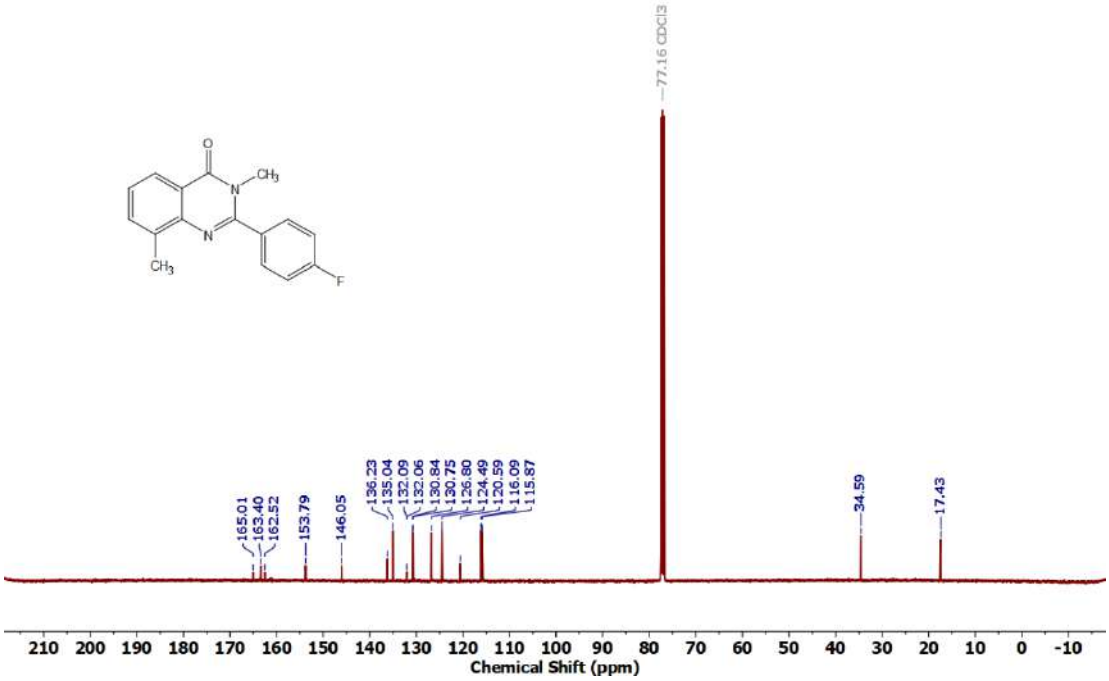

Figure 4.6.A122: $^{13}C\{^{1}H\}$ NMR spectrum of **8aj**

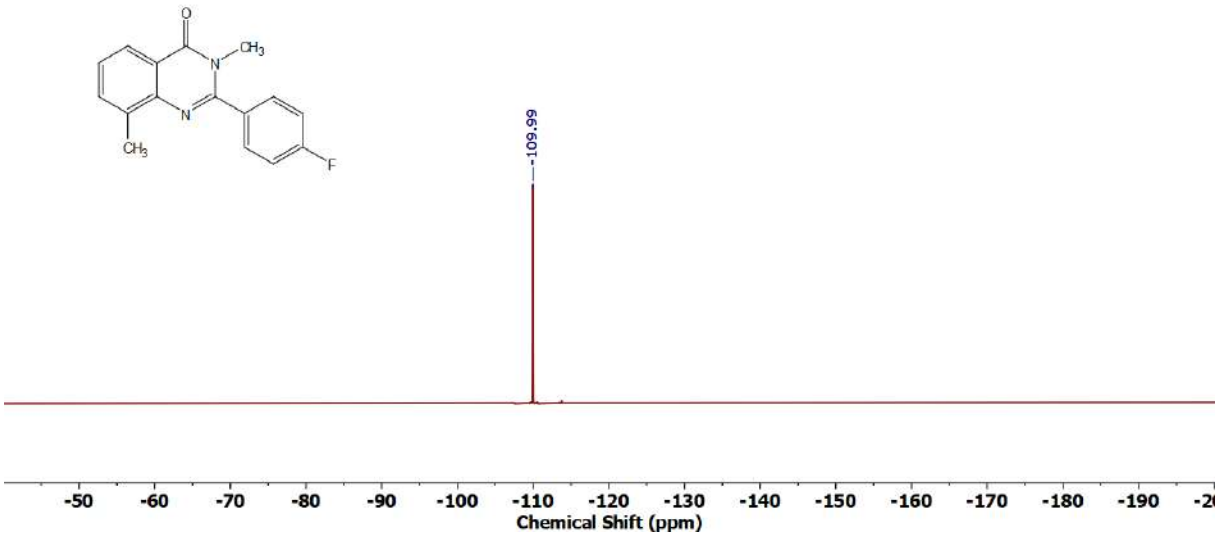

Figure 4.6.A123: ^{19}F NMR spectrum of **8aj**

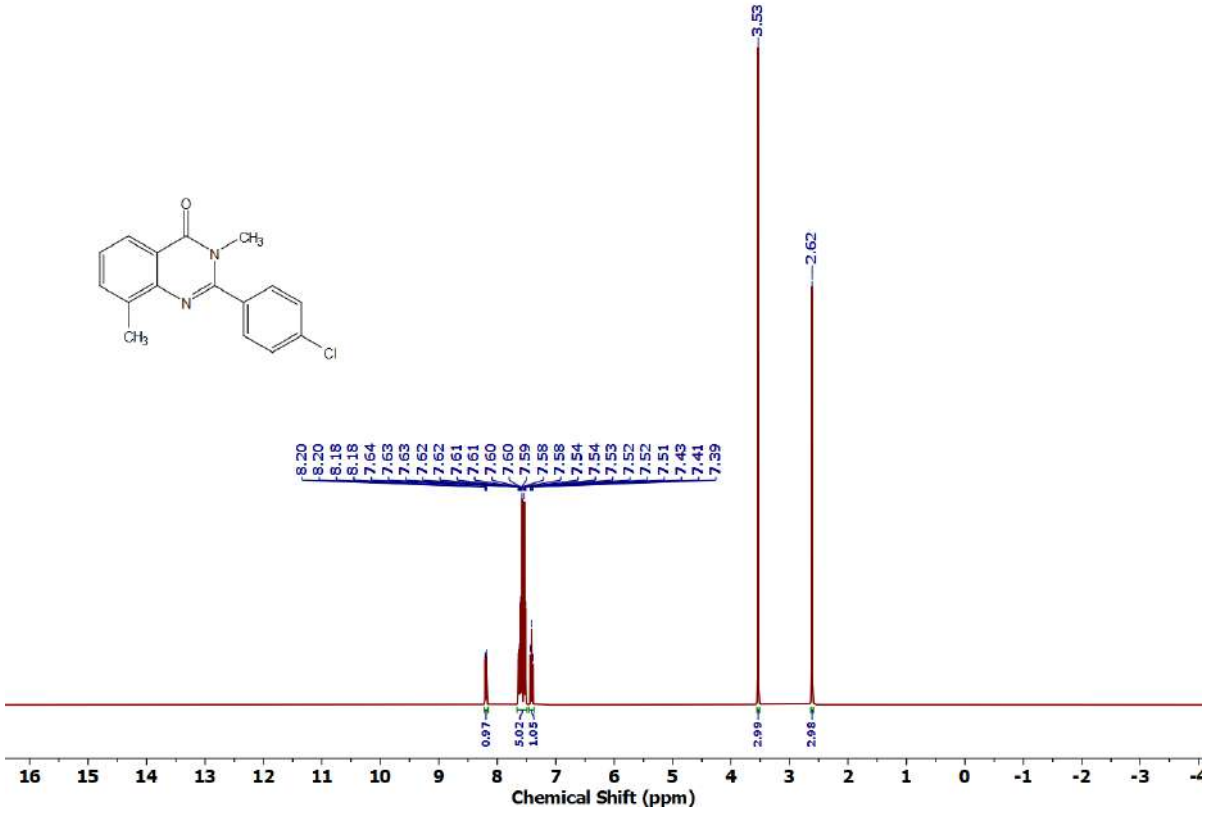

Figure 4.6.A124: ^{1}H NMR spectrum of **8ak**

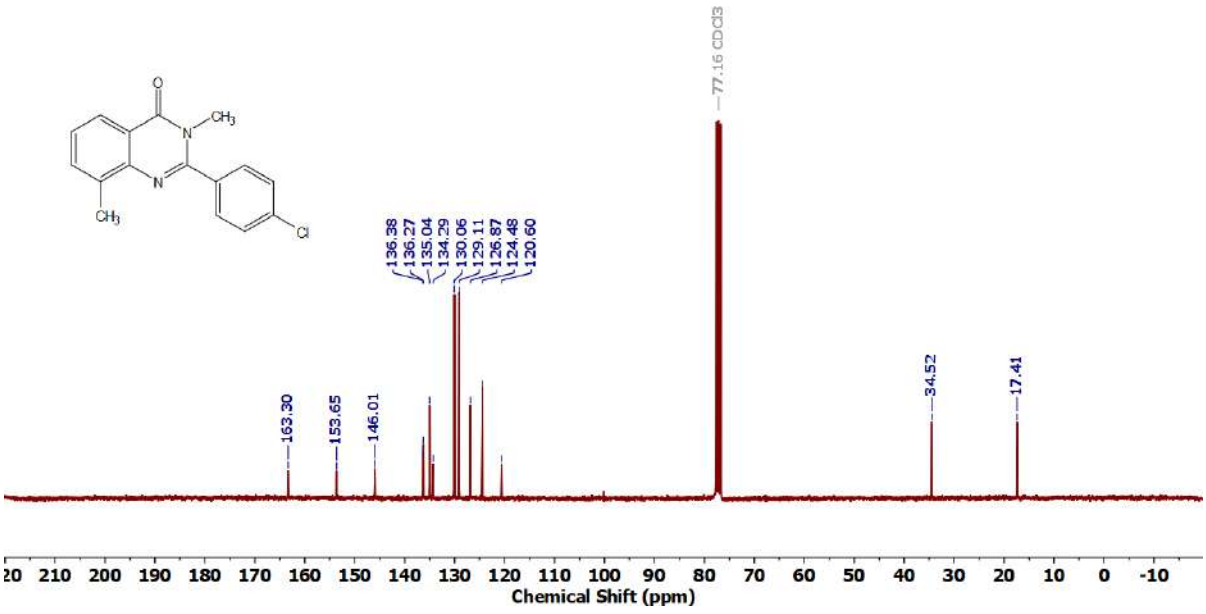

Figure 4.6.A125: ^{13}C{^{1}H} NMR spectrum of **8ak**

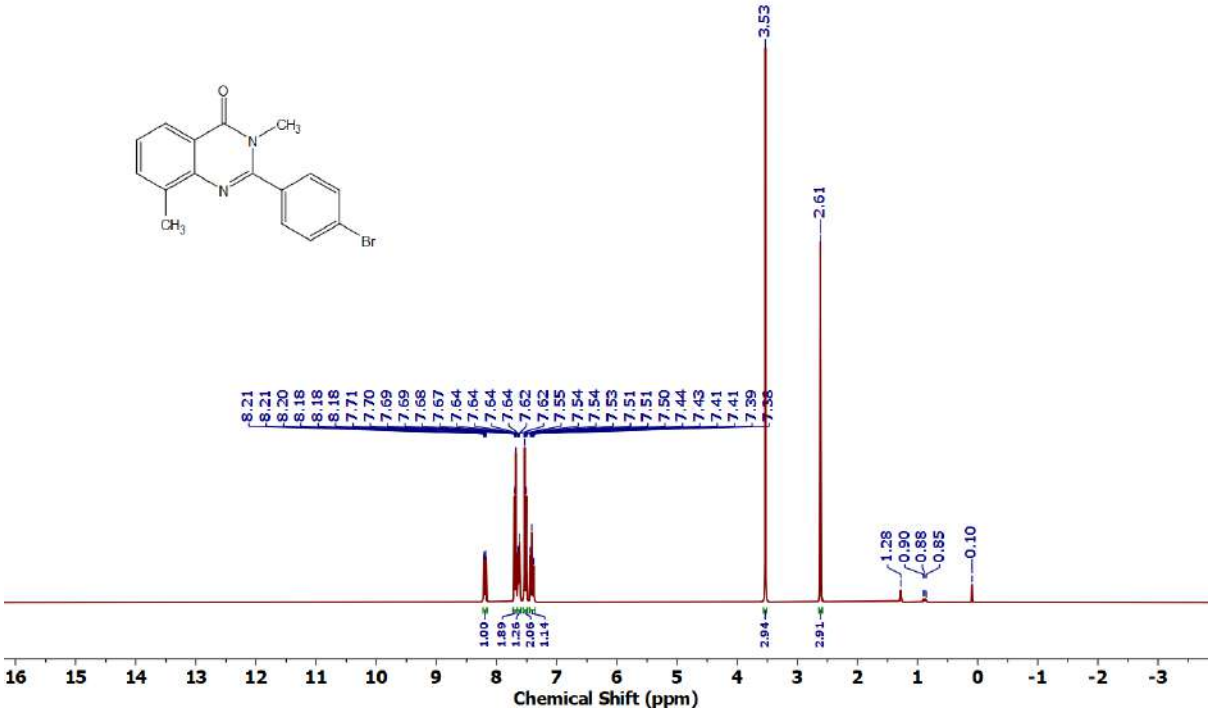

Figure 4.6.A126: ^{1}H NMR spectrum of **8al**

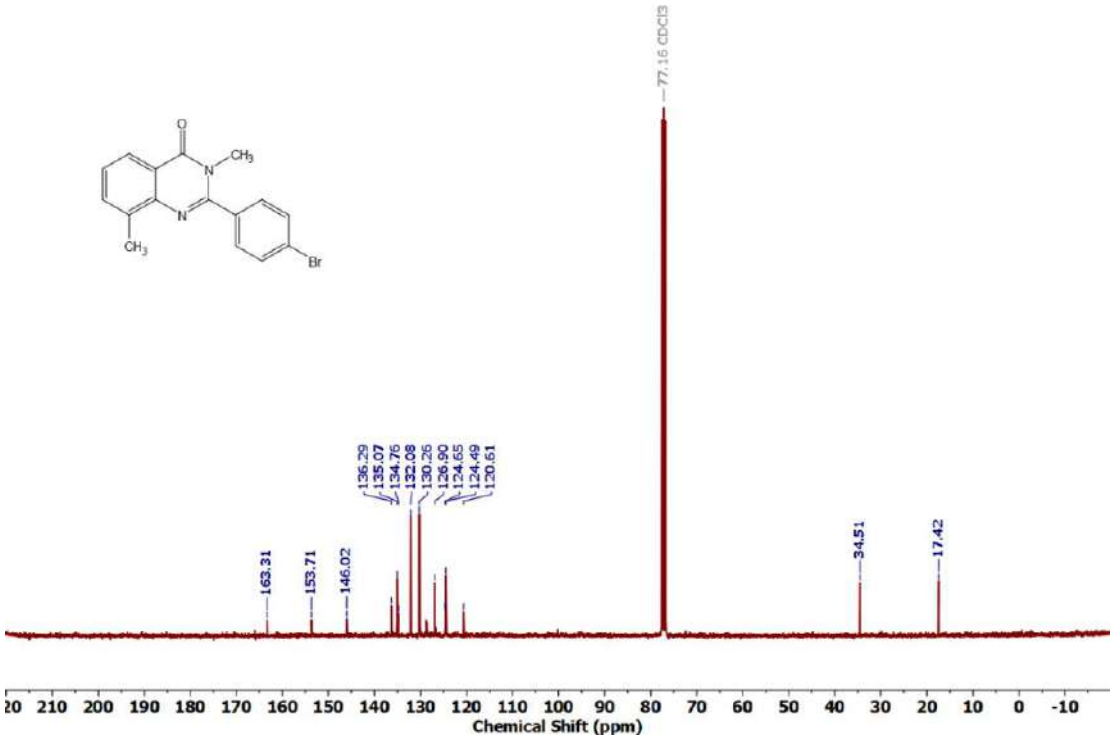

Figure 4.6.A127: ^{13}C{^{1}H} NMR spectrum of **8al**

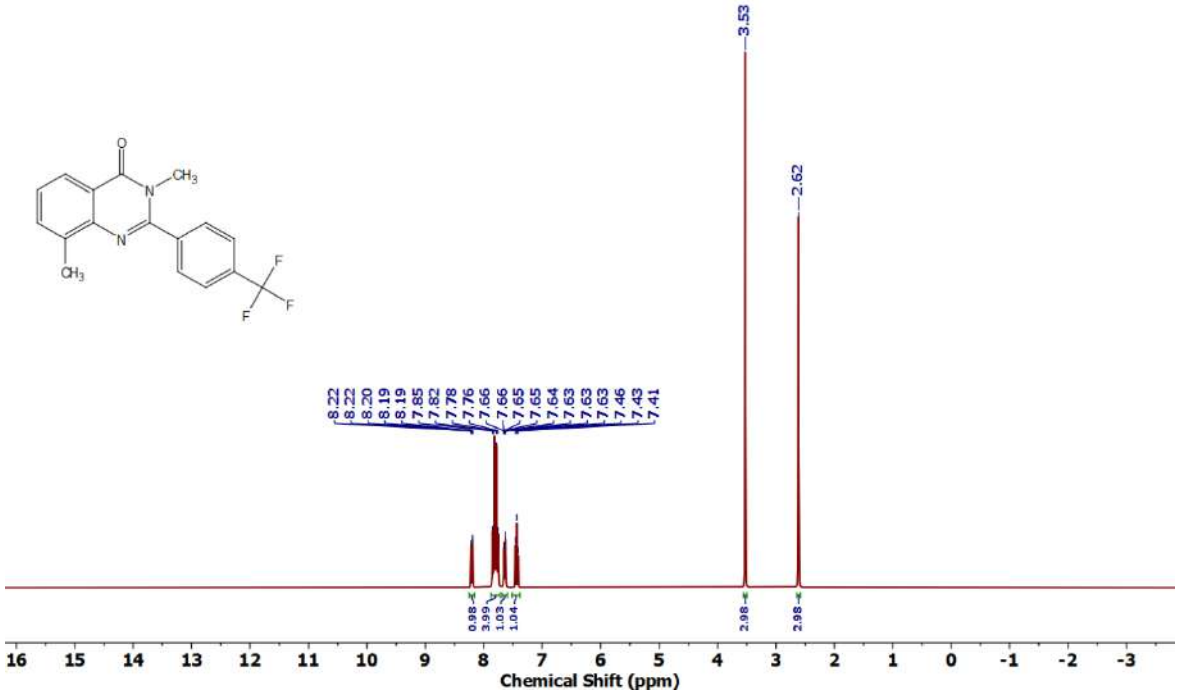

Figure 4.6.A128: ^{1}H NMR spectrum of **8am**

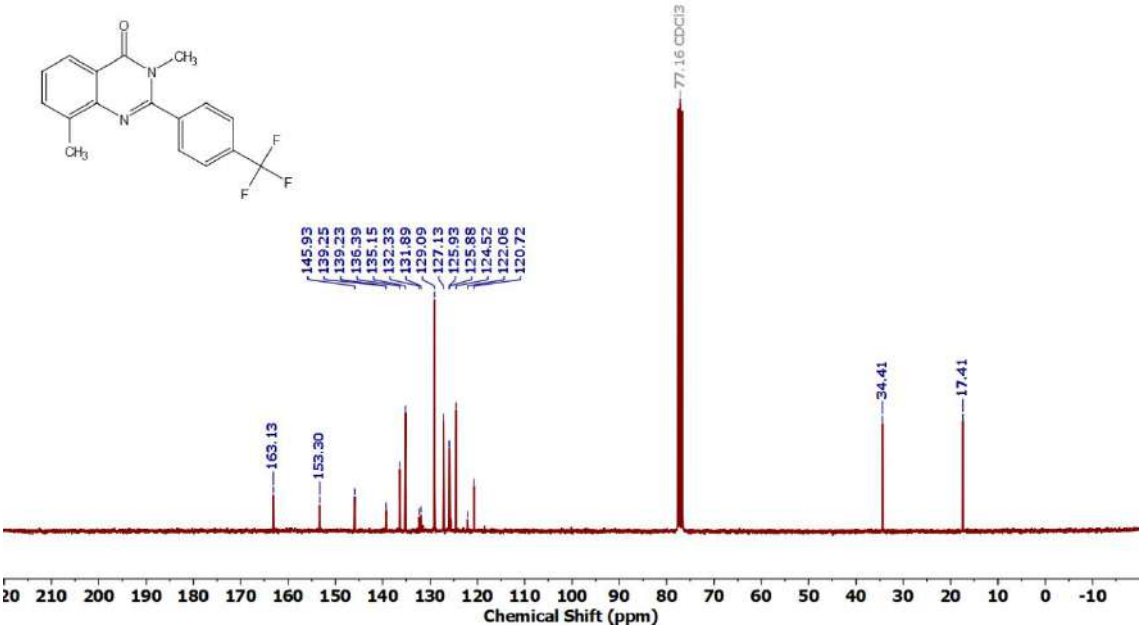

Figure 4.6.A129: ^{13}C{^{1}H} NMR spectrum of **8am**

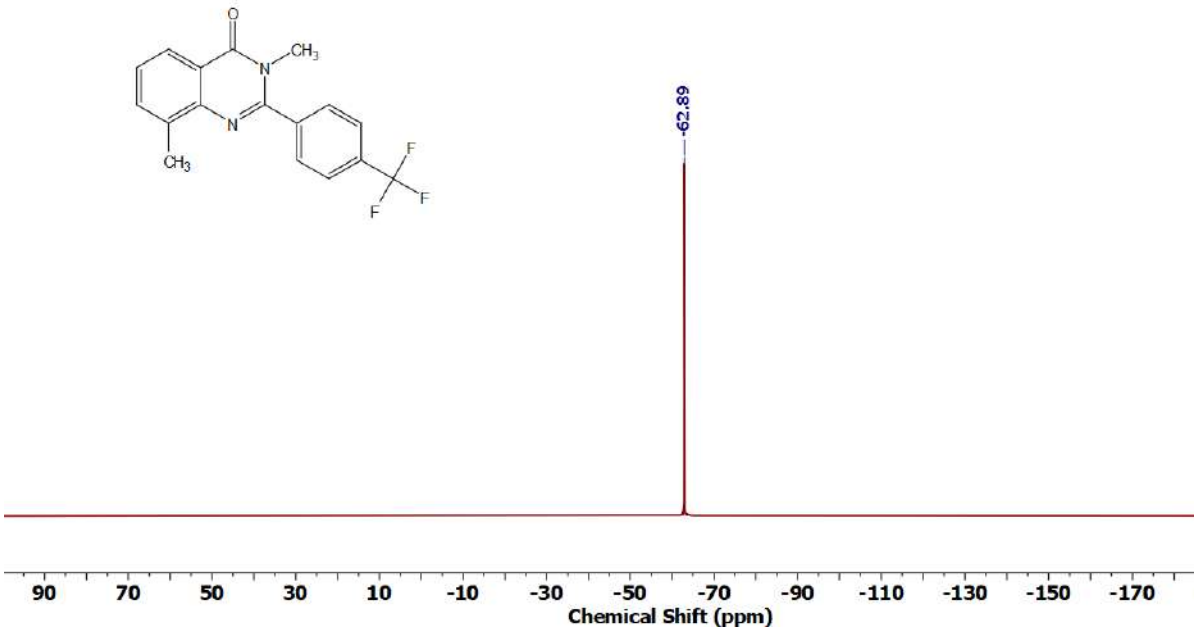

Figure 4.6.A130: ^{19}F NMR spectrum of **8am**

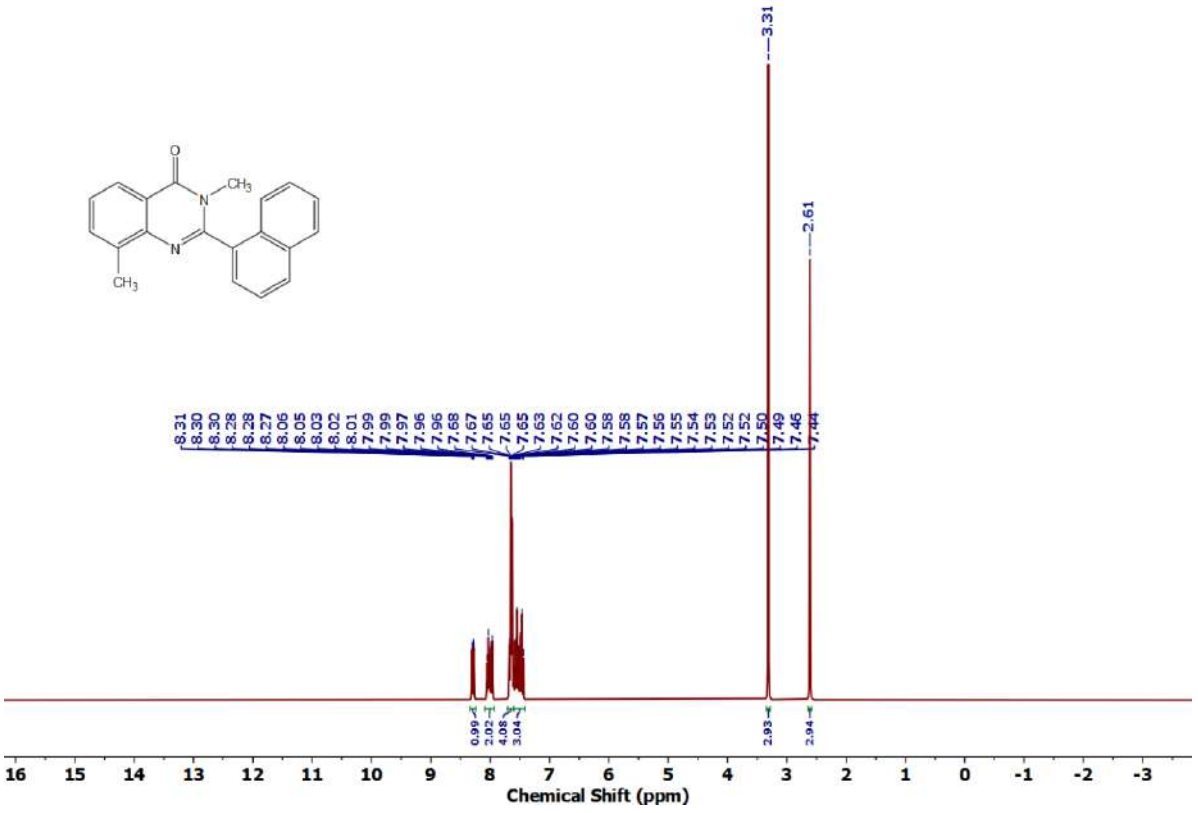

Figure 4.6.A131: ^{1}H NMR spectrum of **8an**

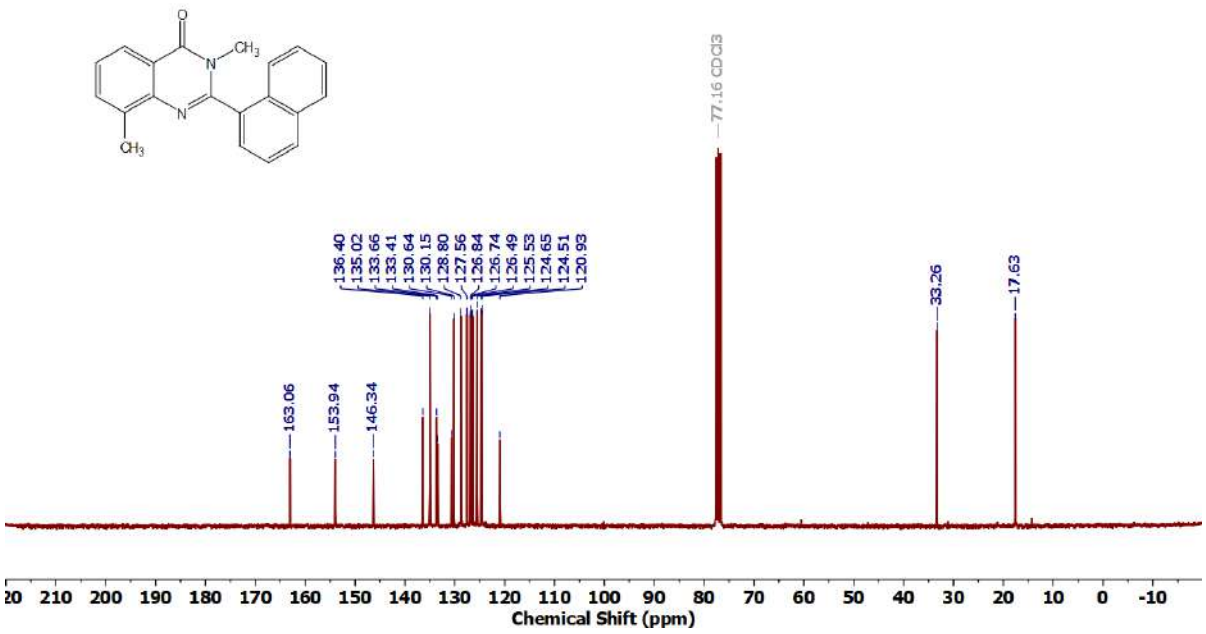

Figure 4.6.A132: $^{13}C\{^{1}H\}$ NMR spectrum of **8an**

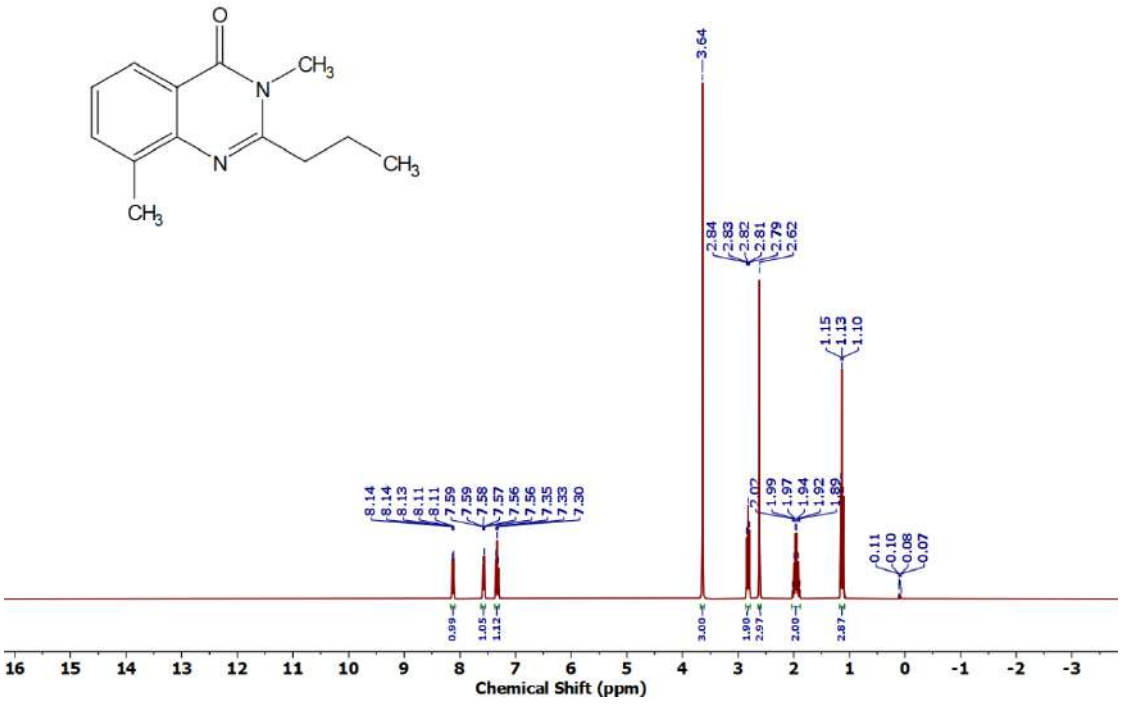

Figure 4.6.A133: ^{1}H NMR spectrum of **8ao**

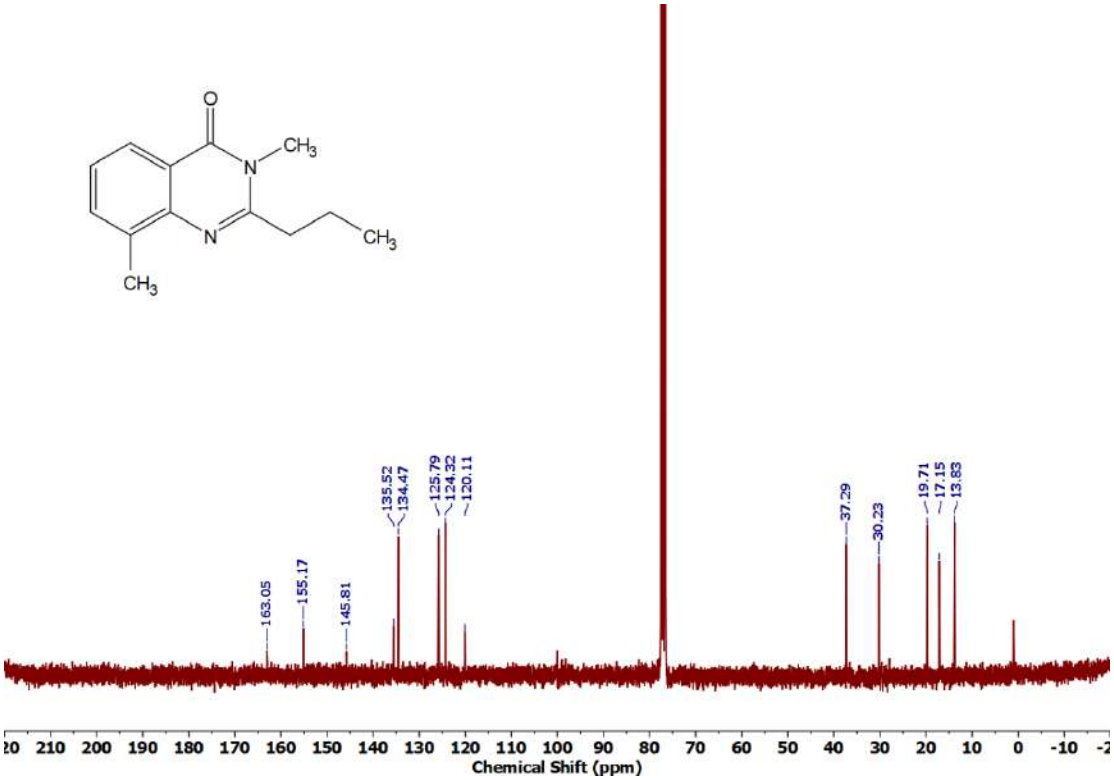

Figure 4.6.A134: $^{13}C\{^{1}H\}$ NMR spectrum of **8ao**

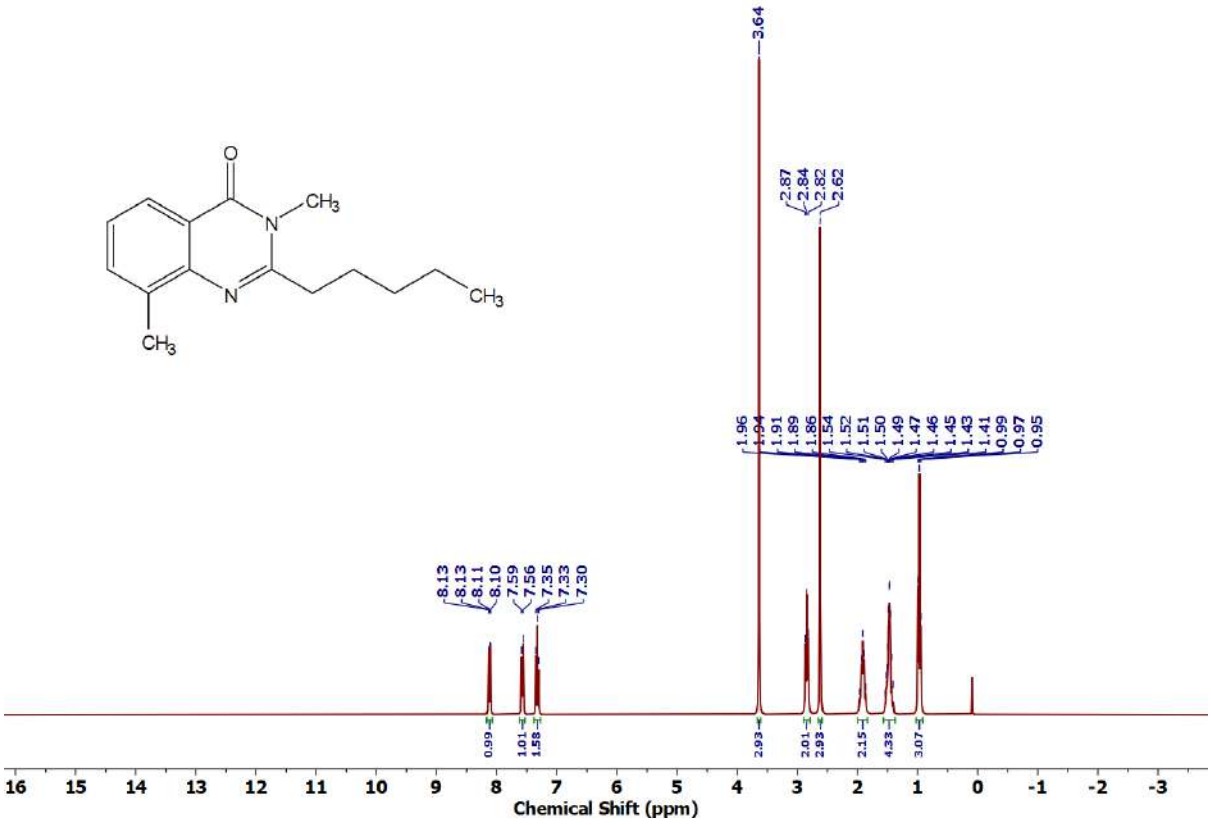

Figure 4.6.A135: ^{1}H NMR spectrum of **8ap**

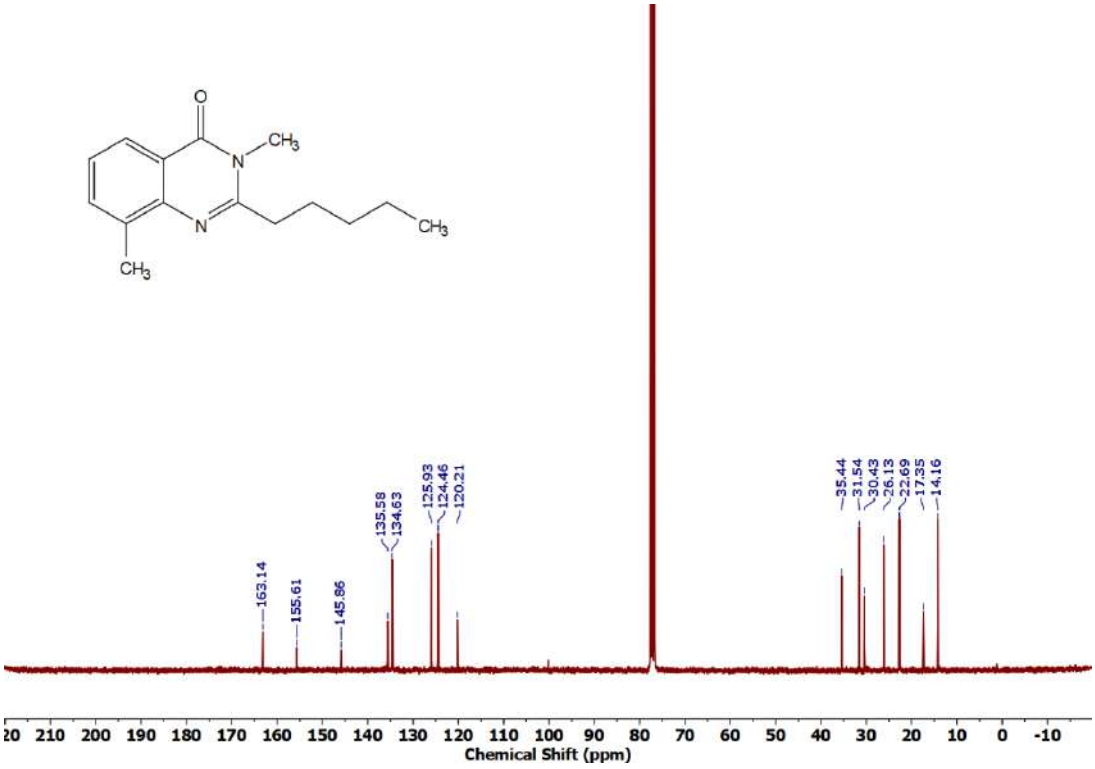

Figure 4.6.A136: $^{13}C\{^{1}H\}$ NMR spectrum of **8ap**

Chapter 5

Coordination Dynamics and Electrocatalytic Activity of a Redox-Active Bis-Azo-Diamine Scaffold in Selective CO_2 Reduction to C_2/C_3 Products

5.1 Introduction

The urgent challenge of climate change necessitates the development of innovative and sustainable technologies.[1] Among these, the electrocatalytic conversion of carbon dioxide (CO_2) into value-added chemicals stands out for its potential to simultaneously reduce atmospheric CO_2 levels and contribute to renewable energy generation.[2] While significant advancements have been made in this field, most efforts have centered on producing one-carbon (C_1) products like formate[3] and formaldehyde,[4] or two-carbon (C_2) compounds such as ethanol and acetic acid.[5] In contrast, the electrosynthesis of three-carbon (C_3) products remains relatively underexplored, despite its promising potential. While the production of C1 and C2 compounds from CO_2 is valuable, it primarily serves as a foundation for advancing toward higher-carbon products (C_3),[6] which are of significant interest for renewable fuel and chemical applications.[7] The direct electrosynthesis of C_3 products from CO_2 marks a critical milestone in achieving efficient carbon utilization and advancing a circular carbon economy. However, this transformation involves a complex interplay of mechanistic, thermodynamic, and kinetic factors,[8] making the C_3 pathway particularly challenging and demanding innovative catalytic strategies to overcome these hurdles.[9] In this work, we report the direct electrocatalytic conversion of CO_2 into C_2 and C_3 products, along with a detailed mechanistic elucidation of the complex reaction pathways involved in this transformation. While most electrocatalytic CO_2 reduction studies have relied on metal-ligand complexes as catalysts,[5,10] our approach is entirely metal-free. We achieve this using a rationally designed organic pre-electrocatalyst, 2,2′-((1E,1′E)-1,2-phenylenebis(diazene-2,1-diyl))dianiline (H_4L, referred to as **1**), which integrates several key features: The molecule contains two electron-deficient azo groups capable of reversible electron acceptance, allowing the ligand to act as an electron reservoir.[11] This electron flow induces coordinative flexibility, enabling dynamic topological changes in the ligand framework. The intrinsic fluxionality of the ligand skeleton mimics the adaptive

coordination behaviour typically offered by transition metal centers, thus fulfilling structural rearrangements required during catalysis. The terminal aromatic amine groups, stabilized by extended conjugation, provide weakly acidic protons, facilitating proton-coupled electron transfer (PCET) events.[12] Upon activation, the organic scaffold transitions into a triplet diradical state, serving as the active catalyst. In this form, it functions both as an electron-proton reservoir and as a topologically adaptive platform for CO_2 binding allowing both end-on and side-on coordination, akin to transition metal complexes. This system represents a rare example of a transition metal-free electrocatalyst that offers: built-in stereoelectronic flexibility for dynamic coordination, efficient electron-proton storage and transfer capabilities, an electronic relay mechanism via ligand twisting, and structurally tunable docking sites for CO_2 binding and product release. Collectively, these properties enable **1** to replicate and even expand upon the catalytic roles typically assigned to transition metal complexes in sustainable CO_2 reduction frameworks. The ligand's ability to (1) accept electrons, (2) form a metastable reactive platform with substrates, and (3) modulate substrate binding and release in response to external electric fields, has been effectively harnessed to drive a cascade reaction sequence converting CO_2 to CH_3COOH, then to CH_3COCH_3, with glyoxal as a key intermediate. In the following section, we delve deeper into the electro-reactive design principles that underpin the functionality of the H_4L catalyst.

5.2 Results and discussion

5.2.1 Synthesis of electrocatalyst

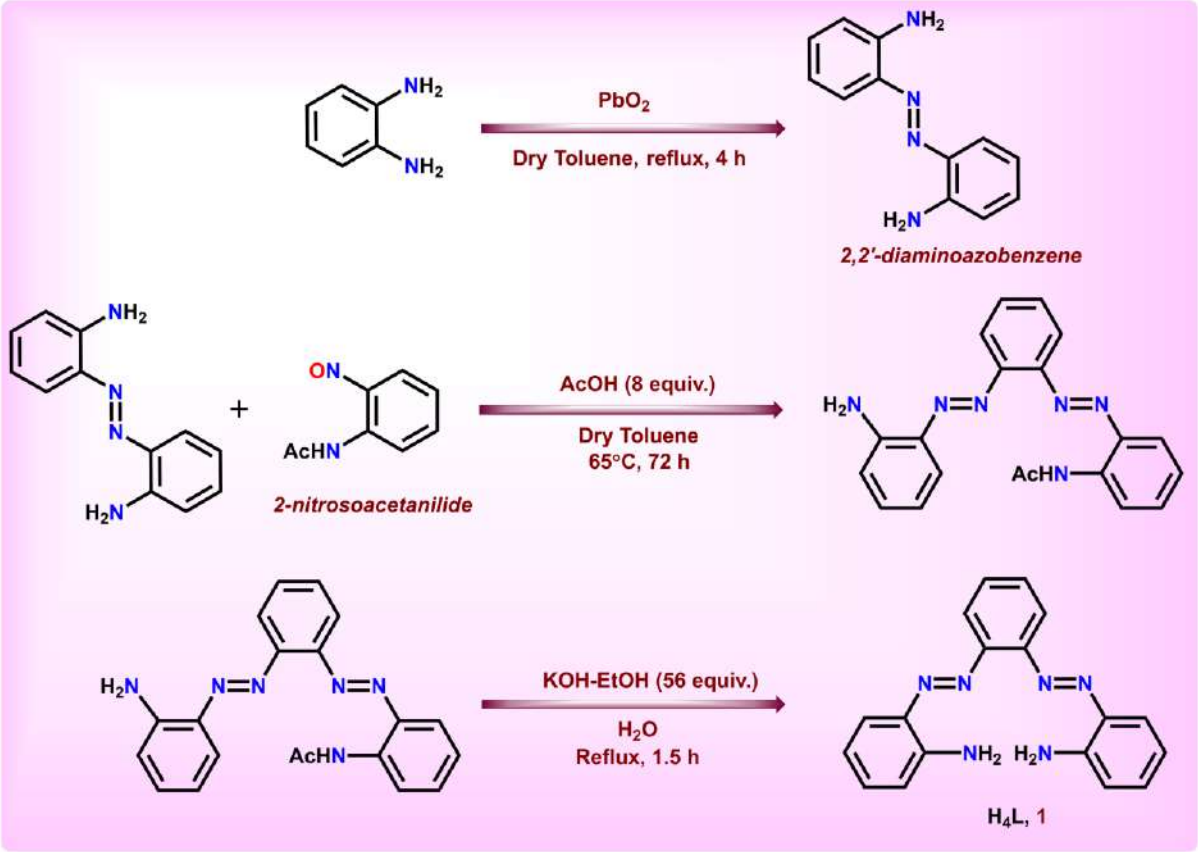

Scheme 5.1 Detailed synthetic procedure for synthesis of catalyst

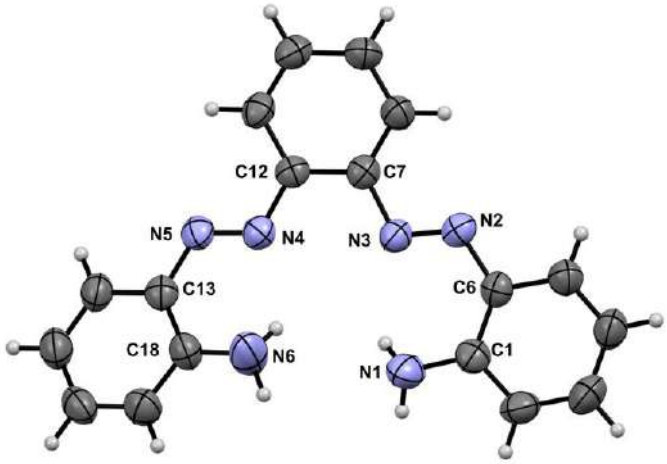

Figure 5.1: ORTEP diagram of **1** (Thermal ellipsoids are set at 50% probability)

Table 5.1: Crystallographic details of **1**

	1
Empirical formula	$C_{18}H_{16}N_6$
T/K	273.15
fw	316.37
Crystal system	Orthorhombic
Space Group	*F* d d 2
a/Å	24.098(2)
b/*Å*	45.696(5)
c/ *Å*	5.8407(5)
α/deg	90
β/deg	90
γ/deg	90
V/ *Å*^{3}	6431.8(10)
Z	16
D_c/Mgm^{-3}	1.307
μ/mm^{-1}	0.083
F(000)	2656
cryst size/mm^3	0.3×0.2×0.2
θ/deg	2.46– 24.38
Measured reflns	46691
Unique reflns	2226
[a]GOF on F^2	1.134
R1[b], wR2[c][*I*>2*σ*(*I*)]	0.0580, 0.1092
R1, wR2	0.0830, 0.1196
[a]GOF = $\{\Sigma[w(F_o{}^2-F_c{}^2)2]/(n-p)\}^{1/2}$. [b]R1 = Σ [$\|F_o\|-\|F_c\|$]/ Σ $\|F_o\|$. [c]wR2 = $[\Sigma [w(F_o{}^2-F_c{}^2)^2]/ \Sigma [w(F_o{}^2)^2]]^{1/2}$ where w = 1/[$\sigma^2(F_o{}^2)+(aP)^2+bP]$, P = $(F_o{}^2+2F_c{}^2)/3$.	

The ligand H_4L (**1**), serving as the pre-electrocatalyst, has been strategically designed to incorporate inherent coordinative fluxionality. This design involves the introduction of two azo groups at the ortho-positions of a central phenyl ring, creating adjacent electron-accepting sites capable of accommodating an electron pair. Upon reduction, these sites are transformed into a triplet azo-anion diradical species, [**1**$^{\bullet\bullet}$]$^{2-}$, which constitutes the catalytically active form.[13] The ability of the ligand to access a diradical state is of significant electronic importance. Each azo-

anion radical[14] center serves not only as an electron reservoir but also as a metastable platform for the activation of kinetically inert CO_2 molecules. The close spatial proximity of the two azo groups facilitates the simultaneous binding of two CO_2 molecules—one in an end-on and the other in a side-on orientation—minimizing steric hindrance while enabling asynchronous, stepwise electron transfer from the ligand's redox-active pockets. Additionally, the ligand features terminal amino groups at both ends, which can become protonated under mildly acidic conditions. These $–NH_2$ functionalities can act as localized proton sources, enabling proton-coupled electron transfer (PCET) steps during CO_2 activation and subsequent transformation into value-added products.

The ligand H_4L was synthesized following a previously reported method with slight modifications.[15] The synthetic route began with the oxidative homocoupling of *o*-phenylenediamine using lead dioxide in refluxing toluene, yielding 2,2′-diaminoazobenzene. This intermediate was then reacted with preformed 2-nitrosoacetanilide under modified Baeyer–Mills conditions to afford the monoprotected bis-azo-diamine ligand. Subsequent alkaline hydrolysis provided the desired ligand H_4L in good yield (see Experimental section for details). The ligand was thoroughly characterized using various analytical and spectroscopic techniques, as well as single-crystal X-ray diffraction. The crystal structure reveals that the molecule adopts a slightly distorted planar conformation, likely due to steric interactions between the two pendant amine ($–NH_2$) groups. The ligand was found to crystallize in the orthorhombic *F*dd2 space group. The molecular structure is shown in Figure 5.1, while detailed crystallographic data and selected bond parameters both experimental and calculated are presented in Table 5.1 and Table 5.2. Intramolecular hydrogen bonding between the pendant amine groups and adjacent azo moieties may play a key role in stabilizing the structure, with donor–acceptor distances of 2.629(6) Å and 2.702(5) Å, respectively (Figure 5.2, Table 5.3). The azo (–N=N–) bond lengths were measured to be 1.273(4) Å and 1.274(4) Å, which

are slightly longer than typical values reported for free azo groups.[16] This elongation is likely attributed to extensive delocalization of electron density from the pendant amine groups toward the azo moieties. The ^{1}H-NMR spectrum of the ligand displays two types of signals: aromatic protons and also for protons from aromatic primary amine group (–NH_2). The aromatic proton signals are observed in the range of 6.76–6.92 ppm, while the signal corresponds to the protons of –NH_2 group appears at 6.26 ppm. (Figure 5.6.A1).

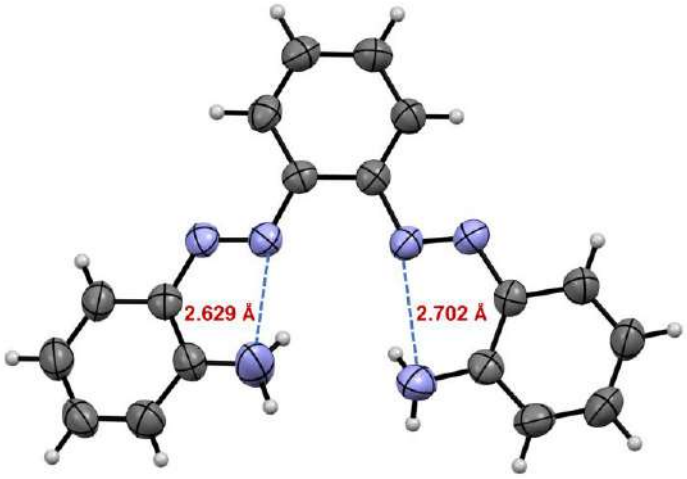

Figure 5.2: The intramolecular H-bonding in **1**

Table 5.2: Crystallographic and theoretical metrical theoretical metrical parameters for **1**

Metrical Parameters	Bond length		Metrical Parameters	Bond angle	
	Expt.	Theo.		Expt.	Theo.
N2–N3	1.273(5)	1.267	N1–C1–C6	122.2(4)	121.75
N4–N5	1.274(4)	1.268	C1–C6–N2	127.3(4)	126.75
C1–N1	1.376(5)	1.360	C6–N2–N3	117.9(4)	117.91
C6–N2	1.406(5)	1.359	N2–N3–C7	112.3(4)	114.53
C7–N3	1.430(5)	1.413	C12–N4–N5	113.2(4)	114.62
C12–N4	1.412(5)	1.413	C13–N5–N4	116.0(4)	117.86
C13–N5	1.412(6)	1.389	C13–C18–N6	121.3(4)	121.73
C18–N6	1.368(5)	1.359	N4–C12–C7	118.2(4)	117.65

Table 5.3: Hydrogen bonding parameter of **1**

Type of H-Bonding	Donor (D)	Acceptor (A)	D – A(Å)	D–H…..A(deg)
Intra-molecular	N1	N3	2.702(5)	119
Intra-molecular	N6	N4	2.629(6)	126

5.2.2 Electrochemistry

The electrochemical properties of compound **1** were investigated using cyclic voltammetry in an anhydrous, deoxygenated mixture of acetonitrile and dichloromethane (9:1 v/v), with 0.2 M tetrabutylammonium hexafluorophosphate (TBAF) serving as the supporting electrolyte. The measurements were carried out using a conventional three-electrode configuration comprising a platinum disk as the working electrode, a platinum wire as the counter electrode, and a saturated Ag/AgCl electrode as the reference electrode. The cyclic voltammogram of **1** reveals a series of reversible one-electron reduction processes occurring at −0.70 V, −1.05 V, −1.36 V, and −1.77 V, with corresponding peak-to-peak separations of 99 mV, 116 mV, 134 mV, and 93 mV, respectively. Additionally, an irreversible oxidation event is observed at +1.45 V (Figure 5.3, Table 5.4). Density Functional Theory (DFT) calculations of neutral ligand **1** indicate that the first reduction wave predominantly involves the azo group within the ligand framework of **1**, accounting for approximately 45% of the electronic contribution (Table 5.5). The subsequent reduction steps are proposed to arise from overlapping electronic contributions originating from both the azo unit and the phenyl rings embedded in the molecular structure of **1**.

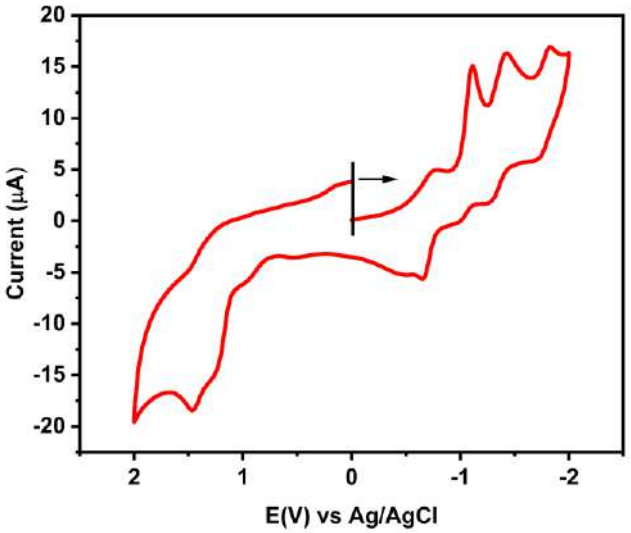

Figure 5.3: Cyclic voltammogram of **1**

Table 5.4: Electrochemical data of **1**

Compound	$E_{1/2}$/V (ΔE/mV)	
	Oxidation	**Reduction**
2	+1.45	−0.70 (99), −1.05 (116), −1.36(134), −1.77(93)
$E_{1/2} = ½(E_{pa} + E_{pa})$, E_{pa} = anodic peak potential; E_{pc} = cathodic peak potential, ΔE = peak-to-peak separation		

Table 5.5: Molecular Orbital Contribution of **1**

Orbital	MO	Energy (eV)	Contribution			Composition
			Azo	Amine	Ph	
89	L+5	0.27	3	4	93	π* (Ph)
88	L+4	0.18	2	7	91	π* (Azo + Amine)
87	L+3	-0.03	2	3	95	π* (Ph)
86	L+2	-0.11	2	1	97	π* (Ph)
85	L+1	-1.91	44	4	52	π* (Azo + Ph)
84	LUMO	-2.46	45	5	50	π* (Azo + Ph)
83	HOMO	-5.47	10	24	66	π (Azo + Amine + Ph)
82	H–1	-5.81	7	26	67	π (Azo + Amine + Ph)
81	H–2	-5.94	71	4	25	Lone Pair (Azo)
80	H–3	-6.45	22	6	72	Lone Pair (Azo) + π (Ph)
79	H–4	-6.50	62	4	33	Lone Pair (Azo)
78	H–5	-6.67	13	2	85	π (Azo + Ph)

5.2.3 Electrocatalytic reduction of CO_2

The electron-accepting nature of the neutral ligand **1** arises from its low-lying π* orbital, which is capable of accepting electrons to generate reduced azo species. Upon accepting one electron, precatalyst **1** forms a monoradical $[–N=N–]^{\bullet-}$, while a two-electron reduction yields a diradical $[–N–N–]^{2-}$, as depicted in Scheme 5.2. These reduced species exhibit nucleophilic character, enabling them to react with electron deficient substrates such as carbon dioxide. Due to its limited solubility in water, ligand **1** can be employed as a heterogeneous electrocatalyst. For electrochemical studies, it is dissolved in acetonitrile (MeCN) and immobilized on a carbon paper electrode *via* drop-casting method, which enhances its operational stability in aqueous environments. Initial electrochemical activation was investigated using cyclic voltammetry with a 10 mM solution of the pre-catalyst in MeCN. The measurements were conducted using carbon paper as the working electrode, a platinum wire as the counter electrode, and a non-aqueous Ag reference electrode filled with 0.1 M $NaClO_4.H_2O$ as supportive electrolyte, Pt, and the scan rate was set at 0.05 mV/s. The cyclic voltammogram (black trace, Figure 5.4) reveals two distinct reduction peaks at $E_{1/2}$ = −0.26 V and $E_{1/2}$ = −1.40 V vs Ag/AgCl, corresponding to successive one-electron reductions of the azo moiety. The first reduction, forming the monoradical, is electrochemically reversible. In contrast, the second reduction process is irreversible under this condition, indicating instability of the two-electron reduced species and suggesting subsequent chemical transformation, likely *via* immediate nucleophilic attack to regain stability. To probe this concept further, a comparative cyclic voltammetry experiment was performed under a CO_2-saturated atmosphere using identical conditions (Red trace, Figure 5.4). Notably, the second reduction peak disappears in the presence of CO_2, implying that the diradical may react with CO_2 to form a stable adduct. This observation signifies the onset of pre-catalyst activation through direct interaction with CO_2. In the

following sections, we delve into the theoretical aspects of the pre-catalyst to gain deeper insights into its activation mechanism and its role in CO_2 reduction to value added products.

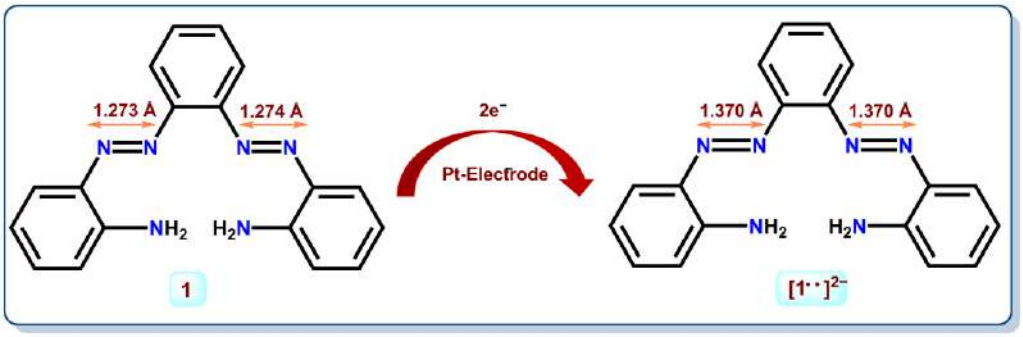

Scheme 5.2: Schematic representation of formation of two electron reduced species $[\mathbf{1}^{\bullet\bullet}]^{2-}$ from **1**

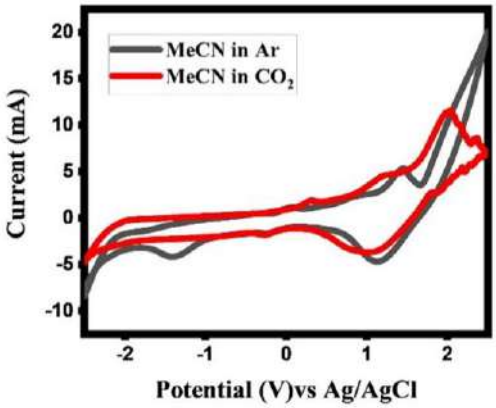

Figure 5.4: Homogeneous cyclic voltammetry Azo-based ligand dissolved in dry and degassed acetonitrile in Ar (black) and after saturating with CO_2 (red) at scan rate 50 mV/s

The single crystal X-ray diffraction study as discussed earlier reveals that the –N=N– lengths are 1.273(5) Å and 1.274(4) Å respectively which is typical for free azo.[16] Theoretical exploration reveals that the HOMO is essentially of π–character having 66% contribution from phenyl rings, 24% from $–NH_2$ and only 10% from the azo moieties (Table 5.5). The feature is in keeping with the role of the amino group during the electrocatalytic process. The π* LUMO is low-lying with significant contribution from the azo groups (45%) (Table 5.4), thereby vindicating our strategy to employ the azo centers as electron receptors to effectuate the electrocatalysis *via* a PCET pathway (Figure 5.5).

Figure 5.5: DFT optimized structures of catalyst forming an adduct with CO_2.

The optimized geometry of the pre-catalyst **1** is shown in Figure 5.6a and it is practically planar owing to extensive π–cloud delocalization. Upon injection of electrons, during the initial step of pre-catalyst activation, theoretical investigations further reveal that the reduction of azo moieties takes place with some involvement from each of the phenyl rings. This is a further indicator that the azo skeletons of the reported ligand can be elegantly exploited as electron sinks to generate the meta-stable triplet diradical. This is the active catalyst for CO_2RR that may further behave as an electron reservoir. In the course of activation, the triplet diradical transfers electrons to CO_2 from the azo electron reservoirs to convert CO_2 to further valorized products as we will see later. In order to have a further insight in the initial steps of the electrocatalytic process, we have optimized the structure of triplet diradical $[\mathbf{1}^{\bullet\bullet}]^{2-}$ (Figure 5.6b) and the spin density plot (Figure 5.6d) reveals that odd electrons reside primarily over the two azo moieties, thereby leading to increase in N–N lengths (Scheme 5.2).[17] The species $[\mathbf{1}^{\bullet\bullet}]^{2-}$, which is in turn is believed to have been formed during electrocatalytic CO_2RR, provide two azo anion radical centres that can behave as docking site for CO_2 activation with subsequent electron relay. We substantiate this theoretical conceptualization by performing spectroelectrochemistry with **1**-based modified electrode (under argon) and comparing the spectral data of $[\mathbf{1}^{\bullet\bullet}]^{2-}$ with the one calculated from TD-DFT (Figure 5.7).

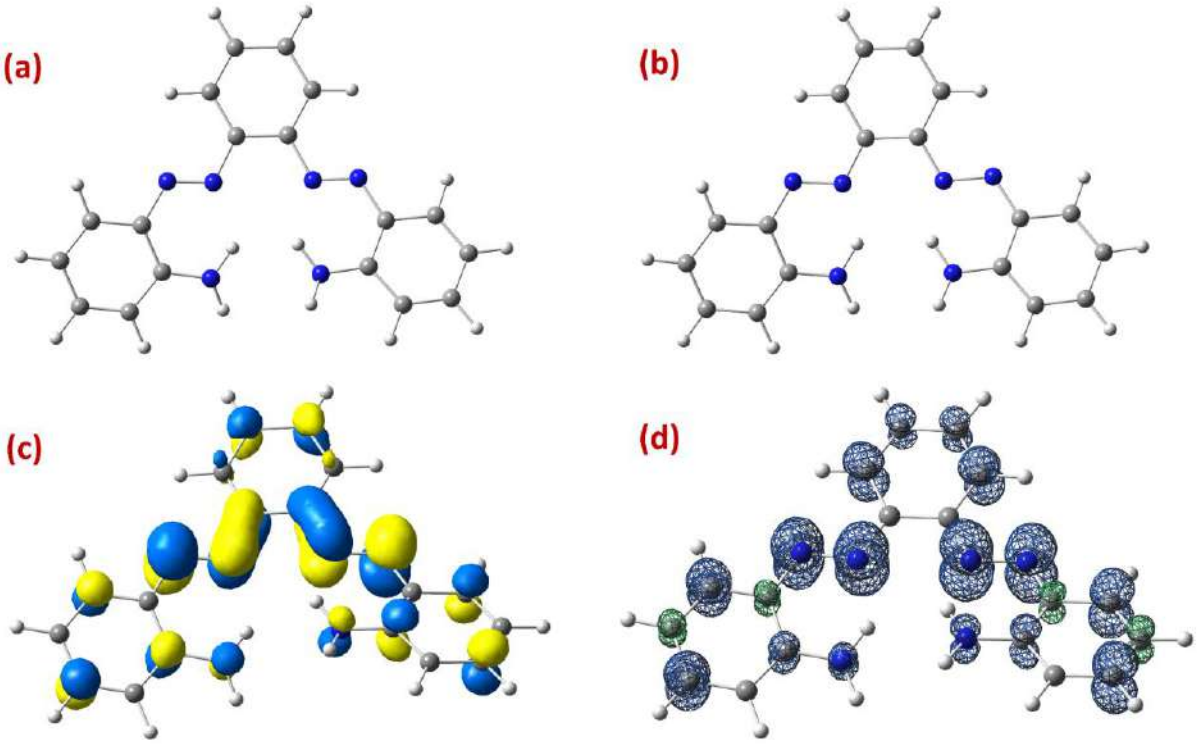

Figure 5.6: (a) Optimised geometry of precatalyst **1** (b) Optimised geometry of triplet diradical [**1**$^{\bullet\bullet}$]$^{2-}$ (c) LUMO of precatalyst **1** (d) Mulliken spin density plot of triplet diradical [**1**$^{\bullet\bullet}$]$^{2-}$

To evaluate the CO_2 reduction products, controlled potential electrolysis (CPE) was carried out in a CO_2-saturated phosphate buffer solution, with continuous bubbling of CO_2 throughout the experiment. The electrolysis was performed at potentials ranging from –0.6 V to –1.0 V vs Ag/AgCl over a period of 5 h. Post electrolysis analysis of the reaction mixture was conducted using ^{1}H NMR spectroscopy. The formation of acetic acid and acetone was confirmed by comparing the spectra with standard reference samples. The characteristic ^{1}H NMR signals for acetic acid and acetone were observed at 2.00 ppm and 2.15 ppm, respectively. To investigate the activation of the pre-catalyst through diradical formation, additional electrochemical experiments were conducted. Following the electrochemical reduction of the pre-catalyst and subsequent purging with CO_2 at room temperature, an EPR spectrum was recorded. The resulting spectrum displays a characteristic S = 1 signal at g ≈ 2 (Figure 5.8), consistent with the presence of a triplet diradical.[18] Given that the pre-catalyst features a low-lying π* LUMO

with significant contribution from the azo moieties (as supported by DFT calculations, Table 5.4),[19] the observed diradical signal can be attributed to the formation of [**1**••]$^{2-}$, in which the two unpaired electrons are delocalized over the two azo moieties. This result provides compelling evidence for the generation of a ligand-centered triplet diradical species during the activation of the pre-catalyst. These results point toward the role of diradical in pre-catalyst activation that are further verified from the electronic absorption spectra that have been monitored during the constant potential electrolysis (CPE) of the pre-catalyst and its conversion to active catalyst. These experimental spectra are in good agreement with the theoretical spectra of the triplet diradical (Figure 5.4). Comprehensive electrochemical analysis and product quantification revealed that at an applied potential of –0.26 V and pH 5.5, the Faradaic efficiencies (FE) for the formation of acetic acid and acetone were 19.6% and 24.2%, respectively. The experimental details of the electrocatalysis including controlled potential electrolysis (CPE) and post-electrolysis analysis have been excluded in this thesis and reported earlier.[20] These results demonstrate efficient electron utilization for the conversion of CO_2 into value-added C_2 and C_3 products. The observed product distribution supports the involvement of the azo centers in electron uptake, leading to the formation of ligand-centered diradical species that serve as the active catalyst during the electrocatalytic CO_2 reduction process.

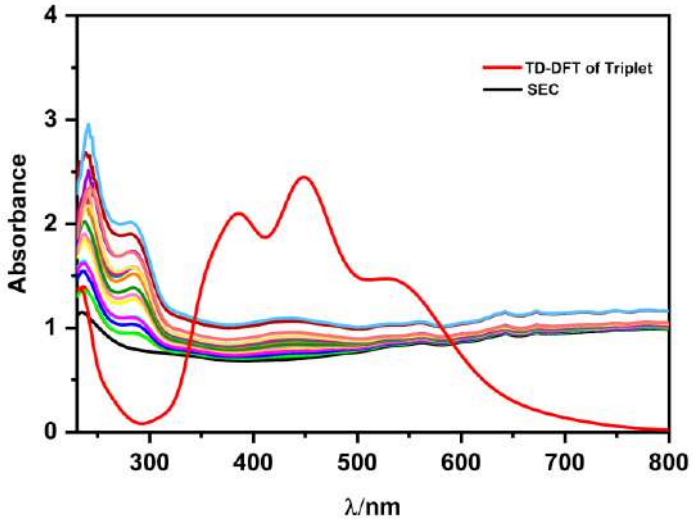

Figure 5.7: Combine plot of SEC with free ligand **1** without CO_2 dosage at interval of 10 min (other colours) and calculated UV-Vis spectrum of $[1^{\bullet\bullet}]^{2-}$ (red)

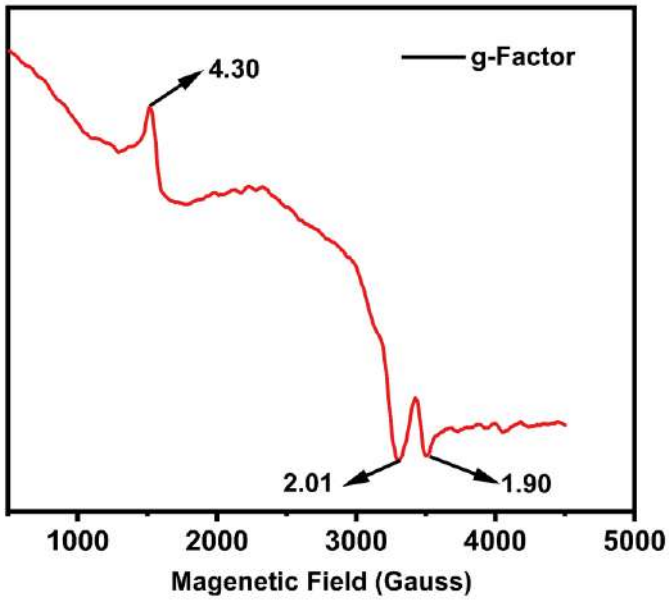

Figure 5.8: Low temperature EPR spectra of the analyte after CPE for 1 hr

5.2.4 Mechanism of electrocatalytic CO_2RR

The proposed mechanism for the electrochemical reduction of CO_2 (CO_2RR) mediated by the bis-azo-diamino ligand **1** appears to share mechanistic similarities with the pathway reported by Koper et al.,[21] as illustrated in Figure 5.9. Upon accepting a pair of electrons, the pre-catalyst **1** undergoes a transformation wherein the azo groups are reduced to generate a triplet diradical species $[\mathbf{1}^{\bullet\bullet}]^{2-}$, which functions as the catalytically active form. In the subsequent step, CO_2 molecules are anchored onto the electron-rich azo sites of the ligand. Density Functional Theory (DFT) calculations suggest that these CO_2 molecules are reduced to the radical anion $CO_2^{\bullet-}$ *via* intramolecular electron transfer from the azo centers. The approach of CO_2 occurs in both end-on and side-on geometries, minimizing steric hindrance and resulting in asynchronous electron transfer events. Initially, one of the CO_2 molecules undergoes one-electron reduction to generate $CO_2^{\bullet-}$, which is then protonated to yield $HCO_2^{\bullet}$. In the very next step $HCO_2^{\bullet}$ is converted to formyl radical ($CHO^{\bullet}$) through accepting of two proton and two

electrons followed by immediate elimination of water molecule. Theoretical modelling indicates a significant conformational twist in the ligand framework during this transformation, likely facilitating this proton coupled electron transfer from the terminal $–NH_2$ groups to the $CO_2^{\bullet-}$ intermediate. Similarly, the second azo moiety also donates an electron to a second CO_2 molecule, forming another $HCO_2^{\bullet}$ radical and finally converted to $CHO^{\bullet}$ following the above-mentioned pathway. The newly generated two formyl radicals now couple to generate glyoxal as a key intermediate. The formation of glyoxal was experimentally verified by performing electrolysis in the presence of formic acid and glyoxal, which led to the detection of acetic acid and acetone by ^1H NMR spectroscopy (Figures 5.6.A6 and 5.6.A7). This supports the hypothesis that glyoxal acts as a precursor to these C_2 and C_3 products. It is proposed that glyoxal undergoes further reduction by the ligand-based electron reservoir (azo diradical centers) in the presence of protons to form acetic acid, which can be further reduced to acetone, thereby regenerating

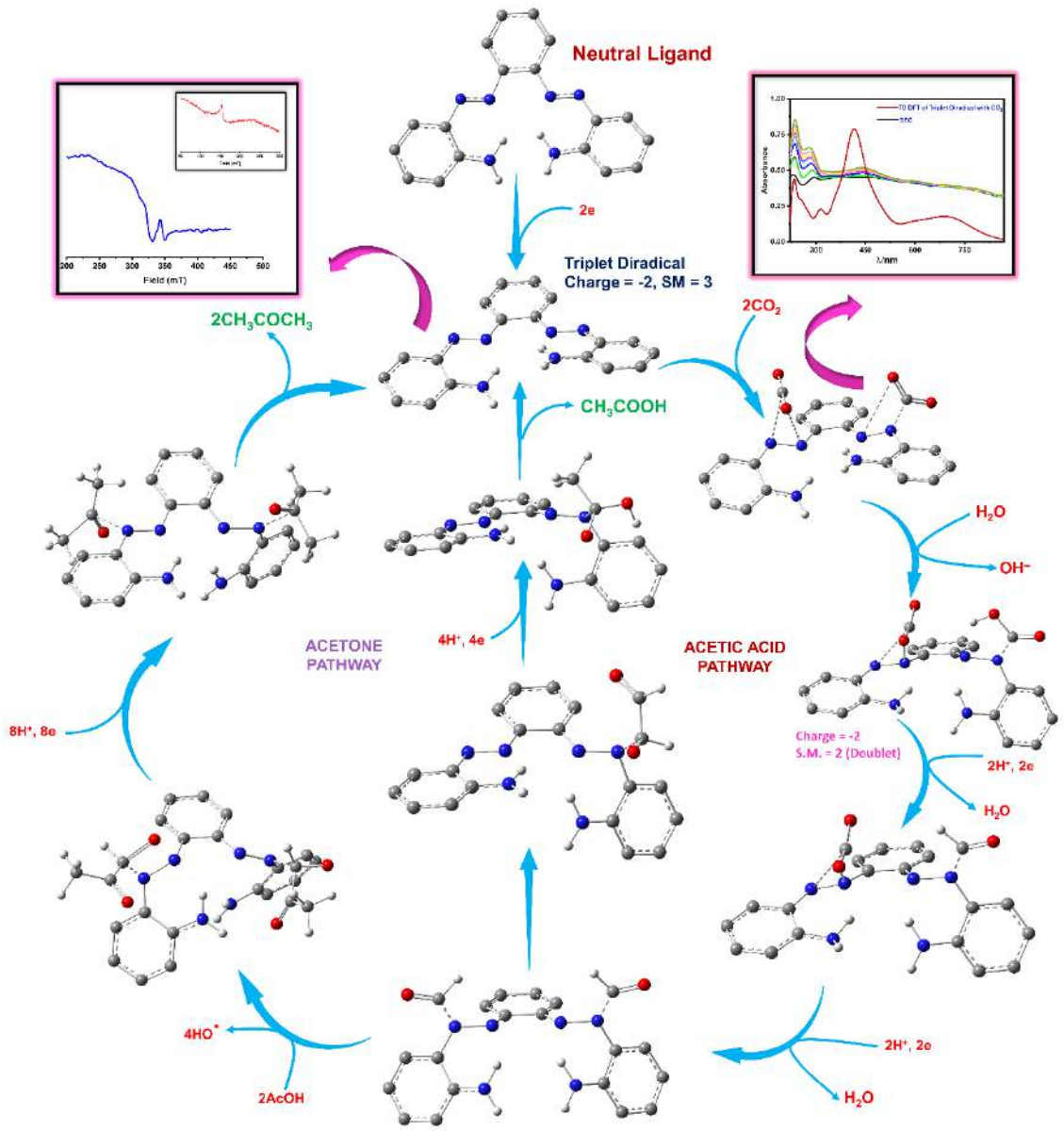

Figure 5.9: Proposed mechanism of electrocatalytic formation of Acetic Acid and Acetone

the active catalyst $[\mathbf{1}^{\bullet\bullet}]^{2-}$ and completing the catalytic cycle. Further mechanistic insights were obtained from electrocatalysis experiments carried out in the presence of formic acid and acetyl chloride, which predominantly yielded acetone as the final product. This observation suggests that acetone formation during CO_2RR likely proceeds *via* coupling of the acetyl radical (derived from acetic acid) and a formyl radical, facilitated by a proton-coupled electron transfer (PCET) mechanism, as outlined in Figure 5.10. Together, these findings provide compelling evidence for a multi-step, ligand-mediated CO_2 reduction pathway that proceeds *via* radical

intermediates and culminates in the formation of value-added C_2 and C_3 products such as acetic acid and acetone.

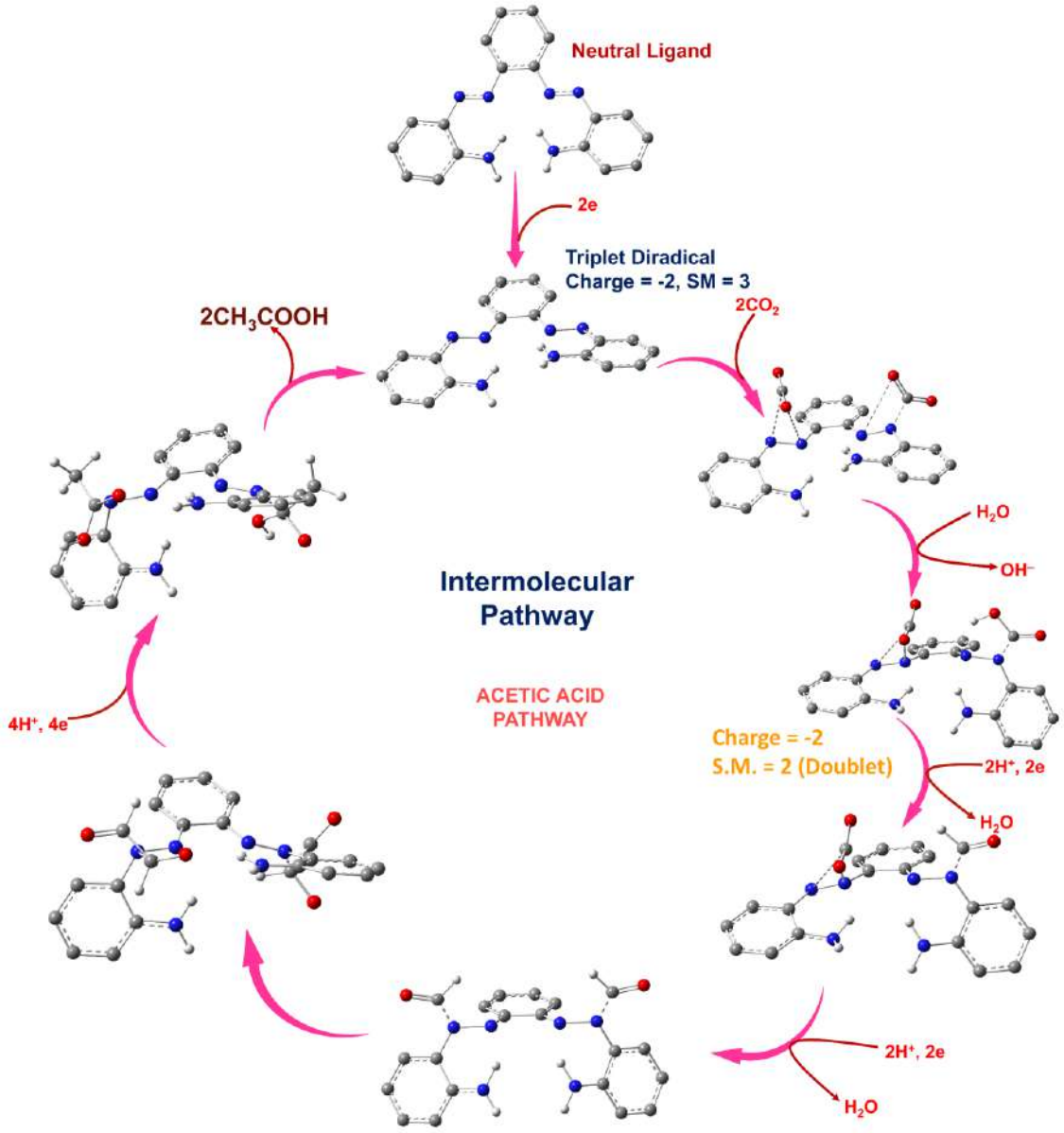

Figure 5.10: Proposed mechanism of electrocatalytic formation of Acetic Acid *via* intermolecular pathway

5.3 Conclusion

This study presents a novel and efficient strategy for the direct conversion of CO_2 into valuable C_3 products using a coordinatively fluxional, redox active precatalyst **1**. The catalyst undergoes transformation into a triplet diradical state, which initiates a cascade of steps leading to the formation of glyoxal and its subsequent conversion into acetic acid. Internal electron transfer enables catalyst regeneration and further transformation of intermediates, with in situ generated acetic acid reacting with formyl units to yield C_3 products. This dual role of product formation and catalyst recycling underscores the efficiency of the system. Overall, the work highlights the promise of metal-free, fluxional electrocatalysts in carbon capture and utilization (CCU), advancing beyond conventional C_1 and C_2 products and offering a path toward sustainable carbon recycling.

5.4 Experimental section

5.4.1 Reagents and materials

All the reagents and solvents used in this investigation are commercially available and were used without further purification. *o*-Phenylenediamine, PbO_2, KOH were purchased from SRL. Water and Acetonitrile were from HPLC grade, $NaClO_4.H_2O$ used was from Loba Chemie. Sodium dihydrogen phosphate dihydrate ($NaH_2PO_4.2H_2O$) and Disodium hydrogen phosphate dihydrate ($Na_2HPO_4.2H_2O$) used for buffer solution were from Merck and Potassium Chloride (KCl) in reference electrode are from Merck. NMR solvent D_2O was purchased from Cambridge Isotopic Laboratory. Toray Carbon paper, TGP-H-60, 19*19 cm was from Alfa Aesar. Pure methanol, acetone, and acetic acid were used as NMR reference standards from Merck, and formic acid, acetyl chloride, and glyoxal used as intermediates are from Merck, Loba Chemie, and SRL respectively. All the glassware was washed with an Acid bath, and

base bath and rinsed with isopropanol or acetone. Dried them in the oven before use. All the electrodes were washed with distilled water.

5.4.2 Synthesis of Catalyst

A solution of *o*-phenylenediamine (3 g, 1.00 equiv.) in dry toluene (15 ml/g) was degassed with argon steam for 20 min. Then PbO_2 (12.0 g, 4.00 equiv.) was added in portion (1.00 equiv/hr) and solution was refluxed for 4 h. After the completion of reaction, the dark red coloured solution was filtered through a Celite 545 bed in order to remove excess PbO_2. The filtrate was collected and solvent was removed under reduced pressure. The residue was subjected to column chromatography using silica gel (100-200 mesh) and toluene as eluent to obtain red shiny crystals of 2,2′-diaminoazobenzene.

The solution of 2,2′-diaminoazobenzene (500mg, 2.35 mmol, 1.00 equiv.) in dry toluene (10 mL/mmol) was degassed with an argon stream for 15 min. Then, the 2-nitrosoacetanilide (386 mg, 2.35 mmol, 1.00 equiv.) and acetic acid (12.00 equiv.) were added. The reaction mixture was stirred at 65°C for 72 h, and the solvent was removed under reduced pressure. The resultant dark red coloured oily residue was purified by column chromatography using silica gel (100-200 mesh) and 2:1 Hexane/EtOAc (v/v) as eluent to get red coloured crystalline monoprotected bis-azo-diamine.

The obtained monoprotected bis-azo-diamine (1.0 equiv) in ethanol (65 mL) was then treated with a solution of KOH (56.0 equiv) in ethanol (20 mL) and water (15 mL). The mixture was refluxed for about 1.5 h, the mixture was poured onto crushed ice (300 g), extracted with CH_2Cl_2, dried over Na_2SO_4, and concentrated to produce a red oil, which is kept in refrigerator for overnight to get solid product. The suitable crystals were grown from warmed solution of hexane through slow evaporation.

5.4.3 Analytical Data of 1

***2,2'-((1E,1'E)-1,2-phenylenebis(diazene-2,1-diyl))dianiline (1)*:** Dark red coloured crystalline solid; Yield: 65%; HRMS [M+H]+: m/z 317.1533 (Calcd. for $C_{18}H_{17}N_6$ 317.1515); ^{1}H NMR (400 MHz, $CDCl_3$): δ 7.91 (dd, *J* = 8.1, 1.6 Hz, 2H), 7.80 (dd, *J* = 6.1, 3.4 Hz, 2H), 7.52 (dd, *J* = 6.1, 3.4 Hz, 2H), 7.28 – 7.20 (m, 2H), 6.86 (t, *J* = 7.6 Hz, 2H), 6.77 (dd, *J* = 8.3, 1.3 Hz, 2H), 6.29 (s, 4H). ^{13}C{^{1}H} NMR (75 MHz, $CDCl_3$): δ 116.71, 117.20, 117.33, 130.24, 130.51, 132.51, 137.97, 142.27, 148.04.

5.4.4 Product Detection and quantification by ^{1}H-NMR

The CO_2 reduction products obtained after controlled potential electrolysis (CPE) were detected and quantified using a Neo Advance Bruker 500 MHz NMR spectrometer. A 6 mL aqueous solution containing 20 mM phenol and 10 mM DMSO was used as the internal standard. For NMR analysis, the sample was prepared by mixing 350 µL of the analyte, 50 µL of the internal standard solution, and 200 µL of D_2O in an NMR tube (7 inches in height, 5 mm in diameter). To enhance the signal intensity, the water peak was suppressed in the ^{1}H NMR spectrum. Characteristic peaks for acetic acid and acetone were observed at 2.00 ppm and 2.17 ppm, respectively. Product quantification was performed by integrating these signals relative to the DMSO reference peak at 2.60 ppm.

5.4.5 EPR Spectroscopy

Electron paramagnetic resonance spectroscopic measurements were performed on a Bruker EMX CW-microX-band EPR spectrometer equipped with an ER4119HS high-sensitivity resonator, with a microwave power of Ca 6.9 mW and modulation frequency and amplitude of 100 kHz and 5 G, respectively. 2 hours after CPE, the analyte from the cell is taken in a capillary tube, kept in an EPR tube, and dipped in liquid Nitrogen to maintain a low temperature. The EPR spectra were recorded for the CPE analyte at low temperatures.

5.5 References

[1] (a) G. Wang, J. Chen, Y. Ding, P. Cai, L. Yi, Y. Li, C. Tu, Y. Hou, Z. Wen, L. Dai, *Chem. Soc. Rev.*, **2021**, *50*, 4993–5061. (b) Y. Chen, T. Mu, *Green. Chem.*, **2019**, *21*, 2544–2574. (c) V. Kumaravel, J. Bartlett, S.C. Pillai, *ACS Energy Lett.*, **2020**, *5*, 486–519.

[2] S. Munir, A.R. Varzeghani, S. Kaya, *Sustain. Energy Fuels*, **2018**, *2*, 2532–2541.

[3] (a) T. Mizukawa, K. Tsuge, H. Nakajima, K. Tanaka, *Angew. Chem. Int. Ed.*, **1999**, *38*, 362–363. (b) K. Zhao, X. Nie, H. Wang, S. Chen, X. Quan, H. Yu, W. Choi, G. Zhang, B. Kim, J. G. Chen, *Nat. Commun.*, **2020**, *11*, 2455. (c) M. -G. Kim, Y. Choi, E. Park, C. -H. Cheon, N.-K. Kim, B.K. Min, W. Kim, *ACS Appl. Energy Mater.*, **2020**, *3*, 11516–11522.

[4] (a) S. Das, S. Kumar, S. Garai, R. Pochamoni, S. Paul, S. Roy, *ACS Appl. Mater. Interfaces*, **2017**, *9*, 35086–35094. (b) S. Barman, S. Das, S. Sreejith, S. Garai, R. Pochamoni, S. Roy, *Chem. Commun.*, **2018**, *54*, 2369–2372. (c) S. Das, S. Biswas, T. Balaraju, S. Barman, R. Pochamoni, S. Roy, *J. Mater. Chem. A*, **2016**, *4*, 8875–8887.

[5] S. Gonglach, S. Paul, M. Haas, F. Pillwein, S.S. Sreejith, S. Barman, R. De, S. Müllegger, P. Gerschel, U.-P. Apfel, *Nat. Commun.*, **2019**, *10*, 3864.

[6] R. De, S. Gonglach, S. Paul, M. Haas, S. Sreejith, P. Gerschel, U.P. Apfel, T. H. Vuong, J. Rabeah, S. Roy, *Angew. Chem.*, **2020**, *132*, 10614–10621.

[7] G. Morello, B. Siritanaratkul, C.F. Megarity, F.A. Armstrong, *ACS Catal.*, **2019**, *9*, 11255–11262.

[8] K.P. Kuhl, E.R. Cave, D.N. Abram, T.F. Jaramillo, *Energy Environ. Sci.*, **2012**, *5*, 7050–7059.

[9] J. Grodkowski, P. Neta, E. Fujita, A. Mahammed, L. Simkhovich, Z. Gross, *J. Phys. Chem. A*, **2002**, *106*, 4772–4778.

[10] (a) L. Sun, Z. Huang, V. Reddu, T. Su, A.C. Fisher, X. Wang, *Angew. Chem. Int. Ed.*, **2020**, *59*, 17104–17109. (b) H. Zhang, C. Xu, X. Zhan, Y. Yu, K. Zhang, Q. Luo, S. Gao, J. Yang, Y. Xie, *Nat. Commun.*, **2022**, *13*, 6029.

[11] (a) T. Bockman, D. Kosynkin, J. Kochi, *J. Org. Chem.*, **1997**, 62, 5811–5820. (b) S. Panda, S. Dhara, A. Singh, S. Dey, G.K. Lahiri, *Coord. Chem. Rev.*, **2023**, *475,* 214895. (c) S. Dinda, S. Roy, S.C. Patra, S. Bhandary, K. Pramanik, S. Ganguly, *New J. Chem.*, **2020**, *44*, 3737–3747.

[12] (a) M. H. V. Huynh, T. J. Meyer, *Chem. Rev.*, **2007**, *107*, 5004–5064. (b) D. R. Weinberg, C. J. Gagliardi, J. F. Hull, C. F. Murphy, C. A. Kent, B.C. Westlake, A. Paul, D. H. Ess, D. G. McCafferty, T. J. Meyer, Chem. Rev. **2012**, *112*, 4016–4093. (c) C. J. Gagliardi, B. C. Westlake, C. A. Kent, J. J. Paul, J. M. Papanikolas, T. J. Meyer, *Coord. Chem. Rev.*, **2010**, *254* 2459–2471. (d) I. Siewert, *Chem. A Eur. J.*, **2015**, *21*, 15078–15091.

[13] (a) W. Wang, G. Tan, R. Feng, Y. Fang, C. Chen, H. Ruan, Y. Zhao, X. Wang, Chem. Commun. **2020**, *56*, 3285–3288. (b) N.D. Paul, U. Rana, S. Goswami, T.K. Mondal, S. Goswami, *J. Am. Chem. Soc.* **2012**, *134*, 6520–6523 (c) S. Roy, S. Pramanik, S.C. Patra, B. Adhikari, A. Mondal, S. Ganguly, K. Pramanik, *Inorg. Chem.*, **2017***, 56*, 12764–12774.

[14] (a) J. L. Sadler, A. J. Bard, *J. Am. Chem. Soc*, 1968, *90*, 1979–1989. (b) S. Das, R. Mondal, A. K. Guin, N. D. Paul, Org. Biomol. Chem., 2022, 20*,* 3105–3117. (c) S. Pramanik, S. Roy, T. Ghorui, S. Ganguly, K. Pramanik, *Dalton Trans.* **2014**, *43*, 5317–5334. (d) A. Das, T. M. Scherer, S. M. Mobin, W. Kaim, G. K. Lahiri, *Chem. A Eur. J.*, **2012**, 18, 11007–11018.

[15] S. Bellotto, R. Reuter, C. Heinis, H. A. Wegner, *J. Org. Chem.* **2011**, *76*, 9826–9834.

[16] (a) J. Bouwstra, A. Schouten, J. Kroon, *Acta Crystallogr. Sect. C: Cryst. Struct. Commun.*, 1983, *39*, 1121–1123. (b) S. Kurihara, D. Yoneyama, T. Nonaka, Chem. Mater. **2001**, *13*, 2807–2812. (c) C. T. Brown, *Acta Crystallogr.*, 1966, *21*, 146–152.

[17] (a) N. M. Gallagher, J. J. Bauer, M. Pink, S. Rajca, A. Rajca, *J. Am. Chem. Soc.*, 2016, 138, 9377–9380. (b) S. Hiraoka, T. Okamoto, M. Kozaki, D. Shiomi, K. Sato, T. Takui, K. Okada, *J. Am. Chem. Soc.*, **2004**, *126*, 58–59. (c) S. Suzuki, T. Furui, M. Kuratsu, M. Kozaki, D. Shiomi, K. Sato, T. Takui, K. Okada, *J. Am. Chem. Soc.*, **2010**, 132, 15908–15910. (d) A. Rajca, M. Takahashi, M. Pink, G. Spagnol, S. Rajca, *J. Am. Chem. Soc.*, **2007**, *129*,10159–10170.

[18] M. Abe, *Chem. Rev.,* **2013**, *113*, 7011–7088.

[19] A. A. Swatiputra, D. Mukherjee, S. Dinda, S. Roy, K. Pramanik, S. Ganguly, *Dalton Trans.*, **2023**, *52*, 15627–15646.

[20] N. Kumari, S. Halder, S. Naskar, S. Ganguly, K. Pramanik, F. Yari, A. Dorniak, W. Schöfberger, S. Roy, *Materials Today Catalysis*, **2024**, *5*, 100049.

[21] J. Shen, M. J. Kolb, A. J. Gottle, M. T. Koper, *J. Phys. Chem. C*, **2016**, *120* ,15714–15721.

5.6 Appendix

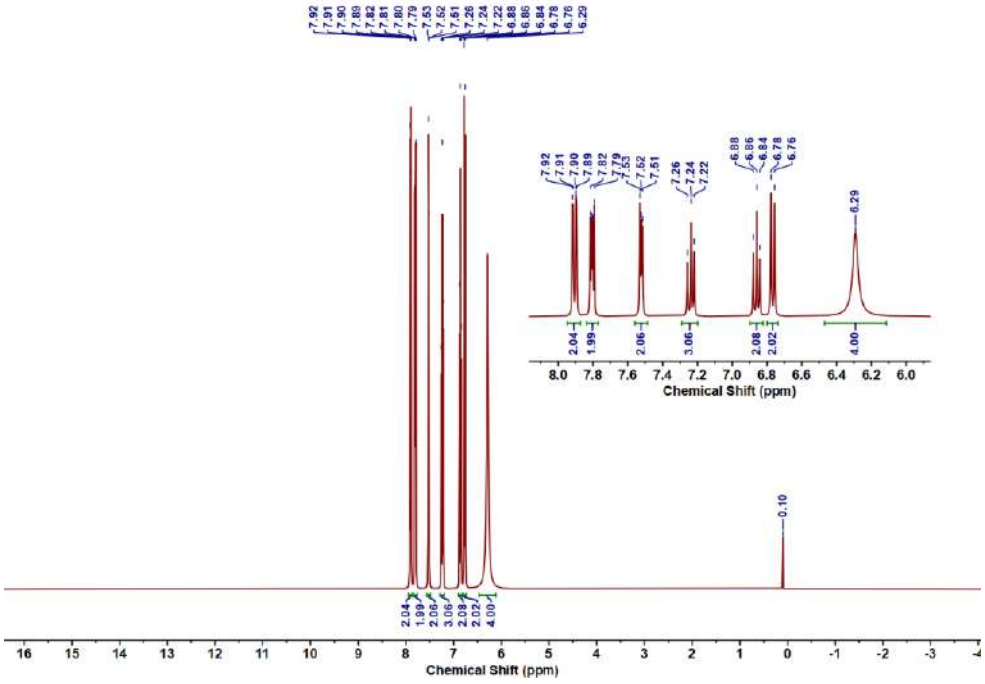

Figure 5.6.A1: ^{1}H NMR spectrum of **1**

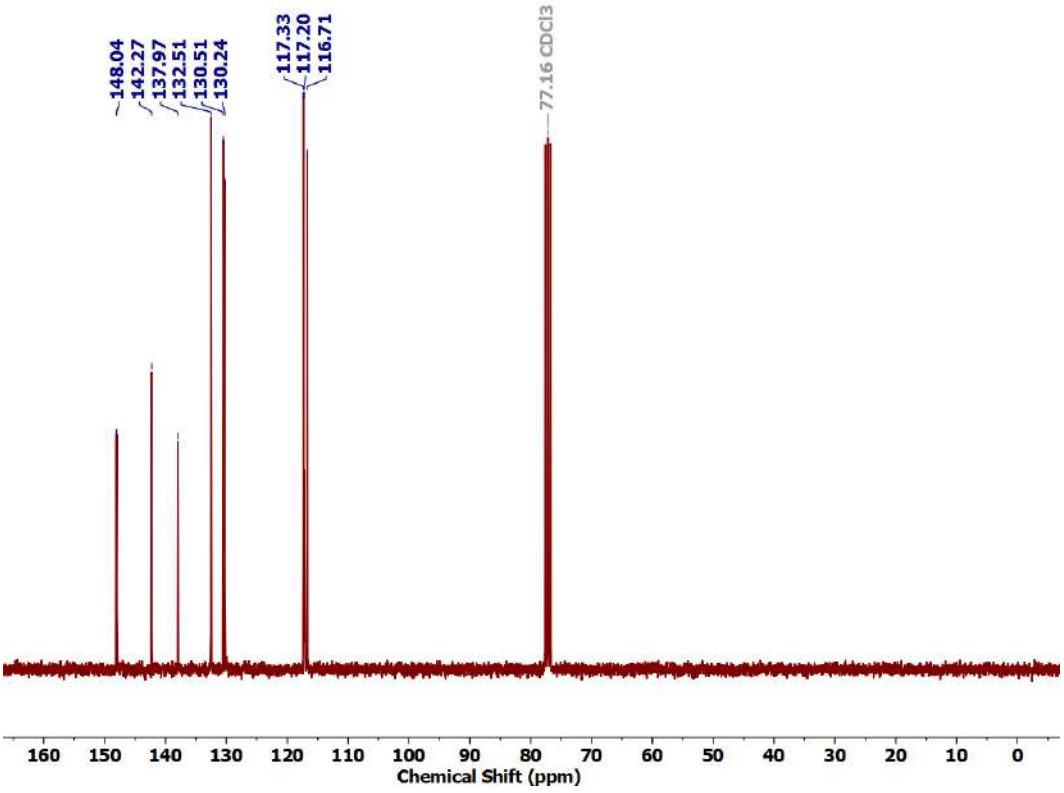

Figure 5.6.A2: $^{13}C\{^{1}H\}$ NMR spectrum of **1**

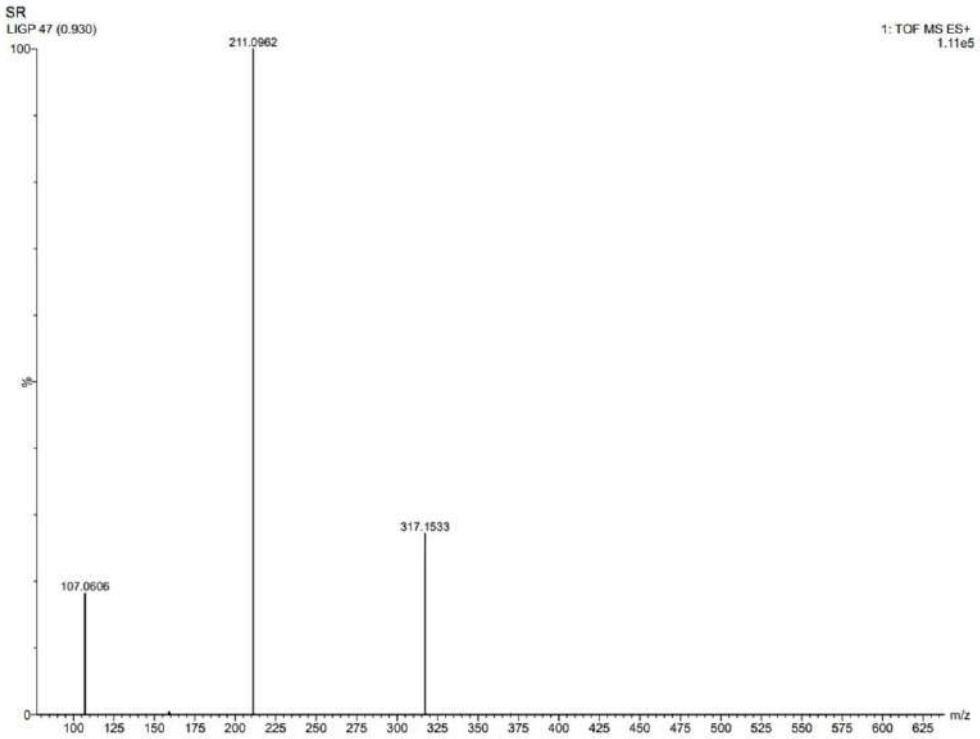

Figure 5.6.A3: HRMS spectrum of **1**

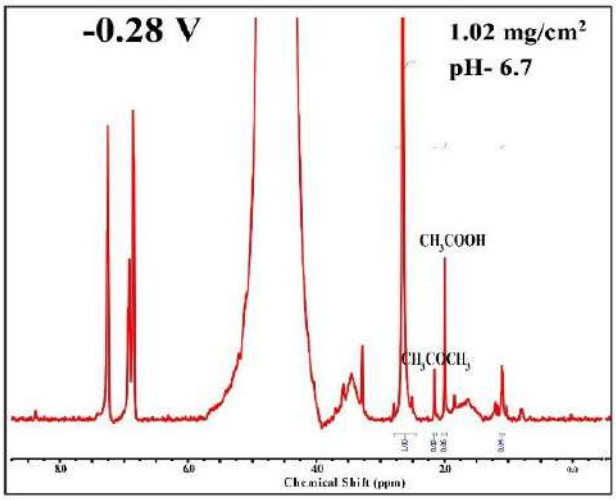

Figure 5.6.A4: ^{1}H NMR spectrum of the analyte after 5 h of CPE at potential –0.28 V vs Ag/AgCl in CO_2 saturated buffer solution and phenol and DMSO used as internal standard

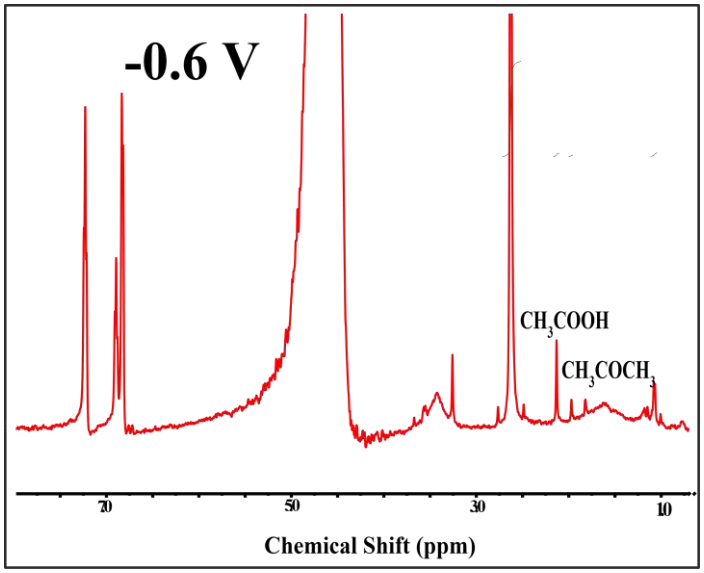

Figure 5.6.A5: ^{1}H-NMR spectrum of liquid product formed after CPE at -0.6 V loading 1 mg/cm^{2} pH 6.7 in 500 MHz instrument

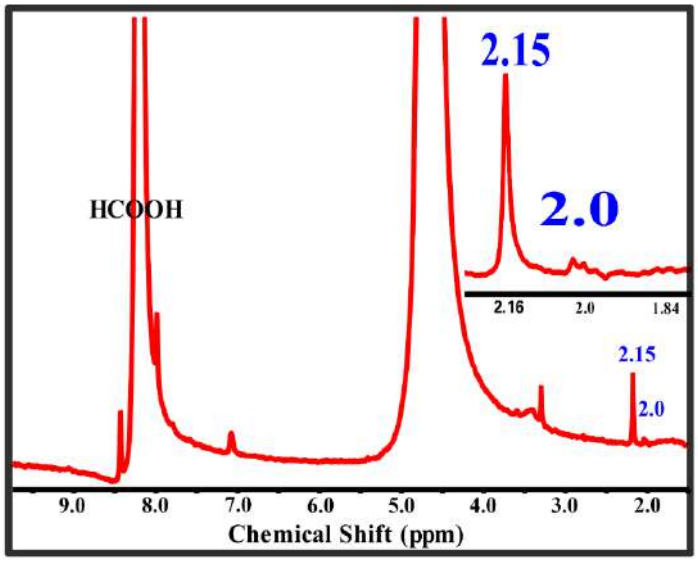

Figure 5.6.A6: ^{1}H NMR spectra of the analyte after CPE by adding Formic acid.

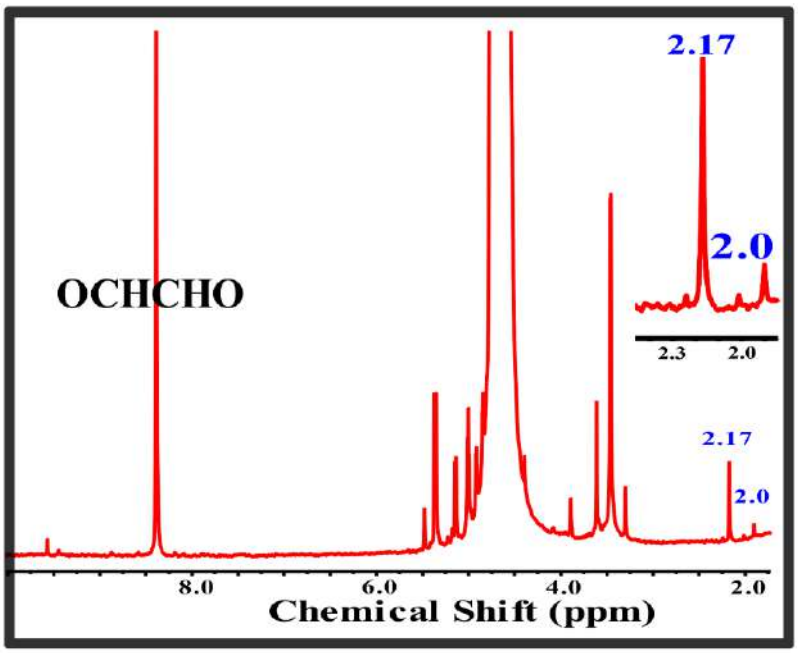

Figure 5.6.A7: ^{1}H NMR spectra of the analyte after CPE by adding glyoxal

Table 5.6.A1: Molecular Orbital Contribution of Triplet Diradical (α-MOs)

Orbital	α-MO	Energy (eV)	Contribution			Composition
			Azo	Amine	Ph	
91	L+5	7.54	27	0	73	π* (Azo + Ph)
90	L+4	7.38	19	0	81	π* (Azo + Ph)
89	L+3	6.67	6	3	91	π* (Azo + Ph + Amine)
88	L+2	6.57	2	5	93	π* (Ph + Amine)
87	L+1	6.31	4	5	91	π* (Ph + Amine)
86	LUMO	6.26	5	3	92	π* (Ph)
85	HOMO	3.43	44	4	52	π (Azo + Ph)
84	H–1	2.82	45	7	48	π (Azo + Amine + Ph)
83	H–2	1.39	64	7	29	Lone Pair (Azo + Amine)
82	H–3	1.14	27	18	55	Lone Pair (Azo) + π (Amine + Ph)
81	H–4	0.91	70	7	23	Lone Pair (Azo + Amine)
80	H–5	0.67	17	25	58	Lone Pair (Azo) + π (Azo + Amine)

Table 5.6.A2: Molecular orbital Contribution of Triplet Diradical (**β-MO**s)

Orbital	β-MO	Energy (eV)	Contribution			Composition
			Azo	Amine	Ph	
89	L+5	6.96	9	2	89	π* (Azo + Amine + Ph)
88	L+4	6.83	5	3	92	π* (Azo + Amine + Ph)
87	L+3	6.54	2	7	91	π* (Amine + Ph)
86	L+2	6.53	3	6	91	π* (Amine + Ph)
85	L+1	5.19	33	2	64	π* (Azo + Ph)
84	LUMO	4.58	36	4	60	π* (Azo + Ph)
83	HOMO	1.71	44	10	46	Lone Pair (Azo + Amine) + π (Ph)
82	H–1	1.48	59	8	34	Lone Pair (Azo + Amine)
81	H–2	1.14	53	10	36	Lone Pair (Azo + Amine)
80	H–3	1.00	38	15	47	Lone Pair (Azo + Amine) + π (Ph)
79	H–4	0.42	9	25	65	π (Azo + Amine + Ph)
78	H–5	0.36	8	18	75	π (Azo + Amine + Ph)

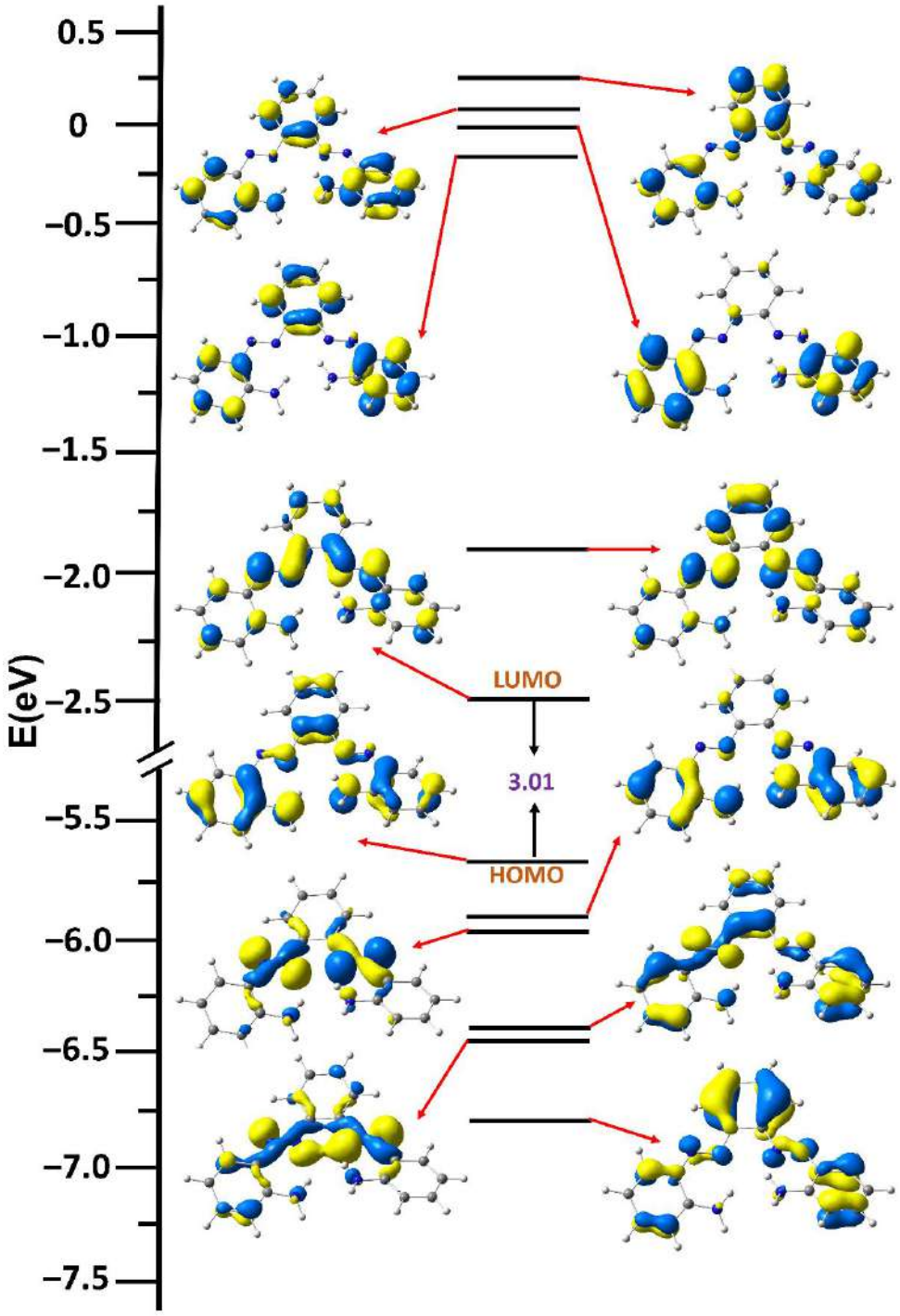

Figure 5.6.A6: Partial FMO (Frontier molecular orbital) diagram and isodensity surface plots (isovalue = 0.06) for selected FMOs of **1**. The arrows are used to highlight the HOMO–LUMO energy gap. All the DFT energy values are given in eV

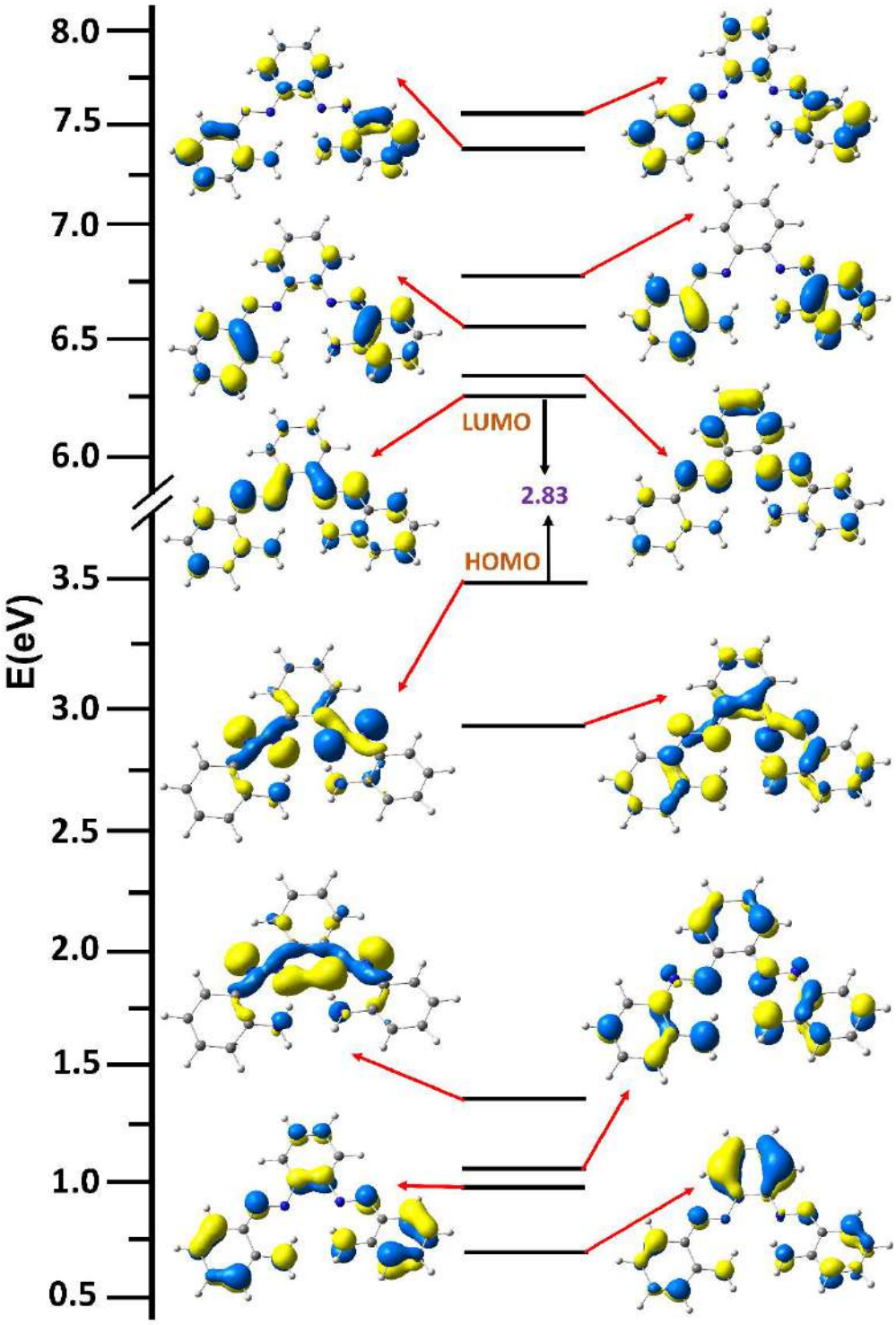

Figure 5.6.A7: Partial FMO (Frontier molecular orbital) diagram and isodensity surface plots (isovalue = 0.06) for selected α-FMOs of $[\mathbf{1}^{\bullet\bullet}]^{2-}$. The arrows are used to highlight the HOMO–LUMO energy gaps. All the DFT energy values are given in eV

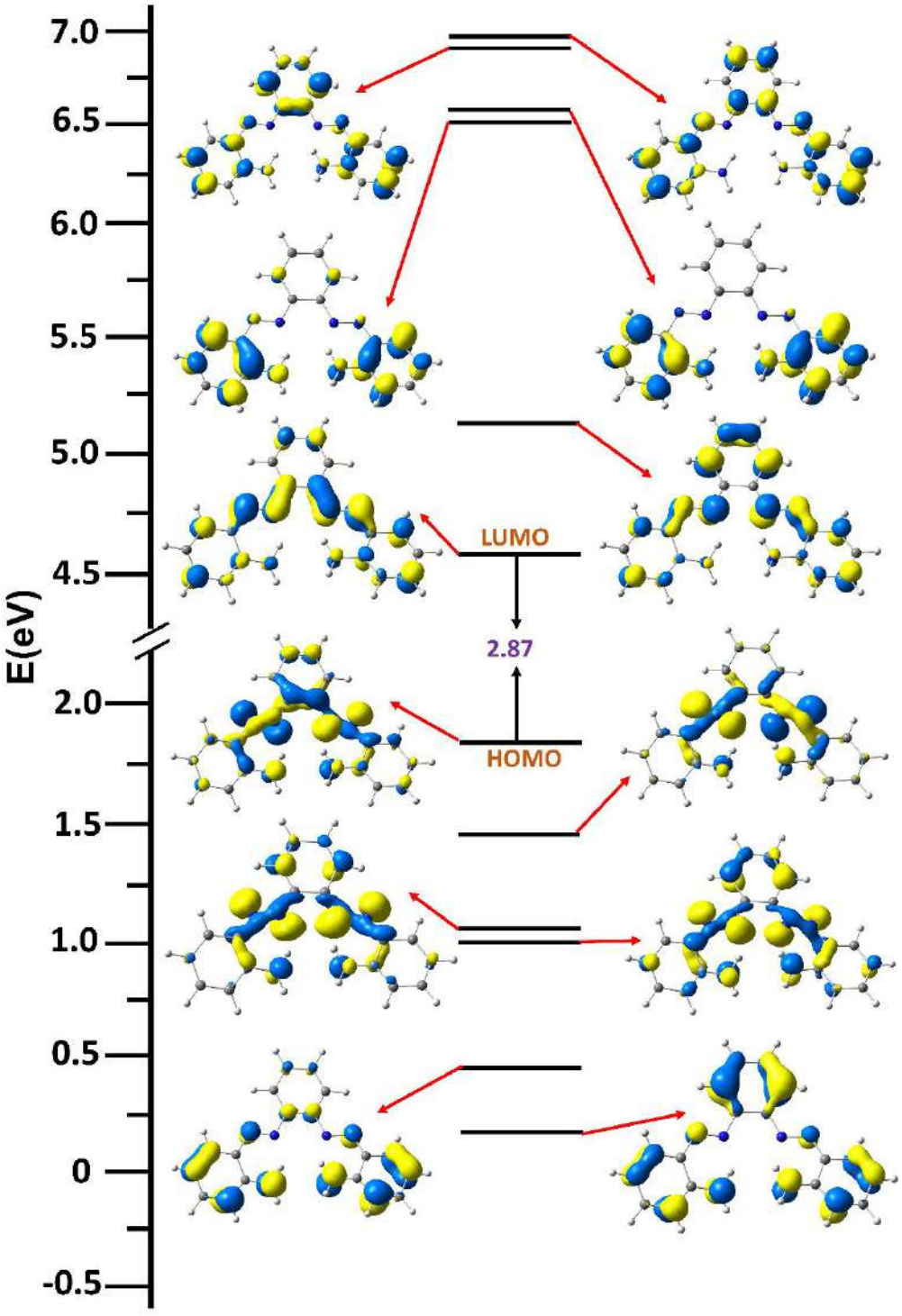

Figure 5.6.A8: Partial FMO (Frontier molecular orbital) diagram and isodensity surface plots (isovalue = 0.06) for selected β-FMOs of $[\mathbf{1}^{\bullet\bullet}]^{2-}$. The arrows are used to highlight the HOMO–LUMO energy gaps. All the DFT energy values are given in eV

Chapter 6

Sustainable Route Towards N-Alkylated Amines via Alcohol Dehydrogenation Catalysed by Bis-Azo-Diamido Coordinated Ruthenium(III) Complex

6.1 Introduction

Nitrogen-based organic compounds play a central role in both modern synthetic chemistry and various industries, particularly pharmaceuticals and fine chemicals. Among these, amines stand out as crucial building blocks, with broad applications in everyday products and high-value materials. Functionalized amines are especially sought after due to their importance in crafting agrochemicals, drugs, and specialty dyes (Scheme 6.1).[1] To meet this demand, chemists have developed a wide range of synthetic strategies.[2] Traditional approaches are still in use, but catalytic methods have gained prominence for their efficiency and versatility. Notable catalytic routes to N-alkylated amines include reactions with alkyl halides,[3] reductive alkylation,[4] hydroamination,[5] and hydroaminoalkylation,[6] each offering unique advantages for tailoring molecular structures (Scheme 6.2). The conversion of alcohols into a variety of fine nitrogen-based materials is a key focus in sustainable chemistry.[7-8] One important example is the alkylation of amines by alcohols, a fundamental alcohol refunctionalization reaction, as illustrated in Scheme 6.3.

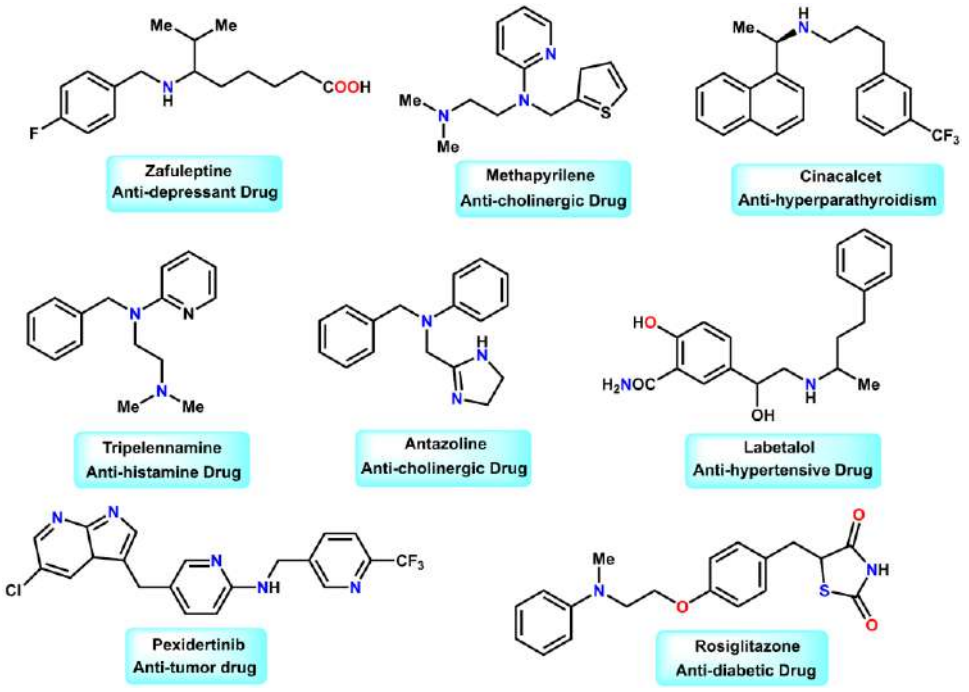

Scheme 6.1: Some representative examples of biologically and medicinally active N-alkylated amine compounds

In this methodology, hydrogen atoms removed from the alcohol are stored on the catalyst, while the resulting carbonyl compound (aldehyde or ketone) condenses with an amine to form an imine. The imine is subsequently reduced by the stored hydrogen equivalents, yielding the corresponding N-alkylated product (Scheme 6.3). The use of readily available alcohols as alkylating agents *via* dehydrogenative coupling (DC) and borrowing hydrogenation (BH) has emerged as one of the most sustainable and atom-economical strategies for forming C–C and C–N bonds.[9-10] This one-pot methodology, which produces only benign water or hydrogen peroxide as by-products, is well-aligned with the principles of green chemistry, offering enhanced efficiency while minimizing waste generation.[11] This homogeneous catalytic strategy was first reported in the early 1980s by Grigg[12a] and Watanabe.[12b] Since then, several research groups including those of Fujita,[13a] Kempe,[13c] Yamaguchi,[13d] Williams, Srivastava,[13e] have advanced this synthetic strategy into a versatile and selective method for the N-alkylation of amines using alcohols. More recently from the research group led by Rit,[14a] Beller,[14b] Paul[14c] and Ghosh[14d] reported ruthenium and palladium-based catalytic systems that furthur advance the N-alkylation reaction using alcohol as alkylating reagent (Scheme 6.4). The borrowing hydrogen (BH) or hydrogen autotransfer (HA) strategy, applied with transition metal catalysts, presents an efficient route for sustainable chemical transformations. Utilizing inexpensive metals at low catalyst loadings for alcohol functionalization, this approach enhances atom economy and promotes the use of renewable feedstocks over conventional resources. These include homogeneous catalysts based on noble metals such as iridium, ruthenium, and palladium, as well as more earth-abundant alternatives like iron, cobalt, manganese, nickel and chromium.

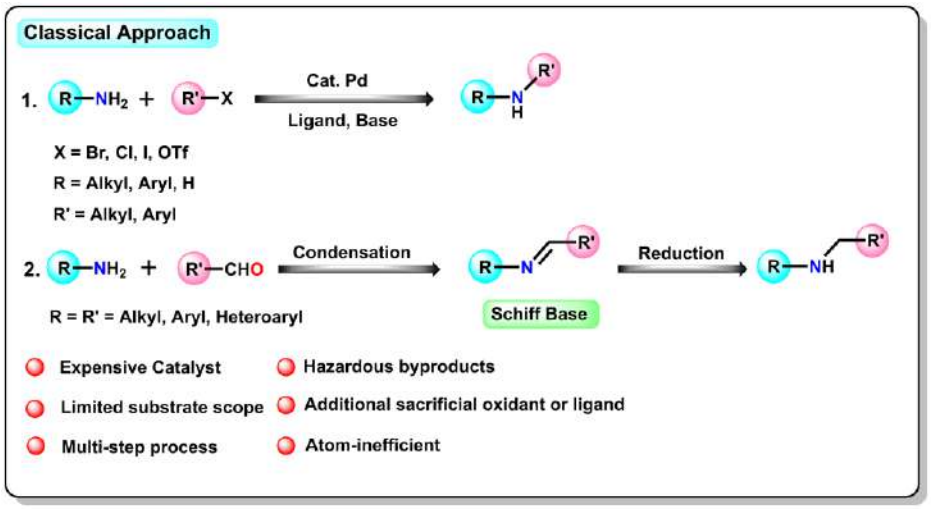

Scheme 6.2: Classical synthetic route for the preparation of N-alkylated amines

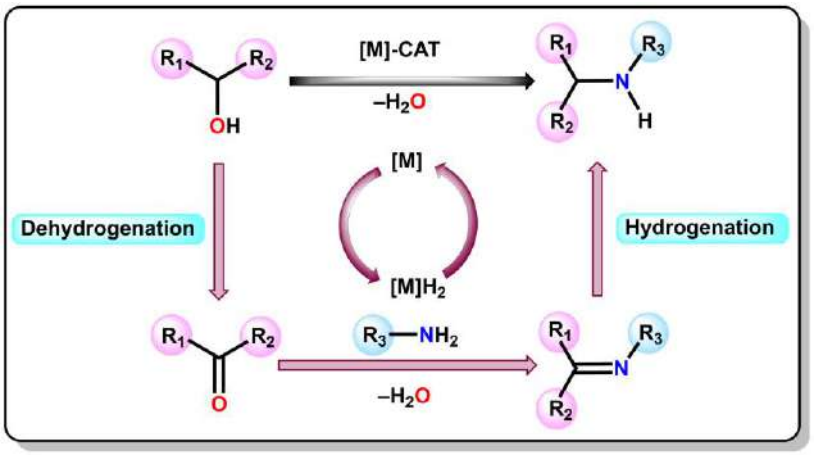

Scheme 6.3: Alkylation of amines by alcohols *via* borrowing hydrogenation or hydrogen auto-transfer strategy

Herein we report the synthesis of an intersting ruthenium(III) complex featuring a planar N4 coordination environment composed of a pair of both strong π-acidic (soft) and σ-donating (hard) donor atoms, forming a robust bisazo-diamido organic scaffold **1**. According to our current knowledge and available litrature, this is probably the first coordination complex based on this tetradentate scaffold to exhibit catalytic activity in the direct N-alkylation of amines using aliphatic primary alcohols. The incorporation of donor atoms with contrasting donor properties was strategically designed to investigate the plausible mechanistic pathway, either

via two-electron Hydride Transfer (HT) or *via* one-electron azo-anion radical pathway followed by Borrowing Hydrogenation (BH). Mechanistic study of N-alkylation of amines by this Ru(III) catalyst has also been scrutinized to understand the prefered pathway in this case. This study thus presents a rare example of a ruthenium(III) complex efficiently promoting N–C bond formation between amines and aliphatic alcohols. The growing emphasis on sustainability in synthetic chemistry emphasizes the demand for atom-efficient and environmentally benign methodologies. Using primary alcohols as alkylating agents offers a compelling solution due to their renewability, low toxicity, and cost-effectiveness. This strategy enables diverse C–N bond formations under relatively mild conditions, offering a valuable green alternative to conventional alkylation methods.

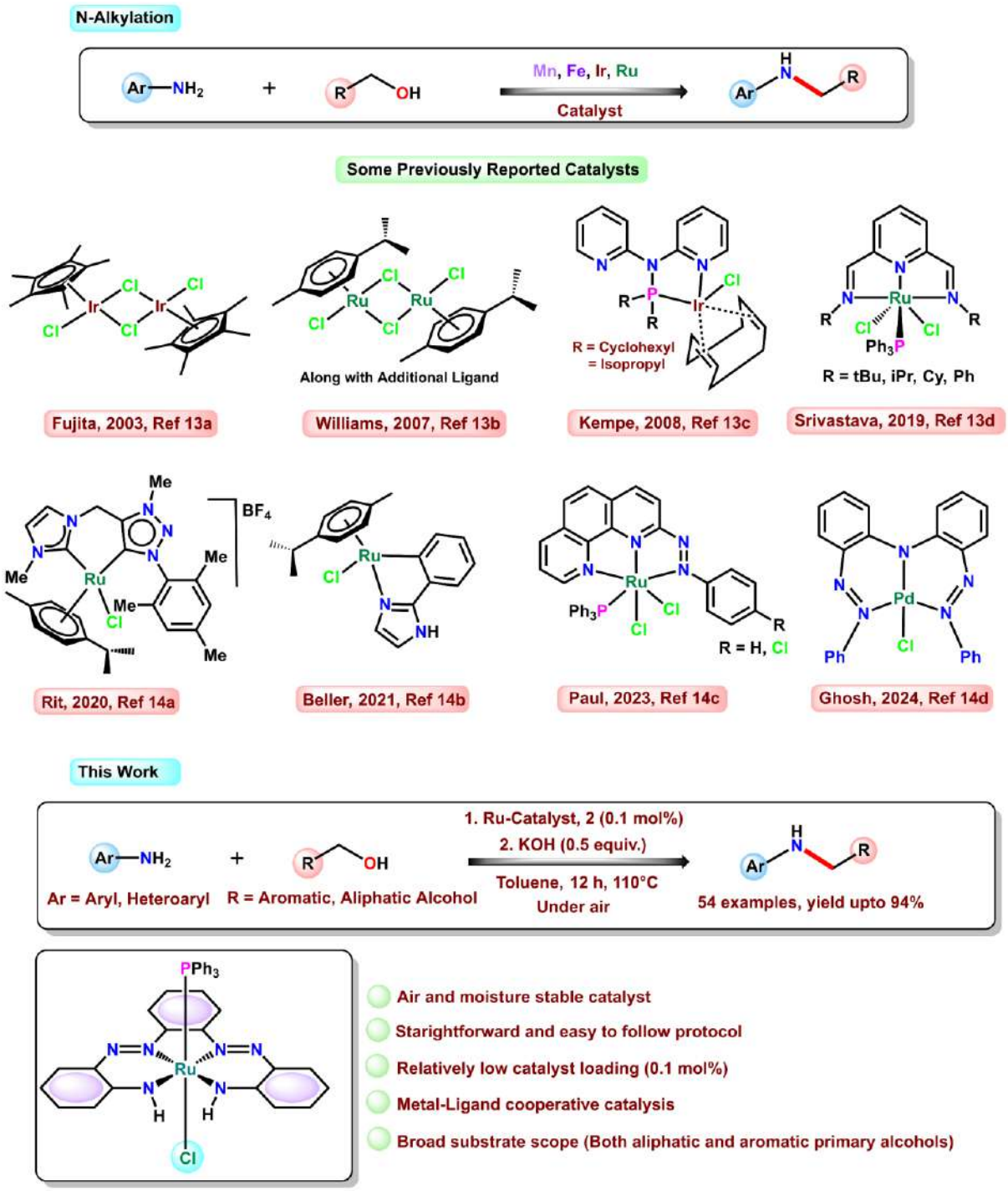

Scheme 6.4: Schematic depiction of some previously reported catalyst and our present work

6.2 Results and Discussion

The current work outlines the synthesis and characterization of a Ru(III) complex **2**, incorporating double deprotonated bis-azo diamine ligand **1**. The ligand was synthesized following previously reported procedure,[15] involving the modified Mills-Baeyer condensation reaction of 2,2'-diaminoazobenzene with 2-nitrosoacetanilide. Subsequent alkaline hydrolysis yielded the target bis-azo amine ligand **1** (Scheme 6.5). Complex **2** was prepared by reacting ligand **1** with $RuCl_2(PPh_3)_3$ in an equimolar ratio in dry, degassed toluene under reflux. This reaction afforded a dark bottle-green solution, from which the complex, *trans*-$[Ru(H_2L)Cl(PPh_3)]$ (**2**), was isolated in good yield *via* column chromatography (see Experimental Section). The complex was comprehensively characterized by single-crystal X-ray diffraction, spectroscopic methods and electrochemical study. Analysis of crystallographic data revealed that ligand **1** coordinates to the Ru(III) centre in a planar, bi-anionic, tetradentate fashion *via* two azo nitrogen atoms (N_{azo}) and two amido nitrogen atoms (N_{amido}), forming a $N_{Amido}N_{Azo}N_{Azo}N_{Amido}$ donor set. The additional coordination sites are occupied by one triphenylphosphine (PPh_3) and one uninegative chloride ligand, positioned trans to each other. This coordination pattern gives rise to a distorted octahedral geometry around the metal centre. The complex was found to crystallize in the triclinic $P\bar{1}$ space group. The molecular structure is depicted in Figure 6.1, while detailed crystallographic data and selected bond parameters (both experimental and calculated) are provided in Table 6.1 and Table 6.2 respectively. Additionally, complex **2** is stabilized by an intramolecular non-covalent π–π stacking interaction involving the phenyl ring of the ligand (Ring **B**), the five-membered chelate ring (Ring **C**), and one of the phenyl rings of the PPh_3 ligand (Ring **A**) (Figure 6.2). The centroid-to-centroid distance between the interacting rings are 3.7979(16) Å and 3.5898(11) Å with a corresponding dihedral angle of 16.29(13) ° and 16.41(9) (Table 6.3).

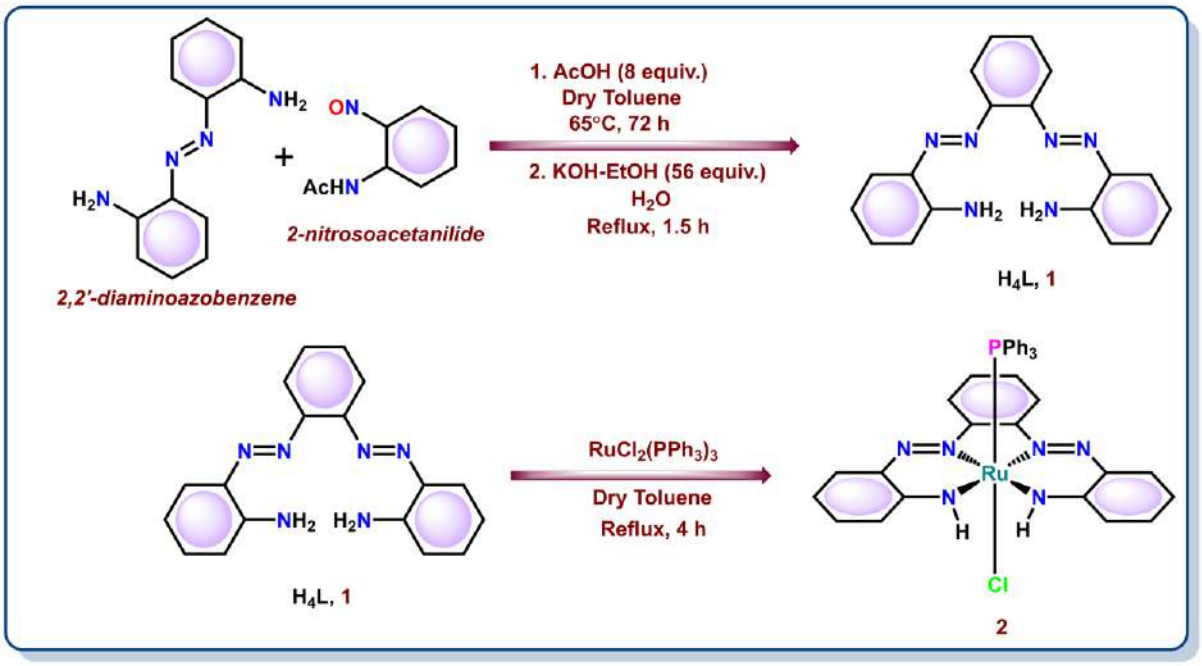

Scheme 6.5: Schematic depiction of synthesis of ligand **1** and its ruthenium(III) complex **2**

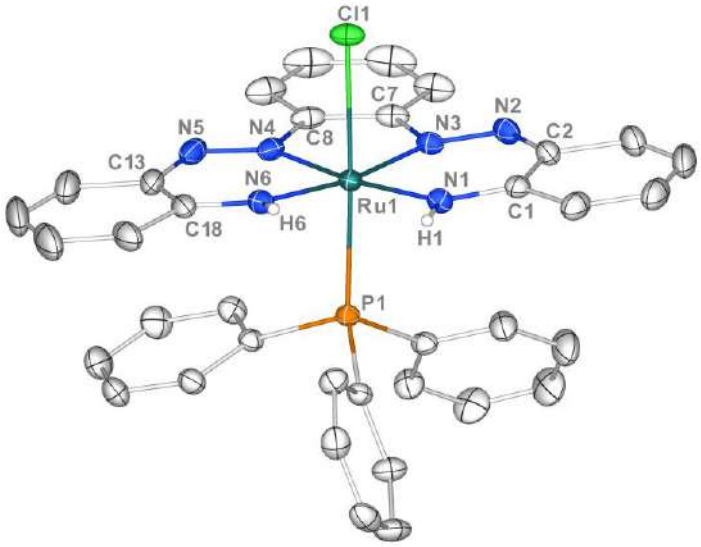

Figure 6.1: ORTEP diagram of **2** with partial atom numbering scheme (Thermal ellipsoids are set at 40% probability, Aromatic H atoms are excluded for clarity), CCDC No. **2433667**

Table 6.1: Crystallographic Details of **2**

	2
Empirical formula	$C_{36}H_{29}N_6ClPRu$
T/K	273.15
f_w	713.14
Crystal system	Triclinic
Space Group	$P\bar{1}$
a/Å	10.1769(8)
b/Å	11.2766(8)
c/Å	16.0950(12)
α/deg	93.284(2)
β/deg	105.880(2)
γ/deg	113.925(2)
V/ *Å*^{3}	1593.9(2)
Z	2
D_c/Mgm^{-3}	1.486
μ/mm^{-1}	0.662
F(000)	726
cryst size/mm^3	0.25 × 0.19 × 0.11
θ/deg	2.48 – 28.75
Measured reflns	64436
Unique reflns	9752
[a]GOF on F^2	1.076
R_1[b], wR_2[c][$I>2\sigma(I)$]	R_1= 0.0254, wR_2= 0.0592
R_1, wR_2	R_1= 0.0314, wR_2= 0.0634
[a]GOF = $\{\Sigma[w(F_o^2-F_c^2)^2]/(n-p)\}1/2$. [b]R1 = Σ $[\|F_o\|-\|F_c\|]/\Sigma\|F_o\|$. [c]wR2 = $[\Sigma[w(F_o^2-F_c^2)^2]/\Sigma[w(F_o^2)^2]]^{1/2}$ where w = $1/[\sigma^2(F_o^2)+(aP)^2+bP]$, P = $(F_o^2+2F_c^2)/3$.	

Table 6.2: Selected metrical parameters of **2**

Metrical Parameter of 2					
Bond lengths (Å)			**Bond Angles (°)**		
	Expt.	**Theo.**		**Expt.**	**Theo.**
Ru1–N1	1.9983(14)	2.037	N1–Ru1–N3	89.70(6)	88.54
Ru1–N3	1.9858(13)	2.026	N4–Ru1–N6	89.51(6)	88.47
Ru1– N4	1.9755(14)	2.027	N1–Ru1–N6	96.59(6)	100.06
Ru1– N6	1.9912(14)	2.042	N3–Ru1–N4	83.77(6)	82.77
Ru1–Cl1	2.5178(5)	2.457	N1–Ru1–P1	92.74(4)	88.45
Ru1–P1	2.3595(4)	2.500	N3–Ru1–P1	95.85(4)	97.69
N2–N3	1.291(2)	1.274	N4–Ru1–P1	91.38(4)	92.97
N4–N5	1.293(2)	1.277	N6–Ru1–P1	90.48(4)	91.07
C1–N1	1.327(2)	1.335	Cl1–Ru1–P1	177.191(16)	176.32
C2 –N2	1.364(3)	1.365	N1–Ru1–Cl1	90.06(4)	89.35
C13–N5	1.371(3)	1.362	N3–Ru1–Cl1	84.39(4)	85.20
C18–N6	1.319(2)	1.335	N4–Ru1–Cl1	85.87(4)	89.63
C1–C2	1.445(3)	1.454	N6–Ru1–Cl1	88.97(4)	86.39
C13–C18	1.442(3)	1.454	N3–Ru1–N6	170.86(6)	167.90

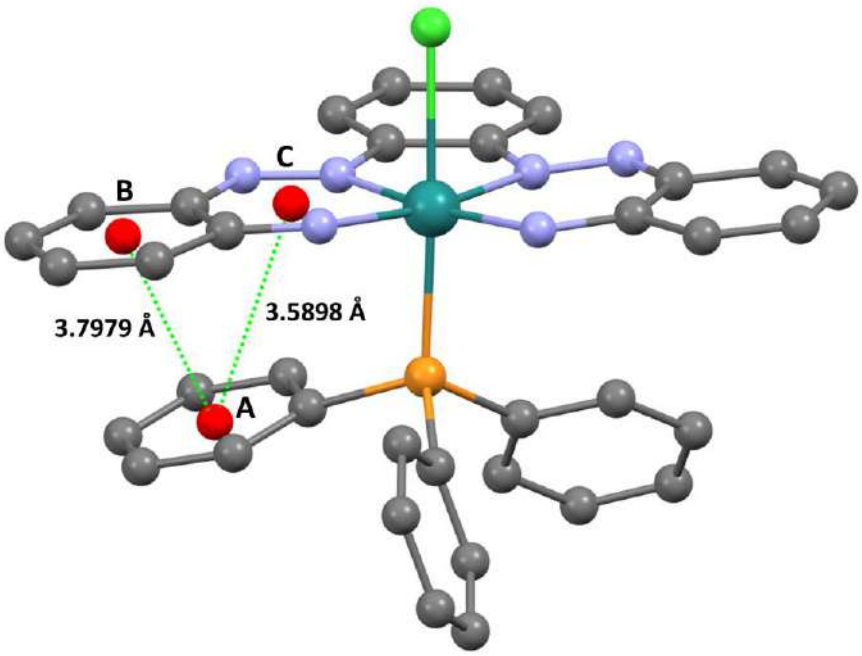

Figure 6.2: Intramolecular pi-pi stacking diagram of complex **2**

Table 6.3: Different stacking parameters* of **2**

Stacking Parameters	Ring A–B	Ring A–C
d[C_g(*I*) – C_g(*J*)] Å/α°	3.7979(16)/11.36(12)	3.5898(11)/16.41(9)
d[Cg(*I*) – R(*J*)] Å/β°	3.4952(12)/30.2	2.9398(7)/23.4
d[Cg(*J*) – R(*I*)] Å/γ°	3.2818(9)/23.0	3.2950(9)/35.0

*Cg(I) = Centroid of ring I, Cg(J) = Centroid of ring J, d[Cg(I) – Cg(J)] = Separation between two ring centroids, d[Cg(I) – R(J)] = Perpendicular distance of Cg(I) on ring J, d[Cg(J) – R(I)] = Perpendicular distance of Cg(J) on ring I, α = Dihedral angle between Planes I of ring I and plane J of ring J, β and γ = Angle between the vector Cg(I) – Cg(J) and the normal to plane P(I) or P(J) from Cg(I) and Cg(J) respectively.

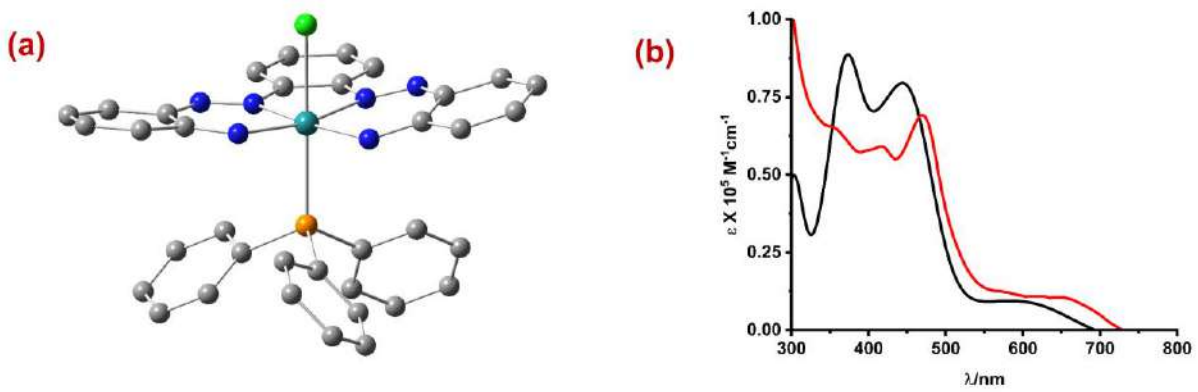

Figure 6.3: (a) Computationally optimized geometry of **2** at (U)B3LYP level of theory using 6-311++G(d,p) basis set for all non-H atoms and LANL2DZ basis set for Ru (b) the experimental (brownish red) and theoretical (black) absorption spectrum of **2** obtained from TD-DFT calculation using CPCM model where dichloromethane (CH_2Cl_2) was selected as solvent

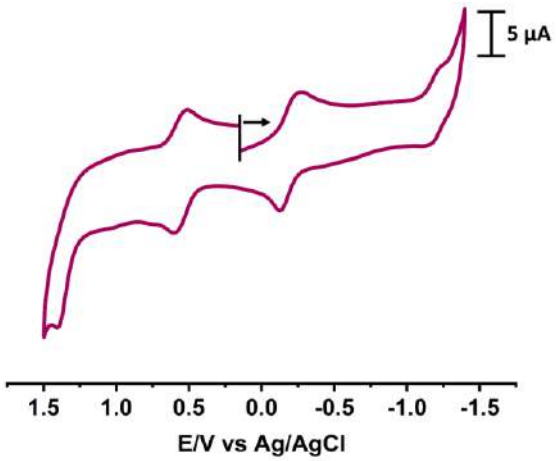

Figure 6.4: Cyclic voltammogram of **2** using Pt working electrode, Pt wire as auxiliary electrode and Ag/AgCl as reference electrode at a scan rate of 100 mV/s

Table 6.4: Cyclic voltametric data of **2** against Ag/AgCl as reference electrode

Complex	$E_{1/2}$/V (ΔE/mV)	
	Oxidation	Reduction
2	+0.56(86)	−0.19 (85), −1.20 (60)
$E_{1/2} = ½(E_{pa} + E_{pa})$, E_{pa} = anodic peak potential; E_{pc} = cathodic peak potential, ΔE = peak-to-peak separation		

The electrochemical behaviour of the complex *trans*-[Ru(H_2L)Cl(PPh_3)] (**2**) was examined *via* cyclic voltammetry in dry and degassed solution of acetonitrile/dichloromethane (9:1, v/v), using 0.2 M tetrabutylammonium hexafluorophosphate (TBAF) as the supporting electrolyte. The measurements were conducted employing a standard three-electrode setup consisting of a platinum disk as working electrode, a platinum wire as the auxiliary electrode, and a saturated Ag/AgCl electrode as the reference electrode. The cyclic voltammogram displays two reversible one-electron reductive responses at −0.19 V and −1.20 V, with peak-to-peak separations of 85 mV and 60 mV, respectively. In addition, a reversible oxidation wave is observed at +0.56 V, showing a peak separation of 86 mV (Figure 6.4, Table 6.4). Density functional theory (DFT) calculations disclose that the first reduction is primarily ligand-centered, involving the coordinated azo functionality, with a relative contribution of 42% (Table 6.5). The second reductive event appears to involve mixed contributions from both the

ruthenium centre and the ligand (Table 6.5 & 6.6). These findings suggest that the redox-active bis-azo framework could play a key role in facilitating ligand-centered electron transfer processes, potentially initiated by the cleavage of the Ru–Cl bond.[10e] The oxidative response, on the other hand, is attributed mainly to ligand oxidation, with a minor involvement of the metal centre (Table 6.5 & 6.6). The computationally optimized molecular geometry of complex **2** is presented in Figure 6.3(a), and the calculated and experimental UV-visible absorption spectra is shown in Figure 6.3(b) (see Computational Studies section, ESI† for details).

Table 6.5: Molecular orbital (**α**-MO) contribution table of **2**

Orbital	MO	Energy (eV)	Contribution						
			Ru	Cl	Azo	Amine	Ph	PPh_3	Composition
174	L+5	-1.11	3	1	0	0	1	95	π*(PPh_3)
173	L+4	-1.21	1	0	0	0	0	99	π*(PPh_3)
172	L+3	-1.31	2	1	0	1	1	96	π*(PPh_3)
171	L+2	-1.57	21	9	5	4	1	60	π*(PPh_3)
170	L+1	-1.93	28	0	35	6	51	0	d_{xz} + π* (PPh_3)
169	LUMO	-2.69	0	0	42	8	50	0	π*(Azo + Amine + Ph)
168	HOMO	-5.11	21	1	9	25	44	0	d_{xy} + π (Azo + Amine + Ph)
167	H–1	-5.33	1	5	9	24	57	4	π (Cl + Azo + Amine + Ph)
166	H–2	-5.81	36	53	6	1	2	1	d_{yz} + π (Cl + Azo)
165	H–3	-6.07	24	68	6	5	2	1	d_{xy} + π (Cl + Azo)
164	H–4	-6.30	29	19	19	8	24	1	d_{xz} + π (Cl + Azo + Amine + Ph)
163	H–5	-6.47	26	19	11	4	40	1	d_{yz} + π (Cl + Azo + Ph)

Table 6.6: Molecular orbital (**β**-MO) contribution table of **2**

Orbital	MO	Energy (eV)	Contribution						
			Ru	Cl	Azo	Amine	Ph	PPh_3	Composition
174	L+5	-1.20	1	0	0	0	0	99	π*(PPh_3)
173	L+4	-1.30	3	1	0	1	0	95	π*(PPh_3)
172	L+3	-1.49	16	7	4	3	1	69	π*(PPh_3)
171	L+2	-1.84	10	0	32	8	50	0	π*(PPh_3)
170	L+1	-2.67	1	0	38	13	47	0	π* (Azo + Amine + Ph)
169	LUMO	-3.12	52	3	7	12	24	2	d_{xz} + π*(Azo + Amine + Ph)
168	HOMO	-5.04	1	4	11	27	54	3	π (Azo + Amine + Ph)
167	H–1	-5.66	41	42	7	1	6	2	d_{xy} + π (Cl + Azo + Ph)
166	H–2	-5.82	19	52	6	10	12	1	d_{yz} + π (Cl + Azo + Ph)

165	H–3	-6.04	60	1	14	10	15	1	d_{xz} + π (Azo + Amine + Ph)
164	H–4	-6.40	9	26	9	1	54	1	d_{xz} + π (Cl + Azo + Ph)
163	H–5	-6.68	9	9	8	3	57	1	d_{xz} + π (Cl + Azo + Ph)

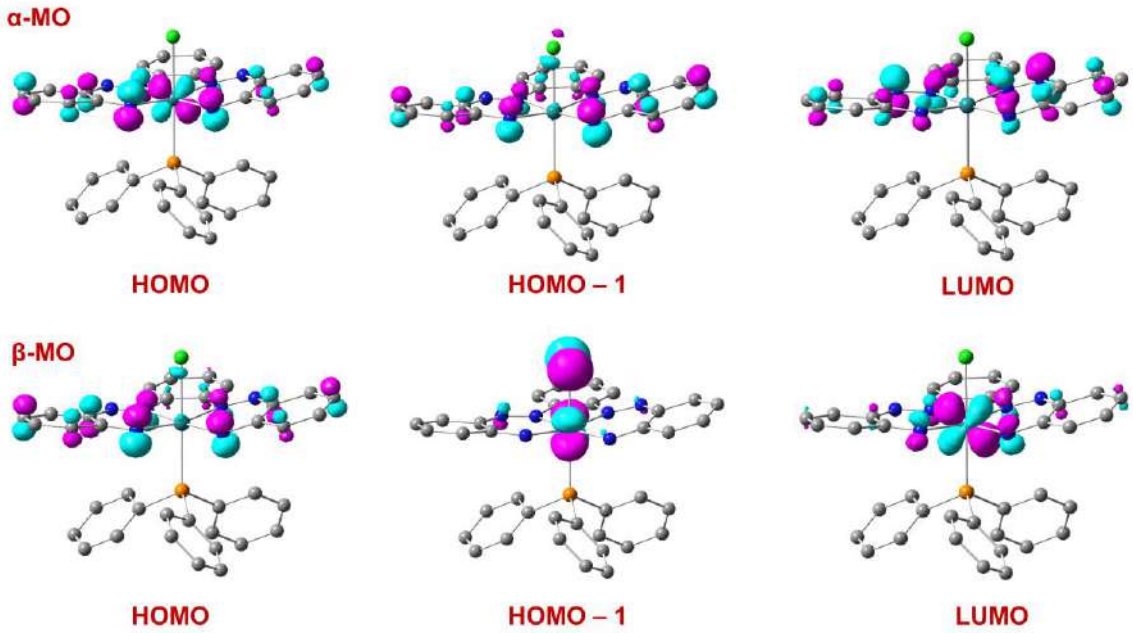

Figure 6.5: Some selected frontier molecular orbital of **2**

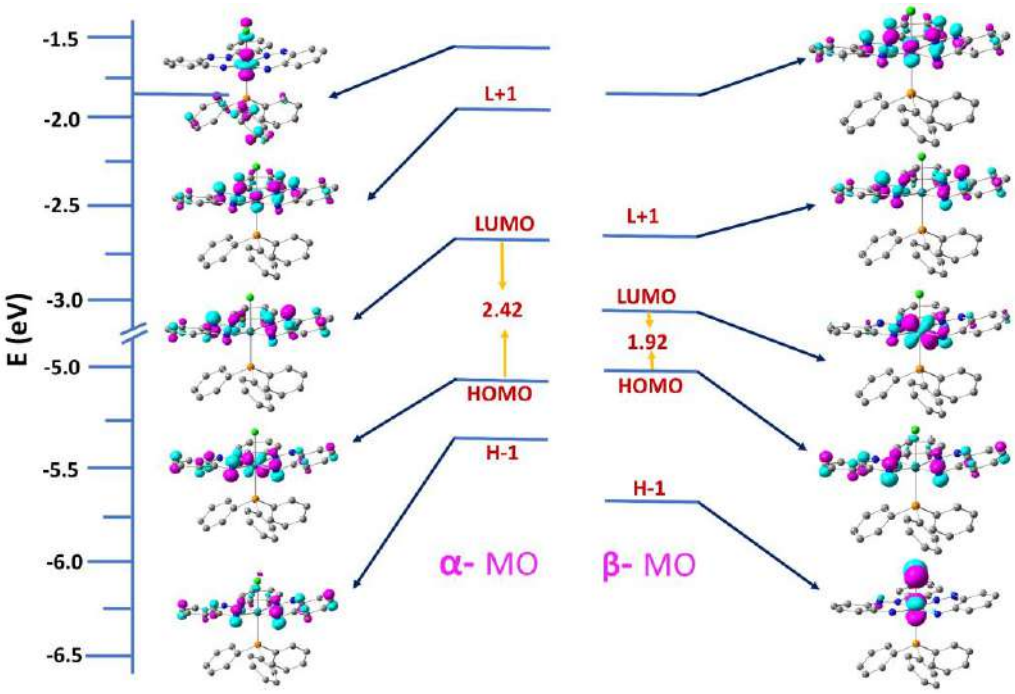

Figure 6.6: Partial MO diagram and isodensity surface plots (isovalue = 0.06) for selected α and β-FMOs of **2**. The arrows are used to highlight the HOMO–LUMO energy gap. All the DFT energy values are given in eV

6.3 Catalytic Activity

The study commenced with the standardization of reaction conditions for the N-alkylation of anilines using aliphatic alcohols. Our investigation began with the reaction of *p*-toluidine (**3b**) and 1-butanol (**4b**) in the presence of 0.1 mol% Ru(III) catalyst (**2**) and 0.5 equiv. of K_2CO_3 in toluene at 100 °C. However, no product formation was observed (Table 6.7, Entry 1 and 2). A similar outcome was noted when K_2CO_3 was replaced with Cs_2CO_3 (Table 6.7, Entry 3 and 4). Subsequently, we employed *t*-BuOK (0.5 equiv.) as a base instead of alkaline earth metal carbonates and increased the reaction temperature slightly to 110°C. Under these conditions, the desired N-alkylated amine **4b** was obtained with a 65% yield (Table 6.7, Entry 5). Increasing the base loading from 0.5 to 1.0 equiv. led to a slight improvement in the yield (Table 6.7, Entry 6)

Table 6.7: Screening of the reaction parameters for ruthenium(III)-catalyzed *N*-alkylation using *p*-toluidine (**3b**) and n-butanol (**4b**)[a,b,c]

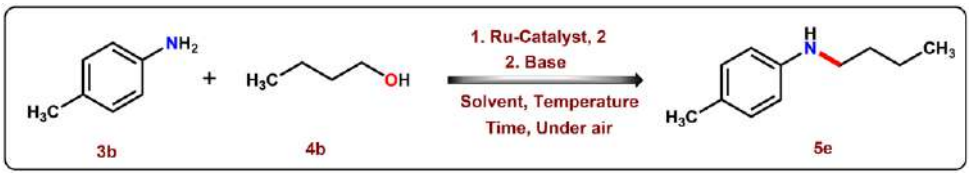

Entry	Catalyst (0.1 mol%)	Base	x (equiv.)	Solvent	T°C	Yield[b] (%)
1	2	K_2CO_3	0.5	Toluene	100	NR
2	2	K_2CO_3	1.0	Toluene	100	trace
3	2	Cs_2CO_3	0.5	Toluene	110	NR
4	2	Cs_2CO_3	1.0	Toluene	110	trace
5	2	t-BuOK	0.5	Toluene	110	65
6	2	t-BuOK	1.0	Toluene	110	71
7	2	t-BuOK	1.5	Toluene	110	72
8	2	NaOH	0.5	Toluene	110	68
9	2	NaOH	1.0	Toluene	110	57
10	**2**	**KOH**	**0.5**	**Toluene**	**110**	**83**
11	2	KOH	1.0	Toluene	110	81

12	2	KOH	1.0	Toluene	130	84
13	2	KOH	1.0	1,4-dioxane	110	12
14	2	KOH	1.0	THF	84	trace
15	2	KOH	0.5	Xylene	110	72
16	2	KOH	1.0	Xylene	110	68
17	2	KOH	0.5	CH_3CN	82	NR
18	2	KOH	1.0	CH_3CN	82	trace
19	2	KOH	0.5	DMF	110	trace
20	2	i-Pr_2NEt	0.5	Toluene	110	NR
21	2	Et_3N	0.5	Toluene	110	NR
22	2	KOH	0.5	–	110	38
23	–	KOH	0.5	Toluene	110	trace
24	2	–	–	Toluene	110	NR
25	$Ru(PPh_3)_2Cl_2$	KOH	0.5	Toluene	110	25
26	$RuH(CO)Cl(PPh_3)_3$	KOH	0.5	Toluene	110	23

[a]*Standardized Reaction conditions:* **3b** (1 mmol), **4b** (1.0 mmol), Catalyst **2** (0.1 mol %), base (x equiv.), solvent (3 mL), 110 ºC (oil bath), 12 h. [b]Isolated yield after column chromatography, [c]Under air.

In an effort to identify a more effective base other than *t*-BuOK, we investigated the use of alternative alkali metal hydroxides, specifically NaOH and KOH, under the same conditions. Surprisingly, both bases efficiently facilitated the formation of the desired N-alkylated amine **5e** with excellent yields (Table 6.7, Entry 8-11). Among them, KOH exhibited superior efficiency affording a significantly higher yield of the desired product compared to NaOH (Table 6.7, Entry 11). Prompted by these findings, we further optimized the reaction conditions by increasing the reaction temperature to 130°C while keeping all other parameters unchanged. However, this modification did not lead to any appreciable improvement in the yield of **5e** (Table 6.7, Entry 12). Subsequently, our attention turned toward identifying a more suitable solvent beyond the commonly used toluene that might enhance the reaction efficiency. A series of organic solvents including 1,4-dioxane, tetrahydrofuran (THF), xylene, acetonitrile, and dimethylformamide (DMF) were evaluated under identical conditions (Table 6.7, Entry 13–19). However, despite our repeated efforts, none of these alternatives proved to be more

effective than toluene. The utilisation of polar solvents such as THF, ethanol, DMF, and acetonitrile resulted in lower yields of **5e**, likely due to their ability to coordinate with the transition metal centre thereby interrupting the catalytic process. The results indicated that toluene remained the most suitable solvent for achieving optimal yield and reaction efficiency. No reaction occurred when organic bases were used as substitutes for alkali metal hydroxides (Table 6.7, Entry 20 & 21). Additionally, we investigated the reaction under solvent-free conditions to assess its feasibility in a more sustainable approach. However, this modification led to a significantly lower isolated yield of **5e** (Table 6.7, Entry 22). To further investigate the fundamental requirements of this N-alkylation reaction, few experiments were performed to assess the necessity of both the catalyst and the base. Notably, when either the catalyst or the base was omitted from the reaction system, no formation of **5e** was observed, emphasizing their vital roles in facilitating the desired transformation (Table 6.7, Entry 23 & 24). Employment of $Ru(PPh_3)_2Cl_2$ and $RuH(CO)Cl(PPh_3)_3$ as catalysts led to the isolation of compound **5e** in yields of 25% and 23%, respectively (Table 6.7, Entry 25 & 26).

After establishing the optimized reaction conditions for N-alkylation of amine using aniline **3a** (1.0 mmol), aliphatic alcohol **4a** (1.1 mmol), KOH (0.5 equiv.), temperature 110ºC and toluene (5 ml), we explored the scope of the reaction with various aliphatic alcohols (C3–C12) and aromatic amines (**3a-3f**) containing different functionalities as well as heteroaromatic amine (**3g**) as summarized in Table 6.8. We started our investigation with the reaction between aniline (**3a**) and 1-propanol (**4a**) which afforded the corresponding N-alkylated **5a** amine in 72% yield. Aromatic amines bearing both electron donating and withdrawing group successfully underwent N-alkylation with a number of aliphatic alcohols. Interestingly, amines with electron donating groups exhibited more efficiency in coupling with aliphatic alcohols compared to those having electron withdrawing groups. For instance, *p*-toluidine (**3b**) was efficiently alkylated with series of primary aliphatic alcohols such as 1-butanol (**4b**), 1-hexanol (**4c**), 1-

heptanol (**4d**), 1-octanol (**4e**), 1-nonanol (**4f**) and 1-dodecanol (**4g**) yielding desired products with good to excellent yield (**5e**: 83%, **5j**: 88%, **5q**: 89%, **5u**: 91%, **5ab**: 94%, **5ah**: 95%). Likewise, *p*-anisidine (**3i**) also effectively coupled with higher alcohols such as **4e**, **4f**, and **4g** to form corresponding N-alkylated amine with the isolated yield up to 92% (**5v**: 86%, **5ac**: 92%, **5ao**: 86%). Equally, chloroaniline derivatives (**3c** & **3d**) also efficiently alkylated with variety of aliphatic alcohols, affording corresponding N-alkylated amines in good to moderate yield (**5b**: 70%, **5c**: 73%, **5f**: 77%, **5g**: 76%, **5k**: 80%, **5l**: 78%, **5r**: 80%, **5w**: 82%, **5x**: 85%, **5z**: 78%, **5ad**: 85%, **5af**: 86%, **5aj**: 87%, **5ak**: 85%, **5ap**: 81%). The scope of the N-alkylation reaction was expanded by employing *p*-bromoaniline which efficiently participated in the reaction, yielding the target products with isolated yield reaching up to 89% (**5h**: 79%, **5m**: 81%, **5s**: 82%, **5al**: 89%).

Additionally, Electron deficient aniline such as 2,4-difluoroaniline, also successfully coupled with higher alcohols like 1-hexanol (**4c**), 1-octanol (**4e**), 1-nonanol (**4f**) and 1-dodecanol (**4g**) with decent yield (**5n**: 70%, **5y**: 75%, **5ae**: 80%, **5am**: 79%). To further explore this catalytic protocol, we also investigated 2-aminopyridine (**3g**) as substrate, when coupled with **4c**, and **4g**, the reaction led to the formation of corresponding N-alkyllpyridine-2-amines with moderate to good yield (**5o**: 69%, **5an**: 72%). Moreover, under the optimized condition cyclohexylmethanol also successfully employed as an alkylating agent for anilines and its derivatives. This transformation proceeded efficiently, affording the corresponding N-alkylated product with yields up to 75% (**5aq**: 66%, **5ar**: 71%, **5as**: 75%, **5at**: 65%, **5au**: 61%).

Further, we tried to demonstrate the practical applicability of this catalytic protocol, we explored its efficiency in gram-scale synthesis of some selected N-alkylated amines. For this purpose, we chose *p*- toluidine (**3b**) and 2-aminopyridine (**3g**) as model substrate and subjected them to alkylation with 1-dodecanol (**4g**) under this standardized condition. The desired N-

Table 6.8: Substrate scope

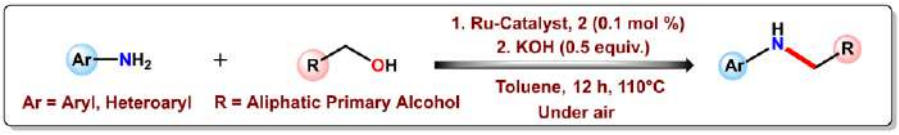

Alcohol	Amine (3a-3g)	Product	
Propan-1-ol (4a)			5a (72%)
			5b (70%)
			5c (73%)
Butan-1-ol (4b)			5d (79%)
			5e (83%)
			5f (77%)
			5g (76%)
			5h (79%)
Hexan-1-ol (4c)			5i (82%)
			5j (88%)
			5k (80%)
			5l (78%)
			5m (81%)
			5n (70%)
			5o (69%)

Alcohol	Amine (3a-3g)	Product	
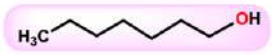 Heptan-1-ol (4d)	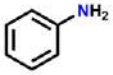	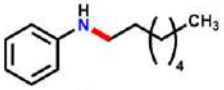	5p (84%)
	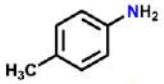	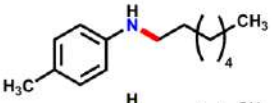	5q (89%)
	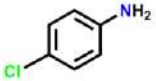	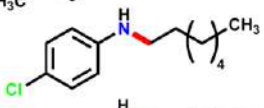	5r (80%)
	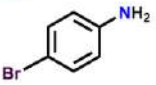	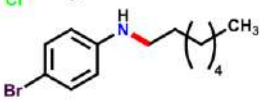	5s (82%)
 Octan-1-ol (4e)	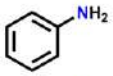	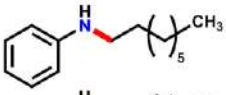	5t (88%)
	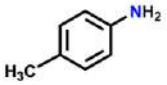	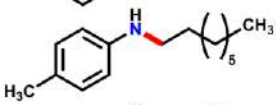	5u (91%)
	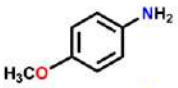	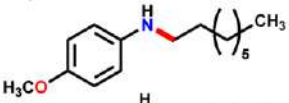	5v (86%)
	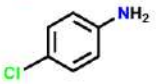	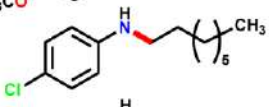	5w (82%)
	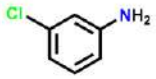	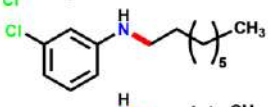	5x (85%)
	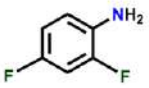		5y (75%)
	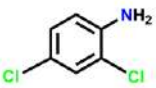		5z (78%)
 Nonan-1-ol (4f)	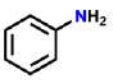	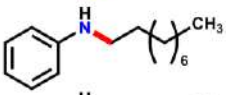	5aa (91%)
	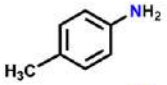	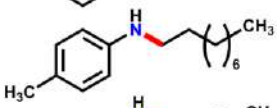	5ab (94%)
	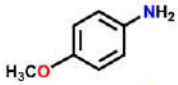	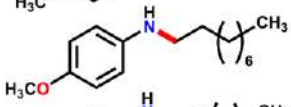	5ac (92%)
	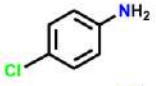	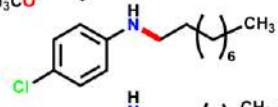	5ad (85%)
	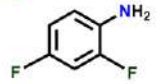		5ae (80%)
	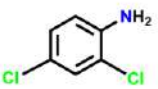		5af (86%)
 Dodecan-1-ol (4g)	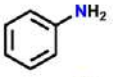	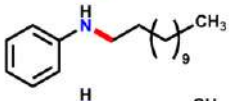	5ag (90%)
	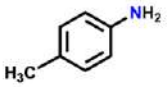	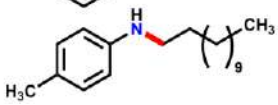	5ah (95%)

Alcohol	Amine (3a-3g)	Product
 Dodecan-1-ol (4g)	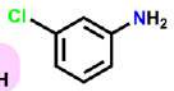	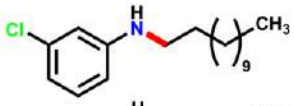 5aj (87%)
	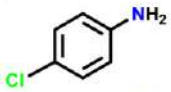	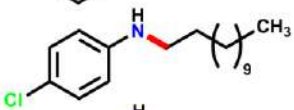 5ak (85%)
	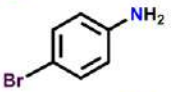	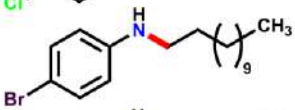 5al (89%)
	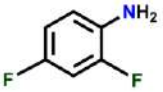	 5am (79%)
	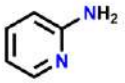	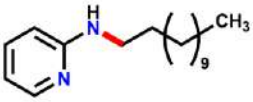 5an (72%)
	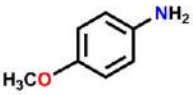	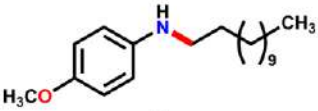 5ao (86%)
	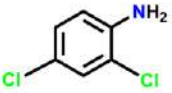	 5ap (81%)
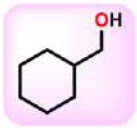 Cyclohexylmethanol (4h)	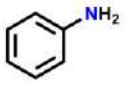	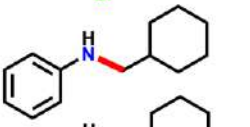 5aq (66%)
	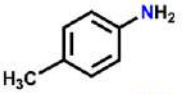	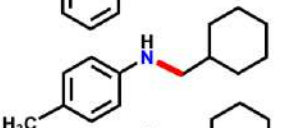 5ar (71%)
	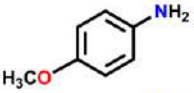	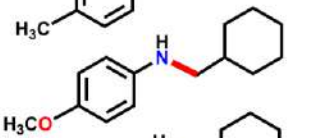 5as (75%)
	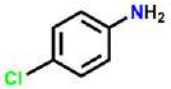	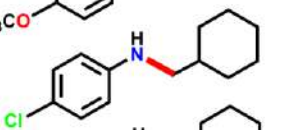 5at (65%)
	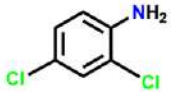	 5au (61%)

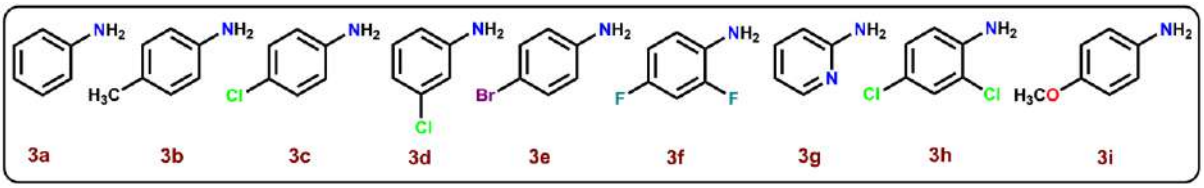

alkylated amines were obtained in admirable yields highlighting the scalability of the method (Scheme 6.6, Entry 1 & 2).

Similarly, we extended the study to *p*-bromoaniline (**3e**) which was successfully coupled with 1-hexanol (**4c**), affording the corresponding N-alkylated product **5m** with an isolated yield of 72% (Scheme 6.6, Entry 3). These results underscore the robustness and efficiency of the developed catalytic system, demonstrating its potential for large scale synthesis while maintaining high product yield.

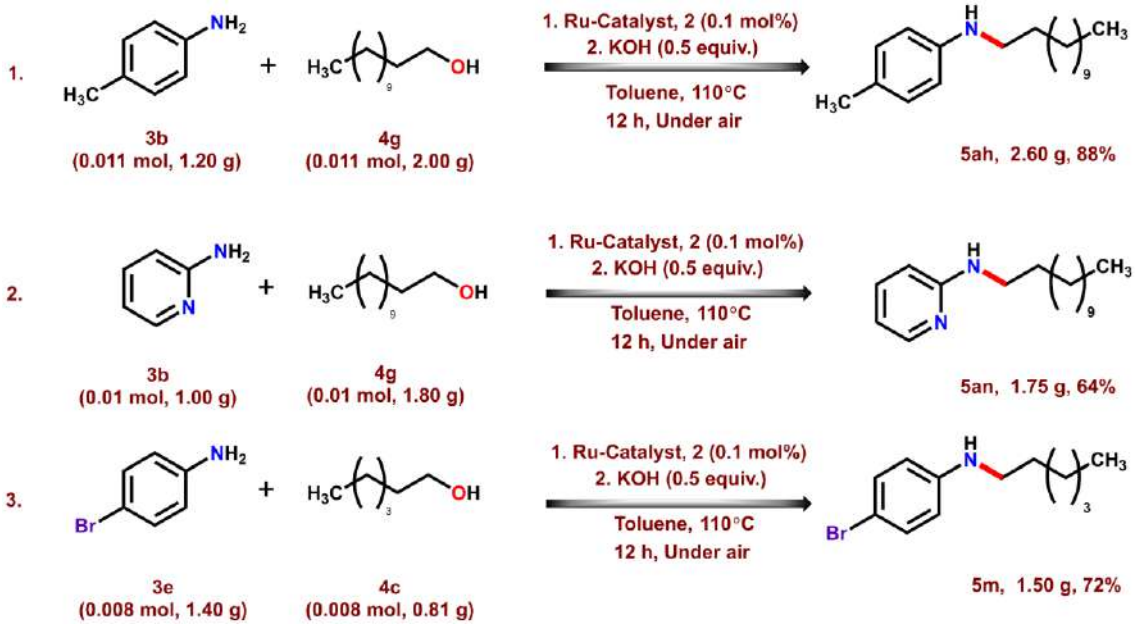

Scheme 6.6: Gram-scale synthesis of some selected N-alkylated amines

To expand the range of substrate compatibility and test the robustness of this protocol, we explored the use of aromatic primary alcohols as alkylating agents as well under the optimized reaction conditions (Table 6.9). As an initial investigation, we selected aniline (**3a**) and subjected it to alkylation with benzyl alcohol (**6a**), *p*-tolylmethanol (**6b**) and (4-chlorophenyl)methanol (**6c**). The reaction proceeded smoothly, leading to the formation of the expected N-benzylated amines in respectable yields (**7a**: 85%, **7b**: 87%, **7c**: 88%). Building on the successful N-alkylation of aniline with benzyl alcohol, we further expanded the scope of this catalytic protocol to other aromatic amines. 4-chloroaniline (**3c**) was efficiently coupled

with benzyl alcohol, yielding the corresponding N-alkylated product **7d** (85%). These observations confirm the generality of the method for a wide array of structurally diverse amines. Furthermore, 4-chloroaniline (**3c**) was also subjected to alkylation with (4-chlorophenyl)methanol, leading to the isolation of the desired N-alkylated product **7e** with 80% yield. Additionally, we extended this approach to heteroaryl amines, specifically 2-aminopyridine (**3g**), which was efficiently alkylated using various aromatic primary alcohols. This transformation resulted in the formation of N-arylated pyridine derivatives (**7f**: 65%, **7g**: 68%, **7h**: 62%) in moderate yields. These findings clearly suggest that the developed catalytic system is not only effective for aliphatic alcohols but also for the aromatic alcohols, further expanding the synthetic utility of this protocol.

Table 6.9: Substrate scope for aromatic primary alcohols

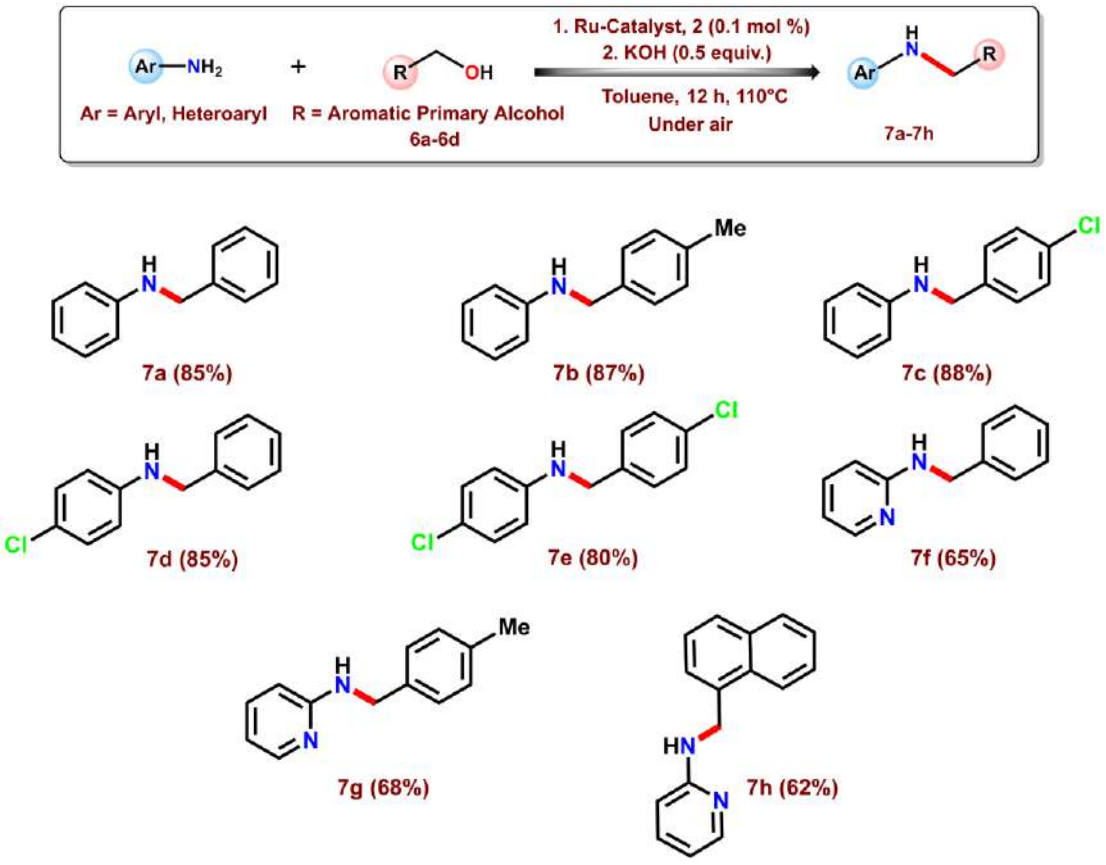

6.4 Mechanistic Studies

Our next focus of investigation is to find out probable mechanism of this ruthenium(III) catalysed dehydrogenative N-alkylation of aromatic/heteroaromatic amines, we conducted some control experiments. Since the N-alkylation reaction was carried out at a relatively higher temperature (110 ºC) we initially asses the catalyst's structural and operational stability. When the catalyst was heated in different organic solvents at elevated temperatures, we observed the catalyst remain intact even at 140 ºC in solvents like toluene xylenes. Based on previous studies, the mechanism of N-alkylation of amines with alcohols involves three key steps: dehydrogenation of the alcohols to a carbonyl compounds, formation of imine intermediates *via* reaction with the amines, and reduction of the imines to produce the final N-alkylated amines.[16] So, we started the investigation with **2**-catalyzed dehydrogenation of *p*-tolylmethanol (**6b**) under aerobic condition which produced corresponding *p*-tolualdehyde (**6b'**) with the isolated yield of 92% (Scheme 6.7a). During this dehydrogenation process hydrogen peroxide (H_2O_2) was produced and detected *via* spectrophotometrically (Scheme 6.8). Nevertheless, when we carried out the N-alkylation reaction between 2-aminopyridine (**3g**) and **6b** also produced H_2O_2 as by-product (Scheme 6.7b). Interestingly, alcohol dehydrogenation of **6b** catalysed by **2** runs efficiently in the presence of easily reducible substrate 4-methoxybenzaldehyde (**8a**) which plays the role of sacrificial hydrogen acceptor, forming the corresponding carbonyl **6b'** with excellent yield (Scheme 6.7c).

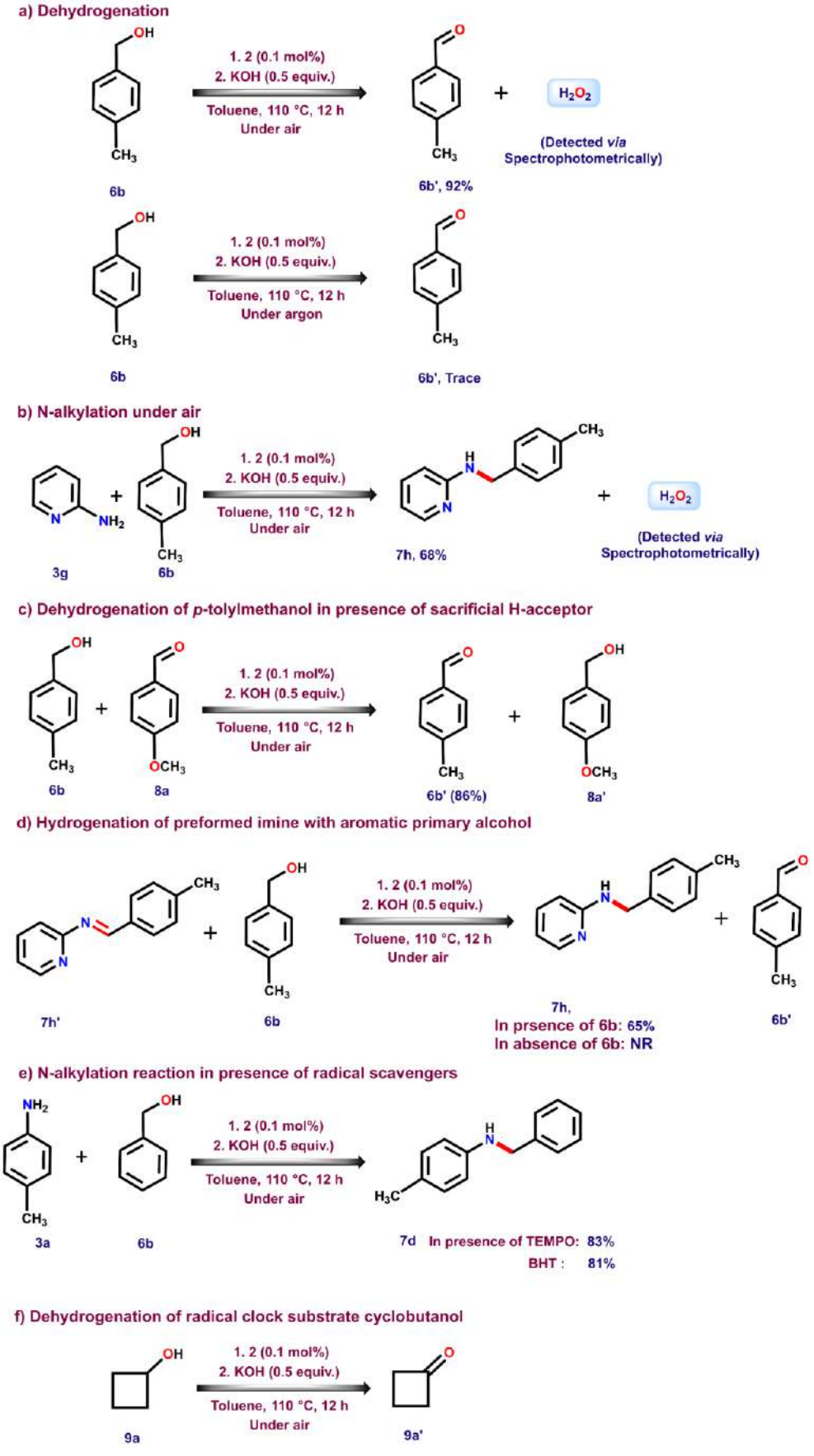

Scheme 6.7: Control experiments

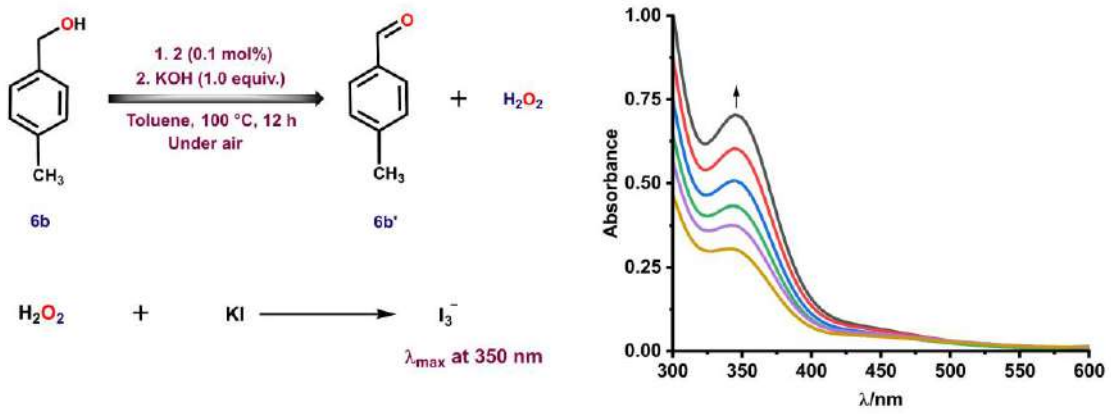

Scheme 6.8: Detection of hydrogen peroxide by spectrophotometry

Interestingly, when a preformed imine (**7g'**) is present, the alcohol dehydrogenation catalyzed by complex **2** still proceeds smoothly, leading to the formation of both the carbonyl compound (**6b'**) and the N-alkylated amine (**7g**) with good yield (Scheme 6.7d). Subsequently, we conducted the hydrogenation of imine **7g'** in the absence of alcohol. Unfortunately, no formation of the desired product **7g** was observed. This result indicates that the reaction did not proceed in the absence of a hydrogen source, further supporting the involvement of an *in-situ* hydrogen transfer mechanism.

Next, we established the homogeneity of this ruthenium(III)-catalysed N-alkylation reaction. To probe the involvement of ruthenium nanoparticles in the catalytic process, both the dehydrogenation of *p*-tolylmethanol (**6b**) and the N-alkylation reaction between 2-aminopyridine (**3g**) and **6b** were conducted in the presence of elemental mercury under the standardized reaction conditions (See Experimental Section). Elemental mercury is known to poison heterogeneous metal nanoparticles, thereby serving as a diagnostic tool to distinguish between homogeneous and heterogeneous catalysis. Notably, both the reactions proceeded smoothly and with comparable efficiency. These results strongly indicate that the catalysis does not involve ruthenium nanoparticles. Instead, the molecular ruthenium complex **2** functions as the active catalytic species throughout the reaction. Subsequently, we investigated the potential

involvement of radical species in the N-alkylation reaction. The alkylation of **3a** with **6b** was performed in the presence of radical scavengers such as **TEMPO** (2,2,6,6-tetramethylpiperidin-1-yl)oxyl) and **BHT** (2,6-di-tert-butyl-4-methylphenol), as depicted in Scheme 6.7e. In both cases, the reaction proceeded smoothly, affording the N-alkylated products with 83% and 81% yields, respectively. These results rule out a ketyl-type radical mechanism involving one-electron hydrogen atom transfer (HAT) and instead point toward a two-electron hydride transfer pathway wherein the hydrogen donor contributing both a proton and two electrons concurrently. In pursuit of more conclusive evidence, we have further conducted the dehydrogenation of a radical clock substrate *viz*., cyclobutanol (**9a**) under optimized reaction condition (Scheme 6.7f). The formation of sole cyclobutanone (**9a'**) in 83% yield, rather than multiple ring-cleavage products, strongly supports a two-electron hydride transfer pathway for alcohol dehydrogenation.[17]

Attempts to detect a ruthenium-hydride (Ru–H) intermediate in the reaction mixture using NMR spectroscopy yielded no observable results, despite repeated attempts. However, IR spectroscopic examination of the reaction mixture obtained from the **2**-catalysed dehydrogenation of methanol (CH_3OH) revealed characteristic N–H stretching vibrations at 2984 cm^{-1} and 3064 cm^{-1} (Figure 6.6.A8). When the reaction was repeated using deuterated methanol (CD_3OH), corresponding N–D stretching bands appeared at 2165 cm^{-1} and 2204 cm^{-1} (Figure 6.6.A9). These observations strongly support the involvement of the azo/hydrazo redox couple in the catalytic process.[18] The involvement of a hydrazo intermediate can be rationalized by a hydrogen transfer mechanism in which a hydride, initially located at the ruthenium center, is relayed to the coordinated azo moiety *via* an intramolecular "hydrogen walking" pathway.[19]

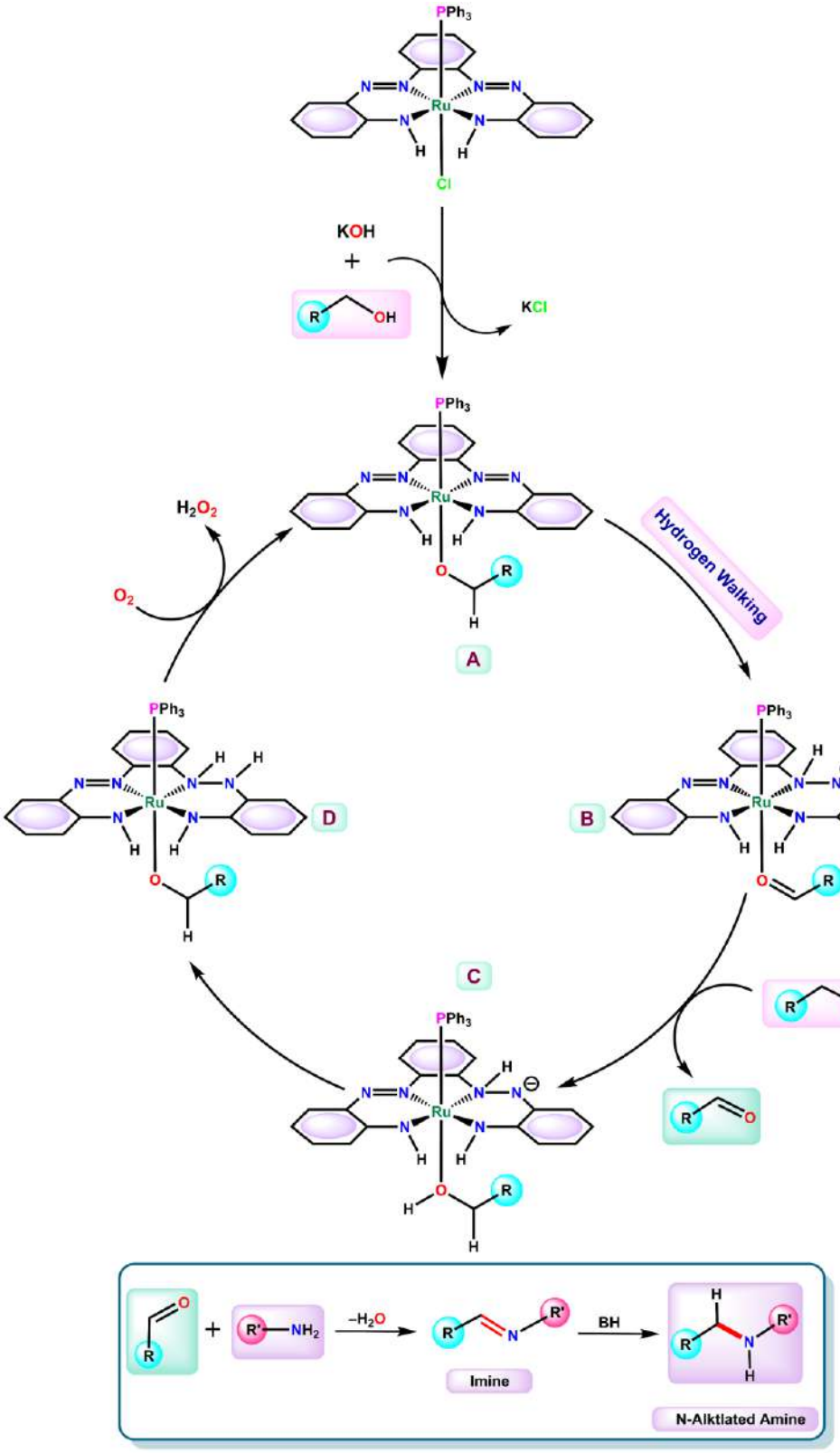

Scheme 6.9: Plausible mechanistic pathway for ruthenium(III) catalyzed dehydrogenative synthesis of N-alkylated amines

Drawing upon the preceding experimental observations and published reports, a probable catalytic mechanism is proposed in Scheme 6.9. The catalytic cycle is initiated by the coordination of a deprotonated alcohol to the Ru(III) centre of complex **2**, affording a Ru(III)-alkoxy intermediate **A**. Subsequent β-hydride elimination from the alkoxide results in the formation of a carbonyl compound (RCHO) and generates intermediate **B**. This step is believed to involve a transient Ru(III)–H species, wherein the hydride is swiftly relayed to the azo unit of the ligand *via* a hydrogen-walking pathway. The resulting vacant coordination site is then occupied by the *in situ* generated carbonyl species (RCHO). In the next step, displacement of the coordinated carbonyl by another molecule of alcohol furnishes intermediate **C**. The newly coordinated alcohol undergoes activation, enabling proton transfer from its hydroxyl group to the partially reduced azo moiety, leading to the formation of a dihydrazo intermediate **D**. This intermediate is subsequently oxidized by atmospheric oxygen, producing hydrogen peroxide as a by-product and regenerating the active Ru(III) catalyst **A**, thus completing the catalytic cycle. The carbonyl compound (RCHO) formed during this sequence undergoes immediate condensation with an aromatic amine to produce imine intermediate. This imine is then reduced *via* a borrowing hydrogenation (BH) pathway, ultimately affording the desired N-alkylated amine product.

6.3 Conclusion

In summary, we have developed and characterized a novel, electronically tuned ruthenium (III) complex featuring a new bis-azo-diamido planar tetradentate N4 coordinating scaffold as an efficient catalyst for the direct N-alkylation of amines with primary aliphatic alcohols. To our knowledge, this is the first Ru(III) catalyst to catalyze the dehydrogenative synthesis of N-alkylated amines using alcohols ranging from C3 to C12 (54 examples). Complex **2** was meticulously characterized using a variety of analytical and spectroscopic techniques. The octahedral complex was structurally ascertained *via* single-crystal X-ray diffraction (SCXRD)

analysis. The complex is electroactive and exhibits reversible couples at mild potential, which have been identified theoretically as primarily ligand-centered reductive responses in nature. Despite the presence of two highly π-acidic azo chromophores, mechanistic investigation reveal that the N-alkylation proceeds *via* a hydride transfer (HT) pathway rather than one-electron azo-anion radical route followed by borrowing hydrogenation (BH). This prediction is supported by certain control experiments. The method is atom-economical, generating only hydrogen peroxide as the sole by-product. By employing an earth-abundant metal at low catalyst loadings, this strategy not only enhances atom economy but also promotes the use of renewable feedstock over conventional petrochemical resources.

6.4 Experimental Section

6.4.1 Synthesis of ligand 1

The ligand was synthesised according to previously reported method.[15]

6.4.2 Synthesis of Complex 2

Ligand **1** (0.2 mmol, 63 mg) was dissolved in dry toluene (25 mL) in a 100 mL round-bottom flask and degassed under a gentle stream of nitrogen for 15 min. $Ru(PPh_3)_3Cl_2$ (192 mg, 0.2 mmol) was then added to the solution, and the reaction mixture was refluxed for 4 h. Upon completion, the dark bottle-green solution was cooled to room temperature and purified by column chromatography on silica gel (100–200 mesh), eluting with acetonitrile. The resulting complex was further purified by recrystallisation from a dichloromethane/hexane (1:4 v/v) solvent mixture.

6.4.3 Analytical data of Complex 2

***trans*-[Ru(H_2L)(PPh_3)Cl] (2)**: Bottle green coloured crystalline solid, Yield: 96 mg, 68%. Anal. Calcd for $C_{36}H_{29}N_6PClRu$: C 60.63, H 4.10, N 11.78. Found: C 60.54, H 4.05, N 11.75.

HRMS: $[M–Cl]^+$ m/z = 678.1029 (calcd. for $C_{36}H_{29}N_6PRu$ 678.1235); FT-IR/cm^{-1} ν = 3044 (w, $\nu_{N–H}$, stretch), 1604 (m, $\nu_{N–H}$, bend), 1436 (m, $\nu_{N=N}$), 521 (m, $\nu_{Ru–P}$).

6.4.4 General procedure for synthesis of N-alkylated amine:

A mixture of catalyst **2** (0.7 mg, 0.1 mol%), KOH (0.5 equiv.), aniline derivative (1.0 mmol, 1.0 equiv.), and primary alcohol (1.0 mmol, 1 equiv.) in 5 mL of dry toluene was added to an oven-dried 20 mL round-bottom flask equipped with magnetic stir bar along with a reflux condenser. The reaction mixture was then placed in an oil bath and heated at designated temperature for about 12 h. Upon completion, the mixture was concentrated under reduced pressure to remove the solvent and other volatile components. The resulting residue was purified by column chromatography on silica gel (60–120 or 100–200 mesh) using a hexane or hexane/diethyl ether mixture as the eluent.

6.4.5 General procedure for 2-catalysed gram-scale synthesis of N-alkylated amines:

A mixture of catalyst **2** (7.7 mg, 0.1 mol%), KOH (308 mg, 0.5 equiv.), **3b** (11.0 mmol, 1.20 g, 1.0 equiv.), and **4g** (11.0 mmol, 2.00 g, 1.0 equiv.) in dry toluene (30 mL) was added to an oven-dried 100 mL round-bottom flask equipped with a magnetic stir bar and a reflux condenser. The reaction mixture was heated in an oil bath at the designated temperature for approximately 12 hours under continuous stirring. Upon completion of the reaction (monitored by TLC), the mixture was concentrated under reduced pressure to remove the solvent and other volatile components. The resulting crude residue was purified by column chromatography on silica gel (100–200 mesh) using hexane or a hexane/diethyl ether mixture as the eluent to afford the pure product with isolated yield of 78% (2.3 g). The same procedure was applied for gram-scale synthesis of **5an** and **5n**.

6.4.6 Alcohol Dehydrogenation and Detection of H_2O_2

During the dehydrogenation of 4-methylbenzyl alcohol (**6b**), the formation of H_2O_2 was detected spectrophotometrically by monitoring the steady increase in the characteristic absorption band of I_3^- at 350 nm. The reaction between 4-methylbenzyl (**6b**) and catalyst **2** was conducted under open-air conditions in a 10 mL oven-dried round-bottomed flask containing 1 mmol of **6b**, 0.1 mol% (0.72 mg) of catalyst **2**, and 0.5 mmol (28 mg) of KOH in 3 mL of dry toluene. The reaction mixture was stirred and heated at 110°C for 12 h. After completion, 15 mL of water was added to the mixture, which was then extracted twice with CH_2Cl_2. The aqueous layer was acidified to pH 2 with dilute H_2SO_4 to prevent further oxidation. Subsequently, 1 mL of a 10% KI solution and a few drops of a 3% $(NH_4)_2MoO_4$ solution were added. In this process, H_2O_2 oxidized I^- to I_2, which then reacted with excess I^- to form I_3^-, as described by the following chemical steps.

1. $H_2O_2 + 2I^- + 2H^+ \rightarrow 2H_2O + I_2$
2. $I_2(aq) + I^- \rightarrow I_3^-$

6.4.7 Mercury Poisoning Test

To a 10 mL round-bottomed flask charged with *p*-toluidine (**3b**) (107 mg, 1.0 mmol, 1 equiv.), n-butanol (**4b**) (74 mg, 0.1 ml, 1.0 mmol, 1 equiv.), KOH (28 mg, 0.5 mmol, 0.5 equiv.), 3 mL of toluene with a magnetic stir bar, catalyst **2** (0.72 mg, 0.1 mol%) and 50 equivalents of mercury (738 mg) were added under an open-air atmosphere. The reaction mixture was stirred and heated at 110°C for 12 h. Upon completion (checked by TLC), the reaction mixture was extracted with dichloromethane (CH_2Cl_2) twice and purified by column chromatography using hexane as the eluent, affording the desired product (**5e**) in 90% isolated yield.

6.4.8 Radical Scavenging Experiment

In an oven dried 20 mL round-bottomed flask, *p*-toluidine (**3b**) (107 mg, 1.0 mmol, 1 equiv.), benzyl alcohol (**6a**) (107 mg, 0.1 ml, 1.0 mmol, 1.0 equiv.), KOH (28 mg, 0.5 mmol, 0.5 equiv.), catalyst **2** (0.72 mg, 0.1 mol%), and (2,2,6,6-Tetramethylpiperidin-1-yl)oxyl (**TEMPO**) (312 mg, 2.0 mmol, 2 equiv.) were combined in 5 mL toluene under an open-air atmosphere. The mixture was stirred at 110°C for 12 h and monitored by TLC. After completion, the reaction mixture was extracted with ethyl acetate (EtOAc) and purified by column chromatography (hexane), yielding the product (**7d**) with 87%.

6.5 References

[1] (a) J. L. McGuire, *Pharmaceuticals: Classes, Therapeutic Agents, Areas of Application*; Wiley-VCH, Weinheim, Germany, **2000**, Vols. 1−4. (b) S. A. Lawrence, *Amines: Synthesis, Properties and Applications; Cambridge University Press*: Cambridge, United Kingdom, **2004**. (c) B. R. Brown, *The Organic Chemistry of Aliphatic Nitrogen Compounds; Cambridge University Press*: Cambridge, United Kingdom, **2004**. (d) A. J. A. Watson, J. M. J. Williams, *Science*, **2010**, *329*, 635– 636 (e) J. Magano, J. R. Dunetz, *Chem. Rev.*, **2011**, *111*, 2177–2250. (f) D. Wang, D. Astruc, *Chem. Rev.*, **2015**, *115*, 6621−6686. (g) M. Baeten, B. U. W. Maes, *Adv. Organomet. Chem.*, **2017**, *67*, 401−481. (h) B. G. Reed-Berendt, K. Polidano, L. C. Morrill, *Org. Biomol. Chem.*, **2019**, *17*, 1595−1607.

[2] (a) J. F. Hartwig, *Acc. Chem. Res.*, **1998**, *31*, 852−860. (b) Y. Ju, R. S. Varma, *Green Chem.*, **2004**, *6*, 219−221. (c) D. S. Surry, S. L. Buchwald, *Angew. Chem., Int. Ed.*, **2008**, *47*, 6338−6361. (d) E. Sperotto, G. P. M.van Klink, G. van Koten, J. G. de Vries, *Dalton Trans.*, **2010**, *39*, 10338−10351. (e) J. Magano, J. R. Dunetz, *Chem. Rev.*, **2011**, *111*, 2177−2250. (f) L. Huang, M. Arndt, K. Gooßen, H. Heydt, L. J. Gooßen, *Chem. Rev.*, **2015**, *115*, 2596− 2697. (g) J. C. Castillo, J. Orrego-Hernandez, J. Portilla, Eur. *J. Org. Chem.*, **2016**, *2016*, 3824−3835. (h) M. Lavoie, M. Stradiotto, *ACS Catal.*, **2018**, *8*, 7228−7250.

[3] K. Eller, E. Henkars, R. Rossbacher, H. Hoke, "Amines, Aliphatic". *Ullmann's Encyclopedia of Industrial Chemistry. Weinheim*: Wiley-VCH. DOI: 10.1002/14356007.a02_001.

[4] (a) C. F. Winans, H. Adkins, *J. Am. Chem. Soc.*, **1932**, *54*, 306−312. (b) W. S. Emerson, "*The Preparation of Amines by Reductive Alkylation*". Organic Reaction, Chapter 3, **2001**, Wiley-VCH. DOI: 10.1002/0471264180.or004.03. (c) Y. Hoshimoto, T. Kinoshita, S. Hazra, M. Ohashi, S. Ogoshi, *J. Am. Chem. Soc.*, **2018**, *140*, 7292−7300.

[5] (a) A. Togni, H. Grutzmacher, *Catalytic heterofunctionalization: from hydroamination to hydrozirconation*, Wiley-VCH Verlag GmbH & Co. KGaA: Weinheim, **2001**, DOI:10.1002/3527600159. (b) K. Alex, A. Tillack, N. Schwarz, M. Beller, *ChemSusChem*, **2008**, *1*, 333 – 338. (c) K. D. Hesp, M. Stradiotto, *ChemCatChem*, **2010**, *2*, 1192 – 1207. (d) J. S. Yadav, A. Antony, T. S. Rao, B. V. S. Reddy, *J. Organomet. Chem.*, **2011**, *696*, 16 – 36.

[6] (a) R. C. DiPucchio, S. -C. Rosca, L. L. Schafer, *J. Am. Chem. Soc.*, **2022**, *144*, 11459−11481. (b) E. Chong, P. Garcia, L. L. Schafer, *SYNTHESIS*, **2014**, *46*, 2884–2896.

[7] (a) A. J. A. Watson, J. M. J. Williams, *Science*, **2010**, *329*, 635–636. (b) S. Bahn, S. Imm, L. Neubert, M. Zhang, H. Neumann, Matthias Beller, *ChemCatChem*, **2011**, *3*, 1853 – 1864.

[8] (a) A. Corma, J. Navas, M. J. Sabater, *Chem. Rev.*, **2018**, *118*, 1410−1459. (b) O. S. Nayal, M. S. Thakur, M. Kumar, N. Kumar, S. K. Maurya, *Adv. Synth. Catal.*, **2018**, *360*, 730−737.

[9] (a) C. Gunanathan, Y. Ben-David, D. Milstein, *Science*, **2007**, *317*, 790−792. (b) C. Gunanathan, D. Milstein, *Science*, **2013**, *341*, 249−260. (c) D. Srimani, Y. Ben-David, D. Milstein, *Angew. Chem., Int. Ed.*, **2013**, *52*, 4012−4015. (d) S. Rösler, M. Ertl, T. Irrgang, R. Kempe, *Angew. Chem., Int. Ed.*, **2015**, *54*, 15046−15050. (e) S. Elangovan, J. Neumann, J. B. Sortais, K. Junge, C. Darcel, M. Beller, *Nat. Commun.*, **2016**, *7*, 12641. (f) R. H. Crabtree, *Chem. Rev.*, **2017**, *117*, 9228−9246. (g) M. Maji, K. Chakrabarti, B. Paul, B. C. Roy, S. Kundu, *Adv. Synth. Catal.*, **2018**, *360*, 722−729. (h) P. Daw, Y. Ben-David, D. Milstein, *J. Am. Chem. Soc.*, **2018**, *140*, 11931−11934. (i) B. G. Reed-Berendt, D. E. Latham, M. B. Dambatta, L. C. Morrill, *ACS Cent. Sci.*, **2021**, *7*, 570−585.

[10] (a) N. A. Espinosa-Jalapa, A. Kumar, G. Leitus, Y. Diskin-Posner, D. Milstein, *J. Am. Chem. Soc.*, **2017**, *139*, 11722−11725. (b) A. Afanasenko, R. Hannah, T. Yan, S. Elangovan, K. Barta, *ChemSusChem*, **2019**, *12*, 3801−3807. (c) A. Porcheddu, G. Chelucci, *Chem. Rec.*, **2019**, *19*, 2398−2435. (d) J. Wu, S. Tongdee, M. Cordier, C. Darcel, *Chem. Eur. J.*, **2022**, *28*, e202201809. (e) J. Li, A. Mao, W. Yao, H. Zhua, D. Wang, *Green Chem.*, **2022**, *24*, 2602–2612. (f) S. Pal, S. Das, S. Chakraborty, S. Khanra, N. D. Paul, *J. Org. Chem.*, **2023**, *88*, 3650−3665. (g) S. Halder, S. Naskar, D. Jana, G. Kanrar, K. Pramanik, S. Ganguly, *New J.*

Chem., **2024**, *48*, 8181–8194. (h) S. Halder, S. Naskar, D. Jana, G. Kanrar, S. C. Mandal, S. Roy, N. Bharadwaj, K. Pramanik, S. Ganguly, *Chem Asian J.*, **2024**, *20*, e202401278. (i) D. Jana, S. Roy, S. Naskar, S. Halder, G. Kanrar, K. Pramanik, *Org. Biomol. Chem.*, **2024**, *22*, 6393−6408. (j) J. Li, S. Ou, X. Sang, R. Chai, D. Wang, *Catal. Sci. Technol.*, **2024**, *14*, 1958–1966. (k) D. Jana, S. Malik, G. Kanrar, S. Halder, S. Naskar, K. Pramanik, *ChemCatChem*, **2025**, *17*, e202401851. (l) S. Naskar, S. Halder, A. Das, S. Malik, G. Kanrar, D. Jana, B. K. Panda, K. Pramanik, S. Ganguly, *Asian J. Org. Chem.* **2025**, e00330, doi.org/10.1002/ajoc.202500330.

[11] (a) M. H. S. A. Hamid, C. L. Allen, G. W. Lamb, A. C. Maxwell, H. C. Maytum, A. J. A. Watson, J. M. J. Williams, *J. Am. Chem. Soc.*, **2009**, *131*, 1766−1774. (b) M. Bertoli, A. Choualeb, A. J. Lough, B. Moore, D. Spasyuk, D. G. Gusev, *Organometallics*, **2011**, *30*, 3479−3482. (c) P. Satyanarayana, G. M. Reddy, H. Maheswaran, M. L. Kantam, *Adv. Synth. Catal.*, **2013**, *355*, 1859−1867. (d) S. Michlik, R. A Kempe, *Nat. Chem.*, **2013**, *5*, 140−144. (e) N. Deibl, R. Kempe, *Angew. Chem., Int. Ed.*, **2017**, *56*, 1663−1666. (f) M. Vellakkaran, K. Singh, D. Banerjee, *ACS Catal.*, **2017**, *7*, 8152−8158. (g) Z. Xu, D.-S. Wang, X. Yu, Y. Yang, D. Wang, *Adv. Synth. Catal.*, **2017**, *359*, 3332 – 3340. (h) M. Mastalir, M. Glatz, E. Pittenauer, G. Allmaier, K. Kirchner, *Org. Lett.*, **2019**, *21*, 1116−1120. (i) Wei Yao, Z. -C. Duan, Y. Zhang, X. Sang, X. -F. Xia, D. Wang, *Adv. Synth. Catal.*, **2019**, *361*, 5695−5703 (j) F. Kallmeier, R. Fertig, T. Irrgang, R. Kempe, *Angew. Chem., Int. Ed.*, **2020**, *59*, 11789−11793. (k) L. Chen, J. Li, L. Wang, Gang Shi, D. Wang, *Asian J. Org. Chem.*, **2023**, *12*, e202300444.

[12] (a) R. Grigg, T. R. B. Mitchell, S. Sutthivaiyakit, N. Tongpenyai, *J. Chem. Soc. Chem. Commun.*, **1981**, 611–612. (b) Y. Watanabe, Y. Tsuji, Y. Ohsugi, *Tetrahedron Lett.*, **1981**, *22*, 2667–2670. (d) Y. Watanabe, Y. Tsuji, H. Ige, Y. Ohsugi, T. Ohta, *J. Org. Chem.*, **1984**, *49*, 3359−3363.

[13] (a) K. Fujita, Z. Li, N. Ozekib, R. Yamaguchi, *Tetrahedron Lett.*, **2003**, *44*, 2687–2690. (b) M. Haniti, S. A. Hamid, J. M. J. Williams, *Chem. Commun.*, **2007**, 725–727 (c) B. Blank, M. Madalska, R. Kempe, *Adv. Synth. Catal.*, **2008**, *350*, 749 – 758. (e) K. Das, P. G. Nandi, K. Islam, H. K. Srivastava, A. Kumar, *Eur. J. Org. Chem.*, **2019**, 6855–6866.

[14] (a) S. N. R. Donthireddy, P. M. Illam, A. Rit, *Inorg. Chem.*, **2020**, *59*, 1835−1847. (b) P. Piehl, R. Amuso, A. Spannenberg, B. Gabriele, H. Neumann, M. Beller, *Catal. Sci. Technol.*, **2021**, *11*, 2512–2517. (c) A. K. Guin, S. Pal, S. Chakraborty, S. Chakraborty, N. D. Paul, *J.*

Org. Chem., **2023**, *88*, 5944−5961. (d) V. K. Chaudhary, P. Kukreti, K. Sharma, K. Kumar, S. Singh, S. Kumaria, K. Ghosh, *Dalton Trans.*, **2024**, *53*, 8740–8749.

[15] (a) P. S. Hallman, T. A. Stephenson, G. Wilkinson, "*Inorganic Syntheses*", **1970**, Volume 12, DOI:10.1002/9780470132432.ch40. (b) S. Bellotto, R. Reuter, C. Heinis, H. A. Wegner, *J. Org. Chem.*, **2011**, *76*, 9826–9834. (c) N. Kumari, S. Halder, S. Naskar, S. Ganguly, K. Pramanik, F. Yari, A. Dorniak, W. Schofberger, S. Roy, *Materials Today Catalysis*, **2024**, *5*,100049.

[16] (a) R. Ramachandran, G. Prakash, S. Selvamurugan, P. Viswanathamurthi, J. G. Malecki, V. Ramkumar, *Dalton Trans.*, **2014**, *43*, 7889−7902. (b) G. Choi, S. H. Hong, *Angew. Chem., Int. Ed.*, **2018**, *57*, 6166−6170. (c) A. Lator, S. Gaillard, A. Poater, J.-L. Renaud, *Org. Lett.*, **2018**, *20*, 5985−5990. (d) M. Subaramanian, S. P. Midya, P. M. Ramar, E. Balaraman, *Org. Lett.*, **2019**, *21*, 8899−8903. (e) B. Emayavaramban, P. Chakraborty, E. Manoury, R. Poli, B. Sundararaju, *Org. Chem. Front.* **2019**, *6*, 852−857. (f) G. Balamurugan, R. Ramesh, J. G. Malecki, *J. Org. Chem.*, **2020**, *85*, 7125−7135. (g) M. Huang, Y. Li, X.-B. Lan, J. Liu, C. Zhao, Y. Liu, Z. Ke, *Org. Biomol. Chem.*, **2021**, *19*, 3451−3461. (h) K. Ganguli, N. Belkova, S. Kundu, *Dalton Trans.*, **2022**, *51*, 4354−4365.

[17] (a) R. Ray, S. Chandra, D. Maiti, G. K. Lahiri, *Chem. Eur. J.*, **2016**, *22*, 8814–8822 (b) S. P. Rath, D. Sengupta, P. Ghosh, R. Bhattacharjee, M. Chakraborty, S. Samanta, A. Datta, S. Goswami, *Inorg. Chem.*, **2018**, *57*, 11995−12009. (c) S. Sinha, S. Das, R. Mondal, S. Mandal, N. D. Paul, *Dalton Trans.*, **2020**, *49*, 8448–8478. (d) B. Goswami, M. Khatua, S. Samanta, *Dalton Trans.*, **2022**, *51*, 1454–1463.

[18] (a) S. P. Rath, D. Sengupta, P. Ghosh, R. Bhattacharjee, M. Chakraborty, S. Samanta, A. Datta, S. Goswami, *Inorg. Chem.*, **2018**, *57*, 11995−12009. (b) A. K. Guin, R. Mondal, G. Chakraborty, S. Pal, N. D. Paul, *J. Org. Chem.*, **2022**, *87*, 7106−7123.

[19] (a) H. Li, M. B. Hall, *J. Am. Chem. Soc.* **2015**, *137*, 12330−12342. (b) A. K. Guin, R. Mondal; G. Chakraborty, S. Pal, N. D. Paul, *J. Org. Chem.*, **2022**, *87*, 7106−7123. (c) S. Bhatt, M. Rana, A. K. Sharma, H. Joshi, *Asian J. Org. Chem.* 2023, *12*, e202300158.

6.6 Appendix

6.6.1 NMR data of all synthesized compounds

***N-propylaniline (5a)*:** Eluent: Hexane / Diethylether (50:1v/v), Light yellow oil, Yield: 97 mg

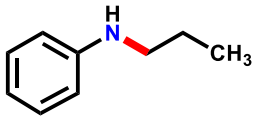

(72%); ^{1}H NMR (400 MHz, $CDCl_3$): δ 7.26 – 7.15 (m, 2H), 6.73 (t, *J* = 7.5 Hz, 1H), 6.65 (d, *J* = 7.9 Hz, 2H), 3.66 (s, 1H), 3.12 (t, *J* = 7.1 Hz, 2H), 1.68 (h, *J* = 7.4 Hz, 2H), 1.03 (t, *J* = 7.5 Hz, 3H). ^{13}C{^{1}H} NMR (101 MHz, $CDCl_3$): δ 148.61, 129.32, 117.20, 112.83, 45.92, 22.83, 11.74.

4-chloro-N-propylaniline (5b): Eluent: Hexane / Diethylether (50:1v/v), Colourless oil, Yield:

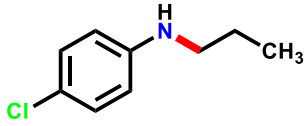

119 mg (70%); ^{1}H NMR (300 MHz, $CDCl_3$): δ 7.23 – 7.09 (m, 2H), 6.63 – 6.47 (m, 2H), 3.46 (br s, 1H), 3.08 (t, *J* = 7.1 Hz, 2H), 1.66 (h, *J* = 7.3 Hz, 2H), 1.03 (t, *J* = 7.4 Hz, 3H). ^{13}C NMR (75 MHz, $CDCl_3$): δ 147.14, 129.07, 121.57, 113.80, 45.96, 22.67, 11.67.

***3-chloro-N-propylaniline (5c)*:** Eluent: Hexane / Diethylether (50:1v/v), Colourless oil, Yield:

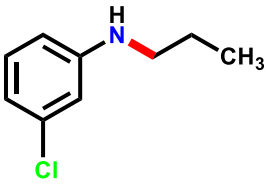

124 mg (73%); ^{1}H NMR (300 MHz, $CDCl_3$): δ 7.09 (t, *J* = 8.0 Hz, 1H), 6.67 (ddd, *J* = 7.9, 2.0, 0.9 Hz, 1H), 6.60 (t, *J* = 2.2 Hz, 1H), 6.49 (ddd, *J* = 8.2, 2.3, 0.9 Hz, 1H), 3.56 (s, 1H), 3.09 (t, *J* = 7.1 Hz, 2H), 1.66 (h, *J* = 7.3 Hz, 2H), 1.03 (t, *J* = 7.4 Hz, 3H). ^{13}C{^{1}H} NMR (75 MHz, $CDCl_3$): δ 149.73, 135.12, 130.24, 116.93, 112.27, 111.16, 45.70, 22.69, 11.70.

***N-butylaniline (5d)*:** Eluent: Hexane / Diethylether (50:1v/v), Light yellow oil, Yield: 118 mg

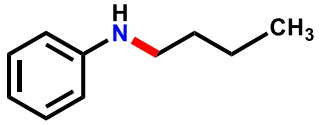

(79%); ^{1}H NMR (300 MHz, $CDCl_3$): δ 7.26 – 7.19 (m, 2H), 6.74 (t, *J* = 7.3 Hz, 1H), 6.68 – 6.62 (m, 2H), 3.63 (s, 1H), 3.16 (t, *J* = 7.0 Hz, 2H), 1.72 – 1.60 (m, 2H), 1.56 – 1.42 (m, 2H), 1.01 (t, *J* = 7.3 Hz, 3H). ^{13}C{^{1}H} NMR (75 MHz, $CDCl_3$): δ 148.68, 129.33, 117.18, 112.80, 43.79, 31.81, 20.43, 14.04.

***N-butyl-4-methylaniline (5e)*:** Eluent: Hexane / Diethylether (50:1v/v), Colourless oil, Yield:

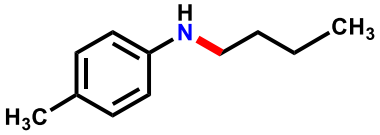

135 mg (83%); ^{1}H NMR (400 MHz, $CDCl_3$): δ 7.08 (d, *J* = 8.1 Hz, 2H), 6.69 – 6.57 (m, 2H), 3.37 (s, 1H), 3.17 (t, *J* = 7.1 Hz, 2H), 2.33 (s, 3H), 1.68 (p, *J* = 7.2 Hz, 2H), 1.51 (h, *J* = 7.3 Hz, 2H), 1.05 (t, *J* = 7.4 Hz, 3H). ^{13}C{^{1}H} NMR (75 MHz, $CDCl_3$): δ 146.39, 129.82, 126.44, 113.07, 44.22, 31.84, 20.48, 20.44, 14.04.

***N-butyl-3-chloroaniline (5f)*:** Eluent: Hexane / Diethylether (50:1v/v), Pale yellow oil, Yield:

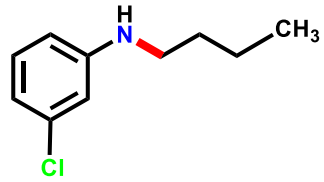

141 mg (77%); ^{1}H NMR (300 MHz, $CDCl_3$): δ 7.11 (t, *J* = 8.0 Hz, 1H), 6.70 (dd, *J* = 8.4, 1.5 Hz, 1H), 6.62 (t, *J* = 2.2 Hz, 1H), 6.50 (ddd, *J* = 8.2, 2.3, 0.9 Hz, 1H), 3.59 (br s, 1H), 3.12 (t, *J* = 7.0 Hz, 2H), 1.73 – 1.57 (m, 2H), 1.47 (dq, *J* = 15.4, 7.1 Hz, 2H), 1.02 (t, *J* = 7.3 Hz, 3H). ^{13}C{^{1}H} NMR (75 MHz, $CDCl_3$): δ 149.73, 135.04, 130.19, 116.82, 112.19, 111.09, 43.53, 31.53, 20.32, 13.95.

***N-butyl-4-chloroaniline (5g)*:** Eluent: Hexane / Diethylether (50:1v/v), Colourless sticky oil,

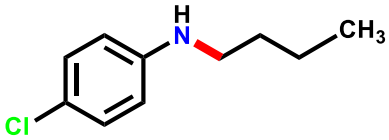

Yield: 139 mg (76%); ^{1}H NMR (400 MHz, $CDCl_3$): δ 7.19 – 7.11 (m, 2H), 6.59 – 6.51 (m, 2H), 3.47 (br s, 1H), 3.10 (t, *J* = 7.1 Hz, 2H), 1.69 – 1.57 (m, 2H), 1.46 (h, *J* = 7.3 Hz, 2H), 1.00 (t, *J* = 7.4 Hz, 3H). ^{13}C{^{1}H} NMR (101 MHz, $CDCl_3$): δ 147.18, 129.11, 121.67, 113.84, 43.92, 31.64, 20.38, 13.99.

***4-bromo-N-butylaniline (5h)*:** Eluent: Hexane / Diethylether (50:1v/v), Colourless oil, Yield:

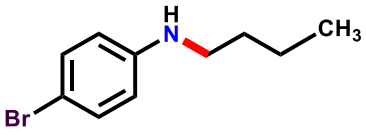

180 mg (79%); ^{1}H NMR (300 MHz, $CDCl_3$): δ 7.34 – 7.22 (m, 2H), 6.57 – 6.45 (m, 2H), 3.50 (br s, 1H), 3.10 (t, *J* = 7.1 Hz, 2H), 1.70 – 1.56 (m, 2H), 1.53 – 1.37 (m, 2H), 1.00 (t, *J* = 7.3 Hz, 3H). ^{13}C{^{1}H} NMR (75 MHz, $CDCl_3$): δ 147.57, 131.93, 114.29, 108.55, 43.75, 31.57, 20.35, 13.99.

***N-hexylaniline (5i)*:** Eluent: Hexane / Diethylether (50:1v/v), Pale yellow oil, Yield: 158 mg

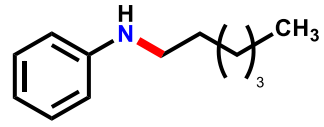

(82%); ^{1}H NMR (400 MHz, $CDCl_3$): δ 7.25 (t, *J* = 7.6 Hz, 2H), 6.72 (dt, *J* = 32.3, 7.4 Hz, 3H), 3.63 (s, 1H), 3.17 (t, *J* = 6.9 Hz, 2H), 1.69 (h, *J* = 6.8 Hz, 2H), 1.43 (tdd, *J* = 15.0, 13.0, 5.5 Hz, 6H), 0.99 (t, *J* = 7.0 Hz, 3H). ^{13}C{^{1}H} NMR (75 MHz, $CDCl_3$): δ 148.65, 129.29, 117.14, 112.78, 44.09, 31.77, 29.65, 26.97, 22.74, 14.15.

***N-hexyl-4-methylaniline (5j)*:** Eluent: Hexane / Diethylether (50:1v/v), Colourless oil, Yield:

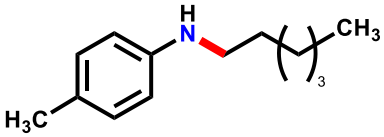

182 mg (88%); ^{1}H NMR (300 MHz, $CDCl_3$): δ 7.04 (d, *J* = 8.1 Hz, 2H), 6.59 (d, *J* = 8.3 Hz, 2H), 3.13 (t, *J* = 7.1 Hz, 2H), 3.06 (s, 1H), 2.29 (s, 3H), 1.53 – 1.29 (m, 8H), 0.96 (t, *J* = 6.5 Hz, 3H). ^{13}C{^{1}H} NMR (75 MHz, $CDCl_3$): δ 146.39, 129.81, 126.41, 113.06, 44.55, 31.79, 29.71, 26.99, 22.76, 20.48, 14.16.

***3-chloro-N-hexylaniline (5k)*:** Eluent: Hexane / Diethylether (50:1v/v), Colourless oil, Yield:

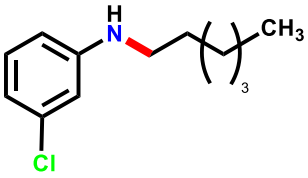

169 mg (80%); ^{1}H NMR (300 MHz, $CDCl_3$): δ 7.11 (t, *J* = 8.0 Hz, 1H), 6.70 (dd, *J* = 7.9, 1.9 Hz, 1H), 6.61 (t, *J* = 2.2 Hz, 1H), 6.50 (dd, *J* = 8.2, 2.3 Hz, 1H), 3.58(s, 1H), 3.11 (t, *J* = 7.1 Hz, 2H), 1.71 – 1.58 (m, 2H), 1.40 (tq, *J* = 8.1, 3.7 Hz, 6H), 0.98 (t, *J* = 7.2 Hz, 3H). ^{13}C{^{1}H} NMR (75 MHz, $CDCl_3$): δ 149.74, 135.06, 130.19, 116.84, 112.21, 111.10, 43.88, 31.70, 29.44, 26.88, 22.72, 14.13.

***4-chloro-N-hexylaniline (5l)*:** Eluent: Hexane / Diethylether (50:1v/v), Colourless oil, Yield:

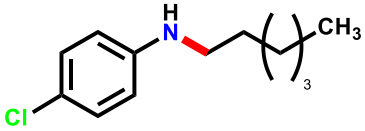

165 mg (78%); ^{1}H NMR (300 MHz, $CDCl_3$): δ 7.24 – 7.06 (m, 2H), 6.67 – 6.46 (m, 2H), 3.45 (s, 1H), 3.09 (t, *J* = 7.1 Hz, 2H), 1.63 (p, *J* = 6.5 Hz, 2H), 1.49 – 1.30 (m, 6H), 0.95 (t, *J* = 6.8 Hz, 3H). ^{13}C{^{1}H} NMR (75 MHz, $CDCl_3$): δ 147.18, 129.12, 121.68, 113.84, 44.26, 31.75, 29.52, 26.93, 22.74, 14.16.

***4-bromo-N-hexylaniline (5m)*:** Eluent: Hexane / Diethylether (50:1v/v), Colourless oil, Yield: 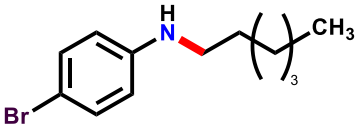 207 mg (81%); ^{1}H NMR (300 MHz, $CDCl_3$): δ 7.37 – 7.17 (m, 2H), 6.66 – 6.37 (m, 2H), 3.52 (s, 1H), 3.09 (t, *J* = 7.1 Hz, 2H), 1.64 (p, *J* = 7.0 Hz, 2H), 1.50 – 1.29 (m, 6H), 0.96 (t, *J* = 6.8 Hz, 3H). ^{13}C{^{1}H} NMR (75 MHz, $CDCl_3$): δ 147.58, 131.94, 114.29, 108.57, 44.09, 31.72, 29.47, 26.91, 22.72, 14.15.

***2,4-difluoro-N-hexylaniline (5n)*:** Eluent: Hexane / Diethylether (50:1v/v), Colourless oil, 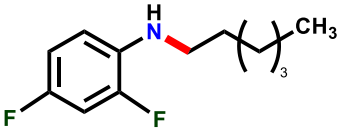 Yield: 149 mg (70%); ^{1}H NMR (400 MHz, $CDCl_3$): δ 6.85 – 6.72 (m, 2H), 6.66 – 6.54 (m, 1H), 3.98 (t, *J* = 6.5 Hz, 1H), 3.12 (t, *J* = 7.1 Hz, 2H), 1.65 (p, *J* = 7.1 Hz, 2H), 1.41 – 1.32 (m, 6H), 0.93 (t, *J* = 6.5 Hz, 3H). ^{13}C{^{1}H} NMR (101 MHz, $CDCl_3$): δ 154.14 (dd, *J* = 236.8, 11.0 Hz), 150.89 (dd, *J* = 241.3, 11.6 Hz), 133.70 (dd, *J* = 11.7, 2.9 Hz), 111.96 (dd, *J* = 8.8, 4.8 Hz), 110.67 (dd, *J* = 21.4, 3.7 Hz), 103.70, 103.45 (d, *J* = 3.8 Hz), 103.21, 44.28, 31.75, 29.57, 26.91, 22.74, 14.16. ^{19}F NMR (377 MHz, $CDCl_3$): δ -126.73, -132.73.

***N-hexylpyridin-2-amine (5o)*:** Eluent: Hexane / Diethylether (40:1v/v), Colourless oil, Yield: 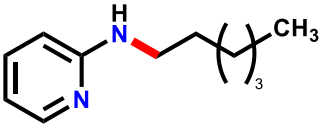 134 mg (69%); ^{1}H NMR (300 MHz, $CDCl_3$): δ 8.11 – 8.05 (m, 1H), 7.43 (ddd, *J* = 8.9, 7.1, 1.9 Hz, 1H), 6.56 (ddd, *J* = 7.1, 5.1, 1.0 Hz, 1H), 6.39 (dt, *J* = 8.4, 1.0 Hz, 1H), 4.61 (s, 1H), 3.35 – 3.18 (m, 2H), 1.75 – 1.56 (m, 2H), 1.43 – 1.27 (m, 6H), 0.91 (t, *J* = 6.5 Hz, 3H). ^{13}C{^{1}H} NMR (101 MHz, $CDCl_3$): δ 159.02, 148.12, 137.65, 112.67, 106.41, 42.46, 31.72, 29.63, 26.87, 22.73, 14.16.

***N-heptylaniline (5p)*:** Eluent: Hexane / Diethylether (50:1v/v), Colourless oil, Yield: 174 mg 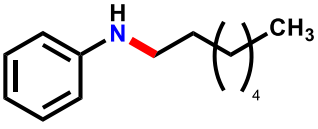 (84%); ^{1}H NMR (300 MHz, $CDCl_3$): 7.33 (q, *J* = 6.4 Hz, 2H), 6.85 (d, *J* = 7.0 Hz, 1H), 6.74 (t, *J* = 6.9 Hz, 2H), 3.61 (s, 1H), 3.24 (t, *J* = 7.1 Hz, 2H), 1.74 (p, *J* = 7.1 Hz, 2H), 1.51 (qt, *J* = 12.8, 6.7 Hz, 8H), 1.08 (t, *J* = 6.6 Hz,

3H).^{13}C NMR (75 MHz, $CDCl_3$): δ 148.67, 129.34, 117.21, 112.83, 44.15, 31.95, 29.72, 29.26, 27.28, 22.76, 14.22.

***N-heptyl-4-methylaniline (5q)*:** Eluent: Hexane / Diethylether (50:1v/v), Colourless oil, Yield: 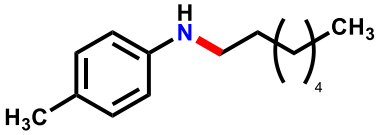 197 mg (89%); ^{1}H NMR (400 MHz, $CDCl_3$): δ 7.13 (dd, *J* = 8.3, 3.7 Hz, 2H), 6.67 (dd, *J* = 8.5, 3.1 Hz, 2H), 3.53 (s, 1H), 3.21 (t, *J* = 7.3 Hz, 2H), 2.39 (s, 3H), 1.73 (qt, *J* = 6.5, 3.2 Hz, 2H), 1.48 (m, 8H), 1.07 (t, *J* = 7.4 Hz, 3H). ^{13}C{^{1}H} NMR (75 MHz, $CDCl_3$): δ 146.41, 129.79, 126.34, 113.01, 44.50, 31.94, 29.75, 29.26, 27.28, 22.74, 20.46, 14.19.

***4-chloro-N-heptylaniline (5r)*:** Eluent: Hexane / Diethylether (50:1v/v), Colourless oil, Yield: 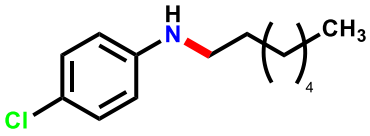 180 mg (80%); ^{1}H NMR (400 MHz, $CDCl_3$): δ 7.14 (d, *J* = 8.8 Hz, 2H), 6.63 – 6.47 (m, 2H), 3.41 (br s, 1H), 3.09 (t, *J* = 7.2 Hz, 2H), 1.63 (p, *J* = 6.9 Hz, 2H), 1.49 – 1.27 (m, 8H), 0.94 (t, *J* = 7.2 Hz, 3H). ^{13}C NMR (75 MHz, $CDCl_3$): δ 147.19, 129.11, 121.65, 113.82, 44.24, 31.92, 29.56, 29.22, 27.22, 22.74, 14.20.

***4-bromo-N-heptylaniline (5s)*:** Eluent: Hexane / Diethylether (50:1v/v), Colourless oil, Yield: 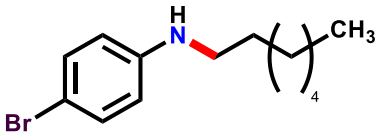 221 mg (82%); ^{1}H NMR (400 MHz, $CDCl_3$): δ 7.36 – 7.22 (m, 2H), 6.61 – 6.41 (m, 2H), 3.50 (br s, 1H), 3.09 (t, *J* = 7.1 Hz, 2H), 1.62 (q, *J* = 7.2 Hz, 2H), 1.48 – 1.33 (m, 8H), 0.94 (t, *J* = 6.6 Hz , 3H). ^{13}C{^{1}H} NMR (75 MHz, $CDCl_3$): δ 147.54, 131.87, 114.22, 108.45, 44.02, 31.87, 29.46, 29.17, 27.16, 22.69, 14.16.

***N-octylaniline (5t)*:** Eluent: Hexane / Diethylether (50:1v/v), Pale yellow oil, Yield: 180 mg 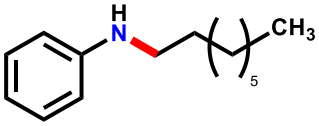 (88%); ^{1}H NMR (300 MHz, $CDCl_3$): δ 7.25 – 7.18 (m, 2H), 6.73 (t, *J* = 7.3 Hz, 1H), 6.67 – 6.61 (m, 2H), 3.61 (s, 1H), 3.14 (t, *J* = 7.1 Hz, 2H), 1.72 – 1.60 (m, 2H), 1.49 – 1.29 (m, 10H), 0.94 (t, *J* = 6.4 Hz, 3H). ^{13}C{^{1}H} NMR

(101 MHz, $CDCl_3$): δ 148.65, 129.29, 117.14, 112.77, 44.09, 31.95, 29.69, 29.54, 29.39, 27.30, 22.78, 14.20.

***4-methyl-N-octylaniline (5u)*:** Eluent: Hexane / Diethylether (50:1v/v), Colourless oil, Yield:

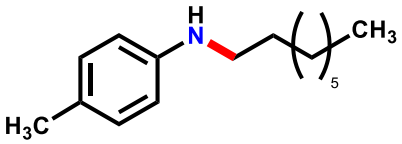

214 mg (91%); ^{1}H NMR (300 MHz, $CDCl_3$): δ 7.04 (d, *J* = 8.1 Hz, 2H), 6.67 – 6.51 (m, 2H), 3.26 (br s, 1H), 3.13 (t, *J* = 7.1 Hz, 2H), 2.29 (s, 3H), 1.66 (p, *J* = 7.0 Hz, 2H), 1.53 – 1.30 (m, 10H), 0.95 (t, *J* = 6.5 Hz, 3H). ^{13}C{^{1}H} NMR (101 MHz, $CDCl_3$): δ 146.40, 129.80, 126.37, 113.03, 44.52, 31.96, 29.74, 29.56, 29.40, 27.32, 22.78, 20.47, 14.21.

***4-methoxy-N-octylaniline(5v)*:** Eluent: Hexane / Diethylether (50:1v/v), Pale yellow oil,

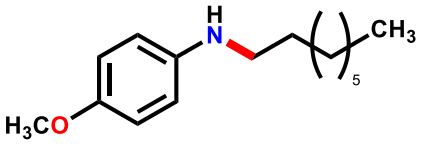

Yield: 216 mg (86%); ^{1}H NMR (400 MHz, $CDCl_3$): δ 6.88 – 6.79 (m, 2H), 6.69 – 6.59 (m, 2H), 3.79 (s, 3H), 3.21 (br s, 1H), 3.10 (t, *J* = 7.2 Hz, 2H), 1.65 (p, *J* = 7.1 Hz, 2H), 1.50 – 1.29 (m, 10H), 0.98 (t, *J* = 6.5 Hz, 3H). ^{13}C{^{1}H} NMR (75 MHz, $CDCl_3$): δ 151.99, 142.94, 114.92, 114.05, 55.78, 45.07, 31.90, 29.75, 29.52, 29.34, 27.28, 22.73, 14.15.

***4-chloro-N-octylaniline (5w)*:** Eluent: Hexane / Diethylether (50:1v/v), Colourless oil, Yield:

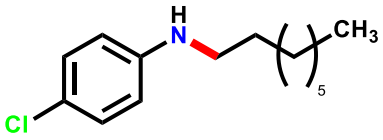

196 mg (82%); ^{1}H NMR (300 MHz, $CDCl_3$): δ 7.19 – 7.11 (m, 2H), 6.59 – 6.51 (m, 2H), 3.59 (s, 1H), 3.09 (t, *J* = 7.1 Hz, 2H), 1.63 (q, *J* = 7.5 Hz, 2H), 1.44 – 1.30 (m, 10H), 0.96 (t, *J* = 6.2 Hz, 3H). ^{13}C{^{1}H} NMR (101 MHz, $CDCl_3$): δ 147.18, 129.11, 121.64, 113.82, 44.24, 31.94, 29.55, 29.52, 29.38, 27.26, 22.78, 14.22.

***3-chloro-N-octylaniline (5x)*:** Eluent: Hexane / Diethylether (50:1v/v), Colourless oil, Yield:

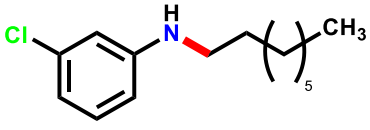

203 mg (85%); ^{1}H NMR (400 MHz, $CDCl_3$): δ 7.10 (d, *J* = 8.1 Hz, 1H), 6.71 (dd, *J* = 7.9, 2.0 Hz, 1H), 6.62 (t, *J* = 2.2 Hz, 1H), 6.50 (dd, *J* = 8.2, 2.4 Hz, 1H), 3.66 (br, s, 1H), 3.11 (t, *J* = 7.2 Hz, 2H), 1.65 (p, *J* = 7.1 Hz,

2H), 1.48 – 1.34 (m, 10H), 0.98 (t, J = 6.8 Hz, 3H). $^{13}C\{^{1}H\}$ NMR (75 MHz, $CDCl_3$): δ 149.74, 135.08, 130.20, 116.86, 112.23, 111.11, 43.89, 31.94, 29.49, 29.49, 29.37, 27.22, 22.78, 14.21.

***2,4-difluoro-N-octylaniline (5y)*:** Eluent: Hexane / Diethylether (50:1v/v), Colourless oil,

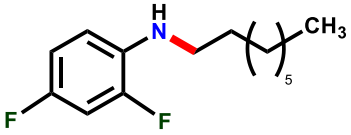

Yield: 180 mg (75%); ^{1}H NMR (400 MHz, $CDCl_3$): δ 6.88 – 6.69 (m, 2H), 6.68 – 6.52 (m, 1H), 3.97 (t, J = 6.5 Hz, 1H), 3.12 (t, J = 7.1 Hz, 2H), 1.71 – 1.60 (m, 2H), 1.34 – 1.28 (m, 10H), 0.91 (t, J = 6.7 Hz, 3H). ^{19}F NMR (377 MHz, $CDCl_3$): δ -126.74, -132.73. $^{13}C\{^{1}H\}$ NMR (101 MHz, $CDCl_3$): δ 154.14 (dd, J = 236.9, 11.2 Hz), 150.89 (dd, J = 241.3, 11.6 Hz), 133.71 (dd, J = 11.8, 2.7 Hz), 111.95 (dd, J = 8.7, 4.7 Hz), 110.66 (dd, J = 21.5, 3.8 Hz), 103.44 (dd, J = 26.7, 22.8 Hz), 44.27, 31.96, 29.60, 29.53, 29.39, 27.24, 22.80, 14.22.

2,4-dichloro-N-octylaniline (5z): Eluent: Hexane / Diethylether (50:1v/v), Colourless oil,

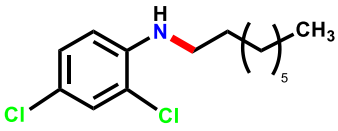

Yield: 211 mg (78%); ^{1}H NMR (400 MHz, $CDCl_3$): δ 7.26 (d, J = 2.4 Hz, 1H), 7.11 (dd, J = 8.8, 2.4 Hz, 1H), 6.58 (d, J = 8.8 Hz, 1H), 4.25 (s, 1H), 3.15 (t, J = 7.1 Hz, 2H), 1.72 – 1.63 (m, 2H), 1.39 – 1.26 (m, 10H), 0.92 (t, J = 6.8 Hz, 3H). $^{13}C\{^{1}H\}$ NMR (101 MHz, $CDCl_3$): δ 143.14, 128.77, 127.86, 120.84, 119.30, 111.74, 43.95, 31.95, 29.49, 29.37, 27.22, 22.79, 14.22.

***N-nonylaniline (5aa)*:** Eluent: Hexane / Diethylether (50:1v/v), Colourless oil, Yield: 200 mg

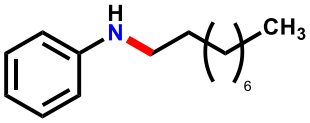

(91%); ^{1}H NMR (300 MHz, $CDCl_3$): δ 7.35 – 7.23 (m, 2H), 6.81 (t, J = 7.1 Hz, 1H), 6.76 – 6.66 (m, 2H), 3.57 (br s, 1H), 3.21 (t, J = 7.1 Hz, 2H), 1.73 (p, J = 7.3 Hz, 2H), 1.53 – 1.38 (m, 12H), 1.04 (t, J = 7.4 Hz, 3H). $^{13}C\{^{1}H\}$ NMR (75 MHz, $CDCl_3$): δ 148.66, 129.32, 117.18, 112.81, 44.12, 32.01, 29.71, 29.69, 29.59, 29.41, 27.31, 22.80, 14.23.

***4-methyl-N-nonylaniline (5ab)*:** Eluent: Hexane / Diethylether (50:1v/v), Colourless oil, 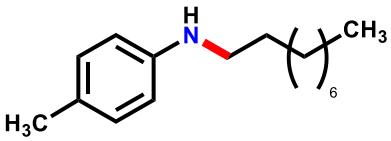 Yield: 219 mg (94%); ^{1}H NMR (300 MHz, $CDCl_3$): δ 7.19 (d, *J* = 8.3 Hz, 2H), 6.81 – 6.63 (m, 2H), 3.58 (s, 1H), 3.26 (t, *J* = 7.1 Hz, 2H), 2.46 (s, 3H), 1.79 (p, *J* = 7.0 Hz, 2H), 1.62 – 1.58 (m, 12H), 1.14 (t, *J* = 7.8 Hz, 3H). ^{13}C{^{1}H} NMR (75 MHz, $CDCl_3$): δ 146.42, 129.81, 126.39, 113.04, 44.54, 32.02, 29.76, 29.70, 29.61, 29.41, 27.32, 22.80, 20.48, 14.23.

***4-methoxy-N-nonylaniline (5ac)*:** Eluent: Hexane / Diethylether (10:1v/v), Pale yellow oil, 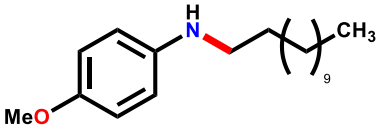 Yield: 244 mg (92%); ^{1}H NMR (400 MHz, $CDCl_3$): δ 6.86 – 6.79 (m, 2H), 6.66 – 6.58 (m, 2H), 3.78 (s, 3H), 3.21 (br s, 1H), 3.10 (t, *J* = 7.1 Hz, 2H), 1.71 – 1.57 (m, 2H), 1.45 – 1.29 (m, 12H), 0.94 (t, *J* = 6.4 Hz, 3H). ^{13}C{^{1}H} NMR (101 MHz, $CDCl_3$): δ 152.04, 142.96, 114.97, 114.10, 55.86, 45.13, 31.98, 29.79, 29.67, 29.59, 29.38, 27.31, 22.77, 14.20.

***4-chloro-N-nonylaniline (5ad)*:** Eluent: Hexane / Diethylether (50:1v/v), Colourless oil, Yield: 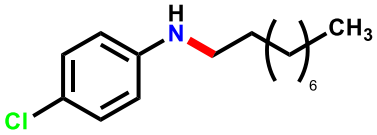 215 mg (85%); ^{1}H NMR (300 MHz, $CDCl_3$): δ 7.24 – 7.04 (m, 2H), 6.63 – 6.48 (m, 2H), 3.58 (s, 1H), 3.09 (t, J = 7.1 Hz, 2H), 1.63 (q, J = 7.5 Hz, 2H), 1.41 – 1.31 (m, 12H), 0.97 (t, *J* = 6.5 Hz, 3H). ^{13}C{^{1}H} NMR (75 MHz, $CDCl_3$): δ 147.19, 129.12, 121.66, 113.83, 44.25, 32.00, 29.68, 29.58, 29.56, 29.40, 27.26, 22.80, 14.23.

***2,4-difluoro-N-nonylaniline (5ae)*:** Eluent: Hexane / Diethylether (50:1v/v), Colourless oil, 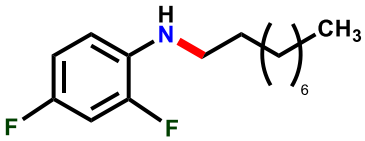 Yield: 204 mg (80%); ^{1}H NMR (300 MHz, $CDCl_3$): δ 6.86 – 6.71 (m, 2H), 6.62 (td, *J* = 9.4, 5.4 Hz, 1H), 3.97 (t, *J* = 6.0 Hz, 1H), 3.12 (t, *J* = 7.1 Hz, 2H), 1.65 (p, *J* = 6.8 Hz, 2H), 1.41 – 1.28 (m, 13H), 0.91 (t, *J* = 6.5 Hz, 3H). ^{19}F NMR (282 MHz, $CDCl_3$): δ -126.74, -132.73. ^{13}C{^{1}H} NMR (75 MHz, $CDCl_3$): δ 155.82 – 152.56 (m), 152.53 – 149.18 (m), 133.71 (dd, *J* = 11.7, 2.9 Hz), 111.95 (dd, *J* = 8.7,

4.8 Hz), 110.66 (dd, *J* = 21.5, 3.7 Hz), 103.44 (dd, *J* = 26.6, 22.8 Hz), 44.26, 32.02, 29.68, 29.61, 29.57, 29.41, 27.23, 22.81, 14.23.

***2,4-dichloro-N-nonylaniline (5af)*:** Eluent: Hexane / Diethylether (50:1v/v), Colourless oil,

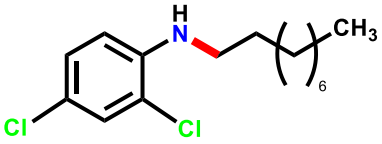

Yield: 248 mg (86%); ^{1}H NMR (300 MHz, $CDCl_3$): δ 7.26 (d, *J* = 2.4 Hz, 1H), 7.11 (dd, *J* = 8.7, 2.4 Hz, 1H), 6.58 (d, *J* = 8.7 Hz, 1H), 4.25 (s, 1H), 3.15 (t, *J* = 7.1 Hz, 2H), 1.79 – 1.56 (m, 2H), 1.51 – 1.22 (m, 12H), 0.98 – 0.86 (m, 3H). ^{13}C{^{1}H} NMR (75 MHz, $CDCl_3$): δ 143.09, 128.74, 127.83, 120.79, 119.25, 111.70, 43.91, 32.01, 29.66, 29.53, 29.40, 29.34, 27.21, 22.82, 14.25.

***N-dodecylaniline (5ag)*:** Eluent: Hexane / Diethylether (50:1v/v), Colourless oil, Yield: 235

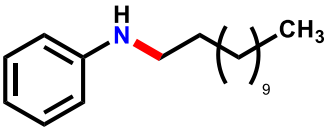

mg (90%); ^{1}H NMR (400 MHz, $CDCl_3$): δ 7.28 (t, *J* = 7.8 Hz, 2H), 6.80 (t, *J* = 7.4 Hz, 1H), 6.70 (d, *J* = 8.0 Hz, 2H), 3.59 (s, 1H), 3.19 (t, *J* = 7.2 Hz, 2H), 1.71 (p, *J* = 7.1 Hz, 2H), 1.61 – 1.30 (m, 18H), 1.02 (t, *J* = 6.9 Hz, 3H). ^{13}C{^{1}H} NMR (75 MHz, $CDCl_3$): δ 148.61, 129.34, 117.25, 112.87, 44.19, 32.06, 29.81, 29.78, 29.76, 29.75, 29.70, 29.60, 29.50, 27.32, 22.84, 14.26.

***N-dodecyl-4-methylaniline (5ah)*:** Eluent: Hexane / Diethylether (50:1v/v), Colourless

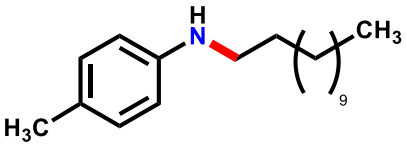

crystalline solid, Yield: 261 mg (95%); ^{1}H NMR (400 MHz, $CDCl_3$) δ 7.02 (d, *J* = 8.1 Hz, 2H), 6.57 (d, *J* = 8.3 Hz, 2H), 3.46 (s, 1H), 3.11 (t, *J* = 7.1 Hz, 2H), 2.27 (s, 3H), 1.63 (p, *J* = 7.0 Hz, 2H), 1.44 – 1.27 (m, 18H), 0.93 (t, *J* = 6.7 Hz, 3H). ^{13}C{^{1}H} NMR (101 MHz, $CDCl_3$): δ 146.40, 129.81, 126.41, 113.06, 44.55, 32.06, 29.81, 29.78, 29.75, 29.61, 29.50, 27.33, 22.83, 20.49, 14.25.

***3-chloro-N-dodecylaniline (5ai)*:** Eluent: Hexane / Diethylether (50:1v/v), Colourless sticky

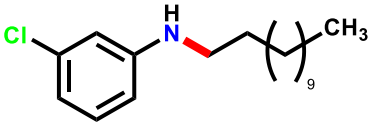

oil, Yield: 257 mg (87%); ^{1}H NMR (300 MHz, $CDCl_3$): δ 7.09 (t, *J* = 8.0 Hz, 1H), 6.68 (ddd, *J* = 7.9, 2.0, 0.9 Hz, 1H), 6.60 (t, *J* = 2.2 Hz, 1H), 6.48 (ddd, *J* = 8.2, 2.3, 0.9 Hz, 1H), 3.46 (br s, 1H) 3.10 (t, *J* = 7.1 Hz, 2H),

1.72 – 1.56 (m, 2H), 1.43 – 1.32 (m, 18H). 0.94 (t, J = 7.2 Hz, 3H). $^{13}C\{^{1}H\}$ NMR (75 MHz, $CDCl_3$): δ 149.74, 135.09, 130.18, 116.86, 112.23, 111.08, 43.89, 32.06, 29.81, 29.78, 29.75, 29.73, 29.68, 29.55, 29.50, 27.24, 22.83, 14.24.

***4-chloro-N-dodecylaniline (5aj)*:** Eluent: Hexane / Diethylether (50:1v/v), Colourless

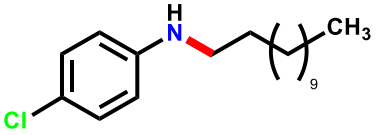

crystalline solid, Yield: 251 mg (85%); ^{1}H NMR (300 MHz, $CDCl_3$): δ 7.21 – 7.08 (m, 2H), 6.60 – 6.48 (m, 2H), 4.09 (t, J = 6.8 Hz, 1H), 3.09 (t, J = 7.1 Hz, 2H), 1.63 (q, J = 7.2 Hz, 2H), 1.44–1.30 (m, 18H), 0.93 (t, J = 6.3 Hz, 3H). $^{13}C\{^{1}H\}$ NMR (75 MHz, $CDCl_3$): δ 147.18, 129.10, 121.66, 113.81, 44.24, 32.06, 29.80, 29.77, 29.74, 29.72, 29.66, 29.56, 29.49, 27.26, 22.83, 14.24.

***4-bromo-N-dodecylaniline (5ak)*:** Eluent: Hexane / Diethylether (50:1v/v), Colourless

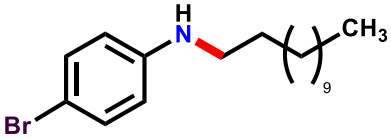

crystalline solid, Yield: 303 mg (89%); ^{1}H NMR (300 MHz, $CDCl_3$) δ 7.33 – 7.20 (m, 2H), 6.58 – 6.44 (m, 2H), 3.64 (br s, 1H), 3.09 (t, J = 7.1 Hz, 2H), 1.74 – 1.57 (m, 2H), 1.31–1.39 (m, 18H), 0.93 (t, J = 6.5 Hz, 3H). $^{13}C\{^{1}H\}$ NMR (75 MHz, $CDCl_3$): δ 147.59, 131.97, 114.30, 108.60, 44.11, 32.06, 29.80, 29.77, 29.74, 29.72, 29.56, 29.53, 29.49, 27.25, 22.83, 14.25.

***N-dodecyl-2,4-difluoroaniline (5al)*:** Eluent: Hexane / Diethylether (50:1v/v), Colourless

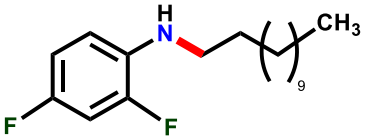

sticky oil, Yield: 235 mg (79%); ^{1}H NMR (300 MHz, $CDCl_3$): δ 6.89 – 6.71 (m, 2H), 6.63 (td, J = 9.4, 5.4 Hz, 1H), 3.69 (br s, 1H), 3.13 (t, J = 7.1 Hz, 2H), 1.75 – 1.59 (m, 2H), 1.34 (d, J = 10.2 Hz, 10H), 0.94 (t, J = 7.2 Hz, 3H). ^{19}F NMR (377 MHz, $CDCl_3$): δ -126.57, -132.62. $^{13}C\{^{1}H\}$ NMR (75 MHz, $CDCl_3$): δ 155.91 – 152.58 (m), 152.57 – 149.20 (m), 133.64 (dd, J = 11.7, 2.8 Hz), 111.99 (dd, J = 8.8, 4.7 Hz), 110.66 (dd, J = 21.5, 3.7 Hz), 103.44 (dd, J = 26.6, 22.8 Hz), 44.30, 32.09, 29.88, 29.83, 29.80, 29.77, 29.74, 29.59, 29.52, 27.25, 22.85, 14.24.

***N-dodecylpyridin-2-amine (5am)*:** Eluent: Hexane / Diethylether (50:1v/v), White crystalline

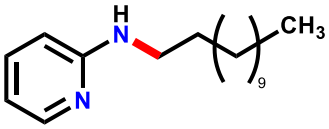

solid, Yield: 189 mg (72%); ^{1}H NMR (400 MHz, $CDCl_3$): δ 8.07 (dd, J = 5.2, 1.8 Hz, 1H), 7.41 (ddd, J = 8.7, 7.2, 1.9 Hz, 1H), 6.55 (dd, J = 7.1, 5.1 Hz, 1H), 6.37 (d, J = 8.4 Hz, 1H), 4.61 (t, J = 5.6 Hz, 1H), 3.24 (q, J = 6.6 Hz, 2H), 1.68 – 1.56 (m, 2H), 1.46 – 1.19 (m, 18H), 0.89 (t, J = 6.7 Hz, 3H). ^{13}C{^{1}H} NMR (75 MHz, $CDCl_3$): δ 159.03, 148.18, 137.55, 112.63, 106.37, 42.42, 32.03, 29.76, 29.74, 29.71, 29.66, 29.58, 29.52, 29.46, 27.19, 22.80, 14.22.

***N-dodecyl-4-methoxyaniline (5an)*:** Eluent: Hexane / Diethylether (18:1v/v), Yellow oil, ^{1}H

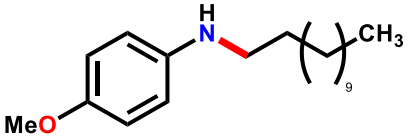

NMR (400 MHz, $CDCl_3$): δ 6.93 – 6.77 (m, 2H), 6.69 – 6.55 (m, 2H), 3.79 (s, 3H), 3.19 (s, 1H), 3.10 (t, J = 7.1 Hz, 2H), 1.65 (p, J = 7.1 Hz, 2H), 1.50 – 1.26 (m, 18H), 0.96 (t, J = 6.7 Hz, 3H). ^{13}C{^{1}H} NMR (75 MHz, $CDCl_3$): δ 152.01, 142.96, 114.93, 114.05, 55.80, 45.09, 32.02, 29.77, 29.74, 29.72, 29.73, 29.59, 29.45, 27.30, 22.78, 14.19.

2,4-dichloro-N-dodecylaniline (5ao): Eluent: Hexane / Diethylether (60:1v/v), Colourless oil,

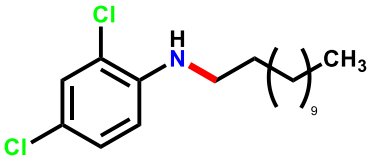

^{1}H NMR (300 MHz, $CDCl_3$): δ 7.26 (d, J = 2.4 Hz, 1H), 7.11 (dd, J = 8.7, 2.4 Hz, 1H), 6.57 (d, J = 8.8 Hz, 1H), 4.25 (s, 1H), 3.13 (t, J = 8.1 Hz, 2H), 1.75 – 1.60 (m, 2H), 1.42 – 1.29 (m, 18H), 0.93 (t, J = 6.4 Hz, 3H). ^{13}C{^{1}H} NMR (101 MHz, $CDCl_3$): δ 143.10, 128.75, 127.84, 120.81, 119.27, 111.71, 43.92, 32.08, 29.81, 29.79, 29.75, 29.71, 29.54, 29.51, 29.35, 27.22, 22.85, 14.27.

N-(cyclohexylmethyl)aniline (5ap): Eluent: Hexane / Diethylether (50:1v/v), Pale yellow

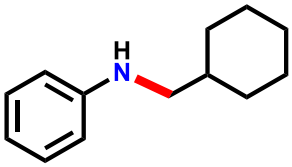

coloured sticky oil, Yield: 125 mg (66%); ^{1}H NMR (300 MHz, $CDCl_3$): δ 7.36 – 7.16 (m, 2H), 6.77 (q, J = 6.5 Hz, 1H), 6.72 – 6.58 (m, 2H), 3.59 (s, 1H), 3.03 (d, J = 6.6 Hz, 2H), 2.04 – 1.74 (m, 5H), 1.72 – 1.57 (m, 1H), 1.31

(qd, *J* = 12.0, 6.7 Hz, 3H), 1.08 (t, *J* = 10.2 Hz, 2H). $^{13}C\{^{1}H\}$ NMR (101 MHz, $CDCl_3$): δ 148.73, 129.33, 117.01, 112.76, 50.74, 37.68, 31.43, 26.71, 26.10.

***N-(cyclohexylmethyl)-4-methylaniline (5aq)*:** Eluent: Hexane / Diethylether (50:1v/v), Pale

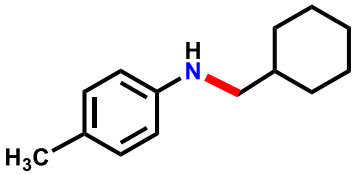

yellow coloured oil, Yield: 142 mg (70%); ^{1}H NMR (300 MHz, $CDCl_3$): δ 7.10 (dd, *J* = 8.4, 2.4 Hz, 2H), 6.73 – 6.56 (m, 2H), 3.54 (s, 1H), 3.05 (d, *J* = 6.7 Hz, 2H), 2.36 (d, *J* = 2.7 Hz, 3H), 2.10 – 1.57 (m, 6H), 1.52 – 1.21 (m, 3H), 1.09 (q, *J* = 11.8 Hz, 2H). $^{13}C\{^{1}H\}$ NMR (75 MHz, $CDCl_3$): δ 146.48, 129.76, 126.09, 112.89, 51.06, 37.63, 31.40, 26.70, 26.08, 20.44.

***N-(cyclohexylmethyl)-4-methoxyaniline (5ar)*:** ^{1}H NMR (400 MHz, $CDCl_3$): δ 6.85 – 6.79 (m,

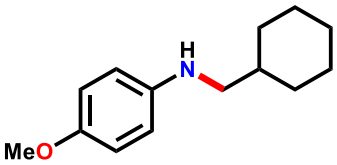

2H), 6.63 – 6.57 (m, 2H), 3.78 (s, 3H), 3.16 (br s, 1H) 2.94 (d, *J* = 6.7 Hz, 2H), 1.91 – 1.69 (m, 5H), 1.68 – 1.53 (m, 1H), 1.38 – 1.16 (m, 3H), 1.01 (q, *J* = 12.0 Hz, 2H). $^{13}C\{^{1}H\}$ NMR (75 MHz, $CDCl_3$): δ 151.89, 143.09, 114.99, 113.98, 55.91, 51.73, 37.69, 31.42, 26.70, 26.09.

***4-chloro-N-(cyclohexylmethyl)aniline (5as)*:** Eluent: Hexane / Diethylether (50:1v/v), Pale

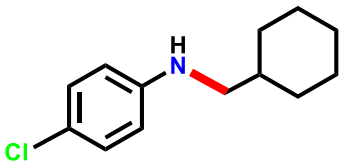

yellow coloured oil, Yield: 134 mg (70%); ^{1}H NMR (400 MHz, $CDCl_3$): δ 7.24 – 7.08 (m, 2H), 6.63 – 6.47 (m, 2H), 3.58 (br s, 1H), 2.94 (d, *J* = 6.7 Hz, 2H), 1.75 (ddd, *J* = 25.7, 19.4, 10.1 Hz, 5H), 1.58 (dqd, *J* = 11.3, 7.6, 3.2 Hz, 1H), 1.26 (dt, *J* = 18.7, 6.4 Hz, 3H), 1.05 – 0.94 (m, 2H). $^{13}C\{^{1}H\}$ NMR (75 MHz, $CDCl_3$): δ 147.27, 129.10, 121.46, 113.78, 50.82, 37.61, 31.37, 26.65, 26.06.

***2,4-dichloro-N-(cyclohexylmethyl)aniline (5at)*:** ^{1}H NMR (300 MHz, $CDCl_3$): δ 7.26 (d, *J* =

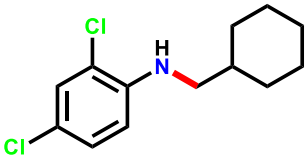

2.4 Hz, 1H), 7.11 (dd, *J* = 8.8, 2.4 Hz, 1H), 6.57 (d, *J* = 8.8 Hz, 1H), 4.36 (s, 1H), 3.00 (d, *J* = 6.7 Hz, 2H), 1.90 – 1.71 (m, 5H), 1.67 – 1.56 (m, 1H), 1.35 – 1.21 (m, 3H), 1.10 – 0.97 (m, 2H). $^{13}C\{^{1}H\}$ NMR (75 MHz, $CDCl_3$): δ 143.15, 128.71, 127.78, 120.58, 119.21, 111.69, 50.41, 37.44, 31.32, 26.61, 26.03.

***N-benzylaniline (7a)*:** Eluent: Hexane / Diethylether (50:1v/v), Colourless oil, Yield: 204 mg (80%); ^{1}H NMR (400 MHz, $CDCl_3$): δ 7.43 (d, *J* = 8.5 Hz, 4H), 7.36 (d, *J* = 6.9 Hz, 1H), 7.26 (d, *J* = 16.7 Hz, 2H), 6.80 (t, *J* = 7.6 Hz, 1H), 6.71 (d, *J* = 7.9 Hz, 2H), 4.39 (s, 2H), 4.09 (s, 1H). ^{13}C{^{1}H} NMR (75 MHz, $CDCl_3$): δ 148.26, 139.55, 129.37, 128.74, 127.61, 127.33, 117.66, 112.95, 48.41.

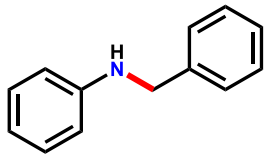

N-(4-methylbenzyl)aniline (7b): ^{1}H NMR (300 MHz, $CDCl_3$): δ 7.34 – 7.27 (m, 2H), 7.26 – 7.16 (m, 4H), 6.75 (t, *J* = 7.3 Hz, 1H), 6.71 – 6.64 (m, 2H), 4.32 (s, 2H), 4.01 (s, 1H), 2.39 (s, 3H). ^{13}C{^{1}H} NMR (75 MHz, $CDCl_3$): δ 148.35, 136.98, 136.48, 129.42, 129.37, 127.64, 117.60, 112.95, 48.19, 21.22.

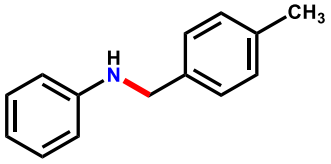

N-(4-chlorobenzyl)aniline (7c): ^{1}H NMR (400 MHz, $CDCl_3$): δ 7.34 (d, *J* = 1.7 Hz, 4H), 7.24 – 7.17 (m, 2H), 6.76 (t, *J* = 7.4 Hz, 1H), 6.68 – 6.60 (m, 2H), 4.34 (s, 2H), 4.09 (s, 1H). ^{13}C{^{1}H} NMR (75 MHz, $CDCl_3$): δ 147.96, 138.13, 132.99, 129.43, 128.87, 128.82, 117.93, 113.02, 47.74.

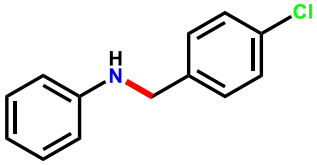

***N-benzyl-4-chloroaniline (7d)*:** ^{1}H NMR (300 MHz, $CDCl_3$): δ 7.40 (dd, *J* = 8.0, 1.6 Hz, 4H), 7.38 – 7.32 (m, 1H), 7.21 – 7.13 (m, 2H), 6.64 – 6.55 (m, 2H), 4.35 (s, 2H), 4.11 (s, 1H). ^{13}C{^{1}H} NMR (75 MHz, $CDCl_3$): δ 146.70, 138.99, 129.08, 128.73, 127.43, 127.38, 122.00, 113.96, 48.28.

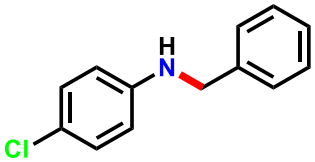

***4-chloro-N-(4-chlorobenzyl)aniline (7e)*:** ^{1}H NMR (400 MHz, $CDCl_3$): δ 7.32 (q, *J* = 8.9 Hz, 4H), 7.13 (d, *J* = 8.2 Hz, 2H), 6.55 (d, *J* = 8.3 Hz, 2H), 4.31 (s, 2H). ^{13}C{^{1}H} NMR (101 MHz, $CDCl_3$): δ 146.29, 137.48, 133.22, 129.26, 128.97, 128.79, 122.68, 114.24, 47.87.

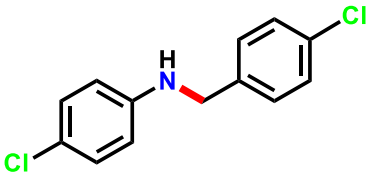

***N-benzylpyridin-2-amine (7f)*:** ^{1}H NMR (400 MHz, $CDCl_3$): δ 8.12 (d, *J* = 5.0 Hz, 1H), 7.45 – 7.39 (m, 2H), 7.38 – 7.26 (m, 4H), 6.61 (t, *J* = 6.2 Hz, 1H), 6.39 (d, *J* = 8.4 Hz, 1H), 4.96 (s, 1H), 4.53 (d, *J* = 5.7 Hz, 2H). ^{13}C{^{1}H} NMR (101 MHz, $CDCl_3$): δ 158.73, 148.32, 139.26, 137.63, 128.76, 127.52, 127.37, 113.29, 106.91, 46.44.

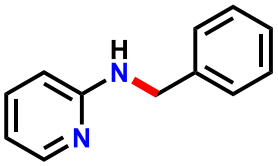

***N-(4-methylbenzyl)pyridin-2-amine (7g)*:** ^{1}H NMR (400 MHz, $CDCl_3$): δ 8.12 (d, *J* = 6.9 Hz, 1H), 7.42 (t, *J* = 8.1 Hz, 1H), 7.27 (dd, *J* = 7.0, 2.5 Hz, 3H), 7.17 (d, *J* = 9.2 Hz, 2H), 6.64 – 6.58 (m, 1H), 6.39 (dd, *J* = 8.5, 2.5 Hz, 1H), 4.90 (s, 1H), 4.47 (q, *J* = 2.5 Hz, 2H), 2.36 (s, 3H). ^{13}C{^{1}H} NMR (101 MHz, $CDCl_3$): δ 158.76, 148.27, 137.63, 137.02, 136.13, 129.43, 127.51, 113.20, 106.86, 46.23, 21.23.

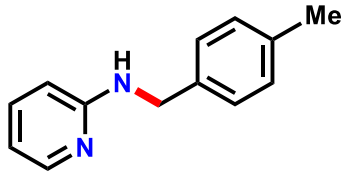

***N-(naphthalen-1-ylmethyl)pyridin-2-amine (7h)*:** ^{1}H NMR (400 MHz, $CDCl_3$): δ 8.26 – 8.03 (m, 2H), 7.97 – 7.77 (m, 2H), 7.50 (ddd, *J* = 39.0, 9.5, 4.9 Hz, 5H), 6.65 (d, *J* = 6.6 Hz, 1H), 6.42 (dd, *J* = 8.5, 2.5 Hz, 1H), 5.19 (s, 1H), 4.97 (s, 2H). ^{13}C{^{1}H} NMR (101 MHz, $CDCl_3$): δ 158.59, 147.92, 137.84, 134.19, 133.97, 131.55, 128.90, 128.30, 126.49, 125.98, 125.82, 125.63, 123.57, 113.18, 107.26, 44.46.

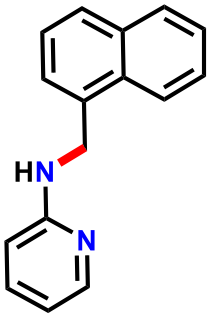

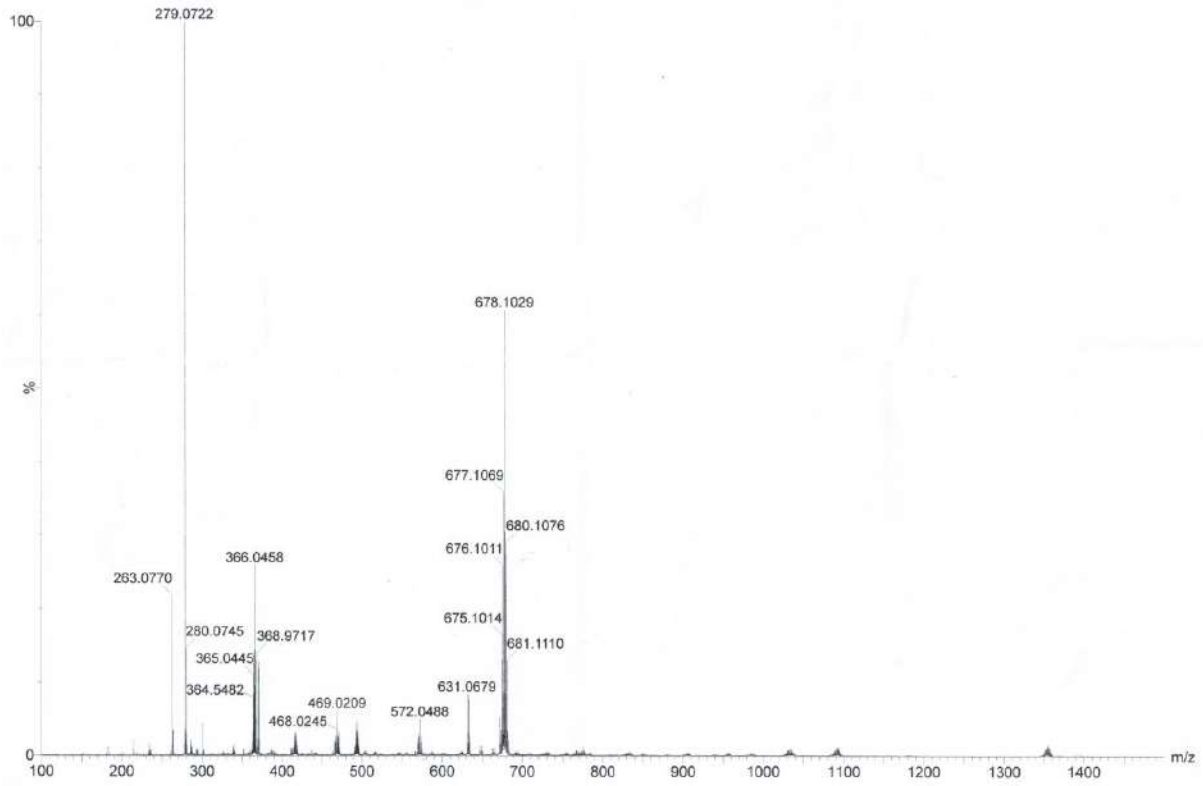

Figure 6.6.A1: HRMS Spectrum of **2**

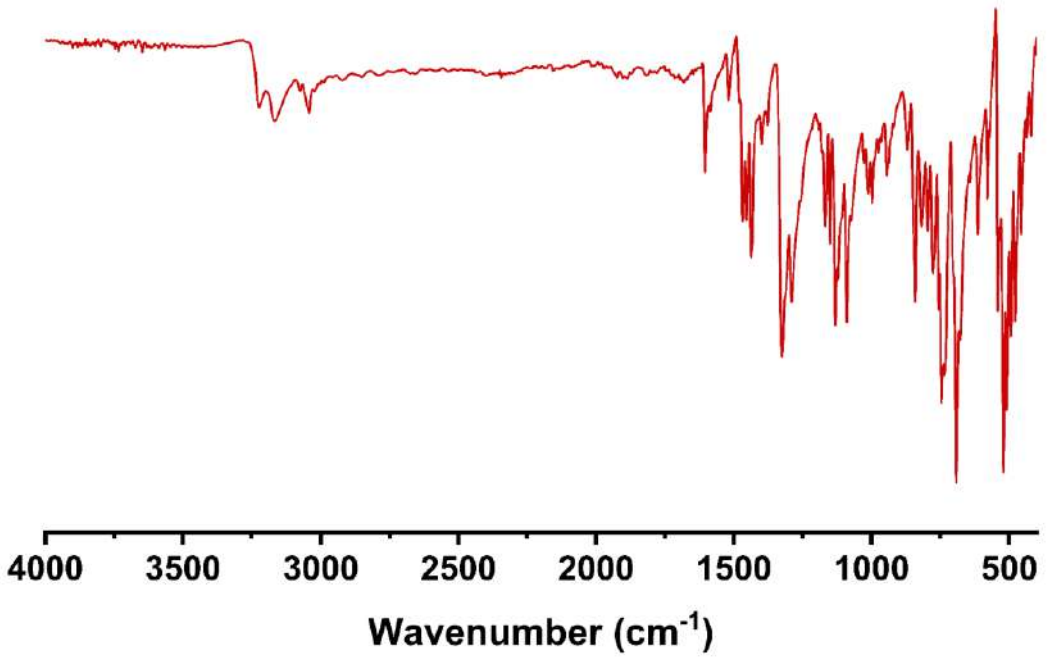

Figure 6.6.A2: IR spectrum of **2**

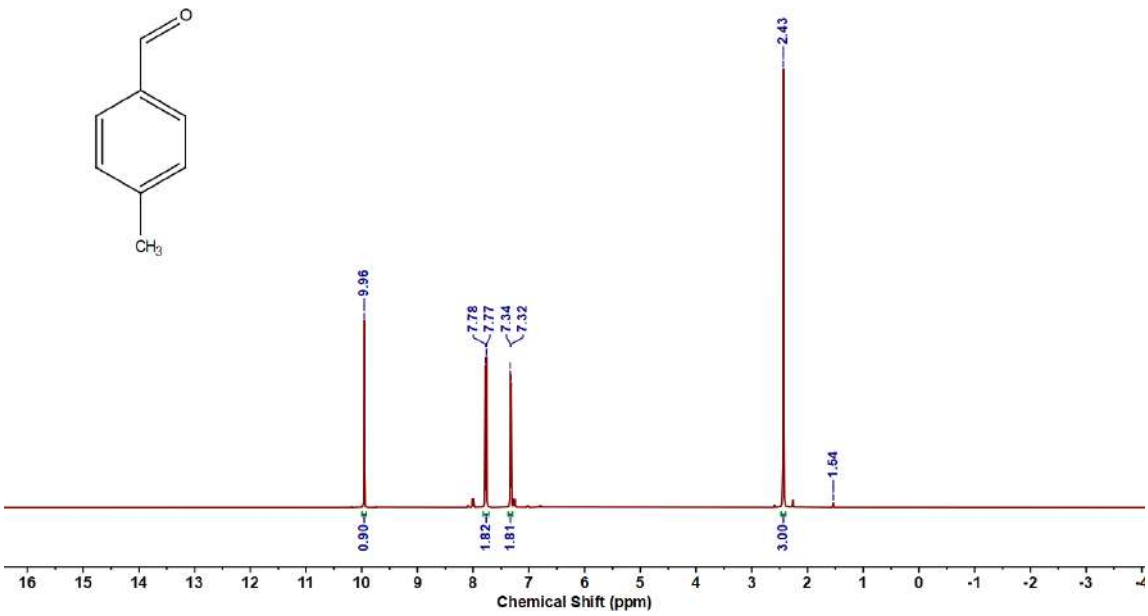

Figure 6.6.A3: ^{1}H NMR spectrum of **6b′**

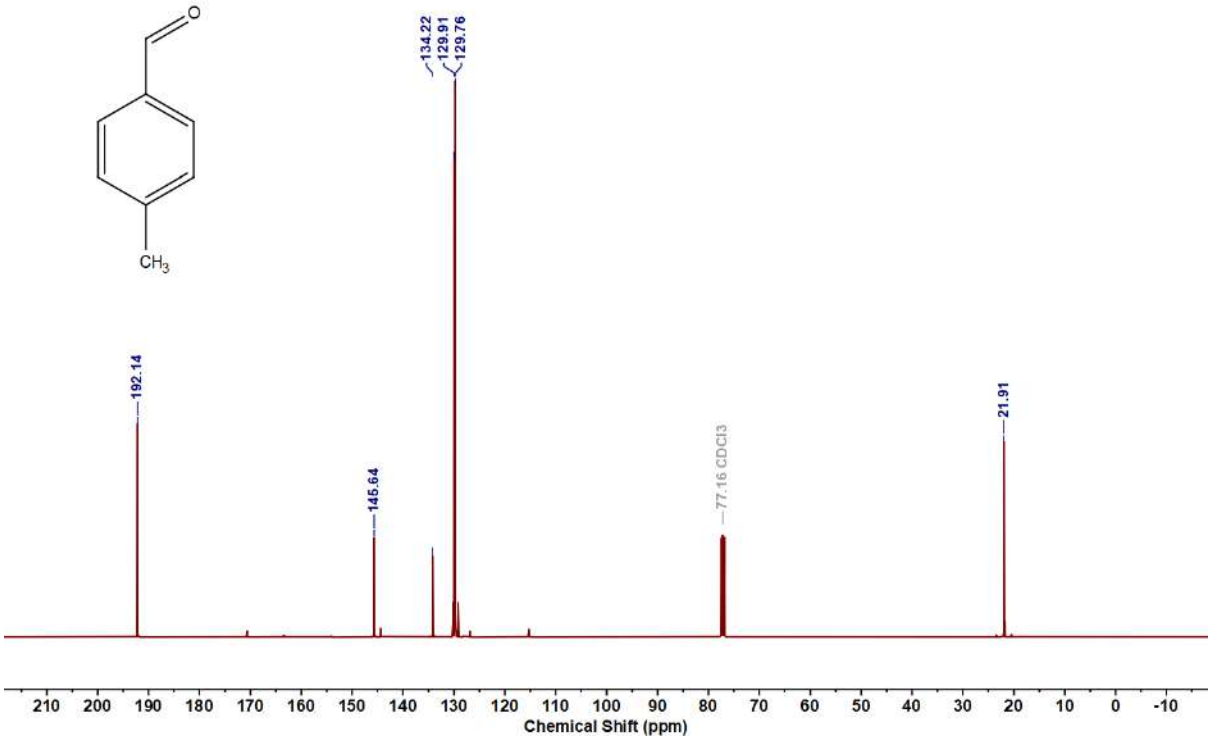

Figure 6.6.A4: ^{13}C{^{1}H} NMR spectrum of **6b′**

NMR data of 4-methylbenzaldehyde (6b′): ^{1}H NMR (400 MHz, $CDCl_3$): δ 9.96 (s, 1H), 7.77 (d, J = 7.9 Hz, 2H), 7.33 (d, J = 7.9 Hz, 2H), 2.43 (s, 3H). ^{13}C NMR (101 MHz, $CDCl_3$) δ 192.14, 145.64, 134.22, 129.91, 129.76, 21.91.

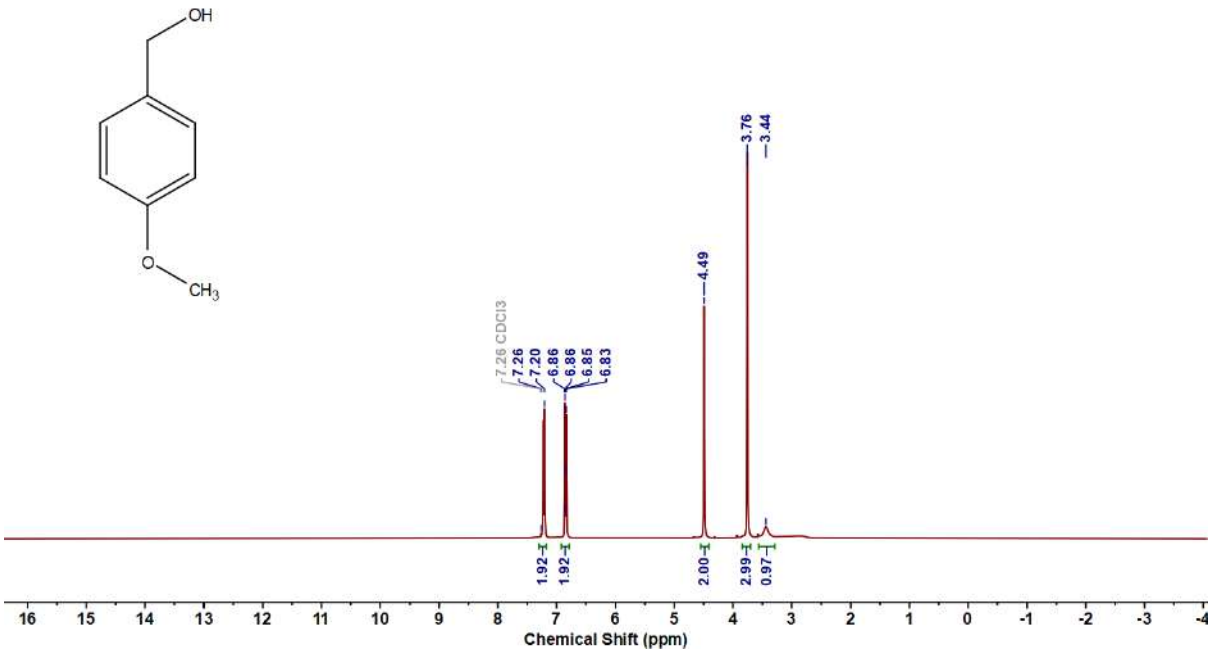

Figure 6.6.A5: ^{1}H NMR spectrum of **8a′**

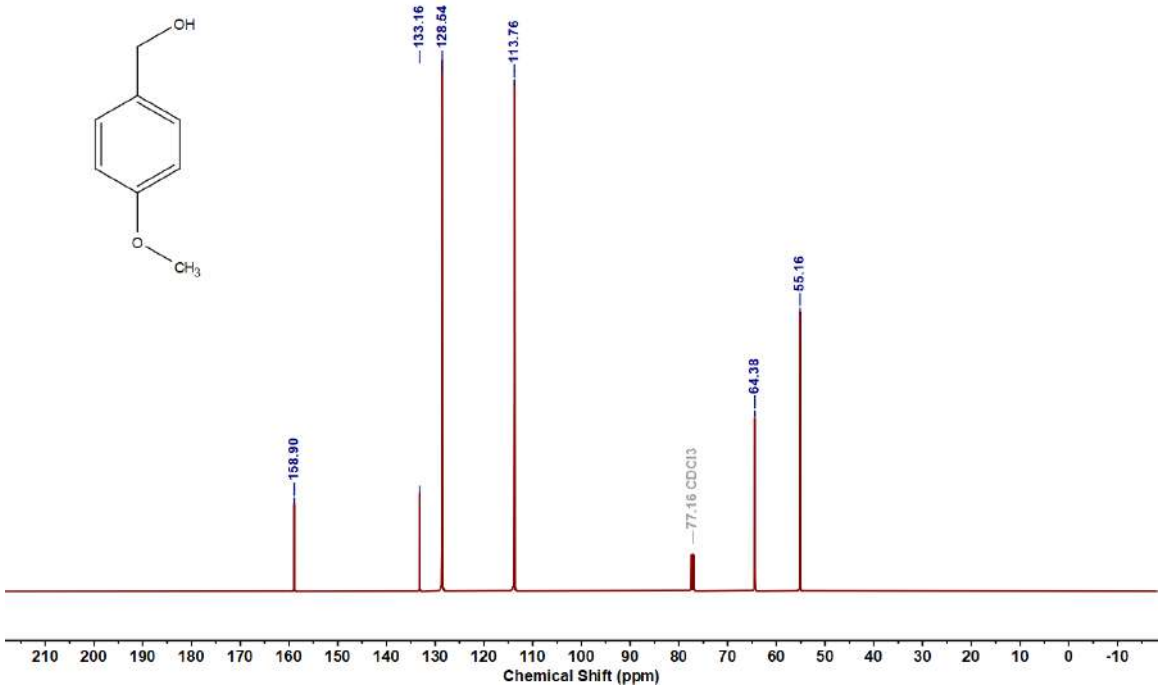

Figure 6.6.A6: ^{13}C{^{1}H} NMR spectrum of **8a′**

(4-methoxyphenyl)methanol (8a′): ^{1}H NMR (400 MHz, $CDCl_3$): δ 7.20 (s, 2H), 6.92 – 6.78 (m, 2H), 4.49 (s, 2H), 3.76 (s, 3H), 3.44 (s, 1H). ^{13}C NMR (101 MHz, $CDCl_3$): δ 158.90, 133.16, 128.54, 113.76, 64.38, 55.16.

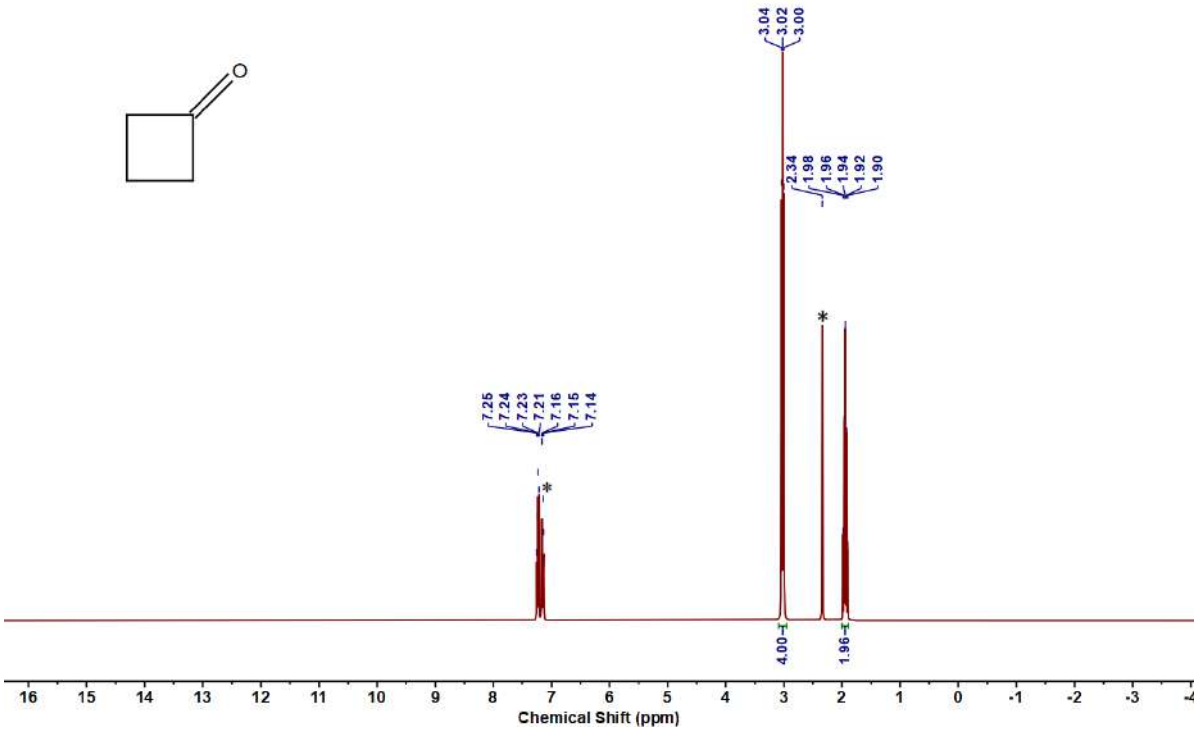

Figure 6.6.A7: ^{1}H NMR of **9a′** (Residual Solvent peak of toluene)

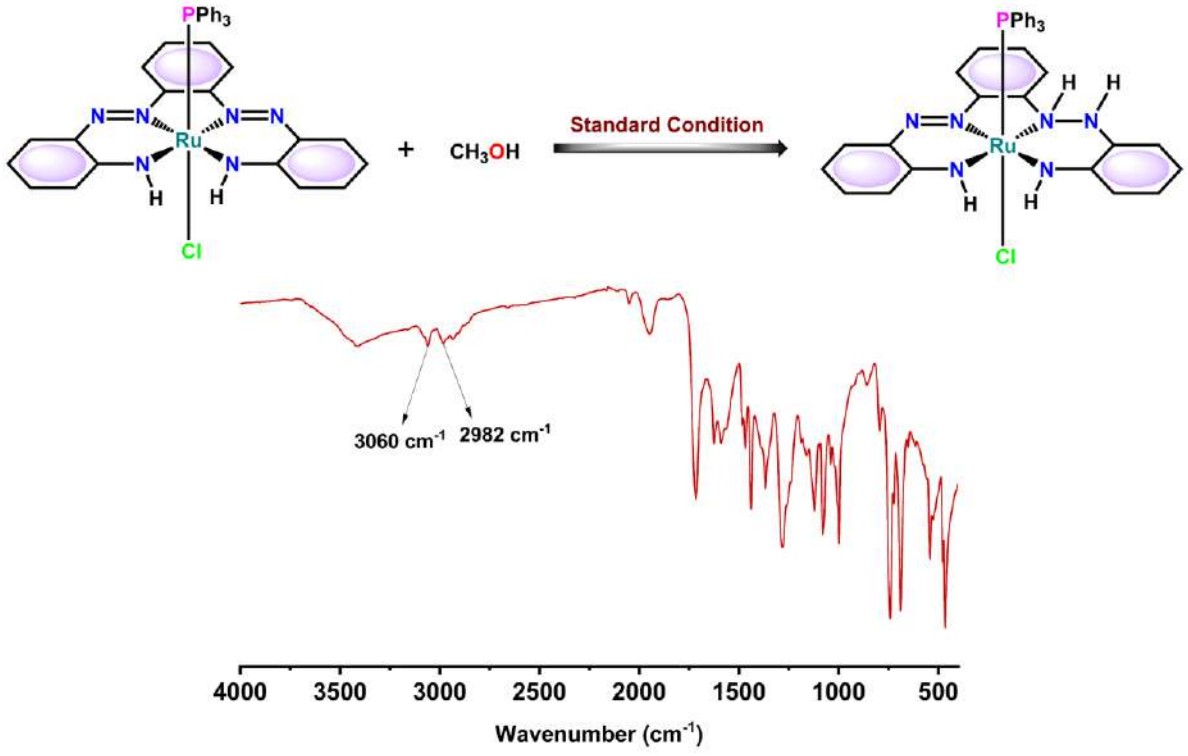

Figure 6.6.A8: IR spectrum of the reaction mixture obtained from stoichiometric alcohol dehydrogenation of methanol (CH_3OH) under argon: involvement of azo/hydrazo redox conversion with catalyst 2.

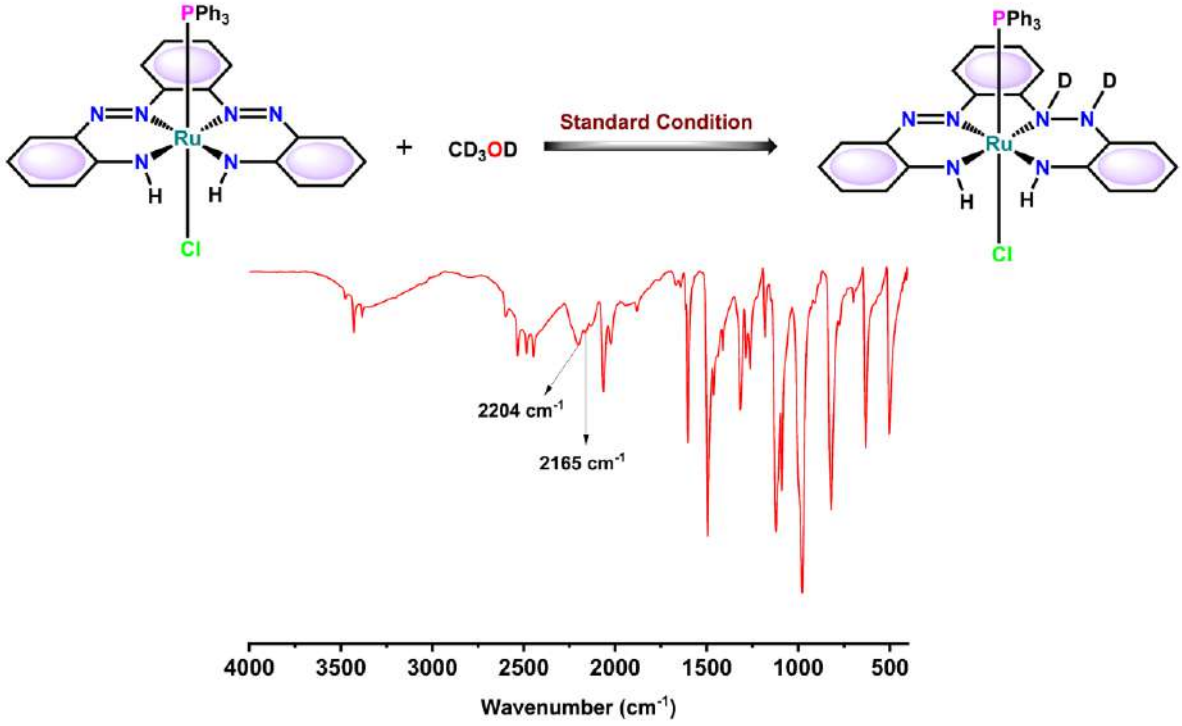

Figure 6.6.A9: IR spectrum of the reaction mixture obtained from stoichiometric alcohol dehydrogenation of deuterated methanol (CD_3OD) under argon: involvement of azo/hydrazo redox conversion with catalyst **2**.

6.8.2 Copies of ^{1}H, $^{13}C\{^{1}H\}$ and ^{19}F NMR spectra of all synthesized N-alkylated amines

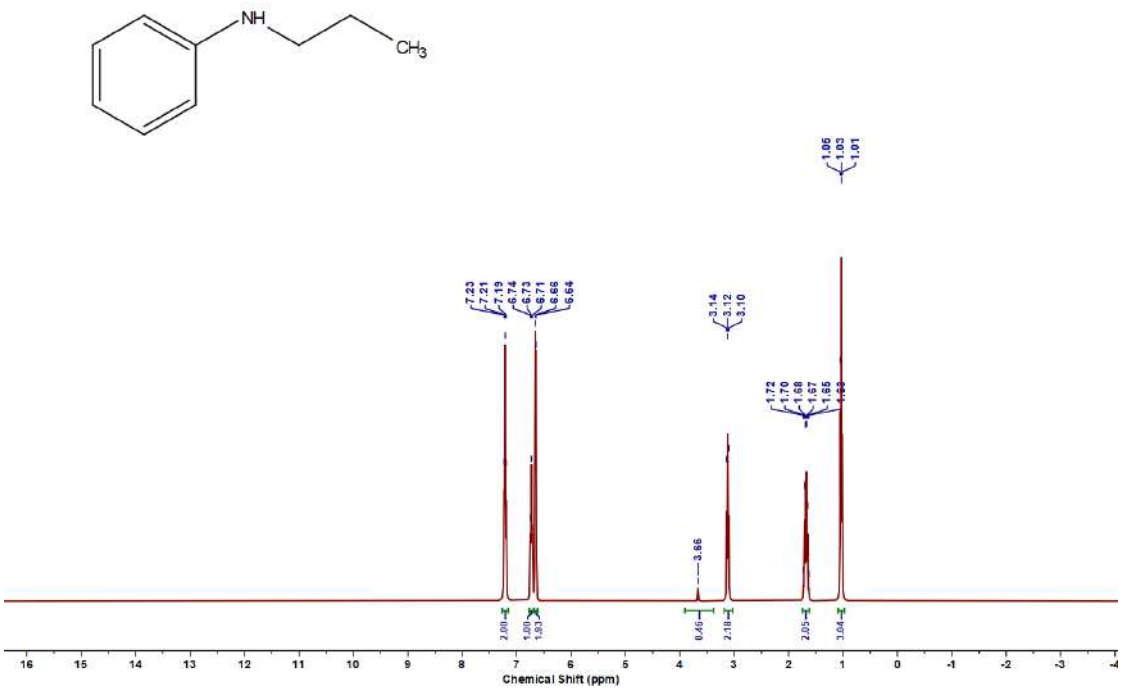

Figure 6.6.A10: ^{1}H NMR spectrum of **5a**

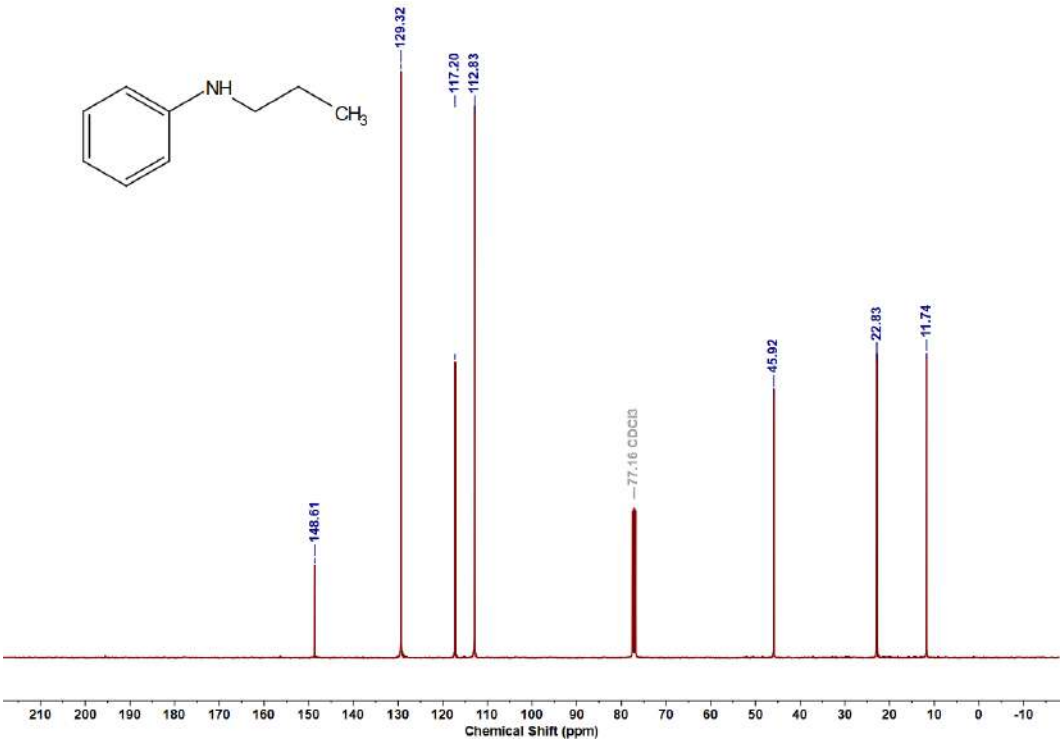

Figure 6.6.A11: $^{13}C\{^{1}H\}$ NMR spectrum of **5a**

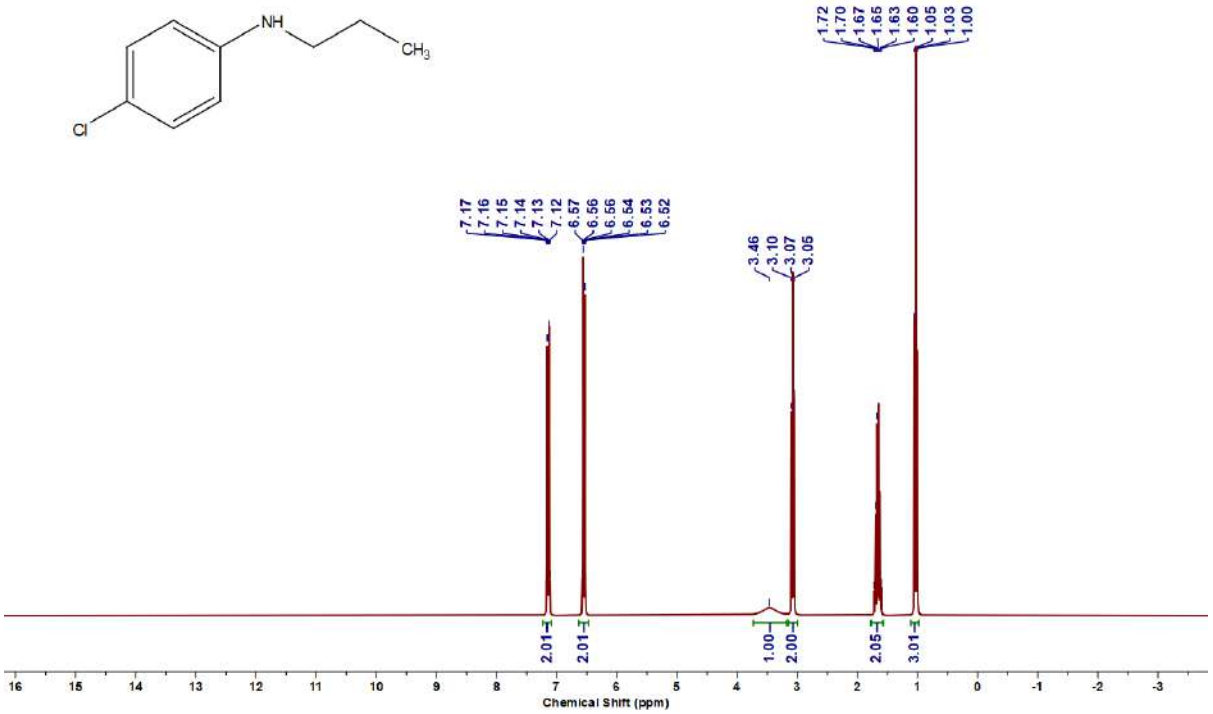

Figure 6.6.A12: ^{1}H NMR spectrum of **5b**

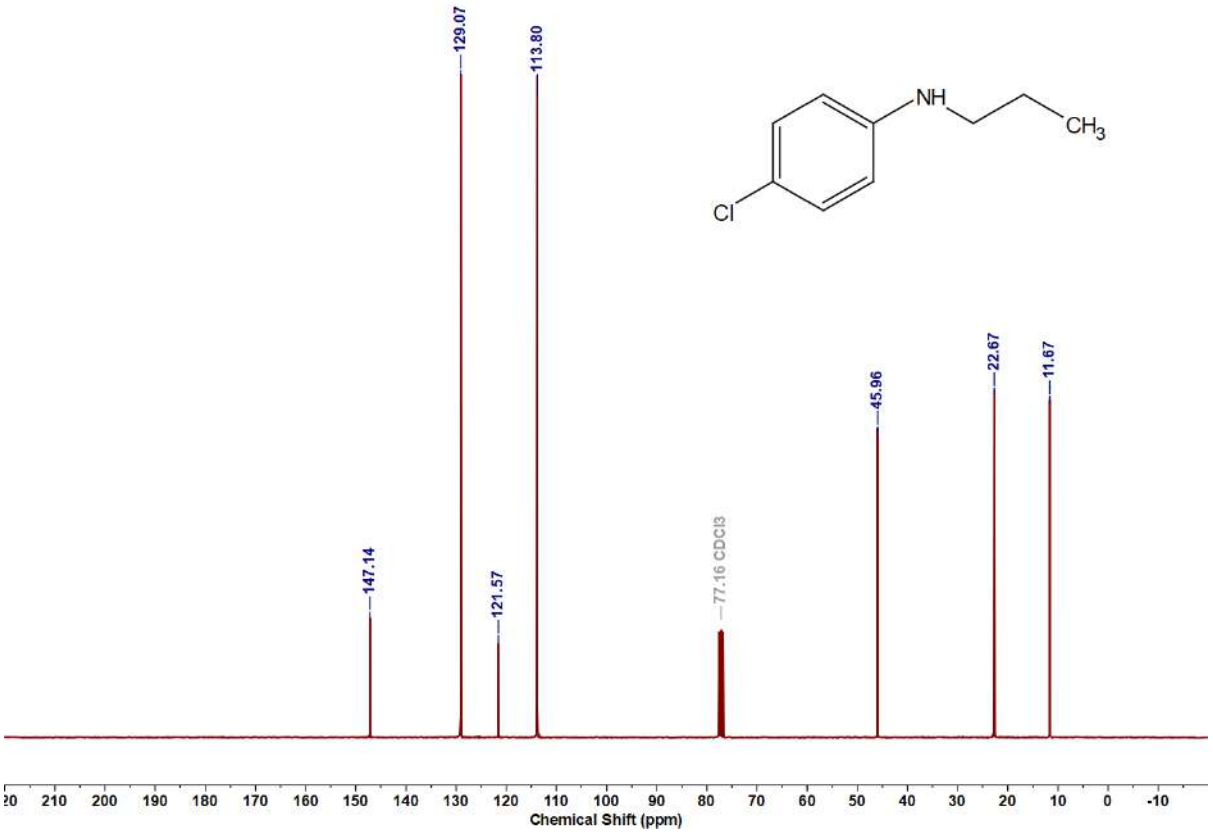

Figure 6.6.A13: ^{13}C{^{1}H} NMR spectrum of **5b**

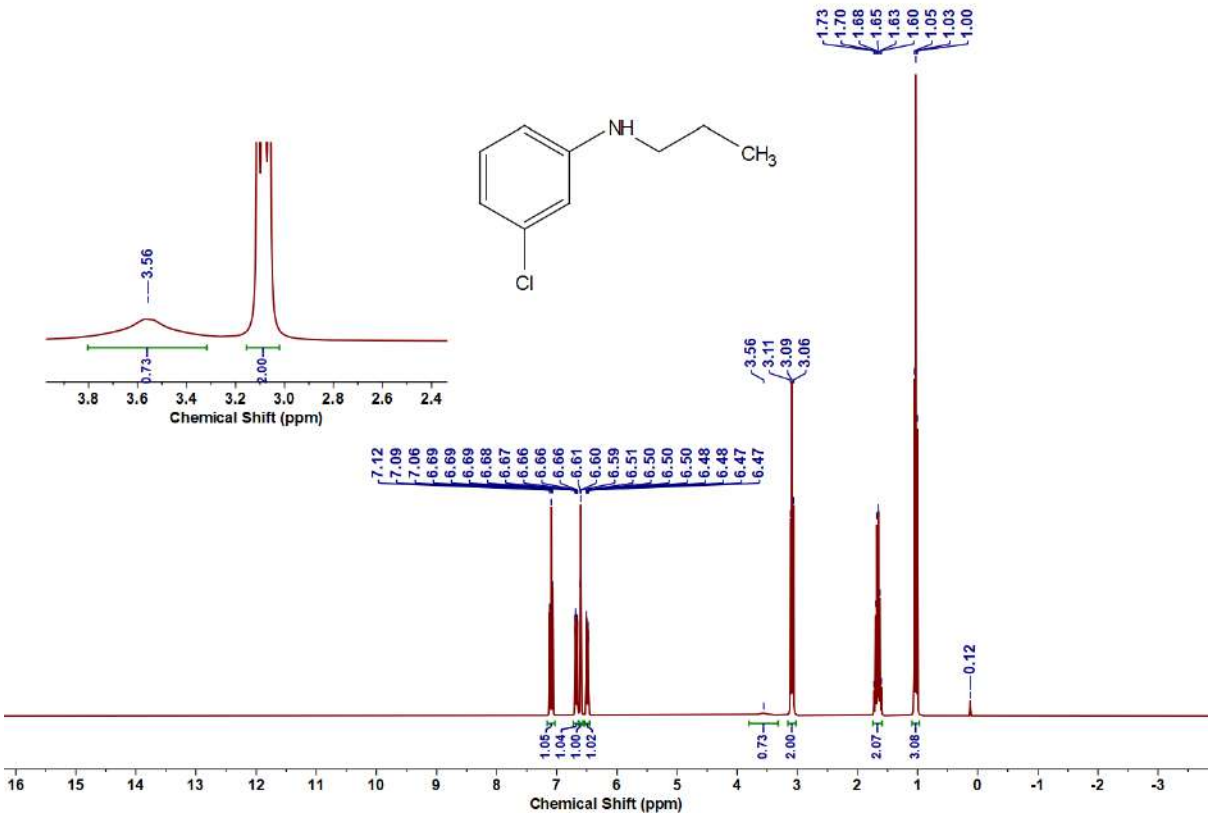

Figure 6.6.A14: ^{1}H NMR spectrum of **5c**

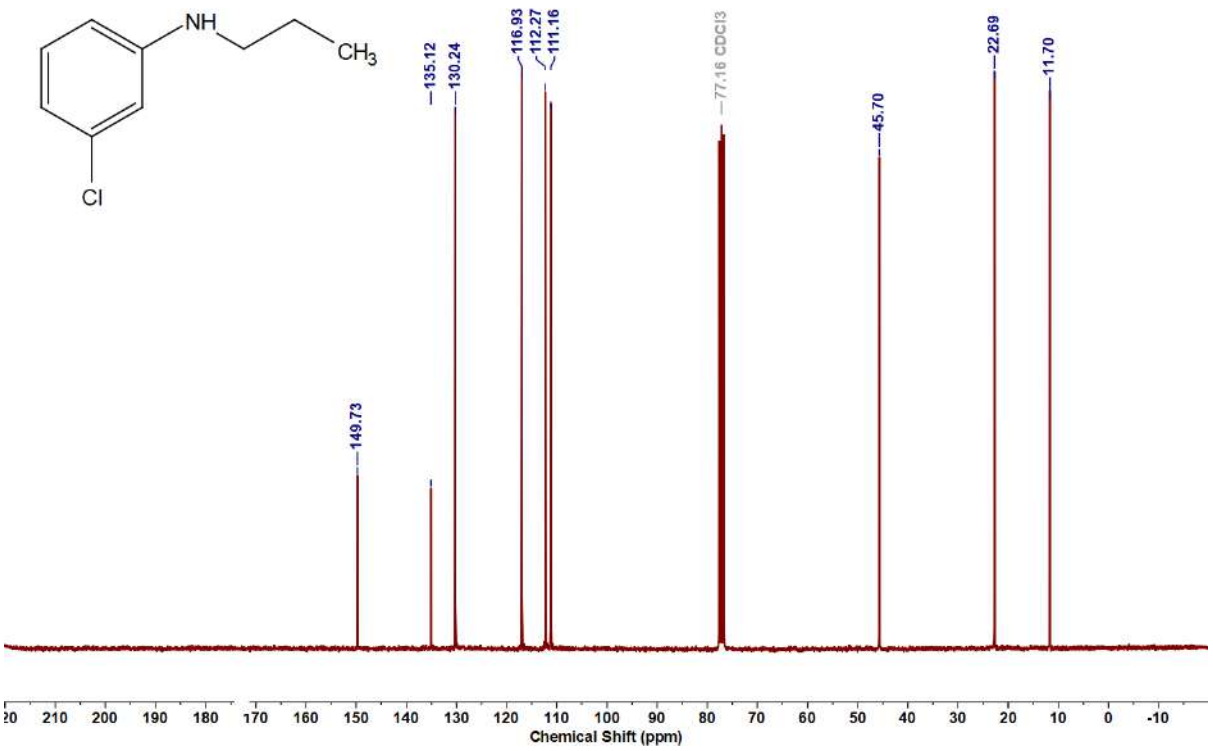

Figure 6.6.A15: $^{13}C\{^{1}H\}$ NMR spectrum of **5c**

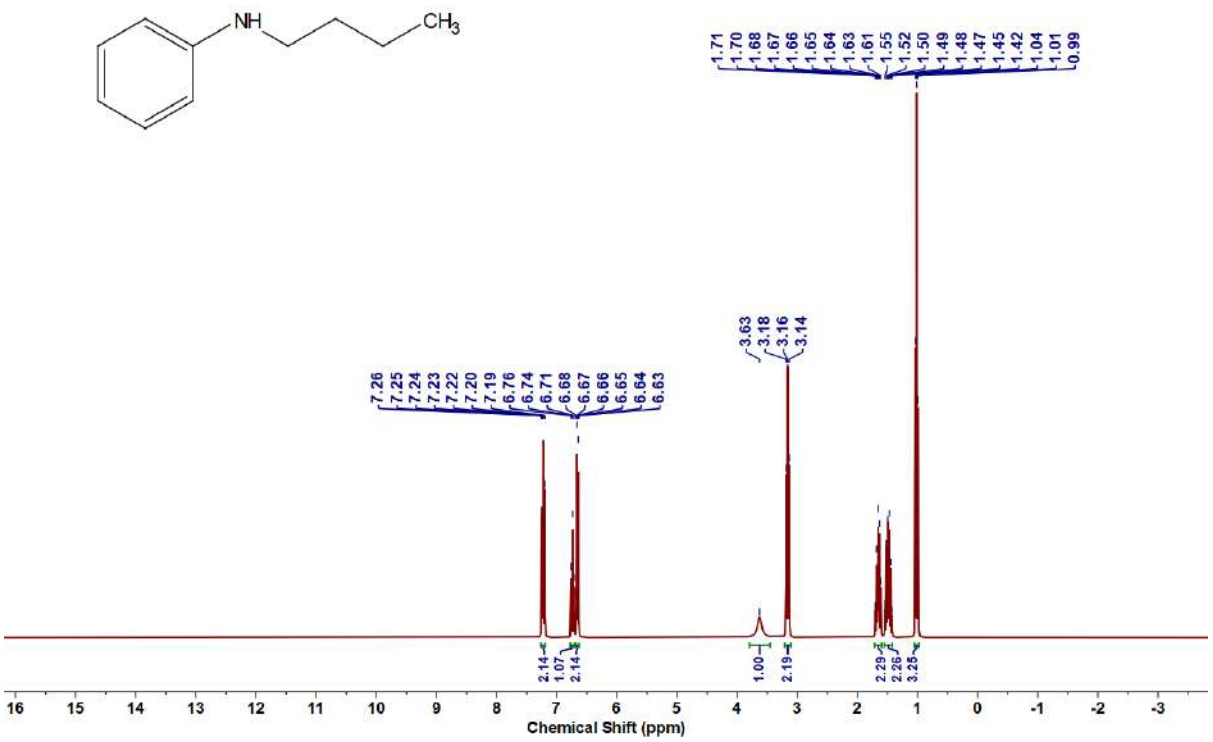

Figure 6.6.A16: ^{1}H NMR spectrum of **5d**

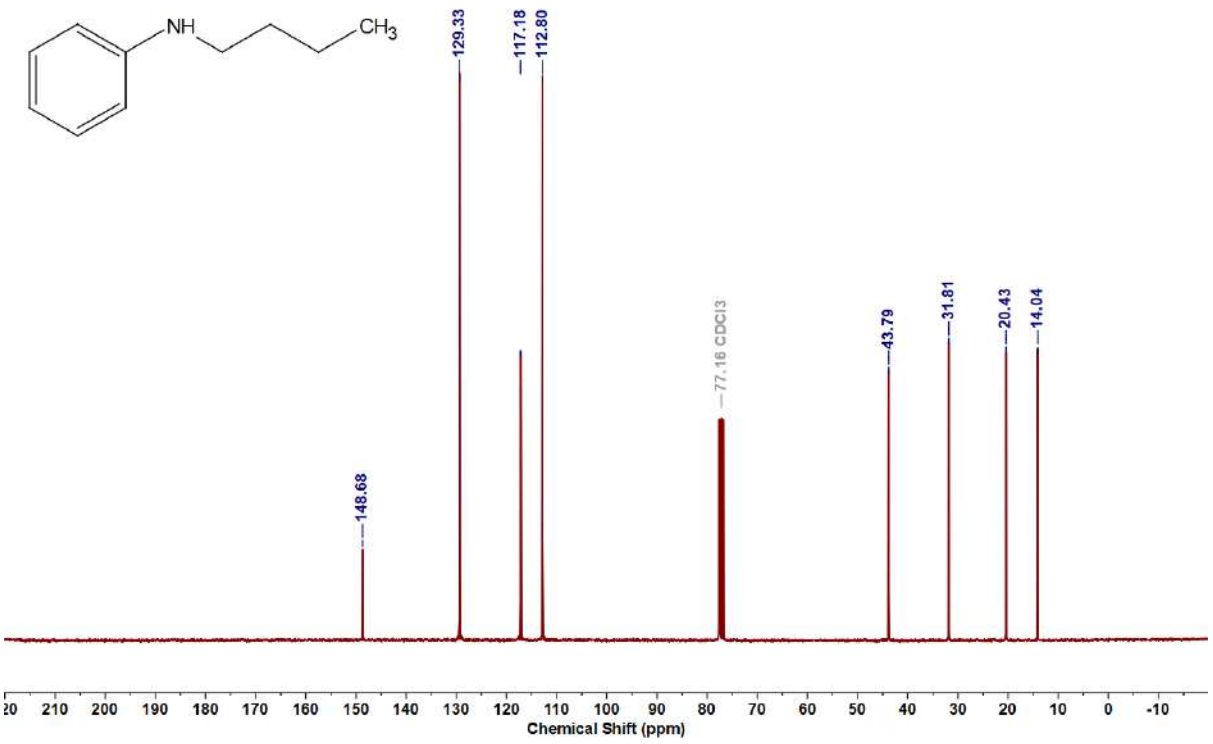

Figure 6.6.A17: ^{13}C{^{1}H} NMR spectrum of **5d**

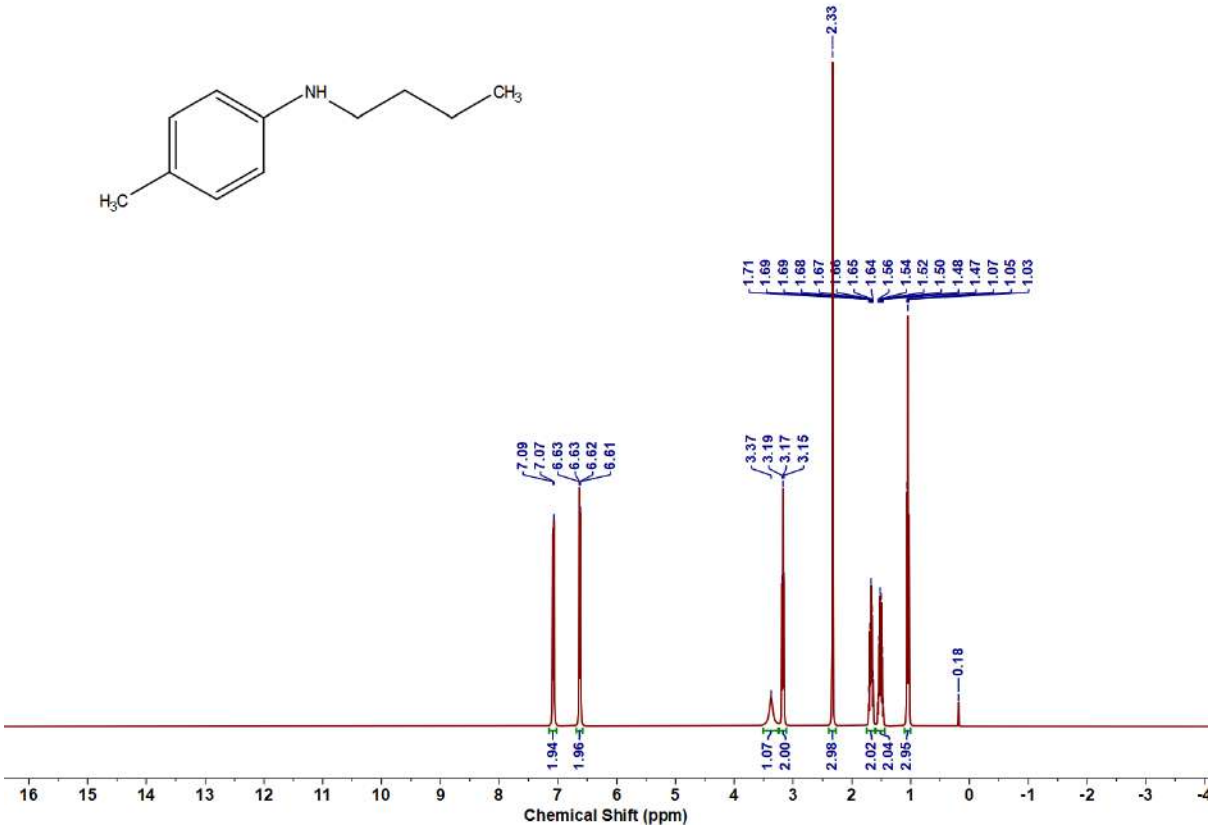

Figure 6.6.A18: ^{1}H NMR spectrum of **5e**

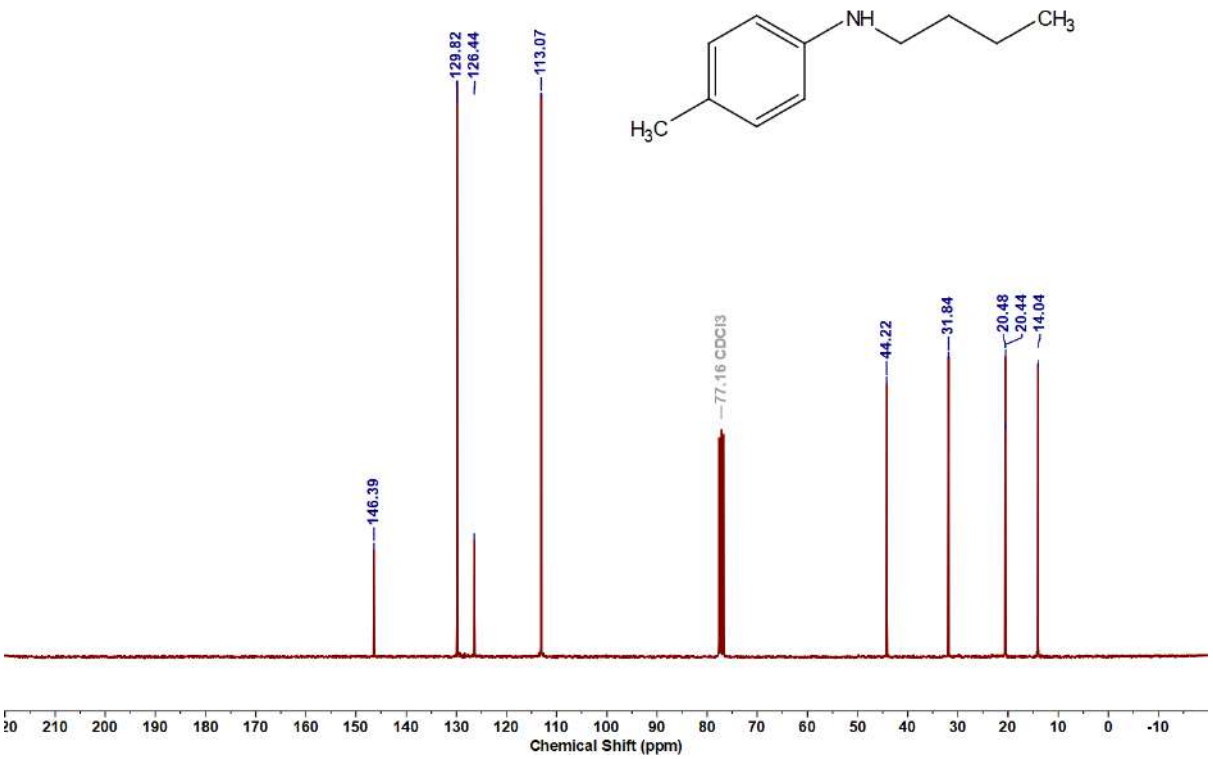

Figure 6.6.A19: $^{13}C\{^{1}H\}$ NMR spectrum of **5e**

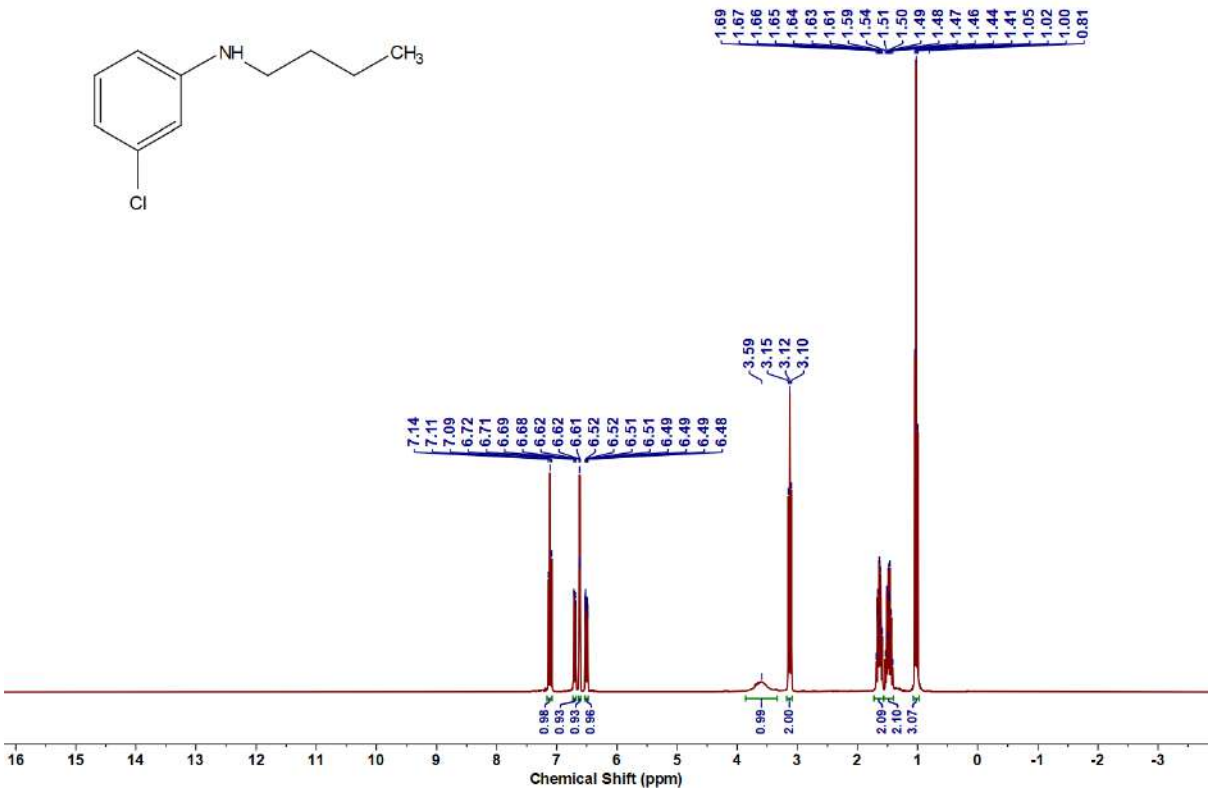

Figure 6.6.A20: ^{1}H NMR spectrum of **5f**

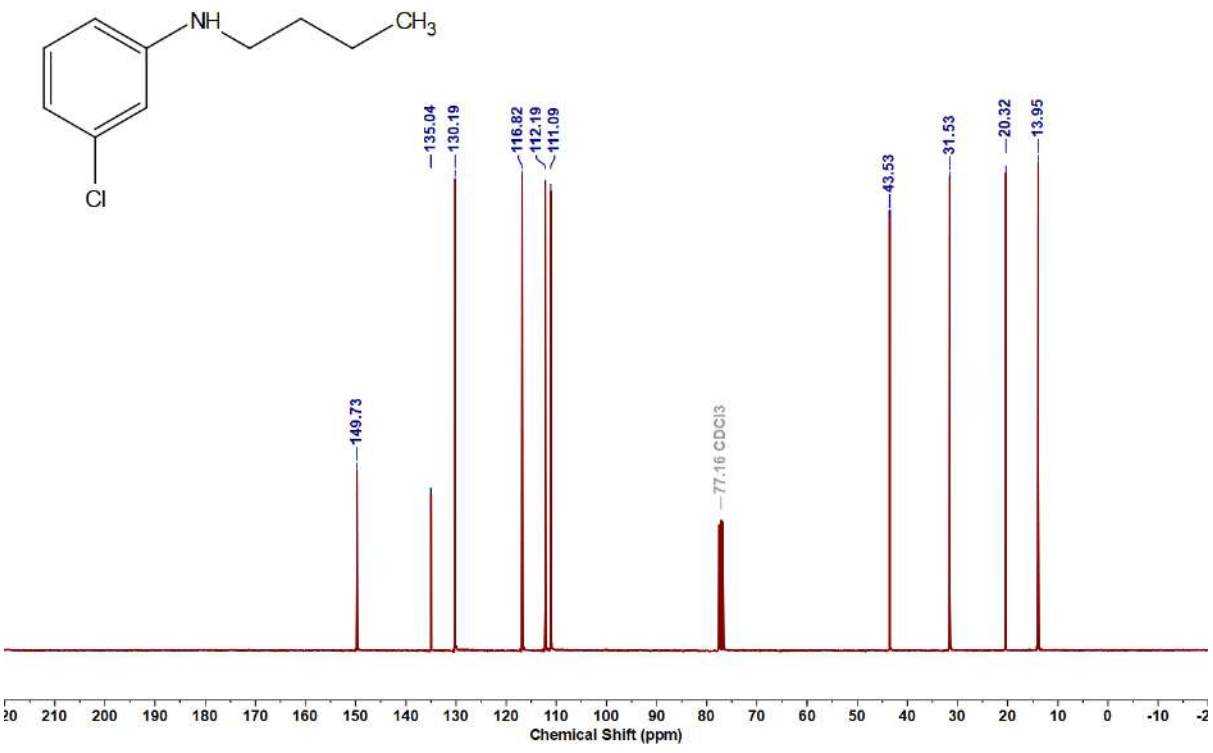

Figure 6.6.A21: ^{13}C{^{1}H} NMR spectrum of **5f**

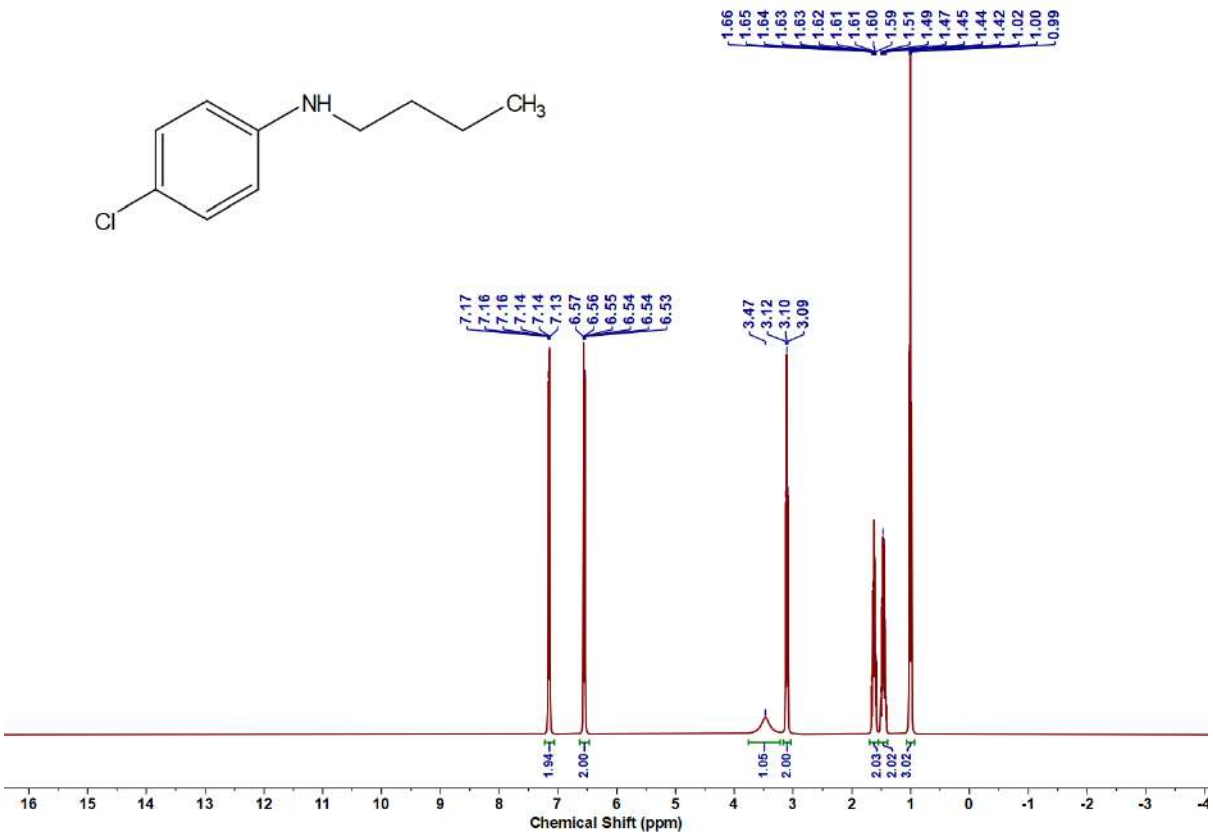

Figure 6.6.A22: ^{1}H NMR spectrum of **5g**

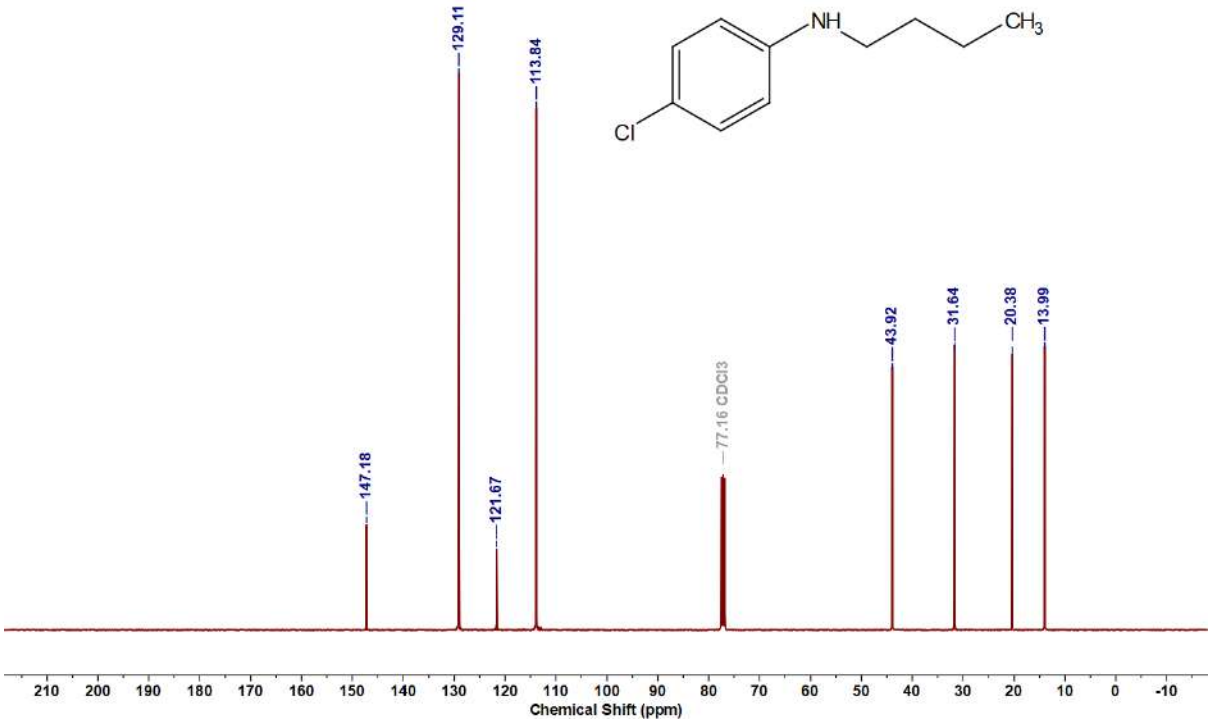

Figure 6.6.A23: ^{13}C{^{1}H} NMR spectrum of **5g**

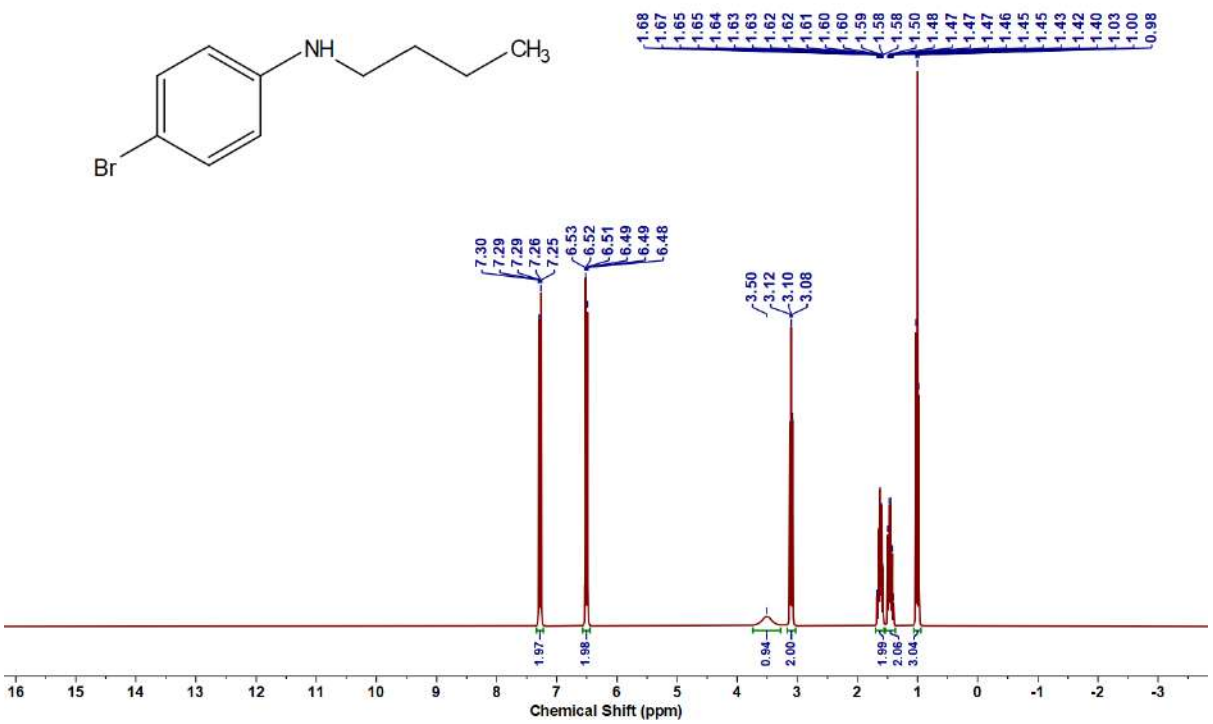

Figure 6.6.A24: ^{1}H NMR spectrum of **5h**

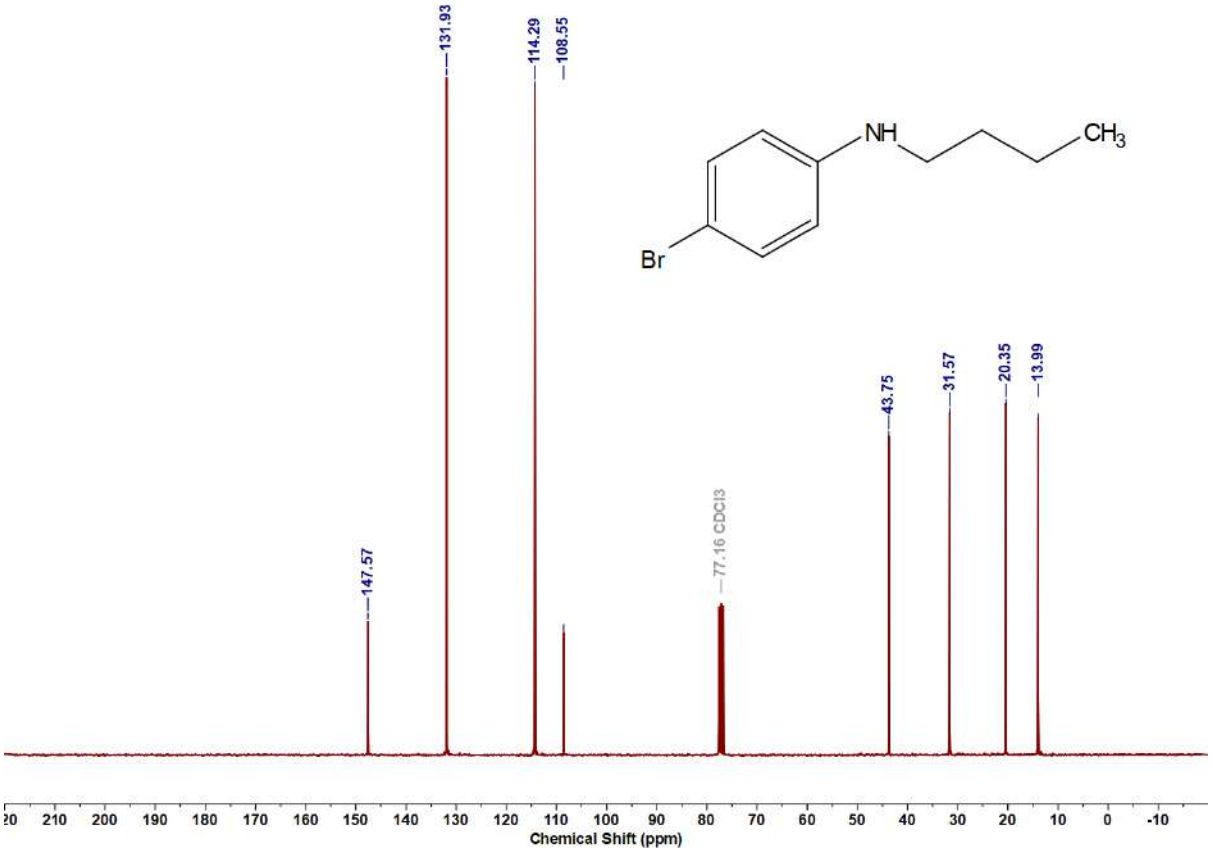

Figure 6.6.A25: ^{13}C{^{1}H} NMR spectrum of **5h**

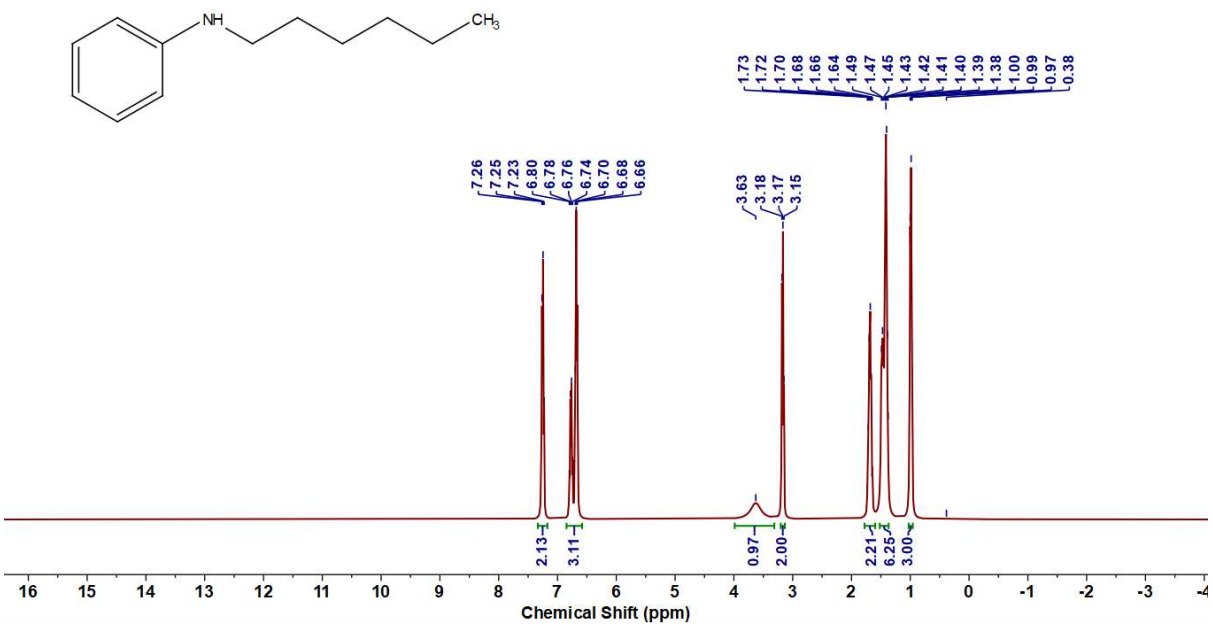

Figure 6.6.A26: ^{1}H NMR spectrum of **5i**

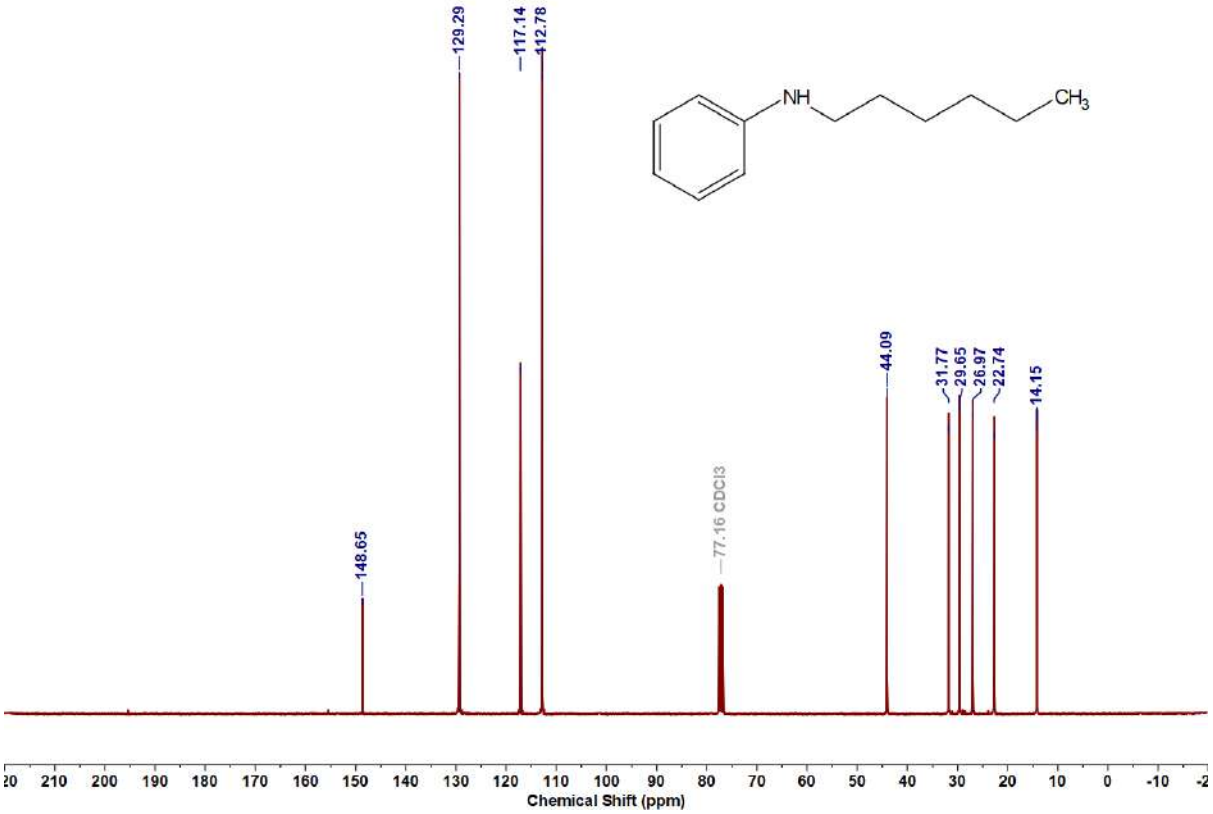

Figure 6.6.A27: ^{13}C{^{1}H} NMR spectrum of **5i**

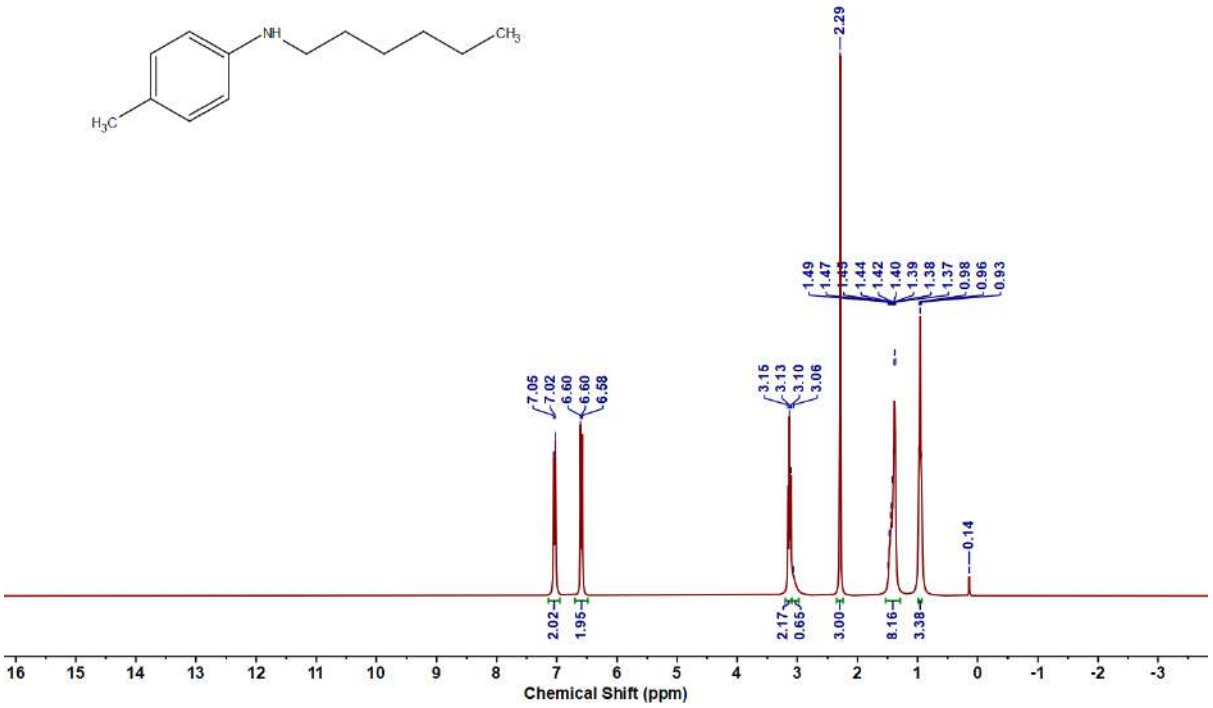

Figure 6.6.A28: ^{1}H NMR spectrum of **5j**

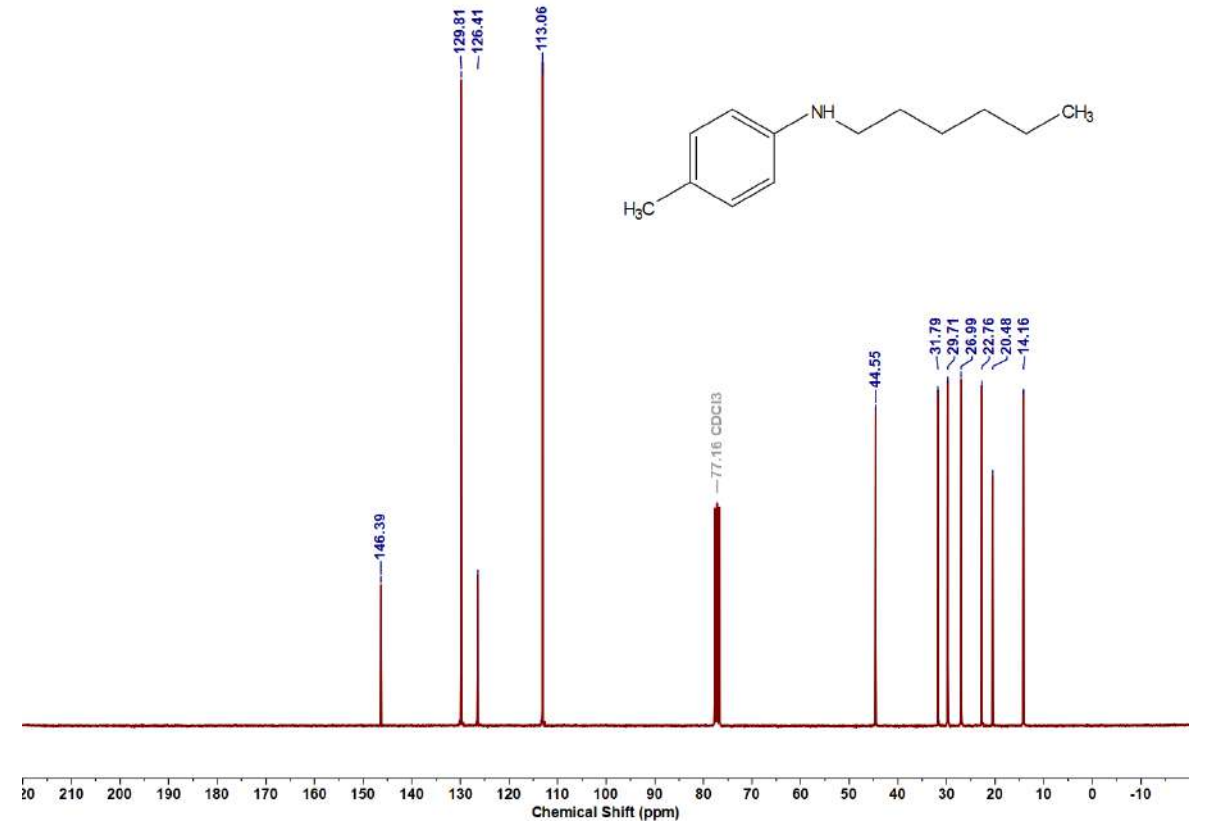

Figure 6.6.A29: ^{13}C{^{1}H} NMR spectrum of **5j**

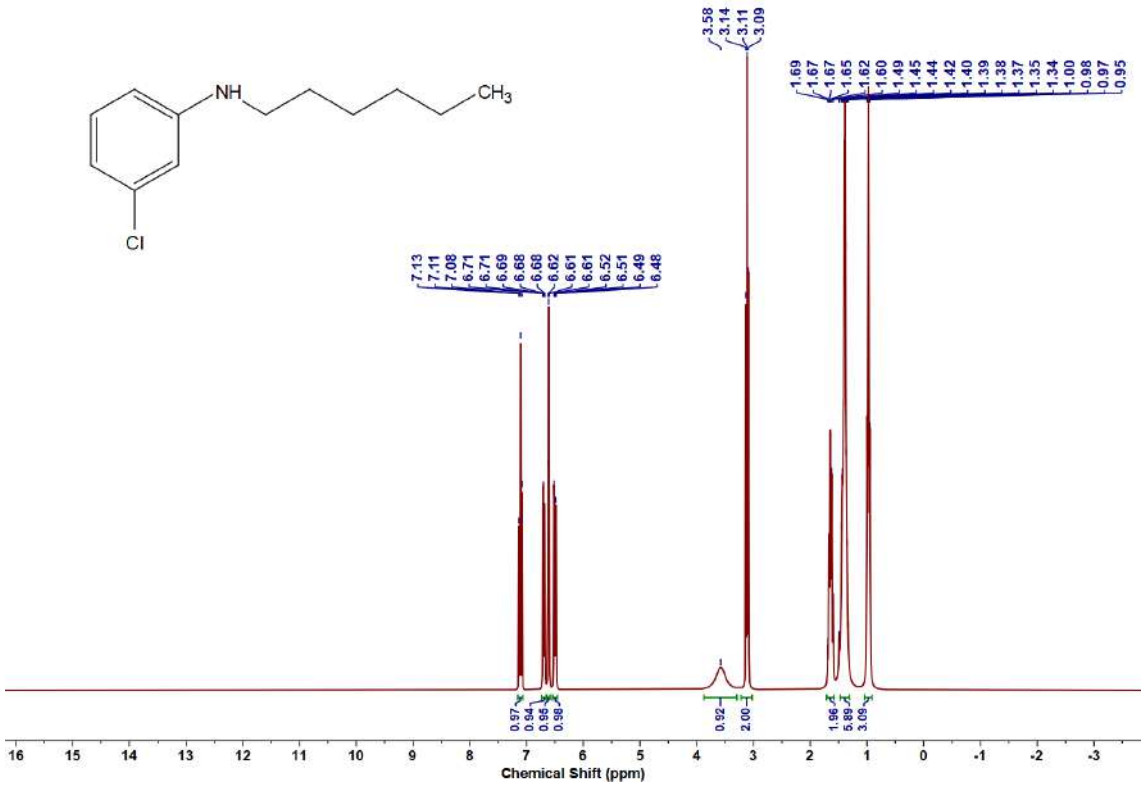

Figure 6.6.A30: ^{1}H NMR spectrum of **5k**

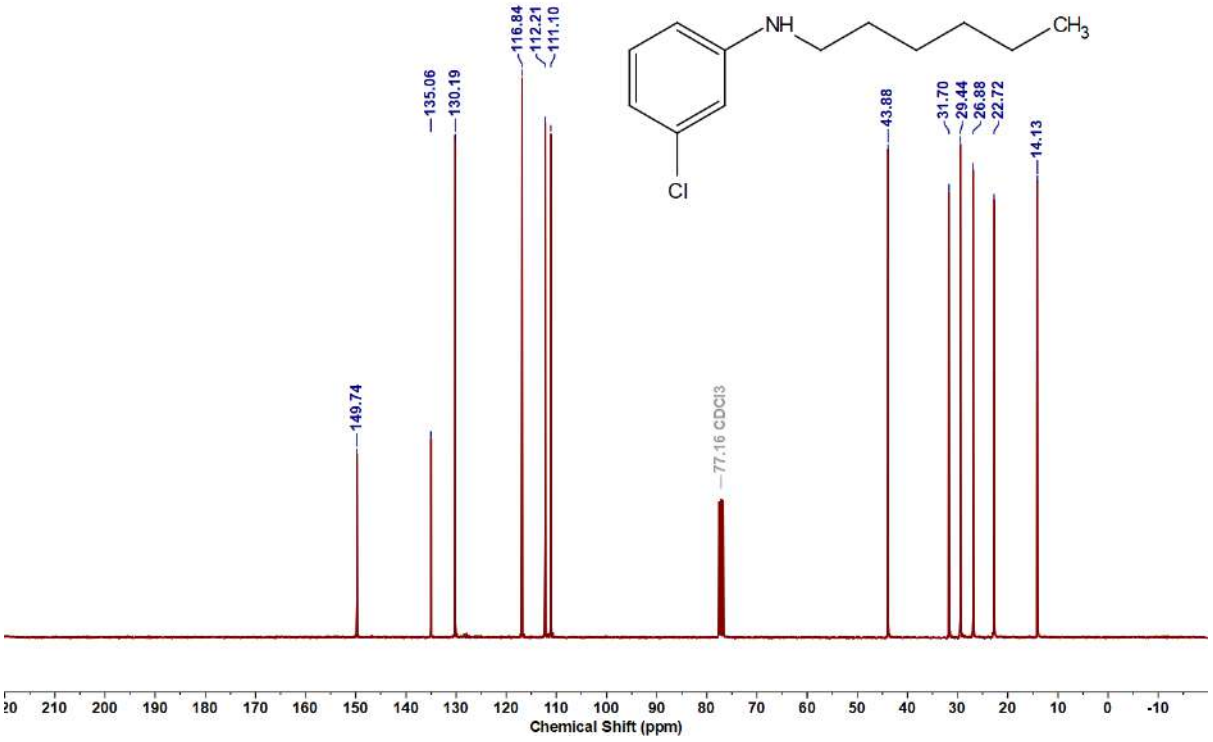

Figure 6.6.A31: ^{13}C{^{1}H} NMR spectrum of **5k**

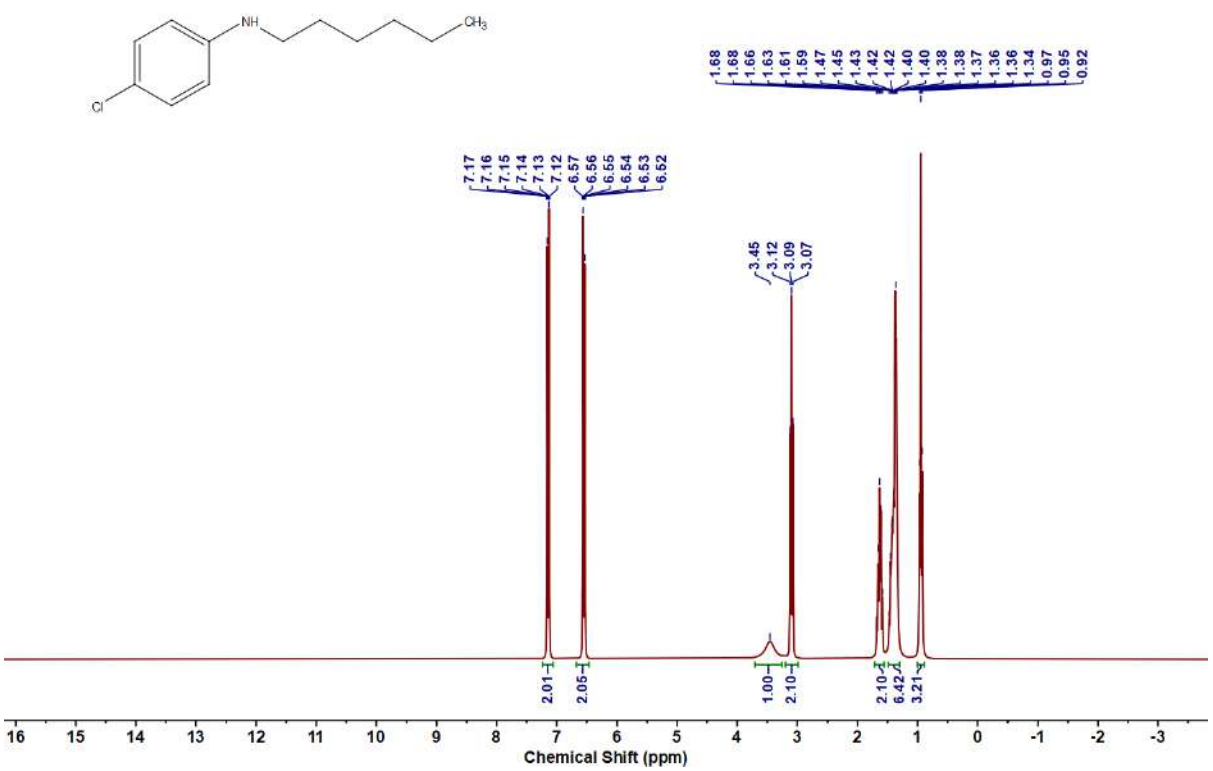

Figure 6.6.A32: ^{1}H NMR spectrum of **5l**

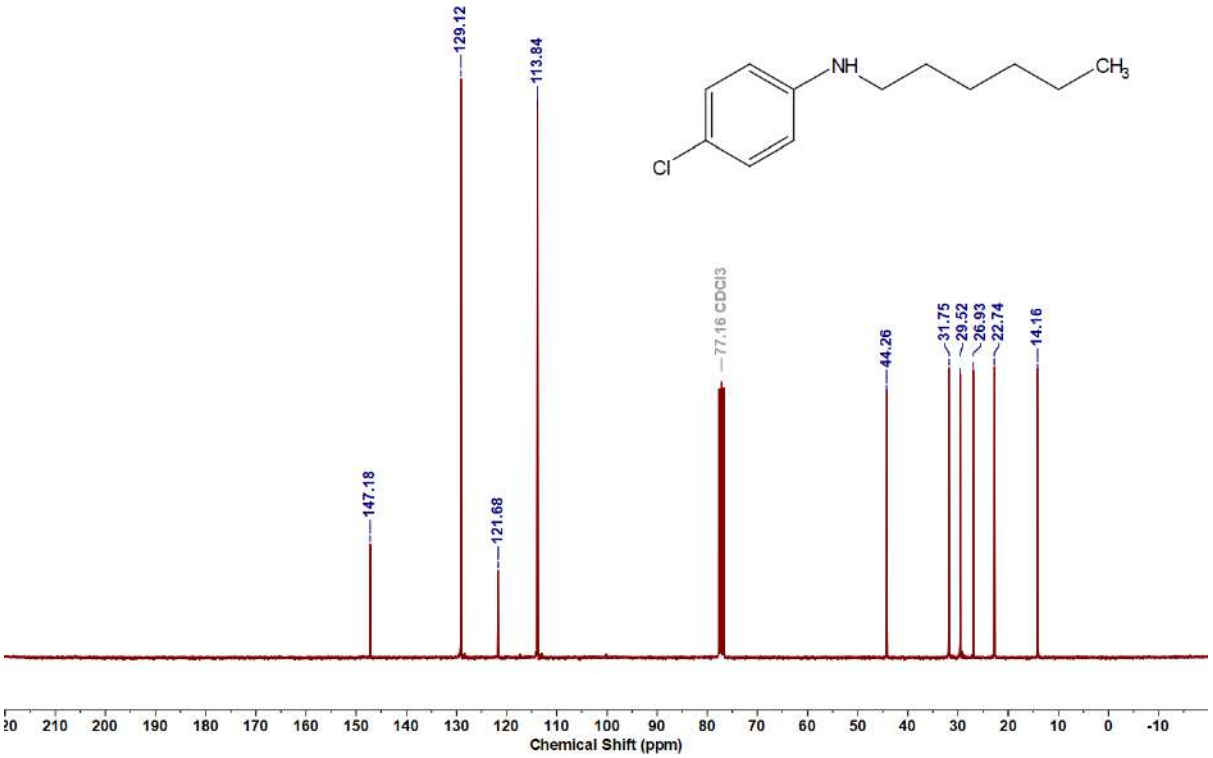

Figure 6.6.A33: ^{13}C{^{1}H} NMR spectrum of **5l**

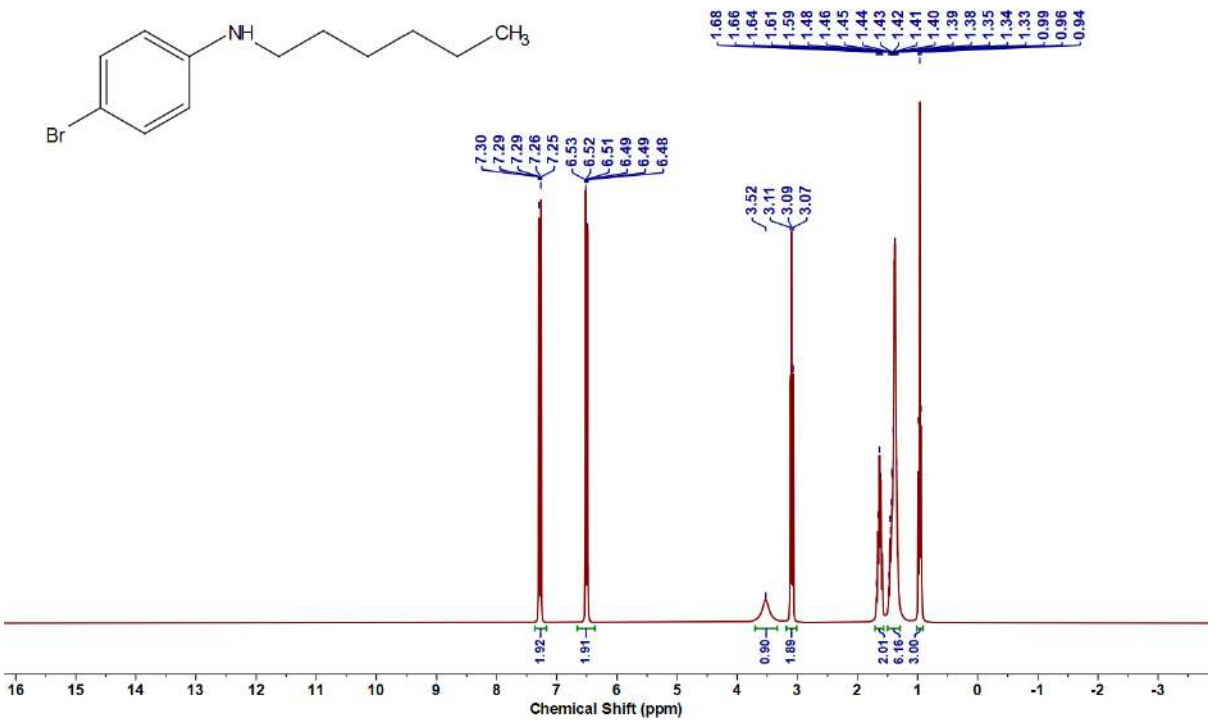

Figure 6.6.A34: ^{1}H NMR spectrum of **5m**

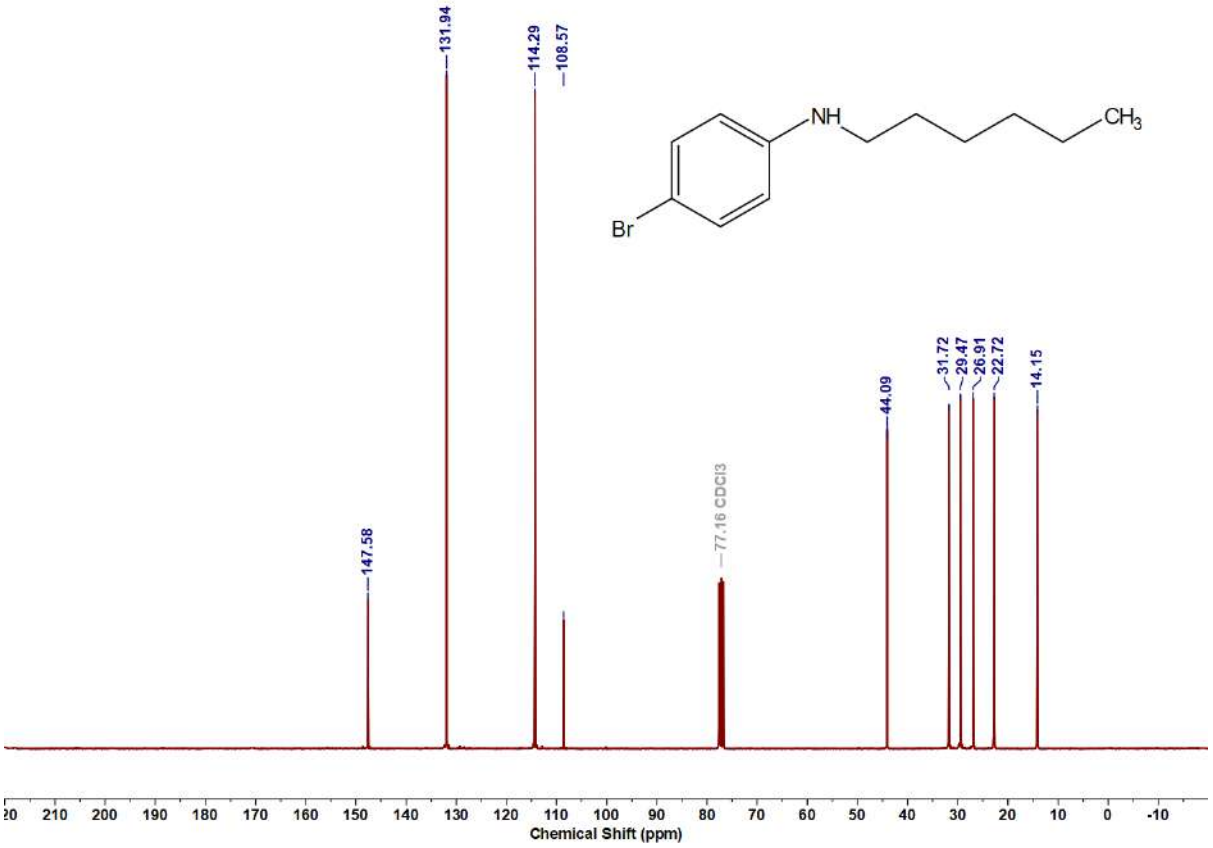

Figure 6.6.A35: $^{13}C\{^{1}H\}$ NMR spectrum of **5m**

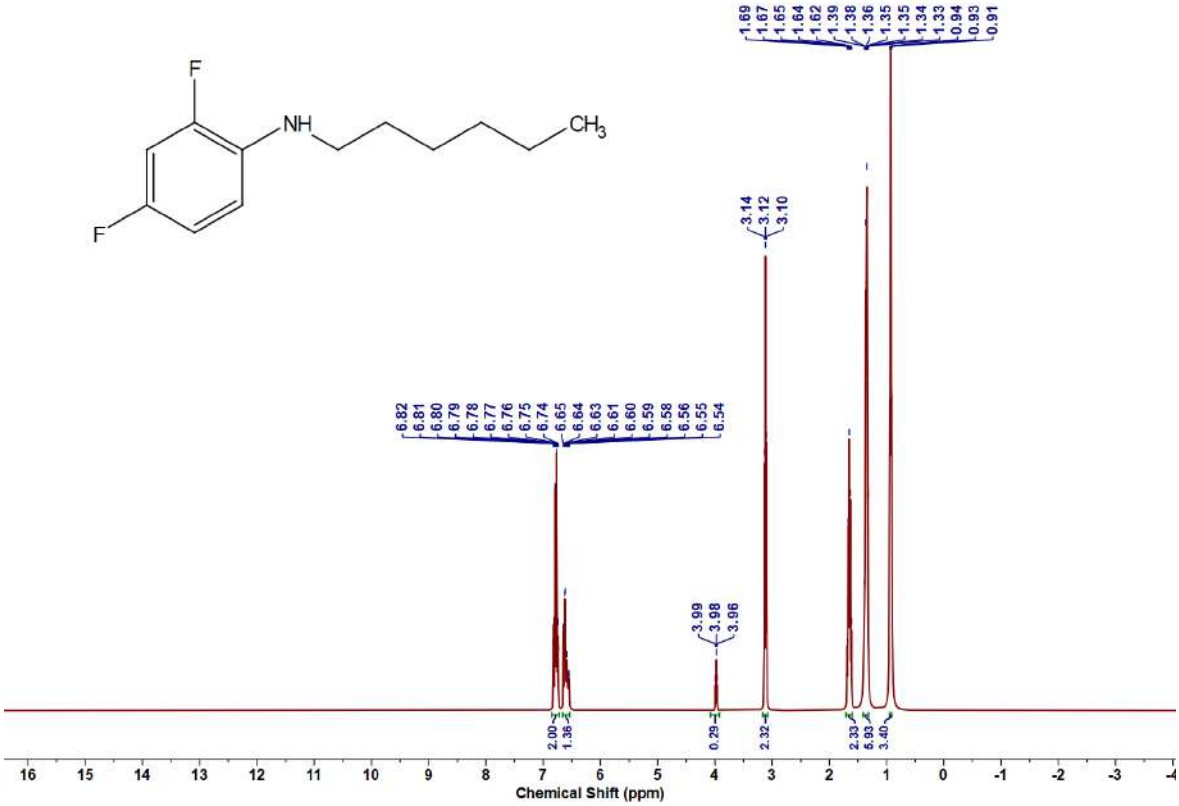

Figure 6.6.A36: ^{1}H NMR spectrum of **5n**

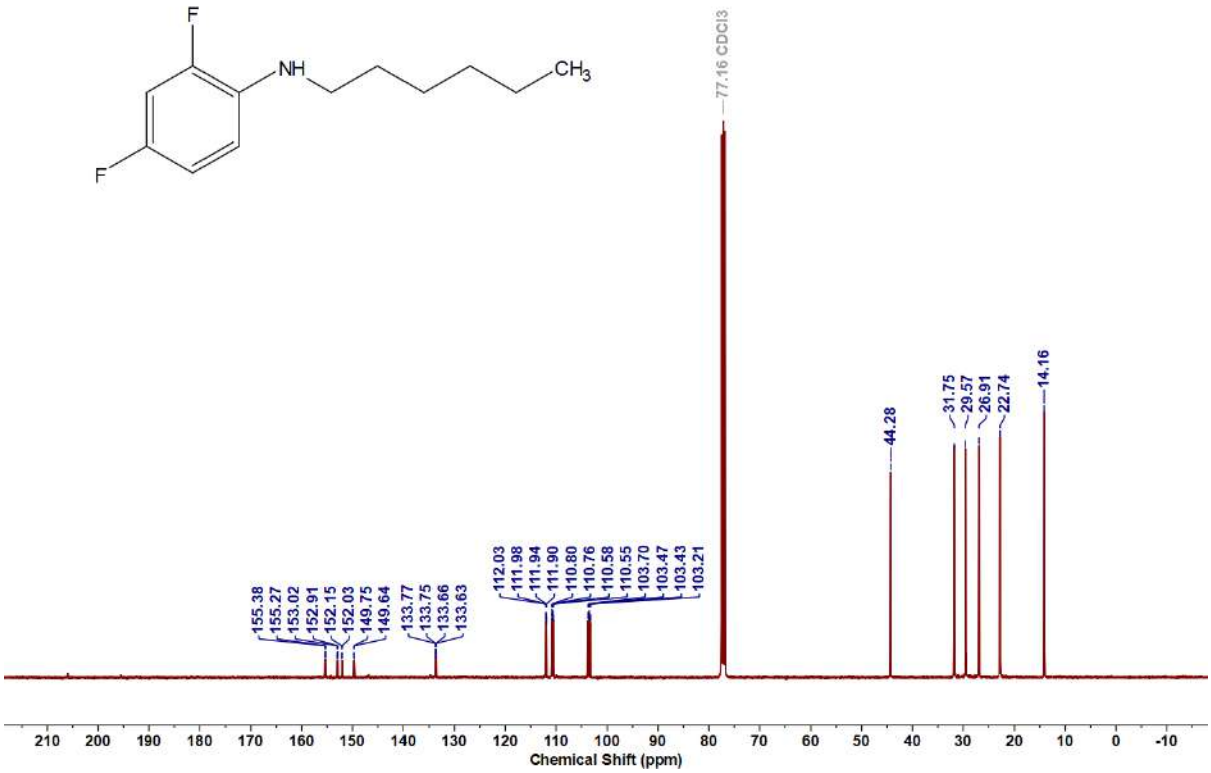

Figure 6.6.A37: $^{13}C\{^{1}H\}$ NMR spectrum of **5n**

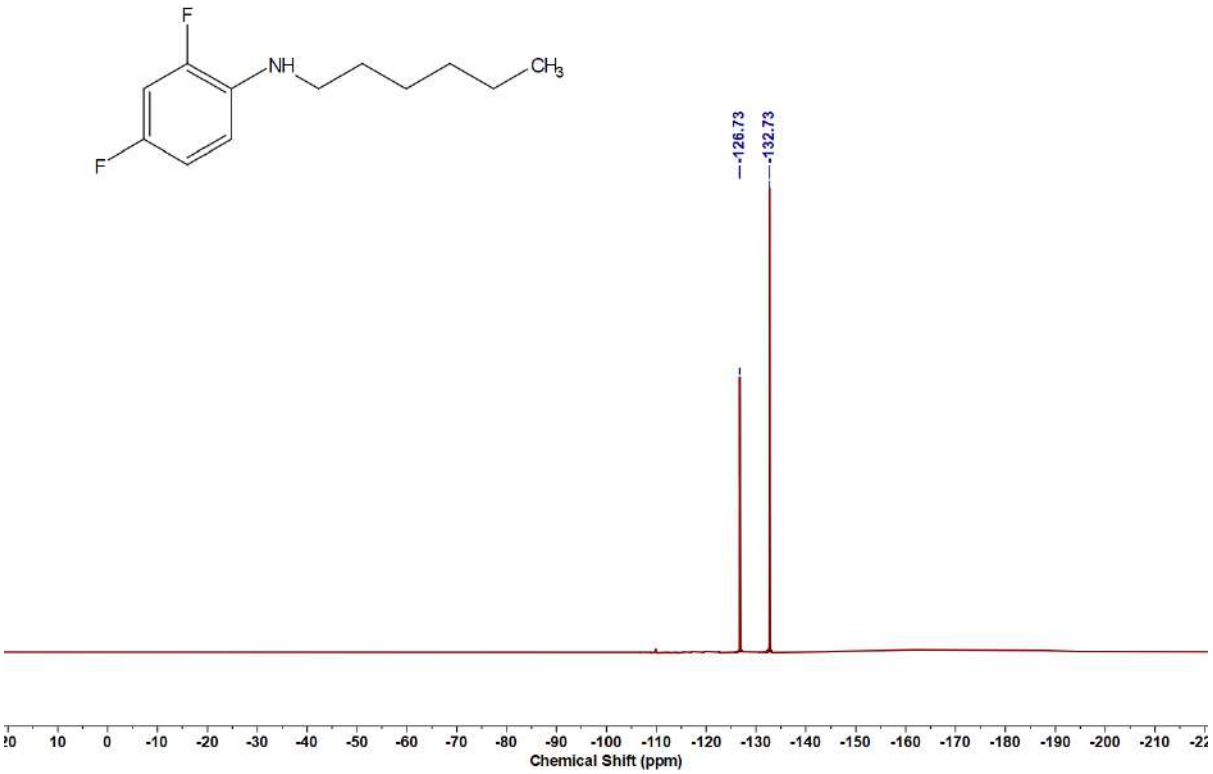

Figure 6.6.A38: ^{19}F NMR spectrum of **5n**

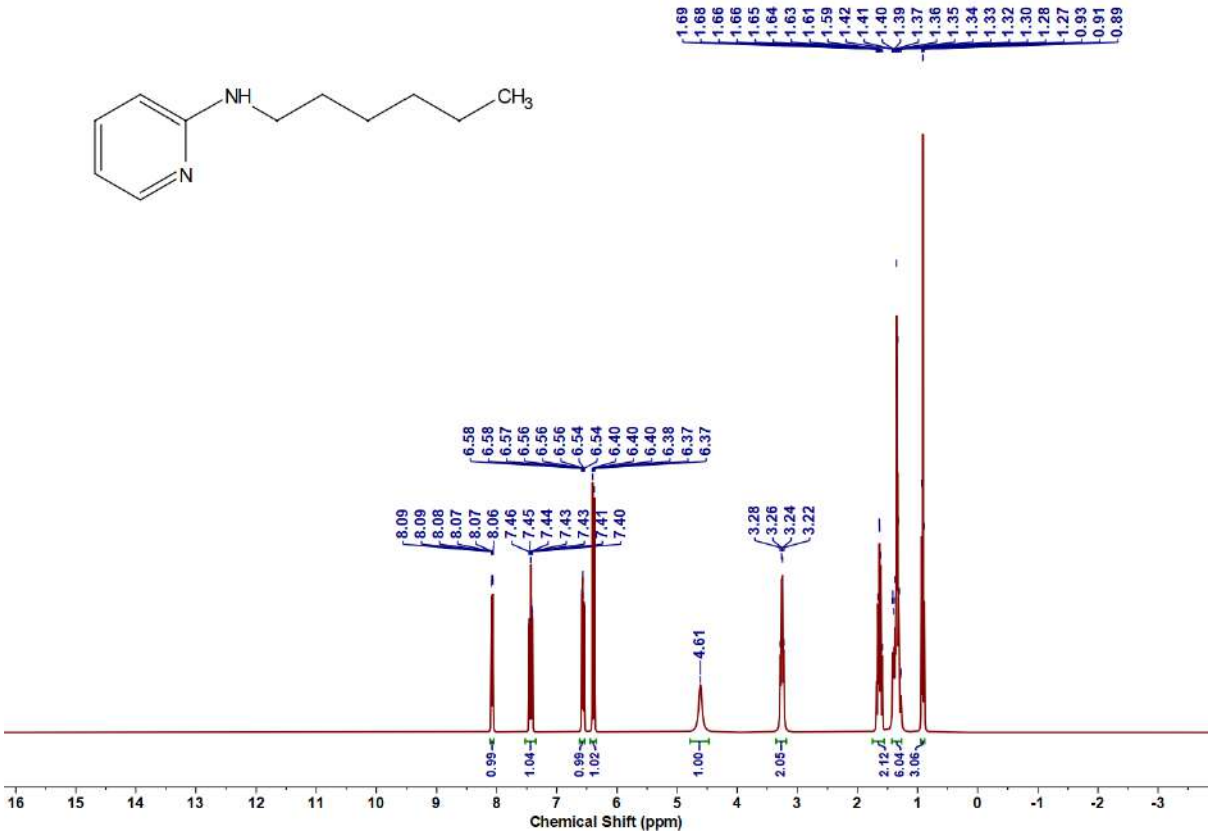

Figure 6.6.A39: ^{1}H NMR spectrum of **5o**

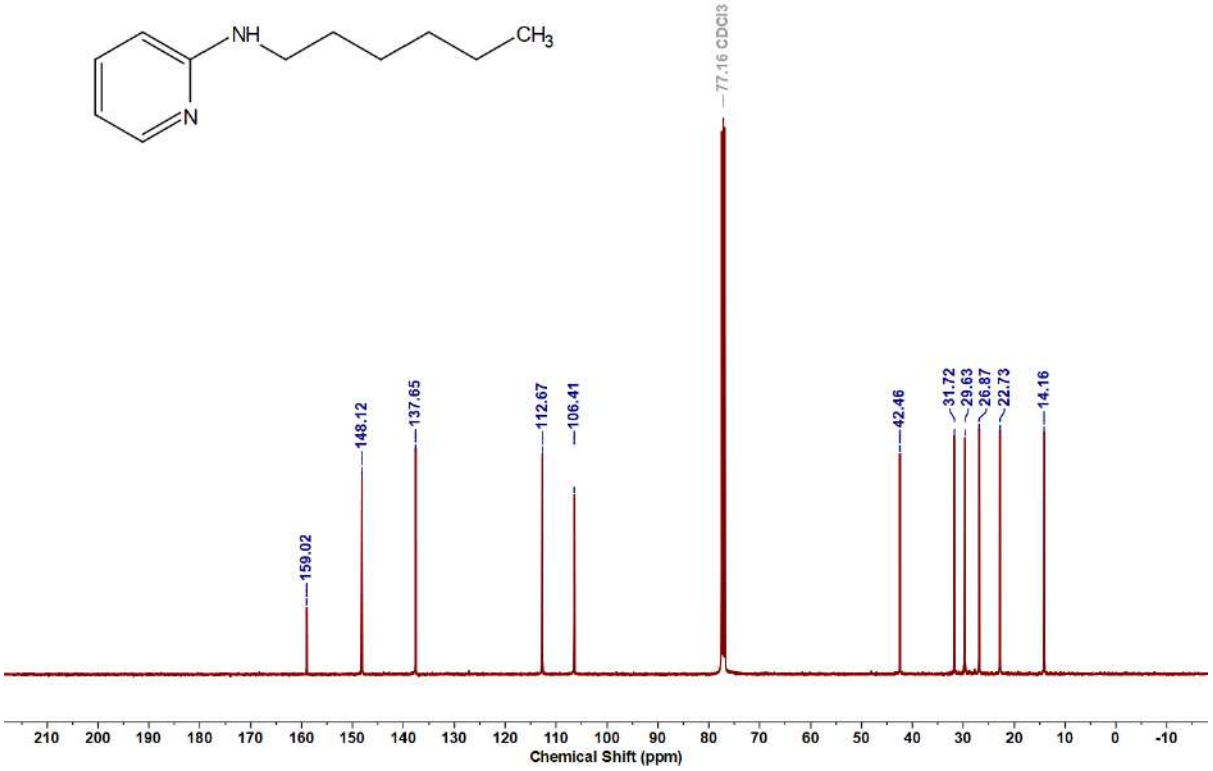

Figure 6.6.A40: $^{13}C\{^{1}H\}$ NMR spectrum of **5o**

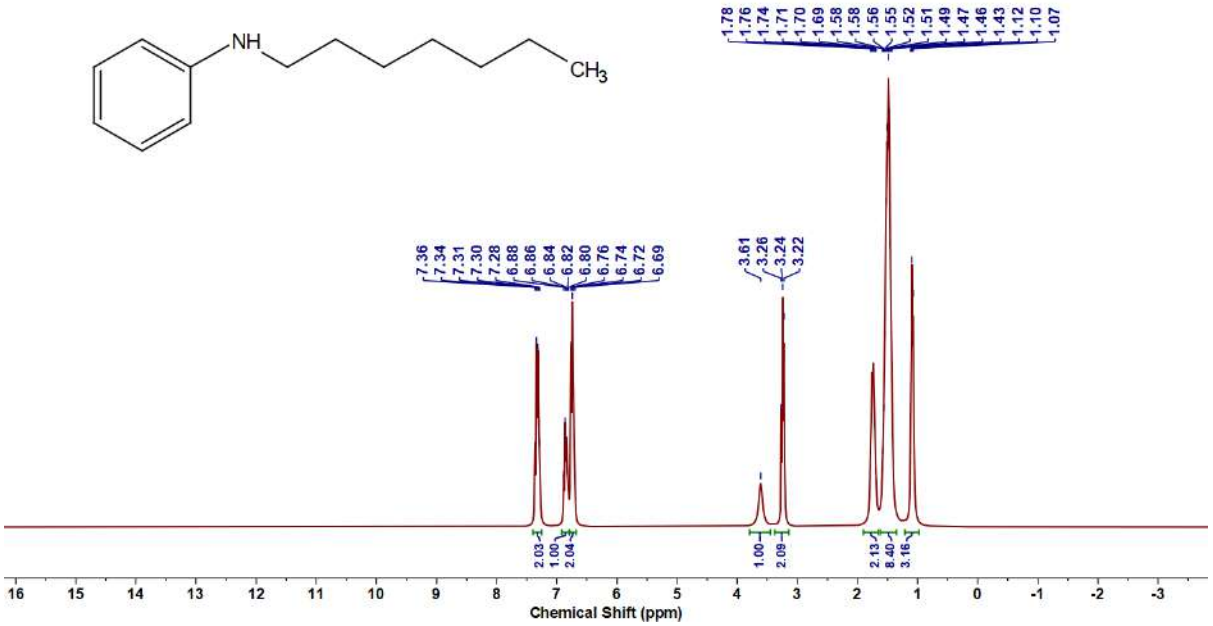

Figure 6.6.A41: ^{1}H NMR spectrum of **5p**

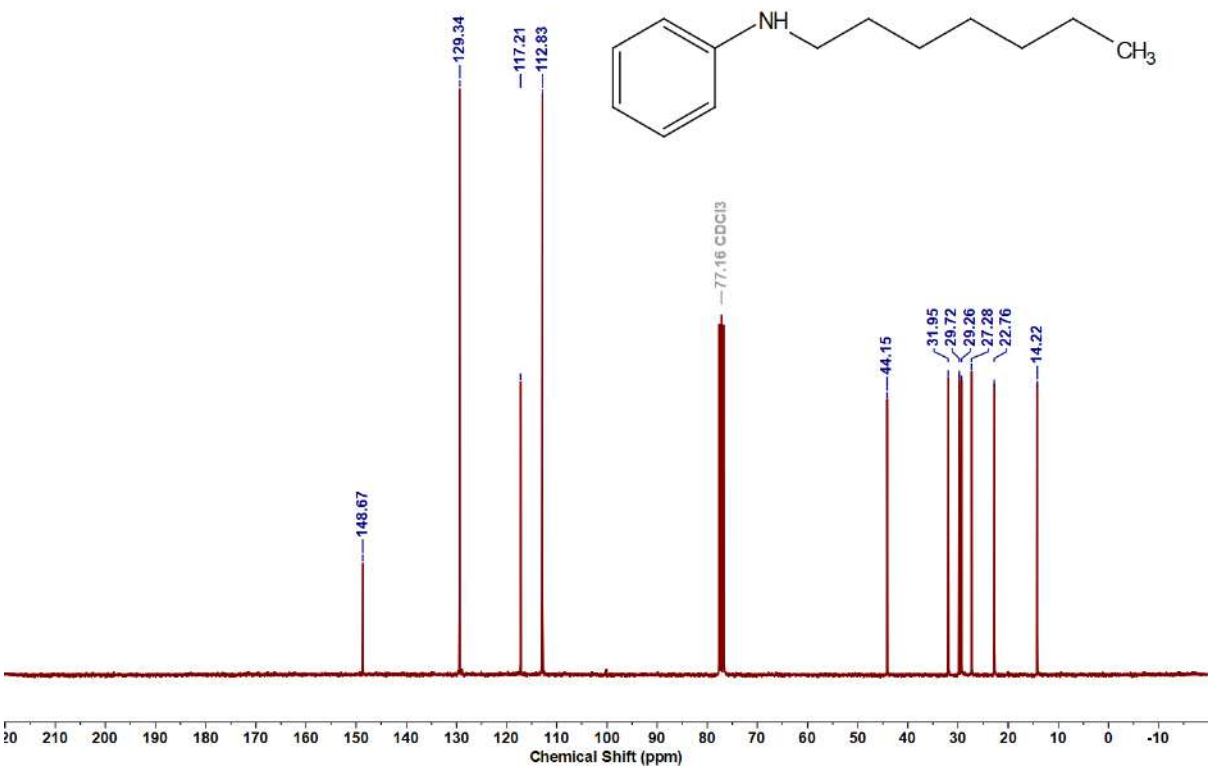

Figure 6.6.A42: $^{13}C\{^{1}H\}$ NMR spectrum of **5p**

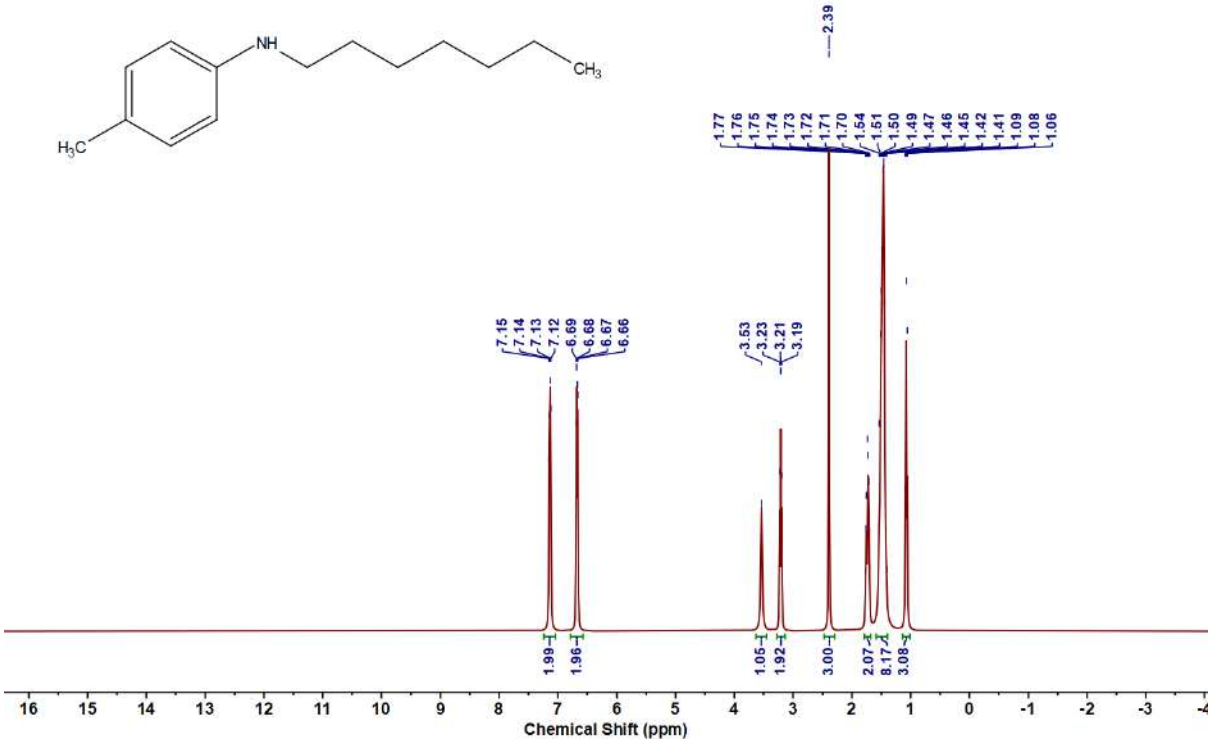

Figure 6.6.A43: ^{1}H NMR spectrum of **5q**

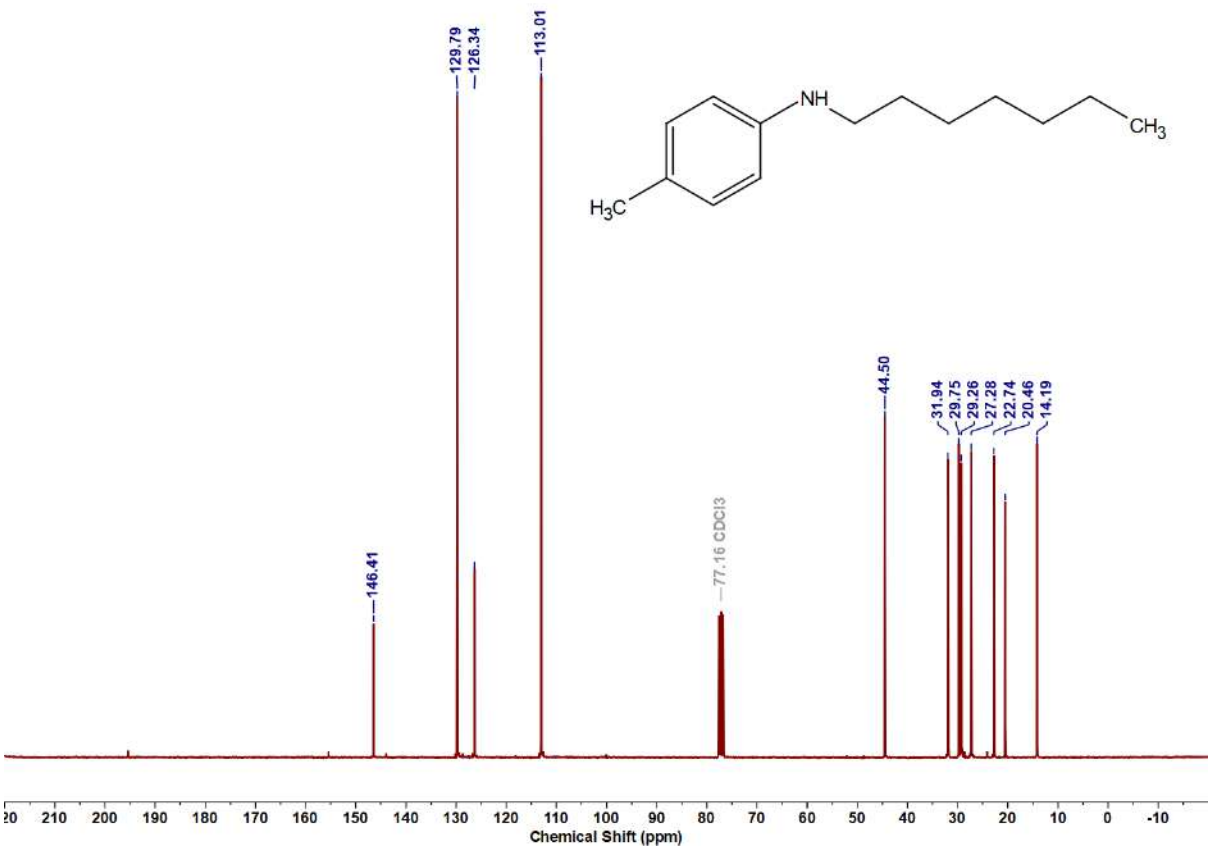

Figure 6.6.A44: $^{13}C\{^{1}H\}$ NMR spectrum of **5q**

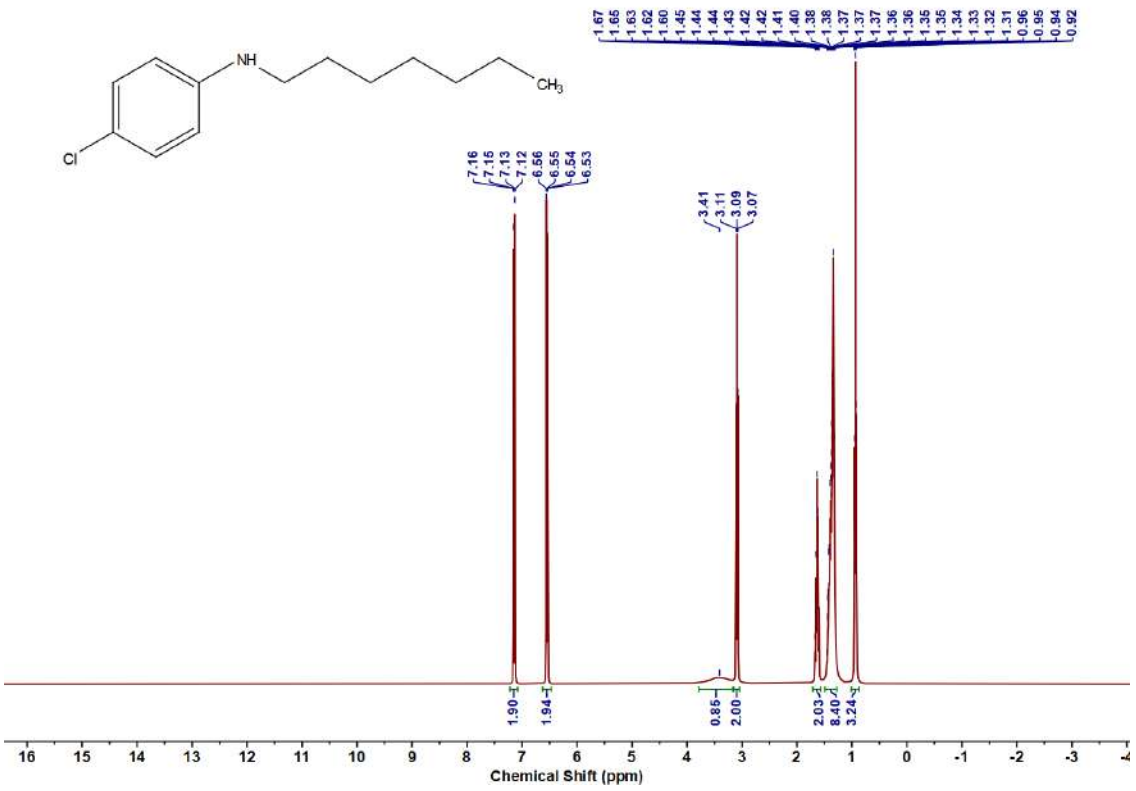

Figure 6.6.A45: ^{1}H NMR spectrum of **5r**

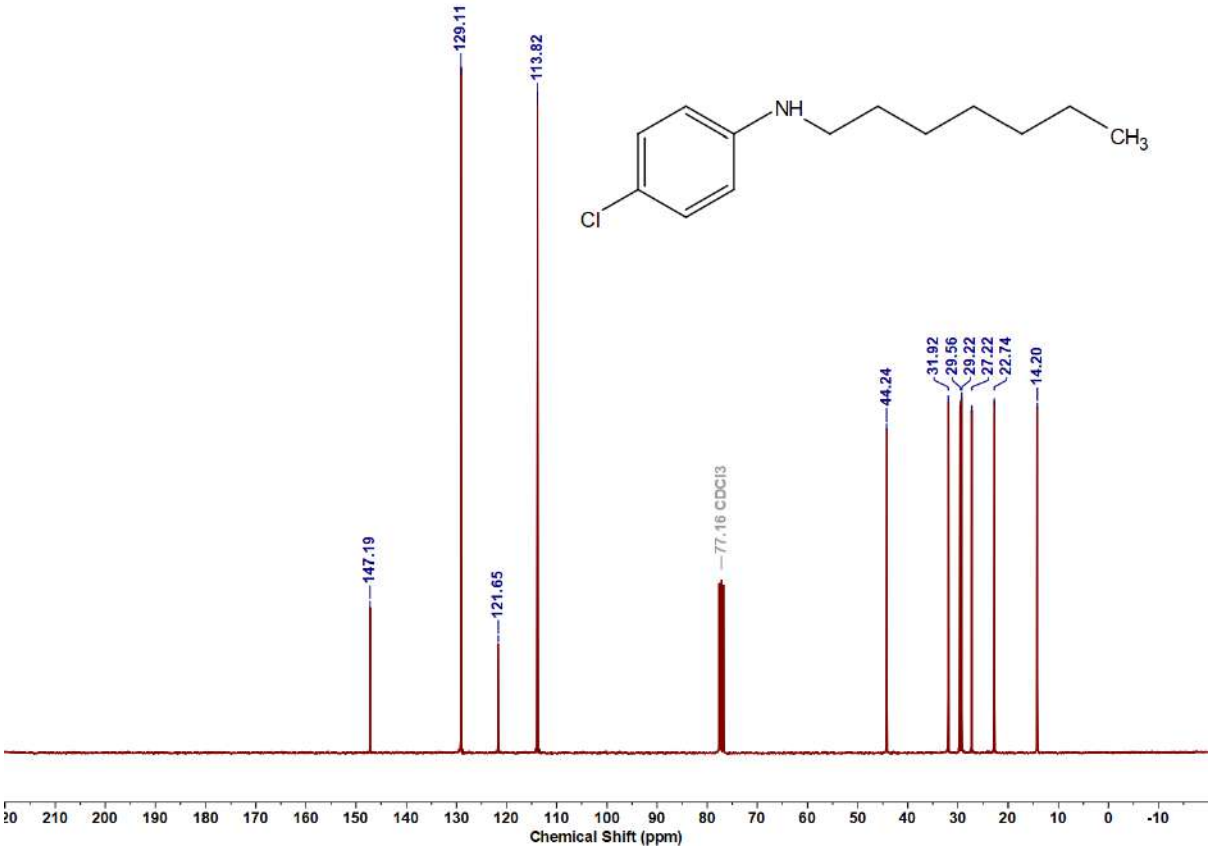

Figure 6.6.A46: $^{13}C\{^{1}H\}$ NMR spectrum of **5r**

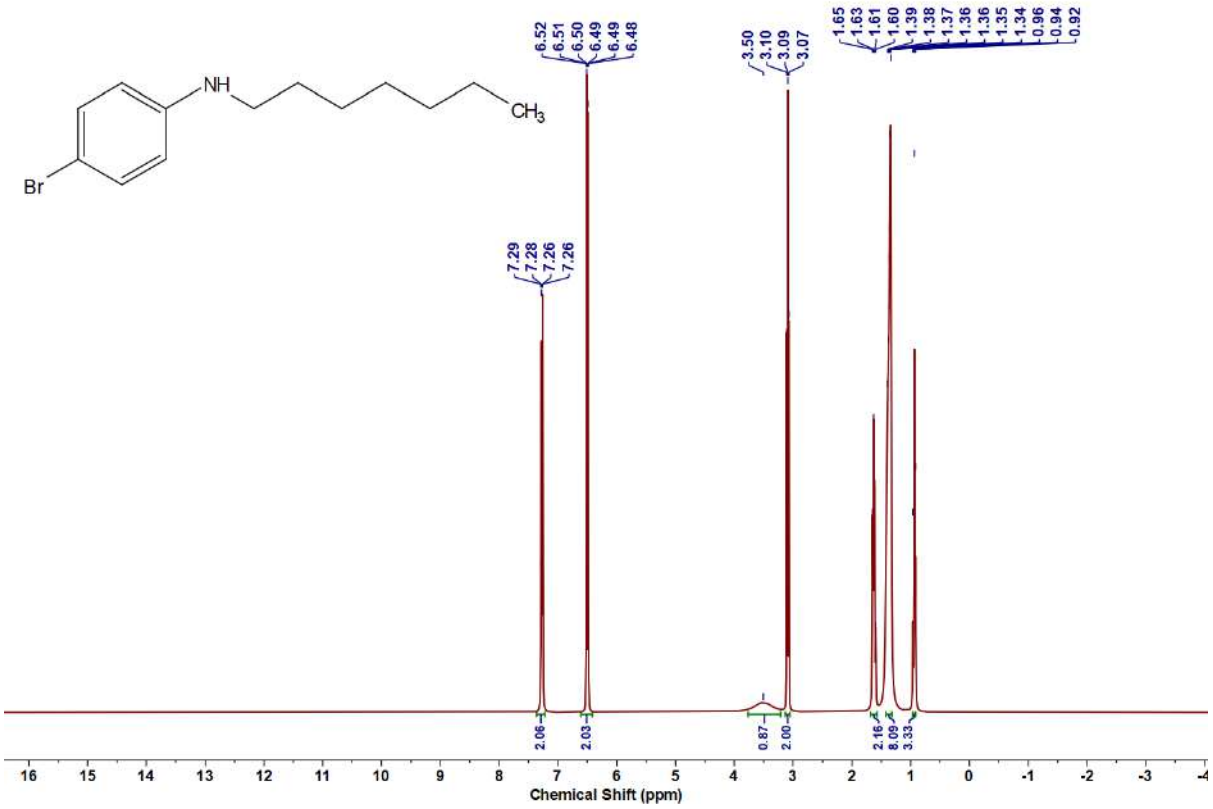

Figure 6.6.A47: ^{1}H NMR spectrum of **5s**

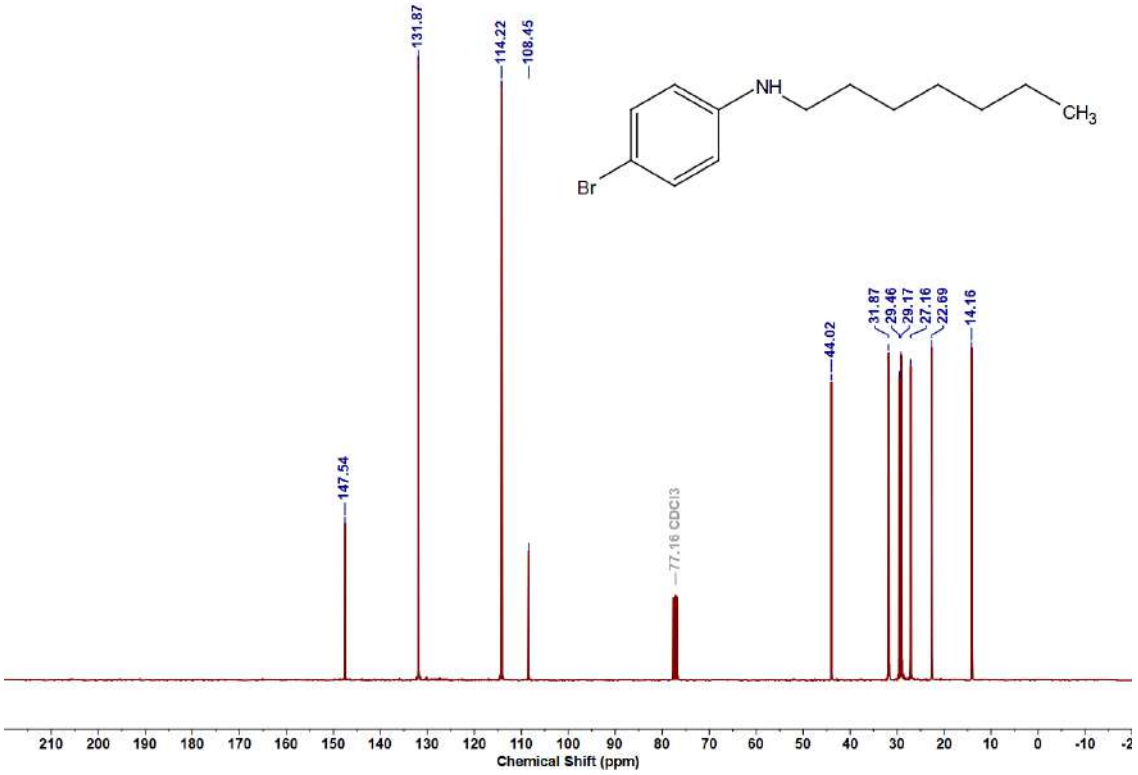

Figure 6.6.A48: $^{13}C\{^{1}H\}$ NMR spectrum of **5s**

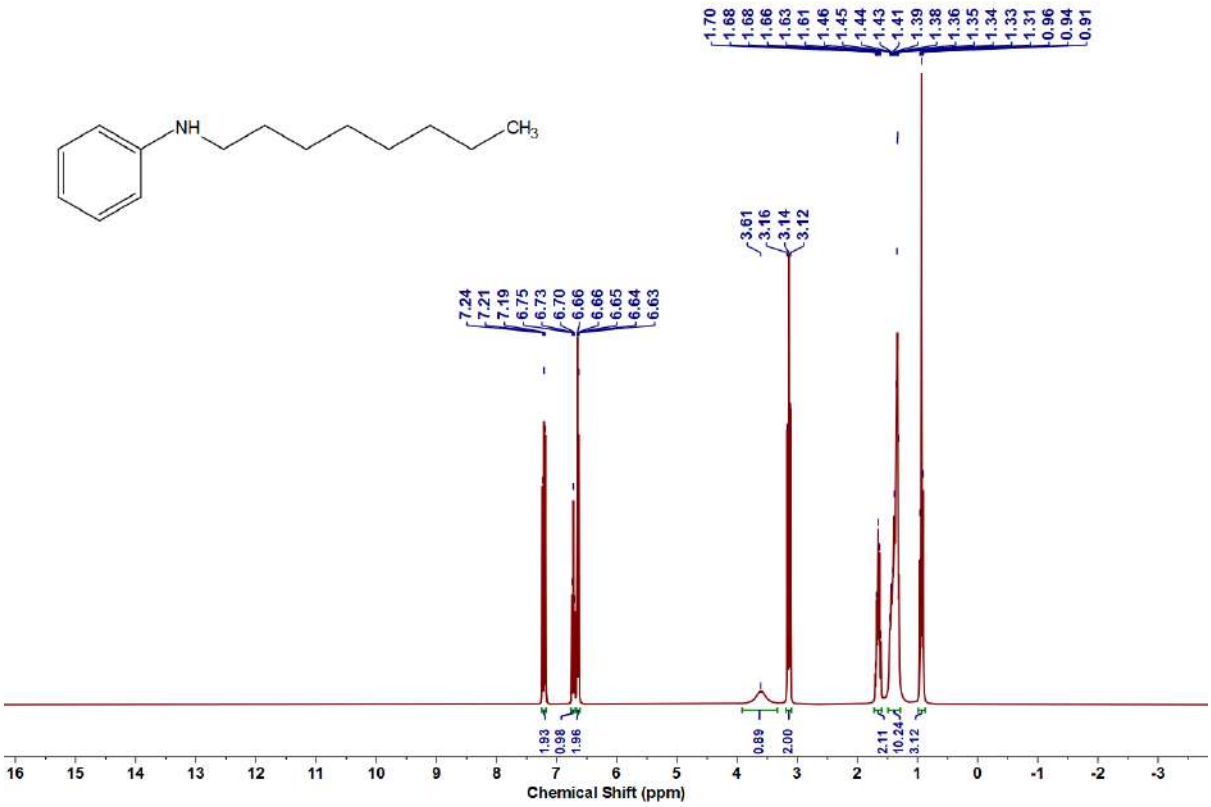

Figure 6.6.A49: ^{1}H NMR spectrum of **5t**

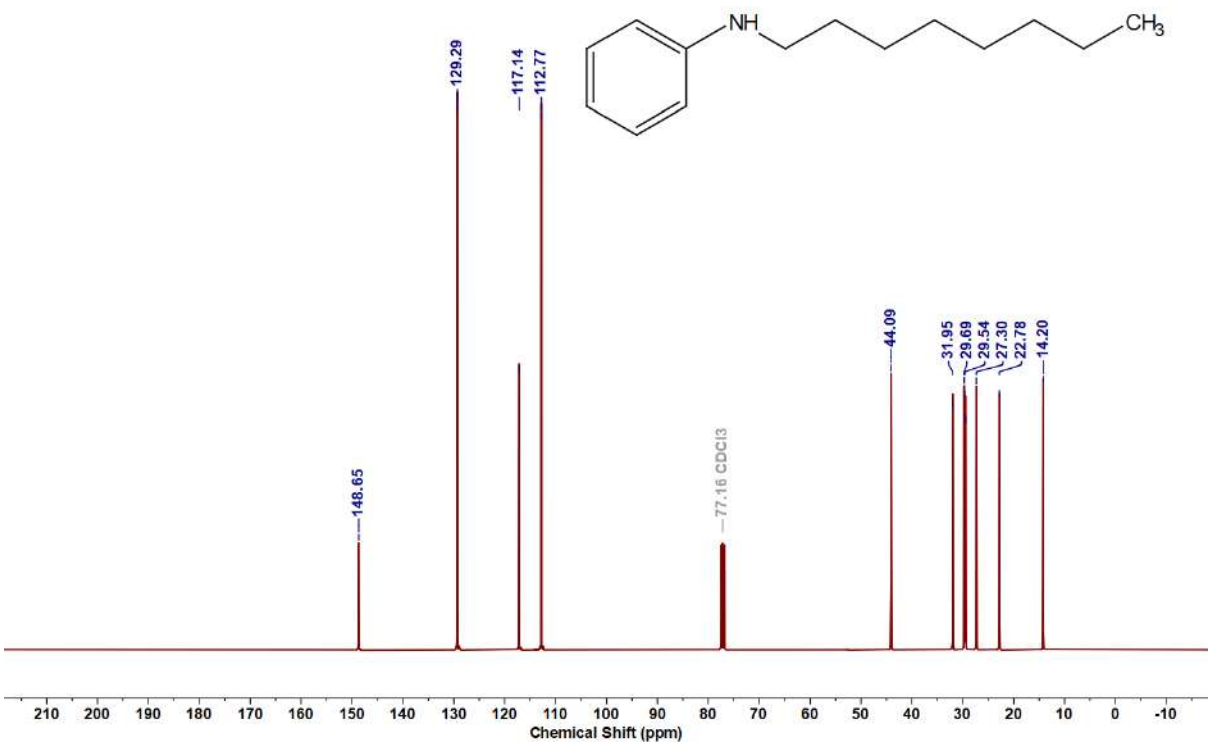

Figure 6.6.A50: $^{13}C\{^{1}H\}$ NMR spectrum of **5t**

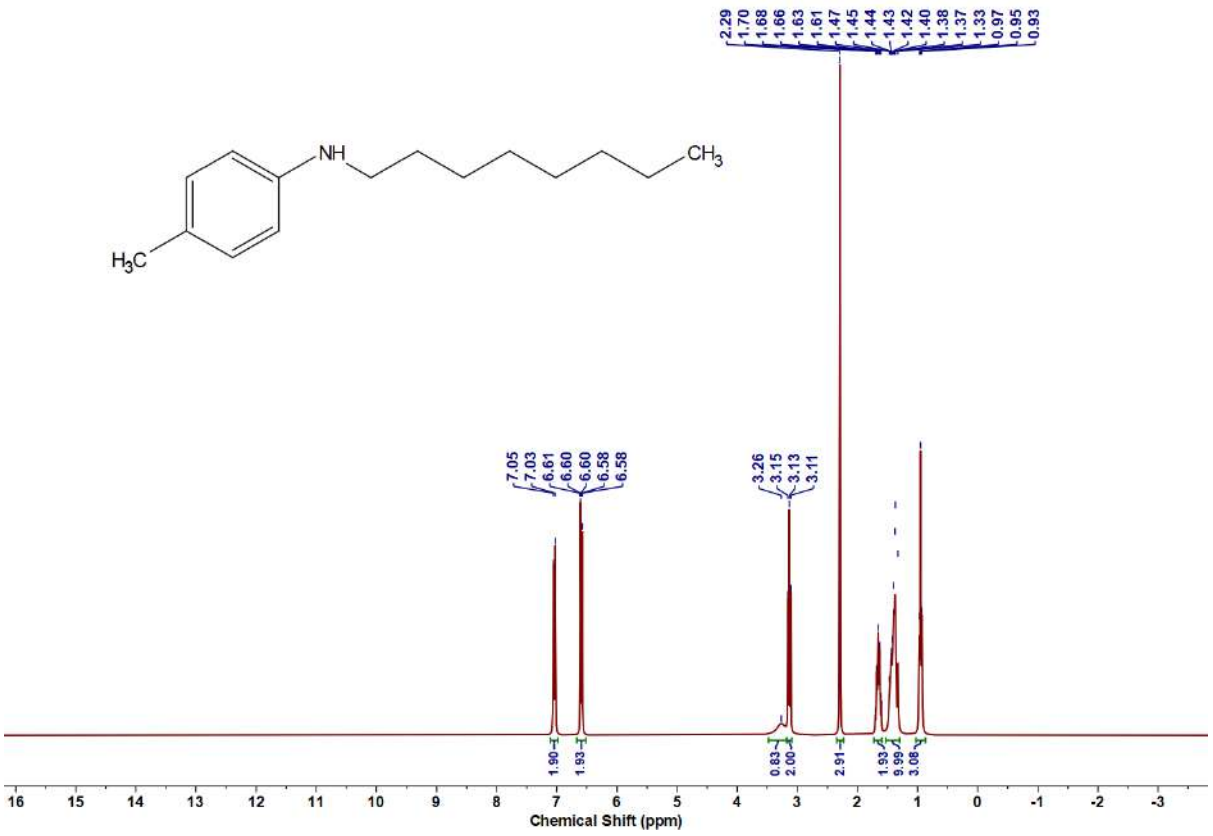

Figure 6.6.A51: ^{1}H NMR spectrum of **5u**

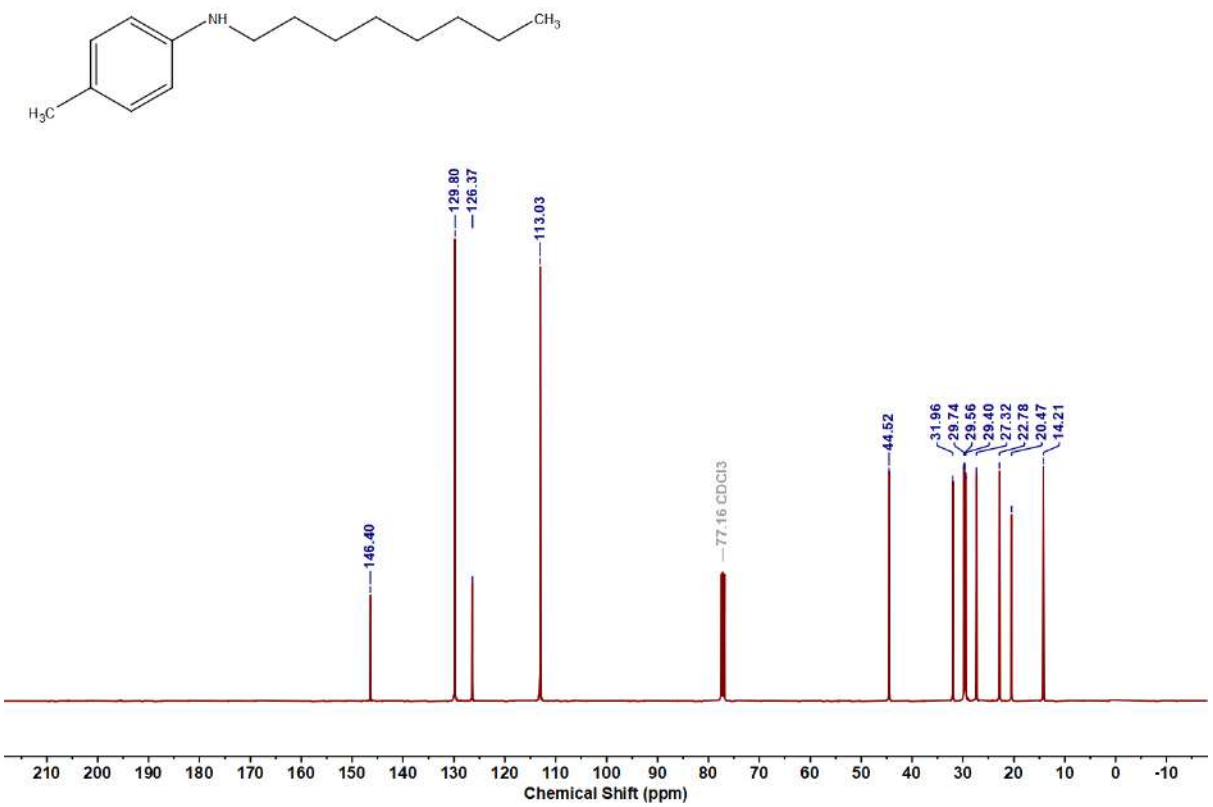

Figure 6.6.A52: $^{13}C\{^{1}H\}$ NMR spectrum of **5u**

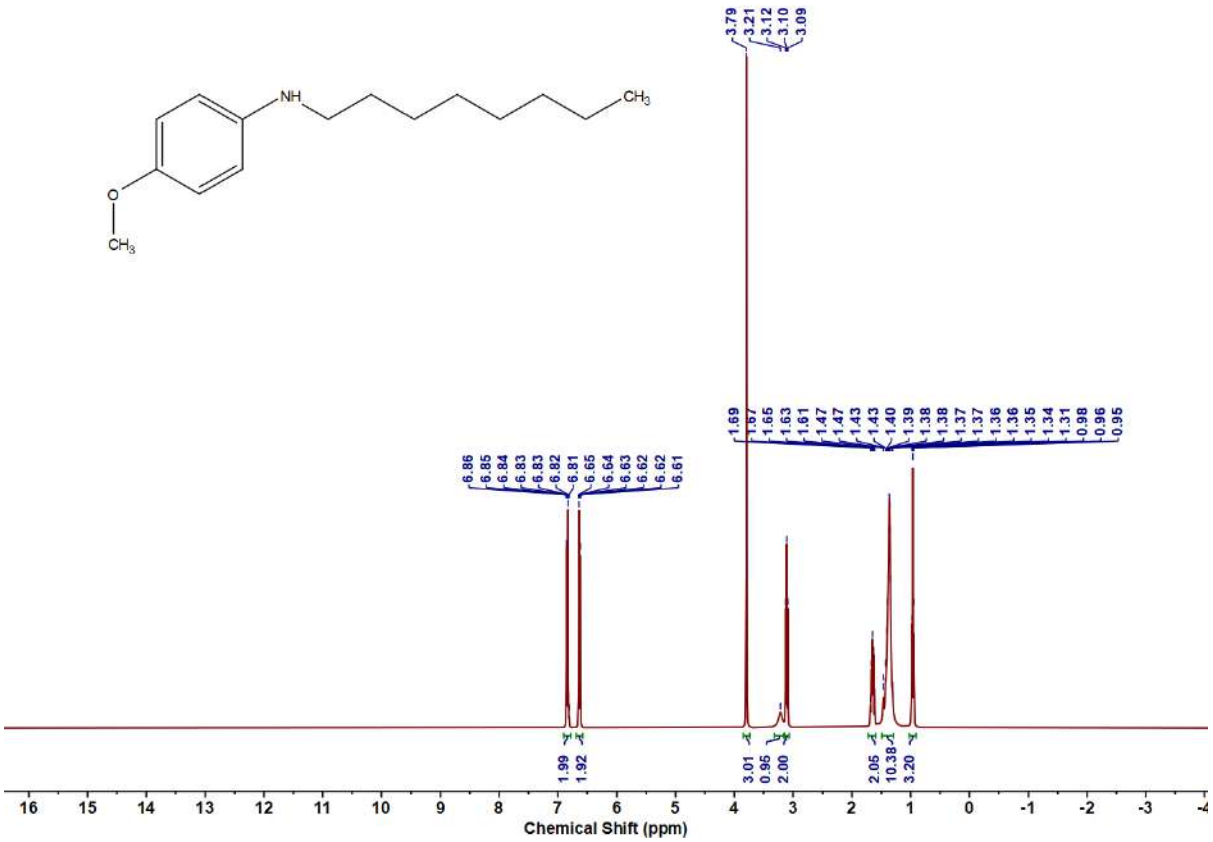

Figure 6.6.A53: ^{1}H NMR spectrum of **5v**

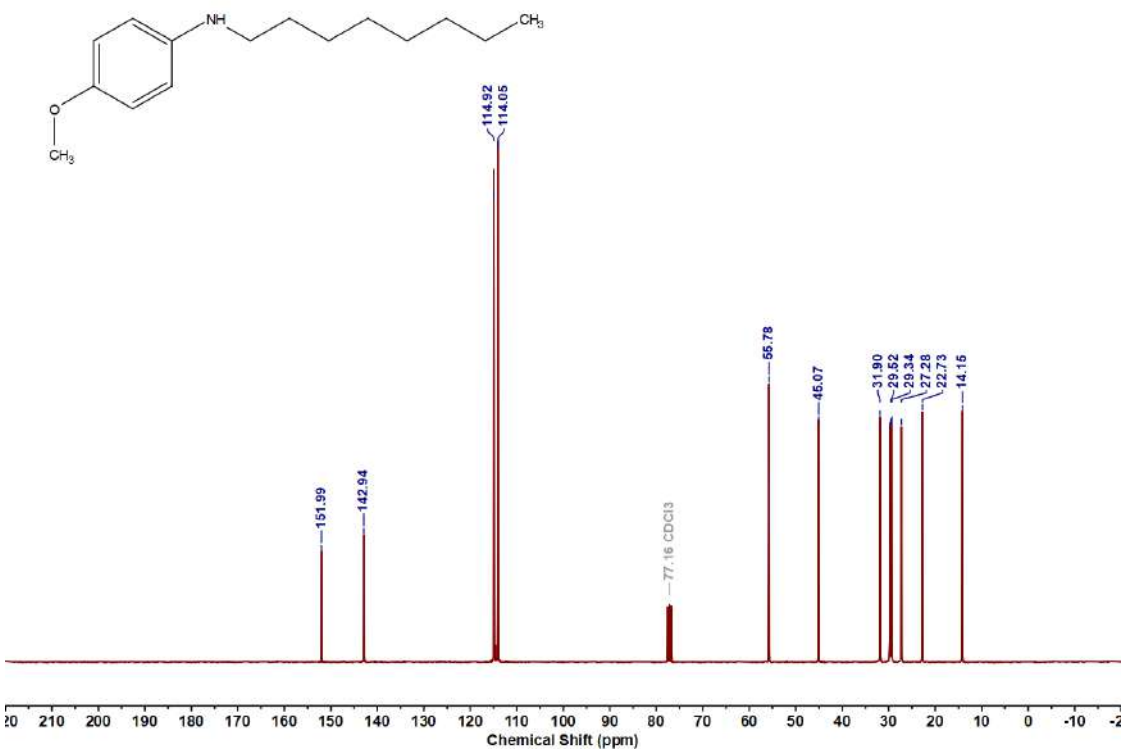

Figure 6.6.A54: $^{13}C\{^{1}H\}$ NMR spectrum of **5v**

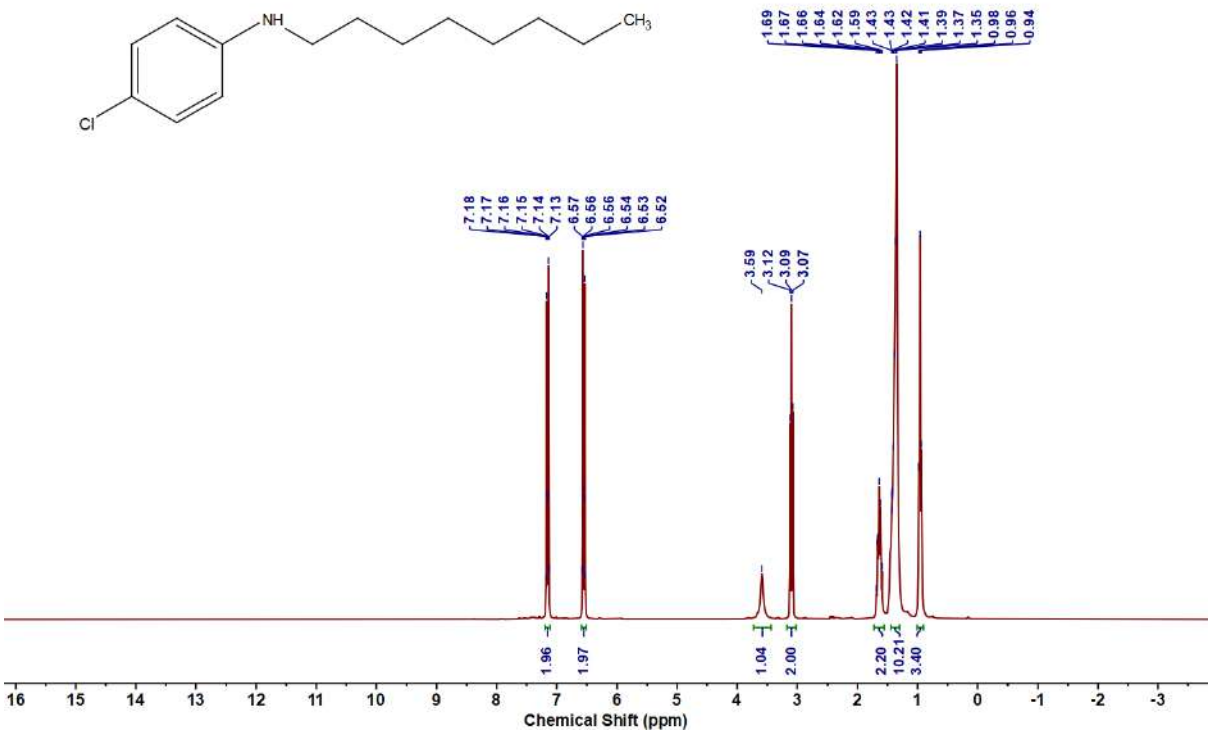

Figure 6.6.A55: ^{1}H NMR spectrum of **5w**

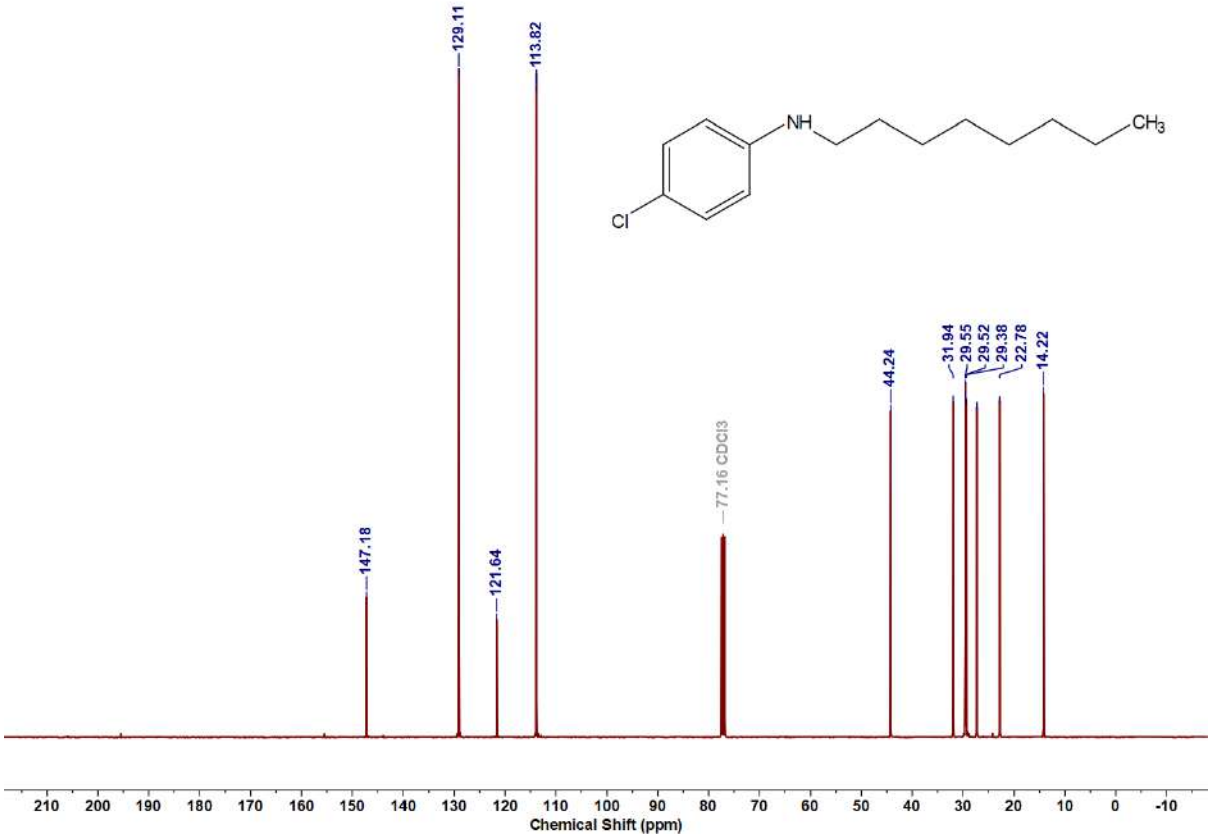

Figure 6.6.A56: $^{13}C\{^{1}H\}$ NMR spectrum of **5w**

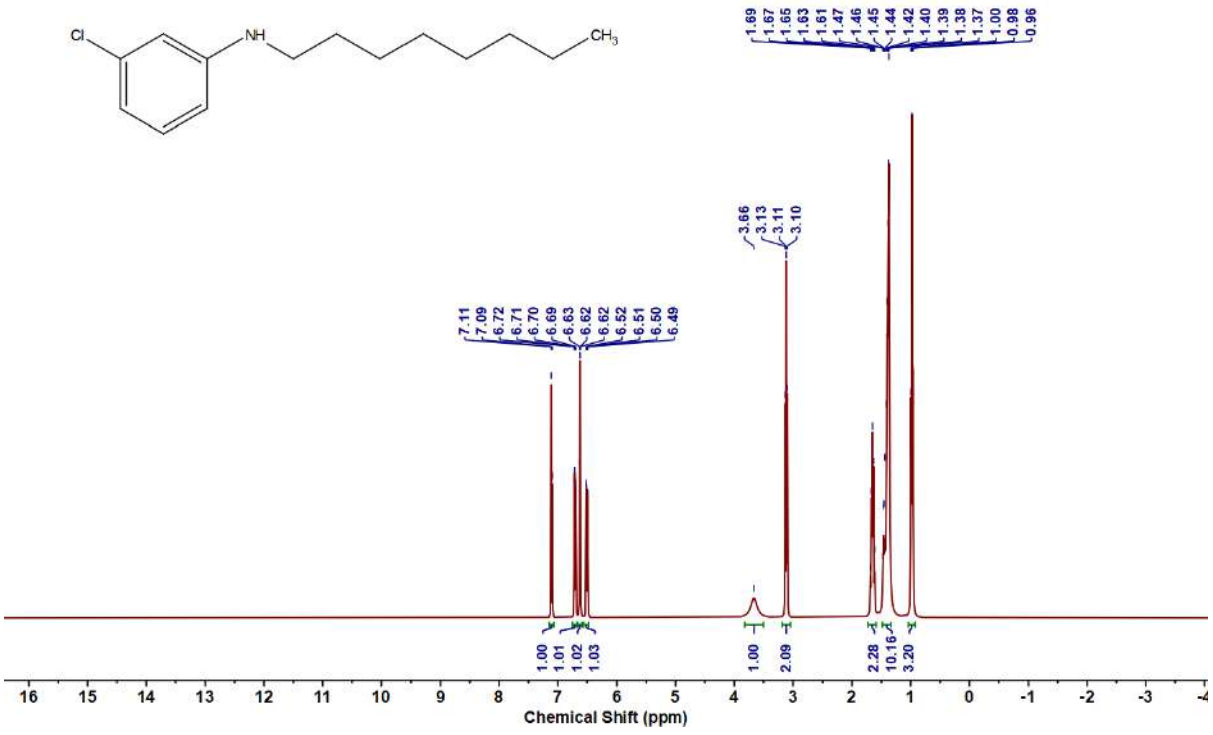

Figure 6.6.A57: ^{1}H NMR spectrum of **5x**

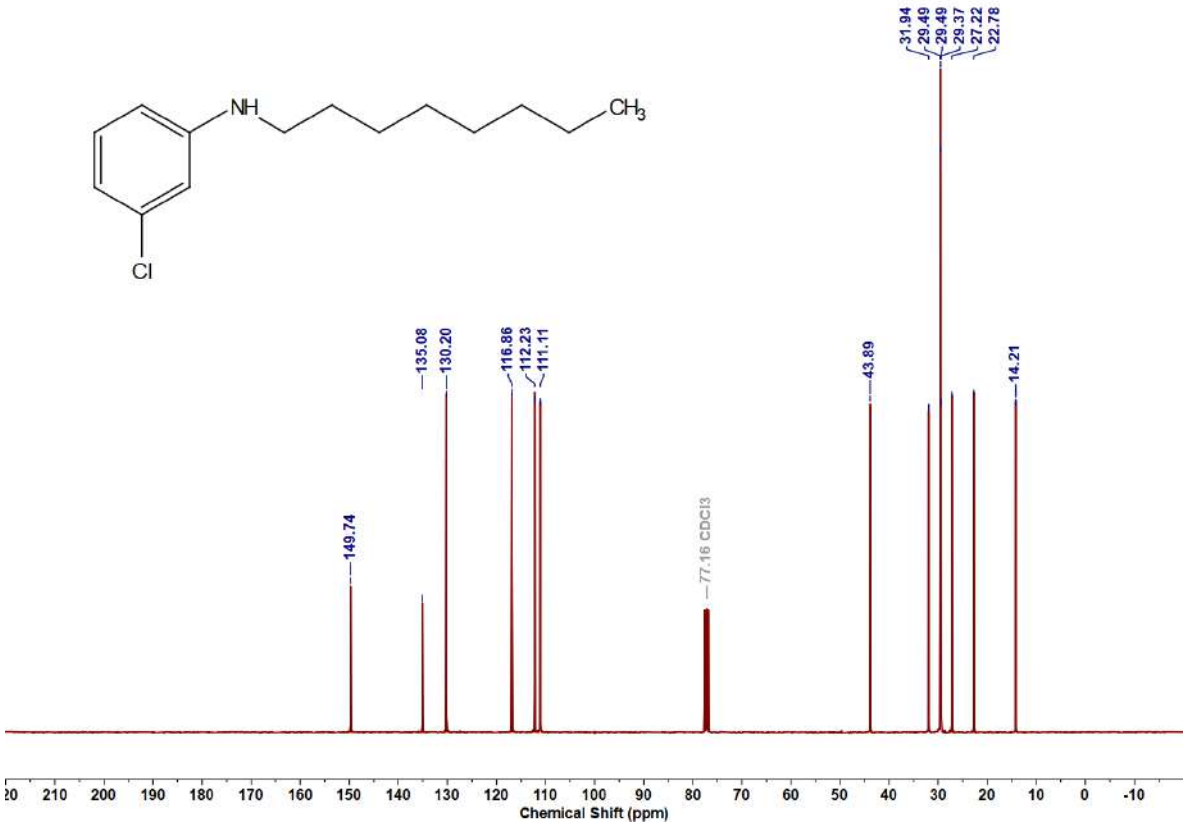

Figure 6.6.A58: $^{13}C\{^{1}H\}$ NMR spectrum of **5x**

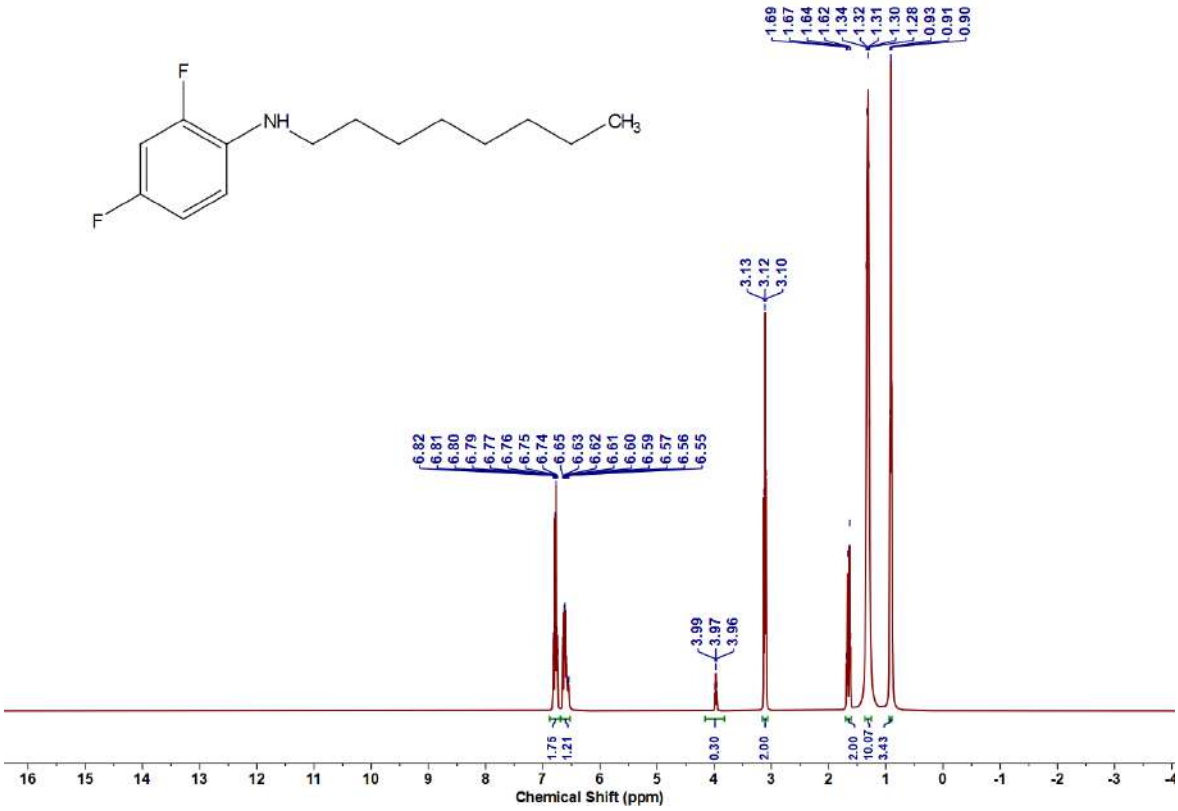

Figure 6.6.A59: ^{1}H NMR spectrum of **5y**

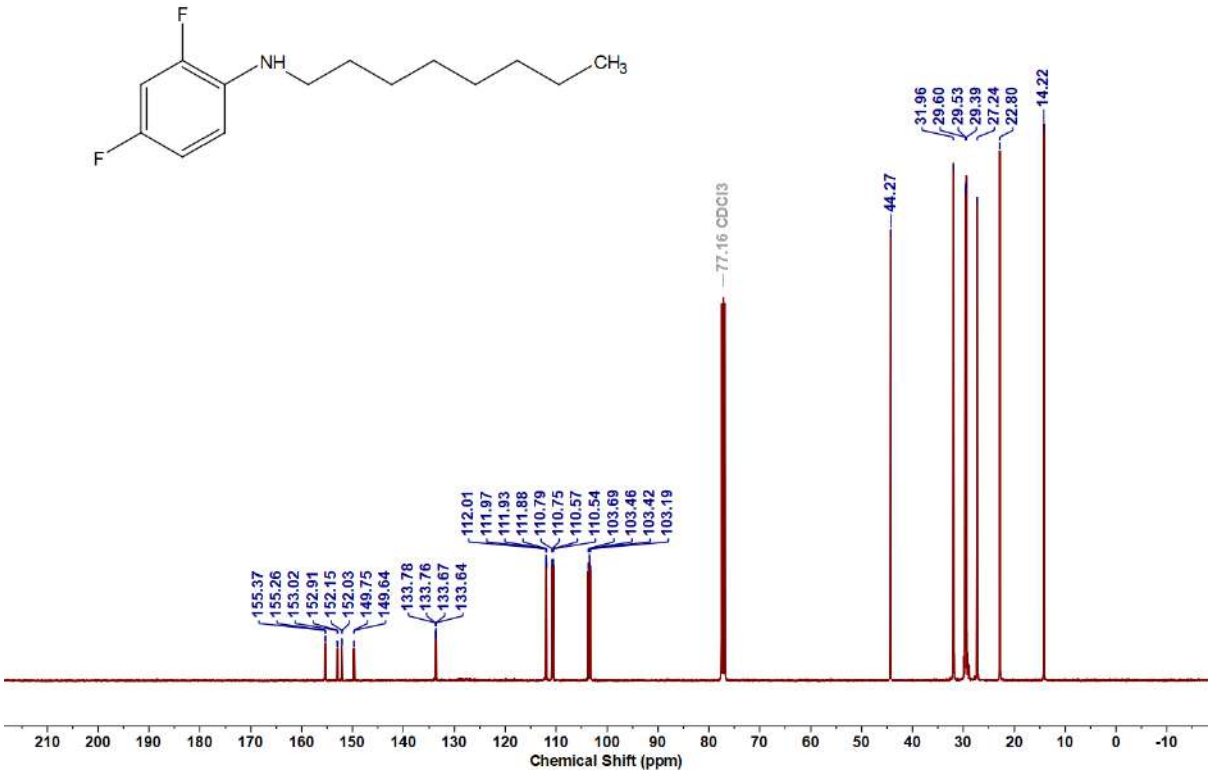

Figure 6.6.A60: $^{13}C\{^{1}H\}$ NMR spectrum of **5y**

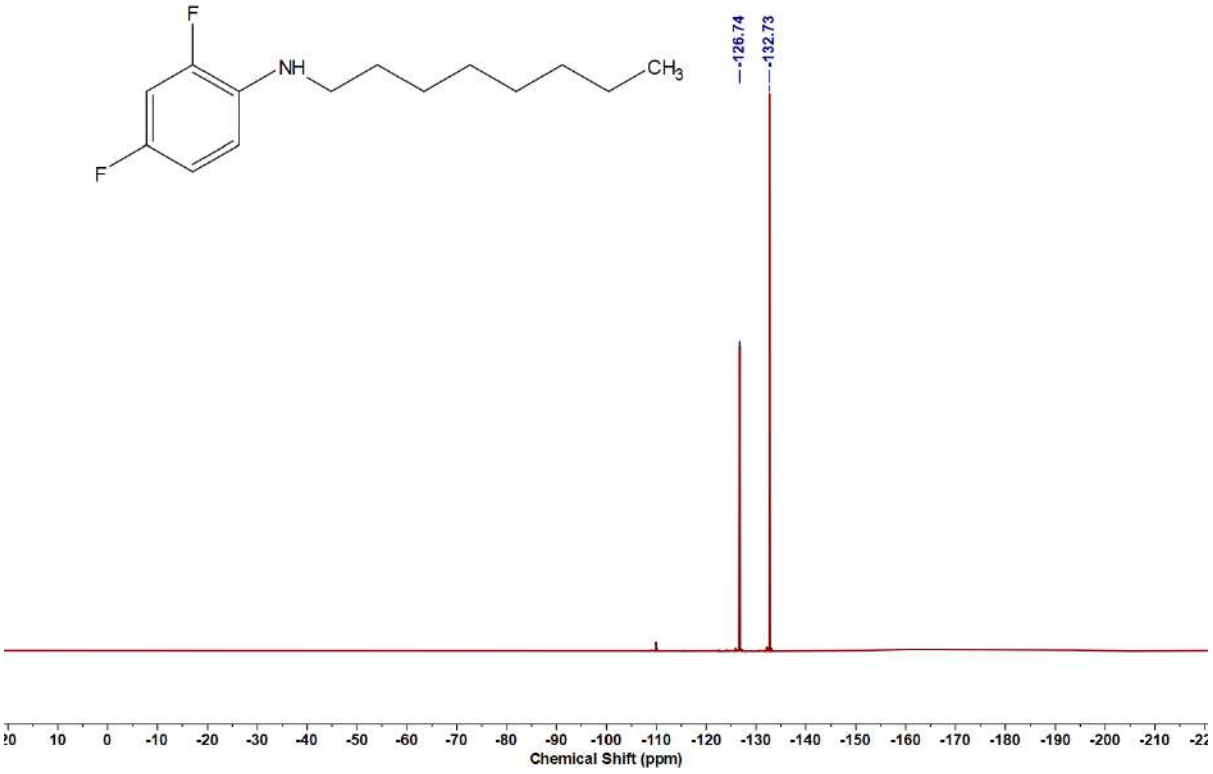

Figure 6.6.A61: ^{19}F NMR spectrum of **5y**

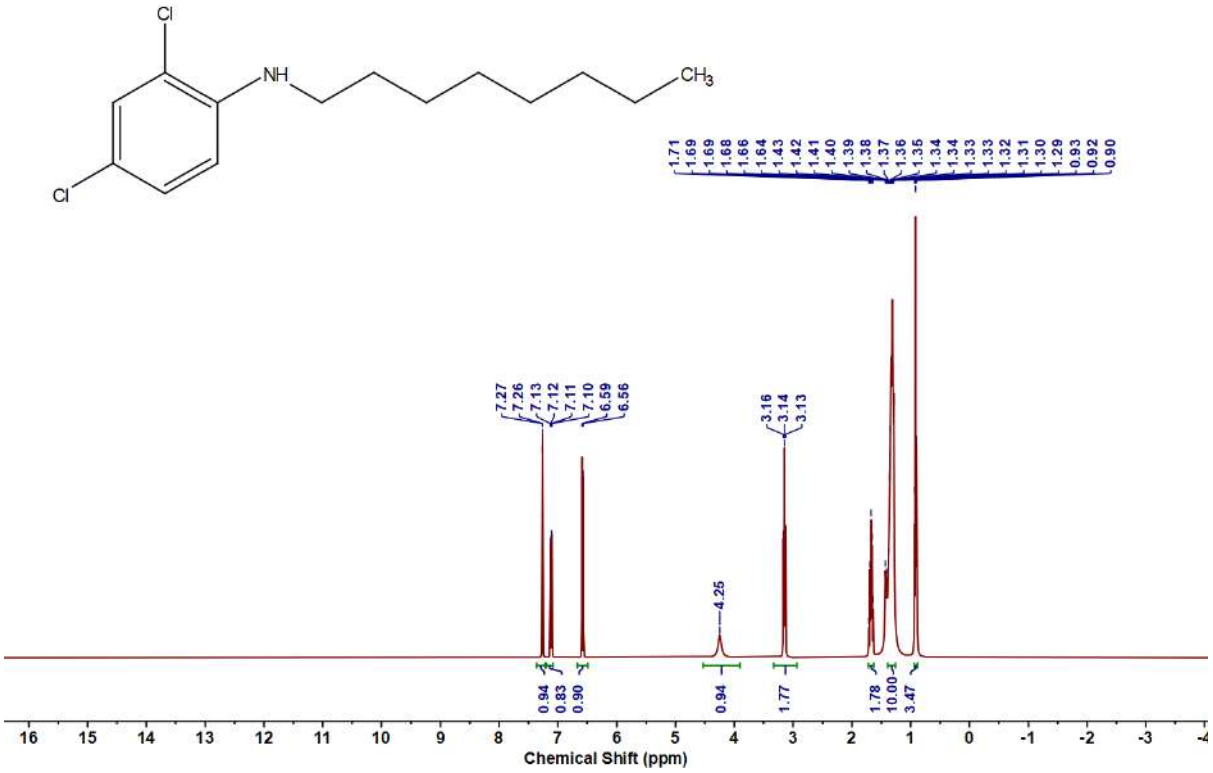

Figure 6.6.A62: ^{1}H NMR spectrum of **5z**

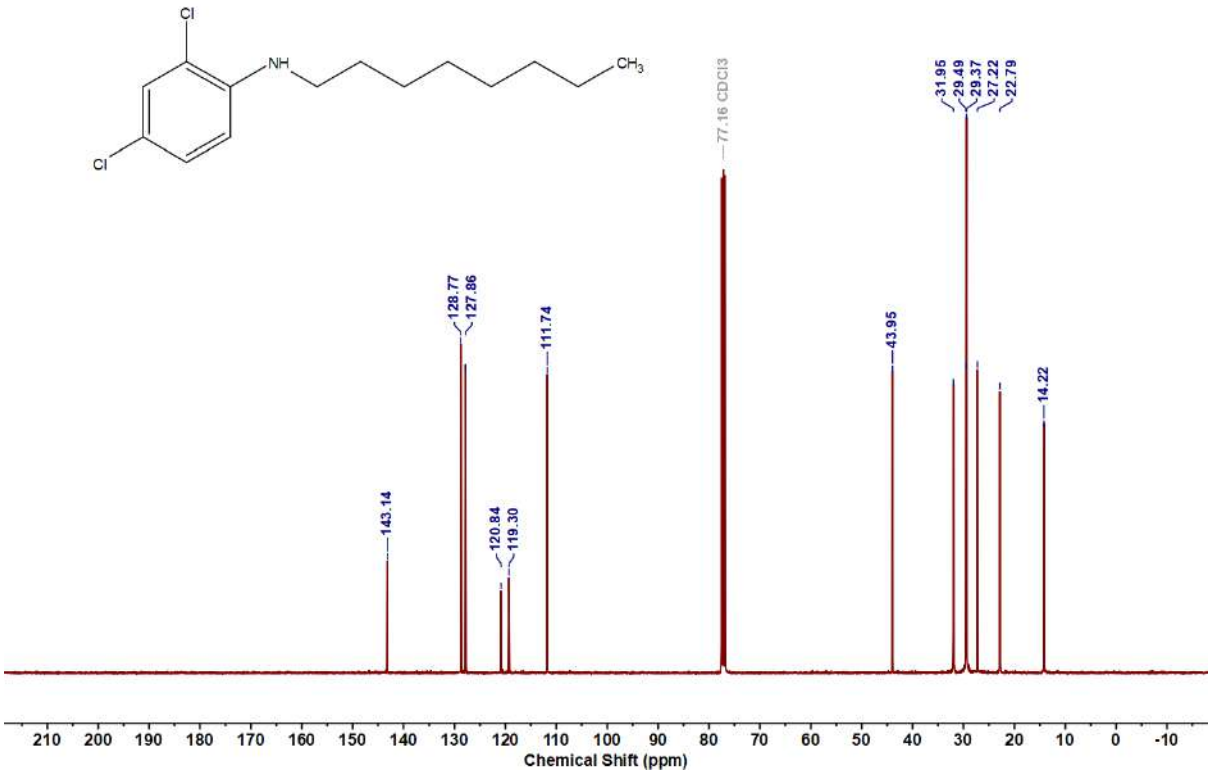

Figure 6.6.A63: $^{13}C\{^{1}H\}$ NMR spectrum of **5z**

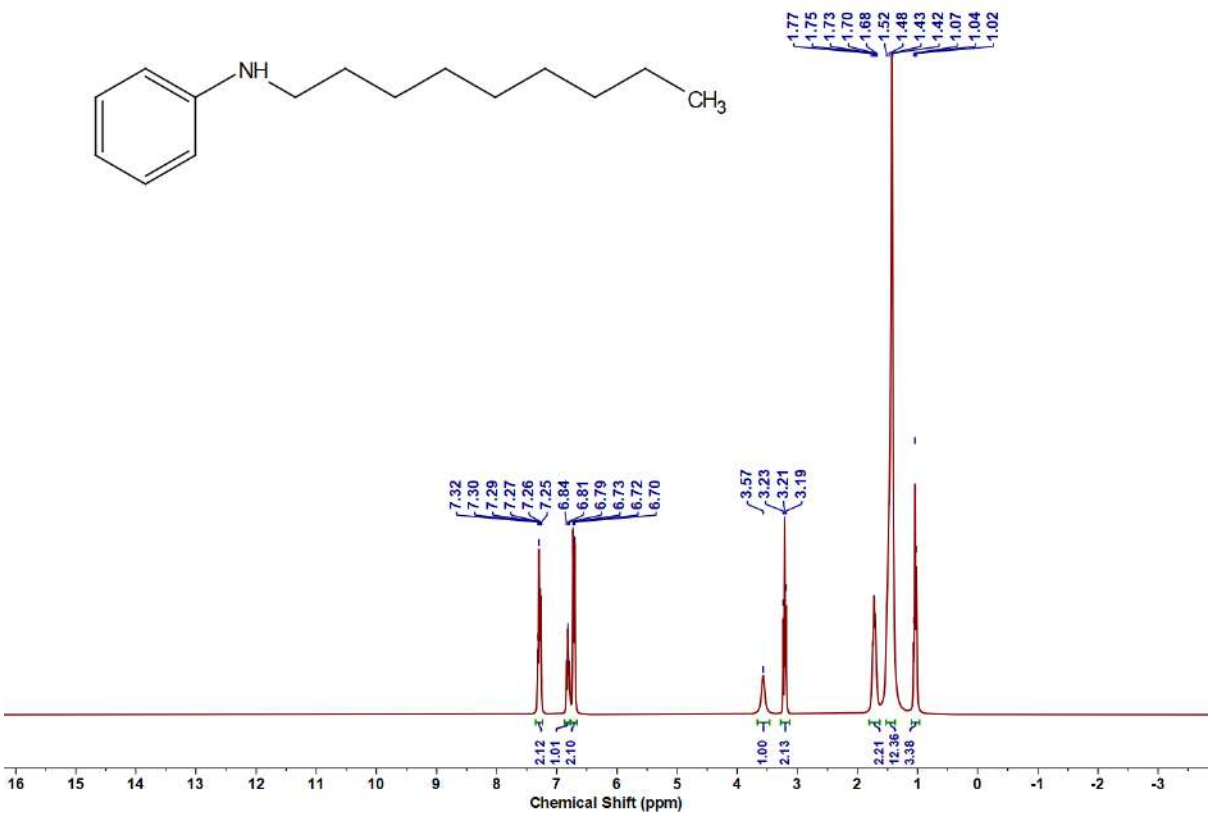

Figure 6.6.A64: ^{1}H NMR spectrum of **5aa**

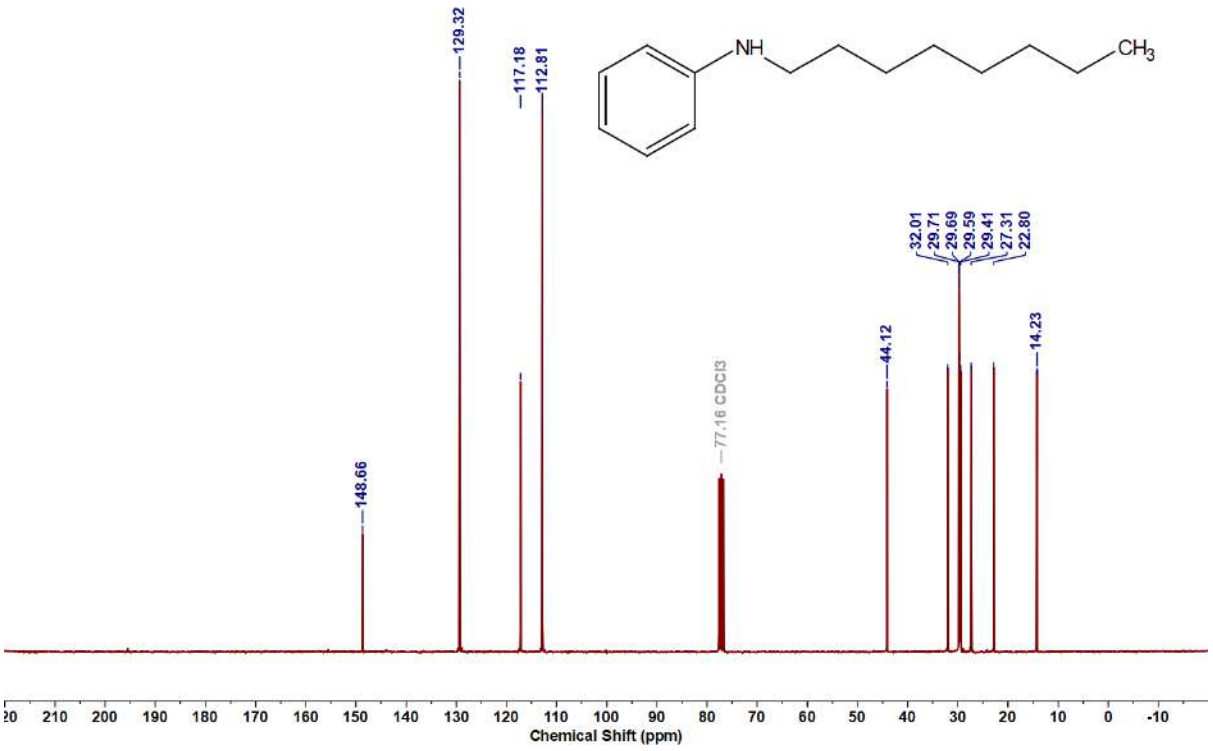

Figure 6.6.A65: ^{13}C{^{1}H} NMR spectrum of **5aa**

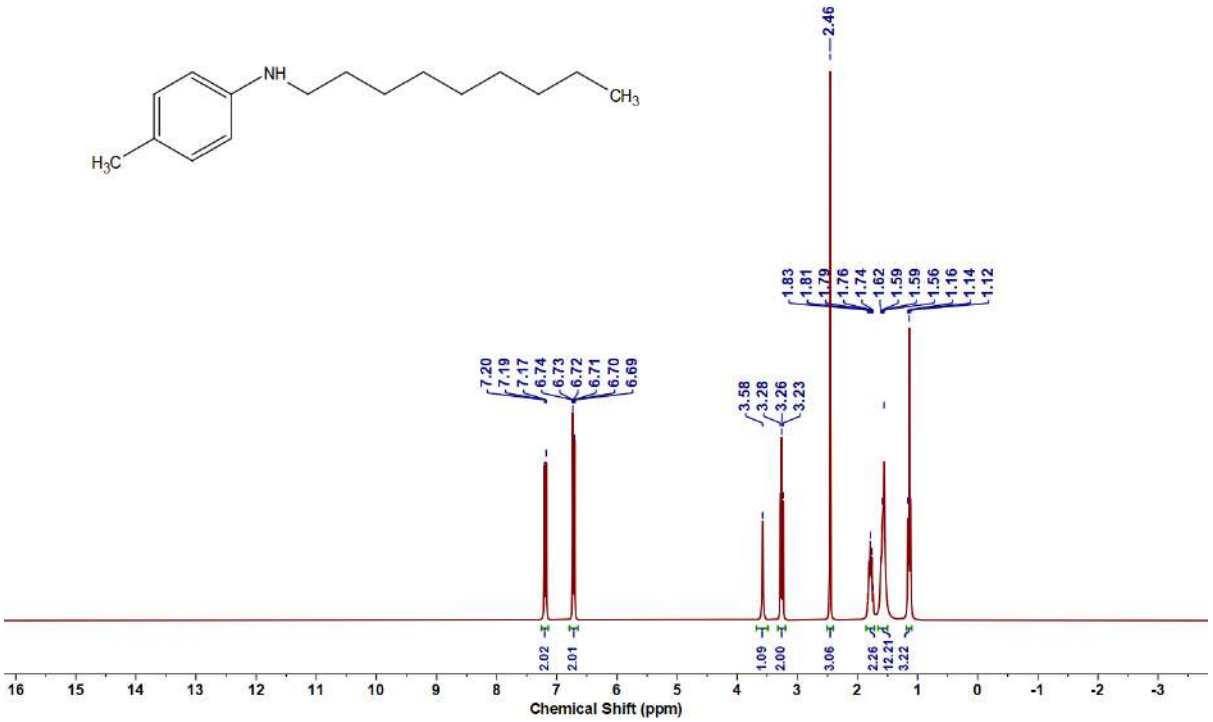

Figure 6.6.A66: ^{1}H NMR spectrum of **5ab**

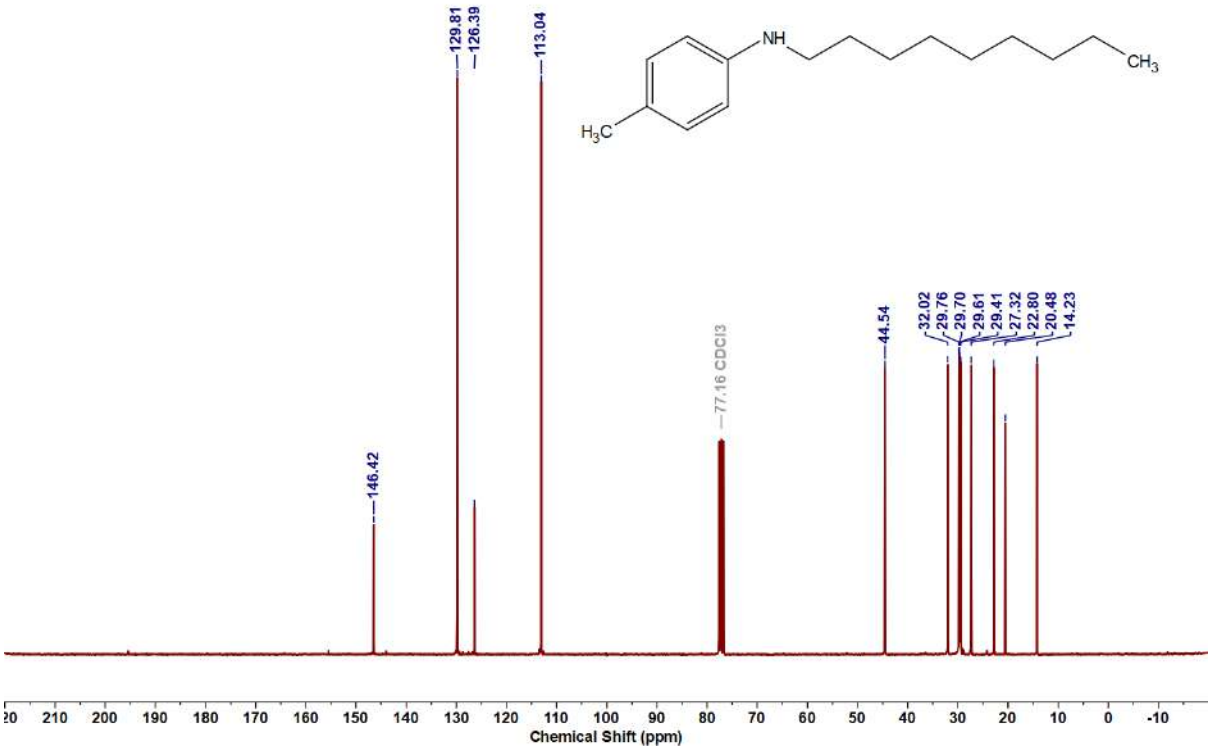

Figure 6.6.A67: ^{13}C{^{1}H} NMR spectrum of **5ab**

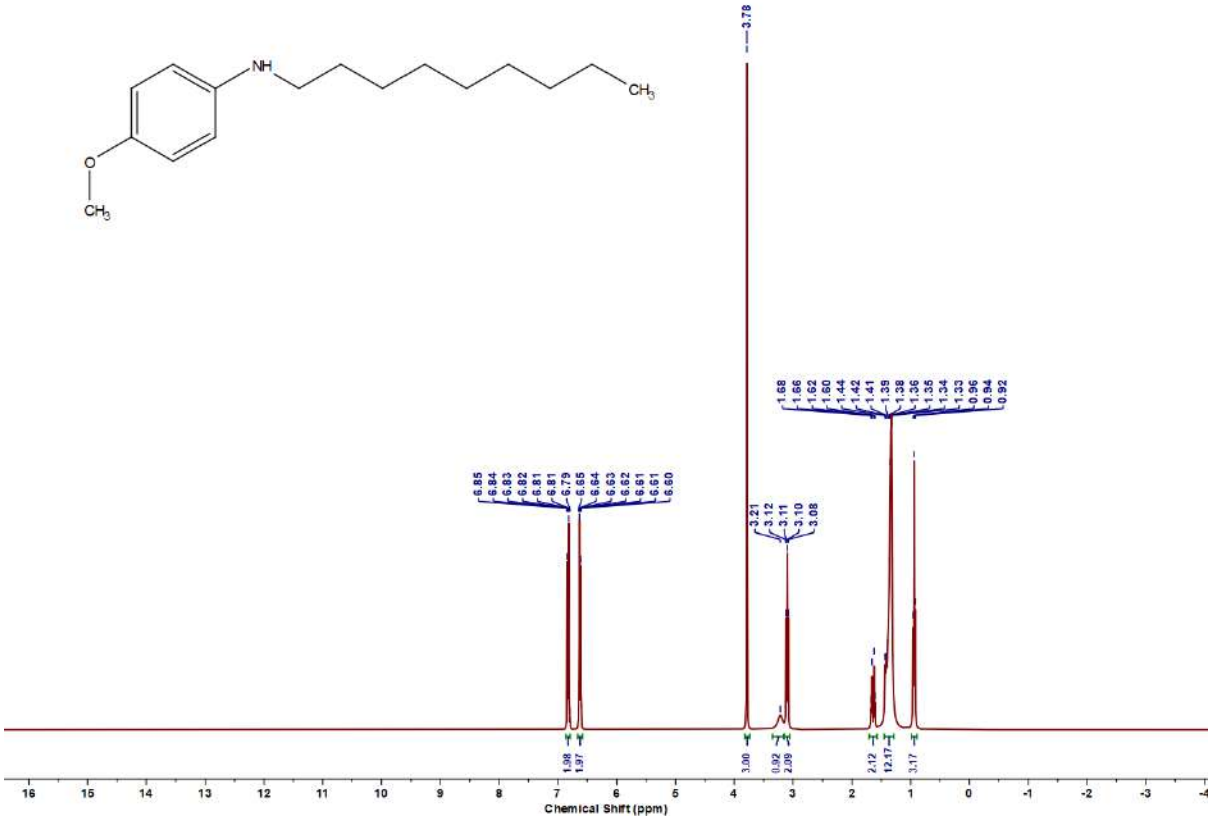

Figure 6.6.A68: ^{1}H NMR spectrum of **5ac**

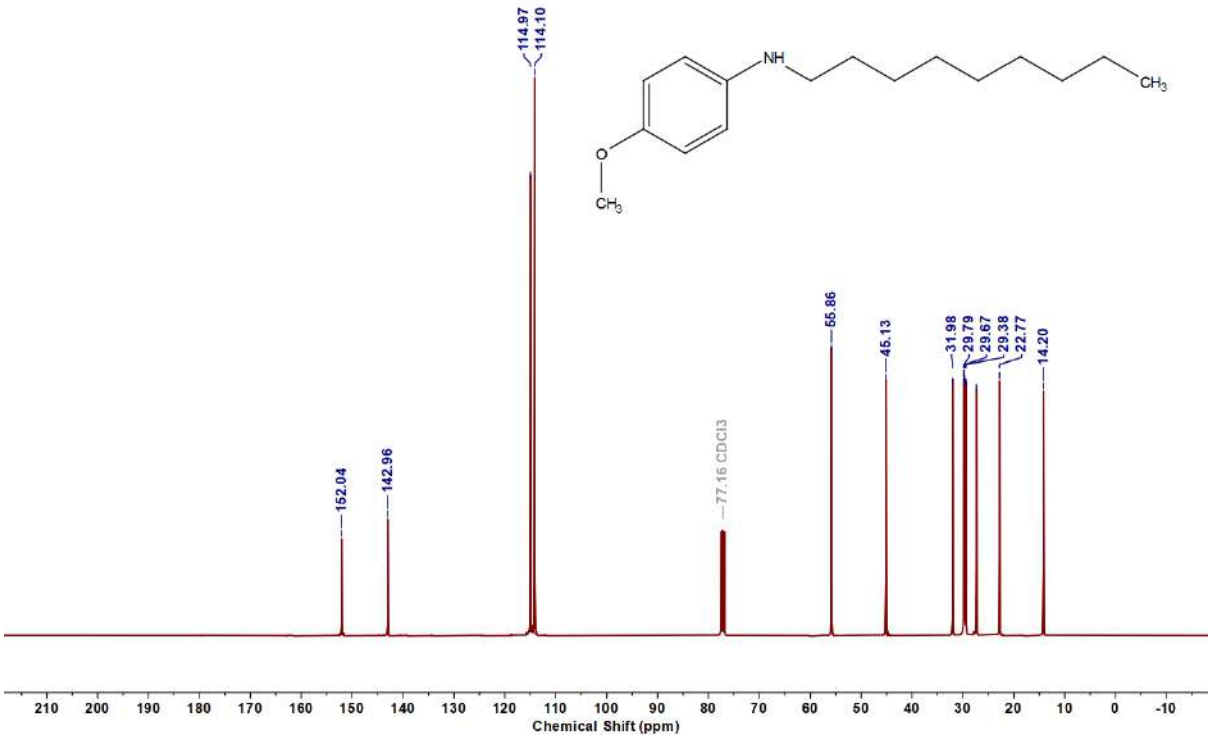

Figure 6.6.A69: ^{13}C{^{1}H} NMR spectrum of **5ac**

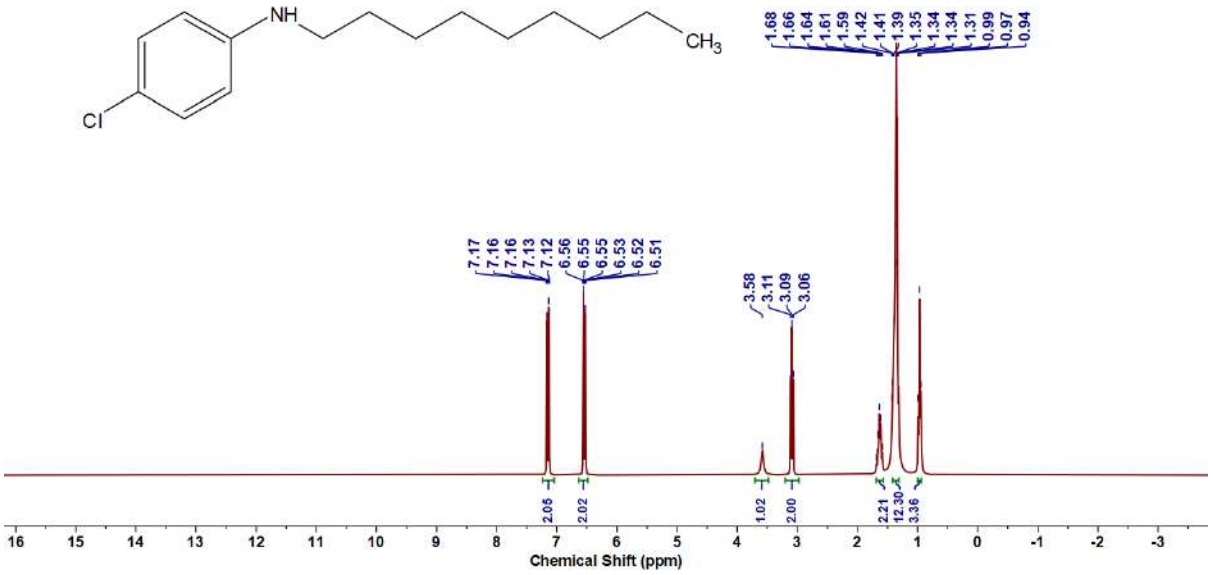

Figure 6.6.A70: ^{1}H NMR spectrum of **5ad**

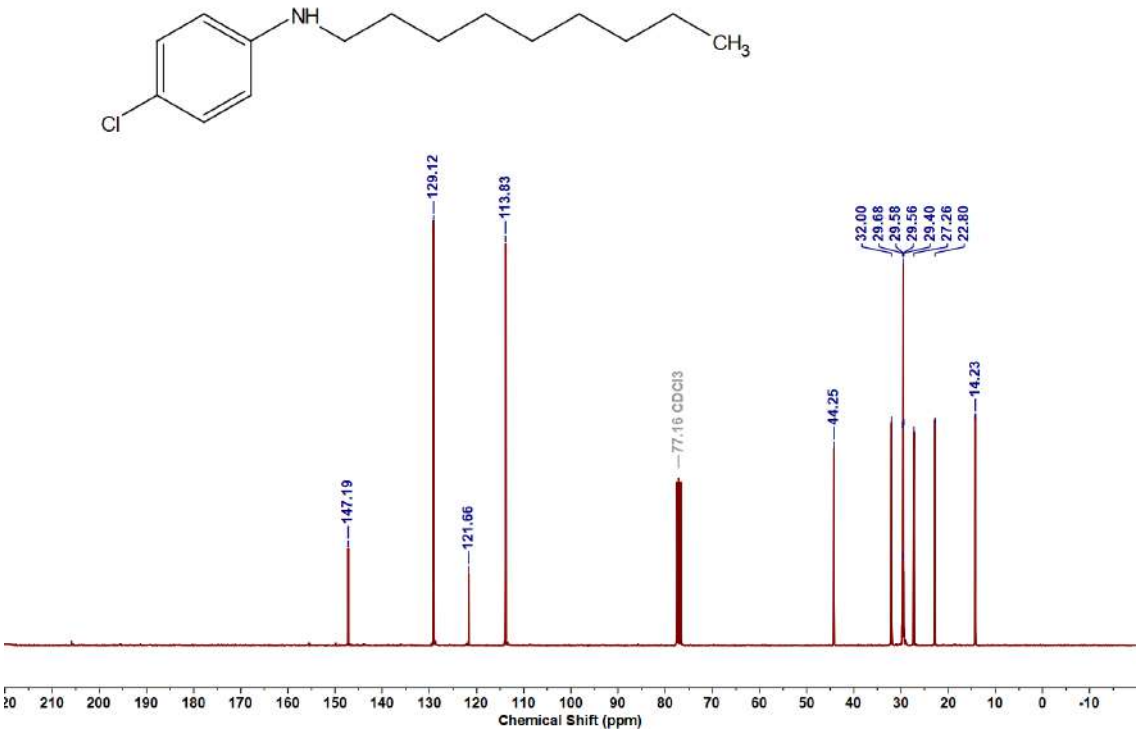

Figure 6.6.A71: ^{13}C{^{1}H} NMR spectrum of **5ad**

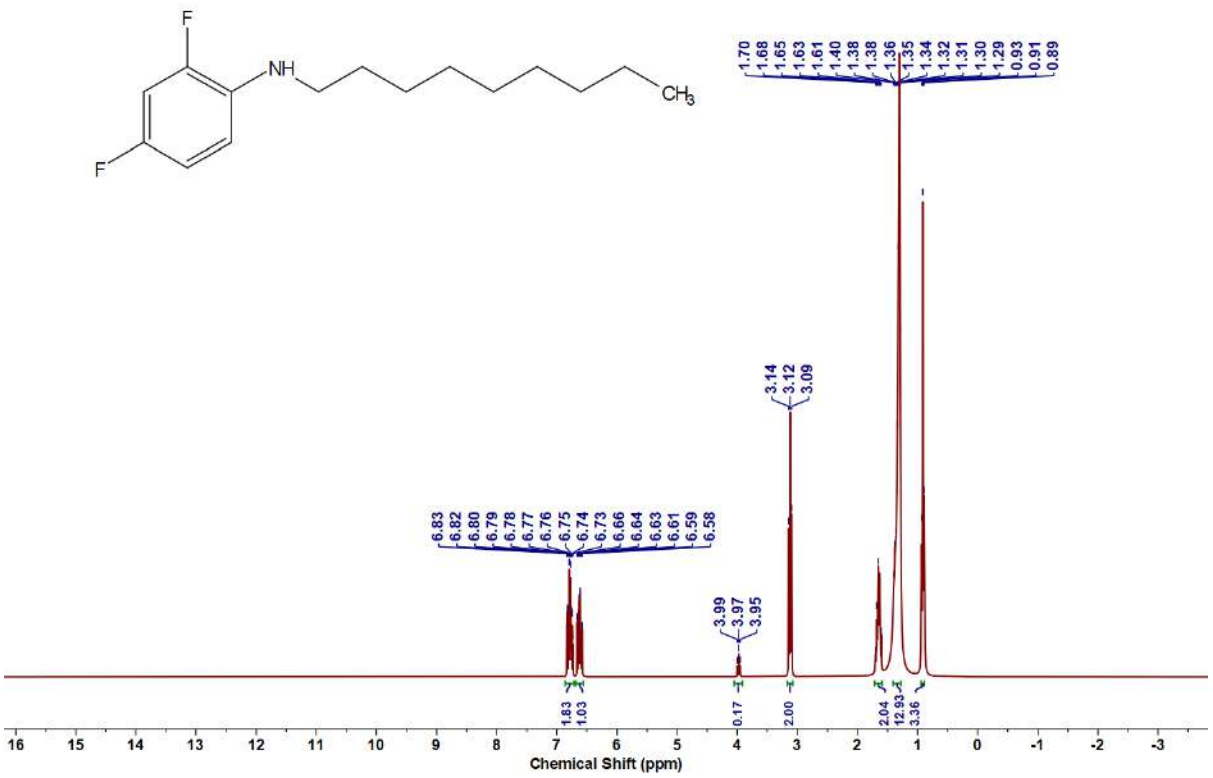

Figure 6.6.A71: ^{1}H NMR spectrum of **5ae**

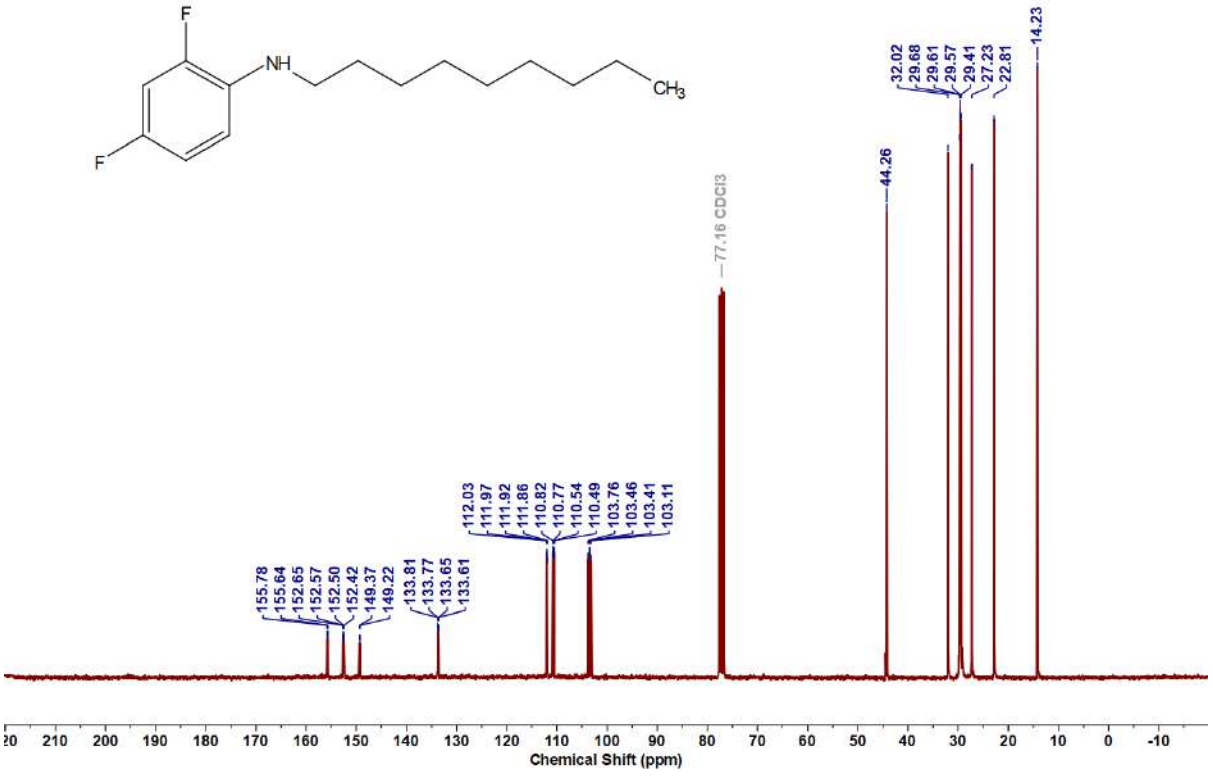

Figure 6.6.A72: ^{13}C{^{1}H} NMR spectrum of **5ac**

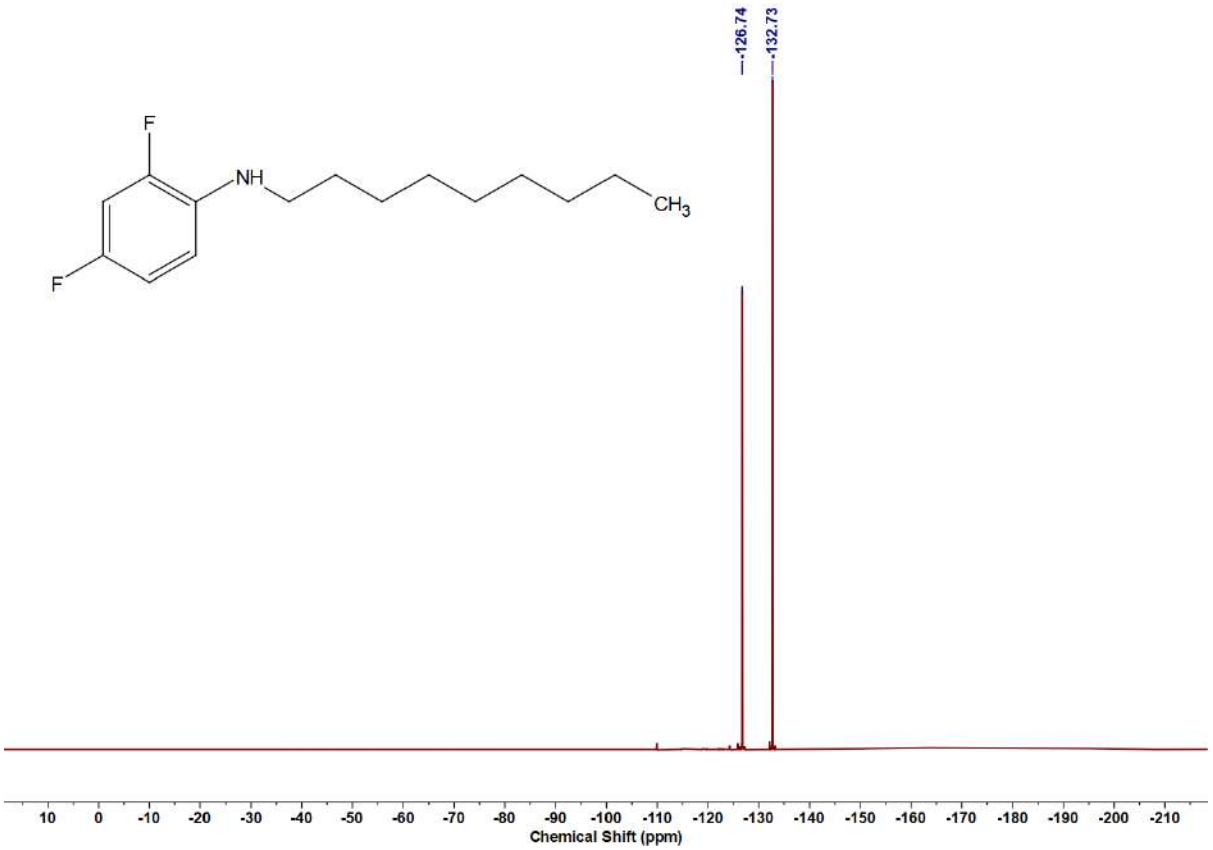

Figure 6.6.A73: ^{19}F NMR spectrum of **5ae**

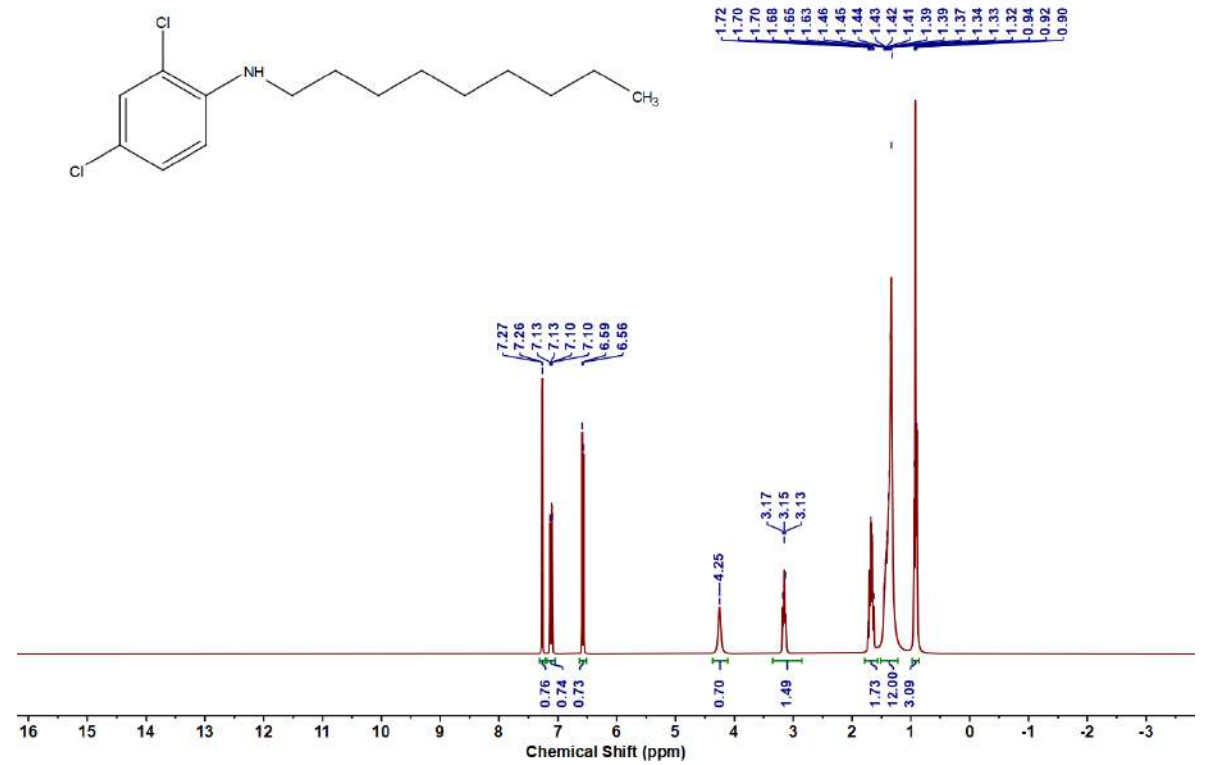

Figure 6.6.A74: ^{1}H NMR spectrum of **5af**

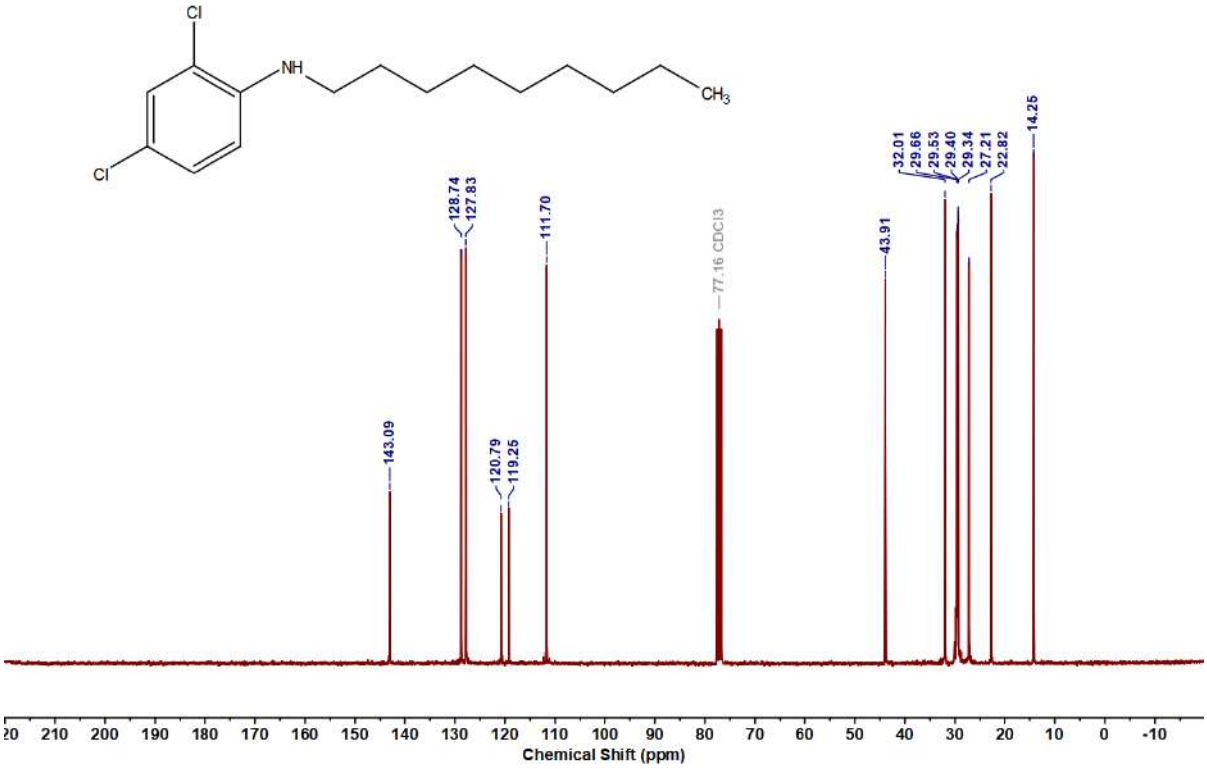

Figure 6.6.A75: $^{13}C\{^{1}H\}$ NMR spectrum of **5af**

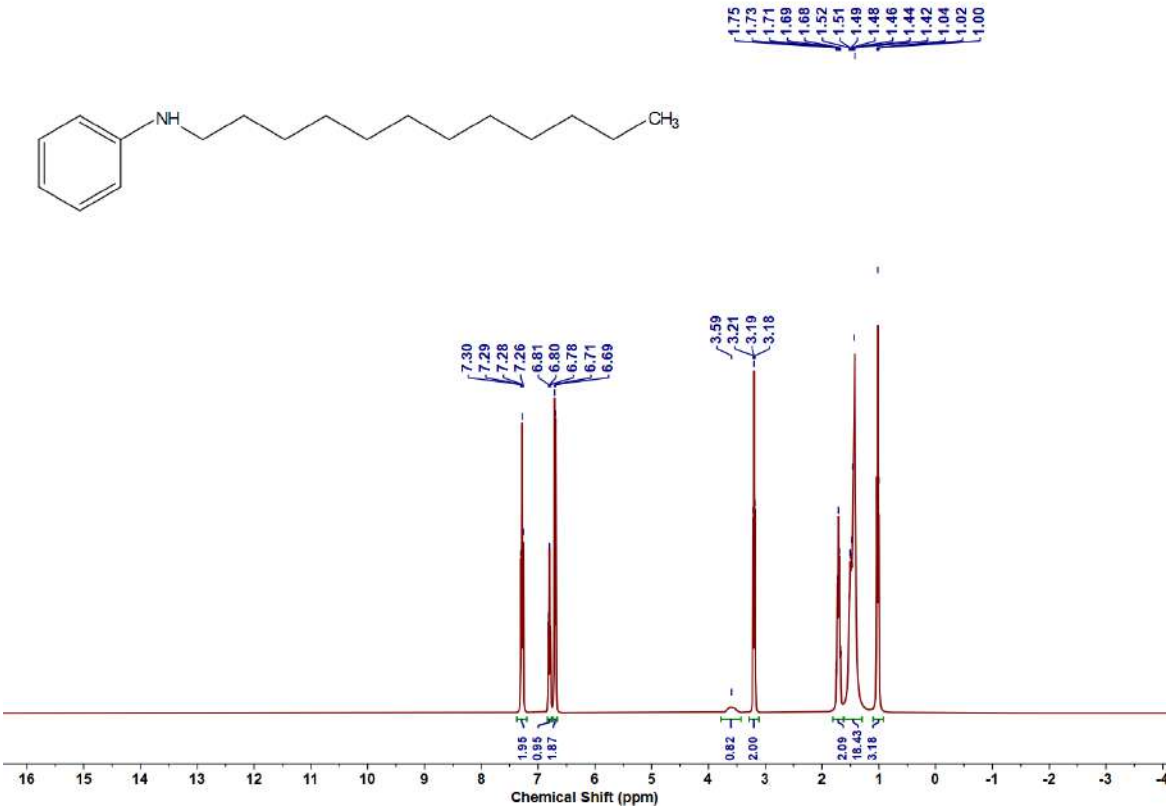

Figure 6.6.A76: ^{1}H NMR spectrum of **5ag**

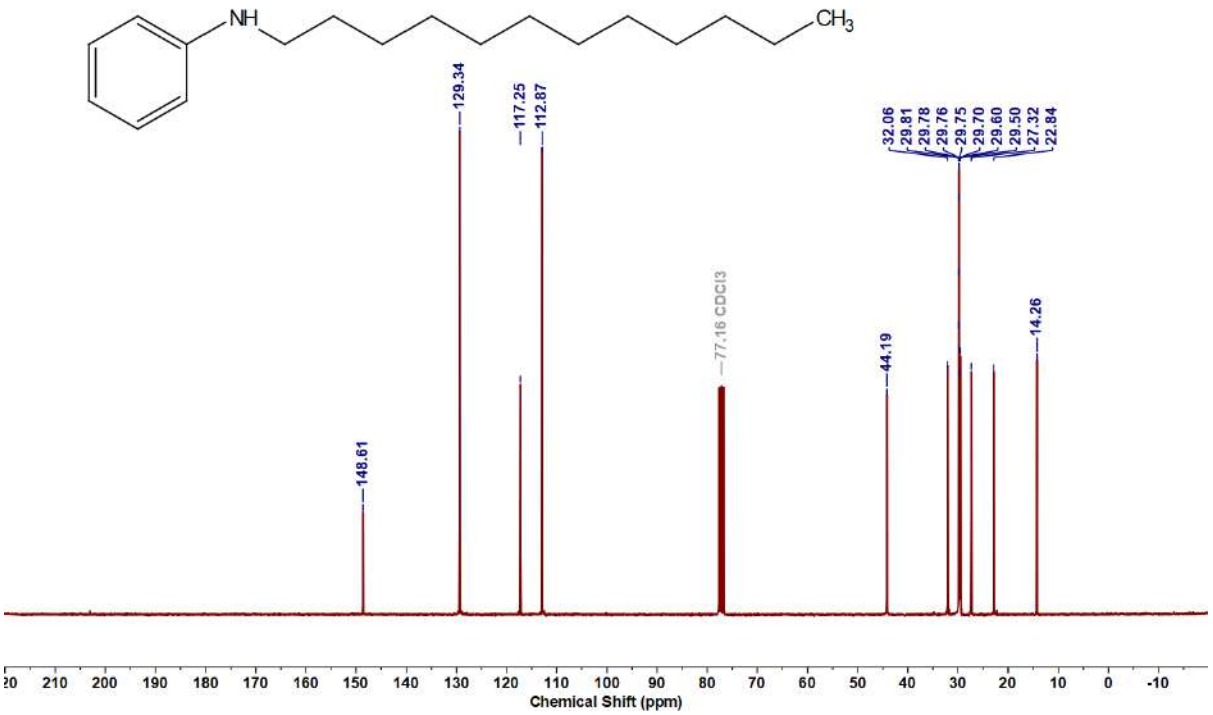

Figure 6.6.A77: $^{13}C\{^{1}H\}$ NMR spectrum of **5ag**

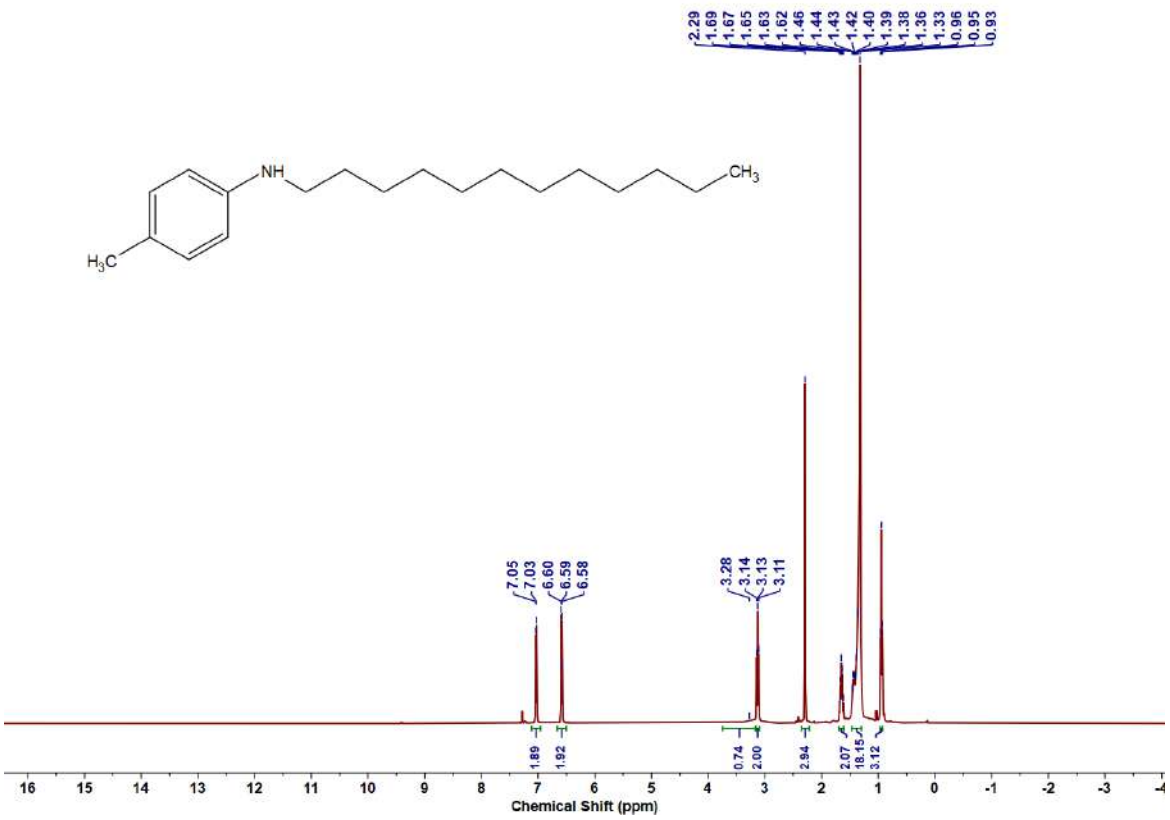

Figure 6.6.A78: ^{1}H NMR spectrum of **5ah**

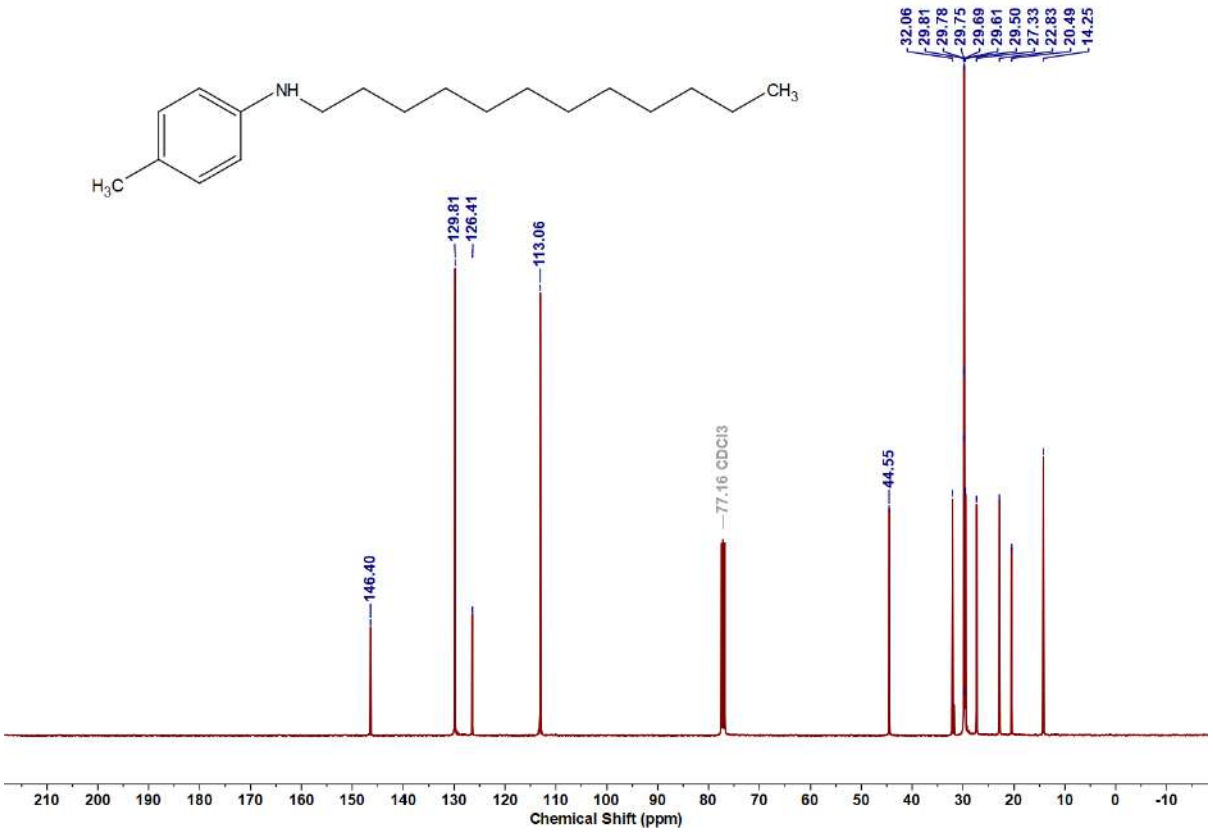

Figure 6.6.A79: $^{13}C\{^{1}H\}$ NMR spectrum of **5ah**

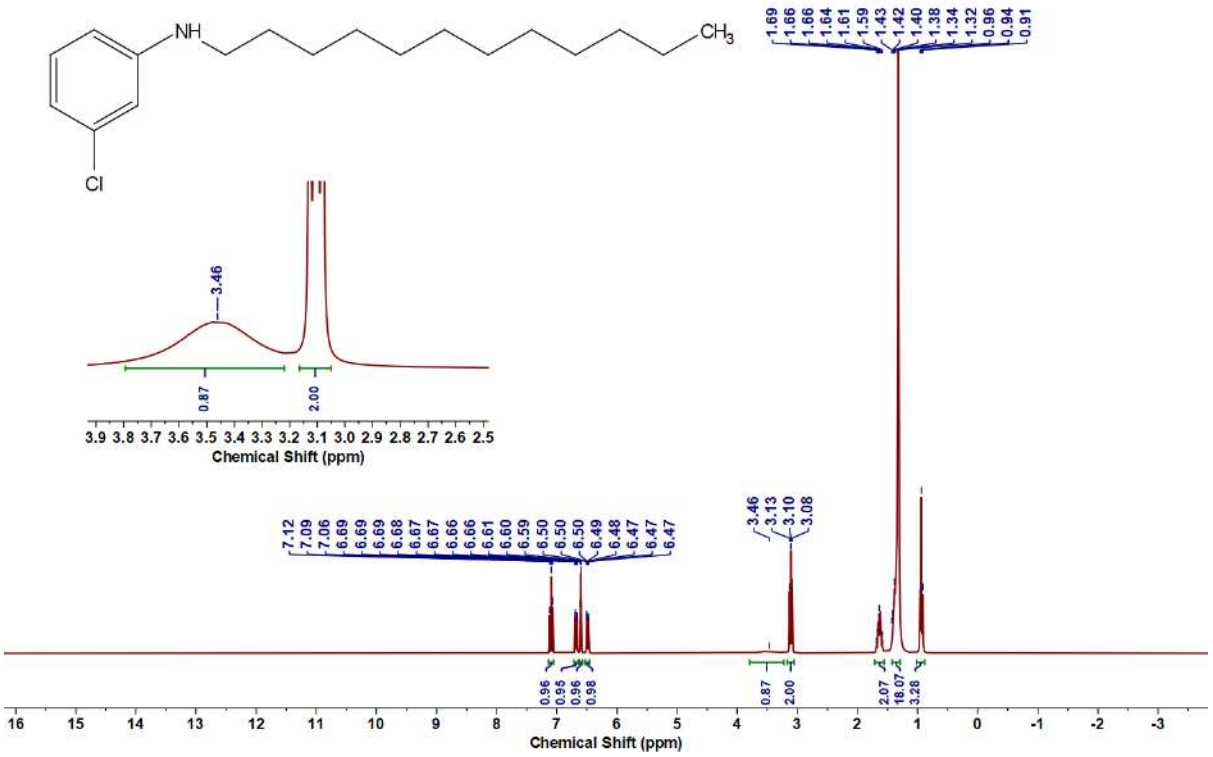

Figure 6.6.A80: ^{1}H NMR spectrum of **5aj**

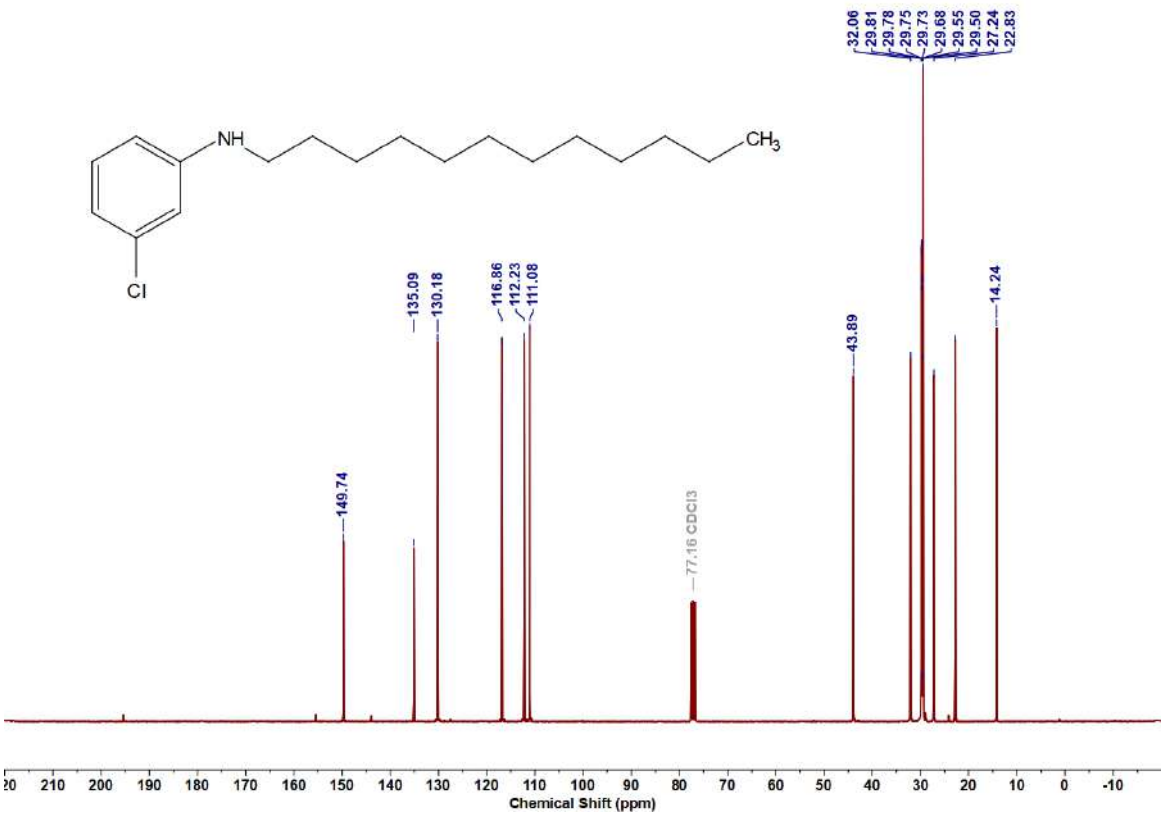

Figure 6.6.A81: $^{13}C\{^{1}H\}$ NMR spectrum of **5aj**

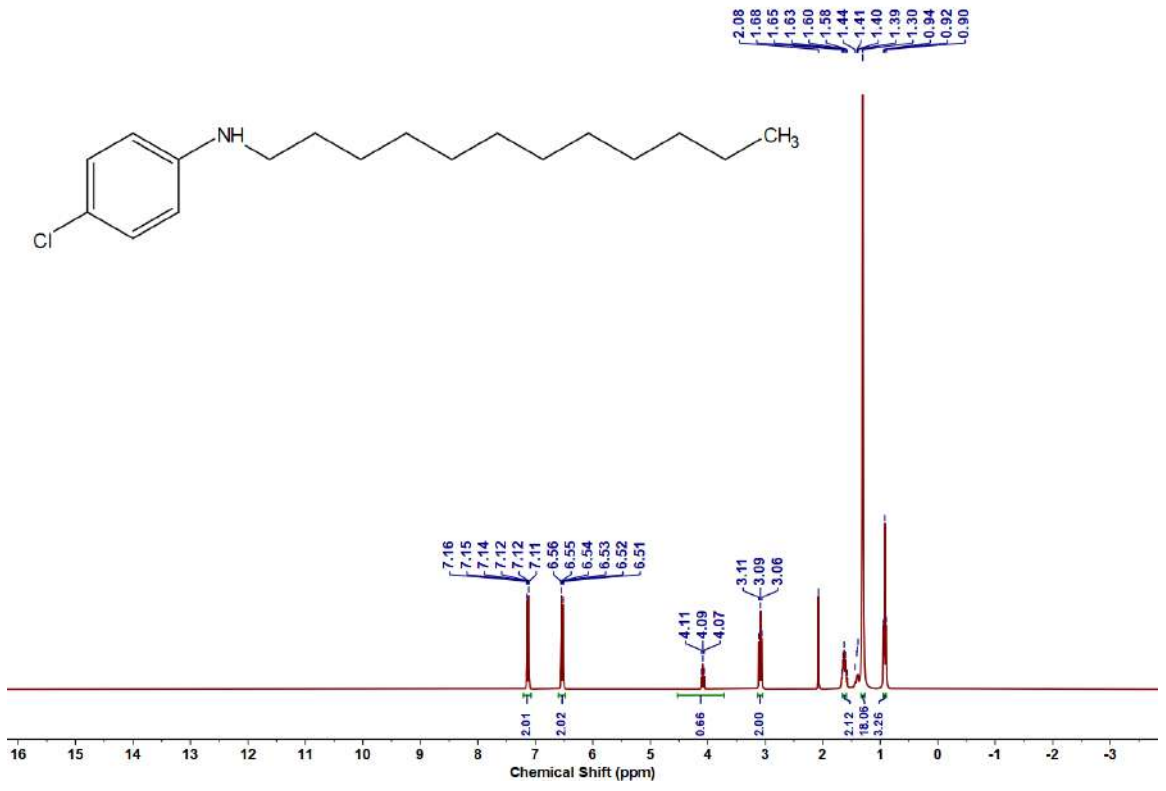

Figure 6.6.A82: ^{1}H NMR spectrum of **5ak**

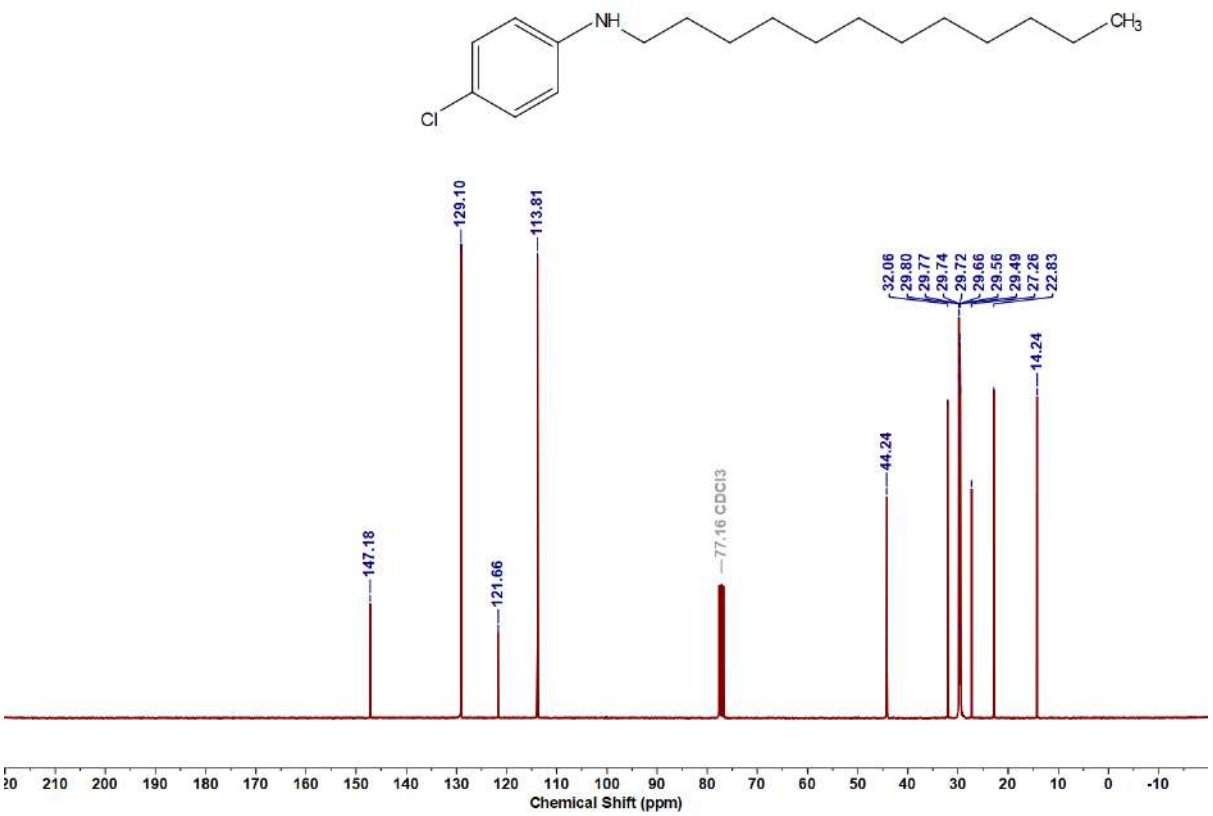

Figure 6.6.A83: $^{13}C\{^{1}H\}$ NMR spectrum of **5ak**

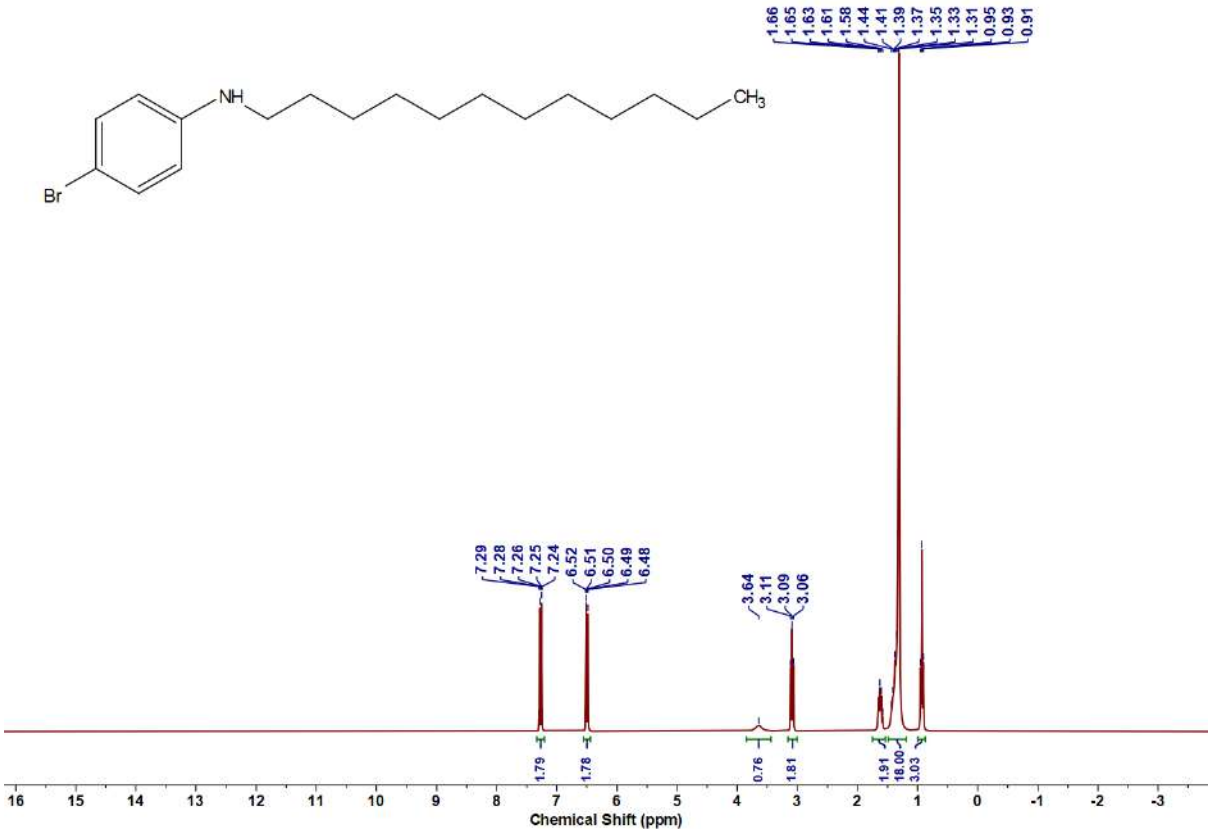

Figure 6.6.A84: ^{1}H NMR spectrum of **5al**

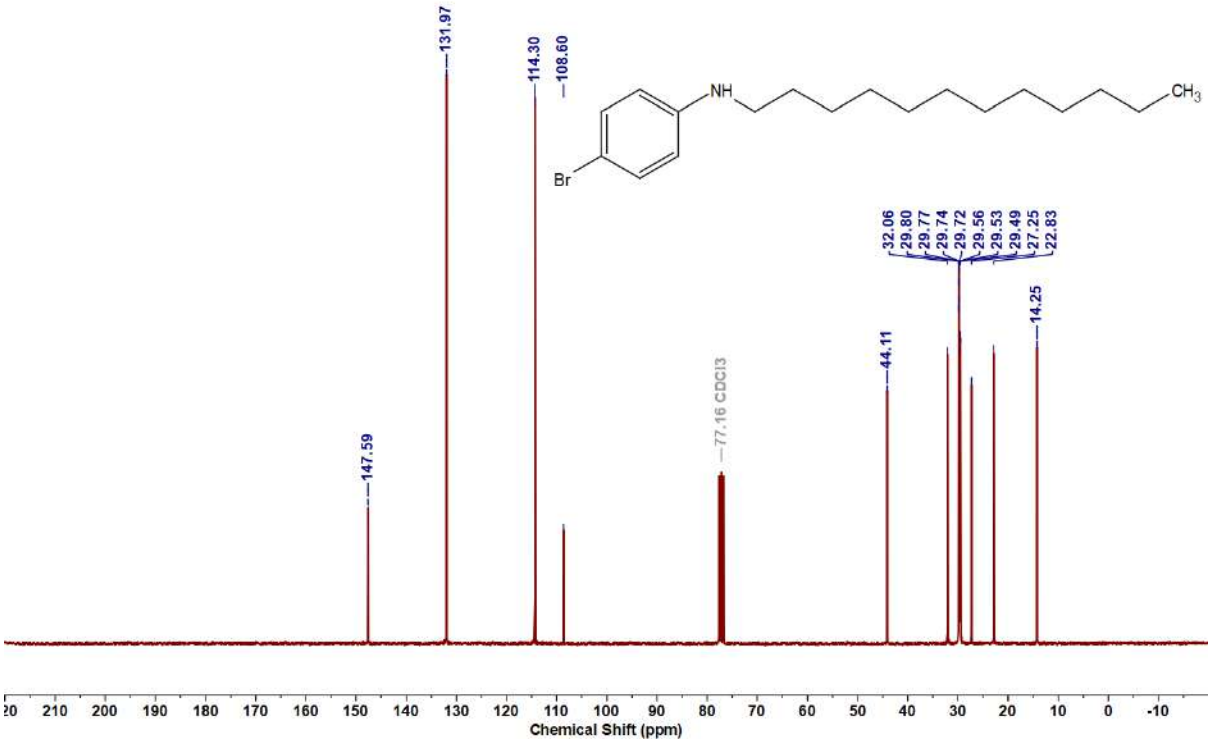

Figure 6.6.A85: $^{13}C\{^{1}H\}$ NMR spectrum of **5al**

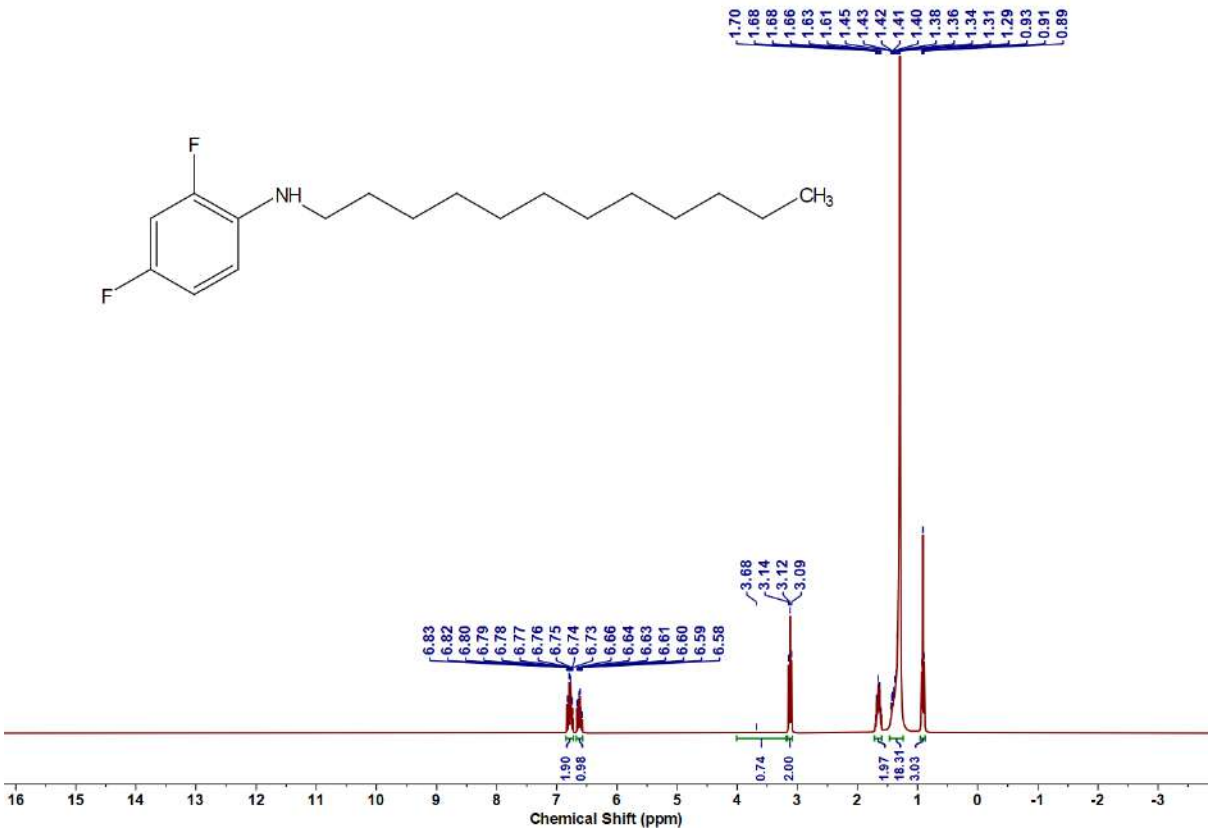

Figure 6.6.A86: ^{1}H NMR spectrum of **5am**

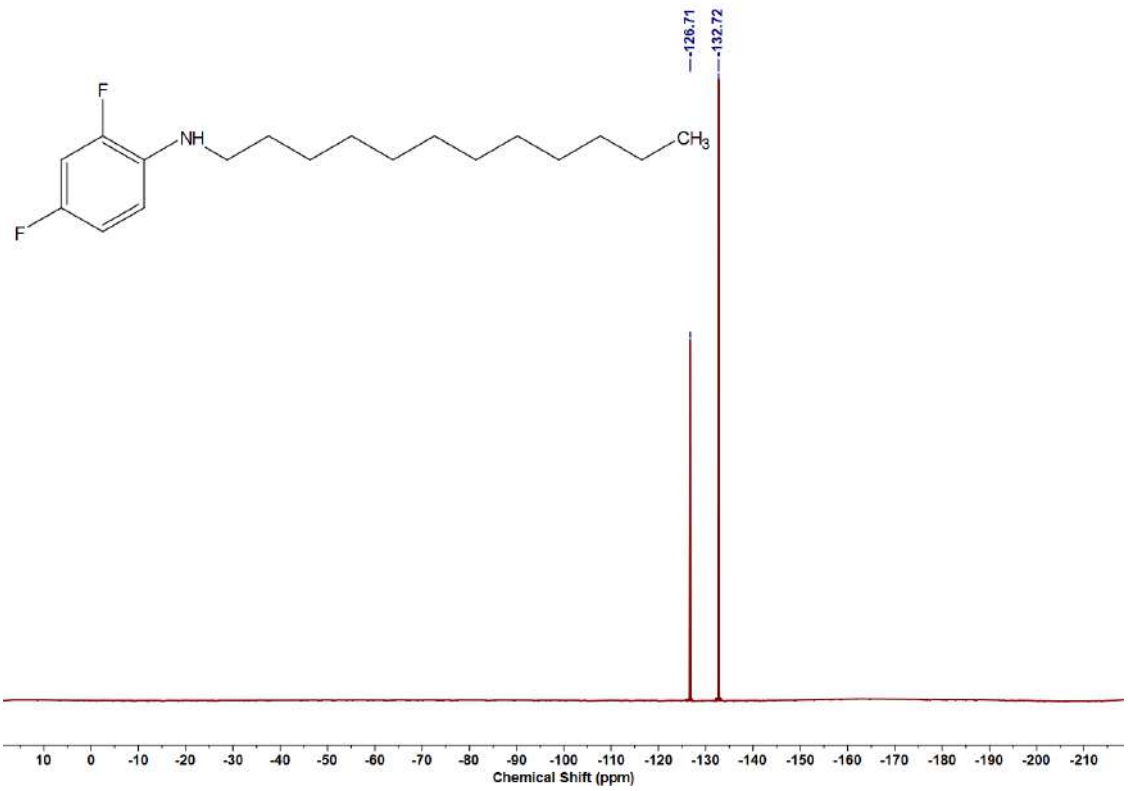

Figure 6.6.A87: ^{19}F NMR spectrum of **5am**

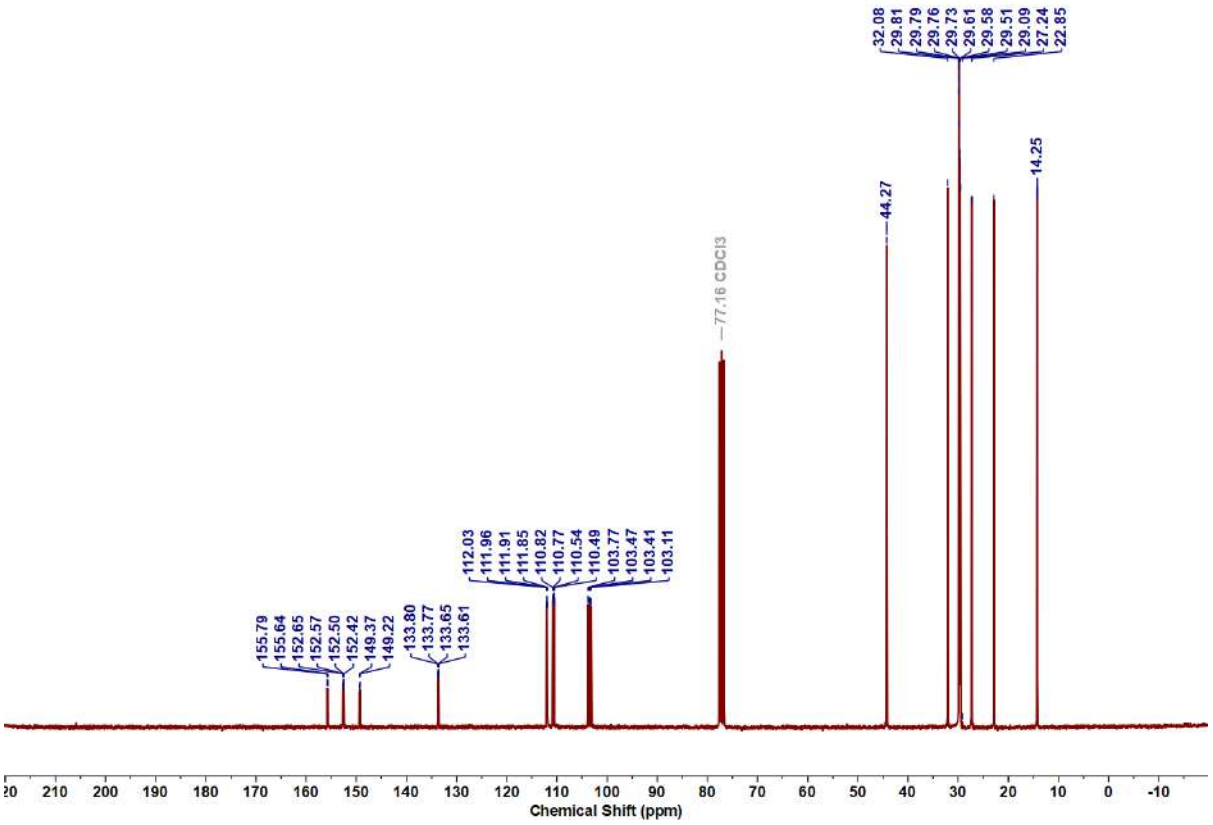

Figure 6.6.A88: $^{13}C\{^{1}H\}$ NMR spectrum of **5am**

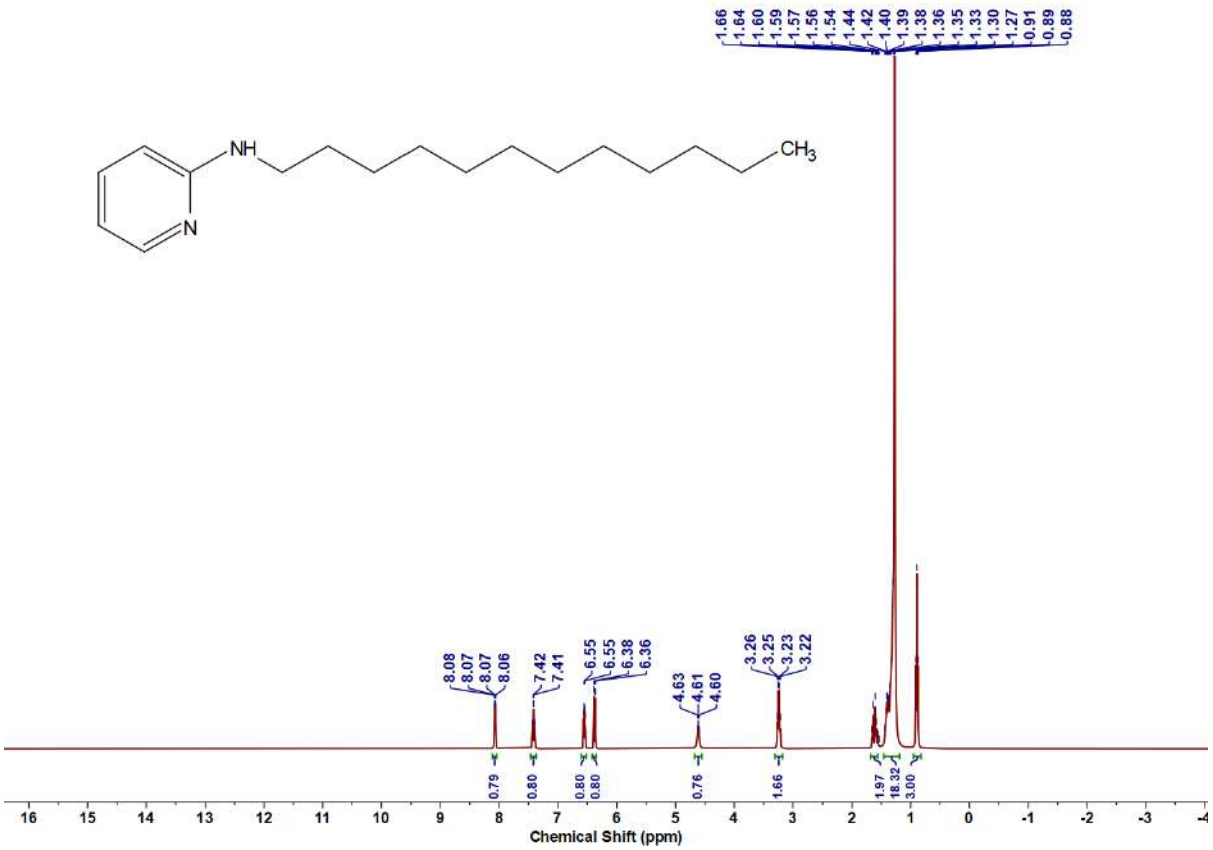

Figure 6.6.A89: ^{1}H NMR spectrum of **5an**

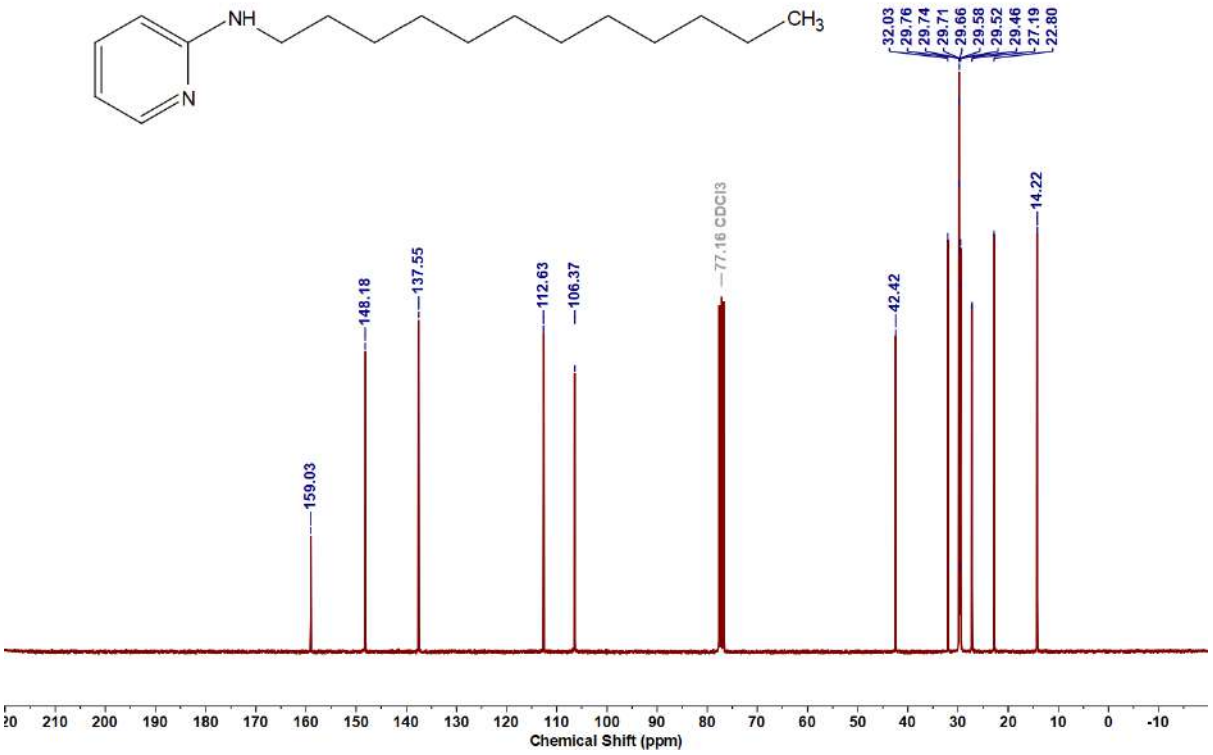

Figure 6.6.A90: $^{13}C\{^{1}H\}$ NMR spectrum of **5an**

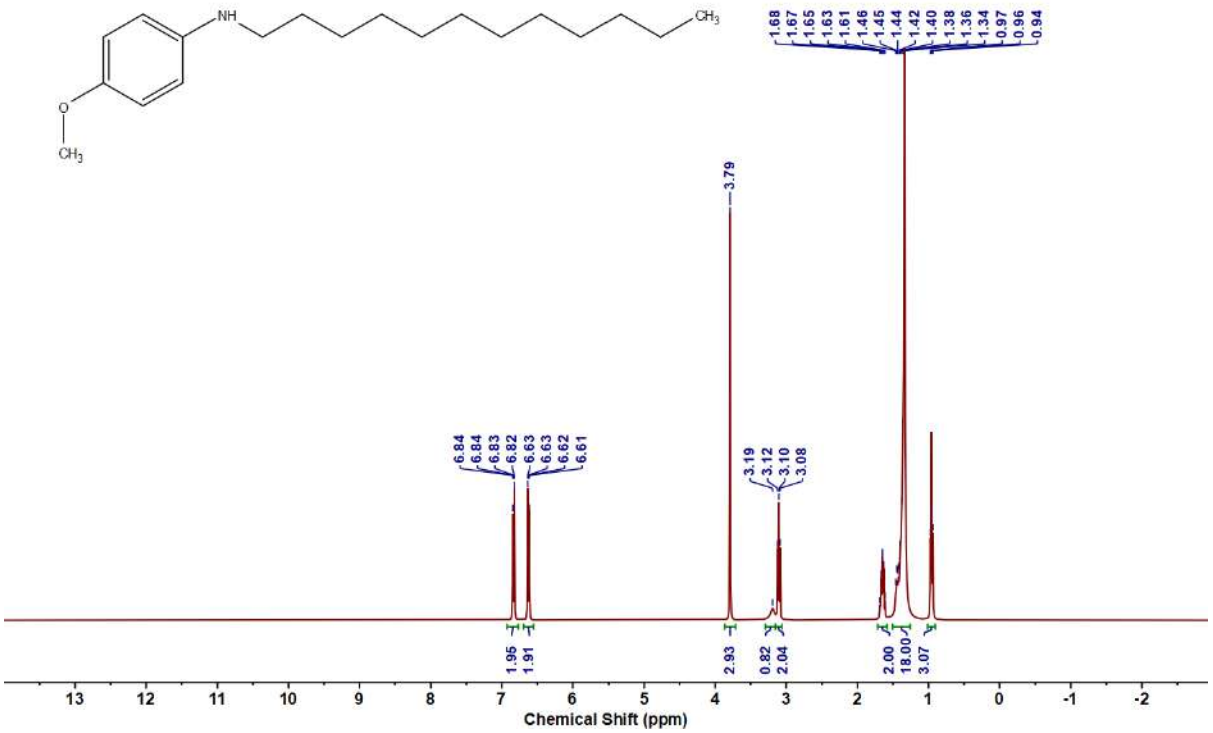

Figure 6.6.A91: ^{1}H NMR spectrum of **5ao**

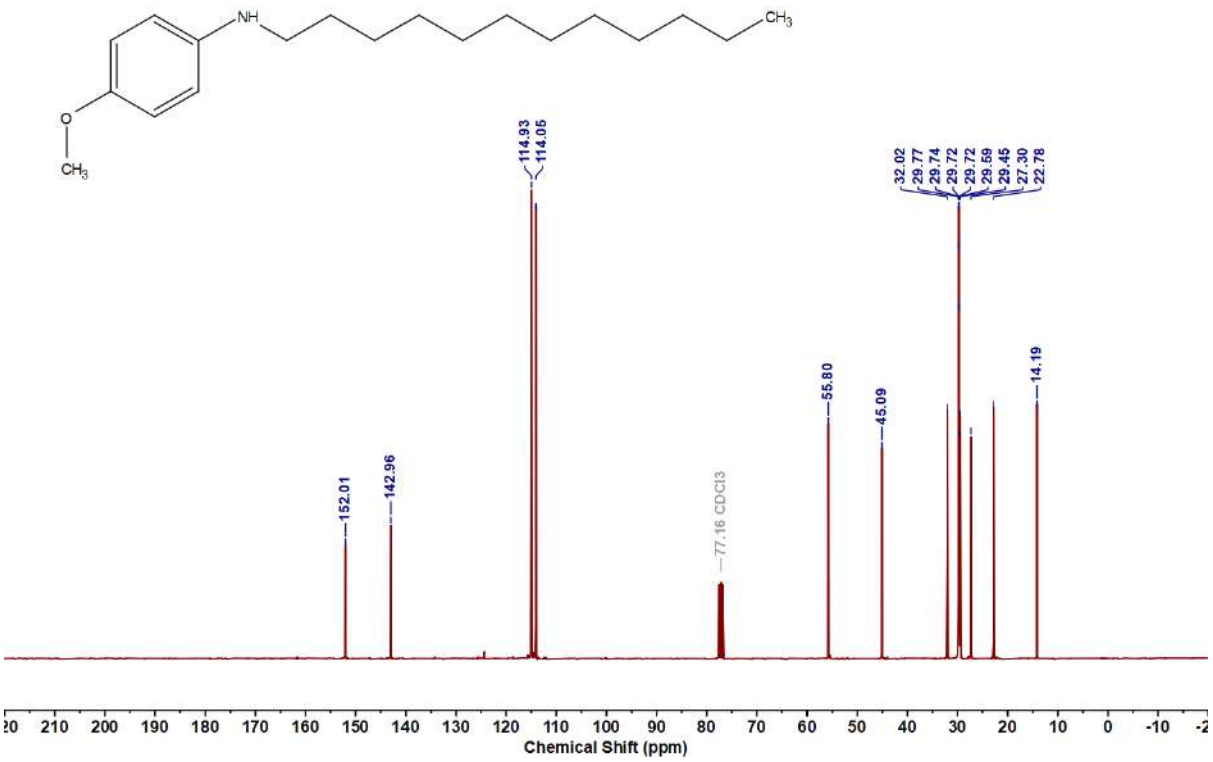

Figure 6.6.A93: ^{13}C{^{1}H} NMR spectrum of **5ao**

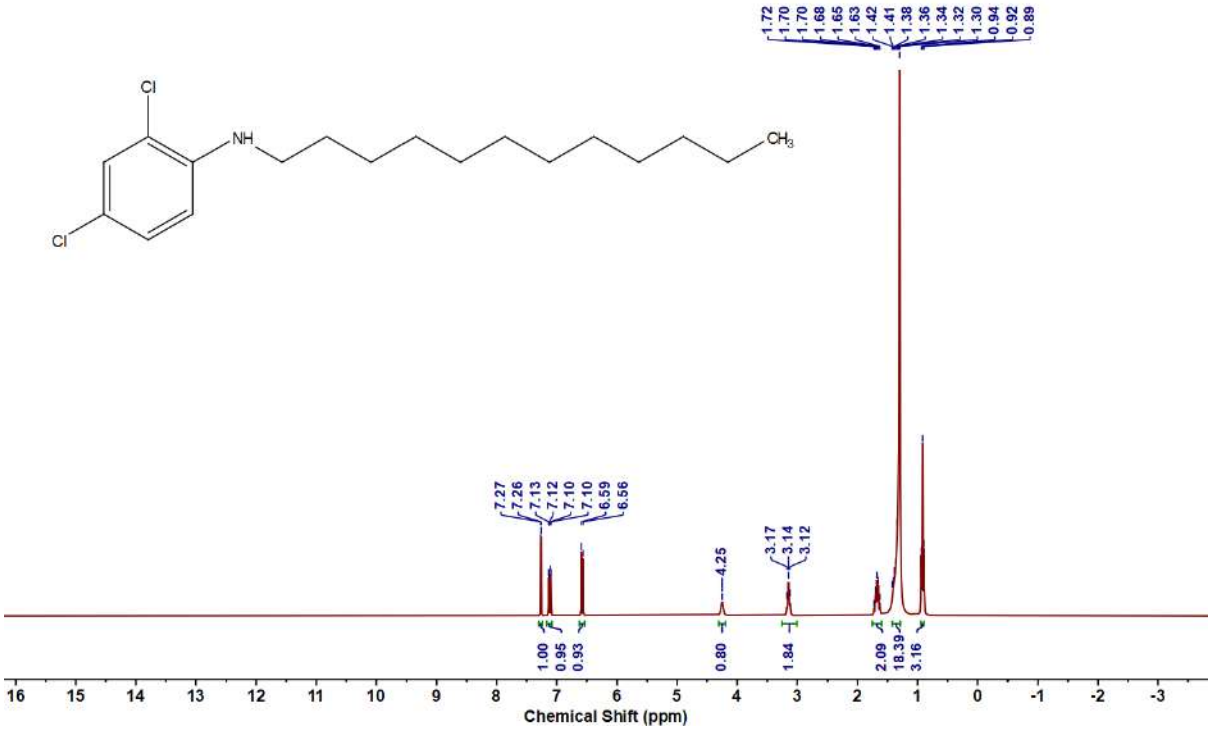

Figure 6.6.A94: ^{1}H NMR spectrum of **5ap**

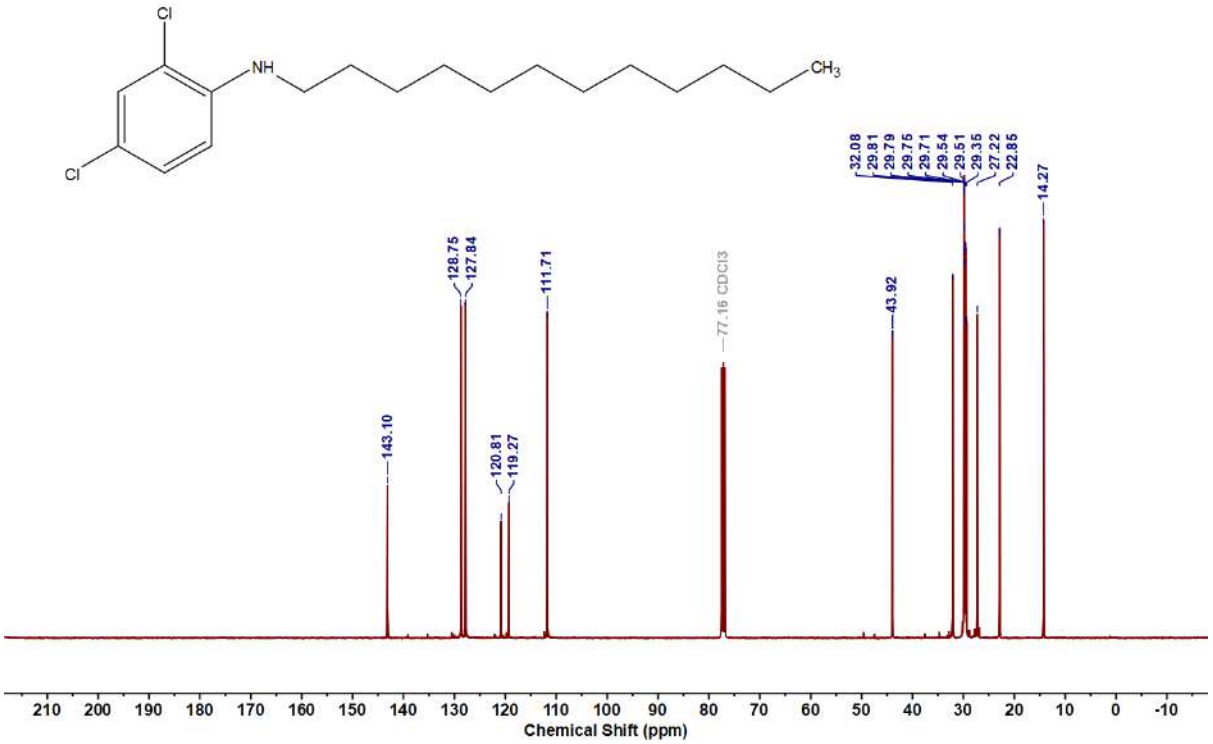

Figure 6.6.A95: ^{13}C{^{1}H} NMR spectrum of **5ap**

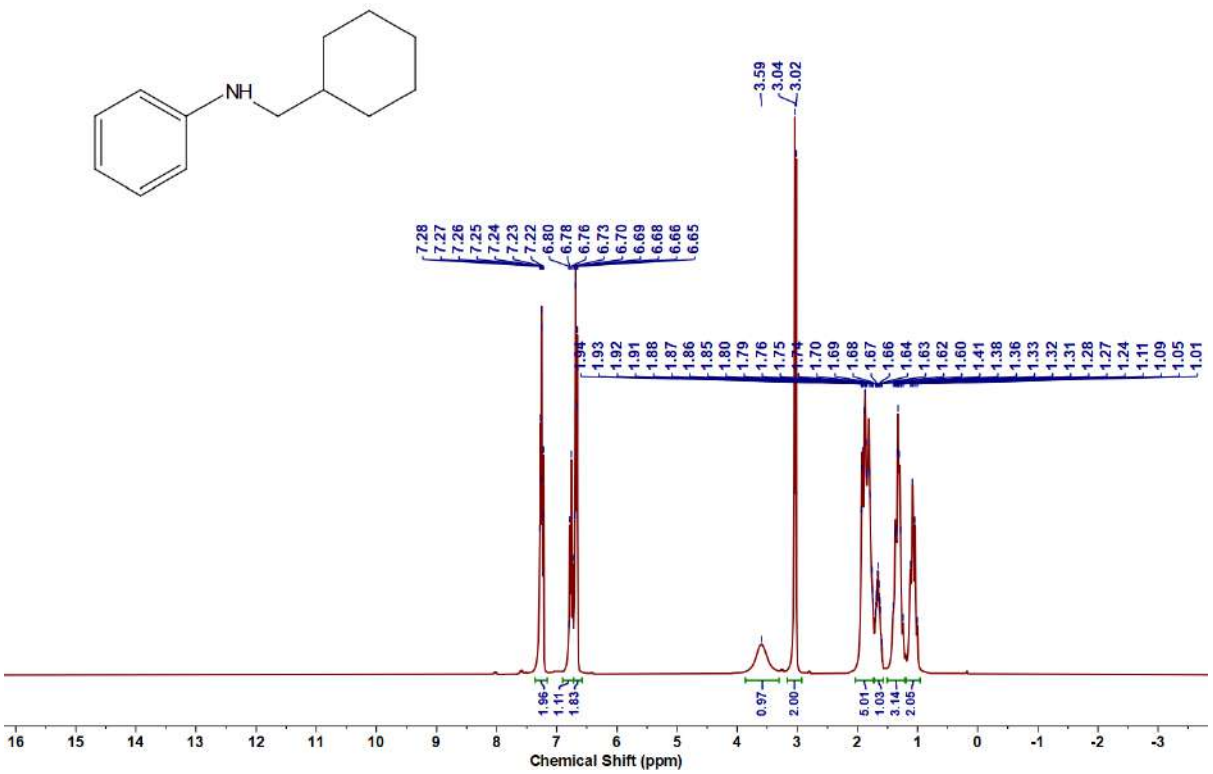

Figure 6.6.A96: ^{1}H NMR spectrum of **5aq**

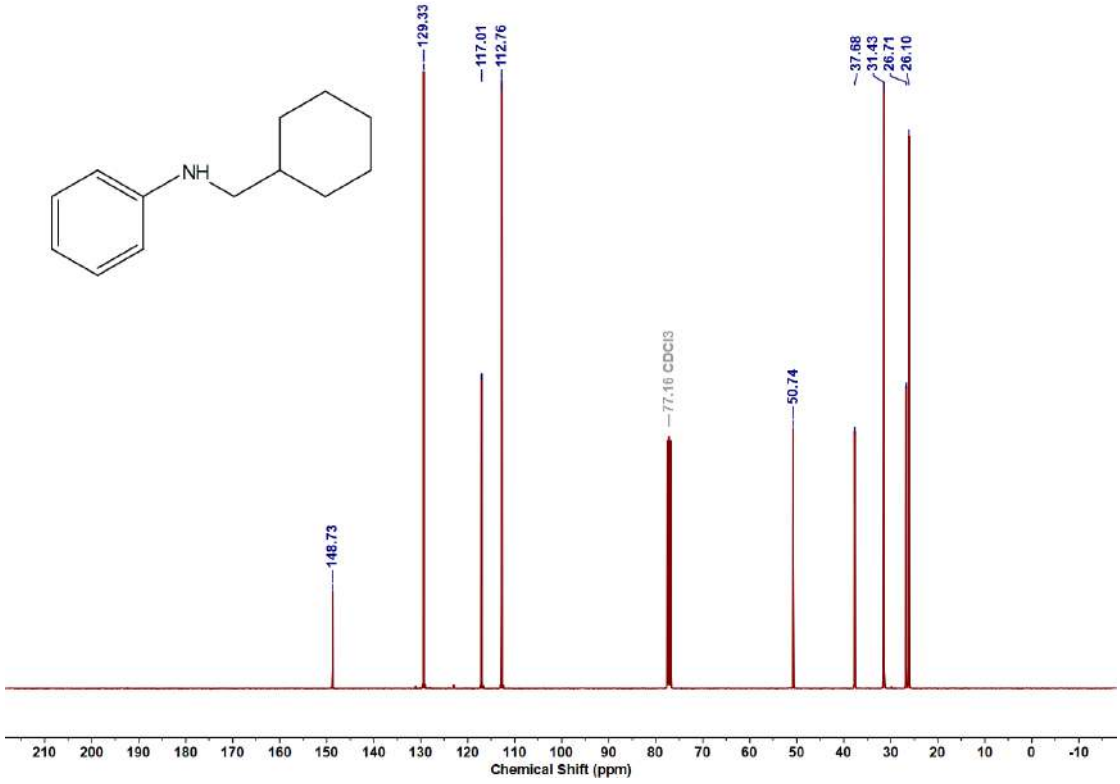

Figure 6.6.A97: $^{13}C\{^{1}H\}$ NMR spectrum of **5aq**

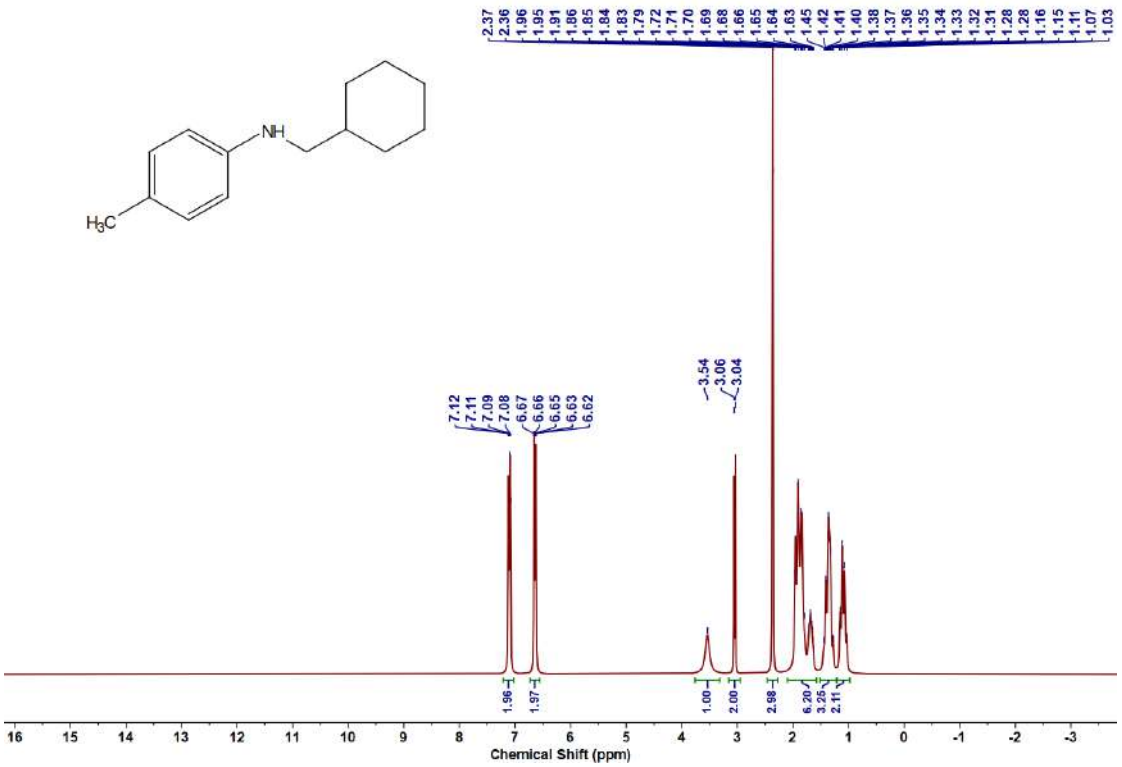

Figure 6.6.A98: ^{1}H NMR spectrum of **5ar**

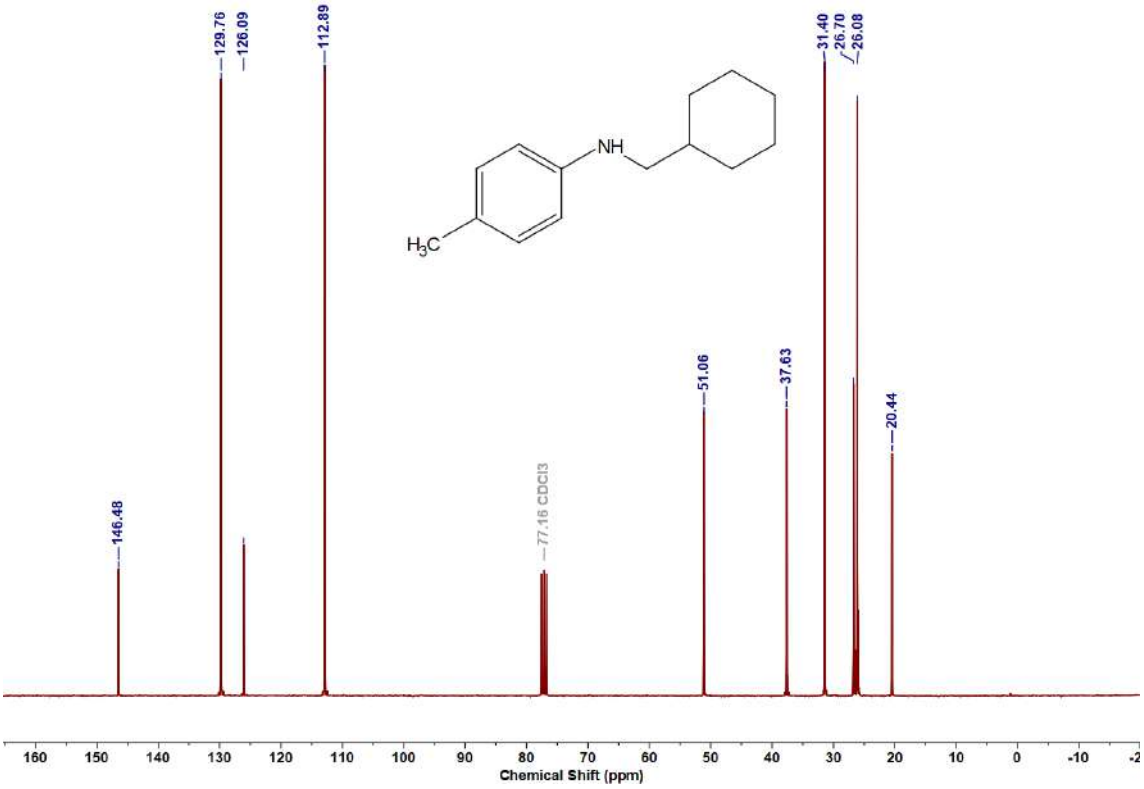

Figure 6.6.A99: $^{13}C\{^{1}H\}$ NMR spectrum of **5ar**

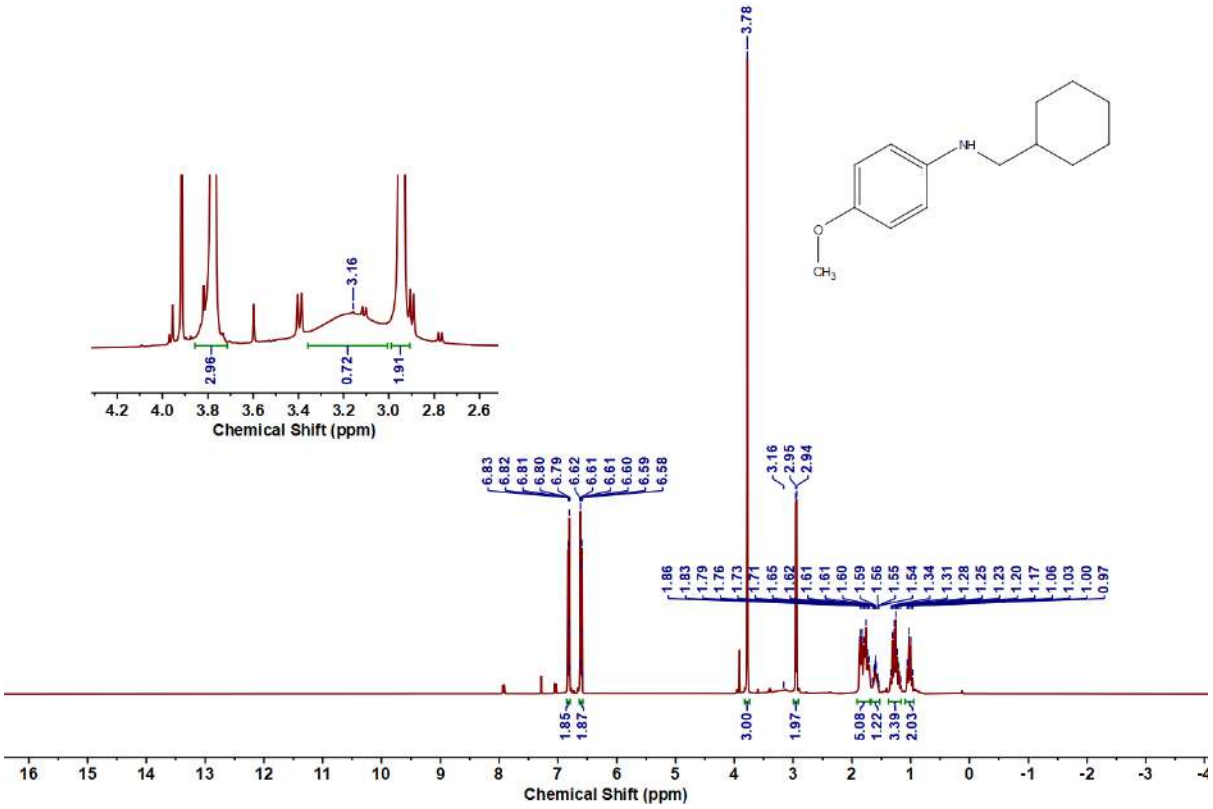

Figure 6.6.A100: ^{1}H NMR spectrum of **5as**

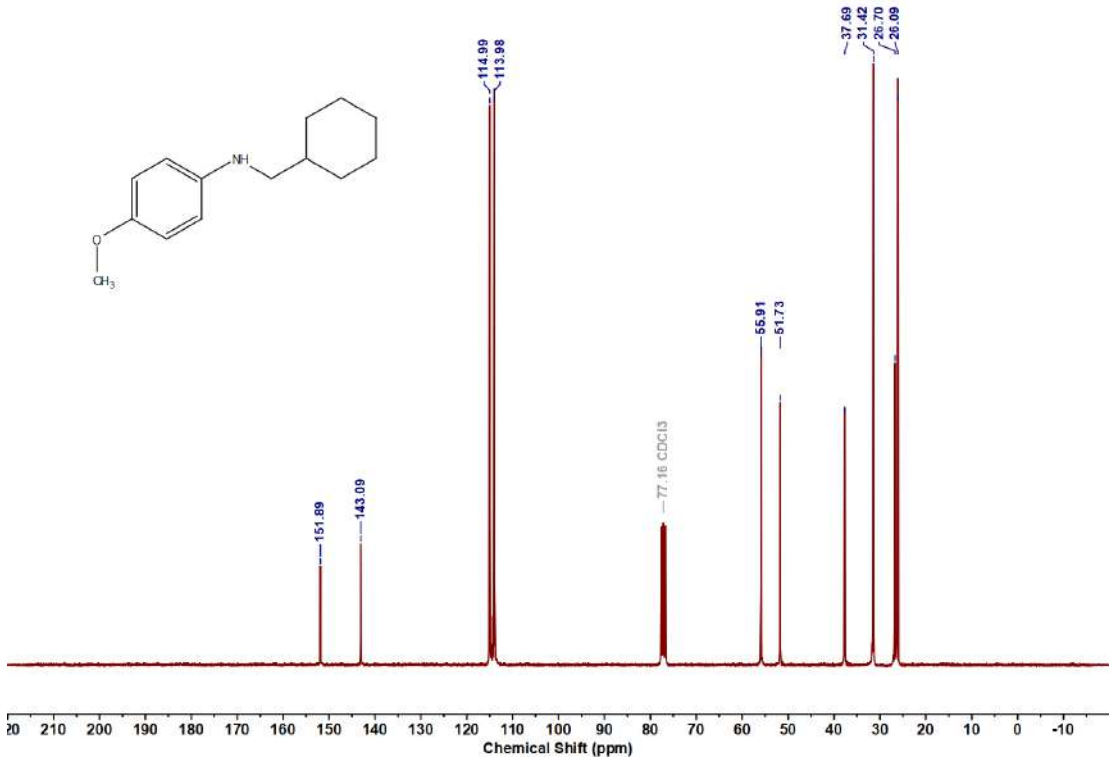

Figure 6.6.A100: $^{13}C\{^{1}H\}$ NMR spectrum of **5as**

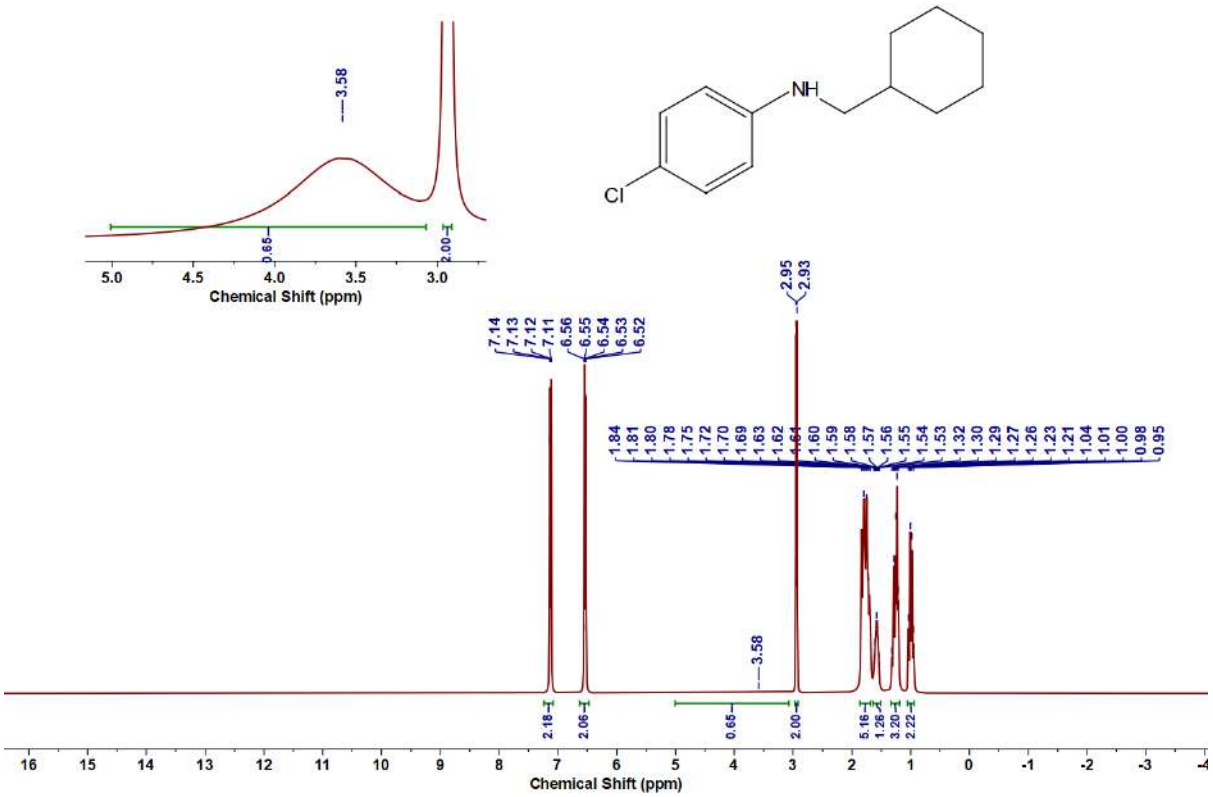

Figure 6.6.A101: ^{1}H NMR spectrum of **5at**

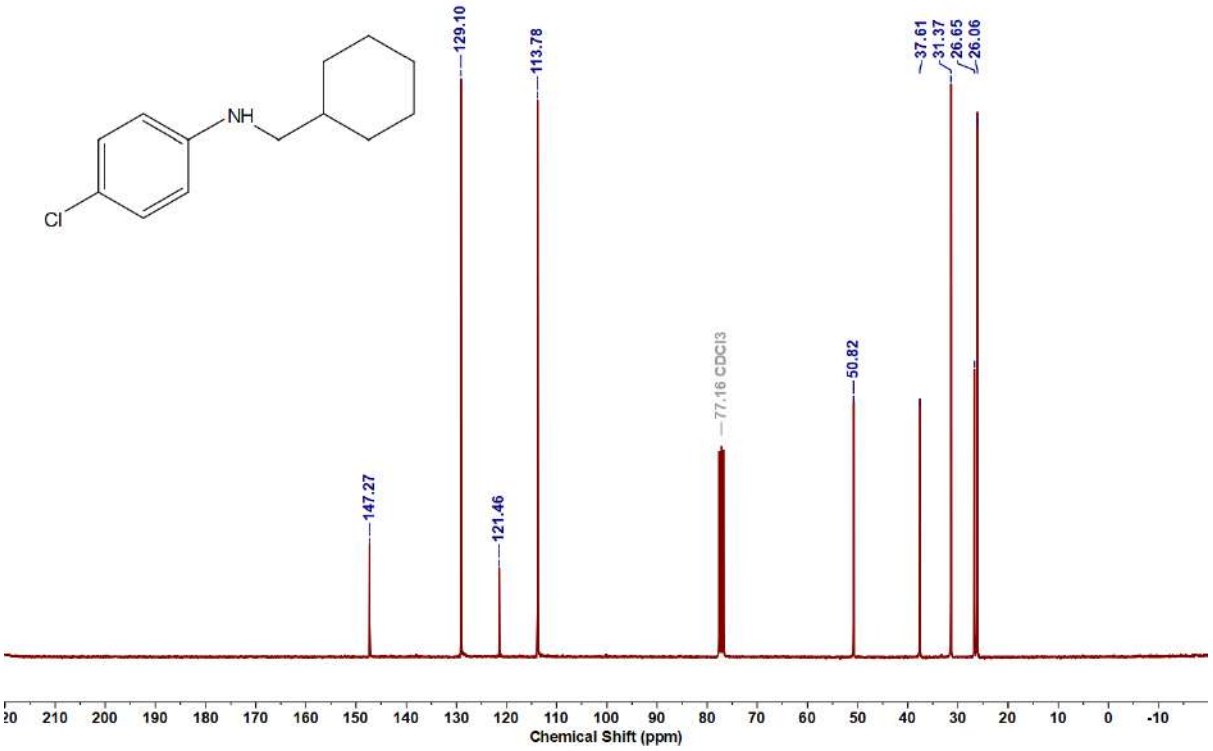

Figure 6.6.A102: ^{13}C{^{1}H} NMR spectrum of **5at**

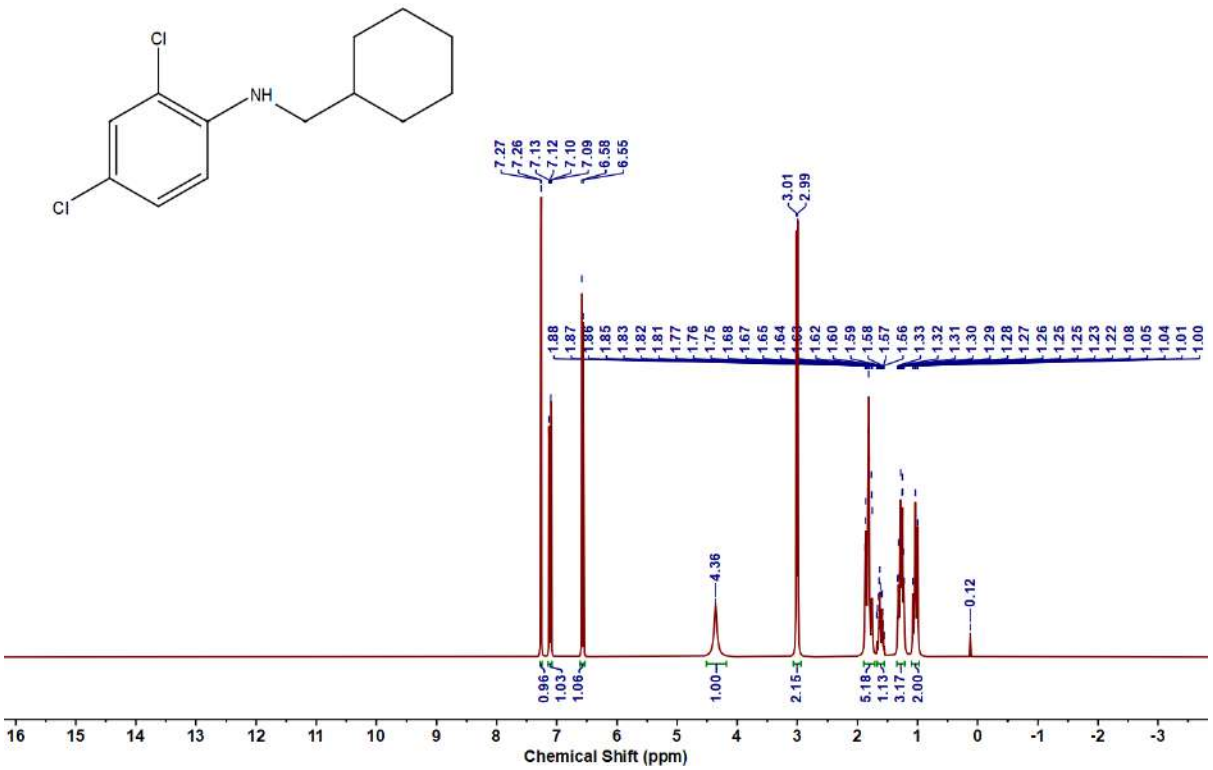

Figure 6.6.A103: ^{1}H NMR spectrum of **5au**

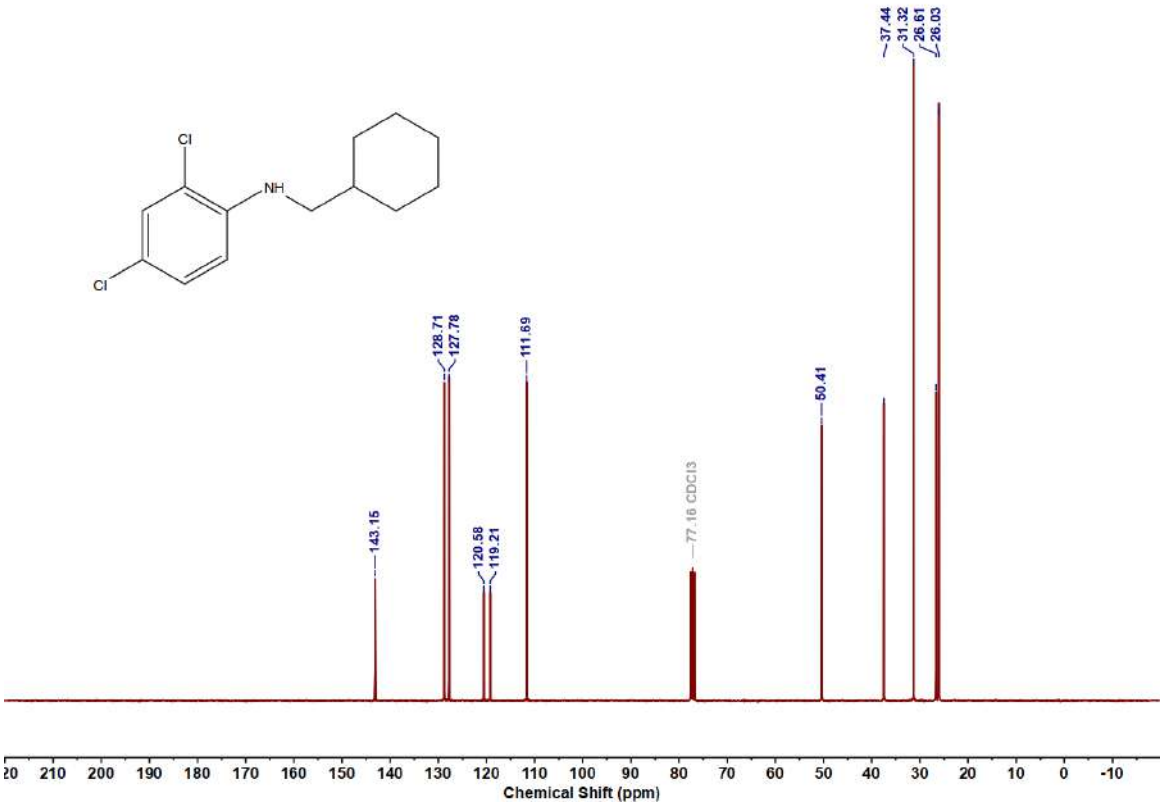

Figure 6.6.104: ^{13}C{^{1}H} NMR spectrum of **5au**

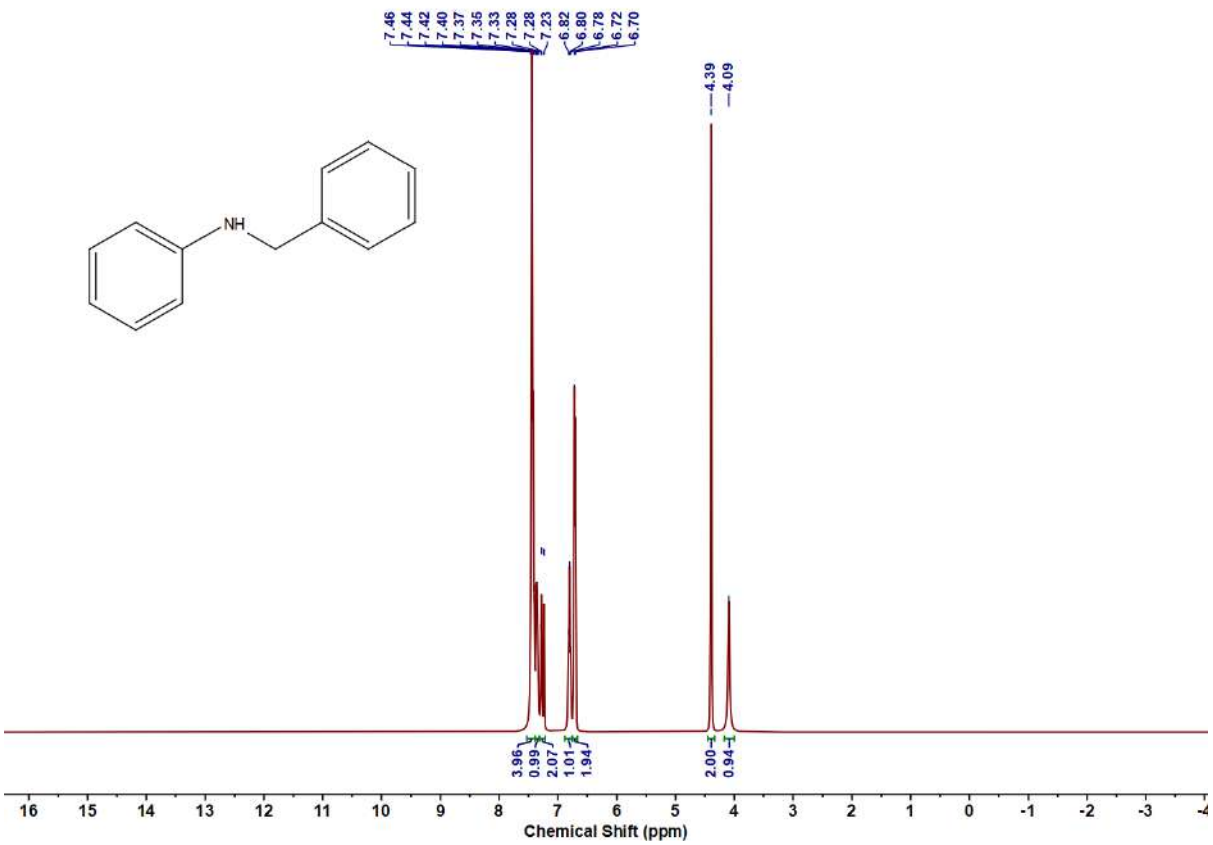

Figure 6.6.A105: ^{1}H NMR spectrum of **7a**

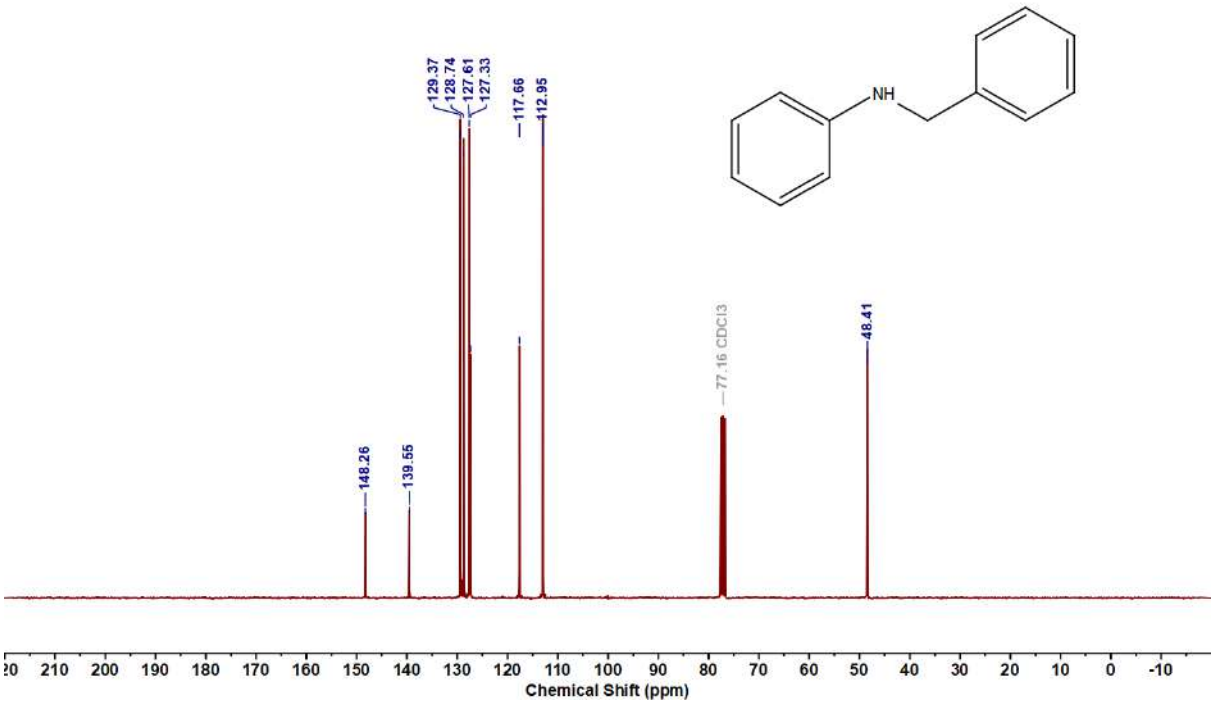

Figure 6.6.A106: $^{13}C\{^{1}H\}$ NMR spectrum of **7a**

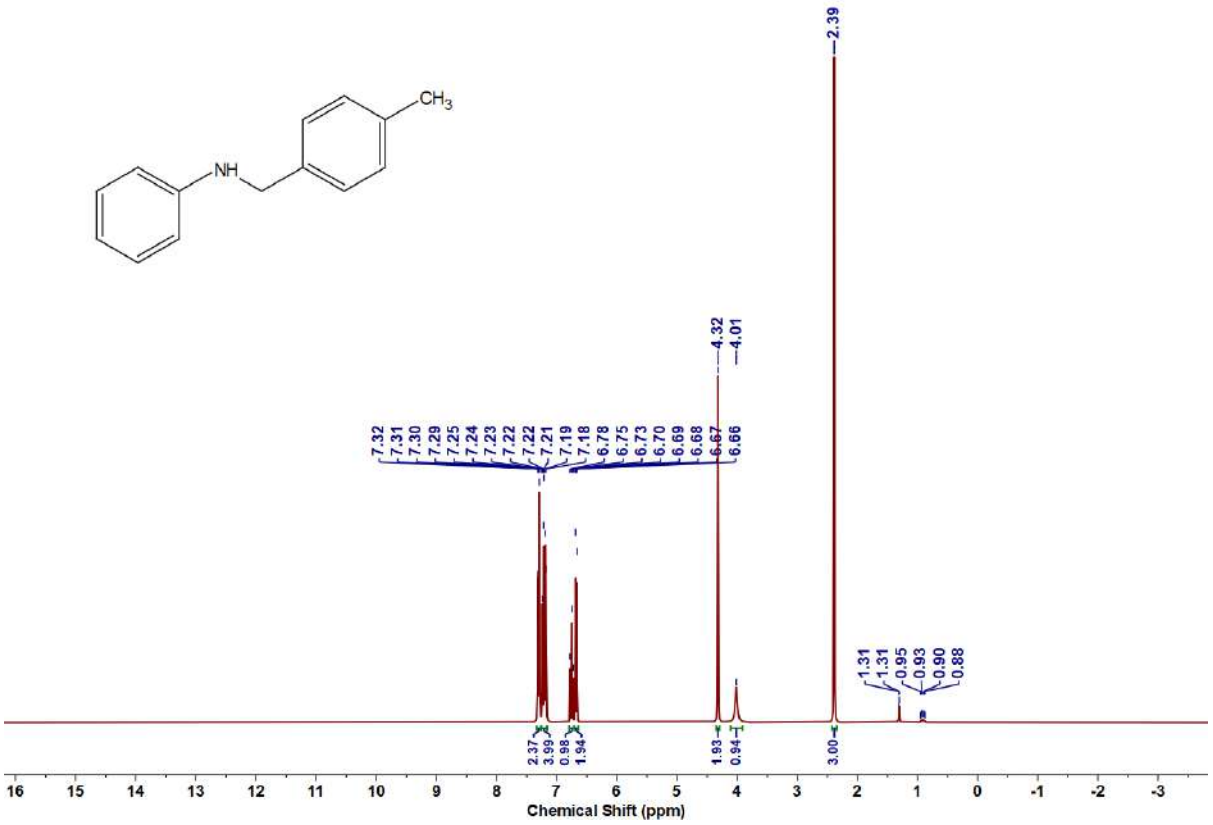

Figure 6.6.A107: ^{1}H NMR spectrum of **7b**

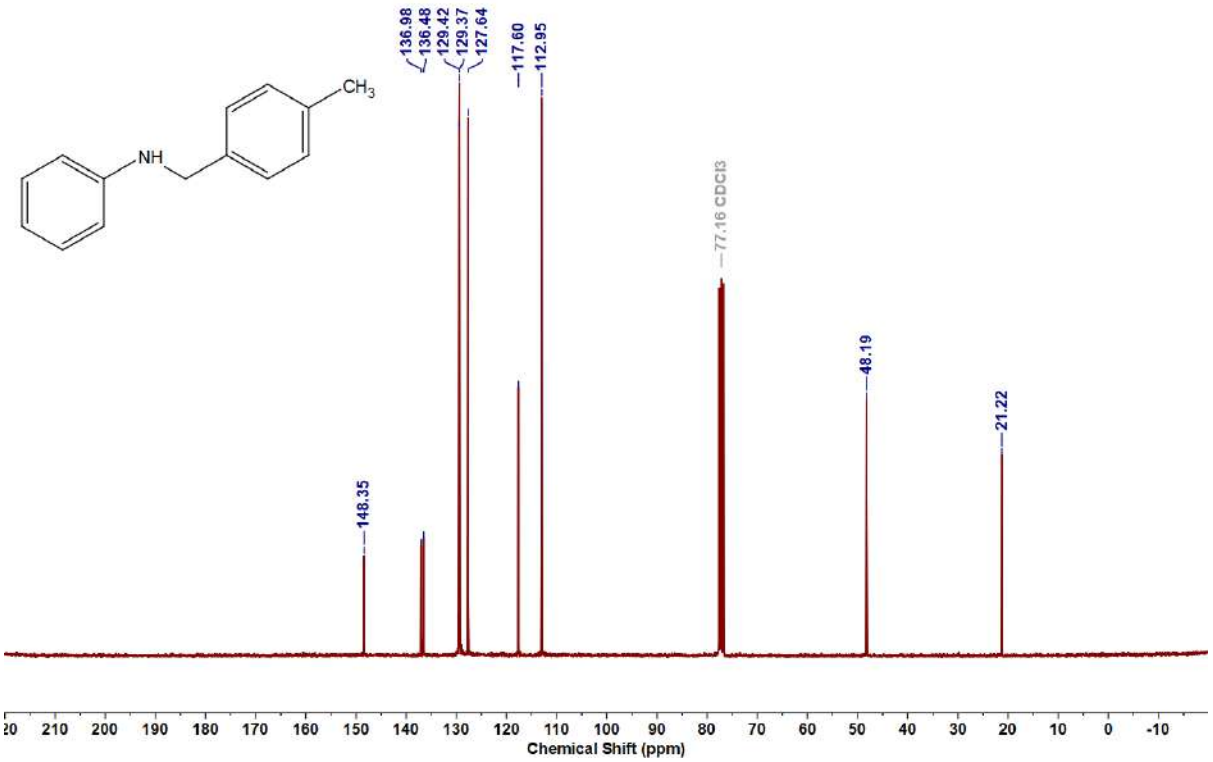

Figure 6.6.A108: $^{13}C\{^{1}H\}$ NMR spectrum of **7b**

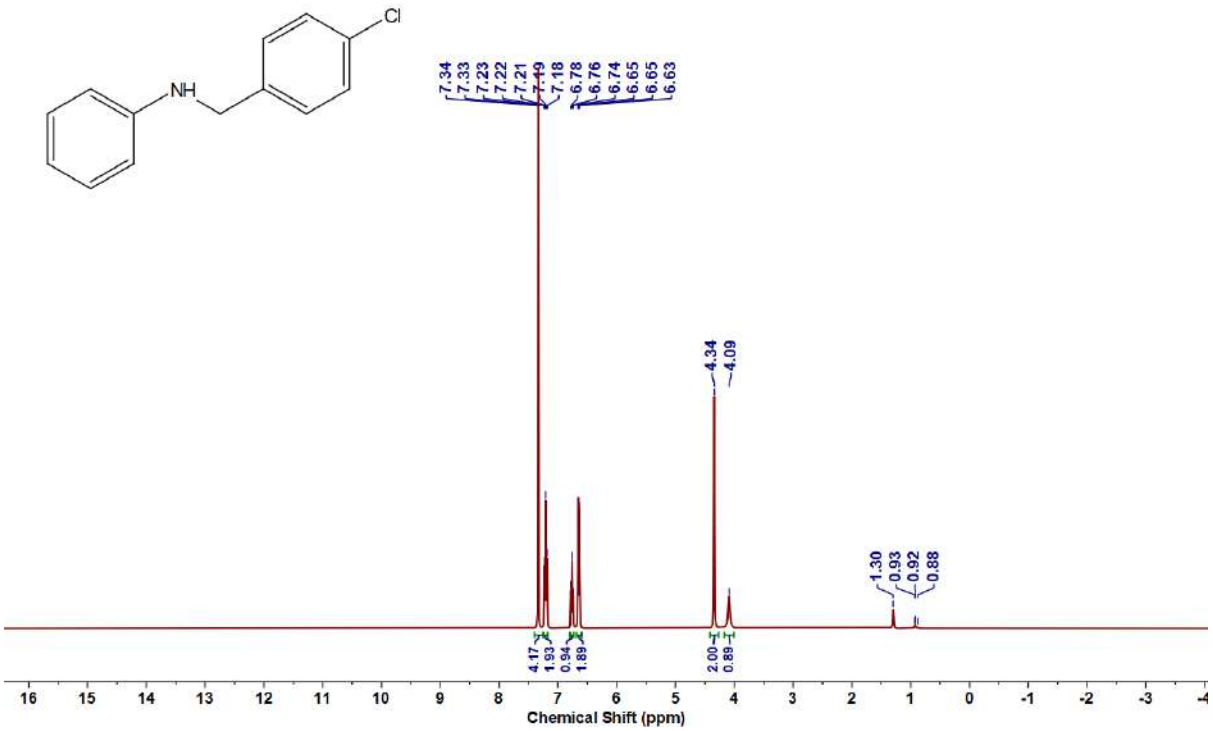

Figure 6.6.A109: ^{1}H NMR spectrum of **7c**

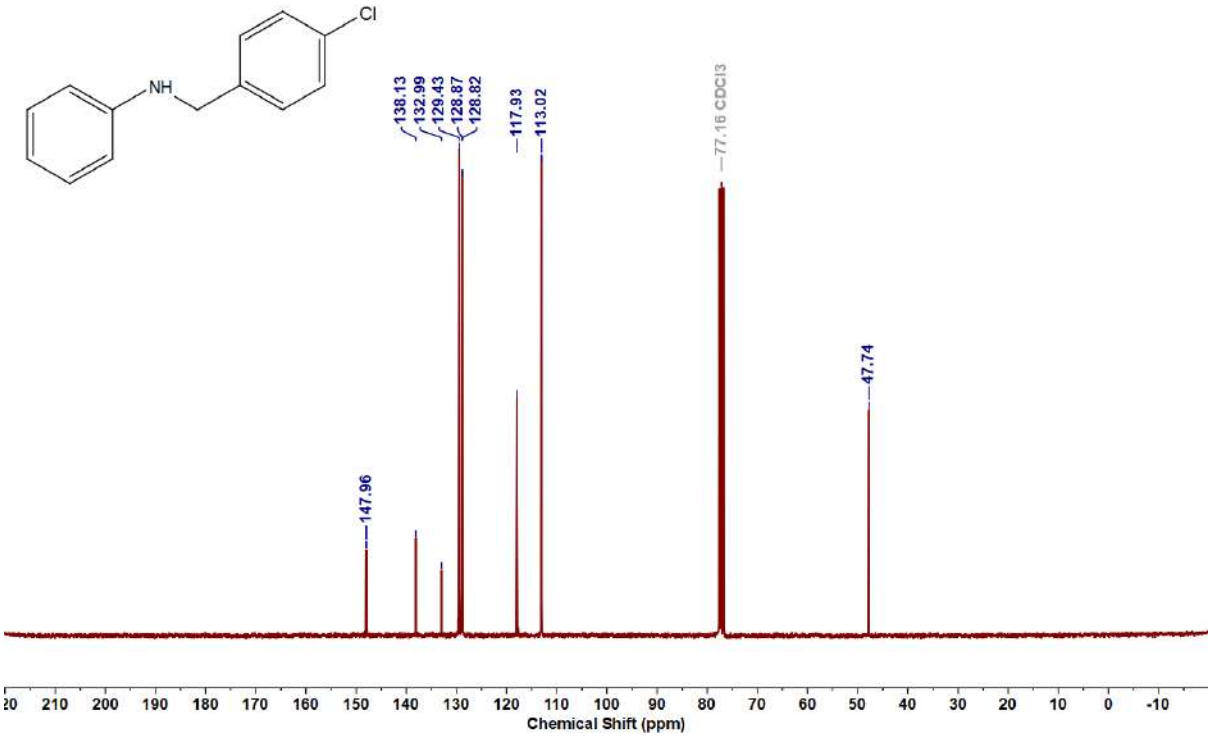

Figure 6.6.A110: ^{13}C{^{1}H} NMR spectrum of **7c**

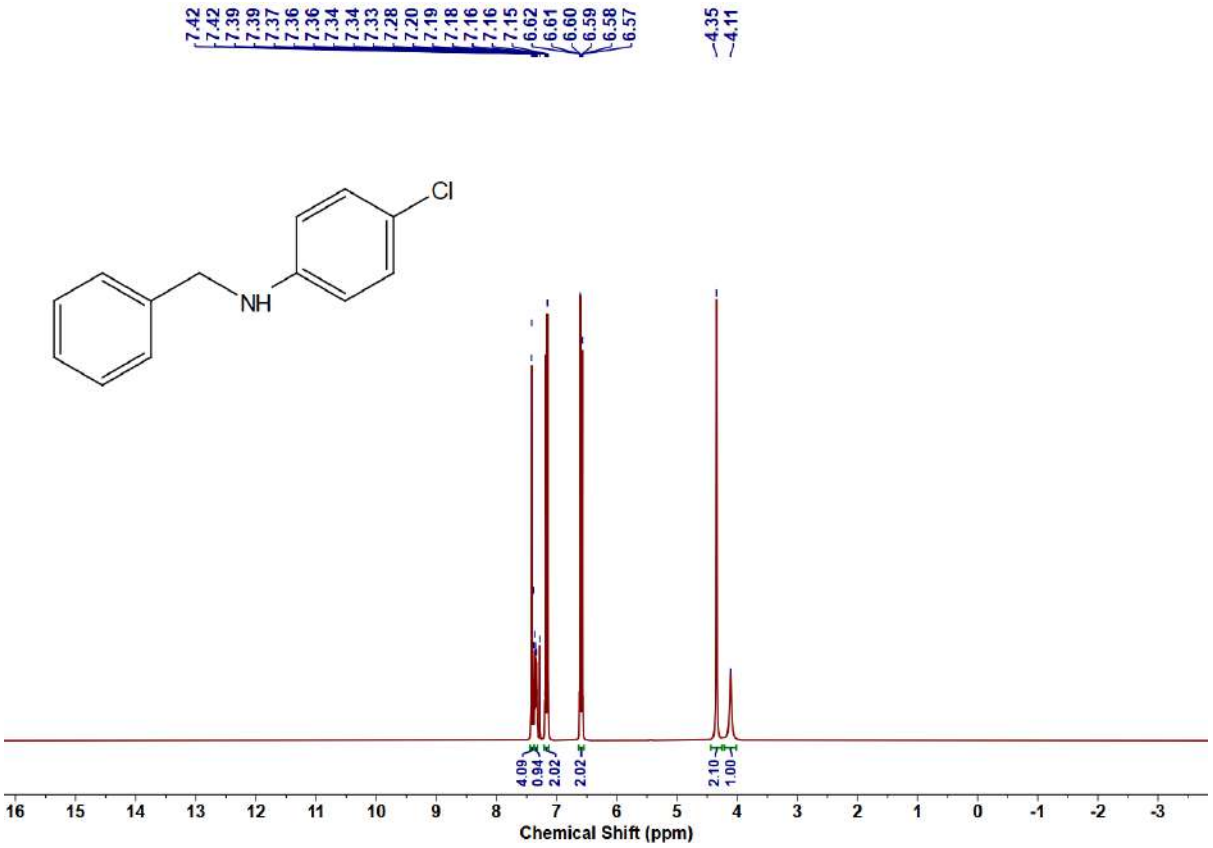

Figure 6.6.A111: ^{1}H NMR spectrum of **7d**

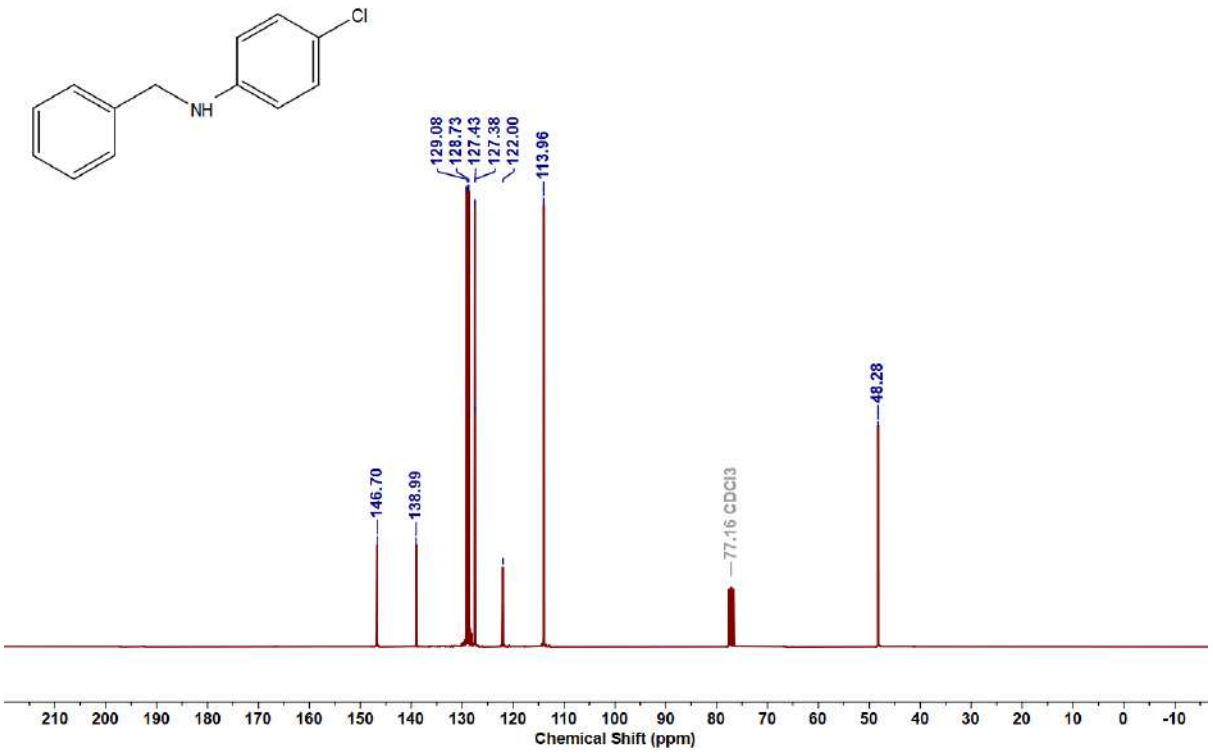

Figure 6.6.A112: ^{13}C{^{1}H} NMR spectrum of **7d**

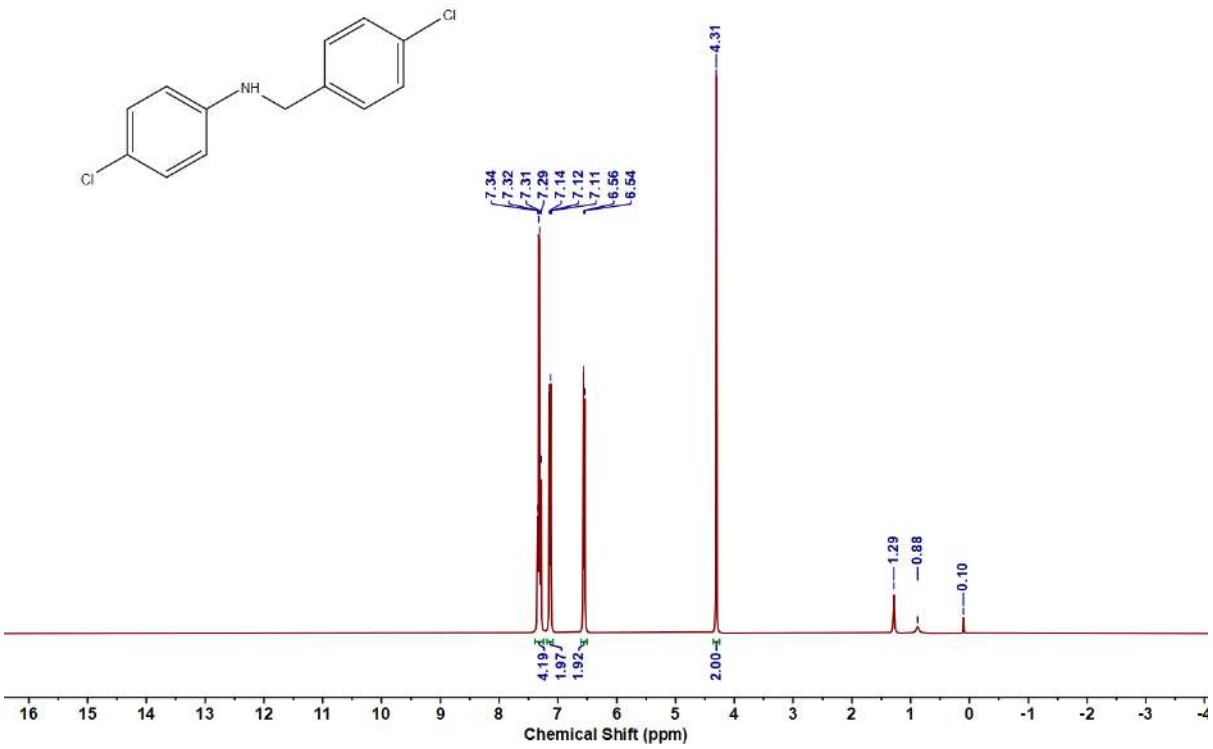

Figure 6.6.A113: ^{1}H NMR spectrum of **7e**

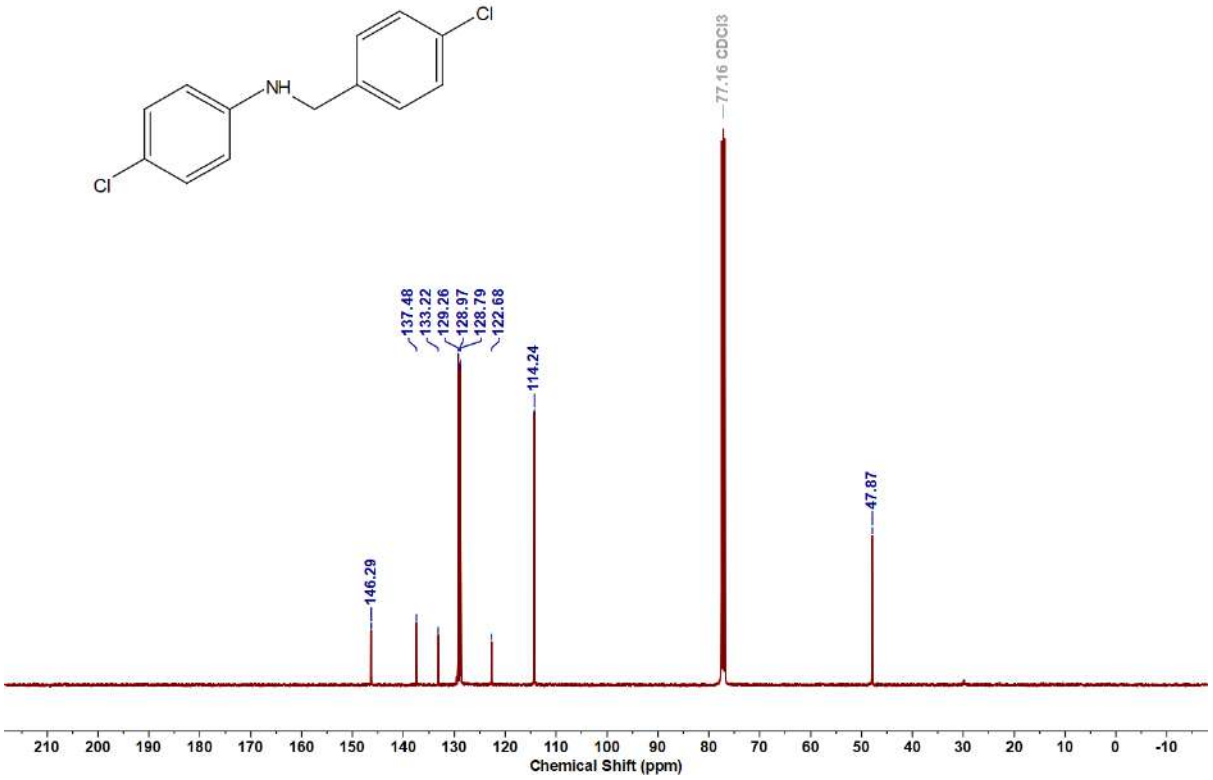

Figure 6.6.A114: ^{13}C{^{1}H} NMR spectrum of **7e**

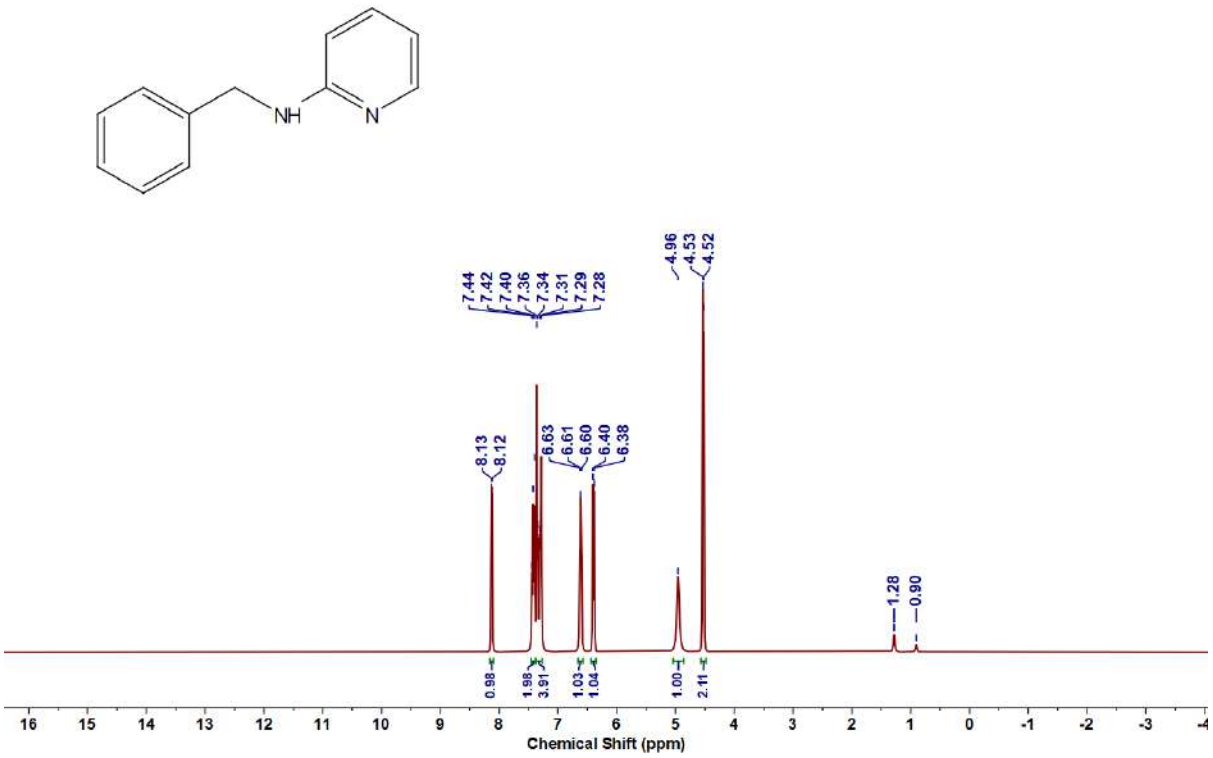

Figure 6.6.A115: ^{1}H NMR spectrum of **7f**

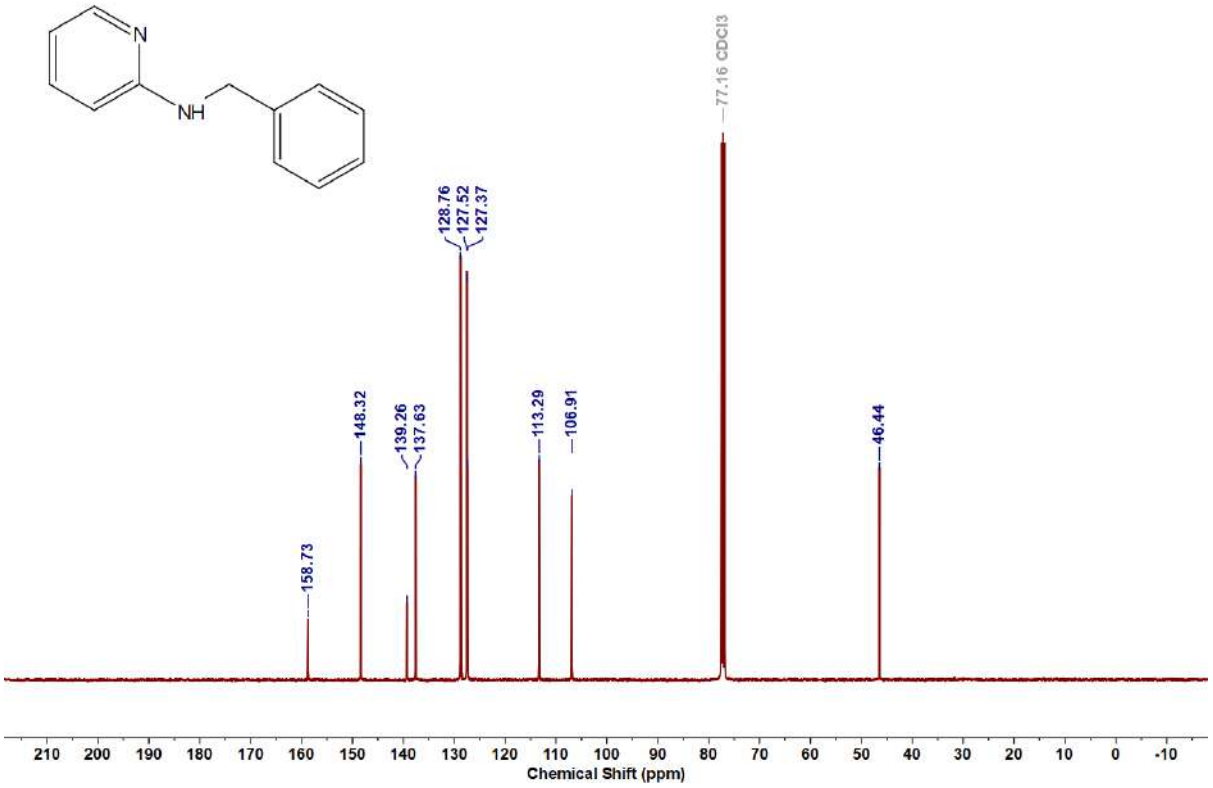

Figure 6.6.A116: ^{13}C{^{1}H} NMR spectrum of **7f**

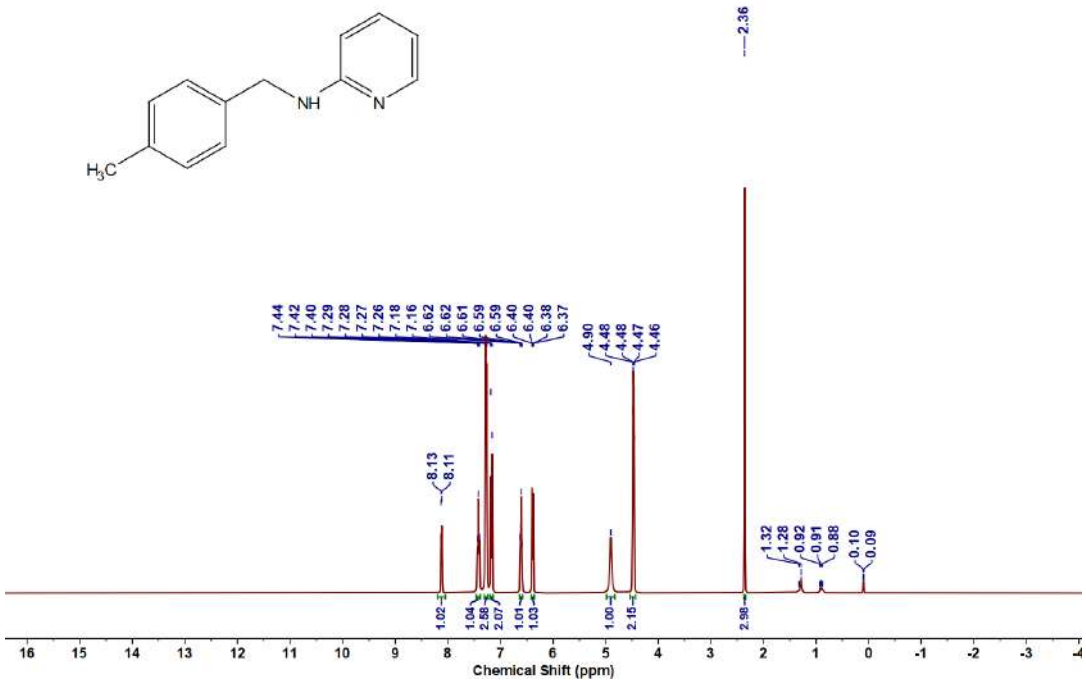

Figure 6.6.A117: ^{1}H NMR spectrum of **7g**

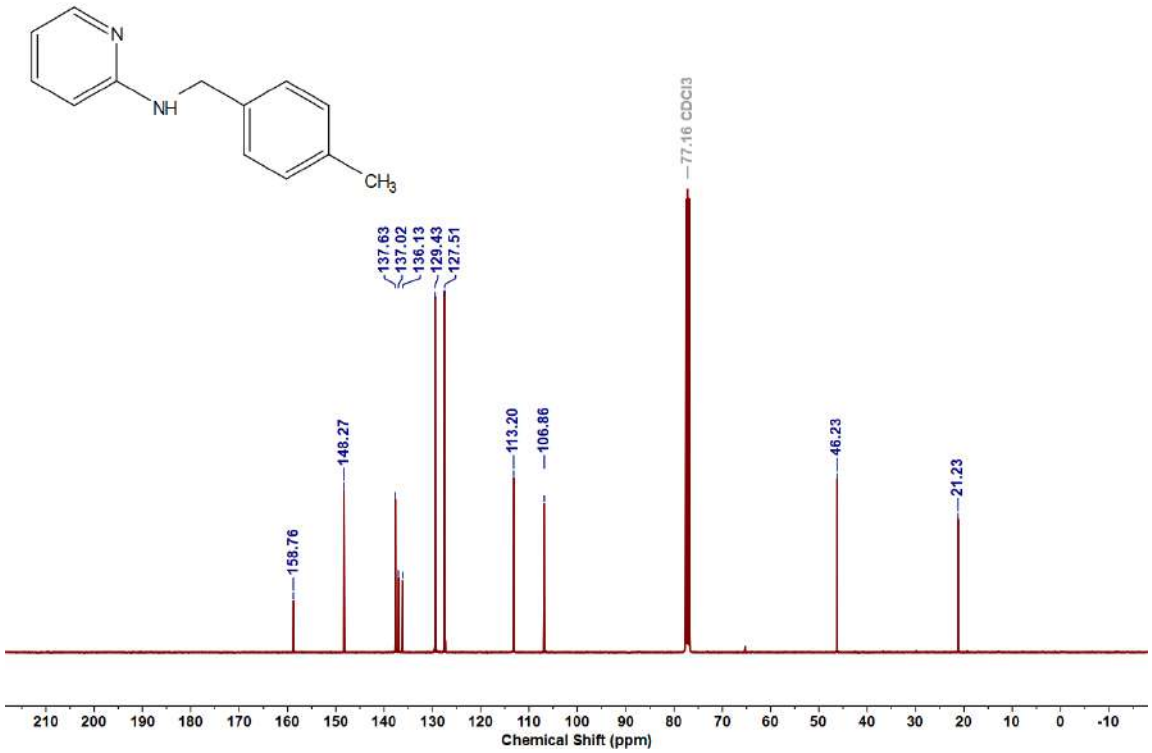

Figure 6.6.A118: $^{13}C\{^{1}H\}$ NMR spectrum of **7g**

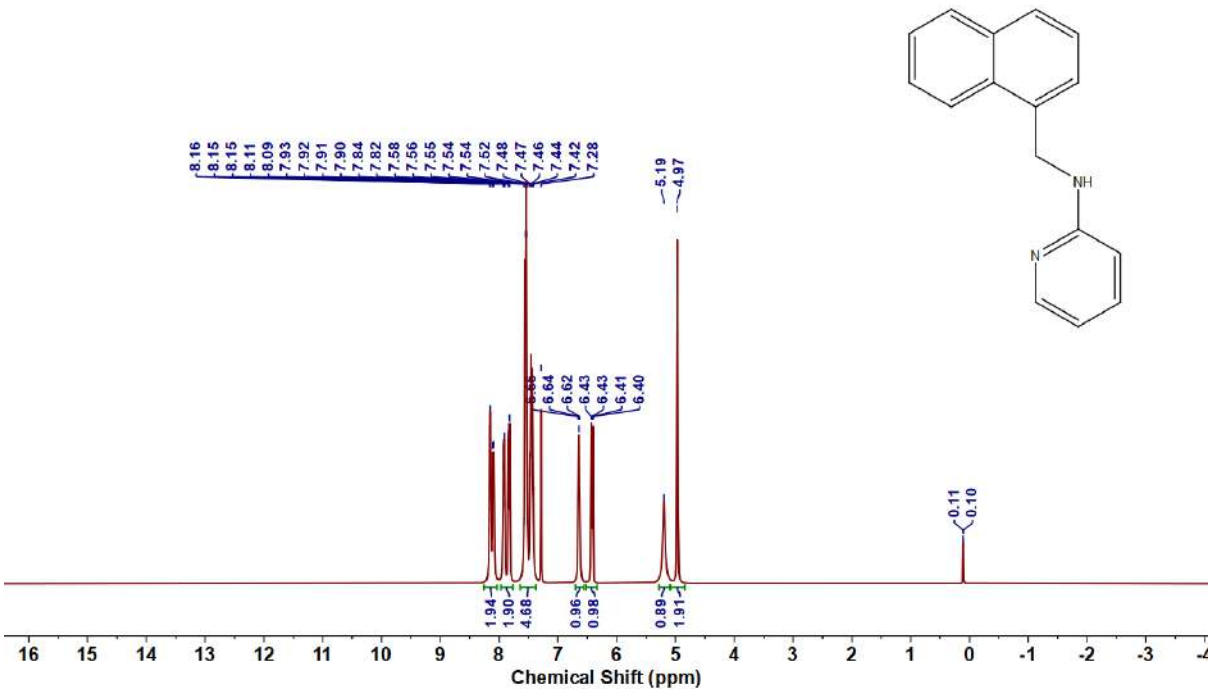

Figure 6.6.A119: ^{1}H NMR spectrum of **7h**

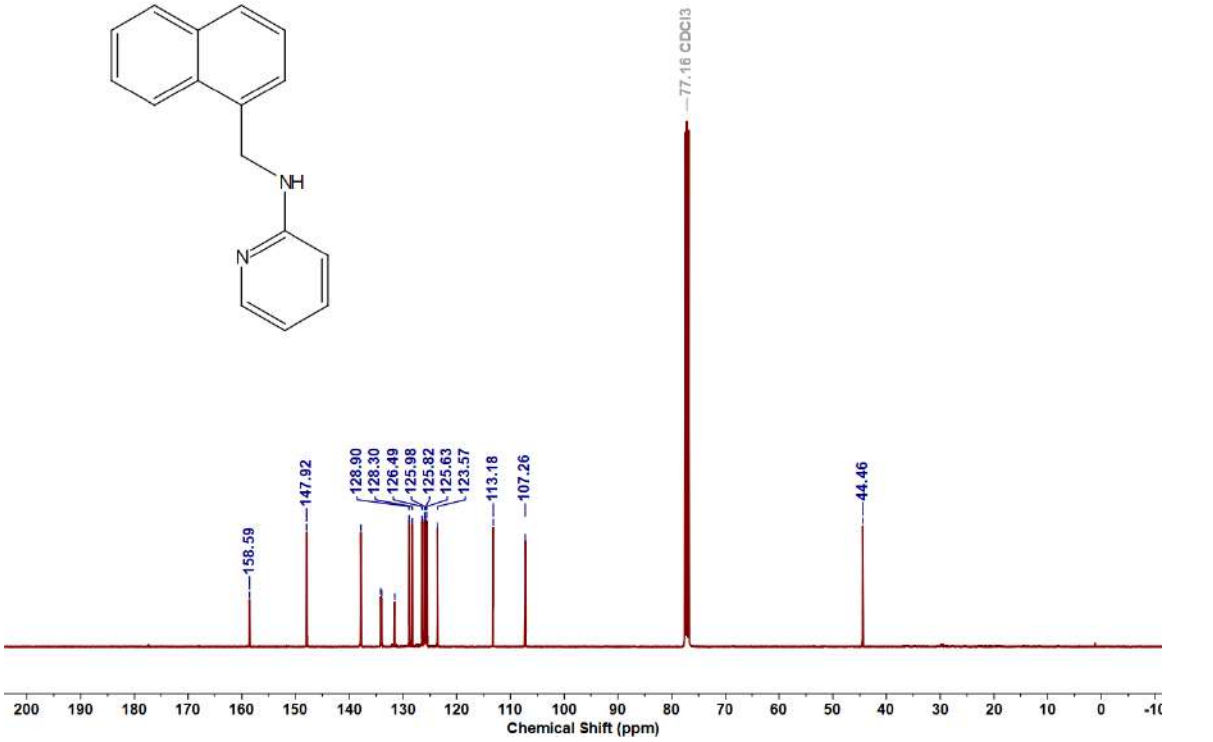

Figure 6.6.A120: ^{13}C{^{1}H} NMR spectrum of **7h**

Summary

This thesis presents a comprehensive account of design, synthesis, and catalytic applications of redox-noninnocent azo-based ligands and their transition metal complexes, with a particular focus on exploring ligand-centered reactivity and its role in facilitating sustainable catalytic transformations.

Chapter 1 provides a general introduction, outlining the fundamental concepts of redox noninnocence with a focus on azo-oxime and bis-azo-diamine ligand systems. It offers a concise summary of the research objectives, methodologies, and major findings, followed by a detailed description of the experimental techniques, instrumentation, and computational approaches employed throughout the study.

Chapter 2 describes the synthesis of four novel ruthenium(II) complexes of the general formula *trans*-[Ru(L)(CO)Cl(PPh_3)$_2$], derived from systematically varied azo-oxime ligands. Structural analyses reveal subtle changes in Ru–N_{azo} and Ru–N_{oxime} bond lengths, influenced by the electronic nature of the aryl substituents. Electrochemical studies demonstrate that the ligand framework undergoes ligand-centered one-electron reductions, forming metastable anion radical species that highlight the redox-responsive nature of the coordinated azo-oxime units.

Chapter 3 establishes the catalytic potential of the *trans*-[Ru(L)(CO)Cl(PPh_3)$_2$] complexes in electron transfer mediated transformations, particularly (i) α-alkylation of ketones with primary alcohols and (ii) dehydrogenative synthesis of 2-substituted quinolines. Mechanistic investigations support a redox-active, ligand-centered pathway initiated via hydrogen atom transfer (HAT) by the azo-oxime anion radical, while the ruthenium center primarily serves as a structural scaffold. The catalytic performance is strongly influenced by the electron-withdrawing nature of the ligand substituents.

Chapter 4 presents the synthesis and characterization of an air- and moisture-stable Ru(II) complex, *trans*-[Ru(NpL)(CO)Cl(PPh_3)$_2$], bearing a phenyl-azo-naphthaldoxime ligand. This complex acts as a pre-catalyst for the aerobic dehydrogenative coupling of benzyl alcohols with *o*-aminobenzamides to synthesize quinazolin-4(3H)-ones. Experimental and computational studies confirm a ligand-centered HAT mechanism where the azo unit drives aldehyde formation, followed by base-mediated condensation. The methodology operates efficiently under mild conditions with low catalyst loading, offering a practical approach to heterocycle synthesis.

Chapter 5 introduces a newly designed bis-azo-diamine ligand, which functions as a metal-free, redox-active organo-catalyst for the electrocatalytic reduction of CO_2. The transformation proceeds through a ligand-centered triplet diradical intermediate, enabling stepwise reduction of CO_2 to glyoxal, which is subsequently converted into acetic acid, ethanol, and acetone. Notably, acetic acid reacts with formyl intermediates to yield C_3 products via a proton-coupled electron transfer (PCET) mechanism. This study demonstrates the promise of coordinatively fluxional, metal-free catalysts in carbon capture and utilization (CCU), laying the groundwork for future catalyst optimization and scale-up.

Chapter 6 explores the synthesis and application of a hexacoordinated Ru(III) complex incorporating a bis-azo-diamido ligand. This complex catalyzes the direct dehydrogenative N-alkylation of aromatic amines using primary alcohols. Mechanistic insights suggest that one azo moiety plays a key role in the initial dehydrogenation step via HAT, while the Ru center remains redox-innocent. The resulting aldehyde undergoes condensation with the amine to form a Schiff base, which is subsequently reduced through a metal-assisted "borrowing hydrogen" (BH) pathway to yield N-alkylated aromatic amines.
This thesis underscores the versatility of redox-noninnocent azo-based ligands in promoting a range of catalytic transformations, both in metal-coordinated and metal-free systems.

Outlook

The ligand-centered electron transfer pathways, particularly involving azo-anion radicals, open new directions for designing sustainable catalysts for small molecule activation, including CO_2. Future work will focus on refining ligand architectures to enhance redox tunability and catalytic selectivity, as well as extending their applicability to other challenging transformations in green and energy-relevant chemistry.

List of Publications

1. Coordinatively fluxional diazo-based organo-electrocatalyst for conversion of CO_2 to C_2 and C_3 products

   Nidhi Kumari,‡ Supriyo Halder,‡ Srijita Naskar, Sanjib Ganguly,* Kausikisankar Pramanik,* Farzaneh Yari, Adrian Dorniak, Wolfgang Schöfberger,* Soumyajit Roy,* *Materials Today Catalysis*, **2024**, *5*, 100049.

2. Ruthenium complexes of redox non-innocent aryl-azo-oximes for catalytic a-alkylation of ketones and synthesis of 2-substituted quinolines

   Supriyo Halder,‡ Srijita Naskar,‡ Debashis Jana, Gopal Kanrar, Kausikisankar Pramanik,* Sanjib Ganguly,* *New J. Chem.*, **2024**, *48*, 8181–8194.

3. Dehydrogenative Coupling for Synthesis of Quinazolin-4(3H)-ones via Tandem Reaction using Ruthenium(II)-Phenyl-Azo-Naphthaldoxime: An Experimental and Theoretical Investigation

   Supriyo Halder,‡ Srijita Naskar, ‡ Debashis Jana, Gopal Kanrar, Shyama Charan Mandal, Subhadip Roy, Nishchal Bharadwaj, Kausikisankar Pramanik,* Sanjib Ganguly,* *Chem Asian J.*, **2025**, *20*, e202401278.

4. Sustainable Route Towards N-Alkylated Amines *via* Alcohol Dehydrogenation Catalyzed by Bis-Azo-Diamido Coordinated Ruthenium(III) Complex

   Supriyo Halder,‡ Srijita Naskar,‡ Sampad Malik, Dipika Roy, Kausikisankar Pramanik*, (*Manuscript under revision*)

Other publications (Not included)

5. Coligand driven diverse organometallation in benzothiazolyl-hydrazone derivatized pyrene: ortho *vs*. peri C–H activation

Soumitra Dinda, Sarat Chandra Patra, Subhadip Roy, Supriyo Halder, Thomas Weyhermuller, Kausikisankar Pramanik,* Sanjib Ganguly,* *New J. Chem.*, **2020**, *44*, 1407–1417.

6. Role of ligand disposition and oxime…oximato hydrogen bonding upon redox non-innocent character of rhodium(III) phenylazooximates

Srijita Naskar, Supriyo Halder, Gopal Kanrar, Debashis Jana, Soumitra Dinda, Kausikisankar Pramanik,* Sanjib Ganguly,* *Polyhedron*, **2023**, *235*,116342.

7. N–N hydrazonyl bond cleavage in benzothiazolyl-hydrazino-phenathrenequinone mediated by ruthenium(II) *via* an anion radical intermediate

Gopal Kanrar, Supriyo Halder, Srijita Naskar, Debashis Jana, Arup Sarkar, Bikash Kumar Panda, Soumitra Dinda, Kausikisankar Pramanik,* Sanjib Ganguly,* *Journal of Molecular Structure*, **2024**, *1314*, 138720.

8. Potent pincer-zinc catalyzed homogeneousnα-alkylation and Friedländer quinoline synthesis reaction of secondary alcohols/ketones with primary alcohols

Debashis Jana, Sima Roy, Srijita Naskar, Supriyo Halder, Gopal Kanrar, Kausikisankar Pramanik,* *Org. Biomol. Chem.*, **2024**, *22*, 6393–6408.

9. Designed Synthesis of Amino-Azo-Quinoline and Their Nickel(II) Complexes: Molecular Structure, Electrochemistry and an Insight Into Their In Vitro Anti-Cancer Activities

Srijita Naskar,‡ Koushik Sarkar,‡ Supriyo Halder, Bidisha Chatterjee, Debjeet Chakraborty, Arka Laha, Rahul Sharma, Arup Kumar Mitra, Kausikisankar Pramanik,* Sanjib Ganguly,* *Chemistry & Biodiversity*, **2025**, *22*, e202402436.

10. One-Pot Cascade [3+2+1] Annulation: Synthesis and Mechanistic Insight of *s*-Triazines and Pyrimidines Using Azo-Supported Metalloradical Nickel Catalyst

Debashis Jana, Sampad Malik, Gopal Kanrar, Supriyo Halder, Srijita Naskar, Kausikisankar Pramanik,* *ChemCatChem*, **2025**, *17*, e202401851.

11. Alcohol Dehydrogenation Catalyzed by Azo-Oxime Coordinated Ruthenium(II): A Strategic and Sustainable Route towards Site-Selective C(sp^3)–H Functionalization of 9H-Fluorene

Srijita Naskar,‡ Supriyo Halder,‡ Aritra Das, Sampad Malik, Gopal Kanrar, Debashis Jana, Bikash Kumar Panda, Kausikisankar Pramanik,* Sanjib Ganguly,* *Asian J. Org. Chem.*, **2025**, e00330.

Materials Today Catalysis 5 (2024) 100049

Contents lists available at ScienceDirect

Materials Today Catalysis

journal homepage: www.journals.elsevier.com/materials-today-catalysis

Coordinatively fluxional diazo-based organo-electrocatalyst for conversion of CO_2 to C_2 and C_3 products

Nidhi Kumari [a,1], Supriyo Halder [b,1], Srijita Naskar [b], Sanjib Ganguly [c,*], Kausikisankar Pramanik [b,*], Farzaneh Yari [d], Adrian Dorniak [d], Wolfgang Schöfberger [d,*], Soumyajit Roy [a,*]

[a] Eco-Friendly Applied Materials Laboratory, Department of Chemical Sciences, Materials Science Centre, Indian Institute of Science Education and Research, Kolkata, West Bengal 741246, India
[b] Department of Chemistry, Jadavpur University, Kolkata, West Bengal 700032, India
[c] Department of Chemistry, St. Xavier's College, Kolkata, West Bengal 700016, India
[d] Institute of Organic Chemistry, Laboratory for Sustainable Chemistry and Catalysis (LSusCat), Johannes Kepler University Linz, Altenberger Straße 69, Linz 4040, Austria

ARTICLE INFO

Keywords:
Metal free
Diazo-based ligand
Catalyst
CO_2 electroreduction
C_2 and C_3 products

ABSTRACT

The conversion of carbon dioxide (CO_2) into valuable chemicals, specifically C_2 and C_3, through metal-free electrocatalysis remains a formidable challenge. Breaking away from traditional transition metal complexes, the focus is on designing and selecting efficient organic catalysts. In this pursuit, a diazo-based organic bulky ligand emerges as a promising candidate, offering a solution that is both sustainable and renewable. The key feature of this ligand is its low-lying π* (LUMO), enabling it to readily accept an electron in an electrochemical environment when a potential is applied. The synthesized Diazo-based ligands have been meticulously characterized using various techniques, including ^{1}H NMR, ^{13}C NMR, UV-Vis, and IR spectroscopy. This diazo-based ligand serves as an electrocatalyst, undergoing reduction to a triplet diradical that acts as a nucleophile. In an aqueous medium, it forms an adduct with CO_2, leading to the generation of a formyl radical. This radical further couples to produce acetic acid and acetone with efficiencies of 19.6% and 24.2%, respectively, at pH 5.5. To provide a deeper understanding, we present a proposed mechanism pathway supported by *in-situ* UV-Vis spectroscopy and a comprehensive Density Functional Theory (DFT) study. These findings mark a significant step forward in the field of metal-free electrocatalysis, offering a sustainable approach to the conversion of CO_2 into valuable chemicals, contributing to the development of renewable and environmentally friendly systems.

1. Introduction

Today's climate change demands the immediate implementation of innovative sustainable technologies [1]. Among these technologies, the electrocatalytic conversion of carbon dioxide (CO_2) into valuable products is of utmost importance due to its dual potential for atmospheric CO_2 reduction and generation of renewable energy. Despite notable progress in this area, the synthesis of three-carbon (C_3) [2] products from CO_2 electro-reduction remains a less explored yet promising frontier [3]. In this article, we address this issue. The present published research paradigm predominantly focuses on the generation of one-carbon (C_1) products such as formaldehyde or formate [4] or two-carbon (C_2) products like ethanol [5] and ethanoic acid [6]. These transformations, although valuable, are stepping stones specifically for higher-carbon products (C_3), that hold considerable potential in the realms of renewable fuels and chemicals [7]. Synthesizing C_3 products from CO_2 electro-reduction represents an essential step towards the direct utilization of CO_2 in chemical synthesis, a goal of paramount practical importance in the context of a circular carbon economy. However, the intricate interplay of mechanistic, thermodynamic, and kinetic factors [8] in the C_3 production pathway present a complex landscape, posing unique challenges for such developments [9].

* Corresponding authors.
E-mail addresses: icsgxav@gmail.com (S. Ganguly), kpramanik@hotmail.com (K. Pramanik), wolfgang.schoefberger@jku.at (W. Schöfberger), s.roy@iiserkol.ac.in (S. Roy).
[1] These authors contributed equally.

https://doi.org/10.1016/j.mtcata.2024.100049
Received 6 February 2024; Received in revised form 5 March 2024; Accepted 8 March 2024
Available online 10 March 2024

NJC

ROYAL SOCIETY OF CHEMISTRY

PAPER

View Article Online
View Journal | View Issue

Cite this: *New J. Chem.*, 2024, **48**, 8181

Ruthenium complexes of redox non-innocent aryl-azo-oximes for catalytic α-alkylation of ketones and synthesis of 2-substituted quinolines†

Supriyo Halder,‡[a] Srijita Naskar,‡[a] Debashis Jana,[a] Gopal Kanrar,[b] Kausikisankar Pramanik *[a] and Sanjib Ganguly *[b]

Received 24th January 2024,
Accepted 3rd April 2024

DOI: 10.1039/d4nj00391h

rsc.li/njc

Ruthenium(II) complexes [RuL(CO)Cl(PPh$_3$)$_2$], **1a**–**4a**, have been synthesized using ligands PhN=NC(Ar)NOH, HL **1**–**4**, respectively, by varying the pendant aryl (Ar) groups. The single crystal X-ray diffraction studies of complexes reveal that there are certain changes in Ru–N$_{azo}$ and Ru–N$_{oxime}$ bond lengths that may be explained primarily on the basis of electronic effects of pendant aryl groups. In **4a**, all Ru–N bond lengths are longer and this is attributed to oximato–O···O (hydroxyphenyl) interactions. Furthermore, there are weak intramolecular F···π interactions in **3a**. The complexes display multiple reductive responses ascribable to electron acceptance within the azo-oxime framework of the coordinated ligand and the corresponding one-electron reduced metastable anion radical complexes of type [Ru(L$^{\bullet-}$)(CO)Cl(PPh$_3$)$_2$]$^-$ **[1]$^{\bullet-}$** have been generated. This property of the complexes has been exploited in electron transfer catalysis *via* trapping of electrons in the azo-oxime skeleton in two types of reactions: (1) α-alkylation of ketones with primary alcohols and (ii) synthesis of 2-substituted quinoline derivatives from 2-aminobenzyl alcohols and substituted acetophenones/alkyl methyl ketones. The scope of catalysis has been studied and the probable catalytic pathway has been established from experimental results. The catalytic pathway is ligand-centric and redox-driven for the dehydrogenation process and the initial step involves formation of a coordinated anion radical. This leads to conversion of the starting 1° alcohol to the corresponding carbonyl *via* the HAT pathway, with the ruthenium(II) centre practically behaving as a template and remaining redox inactive. The catalytic reactions have been proven to be affected by the nature of pendant aryl (Ar) groups within the coordinated ligand.

Introduction

The redox non-innocence[1] of coordinated ligands is gaining profound importance in the field of electron transfer catalysis since the metal center and the ligand skeleton have the ability to stimulate a process in a collaborative manner, with the catalyst switching from one spin isomeric state to another.[2–16] Such reactions may proceed *via* formation of a meta-stable ligand-centric coordinated radical and it is usually accompanied by proton coupled electron transfer (PCET)[17–22] or hydrogen atom transfer (HAT).[23–29] The chemistry of redox non-innocent ligands containing azo functions has developed over the past two and a half decades[30–43] and at present the catalytic role of their complexes is under intense investigation.[44–62] In the majority of the cases, ligands are of tridentate azo pincer type, where the ligated azo moieties have the ability to behave as electron pockets to store electron/s in the form of an azo anion-radical. In addition, the reserved electron/s may be transferred to suitable centres to bring about catalytic reduction and this concept has been widely employed to synthesize several value-added chemicals of pharmaceutical and industrial importance, in a cost effective and atom efficient manner.

We have been striving to explore and figure out the electron extracting ability of coordinated diaryl-azo-oximes in order to effectuate certain unusual redox transformations.[63–67] We are further motivated to synthesize suitable complexes of azo-oximes where the ligand skeleton may become redox active in the presence of ruthenium(II) and they may be skillfully employed to bring about electron-transfer catalysis for synthesis of useful organic compounds in an atom efficient manner. It is worth mentioning that there has been no report on

[a] *Department of Chemistry, Jadavpur University, Kolkata–700032, India. E-mail: kpramanik@hotmail.com; Tel: +91 33 2457 2781*
[b] *Department of Chemistry, St. Xavier's College (Autonomous), Kolkata–700016, India. E-mail: icsgxav@gmail.com, icsg@sxccal.edu; Tel: +91 33 2255 1266*

† Electronic supplementary information (ESI) available. CCDC 2303589, 2303590, 2303602, 2303603, 2303607 and 2303608. For ESI and crystallographic data in CIF or other electronic format see DOI: https://doi.org/10.1039/d4nj00391h

‡ Authors contributed equally to this work.

ACES Asian Chemical Editorial Society

doi.org/10.1002/asia.202401278

CHEMISTRY
AN ASIAN JOURNAL
Research Article

www.chemasianj.org

Dehydrogenative Coupling for Synthesis of Quinazolin-4(3H)-ones *via* Tandem Reaction using Ruthenium(II)-Phenyl-Azo-Naphthaldoxime: An Experimental and Theoretical Investigation

Supriyo Halder[+],[a] Srijita Naskar[+],[a] Debashis Jana,[a] Gopal Kanrar,[b] Shyama Charan Mandal,[c] Subhadip Roy,[d] Nishchal Bharadwaj,[e] Kausikisankar Pramanik,*[a] and Sanjib Ganguly*[b]

The bidentate N, N, donor phenyl-azo-naphthaldoxime NpLH, **1** was used to synthesize the ruthenium(II) complex trans-[Ru(NpL)(CO)Cl(PPh$_3$)$_2$], **2**. It has been characterized by SCXRD, electrochemical and spectral studies. Computational analysis indicates that the low-lying π*-LUMO of the complex has substantial azo-character of coordinated ligand. This property has been exploited to form an efficient electron transfer pre-catalyst to effectuate dehydrogenative functionalization of a large number of benzyl alcohols to quinazolin-4(3H)-ones via condensation with diverse o-amino benzamides as well as N-substituted benzamides under aerobic conditions (57 entries). A reaction mechanism has been projected via isolation of intermediates and certain control experiments. Furthermore, it has been substantiated by theoretical scrutiny using density functional theory (DFT) calculation. The catalytic cycle involves stepwise hydrogen atom transfer (HAT) from benzyl alcohols to the N_{azo} atoms of the coordinated ligand with subsequent removal of the H-atoms from the N_{azo} atoms to regenerate the active catalyst.

Introduction

N-heterocycles have been found to be in plenitude in natural products due to their intimate biological relevance. This leads to extensive research towards the development of innovative, sustainable and greener methods for synthesis of aza-heterocycles.[1] The quinazolinone moiety is present as a building block in a wide range of naturally occurring alkaloids that have been sequestered from natural resources like micro-organisms, plants, and animals.[2,3] Quinazolin-4(3H)-ones and their substituted analogues have gained significant attention owing to various pharmacological activities, such as anti-inflammatory,[4] antimicrobial,[5] anticancer,[6,7] antihypertensive,[8] dihydrofolate reductase inhibition,[9] and Tyrosine Kinase inhibition.[10] Despite significant progress in this area, it has been found that in most cases multi-step synthesis is required. This creates unwanted byproducts and often needed hazardous chemicals for catalytic transformation. Furthermore, the precursor molecules are often expensive and less available.[11,12] Accordingly, it is always challenging to develop cost-effective and atom efficient production of substituted quinazolin-4(3H)-ones. There have been some reports of transition metal catalysed synthesis of substituted quinazolin-4(3H)-ones via dehydrogenative functionalization of aliphatic and aromatic alcohols and this strategy is quite promising since it is a single-step, economical, environment friendly synthesis starting from readily available precursors and generates hydrogen or water as the only byproducts (Scheme 1).[13–15]

We were inquisitive regarding the electron trapping aptitude of coordinated azooximes[16] for the past few years and this led us to explore their ability to bring about dehydrogenative functionalization of aliphatic and aromatic alcohols to form value added products.[17–19] As a continuation of our previous work, in this paper we have utilized phenyl-azo-naphthaldoxime NpLH, **1** to synthesize a ruthenium(II) complex trans-[Ru(NpL)(CO)Cl(PPh$_3$)$_2$], **2** (Scheme 2). The structural, electrochemical, and theoretical studies of **2** have been performed in order to have a comprehension of their competence to bring about electron transfer catalysis. The ruthenium(II) complex

[a] S. Halder,[+] S. Naskar,[+] D. Jana, K. Pramanik
Department of Chemistry, Jadavpur University, Kolkata 700032, India
Tel: +91 33 2457 2781
E-mail: kpramanik@hotmail.com

[b] G. Kanrar, S. Ganguly
Department of Chemistry, St. Xavier's College (Autonomous), Kolkata – 700016, India
Tel: +91 33 2255 1266
E-mail: icsgxav@gmail.com
icsg@sxccal.edu

[c] S. C. Mandal
SUNCAT Center for Interface Science and Catalysis, SLAC National Accelerator Laboratory
2575 Sand Hill Road, Menlo Park, CA 94025 (USA)

[d] S. Roy
Department of Chemistry, The ICFAI University Tripura, Agartala, Tripura 799210, India

[e] N. Bharadwaj
Department of Chemistry, Indian Institute of Technology (IIT) Indore, Indore, Madhya Pradesh 453552

[+] Authors contributed equally to this work

Supporting information for this article is available on the WWW under https://doi.org/10.1002/asia.202401278

NJC

ROYAL SOCIETY OF CHEMISTRY

PAPER

View Article Online
View Journal | View Issue

Cite this: *New J. Chem.*, 2020, **44**, 1407

Coligand driven diverse organometallation in benzothiazolyl-hydrazone derivatized pyrene: *ortho vs. peri* C–H activation†

Soumitra Dinda, [a] Sarat Chandra Patra, [b] Subhadip Roy, [c] Supriyo Halder, [b] Thomas Weyhermüller, [d] Kausikisankar Pramanik *[b] and Sanjib Ganguly *[a]

Benzothiazolyl hydrazones **1** (H_2L^{PAH}) incorporating polycyclic aromatic hydrocarbons (PAHs) have been fabricated as hemilabile scaffolds and elegantly utilized the inbuilt nitrogen donors as a proficient directing group (DG) to bring about ruthenium(II) assisted C–H activation in PAHs at both the *peri* and *ortho* positions. An isomeric pair of organometallics having formula $[Ru^{II}(L^{Pyr})(CO)(PPh_3)_2]$ (*peri*: **3a**, *ortho*: **5a**) have been conveniently prepared by varying the $[Ru^{II}]$ precursors with H_2L^{Pyr}. In contrast, only one type of activated product *viz.* $[Ru^{II}(L^{Anc})(CO)(PPh_3)_2]$ **3b** has been obtained with the 9-anthracene derivative of **1**, H_2L^{Anc}, under analogous reaction conditions. The underlying mechanistic aspects have been elucidated by isolating the thermally unstable intermediates *viz.* $[Ru^{II}(HL^{Pyr})Cl(CO)(PPh_3)_2]$ **2a** and $[Ru^{II}(HL^{Pyr})H(CO)(PPh_3)_2]$ **4a** in the course of the *peri* and *ortho* C–H activation processes, respectively. The coligand (Cl/H) plays a vital role to bring about the C–H activation at the desired positions *via* formation of either a four- or five-membered metallacycle in **2a** and **4a**, respectively. The activation process *vis-à-vis* Ru–C bond formation in **3a** can be achieved smoothly from **2a** by a thermal transformation route, which proceeds *via* an initial rupture of the $Ru–N_{hydrazonyl}$ bond. In contrast, the *trans* influential hydride coligand prefers a five-membered chelate to avoid confrontation with $N_{hydrazone}$ in **4a**, which in turn furnishes exclusively *ortho* activation owing to the close approach of the Ru–H bond towards *ortho*-H in pyrene. The organometallated complexes exhibit oxidative responses at mild potential. EPR and computational studies indicate that the redox activity originates from the ligand-centered orbitals. The observed rich optoelectronic features are analysed primarily as ^{1}ILCT admixed with ^{1}MLCT components by theoretical means, indicating an appreciable accumulation of electron density over the ligand backbone in their ground states.

Received 9th October 2019,
Accepted 12th December 2019

DOI: 10.1039/c9nj05088d

rsc.li/njc

Introduction

C–H bond activation is a long-standing issue under exploration in synthetic organic chemistry, primarily owing to its prospects in simplifying varied chemical conversion in an atom-efficient technique.[1] The efficacy of this ingenious synthetic approach has been efficiently applied to the fabrication of pharmaceuticals[2] and agrochemicals[3] as well as certain materials.[4,5] One of the prime strategies involved in the activation of the aromatic C–H bond is by introducing a directing group (DG) that coordinates a transition metal lying in the vicinity of the aromatic C–H bond, with subsequent activation *via* cyclometallation.[6] Since the C–H bond strength is much higher than that of M–C, the thermodynamic barrier for C–H bond cleavage is expected to be high.[7] Nevertheless, this can be attained with the aid of chelation of a directing group enabled ligand, which in turn affords an organometallacycle at a target specific position.[8] Although C–H transformation of aldehyde-derived hydrazones is documented,[9] the directing ability of benzothiazole blended hydrazones is yet to be explored to bring about aromatic C–H functionalization in polyaromatic hydrocarbons (PAHs). Indeed, bifunctional groups are enviable for diverse chemical reactivity as they can typically exhibit supplementary flexibility during coordination.

Controlling the site-selectivity of C–H activation is a prime barrier for the advancement of synthetically convenient methodology. In the present work, we report the designed synthesis

[a] *Department of Chemistry, St. Xavier's College (Autonomous), Kolkata 700016, India. E-mail: icsgxav@gmail.com, icsg@sxccal.edu; Tel: +91 33 2255 1266*
[b] *Department of Chemistry, Inorganic Chemistry Section, Jadavpur University, Kolkata 700032, India*
[c] *Department of Chemistry, The ICFAI University Tripura, Tripura 799210, India*
[d] *Max-Planck-Institut für Chemische Energiekonversion, Stiftstrasse 34-36, D-45470 Mülheim, Germany*

† Electronic supplementary information (ESI) available: X-ray crystallographic data for **2a**, **3a**, **3b**, **4a** and **5a**, selected experimental and theoretical bond parameters, absorption spectra, electrochemical data, π–π stacking interactions in **2a** and **4a**, NMR spectra of all compounds, relevant DFT results. CCDC 1887301, 1908528, 1908529, 1943129 and 1943130. For ESI and crystallographic data in CIF or other electronic format see DOI: 10.1039/c9nj05088d

Polyhedron 235 (2023) 116342

Contents lists available at ScienceDirect

Polyhedron

journal homepage: www.elsevier.com/locate/poly

Role of ligand disposition and oxime…oximato hydrogen bonding upon redox non-innocent character of rhodium(III) phenylazooximates

Srijita Naskar [a], Supriyo Halder [a], Gopal Kanrar [b], Debashis Jana [a], Soumitra Dinda [b], Kausikisankar Pramanik [a,*], Sanjib Ganguly [b,*]

[a] Department of Chemistry, Jadavpur University, Kolkata 700032, India
[b] Department of Chemistry, St. Xavier's College (Autonomous), Kolkata 700016, India

A B S T R A C T

The diaryl-azo-oxime ligands HL, **1** undergoes oxidative coordination reaction with Wilkinson's catalyst to form two isomeric complexes of type *cis*-[$Rh^{III}L_2Cl(PPh_3)$], **2a** (Cl and PPh_3 are *cis*) and *trans*-[$Rh^{III}L_2Cl(PPh_3)$], **2b** where they are *trans* with respect to each other. Unlike the case of **2a**, the complex **2b** upon treatment with sodium borohydride, can be transformed to *trans*-[$Rh^{III}(HL^{\bullet})(L^{-})Cl(PPh_3)$], **3** and the reaction appears to progress *via* PCET. The disposition of ligand frameworks as well as the formation of oxime…oximato hydrogen bond appears to have a significant function for phenylazooxime to exhibit redox non-innocent behaviour in presence of rhodium(III). The compounds were characterized by electrochemical analysis, different spectral methods, single crystal XRD and optoelectronic properties, particularly the nature of transitions in the chelates were scrutinized by TD-DFT.

1. Introduction:

Redox non-innocent ligands are interesting owing to their inherent capacity to exhibit various ligand redox levels upon coordination [1–23] and such systems have the aptitude to embrace and reject electron(s) during the course of catalytic processes [24–30], in chemical and biochemical reactions [31–33]. Coordinated azo-aromatic systems have been found to act as apposite precursors for stabilizing ligand centered anion radical complexes since they possess low-lying azo-π* orbital [34–47]. It has been well understood that structure of the ligand skeleton and redox character of the metal centre has a significant role for controlling the stabilisation of these type of complexes and ligand–metal π-interaction can further adjust the electronic structural features for maximum stabilization [48–50]. Moreover, ligand environment around the metal centre may also influence the aptitude of these chelated azo-ligands in conjunction with other moieties to receive or donate odd electron(s) and this may be attributed to electronic or steric factors. The impact of electronic environment of auxiliary ligands in supporting extra electron(s) within π* LUMO of these ligands have been much less reported [48,51]. As a continuation of our study on stabilization of odd electron in coordinated azooximes [51–53], we have tried to investigate the competence of these ligand to retain an unpaired electron over azo-oxime framework in presence of rhodium(III) and to stabilize the corresponding open shell complexes. In this regard, we have started with the diaryl-azo-oxime HL, **1** which possesses low lying π* LUMO, thereby having the aptitude to perform as an electron-sink upon ligation, and have successfully isolated two isomeric complexes of type *cis*-[$Rh^{III}L_2Cl(PPh_3)$] (**2a**), where Cl and PPh_3 are in *cis* positions and *trans*-[$Rh^{III}L_2Cl(PPh_3)$] (**2b**), where they are *trans* with respect to each other. The complex **2b** can be reduced to the azo-oxime radical anion complex of type *trans*-[$Rh^{III}(HL^{\bullet})(L^{-})Cl(PPh_3)$] (**3**) and the reaction appears to progress *via* PCET but the corresponding anion radical analog of the *cis* isomer could not be isolated. Thus, the *trans* isomer behaves as a superior electron carrier and this has been attributed to stereochemical control around the rhodium centre. In fact, in the *trans* isomer **2b**, there is scope for unpaired electron to be delocalized on both the ligands much more efficiently since they are practically coplanar. Furthermore, the stabilization of **3** may also be attributed to formation of oxime…oximato intramolecular hydrogen bonding during the course of electron acceptance in presence of protons and this is also consistent with theoretical scrutiny. (see Scheme 1.)

2. Experimental details

2.1. General information

Drying and purification of solvents were performed using literature procedure and distilled out before using as required. The required chemicals were purchased from following sources: Phenyl hydrazine and Benzaldehyde from TCI Chemical (India) Pvt. ltd. Wilkinson's

* Corresponding authors.
E-mail address: icsg@sxccal.edu (S. Ganguly).

https://doi.org/10.1016/j.poly.2023.116342
Received 21 December 2022; Accepted 14 February 2023
Available online 19 February 2023

Journal of Molecular Structure 1314 (2024) 138720

Contents lists available at ScienceDirect

Journal of Molecular Structure

journal homepage: www.elsevier.com/locate/molstr

N–N hydrazonyl bond cleavage in benzothiazolyl-hydrazino-phenathrenequinone mediated by ruthenium(II) via an anion radical intermediate

Gopal Kanrar [a], Supriyo Halder [b], Srijita Naskar [b], Debashis Jana [b], Arup Sarkar [a], Bikash Kumar Panda [c], Soumitra Dinda [a], Kausikisankar Pramanik [b,*], Sanjib Ganguly [a,*]

[a] Department of Chemistry, St. Xavier's College (Autonomous), Kolkata 700016, India
[b] Department of Chemistry, Jadavpur University, Kolkata 700032, India
[c] Department of Chemistry, Jangipur College, Jangipur, Murshidabad, West Bengal 742213, India

ARTICLE INFO

Keywords:
Redox non-innocent ligand
Crystallography
DFT
NMR
Cyclic voltammetry

ABSTRACT

The complexes [Ru(L^{Benz})H(CO)(PPh_3)$_2$] **2**, [Ru(L^{Benz})Cl(CO)(PPh_3)$_2$] **3**, (ligand behaving as bidentate monoanionic) and [Ru(L^{Benz})Cl(CO)(PPh_3)] **4**, (ligand is tridentate monoanionic) have been synthesized starting from benzothiazolyl-hydrazino-phenathrenequinone (HL) **1** and [RuH(CO)Cl(PPh_3)$_3$]. These are characterized by electrochemical and spectral methods as well as single crystal X-ray diffractometry (SCXRD). Upon treating with $NaBH_4$, **3** accepts an electron within the coordinated ligand framework and the anionic hydrazonyl-*N* takes up a proton to be transformed to meta-stable hydrazinoquinone anion radical complex of ruthenium(II) [Ru($HL^{Benz\bullet-}$)Cl(CO)(PPh_3)$_2$] **5**, possibly *via* concerted proton electron transfer process (CPET). Thus, the redox non-innocent character of the ligand upon complexation with ruthenium(II), has been disclosed and it is attributed to presence of low lying π* orbitals of almost entirely of phenanthraquinone and hydrazone character. In **5**, the π–acceptor ability of the ligand donor centres are reduced due to the existence of an odd electron in SOMO and hence the M-L distances around the coordination sphere are altered. The N–N (hydrazonyl bond length increases from 1.296 (6) Å in **3** to 1.429 Å in **5**, leading to lesser thermodynamic stability of the latter and upon standing, the N–N bond is cleaved to be transformed to $\mathbf{6}^+$, possibly *via* the formation of iminoquinone anion radical complex, [6] (reported elsewhere). Also, it is *via* the dissociation of N–N (hydrazonyl) bond, the biologically important molecule 2-aminobenzothiazole is formed along with $\mathbf{6}^+$, so as to provide a novel route for its synthesis.

1. Introduction

It has been well understood that concerted proton-electron transfer (CPET) has consequential roles in a diverse field of biological processes as well as in efficient energy conversions. [1–7] The most demanding and challenging illustration is the biological nitrogen fixation, which comprises of successive transfer and swapping of protons as well as electrons to coordinated nitrogen, [8–12] although the exact reaction pathway is still a matter of conjecture. In this regard, well-defined complexes having N–N bonds are good candidates to provide some illustrative clarification with respect to reduction sequences since they may be suitably engineered to comprehend the redox transformations accompanying the cleavage of N–N bonds. [13–24] Moreover, it has also been reported that metal–ligand synergy [25–27] is one of the significant aspects that regulate the activity of several redox metalloenzymes like cytochrome P450, galactose oxidase and hydrogenases etc. [28–30] In these cases, both ligands (of the prosthetic group) and metal centres contribute to the redox events as well as in bond cleavage or activation. In fact, these types of ligands are often referred to as redox non-innocent [31–44] and they have the distinctive aptitude to confer unprecedented reactivity to the metal complexes by regulating loss or gain of electrons and protons.

We have been working with redox non-innocent ligands [45–56] and their roles in metal mediated redox transformations for a considerable period of time [57–61] and as an extension of our work in this field, we were motivated towards exploration of cooperative effect of metal along with redox active ligand comprising of hydrazone and iminoquinone moieties, to foster the cleavage of N–N bonds. [62–64] In the present

* Corresponding authors.
E-mail addresses: icsgxav@gmail.com, icsg@sxccal.edu (S. Ganguly).

https://doi.org/10.1016/j.molstruc.2024.138720
Received 19 March 2024; Received in revised form 17 May 2024; Accepted 21 May 2024
Available online 22 May 2024

Organic & Biomolecular Chemistry

ROYAL SOCIETY OF CHEMISTRY

PAPER

View Article Online
View Journal | View Issue

Cite this: *Org. Biomol. Chem.*, 2024, **22**, 6393

Potent pincer-zinc catalyzed homogeneous α-alkylation and Friedländer quinoline synthesis reaction of secondary alcohols/ketones with primary alcohols†

Debashis Jana, [a] Sima Roy, [a] Srijita Naskar,[a] Supriyo Halder,[a] Gopal Kanrar[b] and Kausikisankar Pramanik *[a]

Received 12th June 2024,
Accepted 10th July 2024

DOI: 10.1039/d4ob00988f

rsc.li/obc

Herein, we describe an air- and moisture-stable, homogeneous zinc catalyst stabilised using an electron deficient N^N^N pincer-type ligand. This ternary, penta-coordinated neutral molecular catalyst [Zn(N^N^N)Cl_2] selectively produces α-alkylated ketone derivatives (14 examples) through a one-pot acceptorless dehydrogenative coupling (ADC) reaction between secondary and primary alcohols using the borrowing hydrogen (BH) approach in good to excellent isolated yields (up to 93%). It is worth noting that this catalyst also provides an eco-friendly route for the synthesis of quinoline derivatives (30 examples) using 2-aminobenzyl alcohols as alkylating agents *via* successive dehydrogenative coupling and N-annulation reactions. This cost effective, easy to synthesize and environmentally benign catalyst shows excellent stability in catalytic cycles under open-air conditions, as evident from its high turnover number (~10^4), and is activated by using a catalytic amount of base under milder conditions.

Introduction

The construction of molecules with diverse functional groups from commonly available small molecules/building blocks by C–C and C–heteroatom bond activation is one of the fundamental aspects of chemical and biochemical syntheses.[1] In reality, the majority of classical methods require expensive and environmentally toxic reagents and discharge hazardous waste even in (over)stoichiometric amounts.[2] Thus, the development of an efficient approach is desirable for selective C–C and C–heteroatom formation reactions. Accordingly, beneficial organic compounds with potential applications in the medical, agrochemical and pharmaceutical industries may be synthesized.[3] In this context, conversion of alcohols to C-alkylated derivatives and N-heterocycles *via* acceptorless dehydrogenation coupling (ADC) and borrowed hydrogen (BH)/N-annulation methodologies using homogeneous catalysts has received considerable attention in recent years.[4] Although such transformation reactions can be accomplished with 0.5–5 mol% platinum-group-metal catalysts (*e.g.*, Ru, Rh, Ir, Pd and Pt) in satisfactory yields.[5–9] In general, catalysis using non-precious first-row transition metals with good turnover numbers (TONs) under open-air conditions for α-alkylation and Friedländer annulation reactions remains challenging for gram-scale production of high-value bio-active molecules.[10] Nonetheless, continuous effort has been made with 3d metal catalysts (Mn, Fe, Co, Ni and Cu) with comparable catalyst loading (0.5–5 mol%), since they provide a more economically viable solution (Schemes 1 and 2).[11–15] A few examples have recently been reported where analogous reactions can be accomplished with 0.05% or less catalyst loading with Ni(II) and Mn(I), respectively.[16]

It is worth noting that the use of zinc(II) is less cited for homogeneous catalysis than other 3d metals plausibly due to its closed-shell, electron-rich, redox innocent nature. Only very recently molecular zinc-catalyzed dehydrogenation reactions of secondary alcohols have been documented.[17] Here, dehydrogenation of an alcohol occurs first to produce an aldehyde or ketone that undergoes an *in situ* condensation reaction with an enolate or amine to form an α,β-unsaturated ketone or imine, where the former is finally reduced to form a new C–C bond (Scheme 3) or the subsequent cyclization of aniline derivatives leads to quinolines because of the aromatization in the case of the C–N annulation reaction (Scheme 4).

In general, the catalytic performance of homogeneous catalysts is superior to that of heterogeneous catalysts.[18] Nonetheless, the disadvantage in the use of homogeneous cat-

[a]*Department of Chemistry, Jadavpur University, Kolkata 700032, India. E-mail: kpramanik@hotmail.com; Tel: +91 94333 66013*

[b]*Department of Chemistry, St. Xavier's College (Autonomous), Kolkata–700016, India*

† Electronic supplementary information (ESI) available. CCDC 2348683, 2348684, 2349095 and 2349099. For ESI and crystallographic data in CIF or other electronic format see DOI: https://doi.org/10.1039/d4ob00988f

Chemistry & Biodiversity

WILEY-VCH

CHEMISTRY & BIODIVERSITY

RESEARCH ARTICLE

Designed Synthesis of Amino-Azo-Quinoline and Their Nickel(II) Complexes: Molecular Structure, Electrochemistry and an Insight Into Their In Vitro Anti-Cancer Activities

Srijita Naskar[1] | Koushik Sarkar[2] | Supriyo Halder[1] | Bidisha Chatterjee[3] | Debjeet Chakraborty[3] | Arka Laha[3] | Rahul Sharma[2] | Arup Kumar Mitra[3] | Kausikisankar Pramanik[1] | Sanjib Ganguly[2]

[1]Department of Chemistry, Jadavpur University, Kolkata, India | [2]Department of Chemistry, St. Xavier's College (Autonomous), Kolkata, India | [3]Department of Microbiology, St. Xavier's College (Autonomous), Kolkata, India

Correspondence: Kausikisankar Pramanik (kpramanik@hotmail.com) | Sanjib Ganguly (icsgxav@gmail.com; icsg@sxccal.edu)

Received: 26 September 2024 | **Revised:** 20 January 2025 | **Accepted:** 21 January 2025

Funding: We would like to express our sincere gratitude to the CAS-II and RUSA 2.0 programs available in the Department of Chemistry, at Jadavpur University. Sanjib Ganguly is grateful to the Intramural Grant (Sanction No. IMSXC2022-23/001) and Koushik Sarkar for Intramural Grant (Sanction No. IMSXC2022-23/011) from St. Xavier's College (Autonomous), Kolkata. Srijita Naskar and Supriyo Halder thank SVMCM, Department of Higher Education, Govt. of West Bengal, and UGC (ref. No. 210/CSIR-UGC NET DEC.2017) New Delhi India, respectively, for the research fellowship. Arup Kumar Mitra is thankful to DBT, New Delhi, for the Grant (Sanction No. BT/INF/22/SP41296/2020, Dated: March 25, 2021).

Keywords: anti-cancer activity | coordination chemistry | DFT study | Molecular Docking study | X-ray crystallography

ABSTRACT

Amino-quinolines are potential candidates that may provide some insight into the current chemotherapeutic research due to their demonstrated anti-cancer activity. This led us to synthesize and explore a new amino-azo-quinoline ligand H_2L **1** and its square planar nickel(II) complexes [Ni(HL) (OAc)], **2** and [Ni(HL)Cl], **3** and the structures were determined by Single Crystal X-Ray Diffraction. Theoretical investigation of redox orbitals of the complexes discloses that the reduction process is due to ligand reduction whereas both metal and ligand are contributing towards oxidation. The anti-cancer properties of the ligand and one of the nickel(II) complexes have been assessed by 3-[4,5-dimethylthiazol-2-yl]-2,5-diphenyltetrazolium bromide assay, cell migration along with the generation of reactive oxygen species using human epithelial cancer cell line cells. The ligand **1** and complex **3** have been found to show effective anti-cancer activity and for the latter, it is more promising. This may be ascribed to the rigid and robust nature of square planar complex **3**, which supports stronger binding with DNA than that of free ligands, possibly due to the flexible nature of the latter. This result has also been validated by molecular docking using nine conformers of the ligand and complex **3** via interaction with B-DNA (PDB ID: 1BNA) where the binding affinity with the complex has been found to be stronger.

1 | Introduction

The fabrication of *cis*-platin as a chemotherapeutic for a wide range of cancer treatments including solid cancers such as bladder, cervical, head and neck, lung cancer, testicular, ovarian, gastric cancer etc. [1–4], has triggered the research on the anti-blastoma activity of several other platinum complexes [5, 6]. Over the years, combination chemotherapy with *cis*-DDP has

Srijita Naskar and Koushik Sarkar contributed equally to this study.

ChemCatChem

Research Article
doi.org/10.1002/cctc.202401851

Chemistry Europe
European Chemical Societies Publishing

www.chemcatchem.org

One-Pot Cascade [3 + 2 + 1] Annulation: Synthesis and Mechanistic Insight of *s*-Triazines and Pyrimidines Using Azo-Supported Metalloradical Nickel Catalyst

Debashis Jana,[a] Sampad Malik,[a] Gopal Kanrar,[b] Supriyo Halder,[a] Srijita Naskar,[a] and Kausikisankar Pramanik*[a]

Highly efficient Ni-catalyzed C—N/C—C bond formation from amidines during the [3 + 2 + 1] annulation by primary alcohols alone or by primary alcohols with secondary alcohols/phenyl acetylenes has been successfully accomplished toward scaled synthesis of *s*-triazine and pyrimidines, respectively. A strongly π-acidic *bis*-azo NNN-pincer scaffold was successfully introduced for dual functionalization such as augmenting the sustainability of the molecular catalyst by enhancing the metal–ligand integrity and interposing a potent electron-sink chromophore. The high yield synthesis (up to 94%) of *poly*-azaheterocycles with merely 0.001 mol% catalyst loading demonstrates the potency of azo-anion radical assisted catalysis. A diverse range of primary and secondary alcohols are successfully used as substrates. Furthermore, use of methanol/ethanol as C1/C2 synthon (alkylating agents) enables the formation of challenging imine intermediates from amidines through dehydrogenation under mild conditions. This facilitates the synthesis of wide varieties of *s*-triazines, and pyrimidines driven by the auto-tandem catalyst. Mechanistic investigations reveal that the formation of C—C and C—N bonds proceed through a metalloradical catalysis (MRC) pathway instead of borrowing hydrogen (BH) method and thereby addresses the challenge of controlling stereoselection. This process is initiated by Ni-catalyzed acceptorless dehydrogenation (AD) of the alcohol substrate, followed by a series of sequential steps, including condensation, aza-Michael addition, cyclization, and subsequent dehydrogenation. The well-defined one-electron reductive response at −0.34 V (versus Fc^+/Fc) is indicative of the involvement of azo anion radical during catalytic annulation. The formation of the ligand radical intermediate was further substantiated by an electron paramagnetic resonance (EPR) study conducted both in the presence and absence of radical scavengers, specifically 2,2,6,6-tetramethyl-1-piperidinyloxy (TEMPO), and butylated hydroxytoluene (BHT).

1. Introduction

Metal-organic catalysts have played an important role in achieving numerous synthetically valuable organic and biomolecules that are otherwise challenging to achieve in realism. Remarkably, palladium continues to rule the field in fine organic synthesis when compared to other metals because it validates reliability and uniformity in metal-mediated catalysis and exhibits a wide substrate tolerance.[1] However, the substantial expense associated with palladium has limited its commercial adequacy, thereby motivating the exploration of catalysts based on earth-abundant, low-cost metals. Being the sibling, cost-effective nickel is the most viable option. Furthermore, they show striking resemblance in a number of organic catalytic transformation.[2] Nevertheless, they differ in many instances as well due to their innate physicochemical aspects. The recent development of homogeneous catalysis using 3d metals in organic synthesis is highly promising as it has only lately begun to challenge the abiding supremacy of late and mostly noble metals in this field and they hold the potency of being able to encompass large-scale synthesis with substantially high turnover number (TON).[3]

The synthesis of bio-active *poly*-azaheterocycles such as pyrroles, pyridines, imidazoles, pyrimidines, and triazines procured from common alcohols is a rapidly expanding area of interest for green sustainable chemistry.[4] Among these *N*-heterocycles, the pyrimidine and *s*-triazine are found in a wide range of bio-relevant molecules and are crucial structural motifs found in many pharmacological, enzyme inhibitor, antifungal, anticancer, antitubercular activity, argochemicals.[5,6] In fact, a variety of synthetic procedures have been cited in the literature depending on the substrates, reagents and reaction conditions; where metal-mediated homogeneous catalysis emerging as a versatile and valuable synthetic protocol due to their gradual improvising catalytic efficiency, sustainability and atom-economy (Scheme 1).[7] Nevertheless, such methods in general suffer from the complications of physical separation of product(s), formation of hazardous by-products, use of stoichiometric or high amounts of base and low TON, i.e., high catalyst loading. The primary drawback of homogeneous catalysts is that they cannot be efficiently reinstated after the reaction cycle, which makes cost reduction challenging in industrial

[a] D. Jana, S. Malik, S. Halder, S. Naskar, K. Pramanik
Department of Chemistry, Jadavpur University, Kolkata 700032, India
E-mail: kausikis.pramanik@jadavpuruniversity.in

[b] G. Kanrar
Department of Chemistry, St. Xavier's College (Autonomous), Kolkata 700016, India

Supporting information for this article is available on the WWW under https://doi.org/10.1002/cctc.202401851

ACES Asian Chemical Editorial Society

doi.org/10.1002/ajoc.202500330

ASIAN JOURNAL OF ORGANIC CHEMISTRY
Research Article

www.asianjoc.org

Alcohol Dehydrogenation Catalyzed by Azo-Oxime Coordinated Ruthenium(II): A Strategic and Sustainable Route towards Site-Selective C(sp^3)–H Functionalization of 9H-Fluorene

Srijita Naskar,[a] Supriyo Halder,[a] Aritra Das,[b] Sampad Malik,[a] Gopal Kanrar,[b] Debashis Jana,[a] Bikash Kumar Panda,[c] Kausikisankar Pramanik,*[a] and Sanjib Ganguly*[b]

The bidentate redox non-innocent azo-oxime ligand *p*-chloro-aryl-azo-oxime (*p*-Cl-aaOH) has been used to synthesize a robust as well as air- and moisture-stable complex *trans*-[Ru(*p*-Cl-aaO)Cl(CO)(PPh_3)$_2$]. It has been thoroughly characterized by various analytical, spectroscopic and Single-Crystal X-Ray Diffraction (SCXRD) analysis. Its electrochemical property has also been investigated and supported by theoretical studies. The complex has functioned as an effective ligand-based catalyst for dehydrogenation of diverse aromatic and aliphatic primary alcohols followed by selective C(sp^3)–H activation of 9H-Fluorene under aerobic conditions through a tandem process. A probable catalytic cycle has been projected from relevant experiments, where the azo group of coordinated ligand plays a key role in both dehydrogenation and borrowing hydrogenation processes, while the ruthenium(II) centre behaves as a passive spectator throughout the reaction. The main advantages of this ruthenium catalyst include its simple synthetic methodology, low catalyst loading, wide substrate scope, shorter reaction times, and the ability to perform catalytic transformations at relatively lower temperatures.

1. Introduction

Fluorene and its derivatives are important group of compounds having a biphenyl skeleton along with a rigid plane, thereby facilitating π-cloud delocalization.[1] These remarkable structural features accounts for their varied properties and they can be further modulated via introducing suitable functional groups into the fluorene ring.[2] The sustainable synthetic strategies of fluorene derivatives is gaining importance in current research owing to their potential applications in electronic and photochromic materials, particularly OLED [3] and solar cells.[4] This is majorly attributed to the rich photophysical and photoelectric properties of fluorene.[5] These features have also been smartly exploited over the years to formulate and synthesize a wide range of polymers[6] and dyes.[7] This polyaromatic hydrocarbon (PAH) framework has been found to exhibit anticancer and antimicrobial properties.[8] It also finds utility for exploration of two-photon fluorescence bioimaging[9] (Scheme 1). As a crucial component of coal tar, this PAH framework enables the C—H functionalization of fluorene derivatives at the 9-position, offering a transformative strategy for advancing environmental sustainability and converting coal tar into valuable, high impact products.

Conventional approaches for 9-alkylation of fluorene involve condensation of aldehydes with fluorene, followed by hydrogenation or an S_N2 reaction of fluorenes with excess alkylating agents like haloalkanes in presence of strong and highly reactive bases, *for example* KOH or t-BuLi. The earliest report published in 1955 by Becker and co-workers defined the base-promoted alkylation of fluorene using several aliphatic alcohols conducted under rigorous conditions that involved the use of excess base and elevated temperatures ranging from 210 to 220 °C. In 1965, Atkin's group at Union Carbide Corporation revealed a method for base-catalysed alkylation of fluorene and indene with aliphatic alcohols.[10] The process, however, demanded excessive amount of base and harsh reaction conditions such as high temperature (250 °C) and pressure (500 psi). The major shortcoming of these strategies is formation of certain undesirable byproducts and poly-alkylated compounds.[11] These methods lack sufficient control, often leading to a higher degree of dialkylation rather than selective monoalkylation. A greener and more selective approach for synthesis is the dehydrogenation of alcohols using appropriate transition metal complexes as catalyst via dehydrogenation and borrowing hydrogenation (BH) or hydrogen auto transfer (HAT).[12] Owing to its operational

[a] S. Naskar, S. Halder, S. Malik, D. Jana, K. Pramanik
Department of Chemistry, Jadavpur University, Kolkata 700032, India
E-mail: kpramanik@hotmail.com
kausikis.pramanik@jadavpuruniversity.in

[b] A. Das, G. Kanrar, S. Ganguly
Department of Chemistry, St. Xavier's College (Autonomous), Kolkata 700016, India
E-mail: icsg@sxccal.edu

[c] B. K. Panda
Department of Chemistry, Jangipur College, Jangipur, Murshidabad, West Bengal 742213, India

Srijita Naskar and Supriyo Halder contributed equally to this work

Supporting information for this article is available on the WWW under https://doi.org/10.1002/ajoc.202500330